COLUMBIA

ACCIDENT INVESTIGATION BOARD



Note: Volumes II – VI contain a number of conclusions and recommendations, several of which were adopted by the Board in Volume I. The other conclusions and recommendations drawn in Volumes II – VI do not necessarily reflect the opinion of the Board, but are included for the record. When there is conflict, Volume I takes precedence.

REPORT VOLUME II
OCTOBER 2003



On the Front Cover

This was the crew patch for STS-107. The central element of the patch was the microgravity symbol, µg, flowing into the rays of the Astronaut symbol. The orbital inclination was portrayed by the 39-degree angle of the Earth's horizon to the Astronaut symbol. The sunrise was representative of the numerous science experiments that were the dawn of a new era for continued microgravity research on the International Space Station and beyond. The breadth of science conducted on this mission had widespread benefits to life on Earth and the continued exploration of space, illustrated by the Earth and stars. The constellation Columba (the dove) was chosen to symbolize peace on Earth and the Space Shuttle Columba. In addition, the seven stars represent the STS-107 crew members, as well as honoring the original Mercury 7 astronauts who paved the way to make research in space possible. The Israeli flag represented the first person from that country to fly on the Space Shuttle.



On the Back Cover

This emblem memorializes the three U.S. human space flight accidents – Apollo 1, Challenger, and Columbia. The words across the top translate to: "To The Stars, Despite Adversity – Always Explore"

The Board would like to acknowledge the hard work and effort of the following individuals in the production of Volumes II – VI.

Maj. Gen. John L. Barry	Executive Director to the Chairman
Dennis R. Jenkins	Investigator and Liaison to the Board
Lt. Col. Donald J. White	Technical Editor
Lt. Col. Patrick A. Goodman	Technical Editor
Joshua M. Limbaugh	Layout Artist
Joseph A. Reid	Graphic Designer
Christine F. Cole	Administrative Assistant
Jana T. Schultz	Administrative Assistant
Lester A. Reingold	Lead Editor
Christopher M. Kirchhoff	Editor
Ariel H. Simon	Assistant Editor
Jennifer L. Bukvics	Lead Project Manager
Donna J. Fudge	Senior Paralegal, Group II Coordinator
Susan M. Plott	Project Supervisor, Group III Coordinator
Ellen M. Tanner	Project Supervisor

Limited First Printing, October 2003, by the Columbia Accident Investigation Board

Subsequent Printing and Distribution by the National Aeronautics and Space Administration and the Government Printing Office Washington, D.C.

VOLUME I

PART ONE	THE ACCIDENT
Chapter 1	The Evolution of the Space Shuttle Program
Chapter 2	*Columbia*'s Final Flight
Chapter 3	Accident Analysis
Chapter 4	Other Factors Considered
PART TWO	WHY THE ACCIDENT OCCURRED
Chapter 5	From *Challenger* to *Columbia*
Chapter 6	Decision Making at NASA
Chapter 7	The Accident's Organizational Causes
Chapter 8	History as Cause: *Columbia* and *Challenger*
PART THREE	A LOOK AHEAD
Chapter 9	Implications for the Future of Human Space Flight
Chapter 10	Other Significant Observations
Chapter 11	Recommendations
PART FOUR	APPENDICES
Appendix A	The Investigation
Appendix B	Board Member Biographies
Appendix C	Board Staff

VOLUME II

CAIB TECHNICAL DOCUMENTS CITED IN THE REPORT

	Reader's Guide to Volume II	5
Appendix D.a	Supplement to the Report	9
Appendix D.b	Corrections to Volume I of the Report	19
Appendix D.1	STS-107 Training Investigation	21
Appendix D.2	Payload Operations Checklist 3	31
Appendix D.3	Fault Tree Closure Summary	75
Appendix D.4	Fault Tree Elements – Not Closed	121
Appendix D.5	Space Weather Conditions	133
Appendix D.6	Payload and Payload Integration	145
Appendix D.7	Working Scenario	159
Appendix D.8	Debris Transport Analysis	235
Appendix D.9	Data Review and Timeline Reconstruction Report	273
Appendix D.10	Debris Recovery	303
Appendix D.11	STS-107 Columbia Reconstruction Report	317
Appendix D.12	Impact Modeling	361
Appendix D.13	STS-107 In-Flight Options Assessment	391
Appendix D.14	Orbiter Major Modification (OMM) Review	413
Appendix D.15	Maintenance, Material, and Management Inputs	421
Appendix D.16	Public Safety Analysis	471
Appendix D.17	MER Manager's Tiger Team Checklist	509
Appendix D.18	Past Reports Review	515
Appendix D.19	Qualification and Interpretation of Sensor Data from STS-107	517
Appendix D.20	Bolt Catcher Debris Analysis	573

VOLUME III — OTHER TECHNICAL DOCUMENTS CITED IN THE REPORT

Reader's Guide to Volume III

Appendix E.1	CoFR Endorsements
Appendix E.2	STS-107 Image Analysis Team Final Report
Appendix E.3	An Assessment of Potential Material Candidates for the "Flight Day 2" Radar Object Observed during the NASA Mission STS-107
Appendix E.4	*Columbia* Early Sighting Assessment Team Final Report

VOLUME IV — OTHER TECHNICAL DOCUMENTS

Reader's Guide to Volume IV

Appendix F.1	Water Absorption by Foam
Appendix F.2	Follow the TPS
Appendix F.3	MADS Sensor Data
Appendix F.4	ET Cryoinsulation
Appendix F.5	Space Shuttle STS-107 Columbia Accident Investigation, External Tank Working Group Final Report – Volume 1

VOLUME V — OTHER SIGNIFICANT DOCUMENTS

Reader's Guide to Volume V

Appendix G.1	Requirements and Procedures for Certification of Flight Readiness
Appendix G.2	Appendix R, Space Shuttle Program Contingency Action Plan
Appendix G.3	CAIB Charter, with Revisions
Appendix G.4	Aero/Aerothermal/Thermal/Structures Team Final Report, Aug 6, 2003
Appendix G.5	Vehicle Data Mapping (VDM) Team Final Report, Jun 13, 2003
Appendix G.6	SRB Working Group Presentation to CAIB
Appendix G.7	Starfire Team Final Report, Jun 3, 2003
Appendix G.8	Using the Data and Observations from Flight STS-107... Exec Summary
Appendix G.9	Contracts, Incentives, and Safety/Technical Excellence
Appendix G.10	ASAP – SIAT – Rogers Detailed Summaries
Appendix G.11	Foam Application and Production Chart
Appendix G.12	Group 1 Investigation Brief
Appendix G.13	Crew Survivability Report

VOLUME VI — TRANSCRIPTS OF BOARD PUBLIC HEARINGS

Reader's Guide to Volume VI

Appendix H.1	March 6, 2003	Houston, Texas
Appendix H.2	March 17, 2003	Houston, Texas
Appendix H.3	March 18, 2003	Houston, Texas
Appendix H.4	March 25, 2003	Cape Canaveral, Florida
Appendix H.5	March 26, 2003	Cape Canaveral, Florida
Appendix H.6	April 7, 2003	Houston, Texas
Appendix H.7	April 8, 2003	Houston, Texas
Appendix H.8	April 23, 2003	Houston, Texas
Appendix H.9	May 6, 2003	Houston, Texas
Appendix H.10	June 12, 2003	Washington, DC

Reader's Guide to Volume II

Volume II of the Report contains appendices that were cited in Volume I. The Columbia Accident Investigation Board produced many of these appendices as working papers during the investigation into the February 1, 2003 destruction of the Space Shuttle *Columbia*. Other appendices were produced by other organizations (mainly NASA) in support of the Board investigation. In the case of documents that have been published by others, they are included here in the interest of establishing a complete record, but often at less than full page size. Full-size versions of these reports are contained on the DVD disc in the back of Volume VI, or hard copies of the documents may be requested through the organizations that originally produced them.

D.a Supplement to the Report

This supplement is presented to augment the Board Report and its condensed list of recommendations. It outlines concerns to prevent the next accident.

D.b Corrections to Volume I of the Report

Volume I of the Columbia Accident Investigation Board report contained minor errors that are detailed here. None of the errors affected the substance of the report.

D.1 STS-107 Training Investigation

The Board conducted a thorough review of all training activities that were performed in preparation for STS-107, including training conducted for the crew, launch controllers, and mission controllers. An analysis of STS-107 Orbiter and payload training requirements was conducted, as well as a complete review of all training records, schedules, instructor logbooks, and related documentation for the crew, flight controller, and launch controller training. Interviews and discussions were held with STS-107 training and operational personnel at both Johnson and Kennedy Space Centers to investigate the STS-107 training process, the effects of launch slips, the performance of the crew, flight controllers, and launch controllers, and the flight readiness of all for the STS-107 mission. Although several issues were identified as a result of this investigation, none were considered causal in the loss of *Columbia*.

The investigator who wrote this report proposed four recommendations, one of which was adopted by the Board for inclusion in the final report. The conclusions drawn in this report do not necessarily reflect the conclusions of the Board; when there is a conflict, the statements in Volume I of the Columbia Accident Investigation Board Report take precedence.

D.2 Payload Checklist

This appendix is a reproduction of the Payload Operations Checklist used by the STS-107 crew during on-orbit operations. It is reproduced here – at smaller than normal page size – to show the level of detailed instruction provided to the crew during on-orbit payload operations.

This is a NASA document and is published here as written, without editing by the Columbia Accident Investigation Board. The conclusions drawn in this report do not necessarily reflect the conclusions of the Board; when there is a conflict, the statements in Volume I of the Columbia Accident Investigation Board Report take precedence.

D.3 Fault Tree Closure Summary

The NASA Accident Investigation Team examined the accident using "fault trees," a common organizational tool in systems engineering. Fault trees are graphical representations of every conceivable sequence of events that could cause a system to fail. The fault tree's uppermost level illustrates the events that could have directly caused the loss of *Columbia* by aerodynamic breakup during re-entry. Subsequent levels comprise all individual elements or factors that could cause the failure described immediately above it. In this way, all potential chains of causation that could have

ultimately led to the loss of *Columbia* can be diagrammed, and the behavior of every subsystem that was not a precipitating cause can be eliminated from consideration.

NASA chartered six teams to develop fault trees, one for each of the Shuttle's major components: the Orbiter, Space Shuttle Main Engine, Reusable Solid Rocket Motor, Solid Rocket Booster, External Tank, and Payload. A seventh "systems integration" fault tree team analyzed failure scenarios involving two or more Shuttle components. These interdisciplinary teams included NASA and contractor personnel, as well as outside experts. Some of the fault trees are very large and intricate. For instance, the Orbiter fault tree, which only considers events on the Orbiter that could have led to the accident, includes 234 elements. In contrast, the Systems Integration fault tree, which deals with interactions among parts of the Shuttle, includes 295 unique multi-element integration faults, 128 Orbiter multi-element faults, and 221 connections to other Shuttle components.

This appendix provides a listing of fault tree elements that were investigated by the Board and closed during the *Columbia* investigation. Some of the elements in this appendix were open at the time the investigation concluded, but are expected to be closed before the Return to Flight. Items marked "Open due to lower element" remained open because a lower level fault tree had yet to be closed; for the most part, the lower-level fault trees are contained in Appendix D.4.

D.4 Fault Tree Elements – Not Closed

This appendix contains fault tree elements that were not closed or could not be completely closed by the end of the *Columbia* investigation. In some cases, a fault tree element may never be closed since neither analysis nor data is available to rule that element out as a potential cause. In some cases, the lower-level fault trees contained in this appendix will cause a higher-level fault tree in Appendix D.3 to remain open as well (annotated as "Open due to lower element" in Appendix D.3).

D.5 Space Weather Conditions

This appendix provides a detailed discussion of space weather (the action of highly energetic particles, primarily from the Sun, in the outer layer of the Earth's atmosphere) and the potential effects of space weather on the Orbiter on February 1, 2003. This investigation was originally prompted by public reports of unusually active space weather conditions during the mission and by a photograph that was claimed to show a lightning bolt striking *Columbia* at an altitude of 230,000 feet over California during re-entry. The report concludes that space weather was unlikely to have played a role in the loss of *Columbia*.

This is a document commissioned by the Columbia Accident Investigation Board and is published here as written, without editing. The conclusions drawn in this report do not necessarily reflect the conclusions of the Board; when there is a conflict, the statements in Volume I of the Columbia Accident Investigation Board Report take precedence.

D.6 Payload and Payload Integration

The Board conducted a thorough review of the STS-107 payload and the payload integration in preparation for the mission. This appendix contains the results of that investigation, which identified several anomalies, but none were determined to be causal in the loss of *Columbia*.

D.7 Working Scenario

The Working Scenario was the result of a joint effort between the Columbia Accident Investigation Board (CAIB) and the NASA Accident Investigation Team (NAIT). The report was written beginning early in the investigation to track the current understanding of the events that led to the loss of *Columbia*. As such, the report evolved over time as facts became known, theories were developed or disproved, and NASA and the Board gained knowledge of the accident sequence.

The report was written to document the collection of known facts, events, timelines, and historical information of particular interest to the final flight of *Columbia*. The Columbia Accident Investigation Board released the final version of the Working Scenario to the public on July 8, 2003. The version contained here has been reformatted to match the overall style of the first volume and has had a few minor editorial corrections, but none affect the substance of the report.

The Working Scenario includes information from numerous analyses, tests, and simulations related to the *Columbia* investigation that had been completed, or were ongoing at the time that this report was completed, i.e., up to and including July 8, 2003.

This effort compiles and documents the principal facts related to specific vehicle element events, timelines, and data. It also includes pertinent historical data surrounding some of the key vehicle element considerations in the investigation. The scenario addresses the chronology of vehicle events from prelaunch, launch countdown, launch/ascent, orbit, and re-entry, as well as specific information for the External Tank and the left wing, including aspects of the Reinforced Carbon-Carbon (RCC) and attachment hardware. Vehicle processing and significant preflight events and milestones are also discussed. The scenario addresses technical aspects only, and does not address management practices or philosophies, or other organizational considerations.

D.8 Debris Transport Analysis

This appendix contains the debris transport analysis used to determine information about the dimensions of the External Tank bipod foam ramp and the conditions in which the foam struck the Orbiter. This data provided inputs into the foam testing conducted at Southwest Research Institute for the foam impact testing.

This is a NASA document and is published here as written, without editing by the Columbia Accident Investiga-

tion Board. The conclusions drawn in this report do not necessarily reflect the opinion of the Board; when there is a conflict, the statements in Volume I of the Columbia Accident Investigation Board Report take precedence. While the report contains many recommendations to improve the data used in this type of analysis for future missions, the Board did not adopt every recommendation into the Columbia Accident Investigation Board Report.

D.9 Data Review and Timeline Reconstruction Report

This appendix contains the basic timeline data that was used to reconstruct the final minutes of *Columbia*'s re-entry on February 1, 2003. The version in this appendix contains all of the timeline events, but in condensed form.

The timeline organized the re-entry data. As such, this appendix contains no conclusions or recommendations. A visual presentation of the timeline has also been included on the DVD that contains this appendix. It shows the timeline laid over a map of the United States along the ground track that *Columbia* flew during the re-entry.

D.10 Debris Recovery

The *Columbia* accident initiated the largest debris search in history. The evidence collected during the effort was instrumental in confirming the working hypothesis that had been developed by the Columbia Accident Investigation Board and the NASA Accident Investigation Team. The Board is very indebted to the thousands of individuals, companies, and organizations that responded to the call to service. We sincerely apologize to anybody inadvertently omitted from this appendix.

D.11 STS-107 Columbia Resconstruction Report

This appendix contains the STS-107 Columbia Reconstruction Report – reproduced at smaller than normal size – written by NASA during the investigation. While the Board investigation eventually focused on the left wing and the forensics evidence from that area, this report looked at Orbiter damage over the entire vehicle.

The Board's conclusions about debris evidence in Chapter 3 of Volume I were based on this report and independent analysis and investigation by Board investigators.

This is a NASA document and is published here as written, without editing by the Columbia Accident Investigation Board. The conclusions drawn in this report do not necessarily reflect the opinion of the Board; when there is a conflict, the statements in Volume I of the Columbia Accident Investigation Board Report take precedence. While the report contains many recommendations to improve the data used in this type of analysis for future missions, the Board did not adopt every recommendation into the Columbia Accident Investigation Board Report.

D.12 Impact Modeling

This appendix contains the independent analysis of the foam impact with the left wing conducted by Southwest Research Institute in support of the Columbia Accident Investigation Board. In addition to the analysis performed by NASA during the investigation, the Board called for a second independent analysis of the foam impact data. This report examines the foam impact data as it might have affected both thermal tiles and the RCC. The results of this analysis were used to predict damage to the RCC and tile and to set conditions for the foam impact testing program.

The conclusions drawn in this report do not necessarily reflect the conclusions of the Board; when there is a conflict, the statements in Volume I of the Columbia Accident Investigation Board Report take precedence.

D.13 STS-107 In-Flight Options Assessment

During the course of the investigation, the Board heard several NASA officials say there was nothing that could have been done to save *Columbia*'s crew, even if they had known about the damage. The Board therefore directed NASA to determine whether that opinion was valid. NASA was to design hypothetical on-orbit repair and rescue scenarios based on the premise that the wing damage events during launch were recognized early during the mission. The scenarios were to assume that a decision to repair or rescue the *Columbia* crew would be made quickly, with no regard to risk. These ground rules were not necessarily "real world," but allowed the analysis to proceed without regard to political or managerial considerations. This report is the full result of that analysis; a summary was presented in Volume I of the report.

This is a NASA document and is published here as written, without editing by the Columbia Accident Investigation Board. The conclusions drawn in this report do not necessarily reflect the conclusions of the Board; when there is a conflict, the statements in Volume I of the Columbia Accident Investigation Board Report take precedence.

D.14 Orbiter Major Modification Review

Investigation Group I of the Columbia Accident Investigation Board conducted a review of the policies and procedures used by NASA during Orbiter Major Modifications (OMM) and Orbiter Maintenance Down Periods (OMPD). As part of this effort, the U.S. Air Force was invited to conduct an independent review. The results of these efforts are documented in this appendix.

The investigators who conducted this review proposed a number of recommendations, several of which were adopted by the Board for inclusion in the final report. The conclusions drawn in this review do not necessarily reflect the conclusions of the Board; when there is a conflict, the statements in Volume I of the Columbia Accident Investigation Board Report take precedence.

D.15 Maintenance and Sustainment Review

Investigation Group I of the Columbia Accident Investigation Board examined maintenance procedures and sustainment policies relevant to the Space Shuttle Program. Since the remaining Orbiters have all been in service for nearly 20 years, the review included "aging aircraft" issues similar to those faced by military and commercial aviation.

This report contains a large spreadsheet containing production data on every External Tank built to date. This table is not reproduced in the report because of its size, but it is included as a PDF file on the DVD included in Volume VI.

The investigators who conducted this review proposed a number of recommendations, several of which were adopted by the Board for inclusion in the final report. The conclusions drawn in this review do not necessarily reflect the conclusions of the Board; when there is a conflict, the statements in Volume I of the Columbia Accident Investigation Board Report take precedence.

D.16 Public Safety Analysis

After *Columbia* disintegrated in flight, many expressed surprise and relief that no one on the ground was injured by falling debris. During the Board's investigation, it became clear that no one had ever assessed the potential for loss of life on the ground if a re-entry mishap ever occurred. The results of this analysis indicated that the *Columbia* accident was not likely to have produced casualties on the ground.

The conclusions drawn in this report do not necessarily reflect the conclusions of the Board; when there is a conflict, the statements in Volume I of the Columbia Accident Investigation Board Report take precedence.

D.17 MER Manager's Tiger Team Checklists

This appendix contains the Mission Evaluation Room Manager's Tiger Team Checklist referenced in Volume I, Chapter 6. The checklist is reproduced at smaller than normal page size.

D.18 Past Reports Review

This appendix is a listing of relevant findings and recommendations concerning the Space Shuttle program issued by various independent review boards over a two-decade period. The list also includes the NASA responses to the findings or recommendations whenever such responses could be found. Although it was the intent of the Board to present this list in Volume II, its size precluded doing this and the list is actually contained in Volume V.

D.19 Qualification and Interpretation of Sensor Data from STS-107

This appendix provides a thorough review of the Modular Auxiliary Data System (MADS) recorder and sensor operation and an analysis of the data that was gathered from the MADS system and used during the investigation.

This appendix also contains several draft recommendations that were reviewed by the Board. Several of these were adopted and are included in their final form in Volume I. The conclusions drawn in this report do not necessarily reflect the conclusions of the Board; when there is a conflict, the statements in Volume I of the Columbia Accident Investigation Board Report take precedence.

D.20 Bolt Catcher Debris Analysis

This appendix contains – reproduced at smaller than normal size – the study of radar returns from past Space Shuttle launches to determine whether the Solid Rocket Booster bolt catchers may have failed during the flight of STS-107. The report concluded that there was the possibility that one of the debris items seen on radar during that flight could have been part of a bolt catcher.

This appendix has no recommendations, but the Board did make recommendations related to the bolt catcher issue in Volume I. The conclusions drawn in this report do not necessarily reflect the conclusions of the Board; when there is a conflict, the statements in Volume I of the Columbia Accident Investigation Board Report take precedence.

Supplement to the Report

by Brigadier General Duane W. Deal, Board Member

With appreciation to Dr. James N. Hallock, Dr. John M. Logsdon, Dr. Douglas D. Osheroff, and Dr. Sally K. Ride for their valuable inputs and editing.

Err on the side of providing too much rather than too little information in the aftermath of a mistake or failure.

–Strock, Reagan on Leadership[1]

Foreword: Preventing "The Next Accident"

The Columbia Accident Investigation Board report is a powerful document. It goes far beyond any previous accident report in the scope and manner with which it tackles a multitude of complex and daunting subjects previously unaddressed. In extensive detail and often in blunt language, it conveys the intricacies of the physical cause of the *Columbia* accident, and places equal weight on the organizational cause. The Board and its staff of professional investigators who produced this landmark report represent the best our nation has to offer – dedicated men and women brought together from many walks of life by an international tragedy, united with a common purpose, and driven to produce a product of substance and worth to the human space flight program. Additionally, its lessons go far beyond the Space Shuttle Program; indeed, the lessons learned are applicable to any large organization, particularly to those operating complex, risky, or aging systems.

This supplement is not written to refute any portion of that report. The Board report contains data, analysis, and conclusions which combine to write a prescription for NASA to recover not only in returning the Space Shuttle safely to the vacuum of space, but also to address NASA's sporadic organizational morass. If NASA will accept this prescription and take the "medicine" prescribed, we may be optimistic regarding the program's future; if, however, NASA settles back into its previous mindset of saying, "Thanks for your contribution to human space flight," summarily ignoring what it chooses to ignore, the outlook is bleak for the future of the program.

The Board report already contains many findings and recommendations. We have confidence that the recommendations carrying a "Return to Flight" annotation will be addressed and fixed prior to the Shuttle launching again. My confidence diminishes somewhat with recommendations that stand alone, not annotated as return-to-flight. In light of the reaction to past studies – even those following the *Challenger* accident – my confidence disappears when we offer NASA items only as "observations" – when Board members and investigators considered them significant – and trust NASA to address each one of them. History shows that NASA often ignores strong recommendations; without a culture change, it is overly optimistic to believe NASA will tackle something relegated to an "observation" when it has a record of ignoring recommendations.

When the original members of the Board first spoke via teleconconference on February 1, hours after the accident, and when we first assembled at Barksdale Air Force Base the evening of February 2, we were presented with the original Board charter. While that charter and the Board itself have expanded since then, the basic charge to the original Board was to (1) determine the cause of the loss of the *Columbia* and her crew, and (2) prevent recurrences – what we termed "the next accident" waiting to happen.

The Board report goes into great depth examining the physical cause of the accident – "the foam did it." Poorly designed, inconsistently manufactured, and inadequately tested, the foam is no longer an accident waiting to happen. The report then goes into a fascinating look at NASA's organizational culture and the pattern of breakdowns that have cost the lives of 14 astronauts.

With the preceding in mind, this supplement is presented to augment the Board report and its condensed list of recommendations. It is written from the perspective of someone who has presided or participated in the investigation of a dozen space and aircraft accidents, who fears the report has bypassed some items that could prevent "the next accident" from occurring – the "next" O-ring or the "next" bipod ramp.

As much or more than that rationale, this comes from the perspective of one who in the course of the investigation has interviewed those in high/medium/low management levels, and also those with hands on equipment "getting their hands dirty." If *they* express concerns, and those concerns are consistent throughout the workforce, those concerns regarding what could cause the next accident if not fixed *must* be heeded.

> *A primary task in taking a company from good to great is to create a culture wherein people have a tremendous opportunity to be heard and, ultimately, for the truth to be heard.*
>
> –Collins, Good to Great[2]

> *In this view [of adaptive leadership], getting people to clarify what matters most, in what balance, with what trade-offs, becomes a central task.*
>
> –Heifetz, Leadership Without Easy Answers[3]

Because of our conviction in the course of the investigation that we should do our very best to prevent the next accident, we must not miss an opportunity to fix something we know about that could cause that next accident and possibly deaths; indeed, we would be negligent to not do so.

Addressing Items Already In The Report … Why?

Why suggest modifications to items already present in the Board report? History reveals NASA has repeatedly demonstrated a lack of regard for outside studies and their findings. Chapter 5 of the Board report contains a 2-page chart conveying that during the course of the Board investigation, more than 50 separate post-Challenger reports were examined for various topics; Appendix D.18 recounts what was found, what was recommended, and NASA's response to findings and recommendations – if any. Board members had these findings and responses available as a benchmark for their lines of investigation to compare to NASA's current programs. Additionally, Dennis R. Jenkins, a Board Investigator and noted space and aviation author, compiled an exhaustive 300-page study of every Aerospace Safety Advisory Panel report; that study is also in Appendix D.18.

Despite this extensive look at the past, many items in the report were characterized as less than recommendations. The introduction to Chapter 10 of the Board report, "Other Significant Observations," says:

> *The significant issues listed in this chapter are potentially serious matters that should be addressed by NASA because they fall into the category of "weak signals" that could be indications of future problems.*

In my view, given the reality of NASA's past record with such issues, a sterner and more effective wording would have been:

> *The significant issues listed in this chapter are serious matters that must be addressed by NASA because they fall into the category of "strong signals" that are indications of present and future problems.*

While much of the following is contained in the Board report, it is repeated here together with related views that were not included in the body of the report.

These portions of the report are included to reflect the concern that the Board report addresses micrometeorites that we cannot predict or prevent with a Board recommendation, but allows things we can see and can prevent – and can predict an outcome – to remain as "NASA-ignorable observations." Items such as corrosion, the Solid Rocket Booster-External Tank attach rings, the Solid Rocket Booster hold-down cable, and the Kennedy Space Center quality assurance program deserve focused attention, as do ATK Thiokol security, the Michoud Assembly Facility quality program, Michoud security, crew cabin insulation, and other findings/recommendations. In my view, we have not done our best to "prevent the next accident" regarding things we've seen with our own eyes, and that individuals ranging from technicians to engineers have conveyed to us directly and via interviews and documentation.

Quality Assurance

Part of preventing the next accident lies in a strong quality assurance program; while you can't inspect quality into a product, the Shuttle Independent Assessment Team, an internal Kennedy Space Center report, and other past reports spotlight what a weak program can potentially cost. Also, as human error has been implicated in 60 to 80 percent of accidents in aviation and other complex systems, a solid quality assurance program may be the last measure of checks and balances in a complex system such as the Space Shuttle.[4]

Unresponsive Management

> *You need an established system for ongoing checks designed to spot expected as well as unexpected safety problems … Non-HROs [Non-High Reliability Organizations] reject early warning signs of quality degradation.*
>
> –Roberts, "High Reliability Organizations"[5]

Interviews and documentation provided by technicians, inspectors, and engineers revealed that when Quality Assurance Specialist inputs are made to improve processes or equipment, regarding issues from safety to discrepancies of out-of-specification items, Kennedy's quality management support is inconsistent.

Quality Assurance Specialists have found they must occasionally go around their management and elevate concerns using the NASA Safety Reporting System. In turn, the NASA Safety Reporting System has been responsive and validated concerns that local management would not. The KSC quality program management is perceived as unresponsive to inspector concerns and inputs toward improvement.

Staffing Levels

Maintaining adequate staffing levels remains a concern expressed by today's workforce and previous reports, including a February 17, 1999, letter to multiple levels of NASA management from John Young, dean of the astronaut corps. NASA Mission Assurance leadership reported that while the number of Quality Assurance Specialists may be adequate, with additional staff, workers would not have to wait for an inspector to close out a job, and would be available for additional quality-related pursuits. One of the more common reasons that quality engineers cited for declining to add government inspections at Kennedy Space Center was indeed inadequate personnel – a poor excuse for not adding inspections deemed necessary. Likewise, Marshall's Mission Assurance staff and the Michoud Defense Contract Management Agency (DCMA) staff also appear short of people for their workload. Columbia Accident Investigation Board recommendations to evaluate Quality Program Requirements Documents should drive decisions on additional staffing; in the interim, staffing to current authorizations with qualified people should be expedited.

Grade Levels

Grade levels also enter the equation, in two respects. First, the KSC Mission Assurance chiefs are at a lower grade than the Chief Engineer or Launch Director. This organizational structure may cause pressure in resolving conflicting priorities between respective organizations. KSC should review the position descriptions and make adjustments to establish parity in leadership and influence. Second, a review of other NASA center quality assurance specialist staffing and grades revealed that Kennedy is the only NASA center evaluated that has Quality Assurance Specialist grades set at GS-11 – other centers have Quality Assurance Specialist grades set at GS-12. An evaluation of this disparity should determine whether those grades are appropriate.

Inspector Qualifications

Examples surfaced where individuals with no previous aviation, space, technical, or inspection background had been selected as Quality Assurance Specialists and were making NASA final inspections. While most inspectors had extensive aviation and/or related military experience, such hiring practices indicate a need to consistently specify and stringently observe job qualifications for new hires that spell out proper criteria.

Employee Training

Workers expressed concerns over the type and amount of training they received. A common theme expressed by 67 percent of those interviewed regards the lack of formal training, particularly for quality engineers, process analysts, and quality assurance specialists of both NASA and DCMA. Instead of formal training, most is simply on-the-job training. Where available, some training is provided in classrooms conducted by and for contractor employees, and numerous examples were provided where a contractor technician had to provide training to the inspector who would be evaluating the technician's work. Quality Program management must work with the rest of NASA (and perhaps with the Department of Defense) to develop training programs for its quality program personnel. These views were expressed predominantly at KSC and the Michoud Assembly Facility. (Note: Board report observation O10.4-3 addresses Kennedy training, but not Michoud or NASA-wide interest.)

Providing Necessary Tools

Irritants preventing inspectors from performing undistracted were discovered at Kennedy: Quality inspectors experienced difficulty and delays in attaining the tools they needed to do their work per specifications. Some purchased their own equipment, leading to concerns about configuration management of the equipment used in final inspections.

Government Inspections

The existing list of NASA Mission Assurance oversight inspections was based on a point-in-time engineering risk assessment with limited application of quality analysis and sampling techniques to determine the scope and frequency of inspections. Tasks were retained for government oversight on the basis of criticality, not process or quality assurance. By comparison, Marshall Mission Assurance retained government oversight options during its government inspections reduction by moving all the former Government Mandatory Inspection Points (GMIPs) into a new category, Surveillance Opportunities. These Surveillance Opportunities are no longer considered mandatory inspection points, but remain an optional area for Mission Assurance inspection. The MSFC Mission Assurance system includes feedback and closed loop systems to use in trend analysis and in development of future Mission Assurance tasks designed to improve quality. Mission Assurance-observed events that result in a Verbal Corrective Action Report are included in this tracking system, and are used to tailor surveillance or government inspections. ATK Thiokol goes further and calls the Mission Assurance office with a 15-minute warning when a Surveillance Opportunity is occurring, but by agreement, will not wait for the inspector in order to maintain job flow.

Quality Program Surveillance

> *Discovering these vulnerabilities and making them visible to the organization is crucial if we are to anticipate future failures and institute change to head them off.*
>
> –Woods and Cook,
> "Nine Steps to Move Forward from Error"[6]

In contrast to other NASA and contractor locations – where inspectors conduct unscheduled evaluations and observations – Quality Assurance Specialist surveillance is essentially nonexistent at Kennedy, despite reports that document organizational inconsistency within the NASA quality assurance construct. For example, the 2000 Space Shuttle Independent Assessment Team report echoed the Rogers Commission report with a lengthy discussion of the need for organizational independence and a strong presence. [7] "The Shuttle Independent Assessment Team

believes strongly that an independent, visible Safety and Mission Assurance function is vital to the safe operation and maintenance of the Shuttle. The Shuttle program and its "one strike and you're out" environment is unlike most other defense or commercial industries. As a consequence, it is believed the industry trend toward reducing Safety and Mission Assurance oversight and functions is inappropriate for the Shuttle."[8] Among the Assessment Team's recommendations was a strong suggestion to restore surveillance.[9] This is consistent with the testimony of numerous Mission Assurance inspectors, technicians, and engineers to the Columbia Accident Investigation Board. Further, this surveillance should include concurrent inspections (for oversight of the contractor Mission Assurance function), and sequential or no-notice evaluations to improve "oversight by spontaneity."

> *Over the years, these organizations [HROs] have learned that there are particular kinds of error, often quite minor, that can escalate rapidly into major, system-threatening failures.*
>
> –Reason, Managing the Risks of Organizational Accidents[10]

> *In discussing such reliable organizations, it's emphasized that, "The people in these organizations … are driven to use a proactive, preventive decision making strategy. Analysis and search come before as well as after errors … [and] encourage:*
> - *initiative to identify flaws in SOPs and nominate and validate changes in those that prove to be inadequate;*
> - *error avoidance without stifling initiative or (creating) operator rigidity ….*
>
> –LaPorte and Consolini, in Reason's Managing the Risks of Organizational Accidents[11]

The Mission Assurance function of United Space Alliance (and other NASA contractors) samples a large amount of its workload and processes. The relatively minimal Kennedy Mission Assurance samples of United Space Alliance work is informal, and results are currently documented only in the Safety & Mission Assurance Reporting Tool database, which is used as a quality problem-tracking tool to help Mission Assurance identify trends and focus its approach to oversight and insight. Problems revealed by the sampling inspections or from the informal Reporting Tool database can be communicated to United Space Alliance through its Quality Control Assessment Tool (QCAT) system, but there is no contractual requirement for United Space Alliance to respond or even take corrective action. The Space Shuttle Processing Independent Assessment Report of 2001 noted succinctly: "Process surveillance as it exists today is not accomplishing its desired goals nor is it a true measure of the health of the work processes, as was its original stated objective."[12] Even in 2003, the Board found this is still true. To achieve greater effectiveness, sample-based inspections should include all aspects of production, and emphasis should go beyond "command performance" (announced and scheduled) inspections to validate United Space Alliance quality inspection results.

Kennedy Quality Assurance Specialist Position Descriptions – what the specialists are hired to do and tasks against which they are evaluated – actually require independent surveillance of contractor activity. However, Kennedy Quality Assurance Specialist surveillance is essentially nonexistent, as the Kennedy quality program manager actively discourages Quality Assurance Specialist unscheduled hardware surveillance. Testimony revealed that the manager actually threatened those who had conducted such activity, even after a Quality Assurance Specialist had found equipment marked "ground test only" installed on an Orbiter.

In an attempt to meet position description requirements and the basics of a solid surveillance program, a thorough surveillance program concept was developed by Kennedy Quality Assurance Specialists, presented, and accepted as "needed" by Space Shuttle Program management. However, rather than adapting it for Kennedy, this concept was never implemented, and Space Shuttle Program management was never informed of that decision. Ignoring surveillance – a Position Description requirement and a basic tenet of quality operations – is setting the stage for reliance upon "diving catches" referred to by the Space Shuttle Independent Assessment Team report.

> *Some HROs design in redundancy to ensure that there are several ways to catch problems before they become catastrophes. U.S. Navy aircraft carrier operations are characterized by much human redundancy in oversight of operations to make sure nothing is missed that can potentially turn into an accident.*
>
> –Roberts and Brea, Must Accidents Happen? Lessons from High Reliability Organizations[13]

Findings:

- Kennedy Space Center's current government mandatory inspection process is both inadequate and difficult to expand even incrementally, inhibiting the ability of quality assurance to respond to an aging system, changing workforce dynamics, and process improvement initiatives.
- The Quality Planning Requirements Document, which defines inspection conditions, was originally well formulated; however, there is no requirement that it be routinely reviewed and updated as applicable.
- KSC has a separate Mission Assurance office working directly for each program, a separate Safety, Health, and Independent Assessment office under the center director, and separate quality engineers under each program. Integration of the quality program would be much better served if these were consolidated under one Mission Assurance office reporting to the center director.
- Past reports (such as the 1986 Rogers Commission, 2000 Shuttle Independent Assessment Team report, and 2003 internal Kennedy Tiger Team) affirmed the need for a strong and independent quality program, though the quality program management at Kennedy took an opposite tack.
- NASA's Kennedy Space Center Quality Assurance Program discrepancy-tracking program is inadequate

to nonexistent. Robust as recently as three years ago, KSC no longer has a "closed loop" system, where discrepancies and their remedies make a full circle back to the person who detected the discrepancy, and in turn to others across the system who may help prevent or detect similar discrepancies.

- Efforts by Kennedy Space Center quality management to move its workforce toward a "hands-off, eyes-off" approach to quality assurance are cause for alarm.
- Evidence underscored the need to expand government inspections, the need for increased surveillance, and a lack of communication between NASA centers and contractors regarding the disposition of "ground test only" components.
- Witness testimony and documentation submitted by witnesses revealed items that had been annotated "Fly as is," without proper disposition by the Material Review Board prior to flight, leading to a concern about a growing acceptability of risk at the Center level.
- KSC quality management discourages inspectors from rejecting contractor work; instead, it insists on working with the contractor to fix things in the process of the work being accomplished, versus rejecting it and returning for a re-evaluation only after it is fixed.
- The NASA Safety Reporting System was viewed as credible, and was effectively used to validate concerns that local management would not.
- Though most inspectors had extensive aviation and/or related military experience, there are examples where some individuals with no previous aviation, space, technical, or inspection background had been selected as Quality Assurance Specialists, and were making NASA final inspections for human space flight components.
- Following the 2000 Shuttle Independent Assessment Team report, some 35 new inspectors were added at Kennedy Space Center; however, most of that increase has eroded through retirements, promotions, departures, and one death.
- A review of other NASA center Quality Assurance Specialist staffing and grades revealed that Kennedy Space Center is the only NASA center evaluated that has Quality Assurance Specialist grades set at GS-11 – other centers have Quality Assurance Specialist grades set at GS-12.
- No formal NASA Kennedy Space Center training exists in the quality program for its quality engineers, process analysts, and quality assurance specialists.
- NASA-KSC Quality Assurance Specialist Position Descriptions require independent surveillance of contractor activity. However, Quality Assurance Specialist surveillance is discouraged and essentially nonexistent at Kennedy Space Center.
- Through extensive interviews at the Michoud Assembly Facility (MAF) – technicians to managers – plus an extensive review of work documents, we conclude that the MAF Quality Program Requirements Document (alternatively, the Mandatory Inspection Points document) is in need of review, for few believe it covers all of the critical items that government inspectors should be reviewing, and that it may force redundant or non-value added inspections.

Recommendations:

- (Note: This item is currently Observation O10.4-1 in the Board report. Due to the potential gravity of this item, it is urged this become a return-to-flight Recommendation.) Perform an independently led, bottom-up review of the Kennedy Space Center Quality Planning Requirements Document to address the entire quality assurance program and its administration. This review should include development of a responsive system to add or delete government mandatory inspections. Suggested Government Mandatory Inspection Point (GMIP) additions should be treated by higher review levels as justifying why they should not be added, versus making the lower levels justify why they should be added. Any GMIPs suggested for removal need concurrence of those in the chain of approval, including responsible engineers.
- (Note: Like the preceding item, this item is currently a subset of Observation O10.4-1 in the Board report; while it is urged this become a Recommendation, it does not need to be characterized as a return-to-flight recommendation.) Kennedy Space Center must develop and institutionalize a responsive bottom-up system to add to or subtract from Government Inspections in the future, starting with an annual Quality Planning Requirements Document review to ensure the program reflects the evolving nature of the Shuttle system and mission flow changes. At a minimum, this process should document and consider equally inputs from engineering, technicians, inspectors, analysts, contractors, and Problem Reporting and Corrective Action to adapt the following year's program.
- NASA Safety and Mission Assurance should establish a process inspection program to provide a valid evaluation of contractor daily operations, while in process, using statistically-driven sampling. Inspections should include all aspects of production, including training records, worker certification, etc., as well as Foreign Object Damage prevention. NASA should also add all process inspection findings to its tracking programs.
- The Kennedy quality program must emphasize forecasting and filling personnel vacancies with qualified candidates to help reduce overtime and allow inspectors to accomplish their position description requirements (i.e., more than the inspectors performing government inspections only, to include expanding into completing surveillance inspections).
- Job qualifications for new quality program hires must spell out criteria for applicants, and must be closely screened to ensure the selected applicants have backgrounds that ensure that NASA can conduct the most professional and thorough inspections possible.
- Marshall Space Flight Center should perform an independently-led bottom-up review of the Michoud Quality Planning Requirements Document to address the quality program and its administration. This review should include development of a responsive system to add or delete government mandatory inspections. Suggested Government Mandatory Inspection Point (GMIP) additions should be treated by higher review levels as justifying why they should not be added, ver-

sus making the lower levels justify why they should be added. Any GMIPs suggested for removal should need concurrence of those in the chain of approval, including responsible engineers.

- Michoud should develop and institutionalize a responsive bottom-up system to add to or subtract from Government Inspections in the future, starting with an annual Quality Planning Requirements Document review to ensure the program reflects the evolving nature of the Shuttle system and mission flow changes. Defense Contract Management Agency manpower at Michoud should be refined as an outcome of the QPRD review.
- (Note: This item is currently Observation O10.4-4 in the Board report; however to avoid further diluting the quality program focus, it is urged this become a Recommendation.) Kennedy Space Center should examine which areas of ISO 9000/9001 truly apply to a 20-year-old research and development system like the Space Shuttle.

Observations:

- As an outcome of the Quality Program Requirements Document review, manpower refinements may be warranted (for example, should a substantial change in Government Inspections justify additional personnel, adjust the manpower accordingly). While Board recommendations to evaluate quality requirement documents should drive decisions on additional staffing, in the interim, staffing with qualified people to current civil service position allocations should be expedited.
- (Note: This item is currently Observation O10.4-3 in the Board report.) NASA-wide quality assurance management must work with the rest of NASA (and perhaps with the Department of Defense) to develop training programs for its quality program personnel.
- An evaluation of the disparity of Quality Assurance Specialist civilian grades at Kennedy Space Center compared to other NASA centers should be accomplished to determine whether the current grade levels are appropriate.

Orbiter Corrosion

> *Dr. Gebman's draft [a RAND Corporation study's draft released to the New York Times] also says NASA has deferred inspections for corrosion, even though standing water had occasionally been found inside the* Atlantis *(which is still available to fly) and the* Columbia *after rainstorms. The* Columbia *and the* Discovery *have each had corrosion behind the crew cabin, a spot that is hard to inspect and hard to repair.*
>
> *At one time, NASA had a "corrosion control board," but the study said it apparently no longer exists.*
>
> –Wald, "Report Criticizes NASA and Predicts Further Fatal Accidents"[14]

Section 10.7 of the Board report does a great job of spelling out the dangers of and current NASA efforts to combat the effects of corrosion. The chapter also offers four observations to encourage NASA to continue to further its efforts. However, rather than remain an observation, O10.7-3 should be slightly reworded and become a recommendation:

Recommendation:

- Develop non-destructive evaluation inspections to detect and, as necessary, correct hidden corrosion.

Hold-down Post Cable Anomaly

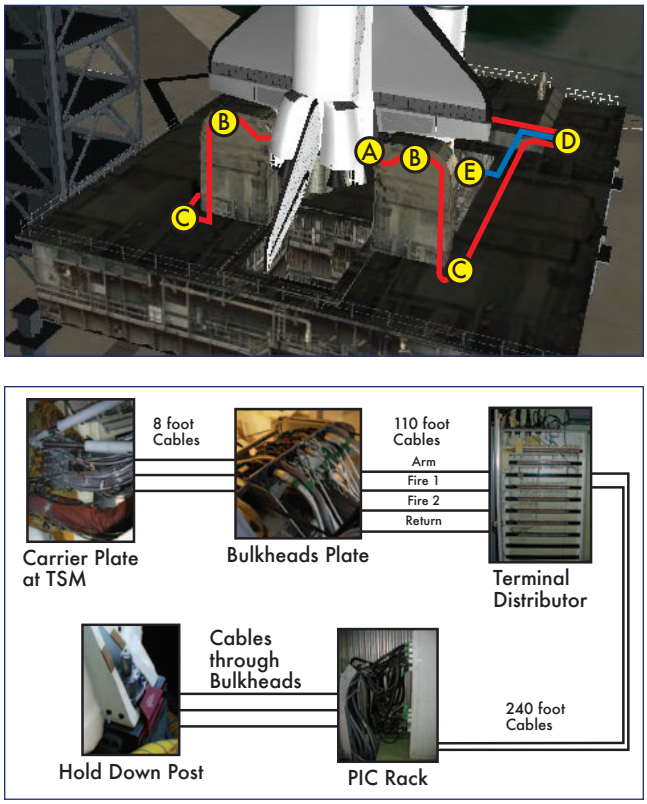


Figure S-1: Hold-Down Post/External Tank Vent Arm Systems diagram with nomenclature below (Note: This figure was not included in the final report Section 10.9; it is provided here for clarity.)

The signal to fire the HDP/ETVAS begins in the General Purpose Computers and goes to both of the Master Events Controllers (MECs). (See Figure S-1 for system routing.) MEC 1 communicates this signal to the A system cable, and MEC 2 feeds the B system. The cabling then goes through the Mobile Launch Platform mast to the Pyrotechnics Initiator Controllers (PICs; there are 16 PICs for A and B Hold-Down Posts, and 4 for A and B External Tank Vent Arm Systems); it then goes to each Solid Rocket Booster and Hold Down Post External Tank Vent Arm System. The A system is hard-wired to one of the initiators on each of the four nuts (eight total) that hold the Solid Rocket Booster to the Mobile Launch Platform. The B system cabling is hard-wired to the secondary initiator on each nut. The A and B systems also send a duplicate signal to the External Tank Vent Arm System. Either Master Events Controller will operate if the other or the intervening cabling fails. To verify cabling integrity, a continuity and ohms check is performed before each launch.

A post-launch review of STS-112 indicated that the A system Hold-Down Post and ETVAS PICs did not discharge. Initial troubleshooting revealed no malfunction, leading to the conclusion that the failure was intermittent. An extensive analysis was initiated, with some 25 different potential fault chains considered as the source of the A-system failure.

Recommendation:

- NASA should evaluate a redesign of the Hold-Down Post Cable, such as adding a cross-strapping cable or utilizing a laser initiator, and consider advanced testing to prevent intermittent failure.

Solid Rocket Booster External Tank Attach Ring

In Chapter 4, the Board noted how NASA's reliance on "analysis" to validate Shuttle components led to the use of flawed bolt catchers. NASA's use of this flawed "analysis" technique is endemic. The Board has found that such analysis was invoked, with potentially disastrous consequences, on the Solid Rocket Booster External Tank Attach Ring. Tests showed that the tensile strength of several of these rings was well below minimum safety requirements. This problem was brought to NASA's attention shortly before the launch of STS-107. To accommodate the launch schedule, the External Tanking Meeting Chair subsequently waived the minimum required safety factor of 1.4 for the Attach Rings (that is, able to withstand NASA-standard 1.4 times the maximum load ever expected in operations). Though NASA has formulated short- and long-term corrections, its long-term plan has not yet been approved by the Space Shuttle Program.

As a result of this finding, the Board issued an observation contained in Section 10.10 of the report. Due to the potential danger of this system experiencing a failure, this observation should become a recommendation.

Recommendation:

- NASA must reinstate a safety factor of 1.4 for the Attach Rings – which invalidates the use of ring serial numbers 15 and 16 in their present state – and replace all deficient material in the Attach Rings.

Other Issues

> *Leaders should listen and listen and listen. Only through listening can they find out what's really going on. If someone comes in to raise an issue with the leader and the leader does not allow the individual to state the full case and to get emotions out in the open, the leader is likely to understand only a piece of the story and the problem probably will not be solved.*
>
> –Smith, Taking Charge[15]

> *It's extremely important to see the smoke before the barn burns down.*
>
> -Creech, The Five Pillars of TQM[16]

Though discussed and submitted by various investigators, the observations that follow did not appear in the Board report. They are offered here to illuminate other aspects of the Space Shuttle Program observed during the course of the investigation.

Crew Survivability

The issues surrounding crew survivability are well covered in Chapter 3 and 10 of the Board report. However, only one observation came from that coverage, and no recommendations, instead deferring to NASA in its long-term evaluation of related issues through the work of the Crew Survivability Working Group. That Group is diligently pursuing improvements to future designs and to today's fleet. One example of a possible improvement to today's fleet is evidence presented to the Board that a small amount of additional insulation or ablative material adhering around the crew cabin (between the inner pressure vessel of the cabin and the outer shell of the Orbiter) might provide the thermal protection needed for the cabin to retain its structural integrity in certain extreme situations. Thus, it seems pertinent to offer a *recommendation* that NASA assess that and other near-term possibilities immediately.

Recommendation:

- To enhance the likelihood of crew survivability, NASA must evaluate the feasibility of improvements to protect the crew cabin of existing Orbiters.

Shiftwork And Overtime

In its Volume 2, Appendix G, on Human Factors Analysis, the Rogers Commission addressed the negative safety impacts of shiftwork and overtime. While Chapter 6 of our report addresses schedule pressure magnificently, it does not address directly issues of workforce morale resulting from that pressure. Workers, had they not been stressed by overtime, may have even highlighted items of concern such as foam fragility, and those concerns could have been acknowledged and potentially acted upon. Issues of excess overtime and staffing are worth including in this supplement, particularly as too much overtime is often indicative of too little manning. Indeed, there were some concerns expressed regarding overtime that provide evidence and resurrect "echoes of *Challenger*," making issues of excess overtime and manning worth including in this supplement:

Findings:

- Workers expressed concern over workflow scheduling. Workflow scheduling in some areas had become so challenging that 69 percent of interviewees related that overtime and its resultant family and workplace stress had become a significant factor in their work environment. Added to that stress, 75 percent related that overtime was not effectively scheduled, often being told on Friday afternoons that overtime would be required over the weekend.
- Workers expressed concern over staffing levels. Using excessive and unpredictable overtime as an indicator,

many employees remained convinced that achieving adequate staffing levels would not only allow adaptation to workflow schedules, but also prevent the stresses that accompany the excessive overtime they found themselves working.

RSRM Segments Shipping Security

The Columbia Accident Investigation Board examined security at NASA and its related facilities through a combination of employee interviews, site visits, briefing reviews, and discussions with security personnel. The Board focused primarily on reviewing the capability of unauthorized access to Shuttle system components. Facilities and programs examined for security and sabotage potential included ATK Thiokol in Utah and its Reusable Solid Rocket Motor production**,** the Michoud Assembly Facility in Louisiana and its External Tank production, and the Kennedy Space Center in Florida for its Orbiter and overall integration responsibilities. The Board also studied specific security preparations for STS-107, which, because the crew included an Israeli astronaut, were the most extensive in NASA history.

The Board visited the Boeing facility in Palmdale, California; Edwards Air Force Base in Edwards, California; Stennis Space Center in Bay St. Louis, Mississippi; Marshall Space Flight Center near Huntsville, Alabama; and Patrick Air Force Base at Cape Canaveral Air Force Station in Florida. These facilities exhibited a variety of security processes, according to each site's unique demands. At Kennedy, access to secure areas requires a series of identification card exchanges that electronically record each entry. The Michoud Assembly Facility employs similar measures, with additional security limiting access to a completed External Tank. The use of closed-circuit television systems complemented by security patrols is universal.

Employee screening and tracking measures appear solid across NASA and at the contractors examined by the Board. The agency relies on standard background and law enforcement checks to prevent the hiring of applicants with questionable records and the dismissal of those who may accrue such a record.

It is difficult for anyone to access critical Shuttle hardware alone or unobserved by a responsible NASA or contractor employee. With the exception of two processes when foam is applied to the External Tank at the Michoud Assembly Facility – and these are the subject of a Board processing recommendation – there are no known final closeouts of any Shuttle component that can be completed with fewer than two people. Most closeouts involve at least five to eight employees before the component is sealed and certified for flight. All payloads also undergo an extensive review to ensure proper processing and to verify that they pose no danger to the crew or the Orbiter.

The handling of redesigned Solid Rocket Motor segments in transit is a concern. Tight security surrounds the transport of completed segments from the ATK Thiokol plant to a Corrine, Utah, railhead, where they are loaded into hardened enclosures on flatbed rail cars. The segments are not loaded at once; it can take up to 12 days for all the segments to arrive at the rail yard. After the first segment is loaded onto a rail car, fences surrounding the railhead are locked, and ATK Thiokol uses occasional patrols and closed-circuit television to maintain security. Although stealing or destroying the segments would require heavy-lift equipment or a rail engine, this situation creates a vulnerability that should be addressed.

Findings:

- When ATK Thiokol completes an order, it transports completed segments to the Corrine, Utah, railhead. The segments are escorted by a host of vehicles on special transporters to the rail spur dedicated to ATK Thiokol that has no common access and is fenced off from public access.
- At the railhead, the segments are cross-loaded onto specially outfitted flatbed rail cars with a hardened enclosure for the booster. At this point the fences are closed and locked, and the booster is left to await delivery of the remaining segments to complete a SRB ship set. This wait time will typically approach 10-12 days.
- During this wait time, ATK Thiokol uses occasional patrols from the main compound and closed circuit TV to maintain vigilance. While theft or destruction of the booster would require heavy lift equipment or a rail engine, it appears to be an unnecessary vulnerability having such a component exposed without more stringent security.

Recommendation:

- NASA and ATK Thiokol perform a thorough security assessment of the RSRM segment security, from manufacturing to delivery to Kennedy Space Center, identifying vulnerabilities and identifying remedies for such vulnerabilities.

Michoud Assembly Facility Security

Findings:

- The Michoud Assembly Facility has a number of natural and manmade provisions to promote its security.
- Several gaps were noted that bear assessment, to include availability of 4-wheel drive vehicles, night vision goggles, and an assessment of security staffing for the large amount of property which must be covered in the manufacture and transport of the Shuttle External Tank.

Recommendation:

- NASA and Lockheed Martin complete an assessment of the Michoud Assembly Facility security, focusing on items to eliminate vulnerabilities in its current stance.

NOTE: ADDITIONAL SUPPLEMENTAL COMMENTS THAT CAN BE APPLIED TO PREVENTING THE NEXT ACCIDENT ARE AVAILABLE IN APPENDIX D.15.

ENDNOTES FOR THE APPENDIX D.a

The citations that contain a reference to "CAIB document" with CAB or CTF followed by seven to eleven digits, such as CAB001-0010, refer to a document in the Columbia Accident Investigation Board database maintained by the Department of Justice and archived at the National Archives.

1 James M. Strock, *Reagan on Leadership* (Roseville, CA: Forum, 1998), p. 104.

2 Jim Collins, *Good to Great* (New York: Harper Business, 2001), p. 88.

3 Ronald A. Heifetz, *Leadership Without Easy Answers* (Cambridge, MA: Harvard University Press, 1994), p. 22.

4 Douglas A. Wiegmann, Institute of Aviation of the University of Illinois, presentation before the Board, May 8, 2003. CAIB document CTF040-08750913.

5 Karlene H. Roberts, High Reliability Organizations, presentation before the Board, May 7, 2003. CAIB document CAB034-00430046.

6 D.D. Woods and R.I. Cook, "Nine Steps to Move Forward from Error," *Cognition, Technology, and Work* (2002), Vol 4, p. 140.

7 *Report of the Presidential Commission on the Space Shuttle Challenger Accident*, June 6, 1986, (Washington: Government Printing Office, 1986), Vol. I.

8 Space Shuttle Independent Assessment Team, Report to Associate Administrator, Oct.-Dec. 1999; March 7, 2001, p. 51.

9 Ibid.

10 James T. Reason, *Managing the Risks of Organizational Accidents* (Hampershire, England: Ashgate, 1997), pp. 214-215.

11 LaPorte and Consolini, as quoted in Reason, *Managing the Risks*, pp. 214-215.

12 Space Shuttle Independent Assessment Report for United Space Alliance, "Maintaining a National Treasure," April 23, 2001, p. 46. CAIB document CTF014-24802586.

13 Karlene H. Roberts and Robert Brea, "Must Accidents Happen? Lessons from High Reliability Organizations," *Academy of Management Executive*, 2001, Volume 15, No. 3, p 73.

14 Matthew L. Wald, "Report Criticizes NASA and Predicts Further Fatal Accidents," *New York Times*, July 15, 2003.

15 Perry M. Smith, *Taking Charge* (Garden City Park, NY: Avery, 1993), p. 89.

16 Bill Creech, *The Five Pillars of TQM* (New York: Truman Talley Books, 1994), p. 239.

THIS PAGE INTENTIONALLY LEFT BLANK

Corrections to Volume I of the Report

ERRATA FOR VOLUME I

Volume I of the Columbia Accident Investigation Board report contained several minor errors, but none of them affected the substance of the report.

The following errors were in the original copies released on 26 August 2003; these were corrected prior to the public printing by NASA and the Government Printing Office. The original electronic copies distributed on www.caib.us and www.nasa.gov also contained these errors; revised files were uploaded the week of 9 September 2003.

Page 11: In the last full paragraph on the page, the altitude was listed as 65,500 feet. It more accurately should have been 65,820 feet.

Page 12: In the next to last paragraph, "culture" was misspelled.

Page 25: The caption for Figure 1.5-1 should have read: "... in the right Solid Rocket Booster."

Page 39: The caption for the photograph at the top of the page should have read: "*Columbia* streaking over the Owens Valley Radio Observatory in Big Pine, California."

Page 223: Observation 10.12-1 should have an "O" in front of the number (O10.12-1).

The following errors were noted after the public printing of the report by NASA and the GPO, and have not been corrected in either the electronic copies or any current (12 September 2003) printing:

Page 34: In the Debris Strike paragraph, the report states, "Further photographic analysis conducted the day after launch revealed that the large foam piece ... " The numbers cited represent the final analysis, so the sentence should have read, "Further photographic analysis conducted after launch revealed that the large foam piece ..."

Page 37: In the second paragraph of the Debris Strike Analysis and Request for Imagery section, the report states, "A large object from the left bipod area of the External Tank struck the Orbiter, apparently impacting the underside of the left wing near RCC panels 5 through 9." Initially, the analysis did not limit the possible strike area to the RCC panels (it extended under the Orbiter as far as the main landing gear door), so the sentence should have read, "A large object from the left bipod area of the External Tank struck the Orbiter, apparently impacting the underside of the left wing.

Page 62: In the first full paragraph, the report states, "Appendix D.8 contains an independent analysis conducted by the Board to confirm that the estimated range of ballistic coefficients of the foam in Figure 3.4-6 ..." The correct figure reference should be 3.4-7.

Page 64: A reference to Appendix D.19 was inadvertently omitted from Section 3.6. The first sentence should read, "For a complete compilation of all re-entry data, see the CAIB/NAIT Working Scenario (Appendix D.7), Qualification and Interpretation of Sensor Data from STS-107 (Appendix D.19), and the Re-entry Timeline (Appendix D.9)."

Page 79: Figure 3.8.1 incorrectly refers to a "30 foot gun barrel" when the actual barrel length was 35 feet.

Page 83: Citation 17 should be on Finding F3.8-5, not F3.8-3.

Page 87: The bottom paragraph in the first column, the report states that "In one test, a bolt catcher failed at 44,000 pounds, which was two percent below the 46,000 pounds generated by a fired separation bolt." The percentage is actually approximately four percent.

Page 102: First column, first partial paragraph "the exceptional quality of the its workforce" should read "of its workforce" (no "the").

Page 105: The title of the sidebar should read "Shuttle Budget Reductions" instead of "Congressional Budget Reductions."

Page 109 Upper right: "... and the Marshall Space Center-managed contracts" should read "... and the Marshall Space Flight Center-managed contracts."

Page 110: Figure 5.4-2. The x-axis scale was inadvertently changed when two graphics were merged into one. The numbers are correct, but the increments change at the midpoint. This is the corrected graph:

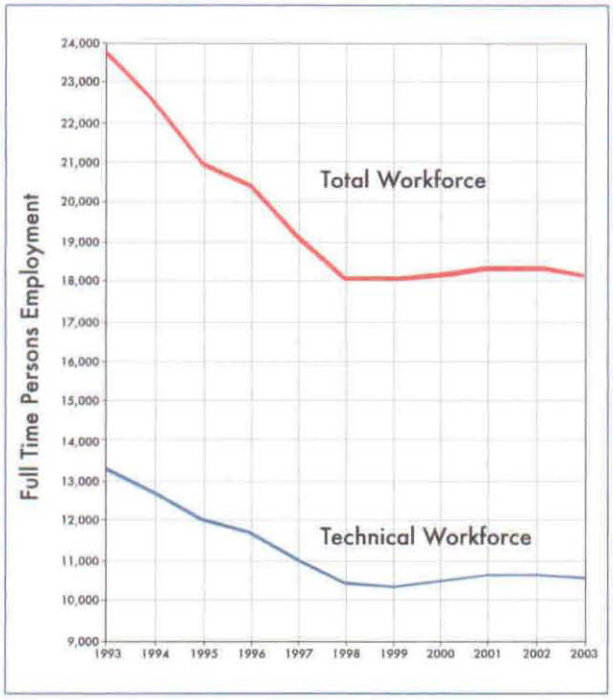


Figure 5.4-2. Downsizing of the overall NASA workforce and the NASA technical workforce.

Page 112: The text before the Past Reports table contains two mistakes. The first is a typographical error: "was to note what factors *that* reports examined" should read "what factors *those* reports examined." The second is a factual error on the last line: "... plus the full text of the reports ..." should be deleted, since the full text is not included in Appendix D.18, only selected Findings and Recommendations.

Page 120: In endnote 54, the citation should read: (New York: Bantam Books, 1986).

Page 120: In endnote 55, the citation should read: (Washington; Government Printing Office, 1982-1991).

Page 120: In endnote 56, the citation should read: (Washington; Government Printing Office, 1999).

Page 144: The 0.45 term in the Crater Model formula should be an exponent for the length-to-diameter [(L/d)] term rather than a multiplicative factor [i.e. "0.0195(L/d)0.45(d) ..." should read "$0.0195(L/d)^{0.45}(d)$ ..."]

Page 156: Trish Petete was incorrectly spelled Petite.

Page 178: At the bottom of the left column, "In January 1967, *months* before the scheduled launch" should read "In January 1967, *weeks* before the scheduled launch".

Page 241: Dr. Ride's middle initial is "K" not "T".

Page 243: Dr. Bagian's middle initial is "P" not "B".

Page 243: CAPT Fraser's middle initial is "R" not "T".

Page 244: Add the following under Group II:
"Col. Donald W. Pitts, Consultant, Air Force Safety Center"

Page 245: CDR (Select) Wolfe's middle initial is "P" not "R".

Page 245: Lt. Col. Woodyard should be listed as Lt. Col. Tyrone M. Woodyard.

Page 246: The correct company name for Mr. Feldman is Press Conference/Hearing Support Federal Networks, Inc.

Page 246: Mr. Gazarek's middle initial should be "G."

Page 246: Mr. Griffin's name should be Douglas S. Griffin.

Page 246: The correct spelling should be "Liaison" in Colonel Anthony's title.

Page 247: Add under Advisors and Consultants:
"Tina L. Panontin, Ph.D., P.E., Advisor, NASA Ames Research Center"

Page 248: Vicci Biondo was incorrectly spelled.

Page 248: Mario Loundermon was incorrectly spelled.

Volume II
Appendix D.1
STS-107 Training Investigation

The Board conducted a thorough review of all training activities that were performed in preparation for STS-107, including training conducted for the crew, launch controllers, and mission controllers. An analysis of STS-107 Orbiter and payload training requirements was conducted, as well as a complete review of all training records, schedules, instructor logbooks, and related documentation for the crew, flight controller, and launch controller training. Interviews and discussions were held with STS-107 training and operational personnel at both Johnson and Kennedy Space Centers to investigate the STS-107 training process, the effect of launch slips, the performance of the crew, flight controllers, and launch controllers, and the flight readiness of all for the STS-107 mission. Although several issues were identified as a result of this investigation, none were considered causal in the loss of *Columbia*.

The investigator who wrote this report proposed four recommendations, one of which was adopted by the Board for inclusion in the final report. The conclusions drawn in this report do not necessarily reflect the conclusions of the Board; when there is a conflict, the statements in Volume I of the Columbia Accident Investigation Board Report take precedence.

Summary 23

Section 1.0 Space Shuttle Training Overview 23
1.1 Space Shuttle Operators and Mission Responsibilities 23
1.1.1 Crew 23
1.1.2 Flight Controllers 24
1.1.3 Launch Controllers 24
1.2 Training Facilities 24
1.2.1 Johnson Space Center (JSC) 24
1.2.2 Other Training Facilities 25
1.3 Space Shuttle Training Process 25
1.3.1 Basic Training and Certification 25
1.3.2 Mission Specific Training 25

Section 2.0 STS-107 Training Factual Information 26
2.1 Crew Training 26
2.2 Flight Controller Training 27
2.3 Launch Controller Training 28
2.4 Readiness Reviews/Certificate of Flight Readiness (CoFR) 28

Section 3.0 Training Investigation and Assessment 28
3.1 Crew 28
3.2 Flight Controllers 28
3.3 Launch Controllers 29
3.4 Mission Performance 29

Section 4.0 Findings 30

Section 5.0 Conclusions 30

Section 6.0 Observations 30

STS-107 Training Investigation

Submitted by Group II
Major General Kenneth W. Hess, Steven B. Wallace, Sally K. Ride, Ph.D.
Lisa Reed

SUMMARY

On February 1, 2003, at 07:59 Central Standard Time, the Space Shuttle *Columbia* broke apart during entry killing all seven crewmembers of mission STS-107.

As part of the ongoing investigation into the cause of the *Columbia* mishap, all aspects of training for mission STS-107 were examined. An analysis of STS-107 Orbiter and payload training requirements was conducted, as well as a complete review of all training records, schedules, instructor logbooks, and related documentation for the crew, flight controller and launch controller training. Interviews and discussions were held with STS-107 training and operational personnel at both Johnson and Kennedy Space Centers to investigate the training process, the effect of launch slips, the performance of the crew, flight controllers, and launch controllers, and the flight readiness of all for the STS-107 mission.

The following report provides an overview of the Space Shuttle mission training process, summarizes the factual information about STS-107 mission training, describes the investigative process used in assessing this information, and presents an analysis of that training. This investigation determined that the crew and controller training for STS-107 was not a contributing factor in the loss of *Columbia* and the STS-107 crew.

1.0 TRAINING OVERVIEW

Training for a Space Shuttle mission begins when a new operator is hired. Space Shuttle operators are the astronauts who fly onboard the Space Shuttle, the launch controllers who work the Launch Control Center (LCC) during launch, and the flight controllers who monitor in the Mission Control Center (MCC) from the vehicle clearing the launch tower until landing.

1.1 SPACE SHUTTLE OPERATORS AND MISSION RESPONSIBILITIES

1.1.1 Crew

A Space Shuttle crew is comprised of pilot astronauts and Mission Specialist astronauts. Payload specialists are "guest astronauts" and may also be assigned to a mission if there is a requirement.

Pilot astronauts may be either a shuttle mission commander (CDR) or a shuttle mission pilot (PLT). They are usually chosen for their extensive flight experience or background as military test pilots. During a mission, the CDR has onboard responsibility for the vehicle, crew, mission success, and safety of flight. The CDR sits in the left seat on the flight deck during ascent and descent. The PLT assists the commander in controlling and operating the vehicle during all phases of flight. The PLT sits in the right seat on the flight deck during ascent and descent. Before being eligible to serve as a mission commander, a pilot astronaut must serve on a shuttle mission in the pilot position at least once.

Mission specialist astronauts are typically scientists or engineers specializing in areas such as aerospace engineering, physics, chemistry, astronomy or medicine. Mission Specialists (MS) are trained in the details of all Orbiter onboard systems, as well as the operational characteristics, mission objectives, and supporting equipment for each of their assigned missions. Mission Specialists perform extravehicular activities (EVA), or space walks, operate the Remote Manipulator System (RMS), and are responsible for payloads and specific experiment operations. One MS is designated as MS2, or flight engineer, for the mission. The MS2 is an integral part of the flight deck crew, assisting the commander and pilot in controlling and operating the vehicle during all phases of flight. At least two MS are chosen to receive extravehicular activity training (EVA) for each mission regardless of whether there is an EVA scheduled for the mission. These EVA crewmembers are trained for Space Shuttle contingencies that would require crewmembers to perform a spacewalk, such as manually closing the payload bay doors should they fail using the normal methods. These

MS are designated EV1 and EV2. Another crewmember, designated "IV," trains to support the EVA crewmembers in donning and doffing their suits and helps coordinate the EVA activities from inside the vehicle.

Payload specialists are persons other than NASA astronauts (including international citizens) who have specialized duties that may be added to shuttle crews if activities that have unique requirements. If Payload Specialists are required, NASA, the foreign sponsor, or the designated payload sponsor nominates them. Although Payload Specialists are not part of the Astronaut Program, they must have the appropriate education and training related to the payload or experiment. All applicants must meet specific physical requirements and must pass NASA space physical examinations with varying standards depending on classification.

1.1.2 Flight Controllers

Flight control teams consisting of Space Shuttle systems experts staff the Flight Control Room (FCR) consoles in the Mission Control Center (MCC) during missions. The primary objectives of the Space Shuttle flight control team are to closely monitor and direct the crew during critical mission phases, to provide support in conducting the mission, and to extend the system analysis capability of the crew by providing systems expertise support on the ground.

Flight controllers who work in the FCR represent only part of the shuttle mission staffing in the MCC. Each of the flight controllers sitting at a console in the FCR has the help of other engineers and flight controllers monitoring and analyzing data in nearby staff support rooms.

There are 19 mission controller consoles in the FCR. Under the direction of the Flight Director, a systems specialist certified in vehicle systems, operations, or flight dynamics operates these consoles. Every position has a "call sign," the name the controller uses when talking to other controllers over the communications loops. Some FCR positions may not be staffed for each mission depending on the flight phase and the requirements of the flight.

1.1.3 Launch Controllers

The Launch Control Center (LCC) at the Kennedy Space Center oversees all aspects of Space Shuttle launch operations. Launch controllers specializing in Space Shuttle systems, test procedures, and launch countdown procedures staff consoles for every launch. There are 17 consoles in Firing Room. Several systems engineers staff each console.

Launch controllers who work in the control room represent only part of the shuttle launch staffing in the LCC. They have the help of other engineers and launch controllers in nearby support rooms.

Under the guidance of the launch director, they oversee the countdown for a shuttle launch beginning at launch minus three (L-3) days through liftoff and tower clear when the MCC in Houston assumes responsibility for vehicle and crew. Each launch controller has a "call sign" that is used when talking to other controllers over the communications loops.

1.2 Training Facilities

1.2.1 Johnson Space Center (JSC)

The Johnson Space Center in Houston, Texas, is the primary training center for NASA's human space flight programs. The majority of training for Space Shuttle missions takes place in facilities in and around the JSC.

Each facility is used to train specific aspects of a shuttle mission. A description of some of the key Space Shuttle training facilities at or nearby the JSC are listed below:

Single System Trainers (SST) – Three SSTs are located in Building 4S. They are used to conduct part-task training in a high-fidelity mockup of the Orbiter flight deck. Classes are instructor led, typically with one or two students. Lessons focus on either nominal operations or malfunction recovery in one Orbiter system.

Shuttle Mission Simulator (SMS) – The SMS is located in Building 5. There are 3 training simulators, 1 motion-base and 2 fixed-base. These are full-fidelity simulators used to provide mission rehearsal in ascent, orbit and entry operations. Simulations can be run "stand-alone", meaning just the crew and instructors – or "integrated" during a simulation combined with the mission control team. The focus of integrated training is on team interaction.

SPACEHAB Volumetric Trainer (SVT) – The SVT is located in Building 5. It is a mockup of the SPACEHAB and its components. This is a low-fidelity trainer used to teach basic SPACEHAB module layout. In some simulations, the SVT is used in conjunction with one of the fixed-base simulators.

Space Vehicle Mockup Facility (SVMF) – The SVMF is located in Building 9. Several high fidelity Orbiter mockups are used to train crew ingress, egress, mission timelines, crew habitability, photo/TV courses, onboard equipment stowage and airlock operations.

Neutral Buoyancy Lab (NBL) – The NBL is located at a facility near JSC. It is a large pool used for Extra Vehicular Activity (EVA) training, EVA tool and procedures verification and extra- and intra-vehicular crewmember coordination. It is also used for bailout training.

Mission Control Center (MCC) – The MCC is located in Building 30S. While it is the nerve center for actual mission operations, it is used to conduct integrated simulations with crewmembers in the SMS. The MCC is critical to training the "team" of crew and mission controllers for a specific mission.

Flight Controller Trainer (FCT) - The FCT is located in Building 4S. It is used to conduct part-task training with flight controllers using a hi-fidelity mockup of a flight

controller console. Classes are instructor led, typically with one or two students. Lessons focus on either nominal operations or malfunction signature recognition for orbiter systems.

Shuttle Training Aircraft (STA) - The STA is a modified Gulfstream II business jet used for training the approach and landing phase of a shuttle mission. The left side of the cockpit is modified to simulate the Orbiter flight deck. It has a rotational hand controller and computer displays that are identical to the Orbiter. The pilot and commander fly approaches to runaway under guidance of an instructor pilot.

1.2.2 Other Training Facilities

Training on crew equipment interfaces, launch terminal countdown, launch pad aborts, and emergency egress training is held with each mission crew at the Kennedy Space Center (KSC). This training is conducted using the actual vehicle, flight hardware and the launch pad facilities. Launch team training is conducted in dedicated computer facilities and also in the actual launch firing rooms in the Launch Control Center.

Depending on the unique payload or flight requirements of each shuttle mission, training can be accomplished at other NASA centers, various international space agency facilities, commercial industry facilities or academic/scientific research facilities.

1.3 Space Shuttle Training Process

1.3.1 Basic Training and Certification

Each operator begins with a phase of Space Shuttle basic training before embarking on detailed training designed to the specifics of his or her job. This comprehensive training includes: immersion in the study of shuttle systems, shuttle flight mechanics, shuttle flight dynamics, mission operations, workbooks, computer-based training lessons, classroom lectures, part-task training classes, hands-on training with vehicle hardware, on-the-job training with mentors and participation in shuttle simulations.

Satisfactory completion of the training certification flow indicates that an operator is eligible to hold a specific position during a Space Shuttle mission and results in a certification for the operator. Obtaining certification for a particular mission position signifies that person is eligible for assignment during a Space Shuttle mission.

After certification, the person enters a period of maintaining proficiency in their knowledge/skill level and participating in periodic training sessions while awaiting flight assignment. The average time required to move from basic training to actual mission flight assignment is four to five years for crewmembers and one to two years for controllers.

The Mission Operations Directorate (MOD) at the JSC is responsible for providing the training and certification for flight crews, mission controllers, and the instructors who train them. Space Shuttle training requirements for the crew are documented in the Crew Training Catalog (CTC). For flight controllers, the training certification process is documented in the "Mission Operations Directorate Space Flight Personnel Certification Plan". For launch controllers, the training certification process is documented in the "KSC Launch Team Certification Plan."

Space Shuttle Program (SSP) training is a Contractor Accountable Function (CAF). The prime contractor responsible for SSP training is the United Space Alliance (USA) under the Space Flight Operations Contract (SFOC).

1.3.2 Mission Specific Training

Mission Specific training consists of: qualification, flight similar, proficiency and flight specific.

Qualifications

Upon flight assignment, each operator begins learning the specifics of the mission. For flight crewmembers, training begins nine months to one year prior to the scheduled launch date depending on the complexity of the mission objectives. The controllers assigned to the mission join the crew in training about three to four months prior to launch. The major reason for the controllers joining the crew late in the training flow is the fact that controllers work multiple missions with more frequency where crewmembers are assigned one a mission at a time and years may have passed since their last mission. Controllers maintain their knowledge-skill level by supporting more missions with more frequency than crewmembers and do not require the extensive mission specific training required by the crewmembers.

A team of instructors is assigned to work with the crewmembers for the duration of their training to provide continuity and consistency. Mission training begins with the crewmembers passing a series of qualifications, or "quals" which may consist of oral examinations or training sessions in a single system trainer requiring the crewmember to demonstrate operational knowledge of a particular shuttle system. These "quals" demonstrate that crewmembers have the expected proficiency in Space Shuttle systems and are ready to begin detailed mission training.

Flight Similar

After meeting qualification requirements, the crew begins "flight similar" training. Flight similar training uses flight products such as Orbiter software and crew procedures that are similar to those they will have for their mission. Mission specific flight products are not usually released until 3 to 4 months prior to launch due to development, testing and verification. Flight similar training offers a standard set of lesson scenarios in crew resource management, ascent, orbit, entry, and other specialized topics. During these lessons, the crew practices working together as a team, performing those tasks they are responsible for during various phases of the mission and responding to anomalous situations that may occur during these mission phases. Early payload training takes place during this time period as well.

Proficiency

If the crew completes all lessons in the flight similar standard set before their flight products are ready for use, they enter a period of "proficiency" training. Proficiency training is scheduled several times a week. By design, it is intended to maintain or advance the crew knowledge or skill level achieved during flight similar training. The proficiency phase can also be entered if there is an extended launch slip.

Flight Specific

After flight products delivery, the crew enters the final phase of mission training called "flight-specific" training. Flight-specific training focuses on rehearsing all aspects of the mission using the actual Orbiter flight software and procedures for that mission. During this period the mission control teams assigned to the mission join the crew for integrated simulations. This integrated training allows the crew and the flight control team to rehearse all aspects of the mission and its major objectives using the flight products they will use during the mission. During flight-specific training, the crew also performs a launch countdown test with launch controllers at the KSC and participates in more detailed payload training. Flight-specific training continues until one week prior to launch when the crew enters quarantine. If there are extended launch slips during this phase of training, the crew and flight controllers may re-enter the proficiency phase.

2.0 STS-107 Training Factual Information

2.1 Crew Training

Seven crewmembers were to be assigned to the STS-107 mission, tentatively scheduled for launch on January 11, 2001. However, the payload specialist and mission specialists were not assigned until July 26, 2000, signaling that the mission launch date would slip. The official press release announcing these assignments ultimately came on September 28, 2000.

The commander and pilot were assigned on October 27, 2000. The official press release announcing these assignments came on December 1, 2000.

The flight assignments were:

Commander:
Rick D. Husband, Colonel, USAF
Pilot:
William C. McCool, Commander, USN
Mission Specialist 1/EV1:
David M. Brown, M.D, Captain, USN
Mission Specialist 2:
Kalpana Chawla, Ph.D
Mission Specialist 3/Payload Cdr/EV2:
Michael P. Anderson, Lieutenant Colonel, USAF
Mission Specialist 4/IV:
Laurel Blair Salton Clark, M.D., Captain, USN
Mission Specialist 5:
Ilan Ramon, Colonel, Israeli Air Force

Commander Husband flew as pilot on STS-96. Mission Specialist Chawla flew on STS-87. Mission Specialist Anderson flew on STS-89.

STS-107 was the first mission for Pilot McCool, Mission Specialists Brown and Clark, and Payload Specialist Ramon.

The primary mission objective of STS-107 was to conduct a variety of science experiments carried in the SPACEHAB Research Double Module (RDM) or on the Orbiter middeck. A secondary mission objective was the operation of the Fast Reaction Experiment Enabling Science, Technology, Applications and Research (FREESTAR) located in the aft payload bay of *Columbia*.

The STS-107 payload crew began training for the mission on August 14, 2000, working toward a June 14, 2001, launch date. For the first few months of training, the crew completed their qualification training, took systems refresher classes, participated in SPACEHAB and mission experiment familiarization, and traveled to see SPACEHAB hardware at the KSC. The commander and pilot joined the crew in training on November 1, 2000.

On November 9, 2000, the launch date was moved to August 2, 2001, delaying the planned start of flight similar training.

Flight similar training began on January 3, 2001. In the following weeks the crew participated in simulator sessions, suited ingress and egress training and attended several payload experiment hands-on training sessions.

On February 13, 2001, the launch date was slipped to October 25, 2001. The crew continued work on the flight similar training requirements.

On March 15, 2001, the launch date was slipped to April 4, 2002 when the STS-109 Hubble servicing mission, which was scheduled to fly on *Columbia*, was assigned a higher priority. The crew continued work on flight similar training requirements and traveled to the European Space Agency (ESA) for hands-on training of ESA-sponsored payload experiments on STS-107. While in Europe for this training, the launch date was slipped to May 23, 2002. The crew completed their flight similar training requirements on July 3, 2001.

After a two-week vacation, the crew began flight specific training the week of July 23, 2001. They participated in mission specific training sessions and traveled to various payload customer facilities for hands-on training for STS-107 experiments.

On October 25, 2001, the launch date was slipped to June 27, 2002. By this date, the crew had been in training for over a year.

The crew entered proficiency training mode due to the extended launch slip. They also traveled to Florida for SPACEHAB timeline training in the SPACEHAB Research Double Module.

On January 24, 2002, the launch date was slipped to July 11, 2002.

On February 5, 2002, the crew resumed flight specific training and continued in-depth payload experiment training including a trip to Goddard Space Flight Center (GFSC) for training on the FREESTAR payload.

On April 11, 2002, the launch date was slipped to July 19, 2002.

Flight specific integrated orbit training, including Joint Integrated Simulations (JIS) with the payload customers, the crew and the orbit flight control teams began on April 23, 2002. Over the next few months, five STS-107 mission JISs were conducted to exercise SPACEHAB activation, deactivation, and experiment portions of the mission timeline.

Integrated ascent and entry training with the crew and ascent/entry flight control team began on May 6, 2002.

On June 8, 2002, the crew traveled to the KSC for the Crew Equipment Interface Test (CEIT). When they returned they continued integrated training with the flight control teams.

On July 22, 2002 and July 31, 2002, two launch slips occurred, to September 26, 2002 and November 29, 2002 respectively.

The crew entered proficiency training mode and remained in that mode for the next month and a half. On September 12, 2002, the launch slipped for a final time to January 16, 2003. The crew had been in training for over two years.

In the final four months of training, the crew traveled to Europe once more for payload experiment training. They repeated ascent and entry integrated training with the flight control team. An additional orbit JIS was added for the orbit flight control team since the last JIS had taken place almost six months prior.

On December 17, 2002, the crew traveled to KSC for the Terminal Countdown Demonstration Test (TCDT), a launch day "dress rehearsal" with the launch control team.

STS-107 mission training was completed on January 9, 2003, with the final ascent integrated simulation with the mission control team. The crew entered quarantine that afternoon. They departed Houston for the Kennedy Space Center on January 11, 2003.

All Space Shuttle mission training requirements defined in the Crew Training Catalog and listed in the Crew Training Plan were completed. Multiple launch slips allowed for additional training to be added or training sessions to be repeated to maintain or enhance crew flight proficiency. According to Space Flight Training Division training records, the cumulative Space Shuttle mission training for the STS-107 crewmembers was 4,811 hours.

Individual crewmember training hours for STS-107 were:

Crewmember	Hours
Husband	822
McCool	830
Brown	766
Chawla	876
Anderson	441
Clark	638
Ramon	437

SPACEHAB, Inc. recorded 3,506.6 hours crew payload experiment training. Fifteen weeks of this payload and experiment training were conducted at payload sponsor facilities at Marshall Space Flight Center, SPACEHAB facilities in Florida, Goddard Space Flight Center, Glenn Research Center and European Space Agency (ESA) facilities.

Experiment training for STS-107 consisted of at least one familiarization briefing for each experiment and one or more hands-ons training sessions with experiment hardware. SPACEHAB subsystem training consisted of familiarization training, part task training, in-flight maintenance training, SPACEHAB activation and deactivation training, and SPACEHAB procedure reviews.

While the STS-107 crew was in training, the launch date slipped a total of 10 times, plus three times prior to the crew being selected. The STS-107 crew never stopped training and maintained their proficiency until launch. By launch time, they had completed 126 weeks of training, about 74 weeks longer than the average duration of Shuttle mission training.

2.2 Flight Controller Training

There were five teams of mission controllers assigned to STS-107: an ascent and entry team, and four orbit teams to support around the clock operations of the dual shift mission.

The Ascent/Entry flight control team began training with the STS-107 crew on October 22, 2002 participating in a total of 16 integrated ascent or entry simulations with the STS-107 crew. Due to the launch slips, training requirements forced some of these simulations to be repeated. The ascent/entry simulations for STS-107 were held on the dates listed below. The repeated simulations are indicated.

Ascent #1	April 22, 2002
Entry # 1	May 6, 2002
Deorbit Prep	May 23, 2002
Ascent #2	May 28, 2002
Ascent #3	June 24, 2002
FDO/BSE	June 14, 2002
Ascent #1(repeated)	October 22, 2002
Entry # 1 (repeated)	October 24, 2002
Ascent # 2 (repeated)	November 8, 2002
FDO/BSE (repeated)	November 19, 2002
Entry #2	December 9, 2002
Deorbit Prep(repeated)	December 13, 2002
Post Insertion	December 16, 2002
Ascent #3 (repeated)	January 3, 2003
Entry # 3	January 7, 2003
Ascent # 4	January 9, 2003

The Orbit flight control team began training with the STS-107 crew on April 23, 2002, participating in a total of six joint integrated simulations with the STS-107 crew and payload customers. Due to the launch slips, one 30-hour JIS was added since the previous JISs has been run almost six months prior. The JISs were held on the dates listed below:

(NOTE: the JIS numbers indicate the name of the JIS and do not imply a numerical order in which they should have been accomplished.)

JIS # 1 – 8 hours	April 23, 2002
JIS # 3 – 17 hours	May 3, 2002
JIS # 4 – 12 hours	May 15, 2002
JIS # 2 – 16 hours	June 21, 2003
JIS # 5 – 10 hours	June 25, 2002
JIS # 6 – 30 hours (added)	December 10, 11, 2002

There were 77 FCR operators assigned to four shifts during the STS-107 mission. All had initial certifications and had worked missions in the past. Seven failed to complete re-certification requirements prior to the STS-107 launch, and by MOD standards, were not re-certified at the time of the mission. Flight controllers are required to re-certify for their positions periodically. For most positions the re-certification requirement is every 18 months. The Board did not consider this paperwork oversight to be a contributing cause to the accident, but believes that the Space Shuttle Program should be more aware of these situations and prevent any reoccurances.

2.3 Launch Controller Training

The STS-107 Launch Control Team participated in the Terminal Countdown Demonstration Test (TCDT) with the STS-107 crew on December 20, 2002. The TCDT was a full "dress rehearsal" of the launch day countdown activities from crew suit-up, walkout, transport to the pad, crew ingress into the Orbiter and terminal launch countdown. The test ended with a simulated anomaly forcing the team and crew to declare a pad abort and emergency pad egress.

All launch controllers were certified to staff their launch control positions for the TCDT and the day of launch.

2.4 Readiness Reviews/Certificate of Flight Readiness (CoFR)

The STS-107 Launch Readiness Review (LRR) was held on December 18, 2002 at the KSC. There were no training issues for launch controllers indicated from either NASA or USA.

For the STS-107 Flight Readiness Review (FRR) held on January 9, 2003, the Mission Operations Directorate (MOD) listed no issues for crew or flight controller training. According to FRR documentation, all personnel were trained and certified or would be trained and certified prior to the flight. This statement was erroneous given the previously-mentioned seven flight controllers assigned to the mission did not have current re-certifications at the time of the FRR, nor were they re-certified by the mission date. This contradicts the MOD Shuttle Certificate of Flight Readiness (CoFR) signed by NASA and USA managers on December 18, 2002.

3.0 Training Investigation and Assessment

STS-107 training requirements for the crew and controllers were reviewed then compared against training records to verify that all required training was completed. The outcome of that training was studied to assess training readiness and identify areas of deficiency in crew or controller performance.

3.1 Crew

A review of documentation outlining STS-107 crew training requirements was conducted. The documentation included the Crew Training Catalog, Crew Training Plan, Assigned Crew Study Guide, Crew Task Assignments, SPACEHAB Mission Specific Training Plan, and Integrated Simulation Plan associated with STS-107. All requirements outlined in the Crew Training Catalog were listed in the STS-107 Crew Training Plan as training objectives to be achieved during the course of training.

Crew training records and weekly crew activity schedules indicated that the prescribed prerequisite flow as outlined in the Crew Training Catalog was strictly followed. Due to launch slips, the appropriate proficiency training lessons were scheduled and training was repeated, if required.

All training requirements were for the STS-107 crew were completed. The crew completed more training than required because of the numerous launch slips.

Interviews, discussions, and a comprehensive review of written instructor training logs and simulation observations notes were conducted to better understand the crew's performance during training and their ultimate readiness for flight. An interview with the STS-107 Training Team Lead revealed no issues with crew performance and described the crew as "more than ready" for flight. Discussions with Training Division management regarding periodic meetings held with Commander Husband indicated that he expressed confidence in his crew's performance and had no problems with the quality of the training the crew received. Independent simulation observations completed monthly by senior training personnel indicated no concerns with crew performance. Individual instructor notes written during crew training sessions show the crew progressed steadily as expected in their knowledge level and readiness, peaking just prior to launch. The training flow was remarkable in length only.

The analysis of training information supports the finding that crew training requirements for STS-107 were complete and the crew was adequately trained for their mission tasks.

3.2 Flight Controllers

A review of documentation for STS-107 flight controller training requirements was conducted. This documentation included the MOD Space Flight Personnel Certification

Plan, flight controller training certification records, and the STS-107 Integrated Simulation Plan.

Training records indicated that flight controllers were qualified to work their respective positions for STS-107. However, seven did not have current certification paperwork in their training folders. Discussions with flight control management for the seven indicated that they had not completed the requisite proficiency re-certification requirements prior to STS-107. Possible explanations offered by managers as to why these certifications were deficient were attributed to smaller numbers of personnel in these groups. This investigation did not identify the reason for the smaller numbers of personnel nor the impact on this issue.

All STS-107 mission specific training requirements for flight controllers were complete. Integrated simulations were repeated to maintain team proficiency as required due to launch slips.

The flight controller performance during training and their readiness for flight, detailed interviews, and a comprehensive review of written instructor training logs and simulation observations were conducted. Interviews with the ascent, orbit, and entry Simulation Supervisors suggest no issue with any of the flight control teams' performance prior to the mission. Instructor written logs and independent simulation observations indicate no performance issues with any flight control team members or teams.

The analysis of training information supports the finding that the STS-107 flight controller training requirements for STS-107 were complete and they were adequately trained for their mission tasks. The board does not believe the recertification issue to be significant in regards to this accident. That said, the Board is somewhat concerned that the absence of re-certification in this instance may be an indication of decreasing standards and management oversight of important training and certification processes.

While reviewing mission control personnel training, it was discovered that Mission Management Team (MMT) simulations are held. There have been six such simulations to date. They were conducted every 18 months.

While these simulations are positive, they were lacking in scope and frequency. All MMT simulations dealt only with ascent abort scenarios that resulted in intact aborts and landings. They were all held at KSC and all participants were briefed that the scenario would be an launch contingency. By stating in advance that this simulation would result in a launch contingency it possibly biased the participants and allowed them to think ahead as to what their reactions would be for just a handful of contingency scenarios. Members of Space Flight Training Division were participants in the last simulation held, but seemed to be in a passive, observation role, rather than actively planning the scenarios and evaluating the performance of the participants.

The MMT would benefit from more frequent simulations with scenarios that include ascent, orbit, and entry problems. Simulations should be conducted at JSC as well. Since the MMT resides in Houston during on-orbit operations, JSC simulations would be beneficial with respect to in-flight crises that require MMT intervention. Space Flight Training Division personnel should be responsible for the planning and execution of the simulations in the future as they are for crew and mission controller training.

3.3 Launch Controllers

A review of documentation outlining STS-107 launch controller training requirements was conducted. This documentation included the Launch Personnel Certification Plan, launch controller training certification records, and the STS-107 Terminal Countdown Demonstration Test (TCDT) training plan and post-TCDT report.

Training records indicate that the launch controllers were certified to work their respective positions for STS-107. All STS-107 training requirements for launch controllers were complete. TCDT documentation and post-TCDT report shows no issues with launch control team performance.

The analysis of training information supports the finding that the STS-107 launch controller training requirements for STS-107 were complete and they were adequately trained for their mission tasks.

3.4 Mission Performance

Since the majority of the STS-107 mission was completed prior to the loss of the vehicle, actual crew, launch controller, and flight controller readiness for flight can be surmised from how they performed their STS-107 mission duties. Launch countdown documentation, mission console logs, and Mission Control Center data were reviewed.

All operators of STS-107 performed satisfactorily during the launch countdown, launch, and subsequent flight. There were a few incorrect switch movements by the crew during the mission, including the configuration of an inter-communications switch and an accidental bump of a rotational hand controller (which affected the Orbiter's attitude) after the de-orbit burn but prior to Entry Interface. The inter-communications switch error was identified and then corrected by the crew; both the crew and Mission Control noticed the bump and took the necessary steps to place the Orbiter in the correct attitude. Neither of these events was a factor in the accident, nor are they considered training or performance issues.

Crew and mission controller actions were unremarkable prior to the loss of vehicle and crew. All actions were in accordance with entry procedures. A review of mission control data supports the finding that there were no crew or mission controller performance issues during the mission or in the moments leading up to loss of signal.

Following the loss of signal and unsuccessful attempts to contact the STS-107 crew, the Entry Flight Director declared a Space Shuttle contingency and implemented the JSC Contingency Plan documented in the Flight Control Operations Handbook.

4.0 Findings

1. Crew and controllers training requirements for STS-107 were completed and the all were adequately trained for their mission tasks.

2. Training records indicated flight controllers were qualified to work their respective positions for STS-107, but seven did not have current re-certification paperwork in their training folders. This contradicts the MOD CoFR and FRR documentation indicating personnel were trained and certified or would be trained and certified prior to the flight.

3. There were no crew or mission controller performance issues during the mission or in the moments leading up to loss of signal.

5.0 Conclusions

1. Crew training was not a factor in the loss of *Columbia* and the STS-107 crew.

2. Mission controller and launch controller training were not factors in the loss of *Columbia* and the STS-107 crew.

6.0 Observations

1. A thorough review of all mission controller certification records should be completed prior to a mission. This should be done early enough to allow time for those lacking current certifications to complete the requirements for them, or to allow replacement by a flight controller with a current certification.

2. Management should ensure the accuracy of the data represented at the Flight Readiness Review and before signing the Certificate of Flight Readiness.

3. Management should examine the flight control organization for causes or factors that might have resulted in several flight controllers not having current re-certifications while working a mission.

4. MOD should conduct MMT simulations with more frequency. These should include ascent, orbit, and entry scenarios. Simulations should be conducted at JSC and KSC. JSC simulations are beneficial with respect to in-flight issues that require MMT intervention. Space Flight Training Division personnel should be responsible for the planning and execution of the simulations as they are for crew and mission controller training.



Volume II
Appendix D.2
Payload Checklist

This appendix is a reproduction of the Payload Operations Checklist used by the STS-107 crew during on-orbit operations. It is reproduced here – at smaller than normal page size – to show the level of detailed instruction provided to the crew during on-orbit payload operations.

This is a NASA document and is published here as written, without editing by the Columbia Accident Investigation Board. The conclusions drawn in this report do not necessarily reflect the conclusions of the Board; when there is a conflict, the statements in Volume I of the Columbia Accident Investigation Board Report take precedence.

THIS PAGE INTENTIONALLY LEFT BLANK

Payload Checklist

Space Shuttle Program
FLIGHT DATA FILE

JSC–48068–107

Payload Operations Checklist

STS–107

Mission Operations Directorate Operations Division

Final, Rev A
June 7, 2002

National Aeronautics and Space Administration

Lyndon B. Johnson Space Center
Houston, Texas

Verify this is the correct version for the pending operation (training, simulation or flight).
Electronic copies of FDF books are available. URL: http://mod.jsc.nasa.gov/fdf

SSP Flight Data File **PAGE CHANGE NOTICE** JSC–48068–107

PAYLOAD OPS C/L STS–107	FINAL, REV A (June 7, 2002)

PCN–3 (Dec 20, 2002) Sheet 1 of 1

List of Implemented Change Requests (482s):

PL OPS–1726 PL OPS–1732
PL OPS–1727 PL OPS–1733
PL OPS–1728 PL OPS–1734
PL OPS–1729 PL OPS–1735
PL OPS–1730 PL OPS–1736
PL OPS–1731 PL OPS–1737

Incorporate the following:

1. Replace iii & iv
2. Replace 1–3 thru 1–6, 1–13 & 1–14, 1–63 thru 1–66, 1–75 & 1–76, 1–83 & 1–84
3. Replace 2–1 & 2–2
4. Replace 3–3 & 3–4
5. Replace 4–1 & 4–2
6. Replace 5–1 & 5–2
7. Replace section 6 (8 pgs)
8. Replace 8–1 & 8–2, 8–5 thru 8–8
9. Replace 9–3 & 9–4
10. Replace 10–3 & 10–4

Prepared by: _____ Book Manager _____ Lead, Cargo Support Operations Group

Approved by: _____ Chief, Cargo Integration and Operations Branch

Encl: 42 pages

File this PCN immediately behind the front cover as a permanent record

JSC–48068–107

MISSION OPERATIONS DIRECTORATE

PAYLOAD OPERATIONS CHECKLIST
STS–107

FINAL, REVISION A
June 7, 2002

PREPARED BY:

_____
Thomas M. Arnold
Book Manager

APPROVED BY:

_____ Robert D. Banfield
Lead, Cargo Support Operations Group

_____ Debbie D. Stapleton
Chief, Cargo Integration and Operations Branch

This document is under the configuration control of the Crew Procedures Control Board (CPCB). All proposed changes must be submitted on JSC Form 482 to DO3/FDF Manager.

Additional distribution of this book for official use must be requested in writing to DO3/FDF Manager. The request must include justification and requester's name, organization, position, and phone number. Contractor requests are made through the NASA or DOD organization supported. Deletions, reduction in quantity, or change of address may be submitted to DO3/FDF Management Office, 281–244–1184.

PL OPS/107/FIN A

Incorporates the following:			
482#:	PL OPS–1698A	PL OPS–1706	PL OPS–1712
	PL OPS–1699B	PL OPS–1707	PL OPS–1713
	PL OPS–1700C	PL OPS–1708	
	PL OPS–1703A	PL OPS–1709	
	PL OPS–1704B	PL OPS–1710	
	PL OPS–1705	PL OPS–1711	

AREAS OF TECHNICAL RESPONSIBILITY

Book Manager	DO53/T. Arnold	281–483–7431
FREESTAR	DO53/T. Arnold	281–483–7431
SPACEHAB	DO53/G. Humble	281–244–1070

PAYLOAD OPERATIONS CHECKLIST
STS–107

LIST OF EFFECTIVE PAGES

FINAL	04/12/02
REV A	06/07/02
PCN–1	06/25/02
PCN–2	11/15/02
PCN–3	12/20/02

Sign Off	* 107/FIN A	1–39	107/FIN A,2
ii	* 107/FIN A	1–40	107/FIN A,2
iii	* 107/FIN A,3	1–41	107/FIN A
iv	* 107/FIN A,3	1–42	107/FIN A,1
v	107/FIN A,1	1–43	107/FIN A
vi	107/FIN A	1–44	107/FIN A
1–1	107/FIN A	1–45	107/FIN A,1
1–2	107/FIN A	1–46	107/FIN A,1
1–3	107/FIN A,3	1–47	107/FIN A
1–4	107/FIN A,3	1–48	107/FIN A
1–5	107/FIN A,3	1–49	107/FIN A
1–6	107/FIN A,1	1–50	107/FIN A
1–7	107/FIN A	1–51	107/FIN A,1
1–8	107/FIN A	1–52	107/FIN A
1–9	107/FIN A,1	1–53	107/FIN A,2
1–10	107/FIN A	1–54	107/FIN A,2
1–11	107/FIN A	1–55	107/FIN A
1–12	107/FIN A	1–56	107/FIN A
1–13	107/FIN A,3	1–57	107/FIN A
1–14	107/FIN A	1–58	107/FIN A,1
1–15	107/FIN A	1–59	107/FIN A
1–16	107/FIN A	1–60	107/FIN A
1–17	107/FIN A	1–61	107/FIN A
1–18	107/FIN A	1–62	107/FIN A
1–19	107/FIN A	1–63	107/FIN A,3
1–20	107/FIN A,1	1–64	107/FIN A
1–21	107/FIN A	1–65	107/FIN A,3
1–22	107/FIN A	1–66	107/FIN A
1–23	107/FIN A	1–67	107/FIN A
1–24	107/FIN A	1–68	107/FIN A
1–25	107/FIN A	1–69	107/FIN A,1
1–26	107/FIN A	1–70	107/FIN A
1–27	107/FIN A,1	1–71	107/FIN A
1–28	107/FIN A	1–72	107/FIN A
1–29	107/FIN A	1–73	107/FIN A,1
1–30	107/FIN A	1–74	107/FIN A,1
1–31	107/FIN A	1–75	107/FIN A,2
1–32	107/FIN A	1–76	107/FIN A,3
1–33	107/FIN A	1–77	107/FIN A,2
1–34	107/FIN A,1	1–78	107/FIN A,2
1–35	107/FIN A	1–79	107/FIN A
1–36	107/FIN A	1–80	107/FIN A,1
1–37	107/FIN A,2	1–81	107/FIN A
1–38	107/FIN A,2	1–82	107/FIN A

* – Omit from flight book

1–83 ..... 107/FIN A,3
1–84 ..... 107/FIN A,1
2–1 ..... 107/FIN A
2–2 ..... 107/FIN A,3
3–1 ..... 107/FIN A
3–2 ..... 107/FIN A,1
3–3 ..... 107/FIN A,3
3–4 ..... 107/FIN A,3
4–1 ..... 107/FIN A
4–2 ..... 107/FIN A,3
5–1 ..... 107/FIN A
5–2 ..... 107/FIN A,3
6–1 ..... 107/FIN A
6–2 ..... 107/FIN A,3
6–3 ..... 107/FIN A
6–4 ..... 107/FIN A,3
6–5 ..... 107/FIN A,3
6–6 ..... 107/FIN A,3
6–7 ..... 107/FIN A,3
6–8 ..... 107/FIN A,3
7–1 ..... 107/FIN A
7–2 ..... 107/FIN A
7–3 ..... 107/FIN A
7–4 ..... 107/FIN A
8–1 ..... 107/FIN A,1
8–2 ..... 107/FIN A,3
8–3 ..... 107/FIN A
8–4 ..... 107/FIN A,1
8–5 ..... 107/FIN A,1
8–6 ..... 107/FIN A,3
8–7 ..... 107/FIN A,3
8–8 ..... 107/FIN A,3
9–1 ..... 107/FIN A
9–2 ..... 107/FIN A,2
9–3 ..... 107/FIN A,3
9–4 ..... 107/FIN A,3
9–5 ..... 107/FIN A,2
9–6 ..... 107/FIN A,1
9–7 ..... 107/FIN A
9–8 ..... 107/FIN A
10–1 ..... 107/FIN A
10–2 ..... 107/FIN A
10–3 ..... 107/FIN A
10–4 ..... 107/FIN A,3
10–5 ..... 107/FIN A,2
10–6 ..... 107/FIN A,2
10–7 ..... 107/FIN A
10–8 ..... 107/FIN A
10–9 ..... 107/FIN A
10–10 ..... 107/FIN A
10–11 ..... 107/FIN A
10–12 ..... 107/FIN A
11–1 ..... 107/FIN A
11–2 ..... 107/FIN A
11–3 ..... 107/FIN A
11–4 ..... 107/FIN A
11–5 ..... 107/FIN A
11–6 ..... 107/FIN A
11–7 ..... 107/FIN A
11–8 ..... 107/FIN A
11–9 ..... 107/FIN A
11–10 ..... 107/FIN A
11–11 ..... 107/FIN A
11–12 ..... 107/FIN A
12–1 ..... * 107/FIN A
12–2 ..... * 107/FIN A
CC 12–3 ..... * 107/FIN A
CC 12–4 ..... * 107/FIN A

PAYLOAD OPS CUE CARDS

TITLE	Ref. Page	Card No.
MEIDEX RECORDING LOG (Front)	CC 12–3	PL OPS–1a/107/O/A
(Back)	CC 12–4	PL OPS–1b/107/O/A

– Color pages for crew copy only
* – Omit from flight book

CONTENTS PAGE

FREESTAR 1–1
FREESTAR ACTIVATION 1–2
DEACTIVATION 1–3
SOLSE PGSC/BIA SETUP 1–4
STOW 1–5
SOLSE/HRIU ACTIVATION 1–6
SOLSE HEALTH CHECK 1–9
SETUP 1–19
SCIENCE 1–29
MONITOR 1–32
CLOSEOUT 1–35
IDLE 1–43
SOLSE/HRIU DEACT 1–46
SOLSE CONTINGENCY RECOVERY 1–49
SHUTDOWN 1–55
MEIDEX PGSC SETUP 1–58
HEATER ACT/HEALTH CHECK 1–60
CHECKOUT 1–62
SETUP 1–71
SCIENCE 1–73
CLOSEOUT 1–79
PRE–DEACTIVATION HEALTH CHECK 1–81
XYBION ACTIVATION 1–83
MEIDEX PGSC STOW 1–84

OARE 2–1
OARE ACT 2–2
DEACT 2–2

DEORBIT PREP 3–1
PAYLOAD DEACT 3–2
REACT 3–2
DEORBIT WAVEOFF 3–2
PAYLOAD ENT SW LIST/VERIF 3–3

CONTINGENCY EVA PL CONFIG 4–1
PRE–EVA PL CONFIG 4–2
POST–EVA PL CONFIG 4–2

ASC PWRDN RECOVERY 5–1
MIDDECK (A PWRDN) 5–2
SPACEHAB (B PWRDN) 5–2

PAYLOAD COMM MALFUNCTIONS 6–1

6.1 PL COMM
STS–107 COMM MALFUNCTION POINTS 6–2
6.1a S62 PDI DECOM FAIL 6–3

PL/DPS RECONFIG 7–1
PL/DPS RECONFIG 7–2

IN–FLIGHT MAINTENANCE (IFM) 8–1
PSP 1 COMMAND SIGNAL BYPASS 8–2
SSP 1 RECOVERY TABLE 8–4
2 RECOVERY TABLE 8–5
KU BAND SIGNAL PROCESSOR BYPASS FOR PL DIG DATA 8–6
SH PL MAX DATA RECOVERY 8–8

CRITICAL EQUIPMENT LOST 9–1
STS–107 BUS LOSS MATRIX 9–2
ELECTRICAL BUS LOSS IMPACTS 9–5
MDM LOSS IMPACTS 9–7

REFERENCE DATA 10–1
L12U SSP 1 10–2
FREESTAR SSP L12U SWITCH ASSIGNMENTS 10–3
L12L SSP 2 10–5
SPACEHAB SSP L12L SWITCH ASSIGNMENTS 10–6
C3A5 PAYLOAD SAFING 10–10
SPACEHAB C3A5 SWITCH ASSIGNMENTS 10–10
PGSC FAILURE RECOVERY OPTIONS 10–11

MEIDEX REFERENCE DATA 11–1
MEIDEX VISIBILITY TARGETS OBSERVATION FORM 11–3
SLANT VISIBILITY TARGETS 11–5

CUE CARD CONFIGURATION 12–1

FREESTAR

FREESTAR ACTIVATION 1–2
DEACTIVATION 1–3
SOLSE PGSC/BIA SETUP 1–4
STOW 1–5
SOLSE/HRIU ACTIVATION 1–6
SOLSE HEALTH CHECK 1–9
SETUP 1–19
SCIENCE 1–28
MONITOR 1–32
CLOSEOUT 1–35
IDLE 1–43
SOLSE/HRIU DEACT 1–46
SOLSE CONTINGENCY RECOVERY 1–49
SHUTDOWN 1–55
MEIDEX PGSC SETUP 1–58
HEATER ACT/HEALTH CHECK 1–60
CHECKOUT 1–62
SETUP 1–71
SCIENCE 1–73
CLOSEOUT 1–79
PRE–DEACTIVATION HEALTH CHECK 1–81
XYBION ACTIVATION 1–83
MEIDEX PGSC STOW 1–84

FREESTAR

FREESTAR ACTIVATION

1. COMMAND CONFIG

A1L S–BD PL CNTL – CMD
PSP CMD OUTPUT – PL UMB
PWR SEL – PSP
SYS – 1

2. DATA CONFIG
Verify PDI/PCMMU config 762
SM 62 PCMMU/PL COMM
TFL: 188
DECOM INPUT FMT FDA ENA
2 1 18
FPM: 508

NOTE
Expect 'S62 PDI DECOM FAIL' msg

DECOM 2 FDA ENA – ITEM 15 EXEC

If reqd, perform LOAD PCMMU FORMAT and LOAD PDI DECOM FORMAT (ORB OPS FS, COMM/INST)

3. PWR CONFIG
On MCC GO:

R1 PL PRI MNC – ON (tb–ON)
CAB – MNA(MNB)
L12U cb DOOR PWR CONT PWR DN ENA – op
HITCHHIKER AV PWR tb – bp
EXP PWR tb – bp
AV PWR – ON (mom) (tb–UP)

* If HITCHHIKER AV PWR tb – bp: *
* SM 62 PCMMU/PL COMM *
* If PDI DECOM 2 – (no ↑): *
* HITCHHIKER AV PWR tb fail, continue nominal ops *
* If PDI DECOM 2 – (↑): *
* HITCHHIKER AV PWR – OFF (pause), ON (hold 5 sec) (tb–UP) *
* If HITCHHIKER AV PWR tb – bp: *
* MCC *
* If HITCHHIKER AV PWR tb – UP: *
* Transient error, continue nominal ops *

HITCHHIKER EXP PWR – ON (mom) (tb–UP)

* If HITCHHIKER EXP PWR tb – bp: *
* MCC to verify POCC has exp pwr on indication *
* If POCC has exp pwr on indication: *
* HITCHHIKER EXP PWR tb fail, continue nominal ops *
* If POCC does not have exp pwr on indication: *
* HITCHHIKER EXP PWR – OFF (pause), ON (hold 5 sec) (tb–UP) *
* If HITCHHIKER EXP PWR tb – bp: *
* MCC *
* If HITCHHIKER EXP PWR tb – UP: *
* Transient error, continue nominal ops *

LPT PWR ENA 1 – ON (tb–bp)
2 – ON (tb–bp)

NOTE
Talkbacks will go gray when POCC cmds pwr to LPT (approximately 10–20 min after activation)

Notify MCC, FREESTAR activated

FREESTAR DEACTIVATION

On MCC GO:

L12U 1. CHECK PWR CONFIG
HITCHHIKER EXP PWR tb – UP
AV PWR tb – UP

LPT PWR ENA 1 tb – bp
2 tb – bp

2. PWR OFF FREESTAR
LPT PWR ENA 2 – OFF
1 – OFF

HITCHHIKER EXP PWR – OFF (mom) (tb–bp)

NOTE
Expect 'PDI DECOM FAIL' msg

HITCHHIKER AV PWR – OFF (mom) (tb–bp)
cb DOOR PWR CONT PWR DN ENA – op

3. Notify MCC, FREESTAR deactivated

SOLSE PGSC/BIA SETUP

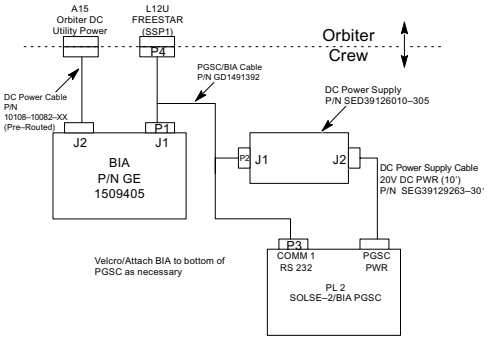
1. CONFIG PGSC/BIA
Unstow:

L11 BIA
PGSC/BIA cable
MF28O DC Power Supply
DC Power Supply cable
PL2 SOLSE–2/BIA PGSC
PCMCIA RF LANCard
MF57K Late update PCMCIA card

Velcro/Attach BIA to bottom of PGSC as necessary

2. VERIFYING SWITCH CONFIG
A15 DC UTIL PWR MNC – OFF

3. CONFIGURING PGSC/BIA
Connect PGSC/BIA cable connectors per diagram



4. BIA PWRUP

BIA BIA PWR – OFF
ENABLE 1 – OFF
2 – OFF

A15 DC UTIL PWR MNC – ON
PWR SUPPLY – ON (lt green)

BIA BIA PWR – ON

5. PGSC PWRUP

PGSC PGSC PWR – ON
Windows initialized
Insert late update PCMCIA card
Run 'Shuttle Apps/Late PGSC Update'
Shut down PGSC
Remove late update card
Insert PCMCIA RF LANCard into PGSC

SOLSE PGSC/BIA STOW

PGSC 1. Shut down Windows
2. PGSC pwr – off
3. DC PWR SUPPLY – OFF (lt not lt)
BIA 4. BIA PWR – OFF
A15 5. DC UTIL PWR MNC – OFF
A15/BIA 6. Disconnect DC pwr cable
L12U/ PGSC/BIA/ Pwr Adapter 7. Disconnect PGSC/BIA cable
8. Disconnect DC Power Supply cable
MF28O 9. Stow PL2 PGSC, DC Power Cable, DC Power Supply
L11 10. Stow BIA, PGSC/BIA cable

SOLSE/HRIU ACTIVATION

NOTE
All SOLSE and HRIU commands require <CTRL–Y> following command selection to execute command.

To clear an error message from active screen, exit to main menu and return to desired screen

* If at any time during procedure execution error *
* messages display in lower left corner of screen, *
* it is possible that an HRIU reset has occurred. *
* To determine if HRIU is reset, if not on *
* HH–JR/SOLSE–2 System Page: *
* Press <ESC> to return to main menu *
* HH–JR/SOLSE–2 Main Menu *
* Sel HH–JR/SOLSE–2 System Page *
* HH–JR/SOLSE–2 System Page *
* If HRIU Status – initialized: *
* Return to nominal ops *
* If HRIU Status – reset: *
* Notify MCC *
* Perform SOLSE CONTINGENCY *
* RECOVERY *

1. CHECK BIA CONFIG AND HRIU POWER
BIA PWR – ON
ENABLE 2 – ON
Log MET: ____/____:____:____

2. SOFTWARE STARTUP
Start SOLSE software:
Go to Shuttle Apps Folder
Sel SOLSE–2 Icon
Follow directions on screen

HH–JR/SOLSE–2 Main Menu
Sel Update MET/GMT

Update MET/GMT
Sel UPDATE MET
Enter Current MET, press enter
Press <ESC> to return to main menu

HH–JR/SOLSE–2 Main Menu
Sel Data Recording and Storage Setup

Data Recording and Storage Setup
HRIU Errors – ON
HRIU Engineering Data – ON
HRIU Diagnostic Data – ON
HRIU Customer Data – ON

* If HRIU Errors – OFF: *
* HRIU Errors – ENAB (ON) *
* *
* If HRIU Engineering Data – OFF: *
* HRIU Engineering Data – ENAB (ON) *
* *
* If HRIU Diagnostic Data – OFF: *
* HRIU Diagnostic Data – ENAB (ON) *
* *
* If HRIU Customer Data – OFF: *
* HRIU Customer Data – ENAB (ON) *

Record PGSC Recording Status (File _____)

Press <ESC> to return to main menu

3. HH–JR STATUS ENABLE
HH–JR/SOLSE–2 Main Menu
Sel HH–JR/SOLSE–2 System Page

HH–JR/SOLSE–2 System Page
HH–JR Polling – ENAB (ON)

* If HH–JR Polling OFF after enable attempt: *
* Reattempt two times *
* If still no joy: *
* Notify MCC *
* Press <ESC> to return to main menu *
* Sel Exit Program, follow directions on screen *
* BIA Enable 2 – OFF *
* Perform hard reboot of PGSC: *
* From Start Menu, Sel Shutdown *
* When Shutdown complete, PGSC pwr – on *
* BIA Enable 2 – ON *
* Repeat steps 1–3 *
* If no joy, MCC *

Commands transmitted incrementing
Data Storage Status = ENABLED

NOTE
Engineering packets are transmitted from payload to PGSC once every 45 sec; depending upon when command is acknowledged during the cycle. It could take up to 45 sec to see a telemetry verification of command sent

After 45 sec:
HRIU Status = initialized

4. PWR HTR & DOOR POWER
Heater & Door Power – ENAB

After 45 sec,
Heater & Door Power – ON

5. RECORD PAYLOAD STATUS
Bus Voltage: >_____ Volts
Bus Current: >_____ Amps
Canister Pressure: _____ PSIA
Door Position: (open/closed) _____ Volts
HRIU temp: _____ °C
HH–JR LEP: _____ °C
Heat Pipe: _____ °C
Bulkhead: _____ °C
Heatsink: _____ °C

Voice payload status values to ground
Notify MCC, SOLSE/HRIU ACTIVATION complete

6. EXIT POLLING & SOFTWARE
HH–JR Polling – DISA (wait ≤ 45 sec, OFF)
Press <ESC> to return to main menu

HH–JR/SOLSE–2 Main Menu
Sel Exit Program, follow directions on screen
From Start Menu, Sel Shutdown

NOTE
SOLSE PGSC may be deactivated when SOLSE software is not in use.

BIA power is reqd for SOLSE heater power. BIA must remain powered from SOLSE activation to SOLSE deactivation unless otherwise instructed

SOLSE HEALTH CHECK

NOTE
All SOLSE and HRIU commands require <CTRL–Y> following command selection to execute command.

Once every 30 sec there is a brief period in which commands to payload will not be accepted. If "S_CMD(L_CMD) Status is NoGo/Wait. Cannot send command to SOLSE(LORE)" message appears at any time after executing S_Cmd Execute or L_Cmd Execute, resend rejected command.

To clear an error message from active screen, exit to main menu and return to desired screen

* If at any time during procedure execution error *
* messages display in lower left corner of screen, *
* it is possible that an HRIU reset has occurred. *
* To determine if HRIU is reset, if not on *
* HH–JR/SOLSE–2 System Page: *
* Press <ESC> to return to main menu *
* HH–JR/SOLSE–2 Main Menu *
* Sel HH–JR/SOLSE–2 System Page *
* HH–JR/SOLSE–2 System Page *
* If HRIU Status – initialized: *
* Return to nominal ops *
* If HRIU Status – reset: *
* Notify MCC *
* Perform SOLSE CONTINGENCY *
* RECOVERY *

1. CHECK BIA CONFIG AND HRIU POWER
BIA PWR – ON
ENABLE 2 – ON

2. SOFTWARE STARTUP
Start SOLSE software:
Go to Shuttle Apps Folder
Sel SOLSE–2 Icon
Follow directions on screen

HH–JR/SOLSE–2 Main Menu
Software MET Time within 10 sec of actual MET

* If Software MET Time > 10 sec off *
* actual MET: *
* Sel Update MET/GMT *
* Update MET/GMT *
* Sel UPDATE MET *
* Enter Current MET, press enter *
* Press <ESC> to return to main menu *

HH–JR/SOLSE–2 Main Menu
Sel Data Recording and Storage Setup

HH–JR/SOLSE–2 Data Storage Setup
HRIU Errors – ON
HRIU Engineering Data – ON
HRIU Diagnostic Data – ON
HRIU Customer Data – ON

* If HRIU Errors – OFF: *
* HRIU Errors – ENAB (ON) *
* *
* If HRIU Engineering Data – OFF: *
* HRIU Engineering Data – ENAB (ON) *
* *
* If HRIU Diagnostic Data – OFF: *
* HRIU Diagnostic Data – ENAB (ON) *
* *
* If HRIU Customer Data – OFF: *
* HRIU Customer Data – ENAB (ON) *

3. SOLSE PGSC RECORDING STATUS AND STORAGE CHECK

PGSC Record MET, PGSC Recording Status (File #), and Total Usage in table

MET	File Number	Total Usage	Percent Used
___/___:___:___		MB	% used
___/___:___:___		MB	% used
___/___:___:___		MB	% used
___/___:___:___		MB	% used
___/___:___:___		MB	% used
___/___:___:___		MB	% used
___/___:___:___		MB	% used
___/___:___:___		MB	% used
___/___:___:___		MB	% used
___/___:___:___		MB	% used
___/___:___:___		MB	% used
___/___:___:___		MB	% used
___/___:___:___		MB	% used
___/___:___:___		MB	% used
___/___:___:___		MB	% used
___/___:___:___		MB	% used
___/___:___:___		MB	% used
___/___:___:___		MB	% used
___/___:___:___		MB	% used
___/___:___:___		MB	% used

Press <ESC> to return to main menu

4. HH–JR STATUS ENABLE

HH–JR/SOLSE–2 Main Menu
Sel HH–JR/SOLSE–2 System Page

HH–JR/SOLSE–2 System Page
HH–JR Polling – ENAB (ON)

* If HH–JR Polling OFF after enable attempt: *
* Reattempt two times *
* If still no joy: *
* Notify MCC *
* Press <ESC> to return to main menu *
* Sel Exit Program, follow directions on screen *
* BIA Enable 2 – OFF *
* Perform hard reboot of PGSC: *
* From Start Menu, Sel Shutdown *
* When Shutdown complete, PGSC pwr – on *
* BIA Enable 2 – ON *
* Repeat steps 2–4 *
* If no joy, MCC *

Commands transmitted incrementing
Data Storage Status – ENABLED
After 45 sec:
HRIU Status – initialized
Heater & Door Power – ON

5. SOLSE STATUS CHECK

HH–JR/SOLSE–2 System Page
Record Payload Status and Voice Values to MCC

Nominal Value Range (SOLSE Primary Pwr Off)	
Bus Voltage:	28 ± 1 V
Bus Current:	0.196 ± .05 Amps
Canister Pressure:	15.257 ± 0.6 PSIA
Door Position:	0.840 ± 0.2 V
HRIU Temp:	0–40°C
HH–JR LEP:	0–40°C
Heat Pipe:	0–40°C
Bulkhead:	0–40°C
Heatsink:	0–40°C

MET	___/___:___:___	___/___:___:___
Bus Voltage:	Volts	Volts
Bus Current:	Amps	Amps
Canister Pressure:	PSIA	PSIA
Door Position:	Open/Closed_____Volts	Open/Closed_____Volts
HRIU Temp:	°C	°C
HH–JR LEP:	°C	°C
Heat Pipe:	°C	°C
Bulkhead:	°C	°C
Heatsink:	°C	°C

MET	___/___:___:___	___/___:___:___
Bus Voltage:	Volts	Volts
Bus Current:	Amps	Amps
Canister Pressure:	PSIA	PSIA
Door Position:	Open/Closed_____Volts	Open/Closed_____Volts
HRIU Temp:	°C	°C
HH–JR LEP:	°C	°C
Heat Pipe:	°C	°C
Bulkhead:	°C	°C
Heatsink:	°C	°C

MET	___/___:___:___	___/___:___:___
Bus Voltage:	Volts	Volts
Bus Current:	Amps	Amps
Canister Pressure:	PSIA	PSIA
Door Position:	Open/Closed_____Volts	Open/Closed_____Volts
HRIU Temp:	°C	°C
HH–JR LEP:	°C	°C
Heat Pipe:	°C	°C
Bulkhead:	°C	°C
Heatsink:	°C	°C

MET	___/___:___:___	___/___:___:___
Bus Voltage:	Volts	Volts
Bus Current:	Amps	Amps
Canister Pressure:	PSIA	PSIA
Door Position:	Open/Closed_____Volts	Open/Closed_____Volts
HRIU Temp:	°C	°C
HH–JR LEP:	°C	°C
Heat Pipe:	°C	°C
Bulkhead:	°C	°C
Heatsink:	°C	°C

MET	___/___:___:___	___/___:___:___
Bus Voltage:	Volts	Volts
Bus Current:	Amps	Amps
Canister Pressure:	PSIA	PSIA
Door Position:	Open/Closed_____Volts	Open/Closed_____Volts
HRIU Temp:	°C	°C
HH–JR LEP:	°C	°C
Heat Pipe:	°C	°C
Bulkhead:	°C	°C
Heatsink:	°C	°C

MET	___/___:___:___	___/___:___:___
Bus Voltage:	Volts	Volts
Bus Current:	Amps	Amps
Canister Pressure:	PSIA	PSIA
Door Position:	Open/Closed_____Volts	Open/Closed_____Volts
HRIU Temp:	°C	°C
HH–JR LEP:	°C	°C
Heat Pipe:	°C	°C
Bulkhead:	°C	°C
Heatsink:	°C	°C

6. SOLSE POWERUP & CALIBRATION, if reqd
Execute Package if step 6 reqd
If reqd, proceed with step 6; otherwise, go to step 10

NOTE
SOLSE Health Calibration will be performed periodically during the mission when SOLSE operations are not planned for a span of three days or more. Door will not be opened during calibration

Set Egg Timer to 00:15:00
HH–JR/SOLSE–2 System Page
All temperatures (five) except TEC Temp: 0°–40°C

If temperatures – 0°–40°C:
SOLSE Primary Power – ENAB (wait ≤ 45 sec, ON)

* If temperatures < 0° or > 40°C *
* Notify MCC *
* On MCC GO: *
* SOLSE Primary Power – ENAB *
* (wait 45 sec, ON) *

* If after 45 sec, SOLSE Primary Power – OFF: *
* Notify MCC *
* Reattempt cmd *
* If still no joy: *
* Notify MCC *
* HH–JR Polling – DISA (wait 45 sec, OFF) *
* Press <ESC> to return to main menu *
* Sel Exit Program, follow directions on screen *
* BIA Enable 2 – OFF *
* Perform hard reboot of PGSC: *
* From Start Menu, Sel Shutdown *
* When Shutdown complete, PGSC pwr – on *
* BIA Enable 2 – ON *
* Record MET ___/___:___:___ *
* Repeat steps 1,2,4,6 *

After 1 min,
SOLSE Packets Rcvd – incremented to 2 or greater

* If after 1 min, SOLSE Packets Rcvd = 0 *
* MCC *

After 1 min 45 sec,
LORE Packets Rcvd – incremented to 2 or greater

* If after 1 min 45 sec, LORE Packets Rcvd = 0 *
* Notify MCC, continue *

Press <ESC> to return to main menu

HH–JR/SOLSE–2 Main Menu
Sel SOLSE/LORE Telemetry Page

SOLSE/LORE Telemetry Page
SOLSE Status – In Sync
LORE Status – In Sync

NOTE
S_Mode will remain in Stby until four packets are received (at ~100 sec after command receipt). When four packets are received S_Mode will indicate Cal

~100 sec after SOLSE Primary Power Enable,
LORE Packets Rcvd ≥ 4
SOLSE Packets Rcvd ≥ 4
S_Mode – Cal

00:15:00 Start Egg Timer

Notify MCC, SOLSE Cal Mode Initiated

SOLSE TEC Temp: –10°C ± 1°C
S_Filter: VIS (if UV, MCC)
S_Fltr Stat: OK (if ERROR, MCC)

NOTE
SOLSE Cal duration = 15 min. No payload commanding reqd during cal. After cal, SOLSE packets rcvd = ~68. Packets will continue to increment following conclusion of cal

00:00:00 SOLSE Status – In Sync
SOLSE Packets Rcvd – ~68
S_Mode – Stby

* If after 15 min, S_Mode – Cal: *
* Notify MCC *
* Press <ESC> to return to main menu *
* HH–JR/SOLSE–2 Main Menu *
* Sel HH–JR/SOLSE–2 System Page *
* HH–JR/SOLSE–2 System Page *
* B2–Standby Mode – PULSE (wait ≤ 45 sec, ON) *
* After 1 min, B2–Standby Mode – OFF *
* Press <ESC> to return to main menu *
* HH–JR/SOLSE–2 Main Menu *
* Sel SOLSE/LORE Telemetry Page *
* SOLSE/LORE Telemetry Page *
* SOLSE Status – In Sync *
* S_Mode – Stby *
* If S_Mode – Cal: *
* Notify MCC *

Press <ESC> to return to main menu

7. SOLSE/LORE DATA DUMP, if reqd
Execute Package if step 7 reqd
If reqd, proceed with step 7; otherwise, go to step 8

NOTE
Data Dump will be performed following calibration

A4 Set Egg Timer to 00:08:00

HH–JR/SOLSE–2 Main Menu
Sel SOLSE/LORE Command Page

a. LORE Data Dump
SOLSE/LORE Command Page
L_Cmd Status – GO/OK
L_Enter Dump Mode – Send (wait ≤ 45 sec, Pending)
L_Execute Cmd Pending – Send (Sent)
Wait ≤ 45 sec, L_Last Cmd Executed: L_Enter Dump Mode

* If after 1 min cmd still pending, reattempt cmd *

NOTE
LORE dark–image dump will complete in 8 min

b. SOLSE Data Dump
S_Cmd Status – GO/OK

S_Enter Dump Mode – Send (wait ≤ 45 sec, Pending)
S_Execute Cmd Pending – Send (Sent)
Wait ≤ 45 sec, S_Last Cmd Executed: S_Enter Dump Mode

* If after 1 min cmd still pending, reattempt cmd *

NOTE
SOLSE post–calibration dump will complete in 4 min

00:08:00 Initiate Egg Timer

c. Status Check
Press <ESC> to return to main menu

HH–JR/SOLSE–2 Main Menu
Sel SOLSE/LORE Telemetry Page

SOLSE/LORE Telemetry Page
SOLSE Status – In Sync
S_Mode – Dump
LORE Status – In Sync
L_Mode – Sci

NOTE
During dump mode, L_Mode will always indicate Sci

d. Dump Completion
00:00:00 L_Mode – Stby
S_Mode – Stby

* If S_Mode – Dump: *
* Press <ESC> to return to main menu *
* HH–JR/SOLSE–2 Main Menu *
* Sel HH–JR/SOLSE–2 System Page *
* HH–JR/SOLSE–2 System Page *
* B2–Standby Mode – PULSE (wait ≤ 45 sec) (ON) *
* Press <ESC> to return to main menu *
* HH–JR/SOLSE–2 Main Menu *
* Sel SOLSE/LORE Telemetry Page *
* SOLSE/LORE Telemetry Page *
* SOLSE Status – In Sync *
* S_Mode – Stby *

Press <ESC> to return to main menu

8. SOLSE/LORE SOFTWARE SHUTDOWN
HH–JR/SOLSE–2 Main Menu
Sel SOLSE/LORE Command Page

a. SOLSE Shutdown
SOLSE/LORE Command Page
S_Cmd Status – GO/OK
S_Shutdown – Send (wait ≤ 45 sec, Pending)
S_Execute Cmd Pending – Send (Sent)
Wait ≤ 45 sec, S_Last Cmd Executed: S_Shutdown

* If after 1 min cmd still pending, reattempt cmd *
* If after 1 min, still no joy: *
* Notify MCC *

b. LORE Shutdown
L_Cmd Status – GO/OK

L_Shutdown – Send (wait ≤ 45 sec, Pending)
L_Execute Cmd Pending – Send (Sent)
Wait ≤ 45 sec, L_Last Cmd Executed: L_Shutdown

* If after 1 min cmd still pending, reattempt cmd *
* If after 1 min, still no joy: *
* Notify MCC *

Press <ESC> to return to main menu

c. Shutdown Verification
HH–JR/SOLSE–2 Main Menu
Sel SOLSE/LORE Telemetry Page

NOTE
SOLSE and LORE Intensity Words progressively fill with asterisks after shutdown command is acknowledged. It may take up to 1 min for asterisks to begin to appear. Final shutdown is indicated when entire field is asterisks

SOLSE/LORE Telemetry Page
SOLSE and LORE Intensity Words = all asterisks

* If after 90 sec, if SOLSE and LORE Intensity Words *
* not all asterisks, repeat step 8a and/or 8b as reqd *

Press <ESC> to return to main menu

9. SOLSE POWERDOWN
Press <ESC> to return to main menu
HH–JR/SOLSE–2 Main Menu
Sel HH–JR/SOLSE–2 System Page

HH–JR/SOLSE–2 System Page
HH–JR Polling – ON
Commands transmitted incrementing
HRIU Status = initialized

SOLSE Primary Power – DISA (wait ≤ 45 sec, OFF)

10. EXIT POLLING & SOFTWARE
HH–JR Polling – DISA (wait ≤ 45 sec, OFF)
Press <ESC> to return to main menu

HH–JR/SOLSE–2 Main Menu
Sel Exit Program, follow directions on screen
Return to Windows

11. FILE TRANSFER

NOTE
Refer to step 3 for most recent data file

Copy most recent SOLSE data file (C:\solse\PGSCdata.00X) and log file (C:\solse2\solse.log) to OCA machine (STS–1) via network.
Downlink location: C:\oca–down\payloads\solse

If network unavailable:
Use PCMCIA card to copy files to OCA machine (STS–1)
Ref: OCA DOWNLINK VIA GROUND COMMAND (ORB OPS, PGSC)

From Start Menu, Sel Shutdown

NOTE
SOLSE PGSC may be deactivated when SOLSE software is not in use.

BIA power is reqd for SOLSE heater power. BIA must remain powered from SOLSE activation to SOLSE Deactivation unless otherwise instructed

SOLSE SETUP

NOTE
Setup must be initiated NLT Terminator Rise – 50 min (per Execute Package).

All SOLSE and HRIU commands require <CTRL–Y> following command selection to execute command.

Once every 30 sec, there is a brief period in which commands to payload will not be accepted. If "S_CMD(L_CMD) Status is NoGo/Wait. Cannot send command to SOLSE(LORE)" message appears at any time after executing S_Cmd Execute or L_Cmd Execute, resend rejected command.

To clear error message from active screen, exit to main menu and return to desired screen

* If at any time during procedure execution error messages display in lower left corner of screen, it is possible that an HRIU reset has occurred. To determine if HRIU is reset, if not on HH–JR/SOLSE–2 System Page:
  Press <ESC> to return to main menu
  HH–JR/SOLSE–2 Main Menu
  Sel HH–JR/SOLSE–2 System Page
  HH–JR/SOLSE–2 System Page
  If HRIU Status – initialized:
    Return to nominal ops
  If HRIU Status – reset:
    Notify MCC
    Perform SOLSE CONTINGENCY RECOVERY

1. P/TV CHECK, if reqd
Execute Pack if step 1 reqd
If reqd, P/TV11 SOLSE, SETUP (PHOTO/TV FS, SCENES) complete; otherwise, proceed to step 2

2. ATTITUDE CHECK
Time reqd to be in attitude for SOLSE SCIENCE per Attitude Timeline

3. CONFIG BIA & FLUSH HRIU BUFFER
PGSC SOLSE–2 software not on
BIA PWR – ON
ENABLE 2 – OFF (wait 5 sec)
ENABLE 2 – ON

Log MET:
____/____:____:____ ____/____:____:____ ____/____:____:____
____/____:____:____ ____/____:____:____ ____/____:____:____
____/____:____:____ ____/____:____:____ ____/____:____:____
____/____:____:____ ____/____:____:____ ____/____:____:____
____/____:____:____ ____/____:____:____ ____/____:____:____

PGSC 4. SOFTWARE STARTUP
Start SOLSE software:
Go to Shuttle Apps Folder
Sel SOLSE–2 Icon
Follow directions on screen

HH–JR/SOLSE–2 Main Menu
Software MET Time within 10 sec of actual MET

* If Software MET Time > 10 sec off actual MET:
  Sel Update MET/GMT
  Update MET/GMT
  Sel UPDATE MET
  Enter Current MET, press enter
  Press <ESC> to return to main menu

HH–JR/SOLSE–2 Main Menu
Sel Data Recording and Storage Setup

HH–JR/SOLSE–2 Data Storage Setup Page
HRIU Errors – ON
HRIU Engineering Data – ON
HRIU Diagnostic Data – ON
HRIU Customer Data – ON

* If HRIU Errors – OFF:
  HRIU Errors – ENAB (ON)
* If HRIU Engineering Data – OFF:
  HRIU Engineering Data – ENAB (ON)
* If HRIU Diagnostic Data – OFF:
  HRIU Diagnostic Data – ENAB (ON)
* If HRIU Customer Data – OFF:
  HRIU Customer Data – ENAB (ON)

Record MET and PGSC Recording Status (File #) in table

MET	File Number	MET	File Number
____/____:____:____		____/____:____:____	
____/____:____:____		____/____:____:____	
____/____:____:____		____/____:____:____	
____/____:____:____		____/____:____:____	
____/____:____:____		____/____:____:____	
____/____:____:____		____/____:____:____	
____/____:____:____		____/____:____:____	
____/____:____:____		____/____:____:____	
____/____:____:____		____/____:____:____	
____/____:____:____		____/____:____:____	
____/____:____:____		____/____:____:____	
____/____:____:____		____/____:____:____	

Press <ESC> to return to main menu

5. HH–JR STATUS ENABLE
HH–JR/SOLSE–2 Main Menu
Sel HH–JR/SOLSE–2 System Page

HH–JR/SOLSE–2 System Page
HH–JR Polling – ENAB (ON)

* If HH–JR Polling – OFF after enable attempt:
  Reattempt two times
  If still no joy:
    Notify MCC
    Press <ESC> to return to main menu
    Sel Exit Program, follow directions on screen
    BIA Enable 2 – OFF
    Perform hard reboot of PGSC:
      From Start Menu, Sel Shutdown
      When Shutdown complete, PGSC pwr – on
    BIA Enable 2 – ON
    Repeat steps 4–5
    If still no joy, MCC

Commands transmitted incrementing
Data Storage Status – ENABLED
After 45 sec:
HRIU Status – initialized
Heater & Door Power – ON

6. SOLSE STATUS CHECK
HH–JR/SOLSE–2 System Page
Record Payload Status in Table

Nominal Value Range (SOLSE Primary Pwr Off)	
Bus Voltage:	28 ± 1 V
Bus Current:	0.196 ± .05 Amps
Canister Pressure:	15.257 ± 0.6 PSIA
Door Position:	2.5 Volts
HRIU Temp:	0–40°C
HH–JR LEP:	0–40°C
Heat Pipe:	0–40°C
Bulkhead:	0–40°C
Heatsink:	0–40°C

MET	____/____:____:____	____/____:____:____
Bus Voltage:	Volts	Volts
Bus Current:	Amps	Amps
Canister Pressure:	PSIA	PSIA
Door Position:	Open/Closed_____Volts	Open/Closed_____Volts
HRIU Temp:	°C	°C
HH–JR LEP:	°C	°C
Heat Pipe:	°C	°C
Bulkhead:	°C	°C
Heatsink:	°C	°C

MET	____/____:____:____	____/____:____:____
Bus Voltage:	Volts	Volts
Bus Current:	Amps	Amps
Canister Pressure:	PSIA	PSIA
Door Position:	Open/Closed_____Volts	Open/Closed_____Volts
HRIU Temp:	°C	°C
HH–JR LEP:	°C	°C
Heat Pipe:	°C	°C
Bulkhead:	°C	°C
Heatsink:	°C	°C

MET	____/____:____:____	____/____:____:____
Bus Voltage:	Volts	Volts
Bus Current:	Amps	Amps
Canister Pressure:	PSIA	PSIA
Door Position:	Open/Closed_____Volts	Open/Closed_____Volts
HRIU Temp:	°C	°C
HH–JR LEP:	°C	°C
Heat Pipe:	°C	°C
Bulkhead:	°C	°C
Heatsink:	°C	°C

MET	____/____:____:____	____/____:____:____
Bus Voltage:	Volts	Volts
Bus Current:	Amps	Amps
Canister Pressure:	PSIA	PSIA
Door Position:	Open/Closed_____Volts	Open/Closed_____Volts
HRIU Temp:	°C	°C
HH–JR LEP:	°C	°C
Heat Pipe:	°C	°C
Bulkhead:	°C	°C
Heatsink:	°C	°C

MET	____/____:____:____	____/____:____:____
Bus Voltage:	Volts	Volts
Bus Current:	Amps	Amps
Canister Pressure:	PSIA	PSIA
Door Position:	Open/Closed_____Volts	Open/Closed_____Volts
HRIU Temp:	°C	°C
HH–JR LEP:	°C	°C
Heat Pipe:	°C	°C
Bulkhead:	°C	°C
Heatsink:	°C	°C

MET	____/____:____:____	____/____:____:____
Bus Voltage:	Volts	Volts
Bus Current:	Amps	Amps
Canister Pressure:	PSIA	PSIA
Door Position:	Open/Closed_____Volts	Open/Closed_____Volts
HRIU Temp:	°C	°C
HH–JR LEP:	°C	°C
Heat Pipe:	°C	°C
Bulkhead:	°C	°C
Heatsink:	°C	°C

Voice telemetry values from table to MCC

7. VENT VALVE OPENING, if reqd
If first door opening, proceed with step 7; otherwise, go to step 8
HH–JR/SOLSE–2 System Page
Vent Command – OPEN (wait 45 sec, OPEN)

8. SOLSE POWERUP & CALIBRATION
A4 Set Egg Timer to 00:15:00

HH–JR/SOLSE–2 System Page
All temperatures (five) except TEC Temp: 0°C–40°C

If temperatures – 0°C–40°C,
SOLSE Primary Power – ENAB (wait 45 sec, ON)

* If temperatures < 0°C or > 40°C, *
* Notify MCC *
* On MCC GO: *
* SOLSE Primary Power – ENAB (ON) *

* If after 45 sec, SOLSE Primary Power – OFF: *
* Notify MCC *
* Reattempt cmd *
* If still no joy: *
* Notify MCC *
* HH–JR Polling – DISA (wait ≤ 45 sec, OFF) *
* Press <ESC> to return to main menu *
* Sel Exit Program, follow directions on screen *
* BIA Enable 2 – OFF *
* Perform hard reboot of PGSC: *
* From Start Menu, Sel Shutdown *
* When Shutdown complete, PGSC pwr – on *
* BIA Enable 2 – ON *
* Repeat steps 4,5,8 *

After 1 min,
SOLSE Packets Rcvd – incremented to 2 or greater

* If after 1 min, SOLSE Packets Rcvd = 0: *
* MCC *

After 1 min 45 sec,
LORE Packets Rcvd – incremented to 2 or greater

* If after 1 min 45 sec, LORE Packets Rcvd = 0: *
* Notify MCC, continue *

Press <ESC> to return to main menu

HH–JR/SOLSE–2 Main Menu
Sel SOLSE/LORE Telemetry Page

SOLSE/LORE Telemetry Page
SOLSE Status – In Sync
LORE Status – In Sync

NOTE
S_Mode will remain in Stby until four packets are received (at ~100 sec after command receipt). When four packets are received S_Mode will indicate Cal

~100 sec after SOLSE Primary Power Enable:
LORE Packets Rcvd ≥ 4
SOLSE Packets Rcvd ≥ 4
S_Mode – Cal

00:15:00 Start Egg Timer

Notify MCC, SOLSE Cal Mode Initiated

SOLSE TEC Temp: –10°C ± 1°C
S_Filter: VIS (if UV, MCC)
S_Fltr Stat: OK (if ERROR, MCC)

9. SOLSE CALIBRATION END

NOTE
SOLSE Cal duration = 15 min. No payload commanding reqd during cal. After cal, SOLSE Packets Rcvd = ~68. Packets will continue to increment following conclusion of cal

00:00:00 SOLSE Status – In Sync
SOLSE Packets Rcvd – ~68
S_Mode – Stby

* If after 15 min S_Mode – Cal: *
* Notify MCC *
* Press <ESC> to return to main menu *
* HH–JR/SOLSE–2 Main Menu *
* Sel HH–JR/SOLSE–2 System Page *
* HH–JR/SOLSE–2 System Page *
* B2–Standby Mode – PULSE (wait ≤ 45 sec, ON) *
* After 1 min, B2–Standby Mode – OFF *
* Press <ESC> to return to main menu *
* HH–JR/SOLSE–2 Main Menu *
* Sel SOLSE/LORE Telemetry Page *
* SOLSE/LORE Telemetry Page *
* SOLSE Status – In Sync *
* S_Mode – Stby *
* If S_Mode – Cal: *
* Notify MCC *

10. SOLSE DATA CHECK
Record number of SOLSE and LORE Packets Rcvd:

MET	SOLSE Packets Rcvd	LORE Packets Rcvd
___/____:____:____		
___/____:____:____		
___/____:____:____		
___/____:____:____		
___/____:____:____		
___/____:____:____		
___/____:____:____		
___/____:____:____		
___/____:____:____		
___/____:____:____		
___/____:____:____		
___/____:____:____		
___/____:____:____		
___/____:____:____		
___/____:____:____		
___/____:____:____		
___/____:____:____		
___/____:____:____		
___/____:____:____		
___/____:____:____		
___/____:____:____		
___/____:____:____		
___/____:____:____		
___/____:____:____		

Voice number of SOLSE and LORE Data Packets Rcvd to ground

Press <ESC> to return to main menu

11. VENT VALVE CLOSING
HH–JR/SOLSE–2 Main Menu
Sel HH–JR/SOLSE–2 System Page

HH–JR/SOLSE–2 System Page

Vent Command – CLOSE

* If Vent Command – OPEN: *
* Vent Command – CLOSE (wait ≤ 45 sec, CLOSED) *

Press <ESC> to return to main menu

12. SOLSE FILTER TOGGLE
HH–JR/SOLSE–2 Main Menu
Sel SOLSE/LORE Telemetry Page
SOLSE/LORE Telemetry Page
Correct filter in place per Execute Package

If correct filter in place, notify MCC SOLSE SETUP complete and proceed to SOLSE SCIENCE

If incorrect filter in place:
Press <ESC> to return to main menu

HH–JR/SOLSE–2 Main Menu
Sel SOLSE/LORE Command Page

HH–JR/SOLSE–2 Command Page

S_Toggle Filter – Send (wait ≤ 45 sec, Pending)
S_Execute Cmd Pending – Send (Sent)
Wait ≤ 45 sec, S_Last Cmd Executed: S_Toggle Filter

NOTE
Timing of filter transition depends on start temperature and direction of motion. For nominal cases at 20 degC, VIS>UV total process takes 120 sec; UV>VIS takes 290 sec. Process will take shorter or longer at a rate of ~4 sec/deg

Press <ESC> to return to main menu

HH–JR/SOLSE–2 Main Menu
Sel SOLSE/LORE Telemetry Page

HH–JR/SOLSE–2 Telemetry Page
After ~120 sec (VIS>UV) or ~290 sec (UV>VIS)
S_Filter – UV or VIS as reqd per Execute Package
S_Fltr_Stat – OK
S_Cmding – GO/OK

* If S_Filter – not UV or VIS as reqd per Execute Package *
* and S_Cmding – GO/OK: *
* Wait 60 sec *
* MCC *

Press <ESC> to return to main menu

Notify MCC SOLSE SETUP complete
Proceed to SOLSE SCIENCE

SOLSE SCIENCE

NOTE
Perform per Execute Package MET (NLT Terminator Rise (TR) –15 min (earth) and TR –10 (limb).

All SOLSE and HRIU commands require <CTRL–Y> following command selection to execute command.

Once every 30 sec there is a brief period in which commands to payload will not be accepted. If "S_CMD(L_CMD) Status is NoGo/Wait. Cannot send command to SOLSE(LORE)" message appears at any time after executing S_Cmd Execute or L_Cmd Execute, resend rejected command.

To clear error message from active screen, exit to main menu and return to desired screen

* If at any time during procedure execution error messages *
* display in lower left corner of screen, it is possible that *
* HRIU reset has occurred. To determine if HRIU is reset: *
* If not on HH–JR/SOLSE–2 System Page: *
* Press <ESC> to return to main menu *
* HH–JR/SOLSE–2 Main Menu *
* Sel HH–JR/SOLSE–2 System Page *
* HH–JR/SOLSE–2 System Page *
* If HRIU Status – initialized: *
* Return to nominal ops *
* If HRIU Status – reset: *
* Notify MCC *
* Perform SOLSE CONTINGENCY RECOVERY *

1. SOLSE CONSTRAINT CHECK
Orbiter in attitude per Attitude Timeline
PLB lights OFF

2. POLLING CHECK
PGSC HH–JR/SOLSE–2 Main Menu
Sel HH–JR/SOLSE–2 System Page

HH–JR/SOLSE–2 System Page
HH–JR Polling – ON

* If HH–JR Polling – OFF: *
* HH–JR Polling – ENAB (ON) *

Heater & Door Power – ON
Commands transmitted incrementing

Press <ESC> to return to main menu

3. SOLSE/LORE SYNC CHECK
HH–JR/SOLSE–2 Main Menu
Sel SOLSE/LORE Telemetry Page

SOLSE/LORE Telemetry Page
SOLSE Status – In Sync
LORE Status – In Sync
SOLSE_Tec Temp: –10°C ± 1°C
S_Mode – Stby
L_Mode – Stby

Press <ESC> to return to main menu

4. SOLSE/LORE SCIENCE MODE INIT
HH–JR/SOLSE–2 Main Menu
Sel SOLSE/LORE Command Page

a. SOLSE Science Mode Init
SOLSE/LORE Command Page
S_Cmd Status – GO/OK
S_Enter Science Mode – Send (wait ≤ 45 sec, Pending)
S_Execute Cmd Pending – Send (Sent)
Wait ≤ 45 sec, S_Last Cmd Executed: S_Enter Science Mode

* If after 1 min cmd still pending, reattempt cmd *

b. LORE Science Mode Init
L_Cmd Status – GO/OK
L_Enter Science Mode – Send (wait ≤ 45 sec, Pending)
L_Execute Cmd Pending – Send (Sent)
Wait ≤ 45 sec, L_Last Cmd Executed: L_Enter Science Mode

* If after 1 min cmd still pending, reattempt cmd *

Press <ESC> to return to main menu

c. Science Mode Verification
HH–JR/SOLSE–2 Main Menu
Sel SOLSE/LORE Telemetry Page

SOLSE/LORE Telemetry Page
SOLSE Status – In Sync
LORE Status – In Sync
S_Mode – Sci
L_Mode – Sci

Press <ESC> to return to main menu

5. COMMAND SOLSE/LORE IT SETTINGS, if reqd
Execute Pack if step 5 commands reqd
If reqd, proceed with step 5; otherwise, go to step 6

HH–JR/SOLSE–2 Main Menu
Sel SOLSE/LORE Command Page

SOLSE/LORE Command Page
Command Instrument Settings per Table as Reqd per Execute Package

#	Command Name	Execution Steps
A	S_Forward IT 1	S_Forward IT 1 – Send (wait ≤ 45 sec, Pending) S_Execute Cmd Pending – Send (Sent) wait ≤ 45 sec, S_Last Cmd Executed: S_Forward IT 1
B	S_Forward IT 2	S_Forward IT 2 – Send (wait ≤ 45 sec, Pending) S_Execute Cmd Pending – Send (Sent) wait ≤ 45 sec, S_Last Cmd Executed: S_Forward IT 2
C	S_Forward IT 3	S_Forward IT 3 – Send (wait ≤45 sec, Pending) S_Execute Cmd Pending – Send (Sent) wait ≤ 45 sec, S_Last Cmd Executed: S_Forward IT 3
D	S_Back IT 1	S_Back IT 1 – Send (wait ≤ 45 sec, Pending) S_Execute Cmd Pending – Send (Sent) wait ≤ 45 sec, S_Last Cmd Executed: S_Back IT 1
E	S_Back IT 2	S_Back IT 2 – Send (wait ≤ 45 sec, Pending) S_Execute Cmd Pending – Send (Sent) wait ≤ 45 sec, S_Last Cmd Executed: S_Back IT 2
F	S_Back IT 3	S_Back IT 3 – Send (wait ≤ 45 sec, Pending) S_Execute Cmd Pending – Send (Sent) wait ≤ 45 sec, S_Last Cmd Executed: S_Back IT 3
G	S_Return to initial IT	S_Return to initial IT – Send (wait ≤ 45 sec, Pending) S_Execute Cmd Pending – Send (Sent) wait ≤ 45 sec, S_Last Cmd Executed: S_Return to initial IT
H	L_Forward IT 1	L_Forward IT 1 – Send (wait ≤ 5 sec, Pending) L_Execute Cmd Pending – Send (Sent) wait ≤ 45 sec, L_Last Cmd Executed: L_Forward IT 1
I	L_Forward IT 2	L_Forward IT 2 – Send (wait ≤ 45 sec, Pending) L_Execute Cmd Pending – Send (Sent) wait ≤ 45 sec, L_Last Cmd Executed: L_Forward IT 2
J	L_Forward IT 3	L_Forward IT 3 – Send (wait ≤ 45 sec, Pending) L_Execute Cmd Pending – Send (Sent) wait ≤ 45 sec, L_Last Cmd Executed: L_Forward IT 3
K	L_Back IT 1	L_Back IT 1 – Send (wait ≤ 45 sec, Pending) L_Execute Cmd Pending – Send (Sent) wait ≤ 45 sec, L_Last Cmd Executed: L_Back IT 1
L	L_Back IT 2	L_Back IT 2 – Send (wait ≤ 45 sec, Pending) L_Execute Cmd Pending – Send (Sent) wait ≤ 45 sec, L_Last Cmd Executed: L_Back IT 2
M	L_Back IT 3	L_Back IT 3 – Send (wait ≤ 45 sec, Pending) L_Execute Cmd Pending – Send (Sent) wait ≤ 45 sec, L_Last Cmd Executed: L_Back IT 3
N	L_Return to initial IT	L_Return to initial IT – Send (wait ≤ 45 sec, Pending) L_Execute Cmd Pending – Send (Sent) wait ≤ 45 sec, L_Last Cmd Executed: L_Return to initial IT

* If after 1 min any cmd still pending, reattempt cmd *

Press <ESC> to return to main menu

6. DOOR OPENING
Perform Per Execute Package MET (NLT TR –4 min (Earth) and TR (limb))

NOTE
Door may be opened early on MCC GO

PGSC HH–JR/SOLSE–2 Main Menu
Sel HH–JR SOLSE–2 System Page

HH–JR/SOLSE–2 System Page
HH–JR Polling – ON

* If HH–JR Polling – OFF: *
* HH–JR Polling – ENAB (wait ≤ 45 sec, ON) *

HRIU Status – initialized
Door Command – OPEN (wait ≤ 45 sec, OPEN)

NOTE
SOLSE door dual motor opening time = ~35 sec, single motor = ~70 sec

~35 sec after sending Door Command Open:
Door Position – OPEN

Press <ESC> to return to main menu
HH–JR/SOLSE–2 Main Menu
Sel SOLSE/LORE Telemetry Page
SOLSE/LORE Telemetry Page
S_Door – Open

Press <ESC> to return to main menu

PGSC HH–JR/SOLSE–2 SYSTEM PAGE
Heater & Door Power – DISA (wait ≤ 45 sec, OFF)

NOTE
Disabling Heater & Door Power ensures that SOLSE door will not close inadvertently in case of an HRIU reset

Press <ESC> to return to main menu
Proceed to SOLSE MONITOR

SOLSE MONITOR

NOTE
All SOLSE and HRIU commands require <CTRL–Y> following command Selection to execute command.

Once every 30 sec there is a brief period in which commands to payload will not be accepted. If "S_CMD(L_CMD) Status is NoGo/Wait. Cannot send command to SOLSE(LORE)" message appears at any time after executing S_Cmd Execute or L_Cmd Execute, resend rejected command.

To clear error message from active screen, exit to main menu and return to desired screen

* If at any time during procedure execution error messages *
* display in lower left corner of screen, it is possible that *
* HRIU reset has occurred. To determine if HRIU is reset: *
* If not on HH–JR/SOLSE–2 System Page: *
* Press <ESC> to return to main menu *
* HH–JR/SOLSE–2 Main Menu *
* Sel HH–JR/SOLSE–2 System Page *
* HH–JR/SOLSE–2 System Page *
* If HRIU Status – initialized: *
* Return to nominal ops *
* If HRIU Status – reset: *
* Notify MCC *
* Perform SOLSE CONTINGENCY RECOVERY *

1. SOLSE OBSERVATION
Perform INTEGRATION COMMANDING, step 1a as reqd per Execute Package and perform SOLSE MONITOR, step 1b, as time allows (every 10 min if possible)

a. Integration Commanding, if reqd
HH–JR/SOLSE–2 Main Menu
Sel SOLSE/LORE Command Page

SOLSE/LORE Command Page
Command Instrument Settings as reqd per Exec Pack

#	Command Name	Execution Steps
A	S_Forward IT 1	S_Forward IT 1 – Send (wait ≤ 45 sec, Pending) S_Execute Cmd Pending – Send (Sent) wait ≤ 45 sec, S_Last Cmd Executed: Forward IT 1
B	S_Forward IT 2	S_Forward IT 2 – Send (wait ≤ 45 sec, Pending) S_Execute Cmd Pending – Send (Sent) wait ≤ 45 sec, S_Last Cmd Executed: Forward IT 2
C	S_Forward IT 3	S_Forward IT 3 – Send (wait ≤ 45 sec, Pending) S_Execute Cmd Pending – Send (Sent) wait ≤ 45 sec, S_Last Cmd Executed: Forward IT 3
D	S_Back IT 1	S_Back IT 1 – Send (wait ≤ 45 sec, Pending) S_Execute Cmd Pending – Send (Sent) wait ≤ 45 sec, S_Last Cmd Executed: Back IT 1
E	S_Back IT 2	S_Back IT 2 – Send (wait ≤ 45 sec, Pending) S_Execute Cmd Pending – Send (Sent) wait ≤ 45 sec, S_Last Cmd Executed: Back IT 2
F	S_Back IT 3	S_Back IT 3 – Send (wait ≤ 45 sec, Pending) S_Execute Cmd Pending – Send (Sent) wait ≤ 45 sec, S_Last Cmd Executed: Back IT 3
G	S_Return to initial IT	S_Return to initial IT – Send (wait ≤ 45 sec, Pending) S_Execute Cmd Pending – Send (Sent) wait ≤ 45 sec, S_Last Cmd Executed: Return to initial IT
H	L_Forward IT 1	L_Forward IT 1 – Send (wait ≤ 45 sec, Pending) L_Execute Cmd Pending – Send (Sent) wait ≤ 45 sec, L_Last Cmd Executed: Forward IT 1
I	L_Forward IT 2	L_Forward IT 2 – Send (wait ≤ 45 sec, Pending) L_Execute Cmd Pending – Send (Sent) wait ≤ 45 sec, L_Last Cmd Executed: Forward IT 2
J	L_Forward IT 3	L_Forward IT 3 – Send (wait ≤ 45 sec, Pending) L_Execute Cmd Pending – Send (Sent) wait ≤ 45 sec, L_Last Cmd Executed: Forward IT 3
K	L_Back IT 1	L_Back IT 1 – Send (wait ≤ 45 sec, Pending) L_Execute Cmd Pending – Send (Sent) wait ≤ 45 sec, L_Last Cmd Executed: Back IT 1
L	L_Back IT 2	L_Back IT 2 – Send (wait ≤ 45 sec, Pending) L_Execute Cmd Pending – Send (Sent) wait ≤ 45 sec, L_Last Cmd Executed: Back IT 2
M	L_Back IT 3	L_Back IT 3 – Send (wait ≤ 45 sec, Pending) L_Execute Cmd Pending – Send (Sent) wait ≤ 45 sec, L_Last Cmd Executed: Back IT 3
N	L_Return to initial IT	L_Return to initial IT – Send (wait ≤ 45 sec, Pending) L_Execute Cmd Pending – Send (Sent) wait ≤ 45 sec, L_Last Cmd Executed: Return to initial IT

Press <ESC> to return to main menu

b. SOLSE Monitor
HH–JR/SOLSE–2 Main Menu
Sel SOLSE/LORE Telemetry Page

SOLSE/LORE Telemetry Page
If available, check SOLSE/LORE telemetry for error status every 10 min through observation conclusion

If Limb View,
If S_Filter – VIS, LORE Target Distance < | 10 | (if > | 10 |, notify MCC)
If S_Filter – UV, LORE Target Distance < | 17 | (if > | 17 |, notify MCC)

SOLSE/LORE Packets Rcvd incrementing at least once per min
SOLSE Status and LORE Status – In Sync
S_Mode and L_Mode – Sci
SOLSE and LORE Intensity Words ≤ 4 asterisks (if > 4 asterisks, notify MCC)

NOTE
S_LORE will nominally alternate between "LORE" and "NoLORE" as LORE only handshakes with SOLSE every other frame. S_Cmding and L_Cmding will also nominally alternate between GO OK and NoGo/Wait

* If SOLSE/LORE packets not incrementing for > 1 min: *
* Notify MCC *
* Perform SOLSE CONTINGENCY RECOVERY *

* If SOLSE (LORE) Status – NoSync: *
* Notify MCC *
* Perform SOLSE CONTINGENCY RECOVERY *

* If L_Mode ≠ Sci: *
* Notify MCC *
* Press <ESC> to return to main menu *
* Sel SOLSE/LORE Command Page *
* SOLSE/LORE Command Page *
* L_Cmd Status – GO/OK *
* L_Enter Science Mode – Send (wait ≤ 45 sec, *
* Pending) *
* L_Execute Cmd Pending – Send (Sent) *
* Wait ≤ 45 sec, L_Last Cmd Executed: L_Enter *
* Science Mode *
* Press <ESC> to return to main menu *
* HH–JR/SOLSE–2 Main Menu *
* Sel SOLSE/LORE Telemetry Page *
* SOLSE/LORE Telemetry Page *
* SOLSE and LORE Status – In Sync *
* L_Mode – Sci *
* If S_Mode ≠ Sci: *
* Notify MCC *
* Press <ESC> to return to main menu *
* HH–JR/SOLSE–2 Main Menu *
* Sel HH–JR System Page *
* HH–JR/SOLSE–2 System Page *
* B3–Science Mode – PULSE (wait ≤ 45 sec, ON) *
* After 1 min, B3–Science Mode – OFF *
* Press <ESC> to return to main menu *
* HH–JR/SOLSE–2 Main Menu *
* Sel SOLSE/LORE Telemetry *
* SOLSE/LORE Telemetry Page *
* SOLSE and LORE Status – In Sync *
* S_Mode – Sci *
* If S_Mode ≠ Sci: *
* MCC *

2. OBSERVATION CONCLUSION
Press <ESC> to return to main menu
Proceed to SOLSE CLOSEOUT per Execute Package MET

SOLSE CLOSEOUT

NOTE
All SOLSE and HRIU commands require <CTRL–Y> following command selection to execute command.

Once every 30 sec there is a brief period in which commands to payload will not be accepted. If "S_CMD(L_CMD) Status is NoGo/Wait. Cannot send command to SOLSE(LORE)" message appears at any time after executing S_Cmd Execute or L_Cmd Execute, resend rejected command.

To clear error message from active screen, exit to main menu and return to desired screen

* If at any time during procedure execution error messages *
* display in lower left corner of screen, it is possible that *
* HRIU reset has occurred. To determine if HRIU is reset: *
* If not on HH–JR/SOLSE–2 System Page: *
* Press <ESC> to return to main menu *
* HH–JR/SOLSE–2 Main Menu *
* Sel HH–JR/SOLSE–2 System Page *
* HH–JR/SOLSE–2 System Page *
* If HRIU Status – initialized: *
* Return to nominal ops *
* If HRIU Status – reset: *
* Notify MCC *
* Perform SOLSE CONTINGENCY RECOVERY *

1. POLLING CHECK
PGSC HH–JR/SOLSE–2 Main Menu
Sel HH–JR SOLSE–2 System Page

HH–JR/SOLSE–2 System Page
HH–JR Polling – ON

* If HH–JR Polling – OFF: *
* HH–JR Polling – ENAB (ON) *

Commands transmitted incrementing
Press <ESC> to return to main menu

2. SOLSE/LORE DATA DUMP INITIATION
A4 Set Egg Timer to 00:15:00

PGSC HH–JR/SOLSE–2 Main Menu
Sel SOLSE/LORE Command Page

SOLSE/LORE Command Page
S_Cmd Status – GO/OK
S_Enter Dump Mode – Send (wait ≤ 45 sec, Pending)
S_Execute Cmd Pending – Send (Sent)
Wait ≤ 45 sec, S_Last Cmd Executed: S_Enter Dump Mode

* If following message appears: "S_CMD Status is NoGo/Wait. *
* Cannot send command to SOLSE.": *
* Reattempt cmd *

L_Cmd Status – GO/OK
L_Enter Dump Mode – Send (wait ≤ 45 sec, Pending)
L_Execute Cmd Pending – Send (Sent)
Wait ≤ 45 sec, L_Last Cmd Executed: L_Enter Dump Mode

* If after 1 min cmd still pending, reattempt cmd *

00:15:00 Initiate Egg Timer

Press <ESC> to return to main menu
HH–JR/SOLSE–2 Main Menu
Sel SOLSE/LORE Telemetry Page

SOLSE/LORE Telemetry Page
SOLSE Status – In Sync
S_Mode – Dump
S_Cmding – No Go/Wait
LORE Status – In Sync
L_Mode – Sci
L_Cmding – NoGo/Wait

NOTE
L_Mode will indicate Sci during dump mode

Press <ESC> to return to main menu

3. DOOR CLOSURE
Execute Package if step 3 reqd

PGSC HH–JR/SOLSE–2 Main Menu
Sel HH–JR/SOLSE–2 System Page
HH–JR/SOLSE–2 System Page
Heater & Door Power – ENAB (wait ≤ 45 sec) (ON)

Door Command – CLOSE (wait ≤ 45 sec, CLOSE)

NOTE
SOLSE door dual motor closing time = ~35 sec;
single motor = ~70 sec

After ~35 sec:
Door position – CLOSED

MON 1 Visually verify SOLSE door position closed

Press <ESC> to return to main menu
HH–JR/SOLSE–2 Main Menu
Sel SOLSE/LORE Telemetry Page

SOLSE/LORE Telemetry Page
S_Door – Closed

Press <ESC> to return to main menu

4. SOLSE STATUS CHECK
Sel HH–JR/SOLSE–2 System Page
HH–JR/SOLSE–2 System Page
Record Payload Status and Voice Values to MCC

Nominal Value Range (SOLSE Primary Pwr On)	
Bus Voltage:	28 ± 1 V
Bus Current:	2.0 ± 0.7 Amps
Canister Pressure:	15.257 ± 0.6 PSIA
Door Position:	≤ 2.5 Volts
HRIU Temp:	0–40°C
HH–JR LEP:	0–40°C
Heat Pipe:	0–40°C
Bulkhead:	0–40°C
Heatsink:	0–40°C
TEC Temp:	–10°C ± 1

MET	____/____:____:____	____/____:____:____
Bus Voltage:	Volts	Volts
Bus Current:	Amps	Amps
Canister Pressure:	PSIA	PSIA
Door Position:	Open/Closed_____Volts	Open/Closed_____Volts
HRIU Temp:	°C	°C
HH–JR LEP:	°C	°C
Heat Pipe:	°C	°C
Bulkhead:	°C	°C
Heatsink:	°C	°C
TEC Temp:	°C	°C

MET	____/____:____:____	____/____:____:____
Bus Voltage:	Volts	Volts
Bus Current:	Amps	Amps
Canister Pressure:	PSIA	PSIA
Door Position:	Open/Closed_____Volts	Open/Closed_____Volts
HRIU Temp:	°C	°C
HH–JR LEP:	°C	°C
Heat Pipe:	°C	°C
Bulkhead:	°C	°C
Heatsink:	°C	°C
TEC Temp:	°C	°C

MET	____/____:____:____	____/____:____:____
Bus Voltage:	Volts	Volts
Bus Current:	Amps	Amps
Canister Pressure:	PSIA	PSIA
Door Position:	Open/Closed_____Volts	Open/Closed_____Volts
HRIU Temp:	°C	°C
HH–JR LEP:	°C	°C
Heat Pipe:	°C	°C
Bulkhead:	°C	°C
Heatsink:	°C	°C
TEC Temp:	°C	°C

MET	____/____:____:____	____/____:____:____
Bus Voltage:	Volts	Volts
Bus Current:	Amps	Amps
Canister Pressure:	PSIA	PSIA
Door Position:	Open/Closed_____Volts	Open/Closed_____Volts
HRIU Temp:	°C	°C
HH–JR LEP:	°C	°C
Heat Pipe:	°C	°C
Bulkhead:	°C	°C
Heatsink:	°C	°C
TEC Temp:	°C	°C

MET	____/____:____:____	____/____:____:____
Bus Voltage:	Volts	Volts
Bus Current:	Amps	Amps
Canister Pressure:	PSIA	PSIA
Door Position:	Open/Closed_____Volts	Open/Closed_____Volts
HRIU Temp:	°C	°C
HH–JR LEP:	°C	°C
Heat Pipe:	°C	°C
Bulkhead:	°C	°C
Heatsink:	°C	°C
TEC Temp:	°C	°C

MET	____/____:____:____	____/____:____:____
Bus Voltage:	Volts	Volts
Bus Current:	Amps	Amps
Canister Pressure:	PSIA	PSIA
Door Position:	Open/Closed_____Volts	Open/Closed_____Volts
HRIU Temp:	°C	°C
HH–JR LEP:	°C	°C
Heat Pipe:	°C	°C
Bulkhead:	°C	°C
Heatsink:	°C	°C
TEC Temp:	°C	°C

MET	____/____:____:____	____/____:____:____
Bus Voltage:	Volts	Volts
Bus Current:	Amps	Amps
Canister Pressure:	PSIA	PSIA
Door Position:	Open/Closed_____Volts	Open/Closed_____Volts
HRIU Temp:	°C	°C
HH–JR LEP:	°C	°C
Heat Pipe:	°C	°C
Bulkhead:	°C	°C
Heatsink:	°C	°C
TEC Temp:	°C	°C

MET	____/____:____:____	____/____:____:____
Bus Voltage:	Volts	Volts
Bus Current:	Amps	Amps
Canister Pressure:	PSIA	PSIA
Door Position:	Open/Closed_____Volts	Open/Closed_____Volts
HRIU Temp:	°C	°C
HH–JR LEP:	°C	°C
Heat Pipe:	°C	°C
Bulkhead:	°C	°C
Heatsink:	°C	°C
TEC Temp:	°C	°C

MET	____/____:____:____	____/____:____:____
Bus Voltage:	Volts	Volts
Bus Current:	Amps	Amps
Canister Pressure:	PSIA	PSIA
Door Position:	Open/Closed_____Volts	Open/Closed_____Volts
HRIU Temp:	°C	°C
HH–JR LEP:	°C	°C
Heat Pipe:	°C	°C
Bulkhead:	°C	°C
Heatsink:	°C	°C
TEC Temp:	°C	°C

Press <ESC> to return to main menu

5. SOLSE/LORE DATA DUMP COMPLETION

HH–JR/SOLSE–2 Main Menu
Sel SOLSE/LORE Telemetry Page
SOLSE/LORE Telemetry Page

00:00:00 S_Mode – Stby
L_Mode – Stby

```
* If S_Mode – Dump:                                  *
*    Press <ESC> to return to main menu              *
*    HH–JR/SOLSE–2 Main Menu                         *
*    Sel HH–JR/SOLSE–2 System Page                   *
*    HH–JR/SOLSE–2 System Page                       *
*    B2–Standby Mode – PULSE (wait ≤ 45 sec,  ON)    *
*    Press <ESC> to return to main menu              *
*    HH–JR/SOLSE–2 Main Menu                         *
*    Sel SOLSE/LORE Telemetry Page                   *
*    SOLSE/LORE Telemetry Page                       *
*    SOLSE Status – In Sync                          *
*    S_Mode – Stby                                   *
*    S_Cmding – GO/OK                                *
```

NOTE

L_Mode cannot be commanded via B1–B4 commands on System Page

Press <ESC> to return to main menu

6. SOLSE CALIBRATION, if reqd

Execute Package if step 6 reqd
If reqd, proceed with step 6; otherwise, go to step 7

NOTE

Step 6 will only be executed at conclusion of observation sequence

Reset Egg Timer to 00:15:00

HH–JR/SOLSE–2 Main Menu
Sel SOLSE/LORE Command Page
SOLSE/LORE Command Page
S_Cmd Status – GO/OK
S_Enter Cal Mode – Send (wait ≤ 45 sec, Pending)

S_Execute Cmd Pending – Send (Sent)
Wait ≤ 45 sec, S_Last Cmd Executed: S_Enter Cal Mode

```
* If after 1 min cmd still pending, reattempt cmd *
```

Press <ESC> to return to main menu

HH–JR/SOLSE–2 Main Menu
Sel SOLSE/LORE Telemetry Page

SOLSE/LORE Telemetry Page
After 1 min:
SOLSE Packets Rcvd – incremented to 2 or greater
LORE Packets Rcvd – incremented to 2 or greater
SOLSE Status – In Sync

NOTE

S_Mode will remain in Stby until four packets are received (at ~100 sec after command receipt). When four packets are received, S_Mode will indicate Cal.

When S–Mode – Cal, notify MCC, SOLSE Cal Mode Initiated

00:15:00 Start Egg Timer

NOTE

SOLSE Cal duration = 15 min. No payload commanding reqd during cal. After cal, SOLSE Packets Rcvd = ~68. Packets will continue to increment following conclusion of cal

00:00:00 SOLSE Status – In Sync
S_Mode – Stby

```
* If S_Mode – Cal after 15 min:                      *
*    Notify MCC                                      *
*    Press <ESC> to return to main menu              *
*    HH–JR/SOLSE–2 Main Menu                         *
*    Sel HH–JR System Page                           *
*    HH–JR/SOLSE–2 System Page                       *
*    B2–Standby Mode – PULSE (wait ≤ 45 sec,  ON)    *
*    After 1 min,  B2–Standby Mode – OFF             *
*    Press <ESC> to return to main menu              *
*    HH–JR/SOLSE–2 Main Menu                         *
*    Sel SOLSE/LORE Telemetry Page                   *
*    SOLSE/LORE Telemetry Page                       *
*    SOLSE Status – In Sync                          *
*    S_Mode – Stby                                   *
*    If S_Mode – Cal:                                *
*       Notify MCC                                   *
```

Notify MCC, SOLSE Cal complete

7. SOLSE FILTER POSITION CHECK

NOTE
At conclusion of observation series, filter should always be in VIS position

SOLSE/LORE Telemetry Page
Correct Filter in Place per Execute Package

If incorrect filter in place:
Press <ESC> to return to main menu

HH–JR/SOLSE–2 Main Menu
Sel SOLSE/LORE Command Page

SOLSE/LORE Command Page
S_Cmd Status – GO/OK
S_Toggle Filter – Send (wait ≤ 45 sec, Pending)
S_Execute Cmd Pending – Send (Sent)
Wait ≤ 45 sec, S_Last Cmd Executed: S_Toggle Filter

NOTE
Timing of filter transition depends on start temperature and direction of motion. For nominal cases at 20 °C, VIS > UV total process takes 120 sec, UV > VIS takes 290 sec. Process will take shorter or longer at a rate of ~4 sec/deg

Press <ESC> to return to main menu
HH–JR/SOLSE–2 Main Menu
Sel SOLSE/LORE Telemetry Page
SOLSE/LORE Telemetry Page

After ~120 sec (VIS > UV) or ~290 sec (UV > VIS)
S_Filter – UV or VIS as reqd
S_Fltr_Stat – OK
S_Cmding – GO/OK

If S_Filter not as reqd and S_Cmding – GO/OK, wait 60 sec prior to proceeding

Press <ESC> to return to main menu

Notify MCC SOLSE CLOSEOUT complete

Proceed to SOLSE SCIENCE or SOLSE IDLE as reqd per Execute Package

SOLSE IDLE

NOTE
All SOLSE and HRIU commands require <CTRL–Y> following command selection to execute command.

Once every 30 sec there is a brief period in which commands to payload will not be accepted. If "S_CMD(L_CMD) Status is NoGo/Wait. Cannot send command to SOLSE(LORE)" message appears at any time after executing S_Cmd Execute or L_Cmd Execute, resend rejected command.

To clear error message from active screen, exit to main menu and return to desired screen

* If at any time during procedure execution error messages *
* display in lower left corner of screen, it is possible that an *
* HRIU reset has occurred. To determine if HRIU is reset: *
* If not on HH–JR/SOLSE–2 System Page: *
* Press <ESC> to return to main menu *
* HH–JR/SOLSE–2 Main Menu *
* Sel HH–JR/SOLSE–2 System Page *
* HH–JR/SOLSE–2 System Page *
* If HRIU Status – initialized: *
* Return to nominal ops *
* If HRIU Status – reset: *
* Notify MCC *
* Perform SOLSE CONTINGENCY RECOVERY *

1. POLLING CHECK

PGSC
HH–JR/SOLSE–2 Main Menu
Sel HH–JR/SOLSE–2 System Page
HH–JR/SOLSE–2 System Page
HH–JR Polling – ON

* If HH–JR Polling – OFF: *
* HH–JR Polling – ENAB (ON) *

Commands transmitted incrementing

2. DATA CHECK
Record number of SOLSE and LORE Packets Rcvd

MET	SOLSE Packets Rcvd	LORE Packets Rcvd
___/____:____:____		
___/____:____:____		
___/____:____:____		
___/____:____:____		
___/____:____:____		
___/____:____:____		
___/____:____:____		
___/____:____:____		
___/____:____:____		
___/____:____:____		
___/____:____:____		
___/____:____:____		
___/____:____:____		
___/____:____:____		
___/____:____:____		
___/____:____:____		

Voice number of SOLSE and LORE Data Packets Rcvd to ground

Press <ESC> to return to main menu

3. SOLSE/LORE SOFTWARE SHUTDOWN

a. SOLSE Shutdown
HH–JR/SOLSE–2 Main Menu
Sel SOLSE/LORE Command Page

SOLSE & LORE Command Page
S_Cmd Status – GO/OK
S_Shutdown – Send (wait ≤ 45 sec, Pending)
S_Execute Cmd Pending – Send (Sent)
Wait ≤ 45 sec, S_Last Cmd Executed: S_Shutdown

b. LORE Shutdown
L_Cmd Status – GO/OK
L_Shutdown – Send (wait ≤ 45 sec, Pending)
L_Execute Cmd Pending – Send (Sent)
Wait ≤ 45 sec, L_Last Cmd Executed: L_Shutdown

Press <ESC> to return to main menu

c. Shutdown Verification
HH–JR/SOLSE–2 Main Menu
Sel SOLSE/LORE Telemetry Page
SOLSE/LORE Telemetry Page

NOTE
SOLSE and LORE Intensity Words progressively fill with asterisks after shutdown command is acknowledged (may take > 1 min for asterisks to begin to appear). Final shutdown is indicated when entire field is asterisks

SOLSE and LORE Intensity Words – all asterisks

* If after 90 sec, SOLSE and LORE Intensity Words *
* not all asterisks: *
* Repeat step 3 *

Press <ESC> to return to the main menu

4. SOLSE POWERDOWN
HH–JR/SOLSE–2 Main Menu
Sel HH–JR/SOLSE–2 System Page

HH–JR/SOLSE–2 System Page
HH–JR Polling – ON

SOLSE Primary Power – DISA (wait ≤ 45 sec, OFF)

5. EXIT POLLING & SOFTWARE
HH–JR Polling – DISA (wait ≤ 45 sec, OFF)
Press <ESC> to return to main menu

HH–JR/SOLSE–2 Main Menu
Sel Exit Program, follow directions on screen

6. FILE TRANSFER

NOTE
Refer to SOLSE SETUP step 5 for most recent data file

Copy most recent SOLSE data file (C:\solse\PGSCdata.00X) and log file (C:\solse/solse.log) to OCA machine (STS–1) downlink location: C:\oca–down\payloads via network

If network unavailable:
Use PCMCIA card to transfer files to OCA machine (STS–1)
Ref OCA DOWNLINK VIA GROUND COMMAND (ORB OPS, PGSC)

From Start Menu, Sel Shutdown

NOTE
SOLSE PGSC may be deactivated when SOLSE software is not in use. BIA power is reqd for SOLSE heater power. BIA must remain powered from SOLSE activation to SOLSE Deactivation unless otherwise instructed

Notify MCC, SOLSE IDLE complete

SOLSE/HRIU DEACT

NOTE
All SOLSE and HRIU commands require <CTRL–Y> following command selection to execute command.

Once every 30 sec there is a brief period in which commands to payload will not be accepted. If "S_CMD(L_CMD) Status is NoGo/Wait. Cannot send command to SOLSE(LORE)" message appears at any time after executing S_Cmd Execute or L_Cmd Execute, resend rejected command.

To clear error message from active screen, exit to main menu and return to desired screen

* If at any time during procedure execution error messages display in lower left corner of screen, it is possible that HRIU reset has occurred. To determine if HRIU is reset:
* If not on HH–JR/SOLSE–2 System Page:
* Press <ESC> to return to main menu
* HH–JR/SOLSE–2 Main Menu
* Sel HH–JR/SOLSE–2 System Page
* HH–JR/SOLSE–2 System Page
* If HRIU Status – initialized:
* Return to nominal ops
* If HRIU Status – reset:
* Notify MCC
* Perform SOLSE CONTINGENCY RECOVERY

1. CONFIG BIA BUFFER

BIA
PWR – ON
ENABLE 2 – ON

2. SOFTWARE STARTUP
Start SOLSE software:
Go to Shuttle Apps Folder
Sel SOLSE–2 Icon
Follow directions on screen

HH–JR/SOLSE–2 Main Menu
Software MET time within 10 sec of actual MET

* If Software MET Time > 10 sec off actual
* MET: Sel Update MET/GMT:
* Update MET/GMT
* Sel UPDATE MET
* Enter Current MET, press enter
* Press <ESC> to return to main menu

HH–JR/SOLSE–2 Main Menu
Sel Data Recording and Storage Setup

HH–JR/SOLSE–2 Data Storage Setup Page
HRIU Errors – ON
HRIU Engineering Data – ON
HRIU Diagnostic Data – ON
HRIU Customer Data – ON

* If HRIU Errors – OFF:
* HRIU Errors – ENAB (ON)
* If HRIU Engineering Data – OFF:
* HRIU Engineering Data – ENAB (ON)
* If HRIU Diagnostic Data – OFF:
* HRIU Diagnostic Data – ENAB (ON)
* If HRIU Customer Data – OFF:
* HRIU Customer Data – ENAB (ON)

Log MET and PGSC Recording Status (File #) below

MET	File Number
____/____:____:____	

Press <ESC> to return to main menu

3. HH–JR STATUS ENABLE
HH–JR/SOLSE–2 Main Menu
Sel HH–JR/SOLSE–2 System Page

HH–JR/SOLSE–2 System Page
HH–JR Polling – ENAB (ON)

* If HH–JR Polling – OFF after enable attempt:
* Reattempt two times
* If still no joy:
* Notify MCC
* Press <ESC> to return to main menu
* Sel Exit Program, follow directions on screen
* BIA Enable 2 – OFF
* Perform hard reboot of PGSC:
* From Start Menu, Sel Shutdown
* When shutdown complete, PGSC pwr – on
* BIA Enable 2 – ON
* Repeat steps 2–3
* If no joy, MCC

Commands transmitted incrementing
Data Storage Status – ENABLED
After 45 sec:
HRIU Status – initialized
Heater & Door Power – ON

4. SOLSE DEACTIVATION
Door Position – CLOSED

PGSC
SOLSE Primary Power – OFF

* If SOLSE Primary Power – ON:
* Execute SOLSE Idle, steps 3 & 4

Vent Command – CLOSE
Door Command – CLOSE

Heater & Door Power – DISA (OFF)
HH–JR Polling – DISA (OFF)

Press <ESC> to return to main menu

HH–JR/SOLSE–2 Main Menu
Sel Exit Program
Follow Directions on Screen
From Start Menu, Sel Shutdown

BIA
5. BIA DEACT
ENABLE 2 – OFF
BIA PWR – OFF

Log MET: ____/____:____:____

Notify MCC, SOLSE/HRIU DEACT complete
Go to SOLSE PGSC/BIA STOW

SOLSE CONTINGENCY RECOVERY

NOTE
This procedure may be requested if SOLSE and LORE payloads lose sync or communications to HRIU during operations. Initiation of this procedure may be delayed depending on where anomaly occurs during data take.

All SOLSE and HRIU commands require <CTRL–Y> following command selection to execute command.

Once every 30 sec there is a brief period in which commands to payload will not be accepted. If "S_CMD(L_CMD) Status is NoGo/Wait. Cannot send command to SOLSE(LORE)" message appears at any time after executing S_Cmd Execute or L_Cmd Execute, resend rejected command.

To clear an error message from active screen, exit to main menu and return to desired screen

BIA
1. RECOVERY SETUP
PWR – ON
ENABLE 2 – ON

HH–JR/SOLSE–2 Main Menu
Sel HH–JR/SOLSE–2 System Page

HH–JR/SOLSE–2 System Page
HH–JR Polling – ON

* If HH–JR Polling – OFF:
* HH–JR Polling – ENAB (ON)

Press <ESC> to return to main menu

2. SOLSE DATA CHECK
HH–JR/SOLSE–2 Main Menu
Sel SOLSE/LORE Telemetry Page

SOLSE/LORE Telemetry Page
SOLSE Status – In Sync

* If SOLSE Status – No Sync:
* Notify MCC
* Press <ESC> to return to main menu
* HH–JR/SOLSE–2 Main Menu
* Sel HH–JR/SOLSE–2 System Page
* HH–JR/SOLSE–2 System Page
* B2–Standby Mode – PULSE (wait ≤ 45 sec, ON)
* After 1 min, B2–Standby Mode – OFF
* Press <ESC> to return to main menu
* Go to step 4

3. SOLSE SOFTWARE SHUTDOWN
Press <ESC> to return to main menu

HH–JR/SOLSE–2 Main Menu
Sel SOLSE/LORE Command Page

SOLSE/LORE Command Page
S_Cmd Status – GO/OK
S_Shutdown – Send (wait ≤ 45 sec, Pending)
S_Execute Cmd Pending – Send (Sent)
Wait ≤ 45 sec, S_Last Cmd Executed: S_Shutdown

```
* If after 1 min, command still pending:                *
*    S_Execute Cmd Pending – Send ( Sent)                *
*    Wait ≤ 30 sec, S_Last Cmd Executed: S_Shutdown      *
*    If after 1 min, command still pending:             *
*       Notify MCC                                      *
*       Press <ESC> to return to main menu              *
*       HH–JR/SOLSE–2 Main Menu                         *
*       Sel HH–JR/SOLSE–2 System Page                   *
*       HH–JR/SOLSE–2 System Page                       *
*       B2–Standby Mode – PULSE (wait ≤ 45 sec, ON)     *
*       After 1 min, B2–Standby Mode – OFF              *
*       Press <ESC> to return to main menu              *
*       Go to step 4                                    *
```

Press <ESC> to return to main menu

HH–JR/SOLSE–2 Main Menu
Sel SOLSE/LORE Telemetry Page

SOLSE/LORE Telemetry Page
When SOLSE Intensity Words (A through P) – *,
proceed to step 4

4. LORE DATA CHECK
SOLSE/LORE Telemetry Page
LORE Status – In Sync

```
* If LORE Status – No Sync:  *
*    Go to step 6            *
```

5. LORE SOFTWARE SHUTDOWN
Press <ESC> to return to main menu

HH–JR/SOLSE–2 Main Menu
Sel SOLSE/LORE Command Page

SOLSE/LORE Command Page
L_Cmd Status – GO/OK

L_Shutdown – Send (wait ≤ 45 sec, Pending)
L_Execute Cmd Pending – Send (Sent)
Wait ≤ 45 sec, L_Last Cmd Executed: L_Shutdown


```
* If after 1 min cmd still pending, reattempt cmd *
*  If after 1 min, still no joy:                  *
*       Go to step 6                              *
```

HH–JR/SOLSE–2 Main Menu
Sel SOLSE/LORE Telemetry Page

SOLSE/LORE Telemetry Page
When LORE Intensity Words (A through P) – *,
proceed to step 6

6. SOLSE POWERDOWN
Press <ESC> to return to main menu

HH–JR/SOLSE–2 Main Menu
Sel HH–JR/SOLSE–2 System Page

HH–JR/SOLSE–2 System Page
SOLSE Primary Power – DISA (wait 45 sec, OFF)
HH–JR Polling – DISA (OFF)

Press <ESC> to return to main menu

HH–JR/SOLSE–2 Main Menu
Sel Exit Program
Follow directions on screen

NOTE
PGSC may remain ON during BIA power cycle

7. BIA CYCLE
BIA
ENABLE 2 – OFF
PWR – OFF

Verify cables securely configured per SOLSE PGSC/BIA SETUP

Wait 5 sec

PWR – ON
ENABLE 2 – ON

Log MET:
____/____:____:____ ____/____:____:____
____/____:____:____ ____/____:____:____
____/____:____:____ ____/____:____:____
____/____:____:____ ____/____:____:____

8. SOLSE SYSTEM RECOVERY
PGSC
PGSC – ON

Start SOLSE software:
Go to Shuttle Apps Folder
Sel SOLSE–2 Icon
Follow directions on screen

HH–JR/SOLSE–2 Main Menu
Software MET time within 10 sec of actual MET

```
* If software MET time > 10 sec off actual MET:  *
*    Sel Update MET/GMT                          *
*    Update MET/GMT                              *
*    Sel UPDATE MET                              *
*    Enter Current MET, press enter              *
*    Press <ESC> to return to main menu          *
```

9. HH–JR STATUS ENABLE
HH–JR/SOLSE–2 Main Menu
Sel HH–JR System Page

HH–JR/SOLSE–2 System Page
HH–JR Polling – ENAB (ON)

```
* If HH–JR Polling – OFF:  *
*    Reattempt cmd         *
*    If still no joy, MCC  *
```

Commands transmitted incrementing
Data Storage Status – ENABLED
After 45 sec:
HRIU Status – initialized

10. SOLSE POWERUP
HH–JR/SOLSE–2 System Page
SOLSE Primary Power – ENAB

After 45 sec, SOLSE Primary Power – ON

```
* If after 45 sec, SOLSE Primary Power – OFF:  *
*    Notify MCC                                 *
*    Reattempt cmd                              *
*    If still no joy:                           *
*       MCC                                     *
```

Press <ESC> to return to main menu

HH–JR/SOLSE–2 Main Menu
Sel SOLSE/LORE Telemetry Page

SOLSE/LORE Telemetry Page
After 1 min:
SOLSE Packets Rcvd – incremented to 2 or greater
SOLSE Status – In sync
After 1 min 30 sec:
LORE Packets Rcvd – incremented to 2 or greater
LORE Status – In Sync

NOTE
SOLSE will remain in Stby mode until four packets are received.
When four packets are received it will indicate Cal mode.

When S–Mode – Cal, notify MCC, SOLSE Cal Mode Initiated

SOLSE_TEC Temp: –10°C ± 1°C
S_Filter Position – VIS (if UV, MCC)
S_Fltr Status – OK (if ERROR, MCC)

Press <ESC> to return to main menu

11. STATUS CHECK, if reqd
MCC if reqd
HH–JR/SOLSE–2 Main Menu
Sel HH–JR/SOLSE–2 System Page

HH–JR/SOLSE–2 System Page
Record Payload Status in table below and voice values to ground

Nominal Value Range (SOLSE Primary Pwr On)	
Bus Voltage:	28 ± 1 V
Bus Current:	0.196 ± .05 Amps
Canister Pressure:	15.257 ± 0.6 PSIA
Door Position:	2.5 Volts
HRIU Temp:	0–40°C
HH–JR LEP:	0–40°C
Heat Pipe:	0–40°C
Bulkhead:	0–40°C
Heatsink:	0–40°C
TEC Temp:	–10°C ± 1

MET	____/____:____:____	____/____:____:____
Bus Voltage:	Volts	Volts
Bus Current:	Amps	Amps
Canister Pressure:	PSIA	PSIA
Door Position:	Open/Closed_____Volts	Open/Closed_____Volts
HRIU Temp:	°C	°C
HH–JR LEP:	°C	°C
Heat Pipe:	°C	°C
Bulkhead:	°C	°C
Heatsink:	°C	°C
TEC Temp:	°C	°C

MET	____/____:____:____	____/____:____:____
Bus Voltage:	Volts	Volts
Bus Current:	Amps	Amps
Canister Pressure:	PSIA	PSIA
Door Position:	Open/Closed_____Volts	Open/Closed_____Volts
HRIU Temp:	°C	°C
HH–JR LEP:	°C	°C
Heat Pipe:	°C	°C
Bulkhead:	°C	°C
Heatsink:	°C	°C
TEC Temp:	°C	°C

MET	____/____:____:____	____/____:____:____
Bus Voltage:	Volts	Volts
Bus Current:	Amps	Amps
Canister Pressure:	PSIA	PSIA
Door Position:	Open/Closed_____Volts	Open/Closed_____Volts
HRIU Temp:	°C	°C
HH–JR LEP:	°C	°C
Heat Pipe:	°C	°C
Bulkhead:	°C	°C
Heatsink:	°C	°C
TEC Temp:	°C	°C

Press <ESC> to return to main menu

12. SOLSE SCIENCE RECOVERY, if reqd
On MCC GO:

HH–JR/SOLSE–2 Main Menu
Sel SOLSE/LORE Command Page

SOLSE/LORE Command Page
S_Cmd Status – GO/OK
S_Enter Science Mode – Send (wait ≤ 45 sec, Pending)
S_Execute Cmd Pending – Send (Sent)
Wait ≤ 45 sec, S_Last Cmd Executed: S_Enter Science Mode

L_Cmd Status – GO/OK
L_Enter Science Mode – Send (wait ≤ 45 sec, Pending)
L_Execute Cmd Pending – Send (Sent)
Wait ≤ 45 sec, L_Last Cmd Executed: L_Enter Science Mode

Press <ESC> to return to main menu

HH–JR/SOLSE–2 Main Menu
Sel SOLSE/LORE Telemetry Page

SOLSE/LORE Telemetry Page
After 1 min:
SOLSE Status – In Sync
LORE Status – In Sync
S_Mode – Sci
L_Mode – Sci

Press <ESC> to return to main menu

Notify MCC, SOLSE CONTINGENCY RECOVERY complete

SOLSE CONTINGENCY SHUTDOWN

NOTE
All SOLSE and HRIU commands require <CTRL–Y> following command selection to execute command.

Once every 30 sec there is a brief period in which commands to payload will not be accepted. If "S_CMD(L_CMD) Status is NoGo/Wait. Cannot send command to SOLSE(LORE)" message appears at any time after executing S_Cmd Execute or L_Cmd Execute, resend rejected command.

To clear an error message from active screen, exit to main menu and return to desired screen

```
* If at any time during procedure execution error   *
*   messages display in lower left corner of screen, *
*   it is possible that an HRIU reset has occurred.  *
*   To determine if HRIU is reset, if not on         *
*   HH–JR/SOLSE–2 System Page:                       *
*     Press <ESC> to return to main menu             *
*     HH–JR/SOLSE–2 Main Menu                        *
*     Sel HH–JR/SOLSE–2 System Page                  *
*     HH–JR/SOLSE–2 System Page                      *
* If HRIU Status – initialized:                      *
*     Return to nominal ops                          *
* If HRIU Status – reset:                            *
*     Notify MCC                                     *
*     Perform SOLSE CONTINGENCY RECOVERY             *
```

1. SOLSE SOFTWARE SHUTDOWN
Press <ESC> to return to main menu

HH–JR/SOLSE–2 Main Menu
Sel SOLSE/LORE Command Page

SOLSE/LORE Command Page
S_Cmd Status – GO/OK
S_Shutdown – Send (wait ≤ 45 sec, Pending)
S_Execute Cmd Pending – Send (Sent)
Wait ≤ 45 sec, S_Last Cmd Executed: S_Shutdown

```
* If after 1 min cmd still pending, reattempt cmd:  *
*   If still no joy:                                *
*     Notify MCC                                    *
*     Press <ESC> to return to main menu            *
*     HH–JR/SOLSE–2 System Page                     *
*     Sel HH–JR/SOLSE–2 System Page                 *
*     HH–JR/SOLSE–2 System Page                     *
*     B2–Standby Mode – PULSE (wait ≤ 45 sec, ON)   *
*     After 1 min, B2–Standby Mode – OFF            *
*     Press <ESC> to return to main menu            *
```

Press <ESC> to return to main menu

HH–JR/SOLSE–2 Main Menu
Sel SOLSE/LORE Telemetry Page

NOTE
SOLSE and LORE Intensity Words progressively fill with asterisks after shutdown command is acknowledged. It may take up to 1 min for asterisks to begin to appear. Final shutdown is indicated when entire field is asterisks

SOLSE/LORE Telemetry Page
SOLSE Intensity Words – all asterisks

```
* If after 90 sec, SOLSE Intensity Words not all asterisks, *
*   Repeat step 1                                          *
```

2. LORE SOFTWARE SHUTDOWN
Press <ESC> to return to main menu

HH–JR/SOLSE–2 Main Menu
Sel SOLSE/LORE Command Page

SOLSE/LORE Command Page
L_Cmd Status – GO/OK
L_Shutdown – Send (wait ≤ 45 sec, Pending)
L_Execute Cmd Pending – Send (Sent)
Wait ≤ 45 sec, L_Last Cmd Executed: L_Shutdown

```
* If after 1 min cmd still pending, reattempt cmd *
*     If after 1 min, still no joy:               *
*       Notify MCC                                *
```

Press <ESC> to return to Main Menu

HH–JR/SOLSE–2 Main Menu
Sel SOLSE/LORE Telemetry Page

NOTE
SOLSE and LORE Intensity Words progressively fill with asterisks after shutdown command is acknowledged. It may take up to 1 min for asterisks to begin to appear. Final shutdown is indicated when entire field is asterisks

SOLSE/LORE Telemetry Page
LORE Intensity Words – all asterisks

```
* If after 90 sec, if LORE Intensity Words not all asterisks, *
*   repeat step 2                                             *
```

Press <ESC> to return to main menu

HH–JR/SOLSE–2 Main Menu
Sel HH–JR System Page

3. SOLSE DOOR CLOSURE, if reqd
HH–JR/SOLSE–2 System Page

Heater & Door Power – ENAB (wait ≤ 45 sec, ON)

Door Command – CLOSE (wait ≤ 45 sec, CLOSE)

NOTE
SOLSE dual motor operating time = ~35 sec; single motor = ~70 sec

After ~35 sec:
Door Command – CLOSED

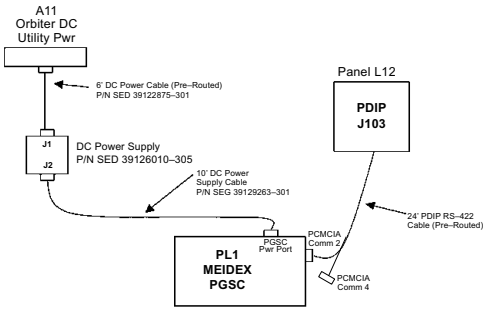
4. SOLSE POWERDOWN
HH–JR/SOLSE–2 System Page
SOLSE Primary Power – DISA (wait 45 sec, OFF)
HH–JR Polling – DISA (OFF)

Notify MCC, SOLSE CONTINGENCY SHUTDOWN complete
MCC for further action

MEIDEX PGSC SETUP

1. UNSTOW
Unstow:
MF28O PL 1 MEIDEX PGSC
PCMCIA RS422 Comm Card
PCMCIA RF LANCard
DC/DC Power Supply
PGSC DC Power Supply Cable
MF57K Late update PCMCIA card

2. CONFIG PGSC
Insert PCMCIA RS422 Comm Card into PGSC; then connect PGSC data and power cables per diagram



3. PGSC PWR ON
A11 DC UTIL PWR MNC – ON
DC PWR SUPPLY – ON (lt green)

PGSC PGSC pwr – on

* If pwr to PL1 fails: *
* Check pwr cable connection *
* Press pwr sw again (both) *

Allow 'Windows' to start

Insert late update PCMCIA card
Run 'Shuttle Apps/Late PGSC Update'
Shutdown PGSC
Remove late update card
Insert PCMCIA RF LAN card into PGSC
PGSC pwr – on
Allow 'Windows' to start

4. MEIDEX SOFTWARE ACTIVATION
PGSC Start MEIDEX software:
Open Shuttle Apps Folder
Sel MEIDEX icon

5. MEIDEX TLM CONFIG
MEIDEX_PGSC_V4_15_0
Sel OpenComm (green)
Sel AutoTlm (green)

GoTo Pages/Cmd Generator Display:
Command Control
Sel IMTAKINGOVER
Sel Xmit
Sel OK
Sel Close (Close Command Control)
MEIDEX_PGSC_V4_15_0
On lower status bar, PGSC_Cntrl

6. MEIDEX EVENT LOG CONFIG
Sel Event (brings up Event Page)

Event page
Log to File –
Report Limits –
Show Auto TLM – no

Sel Event (closes Event Page)
MEIDEX_PGSC_V4_15_0
No Red/Yellow limit violations (limit check boxes in upper right of display = 0,0)

* If Red/Yellow limit violations: *
* Sel Event (brings up Event Page) *
* Determine red/yellow limit violation *
* Voice to MCC *

Notify MCC, MEIDEX PGSC SETUP complete

MEIDEX HEATER ACT/HEALTH CHECK

* If at any time during procedure lower status bar *
* reads PGSC_Not_Cntrl, perform the following: *
* Go to Pages/Cmd Generator Display *
* Command Control *
* Sel IMTAKINGOVER *
* Sel Xmit *
* Sel OK *
* Sel Close (Close Command Control) *
* MEIDEX_PGSC_V4_V15_0 *
* On lower status bar, PGSC_Cntrl *

NOTE
Heater activation will nominally be performed by POCC. Crew will only be reqd to execute if cmd and/or telemetry capability at POCC is lost

1. PGSC CONFIG
PGSC PGSC powered up and MEIDEX software active

* If PGSC OFF: *
* Laptop pwr (side) – on *
* If MEIDEX software not ON start MEIDEX software: *
* Open Shuttle Apps Folder *
* Sel MEIDEX icon *

2. TLM CONFIG
MEIDEX_PGSC_V4_15_0
OpenComm – green
AutoTlm – green

3. EVENT LOG CONFIG
Sel Event (brings up Event Page)

Event page
Configure as follows:
Log to File –
Report Limits –
Show Auto TLM – no

Sel Event (closes Event Page)
MEIDEX_PGSC_V4_15_0
No Red/Yellow limit violations (limit check boxes in upper right of display = 0,0)

* If Red/Yellow limit violations: *
* Sel Event (brings up Event Page) *
* Determine red/yellow limit violation *
* Voice to ground *

4. TELEMETRY CHECK
Sel DigTlm (brings up Digital Telemetry Page)

DigitalTelemetry
Control:
PGSC in Cntrl – green
Truss:
Forward Direction or Reverse Direction – green
All other indicators – white

Sel DigTlm (closes Digital Telemetry Page)

5. TEMPERATURE CHECK
Sel Temps (brings up Temperatures (Deg C) Page)

Temperatures (Deg C)
Htr2: 20°–60°
All other Temperatures: 20°–40°

* If temps out of range: *
* Report to MCC *

Sel Temps (closes Temperatures (Deg C) Page)

6. HEATER ACTIVATION CHECK
Sel RelayCmds (brings up Relay Commanding Page)

Relay Commanding
If Heater1 – white:
Sel Heater1 – On (RELAY K20 ON)
Sel Xmit
Heater1 – green

Sel RelayCmds (closes Relay Commanding Page)

7. TRUSS CONTROL CHECK
Sel TrussCntrl (brings up Truss Pointing Display)

Truss Pointing Display
Limit Switch1 – Not_Limit
Limit Switch2 – Not_Limit
Rvrs Lim Violat – No
Fwrd Lim Violat – No
OverCurr Violat – No

* If out of range: *
* Report to MCC *

Sel TrussCntrl (closes Truss Pointing Display)

Report to MCC, MEIDEX HEALTH CHECK complete

MEIDEX CHECKOUT

```
        * If at any time during procedure lower status bar  *
        *  reads PGSC_Not_Cntrl, perform the following:     *
        *     Go to Pages/Cmd Generator Display             *
        *     Command Control                               *
        *     Sel IMTAKINGOVER                              *
        *     Sel Xmit                                      *
        *     Sel OK                                        *
        *     Sel Close (Close Command Control)             *
        *     MEIDEX_PGSC_V4_V15_0                          *
        *     On lower status bar, PGSC_Cntrl               *

    1.  READINESS CHECK
        P/TV10 MEIDEX OPS, SETUP (PHOTO/TV FS, SCENES) complete

                        NOTE
        MON 1 is used for CCTV and Sekai video.
        MON 2 is used for Xybion video

    2.  TLM CONFIG
        MEIDEX_PGSC_V4_15_0
        OpenComm – green
        AutoTlm – green

    3.  EVENT LOG CONFIG
        Sel Event (brings up Event Page)

        Event Page
        Configure as follows:
            Log to File       –
            Report Limits     –
            Show Auto TLM     – no

        Sel Event (closes Event Page)
        MEIDEX_PGSC_V4_15_0
        No Red/Yellow limit violations (limit check boxes in upper right
          of display = 0,0)

        * If Red/Yellow limit violations:                  *
        *     Sel Event (brings up Event Page)             *
        *     Determine red/yellow limit violation         *
        *     Report to MCC                                *

    4.  DOOR OPENING
L12U    cb DOOR PWR CONT PWR DN ENA – cl

R14     Camera D Illuminator ON, if reqd (TV Cue Card, ILLUMINATOR OPS)
A7      VID OUT pb  – MON 1
          IN pb     – D
        ALC pb      – press
        AVG pb      – press
        VID OUT pb  – ANALOG DNLK
          IN pb     – D
        PAN (TILT,ZOOM) as reqd to view MEIDEX Door
```



```
V10     PWR – ON
        Verify tape installed
        REC pb (two simo) – press (  red dot displayed)

                        NOTE
        MEIDEX door requires ~35 sec to open with dual motor operations;
        ~70 sec to open with single motor ops.  tb will read gray when door
        is > ~94 deg open
L12U    MEIDEX DOOR – OPEN
        After 35 sec,
          MEIDEX DOOR FULL OPEN tb – gray

MON 1   Visually verify MEIDEX Door Full Open
        Report door position to MCC

V10     STOP pb – press
R14     Camera D Illuminator OFF, if reqd (TV Cue Card, ILLUMINATOR OPS)
A7      VID OUT pb  – MON 1
          IN pb     – SEKAI/PAO (FD)
          OUT pb    – DTV/MON 2
          IN pb     – XYBION (MD)

    5.  SEKAI POWERUP
PGSC    Sel RelayCmds (brings up Relay Commanding Page)
        Relay Commanding
        Sel Sekai – On (  RELAYK4 ON)
        Sel Xmit
        Sekai – green

MON 1   If Sekai video signal not displayed:
A7          VID OUT pb  – MON 1
              IN pb     – SEKAI/PAO (FD)

    6.  DSR–20 RECORD
L10(MUX)    VTR/CC PWR – on (LED on)
            MUX/VTR/CC PWR – on (LED on)
            MUX BYPASS – VTR DNLK
  (VIP)     PWR – on (LED on)
VTR/DSR–20  ON/STANDBY LED  green
            Verify tape installed
            REC pb – press, hold
            PLAY pb – press simo (  red dot displayed)

    7.  XYBION PWR CHECK
        Relay Commanding
        Xybion – green
MON 2   Xybion video signal displayed

        * If Xybion – white:                               *
        *     Perform XYBION ACTIVATION, 1–83              *

    8.  DSR–20 RECORD CHECK
VTR/DSR–20  STOP pb – press
            REW pb – press (to tape start)
            PLAY pb – press
MON 2       Verify signal is correctly displayed
VTR/DSR–20  STOP pb – press
            REW pb – press (to tape start)
            REC pb – press, hold
            PLAY pb – press, simo (  red dot displayed)
```



```
    9.  XYBION TIME CONFIG
        Sel XybCmd (brings up Xybion CmdForm Display)
        Sel XybTlm (brings up Xybion Camera Display)

        a.  Date Check
MON 2       Date not 00/00/00

            * If Date is 00/00/00:                         *
            *     Perform XYBION ACTIVATION step 2a, 1–83  *

        b.  MET "Time" Check
MON 2       Time offset between Xybion MET Video signal and MET clock ≤ 3 sec

            * If time offset > 3 sec:                      *
            *     Perform XYBION ACTIVATION step 2b, 1–83  *

PGSC    10. XYBION CAMERA CONFIG
        a.  Current Settings Report
            XybionCmdForm
            Sel Report Current Settings (  T C)
            Sel Xmit

            Xybion Camera Display
            Wait 30 sec (until IMC > appears)
            CCD Temperature:  20°–40°

            * If CCD temperature out of range:             *
            *     Report to MCC                            *

        b.  Enter Lock Settings
            XybionCmdForm
            Enter Lock = 3
            Sel Lock (  L 3)
            Sel Xmit

            Xybion Camera Display
            IMC > L3
MON 2       Filter:  3

PGSC    c.  Enter Gain Settings
            XybionCmdForm
            Enter Gain = 70
            Sel Gain (  G 70)
            Sel Xmit

MON 2       Gain:  70% ± 1

PGSC    d.  Return to Gain Settings
            XybionCmdForm
            Enter Gain = 65
            Sel Gain (  G 65)
            Sel Xmit

MON 2       Gain:  65% ± 1
```



```
PGSC    e.  Enter Exposure Mode
            XybionCmdForm
            Sel Exposure Video Mode Average Video (  EVA)
            Sel Xmit
            Sel Report Current Settings (  T C)
            Sel Xmit

            Xybion Camera Display
            Wait 30 sec (until IMC > appears)
            Auto Exposure Mode:  Average

        f.  Return to Unlocked Filter
            XybionCmdForm
            Sel Run (  R)
            Sel Xmit

            Xybion Camera Display
            IMC > R
MON 2       Filter and display changing

        g.  Return to Nominal Exposure Mode
            XybionCmdForm
            Sel Exposure Video Mode Peak Video (  EVP)
            Sel Xmit

            Sel Report Current Settings (  TC)
            Sel Xmit
            Xybion Camera Display
            Wait 30 sec (until IMC> appears)
            Auto Exposure Mode:  Peak

            MEIDEX_PGSC_V4_15_0
            Sel XybCmd (closes XybionCmdForm Page)
            Sel XybTlm (closes Xybion Camera Display Page)

    11. DSR 20 RECORD STOP
VTR/DSR–20  STOP pb – press
            ON/STANDBY pb – press (red LED on)
L10(VIP)    PWR – OFF (LED off)
  (MUX)     VTR/CC – off (LED off)
            MUX BYPASS – SH PL DATA
            MUX/VTR/CC PWR – off (LED off)

            Perform MEIDEX RECORDING LOG (Cue Card)
            Enter Tape # and VTR/DSR–20 Time Remaining for current tape

    12. VCR1 CONFIG
        Sel RelayCmds (brings up Relay Commanding Page)
        Sel DigTlm (brings up Digital Telemetry Page)

        a.  VCR Record On
            Relay Commanding
            Sel VCR1 – On (  RELAYK1 ON)
            Sel Xmit
            VCR1 – green

            Sel Record1 – On (  RELAYK2 ON)
            Sel Xmit
```

DigitalTelemetry
VCR1 Record – green
VCR1 Standby – white
Verify VCR Elapsed Secs increasing by steps of 10–20 sec

b. VCR Record Off

NOTE
MEIDEX has a limited amount of VCR recording space. If VCR Recording is left ON inadvertently, all of available tape will be used

Relay Commanding
Sel Record1 – Off (RELAYK2 OFF)
Sel Xmit

DigitalTelemetry
VCR1 Standby – green
VCR1 Record – white
Record Elapsed Secs: _____

Relay Commanding
Sel Unthrd1 – On (RELAYK3 ON)
Sel Xmit
Unthrd1 – green

Sel VCR1 – Off (RELAYK1 OFF)
Sel Xmit
VCR1 – white

Sel Unthrd1 – Off (RELAYK3 OFF)
Sel Xmit
Unthrd1 – white

13. VCR2 CONFIG
a. VCR Record On
Sel VCR2 – On (RELAYK9 ON)
Sel Xmit
VCR2 – green

Sel Record2 – On (RELAYK10 ON)
Sel Xmit

DigitalTelemetry
VCR2 Record – green
VCR2 Standby – white
Verify VCR Elapsed Secs increasing by steps of 10–20 secs

b. VCR Record Off

NOTE
MEIDEX has a limited amount of VCR recording space. If VCR Recording is left ON inadvertently, all of available tape will be used

Relay Commanding
Sel Record2 – Off (RELAYK10 OFF)
Sel Xmit

DigitalTelemetry
VCR2 Standby – green
VCR2 Record – white
Record Elapsed Secs: _____

Relay Commanding
Sel Unthrd2 – On (RELAYK11 ON)
Sel Xmit
Unthrd2 – green

Sel VCR2 – Off (RELAYK9 OFF)
Sel Xmit
VCR2 – white

Sel Unthrd2 – Off (RELAYK11 OFF)
Sel Xmit
Unthrd2 – white

14. VCR3 CONFIG
a. VCR Record On
Relay Commanding
Sel VCR3 – On (RELAYK17 ON)
Sel Xmit
VCR3 – green

Sel Record3 – On (RELAYK18 ON)
Sel Xmit

DigitalTelemetry
VCR3 Record – green
VCR3 Standby – white
Verify VCR Elapsed Secs increasing by steps of 10–20 sec

b. VCR Record Off

NOTE
MEIDEX has a limited amount of VCR recording space. If VCR Recording is left ON inadvertently, all of available tape will be used

Relay Commanding
Sel Record3 – Off (RELAYK18 OFF)
Sel Xmit

DigitalTelemetry
VCR3 Standby – green
VCR3 Record – white
Record Elapsed Secs: _____

Relay Commanding
Sel Unthrd3 – On (RELAYK19 ON)
Sel Xmit
Unthrd3 – green

Sel VCR3 – Off (RELAYK17 OFF)
Sel Xmit
VCR3 – white

Sel Unthrd3 – Off (RELAYK19 OFF)
Sel Xmit
Unthrd3 – white

Enter VCR1,2,3 Elapsed Sec in MEIDEX RECORDING LOG (Cue Card)
Voice VCR 1,2,3 Elapsed Sec to ground

Sel RelayCmds (closes Relay Commanding Page)
Sel DigTlm (closes Digital Telemetry Page)

15. V10 CONFIG
V10 PWR – ON
REC pb (two simo) – press (red dot displayed)
Wait 10 sec
STOP pb – press
REW pb – press (to start of tape)
PLAY pb – press
Verify signal is correctly displayed on V10 Display
STOP pb – press
REW pb – press (to start of tape)
PWR – OFF

16. TRUSS POINTING CONFIG
Sel TrussCntrl (brings up Truss Pointing Display)

CAUTION
Truss movement is + to orbiter port and – to orbiter starboard. Limits are ± 22 deg

Truss Pointing Display
Record Truss Angle: _____
If Truss Angle > | 2 |, Enter Truss Pointing commanding:
X (X = ± value reqd to return to 0)
Sel Xmit
Verify truss moving on monitors
Truss angle = 0 deg ± 2.0
Enter Truss Point Commanding: –5
Sel Xmit

MON1(2) Verify truss moving
PGSC Truss angle = –5 deg ± 2.0
Enter Truss Point Commanding: 5
Sel Xmit

MON1(2) Verify truss moving
PGSC Truss angle = 0 deg ± 2.0

Enter Truss Point Commanding: 5
Sel Xmit
MON1(2) Verify truss moving
PGSC Truss angle = 5 deg ± 2.0

Enter Truss Point Commanding: –5
Sel Xmit
MON1(2) Verify truss moving
If Truss Angle > | 2 |:
Enter Truss Point Commanding: X (X = ± value reqd to return to 0)
Sel Xmit
Verify truss moving on monitors
PGSC Truss angle = 0 deg ± 2.0

Sel TrussCntrl (closes Truss Pointing Display)

PGSC 17. CAMERA DEACT
Sel XybCmd (brings up XybionCmdForm display)
Sel XybTlm (brings up Xybion Camera Display)

Xybion CmdForm
Sel Report Current Settings (TC)
Sel Xmit

Xybion Camera Display
Wait 30 sec (until IMC> appears)
Sel XybCmd (closes XybionCmdForm Display)
Sel XybTlm (closes Xybion Camera Display)
Sel RelayCmds (brings up Relay Commanding Page)
Relay Commanding
Sel Sekai – Off (RELAYK4 OFF)
Sel Xmit
Sekai – white

Sel Xybion – Off (RELAYK5 OFF)
Sel Xmit
Xybion – white

Sel VideoBuff – Off (RELAYK8 OFF)
Sel Xmit
Video Buff – white

Sel RelayCmds (closes Relay Commanding Page)

18. DOOR CLOSURE, if reqd
Execute Package if step 18 reqd

NOTE
MEIDEX door requires ~35 sec to close with dual motor operations, ~70 sec to close with single motor ops. tb will read bp when door is < ~94 deg open

L12U MEIDEX DOOR – CLOSE
DOOR FULL OP tb – bp

Camera D On visual confirmation of door full closed:
cb DOOR PWR CONT PWR DN ENA – op

19. FILE TRANSFER
Exit MEIDEX software
Copy most recent MEIDEX data files to OCA machine (STS–1) downlink location:
c:\oca–down\payloads via network
Files reqd:
c:\meidex\RawTlmData<MMDDYYYYhhmm>.bin (211 kb) – Downlink all RawTlmData files from current observation set
c:\meidex\EventLog<MMDDYYYYhhmm>.txt, variable size – Downlink EventLog from current observation set
c:\meidex\XybionLog<MMDDYYYYhhmm>.txt, variable size – Downlink XybionLog from current observation set

If network unavailable:
Use PCMCIA card to transfer files to OCA machine (STS–1)
Ref: OCA DOWNLINK VIA GROUND COMMAND (ORB OPS, PGSC)

Open Shuttle Apps Folder
Sel MEIDEX icon
MEIDEX_PGSC_V4_15_0
Sel OpenComm (green)
Sel AutoTlm (green)

Notify MCC when PGSC file ready for OCA downlink, MEIDEX CHECKOUT complete

NOTE
MEIDEX PGSC must remain ON with AUTOTLM enabled in order to ensure steady telemetry downlinked to ground

MEIDEX SETUP

* If at any time during procedure lower status bar reads PGSC_Not_Cntrl, perform the following:
* Go to Pages/Cmd Generator Display
* Command Control
* Sel IMTAKINGOVER
* Sel Xmit
* Sel OK
* Sel Close (Close Command Control)
* MEIDEX_PGSC_V4_V15_0
* On lower status bar, PGSC_Cntrl

NOTE
Setup must be initiated 45 min prior to observation start (T) as documented in Execute Package

1. TIMER SETUP
A4 Determine time until observation Start (T)
Set Egg Timer
Initiate Egg Timer

2. P/TV CHECK
P/TV10 MEIDEX OPS, SETUP (PHOTO/TV FS, SCENES) complete

3. TAPE VERIFICATION
Go to MEIDEX RECORDING LOG (Cue Card)
Check tapes, replace and log if necessary

Observation Type	Replace Criteria
ROI/Moon Cal	replace tape if time remaining < 15 min
Sprite	replace tape

4. TLM CONFIG
NLT T–40 min MEIDEX_PGSC_V4_15_0
OpenComm – Green
Auto Tlm – Green

5. EVENT LOG CONFIG
Sel Event (brings up Event Page)

Event Page
Configure as follows:
Log to File –
Report Limits –
Show Auto TLM – no
Sel Event (closes Event Page)

MEIDEX_PGSC_V4_15_0
No Red/Yellow limit violations (limit check boxes in upper right of display = 0, 0)

* If Red/Yellow limit violations:
* Sel Event (brings up Event Page)
* Determine red/yellow limit violation
* Report to MCC

6. PLD VCR ACTIVATION
PGSC Execute Package if step 6 reqd

Sel RelayCmds
Relay Commanding
Sel VCR3(2,1) – On (RELAYK17(K9,K1) ON)
Sel Xmit
VCR3(2,1) – green

7. SEKAI ACTIVATION
Execute Package if step 7 reqd
Relay Commanding
Sel Sekai – On (RELAYK4 ON)
Sel Xmit
Sekai – green

MEIDEX SCIENCE

* If at any time during procedure lower status bar reads PGSC_Not_Cntrl, perform the following:
* Go to Pages/Cmd Generator Display
* Command Control
* Sel IMTAKINGOVER
* Sel Xmit
* Sel OK
* Sel Close (Close Command Control)
* MEIDEX_PGSC_V4_V15_0
* On lower status bar, PGSC_Cntrl

T–15 1. XYBION PWR CHECK
On MCC GO:
PGSC MEIDEX_PGSC_V4_15_0
OpenComm – green
AutoTlm – green

Sel RelayCmds (brings up Relay Commanding Page)
Relay Commanding
Xybion – green

* If Xybion – white:
* Perform XYBION ACTIVATION, 1–83

2. XYBION TIME/DATE CHECK
Sel XybCmd (brings up XybionCmdForm Page)
Sel XybTlm (brings up Xybion Camera Display)

MON 2 a. Date Check
Date not 00/00/00

* If Data is 00/00/00:
* Perform XYBION ACTIVATION step 2a, 1–83

b. MET "Time" Check
Time offset between Xybion MET Video signal and MET clock ≤ 3 sec

* If time offset > 3 sec:
* Perform XYBION ACTIVATION step 2b, 1–83

T–10 3. DOOR OPENING, if reqd
L12U If MEIDEX DOOR FULL OPEN tb – gray, proceed to step 4

Execute Package for Door Open Time
Continue with MEIDEX SCIENCE and perform step 3a per Execute Package MET

NOTE
MEIDEX Door will nominally be opened at T–10; however opening may be delayed per Execute Package instructions during some operations to protect against violation of sun/ram constraints

a. Door Opening
cb DOOR PWR CONT PWR DN ENA – cl
MEIDEX DOOR – OPEN

NOTE
MEIDEX door requires ~35 sec to open with dual motor operations, ~70 sec to open with single motor ops. tb will read gray when door is > ~94 deg open

After 35 sec, MEIDEX DOOR FULL OPEN tb – gray
MON 1 Visually verify MEIDEX door open
Report door position to MCC

4. XYBION CAMERA CONFIG
Execute Package if step 4 reqd and determine Payload Setup

Sel XybCmd (brings up XybionCmdForm display)
Sel XybionTlm (brings up Xybion Camera display)
Perform following PGSC cmds and checks per table:

NOTE
Press Xmit button to transmit each cmd in table below

Command/Check	PAYLOAD SETUP		
	ROI	MOON CAL	SPRITE
Lock			5 (L 5)
Gain	65 (G 65)	65 (G 65)	80 (G 80)
Exposure Video Mode	Peak Video (EVP)	Peak Video (EVP)	Peak Video (EVP)
Configuration Peak Video Level	180 (C P 180)	120 (C P 120)	120 (C P 120)
Report Current Settings	T C	T C	T C
On Xybion Camera Display, wait 30 sec (until IMC > appears)			
Target Levels, Peak	180	120	120

5. MONITOR 2 CHECKS
Perform following Monitor 2 checks per table:

Check	PAYLOAD SETUP		
	ROI	MOON CAL	SPRITE
Filter	Variable (changing rapidly)	Variable (changing rapidly)	5
Gain	65% ± 1	65% ± 1	80% ± 1
Exp	Variable (changing rapidly)	Variable (changing rapidly)	Variable (changing rapidly)
Temp	20° – 40°	20° – 40°	20° – 40°
Current Date	01/DD/01 (DD = MET day)	01/DD/01 (DD = MET day)	01/DD/01 (DD = MET day)
Current MET	HH:MM:SS (± 3 sec)	HH:MM:SS (± 3 sec)	HH:MM:SS (± 3 sec)

* If Filter not variable (ROI/MOON CAL only): *
* XybCmdForm *
* Sel Run (R) *
* Sel Xmit *
* Xybion Camera Display *
* IMC>R *
* On Monitor 2, Filter variable *

* If Gain not as expected: *
* XybCmdForm *
* Enter Gain = XX *
* Sel Gain (G XX) *
* Sel Xmit *
* Xybion Camera Display *
* IMC>G XX *
* On Monitor 2, Gain = XX ± 1 *

* If Exp not variable: *
* Notify MCC and continue *

Sel XybCmd (closes XybionCmdForm display)
Sel XybionTlm (closes Xybion Camera display)

6. TRUSS POINTING CONFIG
Execute Package if step 6 reqd

MEIDEX_PGSC_V4_15_0
Sel TrussCntrl (brings up Truss Pointing display)
Truss Pointing Display
If Truss Angle > 2 deg off reqd angle:

NOTE
Truss movement is '+' to orbiter port and '–' to orbiter starboard.
Limits are ± 22 deg

Enter Truss Point Commanding: X (X = value necessary to get to reqd truss position per Execute Package)
Sel Xmit

AFD Verify Truss moving on monitors (1,2)

Truss Pointing Display
PGSC Truss angle = reqd angle ± 2.0 deg

Sel TrussCntrl (closes Truss Pointing display)

T–6 7. IN CABIN RECORD START
L10(MUX) VTR/CC PWR – on (LED on)
Execute Package, if real time digital dnlk:
MUX/VTR/CC PWR – on (LED on)
MUX BYPASS – VTR DNLK
(VIP) PWR – on (LED on)
DSR–20 ON/STANDBY LED green
REC pb – press, hold
PLAY pb – press simo (red dot displayed)

V10 PWR – ON
REC pb (two simo) – press (red dot displayed)

A7 VID OUT pb – MON 1
IN pb – SEKAI/PAO (FD)

T–1 **8. PLD VCR ACTIVATION, if reqd**
Execute Package if step 8 reqd

NOTE
Payload VCRs will not nominally be used during Sprite observations

PGSC **Sel RelayCmds (brings up Relay Commanding Page)**
Sel DigTlm (brings up Digital Telemetry Page)

Relay Commanding
Sel Record3(2,1) – On (RELAYK18(K10,K2) ON)
Sel Xmit

Digital Telemetry
VCR3(2,1) Record – green
VCR3(2,1) Standby – white

9. MEIDEX OBSERVATION
Sel TrussCntrl (brings up Truss Pointing display)

Adjust truss towards target as reqd per visual
If Truss Pointing Angle adjustments reqd:
Truss Pointing Display
Enter Truss Point Commanding = X (as reqd to track target)
Sel Xmit

Voice observations to MCC per table:

Dust	Sprite	Moon
1) If Sea Surface: note presence of small clouds (scattered/gathered, % sea obscured)? 2) Are narrow, long dust streaks/plumes evident at land sea interface (average width = 1/10 of length)? Note number	1) Intensity of lightning activity (high/moderate/low) 2) Sprites visible above lightning (yes/no)? 3) Color of Sprite(s) (red/blue)?	Moon outside Xybion FOV? If yes, note location of moon on Sekai (Xybion FOV = ~1/3 of Sekai FOV)

At observation end:
Sel TrussCntrl (closes Truss Pointing display)

NOTE
Step 10 will not be performed until observation end per execute package

10. PLD VCR RECORD STOP

NOTE
MEIDEX has a limited amount of PLD VCR recording space. If PLD VCR Recording is left ON inadvertently, all of available tape will be used

Perform per Execute Package MET:
Relay Commanding
If Record3(2,1) – On
Sel Record3(2,1) – Off (RELAYK18(K10,K2) OFF)
Sel Xmit

Digital Telemetry
VCR3(2,1) Record – white
VCR3(2,1) Standby – green

11. IN CABIN RECORD STOP
V10 STOP pb – press
VTR/
DSR–20 STOP pb – press

Voice PLD VCR Elapsed Sec to ground

Go to MEIDEX RECORDING LOG (Cue Card):
Enter Obs Type (D = Dust, S = Sprite, M = Moon Cal)
Enter Orbit # and V10 Time Remaining for current tape
Enter VTR/DSR–20 Time Remaining for current tape
Enter VCR3(2,1) Elapsed Sec

Replace tapes if necessary

Observation Type	Replace Criteria
ROI/Moon Cal	replace tape if time remaining < 15 min
Sprite	replace tape

12. P/TV PWRDN
Execute Package if step 12 reqd

VTR/
DSR–20 ON/STANDBY – press (red LED on)
V10 PWR – OFF
L10
(VIP) PWR – off (LED off)
(MUX) VTR/CC PWR – off (LED off)

If MUX powered:
MUX BYPASS – SH PL DATA
MUX/VTR/CC PWR – off (LED off)

13. DOOR CLOSE
Execute Package if step 13 reqd

L12U MEIDEX DOOR – CLOSE
DOOR FULL OPEN tb – bp

MON 1 On visual verification of door fully closed:
L12U cb DOOR PWR CONT PWR DN ENA – op
Notify MCC door closed

14. PLD VCR SWAP
Execute Package if step 14 reqd

Sel Unthrd3(2,1) – On (RELAYK19(K11,K3) ON)
Sel Xmit
Unthrd3(2,1) – green

Sel VCR3(2,1) – Off (RELAYK17(K9,K1) OFF)
Sel Xmit
VCR3(2,1) – white
Sel Unthrd3(2,1) – Off (RELAYK19(K11,K3) OFF)
Sel Xmit
Unthrd3(2,1) – white

Execute Package for alt. VCR

Sel VCR3(2,1) – On (RELAYK17(K9,K1) ON)
Sel Xmit
VCR3(2,1) – green

15. STATUS CHECK
Execute Package if step 15 reqd

Sel XybCmd (brings up XybionCmdForm Page)
Sel XybTlm (brings up Xybion Camera Display)

[XybionCmdForm]
Sel Report Current Settings (T C)
Sel Xmit

[Xybion Camera Display]
Wait 30 sec (until IMC > appears)

Sel XybCmd (closes XybionCmdForm Page)
Sel XybTlm (closes Xybion Camera Display)

16. TRUSS RECONFIG
Execute Package if step 16 reqd

PGSC Sel TrussCntrl (brings up Truss Pointing Display)
[Truss Pointing Display]
If Truss Angle > | 2 | :
Enter Truss Point Commanding: X (X = ± value reqd to return to 0)
Sel Xmit
Verify truss moving on monitors
Truss angle = 0 deg ± 2.0
Sel TrussCntrl (closes Truss Pointing Display)

MEIDEX CLOSEOUT

1. PLD VCR DEACT
PGSC Sel RelayCmds (opens Relay Commanding Page)

[Relay Commanding]
Sel Unthrd3(2,1) – On (RELAYK19(K11,K3) ON)
Sel Xmit
Unthrd3(2,1) – green

Sel VCR3(2,1) – Off (RELAYK17(K9,K1) OFF)
Sel Xmit
VCR3(2,1) – white

Sel Unthrd3(2,1) – Off (RELAYK19(K11,K3) OFF)
Sel Xmit
Unthrd3(2,1) – white

2. SEKAI DEACT
[Relay Commanding]
Sel Sekai – Off (RELAYK4 OFF)
Sel Xmit
Sekai – white

3. XYBION DEACT
Sel XybCmd (brings up XybionCmdForm Page)
Sel XybTlm (brings up Xybion Camera Display)

[XybionCmdForm]
Sel Report Current Settings (T C)
Sel Xmit

[Xybion Camera Display]
Wait 30 sec (until IMC> appears)

Sel XybCmd (closes XybionCmdForm Page)
Sel XybTlm (closes Xybion Camera Display)

[Relay Commanding]
Sel Xybion – Off (RELAYK5 OFF)
Sel Xmit
Xybion – white

Sel VideoBuff – Off (RELAYK8 OFF)
Sel Xmit
Video Buff – white

4. TRUSS RECONFIG
Sel TrussCntrl (brings up Truss Pointing Display)
[Truss Pointing Display]
If Truss Angle > | 2 | :
Enter Truss Point Commanding: X (X = ± value reqd to return to 0)
Sel Xmit
Verify truss moving on monitors
Truss Angle = 0 deg ± 2.0
Sel Truss Cntrl (closes Truss Pointing Display)

5. FILE TRANSFER
Exit MEIDEX software
Copy most recent MEIDEX data files to OCA machine (STS–1) via network; downlink location: c:\oca–down\payloads
Files reqd:
c:\meidex\RawTlmData <MMDDYYYYhhmm>.bin (211 kb) –
Downlink all RawTlmData files from current observation set
c:\meidex\EventLog <MMDDYYYYhhmm>.txt, variable size –
Downlink EventLog from current observation set
c:\meidex\XybionLog <MMDDYYYYhhmm>.txt, variable size –
Downlink XybionLog from current observation set
If network unavailable:
Use PCMCIA card to transfer files to OCA machine (STS–1)
Ref: OCA DOWNLINK VIA GROUND COMMAND (ORB OPS, PGSC)

Open Shuttle Apps Folder
Sel MEIDEX icon
[MEIDEX_PGSC_V4_15_0]
Sel OpenComm (green)
Sel AutoTlm (green)

Notify MCC when PGSC file ready for OCA downlink

NOTE
MEIDEX PGSC must remain ON with AUTO TLM enabled to ensure steady telemetry downlinked to ground

MEIDEX PRE–DEACTIVATION HEALTH CHECK

* If at any time during procedure lower status bar *
* reads PGSC_Not_Cntrl, perform the following: *
* Go to Pages/Cmd Generator Display *
* [Command Control] *
* Sel IMTAKINGOVER *
* Sel Xmit *
* Sel OK *
* Sel Close (Close Command Control) *
* [MEIDEX_PGSC_V4_V15_0] *
* On lower status bar, PGSC_Cntrl *

NOTE
Procedure will nominally be performed by POCC and will only be reqd if cmd capability from ground is lost

1. DOOR POSITION CHECK
L12U MEIDEX DOOR – CLOSE
DOOR FULL OPEN tb – bp

2. TLM CONFIG
[MEIDEX_PGSC_V4_15_0]
OpenComm – green
AutoTlm – green

3. EVENT LOG CONFIG
Sel Event (brings up Event Page)

[Event Page]
Configure as follows:
Log to File –
Report Limits –
Show Auto TLM – no

Sel Event (closes Event Page)
[MEIDEX_PGSC_V4_15_0]
No Red/Yellow limit violations (limit check boxes in upper right of display = 0,0)

* If Red/Yellow limit violations: *
* Sel Event (brings up Event Page) *
* Determine red/yellow limit violation *
* Report to MCC *

4. PRE–DEACT CONFIG CHECK
Sel RelayCmds (brings up Relay Commanding Page)
[Relay Commanding]

If Heater1 – green
Sel Heater1 – Off (RELAYK20 OFF)
Sel Xmit
Heater1 – white

All relays – white
Sel RelayCmds (closes Relay Commanding Page)

5. TRUSS POSITION CHECK
Sel TrussCntrl (brings up Truss Pointing Display)

Truss Pointing Display
Limit Switch1 – Not_Limit
Limit Switch2 – Not_Limit
Rvrs Lim Violat – No
Fwrd Lim Violat – No
OverCurr Violat – No

If Truss Angle > | 2 |:
Enter Truss Point Commanding: X (X = ± value reqd to return to 0)
Sel Xmit
Verify Truss moving on monitors
Truss angle = 0 deg ± 2.0

Sel TrussCntrl (closes Truss Pointing Display)

Report Status to MCC

Exit PGSC software

XYBION ACTIVATION

1. XYBION PWRUP
Sel RelayCmds (brings up Relay Commanding Page)

PGSC Relay Commanding
Sel VideoBuff – On (RELAYK8 ON)
Sel Xmit
VideoBuff – green

Sel Xybion – On (RELAYK5 ON)
Sel Xmit
Xybion – green

MON 2 Xybion video signal displayed

* If errors on Xybion video signal: *
* Notify MCC *
* Once problem resolved, continue *

Sel RelayCmds (closes Relay Commanding Page)

2. TIME/DATE CONFIG

PGSC Sel XybCmd (brings up XybionCmdForm Page)
Sel XybTlm (brings up Xybion Camera Display)

a. Date Check

NOTE
If MET day is "00", enter "31", as Xybion will not accept an entry of "00" in this field

XybCmdForm
In cursor field above and to left of XMIT button, complete as follows, with "DD" = current MET day: C D 01 DD 02

Sel XMIT

Xybion Camera Display
Prompt reads IMC>C D 01 DD 02
No error messages

MON 2 Date updated within Xybion video signal

b. MET "Time" Update

NOTE
MEIDEX requires highly accurate time stamping on Xybion video. As ~4 sec lag is encountered during command acceptance sequence, MET time keyed in must be 4 sec later than actual time at command transmission

PGSC XybionCmdForm
In cursor field above and to left of XMIT button, complete as follows, with "HH", "MM" and "SS" as current MET time, hr, min, sec:
C T HH MM SS

Sel XMIT 4 sec prior to target time
Xybion Camera Display
Prompt reads IMC>C T HH MM SS
No error messages

MON 2 If time offset between Xybion video signal and MET clock >3 sec:
Repeat step 2b

PGSC Sel XybCmd (closes XybionCmdForm Page)
Sel XybTlm (closes Xybion Camera Display)

MEIDEX PGSC STOW

1. POWER OFF PGSC AND UTILITY PANEL

PGSC Laptop pwr (side) – OFF
DC PWR SUPPLY – OFF (lt not lit)
A11 DC UTIL PWR MNC – OFF

2. DISCONNECT CABLES

PDIP Disconnect: Data cable from MEIDEX PGSC outlet
PGSC Data cable from Comm 2 port
Pwr cable from PGSC Power Port
Pwr cable from DC Power Supply J2
Pwr cable from DC Power Supply J1
A11 Pwr cable from DC UTIL PWR MNC

PGSC Remove PCMCIA RS422 Comm Card from PGSC
Remove PCMCIA RF LANCard from PGSC

3. STOW MEIDEX PGSC

MF28O Stow:
PL1 MEIDEX PGSC
PCMCIA RS422 Comm Card
PCMCIA RF LANCard
DC/DC Power Supply
DC Power Supply Cable
PGSC DC Power Supply Cable

Notify MCC, MEIDEX PGSC STOW complete

OARE

OARE ACT 2–2
DEACT 2–2

OARE

OARE ACT

L12U cb OARE PWR CAB P/L BUS CB3 – cl

cb OARE PWR CAB P/L BUS CB1 – cl
OARE PWR – ON

OARE DEACT

L12U OARE PWR – OFF
cb OARE PWR CAB P/L BUS CB1 – op

cb OARE PWR CAB P/L BUS CB3 – op

DEORBIT PREP

PAYLOAD DEACT 3–2
REACT 3–2
DEORBIT WAVEOFF 3–2
PAYLOAD ENT SW LIST/VERIF 3–3

DEORBIT PREP

PAYLOAD DEACT

N/A

PAYLOAD REACT

On MCC GO:
L1 FLOW PROP VLV LOOP 1 – PL HX (tb–PL)

DEORBIT WAVEOFF

Perform FREESTAR ACTIVATION (FREESTAR)

Perform SOLSE PGSC/BIA SETUP (FREESTAR)

Go to SOLSE/HRIU ACTIVATION (FREESTAR)

PAYLOAD ENT SW LIST/VERIF

PAYLOAD PWR CONFIG

R1
PL CAB – MNA(MNB)
PRI MNB – ctr (tb–OFF)
FC3 – ctr (tb–OFF)
MNC – ctr (tb–ON)
AUX – ON
AFT MNB – ON
MNC – OFF

MA73C:E
cb AC2 PL 3Φ – cl
AC3 PL 3Φ – cl

L12U
(OARE)
OARE PWR – OFF
cb OARE PWR CAB P/L BUS CB1 – op
SW PWR – op

(FREESTAR)
HITCHHIKER AV PWR – ctr (tb–bp)
EXP PWR – ctr (tb–bp)
LPT PWR ENA 1 – OFF (tb–bp)
2 – OFF (tb–bp)

MEIDEX DOOR – CLOSE (tb–bp)
cb DOOR PWR/CONT PWR DN ENA – op
OARE PWR CAB P/L BUS CB3 – op

L12L
(SSP–2)
ORB H2O LN HTR – ctr
cb PDIP PWR 1 – op

(SPACEHAB)
FIRE SUPPR FSCU (two) – ctr (tb–DN)
CAB DEPRESS VLV ARM/SAFE – SAFE (tb–bp)
OP/CL – CL
FULL OPEN tb – bp
NOT CL tb – bp
SMOKE SNSR RESET/TEST – ctr
A – ENA (tb–gray)
B – ENA (tb–gray)

MN PWR – NO–OP
PDU SS DC BUS – ctr (tb–gray)
PDU MN DC BUS – ON (tb–gray)
FWD INV – NO–OP (tb–gray)
PDU EXP DC BUS – ctr (tb–gray)
cb SW PWR – cl
ORB H2O LN HTR PWR – op

C3A5
SH FIRE SPPR MCP – SAFE
MCP – NO–OP
FSCU – SAFE
FSCU – NO–OP
H2O LINE HTRS – OFF

ML86B:E
cb MNB MAR 1 – cl
2 – cl

ML85E
AC S1 – OFF
cb AC CB1 – op
DC 10 AMP MNB S2,S3 (two) – ON
cb DC 10 AMP MNB CB2,CB3 (two) – cl
DC 10 AMP MNB S4,S5 (two) – OFF
cb DC 10 AMP MNB CB4,CB5 (two) – op
PUMPS S6 – OFF
cb PUMPS CB6 – op
PUMPS CB7 – op

MO13Q
DC UTIL PWR MNB – ON

MIDDECK
(TEPC)
SW–1 – OFF

MF28G/H
(Biopack)
CENTRIF 1,2,3 (three) – ON
INCUB – ctr
RESET – ctr
COOLER – ctr
FREEZER ON/OFF – ctr
COOL/FREEZE – ctr
ETL – ctr
rotary sw – T COOLER
UP/DOWN – ctr
MAIN POWER – ON
POWER MAIN FAN – ON
COOLER/FREEZER – ON
INCUBATOR – ON
BIOPACK ELECTRONICS – ON
EXPERIMENT ELECTRONICS – ON
AUXILIARY – OFF

MF71C
(CEBAS)
cb PWR – on
PWR lt – on
RECORD lt – off

MF71G
(OSTEO)
cb CB1 – cl
S1 (four) – OFF (dn)
L1 lt (four) – off

MF71O
(BRIC)
cb CB1 – op (out)
POWER lt – off

MA16D
(CMPCG)
cb MAIN – cl
FAN – cl
BATT – cl
28V – cl
LCD – not blank
pb (four) – not blinking
FAN – running

CONTINGENCY EVA PL CONFIG

PRE–EVA PL CONFIG 4–2
POST–EVA PL CONFIG 4–2

CONT EVA PL CONFIG

PRE–EVA PL CONFIG

SPACEHAB PREP
If Spacehab to remain isolated for remainder of mission:
Perform ENTRY PREP (RDM OPS)
If Spacehab will be reentered:
Perform SPACEHAB PREP FOR EVA (RDM OPS, CONTINGENCY PROCEDURES)

FREESTAR PREP
Visually verify MEIDEX, SOLSE, and SOLCON doors closed
MCC pwr removed from MEIDEX, SOLSE, and SOLCON doors

L12U
LPT PWR ENA 1 – OFF (tb–bp)
2 – OFF (tb–bp)

POST–EVA PL CONFIG

SPACEHAB RECONFIG
If Spacehab will be reentered:
Perform SPACEHAB RECONFIG POST EVA (RDM OPS, CONTINGENCY PROCEDURES)
Else, no actions reqd
Spacehab configured for entry

L12U
FREESTAR RECONFIG
LPT PWR ENA 1 – ON (tb–gray)
2 – ON (tb–gray)

CONT EVA PL CONFIG

ASC PWRDN RECOVERY

MIDDECK (A PWRDN) 5–2
SPACEHAB (B PWRDN) 5–2

ASC PWRDN RECOVERY

MIDDECK (A PWRDN)

NOTE
When orbiter pwr removed, science degradation will occur to Biopack, BRIC, CEBAS, OSTEO, and CMPCG

1. Perform MIDDECK EXPERIMENT POWER LOSS CONFIGURATION (SH EH, EXPERIMENT POWER LOSS CONFIGURATION)

ML86B:E 2. cb MNB MAR 1,2 (two) – cl

MO13Q 3. DC UTIL PWR MNB – ON

4. Go to MIDDECK EXPERIMENT RECOVERY AFTER POWER LOSS (SH EH, EXPERIMENT RECOVERY AFTER POWER LOSS)

SPACEHAB (B PWRDN)

R1 1. PL CAB – MNA
AFT MNB – ON
AUX – ON

L12L 2. MN PWR – KILL

R1 3. PL PRI MNC – ON (tb–ON)

L12L 4. cb ORB H2O LN HTR PWR – cl
ORB H2O LN HTR – A
C3A5 H2O LN HTRS – ON

ASC PWRDN RECOVERY

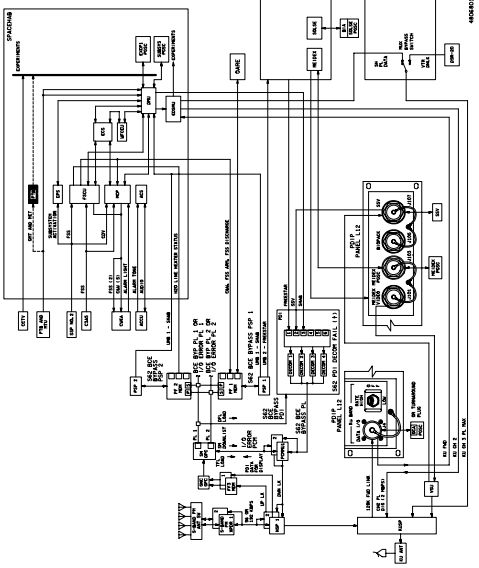
PAYLOAD COMM MALFUNCTIONS

6.1 PL COMM
STS–107 COMM MALFUNCTION POINTS 6–2
6.1a S62 PDI DECOM FAIL 6–3

PAYLOAD COMM MALS

PAYLOAD COMM MALS

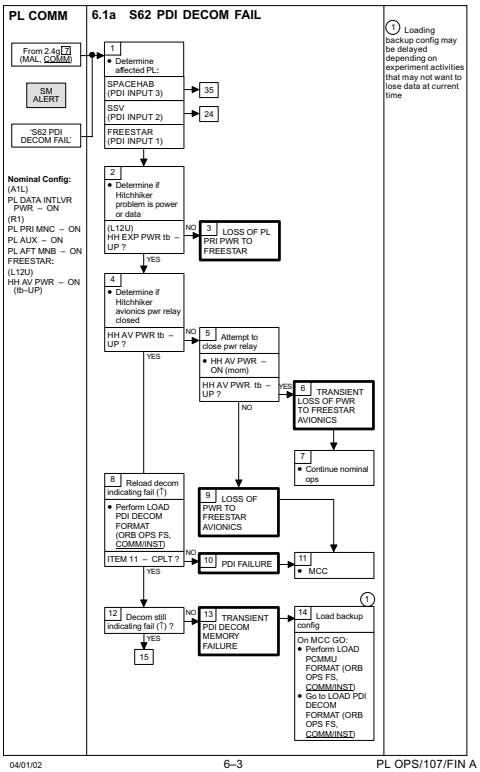
STS–107 COMM MALFUNCTION POINTS

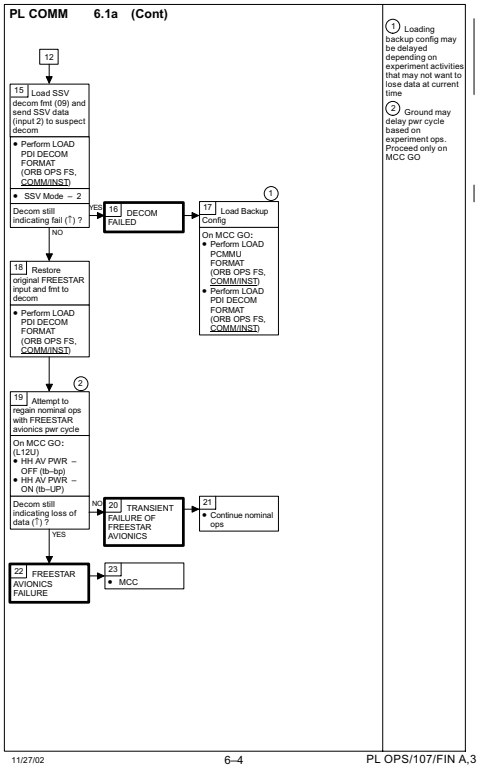


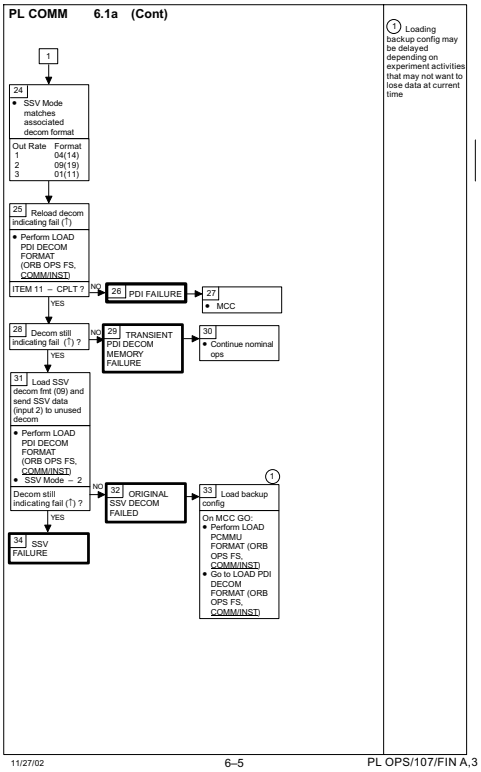
PL OPS/107/FIN A,3

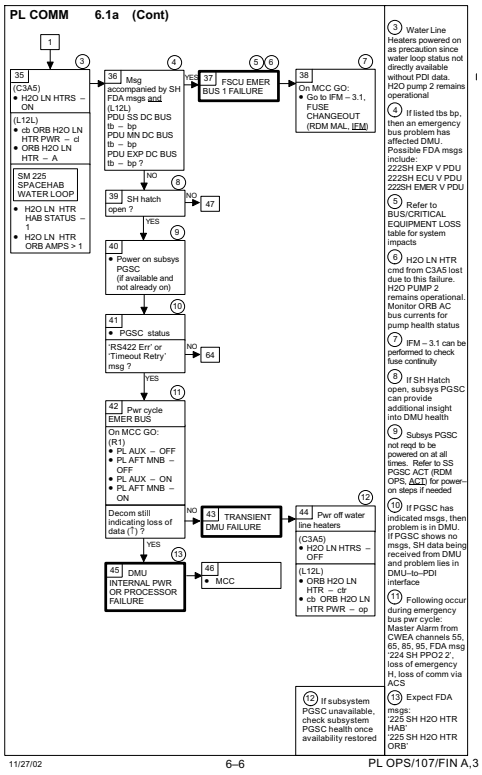
PL COMM

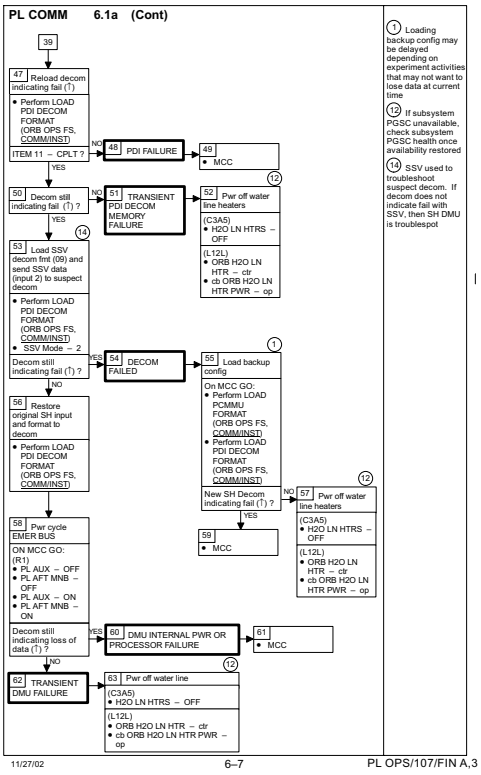
6.1a S62 PDI DECOM FAIL

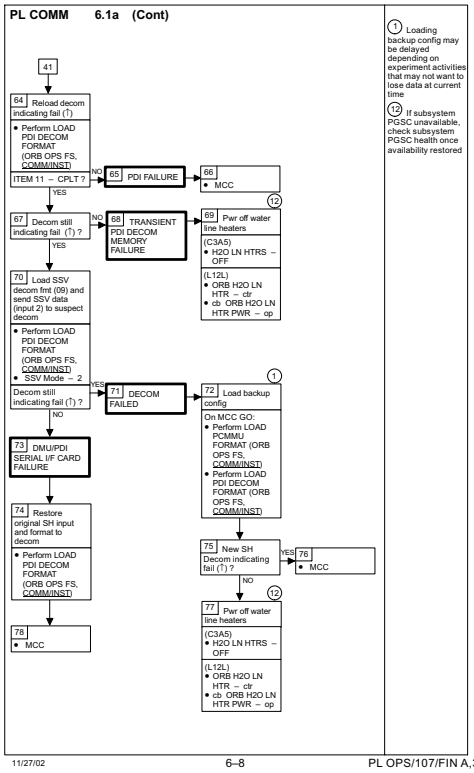



PL COMM 6.1a (Cont)
12
15 Load SSV decom fmt (09) and send SSV data (input 2) to suspect decom
• Perform LOAD PDI DECOM FORMAT (ORB OPS FS, COMM/INST)
• SSV Mode – 2
Decom still indicating fail (↑) ?
YES
16 DECOM FAILED
17 Load Backup Config
On MCC GO:
• Perform LOAD PCMMU FORMAT (ORB OPS FS, COMM/INST)
• Perform LOAD PDI DECOM FORMAT (ORB OPS FS, COMM/INST)
NO
18 Restore original FREESTAR input and fmt to decom
• Perform LOAD PDI DECOM FORMAT (ORB OPS FS, COMM/INST)
19 Attempt to regain nominal ops with FREESTAR avionics pwr cycle
On MCC GO: (L12U)
• HH AV PWR – OFF (tb–bp)
• HH AV PWR – ON (tb–UP)
Decom still indicating loss of data (↑) ?
NO
20 TRANSIENT FAILURE OF FREESTAR AVIONICS
21
• Continue nominal ops
YES
22 FREESTAR AVIONICS FAILURE
23
• MCC
1 Loading backup config may be delayed depending on experiment activities that may not want to lose data at current time
2 Ground may delay pwr cycle based on experiment ops. Proceed only on MCC GO
11/27/02
6–4
PL OPS/107/FIN A,3


PL COMM 6.1a (Cont)
1
24
• SSV Mode matches associated decom format
Out Rate Format
1 04(14)
2 09(19)
3 01(11)
25 Reload decom indicating fail (↑)
• Perform LOAD PDI DECOM FORMAT (ORB OPS FS, COMM/INST)
ITEM 11 – CPLT ?
NO
26 PDI FAILURE
27
• MCC
YES
28 Decom still indicating fail (↑) ?
NO
29 TRANSIENT PDI DECOM MEMORY FAILURE
30
• Continue nominal ops
YES
31 Load SSV decom fmt (09) and send SSV data (input 2) to unused decom
• Perform LOAD PDI DECOM FORMAT (ORB OPS FS, COMM/INST)
• SSV Mode – 2
Decom still indicating fail (↑) ?
NO
32 ORIGINAL SSV DECOM FAILED
33 Load backup config
On MCC GO:
• Perform LOAD PCMMU FORMAT (ORB OPS FS, COMM/INST)
• Go to LOAD PDI DECOM FORMAT (ORB OPS FS, COMM/INST)
YES
34 SSV FAILURE
1 Loading backup config may be delayed depending on experiment activities that may not want to lose data at current time
11/27/02
6–5
PL OPS/107/FIN A,3


PL COMM 6.1a (Cont)
1
3
35
(C3A5)
• H2O LN HTRS – ON
(L12L)
• cb ORB H2O LN HTR PWR – cl
• ORB H2O LN HTR – A
SM 225 SPACEHAB WATER LOOP
• H2O LN HTR HAB STATUS – 1
• H2O LN HTR ORB AMPS > 1
4
36 Msg accompanied by SH FDA msgs and (L12L) PDU SS DC BUS tb – bp PDU MN DC BUS tb – bp PDU EXP DC BUS tb – bp ?
YES
5 6
37 FSCU EMER BUS 1 FAILURE
7
38 On MCC GO:
• Go to IFM – 3.1, FUSE CHANGEOUT (RDM MAL, IFM)
NO
8
39 SH hatch open ?
NO
47
YES
9
40
• Power on subsys PGSC (if available and not already on)
10
41
• PGSC status
'RS422 Err' or 'Timeout Retry' msg ?
NO
64
YES
11
42 Pwr cycle EMER BUS
On MCC GO: (R1)
• PL AUX – OFF
• PL AFT MNB – OFF
• PL AUX – ON
• PL AFT MNB – ON
Decom still indicating loss of data (↑) ?
NO
43 TRANSIENT DMU FAILURE
12
44 Pwr off water line heaters
(C3A5)
• H2O LN HTRS – OFF
(L12L)
• ORB H2O LN HTR – ctr
• cb ORB H2O LN HTR PWR – op
YES
13
45 DMU INTERNAL PWR OR PROCESSOR FAILURE
46
• MCC
3 Water Line Heaters powered on as precaution since water loop status not directly available without PDI data. H2O pump 2 remains operational
4 If listed tbs bp, then an emergency bus problem has affected DMU. Possible FDA msgs include: 222SH EXP V PDU 222SH ECU V PDU 222SH EMER V PDU
5 Refer to BUS/CRITICAL EQUIPMENT LOSS table for system impacts
6 H2O LN HTR cmd from C3A5 lost due to this failure. H2O PUMP 2 remains operational. Monitor ORB AC bus currents for pump health status
7 IFM – 3.1 can be performed to check fuse continuity
8 If SH Hatch open, subsys PGSC can provide additional insight into DMU health
9 Subsys PGSC not reqd to be powered on at all times. Refer to SS PGSC ACT (RDM OPS_ACT) for power–on steps if needed
10 If PGSC has indicated msgs, then problem is in DMU. If PGSC shows no msgs, SH data being received from DMU and problem lies in DMU–to–PDI interface
11 Following occur during emergency bus pwr cycle: Master Alarm from CWEA channels 55, 65, 85, 95, FDA msg '224 SH PPO2 2', loss of emergency H, loss of comm via ACS
12 If subsystem PGSC unavailable, check subsystem PGSC health once availability restored
13 Expect FDA msgs: '225 SH H2O HTR HAB' '225 SH H2O HTR ORB'
11/27/02
6–6
PL OPS/107/FIN A,3


PL COMM 6.1a (Cont)
39
47 Reload decom indicating fail (↑)
• Perform LOAD PDI DECOM FORMAT (ORB OPS FS, COMM/INST)
ITEM 11 – CPLT ?
NO
48 PDI FAILURE
49
• MCC
YES
50 Decom still indicating fail (↑) ?
NO
51 TRANSIENT PDI DECOM MEMORY FAILURE
12
52 Pwr off water line heaters
(C3A5)
• H2O LN HTRS – OFF
(L12L)
• ORB H2O LN HTR – ctr
• cb ORB H2O LN HTR PWR – op
YES
14
53 Load SSV decom fmt (09) and send SSV data (input 2) to suspect decom
• Perform LOAD PDI DECOM FORMAT (ORB OPS FS, COMM/INST)
• SSV Mode – 2
Decom still indicating fail (↑) ?
YES
54 DECOM FAILED
1
55 Load backup config
On MCC GO:
• Perform LOAD PCMMU FORMAT (ORB OPS FS, COMM/INST)
• Perform LOAD PDI DECOM FORMAT (ORB OPS FS, COMM/INST)
NO
56 Restore original SH input and format to decom
• Perform LOAD PDI DECOM FORMAT (ORB OPS FS, COMM/INST)
New SH Decom indicating fail (↑) ?
NO
57 Pwr off water line heaters
12
(C3A5)
• H2O LN HTRS – OFF
(L12L)
• ORB H2O LN HTR – ctr
• cb ORB H2O LN HTR PWR – op
YES
58 Pwr cycle EMER BUS
59
• MCC
ON MCC GO: (R1)
• PL AUX – OFF
• PL AFT MNB – OFF
• PL AUX – ON
• PL AFT MNB – ON
Decom still indicating loss of data (↑) ?
YES
60 DMU INTERNAL PWR OR PROCESSOR FAILURE
61
• MCC
NO
12
62 TRANSIENT DMU FAILURE
63 Pwr off water line
(C3A5)
• H2O LN HTRS – OFF
(L12L)
• ORB H2O LN HTR – ctr
• cb ORB H2O LN HTR PWR – op
1 Loading backup config may be delayed depending on experiment activities that may not want to lose data at current time
12 If subsystem PGSC unavailable, check subsystem PGSC health once availability restored
14 SSV used to troubleshoot suspect decom. If decom does not indicate fail with SSV, then SH DMU is troublespot
11/27/02
6–7
PL OPS/107/FIN A,3



PL/DPS RECONFIG

PL/DPS RECONFIG 7–2

PL/DPS RECONFIG

PROCEDURE	SECURE ACTION	RECOVERY ACTION	INFO ONLY
PL 1(2) MDM I/O ERROR; PL 1(2) MDM OUTPUT (ORB PKT, DPS)	N/A	N/A	C
5.3c I/O ERROR PL 1(2); MDM OUTPUT PL 1(2) (MAL, DPS)	N/A*	N/A	C
PASS SM GPC FAIL (ORB PKT, DPS)	N/A	B	D
GNC RECOVERY VIA G2FD (ORB PKT, DPS)	N/A	A,B	D
5.1a CS SPLIT (MAL, DPS)	N/A	A,B**	D
5.3e BCE I/O ERROR FLEX (MAL, DPS)	N/A	N/A	
5.3f BCE BYP FLEX (MAL, DPS)	N/A	N/A	
5.3g BCE BYP PL 1(2) (MAL, DPS)	N/A*	N/A**	C
GPC FRP–4 PASS RECOVERY AFTER BFS ENGAGE (ASCENT/ORBIT/ENTRY) (MAL, DPS)	N/A*	A,B**	D
GPC FRP–7 DPS RECONFIG FOR LOSS OF AV BAY COOLING (ASCENT/ORBIT) (MAL, DPS)	N/A	A,B**	D
DPS SSR–3 GNC REASSIGNMENT (MAL, DPS)	N/A*	N/A	D
DPS SSR–4 SM REASSIGNMENT (MAL, DPS)	N/A	A,B	D
ECLS SSR–10 H2O PUMP OPS VIA GPC (MAL, ECLS)	N/A	A,B**	D

*Note: Procedure does not call out PL/DPS RECONFIG, Secure
**Note: Procedure does not call out PL/DPS RECONFIG, Recovery

ACTION A

If PSP I/O reset not previously performed:
SM 62 PCMMU/PL COMM
I/O RESET PSP 1(2) – ITEM 6(7) EXEC
Notify MCC when complete

ACTION B

Reload PDI DECOM FORMAT (ORB OPS FS, COMM/INST)
Re–enable PDI DECOM FDA as reqd
Resume SPEC 62

INFO C

If 'I/O ERROR PL1' msg:
Loss of cmd capability (onboard and ground) and telemetry via PL comm string 1 for SPACEHAB, FREESTAR. (MCC will consider PSP COMMAND SIGNAL BYPASS IFM)
Loss of PL1 tlm on SPECs 206, 222, 223, 224, 225 denoted by 'M'. Failed IOM can be determined using chart from PF MDM CHANNELIZATION (RDM MAL, CRITICAL EQUIP LOSS)
Loss of command to Ku Band
Loss of command to OARE and PLR
Failure at IOP XMTR/RCVR at SM GPC recovered via port mode to PL2

If 'I/O ERROR PL2' msg:
Loss of cmd capability (onboard and ground) and telemetry via PL comm string 2 for SPACEHAB (FREESTAR if PSP COMMAND SIGNAL BYPASS IFM previously performed)
Note associated loss H2O LN HTR HAB status and Orbiter H2O LN HTR current on SPEC 225 denoted by 'M'
Loss of SPACEHAB FSS DISCHARGE (FSCU) onboard and ground discrete cmd via PL2
Loss of ground command to the CCTV system
Failure at IOP XMTR/RCVR at SM GPC recovered via port mode to PL1

INFO D

If affected GPC SM:
Loss of command capability (onboard and ground) via SM GPC until SM GPC restored and/or PL 1(2) I/F restored

If affected GPC GNC:
Loss of ground command capability until GNC GPC restored

This Page Intentionally Blank

IN–FLIGHT MAINTENANCE (IFM)

PSP 1 COMMAND SIGNAL BYPASS 8–2
SSP 1 RECOVERY TABLE 8–4
2 RECOVERY TABLE 8–5
KU BAND SIGNAL PROCESSOR BYPASS FOR PL DIG DATA 8–6
SH PL MAX DATA RECOVERY 8–8

IFM

IFM

PSP 1 COMMAND SIGNAL BYPASS (1:00 hr)

OBJECTIVE: To recover payload commands lost due to PSP 1 failure by rerouting signal to PSP 2 with test jumper leads

LOCATION: J1391 FREESTAR on Payload Station Distribution Panel (PSDP) behind L17

TOOLS REQD: Gray Tape
Power Screwdriver
Torque Wrench
5/32–in Allen Head Driver
Pin Kit
Connector Strap Wrench

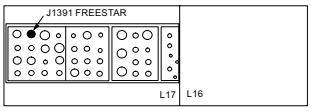
Expect 'S62 BCE BYPASS PSP 1' msg

A1L 1. S–BD PL CNTL – PNL
PWR SYS – OFF

L17 2. Remove pnl L17 (seventeen fasteners, 5/32–in Allen Head Driver)

3. Demate Connector Plug P1 from J1391 FREESTAR on Payload Station Distribution Panel

PAYLOAD STATION DISTRIBUTION PANEL
(Looking through pnl L17 opening)



4. Position Gray Tape over face of Connector Plug P1 FREESTAR. Place in Ziplock Bag from Post Insertion locker MF43G. Label Ziplock as PSDP P1. Stow Ziplock in FDF locker MF57K

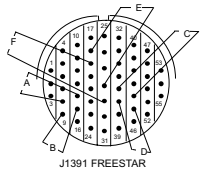
5. Obtain four 5–in (22 ga) Pin/Pin Test Jumper Leads from Pin Kit (insert)

6. Obtain 22–ga Wire (flap 3) and 22–ga pins (four) (flap 6) and fabricate two, 5–in (22 ga) Pin/Pin Test Jumper Leads for a total of six, 5–in Pin/Pin Test Jumper Leads. Place Gray Tape over collar of pins for strain relief and insulation

7. Install Pin/Pin Test Jumper Leads into following socket positions as indicated:

ORBITER SIGNAL		J1391 FREESTAR sockets		FREESTAR
PTB (MET 1 HI)	8	A	14	MET +
PTB (MET 1 LO)	9	B	15	MET –
PDI (TLM 1)	36	C	44	LOW RATE DATA +
PDI (RTN)	37	D	45	LOW RATE DATA –
PSP 2 (CMD 1 OUT)	28	E	18	COMMAND DATA +
PSP 2 (RTN)	29	F	19	COMMAND DATA –

NOTE: (22 ga) 5–in Pin/Pin Test Jumper Leads



J1391 FREESTAR

NOTE: J1391 FREESTAR row type connector.
Pins/sockets numbered at top,bottom of each row

A1L 8. S–BD PL PWR SEL – PSP
SYS – 2
CNTL – CMD
SM 62 PCMMU/PL COMM
ITEM 7 – EXEC

9. Report results to MCC

L17 10. Reinstall pnl L17, torque fasteners (25 in–lb)

11. Stow tools, Gray Tape

SSP 1 RECOVERY TABLE

Note: This table will be used in conjunction with SSP CABLE CHANGEOUT (IFM) to regain functionality of failed L12U control.

PANEL	FAILED CONTROL	WIRED THRU	POWERDOWN ACTION	SWAP ACTION	RECOVERY ACTION	IMPACT OF ACTION
L12U	HITCHHIKER AV PWR (S13) HITCHHIKER EXP PWR (S14)	J2	PL PRI MNC – OFF (tb – OFF) cb DOOR PWR CONT PWR DN ENA – op HH EXP PWR – OFF (tb –bp) HH AV PWR – OFF (tb – bp) OARE PWR – OFF cb OARE PWR CAB PL BUS (two) – op	Swap J2,J6 cables	PL PRI MN C – ON (tb – ON) HH AV PWR – ON (tb – UP) HH EXP PWR – ON (tb – UP) cb OARE PWR CAB PL BUS (two) – cl OARE PWR – ON	S13 function on S1 S14 function on S2 S11 function on S23
	OARE PWR (S11)	J6				
	LPT PWR ENA 1 (S15) LPT PWR ENA 2 (S19) MEIDEX DOOR (S18) cb DOOR PWR CONT PWR DN ENA	J8	HH POCC pwrs down LPT LPT PWR ENA 1 – OFF (tb – bp) LPT PWR ENA 2 – OFF (tb – bp) cb DOOR PWR CONT PWR DN ENA – op MEIDEX DOOR – CLOSE	Swap J8, J12 cables	LPT PWR ENA 1 – ON LPT PWR ENA 2 – ON HH POCC pwrs on LPT	S15 function on S3 S19 function on S7 S18 function on S6 cb4 function on cb2
	N/A	J12				
	HITCHHIKER AV PWR tb (DS13) HITCHHIKER EXP PWR tb (DS14) LPT PWR ENA 1 tb (DS15) MEITDEX DOOR tb (DS18) LPT PWR ENA 2 tb (DS19)	J1	HH EXP PWR – OFF (tb –bp) HH AV PWR – OFF (tb – bp) HH POCC pwrs down LPT LPT PWR ENA 2 – OFF (tb – bp) LPT PWR ENA 1 – OFF (tb – bp) cb DOOR PWR CONT PWR DN ENA – op MEIDEX DOOR – CLOSE	Swap J1, J5 cables	HH AV PWR – ON (tb – UP) HH EXP PWR – ON (tb – UP) LPT PWR ENA 1 – ON LPT PWR ENA 2 – ON HH POCC pwrs on LPT	DS13 function on DS1 DS14 function on DS2 DS15 function on DS3 DS18 function on DS6 DS19 function on DS7
	N/A	J5				
	GAS/FREESTAR connector (J14)	J13	Perform SOLSE/HRIU DEACT (FREESTAR)	Remove J13 cable, connect to L12L J13	Perform SOLSE/HRIU ACT (FREESTAR)	GAS/FREESTAR connector function on L12L AUX I/O (J14) connector

8–4 PL OPS/107/FIN A,1

SSP 2 RECOVERY TABLE

Note: This table will be used in conjunction with SSP CABLE CHANGEOUT (IFM) to regain functionality of failed L12L control.

PANEL	FAILED CONTROL	WIRED THRU	POWERDOWN ACTION	SWAP ACTION	RECOVERY ACTION	IMPACT OF ACTION
L12L	FIRE SUPPR FSCU ARM (S13) FIRE SUPPR FSCU DISCH (S14) MAIN PWR KILL (S20) PDU SS DC BUS (S21) FWD INVERTER (S23) PDU EXP DC BUS (S24)	J2	PL AUX – OFF PL AFT B – OFF cb ORBITER H2O LN HTR PWR – op cb SW PWR – op	Swap J2, J6 cables Swap J8, J12 cables	PL AUX – On PL AFT B – On cb ORBITER H2O LN HTR PWR – cl cb SW PWR – cl	S12 function on S24 S13 function on S1 S14 function on S2 S15 function on S3 S16 function on S4 S17 function on S5 S18 function on S6 S19 function on S7 S20 function on S8 S21 function on S9 S22 function on S10 S23 function on S11 S24 function on S12
	ORBITER H2O LN HTR (S12)	J6				
	CAB DEPRESS VLV ARM (S15) CAB DEPRESS VLV OPEN (S16) SMOKE SENSOR RESET (S17) SMOKE SENSOR A (S18) SMOKE SENSOR B (S19) PDU MN DC BUS (S22)	J8				
	N/A	J12				

8–5 PL OPS/107/FIN A,1

KU BAND SIGNAL PROCESSOR BYPASS FOR PL DIG DATA (1:30 hr)

OBJECTIVE: Recover realtime data for SH PL DIG DATA by routing signal through S Band FM Signal Processor

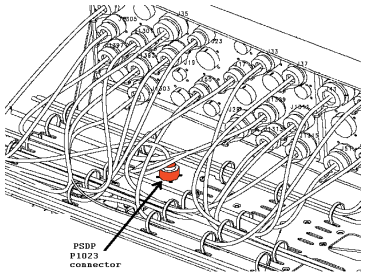
LOCATION: Connector J1023 on wire tray running in front of Payload Station Distribution Panel (PSDP) panel behind L14

TOOLS REQD: Gray Tape
Pin Kit (for Test Jumper Leads and Minigrabber)
Pwr Screwdriver
5/32–in Allen Head Driver
Connector Strap Wrench (if reqd)
Torque Wrench
#10 Torque Tip
–in to 3/8–in Adapter

1. MCC
   S–Band FM Sys – OFF

L14 2. Remove panel L14 (six, #10 Torque Tip; twelve, 5/32–in Allen Head Driver)

3. Locate, demate connector 38P77W469P1023 from J1023 on PSDP wire tray (see diagram for connector location)

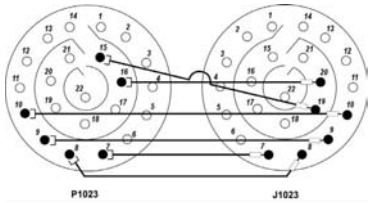


4. Position connector 38P77W469P1023 onto wire tray pointing connector face inboard; secure with Gray Tape

8–6 PL OPS/107/FIN A,3

5. Obtain four, 5–in (22–ga) pin/socket Test Jumper Leads from Pin Kit and two, 24–in (22–ga) pin/socket Test Jumper Leads from Fuse and Test Jumper Lead Container Assy inside Pin Kit. Install into following pin/socket positions on J1023 and P1023:

SPACEHAB	PINS (P1023)	TO	SOCKETS (J1023)	ORBITER
Ku Fwd Link Data –	7	———	7	Ku Fwd Link Data –
Ku Fwd Link Data +	8	———	8	Ku Fwd Link Data +
Ku Fwd Link Clock –	9	———	9	Ku Fwd Link Clock –
Ku Fwd Link Clock +	10	———	10	Ku Fwd Link Clock +
Ku Chan 2 Data +	15	———	19	S BAND FMSP W/B DIG +
Ku Chan 2 Data –	16	———	20	S BAND FMSP W/B DIG –



6. Obtain one 24–in Minigrabber, install between connector shells (from P1023 to J1023) for chassis ground; secure with Gray Tape

7. Reinstall pnl L14, torque fasteners (30 in–lb)

8. Stow tools, Gray Tape

8–7 PL OPS/107/FIN A,3

SH PL MAX DATA RECOVERY

OBJECTIVE: Recover SH PL MAX Data

LOCATION: Payload Station Distribution Panel (PSDP)

TOOLS REQD: 5/32–in Allen Head Driver
Gray Tape
Pwr Screwdriver
Torque Wrench
Wire Cutters

CHCK DTV Cables (two, V710–743700–001 DATA CABLE and V710–743700–002 CLOCK CABLE)

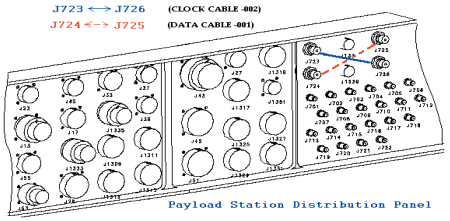
L10 1. MUX/VTR/CC – OFF (0), VTR/CC – OFF (0)

2. Remove L16 closeout panel (seventeen fasteners, 5/32–in Allen Head Driver)

3. Demate PSDP Coax Cables connected to J723, J724, J725, and J726
Cut safety wire as reqd

4. Tape face of Coax Cable (4) connectors; secure cables to structure
(Gray Tape)

5. As shown below, install V710–743700–001 DTV Data Cable between J724 and J725, and install V710–743700–002 DTV Clock Cable between J723 and J726



6. Install closeout panel (torque fasteners, 30 in–lb)

L10 7. VTR/CC – ON (1)

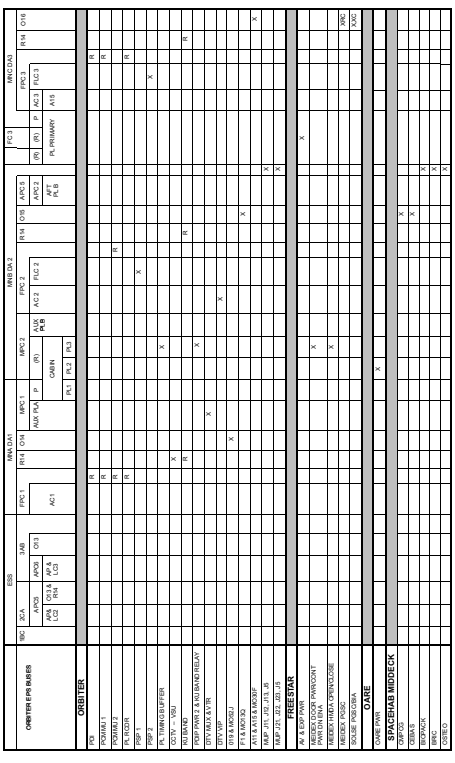
8. Stow tools

CRITICAL EQUIP LOST

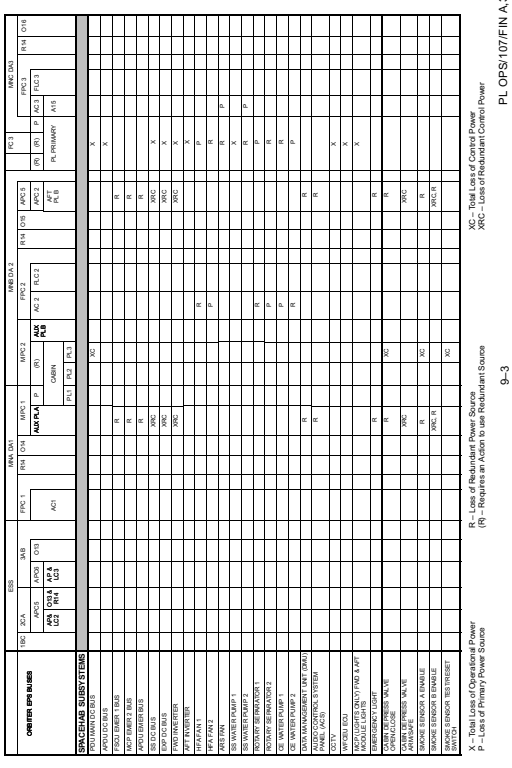
STS–107 BUS LOSS MATRIX 9–2
ELECTRICAL BUS LOSS IMPACTS 9–5
MDM LOSS IMPACTS 9–7

CRITICAL EQUIP LOST

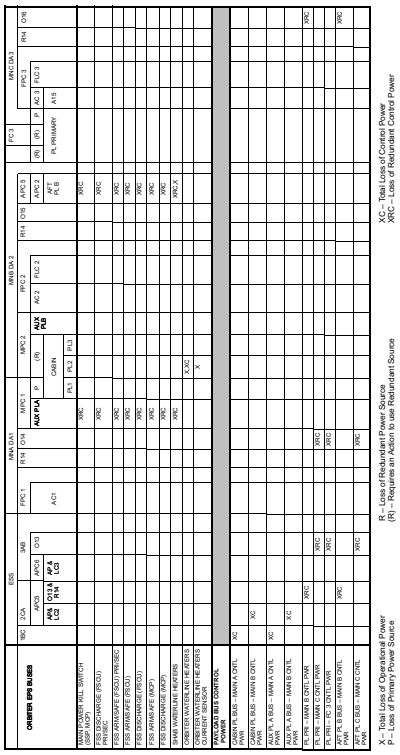
STS–107 BUS LOSS MATRIX



STS–107 BUS LOSS MATRIX (Cont)



STS–107 BUS LOSS MATRIX (Cont)



PL OPS/107/FIN A,3

9–4

ELECTRICAL BUS LOSS IMPACTS

MNA DA1
- MNA FPC1
  - PDI (REDUN POWER)
  - PCMMU (REDUN POWER)
  - AC1
  - PL RCDR (REDUN PWR)
- MNA O14
  - DC UTIL PWR O19/MO52J
- MNA MPC1
  - CABIN PL2 (REDUN POWER AVAILABLE)
    - SSP 1
      - CB 1
        - OARE PWR (REDUN POWER)
      - CB 3
        - OARE PWR (REDUN POWER)
    - SSP 2
      - CB 1
        - PDIP PWR 1
      - CB 3
        - S12 – ORBITER H2O LN HTR
        - ORBITER H2O LN HTR CURRENT SENSOR
  - CABIN PL3 (REDUN POWER AVAILABLE)
    - SSP 1
      - CB 4
        - FREESTAR CONT PWR DN ENA
        - S18 – HMDA OPEN/CLOSE
    - SSP 2
      - CB 4
        - S16 – CAB DEPRESS VLV OPEN/CLOSE
        - S17 – SMOKE SENSOR TEST/RESET
        - S18 – SMOKE SENSOR A ENA/INHB
        - S22 – SEC DC BUS
      - F1
        - PAYLOAD TIMING BUFFER
        - PDIP – S2 DC PWR 2
        - PDIP – S3 KuBAND RATE
  - AUX PL A
    - SPACEHAB FSCU EMER 1 BUS (REDUN PWR)
      - SSP 2
        - S13 – FIRE SUPPR FSCU ARM/SAFE
        - S14 – FIRE SUPPR FSCU DISCH
        - S20 – MAIN PWR KILL
        - S21 – PDU SS DC BUS ON/OFF
        - S23 – FWD INVERTER ON
        - S24 – PDU EXP DC BUS ON/OFF
    - SPACEHAB MCP EMER 2 BUS (REDUN PWR)
      - SSP 2
        - S15 – CAB DEPRESS VLV ARM
        - S19 – SMOKE SENSOR B ENA
    - DTV MUX & VTR
  - MNA R14
    - CCTV – VSU

9–5

PL OPS/107/FIN A,2

MNB DA2
- MNB MPC2
  - CABIN PL1 (REDUN POWER AVAILABLE)
  - CABIN PL2 (REDUN POWER AVAILABLE)
  - CABIN PL3 (REDUN POWER AVAILABLE)
- MNB APC 5
  - MNB APC 2
    - AFT PL B
      - SPACEHAB FSCU EMER 1 BUS (REDUN POWER)
      - SPACEHAB MCP EMER 2 BUS (REDUN POWER)
- MNB FPC 2
  - AC2
    - DTV VIP
  - PCMMU 2 (REDUN POWER)
  - MNB FLC 2
    - PSP 1
- MNB ML86B (MUP DC)
  - ML85E (MUP)
    - BRIC PWR
    - BIOPACK PWR
    - OSTEO PWR
- MNB R14
  - KU BAND – SPA
- MNB O15
  - DC UTIL PWR F1/MO13Q
    - CMPCG PWR
    - CEBAS PWR
- PL PRI (REDUN POWER AVAIL)

MNC DA3
- MNC FPC 2
  - PL RCDR (REDUN POWER)
  - PCMMU 1 (REDUN POWER)
  - PDI (REDUN POWER)
  - AC3
- MNC FLC 3
  - PSP 2
- MNC R14
  - KU BAND – EA1 AND DA
- MNC O16
  - PL AFT MNB CNTRL PWR (REDUN POWER AVAILABLE)
  - DC UTIL PWR A11/A15/MO30F
    - SOLSE PGSC/BIA (LOSS OF OPERATIONAL POWER)
    - MEIDEX PGSC (LOSS OF REDUNDANT CONTROL POWER)
- PL PRI (REDUN POWER AVAILABLE)
  - SPACEHAB MAIN PWR
  - FREESTAR EXP & AV PWR

9–6

PL OPS/107/FIN A,1

MDM LOSS IMPACTS

FF1
- Uplink Through NSP 1 (Secondary)

FF3
- Uplink Through NSP 2 (Primary)

PF1(PL1)
- Spacehab Cmd Path via PSP 1
- FREESTAR Cmd Path via PSP1
- Ku–Band Antenna Cntl
- OARE Discrete Commands
  - Record Ready
  - Quiet Mode
  - Re–entry Mode
- Spacehab Discrete Commands
  - Water Pump 2 to Orbiter
  - Water Pump 2 to Inverter
  - Water Pump 1 On/Water Pump 2 Off
  - Water Pump 2 On/Water Pump 1 Off
  - FSS Arm (MCP)
  - FSS Safe (MCP)
  - ARS Fan On
  - ARS Fan Off
  - HFA Fan #1 Off
  - HFA Fan #2 On
- Spacehab Discrete Monitors
  - Smoke Sensor A Alarm
  - Smoke Sensor B Alarm
  - Water Pump 1 Off/On
  - Water Pump 2 Off/On
  - FSS Discharged
  - FSS Arm/Safe (MCP)
  - FSS Arm/Safe (FSCU)
  - Multi–Bottle Halon Discharge
- Spacehab Analog Monitors
  - PPO2 #2
  - PPCO2 #2
  - Orbiter Water Line Htr Current

PF2(PL2)
- Uplink cmd to CCTV – VSU AND CCTV CAMERAS
- Spacehab Redundant Command Path via PSP 2
- Spacehab Analog Monitor
  - Orbiter Waterline Htr Status
- Spacehab Discrete Command
  - FSS Discharge (FSCU)
- C/W Annunciation (PL CAUTION Alarm)

OF1
- Ku–Band Gyro Temp
- PCMMU 1 FORMAT mon
- PCMMU PWR 1,2 mon
- BFS Auto TFL
- PL AUX A RPC ON mon

DSC OF1
- Ku–Band Gyro Temp
- PCMMU 1 – Mode Select

9–7

PL OPS/107/FIN A

OF2
PSP 1,2 – Bit & Frame Sync
PCMMU 2 FORMAT mon
PL AUX B RPC ON/OFF mon

DSC OF2
PCMMU 2 – Mode Select

OF3
Orbiter Comm Telemetry (S–Band PM/FM,Ku–Band,UHF,NSP 1&2,COMSEC)
GCIL Telemetry (revert to panel)
PL PRI FC3 ON tlm
MNB ON tlm
MNC ON tlm
Ku–Band Alpha/Beta Gimbal Temp

DSC OF3
Ku–Band Alpha Gimbal Temp

OF4
KU–BAND RADAR PWR mon
S–BAND (P/L,PM,FM) & KU–BAND CONTROL mon
Orbiter Comm – GCIL Driver Telemetry (S–Band PM,P/L,FM,Ku–Band,CCTV)
PSP, PL GCIL, COMSEC – ON/OFF Telemetry
CAB P/L MNA(MNB) ON tlm
PL AUX ON tlm

DSC OF4
No P/L impacts

DSC OM2
Ku–Band Beta Gimbal Temp

OA1
No P/L impacts

DSC OA1
No P/L impacts

OA2
PL AFT MNB PWR ON mon
PL AFT MNB AMPS mon

DSC OA2
No P/L impacts

OA3
PL AFT MNC ON mon
PL AFT MNC AMPS mon

DSC OA3
No P/L impacts

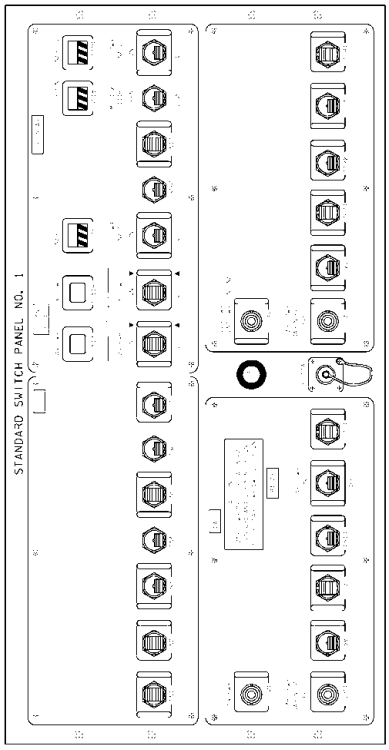
REFERENCE DATA

L12U SSP 1 10–2
FREESTAR SSP L12U SWITCH ASSIGNMENTS 10–3
L12L SSP 2 10–5
SPACEHAB SSP L12L SWITCH ASSIGNMENTS 10–6
C3A5 PAYLOAD SAFING 10–10
SPACEHAB C3A5 SWITCH ASSIGNMENTS 10–10
PGSC FAILURE RECOVERY OPTIONS 10–11

REF DATA

REF DATA

L12U SSP 1



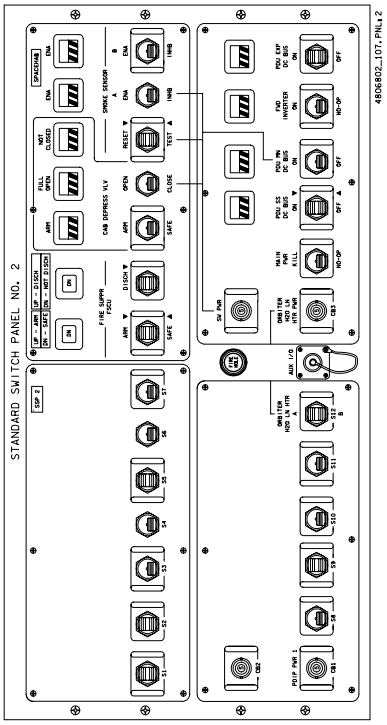
PL OPS/107/FIN A

FREESTAR SSP L12U SWITCH ASSIGNMENTS

CONTROL/LABEL	DEVICE TYPE	POSITION – FUNCTION	USAGE (TIME AND FREQUENCY)
S13 HITCHHIKER AV PWR	Three–position toggle switch with wicket cover: (up, down – momentary, center – maintained)	ON (up) – Closes latching relay K9 applying PL PRI power to HH avionics Not labeled (center) – Not wired OFF (down) – Opens latching relay K9 unpowering HH avionics	Used to control power to HH Avionics during activation and deactivation
DS13	Three–position talkback	UP – Indicates relay K9 closed, PL PRI power supplied to HH avionics bp – Indicates power not supplied to the HH avionics DN – not wired	
S14 HITCHHIKER EXP PWR	Three–position toggle switch with wicket cover: (up, down – momentary, center – maintained)	ON (up) – Closes latching relay ZL applying PL PRI power to HH experiment power bus Not labeled (center) – Not wired OFF (down) – Opens latching relay K9 unpowering HH experiment power bus	Used to control power to HH experiment bus during activation and deactivation
DS14	Three–position talkback	UP – Indicates relay ZL closed, PL PRI power supplied to experiment power bus bp – Indicates power not supplied to power bus DN – not wired	
S15 LPT PWR ENA 1	Two–position toggle switch: (up, down – maintained)	ON (up) – Removes one of the LPT transmitter inhibits OFF (down) – Applies one of the LPT transmitter inhibits	Used during activation and deactivation to remove and provide inhibits to LPT transmission. Also used to provide tranmission inhibits during a contingency EVA
DS15 ENABLED	Two–position talkback	gray – Indicates that one of the LPT transmitter inhibits has been removed bp – Indicates that one of the LPT transmitter inhibits is in place	
S18 MEIDEX DOOR	Two–position toggle switch: (up, down – maintained)	OPEN (up) – Provides power to open the MEIDEX HMDA CLOSE (down) – Provides power to close the MEIDEX HDMA	Used to open and close MEIDEX HMDA during experiment ops
DS18 FULL OPEN	Two–position talkback	gray – Indicates that the HDMA open limit switch has been tripped bp – Indicates that the HDMA open limit switch has not been tripped	
S19 LPT PWR ENA 2	Two–position toggle switch: (up, down – maintained)	ON (up) – Removes one of the LPT transmitter inhibits OFF (down) – Applies one of the LPT transmitter inhibits	Used during activation and deactivation to remove and provide inhibits to LPT transmission. Also used to provide tranmission inhibits during a contingency EVA

FREESTAR SSP L12U SWITCH ASSIGNMENTS (Cont)

CONTROL/LABEL	DEVICE TYPE	POSITION – FUNCTION	USAGE (TIME AND FREQUENCY)
DS19 ENABLED	Two–position talkback	gray – Indicates that one of the LPT transmitter inhibits has been removed bp – Indicates that one of the LPT transmitter inhibits is in place	
CB4 DOOR PWR/CONT PWR DN ENA	Two–position circuit breaker	cl – Provides CAB PL3 power MEIDEX HMDA and to ZL relay open coil controlled by EXP PWR switch op – Interrupts CAB PL3 power to ZL relay open coil and MEIDEX HMDA	Used to provide power to the MEIDEX HMDA during experiment ops. Also used to open the ZL relay and safe the HH experiment power bus in contingency situations when PRI PL power has been temporarily lost
J14 FREESTAR	Connector	PGSC/Bus Interface Adapter (BIA) connection for command and data bus interface to SOLSE	
CB 1 OARE PWR CABIN P/L BUS	Two–position circuit breaker	cl – Provides CAB PL 2 power to OARE via S11. This is 1 of 2 reqd feeds for OARE power op – Removes 1 of 2 power feeds to OARE via S11	Closed during ascent and opened after reaching orbit and then closed a 2nd time prior to SOFBALL ops
CB 3 OARE PWR CABIN P/L BUS	Two–position circuit breaker	cl – Provides CAB PL 2 power to OARE via S11. This is 1 of 2 reqd feeds for OARE power op – Removes 1 of 2 power feeds to OARE via S11	Closed during ascent and opened after reaching orbit and then closed a 2nd time prior to SOFBALL ops
S11 OARE PWR ON	Two–position toggle switch: (up, down – maintained)	ON (up) – Provides CAB PL 2 power to OARE OFF (down) – Removes CAB PL 2 power from OARE	On during ascent and Off after reaching orbit and then On a 2nd time prior to SOFBALL ops



SPACEHAB SSP L12L SWITCH ASSIGNMENTS

ITEM	TYPE DEVICE	FUNCTION	USAGE (TIME AND FREQUENCY)
CB1 PDIP PWR 1	Circuit breaker, 5–ampere: IN – closed OUT – open with wickets	IN – Applies orbiter pwr to PDIP DC PWR 1 SW and J2 connector OUT – Removes orbiter pwr from PDIP DC PWR 1 SW and J2 connector	
S12 ORBITER H2O LN HTR A (not labeled) B	Three position sw: (Maintained–Maintained–Maintained) with wickets	A – Applies pwr to ORBITER H2O LN HTR, sys A Center – Turns off heaters B – Applies pwr to ORBITER H2O LN HTR, sys B	Used to prevent line freezing after failure results in H2O flow being lost to PHX This is normal sw position Used to prevent water line freezing after failure of orbiter heater set A
CB3 ORBITER H2O LN HTR PWR	Circuit breaker, 5–ampere: IN – closed OUT – open with wickets	IN – Applies 28 VDC pwr to ORBITER H2O LN HTR sw (S12) and heater current sensor OUT – Removes 28 VDC pwr from ORBITER H2O LN HTR sw (S12) and sensor	Used to prevent line freezing after failure results in H2O flow being lost to PHX This is normal cb position
S13 FIRE SUPPR FSCU ARM	Momentary sw, 3 positions	ARM – Applies 28 VDC command to FSS discharge logic within FSCU. This command combined with DISCHARGE command, detonates Halon bottles SAFE – Removes 28 VDC command above, which interrupts ARM command or DISCHARGE command	Used when extinguishing confirmed fire during orbit or manned ground operations Used when safing firing circuitry after an inadvertent ARM command or discharge of bottles during orbit or manned ground operations
DS13 FIRE SUPPR FSCU ARM	Event indicator, 3 positions: Down Up bp	Provides status of FSS firing circuitry in FSCU Down – SAFE Up – ARM bp – unpowered	Used when preparing to fire Halon bottles to extinguish a fire
S14 FIRE SUPPR FSCU DISCH	Momentary sw, 3 positions	DISCHARGE – Applies 28 VDC command to FSS discharge logic within FSCU. This command detonates Halon bottles once ARM command is present Other two switch positions not used	Used when extinguishing confirmed fire during orbit or manned ground operations
DS14 FIRE SUPPR FSCU DISCH	Event indicator, 3 positions: Up Down bp	Provides status of Halon bottles Up – 9 bottles have discharged Down – Less than 9 bottles have discharged bp – unpowered	Used after DISCHARGE command has been issued to determine if enough bottles have discharged to extinguish fire

SPACEHAB SSP L12L SWITCH ASSIGNMENTS (Cont)

ITEM	TYPE DEVICE	FUNCTION	USAGE (TIME AND FREQUENCY)
S15 CAB DEPRESS VLV	Toggle sw, 2 positions: (Maintained–Maintained)	ARM – Applies 28 VDC command to CDV control logic within MCP. This command combined with OPEN command from S16 opens CDV SAFE – Removes 28 VDC pwr from CDV control logic. This position not electrically wired	Used when venting SH module to extinguish a fire after FSS has failed, or when toxic agents are present in SH module, during orbit operations Used when safing CDV control logic after an inadvertent ARM command. This is normal position of switch
DS15 CAB DEPRESS VLV ARM	Event indicator, 2 positions: gray bp	gray – (ARM) indicates CDV control logic has been armed bp – (SAFE) indicates CDV control logic has not received power and valve is safed	Indicates status in response to command from S15
S16 CAB DEPRESS VLV	Toggle sw, 2 positions: (Maintained–Maintained)	OPEN – Applies 28 VDC command to CDV control logic in MCP which opens CDV if ARM command from S15 present CLOSED – Applies 28 VDC command to CDV control logic in MCP which closes CDV if ARM command present	Used when venting SH module to extinguish a fire after FSS has failed, or when toxic agents are present in SH module, during orbit operations Used after CDV has been opened (see above) to close valve and safe module. This is normal position of switch
DS16 CAB DEPRESS VLV FULL OPEN	Event indicator, 2 positions: gray bp	gray – (Full open) indicates CDV has reached full open position bp – (Not full open) indicates CDV has not reached full open position	Used to indicate status of CDV in response to command from S16
DS17 CAB DEPRESS VLV NOT CLOSED	Event indicator, 2 positions: gray bp	gray – (Not closed) indicates CDV not closed (partially open) bp – (Closed) indicates CDV closed	Used to indicate status of CDV in response to cabin pressure alarm or command from S16
S17 SMOKE SENSOR	Momentary sw, 3 positions	TEST – Applies 28 VDC test input to both smoke sensors causing them to produce an alarm signal if sensors checkout RESET – Applies 28 VDC signal to reset input cf both smoke sensors returning them to normal operational mode	Verification of smoke sensors during module activation or fire suppression procedures Used after verification of smoke sensors during module activation and to confirm smoke alarm once it has occurred during orbital operations

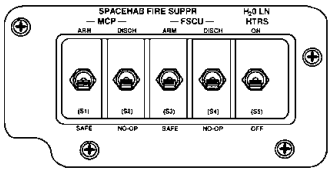
SPACEHAB SSP L12L SWITCH ASSIGNMENTS (Cont)

ITEM	TYPE DEVICE	FUNCTION	USAGE (TIME AND FREQUENCY)
S18 SMOKE SENSOR A	Toggle sw, 2 positions: (Maintained–Maintained)	ENA – Applies 28 VDC to relay inside FSCU which allows Smoke Sensor A alarm signal to travel to the CWEA and the MDM INHB – Other switch position not wired to the SH. However, inhibit signal occurs by removing 28 VDC from above relay at this switch position	Used to return Smoke Sensor A to its normal operational state, after it has been inhibited. This is normal position of switch Used to verify Smoke Sensor B during module activation and to confirm smoke alarm, once it has occurred, during orbit operations
DS18 SMOKE SENSOR A ENA	Event indicator, 2 positions: gray bp	Provides status of Smoke Sensor A gray – Smoke Sensor A ENABLED bp – Smoke Sensor A is INHIBITED	Used to verify Smoke Sensor A status during SH activation and to confirm smoke alarm during orbit operations
S19 SMOKE SENSOR B	Toggle sw, 2 positions: (Maintained–Maintained)	ENA – Applies 28 VDC to relay inside the MCP which allows Smoke Sensor B alarm signal to travel to the CWEA and the MDM INHB – Other switch position not wired to SH. However, inhibit signal occurs by removing 28 VDC from above relay at this switch position	Used to return Smoke Sensor B to its normal operational state, after it has been inhibited. This is normal position of switch Used to verify Smoke Sensor A during module activation and to confirm smoke alarm, once it has occurred, during orbit operations
DS19 SMOKE SENSOR B ENA	Event indicator, 2 positions: gray bp	Provides status of Smoke Sensor B gray – Smoke Sensor B ENABLED bp – Smoke Sensor B INHIBITED	Used to verify Smoke Sensor B status during SH activation and to confirm smoke alarm during orbit operations
CB4 SW PWR	Circuit Breaker—5 ampere: IN – closed OUT – open	IN – Applies orbiter power to CAB DEPRESS VLV (S16), SMOKE SENSOR (S17), SMOKE SENSOR A (S18), PDU MN DC BUS (S22) OUT – Removes power from to CAB DEPRESS VLV (S16), SMOKE SENSOR (S17), SMOKE SENSOR A (S18), PDU MN DC BUS (S22)	This is normal cb position
S20 MAIN PWR	Toggle sw, 2 positions: (Maintained–Maintained)	KILL – Applies 28 VDC command to open PDU relays K1, K13, K14, K15, K16, K18, K21, and APDU relays AK1–AK20, AK31, and AK32 pwr contactors 1,2. This effectively removes AC and DC pwr from all SH subsystem and experiment equipment, except ARS fan, Water Pump 2, and emergency bus powered equipment NO–OP – not wired to SH	Used to remove pwr from SH module after confirmed fire or during contingency safing operations This is normal position of switch

SPACEHAB SSP L12L SWITCH ASSIGNMENTS (Cont)

ITEM	TYPE DEVICE	FUNCTION	USAGE (TIME AND FREQUENCY)
S21 PDU SS DC BUS	Momentary sw, 3 positions	ON – Applies 28 VDC command to close PDU relays K13,K14 which enables distribution of DC pwr to SH subsystem Not wired OFF – Applies 28 VDC command to open above relays removing pwr from SH subsystem equipment	Subsystem will remain ON for duration of mission Nominal position Used during off nominal total module deactivation
DS21 SS DC BUS	Event indicator, 2 positions: gray bp	gray – Indicates both PDU relays K13,K14 closed bp – Indicates both PDU relays K13,K14, or both open	Indicates status in response to command from S21
S22 PDU MN DC BUS	Toggle sw, 2 positions: (Maintained–Maintained)	ON – Used to activate PDU pwr contactor 1 and relay K15 which allow distribution of main DC feed OFF – Applies 28 VDC command to open above relays removing main DC power from subsystems and experiments	Used during SH module activation. Switch will remain in ON position for duration of mission Used during off nominal total SH module deactivation
DS22 PDU MN DC BUS	Event indicator, 2 positions: gray bp	gray – Indicates PDU pwr contactor 1 open bp – Indicates PDU pwr contactor 1 closed	Indicates status in response to command from S22. PDU relay K15 not statused by this indicator
S23 FWD INVERTER	Toggle sw, 2 positions: (Maintained–Maintained)	ON – Applies 28 VDC command to close PDU relay K1 which sends DC pwr to inverter for AC conversion NO–OP – Switch position not wired to SH	Redundant method to turn ON inverter, with MCDS being primary method This is normal position of switch
DS23 FWD INVERTER	Event indicator, 2 positions: gray bp	gray – Indicates PDU relay K1 closed bp – Indicates PDU relay K1 open	Indicates status in response to command from S23 or MCDS
S24 PDU EXP DC BUS	Toggle sw, 3 positions: (Maintained–Maintained)	ON – Applies 28 VDC command to close PDU pwr contractor 2 and relay K16 which allow distribution of DC pwr to locker and rack experiments Not wired OFF – Applies 28 VDC command to above relays removing DC pwr from all experiments	Left ON for duration of mission Used during off nominal total SH module deactivation
DS24 PDU EXP DC BUS	Event indicator, 2 positions: gray bp	gray – Indicates PDU pwr contactor 2 closed bp – Indicates PDU pwr contactor 2 open	Indicates status in response to command from S24 or MCDS. PDU relay K16 not statused by this indicator

C3A5 PAYLOAD SAFING



SPACEHAB C3A5 SWITCH ASSIGNMENTS

ITEM	TYPE DEVICE	FUNCTION	USAGE (TIME AND FREQUENCY)
S1 SPACEHAB FIR SUPPR MCP ARM/SAFE	Two–position toggle switch: (up, down – maintained)	ARM (up) – Sends Arming signal to MCP FSS Discharge Circuitry which closes ground path for pyro circuit SAFE (down) – Sends Safing signal to MCP FSS Discharge Circuitry	Contingency use only
S2 SPACEHAB FIR SUPPR MCP DISCH/NO–OP	Two–position toggle switch: (up, down – maintained)	DISCH (up) – Sends Fire signal to MCP FSS Discharge circuitry. If circuit is armed, will send firing pulses to pyro circuits NO–OP (down) – not wired	Contingency use only
S3 SPACEHAB FIR SUPPR FSCU ARM/SAFE	Two–position toggle switch: (up, down – maintained)	ARM (up) – Sends arm signal to FSCU FSS Discharge Circuitry, and closing ground path for pyro circuit SAFE (down) – Removes arm signal from FSCU FSS Discharge Circuitry	Contingency use only
S4 SPACEHAB FIR SUPPR FSCU DISCH/NO–OP	Two–position toggle switch: (up, down – maintained)	DISCH (up) – Sends Fire signal to FSCU FSS Discharge circuitry. If circuit is armed, will send firing pulses to pyro circuits NO–OP (down) – not wired	Contingency use only
S5 H_2O LN HTRS	Two–position toggle switch: (up, down – maintained)	ON (up) – Closes relays allowing PL AFT B to power SH Water Line heaters. OFF (down) – not wired	Contingency use only

PGSC FAILURE RECOVERY OPTIONS

PGSC	FUNCTION	CONFIGURATION [1]	BACKUP HARDWARE (AS REQUIRED) [2]
STS1	OCA	760XD PGSC ON SINGLE SLOT AC EXPANSION UNIT CONFIGURED WITH OCA PC MOD BOARD	760XD PGSC, OCA PC BOARD, OCA HARDDRIVE, EXPANSION UNIT
STS2	WINDECOM	760XD PGSC ON SINGLE SLOT AC EXPANSION UNIT CONFIGURED WITH PCMMU BOARD	760XD PGSC, EXPANSION UNIT, STS HARDDRIVE
STS3	PROSHARE	760XD PGSC ON SINGLE SLOT AC EXPANSION UNIT CONFIGURED WITH PROSHARE BOARD	760XD PGSC, EXPANSION UNIT, STS HARDDRIVE [3]
STS4	WORLDMAP	760XD PGSC WITHOUT EXPANSION UNIT, DC POWER	760XD PGSC, STS HARDDRIVE
PL1	MEIDEX	760XD PGSC WITHOUT EXPANSION UNIT, DC POWER	760XD PGSC, STS HARDDRIVE
PL2	SOLSE–2	760XD PGSC WITHOUT EXPANSION UNIT, DC POWER	760XD PGSC, STS HARDDRIVE, BIA
PL3	SH SUBSYSTEM, HLS PHAB–4 BAR CODE READER	760XD PGSC ON SINGLE SLOT AC EXPANSION UNIT WITH RS–422 BOARD	760XD PGSC, EXPANSION UNIT, STS HARDDRIVE [4]
PL4	AST, MGM, BDS–05, & ZCG	760XD PGSC WITHOUT EXPANSION UNIT, DC POWER	760XD PGSC, STS HARDDRIVE
PL5	CM–2	760XD PGSC WITHOUT EXPANSION UNIT, DC POWER (WINDOWS 95 OS)	760XD PGSC [5], CM–2 HARDDRIVE
PL6	VCD FE	760XD PGSC WITHOUT EXPANSION UNIT, DC POWER (WINDOWS 95 OS)	760XD PGSC [5], VCD–FE HARDDRIVE
HLS	HLS MPFE	CUSTOMER SUPPLIED 755C THINKPAD WITHOUT EXPANSION UNIT, DC POWER	N/A
ARMS	ARMS	CUSTOMER SUPPLIED 760ED THINKPAD WITHOUT EXPANSION UNIT, DC POWER	760XD PGSC, ARMS HARDDRIVE

[1] All PGSCs are loaded with Microsoft Windows '98 OS unless specified otherwise

[2] On–board backup PGSC hardware includes:
Two IBM Thinkpad 760XD laptops with STS load harddrives
Single Slot AC Expansion Unit with PCMMU board
OCA PC MOD board
OCA load harddrive (has STS load on separate partition)
STS load harddrive
Spare BIA
CM–2 harddrive (Windows '95)
VCD–FE harddrive (Windows'95)
ARMS harddrive

[3] There is no backup Proshare board. The Proshare board provides video teleconferencing capability

[4] There is no backup RS–422 board. The RS–422 board provides capabilities for SH subsystem monitoring and SH video system control. Subsystem monitoring capability is also available to the crew via the orbiter SPEC pages. Backup for SH video system control is only available via ground command

[5] May require CMOS reconfig using Windows 95 OS CMOS Flash diskette

This Page Intentionally Blank

MEIDEX REFERENCE DATA

MEIDEX VISIBILITY TARGETS OBSERVATION FORM 11–3
SLANT VISIBILITY TARGETS 11–5

This Page Intentionally Blank

MEIDEX SLANT VISIBILITY OBSERVATION FORM

Orbit #	Target Name	Target AOS		Target LOS		Comments	Crewmember
		Time Acquired	Window Used	Time Lost	Window Used		

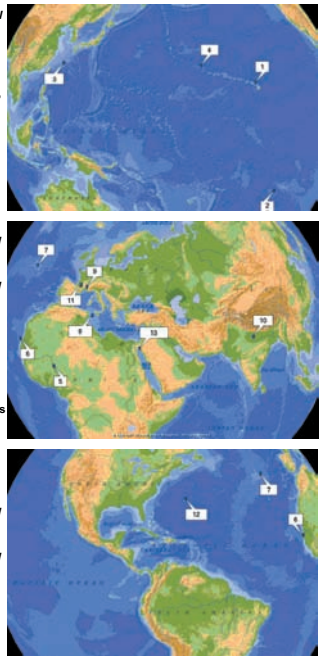
MEIDEX SLANT VISIBILITY OBSERVATION FORM (Cont)

Orbit #	Target Name	Target AOS: Time Acquired	Target AOS: Window Used	Target LOS: Time Lost	Target LOS: Window Used	Comments	Crewmember

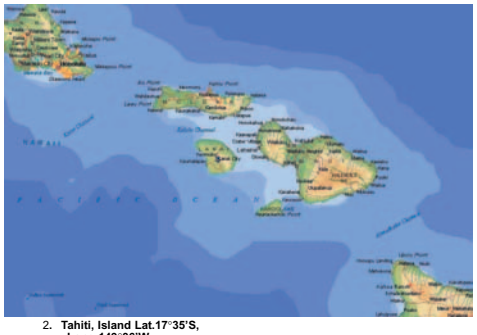
PL OPS/107/FIN A

MEIDEX SLANT VISIBILITY TARGETS

1. **Lanai, Hawaii, Coast Line Lat.20°50'N, Long.156°59'W**
2. **Tahiti, Island Lat.17°35'S, Long.149°36'W**
3. **Okinawa, Island Lat.23°34'S, Long.127°46'E**
4. **Midway Island Lat.28°13'N, Long.177°23'W**
5. **Niger, River Lat.13°32'N, Long.2°40'E**
6. **Dakar, Coast Line Lat.14°44'N, Long.17°31'W**
7. **Azores, Island Lat.38°32'N, Long.28°38'W**
8. **Lampedusa Island, Med. Lat.35°31'N, Long.12°38'E**
9. **Avignon, River Rhone Lat.43°23'N, Long.4°49'E**
10. **Kanpur, India, River Ganges Lat.26°45'N, Long.80°20'E**
11. **Toulouse, River Garonne Lat.43°36'N, Long.1°25'E**
12. **Bermuda Island Lat.32°37'N, Long.64°47'W**
13. **Strait of Tiran Lat.28°18'N, Long.34°32'W**



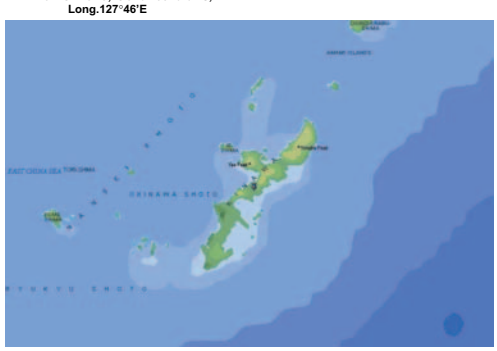
1. **Lanai, Hawaii, Coast Line Lat.20°50'N, Long.156°59'W**



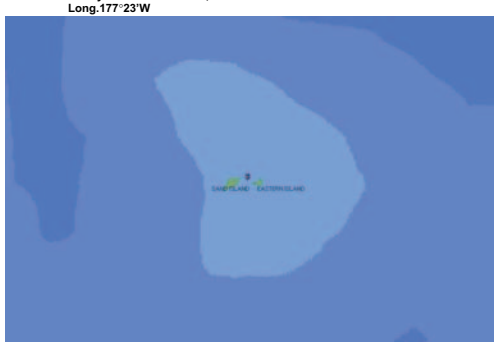
2. **Tahiti, Island Lat.17°35'S, Long.149°36'W**



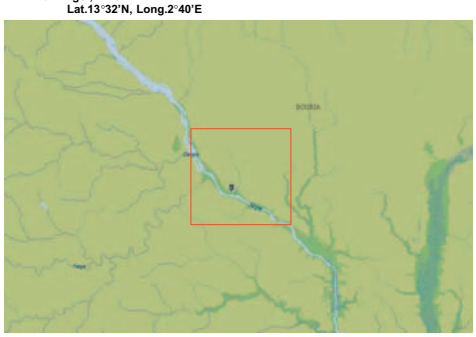
3. **Okinawa, Island Lat.23°34'S, Long.127°46'E**



4. **Midway Island Lat.28°13'N, Long.177°23'W**



5. **Niger, River**
Lat.13°32'N, Long.2°40'E

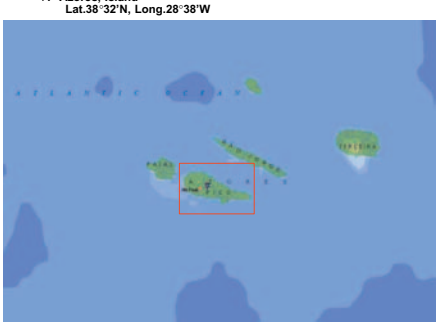


6. **Dakar, Coast Line**
Lat.14°44'N, Long.17°31'W



11–8 PL OPS/107/FIN A

7. **Azores, Island**
Lat.38°32'N, Long.28°38'W



8. **Lampedusa Island, Med.**
Lat.35°31'N, Long.12°38'E

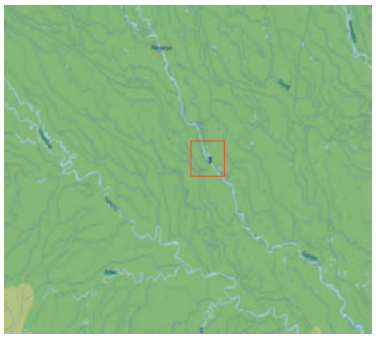


11–9 PL OPS/107/FIN A

9. **Avignon, River Rhone**
Lat.43°23'N, Long.4°49'E

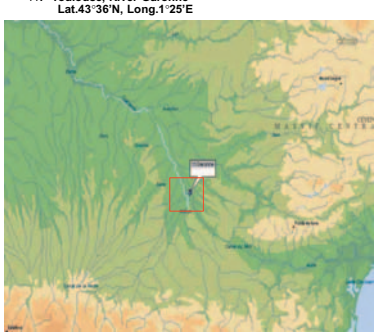


10. **Kanpur, India, River Ganges**
Lat.26°45'N, Long.80°20'E

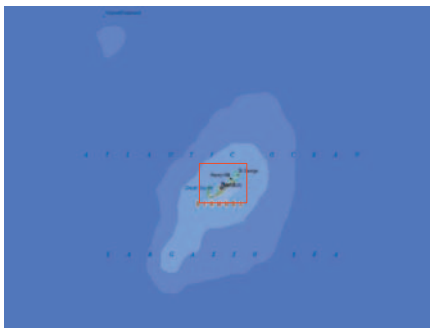


11–10 PL OPS/107/FIN A

11. **Toulouse, River Garonne**
Lat.43°36'N, Long.1°25'E



12. **Bermuda Island**
Lat.32°37'N, Long.64°47'W



11–11 PL OPS/107/FIN A

13. **Strait of Tiran**
Lat.28°18'N, Long.34°32'W



11–12 PL OPS/107/FIN A

CUE CARD CONFIG

CUE CARD CONFIGURATION

FAB USE ONLY 12–1 PL OPS/107/FIN A

CUE CARD CONFIG

This Page Intentionally Blank

FAB USE ONLY 12–2 PL OPS/107/FIN A

TOP

HOOK VELCRO

HOOK VELCRO

MEIDEX RECORDING LOG

Obs. Type	Orb #	V10 Tape #	V10 Time Rem.	VTR/DSR–20 Tape #	VTR/DSR–20 Time Rem.	MEIDEX VCR OFFSETS VCR 1 Elapsed Sec	VCR 2 Elapsed Sec	VCR 3 Elapsed Sec

PL OPS–1a/107/O/A

NOTE: 2 copies reqd for flight

(reduced copy)

FAB USE ONLY CC 12–3 PL OPS/107/FIN A

TOP
BACK OF 'MEIDEX RECORDING LOG'

HOOK VELCRO

HOOK VELCRO

Obs. Type	Orb #	V10 Tape #	V10 Time Rem.	VTR/DSR–20 Tape #	VTR/DSR–20 Time Rem.	MEIDEX VCR OFFSETS VCR 1 Elapsed Sec	VCR 2 Elapsed Sec	VCR 3 Elapsed Sec

PL OPS–1b/107/O/A

NOTE: 2 copies reqd for flight

(reduced copy)

FAB USE ONLY CC 12–4 PL OPS/107/FIN A

JSC–48068–107
FINAL, REV A



Space Shuttle Program
FLIGHT DATA FILE

PAYLOAD OPS CHECKLIST

STS 107

Flight Cover (trim bottom to expose tabs)

THIS PAGE INTENTIONALLY LEFT BLANK

Volume II
Appendix D.3
Fault Tree Closure Summary

The NASA Accident Investigation Team examined the accident using "fault trees," a common organizational tool in systems engineering. Fault trees are graphical representations of every conceivable sequence of events that could cause a system to fail. The fault tree's uppermost level illustrates the events that could have directly caused the loss of Columbia by aerodynamic breakup during re-entry. Subsequent levels comprise all individual elements or factors that could cause the failure described immediately above it. In this way, all potential chains of causation that could have ultimately led to the loss of *Columbia* can be diagrammed, and the behavior of every subsystem that was not a precipitating cause can be eliminated from consideration.

NASA chartered six teams to develop fault trees, one for each of the Shuttle's major components: the Orbiter, Space Shuttle Main Engine, Reusable Solid Rocket Motor, Solid Rocket Booster, External Tank, and Payload. A seventh "systems integration" fault tree team analyzed failure scenarios involving two or more Shuttle components. These interdisciplinary teams included NASA and contractor personnel, as well as outside experts. Some of the fault trees are very large and intricate. For instance, the Orbiter fault tree, which only considers events on the Orbiter that could have led to the accident, includes 234 elements. In contrast, the Systems Integration fault tree, which deals with interactions among parts of the Shuttle, includes 295 unique multi-element integration faults, 128 Orbiter multi-element faults, and 221 connections to the other Shuttle components.

This appendix provides a listing of fault tree elements that were investigated by the Board and closed during the *Columbia* investigation. Some of the elements in this appendix were open at the time the investigation concluded, but are expected to be closed before the Return to Flight. Items marked "Open due to lower element" remained open because a lower level fault tree had yet to be closed; for the most part, the lower-level fault trees are contained in Appendix D.4.

Section A Columbia Accident Investigation Fault Tree (Orbiter) Closures 77
Section B Space Shuttle Main Engine (SSME) Fault Tree Closures 87
Section C Solid Rocket Booster (SRB) Fault Tree Closures 89
Section D Reusable Solid Rocket Motor (RSRM) Fault Tree Closures 92
Section E Multi-Element (Integration) Fault Tree Closures 93
Section F External Tank (ET) Fault Tree Closures 94

Fault Tree Closure Summary

By Group III
James N. Hallock, Ph.D., G. Scott Hubbard, Douglas D. Osheroff, Ph.D.,
Roger E. Tetrault, Sheila E. Widnall, Ph.D.
Captain David Bawcom, Captain Anne-Marie Contraras

Note: Some of the element closures will extend beyond the writing of this report. In addition, there are some elements that can never be closed as neither data nor analysis can unambiguously rule out a contribution to the Columbia accident. Those are listed and described in Appendix D.4. This appendix contains the fault tree elements that were closed by the Columbia Accident Investigation Board as well as the open fault tree elements that have closure strategies and are expected to be closed.

SECTION A

– *Not Reviewed by CAIB, expected closure as 'not a contributor '*

– *Reviewed and closed by CAIB as 'not a contributor'*

ELEMENT NUMBER	*DESCRIPTION OF FAULT TREE ELEMENT*
AC	AERODYNAMIC BREAKUP DUE TO IMPROPER ATTITUDE / TRAJECTORY CONTROL
ACCF	IMPROPER ATTITUDE/TRAJECTORY CONTROL DUE TO COMMAND FAILURE
ACCF-CALC	COMMAND FAILURE DUE TO INCORRECT CALCULATION
ACCF-CALC-5-01	INCORRECT CALCULATION DUE TO NAVIGATION ERROR
ACCF-CALC-5-02	INCORRECT CALCULATION DUE TO GUIDANCE ERROR
ACCF-CALC-5-03	INCORRECT CALCULATION DUE TO FLIGHT CONTROL ERROR
ACCF-CALC-6-01	NAV ERROR DUE TO IMU FAILURE
ACCF-CALC-6-02	NAV ERROR DUE TO BAD NAV STATE UPLOAD
ACCF-CALC-6-03	NAV ERROR DUE TO SOFTWARE ERROR
ACCF-CALC-6-04	GUIDANCE ERROR DUE TO BAD I-LOAD
ACCF-CALC-6-05	GUIDANCE ERROR DUE TO BAD LOGIC
ACCF-CALC-6-06	FLIGHT CONTROL ERROR DUE TO RATE SENSOR FAILURE

ELEMENT NUMBER	*DESCRIPTION OF FAULT TREE ELEMENT*
ACCF-CALC-6-07	FLIGHT CONTROL ERROR DUE TO ACCELEROMETER FAILURE
ACCF-CALC-6-08	FLIGHT CONTROL ERROR DUE TO FC SOFTWARE ERROR
ACCF-CALC-6-09	GUIDANCE SOFTWARE ERROR DUE TO BAD DEORBIT BURN TARGET UPLOAD
ACCF-CALC-7-01	SOFTWARE ERROR DUE TO BAD I-LOAD
ACCF-CALC-7-02	SOFTWARE ERROR DUE TO BAD LOGIC
ACCF-CALC-7-03	FC SOFTWARE ERROR DUE TO BAD I-LOAD
ACCF-CALC-7-04	FC SOFTWARE ERROR DUE TO BAD LOGIC
ACCF-SIG	COMMAND FAILURE DURING DATA PROCESSING TRANSMISSION
ACCF-SIG-5-01	DATA P/T ERROR DUE TO GPC FAILURE
ACCF-SIG-5-02	DATA P/T ERROR DUE TO BROKEN WIRE
ACCF-SIG-5-03	DATA P/T ERROR DUE TO MDM FAILURE
ACCF-SIG-5-04	DATA P/T ERROR DUE TO EMI (ME)
ACCF-SIG-6-01	EMI CAUSED BY INTERNAL SOURCE
ACCF-SIG-6-02	EMI CAUSED BY EXTERNAL SOURCE
ACCF-SIG-6-06	HARDWARE FAILURE CAUSES GPC FAILURE
ACCF-SIG-6-07	SOFTWARE FAILURE CAUSES GPC FAILURE
ACCF-SIG-6-08	HARDWARE FAILURE CAUSES MDM FAILURE
ACCF-SIG-6-09	FIRMWARE ERROR CAUSES MDM FAILURE
ACCG	VEHICLE CONFIGURATION OUTSIDE ENVELOPE DUE TO CENTER OF GRAVITY (CG) (ME)
ACCG-CG	INCORRECT CENTER OF GRAVITY
ACCG-INER	INCORRECT MOMENTS OF INERTIA
ACCG-WT	INCORRECT WEIGHT
ACEF	IMPROPER ATTITUDE/ TRAJECTORY CONTROL DUE TO CONTROL EFFECTOR FAILURE
ACEF-AE	CONTROL EFFECTOR FAILURE DUE TO AEROSURFACE FAILURE
ACEF-AE-5-01	AEROSURFACE FAILURE DUE TO ELEVON FAILURE
ACEF-AE-5-02	AEROSURFACE FAILURE DUE TO RUDDER / SPEED BRAKE FAILURE
ACEF-AE-5-03	AEROSURFACE FAILURE DUE TO BODY FLAP FAILURE
ACEF-AE-6-01	ELEVON FAILURE DUE TO DEBRIS
ACEF-AE-6-02	ELEVON FAILURE DUE TO ACTUATOR FAILURE (INCLUDING ASA)

ELEMENT NUMBER	*DESCRIPTION OF FAULT TREE ELEMENT*
ACEF-AE-6-03	R/S FAILURE DUE TO DEBRIS
ACEF-AE-6-04	RUDDER/SPEEDBRAKE FAILURE DUE TO ACTUATOR FAILURE (INCLUDING ASA)
ACEF-AE-6-05	BODY FLAP FAILURE DUE TO DEBRIS
ACEF-AE-6-06	BODY FLAP FAILURE DUE TO ACTUATOR FAILURE (INCLUDING ASA)
ACEF-AE-7-01	ACTUATOR FAILURE DUE TO ELECTRICAL POWER/DISTRIBUTION FAILURE
ACEF-AE-7-02	ACTUATOR FAILURE DUE TO APU/HYDRAULICS FAILURE (ME)
ACEF-AE-7-03	ACTUATOR FAILURE DUE TO ELECTRICAL POWER/DISTRIBUTION FAILURE
ACEF-AE-7-04	ACTUATOR FAILURE DUE TO APU/HYDRAULICS FAILURE
ACEF-AE-7-05	ACTUATOR FAILURE DUE TO ELECTRICAL POWER/DISTRIBUTION FAILURE
ACEF-AE-7-06	ACTUATOR FAILURE DUE TO APU/HYDRAULICS FAILURE (ME)
ACEF-AE-7-07	MECHANICAL FAILURE OF ELEVON ACTUATOR
ACEF-AE-7-08	MECHANICAL FAILURE OF R/S ACTUATOR
ACEF-AE-7-09	MECHANICAL FAILURE OF BODY FLAP
ACEF-AE-7-10	SSME CONTACTS BODY FLAP (ME)
ACEF-OMS	CONTROL EFFECTOR FAILURE DUE TO OMS FAILURE
ACEF-RCS	CONTROL EFFECTOR FAILURE DUE TO RCS JET FAILURE
ACEF-RCS-5-1	RCS JETS FAIL TO BURN WHEN COMMANDED CAUSES LOSS OF ATTITUDE
ACEF-RCS-5-2	RCS JETS BURN INCORRECTLY WHEN COMMAND CAUSES LOSS OF ATTITUDE
SFOML-AFT	LOSS OF OML DUE TO AFT FUSELAGE FAILURE
SFOML-BAY	LOSS OF OML DUE TO PAYLOAD BAY DOOR FAILURE
SFOML-CABIN	LOSS OF OML DUE TO CREW CABIN MODULE FAILURE
SFOML-FLAP	LOSS OF OML DUE TO BODY FLAP FAILURE
SFOML-FRCS	LOSS OF OML DUE TO FRCS STRUCTURAL FAILURE
SFOML-FWD	LOSS OF OML DUE TO FWD FUSELAGE FAILURE
SFOML-INTPLB	LOSS OF OML DUE TO FAILURE SOURCE INTERNAL TO PAYLOAD BAY
SFOML-MID	LOSS OF OML DUE TO MID FUSELAGE FAILURE
SFOML-OMS	LOSS OF OML DUE TO OMS POD FAILURE
SFOML-SSME	LOSS OF OML DUE TO SSME OUT OF CONFIGURATION (ME)
SFOML-TAIL	LOSS OF OML DUE TO TAIL FAILURE

ELEMENT NUMBER	*DESCRIPTION OF FAULT TREE ELEMENT*
SFOML-WINDOW	LOSS OF OML DUE TO WINDOW FAILURE
SFOML-WING-5-1	WING/ELEVON STRUCTURAL FAILURE DUE TO WING OVERLOAD
SFOML-WING-5-2	WING/ELEVON STRUCTURAL FAILURE DUE TO OVERPRESSURIZATION OR COLLAPSE
SFOML-WING-5-4	WING/ELEVON STRUCTURAL FAILURE DUE TO WEAKENED WING STRUCTURE
SFOML-WING-6-1	WING OVERLOAD DUE TO FLIGHT OUTSIDE ENVELOPE (ME)
SFOML-WING-6-2	WING OVERLOAD DUE TO INTEGRATED ENVIROMENT DIFFERENT THAN DESIGN
SFOML-WING-6-3	WING OVERLOAD DUE TO IMPROPER VEHICLE CONFIGURATION
SFOML-WING-6-4	WING OVERLOAD DUE TO WING/ELEVON FLUTTER
SFOML-WING-6-5	WING OVERPRESS OR COLLAPSE DUE TO BLOCKED VENT RESULTING IN FAILURE TO REPRESS
SFOML-WING-6-6	WING OVERPRESS. OR COLLAPSE DUE TO PRESSURE SYSTEM FAILURE CAUSING INADVERTENT PRESSURIZATION
SFOML-WING-6-7	WING OVERPRESS OR COLLAPSE DUE TO BLOWN TIRE CAUSING INADVERTENT PRESSURE
SFOML-WING-6-8	THERMAL DAMAGE BURN THROUGH DUE TO HIGHER HEATING
SFOML-WING-6-9	OVERHEAT/ THERMAL DAMAGE/ BURN THROUGH DUE TO INADVERTENT OPENING IN WING ALLOWING PLASMA FLOW
SFOML-WING-6-11	WEAKENED WING STRUCTURE DUE TO FATIGUE FAILURE IN WING/ELEVON
SFOML-WING-6-12	WEAKENED WING STRUCTURE DUE TO STRUCTURE CONFIGURATION NOT PER DESIGN STRENGTH
SFOML-WING-6-13	WEAKENED WING STRUCTURE DUE TO SPACE ENVIRONMENT (“Space Weather”)
SFOML-WING-6-14	WEAKENED WING STRUCTURE DUE TO PLASMA/ELECTRICAL DISCHARGE
SFOML-WING-6-15	WEAKENED WING STRUCTURE DUE TO INTERNAL FIRE (ME)
SFOML-WING-6-16	WEAKENED WING STRUCTURE DUE TO MMOD
SFOML-WING-6-18	WING OVERPRESS OR COLLAPSE DUE TO PAYLOAD BAY SOURCE (ME)
SFOML-WING-7-1	FLIGHT OUTSIDE ENVELOPE DUE TO MISSION DESIGN ERROR
SFOML-WING-7-2	FLIGHT OUTSIDE ENVELOPE DUE TO FLIGHT CONTROL SURFACE LOAD PATH
SFOML-WING-7-3	FLIGHT OUTSIDE ENVELOPE DUE TO OVERWEIGHT / CENTER OF GRAVITY OUT OF LIMITS
SFOML-WING-7-5	IMPROPER WING CONFIGURATION DUE TO EARLY GEAR DEPLOYMENT (ME)
SFOML-WING-7-7	WING/ELEVON FLUTTER DUE TO CHANGE IN AIR FLOW
SFOML-WING-7-8	WING/ELEVON FLUTTER DUE TO HIGHER SPEED THAN PLANNED
SFOML-WING-7-9	WING/ELEVON FLUTTER DUE TO IMPROPER MASS PROPERTIES
SFOML-WING-7-10	WING/ELEVON FLUTTER DUE TO FCS LINKAGE FAILURE
SFOML-WING-7-11	WING/ELEVON FLUTTER DUE TO LOOSE COMPONENT

ELEMENT NUMBER	*DESCRIPTION OF FAULT TREE ELEMENT*
SFOML-WING-7-12	INADVERTENT PRESSURIZATION DUE TO PRSD/ECLSS TANK FAILURE
SFOML-WING-7-13	INADVERTENT PRESSURIZATION DUE TO OTHER EVENT
SFOML-WING-7-14	HIGHER HEATING DUE TO OFF NOMINAL TRAJECTORY
SFOML-WING-7-15	HIGHER HEATING DUE TO UNEXPECTED FLOW
SFOML-WING-7-16	HIGHER HEATING DUE TO UNUSUAL ENVIRONMENT
SFOML-WING-7-17	HIGHER HEATING DUE TO HEAVY ENTRY WEIGHT
SFOML-WING-7-18	INADVERTENT DOOR OPEN OR BREACH OF THERMAL SEAL (GEAR REMAINS UP)
SFOML-WING-7-19	INADVERTENT OPENING IN WING ALLOWING PLASMA FLOW DUE TO FLIPPER DOOR FAILURE
SFOML-WING-7-21	TPS MALFUNCTION DUE TO TILE FAILURE
SFOML-WING-7-22	TPS MALFUNCTION DUE TO BLANKET FAILURE
SFOML-WING-7-23	TPS MALFUNCTION DUE TO SEAL FAILURE
SFOML-WING-7-24	FATIGUE FAILURE IN WING/ELEVON DUE TO DEGRADED PROPERTIES
SFOML-WING-7-25	FATIGUE FAILURE IN WING/ELEVON DUE TO SPECTRA EXCEEDED CERTIFICATION PREVIOUS FLIGHT
SFOML-WING-7-26	FATIGUE FAILURE IN WING/ELEVON DUE TO FRACTURE CRITICAL ITEM
SFOML-WING-7-27	STRUCTURE CONFIGURATION NOT PER DESIGN STRENGTH DUE TO LOADS EXCEED PREVIOUS FLIGHTS (ME)
SFOML-WING-7-28	STRUCTURAL CONFIGURATION NOT PER DESIGN STRENGTH DUE TO DEGRADED STRUCTURAL PROPERTIES
SFOML-WING-7-29	STRUCTURE CONFIGURATION NOT PER DESIGN CERTIFICATION DUE TO UNDETECTED NEGATIVE MARGINS
SFOML-WING-7-30	STRUCTURE CONFIGURATION NOT PER DESIGN
SFOML-WING-7-31	MICRO METEROID
SFOML-WING-7-32	ORBITAL DEBRIS
SFOML-WING-7-35	ENTRY LOADS OUTSIDE CERTIFICATION (ME)
SFOML-WING-7-36	INTEGRATED VEHICLE ASCENT ENVIRONMENT OUT OF FAMILY (ME)
SFOML-WING-7-37	ON-ORBIT LOADS OUTSIDE CERTIFICATION (ME)
SFOML-WING-7-38	GROUND PROCESSING INDUCED LOADS OUT OF CERTIFICATION (ME)
SFOML-WING-7-39	FERRY FLIGHT INDUCED LOADS OUTSIDE CERTIFICATION
SFOML-WING-7-40	ON-ORBIT PLASMA/ELECTRICAL DISCHARGE
SFOML-WING-7-41	ENTRY PLASMA/ELECTRICAL DISCHARGE
SFOML-WING-8-1	STS-107 ORBITER LOADS
SFOML-WING-8-7	UNEXPECTED FLOW DUE TO EARLY TRANSITION (STEP/GAP)

ELEMENT NUMBER	*DESCRIPTION OF FAULT TREE ELEMENT*
SFOML-WING-8-8	UNEXPECTED FLOW DUE TO AERO PHENOMENA (ASYMMETRIC TRANSITION SHOCK WAVE)
SFOML-WING-8-9	UNEXPECTED FLOW DUE TO CHEMISTRY OR MATERIALS PROBLEM (CATALYSIS OR CONTAMINATION)
SFOML-WING-8-11	RCC FAILURE DUE TO CRACK/HOLE < 0.25 IN ON BOTTOM 1.0 IN ON TOP NOT SIGNIFICANT
SFOML-WING-8-12	RCC FAILURE DUE TO DEGRADED COATING EXPOSES RCC SUBSTRATE
SFOML-WING-8-13	RCC FAILURE DUE TO ENVIRONMENT OUTSIDE RCC CERTIFICATION ("SPACE WEATHER")
SFOML-WING-8-15	TILE FAILURE DUE TO TILE DEBOND
SFOML-WING-8-16	TILE FAILURE DUE TO BROKEN TILE
SFOML-WING-8-17	TILE FAILURE DUE TO FAILED REPAIR
SFOML-WING-8-18	TILE FAILURE DUE TO LOST CARRIER PANEL
SFOML-WING-8-19	BLANKET FAILURE DUE TO BLANKET INTEGRITY LOSS
SFOML-WING-8-20	BLANKET FAILURE DUE TO LOST CARRIER PANEL
SFOML-WING-8-21	BLANKET FAILURE DUE TO DEBOND
SFOML-WING-8-22	SEAL FAILURE DUE TO THERMAL BARRIER FAILURE
SFOML-WING-8-23	SEAL FAILURE DUE TO ELEVON COVE SEAL FAILURE
SFOML-WING-8-24	SEAL FAILURE DUE TO ENVIRONMENTAL SEAL FAILURE
SFOML-WING-8-25	FATIGUE FAILURE DUE TO CORROSION
SFOML-WING-8-26	FATIGUE FAILURE DUE TO FRACTURE TOUGHNESS DEGRADATION
SFOML-WING-8-27	STS-109/PAST ORBITER ASCENT SPECTRUM (ME)
SFOML-WING-8-28	STS-109/PAST ORBITER ON-ORBIT SPECTRUM (ME)
SFOML-WING-8-29	STS-109/PAST ORBITER DESCENT SPECTRUM (ME)
SFOML-WING-8-30	FAILURE OF <100 FLIGHT LIFE FRACTURE CRITICALITY ITEM
SFOML-WING-8-31	FAILURE OF FRACTURE CRITICALITY ITEM OF 100 TO 300 FLIGHT LIFE
SFOML-WING-8-32	PREVIOUS STS-109/ORBITER DESCENT LOADS
SFOML-WING-8-33	PREVIOUS STS-109/ORBITER ASCENT LOADS
SFOML-WING-8-34	PREVIOUS STS-109/ORBITER ON ORBIT LOADS
SFOML-WING-8-35	DEGRADED STRENGTH DUE TO CORROSION
SFOML-WING-8-36	DEGRADED STRENGTH FROM TEMPERATURE EXPOSURE
SFOML-WING-8-37	DEGRADED STRENGTH DUE TO CREEP
SFOML-WING-8-38	ANALYSIS MISSED ON LOW SAFETY MARGIN (M.S. < 0.20) ITEM

ELEMENT NUMBER	*DESCRIPTION OF FAULT TREE ELEMENT*
SFOML-WING-8-39	ANALYSIS MISSED DEFLECTIONS CRITICAL TO TPS
SFOML-WING-8-40	PROCEDURAL ERRORS
SFOML-WING-8-41	INCORRECT DISPOSITION OF BUILD MR OR STS-109 AND STS-107 FROM PR
SFOML-WING-8-42	TILE FAILURE DUE TO FLIGHT OUTSIDE CERTIFIED ENVIRONMENT (ME)
SFOML-WING-8-44	BLANKET LOSS DUE TO FLIGHT OUTSIDE CERTIFIED ENVIRONMENT (ME)
SFOML-WING-8-46	PRSD RUPTURE OR FIRE/EXPLOSION
SFOML-WING-8-47	ECLSS TANK FAILURE
SFOML-WING-8-48	LEAKS PRIOR TO FLIGHT
SFOML-WING-8-49	SPILLS PRIOR TO FLIGHT
SFOML-WING-8-50	INFLIGHT LEAKS
SFOML-WING-8-52	UNEXPECTED FLOW DUE TO ASYMMETRICAL BOUNDRY LAYER TRANSITION
SFOML-WING-8-53	RCC FAILURE DUE TO IMPROPER RCC REPAIR
SFOML-WING-9-1	HEAVY WEIGHT HEAVE ENTRY WT CAUSED SF OF OML SING/ELEVON (ME)
SFOML-WING-9-2	OTHER
SFOML-WING-9-12	DEGRADED COATING EXPOSES RCC SUBSTRATE DUE TO PINHOLES
SFOML-WING-9-13	DEGRADED COATING EXPOSES RCC SUBSTRATE DUE TO CONTAMINATION
SFOML-WING-9-14	DEGRADED COATING EXPOSES RCC SUBSTRATE DUE TO IMPACT
SFOML-WING-9-15	DEGRADED COATING EXPOSES RCC SUBSTRATE DUE TO ATOMIC OXYGEN DIATOMIC OXYGEN
SFOML-WING-9-16	DEGRADED COATING EXPOSES RCC SUBSTRATE DUE TO AGING
SFOML-WING-9-17	DEGRADED COATING EXPOSES RCC SUBSTRATE DUE TO IMPROPER COATING REPAIR
SFOML-WING-9-21	LOSS OF RCC PANEL DUE TO ADJACENT LOSS OF CARRIER PANEL
SFOML-WING-9-22	TILE DEBOND DUE TO IMPROPER INSTALLATION
SFOML-WING-9-23	TILE DEBOND DUE TO FAULTY BOND INTEGRITY
SFOML-WING-9-24	FASTENER FAILURE DUE TO SNEAK FLOW
SFOML-WING-9-25	TILE NOT WATER-PROOFED
SFOML-WING-9-26	ANALYSIS MISSED OUT-OF-PLANE DEFLECTION FOR TILE
SFOML-WING-9-27	LOST CARRIER PANEL DUE TO FAILED FASTENERS
SFOML-WING-9-28	LOST CARRIER PANEL DUE TO FLOW PENETRATING WING SEAL
SFOML-WING-9-29	BLANKET INTEGRITY LOST DUE TO FAILED REPAIR

ELEMENT NUMBER	*DESCRIPTION OF FAULT TREE ELEMENT*
SFOML-WING-9-30	DEBOND DUE TO IMPROPERLY INSTALLATION
SFOML-WING-9-31	DEBOND DUE TO BOND INTEGRITY FAILURE
SFOML-WING-9-32	THERMAL BARRIER FAILURE DUE TO LANDING GEAR THERMAL BARRIER FAILURE
SFOML-WING-9-33	THERMAL BARRIER FAILURE DUE TO ET UMBILICAL DOOR THERMAL BARRIER FAILURE
SFOML-WING-9-35	ENVIRONMENTAL SEAL FAILURE DUE TO LANDING GEAR DOOR FAILURE
SFOML-WING-9-36	ENVIRONMENTAL SEAL FAILURE DUE TO ET UMBILICAL DOOR FAILURE
SFOML-WING-9-37	DESCENT SPECTRA EXCEEDED CERTIFICATION PREVIOUS FLIGHT DUE TO CAUSES OTHER THAN WEIGHT
SFOML-WING-9-38	PAST HEAVY WEIGHT
SFOML-WING-9-39	OTHER LOADS EXCEEDING PREVIOUS FLIGHT CERTIFICATION
SFOML-WING-9-40	PREVIOUS FLIGHT HEAVY WEIGHT
SFOML-WING-9-41	STS-107 FLOW OPERATIONS IN WING
SFOML-WING-9-42	STS-109 OMM OPERATIONS IN WING
SFOML-WING-9-43	"USE AS IS" HARDWARE
SFOML-WING-9-44	MODIFIED HARDWARE
SFOML-WING-9-46	LANDING GEAR THERMAL BARRIER FAILURE DUE TO FLIGHT OUTSIDE ENVELOPE (ME)
SFOML-WING-9-47	ANALYSIS MISSED OUT-OF-PLANE DEFLECTION FOR TILE
SFOML-WING-9-53	IMPACT
SFOML-WING-9-54	IMPACT
SFOML-WING-9-56	IMPACT
SFOML-WING-9-57	IMPACT
SFOML-WING-9-58	TILE DEBOND DUE TO IMPROPER WATER PROOFING
SFOML-WING-9-59	DEGRADED COATING DUE TO ENVIRONMENTS (ME)
SFOML-WING-10-6	PRE LAUNCH UNIDENTIFIED IMPACT WHILE IN VEHICLE ASSEMBLY BUILDING (ME)
SFOML-WING-10-7	PRE LAUNCH UNIDENTIFIED IMPACT WHILE IN ORBITER PROCESSING FACILITY (ME)
SFOML-WING-10-8	SUPPORTING STRUCTURAL FAILURE DUE TO INTERNAL INSULATION FAILURE
SFOML-WING-10-9	WING LEADING EDGE STRUCTURE FAILURE
SFOML-WING-10-10	LOSS OF CARREIR PANEL DUE TO FASTENER FAILURE
SFOML-WING-10-11	LOSS OF CARRIER PANEL DUE TO FLOW PENETRATING WING SEAL
SFOML-WING-10-12	FAULTY BOND INTEGRITY DUE TO AGE

ELEMENT NUMBER	*DESCRIPTION OF FAULT TREE ELEMENT*
SFOML-WING-10-13	FAULTY BOND INTEGRITY DUE TO OTHER FLUIDS
SFOML-WING-10-14	FAILED FASTENERS DUE TO IMPROPER INSTALLATION
SFOML-WING-10-15	BOND INTEGRITY FAILURE DUE TO AGE
SFOML-WING-10-16	BOND INTEGRITY FAILURE DUE TO OTHER FLUIDS
SFOML-WING-10-17	LANDING GEAR T/B FAILURE DUE TO DEGRADATION OF THERMAL BARRIER MATERIAL
SFOML-WING-10-18	LANDING GEAR T/B FAILURE DUE TO INPROPER INSTALL / CLOSING
SFOML-WING-10-19	ET UMBILICAL DOOR T/B FAILURE DUE TO IMPROPER INSTALL / CLOSING
SFOML-WING-10-20	ET UMBILICAL DOOR T/B FAILURE DUE TO DEBRIS DURING CLOSING
SFOML-WING-10-21	ET UMBILICAL DOOR T/B FAILURE DUE TO THERMAL BARRIER FAILURE INSIDE LIFETIME
SFOML-WING-10-22	MID FUSELAGE SIDEWALL OIL CAN
SFOML-WING-10-23	WING / FUSELAGE ATTACHMENT BOLTS
SFOML-WING-10-24	UNSEALED BLIND RIVETS
SFOML-WING-10-26	OTHER
SFOML-WING-10-27	HARD LANDING
SFOML-WING-10-28	THIN STRUTS
SFOML-WING-10-29	ELEVON COVE LEAKAGE BLADE SEAL REWORK
SFOML-WING-10-30	CLAM - SHELL REPAIR STRUTS
SFOML-WING-10-31	UNSEATED BLIND RIVETS
SFOML-WING-10-32	FACILITY, GSE, SPECIAL TEST EQUIPMENT, TOOLING, AND OTHER HARDWARE
SFOML-WING-10-33	PRE LAUNCH UNIDENTIFIED IMPACT DURING TRANSPORTATION (SCA, ORBITER TRANSPORTER) (ME)
SFOML-WING-10-35	ET UMBILICAL DOOR T/B FAILURE DUE TO FLIGHT OUTSIDE CERTIFIED ENVIRONMENT (ME)
SFOML-WING-10-36	SPILLS
SFOML-WING-10-48	IMPACT
SFOML-WING-10-49	IMPACT
SFOML-WING-10-52	ET UMBILICAL DOOR T/B FAILURE DUE TO OFF NOMINAL ET SEPARATION (ME)
SFOML-WING-11-1	ORBITER CAUSED INFLIGHT IMPACT
SFOML-WING-11-7	RSRM DEBRIS IMPACT ON ASCENT (ME)
SFOML-WING-11-11	SNEAK FLOW DUE TO TILE DAMAGE
SFOML-WING-11-13	SNEAK FLOW DUE TO STRUCTURAL DEFLECTION

ELEMENT NUMBER	*DESCRIPTION OF FAULT TREE ELEMENT*
SFOML-WING-11-14	FASTENER FAILURE DUE TO IMPROPER INSTALL
SFOML-WING-11-19	SNEAK FLOW DUE TO STRUCTURAL DEFLECTION
SFOML-WING-11-34	IMPACT
SFOML-WING-11-60	TPS IMPACTS ORBITER
SFOML-WING-11-61	ORBITER ACCESS PANEL
SFOML-WING-11-62	SSME INDUCED IMPACT INFLIGHT (ME)
SFOML-WING-11-64	SSME DEBRIS IMPACT (ASCENT)
SFOML-WING-11-65	SNEAK FLOW DUE TO MISSING / DISPLACED GAP FILLER
SFOML-WING-11-67	LOSS OF RCC PANEL DUE TO ANGEL-SEAL FAILURE
SFOML-WING-11-68	LOSS OF RCC PANEL DUE TO BUTTERFLY-SEAL FAILURE
SFOML-WING-12-1	ICICLE FORMS ON WASTE WATER OR SUPPLY WATER NOZZLE AND BREAKS OFF CAUSING INFLIGHT IMPACT
SFOML-WING-12-2	OTHER ORBITER CAUSED DEBRIS IMPACT
SFOML-WING-12-5	ICICLE FORMS ON WASTE WATER OR SUPPLY WATER NOZZLE AND BREAKS OFF ON ENTRY
SFOML-WING-12-6	OTHER ORBITER CAUSED DEBRIS IMPACT
SFOML-WING-12-10	RCC DAMAGE DUE TO OTHER EVENT
SFOML-WING-12-11	TILE DAMAGE DUE TO IMPACT
SFOML-WING-12-12	TILE DAMAGE DUE TO OTHER EVENT
SFOML-WING-12-13	SNEAK FLOW DUE TO SEAL DAMAGE INDUCED BY OTHER EVENT
SFOML-WING-12-19	ICE FORMED ON ORBITER SURFACE DUE TO SUPPLY/WASTE DUMP IMPINGEMENT
SFOML-WING-12-20	ET ATTACH CAUSES INFLIGHT IMPACT (ME)
SFOML-WING-12-21	ACCESS PANEL CAUSES INFLIGHT IMPACT
SFOML-WING-12-22	ICE FORMED ON ORBITER SURFACE DUE TO SUPPLY/WASTE DUMP IMPINGEMENT
SFOML-WING-12-23	LOST ACCESS PANEL IMPACTS ON ENTRY
SFOML-WING-12-24	FOD
SFOML-WING-12-90	Orbital Contact with External Tank (ME)
SFOML-WING-12-91	Orbiter Contact with SRB/RSRM (ME)
SFOML-WING-12-92	Contact with launch pad
SFOML-WING-12-93	SSME Debris impact (Entry)
SFSM	STRUCTURAL FAILURE OF ORBITER DUE TO LOSS OF STRUCTURAL MEMBER

ELEMENT NUMBER	*DESCRIPTION OF FAULT TREE ELEMENT*
SFSM-AFT	LOSS OF STRUCTURAL MEMBERS DUE TO AFT FUSELAGE FAILURE (ME)
SFSM-BAY	LOSS OF STRUCTURAL MEMBERS DUE TO PAYLOAD BAY DOOR FAILURE
SFSM-CABIN	LOSS OF STRUCTURAL MEMBERS DUE TO CREW CABIN MODULE FAILURE (ME)
SFSM-FLAP	LOSS OF STRUCTURAL MEMBERS DUE TO BODY FLAP FAILURE
SFSM-FRCS	LOSS OF STRUCTURAL MEMBERS DUE TO FRCS STRUCTURAL FAILURE
SFSM-FWD	LOSS OF STRUCTURAL MEMBERS DUE TO FWD FUSELAGE FAILURE
SFSM-MID	LOSS OF STRUCTURAL MEMBERS DUE TO MID-FUSELAGE FAILURE
SFSM-OMS	LOSS OF STRUCTURAL MEMBERS DUE TO ORBITAL MANEUVERING SYSTEM POD FAILURE
SFSM-PAY	LOSS OF STRUCTURAL MEMBER DUE TO FAILURE INTERNAL TO PAYLOAD BAY
SFSM-PAY-6-1	FAILURE INTERNAL TO PAYLOAD BAY DUE TO FAILURE OF CARGO INTEGRATED HARDWARE (ME)
SFSM-PAY-6-2	FAILURE INTERNAL TO PAYLOAD BAY DUE TO PAYLOAD HARDWARE (ME)
SFSM-PAY-6-3	FAILURE INTERNAL TO PAYLOAD BAY DUE TO ORBITER HARDWARE (ME)
SFSM-TAIL	LOSS OF STRUCTURAL MEMBERS DUE TO TAIL-RUDDER SPEED BREAK FAILURE
SFSM-WINDOW	LOSS OF STRUCTURAL MEMBERS DUE TO WINDOW FAILURE
SFSM-WING	LOSS OF STRUCTURAL MEMBERS DUE TO WING FAILURE

Section B

SSME: (Space Shuttle Main Engine)

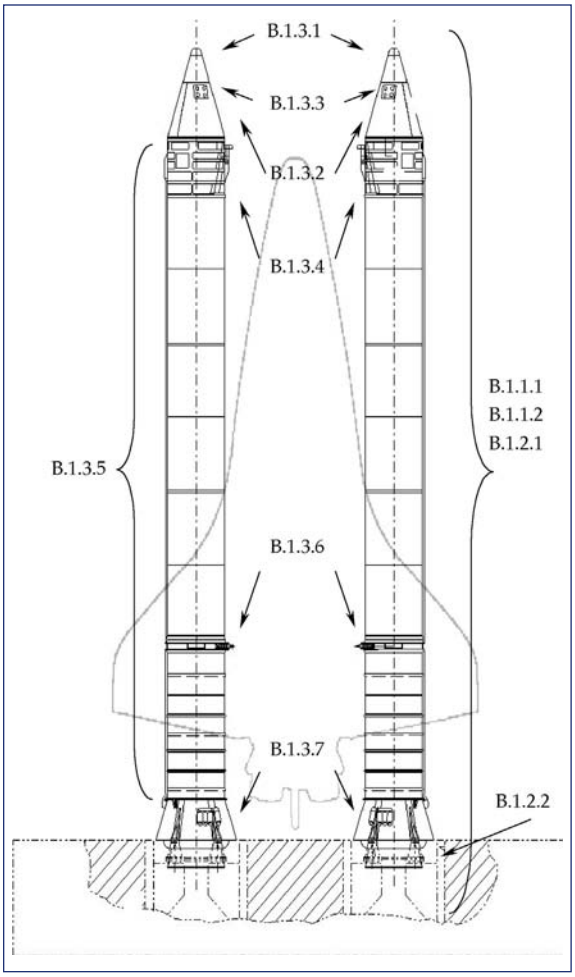


ELEMENT NUMBER	*DESCRIPTION OF FAULT TREE ELEMENT*
SSME-E1.0	SSME Causes Structural Failure of Orbiter
SSME-E1.1	SSME Provides Constituent For Explosion/Combustion During Reentry

ELEMENT NUMBER	*DESCRIPTION OF FAULT TREE ELEMENT*
SSME-E1.1.1	SSME Hydraulic Leak Provides Fuel for Explosion/Combustion
SSME-E1.1.2	Residual Hydrogen or Oxygen Remain in the Engine (i.e. Propellant Dump Anomaly)
SSME-E1.1.3	SSME Electrical System Causes Ignition
SSME-E1.2	SSME Produces Debris Which Damages Orbiter Structure
SSME-E1.2.1	Debris Damages Aft Compartment
SSME-E1.2.2	Debris Damage Occurs External to Aft Compartment
SSME-E1.2.2.1	SSME Exhaust Causes Debris During Launch
SSME-E1.2.2.2	Off-Nominal SSME Operation Causes STS Debris
SSME-E1.2.2.3	SSME Causes Debris Damage on Orbit (i.e. Nozzle Debris Impact)
SSME-E1.3	SSME Imparts Off-Nominal Loads Which Cause Structural Failure of Orbiter
SSME-E1.3.1	Off-Nominal Thrust Vector
SSME-E1.3.2	Off-Nominal Vibrations
SSME-E1.3.3	Off-Nominal Thermal Loads
SSME-E1.3.4	Over-Pressurization of Aft Compartment Due to an SSME Fluid System Leak
SSME-E1.3.5	Off-Nominal Acoustics
SSME-E1.4	Engine Configuration Effects Result in Structural Failure of Orbiter
SSME-E2.0	SSME Causes Failure of Orbiter System
SSME-E2.1	SSME Causes Orbiter Hydraulic System Failure
SSME-E2.1.1	SSME Hydraulic System Leak Causes Failure of Orbiter Hydraulic System
SSME-E2.1.2	SSME Actuators or Hydraulic Line Source of Contamination to Orbiter Hydraulic System
SSME-E2.2	SSME Causes Orbiter Pneumatic System Failure (i.e. SSME Pneumatic System Leak Causes Failure of Orbiter Pneumatic System)
SSME-E2.3	SSME Electrical System Negatively Affects Orbiter Control Capability (e.g. GPCs)
SSME-E2.4	SSME Obstructs Orbiter Control Surfaces
SSME-E2.4.1	Nozzle Debris (TPS or Ablative) Obstructs Aerodynamic Control Surface(s)
SSME-E2.4.2	Nozzle Position Obstructs Movement of Body Flap
SSME-E2.5	SSME Causes Condition that Exceeds Capability of Orbiter Flight Control System
SSME-E2.5.1	Off-Nominal SSME position Disrupts Orbiter Aerodynamics
SSME-E2.5.2	Structural Failure of SSME Component – Orbiter Mass and or CG shift
SSME-E2.6	Block II Engine Configuration Affects Result in Failure of Orbiter System

SECTION C

SRB: (SOLID ROCKET BOOSTERS)



LEGEND

B.1.1.1 Extreme Environments Adversely Affect SRB or SRB/ET Interface
B.1.1.2 Anomalous Loads Adversely Affect SRB or SRB/ET Interfaces
B.1.2.1 Electrical & Instrumentation Subsystem
B.1.2.2 Thrust Vector Control Subsystem
B.1.3.1 Nose Cap Assembly Damage/Malfunction Causes Debris
B.1.3.2 Frustum Assembly Damage/Malfunction Causes Debris
B.1.3.3 Premature Parachute Operation Causes Debris
B.1.3.4 Forward Skirt Assembly Damage/Malfunction Causes Debris
B.1.3.5 Tunnel Cover / Floor Plate Assembly Damage/ Malfunction Causes Debris
B.1.3.6 ETA Ring/Aft Attach Strut Assembly Damage/ Malfunction Causes Debris
B.1.3.7 Aft Skirt Assembly Damage/Malfunction Causes Debris

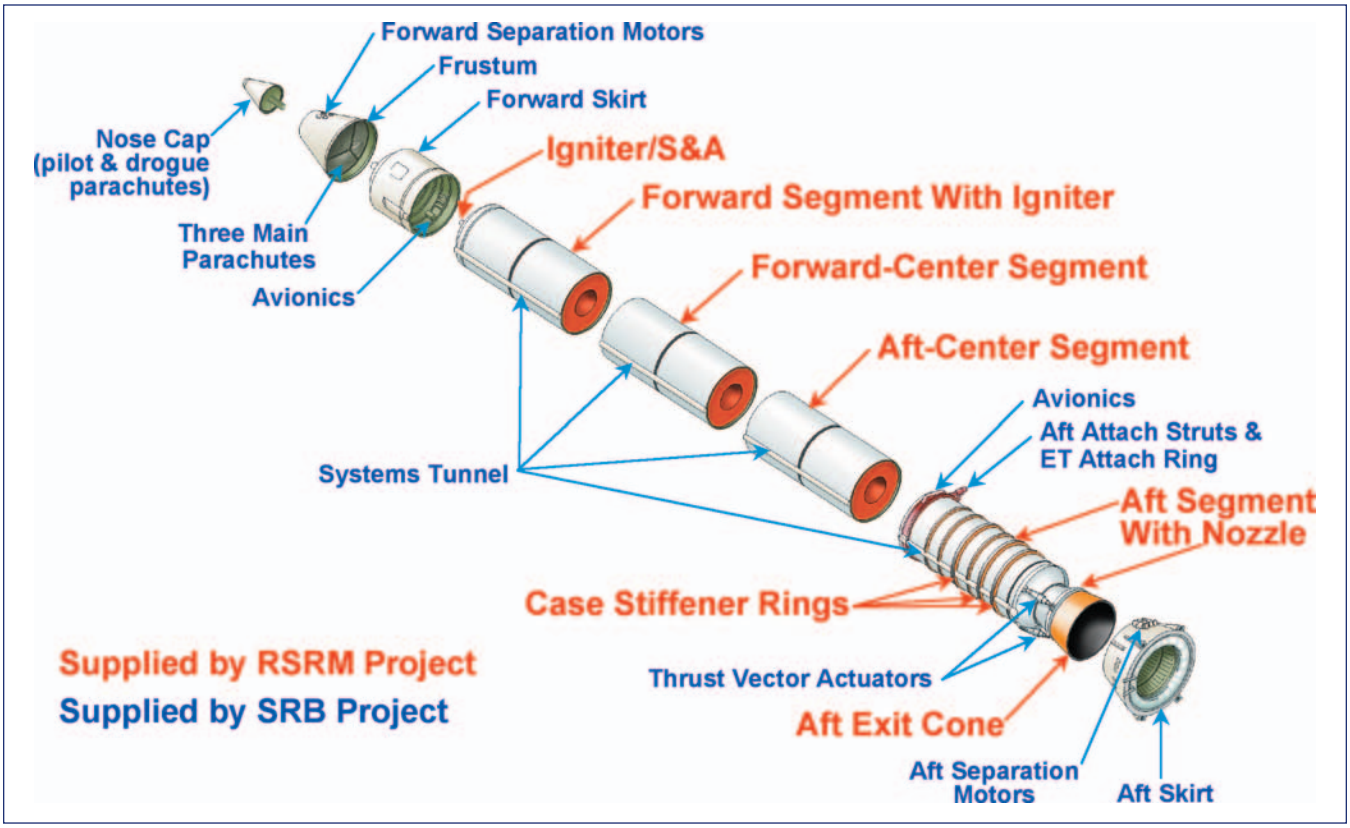
ELEMENT NUMBER	*DESCRIPTION OF FAULT TREE ELEMENT*
B.1.1.1	Extreme Environments Adversely affect SRB or SRB/ET Interface
B.1.1.1.1	Extreme Natural Environments Adversely Affect SRB or SRB/ET Interface
B.1.1.1.2.A	Adverse Effects From Conducted or Radiated Electro Magnetic Interface (EMI)
B.1.1.1.2.B	Adverse Aerothermal Effects During Ascent
B.1.1.1.2.C	Adverse Vibro-Acoustic Effects While on Pad or During Ascent
B.1.1.1.2.D	Adverse Vehicle dynamics Effects While on Pad or During Ascent
B.1.1.1.2.E	Adverse Aerodynamic Effects During Ascent
B.1.1.1.2.F	Improper Venting During Ascent
B.1.1.1.2.G	Pyro Shock While on Pad or During Ascent
B.1.1.2	Anomalous Loads Adversely Affect SRB or SRB/ET Interfaces
B.1.1.2.A	Anomalous Loads Caused by Holddown Stud Hang-up
B.1.1.2.B	Anomalous Loads During Liftoff
B.1.1.2.1	Anomalous Loads During Prelaunch Operations

ELEMENT NUMBER	*DESCRIPTION OF FAULT TREE ELEMENT*
B.1.1.2.1.D	Adverse Loads Induced by SSME Thrust Build up
B.1.1.2.2	Anomalous Loads During Ascent
B.1.1.2.3	Anomalous Loads During Booster Separation
B.1.1.2.3.1.1.1	Premature Ignition (AFT BSM)
B.1.1.2.3.1.1.2	Low/Inadequate Thrust Output for any Two BSMs (AFT BSM)
B.1.1.2.3.1.2.1	Premature Ignition (Forward BSM)
B.1.1.2.3.1.2.2	Low/Inadequate Thrust Output for any Two BSMs (Forward BSM)
B.1.2.1	Anomalous Electrical and Instrumentations Subsystem Performance
B.1.2.2	Anomalous Thrust Vector Control (TVC) Subsystem Performance
B.1.3.2	Frustum Assembly Damage/Malfunction Causes Debris
B.1.3.2.A	Loss of Electrical Cables and Connect Components Causes Debris
B.1.3.2.B	Frustum Structural Failure Causes Debris
B.1.3.2.1	Loss of TPS Causes Debris
B.1.3.2.2	Loss of Frustum Components Causes Debris
B.1.3.2.4.A	Debris from Missing Cover Seal
B.1.3.2.4.3	Debris from Aeroheat Shield Structural Failure
B.1.3.2.4.4	Debris from Aeroheat Shield Failure to Achieve Minimum Opening Angle
B.1.3.2.5	Improper Operation of Pyrotechnic Components Causes Debris
B.1.3.3	Premature Parachute Operation Causes Debris
B.1.3.4	Forward Skirt Assembly Damage/Malfunction Causes Debris
B.1.3.4.A	Forward Skirt Structural Failure Causes Debris
B.1.3.4.B	Loss of Electrical Breakaway Cables and Connector Components (Sep. Plane) Causes Debris
B.1.3.4.1	Loss of TPS Causes Debris
B.1.3.4.1.1	Loss of Forward Separation Area ET Side TPS Causes Debris
B.1.3.4.2	Loss of Forward Skirt Components Causes Debris
B.1.3.4.2.C	Loss of Ordnance Ring Attach Pins and Retainer Clips Causes Debris
B.1.3.4.2.M	Loss of RSS Antennas Causes Debris
B.1.3.4.2.N	Loss of C-Band Antenna Causes Debris
B.1.3.4.3	Improper Operation of Pyrotechnic Components Causes Debris
B.1.3.4.4.1.A	Debris Due to No Separation
B.1.3.4.4.1.B	Debris Due to Premature Separation
B.1.3.4.4.1.1.A	Failure Outside of Fracture Plane Causes Debris
B.1.3.4.4.1.1.B	Recontact Causes Debris
B.1.3.4.4.1.1.1	Material Defects Causes Debris
B.1.3.4.4.1.1.2	Manufacturing Defect Causes Debris
B.1.3.4.4.2	Debris Generation from Range Safety System Crossover (ET side)
B.1.3.5	Tunnel Cover/Floor Plate Assembly Damage/Malfunction Causes Debris

ELEMENT NUMBER	*DESCRIPTION OF FAULT TREE ELEMENT*
B.1.3.5.A	Structural Damage to Tunnel Cover Assembly Causes Debris
B.1.3.5.B	Loss of Electrical Cables and Connector Components Causes Debris
B.1.3.5.C	Improper Operation of Pyrotechnic Components Causes Debris
B.1.3.5.1	Loss of Thermal Protection System (TPS) Causes Debris [Tunnel Cover/Floor Plate Assembly]
B.1.3.5.2	Loss of Tunnel over/Floor Plate Components Causes Debris (SRB/RSRM)
B.1.3.6	ETA Ring/Aft Attach Strut Assembly Damage/Malfunction Causes Debris
B.1.3.6.A	Loss of Electrical Breakaway Cables and Connector Components (Separation Plane)
B.1.3.6.B	External Tank Attach Ring Structural Failure
B.1.3.6.1	Loss of Thermal Protection System (TPS) Causes Debris
B.1.3.6.1.1	Loss of Aft Separation Area ET Side TPS Causes Debris
B.1.3.6.2	Aft Strut Component Failure (ET Strut Half)
B.1.3.6.3	Loss of ETA Ring Components/SRB Strut Half Causes Debris
B.1.3.6.3.G	Loss of Diagonal Strut Restraint Cable Causes Debris
B.1.3.6.4.A	No Separation Causes Debris
B.1.3.6.4.B	Premature Separation Causes Debris
B.1.3.6.4.1.A	Failure Outside Fracture Plane Causes Debris
B.1.3.6.4.1.B	Recontact of the Aft Separation Bolt Halves after Separation Causes Debris
B.1.3.6.4.1.1	Material Defects Causes Debris
B.1.3.6.4.1.2	Manufacturing Defect Causes Debris
B.1.3.6.5	Aft Attach Strut Pyrotechnics Causes Debris
B.1.3.7	Aft Skirt Assembly Damage/Malfunction Causes Debris
B.1.3.7.A	Loss of Electrical Breakaway Cables and Connector Components (Separation Plane)
B.1.3.7.B	Aft Skirt Assembly Structural Failure Causes Debris
B.1.3.7.1	Loss of TPS Causes Debris
B.1.3.7.1.1.A	Loss of Cork with Hypalon Causes Debris
B.1.3.7.1.1.B	Loss of BTA with Hypalon Causes Debris
B.1.3.7.2	Loss of Aft Skirt Components Causes Debris
B.1.3.7.2.B	Loss of Debris Containment Device Causes Debris
B.1.3.7.2.M	Loss of Blast Container Causes Debris
B.1.3.7.2.S	Loss of Thermal Curtains Causes Debris (Fabric)
B.1.3.7.3	Debris from Aft Booster Separation Motor Components
B.1.3.7.4.1	Improper Operation of SRB/MLP Holddown Release
B.1.3.7.4.2	Improper Operation of Booster Separation Motor Ignition Components
B.1.3.7.5	Debris from Thrust Vector Control (TVC)
B.1.3.7.6.A	Loss of Aft Skirt Shoe Hardware Causes Debris (includes shims and ground straps)
B.1.3.7.6.B	Loss of GN2 Purge Line Assembly Causes Debris
B.1.3.7.6.C	Loss of Holddown Hardware Causes Debris (includes stud washer, nut and breaklink nut)

SECTION D

RSRM: (REUSABLE SOLID ROCKET MOTOR)



ELEMENT NUMBER	*DESCRIPTION OF FAULT TREE ELEMENT*
RSRM	Loss of Orbiter During Reentry Due to Anomalous RSRM Behavior
RSRM-M1.0	RSRM Generates Debris/FOD During Ascent
RSRM-M1.1	Thrown/Rebound Debris During Ignition/Lift-off Strikes Other Element
RSRM-M1.1.1	Nozzle Plug
RSRM-M1.1.2	Debris from Non-RSRM Source
RSRM-M1.1.3	RSRM Components
RSRM-M1.1.3.1	RSRM Internal Components
RSRM-M1.1.3.2	RSRM External Components
RSRM-M1.2	Systems Tunnel Floor Plate(s) Departs RSRM
RSRM-M1.3	Joint Protection System Departs RSRM
RSRM-M1.4	Anomalous Loss of Paint from RSRM
RSRM-M1.5	Instrumentation & Associated Hardware Departs RSRM
RSRM-M1.6	Stiffener Ring Insulation Departs RSRM
RSRM-M1.7	Stiffener Rings Depart RSRM
RSRM-M1.8	Ice Forms and Departs RSRM
RSRM-M1.9	Slice Plate Departs RSRM

ELEMENT NUMBER	*DESCRIPTION OF FAULT TREE ELEMENT*
RSRM-M1.10	Failure to Contain Motor Combustion Gases
RSRM-M2.0	RSRM Transfers Anomalous Loads Through Attach Points
RSRM-M2.1	Anomalous Structural Loads
RSRM-M2.1.1	Unsteady (>1 Hz) & Transient
RSRM-M2.1.1.1	RSRM Produces and Anomalous Initial Impulse
RSRM-M2.1.1.1.1	Anomalous Ignition
RSRM-M2.1.1.1.2	Anomalous but Balanced, Rises Rates
RSRM-M2.1.1.1.3	Unbalanced Rise Rates Between the RSRMs
RSRM-M2.1.1.2	RSRM Produces Anomalous Thrust Oscillations
RSRM-M2.1.1.3	Anomalous SRB Separation Due to RSRM
RSRM-M2.1.1.3.1	Anomalous Tail-off
RSRM-M2.1.1.3.2	Anomalous Separation Sequence Cueing Pressure Measurement/Transmission
RSRM-M2.1.1.4	RSRM Nozzle Deflection
RSRM-M2.1.2	Steady
RSRM-M2.1.2.1	RSRM Produces Anomalous, But Balanced Thrust
RSRM-M2.1.2.2	RSRM Produces Anomalous Unbalanced Thrust
RSRM-M2.1.2.3	RSRM Produces Anomalous Pressure Perturbations
RSRM-M2.1.2.4	RSRM Nozzle Deflection
RSRM-M2.2	Anomalous Thermal Loads
RSRM-M3.0	RSRM Generates Anomalous Induced Environments
RSRM-M3.1	Acoustic Anomalies
RSRM-M3.1.1	Excessive Ignition Acoustic Loading
RSRM-M3.1.2	Excessive In-Flight Acoustic Loading
RSRM-M3.2	Thermal Anomalies
RSRM-M3.2.1	RSRM Ignition/Plume Rebound
RSRM-M3.2.2	RSRM Excessive Plume Convective Recirculation
RSRM-M3.2.3	Failure to Contain Motor Combustion Gases

SECTION E

INTEGRATION

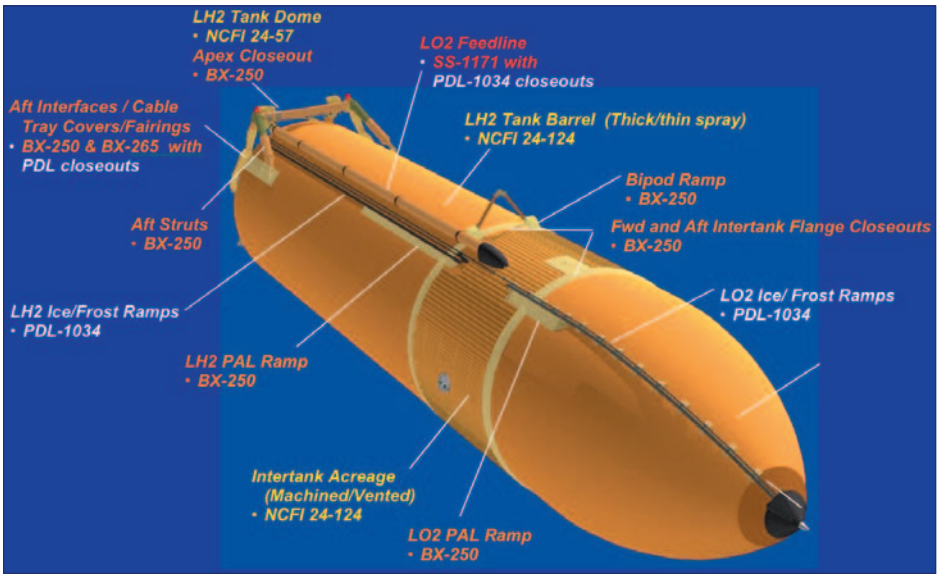
ELEMENT NUMBER	*DESCRIPTION OF FAULT TREE ELEMENT*
B072	POGO Fault
B392	Thermal Environmental Fault/Out of Family
B396	Acoustic Fault/Out of Family
B397	Vibration Fault
G069	Integrated Vehicle Ascent Loads Fault/Out of Family

ELEMENT NUMBER	*DESCRIPTION OF FAULT TREE ELEMENT*
B523	ET Orbiter Umbilical Fire Causes Debris
B751	Airloads
B752	Aero/Plume Heating
B754	Vibration Fault/Out of Family
G386	Payload Induced Fires
B816	T-0 Umbilical Separation Anomaly
B817	Cargo Integration Hardware Induced Fires
B819	HDP Separation Anomaly
B820	GUCP/ET LH2 Vent Arm Separation Anomaly
G821	OLF/MDD Operation Load Fault/Out of Family
G824	OPF Operations Fault/Out of Family
B873	SRB Setdown Anomaly
B874	SRB Stacking Anomaly
B876	ET Mate Anomaly
B877	Orbiter Mate Anomaly
B878	Crawler Transporter Anomaly
B879	Payload Installation Anomaly
B880	ET Cryo Load Anomaly
B137	Ground Handling Non Integrated
G138	Crawler Transporter Loads Fault/Out of Family
G139	On Pad Loads Fault/Out of Family
G140	Integrated VAB Operations Loads Fault/Out of Family

SECTION F

ET: (EXTERNAL TANK)

Elements listed as "open due to lower element" refer to Fault Tree Elements contained in Appendix D.4.



ELEMENT NUMBER	*DESCRIPTION OF FAULT TREE ELEMENT*
1.1.1.1 Open due to lower element	NCFI 24-124
1.1.1.1.1 Open due to lower element	LO2 Tank Acreage
1.1.1.1.1.1	Foam Application-LO2 Tank Ogive & Barrel
1.1.1.1.1.1.1	Debris Due to Design Resulting in a Cohesive, Shear, Delamination, or Crack Failure of the TPS
1.1.1.1.1.1.1.2 Open due to lower element	Debris Due to Vendor Manufacturing/Processing Resulting in a Cohesive, Shear, Delamination, or Crack Failure of the TPS
1.1.1.1.1.1.2.1	NCFI 24-124 Raw Material
1.1.1.1.1.1.2.2	Cleaning Raw Material
1.1.1.1.1.1.2.3	Primer Raw Material
1.1.1.1.1.1.2.4	Ducommun/MAF Material Processing
1.1.1.1.1.1.3 Open due to lower element	Debris Due to Anomalous MAF Processing Resulting in a Cohesive, Shear, Delamination, or Crack Failure of the TPS
1.1.1.1.1.1.3.1	Debris Due to MAF Process Training
1.1.1.1.1.1.3.2	Debris Due to Manufacturing Process Plan
1.1.1.1.1.1.3.3	Debris Due to MAF NCFI 24-124 Material Processing
1.1.1.1.1.1.3.4	Debris Due to MAF Cleaning Material Processing
1.1.1.1.1.1.3.5	Debris Due to MAF Primer Material Processing
1.1.1.1.1.1.3.6	Debris Due to MAF Weld Processing
1.1.1.1.1.1.3.7	Debris Due to External Elements During MAF Processing
1.1.1.1.1.1.3.8	Debris Due to Incipient Weld Leak
1.1.1.2 Open due to lower element	Intertank Acreage
1.1.1.2.1 Open due to lower element	Foam Application-Intertank, Outside Surface
1.1.1.1.2.1.1	Debris Due to Design Resulting in a Cohesive, Shear, Delamination, or Crack Failure of the TPS
1.1.1.1.2.1.2 Open due to lower element	Debris Due to Vendor Manufacturing/Processing Resulting in a Cohesive, Shear, Delamination, or Crack Failure of the TPS
1.1.1.1.2.1.2.1	NCFI 24-124 Raw Material
1.1.1.1.2.1.2.2	DPTU Adhesive Raw Material
1.1.1.1.2.1.2.3	LearJet Cleaning Raw Material
1.1.1.1.2.1.2.4	LearJet Primer Raw Material
1.1.1.1.2.1.2.5	Debris Due to LearJet Manufacturing Process Plan
1.1.1.1.2.1.2.6	Debris Due to LearJet Cleaning Material Processing
1.1.1.1.2.1.2.7	Debris Due to LearJet Primer Material Processing

ELEMENT NUMBER	*DESCRIPTION OF FAULT TREE ELEMENT*
1.1.1.1.2.1.3 Open due to lower element	Debris Due to Anomalous MAF Processing Resulting in a Cohesive, Shear, Delamination, or Crack Failure of the TPS
1.1.1.1.2.1.3.1	Debris Due to MAF Process Training
1.1.1.1.2.1.3.2	Debris Due to Manufacturing Process Plan
1.1.1.1.2.1.3.3	Debris Due to MAF NCFI 24-124 Material Processing
1.1.1.1.2.1.3.4	Debris Due to MAF DPTU Adhesive Material Processing
1.1.1.1.2.1.3.5	Debris Due to External Events During MAF Processing
1.1.1.1.2.1.3.6	Debris Due to Mechanical Assembly Anomaly
1.1.1.1.2.2 Open due to lower element	I/T Foam Machining, Cell "L", +Z Stringer Panels and Thrust Panels
1.1.1.1.2.2.1	Debris Due to Design Resulting in a Cohesive, Shear, Delamination, or Crack Failure of the TPS (Ref. 1.1.1.1.2.1.1)
1.1.1.1.2.2.2 Open due to lower element	Debris Due to Anomalous MAF Processing Resulting in a Cohesive, Shear, Delamination, or Crack Failure of the TPS
1.1.1.1.2.2.2.1	Debris Due to MAF Process Training
1.1.1.1.2.2.2.2	Debris Due to Manufacturing Process Plan
1.1.1.1.2.2.2.3	Debris Due to External Events During MAF Processing
1.1.1.1.2.2.2.4	Debris Due to Mechanical Assembly Anomaly
1.1.1.1.2.3 Open due to lower element	Intertank Foam Venting
1.1.1.1.2.3.1	Debris Due to Design Resulting in a Cohesive, Shear, Delamination, or Crack Failure of the TPS (Ref. 1.1.1.1.2.1.1)
1.1.1.1.2.3.2 Open due to lower element	Debris Due to Anomalous MAF Processing Resulting in a Cohesive, Shear, Delamination, or Crack Failure of the TPS
1.1.1.1.2.3.2.1	Debris Due to MAF Process Training
1.1.1.1.2.3.2.2	Debris Due to Manufacturing Process Plan
1.1.1.1.2.3.2.3	Debris Due to External Events During MAF Processing
1.1.1.1.2.3.2.4	Debris Due to Mechanical Assembly Anomaly
1.1.1.1.3 Open due to lower element	LH2 Tank Acreage
1.1.1.1.3.1 Open due to lower element	Foam Spray-LH2 Barrel
1.1.1.1.3.1.1	Debris Due to Design Resulting in a Cohesive, Shear, Delamination, or Crack Failure of the TPS
1.1.1.1.3.1.2 Open due to lower element	Debris Due to Vendor Manufacturing/Processing Resulting in a Cohesive, Shear, Delamination, or Crack Failure of the TPS
1.1.1.1.3.1.2.1	NCFI 24-124 Raw Material
1.1.1.1.3.1.2.2	Cleaning Raw Material
1.1.1.1.3.1.2.3	Primer Raw Material
1.1.1.1.3.1.2.4	Ducommun/Grumman/Reynolds Material Processing

ELEMENT NUMBER	*DESCRIPTION OF FAULT TREE ELEMENT*
1.1.1.1.3.1.3 Open due to lower element	Debris Due to Anomalous MAF Processing Resulting in a Cohesive, Shear, Delamination, or Crack Failure of the TPS
1.1.1.1.3.1.3.1	Debris Due to MAF Process Training
1.1.1.1.3.1.3.2	Debris Due to Manufacturing Process Plan
1.1.1.1.3.1.3.3	Debris Due to MAF NCFI 24-124 Material Processing
1.1.1.1.3.1.3.4	Debris Due to MAF Cleaning Material Processing
1.1.1.1.3.1.3.5	Debris Due to MAF Primer Material Processing
1.1.1.1.3.1.3.6	Debris Due to MAF Weld Processing
1.1.1.1.3.1.3.7	Debris Due to External Events During MAF Processing
1.1.1.1.3.1.3.8	Debris Due to Incipient Weld Leak
1.1.1.2	NCFI 24-57
1.1.1.3 Open due to lower element	PDL-1034
1.1.1.3.1 Open due to lower element	Bipod
1.1.1.3.2 Open due to lower element	LH2 & I/T Splice
1.1.1.3.3 Open due to lower element	LO2 & I/T Splice, P/L Bracket 861, & Aero Vents
1.1.1.3.3.1 Open due to lower element	LO2 Tank to I/T Splice, P/L Bracket Sta. 861 Aero Vents
1.1.1.3.3.1.1	Debris Due to Design Resulting in a Cohesive, Shear, Delamination, or Crack Failure of the TPS
1.1.1.3.3.1.2	Debris Due to Vendor Manufacturing/Processing Resulting in a Cohesive, Shear, Delamination, or Crack Failure of the TPS
1.1.1.3.3.1.3 Open due to lower element	Debris Due to Anomalous MAF Processing Resulting in a Cohesive, Shear, Delamination, or Crack Failure of the TPS
1.1.1.3.3.1.3.1	Debris Due to MAF Process Training
1.1.1.3.3.1.3.2	Debris Due to Manufacturing Process Plan
1.1.1.3.3.1.3.4	Debris Due to MAF DPTU Adhesive Material Processing
1.1.1.3.3.1.3.5	Debris Due to External Events During MAF Processing
1.1.1.3.3.1.3.6	Debris Due to Mechanical Assembly Anomaly
1.1.1.3.4 Open due to lower element	LO2 P/L & C/T Brackets
1.1.1.3.4.1 Open due to lower element	TPS Application-LO2 Tank Ice Frost Ramps-Cell "G" & "H"
1.1.1.3.4.1.1	Debris Due to Design Resulting in a Cohesive, Shear, Delamination, or Crack Failure of the TPS
1.1.1.3.4.1.2	Debris Due to Vendor Manufacturing/Processing Resulting in a Cohesive, Shear, Delamination, or Crack Failure of the TPS
1.1.1.3.4.1.3 Open due to lower element	Debris Due to Anomalous MAF Processing Resulting in a Cohesive, Shear, Delamination, or Crack Failure of the TPS
1.1.1.3.4.1.3.1	Debris Due to MAF Process Training

ELEMENT NUMBER	*DESCRIPTION OF FAULT TREE ELEMENT*
1.1.1.3.4.1.3.2	Debris Due to Manufacturing Process Plan
1.1.1.3.4.1.3.4	Debris Due to MAF DPTU Adhesive Material Processing
1.1.1.3.4.1.3.5	Debris Due to External Events During MAF Processing
1.1.1.3.4.1.3.6	Debris Due to Mechanical Assembly Anomaly
1.1.1.3.4.2 Open due to lower element	TPS Closeout-ET Complete, Bldg 420 (Xt371 CO)
1.1.1.3.6 Open due to lower element	I/T Wedges
1.1.1.3.6.1 Open due to lower element	Foam Wedge Application- I/T Position #3
1.1.1.3.6.1.1	Debris Due to Design Resulting in a Cohesive, Shear, Delamination, or Crack Failure of the TPS
1.1.1.3.6.1.2	Debris Due to Vendor Manufacturing/Processing Resulting in a Cohesive, Shear, Delamination, or Crack Failure of the TPS
1.1.1.3.6.1.3 Open due to lower element	Debris Due to Anomalous MAF Processing Resulting in a Cohesive, Shear, Delamination, or Crack Failure of the TPS
1.1.1.3.6.1.3.1	Debris Due to MAF Process Training
1.1.1.3.6.1.3.2	Debris Due to Manufacturing Process Plan
1.1.1.3.6.1.3.4	Debris Due to External Events During MAF Processing
1.1.1.3.6.1.3.5	Debris Due to Mechanical Assembly Anomaly
1.1.1.3.7 Open due to lower element	I/T P/L & C/T Brackets & Fairings
1.1.1.3.7.1 Open due to lower element	Support Bracket-GO2 P/L & C/T, I/T, Foam Application
1.1.1.3.7.1.1	Debris Due to Design Resulting in a Cohesive, Shear, Delamination, or Crack Failure of the TPS
1.1.1.3.7.1.2	Debris Due to Vendor Manufacturing/Processing Resulting in a Cohesive, Shear, Delamination, or Crack Failure of the TPS
1.1.1.3.7.1.3 Open due to lower element	Debris Due to Anomalous MAF Processing Resulting in a Cohesive, Shear, Delamination, or Crack Failure of the TPS
1.1.1.3.7.1.3.1	Debris Due to MAF Process Training
1.1.1.3.7.1.3.2	Debris Due to Manufacturing Process Plan
1.1.1.3.7.1.3.4	Debris Due to MAF DPTU Adhesive Material Processing
1.1.1.3.7.1.3.5	Debris Due to External Events During MAF Processing
1.1.1.3.7.1.3.6	Debris Due to Mechanical Assembly Anomaly
1.1.1.3.7.2 Open due to lower element	Foam CO- I/T Fairings, RSS Antennas & Xt 1082.8 P/L & C/T Support
1.1.1.3.7.2.1	Debris Due to Design Resulting in a Cohesive, Shear, Delamination, or Crack Failure of the TPS
1.1.1.3.7.2.2	Debris Due to Vendor Manufacturing/Processing Resulting in a Cohesive, Shear, Delamination, or Crack Failure of the TPS
1.1.1.3.7.2.3 Open due to lower element	Debris Due to Anomalous MAF Processing Resulting in a Cohesive, Shear, Delamination, or Crack Failure of the TPS
1.1.1.3.7.2.3.1	Debris Due to MAF Process Training

ELEMENT NUMBER	*DESCRIPTION OF FAULT TREE ELEMENT*
1.1.1.3.7.2.3.2	Debris Due to Manufacturing Process Plan
1.1.1.3.7.2.3.4	Debris Due to MAF DPTU Adhesive Material Processing
1.1.1.3.7.2.3.5	Debris Due to External Events During MAF Processing
1.1.1.3.7.2.3.6	Debris Due to Mechanical Assembly Anomaly
1.1.1.3.7.3 Open due to lower element	Foam Closeout-Intertank Press Line & Cable Tray Support Brackets
1.1.1.3.7.3.1	Debris Due to Design Resulting in a Cohesive, Shear, Delamination, or Crack Failure of the TPS
1.1.1.3.7.3.2	Debris Due to Vendor Manufacturing/Processing Resulting in a Cohesive, Shear, Delamination, or Crack Failure of the TPS
1.1.1.3.7.3.3 Open due to lower element	Debris Due to Anomalous MAF Processing Resulting in a Cohesive, Shear, Delamination, or Crack Failure of the TPS
1.1.1.3.7.3.3.1	Debris Due to MAF Process Training
1.1.1.3.7.3.3.2	Debris Due to Manufacturing Process Plan
1.1.1.3.7.3.3.4	Debris Due to MAF DPTU Adhesive Material Processing
1.1.1.3.7.3.3.5	Debris Due to External Events During MAF Processing
1.1.1.3.7.3.3.6	Debris Due to Mechanical Assembly Anomaly
1.1.1.3.8 Open due to lower element	LO2 Feed Line & Supports (External)
1.1.1.3.8.1 Open due to lower element	TPS Closeout-Final Assy Feedline Yokes & Base Fittings
1.1.1.3.8.1.1	Debris Due to Design Resulting in a Cohesive, Shear, Delamination, or Crack Failure of the TPS
1.1.1.3.8.1.2	Debris Due to Vendor Manufacturing/Processing Resulting in a Cohesive, Shear, Delamination, or Crack Failure of the TPS
1.1.1.3.8.1.3 Open due to lower element	Debris Due to Anomalous MAF Processing Resulting in a Cohesive, Shear, Delamination, or Crack Failure of the TPS
1.1.1.3.8.1.3.1	Debris Due to MAF Process Training
1.1.1.3.8.1.3.2	Debris Due to Manufacturing Process Plan
1.1.1.3.8.1.3.4	Debris Due to MAF DPTU Adhesive Material Processing
1.1.1.3.8.1.3.5	Debris Due to External Events During MAF Processing
1.1.1.3.8.1.3.6	Debris Due to Mechanical Assembly Anomaly
1.1.1.3.8.2 Open due to lower element	CO-LO2 F/L Flanges & Elbow Tie, Xt1115-2053 & LH2 F/L Base CO
1.1.1.3.8.2.1	Debris Due to Design Resulting in a Cohesive, Shear, Delamination, or Crack Failure of the TPS
1.1.1.3.8.2.2	Debris Due to Vendor Manufacturing/Processing Resulting in a Cohesive, Shear, Delamination, or Crack Failure of the TPS
1.1.1.3.8.2.3 Open due to lower element	Debris Due to Anomalous MAF Processing Resulting in a Cohesive, Shear, Delamination, or Crack Failure of the TPS
1.1.1.3.8.2.3.1	Debris Due to MAF Process Training
1.1.1.3.8.2.3.2	Debris Due to Manufacturing Process Plan

ELEMENT NUMBER	*DESCRIPTION OF FAULT TREE ELEMENT*
1.1.1.3.8.2.3.4	Debris Due to MAF DPTU Adhesive Material Processing
1.1.1.3.8.2.3.5	Debris Due to External Events During MAF Processing
1.1.1.3.8.2.3.6	Debris Due to Mechanical Assembly Anomaly
1.1.1.3.8.3 Open due to lower element	Feedline-LO2 Aluminum Straight Section Foam Application
1.1.1.3.8.3.1	Debris Due to Design Resulting in a Cohesive, Shear, Delamination, or Crack Failure of the TPS
1.1.1.3.8.3.2	Debris Due to Vendor Manufacturing/Processing Resulting in a Cohesive, Shear, Delamination, or Crack Failure of the TPS
1.1.1.3.8.3.3 Open due to lower element	Debris Due to Anomalous MAF Processing Resulting in a Cohesive, Shear, Delamination, or Crack Failure of the TPS
1.1.1.3.8.3.3.1	Debris Due to MAF Process Training
1.1.1.3.8.3.3.4	Debris Due to External Events During MAF Processing
1.1.1.3.8.3.3.5	Debris Due to Mechanical Assembly Anomaly
	Strut, LO2 Feedline, Foam Application
1.1.1.3.8.4.1	Debris Due to Design Resulting in a Cohesive, Shear, Delamination, or Crack Failure of the TPS (Ref. 1.1.1.3.8.1.1)
1.1.1.3.8.4.2	Debris Due to Vendor Manufacturing/Processing Resulting in a Cohesive, Shear, Delamination, or Crack Failure of the TPS
1.1.1.3.8.4.3 Open due to lower element	Debris Due to Anomalous MAF Processing Resulting in a Cohesive, Shear, Delamination, or Crack Failure of the TPS
1.1.1.3.8.4.3.1	Debris Due to MAF Process Training
1.1.1.3.8.4.3.2	Debris Due to Manufacturing Process Plan
1.1.1.3.8.4.3.4	Debris Due to External Events During MAF Processing
1.1.1.3.8.4.3.5	Debris Due to Mechanical Assembly Anomaly
1.1.1.3.8.5	Foam CO-Final Assembly, LO2 & LH2 F/L Inboard Support To Xbeam
1.1.1.3.8.6	Foam Closeout-Cell "C", LO2 Feedline Support Sta 1623.8, 1871.0, And 1973.5, LH2 Tank
1.1.1.3.9 Open due to lower element	LO2 PAL Ramp
1.1.1.3.10	Vent Lines
1.1.1.3.11	Aft Feed Line & Supports (External)
1.1.1.3.12	LH2 PAL Ramp
1.1.1.3.13	LH2 P/L & C/T Brackets & Fairings
1.1.1.3.14	LH2 Barrel
1.1.1.3.15	Aft I/F Hardware & Closeouts
1.1.1.3.16	Aft Fairings
1.1.1.3.17	SRB PAL Ramps

ELEMENT NUMBER	*DESCRIPTION OF FAULT TREE ELEMENT*
1.1.1.3.18	LH2 Aft Dome
1.1.1.3.19	KSC TPS 3rd Hardpoint
1.1.1.3.20	Nose Cone Closeout (Internal)
1.1.1.3.21	TPS Closeout-ET Complete, Bldg 420 (I/T CO GH2 VV Sensor Port)
1.1.1.4 Open due to lower element	BX-250
1.1.1.4.1 Open due to lower element	Bipod
1.1.1.4.1.1 Open due to lower element	TPS Closeout-Final Assembly, Forward Bipod Fittings
1.1.1.4.1.1.1 Open due to lower element	Debris Due to Design Resulting in a Cohesive, Shear, Delamination, or Crack Failure of the TPS
1.1.1.4.1.1.1.2	Inadequate Design Implementation
1.1.1.4.1.1.1.3	Inadequate Design Requirements (Loads & Environments)
1.1.1.4.1.1.2	Debris Due to Vendor Manufacturing/Processing Resulting in a Cohesive, Shear, Delamination, or Crack Failure of the TPS
1.1.1.4.1.1.3 Open due to lower element	Debris Due to Anomalous MAF Processing Resulting in a Cohesive, Shear, Delamination, or Crack Failure of the TPS
1.1.1.4.1.1.3.1 Open due to lower element	Debris Due to MAF Process Training
1.1.1.4.1.1.3.1.2	Uncertified Operator
1.1.1.4.1.1.3.2 Open due to lower element	Debris Due to Manufacturing Process Plan
1.1.1.4.1.1.3.3	Debris Due to Operator Not Following Manufacturing Process Plan
1.1.1.4.1.1.3.3 Open due to lower element	Debris Due to MAF BX-250 Material Processing
1.1.1.4.1.1.3.3.1	Shelf Life Issue
1.1.1.4.1.1.3.3.3	Contamination During Processing
1.1.1.4.1.1.3.3.4	Improper Surface Preparation
1.1.1.4.1.1.3.3.7	Improperly Performed Acceptance Testing
1.1.1.4.1.1.3.3.8	Inadequate Resolution of Identified Anomaly
1.1.1.4.1.1.3.4	Debris Due to MAF DPTU Adhesive Material
1.1.1.4.1.1.3.5	Debris Due to External Events During MAF Processing
1.1.1.4.1.1.3.6	Debris Due to Mechanical Assembly Anomaly
1.1.1.4.2 Open due to lower element	LH2 & I/T Splice
1.1.1.4.2.1 Open due to lower element	TPS CO-I/T To LH2 Tank, Cell "A" Stack & LH2 Aft Dome Apex
1.1.1.4.2.1.1 Open due to lower element	Debris Due to Design Resulting in a Cohesive, Shear, Delamination, or Crack Failure of the TPS
1.1.1.4.2.1.1.2	Inadequate Design Implementation

ELEMENT NUMBER	*DESCRIPTION OF FAULT TREE ELEMENT*
1.1.1.4.2.1.1.3	Inadequate Design Requirements (Loads & Environments)
1.1.1.4.2.1.2	Debris Due to Vendor Manufacturing/Processing Resulting in a Cohesive, Shear, Delamination, or Crack Failure of the TPS
1.1.1.4.2.1.2.1	BX-250 Raw Material
1.1.1.4.2.1.2.2	DPTU Adhesive Raw Material
1.1.1.4.2.1.2.3	26L26 Bolt
1.1.1.4.2.1.2.4	21L1 Washer
1.1.1.4.2.1.2.5	33L19 Nut
1.1.1.4.2.1.2.6	Undetected Anomaly
1.1.1.4.2.1.3 Open due to lower element	Debris Due to Anomalous MAF Processing Resulting in a Cohesive, Shear, Delamination, or Crack Failure of the TPS
1.1.1.4.2.1.3.1 Open due to lower element	Debris Due to MAF Process Training
1.1.1.4.2.1.3.1.2	Uncertified Operator
1.1.1.4.2.1.3.2	Debris Due to Manufacturing Process Plan
1.1.1.4.2.1.3.2.1	Debris Due to Inadequate Manufacturing Process Plan
1.1.1.4.2.1.3.2.2	Debris Due to Operator Not Following Manufacturing Process Plan
1.1.1.4.2.1.3.3 Open due to lower element	Debris Due to MAF BX-250 Material Processing
1.1.1.4.2.1.3.3.1	Shelf Life Issue
1.1.1.4.2.1.3.3.3	Contamination During Processing
1.1.1.4.2.1.3.3.4	Improper Surface Preparation
1.1.1.4.2.1.3.3.	Improperly Performed Acceptance Testing
1.1.1.4.2.1.3.3.8	Inadequate Resolution of Identified Anomaly
1.1.1.4.2.1.3.4	Debris Due to MAF DPTU Adhesive Material Processing
1.1.1.4.2.1.3.4.1	Shelf Life Issue
1.1.1.4.2.1.3.4.2	Improper Storage
1.1.1.4.2.1.3.4.3	Contamination During Processing
1.1.1.4.2.1.3.4.4	Improper Surface Preparation
1.1.1.4.2.1.3.4.5	Improper Application Process
1.1.1.4.2.1.3.4.6	Inadequately Defined Acceptance Testing
1.1.1.4.2.1.3.4.7	Improperly Performed Acceptance Testing
1.1.1.4.2.1.3.4.8	Inadequate Resolution of Identified Anomaly

ELEMENT NUMBER	*DESCRIPTION OF FAULT TREE ELEMENT*
1.1.1.4.2.1.3.5	Debris Due to MAF Bolt Installation Processing
1.1.1.4.2.1.3.6	Debris Due to External Events During MAF Processing
1.1.1.4.2.1.3.7	Debris Due to Mechanical Assembly Anomaly
1.1.1.4.3 Open due to lower element	LO2 & IT Splice, P/L Brkt 861, & Aero Vents
1.1.1.4.3.1 Open due to lower element	Foam appl.-LO2 Tank to I/T Splice, P/L Brkt Sta. 861 aero Vents
1.1.1.4.3.1.1	Debris Due to Design Resulting in a Cohesive, Shear, Delamination, or Crack Failure of the TPS
1.1.1.4.3.1.1.1	Inadequate Design Methodology
1.1.1.4.3.1.1.2	Inadequate Design Implementation
1.1.1.4.3.1.1.2.1	Incorrect Materials Identified
1.1.1.4.3.1.1.2.2	Incorrect Processes Identified
1.1.1.4.3.1.1.2.3	Incorrect Configuration/Dimensions Identified
1.1.1.4.3.1.1.2.4	Incorrect ET Effectivity Identified
1.1.1.4.3.1.1.3	Inadequate Design Requirements (Loads & Environments)
1.1.1.4.3.1.2	Debris Due to Vendor Manufacturing/Processing Resulting in a Cohesive, Shear, Delamination, or Crack Failure of the TPS
1.1.1.4.3.1.2.1	BX-250 Raw Material
1.1.1.4.3.1.2.1.1	Incorrect Material
1.1.1.4.3.1.2.1.2	Shelf Life Issue
1.1.1.4.3.1.2.1.3	Improper Storage
1.1.1.4.3.1.2.1.4	Contamination During Processing
1.1.1.4.3.1.2.1.5	Improper Shipping
1.1.1.4.3.1.2.1.6	Inadequate Resolution of Identified Anomaly
1.1.1.4.3.1.2.2	DPTU Adhesive Raw Material
1.1.1.4.3.1.2.3	26L26 Bolt
1.1.1.4.3.1.2.4	21L1 Washer
1.1.1.4.3.1.2.5	33L19 Nut
1.1.1.4.3.1.2.6	Undetected Anomaly
1.1.1.4.3.1.3 Open due to lower element	Debris Due to Anomalous MAF Processing Resulting in a Cohesive, Shear, Delamination, or Crack Failure of the TPS
1.1.1.4.3.1.3.1 Open due to lower element	Debris Due to MAF Process Training
1.1.1.4.3.1.3.1.2	Uncertified Operator

ELEMENT NUMBER	*DESCRIPTION OF FAULT TREE ELEMENT*
1.1.1.4.3.1.3.2	Debris Due to Manufacturing Process Plan
1.1.1.4.3.1.3.2.1	Debris Due to Inadequate Manufacturing Process Plan
1.1.1.4.3.1.3.2.2	Debris Due to Operator Not Following Manufacturing Process Plan
1.1.1.4.3.1.3.3 Open due to lower element	Debris Due to MAF BX-250 Material Processing
1.1.1.4.3.1.3.3.1	Shelf Life Issue
1.1.1.4.3.1.3.3.3	Contamination During Processing
1.1.1.4.3.1.3.3.4	Improper Surface Preparation
1.1.1.4.3.1.3.3.6	Inadequately Defined Acceptance Testing
1.1.1.4.3.1.3.3.7	Improperly Performed Acceptance Testing
1.1.1.4.3.1.3.3.8	Inadequate Resolution of Identified Anomaly
1.1.1.4.3.1.3.4	Debris Due to MAF DPTU Adhesive Material Processing
1.1.1.4.3.1.3.4.1	Shelf Life Issue
1.1.1.4.3.1.3.4.2	Improper Storage
1.1.1.4.3.1.3.4.3	Contamination During Processing
1.1.1.4.3.1.3.4.4	Improper Surface Preparation
1.1.1.4.3.1.3.4.5	Improper Application Process
1.1.1.4.3.1.3.4.6	Inadequately Defined Acceptance Testing
1.1.1.4.3.1.3.4.7	Improperly Performed Acceptance Testing
1.1.1.4.3.1.3.4.8	Inadequate Resolution of Identified Anomaly
1.1.1.4.3.1.3.5	Debris Due to MAF Bolt Installation Processing (80911100000)
1.1.1.4.3.1.3.6	Debris Due to External Events During MAF Processing
1.1.1.4.3.1.3.7	Debris Due to Mechanical Assembly Anomaly
1.1.1.4.4 Open due to lower element	I/T Wedges
1.1.1.4.4.1 Open due to lower element	Foam Wedge Appl- I/T Position #3
1.1.1.4.4.1.1	Debris Due to Design Resulting in a Cohesive, Shear, Delamination, or Crack Failure of the TPS
1.1.1.4.4.1.1.1	Inadequate Design Methodology
1.1.1.4.4.1.1.2	Inadequate Design Implementation
1.1.1.4.4.1.1.2.1	Incorrect Materials Identified
1.1.1.4.4.1.1.2.2	Incorrect Processes Identified

ELEMENT NUMBER	*DESCRIPTION OF FAULT TREE ELEMENT*
1.1.1.4.4.1.1.2.3	Incorrect Configuration/Dimensions Identified
1.1.1.4.4.1.1.2.4	Incorrect ET Effectivity Identified
1.1.1.4.4.1.1.3	Inadequate Design Requirements (Loads & Environments)
1.1.1.4.4.1.2	Debris Due to Vendor Manufacturing/Processing Resulting in a Cohesive, Shear, Delamination, or Crack Failure of the TPS
1.1.1.4.4.1.2.1	BX-250 Raw Material
1.1.1.4.4.1.2.1.1	Incorrect Material
1.1.1.4.4.1.2.1.2	Shelf Life Issue
1.1.1.4.4.1.2.1.3	Improper Storage
1.1.1.4.4.1.2.1.4	Contamination During Processing
1.1.1.4.4.1.2.1.5	Improper Shipping
1.1.1.4.4.1.2.1.6	Inadequate Resolution of Identified Anomaly
1.1.1.4.4.1.2.2	Undetected Anomaly
1.1.1.4.4.1.3 Open due to lower element	Debris Due to Anomalous MAF Processing Resulting in a Cohesive, Shear, Delamination, or Crack Failure of the TPS
1.1.1.4.4.1.3.1	Debris Due to MAF Process Training
1.1.1.4.4.1.3.1.1	Inadequately Trained Operator
1.1.1.4.4.1.3.1.2	Uncertified Operator
1.1.1.4.4.1.3.2	Debris Due to Manufacturing Process Plan
1.1.1.4.4.1.3.2.1	Debris Due to Inadequate Manufacturing Process Plan
1.1.1.4.4.1.3.2.2	Debris Due to Operator Not Following Manufacturing Process Plan
1.1.1.4.4.1.3.3 Open due to lower element	Debris Due to MAF BX-250 Material Processing
1.1.1.4.4.1.3.3.1	Shelf Life Issue
1.1.1.4.4.1.3.3.3	Contamination During Processing
1.1.1.4.4.1.3.3.4	Improper Surface Preparation
1.1.1.4.4.1.3.3.6	Inadequately Defined Acceptance Testing
1.1.1.4.4.1.3.3.7	Improperly Performed Acceptance Testing
1.1.1.4.4.1.3.3.8	Inadequate Resolution of Identified Anomaly
1.1.1.4.4.1.3.4	Debris Due to External Events During MAF Processing
1.1.1.4.4.1.3.5	Debris Due to Mechanical Assembly Anomaly
1.1.1.4.5 Open due to lower element	LO2 Feed Line Supports (External)

ELEMENT NUMBER	*DESCRIPTION OF FAULT TREE ELEMENT*
1.1.1.4.5.1 Open due to lower element	TPS Closeout-Final Assy Feedline Yokes & Base Fittings
1.1.1.4.5.1.1	Debris Due to Design Resulting in a Cohesive, Shear, Delamination, or Crack Failure of the TPS
1.1.1.4.5.1.2	Debris Due to Vendor Manufacturing/Processing Resulting in a Cohesive, Shear, Delamination, or Crack Failure of the TPS
1.1.1.4.5.1.2.1	BX-250 Raw Material
1.1.1.4.5.1.2.1.1	Incorrect Material
1.1.1.4.5.1.2.1.2	Shelf Life Issue
1.1.1.4.5.1.2.1.3	Improper Storage
1.1.1.4.5.1.2.1.4	Contamination During Processing
1.1.1.4.5.1.2.1.5	Improper Shipping
1.1.1.4.5.1.2.1.6	Inadequate Resolution of Identified Anomaly
1.1.1.4.5.1.2.2	DPTU Adhesive Raw Material
1.1.1.4.5.1.2.3	Undetected Anomaly
1.1.1.4.5.1.3 Open due to lower element	Debris Due to Anomalous MAF Processing Resulting in a Cohesive, Shear, Delamination, or Crack Failure of the TPS
1.1.1.4.5.1.3.1	Debris Due to MAF Process Training
1.1.1.4.5.1.3.1.1	Inadequately Trained Operator
1.1.1.4.5.1.3.1.2	Uncertified Operator
1.1.1.4.5.1.3.2	Debris Due to Manufacturing Process Plan
1.1.1.4.5.1.3.2.1	Debris Due to Inadequate Manufacturing Process Plan
1.1.1.4.5.1.3.2.2	Debris Due to Operator Not Following Manufacturing Process Plan
1.1.1.4.5.1.3.3 Open due to lower element	Debris Due to MAF BX-250 Material Processing
1.1.1.4.5.1.3.3.1	Shelf Life Issue
1.1.1.4.5.1.3.3.3	Contamination During Processing
1.1.1.4.5.1.3.3.4	Improper Surface Preparation
1.1.1.4.5.1.3.3.6	Inadequately Defined Acceptance Testing
1.1.1.4.5.1.3.3.7	Improperly Performed Acceptance Testing
1.1.1.4.5.1.3.3.8	Inadequate Resolution of Identified Anomaly
1.1.1.4.5.1.3.4	Debris Due to MAF DPTU Adhesive Material Processing
1.1.1.4.5.1.3.4.1	Shelf Life Issue
1.1.1.4.5.1.3.4.2	Improper Storage

ELEMENT NUMBER	*DESCRIPTION OF FAULT TREE ELEMENT*
1.1.1.4.5.1.3.4.3	Contamination During Processing
1.1.1.4.5.1.3.4.4	Improper Surface Preparation
1.1.1.4.5.1.3.4.6	Inadequately Defined Acceptance Testing
1.1.1.4.5.1.3.4.7	Improperly Performed Acceptance Testing
1.1.1.4.5.1.3.4.8	Inadequate Resolution of Identified Anomaly
1.1.1.4.5.1.3.5	Debris Due to External Events During MAF Processing
1.1.1.4.5.1.3.6	Debris Due to Mechanical Assembly Anomaly
1.1.1.4.5.2	CO-LO2 F/L Flanges & Elbow Tie, Xt 1115-2053 & LH2 F/L Base CO
1.1.1.4.5.3	Foam CO-Cell "C", LO2 F/L Support Xt 1623.8, 1871.0, and 1973.5, LH2 Tank
1.1.1.4.6 Open due to lower element	LO2 PAL Ramp
1.1.1.4.6.1 Open due to lower element	Foam Application-LO2 Tank/Intertank Pal Ramp
1.1.1.4.6.1.1	Debris Due to Design Resulting in a Cohesive, Shear, Delamination, or Crack Failure of the TPS
1.1.1.4.6.1.2	Debris Due to Vendor Manufacturing/Processing Resulting in a Cohesive, Shear, Delamination, or Crack Failure of the TPS
1.1.1.4.6.1.3 Open due to lower element	Debris Due to Anomalous MAF Processing Resulting in a Cohesive, Shear, Delamination, or Crack Failure of the TPS
1.1.1.4.6.1.3.1 Open due to lower element	Debris Due to MAF Process Training
1.1.1.4.6.1.3.1.2	Uncertified Operator
1.1.1.4.6.1.3.2	Debris Due to Manufacturing Process Plan
1.1.1.4.6.1.3.2.1	Debris Due to Inadequate Manufacturing Process Plan
1.1.1.4.6.1.3.2.2	Debris Due to Operator Not Following Manufacturing Process Plan
1.1.1.4.6.1.3.3 Open due to lower element	Debris Due to MAF BX-250 Material Processing
1.1.1.4.6.1.3.3.1	Shelf Life Issue
1.1.1.4.6.1.3.3.3	Contamination During Processing
1.1.1.4.6.1.3.3.4	Improper Surface Preparation
1.1.1.4.6.1.3.3.7	Improperly Performed Acceptance Testing
1.1.1.4.6.1.3.3.8	Inadequate Resolution of Identified Anomaly
1.1.1.4.6.1.3.4	Debris Due to MAF DPTU Adhesive Material Processing
1.1.1.4.6.1.3.4.1	Shelf Life Issue
1.1.1.4.6.1.3.4.2	Improper Storage
1.1.1.4.6.1.3.4.3	Contamination During Processing

ELEMENT NUMBER	*DESCRIPTION OF FAULT TREE ELEMENT*
1.1.1.4.6.1.3.4.4	Improper Surface Preparation
1.1.1.4.6.1.3.4.5	Improper Application Process
1.1.1.4.6.1.3.4.6	Inadequately Defined Acceptance Testing
1.1.1.4.6.1.3.4.7	Improperly Performed Acceptance Testing
1.1.1.4.6.1.3.4.8	Inadequate Resolution of Identified Anomaly
1.1.1.4.6.1.3.5	Debris Due to External Events During MAF Processing
1.1.1.4.6.1.3.6	Debris Due to Mechanical Assembly Anomaly
1.1.1.4.7	LO2 Dome
1.1.1.4.8	GO2 Vent Lines
1.1.1.4.9	LH2 PAL Ramp
1.1.1.4.10	Aft Feed Line Supports (External)
1.1.1.4.11	Aft I/F Hardware Closeouts
1.1.1.4.12	LH2 Aft Dome
1.1.1.4.13	LH2 Fwd Dome
1.1.1.4.14	LH2 C/T Fairing & Fwd PAL Ramp
1.1.1.4.15	Aft C/Ts
1.1.1.4.16	SRB PAL Ramps
1.1.1.4.17	KSC TPS 3rd Hardpoint
1.1.1.5 Open due to lower element	SLA-561
1.1.1.5.1 Open due to lower element	Bipod
1.1.1.5.1.1 Open due to lower element	TPS Closeout-Final Assembly, Forward Bipod Fittings
1.1.1.5.1.1.1 Open due to lower element	Debris Due to Design Resulting in a Cohesive, Shear, Delamination, or Crack Failure of the TPS
1.1.1.5.1.1.1.2	Inadequate Design Implementation
1.1.1.5.1.1.1.3	Inadequate Design Requirements (Loads & Environments)
1.1.1.5.1.1.2	Debris Due to Vendor Manufacturing/Processing Resulting in a Cohesive, Shear, Delamination, or Crack Failure of the TPS
1.1.1.5.1.1.3 Open due to lower element	Debris Due to Anomalous MAF Processing Resulting in a Cohesive, Shear, Delamination, or Crack Failure of the TPS
1.1.1.5.1.1.3.1	Debris Due to MAF Process Training
1.1.1.5.1.1.3.2	Debris Due to Manufacturing Process Plan
1.1.1.5.1.1.3.3	Debris Due to Manufacturing Process Plan – Materials

ELEMENT NUMBER	*DESCRIPTION OF FAULT TREE ELEMENT*
1.1.1.5.1.1.3.4	Debris Due to Manufacturing Process Plan - Acceptance
1.1.1.5.1.1.3.5	Debris Due to External Events During MAF Processing
1.1.1.5.1.1.3.6	Debris Due to Mechanical Assembly Anomaly
1.1.1.5.1.2 Open due to lower element	Plate Connector-Bipod Fitting, SLA Application
1.1.1.5.1.2.1 Open due to lower element	Debris Due to Design Resulting in a Cohesive, Shear, Delamination, or Crack Failure of the TPS
1.1.1.5.1.2.1.2	Inadequate Design Implementation
1.1.1.5.1.2.1.3	Inadequate Design Requirements (Loads & Environments)
1.1.1.5.1.2.2	Debris Due to Vendor Manufacturing/Processing Resulting in a Cohesive, Shear, Delamination, or Crack Failure of the TPS
1.1.1.5.1.2.2.3	Undetected Anomaly
1.1.1.5.1.2.3 Open due to lower element	Debris Due to Anomalous MAF Processing Resulting in a Cohesive, Shear, Delamination, or Crack Failure of the TPS
1.1.1.5.1.2.3.1	Debris Due to MAF Process Training
1.1.1.5.1.2.3.2	Debris Due to Manufacturing Process Plan
1.1.1.5.1.2.3.3	Debris Due to Manufacturing Process Plan – Materials
1.1.1.5.12.3.4	Debris Due to Manufacturing Process Plan - Acceptance
1.1.1.5.1.2.3.5	Debris Due to External Events During MAF Processing
1.1.1.5.1.2.3.6	Debris Due to Mechanical Assembly Anomaly
1.1.1.5.1.3 Open due to lower element	Bipod Struts, TPS Application
1.1.1.5.1.3.1	Debris Due to Design Resulting in a Cohesive, Shear, Delamination, or Crack Failure of the TPS
1.1.1.5.1.3.1.1	Inadequate Design Methodology
1.1.1.5.1.3.1.2	Inadequate Design Implementation
1.1.1.5.1.3.1.2.1	Incorrect Materials Identified
1.1.1.5.1.3.1.2.2	Incorrect Processes Identified
1.1.1.5.1.3.1.2.3	Incorrect Configuration/Dimensions Identified
1.1.1.5.1.3.1.2.4	Incorrect ET Effectivity Identified
1.1.1.5.1.3.1.3	Inadequate Design Requirements (Loads & Environments)
1.1.1.5.1.3.2	Debris Due to Vendor Manufacturing/Processing Resulting in a Cohesive, Shear, Delamination, or Crack Failure of the TPS
1.1.1.5.1.3.2.3	Undetected Anomaly
1.1.1.5.1.3.3	Debris Due to Anomalous MAF Processing Resulting in a Cohesive, Shear, Delamination, or Crack Failure of the TPS
1.1.1.5.1.3.3.1	Debris Due to MAF Process Training

ELEMENT NUMBER	*DESCRIPTION OF FAULT TREE ELEMENT*
1.1.1.5.1.3.3.2	Debris Due to Manufacturing Process Plan
1.1.1.5.1.3.3.3	Debris Due to Manufacturing Process Plan - Material
1.1.1.5.1.3.3.4	Debris Due to Manufacturing Process Plan - Acceptance
1.1.1.5.1.3.3.5	Debris Due to External Events During MAF Processing
1.1.1.5.1.3.3.6	Debris Due to Mechanical Assembly Anomaly
1.1.1.5.2 Open due to lower element	LO2 C/Ts & Fairings
1.1.1.5.2.1 Open due to lower element	CO GO2 P/L Barry Mounts on LO2 Tank, Sta.371.0 C/T Brkt, & Foam Trims for GO2 P/L Flange
1.1.1.5.2.1.1	Debris Due to Design Resulting in a Cohesive, Shear, Delamination, or Crack Failure of the TPS
1.1.1.5.2.1.1.1	Inadequate Design Methodology
1.1.1.5.2.1.1.2	Inadequate Design Implementation
1.1.1.5.2.1.1.2.1	Incorrect Materials Identified
1.1.1.5.2.1.1.2.2	Incorrect Processes Identified
1.1.1.5.2.1.1.2.3	Incorrect Configuration/Dimensions Identified
1.1.1.5.2.1.1.2.4	Incorrect ET Effectivity Identified
1.1.1.5.2.1.1.3	Inadequate Design Requirements (Loads & Environments)
1.1.1.5.2.1.2	Debris Due to Vendor Manufacturing/Processing Resulting in a Cohesive, Shear, Delamination, or Crack Failure of the TPS
1.1.1.5.2.1.2.3	Undetected Anomaly
1.1.1.5.2.1.3 Open due to lower element	Debris Due to Anomalous MAF Processing Resulting in a Cohesive, Shear, Delamination, or Crack Failure of the TPS
1.1.1.5.2.1.3.1	Debris Due to MAF Process Training
1.1.1.5.2.1.3.2	Debris Due to Manufacturing Process Plan
1.1.1.5.2.1.3.3	Debris Due to Manufacturing Process Plan - Material
1.1.1.5.2.1.3.4	Debris Due to Manufacturing Process Plan - Acceptance
1.1.1.5.2.1.3.5	Debris Due to External Events During MAF Processing
1.1.1.5.2.1.3.6	Debris Due to Mechanical Assembly Anomaly
1.1.1.5.2.2 Open due to lower element	SLA CO-Cell "M", LO2 P/L Brackets Sta. 404.34 thru Sta 718.04
1.1.1.5.2.2.1	Debris Due to Design Resulting in a Cohesive, Shear, Delamination, or Crack Failure of the TPS
1.1.1.5.2.2.2	Debris Due to Vendor Manufacturing/Processing Resulting in a Cohesive, Shear, Delamination, or Crack Failure of the TPS
1.1.1.5.2.2.3 Open due to lower element	Debris Due to Anomalous MAF Processing Resulting in a Cohesive, Shear, Delamination, or Crack Failure of the TPS
1.1.1.5.2.2.3.1	Debris Due to MAF Process Training

ELEMENT NUMBER	*DESCRIPTION OF FAULT TREE ELEMENT*
1.1.1.5.2.2.3.2	Debris Due to Manufacturing Process Plan
1.1.1.5.2.2.3.3	Debris Due to Manufacturing Process Plan - Material
1.1.1.5.2.2.3.4	Debris Due to Manufacturing Process Plan - Acceptance
1.1.1.5.2.2.3.5	Debris Due to External Events During MAF Processing
1.1.1.5.2.2.3.6	Debris Due to Mechanical Assembly Anomaly
1.1.1.5.2.3 Open due to lower element	LO2 Tank Cable Tray Segment, SLA Application
1.1.1.5.2.3.1	Debris Due to Design Resulting in a Cohesive, Shear, Delamination, or Crack Failure of the TPS
1.1.1.5.2.3.2	Debris Due to Vendor Manufacturing/Processing Resulting in a Cohesive, Shear, Delamination, or Crack Failure of the TPS
1.1.1.5.2.3.2.3	Undetected Anomaly
1.1.1.5.2.3.3 Open due to lower element	Debris Due to Anomalous MAF Processing Resulting in a Cohesive, Shear, Delamination, or Crack Failure of the TPS
1.1.1.5.2.3.3.1	Debris Due to MAF Process Training
1.1.1.5.2.3.3.2	Debris Due to Manufacturing Process Plan
1.1.1.5.2.3.3.3	Debris Due to Manufacturing Process Plan - Material
1.1.1.5.2.3.3.4	Debris Due to Manufacturing Process Plan - Acceptance
1.1.1.5.2.3.3.5	Debris Due to External Events During MAF Processing
1.1.1.5.2.3.3.6	Debris Due to Mechanical Assembly Anomaly
1.1.1.5.2.4 Open due to lower element	LO2 Tank P/L & C/T Support Sta. 371.0, SLA Application
1.1.1.5.2.4.1	Debris Due to Design Resulting in a Cohesive, Shear, Delamination, or Crack Failure of the TPS
1.1.1.5.2.4.2	Debris Due to Vendor Manufacturing/Processing Resulting in a Cohesive, Shear, Delamination, or Crack Failure of the TPS
1.1.1.5.2.4.3 Open due to lower element	Debris Due to Anomalous MAF Processing Resulting in a Cohesive, Shear, Delamination, or Crack Failure of the TPS
1.1.1.5.2.4.3.1	Debris Due to MAF Process Training
1.1.1.5.2.4.3.2	Debris Due to Manufacturing Process Plan
1.1.1.5.2.4.3.3	Debris Due to Manufacturing Process Plan - Material
1.1.1.5.2.4.3.4	Debris Due to Manufacturing Process Plan – Acceptance
1.1.1.5.2.4.3.5	Debris Due to External Events During MAF Processing
1.1.1.5.2.4.3.6	Debris Due to Mechanical Assembly Anomaly
1.1.1.5.2.5 Open due to lower element	Cover, Cable Tray, TPS Application
1.1.1.5.2.5.1	Debris Due to Design Resulting in a Cohesive, Shear, Delamination, or Crack Failure of the TPS
1.1.1.5.2.5.2	Debris Due to Vendor Manufacturing/Processing Resulting in a Cohesive, Shear, Delamination, or Crack Failure of the TPS

ELEMENT NUMBER	*DESCRIPTION OF FAULT TREE ELEMENT*
1.1.1.5.2.5.3 Open due to lower element	Debris Due to Anomalous MAF Processing Resulting in a Cohesive, Shear, Delamination, or Crack Failure of the TPS
1.1.1.5.2.5.3.1	Debris Due to MAF Process Training
1.1.1.5.2.5.3.2	Debris Due to Manufacturing Process Plan
1.1.1.5.2.5.3.3	Debris Due to Manufacturing Process Plan - Material
1.1.1.5.2.5.3.4	Debris Due to Manufacturing Process Plan - Acceptance
1.1.1.5.2.5.3.5	Debris Due to External Events During MAF Processing
1.1.1.5.2.5.3.6	Debris Due to Mechanical Assembly Anomaly
1.1.1.5.2.6 Open due to lower element	LO2 Tank C/T Covers & LO2 C/T Fairing Cover, SLA Application
1.1.1.5.2.6.1	Debris Due to Design Resulting in a Cohesive, Shear, Delamination, or Crack Failure of the TPS
1.1.1.5.2.6.2	Debris Due to Vendor Manufacturing/Processing Resulting in a Cohesive, Shear, Delamination, or Crack Failure of the TPS
1.1.1.5.2.6.3 Open due to lower element	Debris Due to Anomalous MAF Processing Resulting in a Cohesive, Shear, Delamination, or Crack Failure of the TPS
1.1.1.5.2.6.3.1	Debris Due to MAF Process Training
1.1.1.5.2.6.3.2	Debris Due to Manufacturing Process Plan
1.1.1.5.2.6.3.3	Debris Due to Manufacturing Process Plan - Material
1.1.1.5.2.6.3.4	Debris Due to Manufacturing Process Plan - Acceptance
1.1.1.5.2.6.3.5	Debris Due to External Events During MAF Processing
1.1.1.5.2.6.3.6	Debris Due to Mechanical Assembly Anomaly
1.1.1.5.2.7 Open due to lower element	Gap Closures-LO2 Tank C/T, SLA Application
1.1.1.5.2.7.1	Debris Due to Design Resulting in a Cohesive, Shear, Delamination, or Crack Failure of the TPS
1.1.1.5.2.7.2	Debris Due to Vendor Manufacturing/Processing Resulting in a Cohesive, Shear, Delamination, or Crack Failure of the TPS
1.1.1.5.2.7.3 Open due to lower element	Debris Due to Anomalous MAF Processing Resulting in a Cohesive, Shear, Delamination, or Crack Failure of the TPS
1.1.1.5.2.7.3.1	Debris Due to MAF Process Training
1.1.1.5.2.7.3.2	Debris Due to Manufacturing Process Plan
1.1.1.5.2.7.3.3	Debris Due to Manufacturing Process Plan - Material
1.1.1.5.2.7.3.4	Debris Due to Manufacturing Process Plan - Acceptance
1.1.1.5.2.7.3.5	Debris Due to External Events During MAF Processing
1.1.1.5.2.7.3.6	Debris Due to Mechanical Assembly Anomaly
1.1.1.5.2.8 Open due to lower element	LO2 Tank P/L & C/T Support Bracket, SLA Application
1.1.1.5.2.8.1	Debris Due to Design Resulting in a Cohesive, Shear, Delamination, or Crack Failure of the TPS

ELEMENT NUMBER	*DESCRIPTION OF FAULT TREE ELEMENT*
1.1.1.5.2.8.2	Debris Due to Vendor Manufacturing/Processing Resulting in a Cohesive, Shear, Delamination, or Crack Failure of the TPS
1.1.1.5.2.8.3 Open due to lower element	Debris Due to Anomalous MAF Processing Resulting in a Cohesive, Shear, Delamination, or Crack Failure of the TPS
1.1.1.5.2.8.3.1	Debris Due to MAF Process Training
1.1.1.5.2.8.3.2	Debris Due to Manufacturing Process Plan
1.1.1.5.2.8.3.3	Debris Due to Manufacturing Process Plan - Material
1.1.1.5.2.8.3.4	Debris Due to Manufacturing Process Plan - Acceptance
1.1.1.5.2.8.3.5	Debris Due to External Events During MAF Processing
1.1.1.5.2.8.3.6	Debris Due to Mechanical Assembly Anomaly
1.1.1.5.2.9 Open due to lower element	Composite Nose Cone, Foam Seal & Blend
1.1.1.5.2.9.1	Debris Due to Design Resulting in a Cohesive, Shear, Delamination, or Crack Failure of the TPS
1.1.1.5.2.9.2	Debris Due to Vendor Manufacturing/Processing Resulting in a Cohesive, Shear, Delamination, or Crack Failure of the TPS
1.1.1.5.2.9.3 Open due to lower element	Debris Due to Anomalous MAF Processing Resulting in a Cohesive, Shear, Delamination, or Crack Failure of the TPS
1.1.1.5.2.9.3.1	Debris Due to MAF Process Training
1.1.1.5.2.9.3.2	Debris Due to Manufacturing Process Plan
1.1.1.5.2.9.3.3	Debris Due to Manufacturing Process Plan - Material
1.1.1.5.2.9.3.4	Debris Due to Manufacturing Process Plan - Acceptance
1.1.1.5.2.9.3.5	Debris Due to External Events During MAF Processing
1.1.1.5.2.9.3.6	Debris Due to Mechanical Assembly Anomaly
1.1.1.5.3 Open due to lower element	Press Line Barrymounts
1.1.1.5.3.1 Open due to lower element	GO2 & GH2 P/L Barry Mount Slide Cap, SLA Application
1.1.1.5.3.1.1	Debris Due to Design Resulting in a Cohesive, Shear, Delamination, or Crack Failure of the TPS
1.1.1.5.3.1.2	Debris Due to Vendor Manufacturing/Processing Resulting in a Cohesive, Shear, Delamination, or Crack Failure of the TPS
1.1.1.5.3.1.3 Open due to lower element	Debris Due to Anomalous MAF Processing Resulting in a Cohesive, Shear, Delamination, or Crack Failure of the TPS
1.1.1.5.3.1.3.1	Debris Due to MAF Process Training
1.1.1.5.3.1.3.2	Debris Due to Manufacturing Process Plan
1.1.1.5.3.1.3.3	Debris Due to Manufacturing Process Plan - Material
1.1.1.5.3.1.3.4	Debris Due to Manufacturing Process Plan - Acceptance
1.1.1.5.3.1.3.5	Debris Due to External Events During MAF Processing
1.1.1.5.3.1.3.6	Debris Due to Mechanical Assembly Anomaly

ELEMENT NUMBER	*DESCRIPTION OF FAULT TREE ELEMENT*
1.1.1.5.4 Open due to lower element	ET/SRB Forward Bolt Catcher
1.1.1.5.4.1 Open due to lower element	Bolt Catcher-Forward SRB Separation
1.1.1.5.4.1.1	Debris Due to Vendor Manufacturing/Processing Resulting in a Cohesive, Shear, Delamination, or Crack Failure of the TPS
1.1.1.5.4.1.2 Open due to lower element	Debris Due to Anomalous MAF Processing Resulting in a Cohesive, Shear, Delamination, or Crack Failure of the TPS
1.1.1.5.4.1.2.1	Debris Due to MAF Process Training
1.1.1.5.4.1.2.2	Debris Due to Manufacturing Process Plan
1.1.1.5.4.1.2.3	Debris Due to Manufacturing Process Plan - Material
1.1.1.5.4.1.2.4	Debris Due to Manufacturing Process Plan - Acceptance
1.1.1.5.4.1.2.5	Debris Due to External Events During MAF Processing
1.1.1.5.4.1.2.6	Debris Due to Mechanical Assembly Anomaly
1.1.1.5.5 Open due to lower element	I/T Fairings
1.1.1.5.5.1	Fairing-LH2 Cable Tray, SLA Application
1.1.1.5.5.2 Open due to lower element	Fairing, LO2 Feedline, SLA Application
1.1.1.5.5.2.1	Debris Due to Design Resulting in a Cohesive, Shear, Delamination, or Crack Failure of the TPS
1.1.1.5.5.2.2	Debris Due to Vendor Manufacturing/Processing Resulting in a Cohesive, Shear, Delamination, or Crack Failure of the TPS
1.1.1.5.5.2.3 Open due to lower element	Debris Due to Anomalous MAF Processing Resulting in a Cohesive, Shear, Delamination, or Crack Failure of the TPS
1.1.1.5.5.2.3.1	Debris Due to MAF Process Training
1.1.1.5.5.2.3.2	Debris Due to Manufacturing Process Plan
1.1.1.5.5.2.3.3	Debris Due to Manufacturing Process Plan - Material
1.1.1.5.5.2.3.4	Debris Due to Manufacturing Process Plan - Acceptance
1.1.1.5.5.2.3.5	Debris Due to External Events During MAF Processing
1.1.1.5.5.2.3.6	Debris Due to Mechanical Assembly Anomaly
1.1.1.5.5.3 Open due to lower element	Fairing-LO2 Tank Cable Tray, SLA Application
1.1.1.5.5.3.1	Debris Due to Design Resulting in a Cohesive, Shear, Delamination, or Crack Failure of the TPS
1.1.1.5.5.3.2	Debris Due to Vendor Manufacturing/Processing Resulting in a Cohesive, Shear, Delamination, or Crack Failure of the TPS
1.1.1.5.5.3.3 Open due to lower element	Debris Due to Anomalous MAF Processing Resulting in a Cohesive, Shear, Delamination, or Crack Failure of the TPS
1.1.1.5.5.3.3.1	Debris Due to MAF Process Training
1.1.1.5.5.3.3.2	Debris Due to Manufacturing Process Plan
1.1.1.5.5.3.3.3	Debris Due to Manufacturing Process Plan – Material

ELEMENT NUMBER	*DESCRIPTION OF FAULT TREE ELEMENT*
1.1.1.5.5.3.3.4	Debris Due to Manufacturing Process Plan - Acceptance
1.1.1.5.5.3.3.5	Debris Due to External Events During MAF Processing
1.1.1.5.5.3.3.6	Debris Due to Mechanical Assembly Anomaly
1.1.1.5.5.4	RSS Cross Strap Details, TPS Application
1.1.1.5.6 Open due to lower element	LO2 Feed Line Supports
1.1.1.5.6.1 Open due to lower element	Yoke LO2 Feedline, TPS Application
1.1.1.5.6.1.1	Debris Due to Design Resulting in a Cohesive, Shear, Delamination, or Crack Failure of the TPS
1.1.1.5.6.1.2	Debris Due to Vendor Manufacturing/Processing Resulting in a Cohesive, Shear, Delamination, or Crack Failure of the TPS
1.1.1.5.6.1.3 Open due to lower element	Debris Due to Anomalous MAF Processing Resulting in a Cohesive, Shear, Delamination, or Crack Failure of the TPS
1.1.1.5.6.1.3.1	Debris Due to MAF Process Training
1.1.1.5.6.1.3.2	Debris Due to Manufacturing Process Plan
1.1.1.5.6.1.3.3	Debris Due to Manufacturing Process Plan - Material
1.1.1.5.6.1.3.4	Debris Due to Manufacturing Process Plan Acceptance
1.1.1.5.6.1.3.5	Debris Due to External Events During MAF Processing
1.1.1.5.6.1.3.6	Debris Due to Mechanical Assembly Anomaly
1.1.1.5.7	LH2 C/Ts & Fairings
1.1.1.5.8	Aft C/Ts & Fairings
1.1.1.5.9	Aft I/F Hardware
1.1.1.5.10	Aft Feed Lines
1.1.1.5.11	LH2 Aft Dome
1.1.1.5.12	LH2 Manhole Covers
1.1.1.6 Open due to lower element	MA-25S
1.1.1.6.1 Open due to lower element	Bipod
1.1.1.6.1.1 Open due to lower element	Bipod Struts, TPS Application
1.1.1.6.1.1.1	Debris Due to Design Resulting in a Cohesive, Shear, Delamination, or Crack Failure of the TPS
1.1.1.6.1.1.2	Debris Due to Vendor Manufacturing/Processing Resulting in a Cohesive, Shear, Delamination, or Crack Failure of the TPS
1.1.1.6.1.1.3 Open due to lower element	Debris Due to Anomalous MAF Processing Resulting in a Cohesive, Shear, Delamination, or Crack Failure of the TPS
1.1.1.6.1.1.3.1	Debris Due to MAF Process Training
1.1.1.6.1.1.3.2	Debris Due to Manufacturing Process Plan

ELEMENT NUMBER	*DESCRIPTION OF FAULT TREE ELEMENT*
1.1.1.6.1.1.3.3	Debris Due to Manufacturing Process Plan - Material
1.1.1.6.1.1.3.4	Debris Due to Manufacturing Process Plan – Shelf Life
1.1.1.6.1.1.3.5	Debris Due to Manufacturing Process Plan - Storage
1.1.1.6.1.1.3.6	Debris Due to Manufacturing Process Plan - Acceptance
1.1.1.6.1.1.3.7	Debris Due to External Events During MAF Processing
1.1.1.6.1.1.3.8	Debris Due to Mechanical Assembly Anomaly
1.1.1.6.2	Nose Cone Closeout (Internal)
1.1.1.7 Open due to lower element	SS-1171
1.1.1.7.1 Open due to lower element	LO2 Feed Line & Supports (External)
1.1.1.7.1.1 Open due to lower element	Feedline-LO2 Aluminum Straight Section Foam Application
1.1.1.7.1.1.1	Debris Due to Design Resulting in a Cohesive, Shear, Delamination, or Crack Failure of the TPS
1.1.1.7.1.1.2	Debris Due to Vendor Manufacturing/Processing Resulting in a Cohesive, Shear, Delamination, or Crack Failure of the TPS
1.1.1.7.1.1.3 Open due to lower element	Debris Due to Anomalous MAF Processing Resulting in a Cohesive, Shear, Delamination, or Crack Failure of the TPS
1.1.1.7.1.1.3.1	Debris Due to MAF Process Training
1.1.1.7.1.1.3.2	Debris Due to Manufacturing Process Plan
1.1.1.7.1.1.3.3 Open due to lower element	Debris Due to MAF SS-1171 Material Processing
1.1.1.7.1.1.3.3.1	Shelf Life Issue
1.1.1.7.1.1.3.3.3	Contamination During Processing
1.1.1.7.1.1.3.3.4	Improper Surface Preparation
1.1.1.7.1.1.3.3.6	Inadequately Defined Acceptance Testing
1.1.1.7.1.1.3.3.7	Improperly Performed Acceptance Testing
1.1.1.7.1.1.3.3.8	Inadequate Resolution of Identified Anomaly
1.1.1.7.1.1.3.4	Debris Due to External Events During MAF Processing
1.1.1.7.1.1.3.5	Debris Due to Mechanical Assembly Anomaly
1.1.1.7.1.2 Open due to lower element	Feedline-LO2 Flex Sections, Foam Application
1.1.1.7.1.2.1	Debris Due to Design Resulting in a Cohesive, Shear, Delamination, or Crack Failure of the TPS
1.1.1.7.1.2.2	Debris Due to Vendor Manufacturing/Processing Resulting in a Cohesive, Shear, Delamination, or Crack Failure of the TPS
1.1.1.7.1.2.3 Open due to lower element	Debris Due to Anomalous MAF Processing Resulting in a Cohesive, Shear, Delamination, or Crack Failure of the TPS
1.1.1.7.1.2.3.1	Debris Due to MAF Process Training

ELEMENT NUMBER	*DESCRIPTION OF FAULT TREE ELEMENT*
1.1.1.7.1.2.3.2	Debris Due to Manufacturing Process Plan
1.1.1.7.1.2.3.3 Open due to lower element	Debris Due to MAF SS-1171 Material Processing
1.1.1.7.1.2.3.3.1	Shelf Life Issue
1.1.1.7.1.2.3.3.3	Contamination During Processing
1.1.1.7.1.2.3.3.4	Improper Surface Preparation
1.1.1.7.1.2.3.3.6	Inadequately Defined Acceptance Testing
1.1.1.7.1.2.3.3.7	Improperly Performed Acceptance Testing
1.1.1.7.1.2.3.3.8	Inadequate Resolution of Identified Anomaly
1.1.1.7.1.2.3.4	Debris Due to External Events During MAF Processing
1.1.1.7.1.2.3.5	Debris Due to Mechanical Assembly Anomaly
1.1.1.7.1.3 Open due to lower element	Yoke LO2 Feedline, TPS Application
1.1.1.7.1.3.1	Debris Due to Design Resulting in a Cohesive, Shear, Delamination, or Crack Failure of the TPS
1.1.1.7.1.3.2	Debris Due to Vendor Manufacturing/Processing Resulting in a Cohesive, Shear, Delamination, or Crack Failure of the TPS
1.1.1.7.13.3 Open due to lower element	Debris Due to Anomalous MAF Processing Resulting in a Cohesive, Shear, Delamination, or Crack Failure of the TPS
1.1.1.7.1.3.3.1	Debris Due to MAF Process
1.1.1.7.1.3.3.2	Debris Due to Manufacturing Process Plan
1.1.1.7.1.3.3.3 Open due to lower element	Debris Due to MAF SS-1171 Material Processing
1.1.1.7.1.3.3.3.1	Shelf Life Issue
1.1.1.7.1.3.3.3.3	Contamination During Processing
1.1.1.7.1.3.3.3.4	Improper Surface Preparation
1.1.1.7.1.3.3.3.6	Inadequately Defined Acceptance Testing
1.1.1.7.1.3.3.3.7	Improperly Performed Acceptance Testing
1.1.1.7.1.3.3.3.8	Inadequate Resolution of Identified Anomaly
1.1.1.7.1.3.3.4	Debris Due to External Events During MAF Processing
1.1.1.7.1.3.3.5	Debris Due to Mechanical Assembly Anomaly
1.1.1.7.2	LO2 & LH2 Covers
1.1.1.7.3	LH2 Feed Line & Recirc Line (External)
1.1.1.7.4	Aft C/Ts & Fairings
1.1.1.7.5	Aft I/F Hardware
1.1.1.8	BX-265

ET 1.1.2 "NON-TPS DEBRIS"

ELEMENT NUMBER	*DESCRIPTION OF FAULT TREE ELEMENT*
1.1.2.1	Debris from Composite Nose Cone and Spike Assy
1.1.2.2	Nosecone Bulkhead Assy
1.1.2.3	IT Access Door Assy
1.1.2.4	GH2 Pressline Fairing Install
1.1.2.5	Presslines and Cable Tray Assy on LH2 tank (aft of XT=1082)
1.1.2.6	LO2 Tank Pressline and Cabletray Assy
1.1.2.7	Aft LO2 Tank Cabletray Fairing Assy.
1.1.2.8	Fwd LH2 Tank Cabletray Fairing Assy.
1.1.2.9	LO2 Feedline Fairing Assy
1.1.2.10	LO2 Feedline Install
1.1.2.11	FOD
1.1.2.12	Aero Vents
1.1.2.13 Open due to lower element	Non-TPS Debris from Other Sources
1.1.2.13.1	Wiring/Electrical
1.1.2.13.3	Internal Components
1.1.2.13.4	Substrate Structure

ET 1. 2 "INTERFACES"

ELEMENT NUMBER	*DESCRIPTION OF FAULT TREE ELEMENT*
1.2.1 Open due to lower element	Structural I/Fs
1.2.1.1 Open due to lower element	EO-1 Fwd Bipod Attach I/F
1.2.1.1.1	Inadequate ICD Design and Implementation
1.2.1.1.2	Inadequate / Incorrect Supplier / GFP Processing
1.2.1.1.3 Open due to lower element	Incorrect/Inadequate MAF processing
1.2.1.1.3.1	Incorrect Part materials Usage
1.2.1.1.3.2	Inadequate Part Processing (Part Marking, Contamination, Shelf Life, Pack and Ship, Etc.)
1.2.1.1.3.3	Incorrect Parts fabrication
1.2.1.1.3.4	Incorrect Parts usage

ELEMENT NUMBER	*DESCRIPTION OF FAULT TREE ELEMENT*
1.2.1.1.3.7	Incorrect NCD Disposition
1.2.1.1.3.8	Incorrect L/C Answer
1.2.1.1.3.9	Incorrect / Deficient Consumables
1.2.1.1.3.10	Incorrect / Inadequate Tooling
1.2.1.1.3.11	Incorrect / Inadequate Inspection
1.2.1.1.3.12	Incorrect / Inadequate Acceptance Test
1.2.1.1.4	Incorrect / Anomalous Ground Processing at KSC
1.2.1.1.5 Open due to lower element	Operational Anomalies (Prelaunch, Ascent, Separation)
1.2.1.1.5.1	Bipod Induces excessive Loads to Orbiter
1.2.1.1.5.2	Bipod Structural Failure imparts anomalous Orbiter load
1.2.1.1.5.3	Bipod Hardware / Components fail and create Debris during Ascent or Separation
1.2.1.1.5.5	Bipod hardware impacts surrounding foam / primary structure
1.2.1.1.5.6	Bipod Anomalous/Incomplete Str. Separation causes I/F hardware to contact orbiter
1.2.1.2	EO-2 Aft Attach, -Y
1.2.1.3	EO-3 Aft Attach, +Y
1.2.1.4	EO-4 LH2 Umbilical Plate (Mechanical)
1.2.1.5	EO-5 LO2 Umbilical Plate (Mechanical)
1.2.1.6	EO-6 LO2 Cross Beam / Orbiter (Aerodynamic)
1.2.1.7 Open due to lower element	EB-1 Fwd SRB Attach -Y & EB-2 Fwd SRB Attach +Y
1.2.1.7.1	Inadequate ICD Design and Implementation
1.2.1.7.2	Inadequate / Incorrect supplier/GFP Processing
1.2.1.7.3 Open due to lower element	Incorrect ICD MAF processing
1.2.1.7.3.12	Incorrect / Inadequate Acceptance Test
1.2.1.7.3.2	Inadequate Part Processing (Part Marking, Contamination, Shelf Life, Pack and Ship, Etc.)
1.2.1.7.3.3	Incorrect Parts fabrication
1.2.1.7.3.4	Incorrect Parts usage
1.2.1.7.3.5	Incorrect Parts Assembly
1.2.1.7.3.6	Incorrect Parts Installation
1.2.1.7.3.7	Incorrect NCD Disposition

ELEMENT NUMBER	*DESCRIPTION OF FAULT TREE ELEMENT*
1.2.1.7.3.8	Incorrect L/C Answer
1.2.1.7.3.9	Incorrect / Deficient Consumables
1.2.1.7.3.10	Incorrect / Inadequate Tooling
1.2.1.7.3.11	Incorrect / Inadequate Inspection
1.1.1.7.4 Open due to lower element	Incorrect / Anomalous Ground Processing at KSC
1.1.1.7.4.1 Open due to lower element	Incorrect / Inadequate Mating
1.2.1.7.4.1.1	Incorrect / Anomalous ET / SRB Mate
1.2.1.7.4.1.1.1	Inadequate Offsite Engineering Requirements (Drawings, Processes, Mod Kits, FECs)
1.2.1.7.4.1.1.2	Incorrect Parts usage
1.2.1.7.4.1.1.3	Incorrect Parts Assembly
1.2.1.7.4.1.1.5	Incorrect AR / PR Disposition
1.2.1.7.4.1.1.6	Incorrect / Inadequate Tooling
1.2.1.7.4.1.1.7	Incorrect / Inadequate Inspection and Acceptance
1.2.1.7.4.1.2	Incorrect / Anomalous Orbiter Mate
1.2.1.7.5	Operational Anomalies (Prelaunch, Ascent, Separation)
1.2.1.8	Canceled (EB-2 Fwd SRB Attach +Y is addressed in 1.2.1.7)
1.2.1.9	Aft SRB Attach -Y (EB-3, EB-5, EB-7)
1.2.1.10	Aft SRB Attach +Y (EB-4, EB-6, EB-8)
1.2.1.11	GUCA (Mechanical)
1.2.1.12	LO2 Vent Hood
1.2.1.13	Post Separation ET / Orb Contact or at ET Break-up
1.2.2	Propulsion Functional I/Fs Functional Performance Impacts Orbiter Systems
1.2.3	Electrical I/Fs Impacts Orbiter / SRB Subsystems
1.2.4	Transportation & Handling I/Fs

Volume II
Appendix D.4
Fault Tree Elements Not Closed

This appendix contains fault tree elements that were not closed or could not be completely closed by the Board by the end of the *Columbia* investigation. In some cases, a fault tree element may never be closed since neither analysis nor data is available to rule that element out as a potential cause. In some cases, the lower-level fault trees contained in this appendix will cause a higher-level fault tree in Appendix D.3 to remain open as well (annotated as "Open due to lower element" in Appendix D.3).

THIS PAGE INTENTIONALLY LEFT BLANK

Fault Tree Elements Not Closed

By Group III
James N. Hallock, Ph.D., G. Scott Hubbard, Douglas D. Osheroff, Ph.D.,
Roger E. Tetrault, Sheila E. Widnall, Ph.D.
Captain David Bawcom, Captain Anne-Marie Contraras

Fault tree analysis is a deductive, top-down method of analyzing an undesirable event (e.g., the loss of crew and vehicle during re-entry) to determine all the ways that the event can happen, based on the behavior of the components, lower-level assemblies, and interfaces. Fault trees are visual representations of all the events that can occur in a system to cause a system to fail.

As noted in Chapter 4, NASA chartered six teams to develop fault trees for each of the Shuttle's major components: the Orbiter, Space Shuttle Main Engine (SSME), Reusable Solid Rocket Motor (RSRM), Solid Rocket Booster (SRB), External Tank (ET), and Payload. In addition, a seventh Systems Integration fault tree team analyzed failures involving two or more Shuttle components.

Some of the element closures will extend beyond the writing of this report. In addition, there will be some elements that can never be closed as neither data nor analysis can unambiguously rule out a contribution to the *Columbia* accident. Below are listed fault tree elements that were not closed by the Board as of the writing of the report. The elements are grouped by their potential for contributing either directly or indirectly to the accident. The first group contains elements that are believed to have contributed to the accident. Here, contributed means that the element was an initiating event or a likely cause of the accident. The second group contains elements that could not be closed and may or may not have contributed to the accident. These elements are potential causes or factors in this accident. The third group contains elements that could not be closed, but are unlikely to have contributed to the accident. Appendix D.3 lists all the elements that were closed and thus eliminated from consideration as a cause or factor of this accident.

Table 1: Fault Tree Elements Not Closed, and Likely Contributed to the Accident.

BRANCH	ELEMENT NUMBER	DESCRIPTION OF FAULT TREE ELEMENT
Orbiter	SFOML-WING-11-5	ET Debris Impact on Ascent. Launch photography and onboard sensors indicated that bipod foam struck the underside of the left wing leading edge.
Orbiter	SFOML-WING-11-66	Loss of RCC Panel Due to T-Seal Failure. The T-seals between RCC panels 7 and 8 and 8 and 9 could have been the initial location of the breach.
Orbiter	SFOML-WING-12-9	RCC Damage Due to Impact Caused Sneak Flow Causing Loss of Panel. Damage could have been initiated at the RCC panel or an adjoining T-seal.
ET	1.1.1.4.1.1.1.1	BX-250/Forward Bipod Fittings/Inadequate Design Methodology. Forward bipod fitting assembly debris due to an inadequate design methodology.
ET	1.1.1.5.1.1.1.1	SLA-561/Forward Bipod Fittings/Inadequate Design Methodology. Forward bipod assembly Super Light Ablator application with inadequate design methodology causes debris.

BRANCH	ELEMENT NUMBER	DESCRIPTION OF FAULT TREE ELEMENT
ET	1.1.1.5.1.2.1.1	SLA-561/Plate Connector-Bipod Fitting/ Inadequate Design Methodology. Forward bipod fitting plate connector Super Light Ablator application with inadequate design methodology causes debris.
ET	1.1.1.4.1.1.3.2.1	BX-250/Forward Bipod Fittings/Debris Due to Inadequate Manufacturing Process Plan. Forward bipod fitting assembly debris due to an inadequate manufacturing process plan.
ET	1.1.1.4.1.1.3.3.6	BX-250/Forward Bipod Fittings/Debris Due to MAF Material Processing. Forward bipod fitting assembly debris due to inadequately defined acceptance testing during Machoud Assembly Facility Processing.
ET	1.1.1.4.1.1.3.7	BX-250/Forward Bipod Fittings/Undetected Anomaly. Forward bipod fitting assembly debris due to undetected anomaly during Machoud Assembly Facility processing.
Integration	B561	Transport Mechanism. There are transport mechanisms to facilitate debris striking the orbiter left wing area from viable debris sources (ET, orbiter, and SRB).

The "likely contributed to the accident" entries address the release of debris from the ET and the impact of this debris on the orbiter wing RCC panels or T-seals. Although the Super Light Ablator has not been implicated in the foam release, it cannot be ruled out.

Table 2: Fault Tree Elements Not Closed, and Possibly Contributed to the Accident.

BRANCH	ELEMENT NUMBER	DESCRIPTION OF FAULT TREE ELEMENT
Orbiter	SFOML-WING-8-51	RCC Panel Improper Installation. Addresses improper installation of the wing leading edge RCC as an initiating cause.
Orbiter	SFOML-WING-8-54	RCC Processing/Material Defect. Addresses the possibility that an initial manufacturing or material defect was present in the RCC from the original manufacturing that led to failure.
Orbiter	SFOML-WING-8-57	RCC Substrate Failure Due to Mission Cycles. The lack of NDE inspection leaves this possibility suspect.
Orbiter	SFOML-WING-8-58	RCC Substrate Failure Due to Ground Cycles. The lack of NDE inspection leaves this possibility suspect.
Orbiter	SFOML-WING-8-59	RCC Failure Due to Aging. Investigates the question of RCC aging over time versus mission cycles.
Orbiter	SFOML-WING-12-3	Micrometeoroid Impact on Orbit. Based on the orbiter orientations, the chance of a micrometeorite or orbital debris hitting the RCC leading edge is 1 in 13,800.
Orbiter	SFOML-WING-12-4	Orbital Debris Impact on Orbit. Based on the orbiter orientations, the chance of a micrometeorite or orbital debris hitting the RCC leading edge is 1 in 13,800.
Orbiter	SFOML-WING-11-8	SRB Debris Impact on Ascent. The SRB bolt catcher and the SRB separation motors are possible sources of debris.
SRB	B.1.3.4.4.3.1	Debris Due to Failure of Attach Fasteners, LMC Supplied.
SRB	B.1.3.4.4.3.2	Debris Due to Failure of Bolt Catcher Structure.
SRB	B.1.3.4.4.3.3	Debris Due to Failure of LMC ET Thrust Fitting or Inserts.
SRB	B.1.3.4.4.3.4	Debris Due to Failure of Insulation (SRB/LMC).

The "possibly contributed to the accident" include a number of different means to cause damage to the wing leading edge. The effect of ageing (both operational and calendar) of the RCC is uncertain at best. Certain debris sources are listed here as they could lead to relatively heavy objects hitting the wing leading edge. Micrometeoroids and space debris can also cause a large enough hole in the RCC to allow superheated air to enter the wing.

Table 3: Fault Tree Elements Not Closed, and Unlikely to have Contributed to the Accident.

BRANCH	ELEMENT NUMBER	DESCRIPTION OF FAULT TREE ELEMENT
Orbiter	SFOML-WING-8-60	RCC Failure Due to Test Cycles. Stress testing was done on the RCC T-seal located between panels 9 and 10, inspected, and returned to OV-102.
Orbiter	SFOML-WING-9-20	Loss of RCC Panel due to RCC Panel Fastener Failure. Portions of all the panels were found in the debris field in Texas.
Orbiter	SFOML-WING-10-5	Prelaunch Unidentified Impact While on the Launch Pad. There is high confidence that pad inspections should detect any RCC damage.
Orbiter	SFOML-WING-11-6	Orbiter Caused In-flight Impact on Ascent. All the access panels have been accounted for and the other materials (e.g., tile) are of low mass.
Orbiter	SFOML-WING-11-18	Lift Off (Pad Debris) Impact. There is good foreign object debris discipline maintained at the launch pad.
Orbiter	SFOML-WING-12-94	Orbiter Debris Source from Loss of Tile During Entry. Tiles are low-density material and there are no indications in the debris and other data of a large tile malfunction.
Integration	SFOML-WING-11-9	Orbiter Bird Strike on Ascent. Photo and video evidence did not record a bird strike.
ET	1.1.1.1.1.1.2.5	NCFI 24-124 LO2 Tank Acreage Undetected Anomaly. NCFI 24-124 undetected LO2 tank acreage anomaly during vendor manufacturing or processing causing TPS debris.
ET	1.1.1.1.1.1.3.9	NCFI 24-124 LO2 Tank Acreage Undetected Anomaly. NCFI 24-124 undetected LO2 tank acreage Machoud Assembly Facility processing anomaly causing TPS debris.
ET	1.1.1.1.1.1.4	NCFI 24-124 LO2 Tank Acreage Debris. NCFI 24-124 LO2 tank acreage debris due to KSC processing resulting in a cohesive, shear, delamination, or crack failure of the TPS.
ET	1.1.1.1.2.1.2.8	NCFI 24-124 Intertank Acreage Undetected Anomaly. NCFI 24-124 undetected intertank acreage outside surface vendor manufacturing or processing anomaly causing TPS debris.
ET	1.1.1.1.2.1.3.7	NCFI 24-124 Intertank Acreage Undetected Anomaly. NCFI 24-124 undetected intertank acreage outside surface anomaly during Machoud Assembly Facility processing causing TPS debris.
ET	1.1.1.1.2.1.4	NCFI 24-124 Intertank Acreage Debris Due to KSC Processing. NCFI 24-124 intertank acreage debris due to KSC processing resulting in a cohesive, shear, delamination, or crack failure of the TPS.
ET	1.1.1.1.2.2.2.5	NCFI 24-124 Intertank Acreage Undetected Anomaly. NCFI 24-124 undetected intertank acreage I/T foam machining, cell "L" and +Z stringer panels and thrust panel anomaly during Machoud Assembly Facility processing causing TPS debris.
ET	1.1.1.1.2.2.3	NCFI 24-124 Intertank Acreage Debris. NCFI 24-124 intertank acreage debris due to KSC processing resulting in a cohesive, shear, delamination, or crack failure of the TPS.
ET	1.1.1.1.2.3.2.5	NCFI 24-124 Intertank Acreage Undetected Anomaly. NCFI 24-124 undetected intertank acreage foam venting anomaly during Machoud Assembly Facility processing causing TPS debris.
ET	1.1.1.1.2.3.3	NCFI 24-124 Intertank Acreage Debris. NCFI 24-124 intertank acreage debris due to KSC processing resulting in a cohesive, shear, delamination, or crack failure of the TPS.
ET	1.1.1.1.3.1.2.5	NCFI 24-124 LH2 Tank Acreage Undetected Anomaly. NCFI 24-124 undetected LH2 tank acreage, barrel foam spray anomaly during vendor manufacturing or processing causing TPS debris.
ET	1.1.1.1.3.1.3.9	NCFI 24-124 LH2 Tank Acreage Undetected Anomaly. NCFI 24-124 undetected LH2 tank acreage, barrel foam spray anomaly during Machoud Assembly Facility processing causing TPS debris.

BRANCH	ELEMENT NUMBER	DESCRIPTION OF FAULT TREE ELEMENT
ET	1.1.1.1.3.1.4	NCFI 24-124 LH2 Tank Acreage Debris. NCFI 24-124 LH2 tank acreage debris due to KSC processing resulting in a cohesive, shear, delamination, or crack failure of the TPS.
ET	1.1.1.1.4	NCFI 24-124 LH2 Tank Acreage Debris. External impacts to ET TPS produce NCFI 24-124 debris.
ET	1.1.1.3.1.1	PDL-1034 Bipod Debris. PDL-1034 bipod closeout/final assembly of the forward bipod fittings PDL application resulting in TPS debris.
ET	1.1.1.3.2.1	PDL-1034 LH2 and I/T Splice Debris. PDL-1034 LH2 and I/T splice TPS – I/T to LH2 tank, cell "A" stack and LH2 aft dome apex application causing TPS debris.
ET	1.1.1.3.3.1.3.3	PDL-1034 LO2 and I/T Splice, P/L Bracket 861, and Aero Vents Debris. PDL-1034 LO2 and I/T splice, P/L bracket 861, and aero vents debris due to Machoud Assembly Facility PDL-1034 material processing.
ET	1.1.1.3.3.1.3.7	PDL-1034 LO2 and I/T Splice, P/L Bracket 861, and Aero Vents Undetected Anomaly. PDL-1034 LO2 and I/T splice, P/L bracket 861, and aero vents undetected Machoud Assembly Facility processing anomaly causes TPS debris.
ET	1.1.1.3.4.1.3.3	PDL-1034 LO2 P/L and C/T Brackets Debris. PDL-1034 LO2 P/L and C/T brackets, LO2 tank ice frost ramp debris due to Machoud Assembly Facility PDL-1034 material processing.
ET	1.1.1.3.4.1.3.7	PDL-1034 LO2 P/L and C/T Brackets Undetected Anomaly. PDL-1034 LO2 P/L and C/T brackets, LO2 tank ice frost ramp undetected Machoud Assembly Facility processing anomaly causes TPS debris.
ET	1.1.1.3.4.1.4	PDL-1034 LO2 P/L and C/T Brackets Debris. PDL-1034 LO2 P/L and C/T brackets, LO2 tank ice frost ramp debris due to KSC processing resulting in a cohesive, shear, delamination, or crack failure of the TPS.
ET	1.1.1.3.4.2.4	PDL-1034 LO2 P/L and C/T Brackets Debris. PDL-1034 LO2 P/L and C/T brackets, Sta.371 fairing bracket, Sta.371 pressline hard mount, and I/T por Sta.1075, -Z application causes debris due to KSC processing resulting in a cohesive, shear, delamination, or crack failure of the TPS.
ET	1.1.1.3.5	PDL-1034 LO2 Tank Debris. PDL-1034 LO2 tank foam, LO2 tank ogive and barrel application causes TPS debris.
ET	1.1.1.3.6.1.3.3	PDL-1034 I/T Wedges Debris. PDL-1034 I/T wedges debris due to Machoud Assembly Facility PDL-1034 material processing.
ET	1.1.1.3.6.1.3.6	PDL-1034 I/T Wedges Undetected Anomaly. PDL-1034 I/T wedges undetected Machoud Assembly Facility processing anomaly causes TPS debris.
ET	1.1.1.3.7.1.3.3	PDL-1034 I/T and C/T Brackets and Fairings Debris. PDL-1034 GO2 P/L and C/T I/T support bracket foam debris due to Machoud Assembly Facility PDL-1034 material processing.
ET	1.1.1.3.7.1.3.7	PDL-1034 I/T and C/T Brackets and Fairings Undetected Anomaly. PDL-1034 GO2 P/L and C/T I/T support bracket foam undetected Machoud Assembly Facility processing anomaly causes TPS Debris.
ET	1.1.1.3.7.1.4	PDL-1034 I/T and C/T Brackets and Fairings Debris. PDL-1034 GO2 P/L and C/T I/T support bracket foam debris due to KSC processing resulting in a cohesive, shear, delamination, or crack failure of the TPS.
ET	1.1.1.3.7.2.3.3	PDL-1034 I/T and C/T Brackets and Fairings Debris. PDL-1034 I/T fairings, RSS antennas and Xt 1082.8 P/L C/T support debris due to Machoud Assembly Facility PDL-1034 material processing.
ET	1.1.1.3.7.2.3.7	PDL-1034 I/T and C/T Brackets and Fairings Undetected Anomaly. PDL-1034 I/T fairings, RSS antennas and Xt 1082.8 P/L C/T support undetected Machoud Assembly Facility processing anomaly causes TPS debris.
ET	1.1.1.3.7.2.4	PDL-1034 I/T and C/T Brackets and Fairings Debris. PDL-1034 I/T fairings, RSS antennas and Xt 1082.8 P/L C/T support debris due to KSC processing resulting in a cohesive, shear, delamination, or crack failure of the TPS.

BRANCH	ELEMENT NUMBER	DESCRIPTION OF FAULT TREE ELEMENT
ET	1.1.1.3.7.3.3.3	PDL-1034 I/T and C/T Brackets and Fairings Debris. PDL-1034 I/T press line and cable tray support bracket foam debris due to Machoud Assembly Facility PDL-1034 material processing.
ET	1.1.1.3.7.3.3.7	PDL-1034 I/T and C/T Brackets and Fairings Undetected Anomaly. PDL-1034 I/T press line and cable tray support bracket foam undetected Machoud Assembly Facility processing anomaly causes TPS debris.
ET	1.1.1.3.7.3.4	PDL-1034 I/T and C/T Brackets and Fairings Debris. PDL-1034 I/T press line and cable tray support bracket foam debris due to KSC processing resulting in a cohesive, shear, delamination, or crack failure of the TPS.
ET	1.1.1.3.8.1.3.3	PDL-1034 LO2 Feed Line and Supports (External) Debris. PDL-1034 LO2 feedline yokes and base fitting assembly causes debris due to Machoud Assembly Facility PDL-1034 material processing.
ET	1.1.1.3.8.1.3.7	PDL-1034 LO2 Feed Line and Supports (External) Undetected Anomaly. PDL-1034 undetected LO2 feedline yoke and base fitting assembly anomaly during Machoud Assembly Facility processing causes TPS debris.
ET	1.1.1.3.8.1.4	PDL-1034 LO2 Feed Line and Supports (External) Debris. PDL-1034 LO2 feedline yokes and base fitting assembly debris due to KSC processing resulting in a cohesive, shear, delamination, or crack failure of the TPS.
ET	1.1.1.3.8.2.3.3	PDL-1034 LO2 Feed Line and Supports (External) Debris. PDL-1034 LO2 F/L flanges and elbow tie, Xt1115-2053, and LH2 F/L base debris due to Machoud Assembly Facility PDL-1034 material processing.
ET	1.1.1.3.8.2.3.7	PDL-1034 LO2 Feed Line and Supports (External) Undetected Anomaly. PDL-1034 undetected LO2 F/L flanges and elbow tie, Xt1115-2053, and LH2 F/L base anomaly during Machoud Assembly Facility processing causes TPS debris.
ET	1.1.1.3.8.2.4	PDL-1034 LO2 Feed Line and Supports (External) Debris. PDL-1034 LO2 F/L flanges and elbow tie, Xt1115-2053, and LH2 F/L base debris due to KSC processing resulting in a cohesive, shear, delamination, or crack failure of the TPS.
ET	1.1.1.3.8.3.3.2	PDL-1034 LO2 Feed Line and Supports (External) Debris. PDL-1034 LO2 Aluminum straight section foam debris due to manufacturing process plan.
ET	1.1.1.3.8.3.3.3	PDL-1034 LO2 Feed Line and Supports (External) Debris. PDL-1034 LO2 Aluminum straight section foam debris due to Machoud Assembly Facility PDL-1034 material processing.
ET	1.1.1.3.8.3.3.6	PDL-1034 LO2 Feed Line and Supports (External) Undetected Anomaly. PDL-1034 undetected LO2 Aluminum straight section foam anomaly during Machoud Assembly Facility processing causes TPS debris.
ET	1.1.1.3.8.4.3.3	PDL-1034 LO2 Feed Line and Supports (External) Debris. PDL-1034 LO2 feed line strut foam debris due to Machoud Assembly Facility PDL-1034 material processing.
ET	1.1.1.3.8.4.3.6	PDL-1034 LO2 Feed Line and Supports (External) Undetected Anomaly. PDL-1034 undetected LO2 feed line strut foam anomaly during Machoud Assembly Facility processing causes debris.
ET	1.1.1.3.8.4.4	PDL-1034 LO2 Feed Line and Supports (External) Debris. PDL-1034 LO2 feed line strut foam debris due to KSC processing resulting in a cohesive, shear, delamination, or crack failure of the TPS.
ET	1.1.1.3.9.1	PDL-1034 LO2 PAL Ramp Debris. PDL-1034 LO2 PAL ramp foam application – LO2 tank/intertank PAL ramp causes TPS debris.
ET	1.1.1.3.22	PDL-1034 External Impacts Causes Debris. External impacts to the ET TPS produces PDL-1034 debris.
ET	1.1.1.4.1.1.3.1.1	BX-250 Bipod Inadequately Trained Operator. BX-250 bipod, forward bipod fitting assembly debris due to inadequately trained operator during Machoud Assembly Facility processing.

BRANCH	ELEMENT NUMBER	DESCRIPTION OF FAULT TREE ELEMENT
ET	1.1.1.4.1.1.3.3.2	BX-250 Bipod Debris. BX-250 bipod, forward bipod fitting assembly debris due to improper storage during Machoud Assembly Facility processing.
ET	1.1.1.4.1.1.3.3.5	BX-250 Bipod Improper Application Process. BX-250 bipod, forward bipod fitting assembly debris due to improper application process during Machoud Assembly Facility processing.
ET	1.1.1.4.1.1.4	BX-250 Bipod Debris. BX-250 bipod, forward bipod fitting assembly debris due to KSC processing resulting in a cohesive, shear, delamination, or crack failure of the TPS.
ET	1.1.1.4.2.1.1.1	BX-250 LH2 and I/T Splice Inadequate Design Methodology. BX-250 LH2 and I/T splice inadequate design methodology causes TPS debris.
ET	1.1.1.4.2.1.3.1.1	BX-250 LH2 and I/T Splice Inadequately Trained Operator. BX-250 LH2 and I/T splice causes TPS debris due to inadequately trained operator during Machoud Assembly Facility processing.
ET	1.1.1.4.2.1.3.3.2	BX-250 LH2 and I/T Splice Improper Storage. BX-250 LH2 and I/T splice causes TPS debris due to improper storage.
ET	1.1.1.4.2.1.3.3.5	BX-250 LH2 and I/T Splice Improper Application Process. BX-250 LH2 and I/T splice causes TPS debris due to improper application process.
ET	1.1.1.4.2.1.3.3.6	BX-250 LH2 and I/T Splice Inadequately Defined Acceptance Testing. BX-250 LH2 and I/T splice causes TPS debris due to inadequately defined acceptance testing.
ET	1.1.1.4.2.1.3.8	BX-250 LH2 and I/T Splice Inadequate Resolution of Identified Anomaly. BX-250 undetected LH2 and I/T splice anomaly during Machoud Assembly Facility material processing causes TPS debris.
ET	1.1.1.4.2.1.4	BX-250 LH2 and I/T Splice Debris. BX-250 LH2 and I/T splice debris due to KSC processing resulting in a cohesive, shear, delamination, or crack failure of the TPS.
ET	1.1.1.4.3.1.3.1.1	BX-250 LO2 and IT Splice, P/L Bracket 861, and Aero Vents Debris. BX-250 LO2 and IT splice, P/L bracket 861, and aero vents causes TPS debris due to inadequately trained operator.
ET	1.1.1.4.3.1.3.3.2	BX-250 LO2 and IT Splice, P/L Bracket 861, and Aero Vents Debris. BX-250 LO2 and IT splice, P/L bracket 861, and aero vents causes TPS debris due to improper storage.
ET	1.1.1.4.3.1.3.3.5	BX-250 LO2 and IT Splice, P/L Bracket 861, and Aero Vents Debris. BX-250 LO2 and IT splice, P/L bracket 861, and aero vents causes TPS debris due to improper application process.
ET	1.1.1.4.3.1.3.8	BX-250 LO2 and IT Splice, P/L Bracket 861, and Aero Vents Debris. BX-250 LO2 and IT splice, P/L bracket 861, and aero vents causes TPS debris due to an anomaly during Machoud Assembly Facility processing.
ET	1.1.1.4.3.1.4	BX-250 LO2 and IT Splice, P/L Bracket 861, and Aero Vents Debris. BX-250 LO2 and IT splice, P/L bracket 861, and aero vents causes TPS debris due to KSC processing resulting in a cohesive, shear, delamination, or crack failure of the TPS.
ET	1.1.1.4.4.1.3.3.2	BX-250 I/T Wedges. BX-250 I/T wedges causes TPS debris due to improper storage.
ET	1.1.1.4.4.1.3.3.5	BX-250 I/T Wedges. BX-250 I/T wedges causes TPS debris due to improper application process during material processing.
ET	1.1.1.4.4.1.3.6	BX-250 I/T Wedges. BX-250 undetected I/T wedge anomaly during Machoud Assembly Facility processing causes TPS debris.
ET	1.1.1.4.5.1.3.3.2	BX-250 LO2 Feed Line Supports (External). BX-250 LO2 feed line supports (external) causes TPS debris due to improper storage.
ET	1.1.1.4.5.1.3.3.5	BX-250 LO2 Feed Line Supports (External). BX-250 LO2 feed line supports (external) causes TPS debris due to improper application process of the Machoud Assembly Facility BX-250 material processing.

BRANCH	ELEMENT NUMBER	DESCRIPTION OF FAULT TREE ELEMENT
ET	1.1.1.4.5.1.3.4.5	BX-250 LO2 Feed Line Supports (External). BX-250 LO2 feed line supports (external) causes TPS debris due to improper application process of the Machoud Assembly Facility DPTU adhesive processing.
ET	1.1.1.4.5.1.3.7	BX-250 LO2 Feed Line Supports (External). BX-250 LO2 feed line supports (external) causes TPS debris due to an anomaly during Machoud Assembly Facility BX-250 materials processing.
ET	1.1.1.4.5.1.4	BX-250 LO2 Feed Line Supports (External). BX-250 LO2 feed line supports (external) causes TPS debris due to KSC processing resulting in a cohesive, shear, delamination, or crack failure of the TPS.
ET	1.1.1.4.6.1.3.1.1	BX-250 LO2 PAL Ramp. BX-250 LO2 PAL ramp causes TPS debris due to inadequately trained operator.
ET	1.1.1.4.6.1.3.3.2	BX-250 LO2 PAL Ramp. BX-250 LO2 PAL ramp causes TPS debris due to improper storage.
ET	1.1.1.4.6.1.3.3.5	BX-250 LO2 PAL Ramp. BX-250 LO2 PAL ramp causes TPS debris due to improper application process.
ET	1.1.1.4.6.1.3.3.6	BX-250 LO2 PAL Ramp. BX-250 LO2 PAL ramp causes TPS debris due to inadequately defined acceptance testing.
ET	1.1.1.4.6.1.3.7	BX-250 LO2 PAL Ramp. BX-250 undetected LO2 PAL ramp anomaly during Machoud Assembly Facility processing causes debris.
ET	1.1.1.4.6.1.4	BX-250 LO2 PAL Ramp. BX-250 LO2 PAL ramp debris due to KSC processing resulting in a cohesive, shear, delamination, or crack failure of the TPS.
ET	1.1.1.4.18	BX-250 External Impacts. BX-250 external impacts to the ET TPS produces debris.
ET	1.1.1.5.1.1.3.7	SLA-561 Bipod. SLA-561 undetected bipod, forward bipod fitting assembly SLA application anomaly during Machoud Assembly Facility processing causes debris.
ET	1.1.1.5.1.2.3.7	SLA-561 Bipod. SLA-561 undetected bipod, forward bipod fitting plate connector SLA application anomaly during Machoud Assembly Facility processing causes debris.
ET	1.1.1.5.1.3.3.7	SLA-561 Bipod. SLA-561 undetected bipod, forward bipod fitting strut SLA application anomaly during Machoud Assembly Facility processing causes debris.
ET	1.1.1.5.2.1.3.7	SLA-561 LO2 C/Ts and Fairings. SLA-561 undetected LO2 GO2 P/L Barry mounts on tank, Sta. 371.0 C/T bracket, and foam trims for P/L flange anomaly during Machoud Assembly Facility processing causes TPS debris.
ET	1.1.1.5.2.1.4	SLA-561 LO2 C/Ts and Fairings. SLA-561 undetected LO2 GO2 P/L Barry mounts on tank, Sta. 371.0 C/T bracket, and foam trims for P/L flange TPS debris due to KSC processing resulting in a cohesive, shear, delamination, or crack failure of the TPS.
ET	1.1.1.5.2.2.3.7	SLA-561 LO2 C/Ts and Fairings. SLA-561 undetected LO2 P/L brackets Sta. 404.34 thru Sta. 718.04 SLA application anomaly during Machoud Assembly Facility processing causes TPS debris.
ET	1.1.1.5.2.2.4	SLA-561 LO2 C/Ts and Fairings. SLA-561 LO2 LO2 P/L brackets Sta. 404.34 thru Sta. 718.04 debris due to KSC processing resulting in a cohesive, shear, delamination, or crack failure of the TPS.
ET	1.1.1.5.2.3.3.7	SLA-561 LO2 C/Ts and Fairings. SLA-561 undetected LO2 tank cable tray SLA application anomaly during Machoud Assembly Facility processing causes TPS debris.
ET	1.1.1.5.2.3.4	SLA-561 LO2 C/Ts and Fairings. SLA-561 LO2 tank cable tray TPS debris due to KSC processing resulting in a cohesive, shear, delamination, or crack failure of the TPS.
ET	1.1.1.5.2.4.3.7	SLA-561 LO2 C/Ts and Fairings. SLA-561 undetected LO2 tank P/L and C/T support Sta. 371.0 SLA application anomaly during Machoud Assembly Facility processing causes TPS debris.

BRANCH	ELEMENT NUMBER	DESCRIPTION OF FAULT TREE ELEMENT
ET	1.1.1.5.2.4.4	SLA-561 LO2 C/Ts and Fairings. SLA-561 LO2 tank P/L and C/T support Sta. 371.0 debris due to KSC processing resulting in a cohesive, shear, delamination, or crack failure of the TPS.
ET	1.1.1.5.2.5.3.7	SLA-561 LO2 C/Ts and Fairings. SLA-561 undetected LO2 cable tray cover SLA application anomaly during Machoud Assembly Facility processing causes TPS debris.
ET	1.1.1.5.2.5.4	SLA-561 LO2 C/Ts and Fairings. SLA-561 LO2 cable tray cover TPS debris due to KSC processing resulting in a cohesive, shear, delamination, or crack failure of the TPS.
ET	1.1.1.5.2.6.3.7	SLA-561 LO2 C/Ts and Fairings. SLA-561 undetected LO2 tank C/T covers and C/T fairing cover SLA application anomaly during Machoud Assembly Facility processing causes TPS debris.
ET	1.1.1.5.2.6.4	SLA-561 LO2 C/Ts and Fairings. SLA-561 LO2 tank C/T covers and C/T fairing cover TPS debris due to KSC processing resulting in a cohesive, shear, delamination, or crack failure of the TPS.
ET	1.1.1.5.2.7.3.7	SLA-561 LO2 C/Ts and Fairings. SLA-561 undetected LO2 tank C/T gap closure SLA application anomaly during Machoud Assembly Facility processing causes TPS debris.
ET	1.1.1.5.2.7.4	SLA-561 LO2 C/Ts and Fairings. SLA-561 LO2 tank C/T gap closure TPS debris due to KSC processing resulting in a cohesive, shear, delamination, or crack failure of the TPS.
ET	1.1.1.5.2.8.3.7	SLA-561 LO2 C/Ts and Fairings. SLA-561 undetected LO2 tank P/L and C/T support bracket SLA application anomaly during Machoud Assembly Facility processing causes debris.
ET	1.1.1.5.2.8.4	SLA-561 LO2 C/Ts and Fairings. SLA-561 LO2 tank P/L and C/T support bracket TPS debris due to KSC processing resulting in a cohesive, shear, delamination, or crack failure of the TPS.
ET	1.1.1.5.2.9.3.7	SLA-561 LO2 C/Ts and Fairings. SLA-561 undetected LO2 composite nose cone seal SLA application anomaly during Machoud Assembly Facility processing causes TPS debris.
ET	1.1.1.5.2.9.4	SLA-561 LO2 C/Ts and Fairings. SLA-561 LO2 composite nose cone seal TPS debris due to KSC processing resulting in a cohesive, shear, delamination, or crack failure of the TPS.
ET	1.1.1.5.3.1.3.7	SLA-561 Press Line Barry Mounts. SLA-561 undetected press line Barry mounts SLA application anomaly during Machoud Assembly Facility processing causes TPS debris.
ET	1.1.1.5.3.1.4	SLA-561 Press Line Barry Mounts. SLA-561 press line Barry mounts debris due to KSC processing resulting in a cohesive, shear, delamination, or crack failure of the TPS.
ET	1.1.1.5.4.1.2.7	SLA-561 ET/SRB Forward Bolt Catcher. SLA-561 undetected ET/SRB forward bolt catcher SLA application anomaly during Machoud Assembly Facility processing causes TPS debris.
ET	1.1.1.5.4.1.3	SLA-561 ET/SRB Forward Bolt Catcher. SLA-561 ET/SRB forward bolt catcher debris due to KSC processing resulting in a cohesive, shear, delamination, or crack failure of the TPS.
ET	1.1.1.5.5.2.3.7	SLA-561 I/T Fairings. SLA-561 undetected I/T fairing LO2 feedline SLA application anomaly during Machoud Assembly Facility processing causes TPS debris.
ET	1.1.1.5.5.2.4	SLA-561 I/T Fairings. SLA-561 I/T fairing LO2 feedline debris due to KSC processing resulting in a cohesive, shear, delamination, or crack failure of the TPS.
ET	1.1.1.5.5.3.3.7	SLA-561 I/T Fairings. SLA-561 undetected I/T fairing LO2 tank cable tray SLA application anomaly during Machoud Assembly Facility processing causes TPS debris.
ET	1.1.1.5.5.3.4	SLA-561 I/T Fairings. SLA-561 I/T fairing LO2 tank cable tray debris due to KSC processing resulting in a cohesive, shear, delamination, or crack failure of the TPS.
ET	1.1.1.5.6.1.3.7	SLA-561 LO2 Feed Line Supports. SLA-561 undetected LO2 yoke feed line supports SLA application anomaly during Machoud Assembly Facility processing causes TPS debris.
ET	1.1.1.5.6.1.4	SLA-561 LO2 Feed Line Supports. SLA-561 LO2 yoke feed line supports debris due to KSC processing resulting in a cohesive, shear, delamination, or crack failure of the TPS.
ET	1.1.1.5.13	SLA-561 External Impacts to ET TPS. External impacts to ET TPS produces SLA-561 debris.

BRANCH	ELEMENT NUMBER	DESCRIPTION OF FAULT TREE ELEMENT
ET	1.1.1.6.1.1.3.9	MA-25S Bipod Undetected Anomaly. MA-25S undetected bipod strut MA-25S application anomaly during Machoud Assembly Facility processing causes TPS debris.
ET	1.1.1.6.1.1.4	MA-25S Bipod Debris Due to Processing. MA-25S bipod strut TPS debris due to KSC processing resulting in a cohesive, shear, delamination, or crack failure of the TPS.
ET	1.1.1.6.3	MA-25S External Impacts to ET TPS. External impacts to ET TPS produces MA-25S bipod debris.
ET	1.1.1.7.1.1.3.3.2	SS-1171 LO2 Feed Line and Supports (External). SS-1171 LO2 feed line aluminum straight section foam application causes TPS debris due to improper storage.
ET	1.1.1.7.1.1.3.3.5	SS-1171 LO2 Feed Line and Supports (External). SS-1171 LO2 feed line aluminum straight section foam application causes TPS debris due to improper application.
ET	1.1.1.7.1.1.3.6	SS-1171 LO2 Feed Line and Supports (External). SS-1171 undetected LO2 feed line aluminum straight section foam application anomaly during Machoud Assembly Facility processing causes debris.
ET	1.1.1.7.1.1.4	SS-1171 LO2 Feed Line and Supports (External). SS-1171 LO2 feed line aluminum straight section foam debris due to KSC processing resulting in a cohesive, shear, delamination, or crack failure of the TPS.
ET	1.1.1.7.1.2.3.3.2	SS-1171 LO2 Feed Line and Supports (External). SS-1171 LO2 feed line flex section foam application causes TPS debris due to improper storage.
ET	1.1.1.7.1.2.3.3.5	SS-1171 LO2 Feed Line and Supports (External). SS-1171 LO2 feed line flex section foam application causes TPS debris due to improper application.
ET	1.1.1.7.1.2.3.6	SS-1171 LO2 Feed Line and Supports (External). SS-1171 undetected LO2 feed line flex section foam application anomaly during Machoud assembly Facility processing causes debris.
ET	1.1.1.7.1.2.4	SS-1171 LO2 Feed Line and Supports (External). SS-1171 LO2 feed line flex section foam debris due to KSC processing resulting in a cohesive, shear, delamination, or crack failure of the TPS.
ET	1.1.1.7.1.3.3.3.2	SS-1171 LO2 Feed Line and Supports (External). SS-1171 LO2 feed line yoke application causes TPS debris due to improper storage.
ET	1.1.1.7.1.3.3.3.5	SS-1171 LO2 Feed Line and Supports (External). SS-1171 LO2 feed line yoke application causes TPS debris due to improper application.
ET	1.1.1.7.1.3.3.6	SS-1171 LO2 Feed Line and Supports (External). SS-1171 undetected LO2 feed line yoke application anomaly during Machoud Assembly Facility processing causes debris.
ET	1.1.1.7.1.3.4	SS-1171 LO2 Feed Line and Supports (External). SS-1171 LO2 feed line yoke foam debris due to KSC processing resulting in a cohesive, shear, delamination, or crack failure of the TPS.
ET	1.1.1.7.6	SS-1171 LO2 Feed Line and Supports (External). External impacts to ET TPS produces SS-1171 debris.
ET	1.1.2.13.2	Non-TPS Debris. Ice - There is no indication from the final inspection results or Ice monitoring activity of STS-107/ET-93 to indicate external ice was a contributor but it cannot be 100% ruled out.
ET	1.1.2.13.5	Non-TPS Debris From Interface. This element investigated debris potential due to design deficiencies, inadequate processing, or mission problems, and found no evidence of non-TPS debris striking the left wing of STS-107 during lift-off and ascent but it cannot be 100% ruled out.
ET	1.2.1.1.3.5	Structural I/Fs EO-1 Forward Attach I/F. Structural I/Fs EO-1 forward bipod attach interface incorrect parts assembly, lack of torque sequencing requirements on strut/fitting assembly bolts could lead to inadequate preloads resulting in one or more bolts/nuts loosening and being released as debris.

BRANCH	*ELEMENT NUMBER*	*DESCRIPTION OF FAULT TREE ELEMENT*
ET	1.2.1.1.3.6	Structural I/Fs EO-1 Forward Attach I/F. Structural I/Fs EO-1 forward bipod attach interface incorrect parts installation, lack of torque requirement on spindle fitting safety wired bolts could cause local TPS debris due to vibration effects.
ET	1.2.1.1.5.4	Structural I/Fs EO-1 Forward Attach I/F. Structural I/Fs EO-1 forward bipod attach interface bipod hardware/components under foam are exposed during ascent and becomes debris, investigated bipod heater connector plate becoming debris.
ET	1.2.1.7.3.1	Structural I/Fs EB-1 Forward SRB Attach –Y and EB-2 Forward SRB Attach +Y. EB-1 forward SRB attach –Y and EB-2 forward SRB attach +Y incorrect part materials usage, investigation found Loctite fastener compound used in the assembly of the SRB fitting did not have recorded traceability. Shelf life could have been exceeded possibly reducing capabilities and allowed associated hardware debris.
ET	1.2.1.7.4.1.1.4	EB-1 Forward SRB Attach –Y & EB-2 Forward SRB Attach +Y Incorrect Parts Installation / SRB Mate. One finding was related to failure of the OMI to call out performance and verification of break away torque on the RSS fairing installation which could potentially result in the loss of a fastener.
SRB	B.1.3.1	Nose Cap Assembly Damage/Malfunction Causes Debris. By design, the SRB nose cap assemblies are ejected from the SRBs during the parachute deployment sequence and are not recovered. There is no evidence (film review and post-flight inspection) of any anomalous behavior.
SRB	B.1.3.1.1	Loss of TPS Causes Debris. Film review confirmed both nose caps were attached during ascent and nominal separation from the external tank and postflight photos and retrieval video review confirmed no loss of MCC-1 from the SRB retrieved hardware other than from splashdown or retrieval and tow back operations. Post flight inspection of the nose cap interface plane on the recovered frustums showed no evidence of abnormalities.
SRB	B.1.3.2.4.1	Debris from BSM Plume. Non-propellants have been identified that ablate during motor firing and generated debris. This debris includes Room Temperature Vulcanizing (RTV) sealant, Conoco grease, ink stamp ID numbers. In addition, contamination / foreign materials have been noted during manufacturing to include RTV, neoprene, lead shot, and paint chips.
SRB	B.1.3.2.4.2	Debris Ejection from Motor (Forward BSM). Standing water in the BSM has occurred in the past and can lead to unburned propellant being a debris source. Enhanced leak tests have been introduced before STS 107 to avoid this problem. During STS 107 pad stay, 8.68 inches of rain was recorded.

There are many ways that the space shuttle can be damaged. Debris sources and manufacturing quality control make up most of the items in the above table. Although "unlikely" in the *Columbia* accident, they must be examined and diligently reviewed so that they do not become contributors in the future.

Volume II
Appendix D.5
Space Weather Conditions

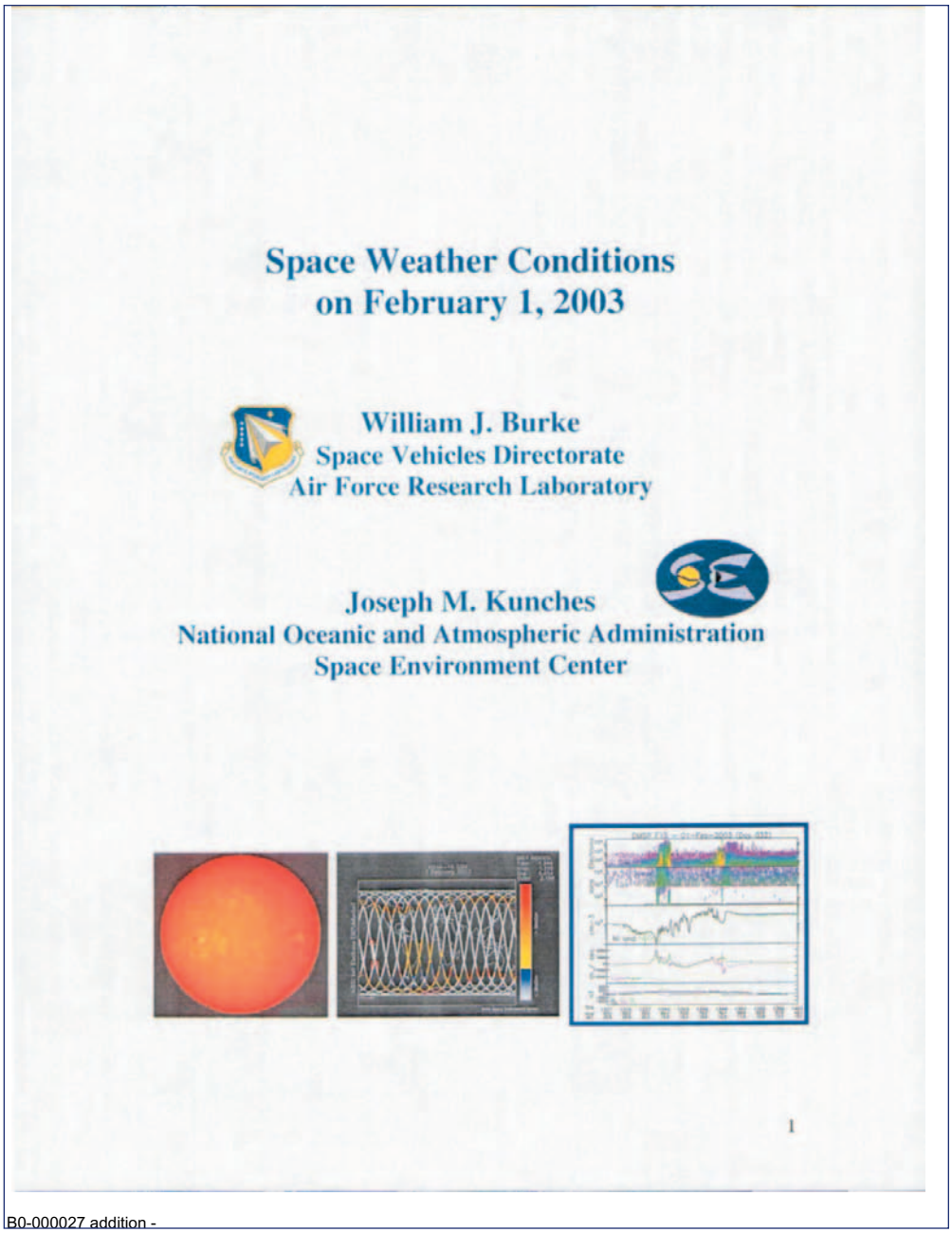
This appendix provides a detailed discussion of space weather (the action of highly energetic particles, primarily from the Sun, in the outer layer of the Earth's atmosphere) and the potential effects of space weather on the Orbiter on February 1, 2003. This investigation was originally prompted by public claims of unusually active space weather conditions during the mission and by a photograph that claimed to show a lightning bolt striking *Columbia* at an altitude of 230,000 feet over California during re-entry. The report concludes that space weather was unlikely to have played a role in the loss of *Columbia*.

This is a document commissioned by the Columbia Accident Investigation Board and is published here as written, without editing. The conclusions drawn in this report do not necessarily reflect the conclusions of the Board; when there is a conflict, the statements in Volume I of the Columbia Accident Investigation Board Report take precedence.

THIS PAGE INTENTIONALLY LEFT BLANK

Space Weather Conditions

Submitted by William J. Burke, Space Vehicle Directorate, Air Force Research Laboratory
Joseph M. Kunches, National Oceanic and Atmosphereic Administration Space Environment Center



Space Weather Conditions
on February 1, 2003

William J. Burke
Space Vehicles Directorate
Air Force Research Laboratory

Joseph M. Kunches
National Oceanic and Atmospheric Administration
Space Environment Center

1

B0-000027 addition -

Table of Contents

1.0 Introduction 3
2.0 A Space Weather Tutorial 3
2.1 Working Definitions 3
2.2 Space Weather Characteristics 4
2.3 Solar Effects 5
2.4 Radiation Effects 9
2.5 Equatorial Plasma Bubbles 11
3.0 Space Weather Conditions on February 1, 2003 12
3.1 Interplanetary Measurements from ACE 12
3.2 LEO Measurements from DMSP 13
3.3 LEO Measurements from POES 18
3.4 Charging Effects 20
3.5 Geostationary Orbit Measurements 21
3.6 Ground Based Measurements 25
4.0 Summary and Conclusions 27
5.0 Acronyms 28

B0-000027 addition - SFOML-WING-6-14.pdf CTF091-1758

Geospace Weather Conditions on February 1, 2003

William J. Burke
Air Force Research Laboratory
Space Vehicles Directorate
Hanscom AFB, MA 01731

Joseph M. Kunches
National Oceanic and Atmospheric Administration
Space Environment Center
Boulder, CO 80305

1.0 Introduction

This report considers the possibility that space weather conditions played a role in the loss of the space shuttle Columbia. It was first presented to the Columbia Accident Investigation Board (CAIB) in Houston, Texas, on March 3, 2003, consequent to reported observations that a coronal mass ejection (CME) driven shock passed the Earth on February 1, 2003. The first part of this report is a tutorial on space weather with emphasis on the electrodynamics of the geospace environment. The second part reviews plasma, particle, and field measurements taken on February 1, 2003, from multiple space and ground based sources. These data clearly show that up to the time of the loss of Columbia, at approximately 14:09 Greenwich Mean Time (GMT), the geospace environment was quiet. Effects of the CME were not observed at Earth until several hours after the accident. It is highly unlikely that any known space weather effect played a role in the loss of Columbia.

2.0 A Space Weather Tutorial

We begin the tutorial with several working definitions, then examine specific space weather characteristics for both typical and stormtime conditions.

2.1 Working Definitions

The term "space weather" describes the systematic variability of geospace environments that occurs on day-to-day or shorter time scales and affects the performance of space related systems. We distinguish weather from climatological effects that occur on year-to-year or solar-cycle time scales. "Systematic variability" refers to repeatedly observed phenomena whose main lines of causality are understood. The "geospace environment" includes the region around the Earth extending from an altitude of approximately 60 km to the magnetopause. The magnetopause is the boundary between regions dominated by the Earth's magnetic field and interplanetary

B0-000027 addition - SFOML-WING-6-14.pdf CTF091-1759

plasmas, particles, and fields. The Sun is the ultimate source of most space weather effects. Meteorites, galactic cosmic rays, and tropospheric electric fields are notable exceptions. However, the internal or coupled electrodynamics of the magnetosphere and ionosphere generally represent the immediate causes of space weather effects. The systems affected by space environmental changes are many, ranging from orbiting satellites to communications links and electrical power distribution networks.

Before considering actual space weather measurements it is useful to recognize that space physicists think in terms of a multi-dimensional world. In addition to the normal three dimensions of our every day lives, they also consider the energies or ionization states as added dimensions characterizing particle environments found in geospace. For example, the "plasmasphere" and the "radiation belts" occupy almost the same region of physical space. However, plasmaspheric particles have thermal energies of a few electron volts (eV) while radiation belt particle energies are in the millions of electron volts (MeV) range. The terms "thermosphere" and "ionosphere" describe different particles of the same energies, neutral and ionized atoms and molecules, respectively, which are found in the same region of space at altitudes above 60 km. Most names given to describe the different regions of space are phenomenological and were assigned by their discoverers. The term "radiation belts" probably reflects the shocked reaction of one of Professor James Van Allen's graduate students to the first Geiger counter measurements on Explorer 1, "Space is radioactive!"

2.2 Space Weather Characteristics

In considering space weather effects it is useful to have some idea of the differences between typical and disturbed conditions (Table 1). The driver for most geospace weather lies in the solar wind that originates in the Sun's corona and terminates at the boundary with interstellar space. At 1 astronomical unit (AU), the distance between the Sun and Earth (~ 1.5 10^8 km), typical solar wind densities and speeds are approximately 5 cm^{-3} and 400 km/s, respectively. Under disturbed conditions they can rise to greater than 20 cm^{-3} and 1,000 km/s, respectively. The dynamic pressure of the solar wind (~1 nano-Pascal (nPa)) compresses the Earth's magnetic field on the dayside and extends it into a long cylinder called the magnetotail. The convenient unit for measuring distance in the magnetosphere is an Earth radius (1 $R_E \approx 6387$ km). Under typical conditions the subsolar magnetopause is at ~10 R_E. When conditions become disturbed the solar wind's dynamic pressure can exceed 10 nPa and the magnetopause is pushed earthward of geostationary orbit (~6.6 R_E).

Table 1. Solar Wind Characteristics

Parameter	Typical	Disturbed
Density	5 – 10 cm^{-3}	20 - 100 cm^{-3}
Velocity	400 km/s	700 km/s
Pressure	1 – 2 nPa	> 10 nPa
IMF	5 - 10 nT	20 - 60 nT

B0-000027 addition - SFOML-WING-6-14.pdf CTF091-1760

plasmas, particles, and fields. The Sun is the ultimate source of most space weather effects. Meteorites, galactic cosmic rays, and tropospheric electric fields are notable exceptions. However, the internal or coupled electrodynamics of the magnetosphere and ionosphere generally represent the immediate causes of space weather effects. The systems affected by space environmental changes are many, ranging from orbiting satellites to communications links and electrical power distribution networks.

Before considering actual space weather measurements it is useful to recognize that space physicists think in terms of a multi-dimensional world. In addition to the normal three dimensions of our every day lives, they also consider the energies or ionization states as added dimensions characterizing particle environments found in geospace. For example, the "plasmasphere" and the "radiation belts" occupy almost the same region of physical space. However, plasmaspheric particles have thermal energies of a few electron volts (eV) while radiation belt particle energies are in the millions of electron volts (MeV) range. The terms "thermosphere" and "ionosphere" describe different particles of the same energies, neutral and ionized atoms and molecules, respectively, which are found in the same region of space at altitudes above 60 km. Most names given to describe the different regions of space are phenomenological and were assigned by their discoverers. The term "radiation belts" probably reflects the shocked reaction of one of Professor James Van Allen's graduate students to the first Geiger counter measurements on Explorer 1, "Space is radioactive!"

2.2 Space Weather Characteristics

In considering space weather effects it is useful to have some idea of the differences between typical and disturbed conditions (Table 1). The driver for most geospace weather lies in the solar wind that originates in the Sun's corona and terminates at the boundary with interstellar space. At 1 astronomical unit (AU), the distance between the Sun and Earth (~ 1.5 10^8 km), typical solar wind densities and speeds are approximately 5 cm^{-3} and 400 km/s, respectively. Under disturbed conditions they can rise to greater than 20 cm^{-3} and 1,000 km/s, respectively. The dynamic pressure of the solar wind (~1 nano-Pascal (nPa)) compresses the Earth's magnetic field on the dayside and extends it into a long cylinder called the magnetotail. The convenient unit for measuring distance in the magnetosphere is an Earth radius (1 $R_E \approx 6387$ km). Under typical conditions the subsolar magnetopause is at ~10 R_E. When conditions become disturbed the solar wind's dynamic pressure can exceed 10 nPa and the magnetopause is pushed earthward of geostationary orbit (~6.6 R_E).

Table 1. Solar Wind Characteristics

Parameter	Typical	Disturbed
Density	5 – 10 cm^{-3}	20 - 100 cm^{-3}
Velocity	400 km/s	700 km/s
Pressure	1 – 2 nPa	> 10 nPa
IMF	5 - 10 nT	20 - 60 nT

4

B0-000027 addition - SFOML-WING-6-14.pdf CTF091-1760

plasmas, particles, and fields. The Sun is the ultimate source of most space weather effects. Meteorites, galactic cosmic rays, and tropospheric electric fields are notable exceptions. However, the internal or coupled electrodynamics of the magnetosphere and ionosphere generally represent the immediate causes of space weather effects. The systems affected by space environmental changes are many, ranging from orbiting satellites to communications links and electrical power distribution networks.

Before considering actual space weather measurements it is useful to recognize that space physicists think in terms of a multi-dimensional world. In addition to the normal three dimensions of our every day lives, they also consider the energies or ionization states as added dimensions characterizing particle environments found in geospace. For example, the "plasmasphere" and the "radiation belts" occupy almost the same region of physical space. However, plasmaspheric particles have thermal energies of a few electron volts (eV) while radiation belt particle energies are in the millions of electron volts (MeV) range. The terms "thermosphere" and "ionosphere" describe different particles of the same energies, neutral and ionized atoms and molecules, respectively, which are found in the same region of space at altitudes above 60 km. Most names given to describe the different regions of space are phenomenological and were assigned by their discoverers. The term "radiation belts" probably reflects the shocked reaction of one of Professor James Van Allen's graduate students to the first Geiger counter measurements on Explorer 1, "Space is radioactive!"

2.2 Space Weather Characteristics

In considering space weather effects it is useful to have some idea of the differences between typical and disturbed conditions (Table 1). The driver for most geospace weather lies in the solar wind that originates in the Sun's corona and terminates at the boundary with interstellar space. At 1 astronomical unit (AU), the distance between the Sun and Earth (~ 1.5 10^8 km), typical solar wind densities and speeds are approximately 5 cm^{-3} and 400 km/s, respectively. Under disturbed conditions they can rise to greater than 20 cm^{-3} and 1,000 km/s, respectively. The dynamic pressure of the solar wind (~1 nano-Pascal (nPa)) compresses the Earth's magnetic field on the dayside and extends it into a long cylinder called the magnetotail. The convenient unit for measuring distance in the magnetosphere is an Earth radius (1 R_E = 6387 km). Under typical conditions the subsolar magnetopause is at ~10 R_E. When conditions become disturbed the solar wind's dynamic pressure can exceed 10 nPa and the magnetopause is pushed earthward of geostationary orbit (~6.6 R_E).

Table 1. Solar Wind Characteristics

Parameter	Typical	Disturbed
Density	5 - 10 cm^{-3}	20 - 100 cm^{-3}
Velocity	400 km/s	700 km/s
Pressure	1 - 2 nPa	> 10 nPa
IMF	5 - 10 nT	20 - 60 nT

4

B0-000027 addition - SFOML-WING-6-14.pdf CTF091-1760

A weak interplanetary magnetic field (IMF) is carried by the solar wind and exerts great influence on geospace weather. Typical values of the IMF are in the 5 to 10 nanotesla (nT) range; this can grow to > 40 nT during disturbed times. The IMF interacts efficiently with the Earth's magnetic field through a process called magnetic merging when the IMF has a southward component. In the vicinity of the Earth there are three distinct magnetic topologies: interplanetary field lines with both "feet" in the solar wind, closed magnetic field lines with both "feet" on Earth, and open field lines with one "foot" in the solar wind and the other on the Earth. The region of open field lines is called the polar cap. Energetic particles in the solar wind have fairly easy access to the ionosphere at polar cap latitudes. The solar wind and IMF impose a potential across the polar cap that ranges from a few tens of kilovolts (kV) during magnetic quiet times to > 200 kV during large magnetic storms. Associated electric fields drive currents in the magnetosphere and ionosphere that produce observable magnetic perturbations on the ground. The three most common measures of geomagnetic activity are the three-hour Kp index of solar particle effects, the one-minute averaged auroral electrojet (AE) index, and the one-hour averaged Disturbance Storm Time (Dst) index (Table 2). Kp reflects the intensity of magnetic disturbances measured at mid latitude stations; it varies from < 3 during quiet / moderate times to > 5 under disturbed conditions. AE is a measure of currents flowing in the ionosphere at auroral latitudes; it has values of < 100 nT during quiet times and > 300 nT during disturbances. The Dst index is a globally averaged measure of the stormtime ring current's intensity. During large magnetic storms the westward ring current produces perturbations < -200 nT at low-latitude magnetic stations. On February 1, 2003 around the time of Columbia's reentry shortly before 1400 GMT, geomagnetic indices were low; Kp ranged from 1- to 3+ and Dst measured between +30 and +34.

Table 2. Geomagnetic Indices

Characteristic	Typical	Disturbed
Kp: 3 - hr midlatitude index	< 3	> 5
Dst: 1 - hr ring current	> - 50 nT	< - 100 nT
AE: 1 - min auroral electrojet	< 100 nT	> 300 nT

2.3 Solar Effects

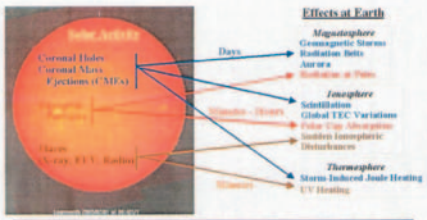
Figure 1 shows a hydrogen alpha image of the Sun taken on February 1, 2003 at Learmonth, Australia, from the National Oceanic and Atmospheric Administration (NOAA) Space Environment Center's Solar Image Archive. It indicates that the chromosphere was relatively quiescent. Also noted are the time scales and geospace locations of three types of solar activity that impact space weather, coronal mass ejections, energetic particles, and flares. For future reference we note that CMEs have broad effects throughout geospace. However, the most significant effects of solar energetic particles (SEPs) are confined to magnetic latitudes of the polar cap.

Figure 2 illustrates the significant differences between simultaneous views of a quiet photosphere in visible light and a turbulent corona seen at extreme ultra violet (EUV) wavelengths. Figure 3 shows the early stage development of a CME as observed

5

B0-000027 addition - SFOML-WING-6-14.pdf CTF091-1761

by a white light coronagraph on the Solar and Heliospheric Satellite (SOHO) which orbits the first Lagrangian point, about one million miles in front of the Earth. Figure 4a plots the range of SEP spectra observed in the solar wind, and Figure 4b demonstrates SEP effects on the active sensor array on SOHO. Random light speckles are excited as MeV SEPs running ahead of a CME pass through elements of the charge coupled device array of the SOHO coronagraph. Fortunately, this type of upset is temporary. A visible-light imager on the Polar satellite acquired the picture of the auroral oval in Figure 4c. It shows that during the great magnetic storm of Bastille Day, July 14, 2000, auroral optical emissions, caused by the impact of energetic electrons on the upper atmosphere, were detected in the southern part of the United States.



The Sun is the principal source of disturbances in the geospace environment

Figure 1. Hydrogen alpha image of the Sun taken on February 1, 2003 at Learmonth, Australia, along with time scales and geospace locations of three types of solar activity that affect space weather.

6

B0-000027 addition - SFOML-WING-6-14.pdf CTF091-1762

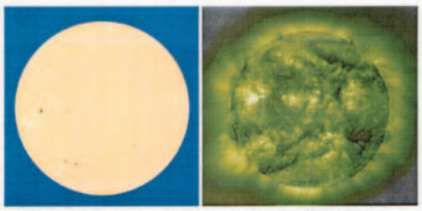


Figure 2. Simultaneous views of a quiet photosphere in visible light and a turbulent corona seen at EUV wavelengths.

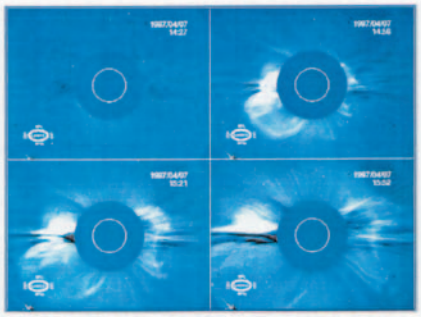


Figure 3. Early stage development of a CME as observed by a white light coronagraph on the SOHO satellite.

7

B0-000027 addition - SFOML-WING-6-14.pdf CTF091-1763

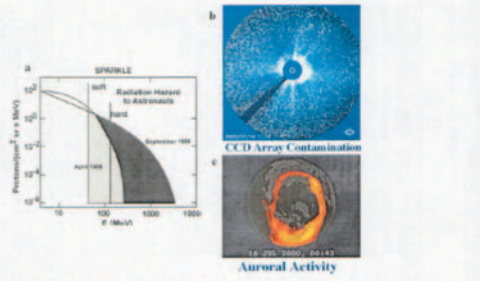


Figure 4. Plot (a) shows the range of SEP spectra observed in the solar wind, (b) SEP effects on the active sensor array on SOHO, and (c) a visible-light image of the auroral oval from the Polar satellite.

Figure 5 shows the most extreme compressional effect of a CME ever observed in the magnetosphere detected by the Combined Release and Radiation Effects Satellite (CRRES) at the onset of the great magnetic storm of March 24, 1991. CRRES flew in a geostationary transfer orbit with perigee at an altitude of ~390 km and apogee at ~6.6 R_E. Figure 5 is a plot of the distribution of protons with energies of ~10.7 MeV in distance from the Earth as a function of orbit number. Attention is directed to the sudden increase in the flux of protons during orbit #587 at radial distances between 2 and 2.5 R_E from the center of the Earth.

CRRES measurements show that the injected high-energy particles were trapped in the magnetosphere and did not have access to the ionosphere. A sudden increase in flux was observed during the inbound pass at ~03:45 UT. This was the first sign of shock-accelerated protons. CRRES then passed through the inner radiation belt, behind the Earth and crossed the spatially extended new radiation belt. The initial injection was narrowly confined in energy to near 40 MeV. During the outbound pass the energies of newly trapped protons filled the 10 to 70 MeV range. These protons were observed continuously for the next seven months (Figure 5) until the spacecraft's battery failed.

8

B0-000027 addition -
SFOML-WING-6-14.pdf
CTF091-1764

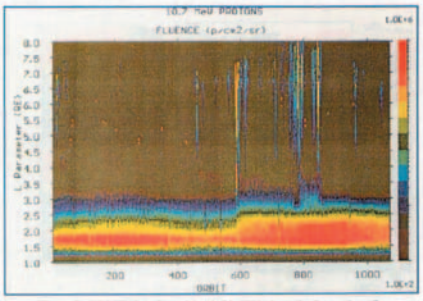


Figure 5. CRRES data from March 24, 1991 show the formation of a new radiation belt.

Modeling studies suggest that the protons first observed near 2 R_E were initially trapped in the outer magnetosphere. They were then accelerated by an intense, earthward-propagating compressional magnetohydrodynamic wave excited after a CME shock impacted the magnetopause. The wave also accelerated and transported energetic electrons into the inner radiation belt. We must emphasize that this was a singular event. The measured amplitude of the compressional magnetic wave that reached the ground at Boulder, Colorado, was 184 nT. During most storms the ground perturbation due to the sudden compression of the magnetosphere is a few tens of nanoTesla.

2.4 Radiation Effects

The CRRES mission objective was to determine the survivability of microelectronic components in natural space-radiation environments. Current national policy calls for using commercial, off the shelf components whenever possible. Without detailed specifications of the radiation environments in which the microelectronic components must operate, this policy would significantly increase the vulnerability of national space assets. The national laboratories are working to reduce this vulnerability in a number of ways, including the Air Force Research Laboratory's (AFRL's) Compact Environmental Anomalies Sensor Experiment (CEASE). CEASE provides real time measurements of total radiation dose to warn of potential space hazards and facilitate

9

B0-000027 addition -
SFOML-WING-6-14.pdf
CTF091-1765

analysis of anomalies such as single event upsets and deep dielectric charging. Other methods include improved prediction and monitoring of space environment hazards and developing practical ways to accelerate the loss of trapped particles from the radiation belts. Figure 6 summarizes the main radiation hazards to which space systems are exposed. The first, called a single event upset, occurs when MeV protons pass through the shielding of microelectronic components leaving trails of ionization and currents that can trigger false commands or altered memory states. Long exposure to doses of energetic protons degrades and destroys the functionality of microelectronic devices.

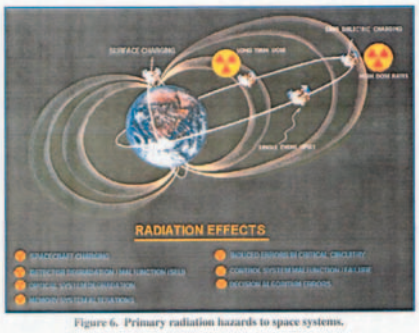


Figure 6. Primary radiation hazards to space systems.

Unexpectedly, the most common upset observed in the CRRES mission derived from a process called deep dielectric charging. This phenomenon occurs when the insulation wrapped around a wire is exposed to prolonged doses of electrons with energies > 100 keV. These energetic electrons penetrate far enough into dielectrics that secondary electrons cannot escape. If enough space charge builds up within the dielectric, Coulomb repulsive forces can exceed the cohesive strength of the material. Charge suddenly starts moving toward the wire and appears as a current burst. The time history of CRRES suggests that dielectrics pass through a long period of slow degradation before deep dielectric events become common. Because the Columbia accident involved failures of insulating tiles, we give special consideration to the susceptibility of the shuttle to deep dielectric charging below.

10

B0-000027 addition -
SFOML-WING-6-14.pdf
CTF091-1766

2.5 Equatorial Plasma Bubbles

The final two figures of the tutorial (Figures 7 and 8) consider a phenomenon known as equatorial plasma bubbles that disrupt transionospheric radio communications. In the post sunset ionosphere, plasma below ~300 km quickly recombines leaving the F layer supported only by the Earth's magnetic field. This is fertile ground for the development of a classic Rayleigh-Taylor instability where a light fluid supports a heavy fluid. Plasma on long magnetic flux tubes interchanges with low-density bubbles that percolate upwards at speeds up to a few kilometers per second. AFRL's Scintillation Network Decision Aid (SCINDA) network (Figure 7) is a ground-based sensor network designed to detect ionospheric scintillations. SCINDA receivers use spaced antenna measurements to provide an estimate of the drift of ionospheric irregularities. The turbulent bubbles and their interactions with radio waves have been modeled extensively in computer simulations at the Naval Research Laboratory. They have also been observed by visible and ultraviolet sensors as elongated streaks of diminished airglow at wavelengths of 6300 and 1356 Å as shown in Figure 8 from the Global Ultraviolet Imager (GUVI) instrument on the Thermosphere, Ionosphere, Mesosphere Energetics and Dynamics Mission (TIMED) satellite. Equatorial plasma bubbles are an evening sector phenomenon and cannot have been responsible for intermittent communications disruptions experienced during Columbia's reentry.

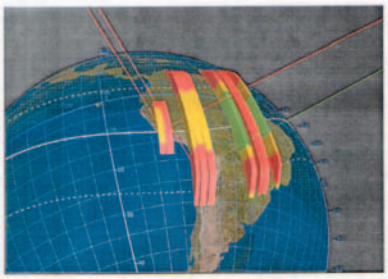


Figure 7. AFRL's SCINDA network of ground-based sensors is designed to detect ionospheric scintillations. SCINDA receivers use spaced antenna measurements to provide an estimate of the drift of ionospheric irregularities.

11

B0-000027 addition -
SFOML-WING-6-14.pdf
CTF091-1767

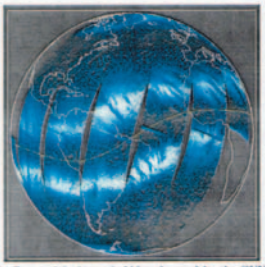


Figure 8. Equatorial plasma bubbles observed by the GUVI visible and ultraviolet sensors on the TIMED satellite.

3.0 Space Weather Conditions on February 1, 2003

The final breakup of Columbia occurred shortly after 1400 UT on February 1, 2003. To understand prevailing space weather conditions and their possible effects on the Columbia accident we have examined measurements from many satellite and ground observatories during the reentry period.

There are several different ways to present geophysical measurements made on the day of the Columbia accident. Interplanetary observations from the Advanced Composition Explorer (ACE) satellite set the stage for all that follows. Somewhat arbitrarily we have chosen to group the remaining measurements from (1) polar-orbiting satellites of the Defense Meteorological Satellite Program (DMSP) and the NOAA Polar Operational Environmental Satellite (POES) program in low Earth orbit (LEO), (2) Los Alamos National Laboratory (LANL) and NOAA Geostationary Operational Environmental Satellites (GOES) in geostationary orbit, and (3) ground observatories.

3.1 Interplanetary Measurements from ACE

The first satellite to observe interplanetary disturbances approaching Earth is the ACE that flies in a halo orbit around the first Lagrangian point about one million miles upstream of the Earth in the solar wind. Typically it takes the better part of an hour for

B0-000027 addition -
SFOML-WING-6-14.pdf
CTF091-1768

the solar wind/IMF observed by ACE to reach the Earth. The traces in Figure 9a show fluxes of energetic protons passing ACE plotted as a function of UT on February 1. The middle three plots indicate that conditions were steady until ~18:00 UT when the fluxes of protons with energies between 0.1 and 2 MeV rose sharply. The increased flux occurred ~ 4 hours after the accident and therefore had no impact upon it. Figure 9b shows the solar wind density (top plot), the IMF magnitude (second plot), and Z (north south), Y (east-west) and X (Sun-Earth) components of the IMF (middle to bottom plots). The solar-wind density was steady and unusually low (< 1 cm^{-3}) throughout the period of interest. At ~13:00 UT the IMF magnitude increased from 9 to 12 nT and the solar wind speed rose from ~400 to 500 km/s (not shown). The middle plot indicates that until 17:30 UT the Z component of the IMF was northward. The observed interplanetary changes should not have interacted strongly with the Earth's magnetic field. This conjecture is borne out by satellite and ground measurements presented below.

At 1344 UT on February 1, 2003 the staff on duty at Space Weather Operations in Boulder, Colorado, issued a warning for a Sudden Impulse, a characteristic step-wise jump in the horizontal geomagnetic field component on the dayside. This warning was based on observations of the solar wind speed increase of ~ 25%, seen by a plasma sensor on ACE at 1308 UT. This increase in speed was accompanied by a small increase in the magnetic field, but no corresponding increase in solar wind density (Figure 9). Typical shocks show simultaneous jumps in speed, density, and magnetic field. As time passed and no subsequent shock or impulse was observed in data acquired nearer to the Earth, this warning came to be regarded as a false alarm.

3.2 LEO Measurements from DMSP

Figures 10 - 12 present measurements from three DMSP satellites F13, F14, and F15. DMSP satellites fly in circular polar orbits at an altitude of ~ 840 km. At an inclination of 98.9° their orbital planes remain at fixed local time (LT) with respect to the sun. The orbit of DMSP F13 is near the dawn-dusk terminator. The orbital planes of DMSP F14 and F15 are near the 09:00 - 2100 LT meridian.

Data from the three DMSP satellites are plotted as functions of UT, magnetic latitude, and magnetic local time (Figures 10-12). The top two plots of each figure show the fluxes of electrons and ions with energies between 30 eV and 30 keV in an energy-versus-time color spectrogram format. The third plot gives the density of ionospheric plasma at the spacecraft altitude. The vertical (green) and horizontal (purple) components of ion drift across the satellite trajectory are presented in the fourth plot. The horizontal drift component is directly proportional to the electric field component along the spacecraft trajectory. Integration of this electric field component along the trajectory gives the cross polar cap potential. The bottom plot gives the three components of magnetic perturbations due to field-aligned currents that electrically couple the magnetosphere and ionosphere. The component of the Earth's magnetic field shown in green is highly correlated with horizontal drift measurements. Drift meters and magnetometers on DMSP satellites serve as voltmeters and ammeters to monitor characteristics of the global magnetosphere-ionosphere circuit.

B0-000027 addition -
SFOML-WING-6-14.pdf
CTF091-1769

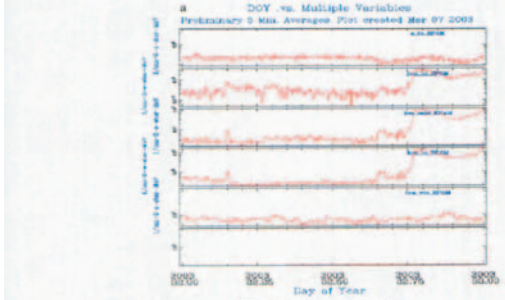


Figure 9. Measurements from ACE on February 1, 2003.

B0-000027 addition -
SFOML-WING-6-14.pdf
CTF091-1770

The gap in DMSP F14 measurements between 13:42 and 13:46 UT occurred in the evening sector of the polar cap and probably reflects an outage that occurred while data were being transmitted to ground. Electron and ion data from all DMSP spacecraft indicate moderate to low auroral activity during the time of Columbia's reentry. This is especially true in the dawn LT sector. Drift meter and magnetometer measurements are also consistent with weak to moderate magnetosphere-ionosphere coupling. In particular we note that neither plasma velocities nor magnetic perturbations due to field-aligned (Birkeland) currents measured by the three DMSP satellites showed any sign of an electromagnetic pulse indicating that the magnetosphere underwent a sudden compression near the time of Columbia's reentry. Data from ground magnetometers also show no sign of a magnetic compression event.

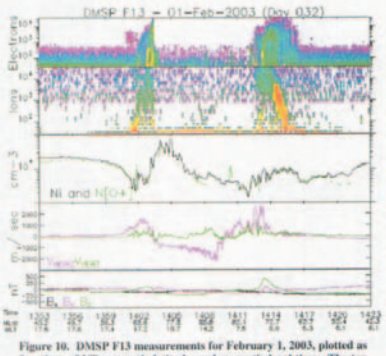


Figure 10. DMSP F13 measurements for February 1, 2003, plotted as functions of UT, magnetic latitude, and magnetic local time. The top two plots show fluxes of electrons and ions from 30 eV to 30 keV in an energy-versus-time color spectrogram. The third plot gives the density of ionospheric plasma at spacecraft altitude. Vertical (green) and horizontal (purple) components of ion drift across the satellite trajectory are presented in the fourth plot. The bottom plot gives the three components of magnetic perturbations due to field-aligned currents that electrically couple the magnetosphere and ionosphere.

B0-000027 addition -
SFOML-WING-6-14.pdf
CTF091-1771

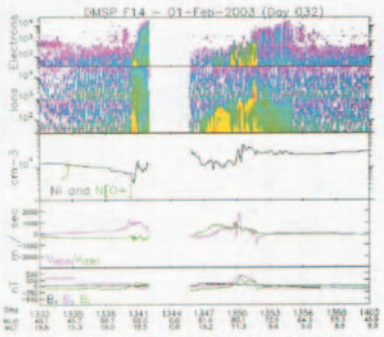


Figure 11. DMSP F14 measurements for February 1, 2003 in the same format as shown in Figure 10.

16

B0-000027 addition - SFOML-WING-6-14.pdf CTF091-1772

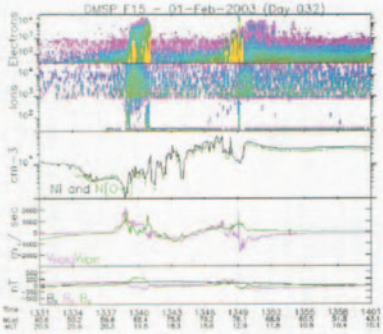


Figure 12. DMSP F15 measurements for February 1, 2003 in the same format as shown in Figure 10.

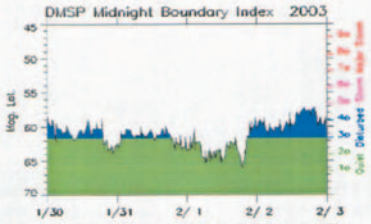


Figure 13. DMSP midnight boundary index for February 1, 2003.

17

B0-000027 addition - SFOML-WING-6-14.pdf CTF091-1773

Figure 13 takes the auroral electron boundaries observed by the DMSP satellites and projects them to the midnight meridian. The Air Force Weather Agency (AFWA) uses the latitude of auroral boundaries at midnight as an operational tool to specify current values of the Kp index. Boundary locations between 12:00 and 14:00 UT indicate magnetically quiet conditions. Kp entered the disturbed range late on February 1, 2003. Both then and on the following day geomagnetic conditions never approached the major storm status of either March 24, 1991, when CRRES observed the birth of a new radiation belt, or Bastille Day July 14, 2000, when auroral emissions appeared in the skies over the southern part of the United States.

3.3 LEO Measurements from POES

NOAA POES 15, 16, and 17 satellites also fly in sun-synchronous circular polar orbits, but near the 02:00 - 14:00 LT meridian. These satellites carry particle detectors covering the energy range from a few hundred eV to ~1 MeV. Standard estimates of the total energy input to the high-latitude ionosphere due to precipitating particle fluxes, as measured by the NOAA satellites, were in the low to moderate range near the time of Columbia's reentry. Although POES measurements were made at local times different from those of DMSP, their observations were similar, showing no indication of a geomagnetic disturbance during the period of interest.

Figures 14 and 15 show the trajectories of the NOAA POES 16 satellite for the full day of February 1, 2003. The trajectories are marked in color to indicate the relative fluxes of protons with energies between 250 and 800 keV and of electrons with energies > 300 keV. The color scales compare fluxes measured on February 1 with the median values observed at that location during the entire previous year. The data show "no higher than normal" (yellow) occurrences of energetic fluxes in the region over and to the east of Chile and Argentina, called the South Atlantic Anomaly (SAA). Within the SAA the Earth's magnetic field is weaker than average and allows radiation belt protons and electrons to penetrate more deeply than normal into the upper atmosphere. The 39° inclination of the STS-107 orbit placed Columbia within the SAA for a small portion of the mission. This was the only place during the entire mission where Columbia was exposed to energetic particles.

18

B0-000027 addition - SFOML-WING-6-14.pdf CTF091-1774

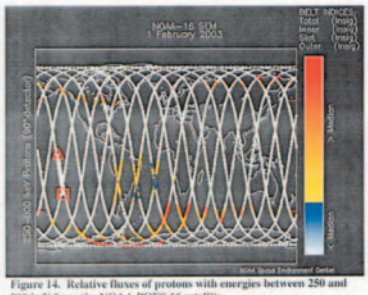


Figure 14. Relative fluxes of protons with energies between 250 and 800 keV from the NOAA POES 16 satellite.

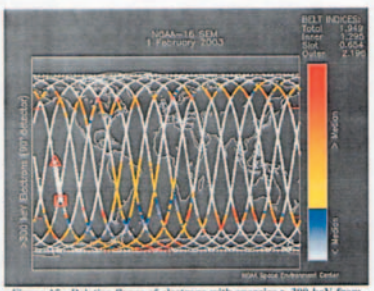


Figure 15. Relative fluxes of electrons with energies > 300 keV from the NOAA POES 16 satellite.

19

B0-000027 addition - SFOML-WING-6-14.pdf CTF091-1775

3.4 Charging Effects

The Columbia accident involved a serious breach of one or more heat tiles on the leading edge of the orbiter's left wing. We must then ask if there is any known space weather effect that could possibly have caused such a breach. In principle, the answer appears to be "yes." If the tiles were subject to prolonged exposure to intense fluxes of electrons with energies >100 keV, space charge could build up within the non-conducting materials. Electrons with lower energies would be stopped in the surface layer of the tiles and would cause surface charging. Electrons with energies >> 1 MeV would simply pass through the tiles. In neither the low nor extremely high energy cases would damage occur. During the Tethered Satellite System mission in 1996, Columbia charged to around a kilovolt with respect to the local plasma but suffered no ill effects.

As indicated in our discussion of deep dielectric charging (Figure 6), if sufficient space charge builds up within an insulating material, Coulomb repulsion forces eventually overwhelm material bonds. If breakdown occurs, a surge of plasma migrates quickly either to the nearest metal or to the outer surface. In the first case, the discharge current would flow to the shuttle's metal frame, to which all other circuits are grounded. Sudden changes in the ground potential induce current surges in all orbiter circuits simultaneously that would be identifiable in the mission telemetry stream. In the second case, negative space charge trapped within the dielectric would attract positive ions from the ionospheric plasma to the outer surfaces of the non-conducting tiles. A massive discharge to the outer surface could cause a breach in a critical surface that would widen as frictional interactions with the atmosphere increased during reentry. Such an event would not easily be identifiable in the telemetry data stream.

Is it likely that Columbia was exposed to a significant level of deep dielectric charging during the course of the mission or that a breach formed in a tile surface? The answer to both questions is negative. The orbital inclination of ~ 39° generally kept Columbia far from significant exposure to radiation in the "horns of the radiation belts" and auroral oval and from SEPs in the polar cap. The only exception lasted a few minutes each day as its orbital trajectory carried Columbia through part of the SAA. The SAA centers near 50° S, 60 ° W. To specify Columbia's exposure we have examined fluxes of electrons with energies >100 keV observed by the NOAA POES 15, 16, and 17 satellites in two orthogonal look directions while crossing the SAA (Figure 15) between January 16 and February 1, 2003. As a worst case scenario, we assumed that Columbia spent 600 seconds each day within the SAA and that every > 100 keV electron that struck a tile became embedded within it and no charge escaped. The estimated dose was ~1.22 $\times 10^{-5}$ Coulombs/m^2. Assuming a dielectric coefficient of 5, Gauss's law predicts a maximum electric field of ~ 10^6 V/m. This is a factor of 3 below breakdown electric fields for air and roughly an order of magnitude below breakdown for most insulating solids. Finally, a cursory glance at Figure 15 indicates that in a 39° inclination orbit, Columbia was more exposed to SAA radiation than orbiters in the standard 28.5° inclined orbit. However, Columbia was much less exposed than orbiters on extended missions to service the International Space Station.

B0-000027 addition -
SFOML-WING-6-14.pdf
CTF091-1776

Silica fibers constitute more than 99% of the shuttle tiles. Individual fibers are <3.2 mm long, between 1.2 and 4 microns in diameter, and are sintered together. The net density is 0.145 g/cc and the dielectric constant is 1.13. A borosilicate glass cover between 0.23 and 0.38 mm thick surrounds the tile fibers. In anticipation of polar-orbiting shuttle missions, sample tiles were irradiated by energetic electrons beams at AFRL to levels of ~ 10^5 Coulombs/m^2. This is similar to the estimated dose applied to Columbia in the SAA. In the experiments the tiles were observed to hold charges for days in the vacuum chamber. Non-destructive, prebreakdown pulses were observed whenever the induced electric field exceeded 10^7 V/m. Full breakdown of tile material never occurred. A full description of the experiments and their results appears in "Charging/discharging of space shuttle tile material under irradiation", by A. R. Frederickson and A. L. Chesley, *IEEE Trans. Nucl. Sci*, **30**, 4296-4301, 1983.

3.5 Geostationary Orbit Measurements

We next turn our attention to observations of energetic particles measured by sensors on five LANL and two GOES satellites that orbit the Earth at geostationary altitude. The left side of Figure 16 shows fluxes of protons with energies between 50 and 400 keV. Electron fluxes measured in the 50 to 315 keV range are shown in the right plot. The yellow and blue vertical lines crossing each spectrogram indicate when a particular satellite crossed the midnight and noon meridians, respectively. Except for small flux increases observed in the lowest (50 keV) channels near 14:00 UT, the environments sampled by all LANL satellites were very steady in the hours leading up to Columbia's reentry. Similarities between proton and electron spectra detected by widely spaced LANL satellites indicate that the geostationary environment was uniform. Consistent with ACE, LEO, and ground measurements, most of the geomagnetic activity encountered by the LANL satellites occurred after 20:00 UT.

B0-000027 addition -
SFOML-WING-6-14.pdf
CTF091-1777

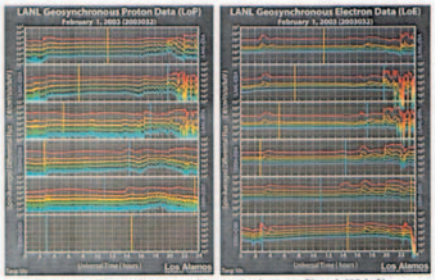


Figure 16. Fluxes of protons with energies between 50 and 400 keV (left) and electron fluxes measured in the 50 to 315 keV range (right) from LANL satellites.

A variety of space environmental parameters measured by GOES satellites appear in the next four figures. Figure 17 depicts the flux of electrons > 600 keV and > 2 MeV, as measured by two GOES satellites for the days January 31 through February 2, 2003. The only noteworthy characteristic is that the fluxes were somewhat elevated for the three-day period. Figure 18 shows fluxes of protons with energies > 10, 50, and 100 MeV for the same three days as measured by GOES 8 located near 75° W. The energetic proton fluxes show no enhancements in magnitude and attest to the presence of persistently benign conditions at geostationary orbit.

Solar flares are monitored by their X-ray outputs. Both the GOES 8 and 10 satellites carry sensors to measure X-ray fluxes in the 0.05 - 0.4 nm and 0.1 - 0.8 nm wavelength bands. Between January 31 and February 2, 2003 (Figure 19), occasional solar X-ray flares occurred. Two X-ray spikes were observed on February 1. However, there is no known association between the occurrence of X-ray photons near Earth and plasma disturbances that would have a significant impact on the predawn ionosphere at reentry altitudes of Columbia.

B0-000027 addition -
SFOML-WING-6-14.pdf
CTF091-1778

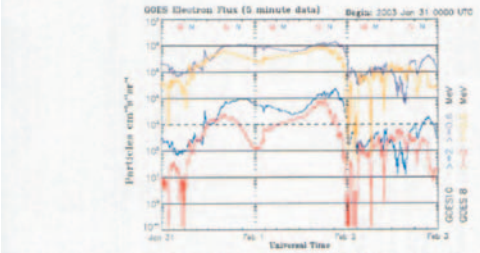


Figure 17. Flux of electrons > 600 keV and > 2 MeV as measured by two GOES satellites for January 31 through February 2, 2003.

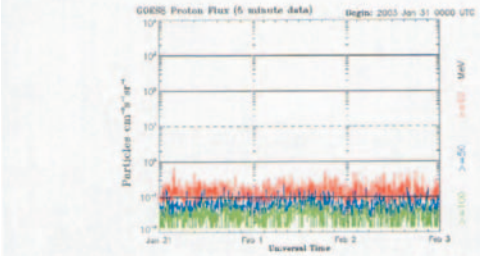


Figure 18. Fluxes of protons with energies greater than 10, 50, and 100 MeV for January 31 through February 2, 2003, as measured by GOES 8 located near 75° W.

B0-000027 addition -
SFOML-WING-6-14.pdf
CTF091-1779

Figure 20 is a composite of four data sets that from top to bottom show: GOES proton fluxes (Figure 18), GOES electron fluxes (Figure 17), the Hp (nearly north-south) component of the Earth's field measured by GOES, and the Kp ground index described previously. This stack plot is useful for comparing various data acquired at the same time. Focusing on the first 15 hours of February 1, we see that regular and quiet conditions are indicated in all four measurements.

It is useful to return to the global distribution of energetic (> 300 keV) electron fluxes observed by NOAA POES 16 as shown in Figure 15 which illustrates the relative fluxes of these particles. The fact that above-average fluxes were detected at high latitudes during virtually all passes is consistent with the presence of relatively high fluxes of > 2 MeV electrons observed by GOES at geostationary orbit (Figure 17). The footprint of the SAA is clearly seen. Elevated electron fluxes were mostly confined to latitudes higher than those accessible to Columbia's low inclination.

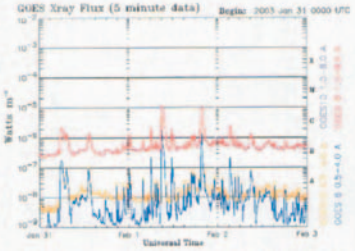


Figure 19. Measurements of X-ray fluxes in the 0.05 - 0.4 nm and 0.1 - 0.8 nm wavelength bands from GOES 8 and 10 satellites for January 31 through February 2, 2003.

B0-000027 addition -
SFOML-WING-6-14.pdf CTF091-1780



Figure 20. Composite of four data sets that from top to bottom show: GOES proton fluxes, GOES electron fluxes, the Hp (nearly north-south) component of the Earth's field measured by GOES, and the Kp ground index described previously for January 31 – 2 February 2003.

3.6 Ground Based Measurements

Our satellite-based estimate of low geomagnetic activity is confirmed by values of the AE and Dst indices measured on February 1, 2003 (Figure 21). During the time of Columbia's reentry, AE and Dst had values of ~100 nT and +34 nT, respectively. Significant auroral electrojet activity only began near 20:00 UT, about six hours after the accident. Steady positive values of Dst indicate that the ring current was inactive. The ring current is mostly carried by ions with energies > 10 keV that drift to the westward in the magnetosphere and produce negative perturbations to the Earth's magnetic field.

Magnetometers distributed over the surface of the Earth monitor the behavior of the Earth's magnetic field. These measurements reflect effects of electrical currents flowing in the ionosphere at altitudes near 120 km. Figures 22 and 23 are records of magnetic field measurements from Kiruna, Sweden, and Gakona, Alaska, respectively. Both of these instruments detected normally quiet conditions until late on February 1, when the effects of a CME began to drive relatively intense ionospheric currents. We also examined the record acquired at the Huancayo, Peru, station at the magnetic equator (not shown). If a CME-driven shock impacted the dayside magnetopause near 14:00 UT, a sudden increase in the north-south component of the magnetic field would have been

B0-000027 addition -
SFOML-WING-6-14.pdf CTF091-1781

detected at Huancayo. Instead, measurements on February 1, 2003 only show the diurnal magnetic variations characteristic of the solar-quiet current system in the ionosphere.

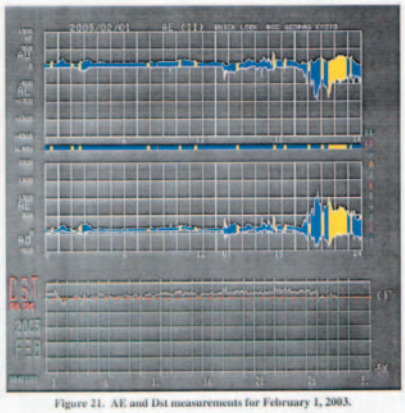


Figure 21. AE and Dst measurements for February 1, 2003.

Finally, to determine whether intense fluxes of SEPs had somehow passed undetected through geostationary and low Earth orbits, we examined fluxes measured at ground-based neutron monitors in Moscow and Apatity, Russia, Oulu, Finland, and Lomnicky Stit, Slovakia. These stations were in the afternoon LT sectors while Columbia was reentering the Earth's atmosphere. On February 1, 2003 these monitors detected only diurnal variations that appear to be similar in form and intensity to those recorded on other days of the month. We conclude that unusually large SEP fluxes did not impact the upper atmosphere near the time of the Columbia's reentry.

B0-000027 addition -
SFOML-WING-6-14.pdf CTF091-1782

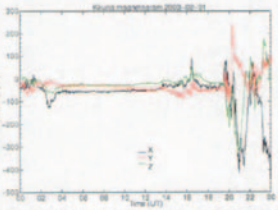


Figure 22. Magnetic field measurements from Kiruna, Sweden for February 1, 2003.

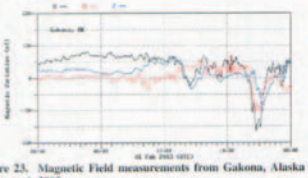
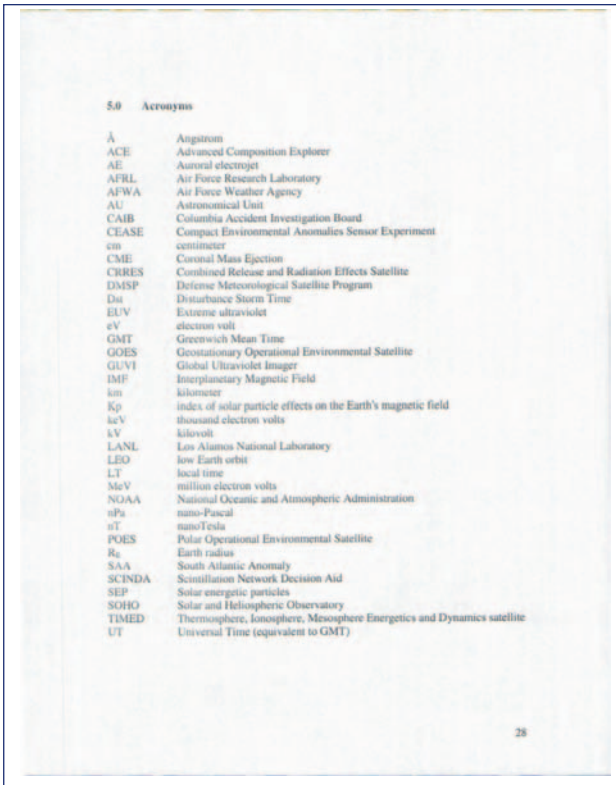


Figure 23. Magnetic Field measurements from Gakona, Alaska for February 1, 2003.

4.0 Summary and Conclusions

We have examined a wide variety of space related parameters measured by satellite and ground based sensors on February 1, 2003. All indications point to the fact that Columbia's reentry occurred during a period of low geomagnetic activity. It is difficult to imagine a more benign space weather environment for Columbia to start its reentry. Signs of moderate activity were not observed until late in the day, six or more hours after the accident. Were it not for the fact that the accident happened on February 1, 2003, it is unlikely that space-weather investigators would have given the day more than cursory inspection.

B0-000027 addition -
SFOML-WING-6-14.pdf CTF091-1783



5.0 Acronyms

Å	Angstrom
ACE	Advanced Composition Explorer
AE	Auroral electrojet
AFRL	Air Force Research Laboratory
AFWA	Air Force Weather Agency
AU	Astronomical Unit
CAIB	Columbia Accident Investigation Board
CEASE	Compact Environmental Anomalies Sensor Experiment
cm	centimeter
CME	Coronal Mass Ejection
CRRES	Combined Release and Radiation Effects Satellite
DMSP	Defense Meteorological Satellite Program
Dst	Disturbance Storm Time
EUV	Extreme ultraviolet
eV	electron volt
GMT	Greenwich Mean Time
GOES	Geostationary Operational Environmental Satellite
GUVI	Global Ultraviolet Imager
IMF	Interplanetary Magnetic Field
km	kilometer
Kp	index of solar particle effects on the Earth's magnetic field
keV	thousand electron volts
kV	kilovolt
LANL	Los Alamos National Laboratory
LEO	low Earth orbit
LT	local time
MeV	million electron volts
NOAA	National Oceanic and Atmospheric Administration
nPa	nano-Pascal
nT	nanoTesla
POES	Polar Operational Environmental Satellite
R_E	Earth radius
SAA	South Atlantic Anomaly
SCINDA	Scintillation Network Decision Aid
SEP	Solar energetic particles
SOHO	Solar and Heliospheric Observatory
TIMED	Thermosphere, Ionosphere, Mesosphere Energetics and Dynamics satellite
UT	Universal Time (equivalent to GMT)

28

B0-000027 addition - SFOML-WING-6-14.pdf CTF091-1784

THIS PAGE INTENTIONALLY LEFT BLANK

Volume II
Appendix D.6

Payload and Payload Integration

The Board conducted a thorough review of the STS-107 payload and the payload integration in preparation for the mission. This appendix contains the results of that investigation which identified several anomalies, none of those were determined to be causal in the loss of *Columbia*.

Section 1.0 Basic Payload Overview 147
1.1 SPACEHAB RDM 147
1.2 FREESTAR 149
1.3 Mid-deck 150

Section 2.0 Payload Integration 150
2.1 Readiness Reviews 150
2.1.1 Payload Readiness Review 150
2.1.2 Pre-Flight Readiness Review 151
2.1.3 Flight Readiness Review 151
2.2 Safety Reviews 151
2.2.1 Integrated Safety Assessments 151
2.2.2 Payload Readiness Review 152
2.2.3 Pre-Flight Readiness Review 152
2.2.4 Payload Safety Review Panel 152
2.3 Pre-Launch Preparation 152

Section 3.0 Mission Overview 153
3.1 Launch 153
3.2 Orbit 153
3.3 Entry 154

Section 4.0 Anomalies 154
4.1 Launch 154
4.2 On-Orbit 154
4.3 Reentry 156

Appendix A Acronyms 157

Payload and Payload Integration

Submitted by Group II
Major General Kenneth W. Hess, Steven B. Wallace, Sally K. Ride, Ph.D.
1st Lt. Matthew Granger

1.0 BASIC PAYLOAD OVERVIEW

The payload bay configuration for the Space Shuttle *Columbia* (OV-102) for the STS-107 mission, from forward to aft, was the SPACEHAB access tunnel, SPACEHAB Research Double Module (RDM), the Fast Reaction Experiment Enabling Science Technology Applications and Research (FREESTAR) payload, the Orbital Acceleration Research Experiment (OARE), and an Extended Duration Orbiter (EDO) kit to accommodate the extended duration flight needed to conduct all on-board research experiments. Additional individual experiments were loaded into the mid-deck of the Orbiter and on the SPACEHAB RDM rooftop (see Figure 1). Total payload weight for STS-107 was 24,536 pounds.

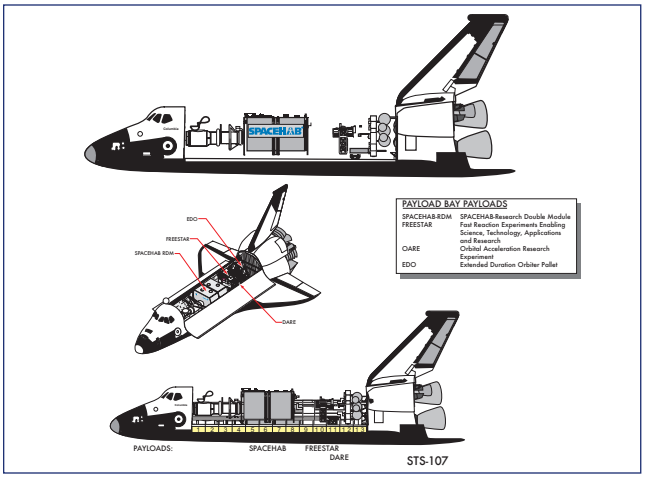


Figure 1. STS-107 Payload bay configuration.

Since STS-107 was a dedicated science research mission, certain payload experiments drove orbital planning requirements. Those requirements were for a 39-degree orbit inclination and a 150 nautical mile altitude, both of which were to support the Miniature Satellite Threat Reporting System (MSTRS), a U.S. Air Force orbital debris avoidance experiment. The STS-107 mission also required approximately 250 attitude maneuvers while on orbit to satisfy the requirements of FREESTAR and the SPACEHAB rooftop experiment payloads.

1.1 SPACEHAB RDM

Founded in 1984, SPACEHAB Incorporated is a company providing commercial space services to NASA and other organizations. The current bulk of products provided to NASA entail research and logistics modules for integration and use aboard the space shuttle within the payload bay. Since 1993 SPACEHAB has produced four major products for use on the Space Shuttle: the Logistics Single Module (LSM), Research Single Module (RSM), Logistics Double Module (LDM), and most recently, the Research Double Module (RDM). Construction of the first SPACEHAB RDM began on August 1, 1996 and was flown aboard OV-102 on the STS-107 mission. The RDM was developed using a flight-proven single forward module (Flight Unit 1, last flown on STS-95) and an identical aft module (Flight Unit 4, new, per existing design). In addition, knowledge learned from the production of the LDM was applied to the RDM.

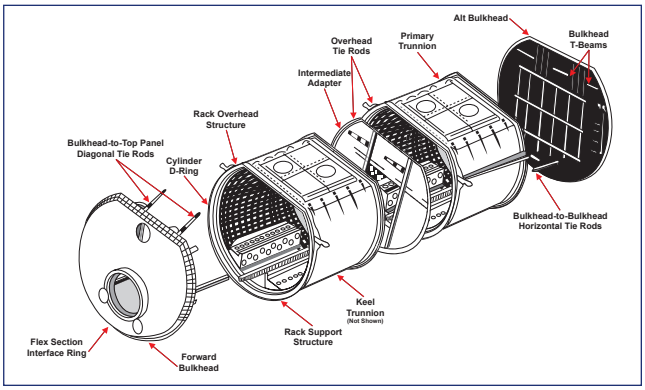


Figure 2. SPACEHAB Research Double Module configuration.

The RDM is a pressurized aluminum research laboratory habitat that connected to the Orbiter via a pressurized access tunnel. It is comprised of two Research Single Modules connected together by an Intermediate Adapter (see Figure 2). It provides a 10,000-pound payload capacity and contains a full array of video, data, command, power, and environment control capabilities. The first flight of a SPACEHAB Research Single Module was in 1993, with the first flight of a Logistics Double Module following in 1996. Below is a list of all SPACEHAB flights:

STS-57 (RSM) June 1993
STS-60 (RSM) February 1994
STS-63 (RSM) February 1995
STS-76 (RSM) March 1996
STS-77 (LSM) May 1996
STS-79 (LDM) September 1996
STS-81 (LDM) January 1997
STS-84 (LDM) May 1997
STS-86 (LDM) September 1997
STS-89 (LDM) January 1998
STS-91 (LSM) June 1998
STS-95 (RSM) October 1998
STS-96 (LDM) May 1999
STS-101 (LDM) May 2000
STS-106 (LDM) September 2000
STS-107 (RDM) January 2003
STS-116 (LSM) June 2003*
STS-118 (LSM) October 2003*

**Planned*

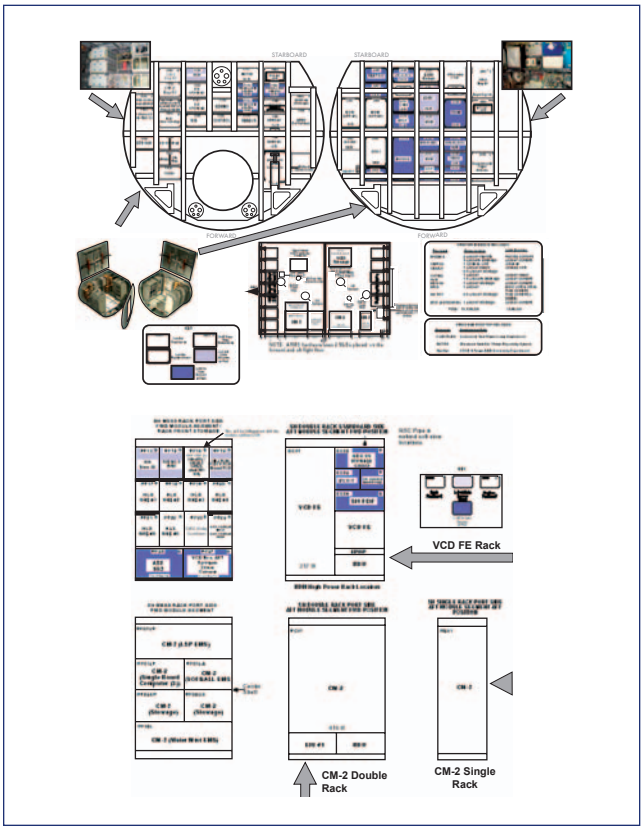


Figure 3. Experiment layout in the SPACEHAB RDM.

The SPACEHAB RDM for STS-107 contained 30 microgravity, space, and life science payloads to include commercial, European Space Agency (ESA), and NASA experiments. The following experiment payloads were flown on OV-102 within the RDM for this mission (see Figure 3 for experiment layout within the module):

NASA Office of Biological & Physical Research Payloads (Managed by NASA Code U)

- Combustion Module-2 (CM-2)
  - LSP
  - SOFBALL
  - Water Mist
- Space Acceleration Measurement System Free Flyer (SAMS FF)
- Mechanics of Granular Materials (MGM)
- Ergometer Hardware
- Johnson Space Center Human Life Sciences (JSC HLS)
  - Microbial Physiology Flight Experiments (MPFE)
  - SLEEP-3
  - Automated Microbial System (AMS)
- Astroculture
  - 10/1 (Plant Growth Chamber) (AST-10/1)
  - 10/2 (Glovebox) (AST-10/2)
- Commercial Protein Crystal Growth – Protein Crystallization Facility (CPCG-PCF)
- Commercial ITA Biomedical Experiment (CIBX)
- Fundamental Rodent Experiments Supporting Health-2 (FRESH-2)
- Gravisensing & Response Systems of Plants (BIOTUBE/MFA)
- Biological Research In Canisters (BRIC)

NASA ISS Risk Mitigation Experiment Payloads

- Vapor Compression Distillation Flight Experiment (VCD FE)

NASA/ESA Sponsored Payloads (Managed by NASA & ESA)

- Facility for Adsorption and Surface Tension (FAST)
- Advanced Protein Crystallization Facility (APCF)
- BIOBOX

Commercial Payloads (Managed by SPACEHAB, Inc.)

- Advanced Respiratory Monitoring System (ARMS)
- Miniature Satellite Threat Reporting System (MSTRS)*
- Combined 2 Phase Loop Experiment (COM2PLEX)*
- Space Technology and Research Students (STARS™)
- Star Navigation (StarNav)*
- European Research in Space and Terrestrial Osteoporosis (ERISTO)
- Johnson Space Center Human Life Sciences (JSC HLS)
  - Physiology and Biochemistry 4 (PhAB4)
  - Enhanced Orbiter Refrigerator/Freezer (EOR/F)

– Thermoelectric Holding Module (TEHM)
– Orbiter Centrifuge

Note: The COM2PLEX, StarNav, and MSTRS were located on the rooftop of the SPACEHAB RDM (see Figure 4).

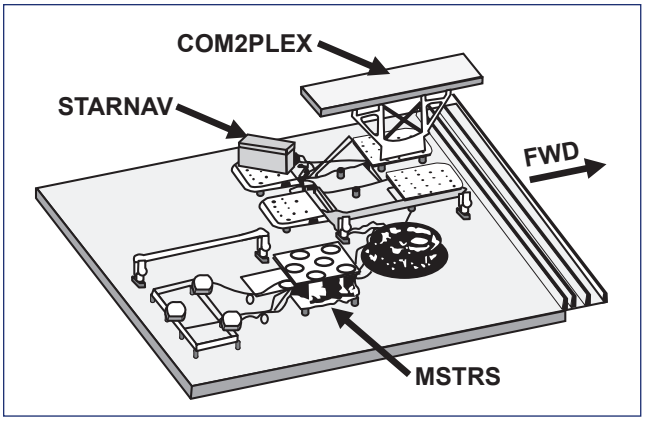


Figure 4. Layout of experiments on the SPACEHAB RDM roof.

Payload experiments for this mission never previously flown included the ARMS, Biopack, BIOTUBE, COM2PLEX, MPFE, MSTRS, StarNav, and VCD FE.

The SPACEHAB RDM required 5500-Watts to power the payload. For ascent/descent, the RDM required 690-Watts DC total and was divided between the module and mid-deck payloads. Main power for the RDM is supplied from the Orbiter by way of two main access cables, entering the module through the forward bulkhead. The power integration between SPACEHAB and OV-102 required the following specific electrical hardware:

- 4 power outlets in order to support 5 powered payloads on ascent
- 7 power outlets in order to support 5 powered payloads on orbit
- 4 power outlets in order to support 4 powered payloads on descent

The environmental control for SPACEHAB required 590 Watts of power for ascent/entry and was designed to provide continuous moisture and atmospheric control and monitoring for three crewmembers, and up to six members for short durations. It was also designed to maintain the SPACEHAB RDM temperature between 65 and 80 degrees Fahrenheit through the use of both air and water-cooling loops, and provide adequate carbon dioxide removal as well. New to the RDM design was the addition of a moisture removal system for added capability to accommodate larger moisture generation rates (i.e. the addition of a human performance ergometer bicycle experiment) and to aid in the overall heat rejection capability (i.e. to accommodate the CM-2 experiment).

A complete fire suppression system was incorporated into the SPACEHAB RDM. Smoke detectors identical to those used aboard the Orbiter provided detection capabilities, and ten Halon bottles built into the module provided the means for fire suppression. A full depressurization capability also existed, enabling the crew to vent the module and remove all oxygen (one of the three requirements for fire to exist). The module also contained emergency breathing systems for up to two crewmembers.

Data and command systems within the RDM included the new Experiment Data System (EDS) to support experiment requirements. Also, a complete RDM display feature is also available to the flight deck crew if needed in order to monitor module readings and warnings via the main flight deck console screens.

When compared to previously flown single and double modules, the RDM contained the following newly developed, first-time use systems, modified systems, and series items:

- Aft Module Segment (FU-4)
- Aft Module Rack Support Structure (RSS) and Overhead Attachment
- Aft Module Floor
- Aft Module Subfloor
- Hab Fan Assembly*
- Air Balancing Box*
- Air By-Pass Valve Assembly*
- Air Mixing Box
- Atmospheric Revitalization System (ARS) Fan Package/Inlet Muffler
- Condensing Heat Exchanger (CHX)*
- Water Separator Assembly (WSA)*
- Condensate Storage System (CSS)*
- CO_2 Control Assembly (CCA)*
- Environmental Control Unit (ECU)
- Centralized Experiment Water Loop (CEWL)*
- Centralized Experiment Rack Suction Cooling
- Aft Power Distribution Unit (APDU)*
- Aft DC-AC Power Inverters*
- Rack Distribution Unit (RDU)
- Emergency Power Distribution Box (EPDB)
- Luminary Switch Box
- Aft Module Luminaries
- EDS Main Unit (EDSMU)
- EDS HUB
- EDS Experiment Interface Unit (EIU)
- EDS Onboard Crew Station (available when required)

** Indicates new hardware added in the aft module subfloor*

The SPACEHAB RDM incorporated no jettison pyrotechnics and, once loaded for launch, weighed 20,249 pounds (this represents both the minimum descent and maximum ascent weight).

1.2 FREESTAR

The Fast Reaction Experiment Enabling Science Technology Applications and Research (FREESTAR) is a Hitchhiker payload managed and operated by Goddard Space Flight Center as part of the Shuttle Small Payloads Project. The FREESTAR payload contained no radioactive or ionizing radiation sources and demonstrated no operational function capability, such as rocket motor firings, appendage deploy-

ments, or separations. FREESTAR weighed 4,427 pounds (FREESTAR and carrier combined) once fully loaded with experiments and, for the STS-107 mission, was mounted on a crossbay Multipurpose Equipment Support Structure and included six Earth science and microgravity experiments as listed below (see Figure 5 for experiment layout):

- Mediterranean Israeli Dust Experiment (MEIDEX)
- Shuttle Ozone Limb Sounding Experiment-2 (SOLSE-2)
- Critical Viscosity of Xenon-2 (CVX-2)
- Solar Constant Experiment-3 (SOLCON-3)
- Space Experiment Module (SEM)
- Low Power Transceiver (LPT)

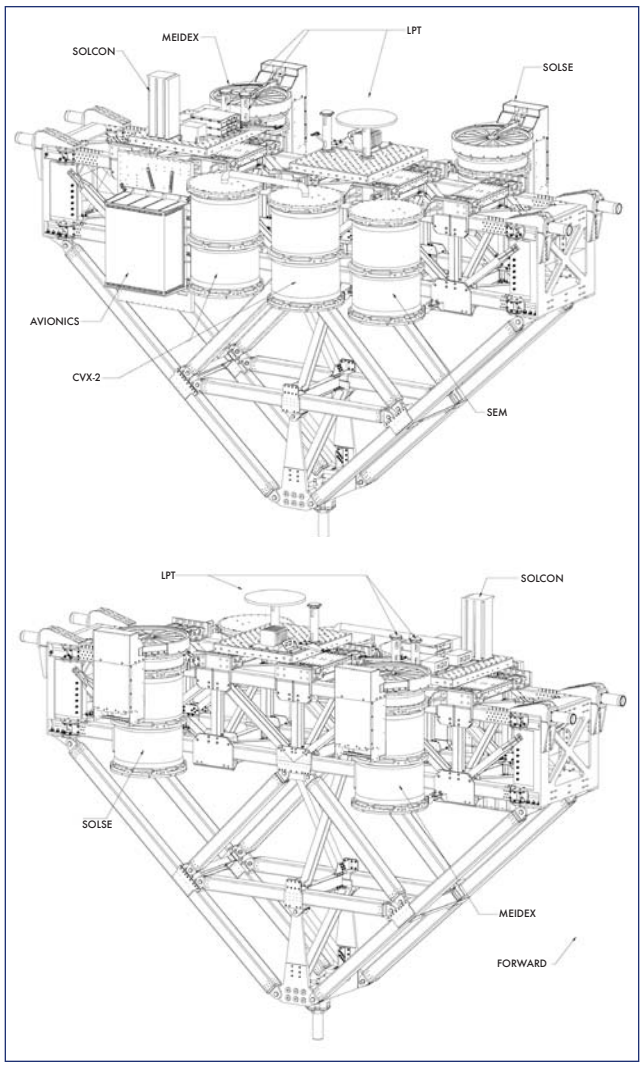


Figure 5. FREESTAR experiment configuration.

1.3 Mid-deck

The mid-deck payloads consisted of experiments housed in the forward bulkhead of the Orbiter mid-deck and were controlled and monitored by SPACEHAB, Inc. The following specific experiments were flown on the mid-deck of OV-102 for STS-107 (see Figure 6 for experiment layout):

- Biopack
- Biopack w/ Passive Thermal Controlled Units (PTCUs)
- Closed Equilibrated Biological Aquatic System (CEBAS)
- Ziolite Crystal Growth-1 (ZCG-1)
- Osteoporosis Experiment in Orbit (OSTEO)
- Bioreactor Demonstration System-05 (BDS-05)
- Biological Research In Canisters (BRIC)
- Commercial Macromolecular Protein Crystal Growth (CMPCG)

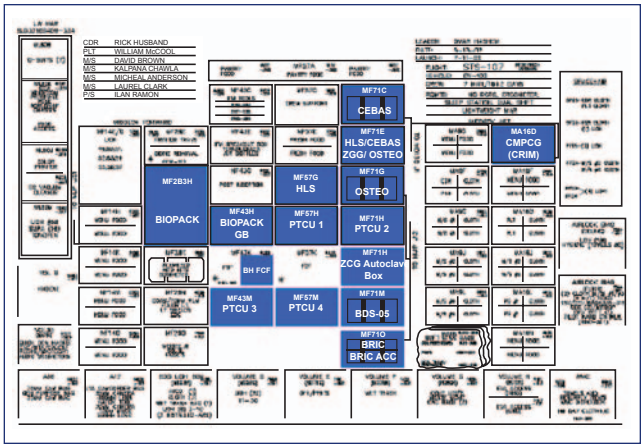


Figure 6. Mid-deck experiment layout.

2.0 Payload Integration

2.1 Readiness Reviews

The original launch date for STS-107 was January 11, 2001. Based on adjustments to estimated rollout dates, the launch was rescheduled for February 22, 2001. In order to support this new launch date, a Cargo Integration Review (CIR) was scheduled for February 22, 2001. The *Triana* payload, designed to observe and study Earth and space-based phenomenon, was originally scheduled to fly aboard OV-102 for the STS-107 mission, along with the SPACEHAB RDM. Command and data inputs (Triana Annex 4) were late for the CIR and forced a one-month launch slip to March 22, 2001. Because of this launch delay and other factors, it was decided to remove the *Triana* payload from the flight manifest for STS-107 and exchange it with the FREESTAR payload. This change-out required an additional launch slip to June 14, 2001. The SPACEHAB RDM then required a Ku-band verification test that required 6 weeks to accomplish and delayed the launch date to August 2, 2001. Other shuttle processing delays, engine flowliner crack repairs, and lower priority of STS-107 behind STS-109, 112, and 113 due in part to space station construction timelines forced several additional launch slips for STS-107 until the final launch date of January 16, 2003 was finalized and executed.

2.1.1 Payload Readiness Review

The initial Payload Readiness Review (PRR) was conducted on May 9, 2002. The purpose of the PRR was to review the

processing of the SPACEHAB RDM and FREESTAR payloads conducted at Kennedy Space Center, ensure readiness for installation of the payloads into the OV-102, and ensure the Orbiter and Ground Support Equipment systems were ready to receive the payloads. OV-102 processing at the Orbiter Processing Facility (OPF) was planned to take place in High Bay 3.

There were no anomalies reported during the PRR by any payload representative, and only one special topic was brought forward. During ground processing, a "ding" was found on the inside wall of the SPACEHAB RDM. Based on results from the inspection and non-destructive analysis, it was deemed non-detrimental to the structural integrity of the RDM and was repaired. The Payload Safety Review Panel (PSRP) closed the topic on April 15, 2002.

All payloads were planned to be integrated together horizontally at the Space Station Processing Facility (SSPF), then loaded horizontally into the Orbiter at the Orbiter Processing Facility (OPF), with several individual time-critical experiments to be installed as part of a late vertical stow on Launch Complex 39A. SPACEHAB Inc. would be responsible for all late stow deliveries to the pad, at which time the individual experiment payloads would be turned over to the Flight Crew Equipment (FCE) team for loading. Ten mission success Launch Commit Criteria (LCC) and three Payload Safety LCCs were identified and approved for this payload (see Figure 4).

As briefed in the engineering status section of the PRR, all Section 20 non-compliances were known to the test team, were generic to SPACEHAB and FREESTAR, and were built into the forward planning. There were no mission specific Interface Control Document (ICD) wavers, deviations, or exceedances identified for this mission. There were also no unexplained anomalies present.

Primary payload software used for this RDM mission was Version 38.01, the Back-up Flight Software (Ascent) was Version 38.24.B.10, and there were no issues or concerns surrounding these software packages. There were also no issues or concerns regarding ground or Orbiter software.

Specifically regarding the SPACEHAB RDM, which was the primary payload for STS-107, there were no open anomalies. This was the first flight of the RDM, but was developed from "flight proven" Research Single Module (RSM) and Logistics Double Module (LDM) designs. The tunnel connecting the SPACEHAB RDM to the Orbiter airlock was developed from previous tunnel designs and all interfaces were similar to previous configurations. The RDM/Orbiter interfaces were identical to the RSM and LDM designs, and changes were minimized to include only those required for payload performance. Changes to the standard SPACEHAB module interfaces are listed below:

- Two Additional DC Power Feeds (4 total – only 3 used for STS-107)
- Additional AC (AC2) Power Feed
- KU-Band Signal Processor (KUSP) Interfaces (channels 2 and 3 for downlink, forward link for commanding)

2.1.1 Pre-Flight Readiness Review

The initial STS-107 Pre-Flight Readiness Review occurred on June 20, 2002, and after a launch slip, the delta review took place on December 11, 2002. Payload processing was reported as complete, except for late stowage of experiments, which was planned to occur at the launch pad prior to launch. No operations requiring payload door opening on the pad were planned in order to complete the late stowage activities, and all integration compatibility requirements were met, all without issue or constraints. The acoustics and hardware branches also reported no outstanding concerns and no constraints to flight.

2.1.2 Flight Readiness Review

The STS-107 Flight Readiness Review occurred on January 9, 2003. An overview of the payload to be flown on this mission was given, as well as key mission considerations, such as time on orbit, altitude, and launch scrub turnaround timelines. It was noted STS-107 was the first Extended Duration Orbiter (EDO) mission since STS-90 in April 1998, and the late addition of six passive sample canisters to the BRIC mid-deck locker was discussed as well. The late addition of the six canisters was approved at the January 8 Payload Safety Review Panel (PSRP).

The Integrated Experiment Hazards Assessment was briefed as complete, all toxicology processes were complete, there were no outstanding Non-Compliance Reports, and the PSRP was complete. There were no payload constraints to launch and all reviews were complete.

2.2 Safety Reviews

2.2.1 Integrated Safety Assessments

The SPACEHAB RDM Phase III Flight Safety Review took place in July 2000, with Boeing/SPACEHAB Inc. presenting information. According to the safety data package, the structural verification of the RDM was accomplished by the maximum use of previously proven hardware, similarity in design to previous modules, and the use of verification tools such as design coupled load analysis, stress analysis and fracture control, and design variation sensitivity analysis.

For the STS-107 mission, there were 14 SPACEHAB RDM Flight Hazard Reports written. Previous Space Shuttle mission hazard reports were reviewed and assessed for applicability to the specifics of the STS-107 mission, and the 14 hazard reports written for the RDM were in addition to previously submitted reports. This mission was the sixth flight for the forward module, FU-1, and fatigue effects were included in the final safety analysis. The module was most recently flown aboard STS-95. The Intermediate Adapter and aft module (FU-4) were new-builds per existing designs. At the conclusion of the SPACEHAB Fracture Control Board, conducted with Boeing, all margins of safety were positive for the primary and secondary structures and all hardware met the 10-mission minimum design life requirements. All subsystems were rated with a design life greater than 50 missions. An RDM Flammability Analysis was also conducted.

The SPACEHAB RDM pressurized environment is identical to the Orbiter environment.

The FREESTAR Phase III Flight Safety Data Package was presented in February 2002 at Goddard Space Flight Center. The FREESTAR payload contained no radioactive or ionizing radiation sources and the Hitchhiker carrier hardware supporting FREESTAR had never experienced any major anomalies or structural failures supporting previous flights. The structural verification plan verified FREESTAR to survive an 11g force about the X, Y, and Z-axis and, for this mission, did not have any operational function capability, such as rocket motor firings, appendage deployments, or separations. There were also no significant heat generation or electromagnetic field sources associated with the payload. It was ultimately determined FREESTAR introduced no additional hazards as a result of integration with the rest of the STS-107 payload or OV-102 and met all payload safety requirements.

2.2.2 Payload Readiness Review

At the Payload Readiness Review (PRR) on May 9, 2002, the Safety and Mission Assurance (S&MA) Division reported all generic payload hazards were properly controlled and there were no unique hazards identified. There were no open ground safety action items, but one "mishap" had occurred during ground processing. A worker was exposed to chemicals during the BRIC-14 processing in Hanger L, but was released back to regular duty soon after. All mission status recommendations from the safety side of the PRR were positive and indicated a readiness for integrated ground operations.

2.2.3 Pre-Flight Readiness Review

During the December 11 Pre-Flight Readiness Review, all payload cargo physical stresses on the Orbiter were reported as within acceptable limits with positive margins of safety. From the Cargo Safety division, the final STS-107 Cargo Integrated Risk Assessment Report was reported as complete and delivered on May 31, 2002, with closure of all tracking log items set for the next day, December 12, 2002. The Payload Environmental Assessment Report was also reported as submitted, as of May 29, with no issues or concerns identified, and the Safety Critical Pin-to-Pin Assessment was reported as completed on the same day. Cargo Safety also reported any open In-Flight Anomalies (IFA) and/or IFA actions from previous flights contained no payload safety concerns specific to the STS-107 mission. Payload Safety reported all safety hazard reports had been approved, all open work remaining was defined and approved, there were no Non-Compliance Reports, and the safety certification process was complete.

2.2.4 Payload Safety Review Panel

The final Payload Safety Review Panel (PSRP) meeting prior to the STS-107 mission was completed on January 8, 2003 where, among other items, the Integrated Safety Assessments conducted for the SPACEHAB RDM and FREESTAR payloads were presented for final approval at Kennedy Space Center. Also presented at the PSRP were the results of the Ground Safety Review Panel and the Flight Safety Review Panel for PSRP approval.

One thing addressed at the PSRP was the issue of hazardous materials. It was reported there were only very limited amounts of hazardous materials within the payload of STS-107. Only negligible amounts of radiological material (i.e. Americium-241 in smoke detectors, the same as in the Orbiter) were on board STS-107 and posed no health hazard. The following material descriptions are for any materials planned to be on board the OV-102 at or above a Toxic Hazard Level 2:

2.3 Pre-Launch Preparation

The EDO kit was loaded into aft section of the Orbiter's payload bay in OPF-3, on April 25, 2002. The SPACEHAB RDM/FREESTAR payload was also loaded horizontally into the Orbiter's payload bay on March 24, 2002 with the Integration Verification Test occurring on June 6. The payload bay doors were closed for flight in the OPF for the last time on October 31 and were not opened prior to launch (all late stow activities were accomplished via the mid-deck and RDM access tunnel). OV-102 rollover from the OPF to the Vehicle Assembly Building (VAB) for external tank and solid rocket booster mating occurred on November 18, 2002. Mating occurred on November 20, and vehicle rollout to Launch Complex 39A occurred without incident from a payload perspective on December 9.

The launch team was exercised in the protocol and flow of the payload LCC through a full Cargo Integration Test Equipment (CITE) simulation performed on December 5, 2002. In the event any payload LCC were violated during the launch count, and required a hold, Kennedy Space Center personnel were responsible for calling the hold from data gathered by the Ground Launch Sequencer (GLS).

Experiment	*Hardware/ Hazard*	*Amount*	*Hazard Level*	*Notes*
ARMS	CO_2 Absorber	20g X 2	2	2 units in storage @ launch – 1 will be mounted on ARMS module #2 on orbit
CM-2	Exhaust vent package – gas filter/LiOH, Silica	590g, 565g	2	None

During the Flight Readiness Review (FRR), all SPACEHAB RDM powered health checks were reported as complete with no anomalies or outstanding issues.

SPACEHAB was ultimately powered up at L-51 hours (January 14, 2003) in order to prepare for the late stowage of time critical experiments. Module Vertical Access op-

erations for SPACEHAB took place at L-46 hours and were completed by L-31 hours without incident. Late mid-deck payload stowage occurred at the launch pad as well. Flight crew equipment loading took place at L-22:30 hours, while mid-deck experiment loading took place from L-19 to L-16 hours. Fourteen experiments were loaded, four of which were powered, all without incident. No LCCs were violated prior to launch at T-0.

3.0 Mission Overview

3.1 Launch

STS-107 performed a successful morning launch from Kennedy Space Center, Launch Complex 39A, on January 16, 2003 at 9:39 a.m. CST, early in the 2.5 hour launch window. The planned orbit inclination was at 39 degrees to the equator and at an altitude of 150 nautical miles. The general mission overview consisted of a dedicated science and research flight lasting 16 days (plus 2 weather extension days if needed) with a crew of seven. Due to the extensive amount of research conducted on this mission (SPACEHAB alone required 468 hours of on-orbit crew time), the crew conducted dual shift operations in order to maintain 24 hour a day operations. Crewmembers were divided into two teams and assigned alternating 12-hour shifts. The "Red Team" consisted of Husband, Chawla, Clark and Ramon. The "Blue Team" consisted of McCool, Brown and Anderson.

The following SPACEHAB RDM experiments were powered for the ascent phase of the mission: Advanced Protein Crystallization Facility (APCF), Astroculture, Bioreactor Demonstration System-05 (BDS-05), BIOBOX, Commercial ITA Biomedical Experiment (CIBX), CPCG-PCF, European Research in Space and Terrestrial Osteoporosis (ERISTO), Fundamental Rodent Experiments Supporting Health-2 (FRESH-02), Space Technology and Research Students (STARS-Bootes), Thermoelectric Holding Module (TEHM).

The following mid-deck experiments were powered for the ascent phase of the mission: Biological Research In Canisters (BRIC), Closed Equilibrated Biological Aquatic System (CEBAS), Commercial Macromolecular Protein Crystal Growth (CMPCG), and Osteoporosis Experiment in Orbit (OSTEO).

FREESTAR was not powered during the ascent phase of the mission.

From downlinked data received by Mission Control and the Payload Operations Control Center (POCC), all payload telemetry was nominal during the launch phase.

3.2 On-orbit

At 11:35 a.m. CST, after orbital insertion, the payload bay doors were opened and the go-ahead was given to begin on-orbit operations. The Blue Team began their first sleep cycle while the Red Team began their first shift of on-orbit payload operations. The SPACEHAB RDM was powered during launch to ensure cooling of all experiments on board and, as their first order of business, the crew successfully activated the RDM and all associated scientific experiments. All on-orbit equipment required for the mission was also unstowed.

On the ground, the first Mission Management Team (MMT) meeting occurred on Friday, January 17, 2003 (for more in-depth descriptions of anomalies listed, see Section 4.2). A SPACEHAB Ku-band Channel 2 anomaly was discussed and a ground systems problem was suspected. Channel 3 data was working nominally and it was determined MOD resources would be made available if needed. The current cryo margin was briefed as 22 hours past nominal end-of-mission due to lower than predicted payload and SPACEHAB RDM power use. A failure of the RDM ICOM B transmission link was also discussed and ICOM A was being used without incident.

The second MMT occurred on Tuesday, January 21, 2003. A SPACEHAB RDM Water Separator Assembly (WSA) leak under the aft sub-floor was discussed in-depth, along with the ensuing electrical short and shutdown of both rotary separators. The possibility of re-starting one of the rotary separators after drying and unclogging was brought forward. An In-Flight Maintenance (IFM) procedure to re-route cooling ducting was discussed and it was determined no new IFM would be carried out without prior approval of the MMT since an electrical short had been confirmed, even if that meant convening a special MMT. A 70mm Hasselblad hand-held camera problem, MSTRS experiment telemetry and command anomalies, and the continuing KU anomaly were also discussed.

The third MMT occurred on Friday, January 24, 2003. The main payload-related topic discussed was the RDM water leak anomaly and IFM development. RDM internal temperature had peaked at 81 degrees Fahrenheit, one degree above maximum allowable (medical was aware of it and it was deemed was acceptable). Airflow adjustments were made and the temperature changes were sufficiently moderated so there was no need to implement the cooling duct re-routing IFM. Instead, a plan is in work to use the DC vacuum to clean up any excessive water under the sub-floor prior to entry.

The fourth MMT occurred on Monday, January 27, 2003. Since adjustments to the air flow from the Orbiter was maintaining sufficient cooling in the SPACEHAB RDM, it was re-stated no further IFM to fix the original RDM problem would be needed. It was also recommended the IFM developed to inspect under the sub-floor prior to entry should be implemented.

The fifth, and final, MMT occurred on Thursday, January 30, 2003. The IFM plan to inspect under the sub-floor of the SPACEHAB RDM was planned for later in the day, as well as a plan to vacuum any residual water with the Orbiter DC vacuum cleaner. It was reported that the crew, during all subsequent inspections since the initial water clean up, still had not observed any visible water remaining. A Combustion Module activation problem was briefed and reported as successfully resolved.

The crew aboard *Columbia* conducted on-orbit research

experiments throughout their 16 days on orbit, completing a total of 255 orbits prior to the de-orbit burn. In preparation for the descent phase of the mission, crewmembers began deactivating experiments and stowing gear on January 31, 2003. One of the Orbiter's three auxiliary power units was activated to perform routine flight control surface checks and the reaction control system jets were also simultaneously test-fired in preparation for re-entry.

A complete accounting of all on-orbit payload-related anomalies is provided in Section 4.2 of this report.

3.3 Reentry

The SPACEHAB RDM was deactivated on the evening of January 31 and was closed for the final time on the morning of February 1. The deorbit burn was performed at 7:15 a.m. CST, February 1, with a scheduled landing time at Kennedy Space Center of 8:16 a.m. CST.

The following SPACEHAB RDM experiments were powered for the descent phase of the mission: Advanced Protein Crystallization Facility (APCF), Astroculture, Bioreactor Demonstration System-05 (BDS-05), BIOBOX, Commercial ITA Biomedical Experiment (CIBX), CPCG-PCF, Enhanced Orbiter Refrigerator/Freezer (EOR/F), Fundamental Rodent Experiments Supporting Health-2 (FRESH-02), Space Technology and Research Students (STARS-Bootes), Thermoelectric Holding Module (TEHM).

The following mid-deck experiments were powered for the descent phase of the mission: BIOPACK, Closed Equilibrated Biological Aquatic System (CEBAS), Commercial Macromolecular Protein Crystal Growth (CMPCG).

FREESTAR was not powered during the descent phase of the mission.
From de-orbit burn through Orbiter Loss of Signal (LOS), all payload telemetry data received by ground control was nominal according to Payload Multi-Purpose Support Room logs, the POCC, and customer downlinks. In addition, the crew did not report any payload-related issues during the entry phase of the mission. Specifically, the following SPACEHAB RDM data telemetry was reviewed, all of which was nominal through LOS:

- Module Pressure
  - Total pressure
  - Partial pressure O_2
- Cooling Loop Parameters
- Module / Orbiter Interface
  - Coolant lines
  - Power
  - Data
  - Electrical current
- CG Parameters

All OARE downlinked telemetry data was nominal through LOS and the attachment base plate was recovered from the wreckage, with all structural fasteners still attached. FREESTAR was powered off for the descent phase of the mission.

4.0 Anomalies

4.1 Launch

There were no anomalies detected regarding the payload or cargo bay by the STS-107 crew or mission control in Houston during launch (from T-0 through MECO).

4.2 On-Orbit

The following is a listing of all on-orbit payload systems anomalies, a brief description of the impact to the mission, corrective actions taken, and effects of the anomaly on the payload and mission (from MECO through de-orbit burn).

1. **No ICOM B Transmission In SPACEHAB (PLD-001)**
   During communication checks between the Orbiter and SPACEHAB on January 17, the crew reported transmissions on ICOM B were not being heard in the RDM. There was no impact to the mission due to other redundant means of communication, such as the use of ICOM A. The problem was traced to an audio switch configuration and full communication was restored.

2. **SPACEHAB Water Loop Degradation (PLD-002)**
   Payload Heat Exchanger, Subsystem Water Pump outlet pressure, and Total Flow rates for the SPACEHAB water loop were observed steadily decreasing, indicating a pump filter blockage or pump degradation. The impact of this would be the inability for SPACEHAB to maintain the required water loop temperature to provide cooling for the operation of several payloads. Pump 2 was allowed to run as long as possible to catch any additional filter debris and was turned off. Pump 1, the backup pump, was subsequently activated for use for the rest of the mission.
3. **MEIDEX Telemetry Corruption (PLD-003)**
   On January 18, corrupt telemetry was occasionally appearing in the Hitchhiker data stream. This corrupt data provided inaccurate MEIDEX health and status parameters. Ground payload controllers performed software patches to their ground unit, which was thought to be the source of the problem, and the system worked accurately thereafter.

4. **MEIDEX VCR Anomaly (PLD-004)**
   MEIDEX VCRs 2 and 3 stopped recording immediately after the activation command was given by ground control. As a result, there was no VCR recording of orbit #28, but the VCRs were successfully activated during orbit #29. The problem was traced to the previous MEIDEX telemetry anomaly.

5. **KU Channel 2 Data Dropouts (PLD-005)**
   Hardware "lock-ups" were occurring within SPACEHAB since the first flight day. The problem was traced to errors received by the Payload Operations Control Center (POCC). The ability to monitor real-time Ku-band Channel 2 data was lost for a few minutes. The crew performed some troubleshooting to try to solve

the anomaly, but did not solve the anomaly and no further troubleshooting was planned for the flight (ground troubleshooting would continue)

6. **BDS-05 Incubator Temperature High (PLD-006)**
   A crewmember observed the BDS-05 incubator temperature was high on the third flight day. Too high of a temperature would result in the loss of the science for that specific experiment. It was found the internal fans stopped running and the crew, with assistance from ground control, reset the payload and the temperature returned to the designed parameters.

7. **RS1 Potentially Failed Due To Flooding (PLD-007)**
   After noticing a constant reading from the Condensate Tank Pressure on Flight Day 4, the crew checked under the SPACEHAB AD-05 subfloor panel to check for the presence of water. The crew reported seeing over 2 quarts of water around the Water Separator Assembly (WSA), water soaked acoustic pads, and water covering the Aft Power Distribution Unit. The crew used towels to soak up the water and Rotary Separator (RS) #1 was turned off for the remainder of the flight, while RS2 was powered on to compensate. The crew also changed control of the Air Bypass Valve to "Bypass Override" so ground could take control the bypass valve. Blockage internal to RS1 was thought to have caused the flooding under the aft subfloor. A more detailed analysis to determine what happened was planned for post-flight.

8. **MPFE Card Tray #6 Jam (PLD-008)**
   Card tray #6 experienced a "motor time out jam" on January 22, creating the potential for other card jams on other trays. The jam was isolated by the crew to tray #6. For the remainder of the mission, further cards were placed in the Flight Checkout card tray to avoid jams.

9. **SH RS2 Failure (PLD-009)**
   On January 20, an electric short to RS2 was detected and alarmed in SPACEHAB. The POCC commanded the RS2 off and inspection of the circuit breakers by the crew confirmed the short. With both Rotary Separators turned off, SPACEHAB lost all condensation collection capability and required the Orbiter to control humidity. To mitigate condensation in the RDM, the SPACEHAB water loop temperature was raised above the RDM dew point and ground control began controlling the bypass valve to regulate the SPACEHAB temperature. In order to maintain the temperature within acceptable margins, the Orbiter water loops were adjusted and heat loads were reduced. Prior to entry, the WSA under the SPACEHAB subfloor was visually inspected by the crew for water and none was reported. All holes in the WSA were covered with tape to keep any remaining water from escaping during entry.

10. **BIOPACK Premature Shut Down (PLD-010)**
    The BIOPACK payload shut down on four separate occasions, twice when the freezer door was opened, twice when it was not. The loss of the cooler/freezer feature would result in the loss of two experiments. The crew re-cycled the power for BIOPACK but the problem persisted. The affected experiments were transferred to the PTCU 1 payload for the remainder of the mission.

11. **CM-2 / MIST Flame Tube Evacuation Leak PLD-011)**
    On January 28, gas from the Combustion Module chamber was leaking into the evacuated MIST flame tube. The crew was unable to start the Water Mist Fire Suppression Experiment. In flight maintenance was performed to seal off the gas sampling line and the crew successfully fixed the leak. The repair delayed the start of the Water Mist Fire Suppression Experiment, but had no other adverse affects and the 34 planned runs of the experiment were still accomplished prior to the end of the flight.

4.2.1 SPACEHAB Condenser Anomaly Description

On January 20, one of two SPACEHAB RDM Rotary Separators failed. These systems are designed to collect and distribute water produced by normal condensation buildup during operation of the cooling system. Rotary Separator #1 (RS1), located under the aft subfloor of the SPACEHAB RDM, began leaking, most likely due to an internal blockage, and was shut down. The exact amount of water released was unknown but estimates ranged from between one cup of water to two liters. Upon inspection under the subfloor, water was observed surrounding the Water Separator Assembly (WSA), soaking into acoustic pads, and covering the Aft Power Distribution Unit. The crew used towels to soak up the water and changed the Air Bypass Valve (ABV) configuration to "Bypass Override", allowing ground control to operate the valve. The secondary system, Rotary Separator #2 (RS2), was turned on and operated normally, adequately compensating for the primary system.

Several hours later on January 20, RS2 experienced an electrical short, most likely due to water from the RS1 leak coming in contact with the electrical connections of RS2. Onboard alarms "223 SH INV AFT PB A" and "225 SH RS2 SPD LO" annunciated, while ground control simultaneously observed an electrical spike via fuel cell and SPACEHAB telemetry (the spike returned to normal shortly after). The crew inspected the circuit breakers on board and verified two of the three related breakers (CB 8 Phase B & C that powered the WSA) were tripped. The crew, at the instruction of ground control, then manually tripped the third circuit breaker (CB 8 Phase A). The POCC commanded the RS2 off, at which time all loads returned to normal.

The shutdown of both Rotary Separators resulted in the loss of the SPACEHAB RDM's ability to collect condensation water and required the Orbiter systems to control humidity within the RDM.

In order to reduce the likelihood of additional condensation within the RDM, the module's water loop temperature

was increased to bring it above the dew point. This raise in water loop temperature would allow operations within the SPACEHAB RDM to continue without the risk of additional condensation. The previous ABV reconfiguration was determined as sufficient to control heating within the RDM, and an additional plan to re-route air ducts from the Orbiter to the module to increase air flow was deemed not necessary. Additional adjustments to the Orbiter water loop, and reductions in the heat load within the SPACEHAB RDM, were sufficient to maintain an acceptable air temperature range of around 73 degrees Fahrenheit (after an initial climb in temperature to 80 degrees).

In preparation for the de-orbit burn and entry, the crew visually inspected under the subfloor of the SPACEHAB RDM one last time to ensure no water was present on January 30. No moisture was found. The crew covered several holes in the WSA with tape as a precaution to ensure any water present, but not visible, did not escape during entry. Since an electrical short occurred earlier in the mission, ground controllers associated with the EGIL console instructed the Orbiters AC power bus to be turned off for entry to prevent a short from propagating to the Orbiter's main power supply, in the event another RDM electrical short occurred.

The SPACEHAB RDM was deactivated as planned on January 31 in preparation for entry and closed for the last time early on the morning of February 1.

4.3 Reentry

There were no anomalies detected regarding the payload or cargo bay by the STS-107 crew or the Mission Control Center in Houston during entry (from de-orbit burn through LOS).

Appendix A: Acronyms

ABV	Air Bypass Valve
AMS	Automated Microbial System
APCF	Advanced Protein Crystallization Facility
APDU	Aft Power Distribution Unit
ARMS	Advanced Respiratory Monitoring System
ARS	Atmospheric Revitalization System
BDS-05	Bioreactor Demonstration System-05
BIOTUBE/MFA	Gravisensing & Response Systems of Plants
BRIC	Biological Research In Canisters
CCA	CO2 Control Assembly
CEBAS	Closed Equilibrated Biological Aquatic System
CEWL	Centralized Experiment Water Loop
CG	Center of Gravity
CHX	Condensing Heat Exchanger
CIBX	Commercial ITA Biomedical Experiment
CIR	Cargo Integration Review
CITE	Cargo Integration Test Equipment
CM-2	Combustion Module-2
CMPCG	Commercial Macromolecular Protein Crystal Growth
COM2PLEX	Combined 2 Phase Loop Experiment
CPCG-PCF	Commercial Protein Crystal Growth – Protein Crystallization Facility
CSS	Condensate Storage System
CVX-2	Critical Viscosity of Xenon-2
DC	Direct Current
ECU	Environmental Control Unit
EDO	Extended Duration Orbiter
EDS	Experiment Data System
EDSMU	Experiment Data System Main Unit
EGIL	Electrical Generation and Integrated Lighting
EIU	Experiment Interface Unit
EOR/F	Enhanced Orbiter Refrigerator/Freezer
EPDB	Emergency Power Distribution Box
ERISTO	European Research in Space and Terrestrial Osteoporosis
ESA	European Space Agency
FAST	Facility for Adsorption and Surface Tension
FCE	Flight Crew Equipment
FD	Flight Day
FREESTAR	Fast Reaction Experiment Enabling Science Technology Applications and Research
FRESH-2	Fundamental Rodent Experiments Supporting Health-2
FRR	Flight Readiness Review
GLS	Ground Launch Sequencer
ICD	Interface Control Document
IFA	In-Flight Anomaly
JSC HLS	Johnson Space Center Human Life Sciences
KUSP	Ku-Band Signal Processor
L•	Launch minus (hours or days)
LCC	Launch Commit Criteria
LDM	Logistics Double Module
LOS	Loss of Signal
LPT	Low Power Transceiver
LSM	Logistics Single Module
LSP	Laboratory Support Processor
LSP	Laminar Soot Processes
MECO	Main Engine Cut-Off
MEIDEX	Mediterranean Israeli Dust Experiment
MGM	Mechanics of Granular Materials
MPFE	Microbial Physiology Flight Experiments
MMT	Mission Management Team
MSTRS	Miniature Satellite Threat Reporting System
NASA	National Aeronautics and Space Administration
OARE	Orbital Acceleration Research Experiment
OPF	Orbiter Processing Facility
OSTEO	Osteoporosis Experiment in Orbit
OV	Orbiter Vehicle
PhAB4	Physiology and Biochemistry 4
POCC	Payload Operations Control Center
PRR	Payload Readiness Review
PSRP	Payload Safety Review Panel
PTCU	Biopack w/ Passive Thermal Controlled Unit
RDM	Research Double Module
RDU	Rack Distribution Unit
RS	Rotary Separator
RSM	Research Single Module
RSS	Rack Support Structure
S&MA	Safety and Mission Assurance
SAMS FF	Space Acceleration Measurement System Free Flyer
SOFBALL	Structure of Flameballs at Low Lewis Numbers
SEM	Space Experiment Module
SOLCON-3	Solar Constant Experiment-3
SOLSE-2	Shuttle Ozone Limb Sounding Experiment-2
SSPF	Space Station Processing Facility
STARSTM	Space Technology and Research Students
STS	Space Transportation System
T•	Time minus (minutes)
TEHM	Thermoelectric Holding Module
VCD FE	Vapor Compression Distillation Flight Experiment
WSA	Water Separator Assembly
ZCG-1	Ziolite Crystal Growth-1

THIS PAGE INTENTIONALLY LEFT BLANK

Volume II
Appendix D.7
Working Scenario

The Working Scenario was the result of a joint effort between the Columbia Accident Investigation Board (CAIB) and the NASA Accident Investigation Team (NAIT). The report was written beginning early in the investigation to track the current understanding of the events that led to the loss of *Columbia*. As such, the report evolved over time as facts became known, theories were developed or disproved, and NASA and the Board gained knowledge of the accident sequence.

The report was written to document the collection of known facts, events, timelines, and historical information of particular interest to the final flight of *Columbia*. The Columbia Accident Investigation Board released the final version of the Working Scenario to the public on July 8, 2003. The version contained here has been reformatted to match the overall style of the first volume and has had a few minor editorial corrections, but nothing that changes the substance of the report.

The Working Scenario includes information from numerous analyses, tests, and simulations related to the *Columbia* investigation that had been completed, or were ongoing at the time that this report was completed, i.e., up to and including July 8, 2003.

This effort compiles and documents the principal facts related to specific vehicle element events, timelines, and data. It also includes pertinent historical data surrounding some of the key vehicle element considerations in the investigation. The scenario addresses the chronology of vehicle events from prelaunch, launch countdown, launch/ascent, orbit, and re-entry, as well as specific information for the External Tank and the left wing, including aspects of the Reinforced Carbon-Carbon (RCC) and attachment hardware. Vehicle processing and significant preflight events and milestones are also discussed. The scenario addresses technical aspects only, and does not address management practices or philosophies, or other organizational considerations.

Preface 165
Section 1.0 Introduction 165
1.1 Scope 165
1.2 Mission Background 165

Section 2.0 Launch Countdown 166

Section 3.0 Launch 168
3.1 Introduction 168
3.2 Launch Debris Impact Observation 168
3.2.1 Launch/Ascent Conditions 168
3.2.2 Launch Debris Impact Area 169
3.2.3 Launch Photo and Transport Analysis 169
3.2.4 Debris Velocity and Size Assessment 171
3.2.5 Impact Damage Testing and Analysis 172
3.3 Launch MADS Data 173
3.4 Launch Area Radar Analysis 175
3.5 Launch Guidance Navigation and Control 177
3.5.1 Wind Shear, Day of Launch Wind Effects 178
3.5.2 Predicted/Actual Loads 179
3.5.3 ET Liquid Oxygen Slosh 181
3.5.4 Nozzle Positions 182
3.5.5 ET Separation Yaw Rate 184
3.5.6 Data Correlation of Flights that Used a LWT and PEs 184
3.5.7 Data Correlation of Flights with ET Bipod Foam Liberation 185

Section 4.0 Orbit 186
4.1 Introduction 186
4.2 Orbital Debris 186
4.2.1 Orbital Debris Risk Assessment 186
4.2.2 Micrometeoroid or Orbital Debris Detection 186
4.3 Flight Day 2 Event 189
4.3.1 Radar Tracking of Flight Day 2 Object 189
4.3.2 Analysis of Mechanisms for Object Release 190
4.3.3 Radar Cross Section and Ballistics Testing 191
4.3.4 KSC Lost and Found Items 192
4.4 Orbit Summary 192

Section 5.0 Deorbit/Entry 192
5.1 Introduction 192
5.2 Weather 192
5.2.1 Upper Atmosphere Weather 192
5.2.2 Landing Weather 192
5.3 Hardware Forensics 193
5.4 Entry Events Timeline 196
5.4.1 Early Entry Heating Events 196
5.4.2 First Roll Maneuver Through Wing Spar Breach 197
5.4.3 Wing Breach and Wire Failures 200
5.4.4 Aerodynamic Events 203
5.4.5 Wheel Well Gas Penetration and Final Aerodynamic Events 207
5.5 Aerodynamic Reconstruction 209

Section 6.0 Re-usable Solid Rocket Motor 212

Section 7.0 Solid Rocket Booster 212

Section 8.0 Space Shuttle Main Engine 212

Section 9.0 Environmental Factors 212
9.1 Introduction 212
9.2 Age and Exposure 213
9.3 Weather Factors 214

Section 10.0 Left Wing Processing and RCC Design 216
10.1 Introduction 216
10.2 Left Wing Processing (Palmdale, J3-OMM) 216
10.3 Left Wing Processing (STS-109) 218
10.4 Left Wing Processing (STS-107) 218
10.5 RCC Design 218
10.6 RCC Impact Resistance 219
10.7 RCC Corrosion 220

Section 11.0 External Tank 222
11.1 Introduction 222
11.2 TPS Requirements 222
11.3 History of Foam Changes and Debris Events 222
11.4 STS-107/ET-93 Chronology 223
11.4.1 Bipod Ramp TPS Configuration 223
11.4.2 Bipod Ramp Certification 227
11.4.3 Bipod Ramp Build Process 227
11.4.4 Bipod Ramp Foam Acceptance/Non-Destructive Evaluation 227
11.4.5 ET Shipping and Handling 228
11.4.6 KSC Processing Activities 228
11.4.7 ET Pre-launch Operations 228
11.4.8 Launch/Ascent 228
11.4.9 Possible Contributors to Strain Energy at ET Separation 229
11.5 STS-107/ET-93 TPS Bipod Debris 229
11.5.1 Bipod Foam Failure Modes and Contributors 229
11.5.2 Test Results for Debris Assessment 230
11.5.3 Max Bipod SLA Temperatures (80 seconds MET) 230
11.5.4 Bipod Ramp As-Built Hardware Assessment 231
11.5.5 Multi-Failure Mode TPS Bipod Debris 231

Section 12.0 Summary 232

Appendix A Acronyms and Abbreviations 233

Appendix B Working Scenario Team 234

TABLES

3-1 Wing damage analysis methods and results. 170
3-2 Transport analysis and ET Working Group estimates of ET bipod debris size, weight, and volume. 172
3-3 STS-107 ascent radar events. 176
3-4 Material samples from post-STS-27 radar calibration tests. 177
3-5 LWT and PE flights. 184
3-6 STS flights with ET left bipod foam liberation. 185

4-1 Summary of analysis of 13 rate events. 187
4-2 Summary of analysis of the lower bound of MMOD (based on body rate data). 187
4-3 Chronology of events related to flight day 2 object. 190
4-4 Summary of nominal launch day events. 190
4-5 Lost tools in *Columbia* processing for STS-107, STS-109, and OMM J3. 191

10-1 RCC refurbishment limits. 220

11-1 STS-Orbiter-ET configuration, age, and exposure. 223

FIGURES

1-1 STS-107 payload bay configuration. 166

2-1 STS-107 Launch Countdown (LCD) overview flowchart. 167
2-2 Shuttle vehicle coordinate system. 168

3-1 Launch of STS-107 at pad 39A at Kennedy Space Center. 169
3-2 STS-107 reconstructed altitude during first stage (prior to SRB separation). 169
3-3 STS-107 flight reconstruction data for mach number and dynamic pressure (Q-bar) prior to SRB separation. Note that Q-bar is highest during first stage (prior to SRB separation), and reduces to a very small number after SRB separation. 169
3-4 Area of most likely wing damage. 169
3-5 Multiple analyses determine foam impacted lower RCC panels 6 through 8 area. 170
3-6 Photographic analysis techniques determined foam size: debris appears almost circular in frame 4914 and elongated in frame 4919. 170
3-7 Camera geometry for ascent video analysis; note that video camera ET208 is at same location as film camera E208. 171
3-8 Orbiter view from cameras E212 and ET208. 171
3-9 Multiple analyses indicate foam is from ET left bipod area. Red line depicts the estimated foam trajectory as it moved from the bipod ramp area toward the left wing. 171
3-10 Video analysis shows impact is below wing leading edge stagnation line. Trajectories of particles are depicted after the impact. 171
3-11 Pre-impact vs. post-impact shows no observable damage within the resolution limits. 171
3-12 Sample CFD flow field with debris modeling. 172
3-13 CFD surface flow with lower left wing pressure sensors. 173
3-14 Unusual behavior of pressure sensor V07P8074A. 173
3-15 Close-out photo shows RCC panel 9 wing leading edge temperature measurement. 174
3-16 Three-bit rise (7.5 degrees F) on MADS wing leading edge spar temperature measurement (V09T9895A) during ascent. 174
3-17 Correlation between simplified thermal math model and STS-107 ascent and entry flight data. 174
3-18 STS-107 ascent and entry heating environments on RCC panel 9. 175
3-19 Limits of dimensional detectability for three simple shapes. 175
3-20 Limits of radar cross section (RCS) detectability and measured STS-107 debris for three radar source sites. 177
3-21 Out-of-plane wind velocity. 178
3-22 Side-slip angle. 178
3-23 Wing loads during wind shear and side-slip angle. 179
3-24 ET interface loads at forward attachment during wind shear and side-slip angle. Q-beta is side-slip angle multiplied by the dynamic pressure and represents the side-slip angle contribution of the interface load. 180
3-25 Slosh effect on ET interface loads. 180
3-26 ET bipod axial aerodynamic loads. 180
3-27 ET bipod side-force aerodynamic loads. 181
3-28 ET bipod radial aerodynamic loads. 181
3-29 STS-107 SRB tilt actuators experienced more than typical 0.6 Hz content. 181
3-30 STS-107 SRB gimbal responses at 0.6 Hz frequency correlated to wind. 181
3-31 Center SSME yaw position. 182
3-32 Right SSME yaw position. 182
3-33 RSRM burn rate at propellant mean bulk temperature (PMBT). 182
3-34 SRB thrust mismatch. 182
3-35 SRB nozzle position for PE flights versus non-PE flights. 183
3-36 ET separation yaw rate. 184

4-1 Jet firing example for vehicle rates. 188
4-2 Sample data from SAMS and ODRC. 189
4-3 SAMS data frequency content. 189
4-4 Tracking of flight day 2 object through various sensor passes. 189
4-5 On-orbit RCS shows increased tumble/rotation rate over time. 189
4-6 Leading edge structural subsystem components matching RCS and ballistics. 191

5-1 Wind profile developed by DAO as part of the STS-107 investigation (time referenced to 8:min:sec EST). 192
5-2 Slag deposition in the RCC panel 8/9 area relative to the other parts of the left wing leading edge. 193
5-3 Samples of severe slag deposition on the panel 8 rib. 193
5-4 Example of rib erosion. 194
5-5 Flow on the lower carrier panel 9 tiles. 194
5-6 CAD drawing of the recovered debris showing overall slag deposition and erosion patterns. 194

5-7 Analysis results show possible flow direction and deposition of metals. 195
5-8 RCC panel debris location. 195
5-9 Three possible orbiter locations of the Littlefield tile on left wing. 196
5-10 STS-107 stagnation heat flux and dynamic pressure. Note that EI was at 8:44:09 EST. 196
5-11 Left wing RCC panel 9 strain gauge is first measurement to indicate an off-nominal event. Note that EI was at 8:44:09 EST. 196
5-12 MADS sensors inside left wing. 196
5-13 Left wing RCC panel 9/10 clevis temp sensor is second measurement to indicate an off-nominal event. 197
5-14 Typical off-nominal OMS pod thermocouple (V07T9220A). 197
5-15 Location of OMS pod thermocouples off-nominal low. 197
5-16 Postulated orbiter leeside flow field associated with wing leading edge damage. 198
5-17 Orbiter wind tunnel model with vent gap along wing leading edge. 198
5-18 Wind tunnel model results for sensitivity of orbiter side fuselage and OMS pod heating patterns to mass addition along WLE leeside vent gap. 198
5-19 Location of left sidewall temperature sensor. 199
5-20 Off-nominal temperature indication on the left sidewall. 199
5-21 Temperature rise on tile surfaces aft of RCC panel 9. 199
5-22 Left wing MADS sensors, including measurement stimulation identification (MSID) number, and start time of loss of signal (EI + sec.). 199
5-23 RCC panel 9 MADS strain and temperature measurements, STS-107. 199
5-24 Off-nominal low OMS pod thermocouple (V07T9972A). 200
5-25 Left side fuselage/OMS pod off-nominal responses indicate increased heating. 200
5-26 Wind tunnel test results for RCC panel 9 missing and resulting in increased heating to OMS pod. 200
5-27 CFD results for no damage, partial damage, and full damage to RCC panel 9 show increased heating on side fuselage and OMS pod. 200
5-28 STS-107 entry heating rate profile. 200
5-29 Cable routing on wing leading edge and wheel well wall. 201
5-30 Thermal model prediction of wing spar burn through. 201
5-31 Hot gas begins to fill left wing. 201
5-32 *Columbia* LH wing and wheel well geometry. 202
5-33 *Columbia* LH wing and wheel well vent model (wheel well leak paths based on *Atlantis* test comparison). 202
5-34 MADS data failure due to wire burning. 202
5-35 View of cables running along outside of wheel wall cavity bulkhead. 202
5-36 Strain measurements on 1040 spar. 203
5-37 Off-nominal temperature rise rate in nose cap RCC attach clevis. 203
5-38 Location of sensors in the LH wing wheel well. 203
5-39 Strain rise in lower 1040 spar cap. 203
5-40 Outboard elevon accelerometer responses at 8:52:25 and 8:52:31 EST (EI + 496 and 502 sec.). 204
5-41 Location of supply dump and vacuum vent nozzles. 204
5-42 Off-nominal temperature for supply nozzle and vacuum vent nozzle. 204
5-43 First noted off-nominal aero event. 205
5-44 Sharp change in rolling moment. 206
5-45 Modeling results show potential area of damage and that significant deformation of the intermediate wing area and/or a recession in the lower surface are possible. 206
5-46 Temperature data in left wheel well trends up. 207
5-47 Hot gas breaches the wheel well. 208
5-48 Kirtland photo with superimposed Orbiter outline.. 208
5-49 Increased wing deformation and wing recession leads to significant vehicle aerodynamic changes. 209
5-50 Wind tunnel testing configurations that match delta roll moment data. 209
5-51 Wind tunnel configurations that match delta yaw moment data. 210
5-52 Wind tunnel configurations that match delta pitch moment data. 210
5-53 Delta roll for lower half and full panel RCC panel missing. 210
5-54 Delta yaw for lower half and full panel RCC panel missing. 210
5-55 Wind tunnel testing results for missing lower carrier panel 8 and a slot and hole through wing. 211
5-56 CFD analysis of wing deformation. 211
5-57 LaRC wind tunnel testing of lower surface depressions. 211

7-1 Details of SRB/ET forward separation bolt catcher assembly. 212

9-1 ET age for all STS missions. 213
9-2 ET age for STS-107 compared to ET age for missions with and without bipod foam loss. 213
9-3 ET exposure time (to weather) prelaunch for all STS missions. 213
9-4 ET exposure time (to weather) for STS-107 compared to ET exposure time for missions with and without bipod foam loss. 214
9-5 Total prelaunch rainfall for all STS missions. 214
9-6 Total rainfall for STS-107 compared to total rainfall for missions with and without bipod foam loss. 214
9-7 Average daily rainfall prelaunch for all STS missions. 215
9-8 Average daily rainfall prelaunch for STS-107 compared to average daily rainfall for missions with and without bipod foam loss. 215
9-9 Day-of-launch average temperature for all STS missions. 215
9-10 Prelaunch average dewpoint for all STS missions. 216
9-11 Prelaunch average humidity for all STS missions. 216

10-1 RCC components. 217
10-2 RCC panel assembly. 217
10-3 Typical tile installation. 217
10-4 Wing leading edge RCC. 218
10-5 RCC cross section. 219
10-6 RCC impact resistance. 220
10-7 RCC corrosion process. 220
10-8 Tee seal crack location. 221
10-9 Tee seal cracking. 221
10-10 RCC pinholes. 221
10-11 RCC impact damage. 221

11-1 History of foam changes. Blowing agent shown in parentheses. No changes to SLA. 222
11-2 Right (+Y) bipod ramp. 226
11-3 Left and right bipod ramp flow differences, CFD results. 227
11-4 ET-93 processing timeline at KSC. 228
11-5 ET LO2 slosh baffle changes – ET-14. 229
11-6 ET LO2 slosh baffle changes – ET-87. 229
11-7 Bipod foam failure modes. 230
11-8 Schematic of bipod ramp - potential cryopumping. 230
11-9 Critical test results in debris assessment. 230
11-10 Max bipod SLA temperatures (80 seconds MET), °F. 231
11-11 Defects found at critical locations. 231
11-12 Weakened plane defect found. 231
11-13 Multi-failure mode bipod TPS debris estimated by the ET Working Group. Note that this size and weight were not used in the RCC impact testing as part of the STS-107 investigation. 231

Working Scenario

Prepared by the Columbia Accident Investigation Board (CAIB)
and the National Aeronautics and Space Administration (NASA) Accident Investigation Team (NAIT)

PREFACE

This Working Scenario report was written to document the collection of known facts, events, timelines, and historical information of particular interest to the final flight of *Columbia*. The report was written with the understanding that it could be published, either in part or in its entirety, as part of the official Columbia Accident Investigation Board (CAIB) report. The report includes information and results from numerous analyses, tests, and simulations related to the *Columbia* investigation that have been completed, or were ongoing at the time that this report was completed. It is anticipated that additional analytical and test results will emerge from ongoing work, as well as from future activities associated with the *Columbia* investigation and efforts related to the Return-To-Flight work. This Working Scenario includes information and results as they existed up to and including July 8, 2003.

1.0 INTRODUCTION

1.1 SCOPE

The Working Scenario is the result of a joint effort between the Columbia Accident Investigation Board (CAIB) and the NASA Accident Investigation Team (NAIT). This effort collates and documents the principal facts related to specific vehicle element events, timelines, and data. It also includes pertinent historical data surrounding some of the key vehicle element considerations in the investigation. The scenario addresses the chronology of vehicle events from prelaunch, Launch Countdown (LCD), launch/ascent, orbit, and entry as well as specific information for the External Tank (ET) and the Left Hand (LH) wing, including aspects of the Reinforced Carbon-Carbon (RCC) and attachment hardware. Vehicle processing and significant preflight events and milestones are also discussed. The scenario addresses technical aspects only, and does not address management practices or philosophies, or other organizational considerations.

The chronological portion of the scenario is contained in Sections 2 through 5 of this report. These sections discuss the prelaunch, launch, orbit, and deorbit/entry portions of the Space Transportation System 107 mission (STS-107). Sections 6 through 8 address the facts related to the Reusable Solid Rocket Motor (RSRM), Solid Rocket Booster (SRB), and Space Shuttle Main Engine (SSME) elements. Section 9 addresses relevant environmental factors such as weather and age of the ET. Section 10 addresses the details of *Columbia* vehicle processing, specifically as it pertains to the LH wing, from the most recent Orbiter Major Maintenance (OMM) at Palmdale, California, through the processing for STS-107. This section also includes a number of design and historical considerations for the LH wing and for the RCC in general. Section 11 addresses several aspects of the ET, including manufacturing, Kennedy Space Center (KSC) processing, Thermal Protection System (TPS) requirements, and numerous aspects of the foam insulation. These discussions provide the history of the bipod foam ramp design, fabrication, testing, and address the details of bipod foam ramp debris failure modes, testing, and analyses. Section 12 briefly summarizes the discussion of the working scenario.

The data sources and types include, but are not limited to, telemetry from all flight phases, Modular Auxiliary Data System (MADS) data from ascent and entry, video and imagery from launch/ascent and entry, and launch/ascent radar. It also includes reconstructed aerodynamic and vehicle loads, Radar Cross Section (RCS) and ballistics, aero/thermal, structural, debris forensics, post-flight test data (TPS impact, ET/SRB bolt catcher, wind tunnel, etc.), and prelaunch processing.

1.2 MISSION BACKGROUND

STS-107 was the 113th mission in the Space Shuttle program and *Columbia*'s 28th trip into space. These 28 missions spanned 22 years with the first being STS-1, launched on April 12, 1981. The STS-107 mission was a science research mission and the payload complement consisted of the

Spacehab Double Research Module and the Fast Reaction Enabling Science, Technology, and Research (FREESTAR). The mission altitude was approximately 150 nautical miles with an inclination of 39 degrees. Figure 1-1 depicts the STS-107 payload bay configuration.

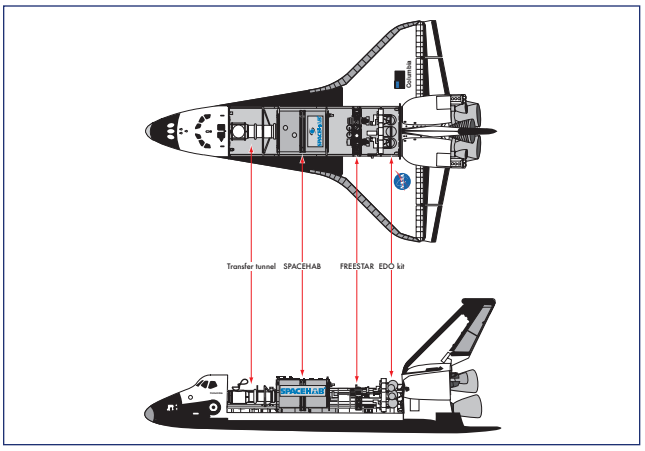


Figure 1-1. STS-107 payload bay configuration.

STS-107 was a Shuttle mission dedicated to investigating human physiology, fire suppression, and other areas of research, with 80-plus experiments representing the latest application of micro-gravity research. The seven-member crew devoted 16 days on-orbit to a mixed complement of research in the space, life, and physical sciences including biology, physics, and chemistry. Other investigations studied factors that control our terrestrial climate. Participants included several NASA centers, universities, and education and research organizations throughout the United States, along with the European Space Agency (ESA), the Canadian Space Agency (CSA), the Japanese National Space Development Agency (NASDA), the German Aerospace Research Establishment (DLR), and the Israeli Space Agency.

The primary payload carrier on STS-107 was the new SPACEHAB Research Double Module (RDM), doubling the volume available for, and significantly increasing the amount and complexity of, micro-gravity research. The RDM was a pressurized environment carried in *Columbia*'s payload bay and accessible to the crew via a tunnel from the Shuttle's middeck.

SPACEHAB Inc., via commercial contracts, enabled many universities, companies, and other government agencies to conduct important research in space on STS-107. As an example, the CSA conducted three bone-growth experiments and the DLR measured the development of the gravity-sensing organs of fish in the absence of gravity's effects. One university grew ultra-pure protein crystals for drug research while another university tested a navigation system for future satellites. The U.S. Air Force conducted communications experiments. Elementary school students in Australia, China, Israel, Japan, Liechtenstein, and the United States studied the effects of space flight on fish, spiders, ants, silkworms, bees, and even inorganic crystals.

Columbia's payload bay also housed six science payloads known as FREESTAR, which were mounted on a Multi-Purpose Experiment Support Structure bridge spanning the width of the Payload Bay (PLB). These experiments performed solar observations, earth science and atmospheric observations, fluid physics, and demonstrated new communications technology for future spacecraft. *Columbia* was also outfitted with an Extended Duration Orbiter (EDO) cryogenic pallet, which provided the required consumables for the long duration of the mission.

The Mediterranean Israeli Dust Experiment (MEIDEX), managed by the Israeli Space Agency and Tel-Aviv University, was one of the key FREESTAR experiments. The primary objective of MEIDEX was to observe dust storms in the Mediterranean and the Atlantic coast of Africa using a radiometric camera mounted in the payload bay, which was remotely controlled by the ground or astronauts in the crew cabin. Secondary objectives of MEIDEX included observations of slant visibility, sea-surface and desert-surface reflectivity, and Transient Luminous Events, such as sprites.

2.0 Launch Countdown

The STS-107 Launch Countdown (LCD) was approximately 24 hours longer than a typical International Space Station (ISS) countdown, but within the experience base of other SPACELAB or SPACEHAB-type missions. There were some differences in this countdown as compared to most LCDs, primarily because this was not an ISS mission. Some of the more significant differences were due to the Extended Duration Orbiter (EDO) pallet that provided additional electrical power generation capability for this 16-day science mission, and the fact that the SPACEHAB module had to receive final stowage late in the countdown to accommodate the live animals and other unique science payloads. Figure 2-1 details the STS-107 LCD overview flowchart.

There were no significant issues during the LCD including the Power Reactants Storage Device (PRSD) cryogenic load or EDO planned offload operations. The crew module activities were in the critical path from L-48 hours (post-PRSD) through the start of External Tank (ET) loading due to the amount of SPACEHAB and middeck stowage items. The SPACEHAB stowage activities were completed approximately 90 minutes late due to configuration issues and the significant amount of equipment to stow. However, the LCD team was back on the critical path timeline by the completion of the communication system activation (~ L-24 hours).

ET propellant loading was delayed by approximately 70 minutes (started at L-7 hours, 20 minutes) due to several factors. These factors included the fuel cell activation/calibration running longer than planned because the time allocated for this activity was not adequate for the additional cryogenic tanks on the EDO pallet. Also, the work to resolve Interim Problem Report 110 (IPR 107V-0110), which was written to document a Liquid Oxygen (LO2) replenish valve problem, required access to the Mobile Launch Platform (MLP) and delayed preparation for ET

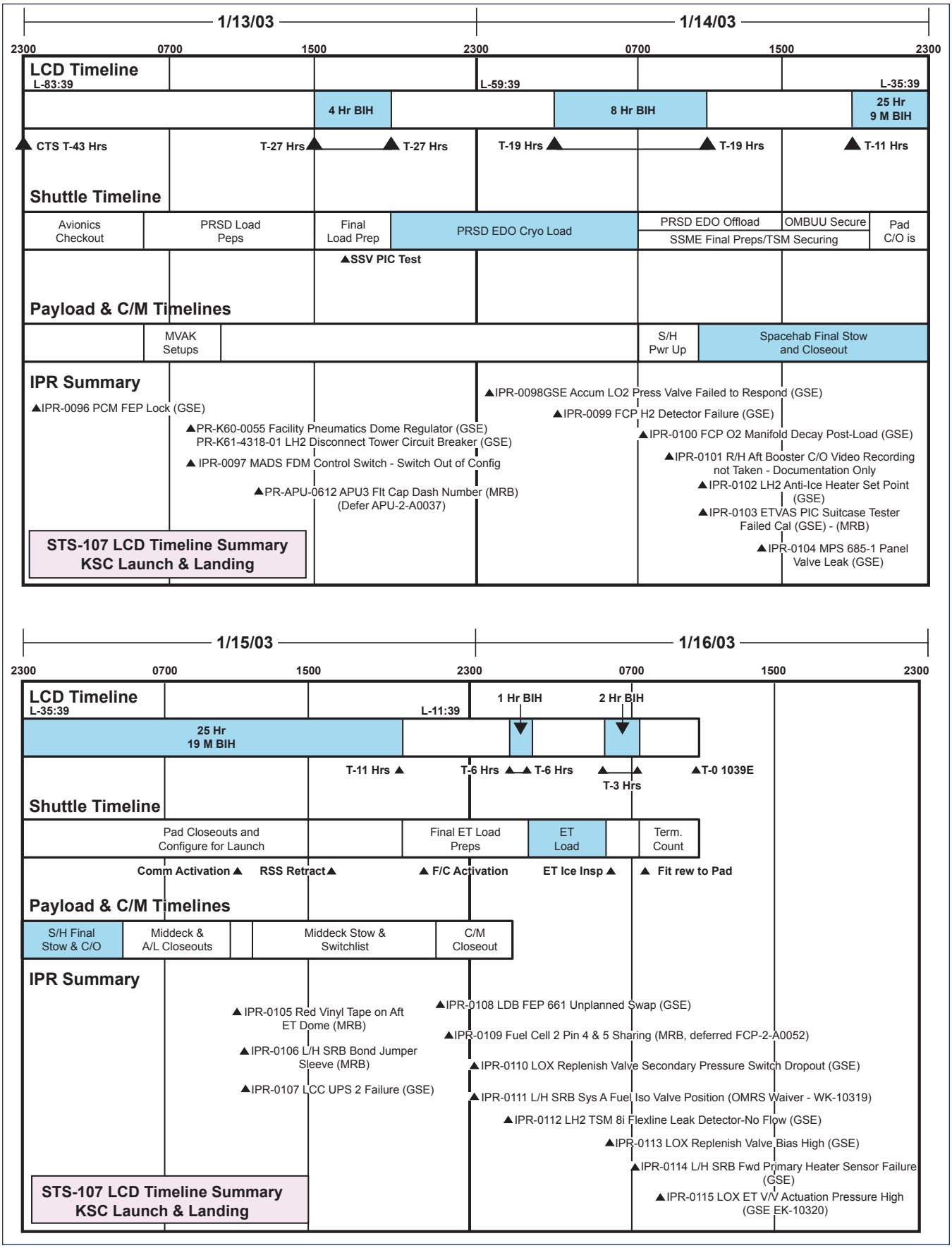


Figure 2-1. STS-107 launch countdown (LCD) overview flowchart.

LO2 filling operations. As a result of troubleshooting for another IPR (IPR 107V-0108, Front-End Processor (FEP) 661 Unplanned Swap), a Launch Processing System (LPS) reconfiguration of the active/standby launch data bus FEP power supplies was required to provide power redundancy for ET loading.

LO2 and LH2 tank loading were both normal, and all loading cycles were within previous experience. According to postflight analysis, at the end of propellant loading (end of replenish), the LH2 tank load was 231,035 pounds mass (lbm), and the LO2 tank load was 1,382,980 lbm. The postflight analysis includes corrections for the specific ET volume for both tanks and helium injection density corrections for the LO2 tank.

The post-ET load Ice Team inspection was performed with no significant issues noted relative to previous inspections. The inspection began at 6:15 EST and finished at 7:45 EST. The weather conditions at the start of inspection were as follows: temperature 48 degrees Fahrenheit, relative humidity 97 percent, winds from 290 degrees at 5 knots. One item of interest was noted with respect to the –Y (left) bipod ramp closeout area (see Figure 2-2 for vehicle coordinate system orientation). The Liquid Hydrogen (LH2) section of the Ice Team report noted that there were visual indications of frost along the bondline of the ET –Y bipod, and that the frost dissipated by 7:15 EST, after sunrise. The ET bipod assembly is located at the forward ET/orbiter attach point, and indications of frost are not unusual in this area.

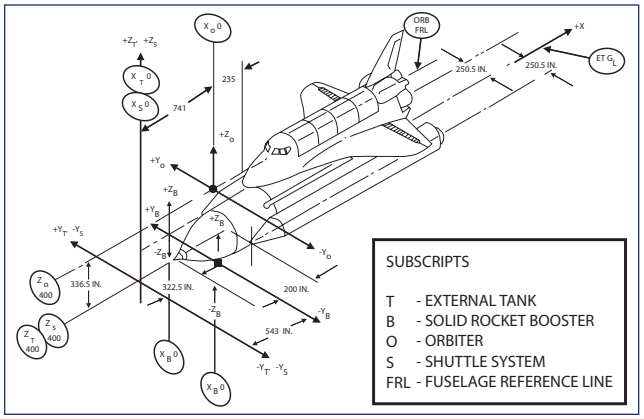


Figure 2-2. Shuttle vehicle coordinate system.

The postlaunch debris walk down was performed at the launch pad per Operations and Maintenance Instruction (OMI) S6444, and no unusual debris or damage was noted. All IPRs and Problem Reports (PRs) recorded during the LCD were evaluated and three were noted as worthy of discussion since they involve possible ascent debris or the ET. The first, IPR 107V-0102, LH2 Anti-Ice Heater Failed Set Point, was written to document a Ground Support Equipment (GSE) heater that did not control to the required set point within the specified time. The Alternating Current (AC) phasing was found incorrectly wired due to a previous modification. The associated power leads were swapped and retested on the second day of the LCD without incident. This system performed nominally for the remainder of the LCD.

The second item, IPR 107V-0105, Red Vinyl Tape on Aft ET Dome, was written to document a small piece of red vinyl tape (1 in. by 1.5 in.), similar to that used in Solid Rocket Booster (SRB) closeout activity, which was found adhered to the +Y side of the ET LH2 aft dome (Y-Y axis approximately 1 ft aft of station XT2058) during the L-1 day walk down. There was no visible Thermal Protection System (TPS) damage noted in the vicinity of the tape. The tape was accepted to use as-is via the Material Review Board (MRB) process. The rationale was that the tape was limited in size and mass, presented no adverse effect to the TPS performance, and was outside of the critical debris zone since it was located on the very bottom part of the ET.

The third item was IPR 107V-0106, Booster Bond Jumper Sleeve Not Removed. This IPR was written for a part marking identification sleeve found on the systems tunnel ground strap 5 feet below the aft web of the right booster ET attach ring near the booster factory joint Xb-1577. The small plastic sleeve was accepted via Material Review (MR) board to use "as-is," because the sleeve and strap would not be affected by aero heating, and if the sleeve melted or tore away during ascent, its trajectory would be outside the orbiter debris zone.

3.0 Launch

3.1 Introduction

This section discusses the launch and ascent phases of STS-107 in four separate sections. The first section outlines some general launch conditions and an introduction to the ET bipod foam impact, including photographic and debris transport analyses, as well as RCC impact testing and analyses. The next section discusses several key MADS measurement signatures from the ET foam impact timeframe. This is followed by a summary of launch and ascent radar, and corresponding analyses. The final section is a detailed discussion of several orbiter Guidance, Navigation, and Control (GNC) system events of interest from the ascent timeframe. These include wind shear, ascent loads, ET propellant slosh, and SSME and SRB nozzle positions. The discussion centers around possible correlation of these events with other families of flights, including the family of flights where it is known that ET bipod foam loss occurred.

3.2 Launch Debris Impact Observation

3.2.1 Launch/Ascent Conditions

Launch occurred at the Kennedy Space Center (KSC), launch pad 39A, on January 16, 2003, at 10:39 EST (see Figure 3-1). The weather at pad 39A, 60-foot level was: temperature 65 degrees Fahrenheit, relative humidity 68 percent, dew point 59 degrees Fahrenheit, with calm winds. Figure 3-2 shows the STS-107 reconstructed altitude data and Figure 3-3 shows the mach number and dynamic pressure during first stage, prior to Solid Rocket Booster (SRB) separation, as a function of Mission Elapsed Time (MET).



Figure 3-1. Launch of STS-107 from pad 39A at Kennedy Space Center.

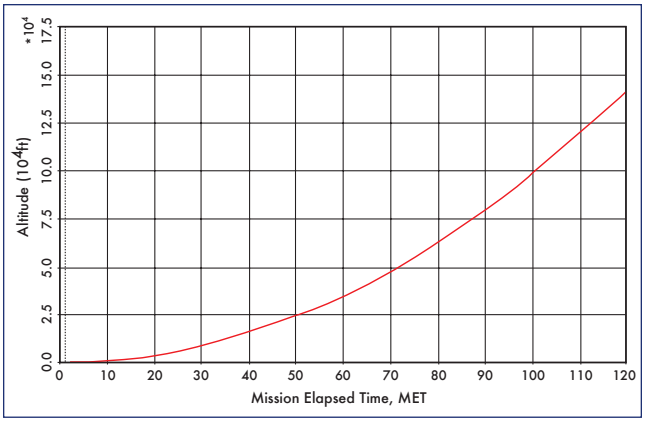


Figure 3-2. STS-107 reconstructed altitude during first stage (prior to SRB separation).

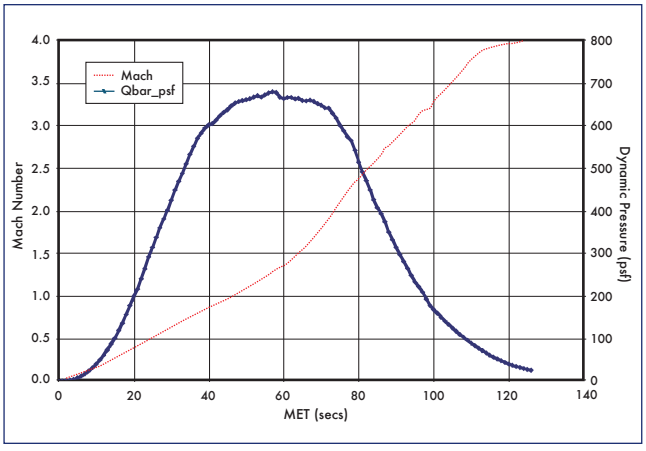


Figure 3-3. STS-107 flight reconstruction data for mach number and dynamic pressure (Q-bar) prior to SRB separation. Note that Q-bar is highest during first stage (prior to SRB separation), and reduces to a very small number after SRB separation.

3.2.2 Launch Debris Impact Area

Postlaunch photographic analysis determined that one major piece of foam and at least two minor pieces departed the External Tank (ET) left bipod ramp area approximately 82 seconds after launch. The primary foam piece impacted *Columbia* in the vicinity of the lower left wing Reinforced Carbon-Carbon (RCC) panels 5 through 9 at 81.86 seconds after launch. There were no indications that any of the minor pieces impacted the left wing based on their post-separation trajectories. The orbiter was at an altitude of ~65,860 feet, traveling at Mach 2.46 at time of impact.

Several approaches were taken to assess the area of left wing damage. The efforts included launch video and photograph analysis, review of launch MADS data, debris transport analysis, forensic analysis of debris found in Texas, wire bundle burn through analysis, and aero/thermal modeling of the entry. The data indicate that the area of the highest probability of damage to the left wing was between RCC panels 5 and 9, with the most likely damage occurring on the lower side of RCC panel 8 or an adjacent Tee seal. The damage was most likely equivalent in size to a 6 to 10 inch diameter hole or area broken from the RCC panel or an adjacent Tee seal. Figure 3-4 shows the area of highest probability of wing damage and Table 3-1 shows the methods used to determine the damage.

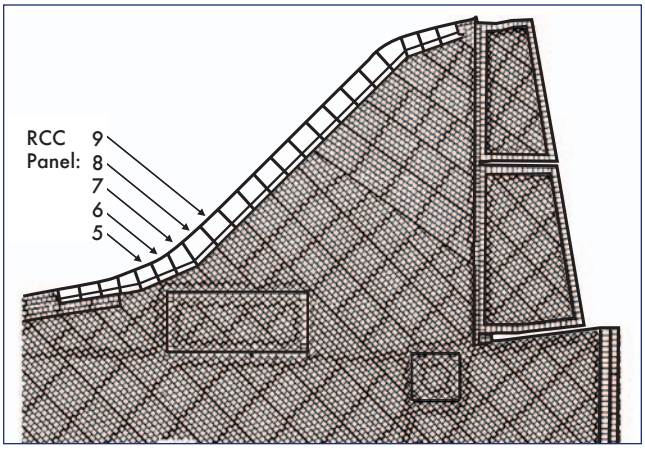


Figure 3-4. Area of most likely wing damage.

3.2.3 Launch Photo and Transport Analysis

Photographic analysis of the debris impact event included participation from the Johnson Space Center, the Marshall Space Flight Center, the Kennedy Space Center, Lockheed Martin Management and Data Systems, Boeing NASA Systems, the Eastman Kodak Company, and the National Imaging and Mapping Agency.

Video and Computer-Aided Design (CAD) analysis determined that the most likely impact location was leading edge RCC panels 6 through 8 (Figure 3-5). Due to the foam size, RCC panels 5 and 9 must also be included in this impact zone. The best estimate of the foam size, based on imagery measurements, is 21 to 27 inches long and 12 to 18 inches

Wing Damage Analysis Method	*Predicted Damage Area*	*Comments*	*Discussion Found In Section*
Launch Video and Photo Analysis	RCC 5 through 9	Most likely area of impact was RCC panels 6 through 8.	3.2
Ascent MADS Data	RCC 6 through 8	Unusual temperature sensor data observed on spar behind RCC panel 9, and temperature rise matches a thermal math model of a 10 inch diameter hole in RCC panel 8.	3.3
Debris Transport Analysis	RCC 5 through 8	Most likely area of impact was RCC panels 6 through 8.	3.2
Hardware Forensics Data	RCC 8 or 9	Fragments of RCC panels 8 and 9 showed extreme temperature indications, knife edge heat erosion patterns, and heavy amounts of slag deposited on the insides of those panels.	5.3
Entry MADS Data	RCC 8 or 9	First unusual indication observed during entry was a strain gauge behind RCC panel 9 (could be due to a strain behind adjacent panel 8).	5.4
Wire Bundle Burn Through	RCC 7 through 9	Burn through from locations forward of panel 7 or aft of panel 9 are very unlikely based on sensor data loss timing.	5.4
Entry Aero/thermal Modeling	RCC 8 or 9	Based on wind tunnel test results and CFD analysis.	5.5

Table 3-1. Wing damage analysis methods and results.

wide. The precise foam shape and thickness cannot be determined from the available imagery; however, a reasonable estimate is that it was a plate-like shape and several inches thick. The foam tumbled at a minimum rate of 18 times per second based on the imagery, although the actual rate may never be known more accurately. Figure 3-6 illustrates a portion of the photographic analysis techniques used to determine the size of the foam.

The most useful video analysis was performed using two cameras that are part of the Eastern Launch Range imaging system. Camera E212 (film), located on the Cape Canaveral Air Force Station, was approximately 17 miles from the orbiter at the time of foam impact and Camera ET208 (video),

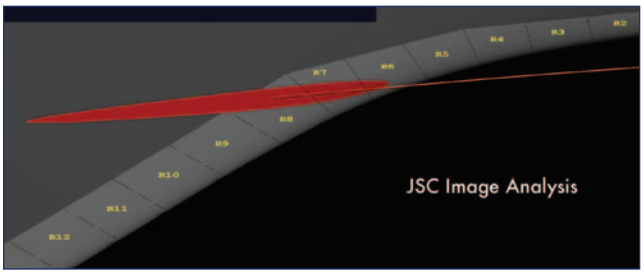


Figure 3-5. Multiple analyses determine foam impacted lower RCC panels 6 through 8 area.

located in Cocoa Beach, Florida, was 26 miles from the orbiter. The overall camera geometry relative to the launch pad and ascent flight path is shown in Figure 3-7. Camera E212 had a better view of the topside of the launch vehicle, while Camera ET208 had a better bottom side view. Figure 3-8 depicts the view from each of the camera systems. A third camera, E208 (film), also recorded the launch but was blurred and contained no useful data for the investigation. There are no Launch Commit Criteria (LCC) regarding cameras, or camera views for ascent, for either onboard or ground.



Figure 3-6. Photographic analysis techniques determined foam size: debris appears almost circular in frame 4914 and elongated in frame 4919.

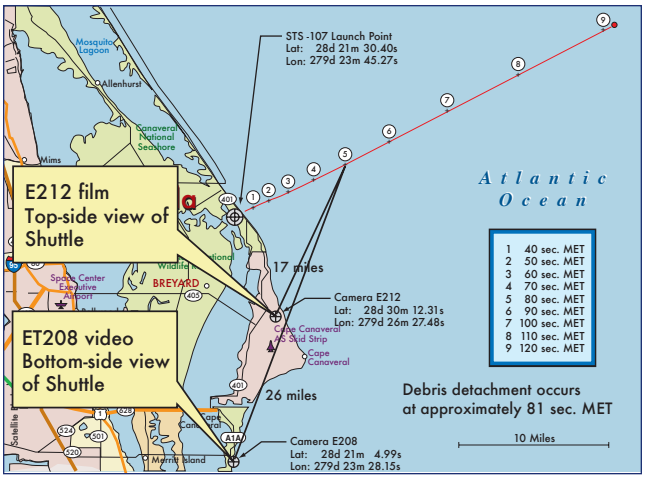


Figure 3-7. Camera geometry for ascent video analysis; note that video camera ET208 is at same location as film camera E208.

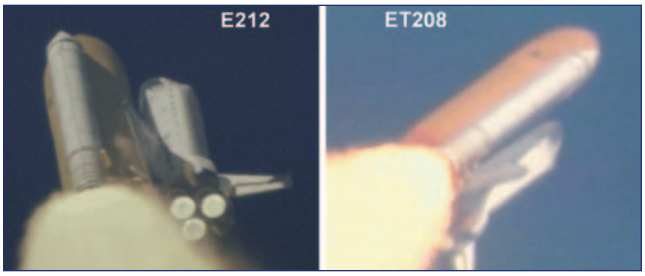


Figure 3-8. Orbiter view from cameras E212 and ET208.

There is significant visual and debris trajectory information to implicate the left bipod ramp area as the source of debris. In Figure 3-9, the red line depicts the estimated foam trajectory as it moved from the bipod ramp area toward the left wing. In addition to locating the impact in the RCC panels 6 through 8 region, the video analysis has also shown that the impact was below the apex of the RCC panels since no foam or post impact debris was observed to traverse over the top of the wing. This is indicative of an impact below the wing leading edge aerodynamic stagnation line (Figure 3-10). The stagnation line, or dividing streamline, is the line along the leading edge of the wing where the airflow comes to rest; above this line, airflow moves over the upper wing surface and below this line, the airflow moves over the lower wing surface.

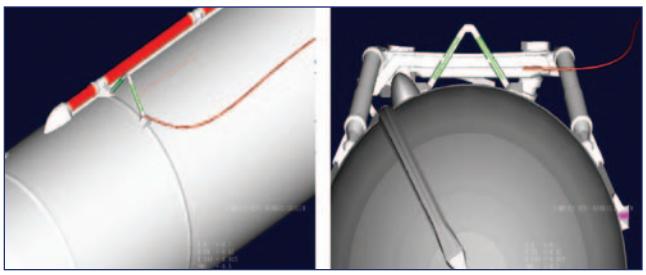


Figure 3-9. Multiple analyses indicate foam is from ET left bipod area. Red line depicts the estimated foam trajectory as it moved from the bipod ramp area toward the left wing.

Enhancements of the ascent video indicated there was no discernable damage to the orbiter wing leading edge or lower tile surface. Figure 3-11 is a sample of these video enhancements. The figure compares 30 pre-impact integrated video fields with 21 post-impact integrated video fields. Based on these enhancements, photo experts have been unable to determine or quantify any damage to any portion of the orbiter vehicle as a result of the impact.

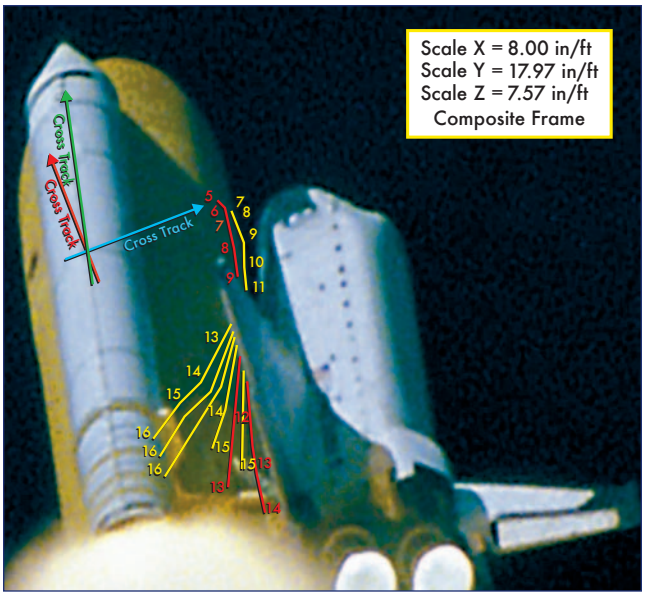


Figure 3-10. Video analysis shows impact is below wing leading edge stagnation line. Trajectories of particles are depicted after the impact.

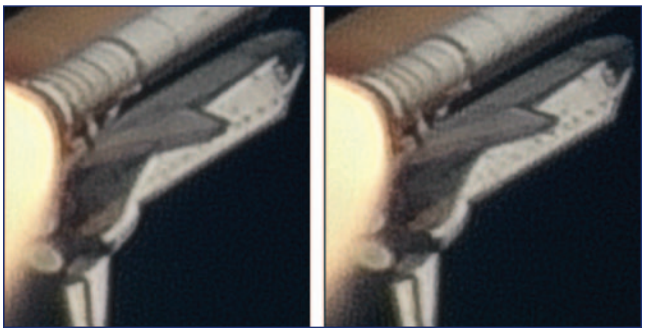


Figure 3-11. Pre-impact vs. post-impact shows no observable damage within the resolution limits.

3.2.4 Debris Velocity and Size Assessment

In addition to size and location of the foam impact, there are several other parameters necessary to complete the post-flight analysis of possible impact damage. These include an estimate of the foam's mass, relative velocity at impact, rotational energy, and the angle of impact with respect to the Shuttle wing at the point of impact. These parameters combine to determine the amount of impulse imparted at impact and are therefore critical to determine whether there was possible damage to the RCC panel, associated attach fitting hardware, or other leading edge structure.

	Transport Analysis Lower Bound	Transport Analysis Upper Bound	ET Working Group Estimate	RCC Impact Testing Target
Ballistic Number (BN)	1.2	1.45	1.0	1.45
Velocity (ft/sec)	820	775	850	775
Volume (in^3) @ 2.4 lb/ft^3	1,025	1,240	855	1,200
Weight (lbs) @ 2.4 lb/ft^3	1.42	1.72	1.19	1.67

Table 3-2. Transport analysis and ET Working Group estimates of ET bipod debris size, weight, and volume.

Photographic analysis was used to establish a range of relative impact velocities, from 625 to 840 feet per second (416 to 573 miles per hour). This large uncertainty is due to the small number of video and film frames between release of the foam and impact with the wing, since the estimated time between the foam release and foam impact is only 0.2 seconds. The predominant direction of motion is toward the aft of the orbiter along the X-axis, although the foam is moving slightly outboard at the time of impact with little to no motion in the Z-axis (see Figure 2-2 for vehicle coordinate system orientation). The direction of motion is from the ET bipod area toward the left wing at an angle of 2 to 10 degrees with respect to the orbiter X-axis in the orbiter X-Y plane. The motion is slightly toward the wing surface at a 0 to 3 degree angle measured in the orbiter X-Z plane.

Three-dimensional trajectories from the launch films and videos were refined using a physics-based trajectory fit that included a realistic flow field model generated using computational fluid dynamics (CFD) techniques. These results indicated that the relative velocity at impact was in the range of 775 to 820 feet per second. The CFD analysis used numerical methods to model the flow field around the orbiter/ET/Solid Rocket Booster (SRB) stack including the SRB and Space Shuttle Main Engine (SSME) plumes. An example of this analysis is shown in Figure 3-12.

The transport analysis was also used to estimate a range of sizes and corresponding weights for the foam, which are summarized in Table 3-2. For an impact velocity of 820 feet per second, the estimated foam volume is approximately 1025 cubic inches with a weight of 1.42 pounds assuming the density of the foam was 2.4 pounds per cubic foot. Similarly, for a velocity of 775 feet per second, the estimated volume is 1240 cubic inches, and the resulting weight is 1.72 pounds. Additional results produced with a more complex CFD model included lift forces and the unsteady rotation of the debris. Table 3-2 also lists the ET Working Group estimate of the bipod foam size and weight. This estimate was for one particular ET bipod ramp configuration and did not account for manufacturing variability. Thus, it was not used as the volume for the RCC impact testing, and more details are included in Section 11.

Numerous factors could affect mass of the foam debris, and the exact volume and mass may never be known. For example, the BX-250 foam could have had a higher than predicted density of 2.4 pounds per cubic foot, since the density can range from 1.8 to 2.6 lb/ft^3. Alternatively, a lower drag coefficient on the debris could also account for a higher ballistic number (BN).

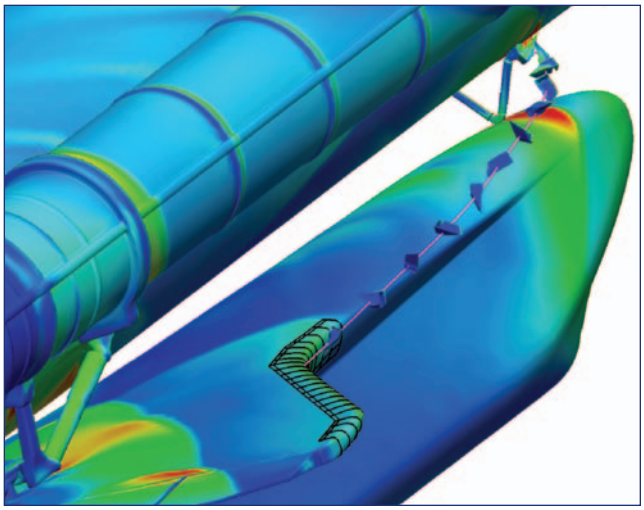


Figure 3-12. Sample CFD flow field with debris modeling.

3.2.5 Impact Damage Testing and Analysis

Analysis and experimental results were used to assess the potential for debris impact to damage *Columbia*'s wing leading edge. The overall concept was to replicate, to the greatest extent feasible, the debris impact event that occurred on *Columbia*'s left wing during ascent, by impacting flight-ready composite panel assemblies with a representative foam projectile fired from a compressed gas gun. The target panel assemblies had a flight history similar to that of *Columbia*, and were mounted on a support structurally equivalent to *Columbia*'s left wing. The attaching hardware and fittings were either flight certified, or built to *Columbia*'s drawings. BX-250 foam, without entrained ablator material, was used for the impacting projectile material because it represented the ascent event and provided a lower bound damage assessment. After significant study and consideration of all inputs by the NAIT and CAIB members, the parameters for representative impacts were established as: foam volume 1200 cubic inches, velocity 775 feet per second, and foam mass 1.67 pounds.

Impact testing has been completed on full size fiberglass panels, an RCC panel 6, and an RCC panel 8 to obtain insight and experimental data important to the understanding and modeling of the response of the wing leading edge components. The RCC panel 6 assembly was from *Discovery* and had flown 30 missions, and the RCC panel 8 was from *Atlantis* and had flown 27 previous missions.

The test of the RCC composite panel assembly 6 demonstrated that a foam impact representative of the debris strike at 82 seconds was capable of damaging RCC material. A 5.5-inch crack was created, extending from a visible 3/4 inch diameter damage area on the outside of the panel to the rib inside the wing. The panel 6/7 Tee seal was also damaged with a 2.5-inch crack, and the Tee seal as well as panel 6 were shifted in position. In addition, a carrier panel on the upper side of the wing was chipped.

Subsequent engineering testing has demonstrated that the localized impact loads imposed on the panel 6 assembly would have been substantially higher with changes in foam impact orientation and location. These changes were included in the RCC panel 8 assembly test and included a 30 degree clocking angle (orientation of the foam projectile relative to the target), a 22 degree angle relative to the impact surface, and an impact location lower and farther outboard relative to the panel 6 test. Impact target location was six inches farther down the trajectory track from the earlier tests. The test generated a 16 inch by 16 inch hole in the lower surface of panel 8, which is the most substantial damage to date in any RCC impact test.

The exact flight damage is unknown but is believed to be bracketed by these two tests. The testing is important in that it confirms that the ET bipod foam can catastrophically damage the RCC.

3.3 Launch MADS Data

There are two other indications that the foam impact occurred in the panels 6 through 8 area. Two Modular Auxiliary Data System (MADS) lower surface pressure measurements behaved anomalously immediately after the time of the impact. Figure 3-13 shows the location of these measurements along with possible areas for post-impact debris re-contact in the vicinity of the sensors. The unusual behavior of one of the sensors is shown in Figure 3-14.

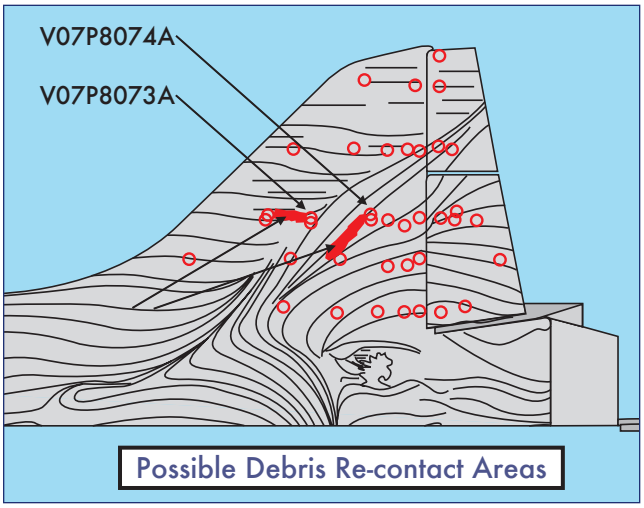


Figure 3-13. CFD surface flow with lower left wing pressure sensors.

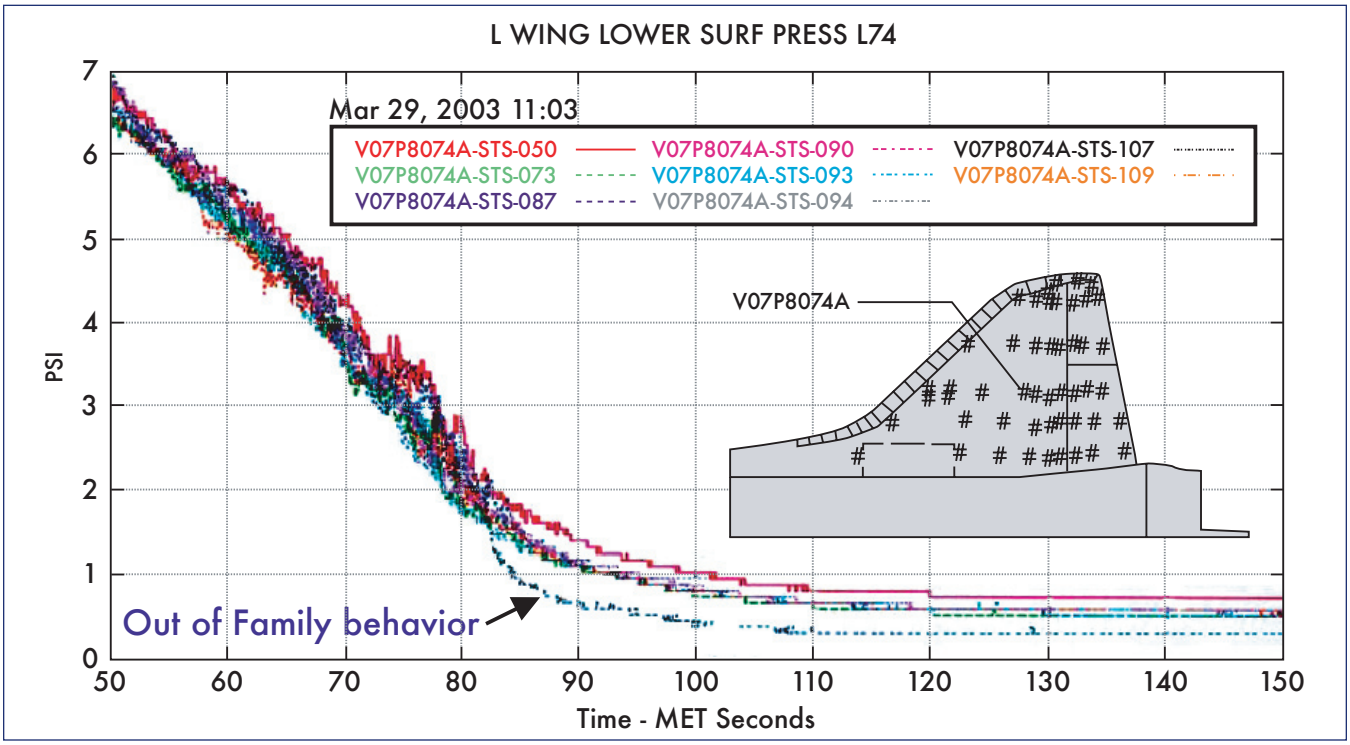


Figure 3-14. Unusual behavior of pressure sensor V07P8074A.

Additionally, there is another MADS measurement that had an off-nominal signature during the ascent timeframe. The temperature sensor on the leading edge spar behind RCC panel 9 showed a slightly higher temperature rise than seen on any previous *Columbia* flight. Figure 3-15 shows the location of the temperature sensor behind the wing leading edge spar inside the wing. The slight temperature rise can be seen in Figure 3-16. Note that most flights show a small rise in this temperature during ascent due to aerodynamic heating.

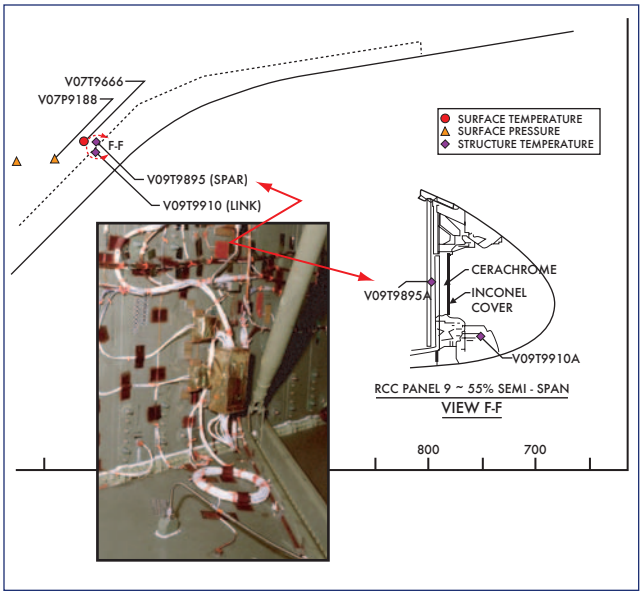


Figure 3-15. Close-out photo shows RCC panel 9 wing leading edge temperature measurement.

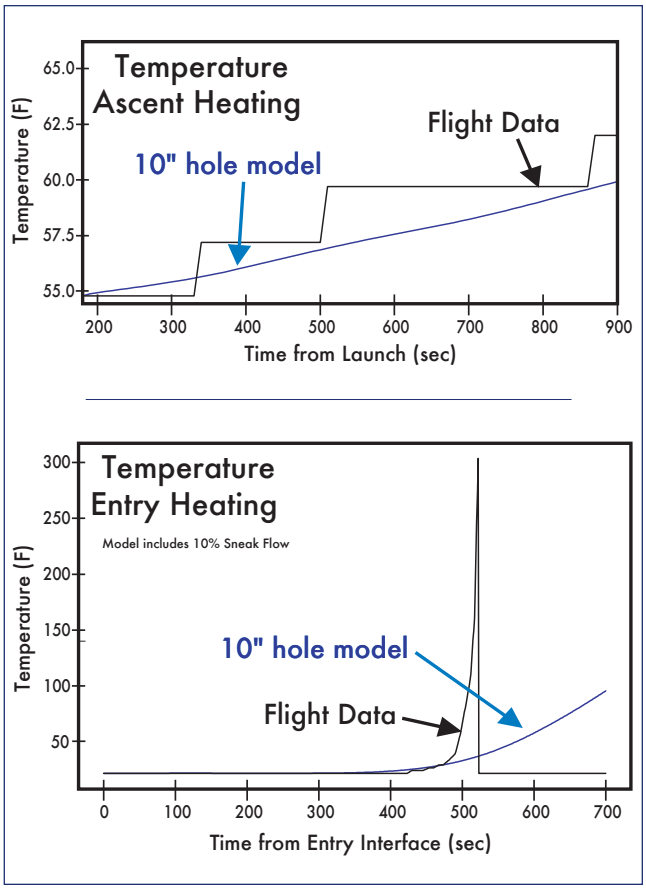


Figure 3-17. Correlation between simplified thermal math model and STS-107 ascent and entry flight data.

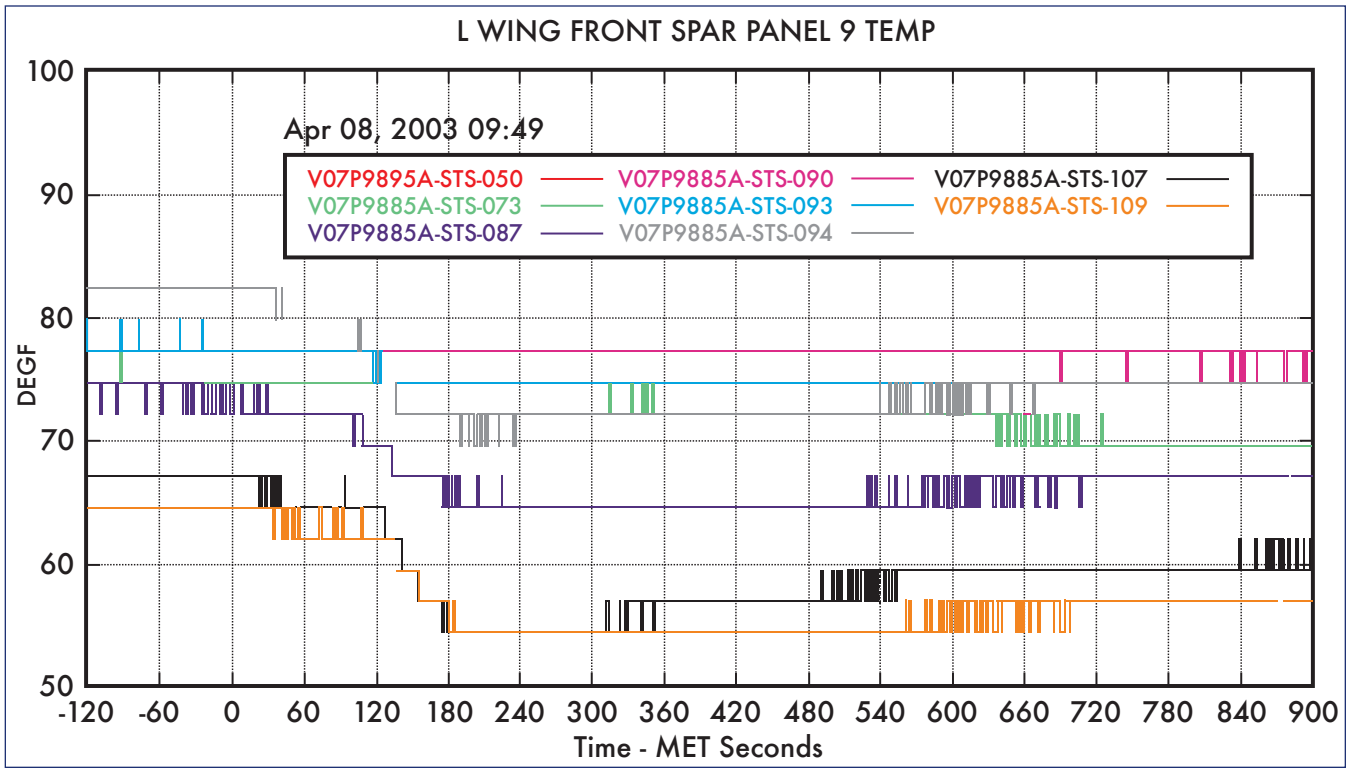


Figure 3-16. Three-bit rise (7.5 degrees F) on MADS wing leading edge spar temperature measurement (V09T9895A) during ascent.

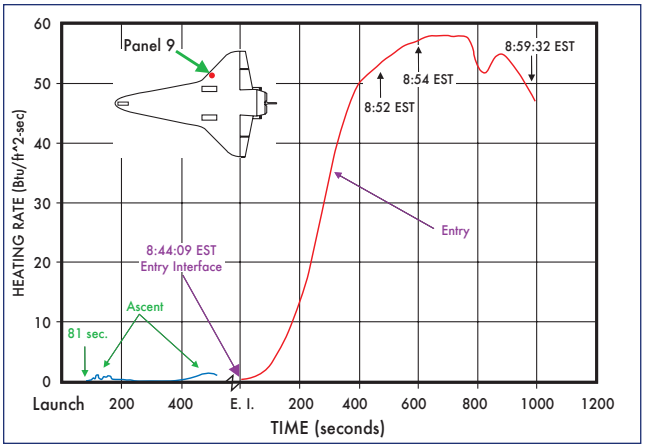


Figure 3-18. STS-107 ascent and entry heating environments on RCC panel 9.

STS-107 had a 7.5 degree Fahrenheit rise that started very early during ascent (five to six minutes after launch). Although the data do not prove that the RCC was breached during ascent, the data are consistent with a possible flow path into the RCC cavity via damage in the RCC panels 6 through 8 area. A simplified thermal math model was constructed and verified with flight data from STS-5. The model was then correlated to the flight data from STS-107. Assuming the equivalent heating from a 10 inch diameter hole in RCC panel 8, this model nearly predicts both the ascent and entry temperature profiles for the wing leading edge spar temperature sensor. Figure 3-17 compares the model with the flight data for both ascent and entry. For comparison, Figure 3-18 shows the overall heating rate of the STS-107 ascent and entry environments on RCC panel 9. As shown, the heating on the wing leading edge is much greater during the entry profile than during the ascent profile.

3.4 Launch Area Radar Analysis

STS-107 was tracked during ascent by the Eastern Range (ER) land-based C-Band radars, and identified debris was analyzed for time of separation, radar cross section (RCS), and range separation rate. In summary, the radars were unable to detect debris prior to SRB separation. Following SRB separation, from Launch + 150 to L + 230 seconds (2:30 to 3:50 Mission Elapsed Time, MET), 46 items were catalogued, of which 27 items are considered to be debris; however, the radar return signal was not of sufficient strength to determine the approximate shape, size, or rigidity of the debris. The radar analysis results are consistent with the debris analyses from previous STS missions. Table 3-3 lists the STS-107 catalogued radar detected events.

The launch radar is optimized for range safety and vehicle trajectory determination, and not for small debris assessment. A better radar for small debris, the Multiple-Object Tracking Radar (MOTR) was not available for use on STS-107. The ER radars used on STS-107 were not designed for signature analysis and were not able to lock onto and track multiple targets simultaneously. Additionally, debris could remain undetected if the debris was emitted at a time and angle where it was shielded from the radar by the vehicle body.

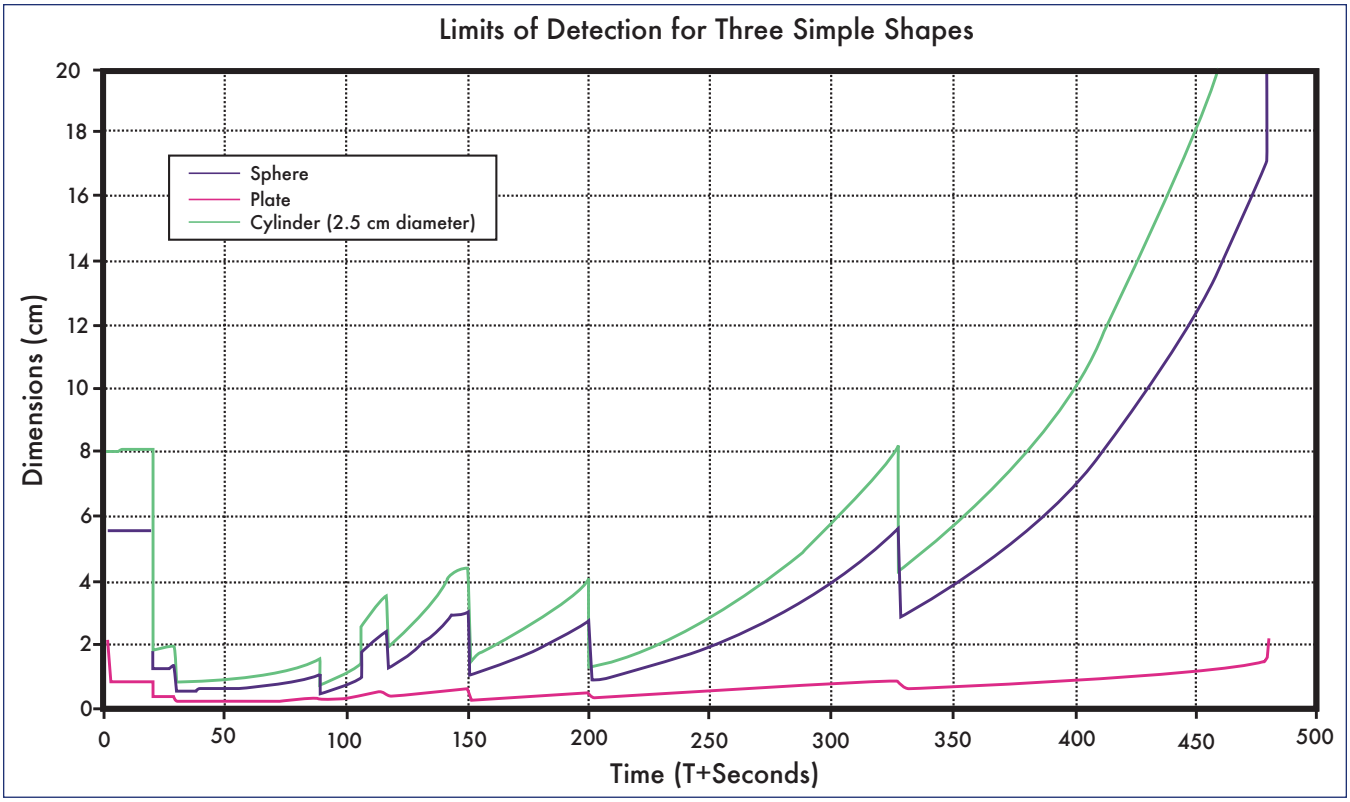


Figure 3-19. Limits of dimensional detectability for three simple shapes.

Catalog number	Radar source (site no.)[a]	First / last appearance (T + sec)	MAX RCS[b] (dBsm)[c]	Separation rate (m/sec)	Lower RSR[d] (m/sec)	Upper RSR[d] (m/sec)
1 [e]	0.14	80.4/87	8	14	44	541
29 [e]	19.14	81.6/86.1	-1	30	36	688
34	19.14	117/121	-15	771	10	1268
30 [f]	0.14	117.5/118	-8	1240	0	1162
31 [f]	28.14	117/118.5	-11	1500	3	616
32	28.14	118/119	-8	350	0	622
35	19.14	121/122	-16	771	4	1286
36	19.14	121/125	-16	372	6	1289
37	19.14	121/123	-15	426	4	1286
38	19.14	123/126	-14	424	1	1294
39	19.14	124/126	-14	480	3	1297
40	19.14	126/127	-12	490	2	1303
41	19.14	126.5/128	-13	490	2	1306
42	19.14	127/128	-14	476	2	1307
43	19.14	128/129	-13	570	0	1310
33	28.14	128/130	1	520	1	710
44	19.14	129.5/131.5	-14	670	2	1320
45	19.14	130/132.5	-15	371	4	1324
46	19.14	130.5/131.5	-13	370	2	1320
23	28.14	152/158.5	-12	187	13	947
2	0.14	152.5/156	-10	210	9	1405
3	0.14	152.5/162.5	-8	326	26	1405
4	0.14	153/160	-9	229	104	1505
24	28.14	154.5/162	-14	400	15	975
5	0.14	156/170	-16	217	38	1465
6	0.14	158.5/171	-17	309	34	1477
7	0.14	164/170	-17	312	17	1493
8	0.14	166.5/173	-21	357	19	1513
25	28.14	167/176.5	-18	221	22	1106
9	0.14	167/184.5	-15	260	53	1557
10	0.14	170/184.5	-15	265	44	1568
11	0.14	174.5/180	-14	290	17	1568
12	0.14	173/180	-16	206	21	1562
13	0.14	174/175.1	-16	244	2	1546
14	0.14	175.5/180	-15	180	14	1572
15	0.14	178/180	-14	296	8	1583
26	28.14	179/187.5	-10	884	22	1221
16	0.14	184/190	-14	236	19	1643
17	0.14	187/192.7	-11	649	19	1665
27 [g]	28.14	201/207	Low signal	Low signal	18	1438
28 [g]	28.14	205/208.5	Low signal	Low signal	11	1468
18 [g]	0.14	204.5/210	Low signal	Low signal	20	1812
19	0.14	204.5/214	-18	326	36	1829
20	0.14	204.5/212	-17	166	28	1820
21	0.14	206/212	-18	225	22	1827
22	0.14	211.5/228	-17	219	66	1926

a - Radar source: 0.14 = Patrick Air Force Base (PAFB), 19.14 = Kennedy Space Center (KSC), 28.14 = Jonathan Dickinson Missile Tracking Annex (JDMTA)

b - Radar cross section (RCS)

c - Decibels relative to one square meter (dBsm)

d - range separation rate (RSR)

e - Objects 1 and 29 are explained as plume artifacts evident by low separation rates from vehicle

f - Objects 30 and 31 are probably SRB slag ejection evident by high separation rates from vehicle

g - Objects 27, 28, and 18 had indeterminable RCS and RSR due to low level of signal returns

Table 3-3. STS-107 ascent radar events.

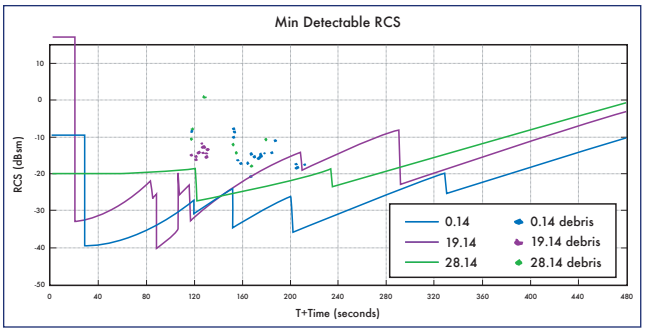


Figure 3-20. Limits of radar cross section (RCS) detectability and measured STS-107 debris for three radar source sites.

Detailed postlaunch radar debris analysis was performed on a regular basis until STS-57. There are reports available from previous flights, and typical observations include low strength radar returns from SRB separation to T + 300 seconds.

In general, the strength of the radar (C-band, AN/FPQ-14 unit) return depends on distance to the object, size of the object, and reflectivity of the object. For the STS-107 analyses, the distance to the objects is known but the object size and reflectivity are unknowns for all objects detected. As such, it was necessary to perform an exclusionary exercise to try to identify the objects. Some basic rules could be applied, such as knowledge that objects with very high separation speed are known to be part of the exhaust plume or products (such as SRB slag). In Table 3-3, items 30 and 31 were determined to be SRB slag. Moderate separation speed indicates solid objects being left behind. Separation rates can also be used to infer the density. There are limits to the debris size and shape that can be detected by the radar (see Figures 3-19 and 3-20).

From Table 3-3, debris item numbers 1 and 29 appear from 80.4 - 87 seconds and 81.6 - 86.1 seconds, respectively. This time coincides with the ET left bipod foam debris generation at 81.7 seconds. However, the low separation rate and relatively large RCS of the two radar objects indicate that they are most likely traveling with the vehicle and are flame (plume) artifacts. There are also several radar objects around the SRB separation time frame, ~126 seconds; however, the data are inadequate to determine the size, shape, or composition of the objects beyond that their moderate separation speed indicates solid objects being left behind. Some known debris objects at the time of SRB separation are the aft Booster Separation Motor (BSM) throat covers. It should be noted that the number and strength of the radar returns are typical as compared to previous Shuttle missions where no significant debris damage occurred.

In an effort to identify the STS-107 launch debris, data was reviewed from a post-STS-27 radar calibration that was performed on several materials. These objects included many applicable Space Shuttle system materials, including various orbiter thermal protection system tiles, various ET insulation foam types, as well as numerous SRB/RSRM materials and potential debris sources. Table 3-4 lists the material samples tested for Orbiter, ET, and SRB/RSRM elements. Additionally, data was used from the 2003 Wright Patterson Air Force Base testing, including Orbiter Felt Reusable Surface Insulation (FRSI), High-Temperature Reusable Surface Insulation (HRSI), and HRSI with Room-Temperature Vulcanized (RTV) sealant and Strain Isolation Pad (SIP).

As a result of the testing, the minimum detectable size for each radar return for selected materials was determined and catalogued. These data were carefully screened and scrutinized, using some reasonableness tests and assumptions, in an attempt to identify STS-107 radar objects as Orbiter, ET, or SRB/RSRM debris.

The radar data are inconclusive with respect to determining identity, size, or shape of any of the debris objects detected. The signal returns were weak and too close to radar noise to allow estimation of object shape. The number and strength of the returns on STS-107 are typical of previous Space Shuttle launches, including those where no debris damage occurred.

3.5 Launch Guidance Navigation and Control

Postflight analysis of the STS-107 ascent data revealed several events that were within the design capability of the

Orbiter	*SRB/RSRM*
Black tile	MSA-1/TPS with Hypalon
White tile	MSA-2/TPS with Hypalon
	Cork with Hypalon
ET	Aft booster separation motor (BSM) cover
PDL (closeout foam)	SRM slag
Ice plate	Cork
CPR 488 (acreage foam)	K5NA
Super Light Ablator (SLA) 561M	Instafoam
MA25	Inhibitor
BX250	EA934 adhesive
Instafoam	Viton thermal curtain
	Quartz cloth blanket

Table 3-4. Material samples from post-STS-27 radar calibration tests.

Shuttle, but considered to be new flight experience. These events were reviewed in detail, primarily because they occurred prior to SRB separation, when the foam loss and wing impact were observed. The items considered new flight experience were environmental (wind relative) side-slip angle during the period of maximum dynamic pressure (Hi-Q), SSME yaw nozzle positions during Hi-Q, and SRB thrust mismatch during SRB tail-off. Other events observed during the flight that were not new flight experience, but were considered worthy of note included the presence of a negative orbiter body yaw rate at ET separation and a period of ET slosh during powered ascent. Each event was separated into the following categories for detailed study and evaluation: wind shear, predicted versus actual vehicle loads, ET slosh, nozzle positions, and ET separation yaw rate.

Those parameters along with several other STS-107 ascent Guidance, Navigation, and Control (GNC) related points of interest were studied to determine if they were significant relative to the scenario. The study included integrated vehicle loads analysis, comparison of the STS-107 data with historical flight experience envelopes, and comparison of STS-107 data with specific families of flights. This section of the report summarizes the integrated GNC flight data review.

3.5.1 Wind Shear, Day of Launch Wind Effects

STS-107 experienced a wind shear during the period of maximum dynamic pressure starting at 57 seconds MET (Mach 1.27). The wind shear was due to a rapid change in the out-of-plane wind velocity of -37.7 feet per second over a 1200 foot altitude range starting at approximately 32,000 ft (as shown in Figure 3-21). Immediately after the vehicle flew through this altitude range, its side-slip angle began to increase in the negative direction, reaching a value of approximately –1.75 degrees at 60 seconds. This value of side-slip angle is a new flight experience value for MET 60 seconds (as shown in Figure 3-22). Post-flight data indicates that the new flight experience side slip event was not the result of the wind shear itself. Instead, it was the direct result of a difference in the L - 4:35 minutes balloon measurement, upon which orbiter guidance commands were updated on launch day, and the actual winds flown through by the orbiter during launch and ascent. Figure 3-21 highlights the difference in these two winds in this altitude region (a 25 foot per second increase in out-of-plane magnitude pre-launch compared to a 12 foot per second reduction in magnitude as experienced by the vehicle).

The L - 4:35 minutes weather balloon is launched to measure atmospheric conditions at the launch site, which are then used as part of a standard process to update the orbiter guidance software to keep it within design limits and minimize loads during ascent. After the Day of Launch I-Load Update (DOLILU) software update but prior to launch, additional balloons are used to verify that the L - 4:35 minutes balloon atmospheric conditions are still valid and meet required tolerance checks required to commit for launch. All STS-107 balloon measurements taken on launch day after L - 4:35 minutes satisfied the required launch commit criteria, and were subsequently verified by balloon data taken 15 minutes after launch.

Several theories consider this wind shear event and the difference between the balloon data to be significant. A negative side-slip angle places the wind vector on the left side

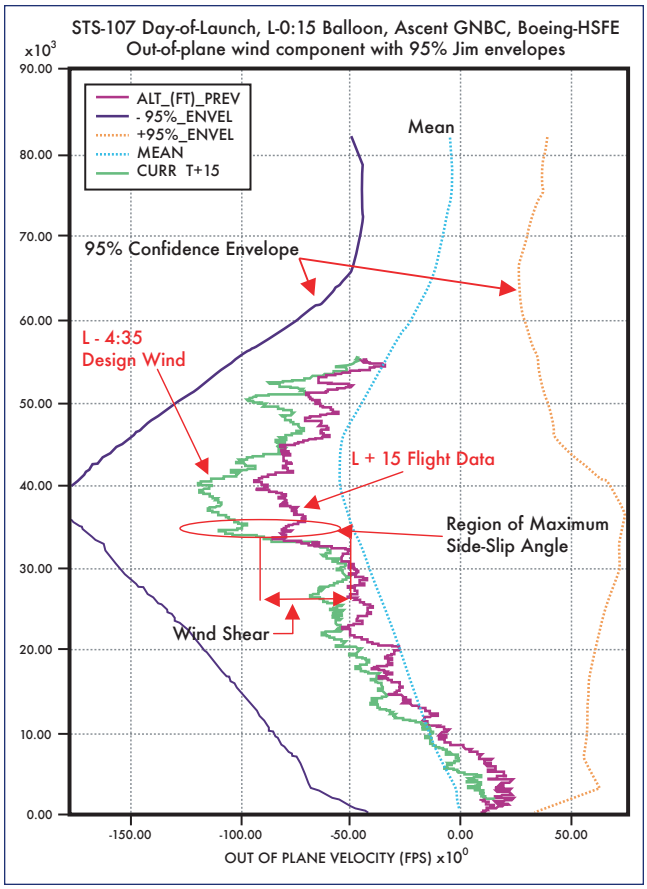


Figure 3-21. Out-of-plane wind velocity.

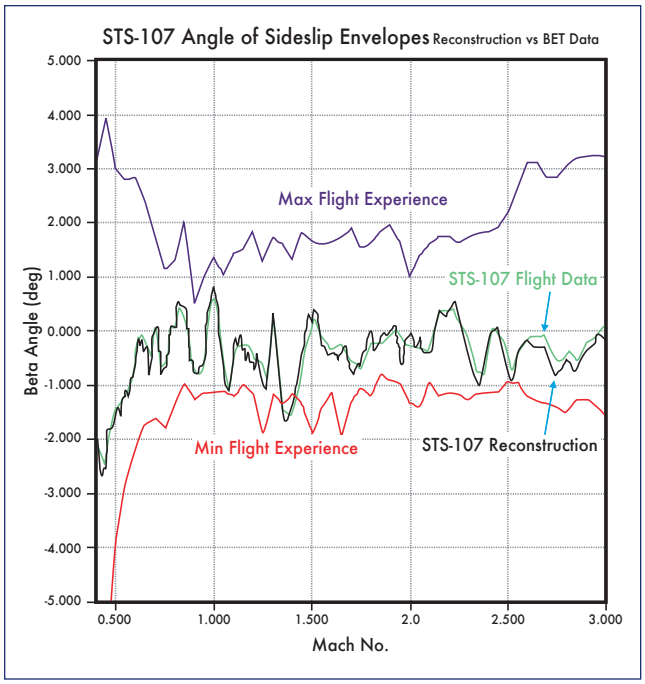


Figure 3-22. Side-slip angle.

of the orbiter, pushing the orbiter to the right, changing the complex aerodynamic flow pattern characteristics in the left ET bipod area. To better understand the conditions on the ET left bipod, several studies were conducted. The studies (1) compared flight data for missions that had ET bipod foam liberation; (2) compared flight data for missions that flew a Light Weight Tank (LWT) in combination with ascent Performance Enhancements (PEs), a package of vehicle software and hardware changes designed to increase overall weight to orbit capability for the ISS; (3) analyzed external aerodynamic loads on the ET forward attach bipod ramp; and (4) studied integrated orbiter/ET vehicle loads.

The flight data correlation studies indicate that a negative side-slip angle during the period of maximum dynamic pressure alone could not explain the liberation of the bipod foam. For both families of flights in the study (LWT and PE flights, and bipod foam liberation flights), a negative side-slip angle was seen on almost every flight. Of the bipod foam loss flights, STS-90 was of particular interest. STS-90 had a larger negative side-slip angle in Hi-Q of -2.0 degrees, when compared to STS-107, yet STS-90 did not lose bipod foam. When flights that shed bipod foam were studied as one family of flights, STS-112 is another outlier that does not support the negative side-slip angle theory. During the STS-112 ascent, video coverage shows the bipod foam liberation occurring prior to Hi-Q, yet the negative side-slip angle on STS-112 did not occur on that flight until after Hi-Q. The details of the flight data correlation studies are summarized in Sections 3.5.6 and 3.5.7 of this report.

To understand the aerodynamic loads on the ET forward attach bipod ramp, a CFD loads assessment was performed. The resulting CFD loads, discussed in more detail in Section 3.5.2, demonstrated that the external aerodynamic loads were below the design requirement.

To measure the orbiter/ET interface loads, an integrated orbiter/ET loads assessment was performed. The assessment, summarized in Section 3.5.2 of this report, also showed all integrated vehicle loads were below design limits.

The day-of-launch wind effects (including the noted wind shear event and associated negative side-slip angle) alone did not cause the ET left bipod foam loss.

3.5.2 Predicted/Actual Loads

Postflight reconstruction analysis of the STS-107 ascent loads characterized the effects of (1) RSRM thrust mismatch, (2) ET slosh dynamics, and (3) wind shear in Hi-Q. The integrated effects of these events were calculated through a flexible body loads assessment. This loads assessment used the STS-107 reconstructed ascent trajectory, and included ET slosh dynamic forces. The assessment produced (1) a wing loads summary, (2) an ET/orbiter interface loads summary, and (3) a summary of external aerodynamic loads on the ET forward attach bipod ramp.

The wing loads analysis used a flexible body structural loads assessment that was validated by the MADS data. The wing loads analysis used reconstructed trajectory parameters to generate the loads on the orbiter wings during ascent. The assessment demonstrated that all orbiter wing loads were 50 to 60% of their design limit, or less, throughout the ascent. This includes the wind shear event at 57 seconds MET, and subsequent side-slip angle at 60 seconds MET (as shown in Figure 3-23).

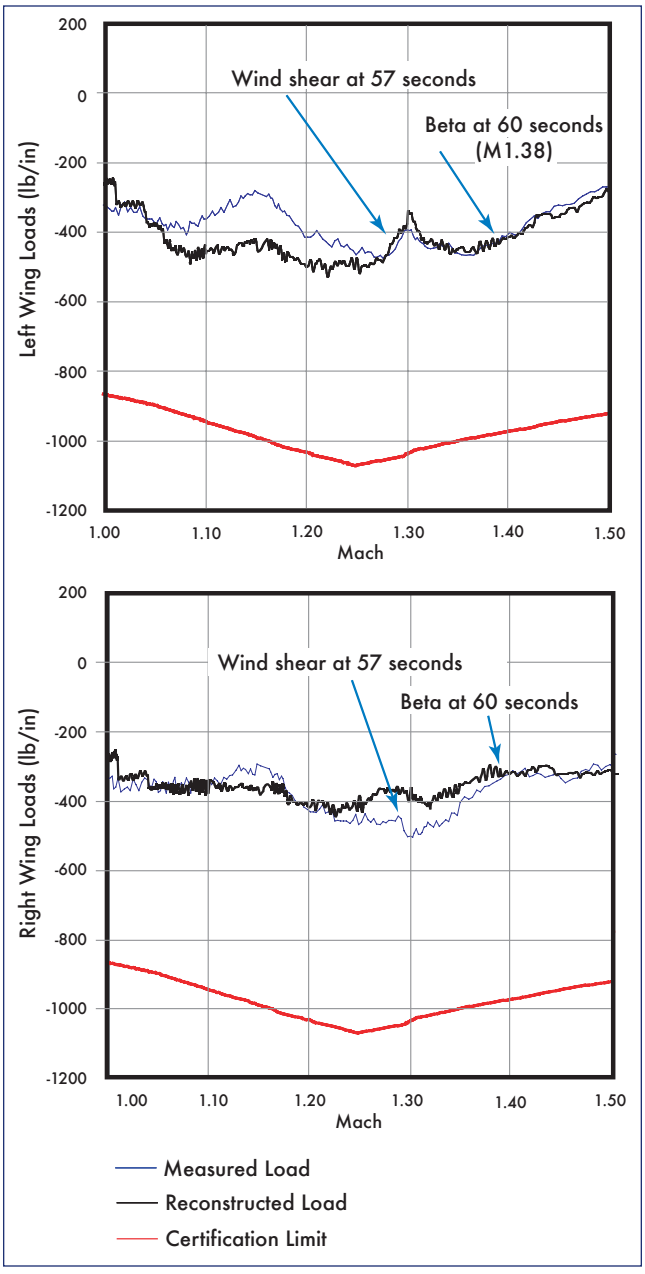


Figure 3-23. Wing loads during wind shear and side-slip angle.

The ET/orbiter interface loads were generated using reconstructed trajectory parameters that included the effects of wind shear/crosswind, side-slip angle, and ET liquid oxygen (LOX) slosh. The loads analysis demonstrated that the ET forward attach loads were within certification requirements at all times. The wind shear event had only a small effect on the overall ET loads relative to the required limits (as shown in Figure 3-24), as did the ET liquid propellant slosh

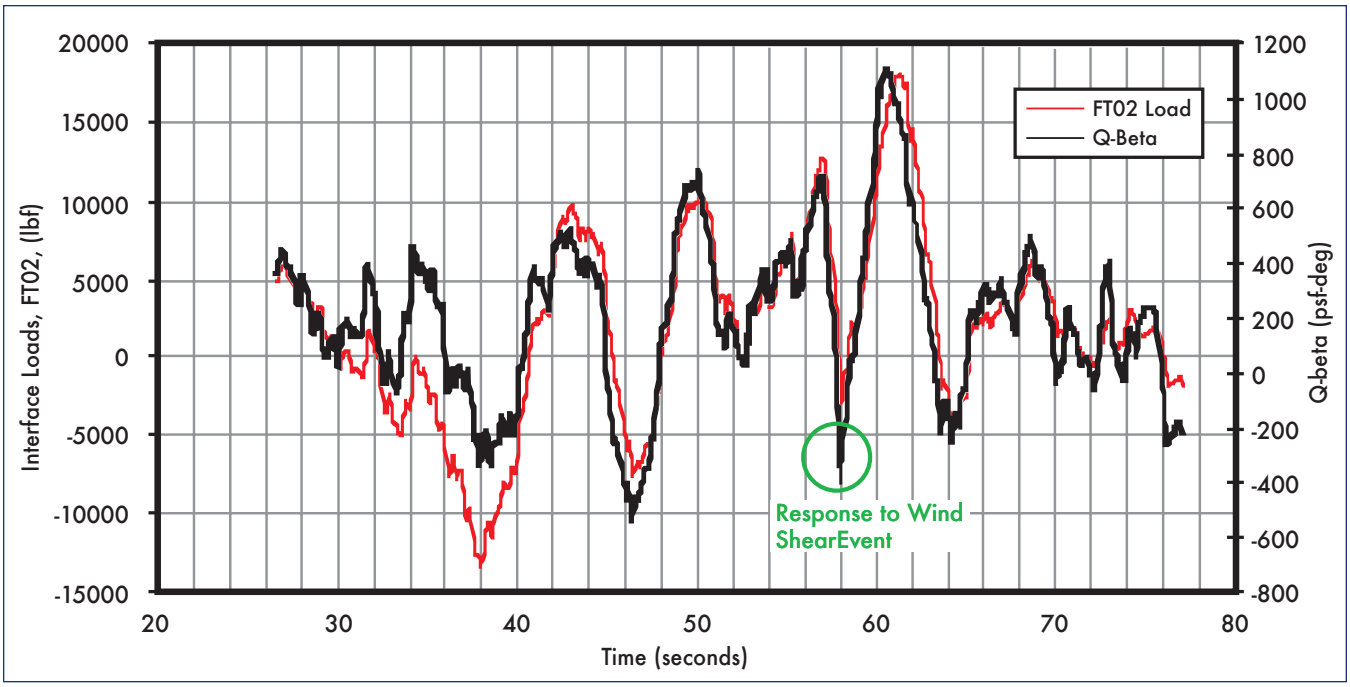


Figure 3-24. ET interface loads at forward attachment during wind shear and side-slip angle. Q-beta is side-slip angle multiplied by the dynamic pressure and represents the side-slip angle contribution of the interface load.

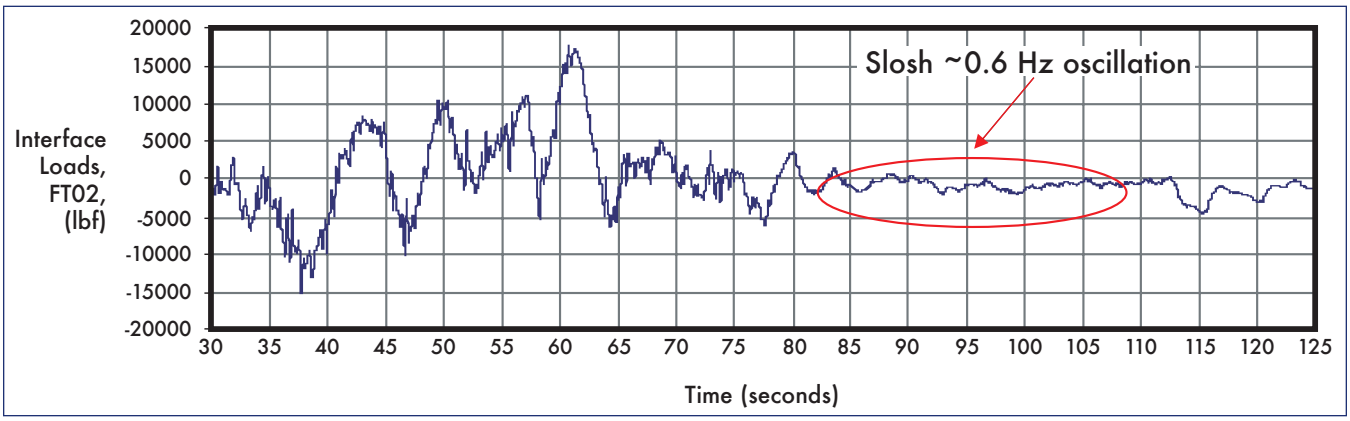


Figure 3-25. Slosh effect on ET interface loads.

(as shown in Figure 3-25). The resulting load from the wind shear event was of the same order magnitude as the roll maneuver and other first stage events prior to SRB separation.

The external aerodynamic loads on the ET forward attach bipod were analyzed using a CFD simulation. The simulation produced axial, side-force, and radial loads as shown in Figure 3-26, Figure 3-27, and Figure 3-28, respectively. The CFD assessment of the bipod area indicated that the external air loads were below the design limit during the Hi-Q region and at the time of the bipod foam liberation.

Flexible body simulation results indicate that all vehicle elements and associated loads were within required limits. The reconstruction loads analyses indicate that the ascent environment-induced loads alone did not cause the ET bipod foam loss.

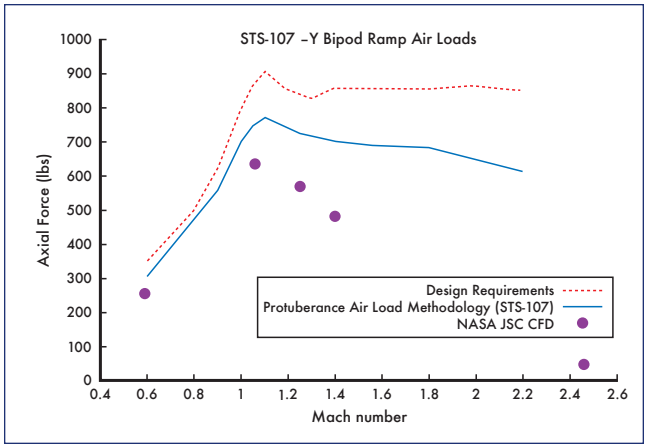


Figure 3-26. ET bipod axial aerodynamic loads.

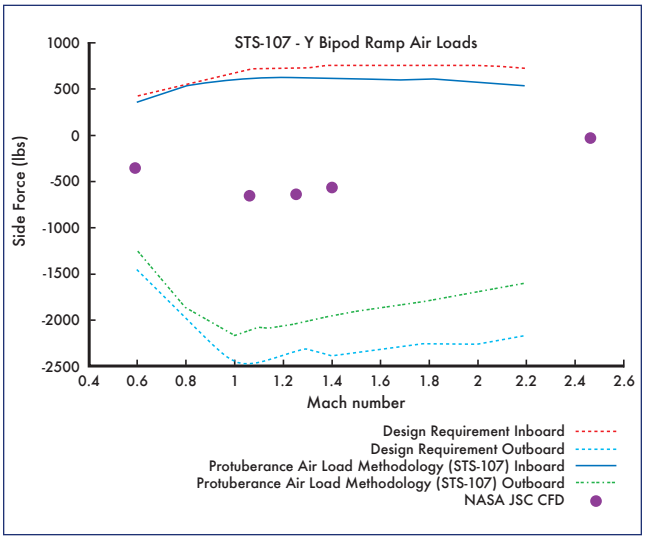


Figure 3-27. ET bipod side-force aerodynamic loads.

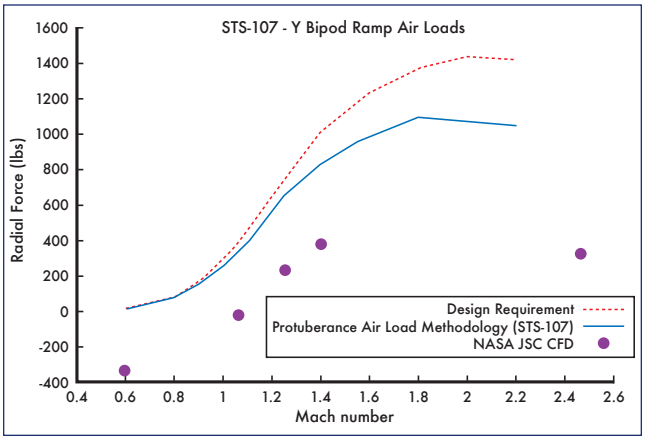


Figure 3-28. ET bipod radial aerodynamic loads.

3.5.3 ET Liquid Oxygen Slosh

The STS-107 ascent data indicate a 0.6 Hz actuator oscillation frequency that peaks in amplitude at 55 seconds, and again at 77 seconds MET and continues through SRB separation. The peaks directly correlate to peaks in 0.6 Hz wind content. A 0.6 Hz oscillation in the Flight Control System output is of interest since it can couple with the ET Liquid Oxygen (LOX) slosh mode. Slosh refers to the repeated side-to-side movement of the center of gravity of the liquid oxidizer propellant in the external tank. The slosh mode frequency and amplitude cannot be measured directly through vehicle data. In order to determine if ET LOX slosh is present, a post-flight process of reviewing the vehicle SRB and SSME actuator frequency content must be conducted, as well as that of the launch wind. When this post-flight process was conducted for STS-107, it revealed that this flight experienced more than typical 0.6 Hz frequency content in the SRB tilt actuators with moderate content in the rock actuators. Figure 3-29 illustrates this point with the results of the SRB left tilt actuator frequency response as compared to previous *Columbia* flight history.

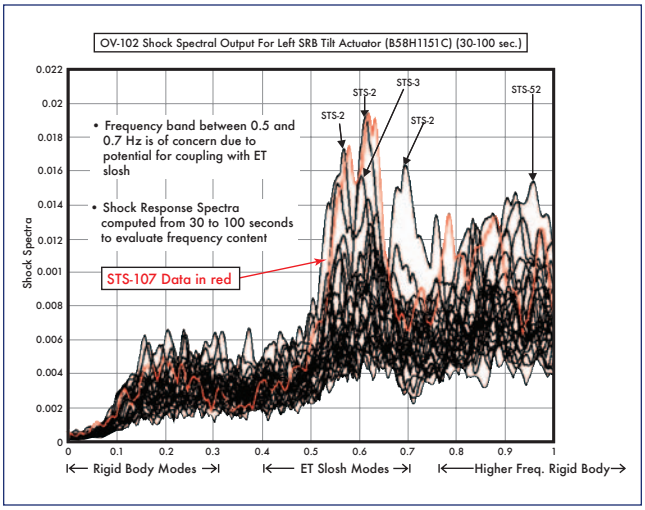


Figure 3-29. STS-107 SRB tilt actuators experienced more than typical 0.6 Hz content.

Figure 3-30 shows the relative time variation of amplitudes of the 0.6 Hz frequency content in wind and actuator data. The close correlation between the peaks in the 0.6 Hz content of the right and left actuator responses and the wind dynamics indicates that the actuators were responding primarily to wind rather than ET LOX slosh at this frequency through most of first stage (prior to SRB separation). As the 0.6 Hz content of the wind dynamics reduces in magnitude late in first stage, the remaining 0.6 Hz content in the actuator response may be attributed to a combination of the remaining wind dynamics and low-amplitude ET LOX slosh. STS-90 shows a similar wind frequency content.

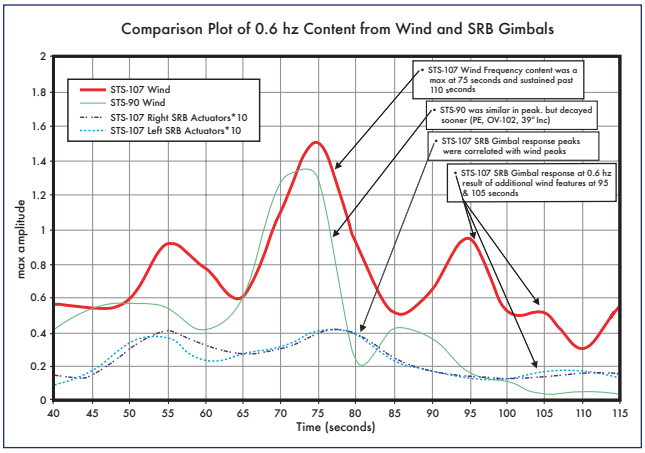


Figure 3-30. STS-107 SRB gimbal responses at 0.6 Hz frequency correlated to wind.

In general, ET LOX slosh is due to (1) commanded vehicle attitude transients, (2) additional wind dynamics after the start of ET LOX slosh, and (3) the 0.2 Hz rigid body vehicle mode. Note that a 0.6 Hz mode is the 3rd harmonic of the 0.2 Hz frequency, and is therefore subject to cross-coupling, and that some wind conditions can naturally contain a 0.6 Hz content.

The data from the ET LOX slosh study indicate that the flight control system operated as designed, and that more than adequate slosh phase stability margin existed. When the ET LOX slosh data is combined with the integrated vehicle loads analysis results (reference Figure 3-25), data indicate that the ET LOX slosh did not result in excessive vehicle loads at the orbiter/ET interface.

3.5.4 Nozzle Positions

A review of the STS-107 ascent data identified two discrete points in time when the SRB and SSME nozzle positions exceeded the flight experience envelope for those respective times in the ascent profile. The first event occurred when the center and right SSME yaw deflections exceeded the previous flight experience envelope during the period of maximum dynamic pressure, as a result of the differences between predicted and actual flight wind conditions (as shown in Figure 3-31 and Figure 3-32).

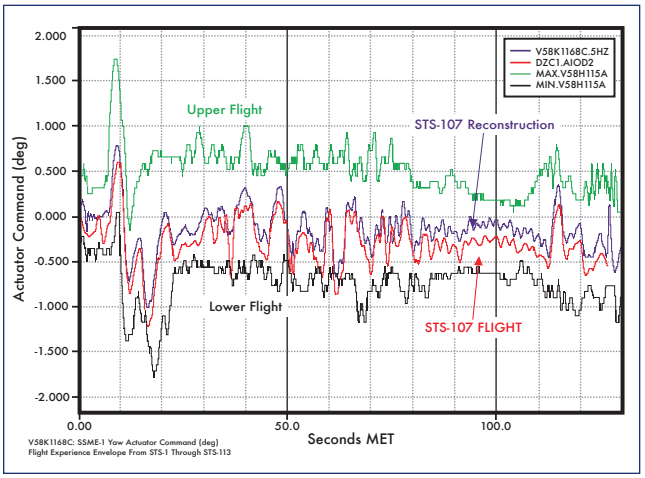


Figure 3-31. Center SSME yaw position.

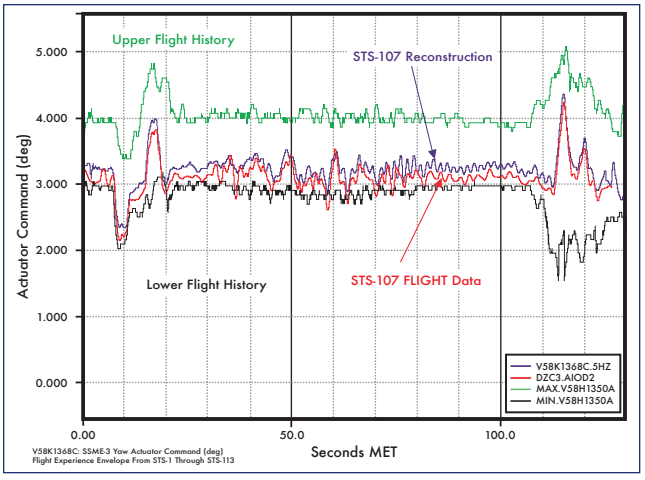


Figure 3-32. Right SSME yaw position.

This nozzle yaw event was coincident with a wind-induced positive lateral acceleration, as sensed via the body mounted accelerometer assemblies and a positive orbiter body yaw rate, as sensed by the orbiter rate gyro assemblies. The yaw event follows the period of greatest change in out-of-plane wind velocity (e.g., the wind shear previously shown in Figure 3-21).

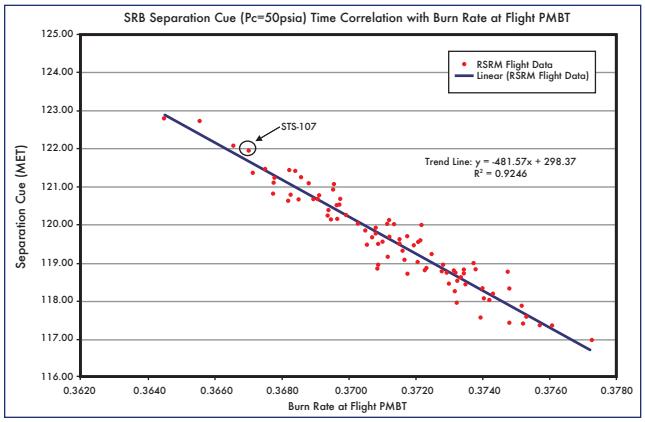


Figure 3-33. RSRM burn rate at propellant mean bulk temperature (PMBT).

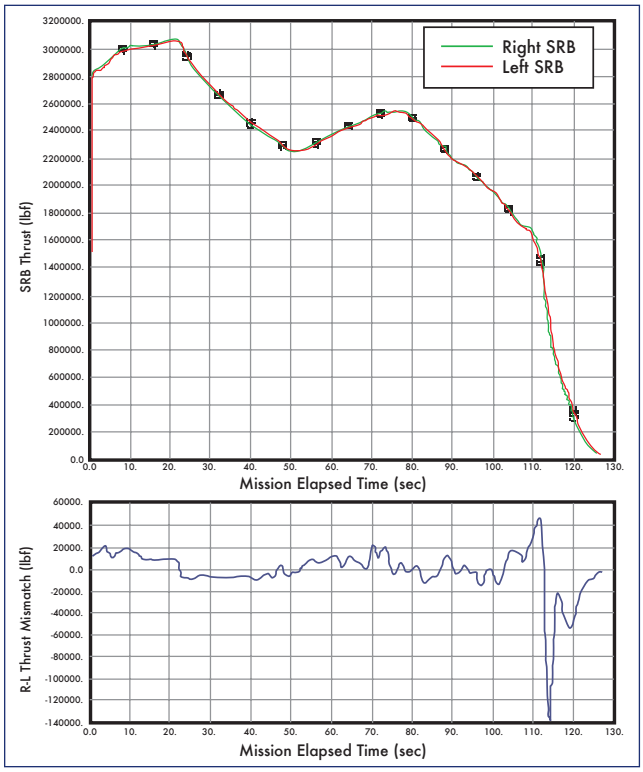


Figure 3-34. SRB thrust mismatch.

The large offset in the Center and Right SSME yaw positions at 62 seconds MET was the reaction of the flight control system to the wind shear event and day-of-launch wind differences as compared to the DOLILU design. The nozzle motion was within the capability of the Shuttle flight control system, and the system operated as designed. As discussed in Section 3.5.1, the reconstruction loads analyses indicate that the ascent environment-induced loads alone did not cause the ET bipod foam loss.

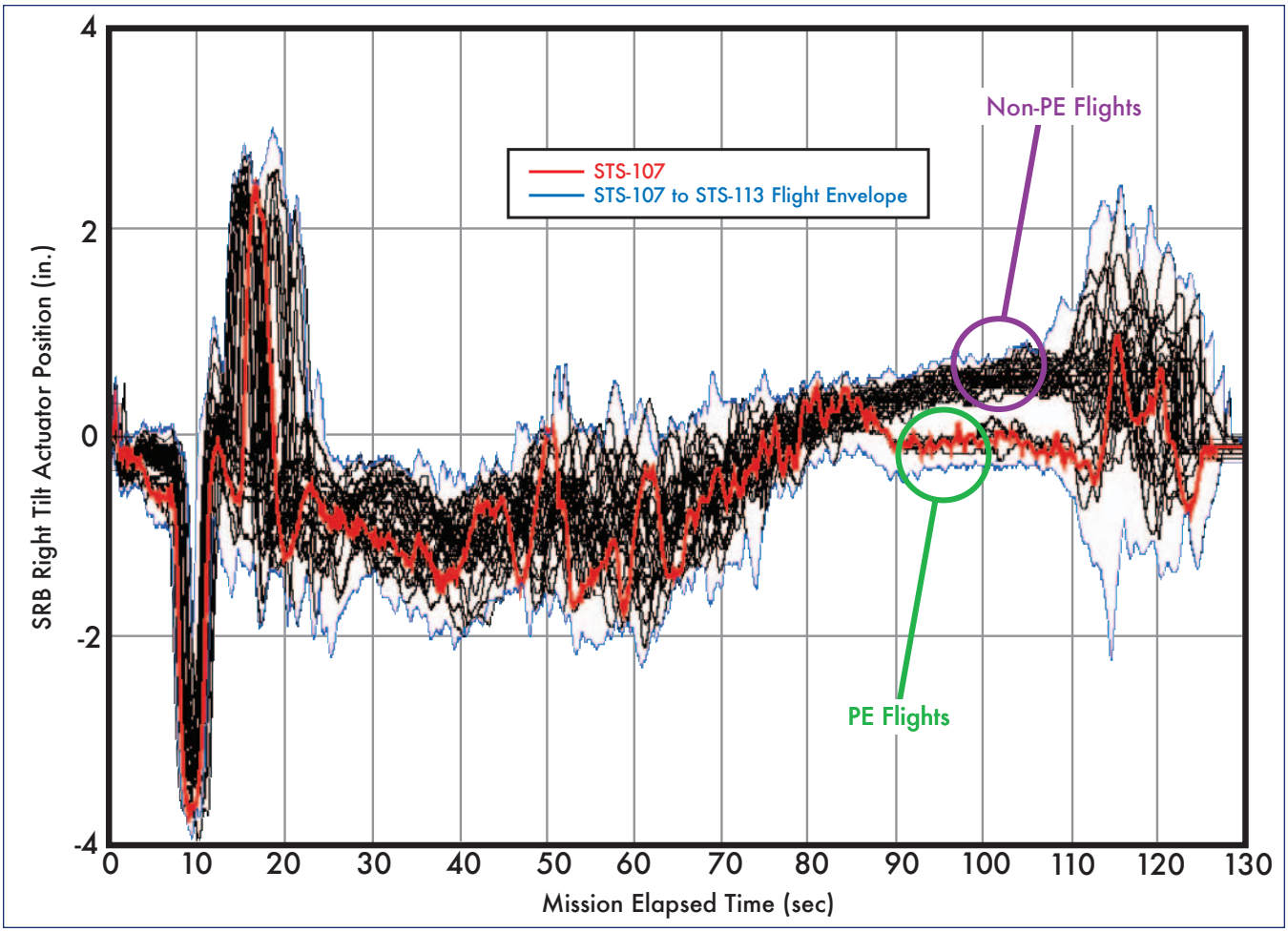


Figure 3-35. SRB nozzle position for PE flights versus non-PE flights.

The second nozzle motion event occurred when the SRB and SSME Thrust Vector Control (TVC) pitch and yaw deflections exceeded the previous flight experience envelope during SRB tail-off (as the SRB thrust diminished). The new flight experience envelope for the SSME and SRB nozzle positions was primarily due to (1) low Reusable Solid Rocket Motor (RSRM) performance that caused a time shift of the SRB tailoff events relative to previous flight experience, as indicated by a low burn rate shown in Figure 3-33, (2) a thrust mismatch between the left and right SRB caused by lower than normal thrust on the right SRB during tail-off, the final seconds of SRB burn (as shown in Figure 3-34), (3) a small bias in the left SRB pitch actuator that shifted the actuator positions farther toward the edge of the flight experience envelope, and (4) flight control trim characteristics unique to PE flights (as shown in Figure 3-35).

The RSRM burn rate is a temperature dependent function, and is determined based on pre-flight tests of small samples of the actual motor propellant at a reference temperature. These values are then adjusted based on a Predicted Mean Bulk Temperature (PMBT) based on the actual weather conditions prior to launch day. For STS-107, the pre-flight predicted motor performance was very close to that determined by post flight reconstruction. A low RSRM burn rate does not affect the total impulse produced by the RSRM during first stage; it only affects the amount of time the RSRMs must burn to achieve the same level of impulse.

The SRB thrust mismatch observed during tail-off was well within the design margin of the flight control system, and similar occurrences have happened numerous times during previous flights.

Due to flight control gain settings unique to PE flights, PE flights have a nozzle position closer to zero inches deflection from 85 to 110 seconds MET. The flight data that coincides with the STS-107 data are all from PE flights, seen clearly in the 85 to 110 seconds MET timeframe in Figure 3-35. The other grouping of flights in this same timeframe (85 to 110 seconds MET) are all non-PE flights and have larger pitch nozzle deflections.

To examine if SRB thrust mismatch during tail-off contributed to the loss of the ET bipod foam, several studies were conducted. The studies included data correlation of (1) flights that used LWT and PEs, and (2) flights that shed ET left bipod foam. The data correlation showed that for both families of flights, SRB thrust mismatches were observed on the majority of flights. The only flights to not have

significant SRB thrust mismatches near SRB tail-off were STS-87 and STS-90. The study of the two families of flights are summarized in Sections 3.5.6 and 3.5.7 of this report.

The data indicate that the SRB thrust mismatch on STS-107 was a direct result of SRB burn rate differences between the left and right SRB. The thrust mismatch observed on STS-107 and the new flight experience nozzle positioning occurred after the foam shedding event. The SRB thrust mismatch occurred on the majority of flights in both families of flights, including those that did not shed foam.

3.5.5 ET Separation Yaw Rate

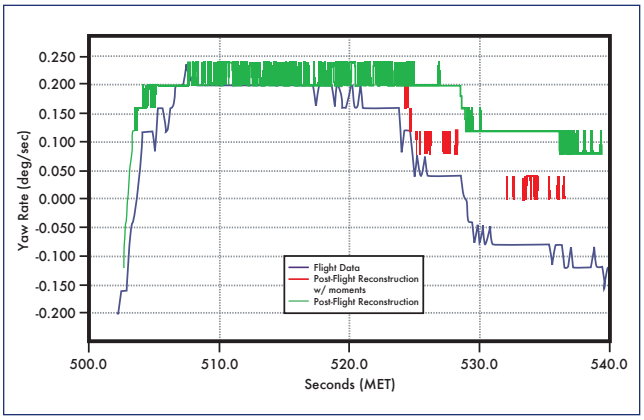


Figure 3-36. ET separation yaw rate.

A higher than typical negative yaw rate was observed at ET separation during STS-107. The yaw rate, shown in Figure 3-36, was approximately -0.12 deg/sec and near the edge of the flight experience envelope. The negative yaw rate is noteworthy because it does not correspond to the flight control system's thruster activity, known vent forces, or any other explained mission activity. Furthermore, the rate appears at the time of physical separation between the orbiter and external tank, which indicates that it is related to the structural release between the two objects. Although the negative yaw rate was unusual, it was well within the design and certification envelope for ET separation. This rate was also well within the flight limits (± 0.7 deg/sec) for ET separation to occur.

A fault tree analysis narrowed down the cause of the negative yaw rate to a release of strain energy at ET separation due to either (1) a misalignment of the orbiter and external tank at structural mating, or (2) a build up of strain energy in the ET structure and associated orbiter attachment strut areas due to thermal differences. STS-107 was one of six flights to have a negative yaw rate at ET separation. The other flights with negative yaw rates at ET separation were STS-2, STS-70, STS-80, STS-92, and STS-98. None of these flights are known to have had bipod foam loss. The ET separation yaw rate on STS-2 was identical to that on STS-107, within the 0.02 deg/sec accuracy limits of the sensors and related data and signal noise.

Data indicate that the yaw rate at ET separation did not result in re-contact between the orbiter and the ET after separation. This observation is based on high rate telemetry (25 Hertz) orbiter body rate data, and MADS accelerometer data analyzed post-flight. The yaw rate was within the expected range of vehicle body rates when taking into account all known error sources, including rate sensor noise. The data indicates that no correlation exists between observed yaw rate at ET separation and bipod ramp foam loss.

3.5.6 Data Correlation of Flights that Used a LWT and PEs

To determine if any of the items considered new flight experience were unique to the use of Light Weight Tank (LWT) and Performance Enhancements (PEs), an evaluation was performed to compare the STS-107 flight data to other flights using LWT and PEs. The STS-107 data was compared to flights STS-87, STS-89, STS-90, and STS-99 (as shown in Table 3-5).

LWT and PEs were also used on STS-85 and STS-86. Neither flight was included in the LWT and PE flight data correlation study because the flights were the first to use the new PE flight software, and as such had very few of the PEs active. One of the most significant PEs not active for STS-85 and STS-86 was the first stage pitch parallel change. Not having the first stage pitch parallel PE in place resulted in STS-85 and STS-86 being outliers when compared to the other five flights, due to significantly different SRB and SSME nozzle positioning during first stage (as previously shown in Figure 3-35).

The LWT and PE flight data correlation study compared the STS-87, STS-89, STS-90, STS-99, and STS-107 flight data for parameters that were considered new flight experience for STS-107. The LWT and PE flight data correlation included a comparison of environmental side-slip angle

Flight	*Tank type*	*ET #*	*Orbiter*	*Flight software*	*Inclination*	*Launch date*
STS-87	LWT	89	*Columbia*	OI-26A	28.45 deg	11/19/97
STS-89	LWT	90	*Endeavour*	OI-26A	51.6 deg	1/22/98
STS-90	LWT	91	*Columbia*	OI-26B	39.0 deg	4/17/98
STS-99	LWT	92	*Endeavor*	OI-27	57.0 deg	2/11/00
STS-107	LWT	93	*Columbia*	OI-29	39.0 deg	1/16/03

Table 3-5. LWT and PE flights.

during Hi-Q, SSME yaw position during Hi-Q, SRB thrust mismatch during Hi-Q, ET separation yaw rate during Hi-Q, and ET slosh.

The LWT and PE flight correlation study indicated that negative side-slip angles of -0.75 degrees or more occurred on all flights, including STS-90, which had the second largest side-slip angle of any flight in Hi-Q of -2.0 degrees. Evaluation of SSME yaw positions during Hi-Q indicated that only STS-90 had a similar signature. The STS-90 SSME yaw was primarily due to a large wind shear on that flight. Evaluation of SRB thrust mismatch shows a similar thrust mismatch and corresponding SRB and SSME TVC gimbal activity on STS-89 and STS-99 only. Within this family of flights, the negative yaw rate at ET separation and ET slosh characteristics were only observed on STS-107.

Of all of the flights studied, STS-90 and STS-107 were the most similar. Both flights were flown on *Columbia*, on a 39.0-degree inclination trajectory, used LWT and PEs, were daytime launches, and had a SPACEHAB module as the primary payload. Furthermore, STS-90 and STS-107 flew through a large wind shear during the Hi-Q region.

The data is inconclusive as to whether ascent GNC parameters/events correlated for flights using a combination of LWT and PEs.

3.5.7 Data Correlation of Flights with ET Bipod Foam Liberation

To examine if any of the items considered new flight experience for STS-107 contributed to the ET bipod foam liberation, a flight data correlation study was performed for all flights known to have lost ET bipod foam during ascent. The flights compared to STS-107 below included STS-7, STS-32, STS-50, STS-52, STS-62, and STS-112 (as summarized in Table 3-6). These are the only flights to have definitive photographic information to show ET bipod foam loss between liftoff and ET separation. An estimate of the ET bipod foam volume obtained from this photographic evaluation can also be found in Table 3-6. It should be noted that STS-32 is under review as a flight that lost ET bipod foam. It is known that STS-32 lost ET foam, but it is not clear at this time if it was acreage foam or bipod foam.

The ET bipod foam liberation flights were compared for parameters that were considered new flight experience for STS-107. The data correlation study included a comparison of environmental side-slip angle during Hi-Q, SSME yaw position during Hi-Q, SRB thrust mismatch during thrust tail-off, ET separation yaw rate, and ET slosh.

The negative side-slip angle of -1.5 degrees or more occurred on all flights in this family, and STS-62 had the

FLIGHT	*STS-7*	*STS-32*	*STS-50*	*STS-52*	*STS-62*	*STS-112*	*STS-107*
BIPOD FOAM LIBERATED ON ASCENT	YES	Under Review	YES	YES	YES	YES	YES
APPROX. DEBRIS VOLUME (cu. in.)	404	295	707	15	1	202	1200
ET NUMBER	06	32	50	55	62	115	93
ET TYPE	SWT	LWT	LWT	LWT	LWT	SLWT	LWT
ORBITER	*Challenger*	*Columbia*	*Columbia*	*Columbia*	*Columbia*	*Atlantis*	*Columbia*
INCLINATION (degrees)	28.45	28.45	28.45	28.45	39.0	51.6	39.0
LAUNCH DATE	06/18/83	01/09/90	06/25/92	10/22/92	03/04/94	10/07/02	01/16/03
LAUNCH TIME (local)	07:33:00 AM EDT	07:35:00 AM EST	12:12:23 PM EDT	1:09:39 PM EDT	08:53:00 AM EST	3:46:00 PM EDT	10:39:00 AM EDT
SIDE-SLIP ANGLE DURING FIRST STAGE	YES	YES	YES	YES	YES	YES	YES
NOZZLE YAW DURING FIRST STAGE	No	No	YES	YES	YES	No	YES
SRB THRUST MISMATCH	YES	YES	YES	YES	YES	YES	YES
ET SLOSH	No	YES	YES	YES	YES	No	YES
NEGATIVE YAW RATE AT ET SEPARATION	No	No	No	No	No	No	YES

Table 3-6. STS flights with ET left bipod foam liberation.

largest side-slip angle of any flight in first stage (prior to SRB separation) at -2.5 degrees. Evaluation of SSME yaw positions in first stage show similar signatures occurred on STS-50, STS-52, and STS-62 (all primarily due to large wind shears). Evaluation shows that similar thrust mismatch and corresponding SRB and SSME TVC gimbal activity occurred on all flights in this family. STS-107 is the only flight in this family to have a negative yaw rate at ET separation. The ET slosh characteristic was present on STS-32, STS-50, STS-52, STS-62, and STS-107.

In summary, the negative side-slip angle and SRB thrust mismatch were evident for all flights on which ET bipod foam loss was observed. For other parameters within this family of flights, no correlations are evident. It is noteworthy that five of the seven flights in the foam loss family were *Columbia* missions, all with the ET slosh characteristic. Finally, the data are inconclusive as to whether any of the new flight experience parameters (individually, or in some combination) by themselves caused bipod foam loss.

4.0 Orbit

4.1 Introduction

While *Columbia* was on-orbit, there was no indication of damage from either the ascent foam impact or a micrometeoroid/orbital debris (MMOD) hypervelocity debris impact based on orbiter telemetry, crew downlinked video and still photography, or crew reports. Multiple comprehensive postflight reviews of the same data indicated that there was nothing unusual with any of *Columbia*'s systems or structure. This included a detailed review of orbiter Inertial Measurement Unit (IMU) accelerometer, body rates, and jet firing data to determine if there were indications of an orbital debris hypervelocity impact. The results of this analysis show that there were no indications of an orbital debris impact, although there are several unexplained events. Data from an additional accelerometer package, known as Space Acceleration Measurement System (SAMS), was used to determine if this more sensitive system was able to detect any unusual activity during these timeframes. Details of the orbital debris analysis can be found in Section 4.2 and the flight day 2 debris event will be discussed in Section 4.3.

4.2 Orbital Debris

4.2.1 Orbital Debris Risk Assessment

There were multiple payload constraints on this mission, which resulted in 239 attitude maneuvers, or orientation changes. For each Shuttle mission the complement of attitude maneuvers is analyzed for orbital debris risk of a critical penetration due to an on orbit hypervelocity impact. This same analysis, performed post-flight, determined that the probability of no critical penetration was 0.9972, which is well below the guideline for critical penetrations. The analysis also included specifics for critical penetrations of the left wing. The results show that the overall probability for no critical penetration is 0.9996 for the entire left wing and 0.9999 for the left wing leading edge RCC.

4.2.2 Micrometeoroid or Orbital Debris Detection

Postflight, a NASA JSC team consisting of members from Mission Operations, Engineering, and Space and Life Sciences with the support of Draper Labs, participated in an effort to use downlisted data to identify any external forces or torques that could be correlated with an MMOD impact. This task was divided into four different areas:

1. Build an inclusive, detailed activity timeline that includes all known Shuttle and payload events (venting, waste control system activities, LiOH canister change out, payload bay door operations, and SPACEHAB systems operations) that would cause attitude and rate errors or momentum changes detectable by the orbiter systems.
2. Review the orbiter IMU rate data for net changes in angular momentum, which would be indicative of an MMOD strike.
3. Screen the 20,000 plus orbiter Vernier Reaction Control System (VRCS) jet firings with an algorithm to determine whether or not each firing was due to the control system response to normal attitude changes or disturbances, or in response to an MMOD strike.
4. Examine SAMS payload experiment data for potential signs of an MMOD strike.

4.2.2.1 IMU Rate Data Review

This study reviewed all orbiter data from various sensors and systems. The only data useful for this study were the orbiter body axis rate data, which are derived from IMU attitude data by the Guidance Navigation and Control (GNC) flight software. This analysis assumed rigid body dynamics; flexural response was covered in the SAMS data analysis (see below).

The entire orbit portion of the mission, from the orbit transition (1 hour MET) to four hours prior to the deorbit, was examined. A total of 238 events of interest were identified which required further examination. All but 13 of these events were correlated to either a known forcing function, or the signature did not match the expected dynamic response of an externally applied impulse (MMOD strike). The remaining 13 unexplained events were analyzed in significantly greater detail.

Additional analysis included the evaluation of the rate transients and a time integration of the change in angular momentum across the event of interest. The guiding principle of this analysis is that unless there is an external force or torque applied to the vehicle, conservation of angular momentum will always apply. This study resulted in the elimination of 10 of the 13 events that did not fit the expected response for an externally applied impulse. One event was inconclusive due to the low resolution of the data, and the remaining two events have the potential to be caused by an MMOD strike; however, other causes are also possible (unknown venting, etc.). The orbiter rate data cannot be used to explicitly determine mass, velocity, or point of impact of an MMOD object. Table 4-1 provides an overview of the original 13 events of interest.

Event	EST* (Day/hour:min:sec)	MET* (Day/hour:min:sec)	External torque, unknown venting, or potential MMOD** strike	Angular momentum conserved (crew motion, other, or unknown)	H_2O dump	Inconclusive
1	18/11:45:00	2/01:06:00		X		
2	19/12:45:50	3/02:06:50		X		
3	19/20:02:20	3/09:23:20	X			
4	19/21:31:30	3/10:52:30		X		
5	24/16:45:10	8/06:06:10			X	
6	25/04:19:20	8/17:40:20	X (possible)			
7	25/05:08:00	8/18:29:00		X		
8	26/03:53:20	9/17:14:20		X		
9	29/00:02:00	12/13:23:00		X		
10	29/15:48:30	13/05:09:30		X		
11	29/17:40:10	13/07:01:10		X		
12	31/11:07:00	15/00:28:00				X
13	32/02:02:30	15/15:23:30		X		

** Times are approximate*
*** Micrometeorite or orbital debris*

Table 4-1. Summary of analysis of 13 rate events.

4.2.2.2 Lower Bound of IMU MMOD Detection Threshold

Two separate techniques were evaluated to attempt to bound the lowest MMOD mass and velocity that could be detected using the orbiter IMU data. The first used measured angular rate data, while the second used the accelerometers to measure a change in velocity.

There were two assumptions for this angular rate analysis. First, the lowest value of angular rate change that can be detected by the Shuttle IMU's is 0.002 deg/sec, based on an evaluation of body rates and engineering judgment. Second, to bound the minimum mass of an MMOD object, the efficiency of transfer of linear momentum of the striking object was assumed to be 100% with optimal geometry. The resulting transfer of the linear momentum is a change of orbiter angular momentum.

The bounding of the lower limit of the linear momentum and/or mass of a potential strike object is not a one-dimensional exercise. Several assumptions must be made to perform this analysis. Strike location on the orbiter is significant. For a fixed orbiter rate change from a strike, the radius from the orbiter center of gravity (CG) to the strike location is inversely proportional to the linear momentum of the striking object. Also, once the linear momentum of the striking object is defined, the mass of the object is inversely proportional to the velocity. The examples shown in Table 4-2 are three of many possible solutions; however, they have

Body Axis	Body Rate (degrees per second)	Angular Momentum (slug*ft²/sec)	Assumed Strike Location of MMOD	Assumed Velocity of MMOD (nmi/sec)	Lower Bound of the Mass of MMOD (Assumes optimal geometry & 100% momentum transfer) (gram)
Roll	0.002	36	Outside edge of the main landing gear door, or about 14 ft Y c.g. offset.	5	1
Pitch	0.002	273	The forward most portion of the wing structure, or about 23 ft in front of the X c.g.	5	6
Yaw	0.002	285	The forward most portion of the wing structure, or about 23 ft in front of the X c.g.	5	6

Table 4-2. Summary of analysis of the lower bound of MMOD (based on body rate data).

been selected to be representative of a strike location roughly associated with the main landing gear door and forward through the leading edge of the wing.

The lowest value of velocity change that can be detected is 0.0344 feet per second based on the minimum integrated acceleration (velocity) pulse size from the IMU's. In order to determine the minimum possible detectable MMOD mass for this orbiter velocity detection capability, the following assumptions were used: conservation of linear momentum, a 100% momentum transfer from the striking object, object impact at the orbiter center of mass, and a relative debris velocity of 5 nmi/sec. Based on these assumptions, the lowest detectable MMOD mass is 127 grams. From this momentum analysis, it is apparent that the orbiter being struck by an approximately one-quarter pound object (at 5 mi/sec) assuming 100% momentum transfer would most likely be noticeable by the crew. Therefore, IMU accelerometers are not considered of significant value in the search for an MMOD strike on-orbit.

4.2.2.3 Vernier Thruster Firing Algorithm

The review of orbiter data accounted for momentum changes due to VRCS jet firings. However, the possibility existed that a debris strike with enough energy or striking the orbiter at the right time could have caused the On-Orbit Digital Auto-Pilot (DAP) to command a jet firing due to a rate deadband exceedance.

The On-Orbit DAP will command jets to fire to maintain attitude errors within attitude deadbands and rate errors within rate deadbands. During periods of attitude hold, the majority of jet firings are due to the attitude deadband. Rate deadband firings typically occur at the beginning and end of attitude maneuvers, and during maneuvers due to changes in the desired rate. Figure 4-1 depicts changes in the vehicle rates due to jet firings and normal gravity gradient forces.

Analysis was undertaken to examine every jet firing and determine the cause of the firing. An algorithm was built to screen all nominal attitude deadband related firings. The remaining firings were examined to determine cause.

The algorithm assumed a VRCS jet was firing any time the downlist (telemetry) indicated a command to fire any one or more of the six VRCS jets. Also, instances of VRCS firings when the DAP attitude error (downlisted at 1 Hz) was less than 95% of the estimated attitude deadband were flagged for further investigation.

A total of 747 jet firings out of 28,779 were identified by the screening process for further investigation. Of these, 19 were due to faulty driver indications (data hits). These were verified via no change in slope of attitude rates, DAP attitude errors, and the six vernier jet fuel and oxidizer injector temperatures.

The remainder were examined and determined to be caused by (1) rate limit firings at the start and stop of attitude maneuvers, (2) rate limit firings that occurred during maneuvers due to changes in the desired rate, and (3) attitude deadband

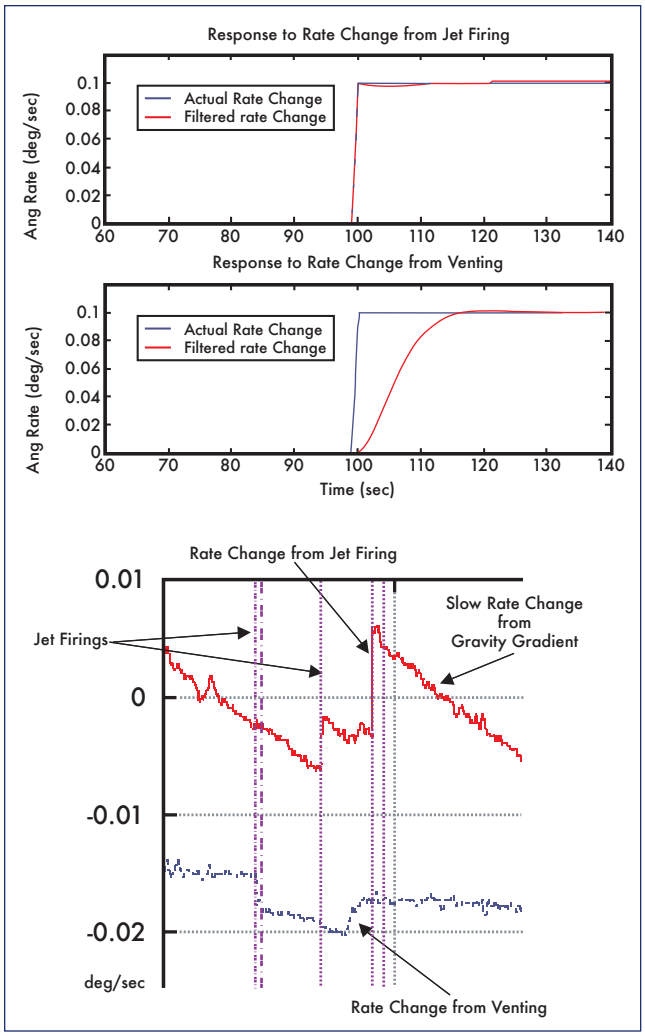


Figure 4-1. Jet firing example for vehicle rates

firings not screened. The final result was that there were no unexplainable jet firings in the STS-107 on-orbit data.

4.2.2.4 SAMS Data Analysis

After a review of the available payload sensors, it was determined that the SAMS data package would be the only suitable sensor that could provide additional data to aid in the detection of an MMOD strike. SAMS provides tri-axial accelerometers to measure the vibratory and transient portion of the microgravity environment. Those vibratory and transient accelerations are composed of disturbances that originate in STS equipment, scientific experiment, and crew operations. The vibratory/transient accelerations are on the order of milli-g's and are sampled at 100 Hz. While the Shuttle IMU's are designed to measure the rigid body accelerations and attitude, SAMS measures the vibratory/transient portion of the micro-gravity environment. The vibratory portion is the dominant part of the SAMS data. Three SAMS sensor sets were aboard STS-107; however, only one had data that was downlinked during the flight. This sensor was located in the SPACEHAB Module near the Combustion Module 2 experiment.

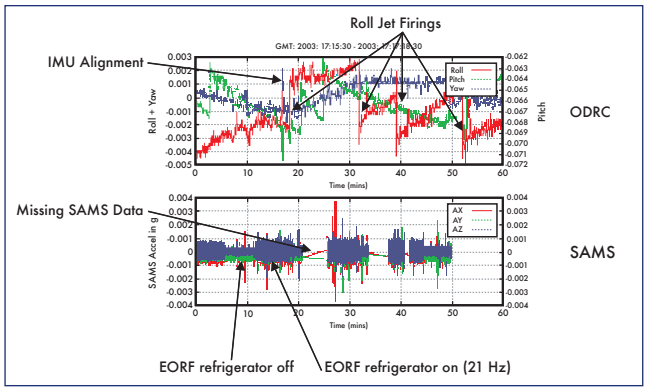


Figure 4-2. Sample data from SAMS and ODRC.

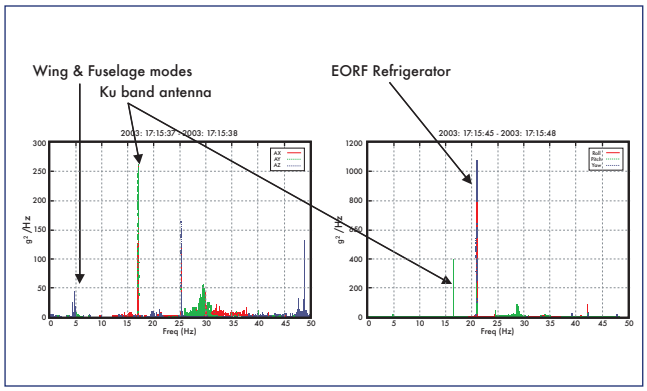


Figure 4-3. SAMS data frequency content.

SAMS data was used to support the aforementioned IMU rate data review. Anomalies in rates from manual review of orbiter body rates were compared to SAMS measurements to help identify sources. Figure 4-2 provides a sample plot of SAMS data and the response signature to an IMU alignment and the Enhanced Orbiter Refrigerator/Freezer (EORF) operation, as well as downlisted telemetry in the Operational Data Retrieval Complex (ODRC) system. SAMS data was also scanned for large transients to identify potential strikes (the assumption is that a hypervelocity impact would "ring" the structure). Various frequencies from nonstructural items were identified, so that they could be filtered out of the data. Figure 4-3 shows the frequency response of several items such as the EORF refrigerator and the Ku-band antenna. A detailed structural model that identifies frequencies of primary structure was developed. This model was used to screen for vibrational transients associated with orbiter wing strikes.

The review of SAMS data has not uncovered any events that could be correlated to a hypervelocity debris strike from micrometeoroids or orbital debris.

4.3 Flight Day 2 Event

4.3.1 Radar Tracking of Flight Day 2 Object

Air Force Space Command post-flight evaluation of radar tracking data indicated an object in the vicinity of the orbiter on flight day 2. The object remained on-orbit for approximately two and a half days, and reentered the atmosphere. Multiple government agencies participated in complex post-mission analysis of this object. These agencies include the Department of Defense *Columbia* Investigation Support Team, United States Strategic Command, Air Force Research Labs (AFRL) at Wright-Patterson Air Force Base, Air Force Space Command (AFSPC), Lincoln Laboratory at the Massachusetts Institute of Technology, and NASA's Johnson and Kennedy Space Centers.

The AFSPC Space Analysis Center estimated the departure time for the object was January 17, between 10:00 and 11:15 EST. Because there was no direct radar observation at the exact time of departure from the orbiter, analysis indicated that the most likely window of departure was between 10:30 EST and 11:00 EST. The analysis was complicated by the high drag profile, making it difficult to determine the precise time when the object left the vicinity of the orbiter.

The calculated departure velocity was relatively low and was estimated to be 0.7 to 3.4 miles per hour with the lower velocity being more likely. An exact departure direction relative to the orbiter could not be determined. Multiple ground sensors including Eglin Air Force Base (AFB), Beale AFB, Cape Cod Air Force Station (AFS), and the Navy Space Surveillance fence radar tracked the object. The object reentered the atmosphere on January 19 between 20:45 EST and 23:45 EST. Figure 4-4 depicts the tracking of the object including various sensor passes.

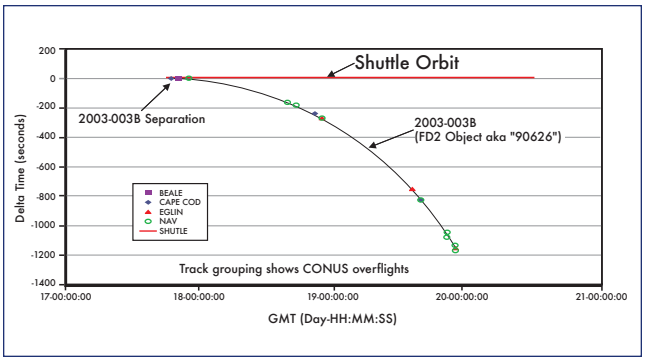


Figure 4-4. Tracking of flight day 2 object through various sensor passes.

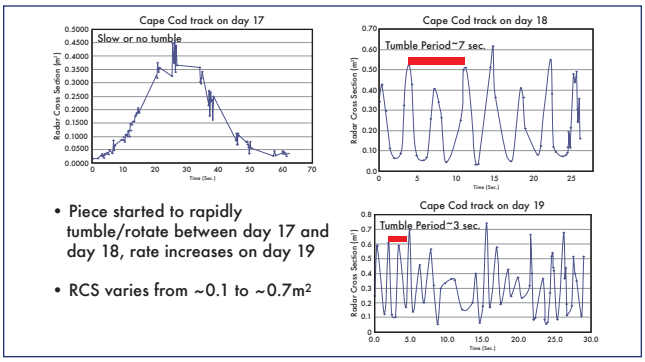


Figure 4-5. On-orbit RCS shows increased tumble/rotation rate over time.

Date/Time (EST hh:mm)	EVENT
January 17 9:42 to 9:46	Attitude maneuver to a biased tail forward bay to earth attitude (biased -ZLV, -XVV)
January 17 10:17 to 10:21	Maneuver back to the bay to earth tail forward attitude (ZLV, -XVV)
January 17 10:30 to 11:00	Best estimate of object departure window
January 17 11:25	Manual fuel cell purge
January 19 16:39	First water dump
January 19 20:45 to 23:45	Object re-enters atmosphere

Table 4-3. Chronology of events related to flight day 2 object.

Based on the observed radar cross sections, the object appeared initially to have a minimal to no tumble/rotation rate, but it gradually developed a rate over the next two days. During a Cape Cod AFS sensor pass on January 18 at 15:29 EST, the tumble/rotation rate had a period of seven seconds. Later, on January 19 at 10:39 EST during another Cape Cod AFS pass, the apparent tumble/rotation rate had increased and the period was approximately three seconds. Figure 4-5 depicts the tumble/rotation rates during the timeframe that the object remained in orbit. The exact physical size and mass of the object are unknown, although it appeared to be a lightweight piece based on the observed ballistic coefficient.

4.3.2 Analysis of Mechanisms for Object Release

The timeframe of estimated departure has been reviewed in detail. There were no unusual crew events, telemetry data, or accelerations in orbiter or payload accelerometer data that can account for the ejection of an object matching this description. SAMS, IMU, and jet firing data indicate that there was no orbital debris impact during the timeframe. Additional reviews indicate that no external mechanical systems such as the radiators or FREESTAR experiment canister doors were active during the time of interest. The port radiator was deployed on January 16 at 13:47 EST and was stowed on January 19 at 17:39 EST.

Crew commentary in the air-to-ground voice transmission during this window was routine and there was no mention of an object being observed. There was no video downlink at the time of interest, but subsequent surveys of downlinked video and still imagery did not reveal any items missing from the payload bay or visible exterior of the vehicle.

The orbiter did not perform any translational maneuvers during this timeframe. Two attitude maneuvers or orientation

MET (hh:mm:ss)	EST (hh:mm:ss)	EVENT
0:00:00	10:39:00	*Columbia* launch
0:01:21.7	10:40:21.7	Foam departs ET left bipod ramp
0:01:21.9	10:40:21.9	Foam impacts Orbiter left wing RCC panels 6 through 8
0:02:06.6	10:41:06.6	SRB separation
0:07:23.6	10:46:23.6	3-G throttling of Space Shuttle Main Engines
0:08:22.5	10:47:22.5	Main Engine cutoff command
0:08:33	10:47:33	Zero thrust
0:08:43.7	10:47:43.7	ET separation translation
0:08:57	10:47:57	Crew +X translation for ET photography
0:10:24 – 0:12:24	10:49:24 – 10:51:24	Main Propulsion System dump
0:13:44 – 0:14:33	10:52:44 – 10:53:33	Manual pitch maneuver for ET photography
0:29:52 – 0:34:24	11:08:52 – 11:13:24	Attitude maneuver to Orbital Maneuvering System (OMS)-2 burn attitude
0:41:24 – 0:43:24	11:20:24 – 11:22:24	OMS-2 burn using left and right OMS engines
~01:15:00	11:54:00	Attitude maneuver to payload bay door opening
~0:02:00	12:39	Configure for vernier attitude control (six small, 24 lb thrusters)

Table 4-4. Summary of nominal launch day events.

changes were accomplished using the small, 24 lb vernier attitude control thrusters. The first maneuver was a 48-degree yaw maneuver to a biased tail forward bay-to-earth attitude that occurred from 09:42 to 09:46 EST. Near the window of estimated departure, there was a maneuver back to the bay-to-earth tail forward attitude from 10:17 to 10:21 EST.

A manual fuel cell purge was performed later at 11:25 EST, outside the window of probable object departure. The first orbiter water dump occurred approximately two days after this event. Table 4-3 lists the chronology of relevant events.

Data indicate that in the timeframe of the object departure there were no unusual forces or mechanisms for liberating the debris that were not also present prior to this timeframe. The orbiter had encountered a more severe loading environment during the ascent and post-insertion timeframe than on-orbit as depicted in Table 4-4. The orbiter was using the large 870 lb primary reaction control system thrusters for attitude maneuvers until the small 24 lb vernier thrusters were activated about two hours after launch. One theory is that 16 orbits of thermal cycling (day/night transitions) caused stored energy from an object in the payload bay or on the orbiter structure to be released. Another theory is that attitude maneuvers in this timeframe could have assisted the object in obtaining the opening rate from the orbiter. The data is inconclusive in determining the cause of the object departing on flight day 2.

4.3.3 Radar Cross Section and Ballistics Testing

In addition to the careful inspection of downlinked orbiter payload bay video and still photography, radar testing and ballistics analysis of various thermal protection system items and thermal blankets have been conducted in an attempt to identify the flight day 2 object. The AFRL Advanced Compact Range Facility at Wright-Patterson AFB in Ohio tested a total of 32 items for radar cross section (RCS) at the Ultra-High Frequency (UHF) frequency of 433 MHz. These items comprise nearly the entire external surface of the orbiter as well as the exposed surfaces in the cargo bay, RCC panels, and carrier panels. The items tested also included four pieces of recovered RCC debris from *Columbia* to better understand the radar characteristics of partial Tee seals and RCC panels.

The results of this radar testing and ballistics analysis have excluded all external Shuttle materials with the exception of 1) a whole Tee seal, 2) a Tee seal fragment that includes an attachment flange and/or apex segment, or 3) RCC panel acreage no less than 90 square inches and roughly square in shape (+/- 20%), although curvature is possible, with a thickness on the order of 0.33 inches. An RCC panel segment matches the RCS and ballistic performance characteristics observed during the STS-107 mission.

A Tee seal fragment with an apex segment matched the RCS characteristics extremely well in any spin orientation; however, the ballistic match required a very specific spin orientation that was shown to be feasible in one analytical simulation. Therefore, it is possible that the flight day 2 object was either a partial Tee seal or RCC panel acreage piece. The Incoflex spanner beam "ear muff" insulation was also a good match for both ballistics and RCS. Because the "ear muff" is situated behind the RCC panel, it is excluded from being considered a very likely candidate because of the lack of a mechanism for exposing it to the space environment. If the damage to the wing were actually a 10-inch diameter, uniformly round hole, then an "ear muff" would be a more plausible candidate. However, it is considered unlikely that the wing damage was a 10-inch diameter round hole. The damage is considered to be the equivalent of that which would provide the same thermal response during entry as a 10-inch diameter hole did in the analyses and simulation. It is not likely that the actual wing damage was geometrically uniform. The damage was more likely a combination of cracks and holes, or a slot, such as a Tee seal or partial Tee seal missing or displaced. Therefore, the ear muff is not considered to be a good candidate for the flight day 2 object. Figure 4-6 shows the three leading edge

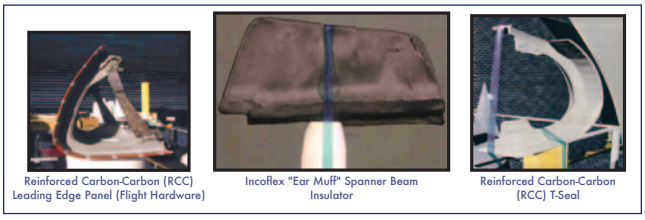


Figure 4-6. Leading edge structural subsystem components matching RCS and ballistics.

Processing Flow	*Tool Description*	*Location*	*PR #*
OMM J3	Allen Socket, 2"x 1/2"	Mid-body	(LAF-2-J3-0550)
OMM J3	Plastic Extraction Tool, 22 gauge	Flight Deck	(LAF-2-J3-0567)
OMM J3	Pliers, 7 3/4"	Hypergolic Maintenance Facility (HMF)	(LAF-RPO5-15-0004)
OMM J3	Screwdriver, 11"	HMF	(LAF-RPO5-15-0005)
OMM J3	Screwdriver, 7"	HMF	(LAF-RPO5-15-0006)
OMM J3	Screwdriver, 8"	HMF	(LAF-RPO5-15-0007)
STS-109	Mini Flashlight, 6"	Forward Reaction Control System (FRCS) 2	(LAF-FRC2-27-0005)
STS-107	Socket, 7/16"x 5/16"	Aft Compartment	(LAF-2-28-0632)

Table 4-5. Lost tools in Columbia *processing for STS-107, STS-109, and OMM J3.*

components that match both RCS and ballistics analysis. It should be noted that a full Tee seal and RCC panel are shown in these photos while there are specific partial Tee seal and RCC panel configurations that match the test results.

4.3.4 KSC Lost and Found Items

A review was conducted of the lost-and-found items from the *Columbia* processing flows of STS-107, STS-109, and the last *Columbia* OMM-J3. The largest tools that were lost and not found are listed in Table 4-5; other smaller items (e.g., washers and nutplates) are not listed. The item, size, location, and Problem Report (PR) number are noted. The largest item documented on a Lost and Found (LAF) PR is a piece of a blanket 6" x 3" lost in the payload bay (LAF-2-27-0611) during STS-109 processing. These items were screened using the ballistic coefficient and RCS criteria. All of the items failed the RCS screening and their RCS is too low to be a candidate for the flight day 2 object.

4.4 Orbit Summary

Extensive data review provided no conclusive indication of damage from either the ascent foam impact or an MMOD hypervelocity impact based on orbiter telemetry, crew downlinked video and still photography, or crew reports.

Orbiter IMU and jet firing data have been reviewed, and this review confirmed that the IMU's were not designed for MMOD detection and data available to detect an MMOD strike is coarse. This data review found 13 events that required additional analysis. After this additional analysis, only two events remained that could not be ruled out as MMOD strikes. An examination of all VRCS jet firings was conducted and showed no unexplainable jet firings during STS-107.

SAMS data were also used in the analysis of the 13 events detected using IMU rate data. SAMS sensor data were also screened for large transients indicative of an MMOD strike; however, none were found. A model was developed that identifies the modal frequencies of the Shuttle structure (including wing modes) to further screen the SAMS data for MMOD strikes.

A review of the flight day 2 event has been performed including RCS testing and ballistics analysis of 41 items, including TPS. The analysis performed to date indicates that a full Tee seal, a partial Tee seal, and RCC panel are the only tested items that have not been excluded.

It is possible that another untested object could match the RCS and ballistics and have departed the orbiter on flight day 2. Objects have departed the payload bay on previous Shuttle missions. The data are inconclusive as to whether the ET ascent foam debris event and the flight day 2 event are related.

5.0 Deorbit/Entry

5.1 Introduction

The deorbit and entry section is divided into four distinct areas. The first section discusses the upper atmosphere weather including high altitude winds, and the Kennedy Space Center (KSC) Shuttle Landing Facility (SLF) weather for the STS-107 landing. The next section includes a detailed discussion of forensics data obtained from testing and analysis of the key items in the recovered debris. The third section is a narrative of the entry events from February 1, 2003, and the fourth section is a brief discussion of key elements of the aerodynamic reconstruction.

5.2 Weather

5.2.1 Upper Atmosphere Weather

As the Shuttle entered the atmosphere, it descended from about 400,000 feet when located over the central Pacific Ocean to roughly 200,000 feet over Texas. The Goddard Space Flight Center Data Assimilation Office (DAO) provided the GEOS-4 model analysis for the investigation in order to provide a best estimate of the density, temperature, and wind along the entry trajectory. The GEOS-4 model assimilates a wide variety of data sources to produce an integrated 3-dimensional analysis of the atmosphere from the Earth's surface to about 250,000 feet. The Global Reference Atmosphere Model (GRAM) was used to provide information about the atmosphere from Entry Interface to the top of the GEOS-4 analysis. In general, the entry environment was characterized by a lower than average density and higher than average winds prior to the vehicle breakup. Comparison of the GEOS-4 analysis to GRAM indicates that the estimated density and winds were within the expected climatology for the upper atmosphere. Figure 5-1 shows the wind profile that was developed by the DAO as part of the STS-107 investigation.

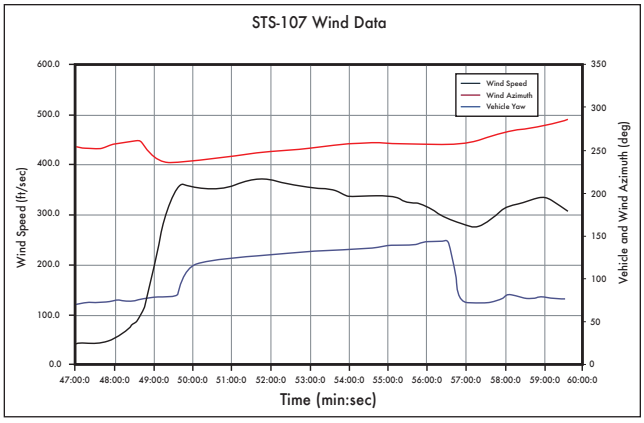


Figure 5-1. Wind profile developed by DAO as part of the STS-107 investigation (time referenced to 8:min:sec EST).

5.2.2 Landing Weather

On the morning of February 1, 2003, there was a concern for ground fog formation at KSC for the first STS-107 landing opportunity. This concern is not uncommon for a morning landing at KSC during the winter months. The landing time for the first KSC opportunity was 9:16 EST. The forecast called for the fog to burn off as the sun rose, producing mixing in the lower levels of the atmosphere. The Shuttle

Training Aircraft (STA), which is used for weather reconnaissance, flew approaches to both the KSC-15 and KSC-33 runways to determine the best runway for landing. The STA is used to evaluate touchdown conditions, visibility, turbulence, crosswind, and overall pilot workload. At the time of deorbit decision, runway visibility was reported as 4 miles in light fog with winds 5 knots from the west. Visibility on final approach was slightly better for Runway 33. The final landing runway decision was not made at that time.

Leading up to the deorbit decision time, the fog had been the main point of discussion until some clouds developed to the northwest of the landing area. Satellite imagery indicated an area of broken clouds (5/8 to 7/8 sky coverage) with bases at approximately 4,000 feet above ground level between 20 and 25 nautical miles northwest of the runway. The forecast was for those clouds to erode as they approached the SLF producing scattered clouds (3/8 or 4/8 sky coverage) at landing time. The Spaceflight Meteorology Group (SMG) stated that if erosion did not occur, the clouds reaching the SLF would be covering the runway for the first landing opportunity. No low clouds were being reported at the SLF at deorbit burn decision time and no surrounding observing sites were reporting low ceilings. The final forecast update was for a few clouds at one thousand feet and scattered clouds at three thousand feet, and the forecast remained "Go" per the flight rules.

At the actual deorbit decision time and at the actual deorbit time, the landing weather satisfied all criteria per the documented Flight Rules, resulting in a "Go" observation and a "Go" forecast. At 9:10 EST, approximately five minutes prior to the expected landing time, the weather observation at the SLF reported a broken ceiling at 3,500 feet with 6/8 sky coverage and visibility 7 miles. The ceiling remained 3,500 broken until 9:25 EST at which time the SLF observer reported scattered clouds with 3/8 sky coverage.

The cloud deck at landing time was below the Flight Rule ceiling minimum requirement of 8,000 feet. Therefore, the commander would have relied in part on computer instrumentation and visible geographic references of the airfield, flying a Microwave Scanning Beam Landing System (MSBLS) approach until breaking out of the clouds at 3,500 feet, a procedure regularly practiced in several landing simulators. The incorporation of MSBLS data provides very accurate onboard navigation, allowing for more accurate instrument information and facilitating instrument approach capability. The opinion among several experienced astronaut commanders, including the Chief of the Astronaut Office, is that the landing would likely not have been affected by this ceiling, when considering all other conditions of the day.

5.3 Hardware Forensics

As discussed earlier in Section 3, *Columbia* entered the upper atmosphere with unknown damage to a Reinforced Carbon-Carbon (RCC) panel or Tee seal in the left wing RCC panels 6 through 9 area. The panel 8/9 area is the most likely area of damage as determined by hardware forensics testing and analysis of MADS entry temperature and strain measurements on the left wing leading edge structure. This damage area is also consistent with the location of the ascent foam impact, and includes the Tee seals adjacent to panel 8, Tee seals 7 and 8.

The forensic data indicate that the panel 8/9 area was subjected to extreme entry heating over a long period of time leading to RCC rib erosion, severely slumped carrier panel tiles, and a substantial slag deposition on the upper portion of RCC panels 8 and 9. Figure 5-2 shows the slag deposition (both metallic and oxide) in the RCC panel 8/9 area relative to the other parts of the wing leading edge, and Figure 5-3 shows samples of the severe slag deposition on the panel 8 rib. A review of all recovered debris indicates that this is the most probable area of a breach into the wing since there are no other debris pieces that exhibit the unique characteristics observed in this area.

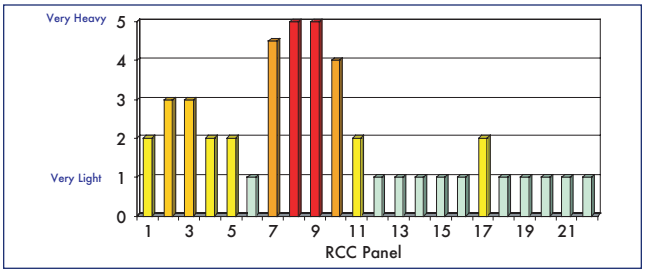


Figure 5-2. Slag deposition in the RCC panel 8/9 area relative to the other parts of the left wing leading edge.

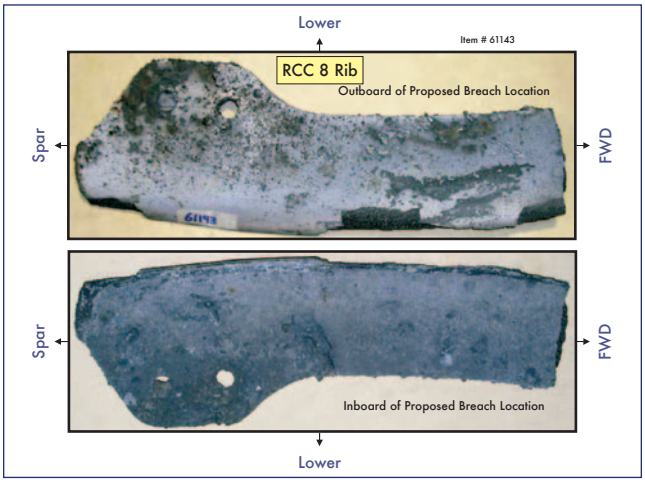


Figure 5-3. Samples of severe slag deposition on the panel 8 rib.

Based on the slag deposition on the upper RCC panel 8 and the rib erosion at the panel 8/9 interface, the most likely area of damage was the bottom portion of RCC panel 8. The outboard apex on the panel 8 upper inboard rib shows knife edge erosion, and the rib tapers from a design thickness of 0.365 inches to 0.05 inches. The surface of the panel 8 outboard rib and matching heel piece show a similar sign of erosion, as does the panel 9 upper inboard rib. The erosion on both the panel 8 and 9 rib is on the inboard side, indicating that flow is coming from the panel 8 location. Additionally, several lower carrier panel tiles in the RCC panel 9 area also show significant slumping and erosion that is consistent with a hole or breach in the lower part of RCC panel 8. Fig-

ure 5-4 and Figure 5-5 show an example of the rib erosion and the flow on the lower carrier panel 9.

Figure 5-6 is a CAD drawing of the recovered debris showing overall slag deposition and erosion patterns. The drawing is a view from behind the RCC panels since this provides the best view of the erosion and slag deposition. Three full Tee seals can be seen in this drawing; the leftmost, Tee seal 9, divides panel 9 and 10; Tee seal 8 in the center divides panel 8 and 9; the rightmost, Tee seal 7, is the division between panel 7 and 8. The drawing shows the heavy slag deposition of the upper portion of panel 8 indicating that the probable breach area was the bottom of panel 8. The severely eroded RCC ribs are also visible near the RCC panel 8/9 Tee seal. The heavy slag on these inner surfaces indicate flow from the panel 8 direction toward panel 9. This is also consistent with the knife-edge erosion shown in Figure 5-4. The proposed flow direction leading to the erosion and slag deposition on the lower carrier panel 9 tiles can be seen in this view as well. The detailed flow, erosion, and deposition are best viewed in Figure 5-5. The last significant feature in Figure 5-6 is the heavy slumping that is observed on the upper carrier panel 8 tile (50336T) in the upper right portion of the drawing.

The data shown in Figure 5-6 is important when combined with the analysis of the slag deposition. The slag deposition on the upper RCC panel 8 was analyzed using sophisticated cross sectional optical and scanning electron microscopy, microprobe analysis, and x-ray diffraction to determine the content and layering of the slag deposition. This analysis indicated that the materials in this area were exposed to extremely high temperatures, since Cerachrome insulation was deposited first and its melting temperature is greater than 3200 degrees Fahrenheit. The analysis also showed no presence of Aluminum 286 in the slag indicating that the RCC attach fittings were not in the direct line of the breach and that the Inconel 718 spanner beam was one of the first internal items to be subjected to heating. Inconel slag was prevalent in much of the analyzed slag indicating melting of the spanner beam, foil, and associated insulation. Aluminum was found in the last deposited layer indicating the wing honeycomb spar was the last area to be subjected to hot gas flow.

Analysis of the slag deposition on the lower carrier panel 9 tiles was also performed. Materials on these tiles are consistent with wing leading edge materials (Aluminum, Inconel, Nickel alloy, and Carbon) indicating an outflow from the panel 8 area across the tiles. Tile slumping in this area is indicative of temperatures in excess of 3000 °F. The upper carrier panel 8 tile was also analyzed and the results were similar to lower carrier panel 9 except that this tile appeared to have more Cerachrome and Nextel fiber deposits. These materials are consistent with the insulator that protects the wing leading edge spar and with flow moving toward the upper wing surface through the vent between the upper carrier panel and RCC.

This forensics analysis further corroborates the breach location to be the lower portion of RCC panel 8 below the apex, approximately midway between the apex and where the RCC panel meets the carrier panel. Based on the flow

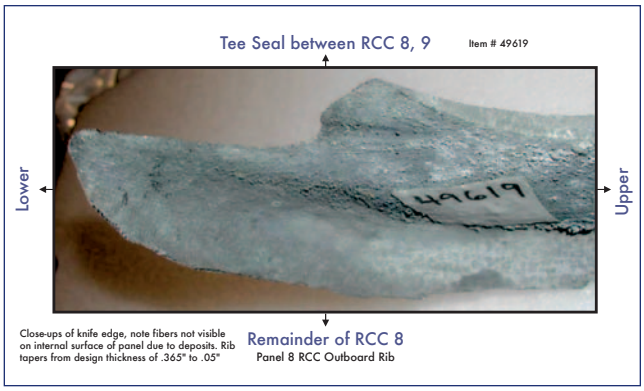


Figure 5-4. Example of rib erosion.

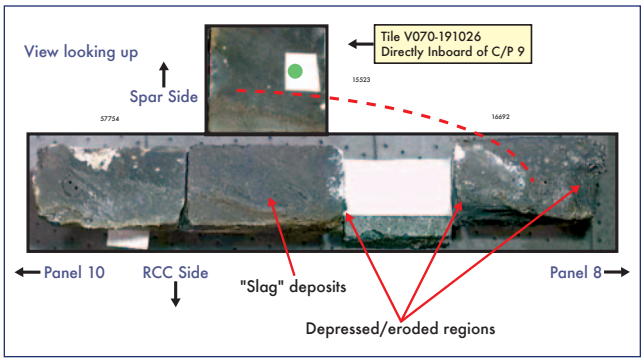


Figure 5-5. Flow on the lower carrier panel 9 tiles.

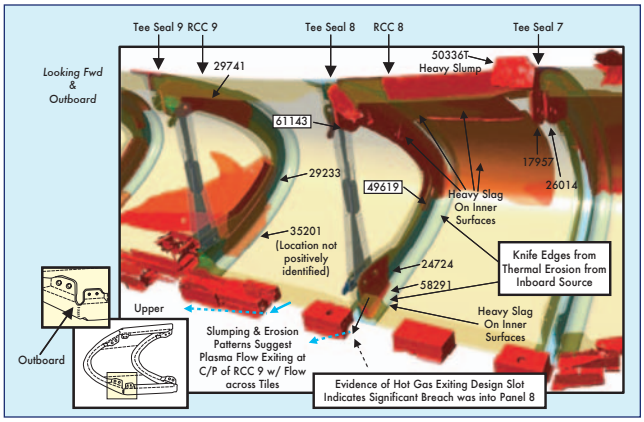


Figure 5-6. CAD drawing of the recovered debris showing overall slag deposition and erosion patterns.

patterns, the breach was in an area that caused the flow to impact the spanner beam associated with Tee seal 8 and create the knife edge erosion shown in this area in Figure 5-6.

The flow appears to have entered through this breach and into the lower aft corner, exiting through a slot toward carrier panel 9. The flow burned through the horse collar and eroded and slumped the carrier panel tiles. The flow continually grew the hole in panel 8 as time progressed and it eroded the remaining aft flange part of RCC panel 8 and the forward flange on RCC panel 9. Although the lower carrier panel 9 tiles are slumped and eroded, there must have been

an RCC rib protecting the adjacent carrier panel 8 tiles since there is no erosion or slumping of these tiles. Compared to the severely eroded carrier panel 9 tiles, the three recovered carrier panel 8 tiles are in relatively pristine condition, and likely separated due to backside heating with no indications of mechanical damage occurring prior to vehicle break-up.

As time progressed, the Cerachrome and Inconel wing spar insulators were eroded, and eventually hot gas flow impinged on the wing leading edge, burning through the honeycomb spar. Figure 5-7 depicts the possible flow direction and deposition of various metals as determined by this analysis.

In addition to the slag deposition and flow analysis, there are two other significant pieces of data that point to a breach in the RCC 8/9 area as the initial damage. The first item is the location of the leading edge RCC in the debris footprint. Figure 5-8 shows the recovered RCC for both the left and right wing and its location in the debris footprint. The eroded RCC pieces from panels 8 and 9 are found in the westernmost part of this debris footprint near Waxahachie, Texas, along with other pieces of RCC panel 8. Left wing RCC panel 9 and other aft panels appear to have been lost relatively early in the break-up sequence since their footprint spans the western to center part of the footprint. This is indicative of a left wing breach in the panel 8/9 area. The forward portion of the RCC panels on both the left and right wings (panels 1 through 7) are found from the center to eastern part of the debris footprint possibly indicating that these were lost in a secondary aerodynamic break-up.

The second additional piece of data is an upper left wing tile recovered near Littlefield, Texas. Littlefield is a small town near the Texas/New Mexico border along *Columbia*'s

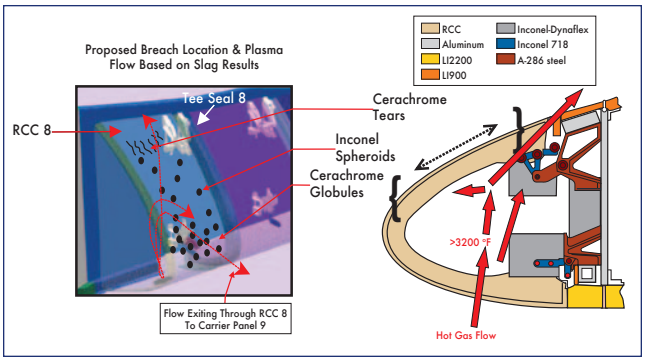


Figure 5-7. Analysis results show possible flow direction and deposition of metals.

ground track. This tile is the westernmost piece of debris that has been found to date in the debris recovery efforts. Due to the unique features of the tile (thickness, shape, paint, etc.), the tile must be from the upper wing area in the RCC panel 9 area. Figure 5-9 shows the only three possible locations for this tile.

The tile departed the orbiter more than one minute prior to final break-up due to prolonged internal heating of the upper wing skin in the area shown in Figure 5-9. The tile shows indications of backside heating and an RTV debond. It was not a failure in the densification layer, which would have been caused by mechanical loading. This piece of recovered debris is not very significant on its own merit; however, it is consistent with the previously discussed forensics data (rib erosion, carrier panel 9 tile slumping, etc.) and other events that will be discussed later in Section 5.4.

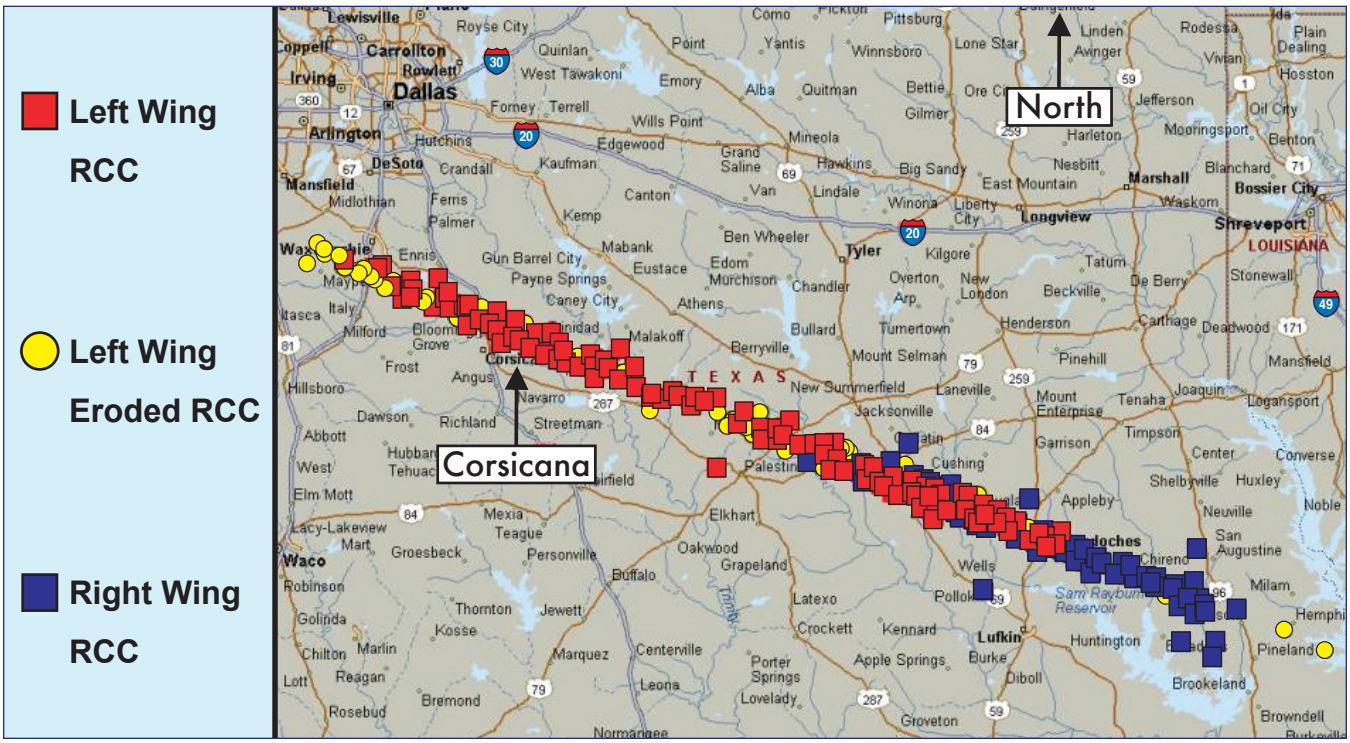


Figure 5-8. RCC panel debris location.

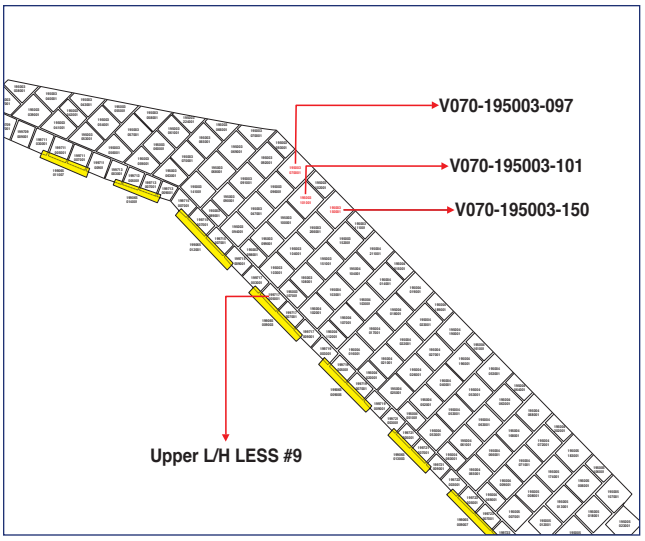


Figure 5-9. Three possible orbiter locations of the Littlefield tile on left wing.

5.4 Entry Events Timeline

5.4.1 Early Entry Heating Events

Columbia successfully completed the deorbit burn at 8:18:08 EST over the Indian Ocean. The deorbit burn and entry targeting were accomplished using well-established Mission Control Center procedures, and there were no problems identified with this process. Both the left and right Orbital Maneuvering System (OMS) engines performed nominally and the post burn residuals were less than 0.2 feet per second indicating a precise burn. The maneuver to the Entry Interface (EI) attitude, the Forward Reaction Control System Dump, and remaining Auxiliary Power Unit (APU) start (APU 1 and APU 3) were accomplished nominally.

At 8:44:09 EST, *Columbia* reached EI, the transition between orbital and atmospheric flight. The altitude was 400,000 feet and the orbiter was traveling Mach 24.6 in wings level (zero degree bank) attitude with a nominal 40-degree angle of attack. The orbiter guidance had been moded to OPS 304 nominally at five minutes prior to entry interface. OPS 304 is the name given to the entry flight software that contains the aerojet digital auto-pilot control mode. It is used from five minutes prior to EI through Mach 2.5. Figure 5-10 is a plot of dynamic pressure and stagnation heating from EI to vehicle break-up. The plot shows that both heating and dynamic pressure were very low during the two to three minutes (120-180 seconds) after EI. The heating rate shown is stagnation heat flux that is the allowable heat flux that could be achieved by the gas if all its thermal and kinetic energy were available. For this plot and others that follow in Section 5, EI occurred at 8:44:09 EST, which corresponds to zero seconds on the plots. This is a convenient reference point for many of the entry events that will be discussed.

At approximately 8:48:39 EST (EI + 270 sec.), a left wing leading edge spar strain gauge began a small off-nominal increase. Figure 5-11 shows the STS-107 response of this

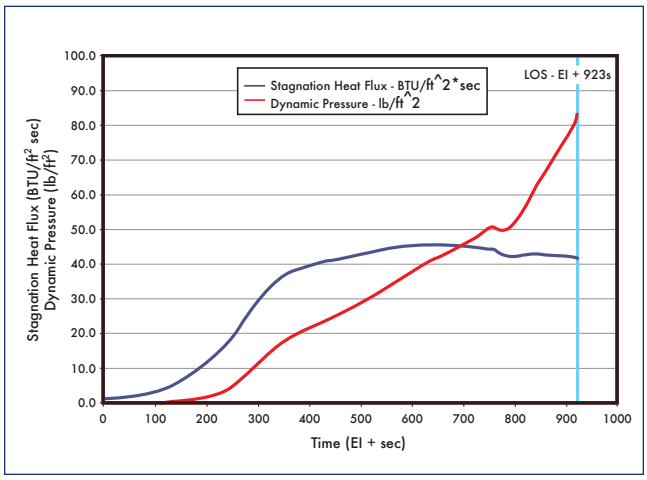


Figure 5-10. STS-107 stagnation heat flux and dynamic pressure. Note that EI was at 8:44:09 EST.

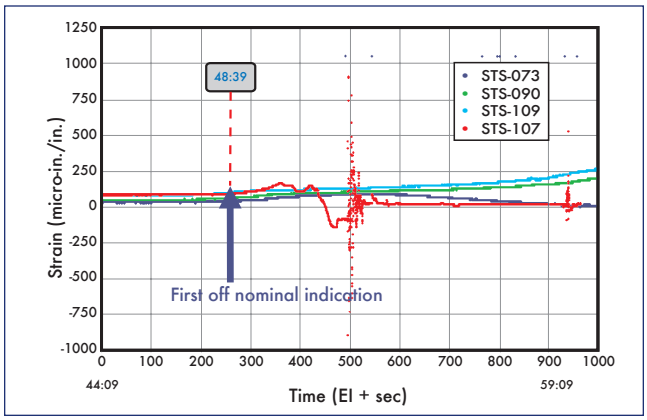


Figure 5-11. Left wing RCC panel 9 strain gauge is first measurement to indicate an off-nominal event. Note that EI was at 8:44:09 EST.

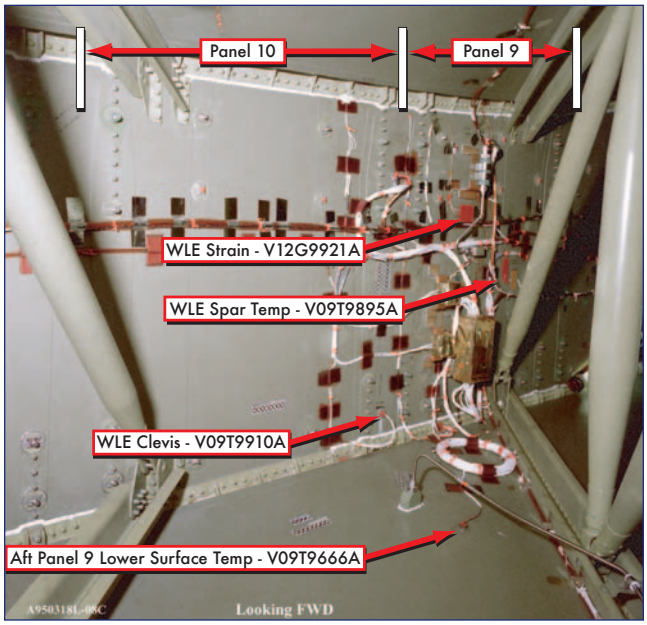


Figure 5-12. MADS sensors inside left wing.

strain measurement along with three other previous *Columbia* missions. Figure 5-12 shows the location of this sensor (WLE Strain V12G9921A) and others on the wing leading edge. The damage in lower RCC panel 8 is believed to be the cause of this strain increase. The breach allowed hot gas intrusion onto the panels 8 through 9 wing leading edge spar area leading to extreme heating and thermally induced strain. The strain increase grew over time and reached a maximum at approximately 8:50:09 EST (EI + 360 sec.). Thermal and structural analyses indicate that a breach would need to be within approximately 15 inches of the strain gauge to create the observed strain increase.

Twenty seconds later at 8:48:59 EST (EI + 290 sec.), the left wing lower attach clevis temperature sensor (between RCC panel 9 and 10) began an early off nominal temperature trend. Figure 5-13 shows the abnormal temperature response when compared to other *Columbia* missions. This temperature rise is consistent with an early entry of hot gas into the RCC cavity. This Modular Auxiliary Data System (MADS) measurement (V09T9910A) is the only temperature measurement located in the RCC cavity along the left wing leading edge. It is positioned on the lower attach fitting between panel 9 and 10 and is well protected thermally by Inconel foil insulation. The sensor is also thermally isolated since it sits on the attach fitting away from other structure as shown in Figure 3-12. In order to get an early temperature rise for this sensor, unlike that observed on any other flight, there must be a path in the RCC cavity to allow hot gas to reach the sensor.

A thermal analysis was performed with heating rates from various hole sizes in the bottom of RCC panel 8 in an attempt to match this temperature rise. The analysis used a thermal math model of the wing leading edge (Inconel Cerachrome insulation, Inconel 718 and A-286 steel attach fittings, and aluminum honeycomb spar). The results indicated that the heating equivalent of a 6 to 10 inch diameter hole with a 10 percent "sneak flow" around the insulation would be required to match the thermal response of the clevis temperature. In the same timeframe several MADS lower surface temperatures on the left wing showed a slight off nominal early temperature rise when compared to previous flights of *Columbia* of the same inclination.

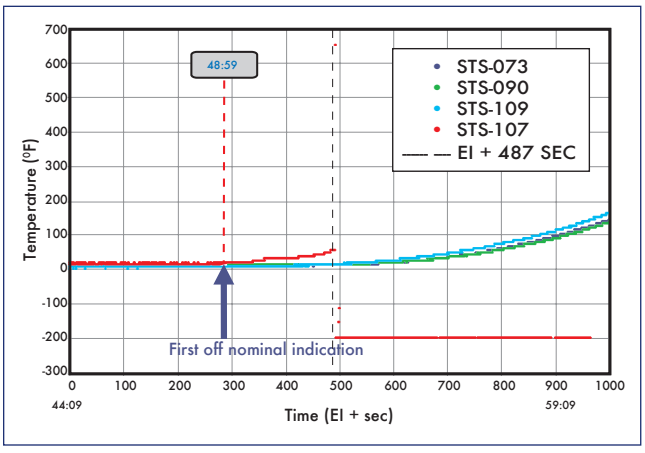


Figure 5-13. Left wing RCC panel 9/10 clevis temp sensor is second measurement to indicate an off-nominal event.

5.4.2 First Roll Maneuver Through Wing Spar Breach

Columbia executed a nominal roll to the right at 8:49:32 EST (EI + 323 sec.) as the entry guidance software began to actively control energy (i.e., closed loop guidance) to land at KSC. This initial roll command is also timed to ensure atmospheric capture by reducing the lift on the vehicle. Within 17 seconds of this maneuver, at 8:49:49 EST (EI + 340 sec.), four left OMS pod surface temperature measurements showed an off-nominal trend with lower temperature rises when compared to similar *Columbia* missions. A sample of these measurements compared to other *Columbia* missions is shown in Figure 5-14, and the location of these measurements on the left OMS pod forward face can be found in Figure 5-15.

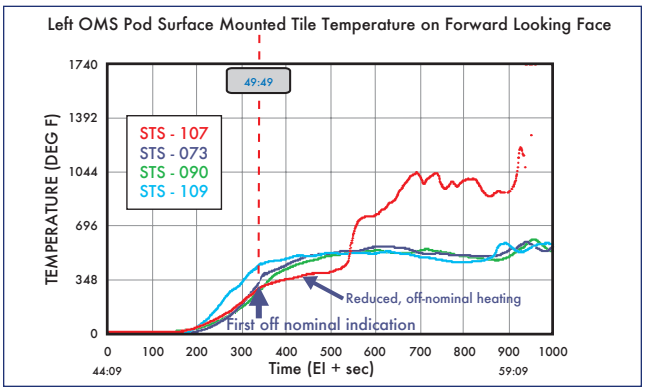


Figure 5-14. Typical off-nominal OMS pod thermocouple (V07T9220A).

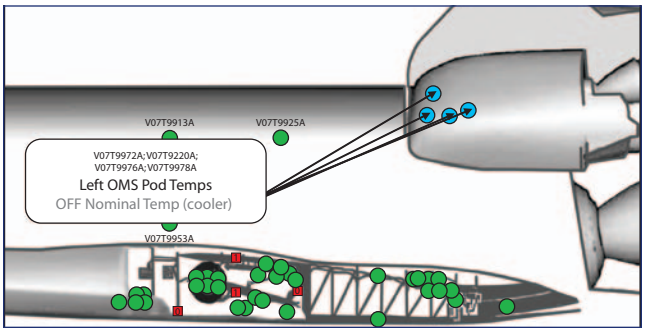


Figure 5-15. Location of OMS pod thermocouples off-nominal low.

The reduced heating is not completely understood since the weak aerodynamic flow field on the upper surface of the orbiter is difficult to model and is extremely sensitive to disturbances. The best explanation for this reduced heating is that flow into the RCC cavity was venting through to the upper surface of the wing through an existing 0.1-inch vent between the RCC and upper surface carrier panels. This vent exists all along the leading edge from RCC panel 1 through panel 22 and has an approximate area of 66 square inches. This upper surface RCC venting and the flow disturbance created by the panel 8 and upper carrier panel 8 damage caused the vortices from the canopy or area where the wing

meets the orbiter fuselage to move from their normal positions, thus reducing the heating on the OMS pod. Figure 5-16 depicts the change in the upper wing surface vortices and the weak upper surface flow.

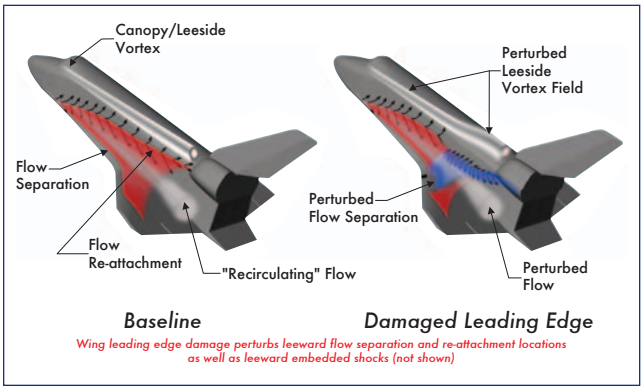


Figure 5-16. Postulated orbiter leeside flow field associated with wing leading edge damage.

In order to verify this theory of a weak upper surface flow being disturbed from venting on the upper surface, several wind tunnel tests were performed in the NASA Langley Research Center Mach 6 Tetraflouromethane (CF4) Wind Tunnel. The use of CF4 as the gas for the flow analysis is required to best replicate the Mach number environment during this timeframe. These wind tunnel tests used a ceramic model and a 0.01-inch leading edge vent to mimic the postulated venting. Nitrogen gas was allowed to flow through this upper surface vent via a gas supply line. A picture of this model is shown in Figure 5-17. Results of this testing show that it is feasible to obtain reduced heating on both the left OMS pod and the left fuselage as a result of flow through the RCC upper surface vent. Figure 5-18 shows the change in heating as the vent velocity is altered.

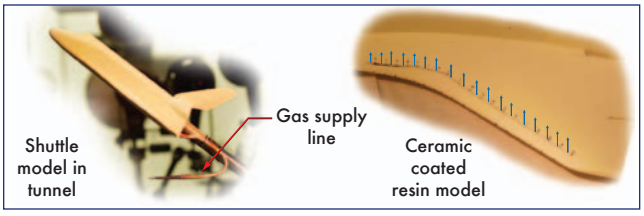


Figure 5-17. Orbiter wind tunnel model with vent gap along wing leading edge.

Over the next 43 seconds, there were five communications dropouts beginning at 8:50:00 EST and ending at 8:50:43 EST (EI + 351 through 394 sec.). It is possible that hot gas in the RCC cavity had begun to erode the Inconel and Cerachrome insulation along the wing leading edge spar. Molten materials could have been ejected into the environment around the orbiter creating multi-path signal scattering with the link between the orbiter and the western Tracking and Data Relay Satellite (TDRS). The best parallel for this explanation is chaff used by some military aircraft to confuse opposing radar systems.

Forensic analysis of the recovered left OMS pod debris indicates that molten Inconel 718 and A-286 cress were sprayed onto the left OMS pod during entry. This OMS pod debris and the left side of a recovered vertical tail debris piece were significantly pitted by this metallic spray supporting the concept that there was vaporized metal in the environment around *Columbia*. These materials must have originated from the RCC panel 8 wing spar damage area since Inconel 718 is used as the wing leading edge insulator and A-286 is used for the RCC attach fittings.

In the same timeframe, at 8:50:09 EST (EI + 360 sec.), a left payload bay fuselage MADS surface temperature measurement (Figure 5-19) showed an off-nominal temperature trend. This trend is a reduced rise rate when compared to other previous *Columbia* missions, as shown in Figure 5-20. The previously discussed theory of venting and or disturbed flow due to panel 8 damage, causing a shift in the vortices on the upper surface of the wing, is also believed to be the cause of this off-nominal behavior. The flow field and venting on the upper surface rate are constantly increasing since the mass flow rate into the RCC breach is increasing as the orbiter descends lower into the atmosphere.

At 8:50:19 EST (EI + 370 sec.), a lower surface thermocouple showed signs of off nominal, increased heating. The best explanation for the increased heating in this area is severely disturbed, turbulent flow caused by the leading edge damage on the bottom of RCC panel 8 and flow from the lower corner of this panel as discussed in Section 5.3. Langley Research Center wind tunnel testing has confirmed that wing leading edge damage (notch or protuberance) near

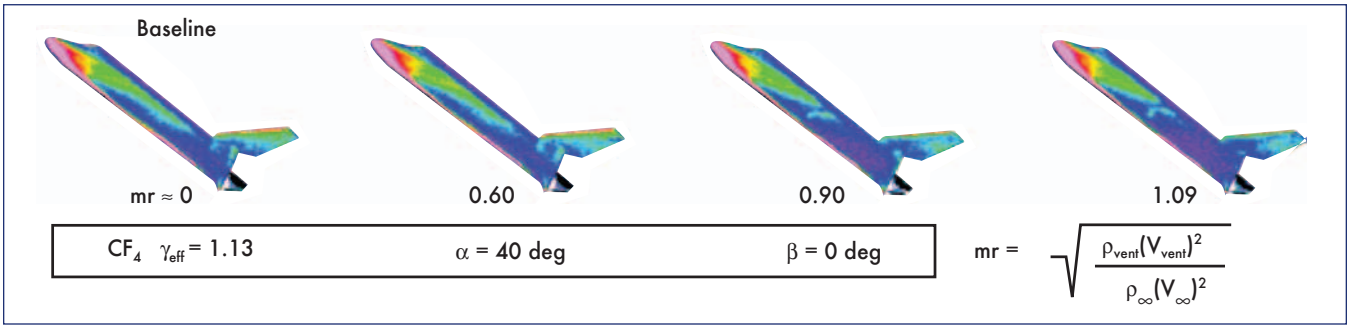


Figure 5-18. Wind tunnel model results for sensitivity of orbiter side fuselage and OMS pod heating patterns to mass addition along WLE leeside vent gap.

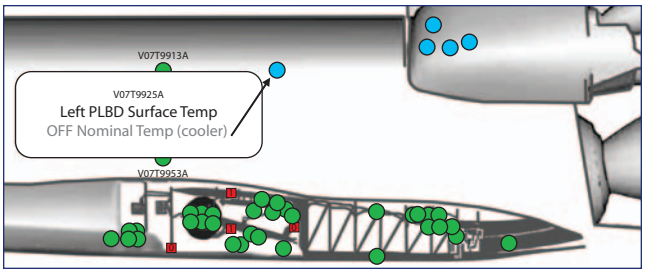


Figure 5-19. Location of left sidewall temperature sensor.

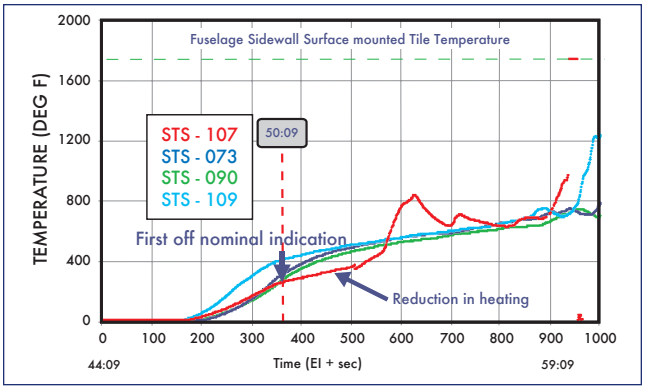


Figure 5-20. Off-nominal temperature indication on the left sidewall.

panel 8 will cause increased heating to the lower wing surface. As previously discussed, the eroded lower carrier panel tiles on panel 9 indicate this strong flow from panel 8. This is consistent with flow patterns observed on many recovered lower surface wing acreage tiles along the flow lines aft of the RCC panel 8 area. Figure 5-21 shows this temperature response as compared to other *Columbia* missions. The location of the sensor can be seen in Figure 5-22.

By 8:51:14 EST (EI + 425 sec.), the wing leading edge spar temperature began an early, off-nominal rise, shown in Figure 5-23. At the same time, the clevis temperature in the RCC panel 9/10 region continued to increase. The initial spar temperature rise was relatively slow and was caused by

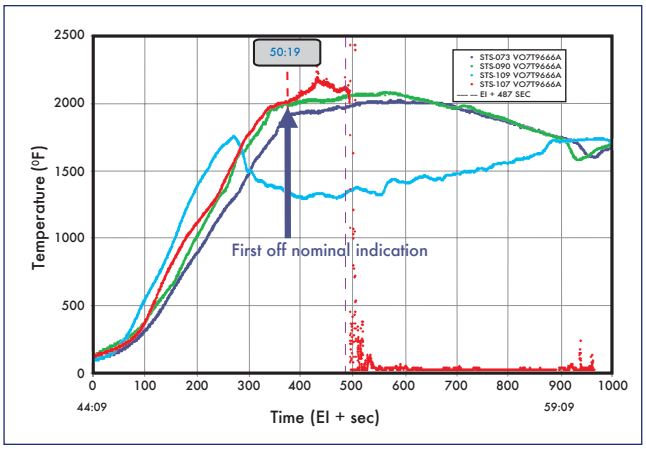


Figure 5-21. Temperature rise on tile surfaces aft of RCC panel 9.

conduction since this measurement is on the backside of the spar in the wing cavity. Eventually, the rise rate increased dramatically as first the Inconel and Cerachrome insulation and later the aluminum honeycomb were destroyed. The exact time of the spar breach is unknown; however, it is estimated to have occurred between 8:51:14 to 8:51:59 EST (EI + 425 to 470 sec.) based on the observed wing leading edge linear decrease in strain during this timeframe. A more detailed discussion of the method used to bracket the time of the wing spar breach is contained in the following section.

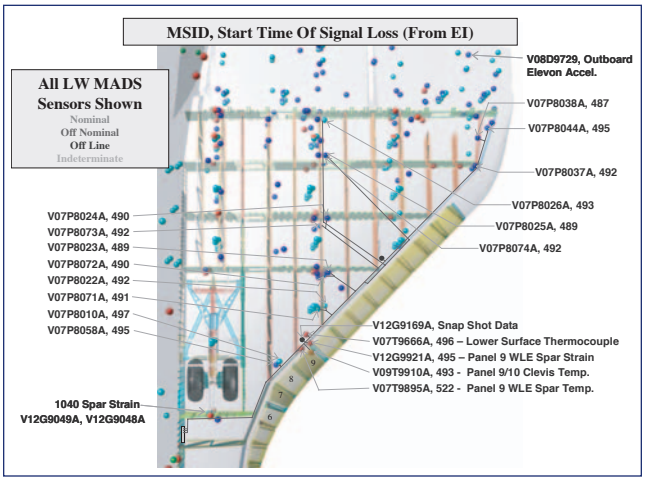


Figure 5-22. Left wing MADS sensors, including Measurement Stimulation Identification (MSID) number, and start time of loss of signal (EI + sec.).

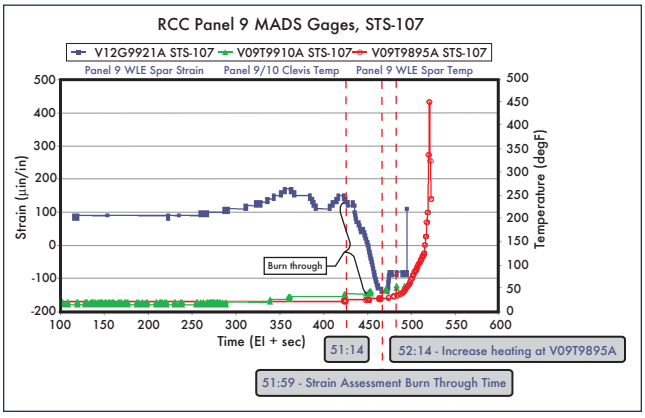


Figure 5-23. RCC panel 9 MADS strain and temperature measurements, STS-107.

At 8:51:49 EST (EI + 460 sec.), one of the left OMS pod measurements (V07T9972A) began to show an increased temperature rise, indicating that the upper surface flow has changed again. This is shown in Figure 5-24 along with this measurement on other *Columbia* missions. It is evident that the measurement rises to a higher temperature and at a faster rate than has been observed on previous missions within the next few minutes. Figure 5-25 shows other left OMS pod and fuselage temperature measurements that exhibit an off-nominal rise later in time. The sensor locations on the left side of the orbiter are also shown in Figure 5-25.

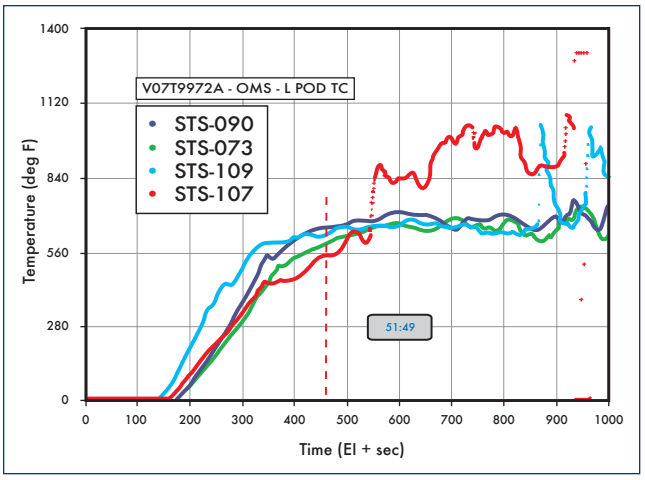


Figure 5-24. Off-nominal low OMS pod thermocouple (V07T9972A).

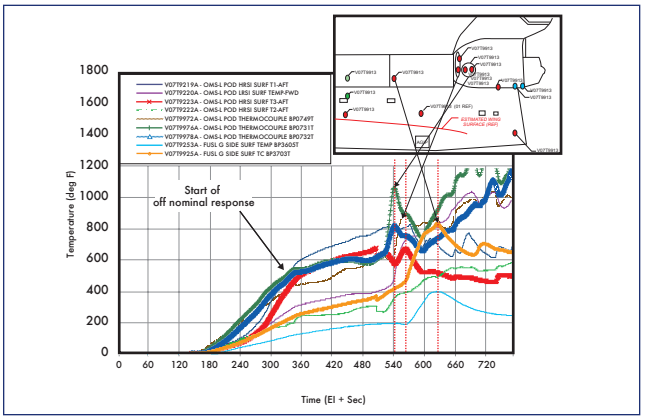


Figure 5-25. Left side fuselage/OMS pod off-nominal responses indicate increased heating.

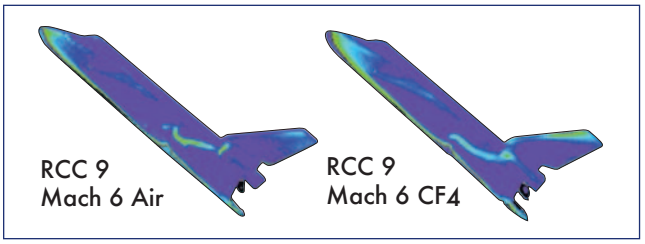


Figure 5-26. Wind tunnel test results for RCC panel 9 missing and resulting in increased heating to OMS pod.

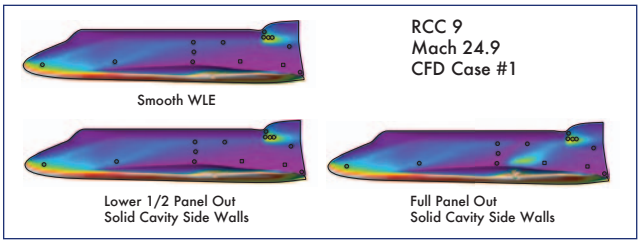


Figure 5-27. CFD results for no damage, partial damage, and full damage to RCC panel 9 show increased heating on side fuselage and OMS pod.

These off-nominal temperature rises were caused by a change in the flow field along the upper portion of the left wing as the wing leading edge (WLE) and wing spar damage progressed. The mechanism was a shift in the vortices due to venting on the upper portion of the wing and is similar to the previous discussions on lower than expected OMS pod temperatures. Wind tunnel testing and CFD analysis confirmed that WLE damage on RCC panels 8 and 9 could cause increased heating to the OMS pod due to disturbed upper surface flow or flow impingement caused by re-directed flow from the lower surface. Additionally, the molten Inconel 718 and A-286 spray onto this area are indications that this flow is the cause of these temperature rises. Figure 5-26 (from wind tunnel test results) is a representative example of increased heating on the left fuselage and OMS pod due to RCC panel 9 damage from wind tunnel test results. Figure 5-27 shows a similar picture of the left side as determined by CFD analysis. Note that neither the wind tunnel testing nor the CFD analysis accounts for increased heating that is likely due to molten metal contacting the OMS pod.

The increased heating implies that damage/erosion to the RCC panel 8 area had increased or that at least one carrier panel had been lost. The increased heating is also consistent with an increased mass flow rate due to the nature of the entry environment. The dynamic pressure and stagnation heat flux had more than doubled by this timeframe when compared to a few minutes after EI. There are three additional communication dropouts that follow at approximately 8:52:09 EST to 8:52:31 EST (EI + 480 to 502 sec.). Again, these dropouts are consistent with molten aluminum and other metals being released into the environment surrounding *Columbia*.

5.4.3 Wing Breach and Wire Failures

The next significant event was a breach through the left wing leading edge spar leading to many wire measurement failures and eventual deformation of the left wing. As discussed in Section 5.4.2, by approximately 8:52:00 EST (EI + 471 seconds), strain and temperature measurements indicated that hot gas had begun to weaken the wing spar. Figure 5-28 shows that the orbiter has entered the peak-heating region during this timeframe and would remain there for many of the ensuing events that will be discussed later.

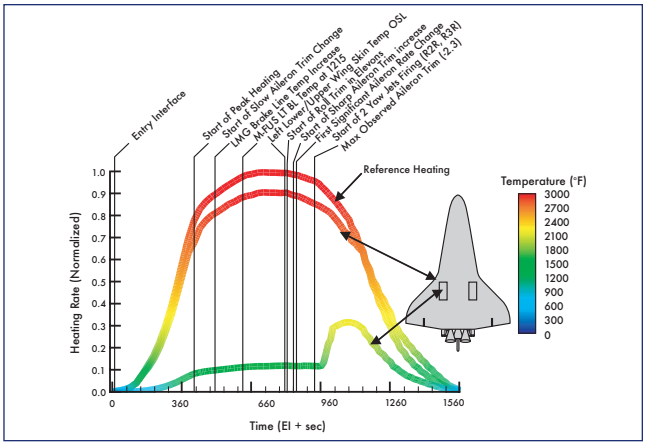


Figure 5-28. STS-107 entry heating rate profile.

The precise timing of the wing spar breach is difficult to determine, and three different techniques were used in an attempt to bound the breach time. These techniques included a structural assessment using the wing leading edge spar measurement, use of a thermal model to predict the time required to burn through the spar insulators and then the honeycomb structure, and a wire failure assessment.

The first technique used the strain response, shown earlier in Figure 5-23. On this plot, the initial strain rise that began at about 8:49:09 EST (EI + 300 sec.) is due to thermal elastic strain. It appears that the spar structural softening occurs at approximately 8:50:09 EST (EI + 360 sec.), followed by loss of the structural integrity, or breach, at approximately 8:51:14 EST (EI + 425 sec.). This appears to be completed by approximately 8:52:00 EST (EI + 471 sec.). A detailed structural model that attempted to reproduce the thermal strain response observed during this timeframe confirmed this timing. This analysis determined that the location of the spar breach must be within about 15 inches of the spar strain measurement. This would locate the spar breach near the intersection of panel 8/9, as shown in Figure 5-29. The flow through the RCC breach maintained some directionality although it was influenced by the shape of the hole, remaining RCC structure, attach hardware, and leading edge insulators. Overall, this strain response is consistent with an RCC breach in the lower part of panel 8 as previously discussed in Section 5.3. Although it is difficult to pinpoint a precise location of the RCC breach, this analysis supports the argument that the breach was closer to the panel 8/9 intersection and Tee seal 8.

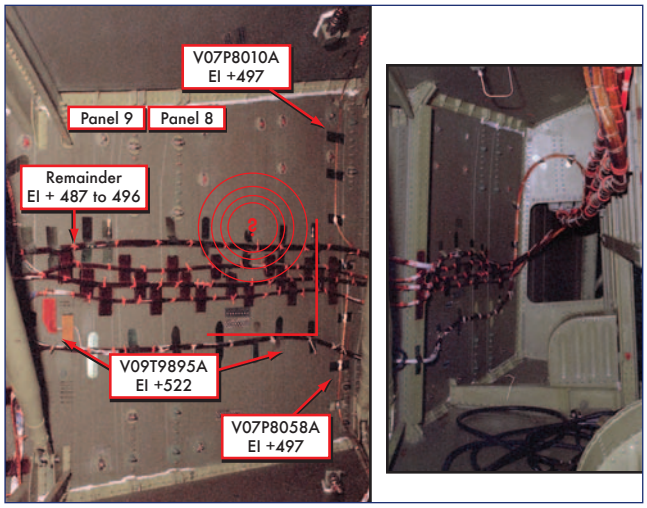


Figure 5-29. Cable routing on wing leading edge and wheel well wall.

The second technique used a detailed thermal model to determine the time required to burn through the various insulations immediately in front of the wing leading edge spar (Inconel, Nextel, Cerachrome) and then the honeycomb spar. This model assumed the equivalent heating of a six-inch diameter hole in the bottom of RCC panel 8. Using the expected aero heating rate and the various material properties, the spar burn through occurred at 8:52:19 EST (EI + 490 sec.). This time would be accelerated slightly for a larger diameter hole. The results of this thermal model are shown in Figure 5-30.

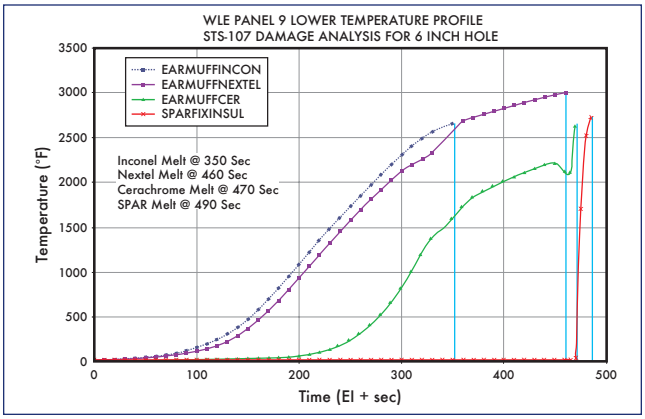


Figure 5-30. Thermal model prediction of wing spar burn through.

The final technique used was an examination of the wire failures on the wing leading edge spar. These wire runs are shown in Figure 5-29. The first measurement loss was a MADS upper left wing pressure measurement, which failed at approximately 8:52:16 EST (EI + 487 sec.). This measurement is contained in the upper wire bundle in the left photo in Figure 5-29. The combination of these three separate and distinct analyses results in a range of wing spar breach times as early as 8:51:14 EST and as late at 8:52:16 EST (EI + 425 to 487 sec.).

Immediately after the breach, hot gas inside the wing began to heat the remaining wire bundles that contained real-time telemetry and the recorded MADS measurements. Figure 5-29 shows an inside-the-wing view of the approximate breach location based on this wire failure analysis. The view on the left is of the panel 8/9 spar location. This area is not visible in the right photo, which contains the transition spar and a view of the three wire bundles along the outside of the wheel well wall. Figure 5-31 shows the overall spar breach location with respect to the rest of the wheel well. The distance from the spar to the wheel well wall in this area is approximately 56 inches, as shown in Figure 5-32. Figure

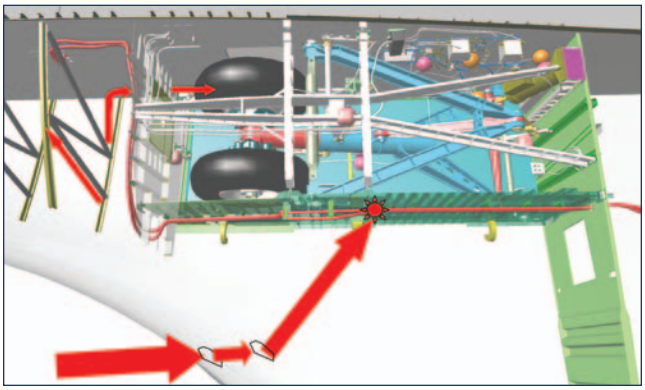


Figure 5-31. Hot gas begins to fill left wing.

5-33 shows a sketch of the venting of the left wing into the payload bay, driving the direction of the internal flow depicted in Figure 5-31. Note the 142 square inch vent into the midbody fuselage located forward of the wheel well.

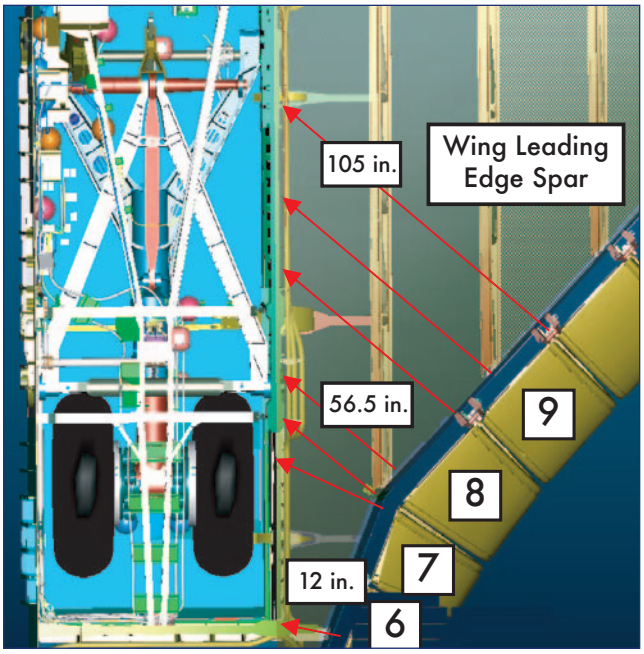


Figure 5-32. Columbia LH wing and wheel well geometry.

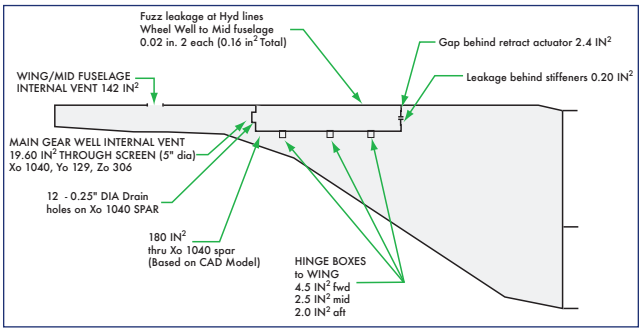


Figure 5-33. Columbia LH wing and wheel well vent model (wheel well leak paths based on Atlantis test comparison).

One hundred sixty-three other measurements failed very quickly over the next two minutes. Figure 5-34 is a plot of the percentage of measurements lost as a function of time from EI. The first measurements to fail are all located on the wing leading edge spar as shown by the purple line on the plot. Bundles 1, 3, and 4 along the wheel well (shown in Figure 5-35) began to fail about 14 seconds after the first spar measurements. This is indicative of a plume impinging on the wire bundles on the wheel well wall.

Arc-jet testing was performed in a facility at JSC to demonstrate how quickly a hole in a 0.1 inch thick aluminum plate would grow in an attempt to determine the feasibility of a rapid spar burn through followed by rapid wire measurement failures. The test configuration had an initial 1-inch diameter hole, and a stagnation heat rate of 12.13 BTU per square foot per second (equivalent to the flight environment at about 8:50 EST, EI ~ 351 sec). During the test, the aluminum plate hole grew from 1 inch in diameter to 5 inches in diameter in approximately 13 seconds. This was consistent with thermal math models developed to analytically predict hole growth. A wire bundle placed 15 inches from the heat source showed very rapid erosion after the hole grew to 5 inches in diameter. The measurement losses in this bundle were very consistent with those observed for wire bundle number 3 (see Figure 5-34). The hole would have grown to a larger diameter; however, the test set-up provided a heat sink that eliminated further hole growth. Overall, the test indicated that a hole in the aluminum honeycomb would grow rapidly, allowing a substantial plume to destroy the wire bundles on the wheel well wall.

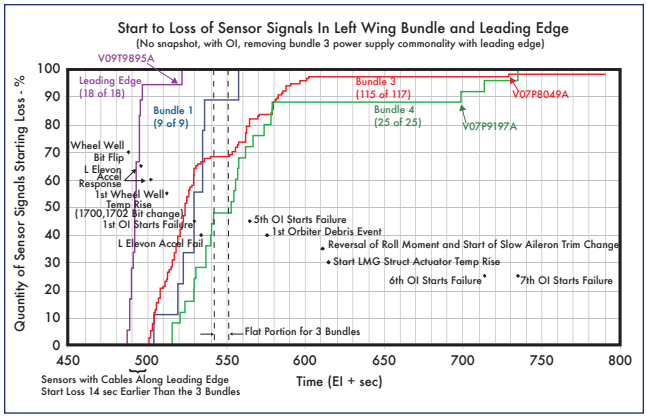


Figure 5-34. MADS data failure due to wire burning.

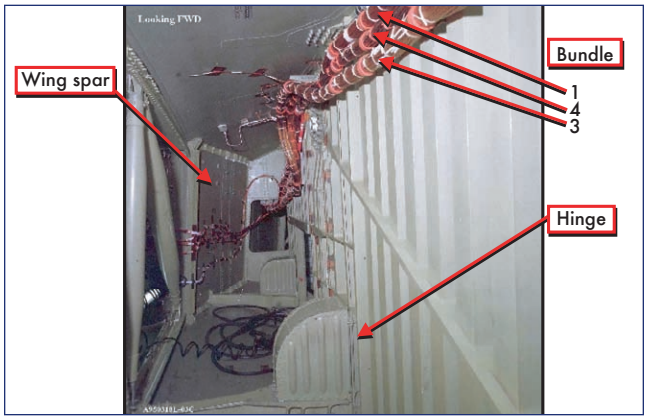


Figure 5-35. View of cables running along outside of wheel wall cavity bulkhead.

Four additional measurements failed after 8:54:16 EST (EI + 605 sec.) with the last starting to fail at 8:56:24 EST (EI + 735 sec.). This last measurement failure took over a minute to fail completely. Figure 5-34 and Figure 5-35 show the measurement loss timing and the wire bundle runs along the wheel well. Although almost all measurements internal to the wing failed, two strain measurements on the 1040 spar (forward of the wheel well) were unaffected and produced data until loss of all MADS data at 9:00:13 EST (EI + 964 sec.). Figure 5-36 shows the location of the sensors on the forward

wheel well spar. The fact that these measurements are available until loss of data are important indicators that the RCC breach could not be forward on the panel 6 area since these measurements would have been lost as well (see Figure 5-32). These measurements also record key changes in strain that help indicate some of the changes that the left wing underwent as the remainder of the entry events unfolded.

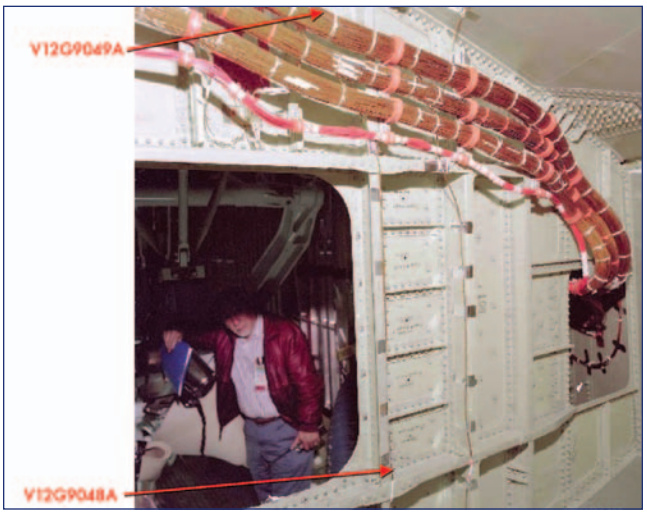


Figure 5-36. Strain measurements on 1040 spar.

A comprehensive evaluation of all MADS measurement failures in the left wing was performed to attempt to determine the spar breach progression. Each measurement's failure signature was evaluated to determine both the start time of the failure and when the wire failure was complete. As the wire burns, the short between the twisted pairs of wiring increases thereby producing the time delay effect between failure initiation and complete failure. Eighteen measurements routed on the wing leading edge and over 100 measurements in three wire bundles routed on the outboard side and external to the wheel well were used for this assessment. Seventeen of the 18 wing leading edge measurements failed in 10 seconds starting at 8:52:16 EST (EI + 487 sec.). No other MADS measurements failed during this time. The one measurement that did not fail in this time span was located in the bottom of five harnesses on the WLE. The remaining 17 measurements are in the upper four harnesses with the majority being in the top harness. This would indicate that the spar breach started near the top wire bundle and worked toward the bottom of the spar. Additionally, two of the 18 measurements join the harnesses at the panel 7 to 8 interface, making the wing spar breach outboard of panel 8 very unlikely.

5.4.4 Aerodynamic Events

Coincident with the spar breach at approximately 8:52:09 EST (EI + 480 sec.), the nose cap RCC attach clevis temperature had an off-nominal change in rise rate when compared to previous missions. This rise rate was abnormal for approximately 30 seconds and ended at 8:52:39 EST (EI + 510 sec.). The exact cause of this abnormal temperature rise is not known, but the timing is coincident with the breach of the wing leading edge spar. An explanation is that the abnormal rise is an instrumentation anomaly caused by multiple wire failures in this timeframe. This measurement response is shown in Figure 5-37 along with the same measurement for several other *Columbia* missions. This figure also shows the location of this internal nose cap measurement on the very forward portion of the left fuselage.

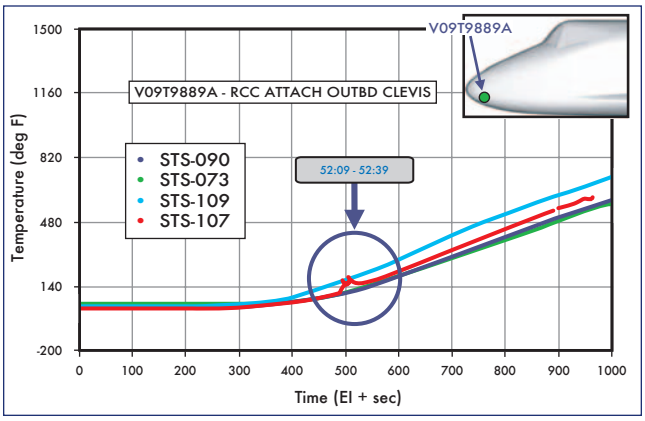


Figure 5-37. Off-nominal temperature rise rate in nose cap RCC attach clevis.

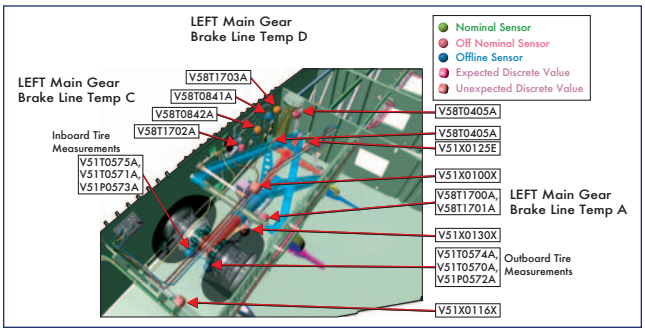


Figure 5-38. Location of sensors in the LH wing wheel well.

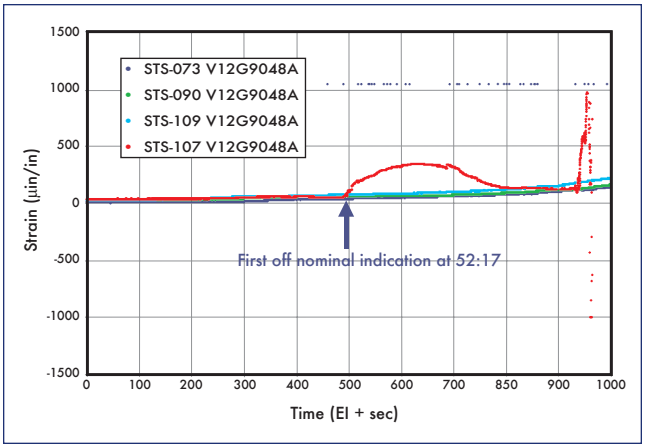


Figure 5-39. Strain rise in lower 1040 spar cap.

Until approximately 8:52:17 EST (EI + 488 sec.), there was no indication of any off-nominal situation that could be observed by the MCC or the crew in real-time. The flight control response and all orbiter telemetry measurements were

nominal. The first indication of any anomalous Operational Instrumentation (OI) was a small increase in the left main gear brake line temperature D measurement at this time (see Figure 5-38). Within one second of this time, there is a lower 1040 spar (forward wall of the wheel well) strain measurement that shows an off-nominal increase in strain (see Figure 5-39). These are both indications that the breach in the wing leading edge spar had allowed hot gas to reach the wheel well area, most likely through vent paths around the hinge covers, which allowed hot gas into the wheel well cavity.

At approximately 8:52:25 EST (EI + 496 sec.), the left outboard elevon wideband accelerometer showed an unusual 2 g peak-to-peak acceleration (see Figure 5-40). This is consistent with the timing of the many wire failures within the left wing and the timeframe when the spar breach occurs. Additionally, there are two unexplained communication dropouts in this same timeframe. Another 3 g peak-to-peak acceleration anomaly was observed at 8:52:31 EST (EI + 502 sec). Additional temperature measurements (left main gear brake line temp A and C) in the wheel well area (see Figure 5-38) began an off-nominal rise at 8:52:41 EST (EI + 512 sec.).

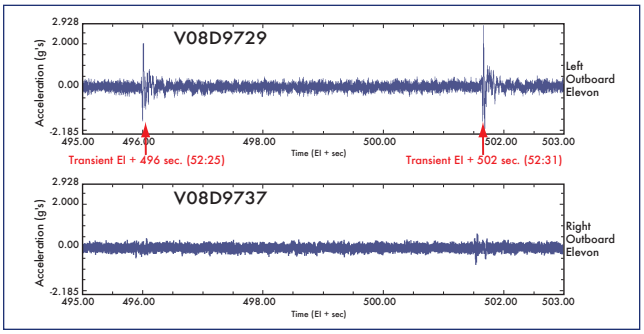


Figure 5-40. Outboard elevon accelerometer responses at 8:52:25 and 8:52:31 EST (EI + 496 and 502 sec.).

The elevon response event was followed by a change in the rise rate for two supply nozzle temperatures and the vacuum vent nozzle temperatures at 8:52:32 EST (EI + 503 sec.). The off-nominal rise rate occurred for approximately 15 seconds for the supply nozzle temperatures and 23 seconds for the vacuum vent temperatures. The location of these nozzles on the left side of the fuselage is shown in Figure 5-41, and the arrow indicates that they could have been located along a line of disturbed flow. The short, abnormal rise rate is unexplained, has not been observed on any previous Shuttle missions, and may not be associated with the upper wing disturbed flow caused by the leading edge damage. Unlike the RCC nose cap clevis temperature, the instrumentation appears to have been valid for both nozzles. Plots of this off-nominal temperature rise for one of the supply nozzle temperatures and the vacuum vent nozzle are shown in Figure 5-42.

Immediately following these events, at 8:52:44 EST (EI + 515 sec.), the aerodynamic roll and yaw coefficients that have been extracted from the flight data showed a slight negative trend (see Figure 5-43). This is indicative of more drag and decreased lift on the left wing.

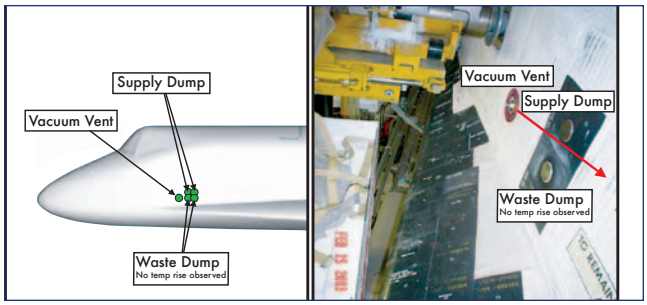


Figure 5-41. Location of supply dump and vacuum vent nozzles.

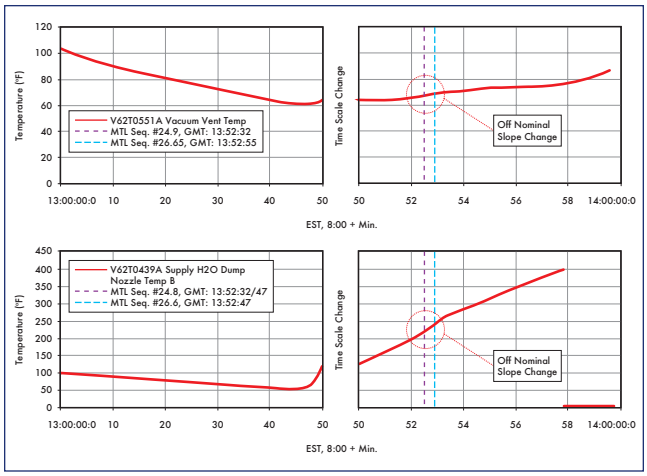


Figure 5-42. Off-nominal temperature for supply nozzle and vacuum vent nozzle.

Hypersonic wind tunnel tests indicate that both the slight negative roll and yaw deltas can be explained by leading edge damage in the lower half of RCC panel 8. This will be discussed in more detail in Section 5.4.5.

The flight control system compensated for the initial aerodynamic disturbance, and the aileron trim continued to match pre-entry predictions. To account for the increased drag the orbiter yawed slightly to the right to balance the yaw moments. The inertial sideslip exceeds flight history at 8:53:38 EST (EI + 569 sec.); however, this small departure was well within the vehicle's capability to control. There was also another communication dropout in this timeframe (8:52:49 to 8:52:55 EST, EI + 520 to 526 sec.).

By 8:53:28 EST (EI + 559 sec.), *Columbia* had crossed the California coast. After this coastal crossing, there are indications of damage progression on the left wing since the temperature response on the upper surface changes and measurement losses continue in the left wing. At 8:53:29 EST (EI + 560 sec.), several left fuselage temperature measurements showed an unusual 400 degree temperature increase over the next minute. These measurement increases were accompanied by another short communications dropout.

At 8:53:39 (EI + 570 sec.), four left OMS temperature measurements also exhibited an unusual temperature rise. This temperature rise is attributed to shifting of the left wing lead-

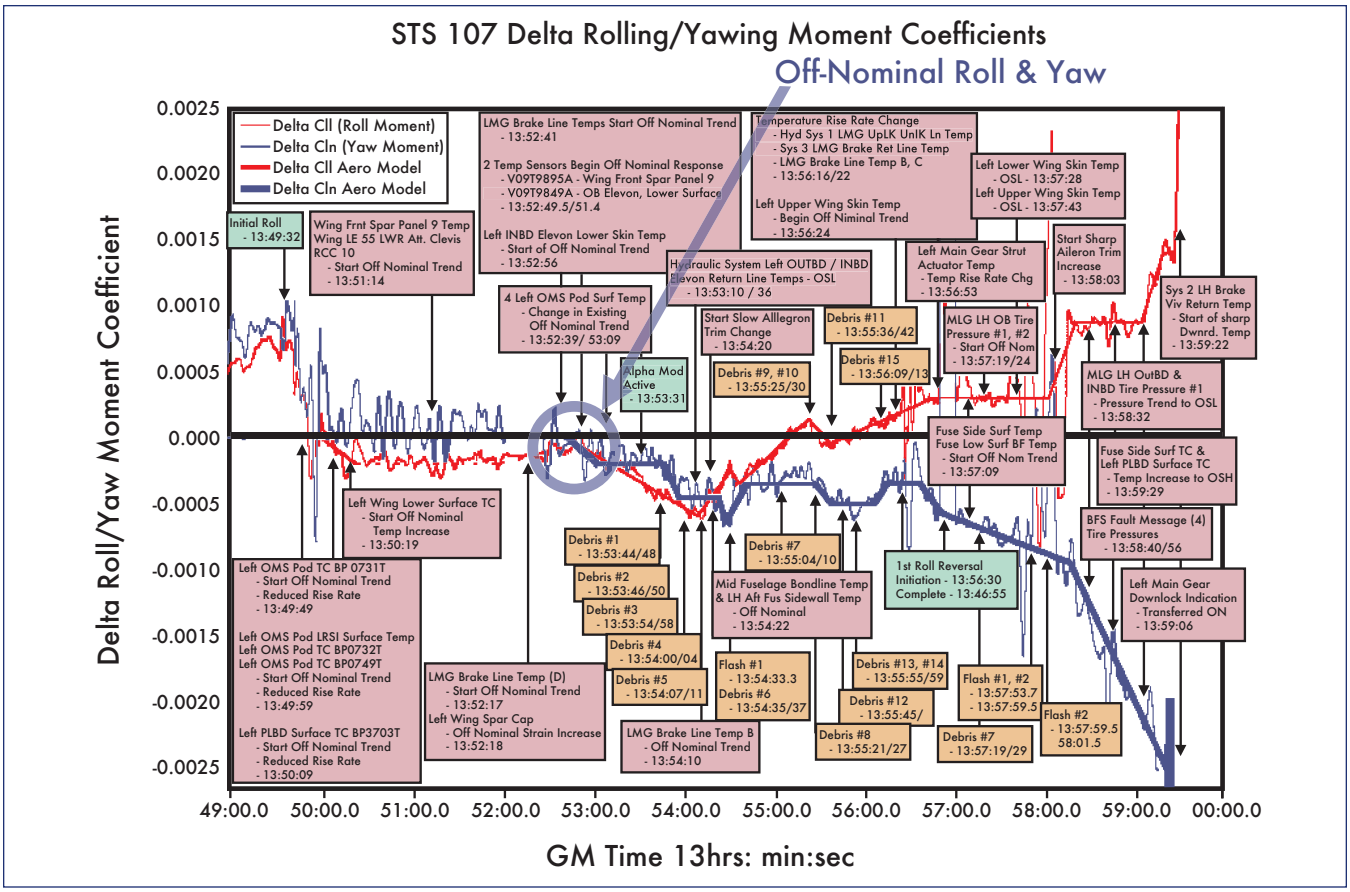


Figure 5-43. First noted off-nominal aero event.

ing edge upper surface vortices due to interaction with disturbed flow caused by damage progression in the RCC panels 8 through 9 area. During this same timeframe, the upper cap strain gauge on the 1040 spar began an off nominal increase indicating continued heating internal to the left wing.

By this point in the entry almost all measurements in the left wing had been lost and there appeared to be a temporary decrease in the measurement failure rate. It is possible that the "lull" in measurement failures was caused by a release of upper wing skin and FRSI. The breach in the upper wing surface and resulting pressure differentials internal to the wing would shift the internal plume impingement location relative to the wiring. In this same timeframe, there were multiple debris events captured on video by public ground observers beginning at 8:53:46 EST (EI + 577 sec., 20 seconds after California coastal crossing) and ending at 8:54:11 EST (EI + 602 sec.). The source of the debris may be upper wing skin and other thermal protection system (TPS) elements.

Since the wing had been ingesting hot gas for over two minutes, it is quite probable that significant internal damage to the wing occurred over this timeframe. The aluminum structure in the wing was not designed for high heating and many of the components are unlikely to survive this heating environment. For example, aluminum's melting point is ~1200 °F, but the ingested gas into the wing may have been up to 8000 °F near the breach. There were other communication dropouts in this timeframe as well (8:53:32 to 8:53:34 EST, EI +563 to 565 sec.).

In the 8:54:10 to 8:54:35 EST (EI + 601 to 626 sec.) timeframe, several key events occurred. The first event at 8:54:10 EST (EI + 601 sec.) was an indication that the temperatures in the wheel well had a greater rise rate, indicating the sneak flow or breach into the wheel area had increased. The roll moment trend changed sign at 8:54:11 EST (EI + 602 sec.) almost simultaneously with the change in wheel well temperature rise rate as shown in Figure 5-44, followed by a debris flash event at 8:54:33 EST (EI + 624 sec.). A large debris item, labeled debris event six, was seen leaving the orbiter two seconds later. This debris event and the roll moment trend change are believed to be created by growing damage to *Columbia*'s left lower wing.

There are several theories that attempt to explain this response including a change in the wing camber or shape due to deformation and a lower wing recession, caused by the loss of much of the support structure internal to the wing. Wing recession here is in reference to structural deformation of the wing surface. In this case, one or more areas on the lower wing form a more concave shaped depression of wing skin and tiles as a result of the structural support in those areas being weakened or lost. A structural analysis of both wing deformation due to the loss of three ribs internal to the wing, and the wing recession concept was performed.

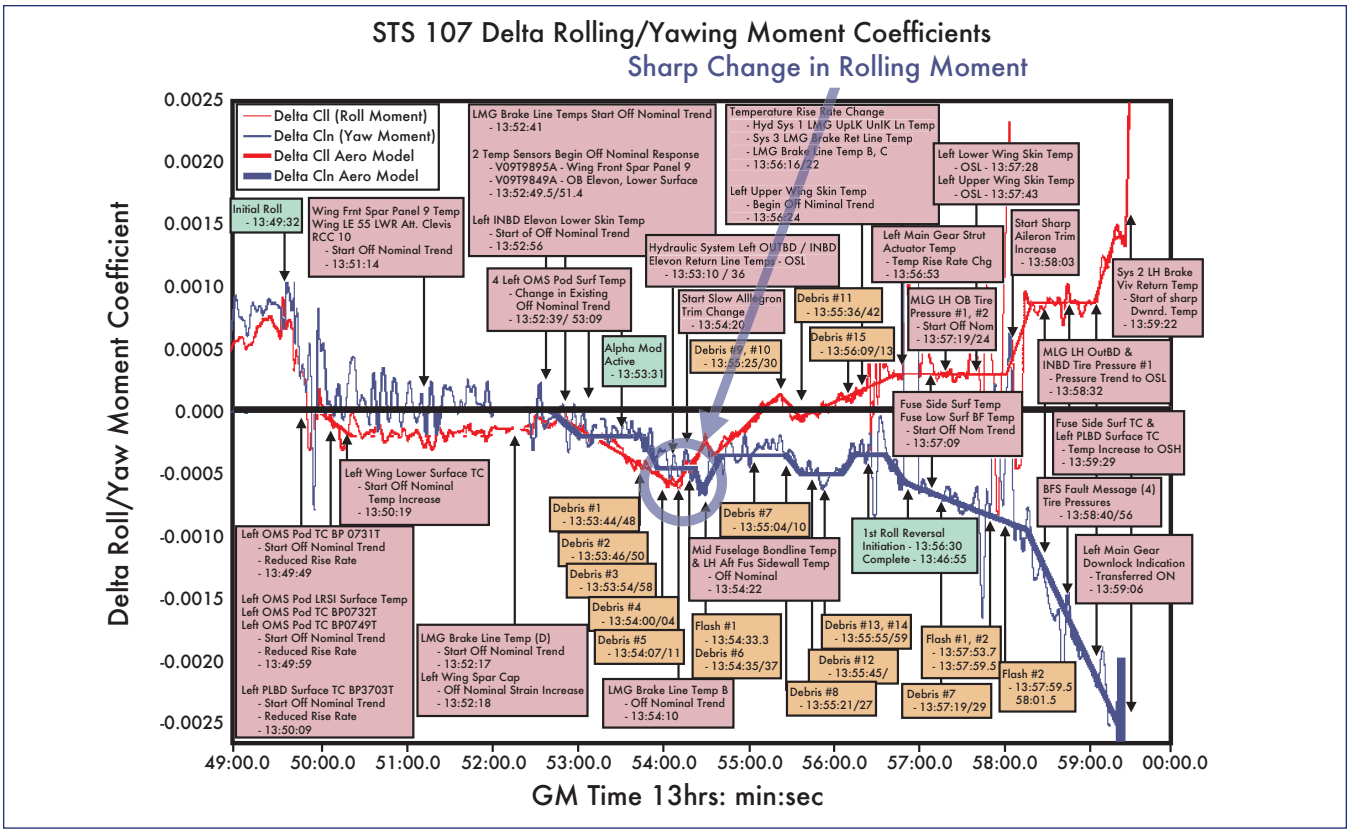


Figure 5-44. Sharp change in rolling moment.

Structural and aerodynamic analysis of wing deformation was performed without any type of recession in the wing lower surface. An assumption of 70 pounds per square foot was used for wing loading. Heat transfer coefficients were updated from previous coupled venting and thermal models for the left wing. A structural model was used along with the heating equivalent of a 10 inch diameter breach in the wing spar beginning at 8:52:16 EST (EI + 487 sec.) assuming 100 percent of the energy from this hole was transferred to the wing interior. Two different cases were analyzed: one with no breach in the upper wing skin and another with a 5 inch diameter breach in the upper skin at 8:54:37 EST (EI + 628 sec.) when a significant visual flash event was observed. Both cases showed that the temperatures of the wing skins, wing spars, and the wheel well wall were high enough by 8:58:19 (EI + 850 sec) that significant damage to the wing structure would occur. Figure 5-45 shows the potential area of damage and that significant deformation of the intermediate wing area and/or a recession in the lower surface is possible.

It is difficult to postulate the exact wing deformation that occurred. One case is localized leading edge damage, resulting in global wing deformation. Local deformation was relatively small, less than 1.0 inch in the damage area with a 0.25-inch global increase in wing tip deflection. Delta rolling and yawing moments were calculated for this case, and they were very small, approximately +0.0001 for roll and -0.0001 for yaw. Another case looked at deformation resulting from the loss of three internal ribs. Again, the local deformation

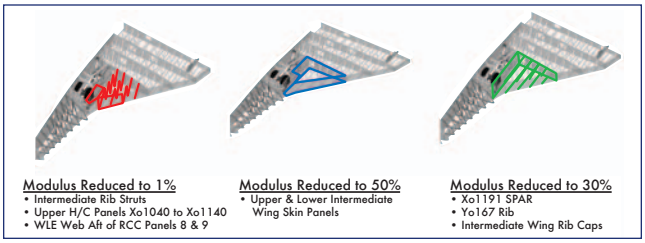


Figure 5-45. Modeling results show potential area of damage and that significant deformation of the intermediate wing area and/or a recession in the lower surface are possible.

was small (approximately 5 inches) and the resulting aerodynamic moments were small. These delta moments are in the correct direction for change in the aerodynamic moments, but are not nearly large enough in magnitude when compared to the flight derived moments for the time after the roll moment trend reversal. To achieve the aerodynamic response observed in the flight data, more significant damage to the wing would have been required.

Based on the structural analysis, it appears feasible that a wing recession occurred and resulted in the large positive slope in the delta rolling moment. The recession was caused by severe prolonged heating internal to the left wing that melted many of the support struts. Once the struts were lost, the wing skin lost structural support, a concave cavity developed, and some lower surface tiles may have been lost.

Wind tunnel testing has shown that this type of cavity can cause the change in delta aero moments derived from the aerodynamics reconstruction in this timeframe. The aero moment change is a negative yaw moment due to increased drag and a positive roll moment due to increased lift on the left wing. This testing will be discussed in more detail in the next section.

The flash event in this timeframe could indicate a loss of either upper surface wing skin or thermal blankets or a release of molten material into the environment around the orbiter. More than 10 debris events followed and were observed by various public videos in the 8:55:04 to 8:56:00 EST (EI + 655 to 720 sec.) timeframe. Several of these events were large, consisting of a shower of particles, and lead to a brightening of the plasma trail. Another communication dropout followed at 8:56:00 EST (EI + 720 sec.).

5.4.5 Wheel Well Gas Penetration and Final Aerodynamic Events

By 8:56:16 EST (EI + 727 sec.), hot gas had penetrated the wheel well wall as indicated by off-nominal rise rates in several hydraulic line temperatures (see Figure 5-46). Preliminary analysis indicates that it is feasible to have had some gas intrusion into the wheel well area as early as 8:52:39 EST (EI + 510 sec.) since a honeycomb access panel could melt as quickly as 22 seconds after the wing spar is breached. Additionally, there are various vent paths into the wheel well around the landing gear door hinge covers.

The centerline of the plume contained enough energy to begin melting the exterior of the wheel well wall by approximately 8:54:00 EST (EI + 594 sec.). The modeling described in the previous sub-section assumed the heating equivalent of a 5 inch diameter hole in the leading edge spar, but does not include the complex thermal interaction with struts and other wing spar structure internal to the wing. The intent of the analysis is to show that it is feasible to obtain the temperature response shown in Figure 5-46, including the early response that was seen in the 8:54:10 to 8:55:10 EST (EI + 601 to 666 sec.) timeframe, when several left main gear brake line temperatures and strut actuator temperatures began an off-nominal rise.

Immediately after the wheel well wall was breached, a hot gas plume began to flow on to the left main gear strut (depicted in Figure 5-47), leading to excessive strut erosion. A wheel well wall breach in this area is consistent with the erosion pattern observed on the recovered left main gear strut. Even after damage had significantly progressed into the wheel well, the orbiter initiated the first roll reversal at 8:56:30 EST (EI+741 sec.). The maneuver was completed by 8:56:55 EST (EI+766 sec.), and the vehicle was in a normal left bank. The guid-

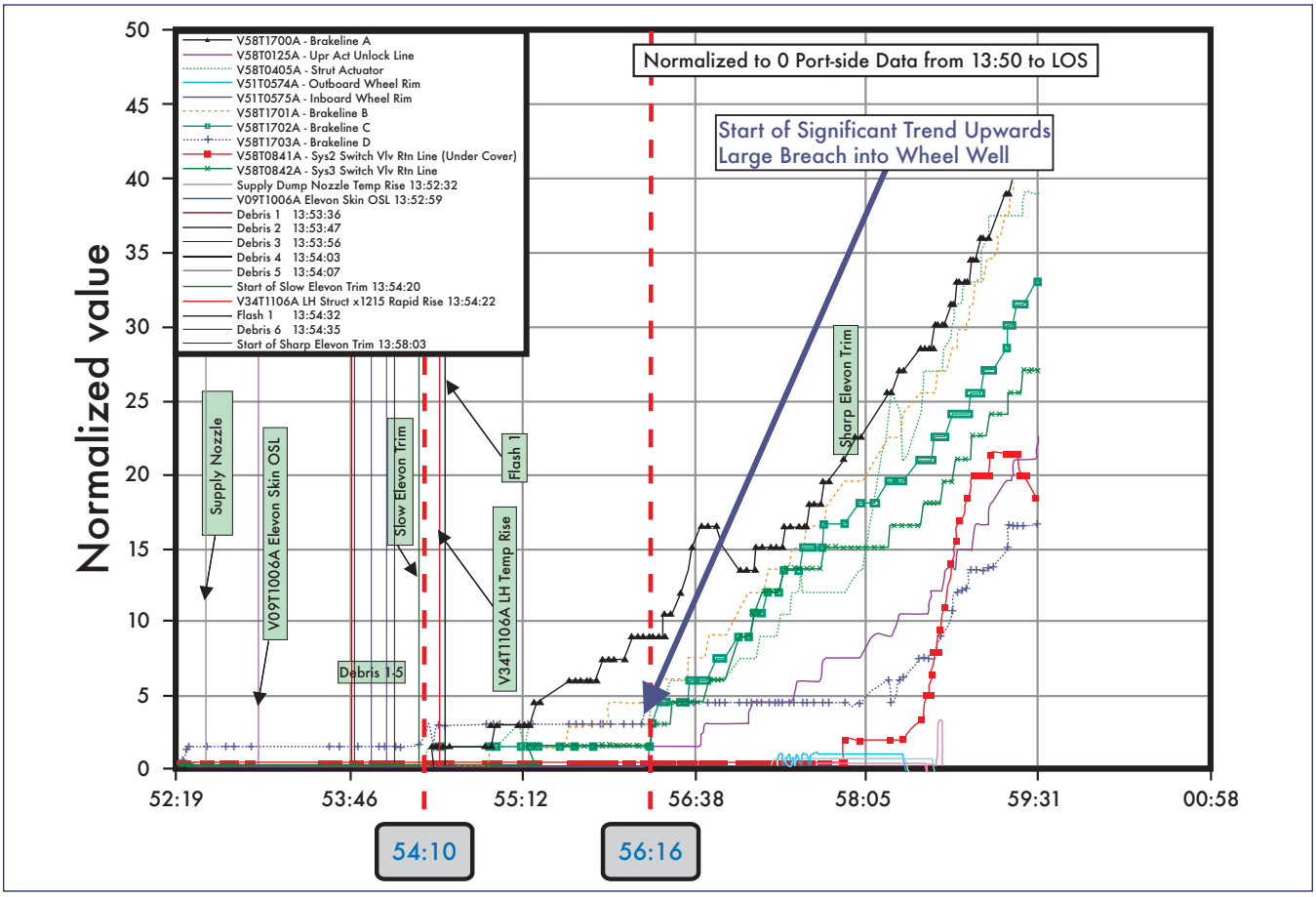


Figure 5-46. Temperature data in left wheel well trends up.

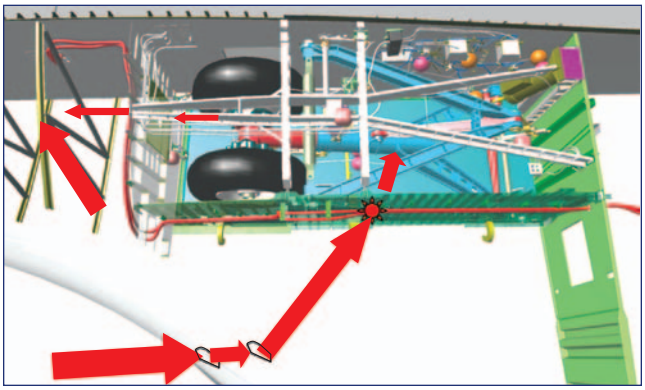


Figure 5-47. Hot gas breaches the wheel well.

ance and flight control systems were performing nominally, although the aileron trim continued to slowly change to counteract the additional drag and lift from the left wing.

Imaged at 8:57:14 EST (EI + 785 sec.), the Kirtland photo could indicate a flow disturbance on the leading edge of the left wing and/or flow leaving the leading edge of the left wing (see Figure 5-48). It also appears to show a disturbed flow leaving the trailing edge of the left wing. Other images, not shown here, also show disturbed flow on the upper side of the left wing, indicating that the damage and venting through the upper RCC vent was deflecting the flow upward. The Kirtland photo is a digital still image taken by off-duty employees of the Starfire Optical Range at Kirtland Air Force Base, New Mexico, during the STS-107 entry using a 3.5 inch telescope through a computer controlled 1 meter rotating mirror.

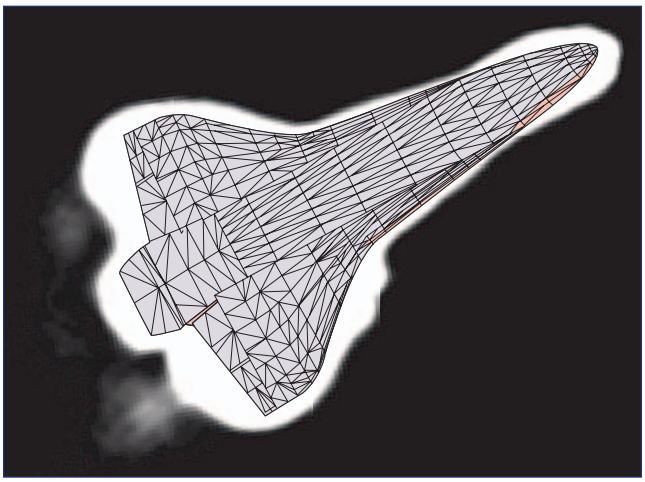


Figure 5-48. Kirtland photo with superimposed Orbiter outline.

At 8:58:32 EST (EI + 863 sec.), there was a change in stress measured on the left wing 1040 spar (main landing gear forward wall spar), as indicated by strain gauge measurements that began trending up at 8:52:18 EST (EI + 489 sec.). At 8:58:32 EST (EI + 863 sec.) the lower cap strain (near the bottom of the 1040 spar) essentially returned to a normal measurement when compared to previous flights (see previous Figure 5-39). The upper strain measurement continued to increase during this timeframe indicating that the heating was different on the upper and lower portions of the wheel well and 1040 spar. Although the response of the 1040 spar strain is not completely understood, structural analysis indicates that the strain response can be completely explained by thermal stresses caused by severe heating of the wheel well wall and internal wing components.

As shown in Figure 5-49, this strain response appears to be consistent with another sharp change in the slope of the derived delta rolling moment coefficient that occurred slightly earlier at 8:58:03 EST (EI + 834 sec.), along with several additional debris events. The vehicle responded to this event with a sharp change in the aileron trim. These events indicate that there was another significant change to the left wing configuration at this time. Wing deformation and an increase in the lower surface recession along with a loss of additional bottom tiles are possible explanations for this behavior.

At the same time as the stress was relieved on the lower 1040 spar, two left main gear outboard tire pressures began trending toward an off-scale low reading. This was preceded by a slight upward trend at 8:57:19 EST (EI + 790 sec.) for both pressure measurements. This is an indication of extreme heating of both the left outboard tire and the surrounding instrumentation. The tire has significant thermal mass and substantial heating would be required to produce the slight temperature rise. By 8:58:56 EST (EI + 887 sec.), all left main gear inboard and outboard tire pressure and wheel temperature measurements were lost indicating a rapid progression of damage or wire burning inside of the wheel well. Figure 5-38 shows the location of these pressure sensors.

At 8:59:06 EST (EI + 897 sec.), the left main gear downlocked position indicator changed state. There are indications that the gear did not come down until after Loss of Signal (LOS) because the left main gear uplock position indicator still showed the gear in the stowed position, and the left main landing gear door latch position indicator showed that the door was still closed. Additionally, there are several measurements on the strut that produce valid data until final loss of telemetry in the MCC.

As shown in Figure 5-49, there was another abrupt change in the vehicle aerodynamics caused by the continued progression of left wing damage at 8:59:26 EST (EI + 917 sec.). This change was a significant increase in the positive delta roll moment and negative delta yawing moment, indicating increased drag and lift from the left wing. *Columbia* attempted to compensate for this by firing all four right yaw jets. By this point the MCC had lost all telemetry data at 8:59:23 EST (EI + 914 sec.). Even with all four right yaw jets and a maximum rate of change of the aileron trim, *Columbia* was unable to control the side-slip angle that was slightly negative (wind on the left side of the fuselage) during much of the entry. The side-slip angle changed sign at 8:59:36 EST (EI + 927 sec.) indicating that vehicle loss of control was imminent (side-slip angle is an aerodynamics term for the angle between the relative wind velocity and the vehicle direction of motion, or velocity vector).

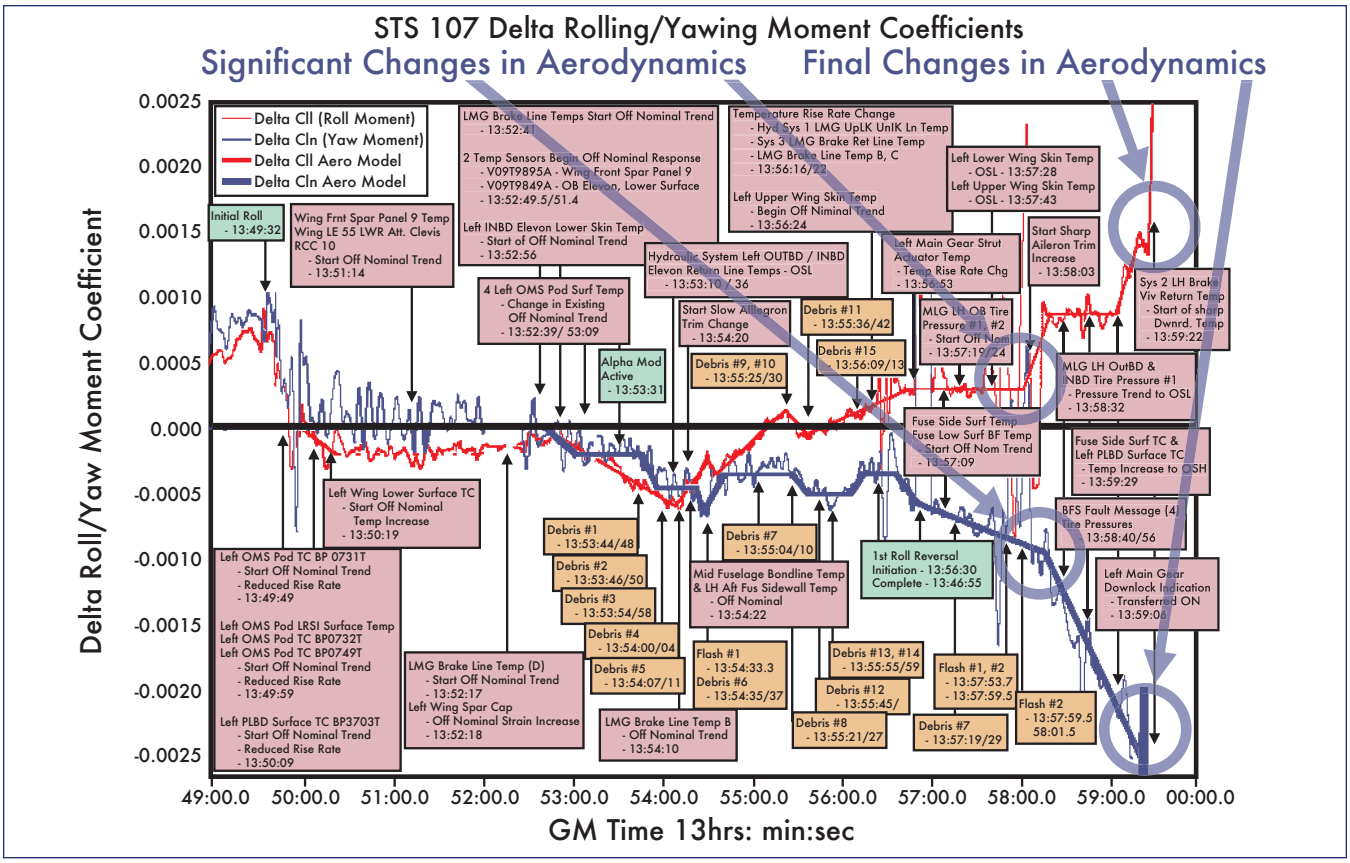


Figure 5-49. Increased wing deformation and wing recession leads to significant vehicle aerodynamic changes.

A large piece of debris was observed leaving the orbiter at approximately 8:59:46 EST (EI + 937 sec.). Five additional debris events and two flash events were observed over the next thirty seconds. MADS recorder data was lost at approximately 9:00:14 EST (EI + 965 sec.) and main vehicle aerodynamic break-up occurred at 9:00:18 EST (EI + 969 sec.), based on video imagery.

In the Mission Control Center, the Entry Flight Control Team waited for tracking data from the Eastern Range and communication link handover to the Merritt Island Launch Area (MILA) ground station. There was no radio frequency (RF) communication received from the vehicle at MILA and no valid tracking data was ever produced at the Eastern Range since the vehicle never crossed the KSC area horizon. Shortly thereafter, Mission Control's Entry Flight Director implemented contingency action procedures.

5.5 Aerodynamic Reconstruction

As previously discussed, the flight-derived aerodynamic moments use the high altitude winds and atmosphere developed by the DAO and represent the most accurate reconstruction that is possible based on available data. Many different scenarios were proposed to define the damage necessary to match this reconstruction using wind tunnel testing and CFD analyses at facilities across the United States. These scenarios include individual and multiple full or partial missing RCC panels, a missing landing gear door, a deployed left main landing gear, missing lower surface tiles, holes through the wing, lower surface deformation, and several others. The details for all of the options that did not match the flight-derived data will not be discussed here and are beyond the scope of this document.

Figures 5-50 through 5-52 show the flight derived delta roll, yaw, and pitch aerodynamic moments, respectively, along with the tested damaged configuration results that are consistent with the flight data. The intent of the remainder of this

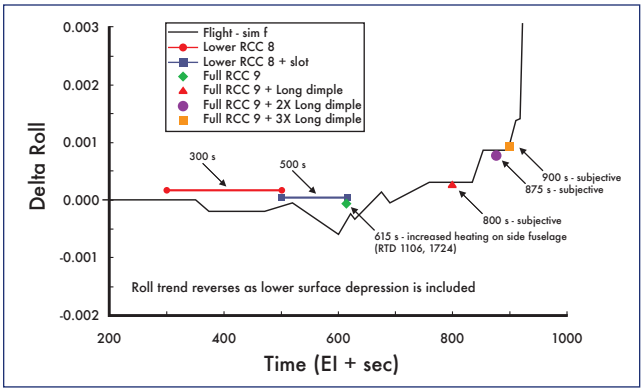


Figure 5-50. Wind tunnel testing configurations that match delta roll moment data.

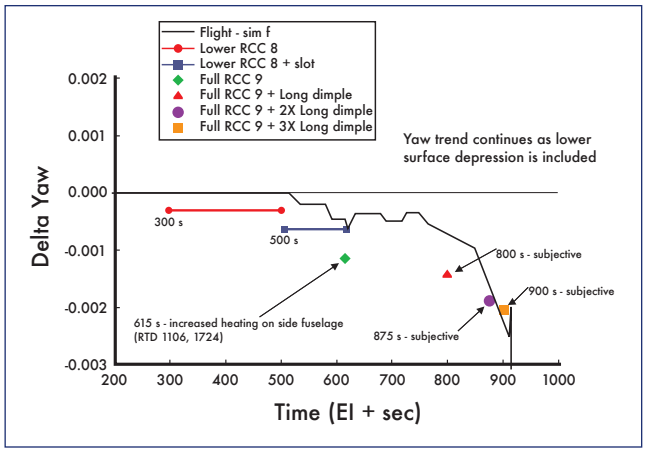


Figure 5-51. Wind tunnel configurations that match delta yaw moment data.

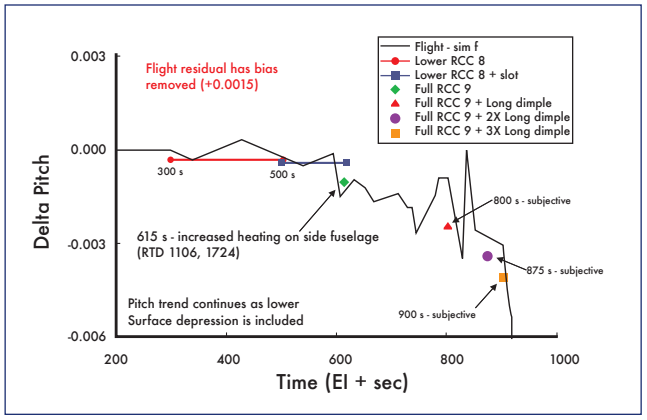


Figure 5-52. Wind tunnel configurations that match delta pitch moment data.

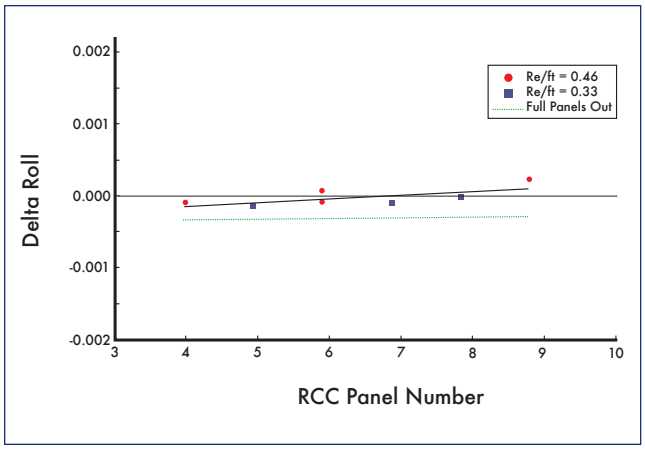


Figure 5-53. Delta roll for lower half and full panel RCC panel missing.

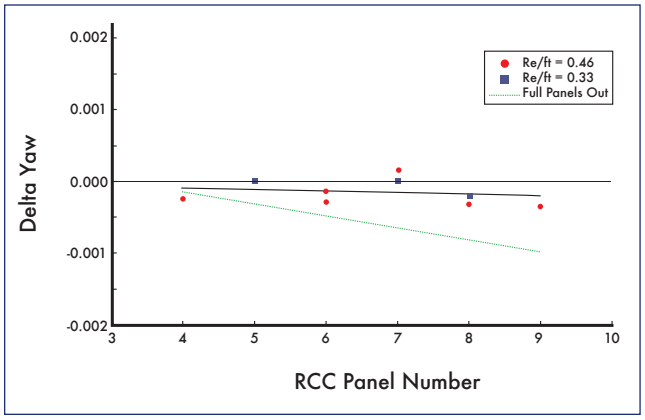


Figure 5-54. Delta yaw for lower half and full panel RCC panel missing.

section is to briefly discuss the CFD analysis and wind tunnel testing used to replicate the derived delta aero moments. Note the time scale on these plots is in seconds from EI.

As discussed previously, the reconstructed aerodynamic moments showed little to no change due to damage through 8:52:29 EST (EI + 500 sec.). Based on the forensics data discussed in Section 5.3, the most likely region of initial damage was in the lower part of RCC panel 8. Wind tunnel testing in the Langley Research Center (LaRC) CF4 tunnel indicated that a missing bottom part of RCC panel 8 (from the apex to the lower carrier panel) matches the initial aerodynamic increments, which show a minimal effect on the overall vehicle aerodynamics. In fact, even a full missing panel 8 produces only a small change to the roll and yaw aero moments. Figure 5-53 and Figure 5-54 show the results of this LaRC evaluation.

The left wing spar was breached in the 8:51:14 EST (EI + 425 sec.) to 8:52:15 EST (EI + 487 sec.) timeframe. Initially, the spar breach had little to no effect on the derived aero moments. Over time the leading edge damage progressed and a slot or upward deflection of the flow through the upper carrier panel 8 developed. The combination of flow through the wing leading edge and flow through a slot onto the upper carrier panel is consistent with the first observed aerodynamic response, which occurs at 8:52:29 EST (EI + 500 sec.). This can be observed in Figure 5-50 and Figure 5-51 as a slow negative trend in delta roll and yaw. Figure 5-55 shows the wind tunnel test results for three different cases: missing lower RCC panel 8, missing panel 8 combined with a 4 inch diameter hole in the upper carrier panel 8, and missing RCC panel 8 with a slot through the upper carrier panel. The slot was shown to produce the increased delta yaw observed during flight as well as the upper surface flow disturbances on the OMS pod and left side fuselage, which were also observed during flight by abnormal temperature rise rates.

It is possible that a hole through the upper wing developed in the 8:54:11 EST (EI + 600 sec.) to 8:54:31 EST (EI + 630 sec.) timeframe. This is consistent with a lull in the measurement failure rate in the wire bundle along the wheel well that was discussed earlier in Section 5.4.3. Wind tunnel testing and CFD analysis have shown that sizable holes through the wing have little to no effect on the aerodynamics and heating on the left side of the fuselage and OMS pod. A representative sample of this work is shown in Figure 5-55 as damage scenario number 2.

The next significant aerodynamic event occurred at 8:54:11 EST (EI + 602 sec.) when a dramatic reversal of the aero rolling moment trend occurs. By this time hot gas and an internal plume environment had severely degraded the structural integrity of some of the intermediate wing support structure leading to wing deformation. Three different configurations were tested to validate the theory of wing deformation. The first involved global wing deflection of up to 0.79 inches due to damage and is depicted in Figure 5-56. CFD analysis of this configuration showed extremely small aero moment response for yaw and roll that does not match the flight derived data. More substantial local wing skin deformation with a maximum deflection of 5.1 inches due to three ribs missing along with other internal wing damage was examined using CFD tools. Again, these results produced only small aerodynamic moment changes, which did not match the flight-derived data.

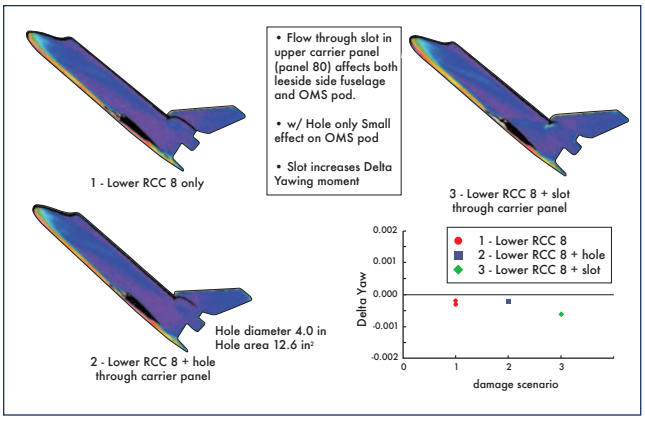


Figure 5-55. Wind tunnel testing results for missing lower carrier panel 8 and a slot and hole through wing.

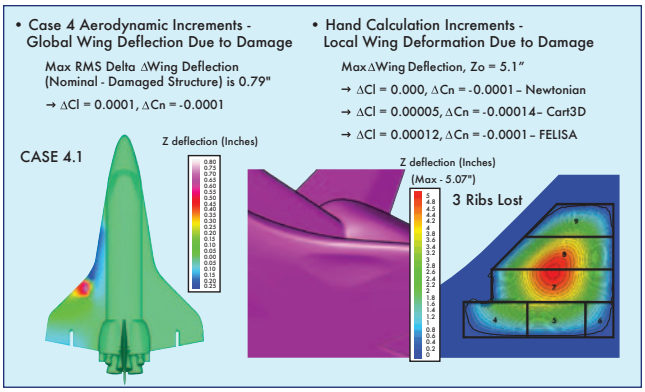


Figure 5-56. CFD analysis of wing deformation.

The third and final configuration that was tested was a depression in the lower surface of the wing caused by the significant structural damage caused by the hot gas plume environment internal to the wing. A previous section (5.4.5) discussed the internal structural damage that was most probable in this timeframe. LaRC wind tunnel testing and CFD analysis were performed for several different configurations of lower surface recessions shown in Figure 5-57. The data shows that it is feasible for a recession to cause the change in the rolling moment sign when combined with some portion of RCC panel 9 missing at 8:54:11 EST (EI + 602 sec.).

Initially, the recessed area would have been relatively small; however, it would gradually grow over time to cause the delta roll moment to increase. By 8:57:29 EST (EI + 800 sec.) wind tunnel testing showed that the depression has to be on the order of 20 feet long, two feet wide, and 5.3 inches deep along with panel 9 missing in order to duplicate the delta roll coefficient shown in Figure 5-50. This configuration provides a delta yaw moment that is slightly larger than was observed, but is consistent with a decreasing negative delta yaw moment observed in this timeframe (Figure 5-51).

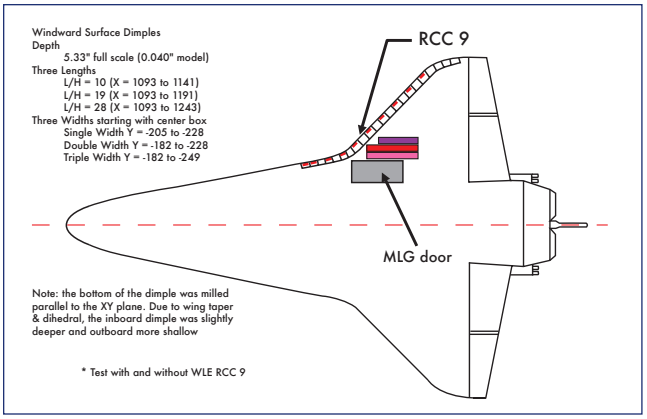


Figure 5-57. LaRC wind tunnel testing of lower surface depressions.

A little more than a minute later, at 8:58:44 EST (EI + 875 sec.), the width of this recession would need to have increased by another two feet to match the aerodynamic delta roll and yaw moments. At this point, the rate of change of the aerodynamic moments and damage progression is so great that it likely grew by about an additional two feet in width over the next 25 seconds at 8:59:09 EST (EI + 900 sec.). Additionally, the delta pitch moment was now observed to deviate from previous mission reconstructions in this timeframe. Figure 5-52 shows that the recession concept is consistent with the delta pitch moment reconstruction. Previous structural analysis indicates that by 8:58:19 EST (EI + 850 sec.) there is large-scale wing deformation and thus the possibility of a large recession is plausible in this timeframe.

In summary, the latest aerodynamic wind tunnel testing and CFD analysis performed to date indicate that the initial damage was probably relatively small, like a hole and/or missing part of the bottom of RCC panel 8. A slot then developed so that there is upward flow through the RCC vent and across the upper 8 carrier panel. Later, more of RCC panel 8 and/or panel 9 is lost along with some substantial wing deformation probably involving a locally depressed area on the lower wing surface. The wing deformation and lower surface recession gradually increased over time, and eventually the yaw and roll moments were too great for the flight control system to manage, leading to a loss of vehicle control and aerodynamic break-up.

Although this aerodynamic reconstruction represents a reasonable sequence of vehicle configurations that led to loss of control during entry, it is not meant to be interpreted as an exact literal sequence of events. The wind tunnel testing and analysis was performed using representative geometries; however, the actual specific vehicle damage is unknown and may never be known completely. The sequence of events discussed here is consistent with the reconstructed aero moments, MADS data, and forensics data and provides the best aerodynamic, thermal, and structural understanding possible for the eventual loss of *Columbia*.

6.0 Re-usable Solid Rocket Motor

All Re-usable Solid Rocket Motor (RSRM) investigation fault tree legs have been closed for the STS-107 RSRM set, RSRM-88. All Contract End Item (CEI) performance specifications were met including all flight individual and paired motor requirements. Postflight inspections revealed a tear in the right-hand nozzle flex boot that is considered an IFA (STS-107-M-01), but the tear is attributed to thrust tail-off or splashdown events. A slightly low out-of-family thrust level was observed for the right-hand motor in the 113.5 to 114.5 second interval during thrust tail-off, but the resultant thrust imbalance was still within family experience and CEI limits. The new experience has been reviewed and accepted as being within the statistical expectations for the RSRM motor population and is attributed to the increased population sample size (see Section 3.4 for more details).

7.0 Solid Rocket Booster

The Solid Rocket Booster (SRB) fault tree for the STS-107 SRB set, SRB BI116, remains open due to possible debris sources at the forward SRB/External Tank (ET) separation bolt catcher assembly and the forward Booster Separation Motors (BSM). The STS-107 SRBs performed nominally and there were no reported SRB IFAs.

Four blocks on the STS-107 SRB fault tree remain open pending completion of forward bolt catcher testing. The bolt catcher, shown in Figure 7-1, was not qualified as an assembly, and structural qualification testing was not representative of the current flight configuration. The exact magnitude of loads transmitted to the bolt catcher housing cannot be determined based on available data. The SLA-561 thermal protection system (TPS) material on the bolt catcher was qualified by test and analysis for general ET application, but no pyrotechnic shock testing was performed. There is no test data available on the bolt catcher honeycomb dynamic crush strength versus separation bolt velocity, and random pressure loading from the NASA Standard Initiator (NSI) ejection was not included in the original qualification tests. Lastly, the running torque/break-away torque was not measured during STS-107 bolt catcher fastener and ET range safety system (RSS) fairing installation, which is used to verify the insert locking feature is in place. A review has determined that the bolt catchers and RSS fairings were installed and secured for flight with the correct bolts and final torque. Testing is in work to close the four remaining fault tree blocks, but initial static tests results show failure below the required safety factor of 1.4.

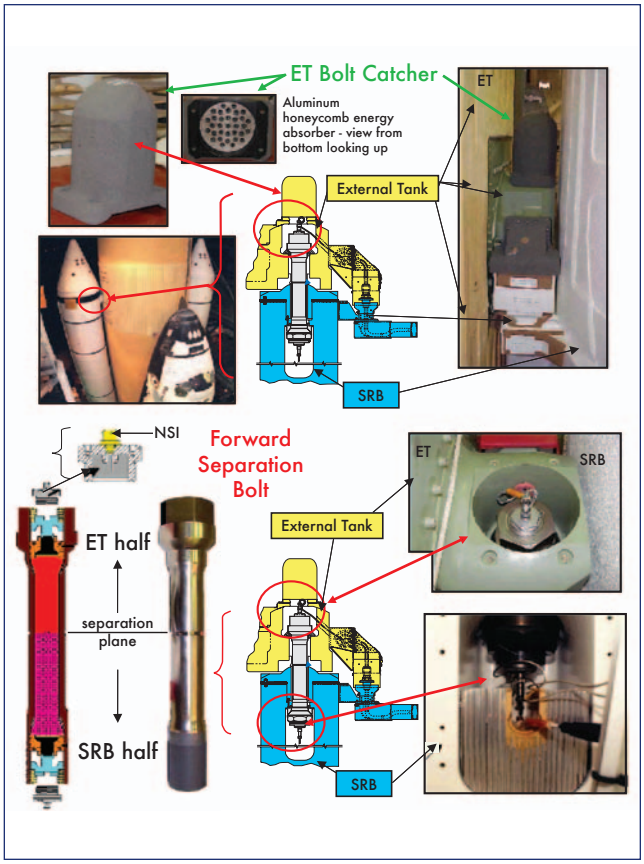


Figure 7-1. Details of SRB/ET forward separation bolt catcher assembly.

Two other blocks on the STS-107 SRB fault tree remain open that pertain to potential debris from the forward BSMs. Inspection of the forward BSMs found no indication of unburned propellant or any indication that the BSMs contained any Foreign Object Debris (FOD). The two debris related fault tree blocks will remain open pending transport and impact analysis.

8.0 Space Shuttle Main Engine

All Space Shuttle Main Engine (SSME) investigation fault tree legs have been closed. The STS-107 Block II SSMEs (center #2055, left #2053, and right #2049) performed nominally and there were no reported SSME In-Flight Anomalies (IFAs).

9.0 Environmental Factors

9.1 Introduction

A survey was conducted of the relevant environmental factors during STS-107/ET-93 processing to determine if a correlation could be drawn between those factors and ET bipod foam loss observed in flight. The data are inconclusive as to whether any correlation can be shown between environmental factors and ET bipod foam loss. The review considered ET age and exposure time, as well as weather factors such as rainfall, temperature, and humidity.

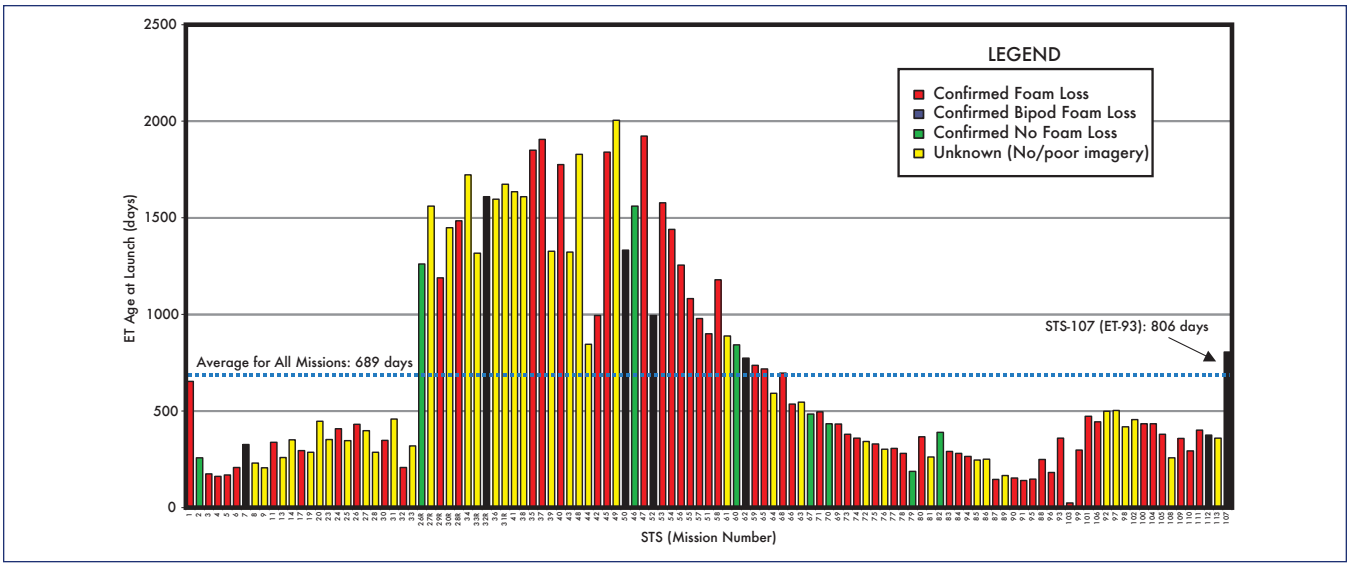


Figure 9-1. ET age for all STS missions.

9.2 Age and Exposure

The ET age was compared for various flights, presented in Figure 9-1. As shown in Figure 9-2, the ET age for STS-107/ET-93, 806 days, falls above the 95% confidence interval upper limit for the average age of all tanks, mean value 689 days, as well as the average age for all tanks with known bipod foam loss. STS-107/ET-93 also falls within the 95% confidence limit for missions with known bipod foam loss. Although the upper bound of the 95% confidence interval of the age of missions with bipod foam loss appears to be greater than the other groups in Figure 9-2, the 95% confidence interval limits of the different groups overlap each other. Therefore, data are inconclusive as to whether a correlation can be drawn about ET age and bipod foam loss.

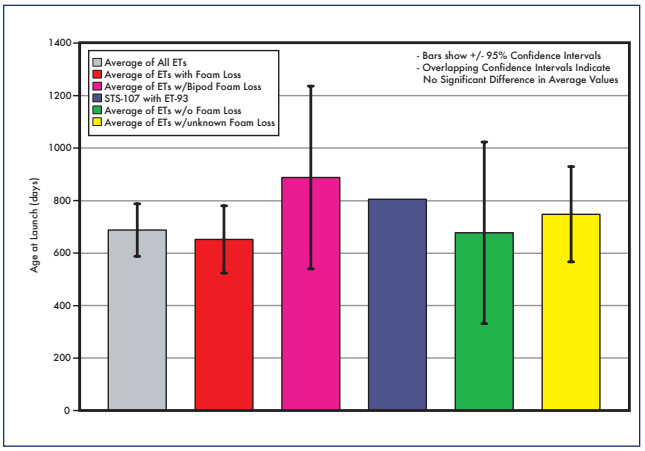


Figure 9-2. ET age for STS-107 compared to ET age for missions with and without bipod foam loss.

A similar comparison was made relating ET exposure time and bipod foam loss across the flight history (see Figure 9-3).

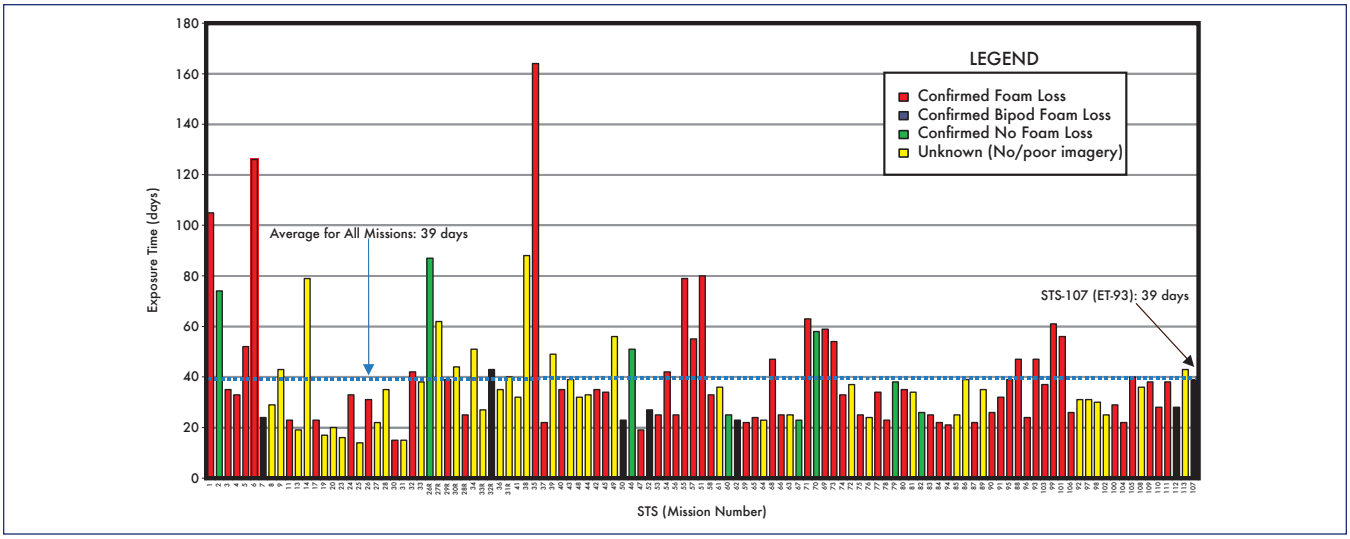


Figure 9-3. ET exposure time (to weather) prelaunch for all STS missions.

Note that the STS-107/ET-93 exposure time, 39 days, is the same as the mean value for all STS flights. As shown in Figure 9-4, the STS-107/ET-93 exposure time falls within the 95% confidence limit of all missions' ET exposure time, as well as the time confidence limits for flights with or without known bipod foam loss. The STS-107/ET-93 exposure time is larger than the 95% confidence upper bound for missions with known bipod foam loss. However, as stated above when discussing ET age, the 95% confidence limits of the different groups in Figure 9-4 overlap each other, and data are inconclusive as to whether ET exposure time and bipod foam loss can be correlated.

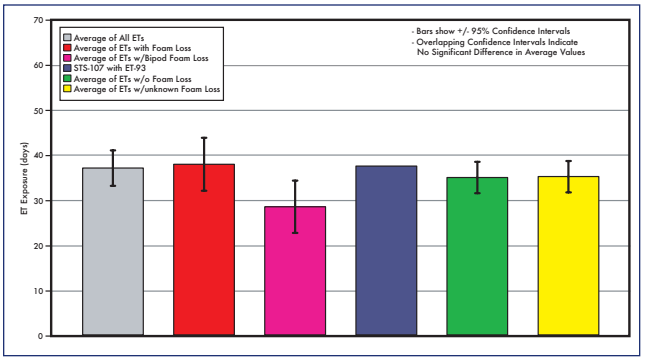


Figure 9-4. ET exposure time (to weather) for STS-107 compared to ET exposure time for missions with and without bipod foam loss.

9.3 Weather Factors

An extensive review of the relevant weather at Kennedy Space Center (KSC) was conducted in order to determine if a correlation could be derived for the weather conditions impact on ET bipod foam loss. The precipitation review examined total rainfall, maximum one-day rainfall, average daily rainfall, launch day rainfall, and L-5 days through lift-off total rainfall. Figure 9-5 shows the total prelaunch rainfall for all STS missions. As shown in Figure 9-6, although the STS-107 value for total prelaunch rainfall, 12.78 inches, is greater than the mean value for all mission, 5.45 inches, the data are inconclusive as to whether a correlation can be

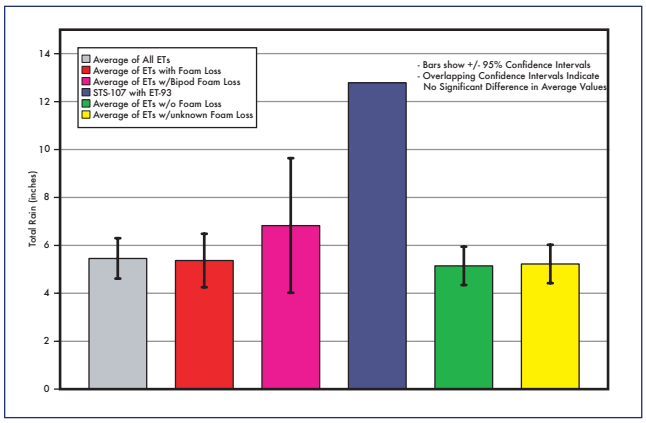


Figure 9-6. Total rainfall for STS-107 compared to total rainfall for missions with and without bipod foam loss.

made for ET bipod foam loss as a function of total rainfall prelaunch. The 95% confidence limit of the missions with ET bipod foam loss overlaps the confidence interval for all missions, as well as missions with no foam loss.

Similarly, the other rainfall parameters studied (e.g., average daily, day-of-launch) reveal no correlations for ET bipod foam loss. Figure 9-7 and Figure 9-8 show the data correlation for average daily prelaunch rainfall. The STS-

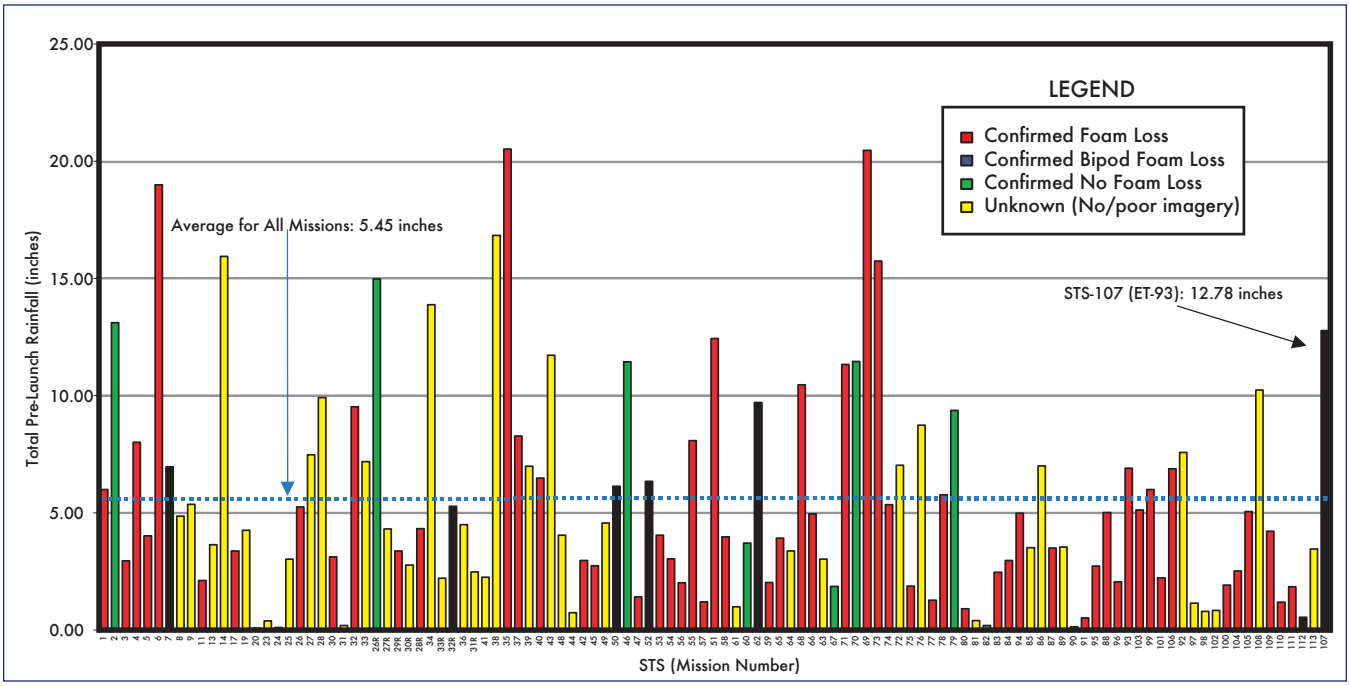


Figure 9-5. Total prelaunch rainfall for all STS missions.

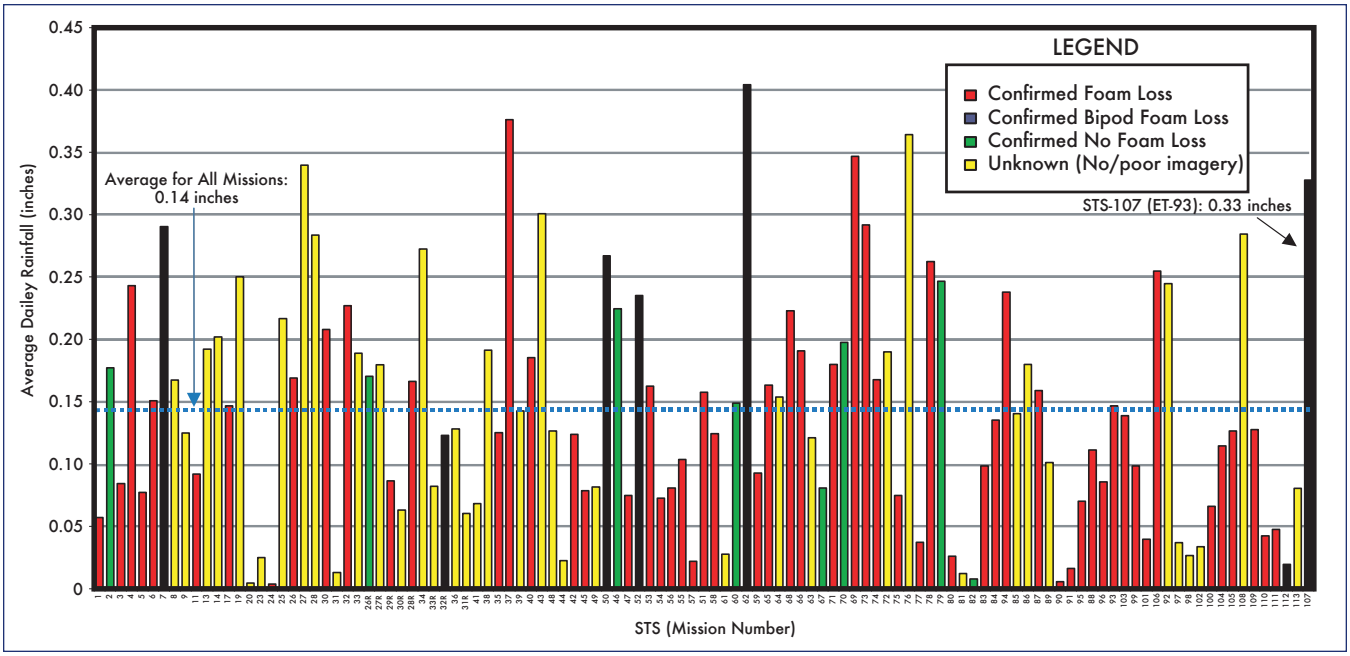
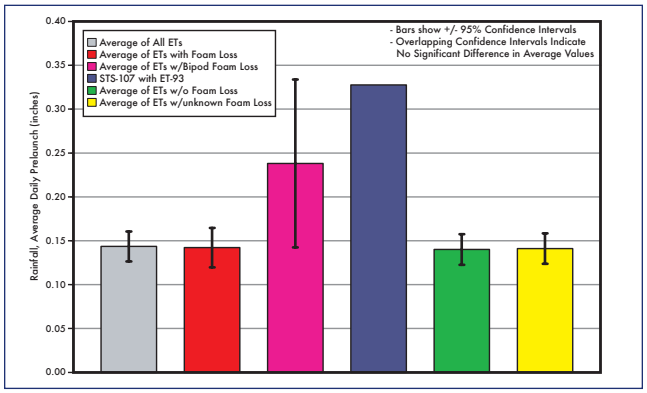
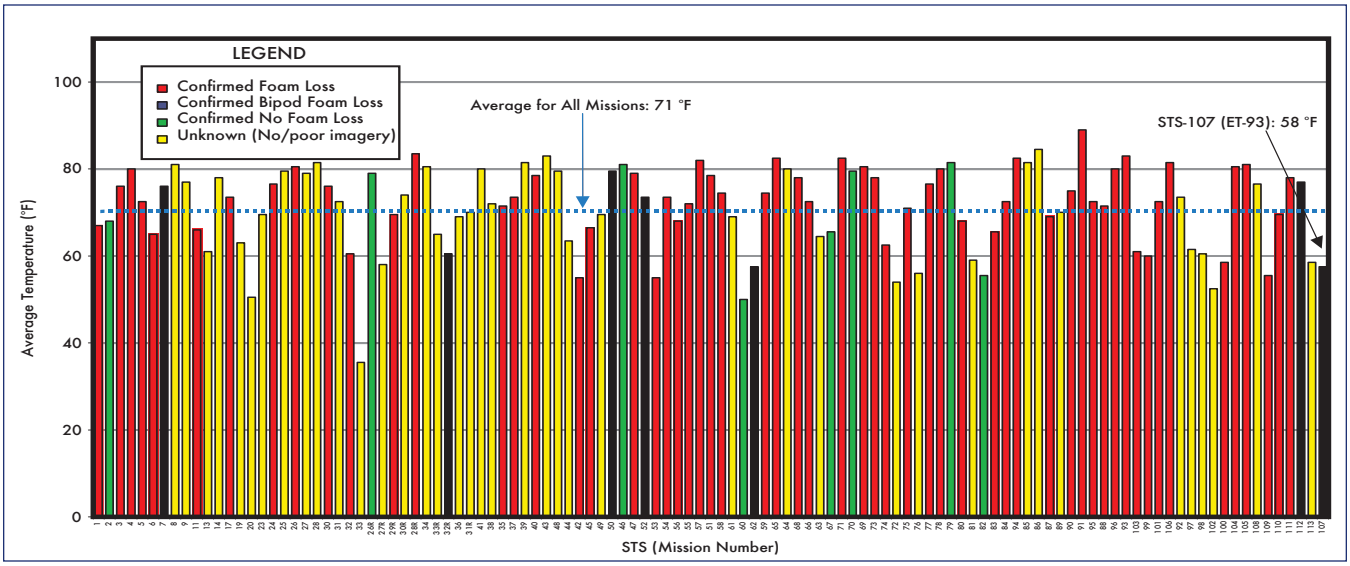


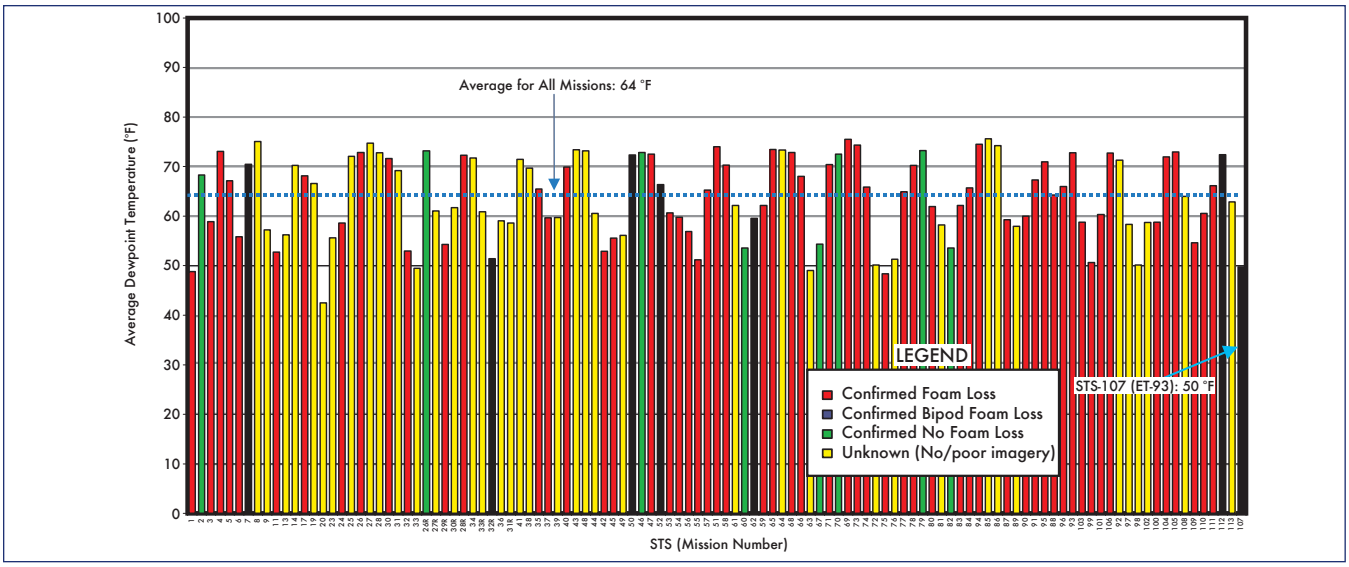
Figure 9-7. Average daily rainfall prelaunch for all STS missions (above).
Figure 9-8. Average daily rainfall prelaunch for STS-107 compared to average daily rainfall for missions with and without bipod foam loss (below).
Figure 9-9. Day-of-launch average temperature for all STS missions (bottom).



107 value, 0.33 inches, and the mean value for missions with bipod foam loss are greater than the average mission value, 0.14 inches. However, the confidence intervals overlap each other, and the data are inconclusive as to whether average daily rainfall and ET bipod foam loss can be correlated.

In addition to rainfall, the study also reviewed average, minimum, and maximum temperature, dew point, and humidity for both prelaunch and day of launch. Figure 9-9 shows the day-of-launch average temperature. The STS-107 day-of-launch average temperature, 58 °F, was less than the mean value for all missions, 71 °F, but no correlation can be made between day-of-launch average temperature and ET bipod





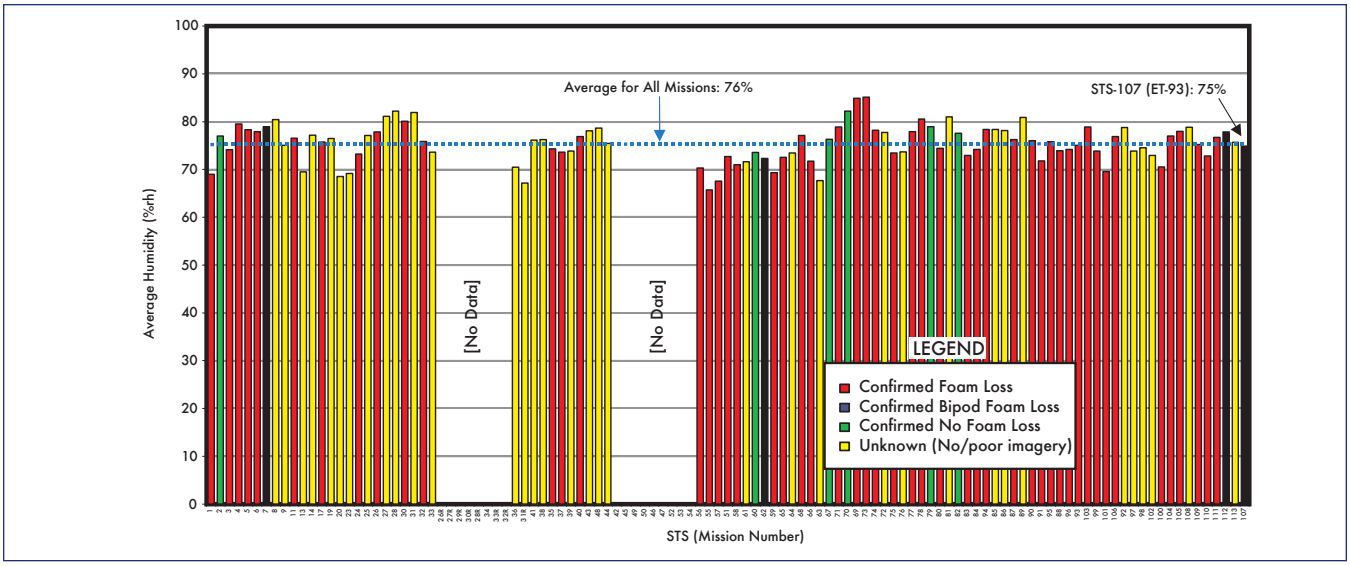


Figure 9-10. Prelaunch average dewpoint for all STS missions (top).
Figure 9-11. Prelaunch average humidity for all STS missions (above).

foam loss. Similar comparisons made for other temperature samplings, dew point (Figure 9-10), and humidity (Figure 9-11), yielded no correlations either.

10.0 Left Wing Processing and RCC Design

10.1 Introduction

This section summarizes the processing effort performed on the left wing of the Space Shuttle *Columbia* from the last Orbiter Major Maintenance (OMM) period through the launch of STS-107, and provides some background on the design of the RCC panels used on the orbiter. The processing includes all work done on *Columbia* from the major maintenance period (*Columbia* J3-OMM) through the flight of the STS-109 mission and all the normal preflight work done in preparation for the STS-107 mission.

10.2 Left Wing Processing (Palmdale, J3-OMM)

Columbia was in Palmdale, California, for its most recent OMM from September 1999 through March 2001. The work performed on the left wing included work on the electrical power and distribution system, instrumentation, mechanisms, structures, and the Thermal Protection System (TPS). There were 29 Problem Reports (PRs) on the electrical system, mostly wire lead discrepancies and wire stow issues. Two pyrotechnic connectors were found out of configuration and repaired. Instrumentation sensors and wire splices accounted for 20 PRs on the left wing and all were appropriately resolved. In the mechanisms area, a main landing gear door rotational pin inspection was partially performed at Palmdale and subsequently completed at the KSC. Slight damage to the Chromium plating of the forward inboard gear door hook was repaired. The gear downlock bungee was sent to the vendor for refurbishment.

Palmdale logged 62 PRs to the left wing structure that addressed elevon cove corrosion, elevon flipper door modification (material change from Inconel to Aluminum), and minor work on the main landing gear door.

All Reinforced Carbon-Carbon (RCC) upper and lower wing Leading Edge Structural Subsystem (LESS) access panels, spar insulators, ear muff insulators, wing leading edge RCC panels, and spar fittings (see Figure 10-1 and Figure 10-2) were removed and inspected for discoloration and damage. Visual pinhole inspections were performed on each RCC panel and the wing leading edge spar was inspected for damage. Oversized pinholes were originally reported in RCC panels 8 and 19, but after further evaluation with an optical comparator, it was determined that the pinholes were acceptable. No other significant damage was noted. Leading edge RCC panels 6 and 13 through 17 were sent to the vendor (Vought) for refurbishment. New shims were installed to accommodate the reinstallation of the spar insulators.

The panels and spar fittings were reinstalled and all step and gap measurements were taken. At that time, gaps were found to be unacceptable in numerous locations. Wing leading edge RCC panels 11, 12, 17, and 18 were removed and additional anomalies were noted, which included insufficient step and gap, spar fitting shims not per design (too small), and the lower access panel nutplates debonded and/or with low running torque. The low torque was due to a combination of the shim problem and a procedural error on the torque sequence. All 22 RCC panels were removed a second time. The nutplate issues were resolved by removing and replacing the nutplates that were accessible and securing with safety wire those that were not accessible. All anomalies identified were repaired, reworked, or accepted by Material Review (MR).

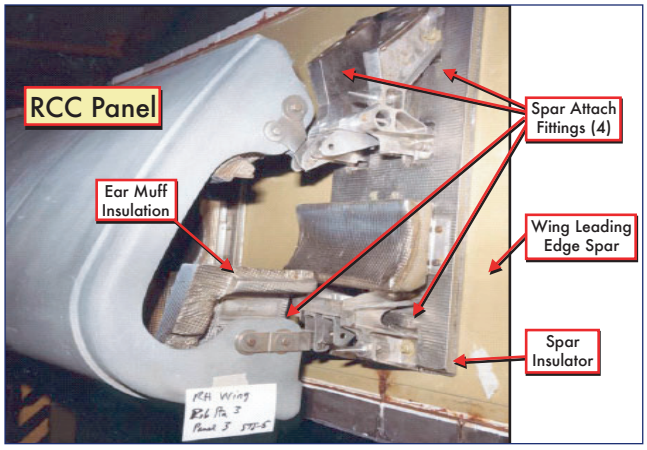


Figure 10-1. RCC components.

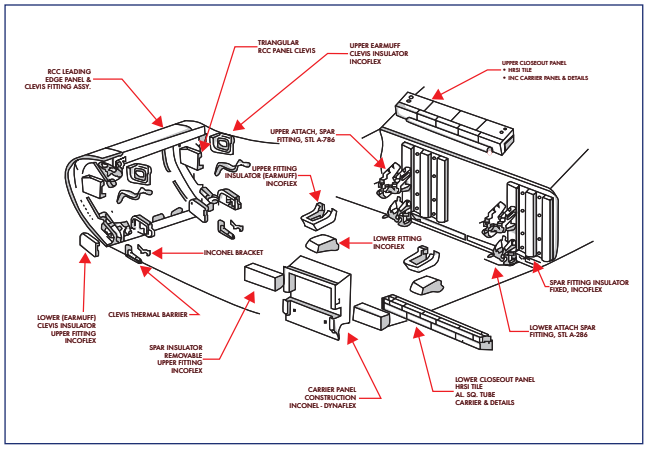


Figure 10-2. RCC panel assembly.

Tiles are attached to a strain isolation pad and then to the orbiter structure by a Room Temperature Vulcanized (RTV) adhesive. The outer tile surfaces must be flush with one another to preclude steps that would lead to excessive heat damage of surrounding tiles due to aerodynamic heating (Figure 10-3). Gaps present between adjacent tiles must be adequately sealed. There were 200 tile PRs worked for step and gap, gap fillers, and repair on the elevon cove area tile. One hundred thirty one (131) upper and lower wing surface tiles were replaced for various reasons, including baseline removal and replacements, damaged tile, instrumentation problems, and structural inspections. Wear and tear accounted for 27 maintenance items. Tile gap filler replacements numbered 58 with no issues noted. There were 100 discrepancy reports for minor tile putty repairs. Six chits (change items) were worked on the left side, mostly in the landing gear area. The main landing gear rotational pins, wheel well wire, and landing gear structural components were all inspected. The left inboard brake interference was slightly out of tolerance, but was corrected. One chit addressed the application of corrosion protection coating to the forward wing spar.

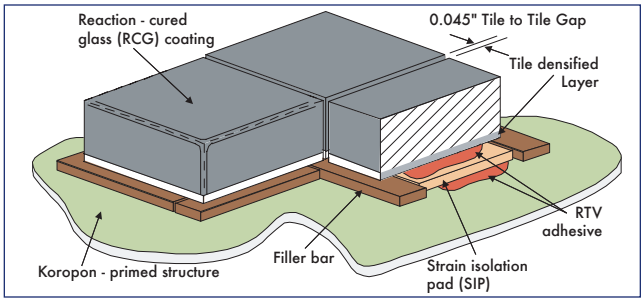


Figure 10-3. Typical tile installation.

Twenty Master Change Records were incorporated during the period. They included the replacement of the aluminized Mylar tape that lines the wheel well walls, the deletion of some non-functional acoustic sensors, and the removal of inactive Modular Auxiliary Data System (MADS) instrumentation. An additional part of that effort was the modification of the elevon columbium seal springs, some wing leading edge protective shielding, and enhancements to various gap fillers.

The 22 left wing Line Replaceable Units (LRUs) that were replaced included the RCC panels previously mentioned, a hydraulic retract valve, the landing gear extend isolation valve, left main landing gear bungee, Tee seals, and an Inconel (Incoflex) insulator.

All items not completed at Palmdale were dispositioned and transferred to KSC for completion.

10.3 Left Wing Processing (STS-109)

Once *Columbia* was delivered to KSC in March 2001, the outstanding main landing gear work was completed. This work included the left inboard axle rework to improve brake clearance and the completion of the rotational pin inspections. The elevon flipper doors had a few PRs for Wear and Tear issues that were resolved. The lower elevon cove columbium seals/springs were out of configuration as compared to drawing requirements, and minor adjustments were successfully made. When it was discovered that there was excessive corrosion protection coating applied to the elevon cove area, work was done to clean that area. There was minor corrosion in the elevon cove area that was removed as well.

There were also numerous tile inspections and verifications performed during the processing flow for STS-109. No work was done on the wing leading edge RCC panels or Tee seals after *Columbia* returned from OMM and prior to STS-109. During that flow work was done on the LESS lower access panels 3, 6, 15, 17, 21, and 22 for step and gap issues and frayed horse collar gap concerns. Upper access panel 14 was replaced due to out-of-tolerance gap and out-of-tolerance Strain Isolation Pad (SIP). No lower tile acreage was replaced during the STS-109 flow, but the upper wing area had a few minor repair areas. All the leading edge and trailing edge panels for the left inboard elevon cove were replaced. Discrepancies were noted at Palmdale and corrected at KSC for the primary and secondary sealing circuits in the elevon cove seal assembly. The seals were operating within acceptable limits, but work was performed to repair leak paths and improve flow rate. There were 1,481 tiles that were suspect and had a manual deflection test performed on them in support of the corrective action required after one wing lower surface tile was found missing/debonded after the STS-103 (orbiter *Discovery*) mission. Thirteen thermal barriers were replaced in the main landing gear door area. There were 14 total MR items for STS-109.

10.4 Left Wing Processing (STS-107)

During the STS-107 flow, damage was noted to the left main landing gear axle sleeve and axle nut. A review of the entire shuttle fleet revealed similar conditions on other vehicles. The tire separation harness for the tire temperature and pressure measurements was found caught in the brake mechanism and had to be removed. The tires were deflated and removed in order to inspect the wheel half-tie bolts. Due to the discovery of corrosion in the tie bolt holes in wheels throughout the fleet, wheels with sleeved tie bolt holes were installed.

The angle seal at RCC panel 1 on the left wing leading edge (see Figure 10-4) was removed to support the evaluation of the horse collar gap filler between the adjacent tiles. During the removal attempt, the upper bushing remained bound with the shipside clevis. During subsequent attempts, the angle seal was manually manipulated to try and remove the preload. During the KSC paper review, structures engineers realized that the load applied to the angle seal was specified to be kept below 20 pounds, but was never recorded in the

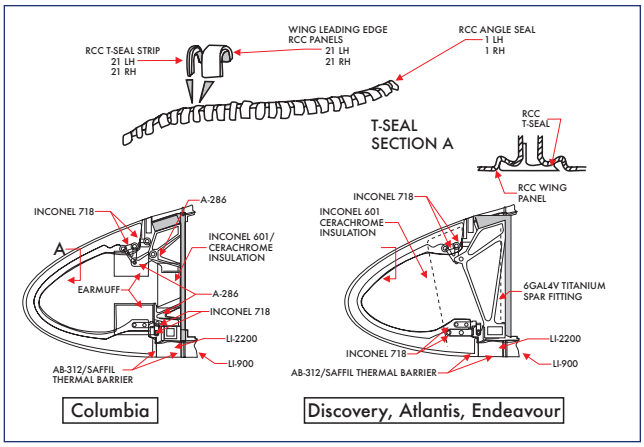


Figure 10-4. Wing leading edge RCC.

paper. The RCC specification requires that RCC panel loads be kept below 30 pounds. Subsequent tests at KSC verified that the angle seal load was below the 30-pound requirement. The LESS prevention and resolution team is addressing the issue of how to measure the load and how to support the seal in future operations. Work continued on the elevon flipper doors. Flipper door 1 blade seal was not making contact with the rub channel, potentially leading to excessive venting from the elevon cove area. This issue surfaced twice during this flow and was Material Review (MR) accepted to fly as is. Modification was made to the Inconel trailing edge seal and bulb seal on the elevon. Additional work was performed on the elevon cove corrosion protection again to reduce the excessiveness of the application.

An uncharacteristic number of access panels were removed during the STS-107 processing flow. Most of the upper (14 of 22) and lower (13 of 22) access panels were removed due to misinterpreted requirements to check for excessive movement in the panels. Wing leading edge upper and lower access panels at RCC 15 had to be removed to retrieve a burned ball of tape that had been inadvertently left from previous work performed during OMM. Upper access panel 18 was removed to investigate the possibility of water intrusion from a water deluge system mishap in the orbiter processing facility, but no damage was noted. Tee seal 10 was removed and shipped to the vendor for repair. No other wing leading edge RCC panels were removed in preparation for the STS-107 mission. Only one access panel was replaced on the left outboard elevon cove area, but there were three other minor tile repairs performed on the left elevons. There were four tiles replaced on the under side of the left wing in front of the left outboard elevon because a gap filler had protruded 0.8 inches. This caused charred filler bar, SIP damage, and instrumentation wiring damage. None of the tiles in these areas is believed to affect the failure scenario. There were 36 total MRs for STS-107.

10.5 RCC Design

The RCC material is the basic structure of the wing leading edge panels (Figure 10-4), the nose cone, the chin panel between the nose cone and the nose landing gear door, and the

forward external tank attach fitting cover plate on the orbiter. Its purpose is to protect the orbiter from local temperatures in excess of 2300 °F. Most RCC panels are designed with a 100-mission fatigue life, but RCC panels 8 through 12 have reduced lives due to higher temperature exposures. Panel 9 has the shortest mission life of 61 missions because it has the highest heating load during entry. RCC panel 17 has the highest aerodynamic load.

The panels were originally arc jet tested. Test data indicated that the multi-use temperature limit of 2960 deg F could be sustained for approximately 600 seconds. They were structurally tested up to a 1.2 factor of safety and eventually certified by analysis up to a 1.4 factor of safety. With these parameters, the panels are certified to 140% of their expected load up to the ultimate strength of the panel. Other significant testing of the RCC panels was not performed due to lack of sufficient time to accomplish the testing prior to the first flight of *Columbia*. RCC panels show no obvious aging effects due to calendar life, but the panels normally lose mission life due to the combined effects of oxygen, high temperature, and high pressure during the entry of each mission.

On *Columbia*, the structure supporting the RCC panels consisted of four attach fittings to mount each RCC panel to the aluminum honeycomb wing leading edge spar. In an effort to reduce the orbiter weight, wing components affecting the RCC installation were redesigned on subsequent vehicles. Beginning with the orbiter *Discovery*, the RCC attachment was accomplished using a single Titanium attach fitting. The wing leading edge spar became a corrugated Aluminum structure. Additional insulation was installed behind each RCC panel on all orbiters to shield the underlying structure from radiative heat damage from the high temperatures that the RCC reaches during entry.

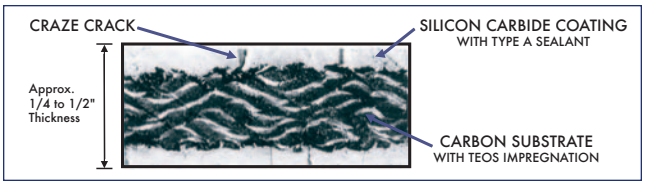


Figure 10-5. RCC cross section.

The RCC is composed of a carbon-based substrate (see Figure 10-5) that provides essentially all of the RCC strength. It is composed of graphitized rayon fabric impregnated with a phenolic resin called Tetraethyl Orthosilicate (TEOS) to provide internal protection against porosity within the laminate. The substrate is covered with a silicon carbide coating also enhanced with TEOS and sealed with a sealant to protect it from oxidation within the substrate. The silicon carbide coating provides no thermal protection for the RCC.

During the manufacturing process, the silicon carbide surface acquires surface craze cracks due to differential contraction during the cooling process. The silicon carbide coating cools faster and contracts more than the carbon substrate during the cooling process. The craze cracks sometimes extend completely through the silicon carbide coating to the carbon substrate. A sodium silicate solution called "Type A Sealant" is applied to the silicon carbide coating to decrease porosity in the surface and fill the crazing cracks. Any erosion of the type A sealant and/or the silicon carbide coating could lead to direct exposure of the carbon fibers in the substrate. This provides a path for oxidation and can potentially lead to subsequent burn through of the RCC panel during entry. Development tests for the RCC never identified a susceptibility to oxidation; therefore, *Columbia* was not treated with the type A sealant until after the first five flights. Beginning in 1992, a double type A (DTA) sealant program was instituted on all vehicles to further enhance the corrosion protection on the wing RCC.

Each time a vehicle returns from space, the entire RCC and Thermal Protection System (TPS) are visually inspected to determine the extent of any damage. Inspections look for RCC impact damage and any indications of flow in the interface between the TPS (tiles) and adjacent RCC. There also exists a test method whereby the RCC panel is pressed with a gloved hand in the vicinity of RCC cracks to determine the integrity of the panel and the existence of potential unacceptable subsurface oxidation. This same test is always performed on RCC panels 6 through 17 near each of the adjoining Tee seals. During each OMM, all RCC components are visually inspected including all the attachment hardware and underlying attachment structure.

During the inspections, a determination is made to either repair, refurbish, or replace the panel as necessary. Repairs are required when there is noticeable damage to the surface of the panel. Field repairs can be made at KSC or Palmdale unless the carbon substrate is exposed. In that case the panels must be sent to the vendor for repair. Refurbishment is required at regular intervals to recoat the panels to increase their resistance to oxidation and mass loss. Occasionally, complete replacement of RCC panels is necessary due to unrepairable damage. Each wing leading edge RCC panel is paired with an associated Tee seal and both of these components are generally replaced/refurbished as a unit.

Columbia has only had three panels/Tee seals replaced over its history. Panels 12R and 10L were removed for destructive testing and pinhole evaluations. Panel 11L had fit problems and was sent to spares. Also, over *Columbia*'s lifetime, seven RCC panels and six seals on the left wing were repaired, and 11 panels and 12 seals were refurbished. All of the *Columbia* RCC panels were within their predicted mission life limits, and most were original panels.

10.6 RCC Impact Resistance

The RCC was not considered part of the TPS for the purposes of impact resistance. The TPS was designed to accommodate particle impacts, such as from hail, rain, runway debris, etc., whose impact energy did not exceed 0.006 foot-pounds to the surface. The wing leading edge RCC impact resistance allowed no damage to the RCC with the application of up to 16 inch-pounds of energy. Figure 10-6 shows RCC impact resistance ranging from 4 to 26 inch-pounds depending on the increasing thickness of the RCC element. Different tests including low velocity and hypervelocity tests have been

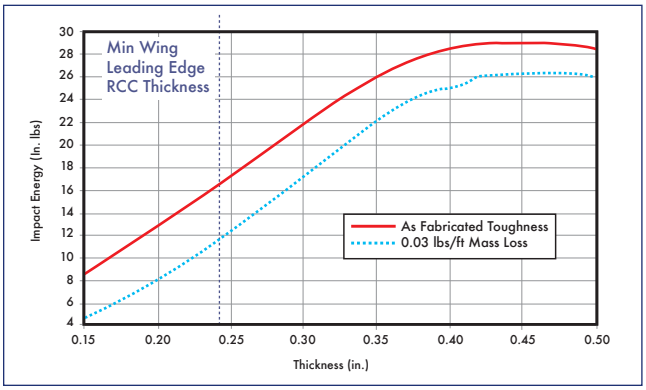


Figure 10-6. RCC impact resistance.

conducted to determine the actual impact resistance of the RCC. Test projectile materials have included nylon, glass, aluminum, steel, lead, and ice and have taken shapes of spheres, bullets, and cylinders. The test results vary widely and appear to be significantly dependent on impact velocity, projectile type, and angle of incidence of impact. Because of the variability of the test results, no actual impact resistance could be defined.

In support of the STS-107 investigation, RCC impact testing was performed at Southwest Research Institute in San Antonio, Texas, by propelling a large piece of foam at high velocity at a previously flown RCC panel. These tests were described earlier in Section 3 and show that RCC material can be damaged by ET foam at impact velocities matching STS-107 debris impact conditions.

10.7 RCC Corrosion

The RCC panels are subject to mass loss due to loss of sealant that can be caused by normal entry heating, impact damage, or even undetected chemical attack. Mass loss results in a decrease in strength, burn resistance, and RCC mission life. Under the high temperatures of entry, the sealant may become molten in the vicinity of pinholes or debris impact areas and migrate, allowing an active oxidation process to begin at the surface. Some mass loss occurs normally during each mission. Mass loss is cumulative over mission life and is determined by analysis. Previously damaged RCC panels have been measured for mass loss using computer tomography, and that data is used in the analysis for all other RCC panels' mass loss determinations. When analysis shows that the 1.4 factor of safety can no longer be maintained, the RCC panel is removed from service. The silicon carbide sealant does not prevent mass loss, but it does help increase corrosion resistance. The sealant must be refurbished periodically, but is usually performed during the most convenient OMM that does not violate the limits listed in Table 10-1.

Subsurface oxidation has been discovered beneath the silicon carbide surface cracks in the sealant and coating which allow the oxidation process to thrive. This process is considered to be an impact to RCC mission design life, but is not generally considered to be a safety of flight issue. This oxidation process (Figure 10-7) starts with the breakdown of

Panels	*Refurbishment Interval*
1-5, 20-22	As required based on visual inspection
6-17	16-18 missions, no calendar limit
18-19	32-36 missions, no calendar limit
Nose Cap	29 missions, no calendar limit

Table 10-1. RCC refurbishment limits.

the coating due to entry heating. Surface craze cracks allow oxygen to migrate to the subsurface carbon fibers and react with them. This increase in oxidation develops into larger crazed areas, which eventually allow pieces to become dislodged due to vibration, aerodynamic, or thermal loads. Once the pieces dislodge, they leave a large path for the oxidation process to continue.

Dry ultrasonic and real-time radiographic inspections have been performed on the panels in the past to look at coating damage. More recently, special non-destructive examinations are being evaluated which include infrared thermography to determine the extent of coating loss.

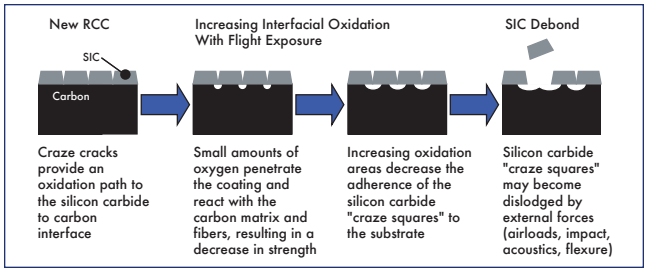


Figure 10-7. RCC corrosion process.

Each wing leading edge RCC panel shares a Tee seal that is used to close the gap between adjacent RCC panels. Following STS-43 (*Atlantis*) in August 1991, routine inspections identified cracks in the web of a Tee seal. The cracks were in the silicon carbide coating and occasionally in the substrate, and were due to normal shrinkage. They were typically less than 1/2 inch long, were not visible to the naked eye, and usually occurred in the web of the seal, on the backside of the seal (Figure 10-8) near the apex rather than on the leading edge. Further examination of the remainder of the shuttle fleet identified 20 (of 132) cracked Tee seals. *Columbia* had 11 Tee seals identified with possible cracks. Detailed inspections determined that all the cracks were typical of the surface craze cracks in the coating. The Tee seal cracks were determined to be caused by warping of the substrate fabric during lay-up during the original build. The Tee seal cracking (Figure 10-9) leads to a reduction in mission life and loss of oxidation protection. All the seals were refurbished with new coating and sealant and were reinstalled. Failure analysis showed that cracks would form after excessive wishbone loading (bending) caused the brittle coating to crack. Crack testing was performed in 1991 on Tee seal 10 (attached to RCC panel 9) from the left wing of *Columbia* to try to determine the crack mechanism. The Tee seal was cycled 400 times in bending up to 70% of its ultimate load and no dis-

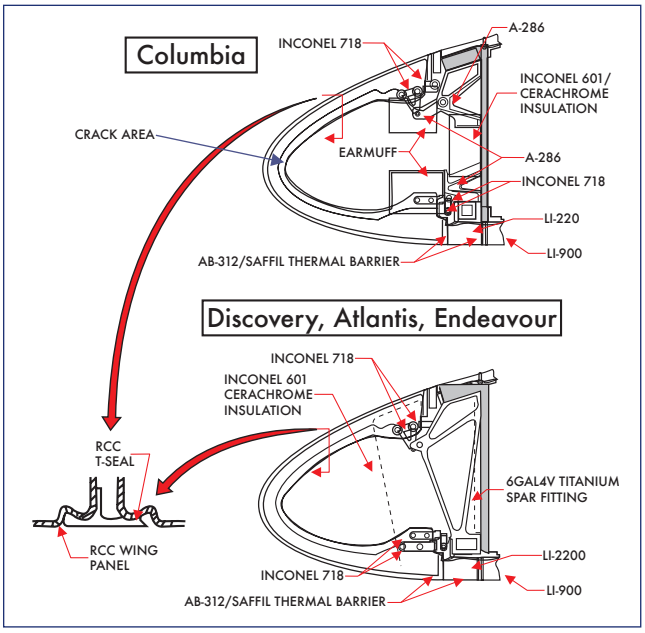


Figure 10-8. Tee seal crack location.

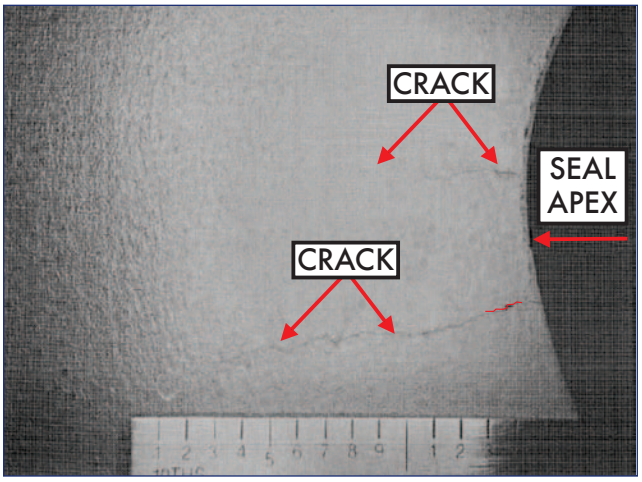


Figure 10-9. Tee seal cracking.

cernable damage was noted. After an engineering evaluation was performed on the health and strength of the Tee seal, it was subsequently reinstalled on *Columbia*.

Another phenomenon, discovered first on *Columbia* after STS-50 landed, was the existence of pinholes (Figure 10-10) in the RCC panels. The pinholes were found primarily in the wing leading edge RCC and were subsequently identified on all orbiters. Testing has shown that the pinholes are most likely the result of the accelerated oxidation process involving zinc oxide and the silicon carbide coating. The reaction of the zinc oxide and the silicon carbide produces a silica (glass) exudate that flows out of the pinhole area. The presence of zinc oxide is theorized to originate from the paint primer used to recondition the launch pad after each mission and is considered an accelerator to the oxidation process. The zinc-based contamination accumulates on the wing leading edge RCC as rainwater drips off of the launch pad. This contamination rests on the RCC without reacting to the surface material while at ambient conditions at the pad. All of the damaging oxidation occurs once the RCC is exposed to the high temperatures, pressures, and excess oxygen of reentry. Only a few pinholes have been observed on the nose cap RCC, most likely because the nose cap remains under a protective cover while at the launch pad. It is also believed that sodium chloride contributes to the oxidation process, but to a much lesser extent than the zinc oxide.

In 1997, pinhole acceptance criteria were established. Pinholes with surface dimensions less than 0.040 inches discovered during routine processing flows are acceptable to fly as is for up to 16 missions unless the carbon substrate is exposed, in which case the panel must be repaired. Pinholes discovered at OMM greater than 0.040 inches are unacceptable. Although the pinholes themselves constitute only a small mass loss, they are not considered to be a safety-of-flight issue by themselves. Analysis has identified that the sustainable thru-hole size in-flight due to orbital debris is 0.25 inches in the lower surfaces of RCC panels 5-13. A hole under 1 inch in diameter anywhere else in the RCC is considered survivable for a single mission.

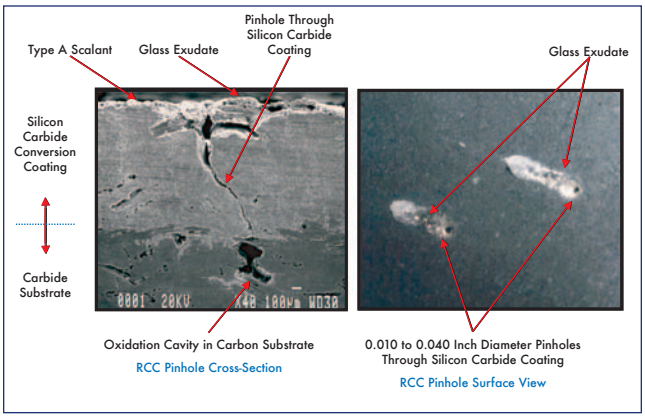


Figure 10-10. RCC pinholes.

There have been damaged RCC panels that were discovered after the vehicle returned from space on various missions. Some of the impact damage was only to the surface, but some even caused damage to the coating on the backside of the panel. In 1992, after STS-45, significant impact damage (overall length of ~1.75 inches) was noted on RCC panel

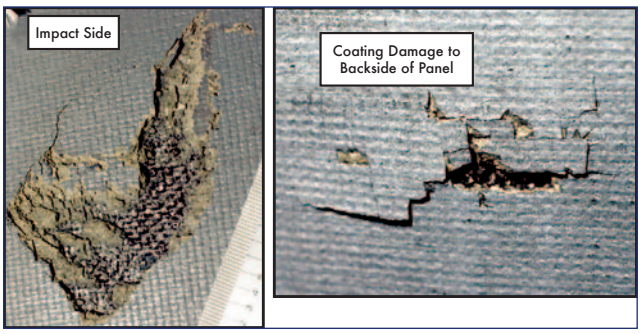


Figure 10-11. RCC impact damage.

10R on *Atlantis*. The damage (Figure 10-11) was theorized to come from orbital debris or micrometeorite impacts during the mission. This type of RCC damage is of particular concern in that a significant impact could cause a hole in the RCC large enough to lead to wing spar burn through and subsequent loss of crew and vehicle. At that time, the maximum acceptable hole size (0.040") criterion was established for processing flows and advanced wing leading edge internal insulation was modified to reduce the risk should hot gas penetrate the RCC.

There has been a history of loose bolts on access panels on all orbiters. Following STS-87, the right-hand lower access panel 4 had a loose bolt. All other installations were inspected and several additional bolts were found with low torque. All bolts were subsequently torqued to their proper values. During STS-95, the OMS pod Y-web door area had some damaged insulation. It was determined post-flight that there were bolts in the area that had low torque. A review of other orbiters identified low torque bolts on *Discovery* and *Endeavour*. Low torque bolts were also found during *Columbia*'s last OMM. The low torque was attributed to the performance of an improper torque sequence. All attach fittings were removed and reinstalled using the correct torque sequence.

11.0 External Tank

11.1 Introduction

The External Tank (ET) used for STS-107 was Light Weight Tank (LWT) number ET-93. This tank was the first LWT to be used with a cluster of three Block-II Space Shuttle Main Engines (SSMEs). As discussed in Section 3, there is significant visual and debris trajectory data to implicate the left bipod ramp area as the source of debris. Contributors to forward bipod thermal protection system (TPS) foam loss were: (1) the design, verification, and process validation did not encompass all material and processing variability or adequately address all failure modes, and (2) the acceptance testing and inspection techniques and procedures were not designed to be capable of rejecting ramps with adverse "as-built" features which would threaten the TPS integrity.

11.2 TPS Requirements

During prelaunch, the ET TPS minimizes ice formation and maintains the quality of cryogenic propellant. During ascent, the ET TPS maintains the structure within design temperature limits. Program requirements (NSTS 07700, Vol. X, Book I, Paragraph 3.2.1.2.14) indicate that the ET "shall be designed to preclude the shedding of ice and/or other debris that would jeopardize the flight crew, vehicle, mission success, or would adversely impact turnaround operations." During ET entry, the TPS assures a predictable, low altitude ET break-up that meets the ET entry impact footprint boundary limits.

The ET TPS itself is designed to have low density to maximize Shuttle payload capacity, high adhesion to cryogenic surfaces (-423 °F), resistance to thermal abrasion and degradation from aerodynamic shear, consistency (material qualified is the material flying), and environmental resistance to ultraviolet radiation, rain, etc. The application of ET TPS materials includes computer controlled automatic spray cells and manual application in normal working environments.

11.3 History of Foam Changes and Debris Events

The ET TPS history is marked by multiple material and configuration changes resulting from ET TPS and ice loss events, design enhancements, environmental regulations (especially blowing agent changes), and supplier changes. The history of foam changes is outlined in Figure 11-1, and Table 11-1 lists the ET flight history, as well as age and exposure data. Thousands of tests have been conducted to develop and qualify the ET TPS. There were no first time ET TPS changes on STS-107/ET-93 except for rework of the TPS on the upper aft ET/Solid Rocket Booster (SRB) fitting fairing (following SRB demate) using BX-265. Basic bipod TPS materials had not changed from the beginning of the program until after ET-93. The bipod TPS configuration has been stable since 1983, when with ET-14 the ramp angle was changed. At ET-76 in 1995, there was one minor change to the ramp intersection with the ET intertank area. At ET-116 in 2002, the bipod material was changed to BX-265, but ET-93 had been constructed with BX-250. No indication has been found that any specific ET TPS foam change or any combination of historical ET TPS foam changes alone caused the bipod foam loss on STS-107/ET-93.

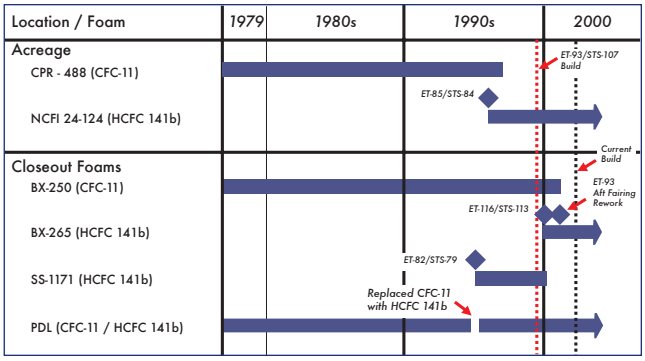


Figure 11-1. History of foam changes. Blowing agent shown in parentheses. No changes to SLA.

ET debris has been observed throughout program history, including both ET TPS and ice debris. Since STS-1, imagery was available on about 80 missions, and debris has been confirmed on at least 62 missions. At least six missions lost portions of the left bipod ramp (see Section 3.5). TPS loss on the right bipod ramp has never been observed. A portion of the left bipod ramp was lost during STS-112 ascent and impacted the left SRB Integrated Electronics Assembly. No changes were made to STS-113 or STS-107 bipod ramp configurations after this event.

The majority of ET debris events have been limited to small mass (< 0.2 lbs). A definitive correlation to orbiter damage is difficult except for major debris events such as STS-27R, which was identified as SRB ablator debris, and STS-87,

which was attributed to ET intertank foam loss. Based on available historical data, the bipod ramp represents the source of the largest pieces of ET debris (estimated > 1.0 lbs), and LO2 feedline bellows ice is second (estimated < 0.3 lbs).

11.4 STS-107/ET-93 Chronology

Ascent film indicates that the origin of STS-107 ET TPS loss was from the forward bipod area (see Section 3). Image-based size estimates support this to be the bipod ramp rather than flange or acreage foam. The history of bipod TPS loss provides additional supporting evidence. Available data supports the bipod ramp as the most probable point of origin of STS-107 debris.

11.4.1 Bipod Ramp TPS Configuration

The forward bipod TPS configuration includes a complex combination of foams, Super Light Ablator (SLA), and underlying bipod structural substrate elements. The bipod ramp configuration has been essentially stable since early in the program. There have been no changes in material until after ET-93 and only minimal changes to configuration, processing, and personnel certification and training. The BX-250 ramp angle has been constant since 1983, when with ET-14, the ramp angle was changed to 30° maximum with a 5.0 ±1.0 inch radius at the forward edge (changed from 45° ± 5.0° with no radius at the forward edge). This was changed as a result of suspected foam debris on STS-7/ET-6. For ET-76 in 1995, there was one minor change to the forward ramp intersection with the ET intertank area; the 5.0 ±1 inch radius was changed to a straight termination line with a 0.25-inch step allowed. At ET-116 in 2002, the bipod material was changed to BX-265, but ET-93 was BX-250. There has been no indication that the bipod ramp configuration changes affected the observed STS-107/ET-93 bipod foam loss.

STS	STS aka	OV	ET	ET wt.	Date	ET Age @ Launch (days)	ET Exposure @ Launch (days)
1		Columbia	1	ET	04/12/81	653	105
2		Columbia	2	ET	11/12/81	258	74
3		Columbia	3	ET	03/22/82	175	35
4		Columbia	4	ET	06/27/82	161	33
5		Columbia	5	ET	11/11/82	169	52
6		Challenger	8	LWT	04/04/83	208	126
7		Challenger	6	ET	06/18/83	327	24
8		Challenger	9	LWT	08/30/83	230	29
9		Columbia	11	LWT	11/28/83	206	43
11	41B	Challenger	10	LWT	02/03/84	339	23
13	41C	Challenger	12	LWT	04/06/84	259	19
14	41D	Discovery	13	LWT	08/30/84	352	79
17	41G	Challenger	15	LWT	10/05/84	295	23
19	51A	Discovery	16	LWT	11/08/84	286	17
20	51C	Discovery	14	LWT	01/24/85	448	20
23	51D	Discovery	18	LWT	04/12/85	353	16
24	51B	Challenger	17	LWT	04/29/85	409	33
25	51G	Discovery	20	LWT	06/17/85	347	14
26	51F	Challenger	19	LWT	07/29/85	431	31
27	51I	Discovery	21	LWT	08/27/85	398	22
28	51J	Atlantis	25	LWT	10/03/85	287	35
30	61A	Challenger	24	LWT	10/30/85	348	15
31	61B	Atlantis	22	LWT	11/26/85	459	15
32	61C	Columbia	30	LWT	01/12/86	208	42
33	51L	Challenger	26	LWT	01/28/86	319	38
26R		Discovery	28	LWT	09/28/88	1261	87
27R		Atlantis	23	LWT	01/02/89	1561	62
29R		Discovery	36	LWT	03/13/89	1189	39

Table 11-1. STS-Orbiter-ET configuration, age, and exposure.

[continued on next page]

STS	STS aka	OV	ET	ET wt.	Date	ET Age @ Launch (days)	ET Exposure @ Launch (days)
30R		*Atlantis*	29	LWT	05/04/89	1450	44
28R		*Columbia*	31	LWT	08/08/89	1484	25
34		*Atlantis*	27	LWT	10/18/89	1723	51
33R		*Discovery*	38	LWT	11/22/89	1317	27
32R		*Columbia*	32	LWT	01/09/90	1609	43
36		*Atlantis*	33	LWT	02/28/90	1597	35
31R		*Discovery*	34	LWT	04/24/90	1674	40
41		*Discovery*	39	LWT	10/06/90	1635	32
38		*Atlantis*	40	LWT	11/15/90	1609	88
35		*Columbia*	35	LWT	12/02/90	1850	164
37		*Atlantis*	37	LWT	04/05/91	1906	22
39		*Discovery*	46	LWT	04/28/91	1327	49
40		*Columbia*	41	LWT	06/05/91	1776	35
43		*Atlantis*	47	LWT	08/02/91	1323	39
48		*Discovery*	42	LWT	09/12/91	1829	32
44		*Atlantis*	53	LWT	11/24/91	846	33
42		*Discovery*	52	LWT	01/22/92	994	35
45		*Atlantis*	44	LWT	03/24/92	1840	34
49		*Endeavour*	43	LWT	05/07/92	2005	56
50		*Columbia*	50	LWT	06/25/92	1333	23
46		*Atlantis*	48	LWT	07/31/92	1561	51
47		*Endeavour*	45	LWT	09/12/92	1923	19
52		*Columbia*	55	LWT	10/22/92	994	27
53		*Discovery*	49	LWT	12/02/92	1577	25
54		*Endeavour*	51	LWT	01/13/93	1440	42
56		*Discovery*	54	LWT	04/08/93	1256	25
55		*Columbia*	56	LWT	04/26/93	1082	79
57		*Endeavour*	58	LWT	06/21/93	979	55
51		*Discovery*	59	LWT	09/12/93	900	80
58		*Columbia*	57	LWT	10/18/93	1180	33
61		*Endeavour*	60	LWT	12/02/93	889	36
60		*Discovery*	61	LWT	02/03/94	842	25
62		*Columbia*	62	LWT	03/04/94	773	23
59		*Endeavour*	63	LWT	04/09/94	737	22
65		*Columbia*	64	LWT	07/08/94	718	24
64		*Discovery*	66	LWT	09/09/94	591	23
68		*Endeavour*	65	LWT	09/30/94	697	47
66		*Atlantis*	67	LWT	11/03/94	535	25
63		*Discovery*	68	LWT	02/03/95	546	25
67		*Endeavour*	69	LWT	03/02/95	484	23
71		*Atlantis*	70	LWT	06/27/95	495	63
70		*Discovery*	71	LWT	07/13/95	435	58

Table 11-1 (continued). STS-Orbiter-ET configuration, age, and exposure. *[continued on next page]*

STS	STS aka	OV	ET	ET wt.	Date	ET Age @ Launch (days)	ET Exposure @ Launch (days)
69		Endeavour	72	LWT	09/07/95	433	59
73		Discovery	73	LWT	10/20/95	381	54
74		Atlantis	74	LWT	11/12/95	360	33
72		Endeavour	75	LWT	01/11/96	342	37
75		Columbia	76	LWT	02/22/96	330	25
76		Atlantis	77	LWT	03/22/96	303	24
77		Endeavour	78	LWT	05/19/96	307	34
78		Columbia	79	LWT	06/20/96	281	23
79		Atlantis	82	LWT	09/16/96	188	38
80		Columbia	80	LWT	11/19/96	368	35
81		Atlantis	83	LWT	01/12/97	262	34
82		Discovery	81	LWT	02/11/97	390	26
51		Discovery	59	LWT	09/12/93	900	80
58		Columbia	57	LWT	10/18/93	1180	33
61		Endeavour	60	LWT	12/02/93	889	36
60		Discovery	61	LWT	02/03/94	842	25
62		Columbia	62	LWT	03/04/94	773	23
59		Endeavour	63	LWT	04/09/94	737	22
65		Columbia	64	LWT	07/08/94	718	24
64		Discovery	66	LWT	09/09/94	591	23
68		Endeavour	65	LWT	09/30/94	697	47
66		Atlantis	67	LWT	11/03/94	535	25
63		Discovery	68	LWT	02/03/95	546	25
67		Endeavour	69	LWT	03/02/95	484	23
71		Atlantis	70	LWT	06/27/95	495	63
70		Discovery	71	LWT	07/13/95	435	58
69		Endeavour	72	LWT	09/07/95	433	59
73		Discovery	73	LWT	10/20/95	381	54
74		Atlantis	74	LWT	11/12/95	360	33
72		Endeavour	75	LWT	01/11/96	342	37
75		Columbia	76	LWT	02/22/96	330	25
76		Atlantis	77	LWT	03/22/96	303	24
77		Endeavour	78	LWT	05/19/96	307	34
78		Columbia	79	LWT	06/20/96	281	23
79		Atlantis	82	LWT	09/16/96	188	38
80		Columbia	80	LWT	11/19/96	368	35
81		Atlantis	83	LWT	01/12/97	262	34
82		Discovery	81	LWT	02/11/97	390	26
83		Columbia	84	LWT	04/04/97	291	25
84		Atlantis	85	LWT	05/15/97	281	22
94		Columbia	86	LWT	07/01/97	266	21
85		Discovery	87	LWT	08/07/97	246	25

Table 11-1 (continued). STS-Orbiter-ET configuration, age, and exposure.

[continued on next page]

STS	STS aka	OV	ET	ET wt.	Date	ET Age @ Launch (days)	ET Exposure @ Launch (days)
86		*Atlantis*	88	LWT	09/25/97	251	39
87		*Columbia*	89	LWT	11/19/97	146	22
89		*Endeavour*	90	LWT	01/22/98	167	35
90		*Discovery*	91	LWT	04/17/98	154	26
91		*Discovery*	96	SLWT	06/02/98	141	32
95		*Discovery*	98	SLWT	10/29/98	147	39
88		*Endeavour*	97	SLWT	12/04/98	249	47
96		*Discovery*	100	SLWT	05/27/99	183	24
93		*Columbia*	99	SLWT	07/23/99	360	47
103		*Discovery*	101	SLWT	12/19/99	24	37
99		*Endeavour*	92	LWT	02/11/00	298	61
101		*Atlantis*	102	SLWT	05/19/00	473	56
106		*Atlantis*	103	SLWT	09/08/00	444	26
92		*Discovery*	104	SLWT	10/11/00	498	31
97		*Endeavour*	105	SLWT	11/30/00	503	31
98		*Atlantis*	106	SLWT	02/07/01	418	30
102		*Discovery*	107	SLWT	03/08/01	455	25
100		*Endeavour*	108	SLWT	04/19/01	434	29
104		*Atlantis*	109	SLWT	07/12/01	435	22
105		*Discovery*	110	SLWT	08/10/01	380	40
108		*Endeavour*	111	SLWT	12/05/01	258	36
109		*Atlantis*	112	SLWT	03/01/02	358	38
110		*Atlantis*	114	SLWT	04/08/02	294	28
111		*Endeavour*	113	SLWT	06/05/02	401	38
112		*Atlantis*	115	SLWT	10/07/02	376	28
113		*Endeavour*	116	SLWT	11/23/02	360	43
107		*Columbia*	93	LWT	01/16/03	805	39

Table 11-1 (concluded). STS-Orbiter-ET configuration, age, and exposure.

11.4.1.1 Left and Right Bipod Ramp Differences

TPS loss on the right bipod ramp has never been observed. Launch/ascent imagery from ground assets is less favorable for seeing right bipod foam loss as compared to the left bipod, and post-ET separation crew imagery is random between imaging the left or right bipod ramps.

There is no flight or test data to explain why the –Y (left) bipod looses foam and the +Y (right) does not. The Shuttle Program only provides the –Y ramp air loads as a worst case for ET project analysis. There are several bipod configuration differences that may contribute to foam not coming off the +Y ramp. First, the foam ramp is configured slightly differently to accommodate the inboard strut for the LO2 feed line support structure (see Figure 11-2). Second, the proximity of the right bipod to the LO2 feedline could potentially influence local surface pressure causing a lower internal to

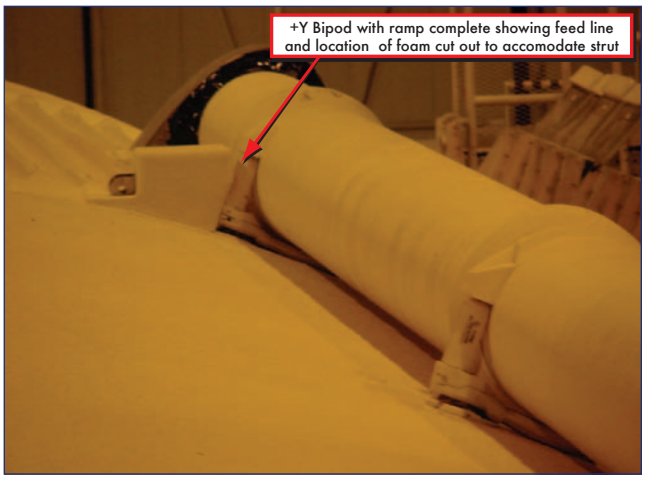


Figure 11-2. Right (+Y) bipod ramp.

external pressure differential (see Figure 11-3). Finally, the outboard and aft facing surface of the –Y bipod may experience lower surface pressure due to flow separation and other local effects relative to the +Y side. If the internal ramp pressure was high due to adverse "as-built" features in the ramp, this could lead to a higher differential pressure on the –Y versus the +Y ramp. However, the aerodynamic loads analysis reviewed in Section 3.5 shows that the loads on both ramps are below their design requirements.

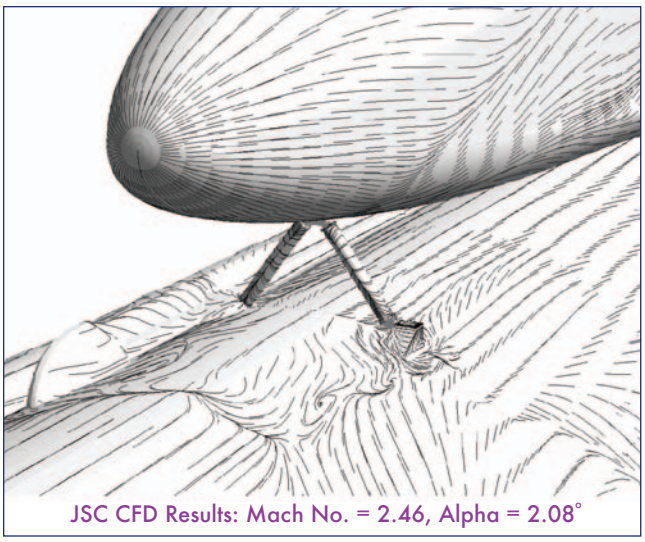


Figure 11-3. Left and right bipod ramp flow differences, CFD results.

11.4.2 Bipod Ramp Certification

The BX-250 foam was supplied to the ET project as a flight verified material from the Saturn Program. A review of material properties certification indicated forward bipod materials met material performance requirements including thermal recession properties at design ascent heating rates, thermal conductivity to preclude ice formation and to maintain cryogenic propellant quality during prelaunch, and mechanical properties.

Process validation was performed by similarity of "flight-like" design substrate configurations. There had been no specific bipod dissection prior to the STS-107/ET-93 investigation. Dissection of the bipod ramps from the production flow provided insight that the bipod ramp could contain unique adverse "as-built" features. The features identified during these recent dissections could potentially reduce the strength of the foam and result in foam failure and subsequent debris.

For the bipod ramp, there was no robust evaluation of the manual spray process. The complexity of the manual spray process of the forward bipod TPS closeout leads to unique defects in this area including voids, rollovers, and TPS discontinuities. The configuration of the forward bipod BX-250 foam was verified based on similarity to the Protuberance Air Load (PAL) ramp, which did not address all aspects and failure mechanisms in combination with critical environments (adverse "as-built" features). The interaction of the underlying SLA configuration interfacial boundary and the potential effects of cryopumping were not considered. The design, verification, and process validation did not encompass all material and processing variability or adequately address all failure modes.

11.4.3 Bipod Ramp Build Process

Experienced certified practitioners performed the ET-93 bipod ramp BX-250 sprays, each with over 20 years experience. No indications of sprayer error were found. Procedures were followed and documented, and processes were within control limits (e.g., material specifications, temperature, and humidity) except that the process plan review found no Quality Control (QC) verification of overlap timing. There is no requirement to verify the overlap timing, and the impact of the overlap timing verification is not known.

Dissection results of five ET TPS configurations demonstrated the forward bipod as the configuration with the most significant defects. Defects are driven by the variable manual spray process and complex contour substrate. This creates the potential for a combination of large voids or defects at critical locations needed to produce a significant foam loss. The designed-in process plan controls related to QC buy-off of critical parameters did not preclude introduction of adverse "as-built" features resulting from the complex and variable forward bipod manual spray operation. There is also variability in the response of the foam based on inherent randomness of the foam cell structure. It may not be possible to control a manual process well enough to preclude defects in the bipod ramp.

11.4.4 Bipod Ramp Foam Acceptance/Non-Destructive Evaluation

ET BX-250 ramp foam build acceptance processes include localized plug pull and core tests of the ramp material prior to final trim configuration. The plug-pulls are taken from trimmed-off over-spray lead-in/lead-out areas (witness, or sample panels) on either side of the ramp to provide density, final visual inspections, and dimensional features. Post-build inspection techniques are limited to visual inspections only. There were no anomalies found with the STS-107/ET-93 forward bipod ramp using inspection and acceptance techniques available at Michoud Assembly Facility (MAF).

Previous efforts to implement robust foam Non-Destructive Evaluation (NDE) techniques were unsuccessful (a variety of techniques were attempted). Some progress was made in certain areas, but it never reached a fully qualified approach and the MAF effort was discontinued in 1993. Development efforts found many false positives and many missed defects. NDE methods in use at MAF were not able to identify adverse "as-built" features in the forward bipod BX-250 ramp, which could combine with nominal environments and create debris. Acceptance testing and inspection techniques and procedures were not designed to be capable of rejecting ramps with adverse "as-built" features that would threaten the TPS integrity.

11.4.5 ET Shipping and Handling

Post-build activities include storage at MAF, shipment to Kennedy Space Center (KSC), storage at KSC, and mating to the SRBs and orbiter. Extensive documentation governs the steps taken to care for the ET. Documentation review found no issues in ET-93 processing paperwork. Storage took place in locked, limited-access facilities. The tanks were shipped pressurized with nitrogen to 6.0 ± 0.5 psi per requirements. At KSC, the LH2 tank pressurant is changed to helium and the pressure on each tank is checked at least twice per week per requirements. Visual inspections were performed every 90 days while in storage. ET-93 was inspected seven times between arrival at KSC and launch, not counting additional daily inspections when mated to the SRBs. Processes were in place and followed to ensure that shipping and handling were performed in a manner that minimizes damage to the ET.

11.4.6 KSC Processing Activities

The shuttle flight manifest was delayed due to cracks found during inspections of Main Propulsion System feedline flow liners on *Atlantis* in June 2002. The final manifest moved STS-112 and STS-113 ahead of STS-107. ET-93 was demated from SRBs BI-114/RSRM-86 and later mated to SRBs BI-116/RSRM-88, and SRBs BI-114/RSRM-86 were used for STS-113. All mate/de-mate operations were carried out in accordance with standard procedures, and are outlined in Figure 11-4. There are no indications that KSC ET processing (ET shipping, handling, and processing) contributed to the bipod foam loss on STS-107/ET-93.

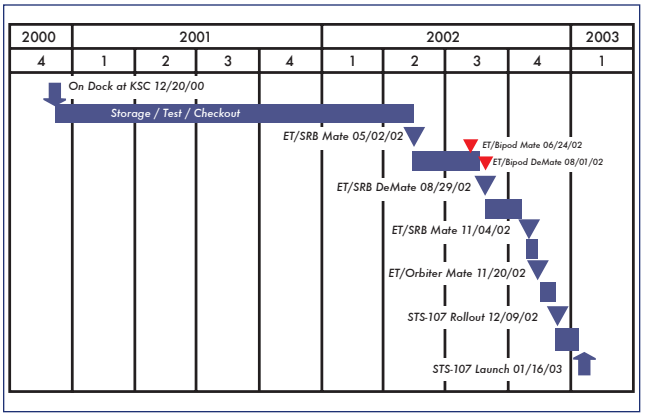


Figure 11-4. ET-93 processing timeline at KSC.

11.4.6.1 ET-93 Mate/De-Mate/Re-Mate

The ET-93 bipod struts were installed, and then later removed during de-mate and re-installed. This process has been performed at least six times during the Shuttle program. ET-11 was used on STS-9, but there is no imagery to confirm ET foam loss. ET-13 was used on STS-14 (41D), but again there is no imagery to confirm ET foam loss. ET-23 was used on STS-27R with handheld video imagery available that does not show the bipod ramps, but no foam loss was observed elsewhere. ET-23 was mated and de-mated during checkout of the Vandenberg Air Force Base facilities. STS-27R had a great amount of tile damage thought to be due to the loss of SRB ablator during launch. ET-37 was used on STS-38 but there is no imagery to confirm ET foam loss. ET-80 was used on STS-80, and there were two lost divots on the flange under the bipod and one 10-inch diameter divot on the intertank forward of the bipods. ET-86 was used on STS-94 and the left bipod strut was installed upside down then re-installed correctly. The bipod ramps were visible and no bipod foam loss was noted.

11.4.6.2 ET-93 Crushed Foam

On ET-93, crushed foam (1.5" x 1.25" x 0.187") was seen after the –Y strut removal at the clevis. The thickness of foam in this area is 2.187 inches. Exposed crushed foam is not permissible outside of specific acceptance criteria, so a Problem Report (PR VG-389216) was written to evaluate the condition. The crushed foam was essentially covered up after mating to a new set of bipod struts. No data is available to determine if this section of foam could have been the source of, or contributed to, a void or leak path for liquid or gas.

Inspection of the region after installation of the bipod struts showed that the crushed foam did not extend farther than 0.75" beyond the bipod fitting-clevis joint, which is within acceptable limits. Dye penetration testing with recreated conditions indicated that the damage extended 0.25 inches from the visible mark and 0.5 inches into the surface of the foam, where the damage stopped.

The Material Review Board (MRB) decided to "use as is," and STS-107 launched with crushed foam contained behind the –Y bipod strut clevis. Crushed foam in this area is a nominal configuration, and the PR was only written for documentation for bipod strut removal and future inspections. Available data indicates that every flight may have crushed foam beneath the bipod strut. Review of the ET-93 PR, MAF testing, and the ET-117 strut removal provided evidence that crushed foam had no impact on performance, both thermal and structural. Data are inconclusive as to whether the crushed foam and bipod foam loss are associated.

11.4.7 ET Pre-launch Operations

The electrical system performance was nominal based on evaluation of pre-launch data and post flight inspection of ground electrical interfaces and SRB hardware. No anomalous conditions were identified during STS-107 visual inspections during launch operations: preflight, tanking ice team, video surveillance, and postflight walk down. There are no indications that ET pre-launch operations at KSC contributed to bipod foam loss on STS-107/ET-93.

11.4.8 Launch/Ascent

The ET-93 propulsion system performance was within design limits based on preflight predictions and postflight reconstruction. Comparison to historical performance showed performance within flight history experience for LWT, Super Light Weight Tank (SLWT), and Block II SSME. The STS-107 trajectory was within design limits through-

out ascent. There were no anomalous angles of attack or dynamic pressure indications (see Section 3.5). STS-107 reconstructed air loads were within design limits, and no unique observations were associated with STS-107/ET-93. It is unlikely that any significant bipod structural loads were associated with the 62 second wind shear event followed by a 0.6 Hz RSRM gimbal reaction associated with LO2 slosh (see Section 3.5 and sections below). No anomalous structural loads have been identified. Best-estimated trajectory loads and flex body loads assessment reconstructions show the ET interfaces to be well within design limits. Bipod interface vehicle loads are not considered "driving" environments for the bipod foam ramp. Adjacent structural stiffness precludes significant induced bipod ramp deflections from the interface strut loads. The majority of flexural loading on the bipod ramp results from cryogenic shrinkage of the LH2 tank prior to lift-off. STS-107 ascent thermal environments were within design limits based on analysis of flight data and ET system performance. A higher LH2 tank ullage preflight pressurization pressure (pre-press) is required for flights with Block-II SSME clusters. This helps reduce spikes in the high-pressure fuel turbopump turbine discharge temperatures during start. The LWT was certified for higher pre-press and approved for ET-92 and subsequent flights by Interface Revision Notice (IRN) IC-1432 on 8-28-98.

Data are inconclusive as to whether the STS-107 ascent environments contributed to the bipod foam loss on ET-93.

11.4.8.1 ET LO2 Slosh Baffle Changes

Eight ET LO2 slosh baffles were used until ET-14 in 1983. Vehicle stability analysis based on development flight instrumentation confirmed minimum LO2 sloshing disturbances and Space Shuttle Program LO2 damping requirements were subsequently reduced. Analysis and sub-scale test showed the baffle count could be reduced from eight to two and still maintain margin, but a reduction to four was selected as a trade off between cost benefit and weight reduction (see Figure 11-5).

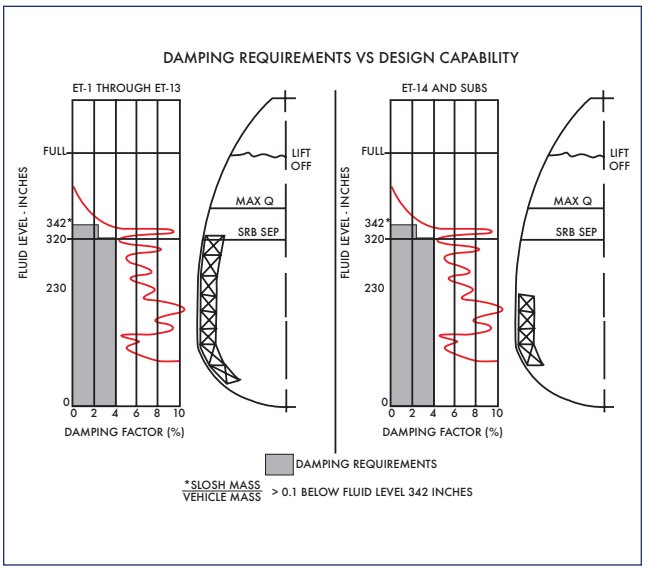


Figure 11-5. ET LO2 slosh baffle changes – ET-14.

One weight saving feature of the SLWT is the removal of one more slosh baffles section, as shown in Figure 11-6. This gives a predicted performance gain of 92 pounds. This feature was incorporated into the LWT at ET-87 in 1996 to reduce weight and diminish the number of first time configuration changes for the subsequent first flight of the SLWT. Dynamics analysis showed available damping remained within requirements and propulsion and stress analysis also remained within requirements. Data are inconclusive as to whether the ET LO2 slosh baffle configuration alone caused bipod foam loss on STS-107/ET-93.

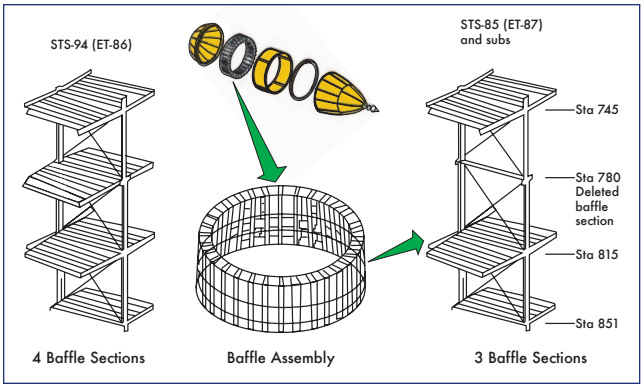


Figure 11-6. ET LO2 slosh baffle changes – ET-87.

11.4.9 Possible Contributors to Strain Energy at ET Separation

The Space Shuttle Program Loads Panel is continuing to work actions to identify potential contributors to strain energy that could have led to the off-nominal yaw rate at ET separation described in Section 3.5. For induced loads during ground operations, KSC is reviewing handling and stacking (orbiter and Ground Ops). For loads that occurred during flight, Boeing GNC is looking into the left side thermal event at 300 seconds MET and if the mechanical load overcomes the joint preload during ascent. The ET project is looking into loads induced through cryogenic and pressurization cycles and the effects on the ET, such as shrinkage of the diagonal strut and overall shrinkage of the ET affecting the forward and aft attachments. The data are inconclusive as to whether potential strain energy at ET separation can be associated with events that caused bipod foam loss on STS-107/ET-93.

11.5 STS-107/ET-93 TPS Bipod Debris

11.5.1 Bipod Foam Failure Modes and Contributors

Four basic possible bipod failure modes have been identified (shown in Figure 11-7) and each may occur alone or act in combination with each other. However, due to lack of bipod instrumentation, it is impossible to know exactly why part of the left bipod foam came off ET-93 during STS-107 ascent. Cracking is a break in the foam, which does not exhibit material loss and is typically perpendicular to the substrate. Debond or delamination is a separation of the material running along the substrate or layer lines. A divot is a piece of

material dislodged from the surface resulting in a cavity, which may or may not expose the substrate. Shear is the removal or separation of material within the cell structure and is not confined to the layer lines of the material, but is parallel to the substrate.

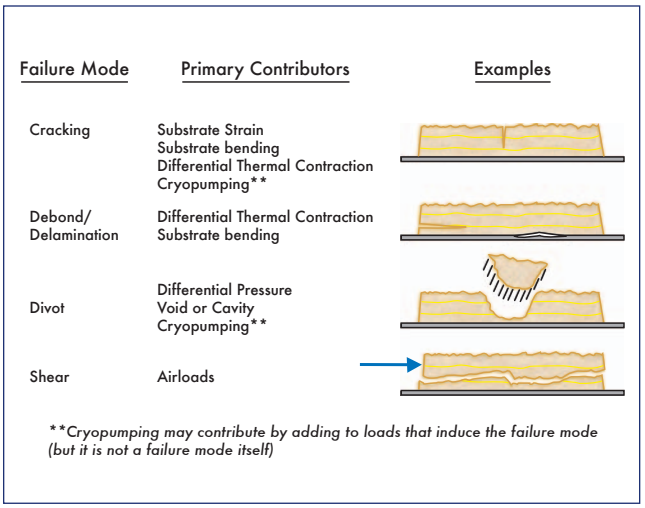


Figure 11-7. Bipod foam failure modes.

Cryopumping could contribute to bipod foam loss, shown schematically in Figure 11-8. The mechanism that drives cryopumping is the transformation of a gas to a liquid at cryogenic temperatures. Gases may condense within a void or porous material at low temperatures. Air in cavities or porous material liquefies when in contact with structure below -297°F for oxygen or -320°F for nitrogen. Pressure is reduced locally due to the condensation. If a leak path exists, more air will be "pumped," providing more gas to condense. When the structure warms, the consequence of cryopumping is that the liquefied air returns to the gaseous state with a local pressure increase. If the leak path is large, gas escapes with no detrimental effect. However, if the leak path is small, cracks may form in the TPS to relieve pressure, or a rapid increase in pressure may result in a divot. In order for this to occur, the inlet source must be blocked off to avoid venting out the inlet. It should be noted that testing has been unable to demonstrate cryopumping in this application.

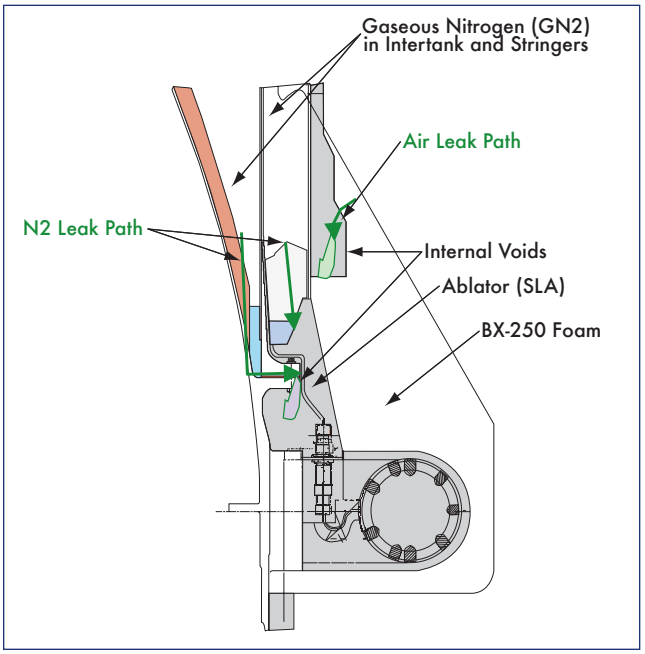


Figure 11-8. Schematic of bipod ramp - potential cryopumping.

11.5.2 Test Results for Debris Assessment

Bipod TPS static and dynamic coupon tests were performed (test ET-TR-003). The objectives of these tests were to evaluate the BX-250/SLA hand-pack (HP) bond line laminate mechanical properties and investigate whether liberated BX-250 material could "pull" or "tear" SLA HP material from the bipod region. Analysis shows the critical bipod Spray-On Foam Insulation (SOFI) ramp failure mode due to direct air load is shear failure between SOFI ramp and bipod fitting substrate.

Testing shows that the potential loss of BX-250 does not liberate hand packed SLA due to impulse loading for cryogenic applications; the BX-250 fails before the SLA. For shear, testing shows BX-250 fails before SLA at all test temperatures. For tension, testing shows BX-250 fails before SLA when SLA temperatures are less than or equal to -100 °F (see Figure 11-9).

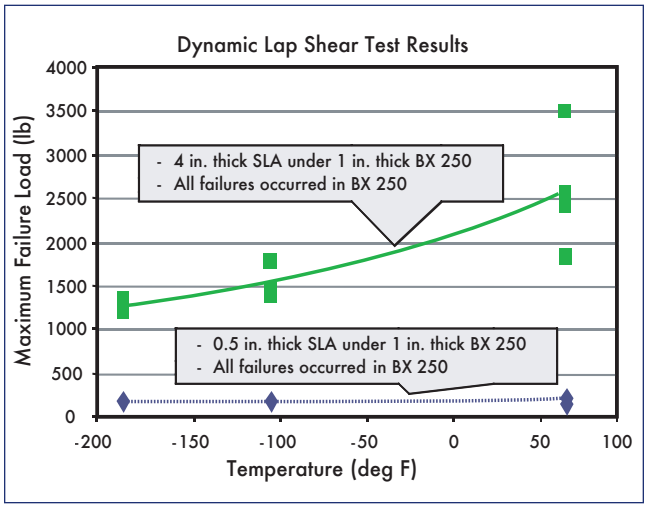


Figure 11-9. Critical test results in debris assessment.

11.5.3 Max Bipod SLA Temperatures (80 seconds MET)

The maximum SLA temperatures possible at 80 seconds were analyzed to determine maximum worst-case multi-event material loss. No cryopumping or cryo ingestion was assumed in order to calculate temperatures as high as possible. STS-107 ambient environments were used. Results showed the maximum SLA temperature possible at 80 seconds MET is less than or equal to -100 °F, as shown in Figure 11-10. Tension testing shows BX-250 fails before SLA at temperatures less than or equal to -100 °F.

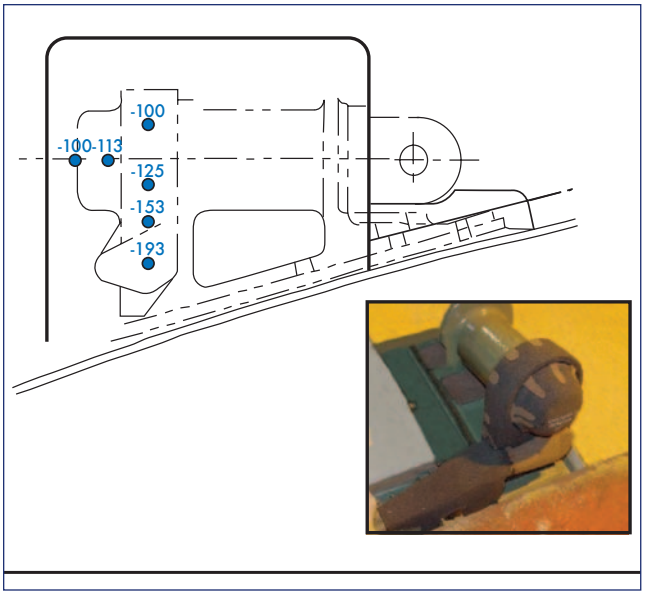


Figure 11-10. Max bipod SLA temperatures (80 seconds MET), °F.

11.5.4 Bipod Ramp As-Built Hardware Assessment

The dissection of six bipod ramps indicated similar patterns for geometry-induced defects in all ramps. Roll-overs were observed at complex substrate elements, and the majority of observations were associated with spraying over complex details at the substrate. Sporadic voids were also observed. One internal delamination and one weak plane at the knit line were observed. Critical locations, or areas at-risk for producing debris, were identified near the edge of the machined foam surface for both voids and roll-overs (see Figure 11-11). Vacuum pressure is the primary driver for divot formation; however, wind shear also contributes to flight loads. A combination of multiple large voids, geometry-induced defects, and critical locations is needed to produce significant foam loss. For example, a large interconnected void at close proximity to the surface plus a "weakened plane" (see Figure 11-12) may produce foam loss.

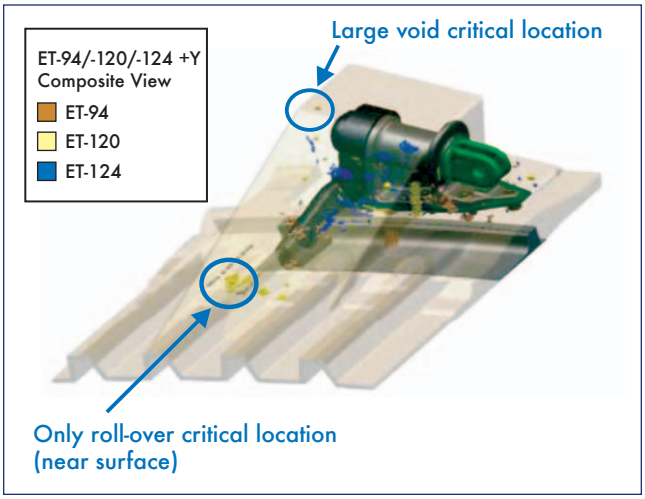


Figure 11-11. Defects found at critical locations.

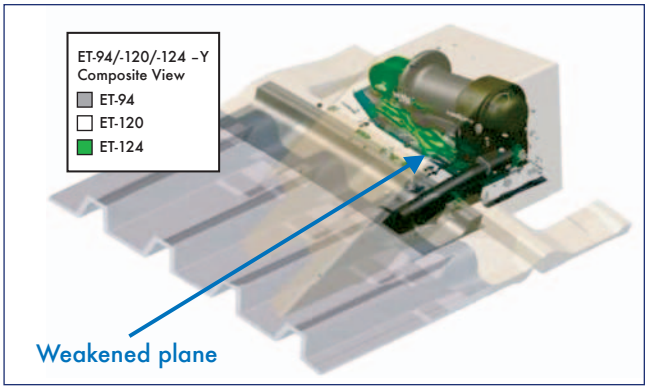


Figure 11-12. Weakened plane defect found.

11.5.5 Multi-Failure Mode TPS Bipod Debris

The ET Working Group conducted an analysis coupled with test data to estimate a multi-failure mode TPS bipod debris size and weight. The ET Working Group scenario includes seven simultaneous and interactive adverse events: A large rollover occurs at the inboard stringer interface immediately below the machined foam surface, side-to-side thermal crack/weak knit line, a large void near the topmost surface one inch below machined foam surface, warm SLA environment, and foam machined to minimum tolerances (not a failure). The specific results are shown in Figure 11-13.

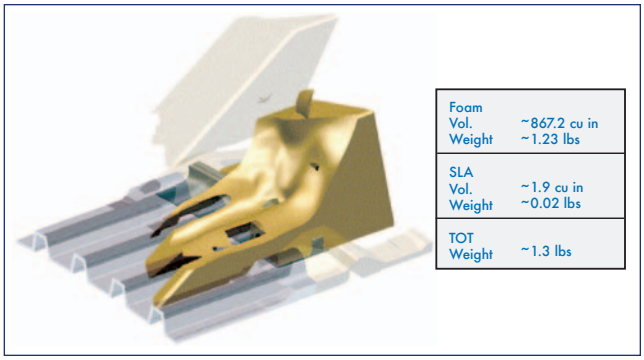


Figure 11-13. Multi-failure mode bipod TPS debris estimated by the ET Working Group. Note that this size and weight were not used in the RCC impact testing as part of the STS-107 investigation.

The determination of the STS-107/ET-93 bipod TPS debris is based on evaluation of fault tree findings, possible TPS failure modes and contributors, and results to date from TPS debris test programs including dissection, foam loss secondary effects assessment (SLA/BX-250), and bipod TPS debris size analysis. The TPS bipod debris size was determined by the ET Working Group to be approximately 870 cubic inches and 1.3 pounds.

The transport analysis presented in Section 3 suggests that the debris object may be heavier than average foam, but the ET Working Group analysis indicates there could not be ice or significant SLA in the debris and that the density of the foam is consistent. Also, the imagery analysis showed that

not all the debris struck the wing, but it broke up prior to impact, with all debris passing beneath the wing, some without impacting the wing. Recall that the transport analysis presented in Section 3 states the bipod TPS debris would be 1026 cubic inches and 1.4 pounds for a 820 ft/sec velocity or 1239 cubic inches and 1.7 pounds for a 775 ft/sec velocity. The RCC foam impact test conducted at Southwest Research Institute was performed at 775 ft/sec with a 1.67-pound foam article.

12.0 Summary

During the first stage of ascent, before SRB separation, the left wing of *Columbia* was struck by debris from the ET –Y bipod foam ramp. Analysis of the bipod foam ramp design, material, and processes suggests that the probable contributing mechanisms for foam liberation were cracks, delamination or debonding, divots, shear loads, or some combination of these. Analytical and test estimates of foam debris size, trajectory, and impact location indicate that the foam struck the left Wing Leading Edge (WLE) in the area between Reinforced Carbon-Carbon (RCC) panels 5 and 9. The impact energy tests conducted at Southwest Research Institute support the theory that the left wing RCC (lower panel 8 area, and/or an adjacent Tee seal) was damaged by the debris impact.

During ascent several new flight experience events occurred. These were all very near existing flight envelopes and well within the certified flight envelope for which the Shuttle was designed. The data indicate that all new flight experiences could be attributed to the winds aloft and SRB performance. The new flight experiences may have individually or collectively contributed to liberation of the bipod foam ramp, but data are inconclusive in this regard.

Launch radar analyses are inconclusive in determining size, shape, or identity of the debris measured after SRB separation. The radar data and analyses are inconclusive as to whether any of the debris impacted the orbiter.

There is data indicating that an object departed the orbiter on flight day 2 with a small relative separation velocity. Ballistics and Radar Cross Section (RCS) testing and analyses have excluded all tested objects except for a partial WLE Tee seal, a whole WLE Tee seal, or a partial WLE RCC panel. Data are inconclusive in determining the identity of the flight day 2 object, or whether the object was associated with the bipod foam debris impact.

Analysis of the RCC damage location and size is consistent with data from ascent. Analyses from orbiter telemetry, Modular Auxiliary Data System (MADS), aerodynamic and aero-thermal reconstruction and simulation, and debris forensics suggest that the RCC was damaged prior to Entry Interface (EI). The best estimate of the damage location is in the panel 8 lower area. Indications from modeling are that the damage size could have produced heating equivalent to a 6 to 10 inch hole diameter in the lower panel 8 area, or in one of the Tee seals adjacent to RCC panel 8.

The damage in the left wing RCC provided a pathway for hot gas to enter the left wing leading edge and support structure during entry. This resulted in significant damage to the left wing and the subsequent loss of vehicle control, leading to aerodynamic breakup.

Appendix A

Acronyms and Abbreviations

AA	Accelerometer Assembly
AC	Alternating Current
AFB	Air Force Base
AFRL	Air Force Research Labs
AFS	Air Force Station
AFSPC	Air Force Space Command
APU	Auxiliary Power Unit
BN	Ballistic Number
BSM	Booster Separation Motor
CAD	Computer-Aided Design
CAIB	Columbia Accident Investigation Board
CEI	Contract End Item
CF4	Tetraflouromethane
CFD	Computational Fluid Dynamics
CG	Center of Gravity
CSA	Canadian Space Agency
DAO	Data Assimilation Office
DAP	Digital Auto Pilot
dBsm	Decibels Relative to One Square Meter
DLR	German Aerospace Research Establishment
DOLILU	Day of Launch I-Load Update
DTA	Double Type A
EDO	Extended Duration Orbiter
EI	Entry Interface
EORF	Enhanced Orbiter Refrigerator/Freezer
ER	Eastern Range
ESA	European Space Agency
EST	Eastern Standard Time
ET	External Tank
FEP	Front End Processor
FOD	Foreign Object Debris
FRCS	Forward Reaction Control System
FREESTAR	Fast Reaction Enabling Science Technology and Research
FRSI	Felt Reusable Surface Insulation
GMT	Greenwich Mean Time
GNC	Guidance Navigation and Control
GRAM	Global Reference Atmosphere Model
GSE	Ground Support Equipment
Hi-Q	Maximum Dynamic Pressure
HMF	Hypergolic Maintenance Facility
HP	Hand Pack
HRSI	High-Temperature Reusable Surface Insulation
IEA	Integrated Electronics Assembly
IFA	In-Flight Anomaly
IMU	Inertial Measurement Unit
IPR	Interim Problem Report
IRN	Interface Revision Notice
ISS	International Space Station
JDMTA	Jonathan Dickinson Missile Tracking Annex
KSC	Kennedy Space Center
LAF	Lost and Found
LaRC	Langley Research Center
LCC	Launch Commit Criteria
LCD	Launch Countdown
LESS	Leading Edge Structural Subsystem
LH2	Liquid Hydrogen
LO2	Liquid Oxygen
LOS	Loss of Signal
LOX	Liquid Oxygen
LPS	Launch Processing System
LRU	Line Replaceable Unit
LWT	Light Weight Tank
MADS	Modular Auxiliary Data System
MAF	Michoud Assembly Facility
MCC	Mission Control Center
MEIDEX	Mediterranean Israeli Dust Experiment
MET	Mission Elapsed Time
MILA	Merritt Island Launch Area
MLP	Mobile Launch Platform
MMOD	Micrometeoroid or Orbital Debris
MOTR	Multiple-Object Tracking Radar
MPS	Main Propulsion System
MR	Management Review
MRB	Material Review Board
MSBLS	Microwave Scanning Beam Landing System
MSID	Measurement Stimulation Identification
NAIT	NASA Accident Investigation Team
NASA	National Aeronautics and Space Administration
NASDA	Japanese National Space Development
NDE	Non-Destructive Evaluation
NSI	NASA Standard Initiator
ODRC	Operational Data Retrieval Complex
OI	Operational Instrumentation
OMDP	Orbiter Maintenance Depot Processing
OMI	Operations and Maintenance Instruction
OMM	Orbiter Major Maintenance
OMS	Orbital Maneuvering System
PAFB	Patrick Air Force Base
PAL	Protuberance Air Load
PAPI	Precision Approach Position Indicator
PE	Performance Enhancement
PLB	Payload Bay
PMBT	Propellant Mean Bulk Temperature
PR	Problem Report
PRSD	Power Reactants Storage Device
QC	Quality Control
RCC	Reinforced Carbon-Carbon
RCS	Radar Cross Section
RDM	Research Double Module
RF	Radio Frequency
RGA	Rate Gyro Assembly
RSR	Range Separation Rate
RSRM	Re-usable Solid Rocket Motor
RSS	Range Safety System
RTV	Room Temperature Vulcanized
SAMS	Space Acceleration Measurement System
SIP	Strain Isolation Pad
SLA	Super Light Ablator
SLF	Shuttle Landing Facility
SLWT	Super Light Weight Tank
SMG	Space Meteorology Group
SOFI	Spray-On Foam Insulation
SRB	Solid Rocket Booster
SSME	Space Shuttle Main Engine
STA	Shuttle Training Aircraft
STS	Space Transportation System
TDRS	Tracking and Data Relay Satellite
TEOS	Tetraethyl Orthosilicate
TPS	Thermal Protection System
TVC	Thrust Vector Control
UHF	Ultra-High Frequency
VRCS	Vernier Reaction Control System
WLE	Wing Leading Edge

Appendix B

Working Scenario Team

Team Leaders

- **Columbia Accident Investigation Board**
  - CAIB Group I Lead: Major General John Barry
  - CAIB Group III Lead: Dr. James Hallock

- **NASA, Johnson Space Center**
  - NASA Lead, Flight Director Office: LeRoy E. Cain
  - NASA Deputy, Flight Director Office: J. Steve Stich

Primary Technical Support and POCs

- **Columbia Accident Investigation Board**
  - Lt. Col. Larry Butkis

- **Cimmaron**
  - Phil Glynn

- **Hernandez Engineering**
  - Ernest Ramirez

- **Johnson Space Center**
  - Flight Director Office: Phil Engelauf
  - Mission Operations Directorate: Jeffrey Kling, Michael Sarafin, Jon Reding, Dr. J.C. Melcher, Barbara Conte
  - Engineering Directorate: Gene Grush, Don Curry, Reynaldo Gomez, Steve Labbe, Jose Caram, Chris Madden, Julie Kramer, Steve Rickman
  - Space Shuttle Progam, Launch Integration Manager: N. Wayne Hale
  - Space Shuttle Systems Integration: Rod Wallace
  - International Space Station Vehicle Program: Tom Martin
  - Human Exploration Science: Greg Byrne

- **Kennedy Space Center**
  - Processing: Mike Leinbach, Charlie Abner, Terri Herst, Shawn Greenwell, Tim Wilson

- **Marshall Space Flight Center**
  - External Tank Working Group: Dr. Paul Munafo
  - External Tank Project: Neil Otte, Jerry Smelser
  - Reusable Solid Rocket Motor: Steve Cash
  - Solid Rocket Booster: Joe Lusk
  - Space Shuttle Main Engine: Mike Kynard

- **Michoud Assembly Facility**
  - Ron Wetmore
  - Eugene Sweet
  - Dan Callan

- **The Boeing Company**
  - Mark Hasselbeck
  - Mike Dunham

- **United Space Alliance**
  - Doug White
  - Pam Madera

Volume II
Appendix D.8
Debris Transport Analysis

This appendix contains the debris transport analysis used to determine information about the dimensions of the External Tank bipod foam ramp and the conditions in which the foam struck the Orbiter, post-mishap. This data provided inputs into the foam testing conducted at Southwest Research Institute for the foam impact testing.

This is a NASA document and is published here as written, without editing by the Columbia Accident Investigation Board. The conclusions drawn in this report do not necessarily reflect the opinion of the Board; when there is a conflict, the statements in Volume I of the Columbia Accident Investigation Board Report take precedence. While the report contains many recommendations to improve the data used in this type of analysis for future missions, the Board did not adopt every recommendation into the Columbia Accident Investigation Board Report.

Section 1.0 Executive Summary 239

Section 2.0 Background 240
2.1 Freestream Conditions 240
2.2 Debris Transport Background 241
2.3 Ballistic Number (BN) Definition 241
2.4 STS-107 Debris Transport Assessment Approach 242

Section 3.0 STS-107 Image Analysis Team Inputs 242
3.1 Assessment of Impact Analysis Inputs 243

Section 4.0 External Tank Project Inputs 243
4.1 Assessment of External Tank Inputs 244

Section 5.0 Static Geometry CFD Solutions 245
5.1 Background 245
5.2 Solver Background/Verification 245
5.3 Other Applications 245

Section 6.0 Ascent Debris Transport Program (ADTP) 246
6.1 Assumptions/Limitations 246
6.2 Code Review Results 246
6.3 Results compared to STS-107 Mission Predictions 247

Section 7.0 Trajectory Analysis/Ballistic Number Determination 247
7.1 Condon Analysis: Least Squares Optimized with Pre-processed and View Vector Data 247
7.2 Lee Analysis: Least Squares Optimized with View Vector Data 256
7.3 Crain Analysis: Batch Least Squares Method with Pre-processed Data 260
7.4 Recommendations (Condon, Lee, and Crain) 263

Section 8.0 6-DOF Unsteady CFD Analysis 264
8.1 Approach 264
8.2 Tool Background 264
8.3 Observations 264
8.4 Results 264

Section 9.0 RCC Impact Testing Inputs 266
9.1 Debris Mass Estimation 266
9.2 Angle of Incidence Inputs 267

Section 10.0 Conclusions/Recommendations 267
10.1 Image Analysis 267
10.2 Debris Transport 268

Section 11.0 Acknowledgements 268

Section 12.0 References 268

Section 13.0 Appendix A 268
13.1 Acronyms and Abbreviations 268

Section 14.0 Appendix B 268
14.1 Bipod Ramp Airloads 268

Section 15.0 Appendix C 270
15.1 Time-dependent position data sets from JSC/ES, JSC/SX, KSC and JSC/EG 270
15.2 Time-dependent ground camera view vector data sets 271
15.3 Time-dependent ground camera view vector data sets 272

Figures & Tables

Table 1-1 Comparison of Debris Impact Parameters 240

Table 2-1 STS-107 Freestream conditions at time of debris release 240
Figure 2-1 Distance from Debris Source to Debris Impact Location 240
Figure 2-2 STS-107Ascent Angle of Attack & Dynamic Pressure History 240
Figure 2-3 STS-107 Ascent Elevon Schedule 241
Figure 2-4 Impact Velocity vs. Mach number (based on freestream conditions) 241
Equation 2-1 Ballistic Number (BN) Definition 241
Equation 2-2 Drag Force Equation 242
Equation 2-3 Aerodynamic Acceleration due to Drag 242
Figure 2-5 Impact Velocity vs. Ballistic Number at STS-107 Conditions 242

Table 3-1 Image Analysis Inputs 243
Figure 3-1 Sample set of 3-dimensional trajectories from various members of the Image Analysis Team 243
Figure 3-2 Initial Trajectory Points from Image Analysis Team 243
Figure 3-3 Weakened plane in bipod ramp foam 243

Figure 4-1 ET93 CAD Model Detail 244
Table 4-1 Allowable range of ramp dimensions and foam densities 244
Table 4-2 Estimated maximum foam volume loss vs. bipod ramp angle 244
Figure 4-2 Initial Maximum Estimated Foam Loss 244
Figure 4-3 Final Maximum Estimated Foam Loss 245

Figure 5-1 Pressure coefficient on the SSLV surface and Mach number in the surrounding flowfield at the TS-107 debris release conditions. 245
Figure 5-2 Mach Number Isosurfaces at Mach number = 2.46 245
Figure 5-3 Surface Flow Lines and Possible Secondary Impact Locations 246

Figure 6-1 STS-107 Mission Debris Impact Results 247

Figure 7-1 Force diagram of Shuttle and foam debris accompanied by associated equations of motion 248
Figure 7-2 Illustration of time-dependent position differences between one of four reference data sets (JSC/ES, JSC/SX, KSC, or JSC/EG) and an integrated trajectory employing a flight-based local velocity flow field. The objective (minimized) function is the sum of the squares of the distances between some or all eleven of these time-dependent position points (ΣDn2). 248
Table 7-1 BN and projected velocity results for reference data sets (JSC/ES, JSC/SX, JSC/EG3, KSC). 249
Figure 7-3 Three-dimensional view of foam debris trajectory as compared to KSC reference data for index range (5-8). Note: Shuttle diagram is for attitude reference only and is not to scale. 249
Figure 7-4 Composite view of foam debris trajectory as compared to KSC reference data for index range (5-8) including top, side and "front" views. Note: Shuttle diagram is for attitude reference only and is not to scale 250
Figure 7-5 Projected velocity of foam debris to position X = 1800 inches, for reference data sets JSC/ES, JSC/SX, JSC/EG, and KSC. The KSC data provides the most consistent projected velocity results 250
Figure 7-6 Three-dimensional view of foam debris trajectory as compared to JSC/EG reference data for index range (5-8). The sum square position error for this case is larger than that based on the KSC reference data set, as shown in Figure 7-3. Note: Shuttle diagram is for attitude reference only and is not to scale. 251
Figure 7-7 Composite view of foam debris trajectory as compared to JSC/EG reference data for index range (5-8) including top, side and "front" views. Note: Shuttle diagram is for attitude reference only and is not to scale. 251
Table 7-2 Single and Multiple BN values and initial states for the JSC/ES reference data set. Note that a maximum allowable BN of 1000 was used for the multiple BN cases. On possible explanation for the arbitrarily high BN is the sparseness and uncertainty in the imagery-based data set. 251
Figure 7-8 Illustration of time-dependent position differences between view vectors for ground cameras 208 and 212 and an integrated trajectory (solid curve) employing a flight-based local velocity flow field. The objective (minimized) function is the sum of the squares of the distances between some or all eleven of these time-dependent position points (ΣDn2). 252

Figure 7-9 The index intervals for the comparison of an integrated trajectory with the view vectors from cameras 208 and 212 are designed to provide similarity to the intervals using in the reference data set comparisons in the previous section. The index ranges used to generate the most probable estimates of key parameters (BN, projected impact velocity, etc.) were 7-13, 7-14, 7-15, 7-16, 8-13, 8-14, 8-15, and 8-16. 253
Figure 7-10 BN vs. index range for selected view vector data comparisons. 253
Figure 7-11 Projected impact velocity at X-position = 1817.45 inches vs. index range for selected view vector data comparisons. 254
Figure 7-12 Projected time of impact at X-position = 1817.45 inches vs. index range for selected view vector data comparisons 255
Table 7-3 BN and projected impact velocity and time (at X = 1817.45 inches) results for comparison of minimum sum square error between ground camera (208 & 212) view vectors and the integrated trajectory. This data is based on movement of the time stamp for camera 208 earlier by 6.75 milliseconds and includes view vector location errors in computation of the sum square perpendicular error between the integrated trajectory and the view vectors at a succession of index points 254
Figure 7-13 Optimized foam debris trajectories for index intervals 7-13, 7-14, 7-15, 7-16, 8-13, 8-14, 8-15, and 8-16, projected to Shuttle impact. Graphic courtesy of Phil Stuart – JSC/EG3 255
Figure 7-14 Close-up of optimized foam debris trajectories for index intervals 7-13, 7-14, 7-15, 7-16, 8-13, 8-14, 8-15, and 8-16, projected to Shuttle impact. Graphic courtesy of Phil Stuart – JSC/EG3. 255
Figure 7-15 Top view of optimized foam debris trajectories for index intervals 7-13, 7-14, 7-15, 7-16, 8-13, 8-14, 8-15, and 8-16, projected to Shuttle impact and showing outboard direction of trajectory at impact. Graphic courtesy of Phil Stuart – JSC/EG3. 256
Table 7-4 Foam debris data for selected index interval trajectories impacting the Shuttle wing as depicted in figures 6-11, 6-12, and 6-13. 256
Figure 7-16 Ballistic Equations of Motion for Debris Object Relative to STS 257
Figure 7-17 Combined uncertainty shape for camera views with small intersection angle 257
Figure 7-18 Debris Object Trajectory Solution with View Vectors (Ballistic Model) 259
Figure 7-19 Debris Object Trajectory Solution with RCC and Bipod Ramp Outlines (Ballistic Model) 260
Figure 7-20 Batch Least Squares Estimation Process 260
Table 7-5 Batch Least Squares Estimates and Confidences for Initial BN by Data Set 261
Table 7-6 Batch Least Squares Estimation Error and Average Interval Estimation Error Table 261
Table 7-7 Ballistic Number Estimates and Statistical Confidences from Fused JSC/EG, JSC/SX, and KSC Data 262
Table 7-8 Foam Impact Characteristics for Each Data Set and Data Start/Stop Number (Courtesy Phillip Stuart JSC/EG) 263
Figure 7-21 Interpolated Impact Points of All Data Sets 263

Figure 8-1 Backward vs. forward flip trajectories 265
Figure 8-2 Impact Velocity for Various Effective Densities 265
Figure 8-3 Ballistic Number Variation along Trajectory (704 in3 foam volume) 265
Figure 8-4 Ballistic Number Variation along Trajectory (855 in3 foam volume) 265
Figure 8-5 Rotation Rates From Unsteady CFD 265
Figure 8-6 Delta Pressure on Vehicle Surface Caused by Debris 266
Figure 8-7 Delta Pressure Near Orbiter Lower Surface Pressure Tap 266

Figure 9-1 Velocity at 1800 inches vs. Ballistic Number 266
Equation 9-1 Ballistic Number As A Function of Density 267
Figure 9-2 Angle of Incidence on RCC Panel (1 foot radius footprint) 267
Figure 9-3 Impact Test Article Rotation about Y-Axis 267
Figure 9-4 Impact Test Article Rotation about Z-Axis 267
Figure 14-1 Bipod Ramp Force Convention 269
Figure 14-2 -Y Bipod Ramp Axial Force vs. Mach Number 269
Figure 14-3 -Y Bipod Ramp Side Force vs. Mach Number 269
Figure 14-4 -Y Bipod Ramp Radial Force vs. Mach Number 269

Debris Transport Analysis

Submitted by NASA Accident Investigation Team
Reynaldo J. Gomez III, Michael Aftosmis, Darby Vicker, Dr. Robert L. Meakin, Phillip C. Stuart, Dr. Stuart E. Rogers, James S. Greathouse, Dr. Scott M. Murman, Dr. William M. Chan, David E. Lee, Gerald L. Condon, and Dr. Timothy Crain

1.0 EXECUTIVE SUMMARY

This report documents the results of the STS-107 Investigation team responsible for characterizing the debris impact on the Orbiter wing during the STS-107 launch. These results provided the inputs for the Orbiter Thermal Protection System Impact Test Team as well as information regarding bipod ramp airloads and characterization of the bipod ramp local flow environment.

The goal of this effort was to characterize the External Tank bipod ramp foam trajectory and subsequent impact on the Orbiter lower wing leading edge at a Mission Elapsed Time (MET) = 81.86 seconds. Determining the mass and impact velocity of the debris that struck the Orbiter was a complex effort requiring the integration of inputs from a number of sources. Inputs from the External Tank (ET) Project and the STS-107 Image Analysis Team were combined with CFD and trajectory analysis tools to determine the mass and impact velocity of the debris that struck the lower Reinforced Carbon Carbon (RCC) surface of the Orbiter left wing. In depth evaluations of the Image analysis products along with CFD simulations were the primary efforts that determined the parameters required to characterize the debris in an enough detail to support impact testing required for the STS-107 investigation.

The bipod ramp aerodynamic loads were assessed using CFD solutions at the STS-107 ascent conditions. These results showed that the air loads on the bipod ramps were well within the design certification limits and were a small fraction of the design limits at the debris release conditions. This implies that a foam ramp without flaws should not have failed due to aerodynamic loads.

Assessments of debris impact velocity potential were performed at a range of Mach numbers along the STS-107 ascent profile. These results showed that the debris release conditions on STS-107 were near the worst case combination of freestream velocity (2324 ft/sec) and dynamic pressure (482 psf), from a debris impact velocity perspective.

Three-dimensional trajectories from the launch films and videos were screened using a physics-based trajectory fit based on a steady state flowfield model generated using high fidelity Computational Fluid Dynamics (CFD) tools. These results refined the most likely range of relative velocities at debris impact to between 775 and 820 feet per second. The debris impact velocity is the difference between the vehicle velocity and the debris velocity as shown in the following equation.

$$\text{Impact Velocity} = \text{Shuttle Velocity} - \text{Debris Velocity}$$

$$775\ (^{ft}/_{sec}) = 2324\ (^{ft}/_{sec}) - 1549\ (^{ft}/_{sec})$$

A parallel effort used a more complex CFD model that included the unsteady rotation of the debris and simulated the effect of the debris on the overall flowfield. These results indicated that an 855 in^3 volume of foam from the –Y bipod ramp would impact the Orbiter wing at approximately 950 feet per second. The unsteady moving body simulations provided insight into the most likely initial conditions for the debris release as well estimates of the debris rotation rate and the effect of the debris on the local pressure distribution. These results show that the 855 in^3 foam volume would require an effective density considerably higher than the allowable foam density to impact at a velocity of 820 ft/sec or that the foam volume was significantly larger than 855 in^3.

These analyses along with the inputs from the Image Analysis Team and the ET Project were used to estimate a range of debris dimensions and corresponding weights for the foam debris. These upper and lower velocity and corresponding weight ranges are listed in Table 1-1 along with one of the debris sizes analyzed during the STS-107 and the values used in RCC impact tests. The STS-107 result corresponds to the debris size and impact location closest to the test article used in the RCC impact tests.

	Transport Analysis Lower Bound	Transport Analysis Upper Bound	Estimate made during STS-107 mission[1]	RCC Impact Test Target Values
Velocity (ft/second)	775	820	720	775
Volume (in^3) ρ_{foam} = 2.4 lb/ft^3	1,025	1,240	1,200	1,200
Weight (lb)	1.42	1.72	1.67	1.67
Incidence Angle (degrees)	Dependent on impact location		21°	20.6°

Table 1-1. Comparison of debris impact parameters.

2.0 Background

2.1 Freestream Conditions

During the STS-107 launch a large piece of debris was observed falling from the External Tank at a MET = 81.699 seconds at the following freestream conditions:

MET	81.7 seconds	
Altitude	6,5820 feet	12.47 miles
Mach number	2.46	
Velocity	2,324.1 feet/second	1,584.6 miles/hour
Dynamic pressure	481.72 lb/ft^2	
Density	1.783e-04 $slug/ft^3$	7.1% Seal level density
Temperature	-88.1°F	
Alpha	2.08 degrees	
Beta	-0.09 degrees	
Inboard elevons	0.26 degrees	
Outboard elevons	-4.85 degrees	

Table 2-1. STS-107 freestream conditions at time of debris release.

The freestream conditions and the vehicle geometry determine the flowfield around the Space Shuttle at the time of the debris release. This flowfield, along with the vehicle acceleration, provides the force that causes the debris to accelerate relative to the Space Shuttle Launch Vehicle. The flowfield density and velocity combine to accelerate the debris and the flowfield direction combined with the aerodynamics of the debris determine the trajectory that the debris will follow.

Figure 2-1 shows that the impact location is approximately 58 feet downstream of the debris release point. Although the downstream distance is 58 feet the SSLV travels more than 370 feet during 0.16 second debris trajectory duration.

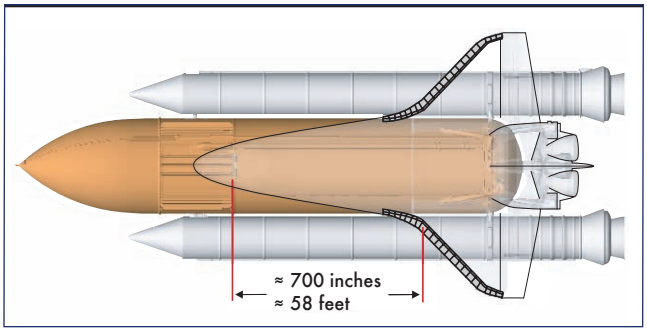


Figure 2-1. Distance from debris source to debris impact location.

At Mach 2.46 the SSLV has transitioned from a negative angle of attack to a positive angle of attack. During the maximum dynamic pressure portion of the ascent profile the SSLV flies at a negative angle of attack to reduce the aerodynamic loads on the Orbiter. Additionally the vehicle has passed the maximum dynamic pressure or max $\bar{q}$, and the region of maximum aerodynamic loading on the vehicle. This data is shown in Figure 2-2.

Figure 2-3 shows that the elevons were moving to their neutral or 0°/0° deflection position during the debris event.

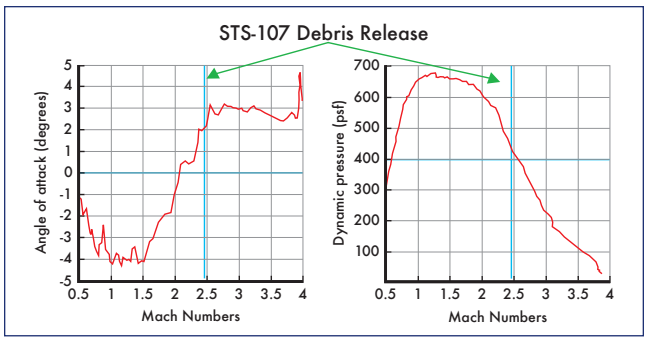


Figure 2-2. STS-107 ascent angle of attack and dynamic pressure history.

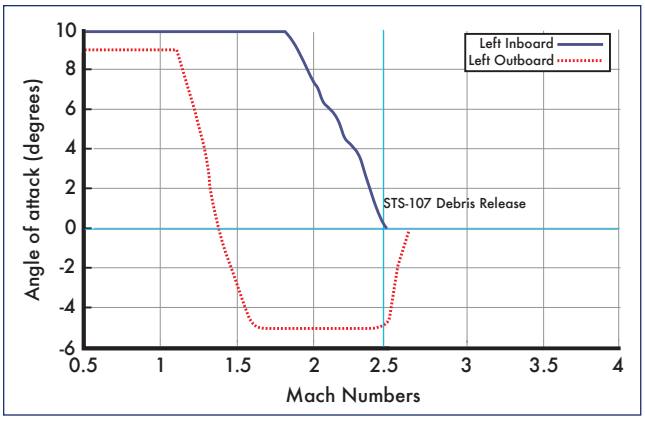


Figure 2-3. STS-107 ascent elevon schedule.

Negative elevon deflections indicate that the elevons are rotated upward, away from the External Tank. The elevon deflection at this point in the ascent trajectory makes debris impacts on the outboard elevon lower surface unlikely.

FIgure 2-4 illustrates the importance of freestream density and velocity on the impact velocity. This figure is based on a constant drag coefficient and does not account for local variations in the flowfield.

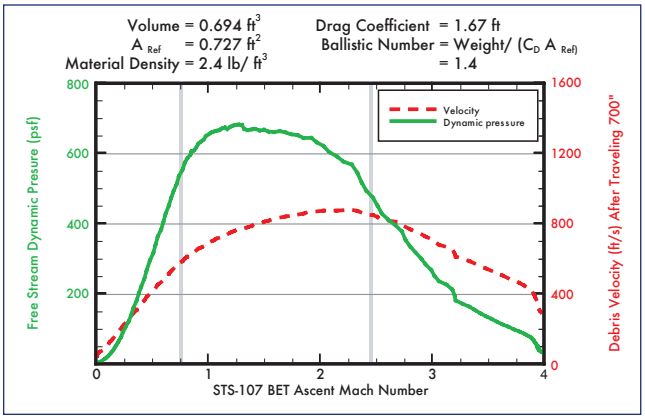


Figure 2-4. Impact velocity vs. Mach number (based on freestream conditions).

Dynamic pressure produces the acceleration force applied to the debris and the freestream velocity determines the maximum relative velocity that the debris can attain. The maximum potential acceleration coincides with the maximum dynamic pressure or max q, which occurred at Mach number = 1.28, however this does not produce the worst case impact velocity. As shown in the previous figure, Mach 2.46 is near the worst case combination of dynamic pressure and freestream velocity in terms of impact velocity potential.

2.2 Debris Transport Background

Typically the size, shape and initial conditions of Space Shuttle ascent debris are unknown. Most debris impacts are assessed after the Shuttle mission ends and the vehicle is inspected on the runway. This is primarily due to the fact that many debris impacts are not visible on ground based launch cameras. Estimating the impact conditions for a specific debris event requires inputs from the Intercenter Photographic Working Group and knowledge of the installed hardware or material at the debris source to refine these assessments. Ideally these inputs would include the following information:

- Debris release time
- Debris source and material properties
- Debris dimensions
- Debris impact location

Currently no single analysis technique can uniquely calculate all of the debris mass and impact conditions. Current Image Analysis tools do not include physical models of the flowfield and debris aerodynamics that would enable them to determine debris mass. The Ascent Debris Transport (ADT) program used to predict debris impact conditions cannot uniquely define debris impact conditions without some knowledge of the debris initial conditions, shape and final velocity. Most debris transport analyses are performed parametrically in an attempt to bound the range of likely debris impact energies for assessment purposes. The ADT program is typically utilized as a statistical tool rather than as an investigative tool. It is useful for looking at ranges of potential debris impacts but it does not have the capability to determine debris volumes and shapes based on an observed trajectory.

Two techniques that have not been employed in previous debris assessments were used to determine the debris mass and drag characteristics. The first technique, discussed in Section 7.0, used physics based trajectory analysis techniques to evaluate three-dimensional trajectories from the Image Analysis Team. The second technique used unsteady moving body CFD codes with the ET Project's maximum estimated foam loss shape to determine the initial conditions required to impact the most likely impact location. It is unlikely that this shape exactly matches the STS-107 debris but it provided a reasonably close shape for evaluation purposes. This is consistent with CFD analysis of various bipod ramp debris shapes that indicated the results are not overly sensitive to the exact debris shape.

2.3 Ballistic Number (BN) Definition

One of the key parameters used to evaluate the mass of the foam debris was the Ballistic Number (BN) sometimes referred to as the ballistic coefficient. This parameter is defined a number of different ways in the literature. In order to avoid confusion the definition used in this document is shown in the following equations.

$$\text{Ballistic Number}\left(\frac{lbs}{ft^2}\right) = \left(\frac{Weight}{C_D A_{ref}}\right) = \left(\frac{Weight}{Drag/Dynamic\ Pressure}\right) \approx \left(\frac{Inertia}{Drag}\right)$$

W = weight (lbs)
C_D = non-dimensional drag coefficient
A_{ref} = reference area (ft2)
$\overline{q}$ = dynamic pressure [???]

Equation 2-1. Ballistic Number (BN) Definition.

Note that the dynamic pressure is shown in terms of local air density (ρ_{local}) and relative velocity ($V^2_{relative}$). The debris and the launch vehicle are in relative motion and consequently the force acting on the debris is proportional to the square of the relative velocity. The local air density is used to account for variation in the flowfield density caused by compressible flow phenomena.

The ballistic number provides an index of the relative sensitivity of an object to aerodynamic forces. The equation shows two different methods for computing the BN: one requires a drag coefficient and a reference area; the other requires measured drag and dynamic pressure. The reference area is typically chosen to correspond to the frontal area of an object or the projected planform area of a wing. The drag coefficient is then calculated based on a measured force where the aerodynamic drag is given by the following equation:

$$\text{Drag force (lb)} = \bar{q}\, C_D A_{ref}$$

Equation 2-2. Drag force equation.

For a tumbling object or an unknown shape the reference area is arbitrary and a C_D value cannot be specified without a definition of the reference area. Fortunately the BN can be calculated without specified values for these variables since the drag force can also be written in the following way:

$$\text{Aerodynamic acceleration} \left(\frac{ft}{sec^2}\right) = \bar{q}\,\frac{g}{BN}$$

$$g = \text{gravitational acceleration} = 32.174 \left(\frac{ft}{sec^2}\right)$$

Equation 2-3. Aerodynamic acceleration due to drag.

The trajectory analysis documented in Section 7 is based on this definition and does not require a specific reference area or drag coefficient. This equation also shows that aerodynamic acceleration is a function of BN. As the ballistic number decreases the drag force and resultant impact velocity increases and as the ballistic number increases the drag decreases and the resultant impact velocity decreases. The Figure 2-5 shows estimated impact velocity vs. ballistic number for a Mach 2.46 flowfield for debris from the bipod region impacting the wing leading edge on RCC panel 8.

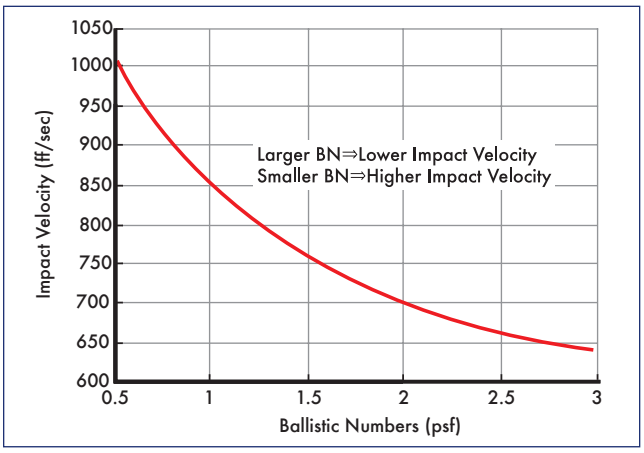


Figure 2-5. Impact velocity vs. ballistic number at STS-107 conditions.

Since the debris is tumbling it has a time varying drag force. This implies that the BN is not a constant but is a function of time. This variation is accounted for in the unsteady CFD analysis in Section 8 and was as documented in Section 7.

2.4 STS-107 Debris Transport Assessment Approach

The overall process consisted of three types of analysis followed by an integration of the results. These steps are listed below:

- Review of relevant inputs from other groups
  - Image Analysis Team
  - ET Project
  - Boeing Debris Transport Program
- Assessment of the STS-107 Image Analysis Team 3-dimensional trajectories using physics based trajectory codes and CFD flowfields
- Simulation of debris trajectories using unsteady 6-DOF CFD codes.
- Integration of results to produce inputs for Southwest Research Institute Impact tests

Results of this analysis included:

- Detailed assessments of the flowfield in the vicinity of the –Y bipod ramp
- Comparisons of these flowfields to wind tunnel and flight data
- Assessment of the Image Analysis impact velocities
- Ranges of most likely impact velocity and incidence angle
- Ranges of most likely debris weights
- Assessment of debris rotational motion

3.0 STS-107 Image Analysis Team Inputs

The STS-107 Image Analysis Team provided inputs that were instrumental in refining the estimated debris size. These results came from a number of different organizations and the ranges shown in the table bracket the results from the various groups that made up the Image Analysis Team. The significant inputs are summarized in Table 3-1 and the following text.

The Image Analysis Team also reported a third debris dimension based on a simplified debris transport analysis by Dwight Divine III of Lockheed-Martin Gaithersburg. The results of this analysis were not used due to the simplified nature of the analysis but the concepts from this analysis were used in the detailed analyses documented in Section 7. These detailed analyses played a key role in evaluating the

Debris release time	MET = 81.699 seconds
Debris source	-Y bipod ramp
Number of impacts	One large debris impact
Impact location	Left wing RCC Panel 5-9 Most likely range 6-8
Impact velocity range	625-840 ft/sec Most likely velocity = 700 ft/sec
Debris dimensions	24″ ± 3″× 15″± 3″
Tumble rate	At least 18 revolutions/second

Table 3-1 Image analysis inputs.

3-dimensional trajectories from the various members of the Image Analysis Team.

One the most important inputs from this group were 3-dimensional trajectories and view vectors extracted from the launch camera film and videos. Four of the trajectories are shown in Figure 3-1. These trajectories provided the reference information needed to narrow the estimated range of the weights and velocities for the debris released from the External Tank. This refinement was required due to the limited number of test articles available for impact testing and the critical nature of these impact tests to determine the foam damage potential.

3.1 Assessment of Impact Analysis Inputs

Based on the initial positions of each of these trajectories and the camera frame rates an initial average velocity can be calculated for each of these trajectories. Figure 3-2 shows the initial positions of four of the 3-dimensional trajectories relative to the bipod ramp. These points are assumed to represent the debris locations 1/2 of a frame (12.25 milliseconds) after release.

The velocities shown are average velocities required to move from the installed location to the first observed debris point. This simple analysis assumes that the debris broke away halfway in time between the last frame before the debris is

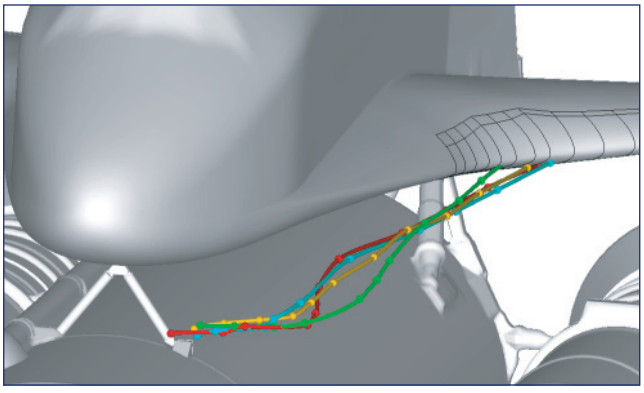


Figure 3-1. Sample set of 3-dimensional trajectories from various members of the Image Analysis Team.

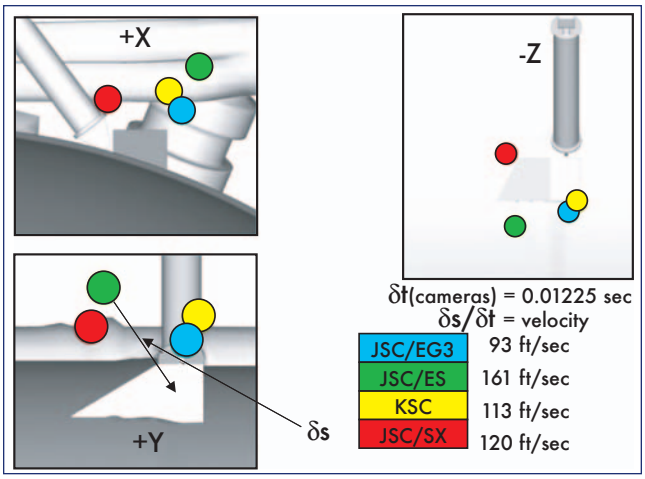


Figure 3-2. Initial trajectory points from Image Analysis Team.

observed to move. It is possible that the debris was released at a slightly different time. A later release time would decrease the δ*t* term and increase the initial velocity estimate. An earlier release time would have the opposite effect.

Note that two of the initial trajectory points shown in the +Y view of Figure 3-2 are actually ahead of the ramp. This implies that the debris somehow moved forward, against the oncoming flow, initially and then traveled aft towards the Orbiter wing. This would require some force acting on the aft edge of the foam ramp that could overcome the aerodynamic forces acting on the ramp at the time of the debris release. Flaws in the bipod ramp shown in Reference 3-2 are in an area where this force could have been applied. However, there is no data on the STS-107 ramp to confirm the existence of similar defects in the STS-107 foam ramps.

The wide range of initial locations and fairly large differences in the observed trajectories could have been caused by optical distortions due to flow gradients caused by shock waves. Shock waves in the bipod vicinity come from the Orbiter and Solid Rocket Boosters. Shock waves ahead of the wing leading edge could have distorted observations of the final portion of the trajectory prior to the debris impact. Images showing the shock waves affecting the bipod region are discussed in Section 5.

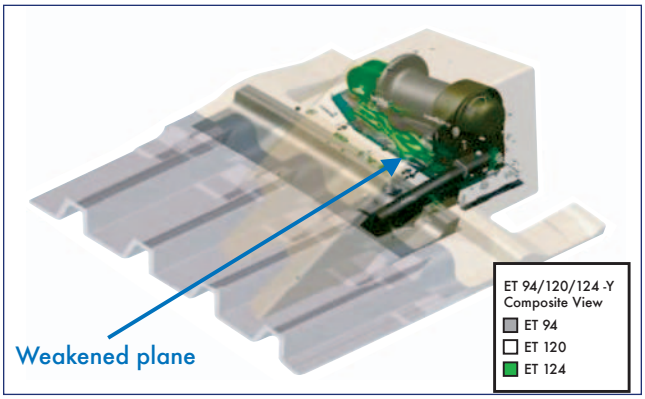


Figure 3-3. Weakened plane in bipod ramp foam.

4.0 External Tank Project Inputs

The External Tank Project provided detailed drawings and material properties for the bipod ramp configuration flown on STS-107. Additionally a Computer Aided Drawing (CAD) model was developed of the outer mold line of the ET that has been incorporated into the latest CFD solutions of the SSLV.

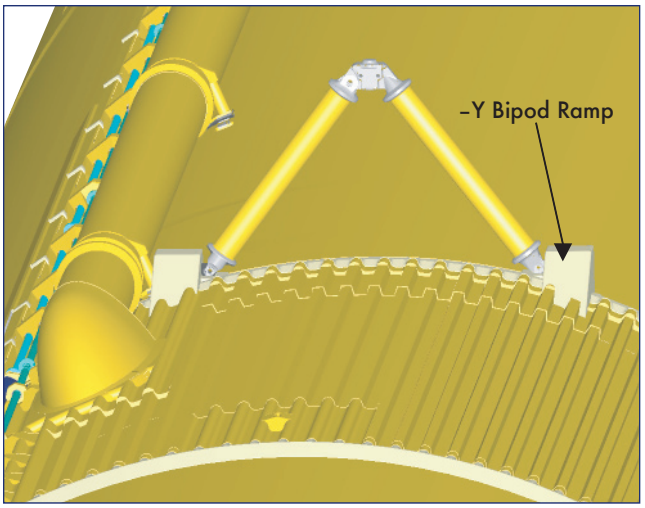


Figure 4-1. ET-93 CAD model detail.

Figure 4-1 includes the bipod struts, LO2 Feedline, cable trays and the stringer geometry ahead of the bipod ramp. These details were not available during the early part of the investigation and most analyses were carried out with simplified geometries that did not include the stringers on the ET Intertank and included simplified representations of the feedline geometry.

4.1 Assessment of External Tank Inputs

The External Tank Project did not have exact measurements for the bipod foam ramp flown on the STS-107 External Tank (ET). The ramp angle on ET93, the tank used on STS-107, was estimated by reviewing closeout photographs to be approximately 25°.

The two primary variables affecting the volume and weight of foam in the bipod ramp are the ramp angle and the BX-250 foam density. The allowable ranges are listed in Table 4-1 below:

	Minimum Allowable	Maximum Allowable
Ramp angle (degrees)	22	30
BX-250 foam density (lb/ft^3)	1.8	2.6

Table 4-1. Allowable range of ramp dimensions and foam densities.

Lower ramp angles increase the volume of foam in the installed ramp. The height remains the same but the length ahead of the bipod strut increases. Measurements from ET94 and ET120, two ETs manufactured at approximately the same time as ET93 had measured ramp angles from 21°-24°. Using similar logic to that used to determine the 855 and 867 in^3 volumes, volume estimates were made for 22 and 30 degree ramp angles, these values are shown in Table 4-2.

Ramp Angle	Max. Volume Loss
22°	1042 in^3
26°	855 in^3
30°	722 in^3

Table 4-2. Estimated maximum foam volume loss vs. bipod ramp angle.

During the STS-107 investigation the ET Project was unable to find any credible scenario that would support the loss of any other hardware or large piece of insulation that would significantly increase the mass of the foam debris.

An estimate was made of the maximum potential foam loss based on this ramp angle. The original estimated maximum foam loss was 855 in^3. Later in the investigation this estimate was increased to 867 in^3. The initial estimate assumed that the thin region aft of the ramp would break off during the debris separation. At a foam density of 2.4 lb/ft^3 these volumes of foam would weigh approximately 1.2 pounds. These estimated volumes are shown in Figures 4-2 and 4-3.

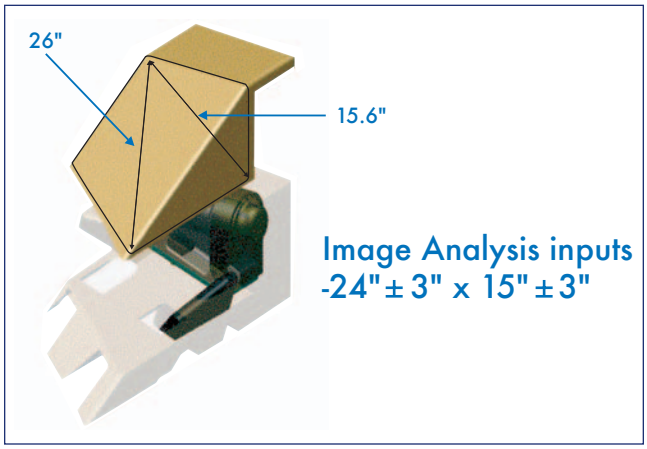


Figure 4-2. Initial maximum estimated foam loss.

The dark outline in Figure 4-2 represents the initial 855 in^3 estimated worst case foam loss. Note that the diagonal dimensions are similar to those reported by the Image Analysis Team. The final estimate included a small amount of Super-Lightweight Ablator SLA.

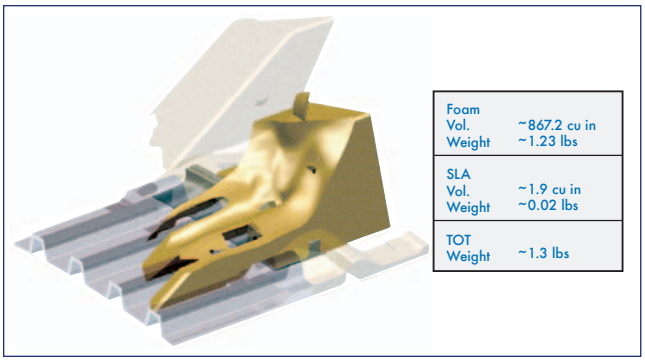


Figure 4-3. Final maximum estimated foam loss.

5.0 Static Geometry CFD Solutions

5.1 Background

Computational Fluid Dynamic (CFD) solutions were used to characterize the flowfield surrounding the Space Shuttle Launch Vehicle (SSLV) at the debris release time. These solutions provided the local aerodynamic acceleration used in the Ascent Debris Transport program and the trajectory analysis used to estimate the debris ballistic number described in Section 7. Additionally these solutions were used compute air loads on the bipod ramp as well as to visualize the flowfield in the bipod vicinity.

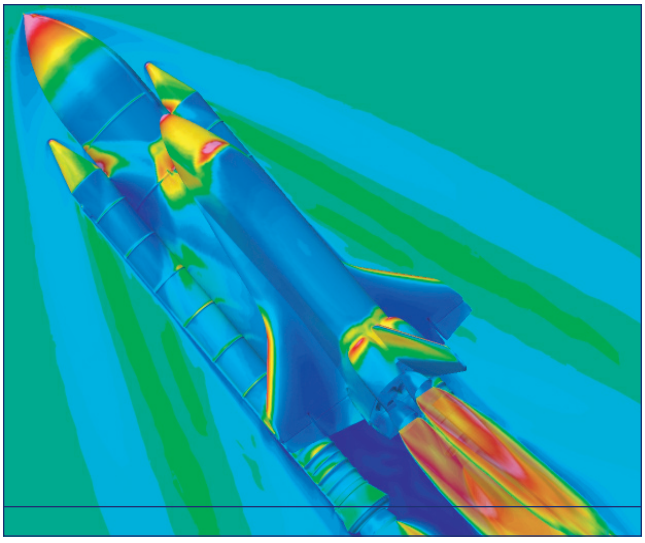


Figure 5-1. Pressure coefficient on the Space Shuttle surface and Mach number in the surrounding flowfield at the STS-107 debris release conditions.

The flowfield in the bipod ramp region, at the STS-107 debris release conditions, has a number of interesting features. Each of the SSLV elements generates a bow shock and the Orbiter and SRB shocks intersect just ahead of the bipod ramp. The left hand SRB shock effect on the local surface pressures is visible as a light blue area in Figure 5-1 on the ET between the SRB nose and the Orbiter nose. These shock-shock interactions with the boundary layer cause the boundary layer ahead of the bipod ramp to separate. Figure 5-2 shows Mach number isosurfaces, colored yellow, at the debris release conditions. These images show the bow shock ahead of the ET as well as the SRB shocks intersecting with the shock off of the Orbiter nose just ahead of the bipod ramps.

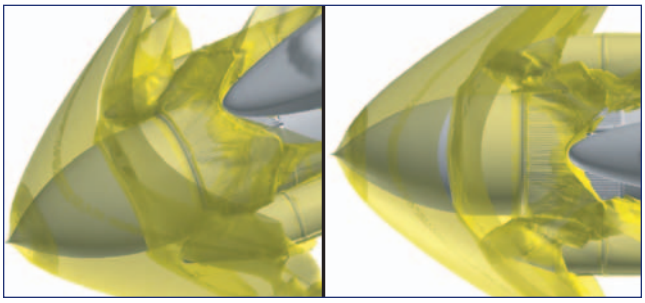


Figure 5-2. Mach number isosurfaces at Mach number = 2.46.

5.2 Solver Background/Verification

The OVERFLOW CFD solver developed by Pieter Buning/NASA Langley Research Center was used to produce these CFD simulations. OVERFLOW is a structured (overset) grid, Navier-Stokes flow solver. It uses a finite-difference formulation, with flow quantities stored at the grid nodes. OVERFLOW has central- and Roe upwind-difference options, and uses a diagonalized, implicit approximate factorization scheme for the time advance. Local time stepping, multigrid and grid sequencing are used to accelerate convergence to a steady state. In this study, 2nd-order central differencing with Jameson-type 2nd/4th-order scalar dissipation is used. Thin-layer viscous terms are computed in wall-normal directions by default and the Spalart-Allmaras 1-equation turbulence model is used to simulate turbulent phenomena.

OVERFLOW has been extensively validated with flight and wind tunnel data. This is documented in references 5-3 through 5-5. The original development of OVERFLOW was funded by the Space Shuttle Systems Integration Office and focused on the development of a capability to accurately simulate transonic aerodynamic loads on the SSLV. During the investigation these results were compared to wind tunnel, previous Operational Flight Test data and STS-107 ascent pressures with good agreement for all of these comparisons. Typical run times for each of these solutions were on the order 10 hours using 128 processors on an SGI Origin 3900 located at NASA Ames Research Center operated by the NASA Advanced Supercomputing Division.

5.3 Other Applications

Bipod ramp air loads were evaluated using these CFD solutions and compared to the aerodynamic loads certification limits used to design the ramp. These results are shown in Appendix B.

A series of numerical experiments were performed to determine if there was any significant unsteadiness in the bipod ramp region. No measurable unsteadiness was found using

the current grid system but there could be subscale unsteadiness that was not resolved due to the local grid spacing in the bipod region.

Surface constrained flow lines, extracted from the static CFD solution, were used to estimate areas where secondary debris strikes may have been detected by the vehicle pressure sensors. Figure 5-3 shows flow lines on the Orbiter lower surface at the debris release freestream conditions the red regions indicate possible secondary impact locations that might have resulted in anomalous pressure measurements during the vehicle ascent. These locations were determined based on their positions relative to the anomalous pressure tap measurements, the local flow direction and further any damage should not affect any other down stream or adjacent pressure instruments which behaved nominally.

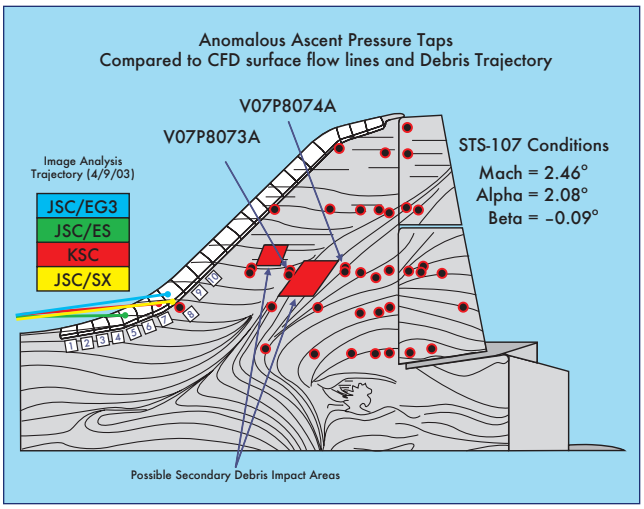


Figure 5-3. Surface flow lines and possible secondary impact locations.

6.0 Ascent Debris Transport Program (ADTP)

The Ascent Debris Trajectory Program is documented in Reference 5-1 and is a Shuttle Systems Design Criteria Critical Math Model (CMM). The following description from CMM 00209 describes the code, its use and required inputs:

> The Debris Trajectory Program is used to calculate the trajectories and resulting impact conditions of ice and other debris particles released from the Space Shuttle during ascent flight, for the purpose of predicting Orbiter tile damage characteristics. The resulting debris impact location and velocity data are used by the Orbiter Project to predict tile impact damage dimensions to determine the acceptability of the debris source for ascent flight and to resolve post-flight debris issues. CFD solutions of the Space Shuttle aerodynamic flowfield are used to calculate the aerodynamic acceleration of the debris as it passes through the flowfield. Required inputs include both debris properties and flight conditions at the time of release.

6.1 Assumptions/Limitations

The ADT program is based on the following assumptions:

1. Debris is tumbling uniformly.
2. Aerodynamic forces act on an area equal to the average area of all exposed surfaces.
3. Aerodynamic drag, gravity and vehicle thrust are the only significant forces acting on the tumbling debris, lift force is not modeled.
4. Debris does not affect the local flowfield.
5. Static flowfields are used; flowfield changes due to vehicle acceleration are not modeled.

Realistically lift forces are relatively large during the initial portion of the trajectory. Initial rotation, during the early portion of the trajectory, has a strong effect on the debris trajectory. Section 7 contains an illustration of the effect of the debris on the local surface pressures as the debris travels down the body.

The program is limited to rectangular solid, circular cylinder and spherical shapes. Approximate solutions can be obtained by selecting the shape most similar to the particle being analyzed. Particle drag coefficient data, as a function of Mach number, is defined for the expected range of Shuttle ascent flight conditions and debris particle sizes corresponding to Reynolds numbers of one or greater. CFD solutions at various conditions are used for parametric debris studies to predict debris impact conditions from subsonic conditions up to Solid Rocket Booster (SRB) separation. When the actual flight conditions at the time of debris release are known CFD flowfield solutions are selected from the available Mach number/angle of attack combinations to bound the time of particle release.

6.2 Code Review Results

During the STS-107 investigation a thorough review of the ADTP was performed. A number of bugs and errors were discovered in the program. The errors included problems in the code's time integration scheme and some incorrect assumptions regarding the input gravity and vehicle acceleration vectors. Additionally several very inefficient routines were identified during this review. Replacement of the inefficient routines resulted in more than 3 orders of magnitude speed improvement in the code along with improved accuracy due to the use of an improved solution interpolation method.

Review of the drag coefficient tables in the ADTP resulted in several findings.

1. Tumbling rectangular solid drag coefficient look up table was actually for a rotating solid disk.
2. Most of the tumbling drag coefficient data dates back to the 1950s and are based on small metal cubes or other simple shapes.
3. The assumption that the reference area is equal to the average exposed surface area not consistent with all of the available drag coefficient data.
4. Update used Hoerner's tumbling cube data for all rectangular solids.

Conventionally the reference area is based on frontal or planform area and the some of the drag tables used in the ADT used planform area rather than average area. This assumption is particularly problematic for thin flat plates, disks or high aspect ratio objects. Using an average area where the drag coefficient is based on a planform area will result in an under prediction of the drag force and result in a lower impact velocity.

Review of this material showed that the there are relatively few sources of information for tumbling debris drag coefficients and that most of the sources are quite old and for very small objects. This is an area that could benefit from additional wind tunnel and CFD analysis.

The static CFD solution described in section 5 was used with the corrected code to obtain a more accurate prediction of the foam debris impact conditions on STS-107. These results are compared to the predictions made during the STS-107 mission in the next sub section.

6.3 Results compared to STS-107 Mission Predictions

During the STS-107 three different foam debris sizes were analyzed. One of the debris sizes, a 20″× 10″× x 6″ volume, is within the final estimated range of foam volumes predicted by detailed ballistic number estimates in Section 7. The original predicted impact velocity on RCC Panel 8 was 710 ft/sec with an impact angle of up to 21° as shown in Figure 6-1. These analyses were performed using relatively coarse grid CFD solutions at a Mach number of 2.5 and at angles of attack of 1.5° and 3.0°. These values compare well with the Mach 2.46 and angle of attack of 2.08° values determined by the post STS-107 ascent reconstruction.

Using a high fidelity flowfield at the STS-107 debris release conditions and a 1200 in^3 debris volume, along with the updated/corrected ADT, resulted in an impact velocity of 830 ft/sec. This result is within 55 ft/sec of the final estimated velocity used in the impact testing performed at the Southwest Research Institute. The final impact test used an angle of incidence equal to 20.6° that was quite close to the 21° value shown in the previous figure.

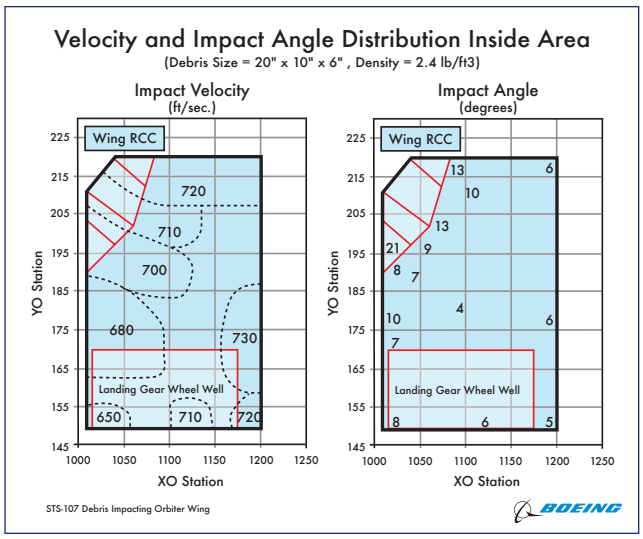


Figure 6-1. STS-107 debris impact results.

7.0 Trajectory Analysis/Ballistic Number Determination

This section details attempts to model the motion of the large debris object that apparently separated from the STS-107 external tank at approximately 81.7 seconds MET and subsequently impacted the left wing of the Orbiter. These analyses used observational data together with dynamical models to determine likely trajectories and properties of the debris object. Three separate coordinated analyses were performed by Condon, Crain, and Lee.

Condon and Lee both took the approach of using optimizer routines to fit trajectories to observational data based on a least-squares fit. They each performed analyses using two forms of observational data: first three-dimensional points estimated by image analysis groups, and later the "view vector" or "view line" form of data from the image analysis groups. Condon focused on a parametric approach to scan the pre-processed three-dimensional point data sets, using these results and other observation data-quality information to provide a better focus for the follow-on "view vector" analysis. Lee attempted to assess input data and specific case results to identify a "most reliable case" estimate.

Crain approached the problem using the more rigorous methods of statistical epoch state estimation. He applied the batch-least-squares method to estimate trajectory initial conditions and average ballistic number. This approach provided a measure of the uncertainties in the solution parameters that is a function of the uncertainty in the observations and the debris path. The Crain analysis was based on the three-dimensional point sets from image analysis.

7.1 Condon Analysis: Least Squares Optimized with Pre-processed and View Vector Data

This analysis was used to predict the impact velocity of foam debris with the Shuttle wing along with an estimate of the average ballistic number of this debris. The first part of the analysis compared integrated trajectory data to pre-processed imagery data sets acquired from four NASA organizations (JSC/ES, JSC/SX, KSC, and JSC/EG).

7.1.1 Approach Trajectory vs. Pre-processed Imagery Data Sets

This analysis attempts to minimize the sum square distance between time-dependent positions along the propagated foam debris trajectory and time-equivalent corresponding positions estimated from ground imagery data. Both parts of the deterministic trajectory analysis required development of the equations of motion for the foam debris relative to the Shuttle External Tank (ET) coordinate frame (Figure 7-1). The sum of the forces on the Shuttle (m_1) include accelerations due to engine thrust, drag, and gravity. The sum of forces on the debris (m_2) include acceleration from drag

and gravity only. The difference in the acceleration between the Shuttle and the debris, in the Shuttle ET coordinate frame, can be expressed as the difference between the drag acceleration of the debris and the Shuttle Orbiter sensed acceleration (due to thrust and drag). Note that the gravitational acceleration term drops out, as the gravity acting on the Shuttle and the debris are essentially the same. The drag force on the debris is a function of the density (ρ), relative velocity (V_{rel}), the drag coefficient (C_D), and the area (A). If we define the ballistic number (BN) as $m_2 g_0/(C_D A)$, then we can express the acceleration of the debris relative to the Shuttle as a function of the dynamic pressure (q), BN, and the Shuttle sensed acceleration.

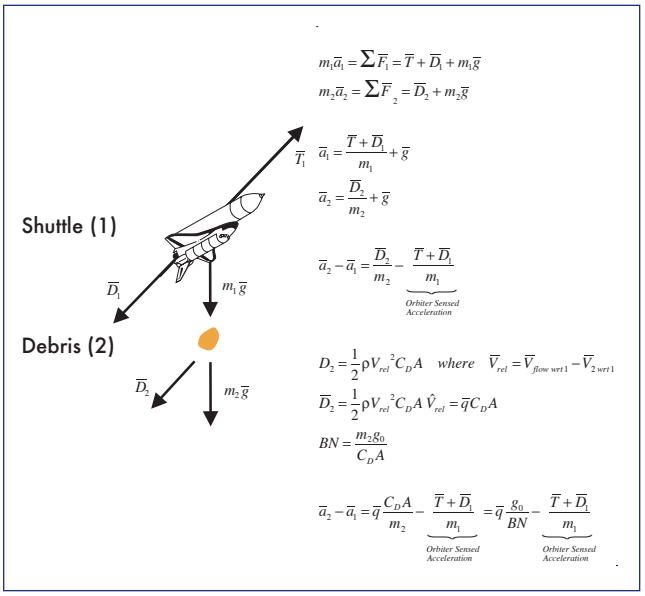


Figure 7-1. Force diagram of Shuttle and foam debris accompanied by associated equations of motion.

The Orbiter sensed acceleration, based on flight data and provided by the JSC/EG3 organization, is assumed to be constant over the approximately 170 milliseconds duration of the foam debris trajectory from the Shuttle bipod to impact on the wing. The sensed acceleration value (at Mach number 2.48) used in the trajectory simulation is:

$$a_sensed = [-75.163\ -0.058\ -2.472]\ ft/s^2.$$

The foam debris trajectory was propagated using a specially developed MATLAB simulation employing a Runge-Kutta fourth order integrator. The trajectory was integrated through a local velocity flow grid, obtained from JSC/EG3, that provided local velocity vectors, density, and speed of sound as a function of position vector components in the Shuttle ET coordinate frame. The 73x36x21 local velocity flow grid matrix covered the following range of position components (in units of inches):

1100 < x < 1820,	-350 < y < 0,	550 < z < 750
positive nose to tail	positive out right wing	positive through tail

The simulation performs an optimization using MATLAB's FMINCON routine to minimize the sum of the square of the time dependent distances (ΣD_n^2) between the integrated trajectory (Figure 7-2, dashed curve with circular icons) and the predetermined position data sets generated by JSC/ES, JSC/SX, KSC, and JSC/EG (Figure 7-2, solid curve with square icons). These four reference data sets are found in Appendix E.1. The MATLAB FMINCON optimization function employs ΣD_n^2 as the objective function to be minimized using 7 controls: the initial state vector (3 initial position controls and 3 initial velocity controls) and a constant BN over the entire debris trajectory. The initial state and BN are numerically perturbed to minimize the sum of the square of the distances at some or all of 11 data index points.

Imagery data suggested that the debris did not enter full ballistic trajectory behavior until around index point 4 or 5. Prior to that (index points 1-4 or 5), the debris appears to be heavily affected by multi-directional lift and drag accelerations. The equations of motion

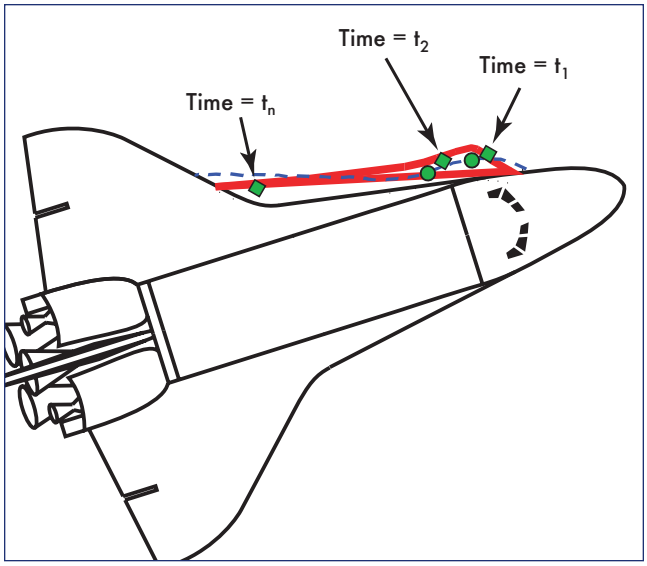


Figure 7-2. Illustration of time-dependent position differences between one of four reference data sets (JSC/ES, JSC/SX, KSC, or JSC/EG) and an integrated trajectory employing a flight-based local velocity flow field. The objective (minimized) function is the sum of the squares of the distances between some or all eleven of these time-dependent position points (ΣD_n^2).

for this part of the analysis employed only drag acceleration and not lift acceleration. For this reason, BN and estimated impact velocity data were generated for trajectories with initial conditions specified in this ballistic debris flow region. Index points 10 and 11 lacked consistent views from one or more (two) camera views, bringing into question the accuracy of the imaging data for these points. Further, preliminary data using the JSC/SX reference database showed relatively consistent BN results in this ballistic flow region away from the lift-affected initial part of the trajectory (index points 1 – 4 or 5) and the questionable end points 10 and 11.
A trajectory comparison analysis was then performed for the region including index points 4 and 5 through 8 and 9 (i.e.,

				Controls							Objective Function (Min)		
				Initial State						Initial Bn			
Data Set	Intervals	Initial Interval Time (sec)	Final Interval Time (sec)	X (in)	Y (in)	Z (in)	Vx (fps)	Vy (fps)	Vz (fps)	Ballistic Number (lb/ft²)	Sum Square Position Error (in²)	Average Error per Interval (in²)	Projected Velocity @ X = 1800 in. (fps)
JSC/ES	4-8	0.050	0.117	1146.73	-151.56	585.43	191.11	-26.58	49.82	2.5134	1207.84	301.96	647
JSC/ES	4-9	0.050	0.133	1149.34	-154.17	585.43	138.61	-10.29	49.85	1.8064	1524.75	304.95	719
JSC/ES	5-8	0.067	0.117	1206.86	-171.86	595.39	96.34	20.44	52.01	1.0854	341.89	113.96	826
JSC/ES	5-9	0.067	0.133	1206.86	-172.32	595.48	94.98	23.35	51.46	1.0782	344.53	86.13	827
JSC/SX	4-8	0.050	0.117	1164.53	-136.26	578.60	-8.72	9.84	59.78	1.2217	623.65	155.91	803
JSC/SX	4-9	0.050	0.133	1164.86	-133.81	579.06	-10.85	-2.14	57.68	1.2168	725.85	145.17	808
JSC/SX	5-8	0.067	0.117	1191.17	-134.75	586.47	83.00	-6.31	66.14	0.8960	451.67	150.56	883
JSC/SX	5-9	0.067	0.133	1190.30	-132.30	587.37	119.10	-23.38	59.52	1.0300	559.47	139.87	847
JSC/EG	4-8	0.050	0.117	1139.89	-116.00	586.27	125.29	-48.72	42.45	1.4103	1215.65	303.91	788
JSC/EG	4-9	0.050	0.133	1134.11	-115.16	586.97	226.07	-56.15	37.72	2.1322	1860.28	372.06	695
JSC/EG	5-8	0.067	0.117	1184.27	-125.81	593.66	224.31	-51.42	42.42	1.1887	1158.66	386.22	823
JSC/EG	5-9	0.067	0.133	1180.98	-124.93	594.49	350.27	-64.02	33.43	2.5056	1804.99	451.25	674
KSC	4-8	0.047	0.109	1168.93	-125.93	583.59	66.63	-45.48	59.27	1.4059	67.62	16.90	772
KSC	4-9	0.047	0.125	1168.57	-126.67	585.00	73.99	-42.20	52.42	1.4516	109.30	21.86	763
KSC	5-8	0.063	0.109	1196.96	-134.85	591.66	183.20	-50.95	61.79	1.2317	46.66	15.55	803
KSC	5-9	0.063	0.125	1196.29	-135.63	593.57	204.68	-47.78	49.41	1.3939	104.83	26.21	771

Table 7-1. BN and projected velocity results for reference data sets (JSC/ES, JSC/SX, JSC/EG3, KSC).

indices 4 – 8, 4 – 9, 5 – 8, and 5 – 9) for each of the reference data sets (JSC/ES, JSC/SX, KSC, and JSC/EG). This analysis produced constant BN values and associated projected impact velocities as shown in Table 7-1. A key comment would be to consider the sparse imagery-based trajectory analysis results in the context of the data available. There were only 11 data points presented of which only about 5 or so are useful (without additional lift modeling in the analysis*).

At this point a caveat about this methodology should be mentioned. One must keep in mind that closely matching a trajectory to the reference data with the minimum sum square position error doesn't necessarily mean that the BN and projected impact velocity is the most accurate. The sparse data coupled with the fact that these data sets represent already pre-processed data suggest that the best trajectory match will only be as good as the original data set. With this in mind, the author attempts to temper results by considering overall consistency of the results and the best possible matching of the data to the methodology using as much appropriate data as possible. For example, this methodology employs only a drag model and will show the best results in region of the trajectory where the debris experiences ballistic motion. Early in the trajectory, imaging suggests the existence of lifting on the debris. The maximum number of useful data points should be employed to provide the best possible representation of the actual debris flight. For example, if only two data points are used, the trajectory simulation could produce a nearly zero sum square error. However, with such few data points, the confidence in the resulting BN and projected velocity would be low.

7.1.2 Observations

The limited data resulted many times in large variations in BN. The 11 data points available for analysis were further limited by unusable data points at the beginning of the trajectory due to unmodeled lift and a couple of questionable or unusable data points at the end of the trajectory due to camera viewing limitations or image analysis limitations.

The KSC data set (see Table 7-1) for ranges (4-8, 4-9, 5-8, and 5-9) produced the most consistent BN values. Trajectory optimization using the KSC reference data set resulted in a BN ranging from 1.2317 – 1.4516 lb/ft² and an associated projected velocity range (at X=1800 inches) of 763 – 803 ft/s. These ranges represent approximately an 18% variation in BN and a 5% variation in predicted velocity at X = 1800 in. (near impact location). The minimum sum square error of all assessed data sets is 15.55 in² per interval in the index interval range 5-8. A 3-dimensional plot of the trajectory positions and the reference data set positions for this portion of the debris trajectory (Figure 7-3) reflects the low sum square

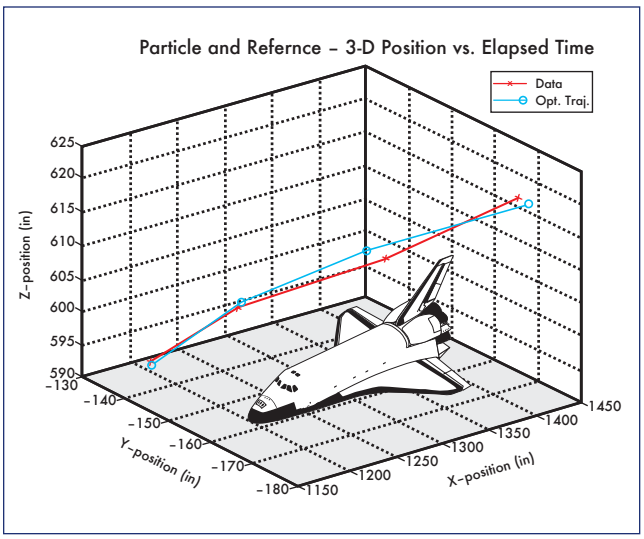


Figure 7-3. Three-dimensional view of foam debris trajectory as compared to KSC reference data for index range (5-8). Note: Shuttle diagram is for attitude reference only and is not to scale.

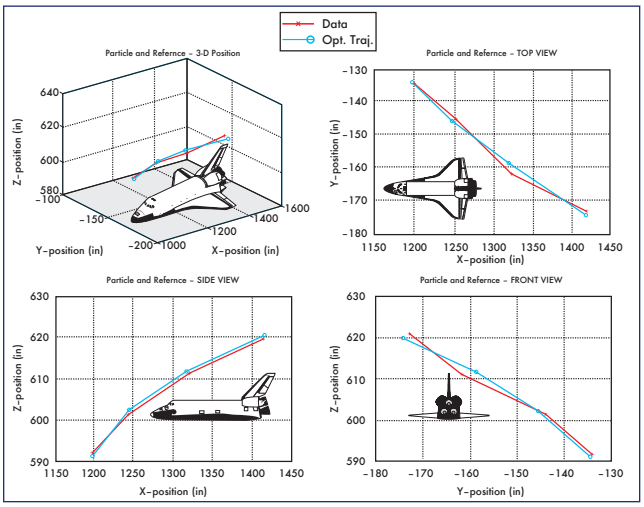


Figure 7-4. Composite view of foam debris trajectory as compared to KSC reference data for index range (5-8) including top, side and "front" views. Note: Shuttle diagram is for attitude reference only and is not to scale.

error. A composite view of the 3-D plus front, side, and top views of the trajectory comparison are shown in Figure 7-4.

The time tags for the JSC/ES, JSC/SX, and JSC/EG data are consistent with each other and with that of a 60 frame/second camera. The first 10 points of the KSC data appear to be taken from a 64 frame/second camera. The interval between the last two KSC data points (10 and 11) is approximately 140% that of a normal 64 frame/second rate and may be spurious. Convergence of trajectories including the 11th reference data point results in high BN values. Other, more consistent data (previously described) suggest these high BN values to be erroneous. They were not considered in the results of this analysis. The JSC/SX data carries a higher sum square error over the selected ranges of integration, however these data also appear to be relatively consistent. The BN values range from 1.0300 – 1.2217 lb/ft^2 over the same index interval ranges as that of the KSC data. This BN range is a bit lower than that of the KSC with a slightly wider variation (approximately 19%), while the projected speed at X = 1800 inches ranges from 803 – 883 ft/s representing a 10% variation between the maximum and minimum values. The BN ranges for the JSC/ES and JSC/EG reference data sets were much more varied (133% and 132%, respectively) and the projected velocity values (at X = 1800 inches) carried a variation of 28% and 22%, respectively. The more consistent BN and projected velocity results fostered better confidence in the KSC and JSC/SX reference data sets.

A plot of the projected velocities at X = 1800 inches (Figure 7-5) shows the consistent velocity results for the KSC based data. The JSC/SX velocities appear to be almost as consistent as the KSC data and are uniformly higher than the KSC data. The results for the JSC/ES and JSC/EG are a bit more "choppy". In contrast to the lower sum square error of the KSC data for index interval range 5-8, the JSC/EG carries a higher sum square position error and associated larger differences between the trajectory and the reference data set (see Figures 7-6 and 7-7).

While the previous analysis sought only constant BN values across the trajectory, a preliminary look was given to minimizing the sum square error between the integrated trajectory and the reference data sets using multiple BNs (and the initial state) as controls. This initial look was done with the JSC/ES reference data set, which as more reference data sets became available, appeared to possess less consistent data than other data sets (i.e., KSC and JSC/SX). The data in Table 7-2 shows BN values, sum square error, and the initial state for trajectory optimizations employing both single and

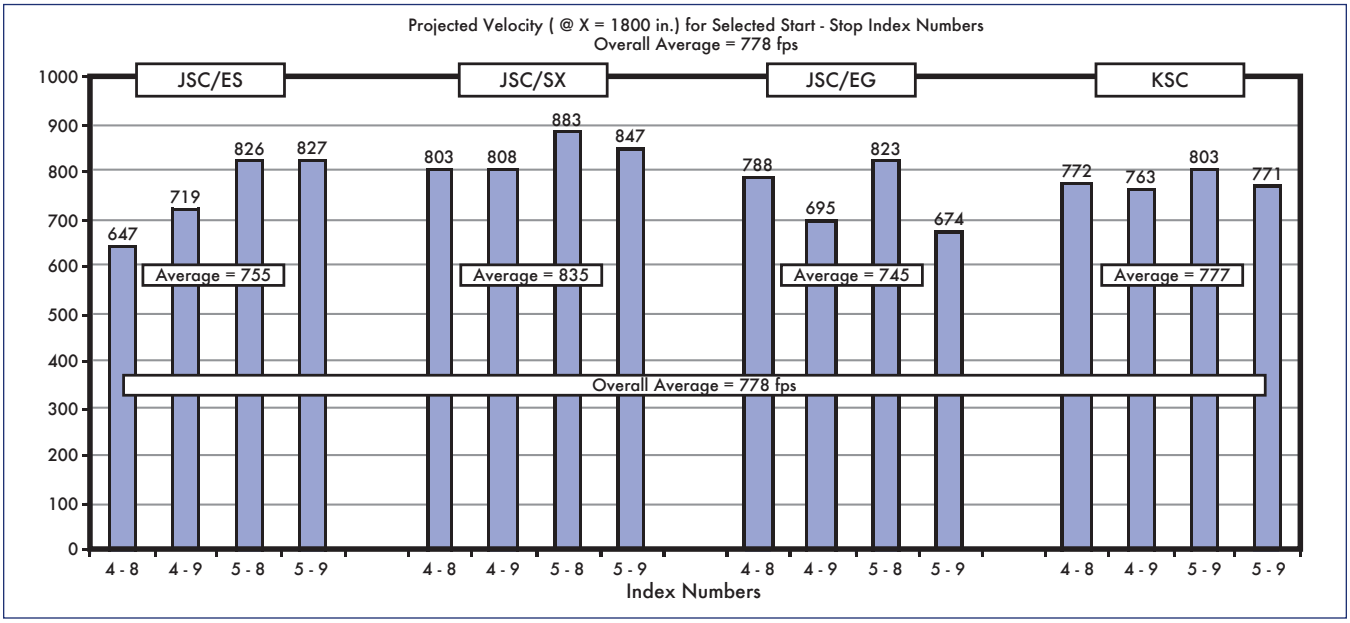


Figure 7-5. Projected velocity of foam debris to position X = 1800 inches, for reference data sets JSC/ES, JSC/SX, JSC/EG, and KSC. The KSC data provides the most consistent projected velocity results.

multiple BN controls. Assumptions used in generation of this particular data include constant local velocity between index intervals and10 internal integration steps between index intervals. While the magnitude of the BNs for the multiple BN trajectories can become exceedingly large, a point of interest to note is that the BNs have a cyclic nature (large to small to large). One could infer from this that the changing BN was a result of a rotating piece of debris. Imagery data confirms this. Further, the multiple BN case using the most data points (i.e., 2-10) indicates a rotation rate of about 20 revolutions/second. This is in relatively good agreement with rotation rates extracted from imagery data.

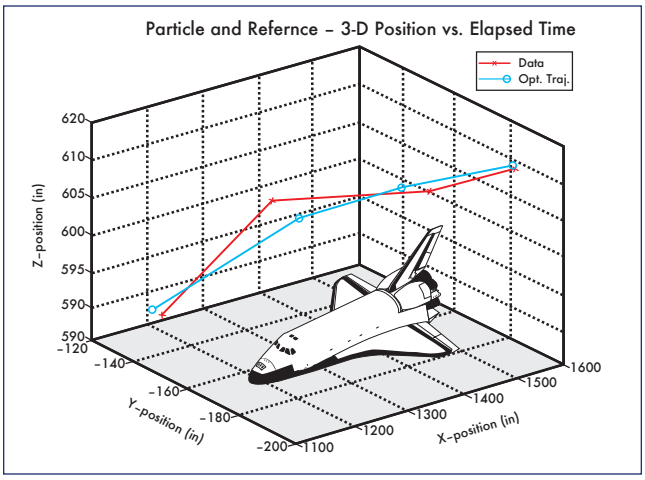


Figure 7-6. Three-dimensional view of foam debris trajectory as compared to JSC/EG reference data for index range (5-8). The sum square position error for this case is larger than that based on the KSC reference data set, as shown in Figure 7-3. Note: Shuttle diagram is for attitude reference only and is not to scale.

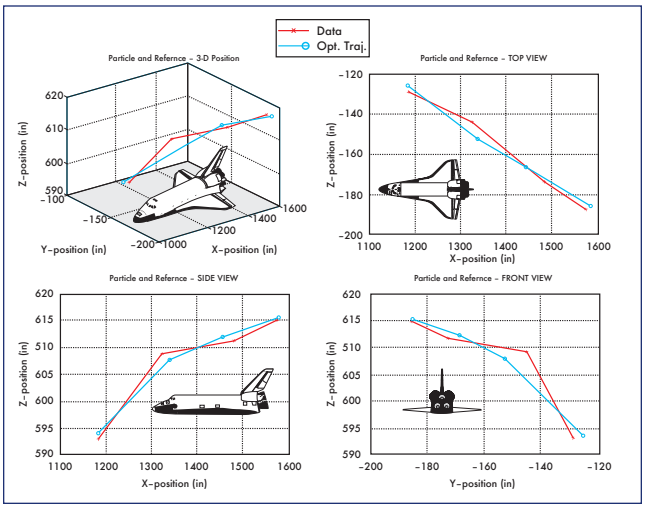


Figure 7-7. Composite view of foam debris trajectory as compared to JSC/EG reference data for index range (5-8) including top, side and "front" views. Note: Shuttle diagram is for attitude reference only and is not to scale.

Index	Elapsed Time (sec)	Single Ballistic Number Optimization Control							Multiple Ballistic Number Optimization Control						
1	0.000	BN1	BN1	BN1	BN1	BN1	BN1	BN1	BN1	BN1	BN1	BN1	BN1	BN1	BN1
2	0.017	BN2	BN2	BN2	BN2	BN2	BN2	BN2	**BN2**	BN2	BN2	BN2	BN2	BN2	BN2
3	0.033	BN3	**BN3**	BN3	BN3	BN3	BN3	BN3	**BN3**	**BN3**	BN3	BN3	BN3	BN3	BN3
4	0.050	BN4	BN4	**BN4**	BN4	BN4	BN4	BN4	**BN4**	**BN4**	**BN4**	BN4	BN4	BN4	BN4
5	0.066	BN5	BN5	BN5	**BN5**	BN5	BN5	BN5	**BN5**	**BN5**	**BN5**	**BN5**	BN5	BN5	BN5
6	0.083	BN6	BN6	BN6	BN6	**BN6**	BN6	BN6	**BN6**	**BN6**	**BN6**	**BN6**	**BN6**	BN6	BN6
7	0.100	BN7	BN7	BN7	BN7	BN7	**BN7**	BN7	**BN7**	**BN7**	**BN7**	**BN7**	**BN7**	**BN7**	BN7
8	0.117	BN8	BN8	BN8	BN8	BN8	BN8	**BN8**	**BN8**	**BN8**	**BN8**	**BN8**	**BN8**	**BN8**	**BN8**
9	0.133	BN9	BN9	BN9	BN9	BN9	BN9	BN9	**BN9**	**BN9**	**BN9**	**BN9**	**BN9**	**BN9**	**BN9**
10	0.150	BN10	BN10	BN10	BN10	BN10	BN10	BN10	**BN10**	**BN10**	**BN10**	**BN10**	**BN10**	**BN10**	**BN10**
11	0.167	BN11	BN11	BN11	BN11	BN11	BN11	BN11	BN11	BN11	BN11	BN11	BN11	BN11	BN11
1	0.000	BN1							1.000	1.000	1.000	1.000	1.000	1.000	1.00
2	0.017	BN2							50.537	1.000	1.000	1.000	1.000	1.000	1.00
3	0.033	BN3	2.15208						1.106	3.474	1.000	1.000	1.000	1.000	1.00
4	0.050	BN4	2.15208	2.28391					5.773	2.251	8.208	1.000	1.000	1.000	1.00
5	0.066	BN5	2.15208	2.28391	1.95284				17.247	42.263	13.833	13.224	1.000	1.000	1.00
6	0.083	BN6	2.15208	2.28391	1.95284	2.58165			1.058	0.671	1.302	0.706	0.298	1.000	1.00
7	0.100	BN7	2.15208	2.28391	1.95284	2.58165	*1000*		1.186	102.181	0.999	1.470	84.813	348.948	1.00
8	0.117	BN8	2.15208	2.28391	1.95284	2.58165	*1000*	*1000*	10.734	1.849	36.370	206.760	302.151	1000.000	729.10
9	0.133	BN9	2.15208	2.28391	1.95284	2.58165	*1000*	*1000*	93.614	17.662	31.179	408.217	263.402	102.980	1000.00
10	0.150	BN10	2.15208	2.28391	1.95284	2.58165	*1000*	*1000*	224.947	55.640	58.044	1000.000	492.291	147.066	889.64
11	0.167	BN11	2.15208	2.28391	1.95284	2.58165	*1000*	*1000*	224.947	55.6405	58.0444	*1000*	492.291	147.0662	889.637
		$R1_{init}$	in.	1129.08	1144.39	1197.90	1248.13	1318.36	1441.46	1125.14	1128.08	1144.05	1205.13	1258.77	1318.44	1441.47
		$R2_{init}$	in.	-144.64	-160.53	-174.63	-175.62	-177.00	-183.49	-123.65	-144.36	-160.83	-176.29	-177.82	-177.01	-183.49
		$R3_{init}$	in.	581.26	589.52	598.97	607.32	615.84	623.45	575.99	581.66	589.20	598.87	607.49	615.83	623.45
		$V1_{init}$	ft/sec	47.39	190.94	238.56	401.49	582.84	574.02	1.91	94.56	258.35	218.58	-70.03	582.20	573.99
		$V2_{init}$	ft/sec	-0.52	5.79	17.09	-2.30	-22.32	-17.48	-19.60	-6.03	-3.51	20.60	71.50	-22.25	-17.47
		$V3_{init}$	ft/sec	39.07	36.81	35.10	27.41	14.83	3.31	38.40	37.47	37.62	35.32	38.60	14.86	3.31
Least Square Position Error (in.^{2})				3556.74	2149.39	1165.66	960.02	138.85	33.73	4834.65	3142.53	1493.01	464.88	185.90	141.20	33.75

Table 7-2. Single and multiple BN values and initial states for the JSC/ES reference data set. Note that a maximum allowable BN of 1000 was used for the multiple BN cases. On possible explanation for the arbitrarily high BN is the sparseness and uncertainty in the imagery-based data set.

7.1.3 Conclusions

The KSC data set for index ranges (4-8, 4-9, 5-8, 5-9) produced the most consistent results, including the lowest sum square position error as compared to the other data sets (JSC/ES, JSC/SX, and JSC/EG). This data set resulted in the smallest overall sum square error (46.66 in^2) and the smallest sum square error per index interval (15.55 in^2). The average projected velocity of 777 fps was, coincidentally, very close to the overall average of 778 fps for velocity results from all data sets. Based on this KSC data, the ballistic number ranges from 1.23 to 1.45 lb/ft^2 and produce a range of velocities of 763 to 803 fps (at an X-position of 1800 in.).

Note that results for the sampling of multiple BN cases appear to support imaging analysis data indicating foam debris rotation. More abundant and accurate trajectory data may have allowed the trajectory analysis to produce a trustworthy time history of the actual BN, aiding analysts in better confirming the orientation of the foam debris as well as its trajectory.

7.1.4 Approach –Trajectory vs. View Vector Data

As mentioned in the previous section, comparisons between an integrated trajectory and pre-processed reference data sets may possess inherent errors due to the nature of these data sets (e.g., curve fitting of imagery data, unknown assumptions made by analysts, etc.). A second approach option employing trajectory comparison directly to camera view vector data attempts to generate the most realistic values for BN and projected velocity. This approach minimized the sum square error (in the ET coordinate frame) between an integrated trajectory and view vector data for cameras 208 and 212, obtained from Marshall Space Flight Center. The diagram and equations of motion in Figure 7-1 also apply to this approach. In fact the overall approach for this trajectory vs. view vector data comparison (part 2) is the essentially the same as that of the trajectory vs. reference data sets (part1). The approaches differ in that the sum square error objective (optimization) function in this approach (part 2) is obtained by comparing the integrated trajectory to the perpendicular distance from the camera view vectors for two ground cameras 208 and 212 (see Figure 7-8).

The time stamps for the cameras were not synchronized, so the view vector data had to be interleaved. After performing some analysis using the interleaved data, MSFC noted that the image analysis team achieved much better "triangulation" of the imaging data when the time stamp for camera 208 was shifted earlier by 6.75 milliseconds (milliseconds). Subsequent analysis was performed using the time shifted time stamp for camera 208. The interleaved data for the original and time shifted camera view vector data are shown in Appendix E-2 along with anchor positions and estimated error associated with the view vectors at each index interval point.

The interleaved camera data result in 19 index intervals covering the imaged flight of the foam debris from just after break-away to impact with the Shuttle's port (left) wing. As in part 1, the drag-based modeling in the equations of motion focused the analysis to consideration of the index points beyond the initial points, which appeared to include uncertain flow interactions including lifting. Further, as in part 1, the latter index points were not considered in the analysis due to poor imagery confidence resulting from blocked debris view from one or both cameras. In order to maintain correlation with the start and stop intervals from the part 1 reference data set comparison, a range of candidate trajectory optimizations was selected on the basis of previous results from pre-processed data sets provided by JSC/ES, JSC/SX, JSC/EG, and KSC. Figure 7-9 shows the index interval selection of the view vector data set of part 2 as compared to that of the reference data sets in part 1. For the view vector based analysis the index interval ranges used were 7-13, 7-14, 7-15, 7-16, 8-13, 8-14, 8-15, and 8-16. This ballistic flow region was considered to be the best range for obtaining the best average BN and impact velocity estimates.

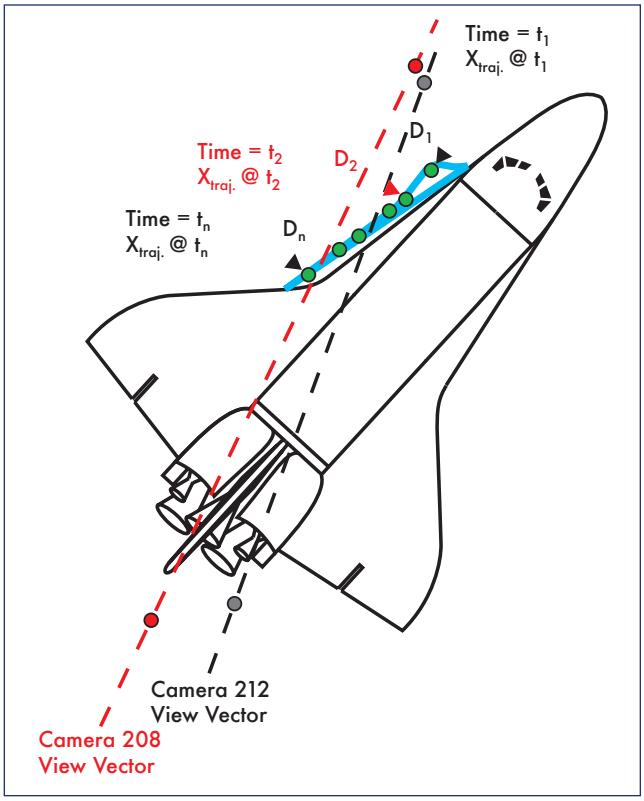


Figure 7-8. Illustration of time-dependent position differences between view vectors for ground cameras 208 and 212 and an integrated trajectory (solid curve) employing a flight-based local velocity flow field. The objective (minimized) function is the sum of the squares of the distances between some or all eleven of these time-dependent position points (ΣD_n^2).

The minimization of the sum square error between the integrated trajectories and the camera (208 and 212) view vectors was confined to these regions. Propagation of the state vector was performed using the position dependent local velocity data grid provided by JSC/EG3 (as used for part 1). In addition to the data associated with the index interval endpoints (i.e., 7-13, 7-16, 8-13, and 8-16), BN, projected impact velocity, projected impact time, and sum square error were

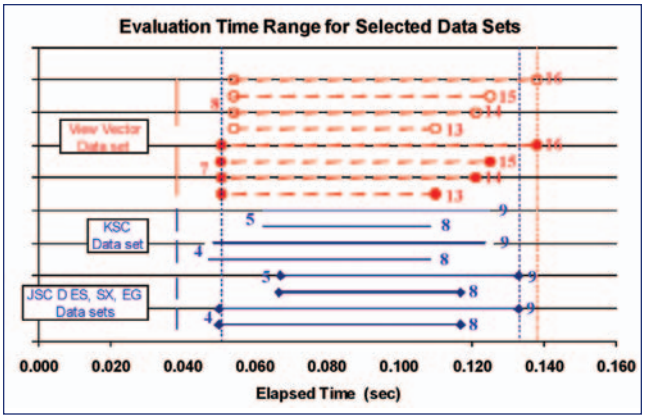


Figure 7-9. The index intervals for the comparison of an integrated trajectory with the view vectors from cameras 208 and 212 are designed to provide similarity to the intervals using in the reference data set comparisons in the previous section. The index ranges used to generate the most probable estimates of key parameters (BN, projected impact velocity, etc.) were 7-13, 7-14, 7-15, 7-16, 8-13, 8-14, 8-15, and 8-16.

evaluated for all internal index point ranges surrounding these endpoints (i.e., 4-8, …, 4-17, 5-9, … , 5-17, … , 13-17). Contour plots of these data are presented in Appendix C.

7.1.5 Observations

The contour plots for BN, projected impact velocity (at X = 1817.45 inches), projected impact time and sum square error (Appendix E3) encompass the index range of interest (7-13, 7-16, 8-13, and 8-16). This index range was the focus for generating the parameters of interest (BN, projected impact velocity, projected impact time). The data in this index range of interest are relatively consistent and homogeneous, given the sparseness and the uncertainty of the image-based comparison data (view vector data). The contour plots show the significant sensitivity of these parameters to the start and stop index values, and appear to reinforce the jittery nature of this sparse data.

Several different trajectory optimization approaches were employed. All impact velocity and time computations were projected to X = 1817.45 inches. The data in figures 6-10(a, b, and c) show the BN, projected impact velocity, and projected impact time for these optimization approaches. The first bar (left most – lightest) in each plot shows the results based on the original MSFC data. Note point 14 (index 7-14 and 8-14) shows a large excursion in the parameters. It is particularly apparent for BN in Figure 7-10. The second plot bars reflect an adjustment to the time stamp of camera 208, which is moved up (earlier) by 6.75 milliseconds. This adjustment was based on feedback from MSFC that it produced the best imaging data results. Again, some excursion in the data can still be seen for point 14. A conversation with MSFC personnel revealed that MSFC had trouble with this particular frame (index) due to image blur. It appears that the trajectory results performed at JSC reflected the uncertainty in the view vector data for index 14. Subsequently, the author performed another trajectory optimization with the data for index 14 removed (3rd more heavily shaded bar). The result was data that appeared to be much more consistent. Finally, the camera view vector errors were used in the computation of the objective function (sum square

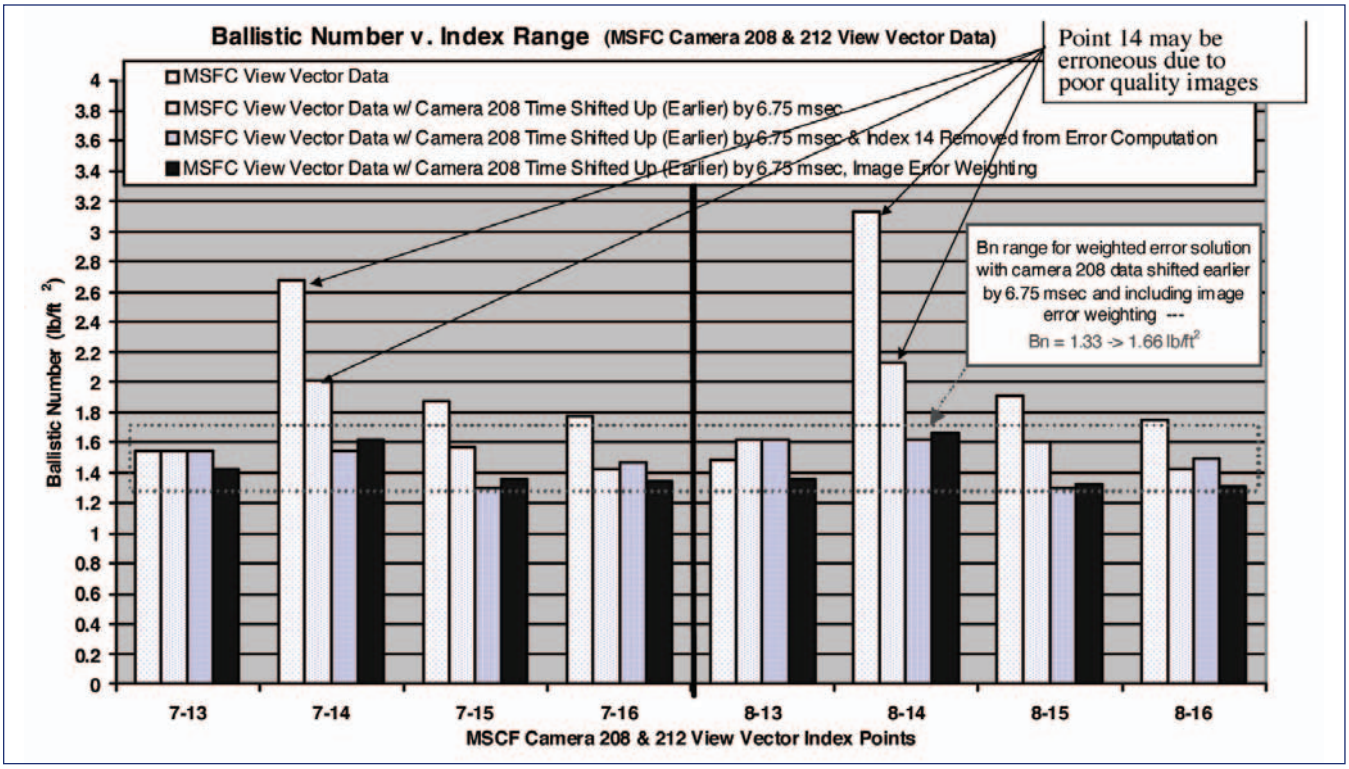


Figure 7-10. BN vs. index range for selected view vector data comparisons.

				Controls							Objective Function (Min)				
				Initial State						Initial Bn					
Data Set	Intervals	Initial Interval Time (sec)	Final Interval Time (sec)	X (in)	Y (in)	Z (in)	Vx (fps)	Vy (fps)	Vz (fps)	Ballistic Number (lb/ft^2)	Sum Square Position Error (in^2)	Average Error per Interval (in^2)	Projected Velocity @ X = 1817 in. (fps)	Projected Impact Time @ X = 1817 in. (sec)
View Vector	7-13	0.04975	0.110	1135.01	-116.45	578.63	81.93	-58.87	55.02	1.426	55	9	796	0.164
View Vector	7-14	0.04975	0.121	1134.17	-116.51	578.76	84.74	-50.61	52.06	1.620	100	14	759	0.170
View Vector	7-15	0.04975	0.125	1137.172	-117.017	579.1242	28.31112	-43.0193	50.10038	1.360	203	25	804	0.166
View Vector	7-16	0.04975	0.138	1136.68	-116.73	579.04	31.15	-45.30	50.77	1.345	208	23	808	0.166
View Vector	8-13	0.05000	0.110	1141.65	-120.80	576.02	120.18	-71.90	66.79	1.353	36	7	814	0.162
View Vector	8-14	0.05000	0.121	1146.41	-124.49	577.01	69.49	-34.24	56.23	1.661	81	14	742	0.172
View Vector	8-15	0.05000	0.125	1143.63	-119.87	577.65	14.74	-38.24	53.23	1.328	199	28	807	0.166
View Vector	8-16	0.05000	0.138	1143.24	-119.50	577.56	15.44	-40.07	53.77	1.314	203	25	811	0.166

Table 7-3. BN and projected impact velocity and time (at X = 1817.45 inches) results for comparison of minimum sum square error between ground camera (208 & 212) view vectors and the integrated trajectory. This data is based on movement of the time stamp for camera 208 earlier by 6.75 milliseconds and includes view vector location errors in computation of the sum square perpendicular error between the integrated trajectory and the view vectors at a succession of index points.

error) to produce a weighted error trajectory comparison to the view vector data (right most solid bar). While this data did include index 14, it appeared to be relatively consistent. This last data set was selected as the most representative of the actual foam debris flight characteristics, given the data available.

Table 7-3 shows a summary of the BN values along with the projected impact velocity and time at X = 1817.45 inches. The table shows the 7 controls used in the trajectory optimization including the initial state and the BN. The optimization minimized the objective function or the sum square perpendicular distance error between the integrated trajectory and the view vectors at successive index points.

For the index intervals evaluated, the resulting BN ranged from 1.314 to 1.661 $lb./ft^2$ and the projected impact velocity of the foam debris at X-position of 1817.45 inches ranged from 742 to 814 fps.

The foam debris trajectories for index ranges (7-13, 7-14, 7-15, 7-16, 8-13, 8-14, 8-15, and 8-16) are depicted in an oblique view of the Shuttle (Figure 7-13). These trajectories represent the optimal selection of the initial state and a constant BN to provide a minimum sum square error over the selected index interval. They begin at the initial state and are projected to impact the left Shuttle wing*. For all cases the debris impacts the Shuttle on Reinforced Carbon-Carbon (RCC) panels 7, 8, or 9.

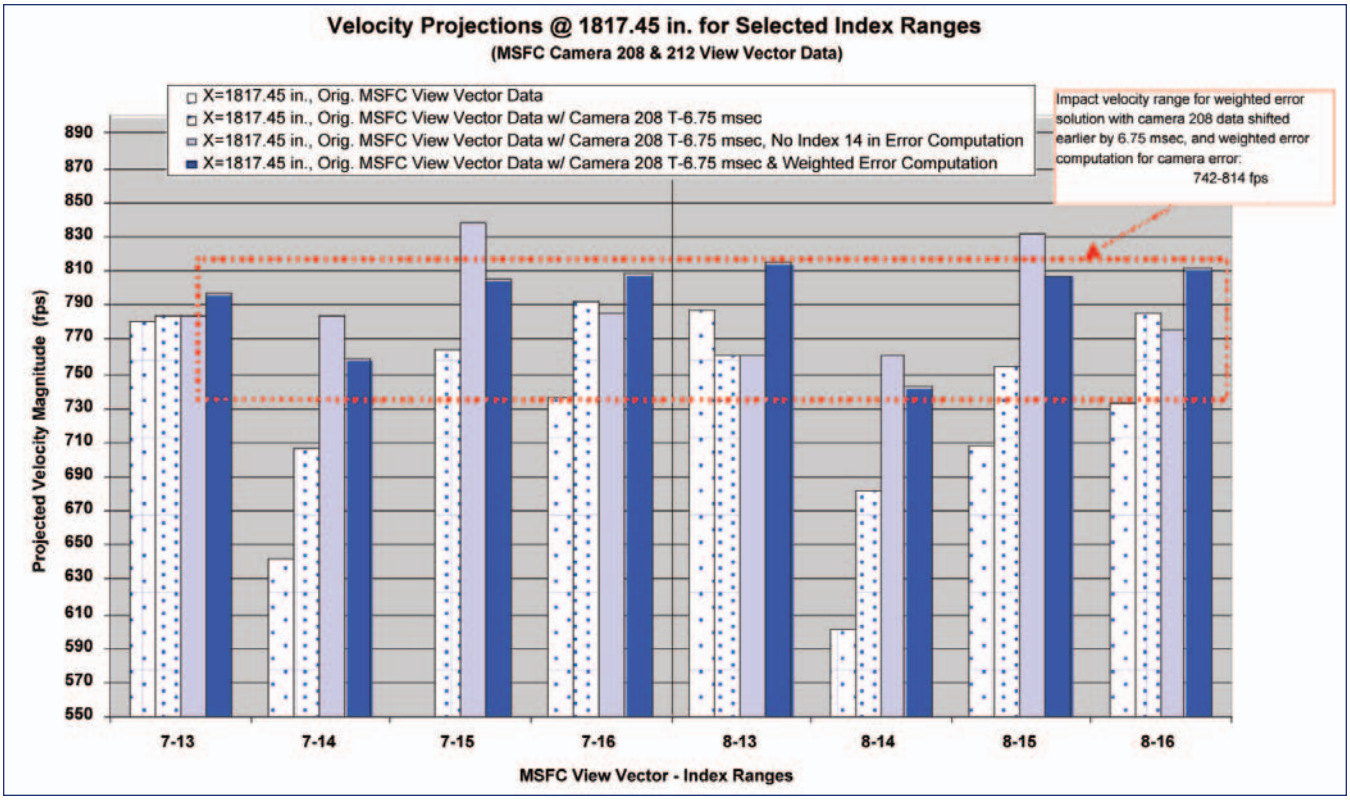


Figure 7-11. Projected impact velocity at X-position = 1817.45 inches vs. index range for selected view vector data comparisons.

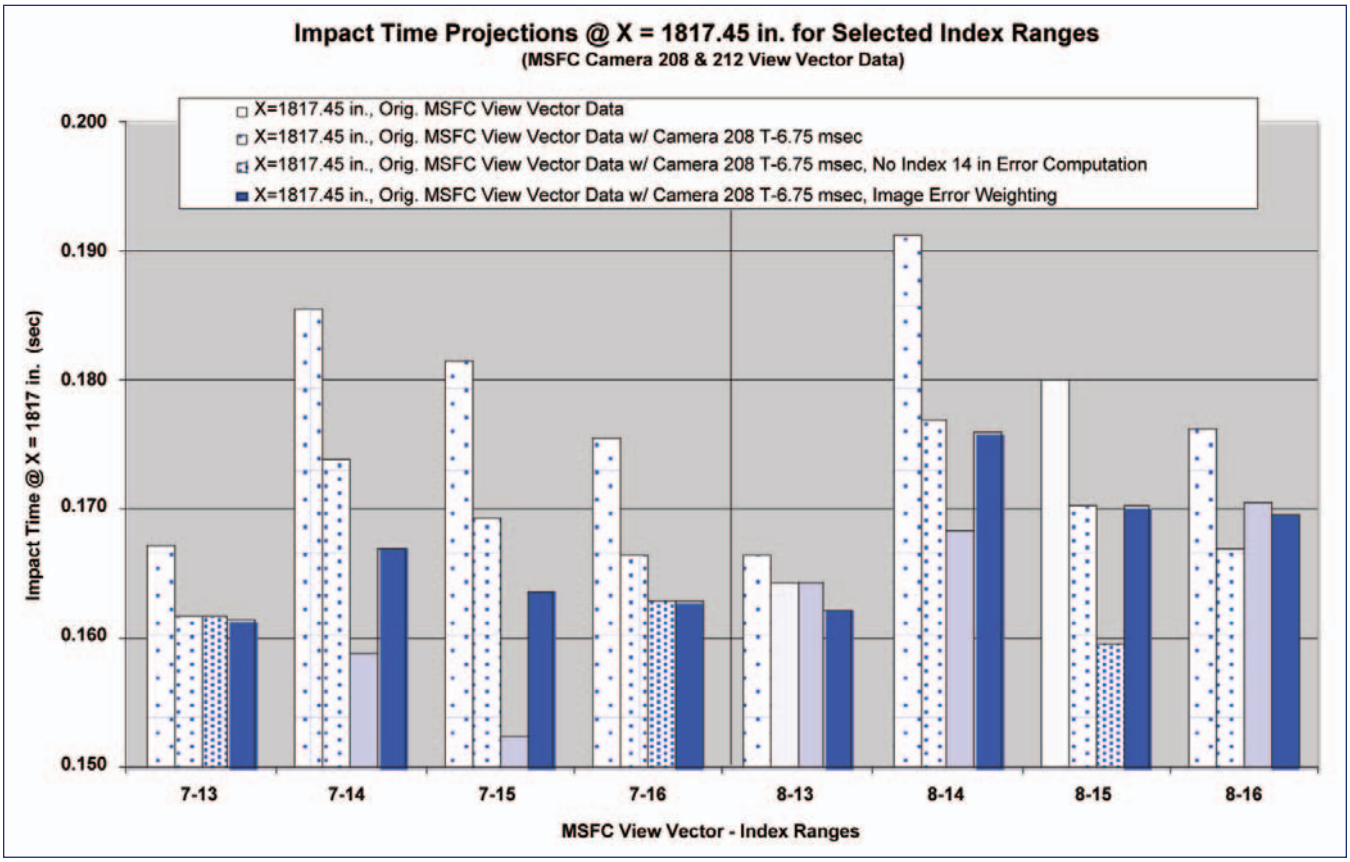


Figure 7-12. Projected time of impact at X-position = 1817.45 inches vs. index range for selected view vector data comparisons.

An enhanced view of the impact locations (Figure 7-12) shows the projected impact locations on the leading edge of the Shuttle wing. While all eight selected index interval trajectories were projected to hit the wing, several appeared to hit high on the wing leading edge (trajectories 8-13 and 8-14, possibly 7-13 and 7-14). Imagery data showing debris emerging from under the wing suggest a debris impact on the lower leading edge. A grouping of four trajectories (7-15, 7-16, 8-15, 8-16) appears on RCC panels 7 & 8 on the lower leading edge. A top view of the Shuttle with these trajectories shows that the impacts occurred with an outboard angle to the trajectory (see Figure 7-14).

The impact velocities for the selected-index-intervals trajectories shown in Figures 7-10 through 7-12 range from 729-815 fps, with the bulk of the velocity component in the ET coordinate frame x-direction (see Table 7-4). The trajectory heading ranges from about 6.5°-7.5° outboard at impact

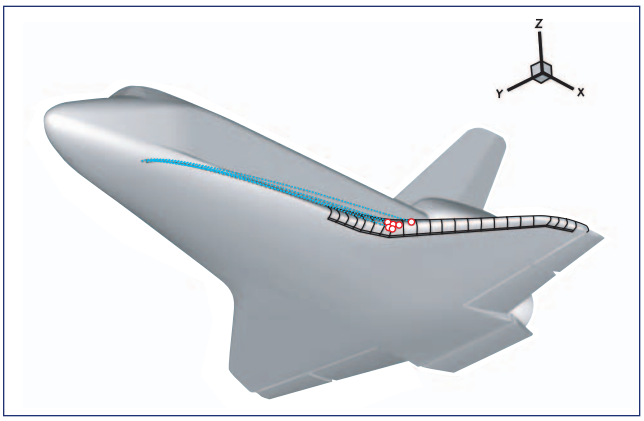


Figure 7-13. Optimized foam debris trajectories for index intervals 7-13, 7-14, 7-15, 7-16, 8-13, 8-14, 8-15, and 8-16, projected to Shuttle impact. Graphic courtesy of Phil Stuart – JSC/EG3.

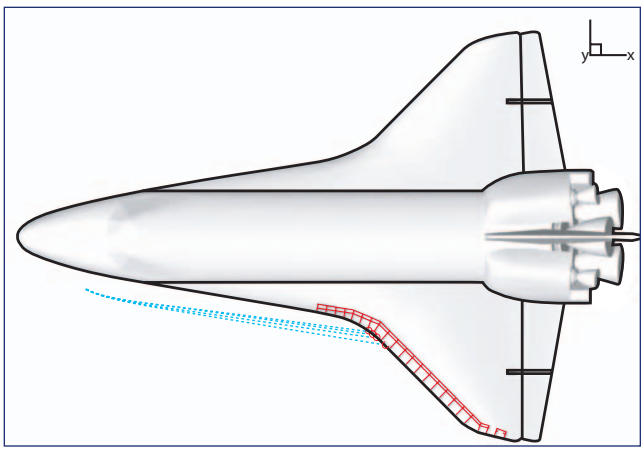


Figure 7-14. Top view of optimized foam debris trajectories for index intervals 7-13, 7-14, 7-15, 7-16, 8-13, 8-14, 8-15, and 8-16, projected to Shuttle impact and showing outboard direction of trajectory at impact. Graphic courtesy of Phil Stuart – JSC/EG3.

	Impact Position			Impact Velocity				Impact angle - relative to Shuttle wing	Trajectory heading - relative to E.T. coordinate frame		
Index Interval	X	Y	Z	Vx	Vy	Vz	Vmag	Impact Angle	Angle X-Y	Angle X-Z	Angle Y-Z
	(inches)	(inches)	(inches)	(fps)	(fps)	(fps)	(fps)	(deg)	(deg)	(deg)	(deg)
7-13	1806.63	-231.14	630.24	784.98	-98.77	28.45	791.68	31.83	2.03	-7.16	82.56
7-14	1796.85	-223.44	630.41	743.94	-91.00	27.65	750.00	29.89	2.13	-6.97	82.71
7-15	1797.70	-217.53	624.55	789.94	-91.46	22.37	795.53	15.46	1.62	-6.60	83.20
7-16	1799.12	-219.39	624.94	794.44	-93.00	22.93	800.20	15.81	1.63	-6.67	83.14
8-13	1827.05	-247.37	637.56	807.41	-107.57	36.85	815.37	29.55	2.59	-7.58	81.98
8-14	1786.80	-215.39	633.33	724.08	-81.86	30.30	729.32	26.08	2.40	-6.44	83.12
8-15	1792.08	-215.63	625.54	790.12	-89.63	23.81	795.54	15.79	1.70	-6.47	83.31
8-16	1793.51	-217.01	625.78	794.47	-90.90	24.18	800.02	16.94	1.71	-6.53	83.25

Table 7-4. Foam debris data for selected index interval trajectories impacting the Shuttle wing as depicted in Fgures 6-11, 6-12, and 6-13.

(as shown in Figure 7-15). The trajectory angle between the incoming debris trajectory and the Shuttle wing leading edge (impact angle) has a range of about 15.5°-31.8°. For all cases, the impacting debris trajectory lies within about 2.5° of the z-plane (angle x-y).

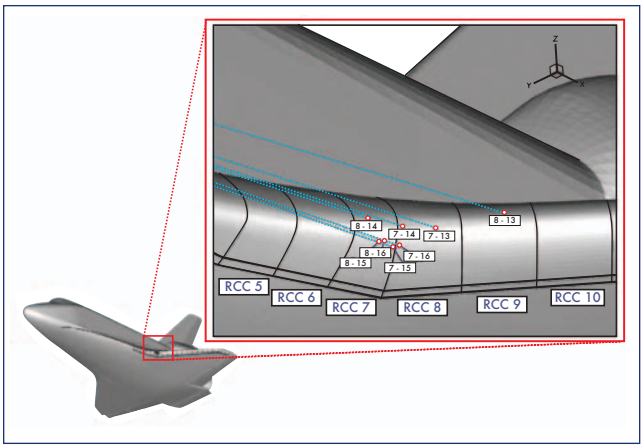


Figure 7-15. Close-up of optimized foam debris trajectories for index intervals 7-13, 7-14, 7-15, 7-16, 8-13, 8-14, 8-15, and 8-16, projected to Shuttle impact. Graphic courtesy of Phil Stuart – JSC/EG3.

7.1.6 Conclusions

The reference data sets (JSC/ES, JSC/SX, KSC, and JSC/EG) and the MSFC view vector data sets provided sparse and choppy sources on which to generate position, velocity, and BN estimates for the foam debris that impacted the Shuttle's left wing. That being said, part 1 of this portion of the trajectory analysis (i.e., comparison to the above-mentioned reference data sets) favored the KSC data as producing the most consistent results. For this part, the BN ranges from 1.23-1.45 lb/ft^2 with an estimated range of impact velocities between 763 and 803 fps (at an X-position of 1800 in.). The author feels, however, that the trajectory comparisons were better served by the MSFC view vector data. This is because view vector data possessed more of a raw measurement characteristic than the pre-processed (approximated, curve fit) data, as shown in part 2. For this case, the integrated trajectories were propagated, in a local velocity flow field, to impact on the Shuttle's left wing. For these minimum sum square error trajectory integration comparisons with the view vector data, the average BN for a selected index interval (shown in Table 7-3) ranges from 1.314 to 1.661 lb/ft^2 with a Shuttle impact velocity magnitude range of 729.3 to 815.4 fps.

7.2 Lee Analysis: Least Squares Optimized with View Vector Data

This study was an attempt to model the motion of the large debris object that apparently separated from the STS-107 external tank at approximately 81.7 seconds MET and subsequently impacted the left wing of the Orbiter. This analysis used image analysis observations together with dynamics models and realistic flow fields to estimate the most likely trajectory of the debris object. The study determined "best fit" debris trajectories including approximate impact velocities, and developed information on the aerodynamic properties of the object, which could be used to infer the likely mass of the debris object.

7.2.1 Approach & Methodology Trajectory vs. Pre-processed Imagery Data Sets

The approach was to find the most likely trajectory of the debris object by fitting the trajectory to observational data from image analysis. The motion of the debris object was modeled using dynamics equations and Runge-Kutta type numerical integrators. The initial conditions and aerodynamic parameters were selected to provide the closest fit between the debris object motion and the image analysis observations, according to an uncertainty-weighted least squares fit approach. An elementary trial-and-error optimization routine was used to seek the initial conditions and aerodynamic parameters for the best fit trajectory.

The objectives were:

1. To develop an estimate of the ballistic number (BN) of the debris object. The ballistic number, which is the weight divided by the product of the coefficient of drag and the corresponding reference area, determines the relative effect of drag versus momentum. For an object primarily influenced by drag, it is the key aerodynamic parameter. Together with knowledge about the material density and approximate shape of the object, the ballistic number could be used to infer an approximate mass.
2. Estimate the impact velocity of the debris.
3. Model the path of the debris to estimate impact location and impact angle.

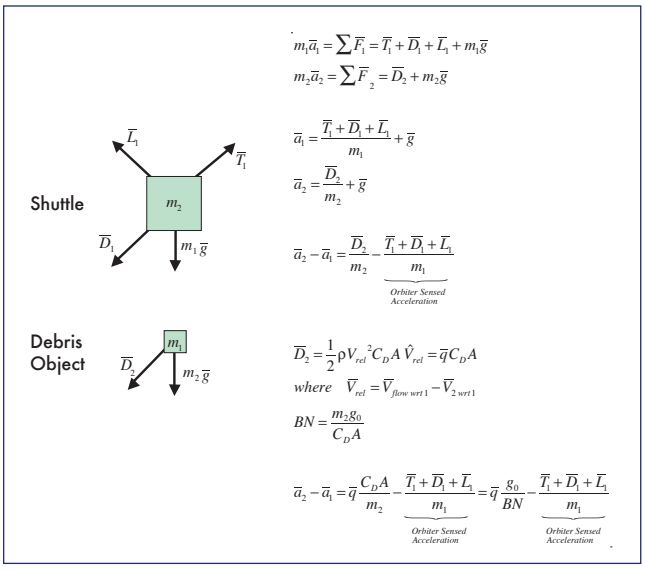


Figure 7-16. Ballistic equations of motion for debris object relative to the Space Shuttle.

Figure 7-16 presents a brief derivation of the equations of motion. This derivation is for a "ballistic" model – That is it includes drag, but no lift force on the debris object. The subscript 1 indicates the STS; subscript 2 indicates the debris object. Overbars indicate vectors, and "hats", or bent bars indicate unit vectors. In general, vector names are as follows:

m – Mass
a – Acceleration
g – The local acceleration due to gravity
g_0 – The sea-level-standard value of the acceleration of gravity
F – Force
T – Thrust
L – Lift
D – Drag
V – Velocity
ρ – Local air flow density
C_D – Coefficient of drag for the debris object
A – Reference area for the C_D
BN – Ballistic number

The final result is the equation for the relative acceleration of the debris object with respect to the STS. This is the equation evaluated in the Runge-Kutta propagation routines. Note that for cases such as this where the STS and the debris object are in close proximity, the local gravitational acceleration cancels out of the relative acceleration equation. Note also how much simplified the equation becomes when the ballistic number term is used – this makes solution for an unknown object much more feasible.

A realistic flow field about the STS was used in calculating the drag force. This flow data was developed using computer models and supplied by Ray Gomez and Darby Vicker of the JSC EG3/Applied Aeroscience and CFD branch. The flow data included velocity components, local air density, and local speed of sound. It was provided in a ten inch grid referenced to STS External Tank structural coordinates, i.e. data points spaced by ten inches in each direction, over the region of interest.

The image analysis data we used was in the form of "view vectors", or "view lines". At first, we were using three-dimensional points derived by the various image analysis groups as the basis for our trajectory fitting approach. However, we decided that the view lines developed by the image analysis groups gave us a better basis for our trajectory estimates. Only the vector-based results will be presented in this section.

Each image, in which the debris object is visible, gives us a line from the camera through the debris object. A single image can't give us a three-dimensional position in this case. And though some are very close, no two images occur at exactly the same time. (Even if they did, observational uncertainties would mean that the view lines don't necessarily pass through the same point in space.) In developing the "imagery only" three-dimensional position estimates, the image analysts had to make assumptions, which were probably geometrically based.

Complicating matters, the angle between the camera views, measured at the Orbiter, was fairly small (only 17.3 degrees). This means a little uncertainty in one view can "stretch out", making a large uncertainty along the view direction. (See Figure 7-17- but note that the situation with simultaneous intersecting view lines is for illustration only.)

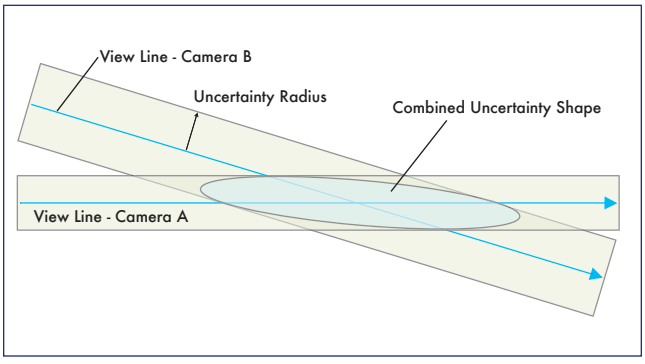


Figure 7-17. Combined uncertainty shape for camera views with small intersection angle.

Using the view lines allows us to take into account the actual shape of the "uncertainty corridor". It allows us to "lace" the observation data together using a physical model of the motion.

The times of the observations also presented challenges. Some image analysis experts felt that the time stamp from the video imagery was not reliable. Also, truncation errors were obvious in both sets of the observation time stamps.

However, the frame rates of the cameras were known with very good precision. In order to develop better estimates of relative observation times, the camera frame rates were used to establish intervals between observations for each camera respectively. The time offset between the first observations from each of the two cameras was then determined as an output of the optimization routine.

In terms of aerodynamic forces, most of this study modeled only the drag force. However, limited work was done to model lift. A rotating disk model was employed, assuming a constant rotational rate and direction. Attempting even a simple model of lift involves fitting several more parameters, and in general, it was felt that there was not enough observational data to resolve the lift properties of the object. Also, convergence times were very long for the optimization routine with the lift model, and schedule constraints made an extensive examination impossible. However, with these caveats, some limited results of the lift model will be discussed in this report.

The orbiter sensed acceleration components used in the simulation, expressed in the STS External Tank structural coordinate frame, were:

Ax = -75.163 ft/s^2
Ay = -0.058 ft/s^2
Az = -2.472 ft/s^2

These values were assumed not to change significantly over the less than 0.2 second transit time of the debris object.

Also, the attitude of the STS was assumed not to change significantly over the time period of the simulation.

7.2.2 Input Data from Image Analysis – View Vectors

Observational data in the form of three-dimensional points was received from image analysis teams at MSFC, KSC, and the SX, ES, and EG divisions of JSC. The view vector form of the data was requested later as analysis methods were developed. Due to time limitations, only the MSFC view vector data was analyzed, and it forms the basis for the analysis presented here.

View vector/line sets were obtained for two cameras: E-212 and ET-208. Info from image analysis is summarized as follows:

E-212 is a film camera with a frame rate of 64 frames per second. The view is from over the wing and aft. It renders the closest and clearest view of the debris transit, but the object is obscured by the Orbiter wing in this view before impact. This camera renders 10 frames of visibility for the debris transit, the last only partial. Image analysis experts give an uncertainty radius for view vectors from this camera of about 8 or 9 inches.

ET-208 is a video camera, and it operates at 60 frames per second. The view is looking under the wing from a position somewhat aft. This view is farther away and the images are somewhat fuzzier, but the object is visible all the way to impact (and past). There are again 10 frames from this camera during the transit of the debris object, but only 7 or 8 frames have a clearly resolvable image of the object. The estimated uncertainty radius for view vector observations from this camera is in the range of 20 to 30 inches.

From camera E-212, view vector observations 1 though 9 were used in this analysis (corresponding to frames 4913 to 4921). The tenth view vector (from frame 4922) was discarded, as it was based only on a view of the edge of the object, with the bulk hidden behind the wing.

From the video camera ET-208, view vectors corresponding to frames 1 to 5, and 9 and 10 of the debris transit were used. No view vectors were used corresponding to frames 6, 7, or 8: The object is not clearly visible in frames 6 and 7. Frame 8 also has very marginal visibility, and this view vector appears to be inconsistent with other view vectors, as noted by Condon. MSFC also presented a view vector corresponding to frame 11 from this camera, but it represents the post-impact debris cloud and was not used in this analysis.

7.2.3 Results

Several ballistic cases were examined, using different start times and therefore including different subsets of the view vectors. (i.e. later start times would exclude the earlier view vectors.) This approach was taken in case the later segment could be better approximated with a ballistic (i.e. non-lifting) model.

The flow field data was provided in a 10 inch grid. This seemed sufficient for most of the flow field. However, interpolation of the flow data required that we start our trajectory calculations an adequate distance away from STS structure, since flow interpolation wasn't accurate if a "buried" grid point was included. Also, flow gradients were largest directly next to structure. This set an effective limit on the start time for our trajectory simulations – the net effect was that the first view vector for each camera could not be included in the solution.

For several of the cases, the best fit-solution included a negative X velocity in the ET coordinate frame (that is the debris object is moving forward at the beginning of the simulated time interval). While the complex aerodynamic forces involved in the separation of the debris object from the bipod ramp region might provide some justification for such a result very early in the trajectory, negative initial X-velocities for simulations starting later in the trajectory suggest spurious solutions. The reasons for these spurious solutions could

have to do with sparsity of data and data noise, and/or with the assumptions of a constant coefficient of drag and no lift.

The most reliable ballistic trajectory solution was selected by eliminating several of these spurious solutions, and using the general rule of thumb that a solution including more observational data is better. The solution selected is one with a start time of 0.014 sec after the first E-212 camera frame. This is depicted in figures 6-16 and 6-17. It includes all of the selected view vector data except the first vector from each camera (as discussed).

Impact velocity is between about 800 and 820 ft/s depending on where contact occurs. The estimated ballistic number is 1.397. The debris object mass center passes close beneath RCC panels 8 and 9 – For an actual finite-sized debris object the initial impact for this trajectory would probably be on these panels. The optimization routine calculated a time shift of -4.127 milliseconds for the ET-208 view vector times (i.e. the first ET-208 frame would occur 0.127 milliseconds before the first E-212 frame).

This trajectory solution fits the view vector data pretty well. The trajectory position and time matches are within 8.51 inches of all view vectors, and the average "miss distance" is only 4.73 inches.

It is worth noting, however, that looking at Figure 7-19 ballistic-model trajectories do not seem to originate from an initial position and direction of motion consistent with departure from the bipod ramp location (pretty close, but not quite). Also, looking at Figure 7-18, while the ballistic model can fit the observational data pretty well, it doesn't seem to follow apparent trends in the Z direction. These discrepancies seem to suggest that lift is a significant factor in the trajectory shape.

Modeling a lifting object is much more complex than an object with constant drag, however. Solving for the motion of an object with constant drag involves fitting only a single parameter – the ballistic number. Determining the aerodynamic and rotational properties of a rotating object with lift is significantly more complex.

In general, the number, quality, and arrangement of observations for the STS-107 ascent debris object were not sufficient to fit a model including aerodynamic lift with any confidence. Also, trajectory solutions using a lift model proved to have very long convergence times using the current rather primitive optimization scheme – schedule limitations prevented a more thorough examination. However, some preliminary modeling was attempted. A simplified "rotating disk" model was employed, with a constant rotation rate and an axis of rotation in the plane of the disk.

A single result is presented for comparison: This solution was selected because it had an impact location approximately matching the location suggested by forensic analysis. The object path in this case fits the observational data somewhat better than the ballistic solution – particularly in the Z-axis direction. It may be a better approximation of the actual object motion. This case was constrained to have a rotation rate

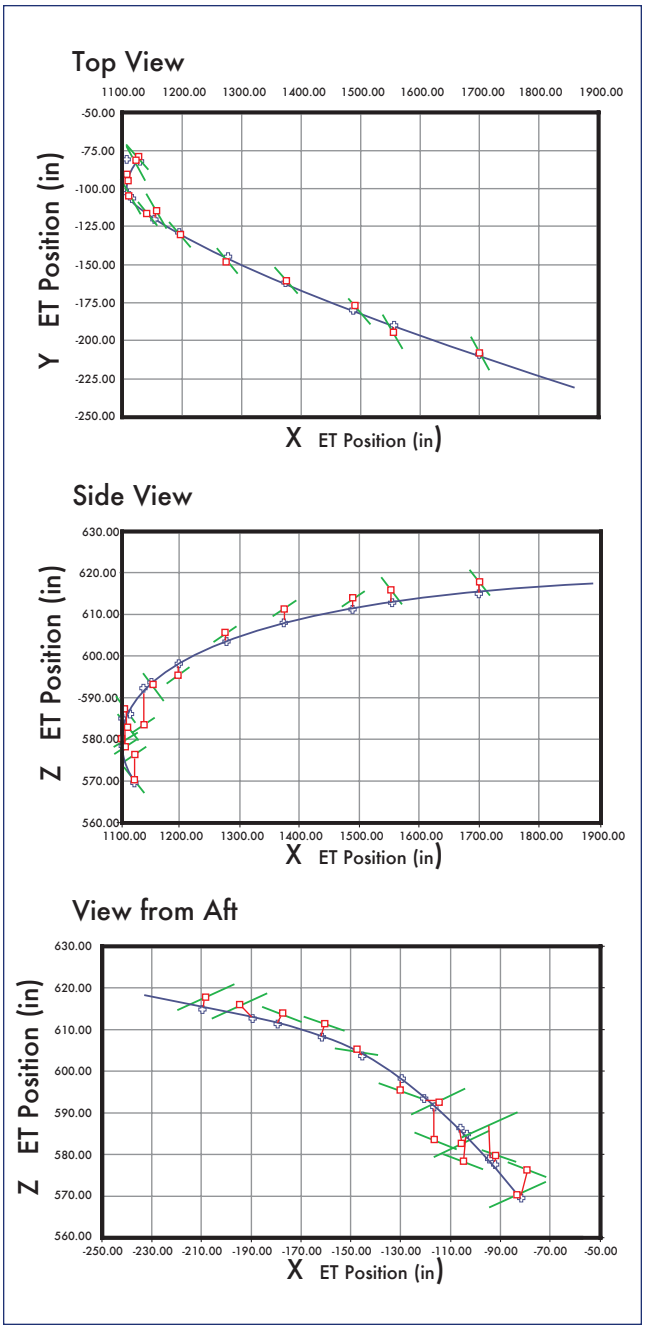


Figure 7-18. Debris object trajectory solution with view vectors (ballistic model).

of 5 rotations per second – much less than the 18 rotations per second result of the color ratio analysis by Svendsen and Salacin of NIMA.

Details of this lift-based trajectory will not be presented because of its preliminary nature, but for purposes of comparison, the impact velocity is presented. The impact velocity for this solution was approximately 760 ft/s, somewhat lower than the ballistic solution. There are several possible reasons for the solution with lift to have a lower impact velocity than the ballistic model. This particular lifting solution had an impact location slightly forward of the impact location for the

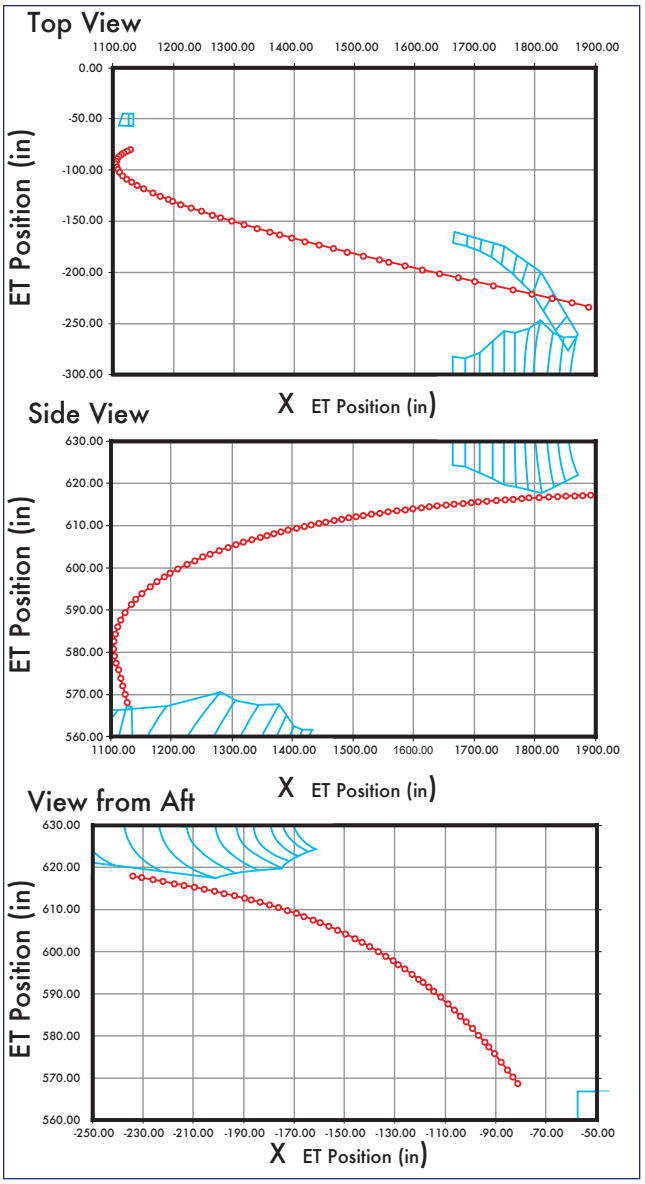


Figure 7-19. Debris object trajectory solution with rcc and bipod ramp outlines (ballistic model).

ballistic model, which means a slightly shorter distance in the flow direction for the debris object to accelerate. The lifting solution has a slightly different path – it travels through different flow regions than the ballistic solution. And the effect of lift and time-varying aerodynamic properties may be that the optimal fit of the motion to the observational data may call for a higher average ballistic number.

7.2.4 Conclusions

Conclusions of the analysis are as follows:

1. Impact location: The ballistic model predicts an impact location in the region of RCC panels 8 and 9.
2. Impact velocity: The ballistic model predicts an impact velocity of approximately 800 to 820 ft/s. A preliminary result of a simplified model including lift predicts an impact velocity of approximately 760 ft/s.
3. The ballistic model estimates a ballistic number of approximately 1.4.
4. Comparison of view vectors with ballistic model trajectory suggests lift was a significant factor in debris motion. However, the number, quality, and arrangement of observations were not really sufficient to fit a model including aerodynamic lift with any confidence.

7.3 Crain Analysis: Batch Least Squares Method with Pre-processed Data

The preprocessed foam position data sets JSC/EG, JSC/ES, JSC/SX, and KSC were also processed in a batch least squares epoch state estimator to refine estimates of the initial foam position, velocity, and ballistic number. This approach refines the initial conditions of the foam debris trajectory (including ballistic number) by minimizing the sum of the squares of the residuals between the predicted foam debris locations, developed by propagating through a Space Shuttle flow field model, and the observed locations (from the image analysis data sets). This process is widely used to reduce data in the scientific community and has the advantage of providing a statistical confidence of the initial conditions that is a function of the assumed measurement accuracy and the system dynamics. A qualitative illustration of this process is provided in Figure 1 and the formulation of this approach is easily obtained from the mathematical and statistical literature.

The specific goal of this approach was to quantify the average ballistic number that best fit the available camera data of the foam debris trajectory. This ballistic number would be accompanied by a batch least squares statistical confidence number derived from the initial estimate covariance produced by the least squares algorithm. Following the lead of the other approaches, not all of the available data was processed together. In fact, varying start and stop points in the data were used to investigate the sensitivity of foam debris passing through different observational or dynamical

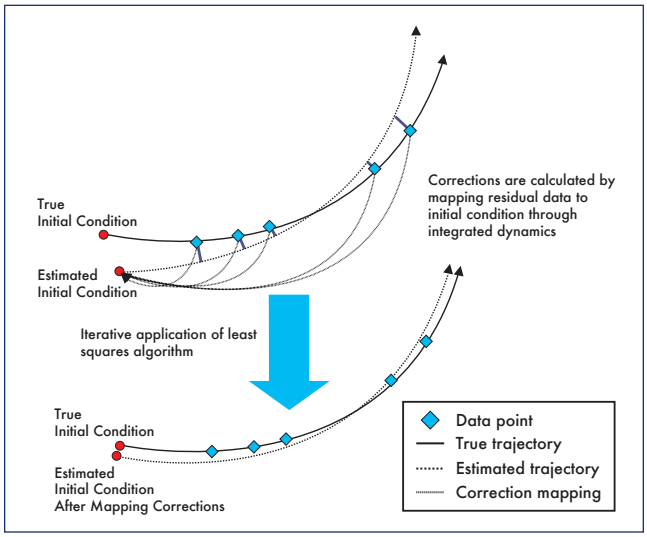


Figure 7-20 Batch least squares estimation process.

regimes of the Space Shuttle vicinity. The initial ballistic number estimates and the 1–σ confidence intervals on these estimates are provided in Table 6-5. The columns within each data set represent final data values while rows characterize initial data values. For example, the EG BN estimate of 1.15 occurs at the 3 row and 7 column indicating that the estimate was obtained from least squares processing of EG data points 3, 4, 5, 6, and 7. The measurement accuracy of each foam debris data point in each preprocessed data set was considered to be 8.0 inches in all three coordinates.

Generally, ballistic number confidences were higher when more data was processed (resulting in smaller 1-sigma values in the '10' column of each data set). The JSC/SX data set had the smallest overall statistical confidence values indicating a higher probability that the ballistic numbers, for most of the available data, were more representative of the foam debris data as compared to other data sets.

EG Data BLS Bn Estimate

From V, To->	7	8	9	10
1				
2				
3	1.15	1.33	1.66	1.82
4	1.01	1.41	2.15	2.29
5		1.21	2.54	2.61
6				

EG Data BLS Bn 1-sigma

From V, To->	7	8	9	10
1				
2				
3	0.12	0.12	0.14	0.13
4	0.20	0.25	0.38	0.31
5	0.00	0.30	0.79	0.57
6				

ES Data BLS Bn Estimate

From V, To->	7	8	9	10
1				
2				
3	3.57	2.14	1.83	1.90
4	0.00	2.48	1.79	1.92
5	0.00	0.00	1.08	1.43
6				

ES Data BLS Bn 1-sigma

From V, To->	7	8	9	10
1				
2				
3	1.55	0.37	0.20	0.16
4	0.00	0.88	0.31	0.26
5	0.00	0.00	0.19	0.23
6				

KSC Data BLS Bn Estimate

From V, To->	7	8	9	10
1				
2				
3	1.87	1.71	1.65	1.65
4	1.35	1.41	1.45	1.52
5	0.00	1.24	1.40	1.53
6				

KSC Data BLS Bn 1-sigma

From V, To->	7	8	9	10
1				
2				
3	0.51	0.28	0.18	0.14
4	0.54	0.33	0.23	0.18
5	0.00	0.51	0.38	0.30
6				

SX Data BLS Bn Estimate

From V, To->	7	8	9	10
1				
2				
3	4.00	1.87	1.65	1.61
4	2.42	1.21	1.21	1.31
5	0.00	0.89	1.03	1.24
6				

SX Data BLS Bn 1-sigma

From V, To->	7	8	9	10
1				
2				
3	1.98	0.29	0.16	0.12
4	1.42	0.21	0.14	0.12
5	0.00	0.23	0.19	0.18
6				

Table 7-5 (above). Batch Least Squares Estimates and Confidences for Initial BN by Data Set.
Table 7-6 (below). Batch Least Squares Estimation Error and Average Interval Estimation Error Table.

EG Data BLS Sum Square Error (in.^2)

From V, To->	7	8	9	10
1				
2				
3	909	1,240	2,313	2,580
4	859	1,216	1,861	1,898
5	0	1,159	1,805	1,816
6				

EG Data BLS Sum Squared Error per Interval (in.^2)

From V, To->	7	8	9	10
1				
2				
3	227	248	385	369
4	286	304	372	316
5	0	386	451	363
6				

ES Data BLS Sum Square Error (in.^2)

From V, To->	7	8	9	10
1				
2				
3	952	1,713	2,209	2,717
4	0	1,208	1,526	1,760
5	0	0	345	716
6				

ES Data BLS Sum Squared Error per Interval (in.^2)

From V, To->	7	8	9	10
1				
2				
3	238	343	368	388
4	0	302	305	293
5	0	0	86	143
6				

KSC Data BLS Sum Square Error (in.^2)

From V, To->	7	8	9	10
1				
2				
3	194	264	321	425
4	57	68	109	186
5	0	47	105	176
6				

KSC Data BLS Sum Squared Error per Interval (in.^2)

From V, To->	7	8	9	10
1				
2				
3	48	53	54	61
4	19	17	22	31
5	0	16	26	35
6				

SX Data BLS Sum Square Error (in.^2)

From V, To->	7	8	9	10
1				
2				
3	965	1,882	2,066	2,093
4	56	624	726	826
5	0	452	560	727
6				

SX Data BLS Sum Squared Error per Interval (in.^2)

From V, To->	7	8	9	10
1				
2				
3	241	376	344	299
4	19	156	145	138
5	0	151	140	145
6				

The summed estimation error for each data set processed is presented in Table 7-6. The KSC data had the best final fit to the least squares solution followed by the JSC/SX data set. This result tends to support the deterministic results of Condon and Lee. The JSC/EG and JSC/ES data were comparable to each other in their final fit to the least squares solution; however, the ES data did not converge to a solution in the cases of ES4-7 (starting with the 4th data point and ending with the 7th) and ES5-8 (starting with the 5th data point and ending with the 8th).

The ballistic numbers of the JSC/EG, JSC/SX, and KSC data sets were fused into a weighted average based upon their statistical confidence levels as presented in Table 7-7. This approach provides the most representative ballistic number of all of the data from these preprocessed data sets

	IMPACT CHARACTERISTICS										
DATA	x in	y in	z in	u ft/s	v ft/s	w ft/s	vel ft/s	ang deg	angxy deg	angxz deg	angyz deg
EG3-7	1823.3	-209.2	617.5	849.1	-92.6	10.8	**854.2**	5.1	0.7	-6.2	83.8
EG3-8	1815.7	-212.4	619.0	803.9	-90.7	13.7	**809.1**	8.0	0.9	-6.4	83.5
EG3-9	1808.6	-215.0	620.9	737.3	-86.7	16.6	**742.6**	10.9	1.3	-6.7	83.2
EG3-10	1807.5	-217.3	621.8	714.1	-86.3	17.8	**719.5**	11.8	1.4	-6.9	82.9
EG4-7	1822.3	-208.5	617.4	885.3	-95.2	10.6	**890.5**	5.2	0.7	-6.2	83.8
EG4-8	1809.4	-212.4	620.1	785.7	-89.9	16.0	**791.0**	8.9	1.2	-6.5	83.4
EG4-9	1802.7	-215.4	622.4	688.3	-84.3	19.6	**693.7**	11.5	1.6	-7.0	82.9
EG4-10	1804.8	-217.7	622.6	677.7	-85.1	19.9	**683.3**	12.5	1.7	-7.2	82.7
EG5-8	1813.5	-212.8	619.5	820.5	-93.1	14.6	**825.9**	8.9	1.0	-6.5	83.4
EG5-9	1802.6	-216.4	622.7	666.8	-84.4	20.1	**672.5**	12.6	1.7	-7.2	82.6
EG5-10	1805.5	-218.6	622.7	663.8	-86.1	20.1	**669.7**	12.5	1.7	-7.4	82.4
ES3-7	DID NOT HIT SURFACE										
ES3-8	1833.5	-252.5	639.1	690.1	-87.0	29.4	**696.2**	28.4	2.4	-7.2	82.4
ES3-9	1812.0	-234.4	635.6	719.0	-81.5	28.2	**724.1**	29.3	2.2	-6.5	83.2
ES3-10	1793.2	-220.1	632.9	699.9	-72.1	26.2	**704.1**	29.5	2.1	-5.9	83.8
ES4-7	LEAST SQUARES SOLUTION DID NOT CONVERGE										
ES4-8	1822.3	-232.3	644.6	653.5	-67.4	35.3	**657.9**	19.7	3.1	-5.9	83.4
ES4-9	1795.7	-219.8	636.8	716.3	-66.4	30.5	**720.0**	25.5	2.4	-5.3	84.2
ES4-10	1777.0	-209.1	633.1	691.3	-57.2	27.1	**694.2**	25.2	2.2	-4.7	84.8
ES5-8	LEAST SQUARES SOLUTION DID NOT CONVERGE										
ES5-9	1772.0	-206.6	631.5	810.8	-57.4	24.0	**813.2**	25.1	1.7	-4.0	85.6
ES5-10	1759.9	-200.1	630.3	733.3	-45.6	22.5	**735.1**	24.3	1.8	-3.6	86.0
KSC3-7	1826.1	-245.9	627.5	710.4	-97.0	21.0	**717.3**	24.3	1.7	-7.8	82.1
KSC3-8	1812.1	-235.8	632.4	725.8	-95.0	25.4	**732.5**	33.8	2.0	-7.5	82.3
KSC3-9	1805.2	-229.3	628.6	731.9	-92.4	22.5	**738.0**	27.6	1.8	-7.2	82.6
KSC3-10	1798.8	-222.7	627.0	728.3	-88.6	21.1	**734.0**	20.7	1.6	-6.9	82.9
KSC4-7	1804.2	-229.1	631.0	781.1	-94.7	26.2	**787.3**	31.7	1.9	-6.9	82.8
KSC4-8	1803.4	-226.4	636.3	767.5	-91.9	30.8	**773.6**	26.8	2.3	-6.8	82.8
KSC4-9	1795.7	-222.5	630.4	755.7	-88.7	25.4	**761.3**	29.6	1.9	-6.7	83.1
KSC4-10	1789.9	-217.4	628.0	741.1	-84.0	23.0	**746.2**	22.1	1.8	-6.4	83.3
KSC5-8	1805.3	-226.1	638.4	798.2	-94.3	34.1	**804.4**	23.9	2.4	-6.7	82.8
KSC5-9	1794.5	-221.6	630.6	763.2	-88.3	25.7	**768.7**	29.6	1.9	-6.6	83.1
KSC5-10	1788.1	-216.0	627.7	739.1	-81.8	22.5	**743.9**	22.2	1.7	-6.3	83.5
SX3-7	DID NOT HIT SURFACE										
SX3-8	1778.6	-204.7	624.3	692.3	-76.5	20.6	**696.8**	13.2	1.7	-6.3	83.5
SX3-9	1785.2	-206.5	623.4	728.6	-80.5	20.0	**733.3**	11.8	1.6	-6.3	83.5
SX3-10	1789.5	-205.9	622.2	736.9	-80.5	18.8	**741.5**	11.2	1.4	-6.2	83.6
SX4-7	1570.7	-148.0	629.7	525.3	-26.3	32.5	**526.9**	8.3	3.6	-2.8	85.4
SX4-8	1730.3	-182.2	624.7	768.8	-64.7	22.4	**771.8**	7.5	1.7	-4.8	84.9
SX4-9	1759.2	-193.8	624.2	785.0	-73.0	21.6	**788.7**	10.7	1.6	-5.3	84.5
SX4-10	1773.0	-198.0	623.0	772.8	-73.9	20.2	**776.6**	10.9	1.5	-5.5	84.3
SX5-8	1739.1	-186.6	625.2	849.7	-76.7	23.0	**853.5**	9.5	1.5	-5.1	84.6
SX5-9	1765.3	-198.1	624.8	824.5	-82.4	22.5	**828.9**	11.4	1.6	-5.7	84.1
SX5-10	1776.9	-201.2	623.3	784.6	-80.3	20.8	**788.9**	10.9	1.5	-5.8	84.0

Table 7-7. Ballistic number estimates and statistical confidences from Fused JSC/EG, JSC/SX, and KSC Data.

Fused Bn Solution from EG/KSC/SX Data

From V, To->	7	8	9	10
1				
2				
3	1.23	1.47	1.66	1.69
4	1.09	1.32	1.39	1.49
5		1.04	1.21	1.44
6				

Fused Bn Solution 1-Sigma from EG/KSC/SX Data

From V, To->	7	8	9	10
1				
2				
3	0.12	0.10	0.09	0.07
4	0.18	0.15	0.12	0.10
5		0.17	0.16	0.15
6				

Table 7-8. Foam impact characteristics for each data set and data start/stop number. (Courtesy Phillip Stuart JSC/EG)

and the best statistical estimate of the average ballistic number of the foam debris, which was between 1.69 and 1.04 ft/lb^2. The statistical 1-σ confidences in this process all ranged from 0.07 to 0.18 ft/lb^2.

The converged initial conditions and ballistic numbers of each data set were integrated in the Space Shuttle vicinity flow field to interpolate the characteristics of their impact on the shuttle wing. The collected results of this interpolation are found in Table7- 4. The (*x, y, z*) columns represent the impact location in ET coordinate frame in inches while the (*u, v, w*) columns represent the velocity components in the ET frame (*x, y, z*) direction in ft/sec. The *vel* column with bold characters represents the magnitude of the impact velocity in ft/sec and the *ang* column is the incidence angle of the impact in degrees where 90 degrees is normal to the surface of the impact point. The (*angxy, angxz, angyz*) columns represent the angles that a foam debris particle would impact the Shuttle wing leading edge and support alignment of a launch mechanism to simulate foam debris impact. Specifically the planes in these angles are +*xy* in the Space Shuttle up direction, +*xz* toward the starboard side, and +*yz* toward the Space Shuttle aft section. Note that data sets ES3-7 and SX3-7 did not impact the Space Shuttle. The velocity magnitudes at interpolated impact points ranged from 669 ft/sec to 853 ft/sec with incidence angles varying from 5 to 33 degrees. The impact point of each data set is represented visually in Figure 7-21.

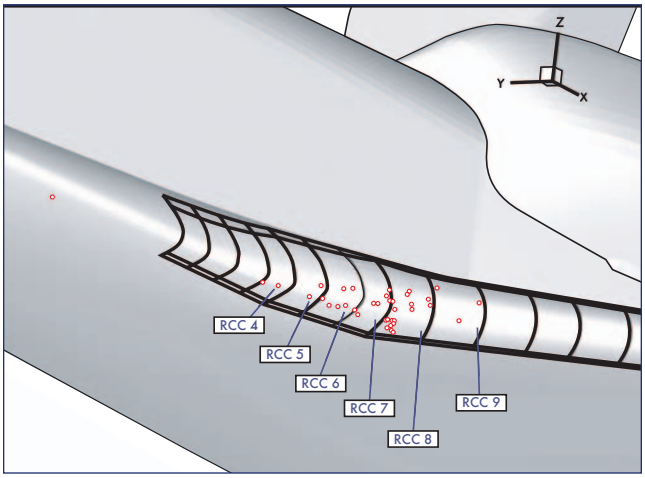


Figure 7-21. Interpolated impact points of all data sets.

7.3.1 Least Squares Analysis Conclusions

A lease squares estimation technique was used to obtain initial foam debris position and velocity and average ballistic number. An important feature of this technique is the calculation of a statistical confidence value that is generated along with the estimate which gives a probabilistic range on the estimate. With the data available, the average ballistic number of foam debris is estimated to be between 1.04 and 1.69 lb/ft^2 with a 1-σ confidence between 0.07 and 0.18 lb/ft^2 depending on the data start and stop points used in the lease squares algorithm. From Table 3, it can be seen that the average ballistic number consistently rises as the data is processed with more data end points from the latter part of the observation set. This indicates that the ballistic number of the foam debris was higher as it neared the end of its trajectory. The results from this analysis can be used to create a probabilistic description of the initial conditions and impact conditions of the foam debris trajectory. This description is based on the post-processed video foam debris impact data, the CFD flow model of the debris trajectory volume, and the inertial acceleration experienced by the Shuttle during the data record time span. Without an increase in the quantity or quality of foam debris observation data, further analysis using the least squares technique will not produce differing results of any statistical significance.

7.4 Recommendations (Condon, Lee, and Crain)

The composite list of recommendations from the analyses of Condon, Lee, and Crain, are as follows:

1. STS ascent tracking system should employ cameras with improved frame rates & reliability for improved debris tracking. Sparse data density and quality were a significant limitation in trajectory estimation.
2. There should be an accurate and consistent time stamp for the ascent video cameras.
3. More digits in the seconds readout of all camera time stamps would be useful for modeling of debris trajectories. The transit time for the STS-107 debris object was very short – less than 0.17 seconds. More precision in the readout would reduce truncation errors, which can currently be significant when modeling motion over so short a time span. At least three more digits in the readout would be useful, i.e. six digits after the decimal for the seconds readout.
4. NASA should have in place a turn-key process to analyze ascent debris events. This process should include image analysts to develop observational data, aerodynamicists to develop realistic flow conditions, and flight dynamics experts to estimate the object path,

velocities, and aerodynamic parameters. The process should include multiple disciplines and organizations.

5. The process for analysis of ascent debris trajectories analysis should include:
   a. Modeling of debris motion based on dynamics equations and CFD based flow fields.
   b. Solution of initial conditions and aerodynamic parameters to fit the debris trajectory to image analysis observations in the form of view vectors/lines.
   c. A more rigorous statistical navigation type methodology should be explored, in parallel with the current brute force approach.
6. There should be a standardized format and process for reporting image analysis debris observations for dynamics analysis:
   a. Debris observations should be reported as view lines in standard anchor point plus vector direction format, expressed in STS External Tank coordinates.
7. Analysis of debris observation view lines should consider frame-to-frame changes in STS position and orientation, i.e. view vector direction.

8.0 6-DOF Unsteady CFD Analysis

8.1 Approach

Viscous and inviscid Computational Fluid Dynamics (CFD) codes were used to carry out unsteady simulations of the coupled aerodynamic and debris motion for Columbia ascent conditions. The debris motion was allowed to translate and rotate in each coordinate direction based on the aerodynamic forces, giving it six degrees of freedom. In all, more than 40 viscous and 200 inviscid solutions were generated. The simulations examined six possible pieces of the debris (ranging in size from 166 cubic inches to 1450 cubic inches), and a range of foam mass densities (from 2.1 to 5.0 lb per cubic foot). In the simulations for both codes the initial velocity and rotation rates were varied, until an initial condition that resulted in an impact of the Orbiter wing was found. The viscous results are products of the OVERFLOW-D code, while the inviscid results are products of the CART3D code. The details of each computational approach are briefly summarized in the following sub sections.

8.2 Tool Background

OVERFLOW-D is based on version 1.6au of the NASA OVERFLOW code, but has been significantly enhanced to accommodate problems that involve bodies in relative motion. The enhancements represent in-core subroutine actuated operations, including a general 6-degrees-of-freedom (6-DOF) model, contact detection algorithms, impact reaction routines, and solution adaptation capability. A near-body/off-body domain partitioning method is used in OVERFLOW-D as the basis of problem discretization. The near-body portion of the domain is defined to include the vehicle surface geometry and the volume of space extending out a short distance. This portion of the domain is discretized with body-fitted viscous grid components. The off-body portion of the domain is defined to encompass the near-body domain and extend out to the far-field boundaries of the problem. The off-body domain is filled with a system of uniform Cartesian grids of variable levels of refinement. The off-body grids are automatically generated by OVERFLOW-D such that all near-body grids are always surrounded by off-body grid components of comparable resolution capacity. These spacing constraints are enforced at each time step for moving body applications. The SSLV near-body and off-body grid systems used for the present Columbia debris breakaway simulations consist of more than 20 million points. Each trajectory has been resolved temporally with more than 10,000 time-steps.

The Cart3D code solves the Euler equations using unstructured Cartesian meshes. Cart3D takes as input the triangulated surface geometry and generates an unstructured Cartesian volume mesh by subdividing the computational domain based upon the geometry, and any pre-specified regions of mesh refinement. In this manner, the space near regions of high surface curvature contains highly refined cells, while areas away from the geometry contain coarser cells. For moving-body problems, Cart3D's solver is based on a dual-time, implicit scheme with multigrid as a smoother on the inner iterations permitting large time steps. The package is tightly coupled with a 6-Degree-Of-Freedom (6-DOF) module so that mesh automatically adjusts as pieces of geometry move under aerodynamic loads. The efficiency of the code with coupled 6-DOF is comparable to the best codes in the literature. Cart3D has been parallelized to efficiently run on shared-memory computers on over 1000 processors. Due to the high degree of automation in the package, simulations of new vehicles can be setup in a matter of hours. Trajectory simulations for the Columbia debris cases typically ran in less than one day on 64 SGI Origin CPUs.

8.3 Observations

With this database of several hundred simulations, several general observations can be made with confidence.

1. The cross flow (Y-Z) position and cross flow velocity are relatively sensitive to release conditions. With the right initial conditions, the debris can be made to fly well above or below the Orbiter wing. Y-Z position, however, is less critical, since we know from the photographic and forensic evidence the approximate Y-Z position of the debris impact. Therefore initial conditions were chosen to give this result (wing impact near RCC panels 6-8).
2. Streamwise (X) position and velocity generally quite insensitive to release conditions (±~ 50 ft/ sec @ impact location), and are primarily dependent upon the density and size of the debris used in the simulations.
3. Of these, the final relative impact velocity shows strong dependence upon the foam density, and is less sensitive to the size and geometry of the foam piece.

8.4 Results

A trajectory that begins with a rotating forward flip (nose-down) is more likely than a backward flip (nose-up) to impact the Shuttle's lower wing leading-edge surface. A backward flip would generate significantly more lift before the

piece starts to tumble, carrying it too far outboard or over the top of the wing. In a forward-flip release, the debris leading edge is pushed down under aerodynamic loads, and begins tumbling almost immediately – experiencing little aerodynamic lift in the process. As a result the forward-flip trajectories follow the Orbiter's surface more closely, and more consistently impact the wing leading edge. Also, trajectories produced by forward-flip releases are closer to the initial positions reported by the Image Analysis Team teams.

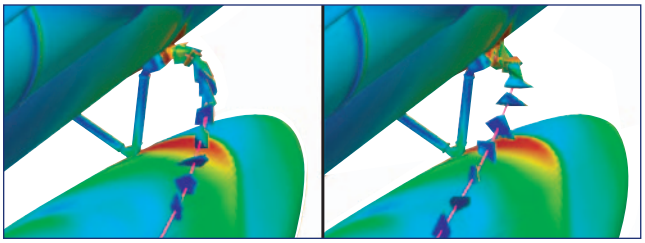


Figure 8-1. Backward vs. forward flip trajectories.

These images also illustrate the tumbling behavior of the debris after it separated from the launch vehicle. The homogeneous wedge shaped foam debris analyzed in these simulations is unstable and will tend to rotate rather than trim out in a stable attitude. To assume a stable attitude, with a correspondingly lower drag coefficient, would require a significantly different debris shape than the shape observed on the launch films or would require some additional mass embedded in the foam debris. No conclusive evidence supports this scenario.

The effect of density variation was investigated for debris pieces ranging in size from 705-1450 cubic inches. The figure below shows streamwise relative velocity of a 705 cubic inch piece as it travels downstream. This chart shows predicted impact speeds of between 1000-750 ft/sec as the foam density is varied from 2.1-5.0 lb/ft^3. While debris with different sizes and shapes had different actual impact speeds, these results are typical. For example, increasing the debris size to 1450 cubic inches only resulted in a decrease of about 100 ft/sec from the results shown in this figure. The prediction of impact velocity between the two simulation codes (Cart3D and OVERFLOW) was very consistent, with results varying by only ±50 ft/sec overall, and results for cases with similar trajectories (and impact points) varying by only 10-20 ft/sec.

Ballistic numbers were computed for the debris pieces of 705, 855, and 1450 cubic inches. The average ballistic number for a given trajectory was found to be primarily a function of the foam density. An increase in foam density results in increased ballistic number. Two figures showing the ballistic number variation as the debris tumbles downstream are included. The first of these figures show the trajectories for foam density variations on a 704 cubic inch wedge shaped debris piece. The second figure shows trajectories for a similar piece of 855 cubic inch and 2.4 lb per cubic foot foam density. These ballistic numbers were used in the correlation with the Image Analysis Team results, as described above.

The rotation rates for these trajectories were collected and are shown in the following figures.

These results are consistent with the Image Analysis assessment indicating a rotation rate of at least 18 revolutions/second and show that the rotation rate could be even higher for this smaller volume of foam.

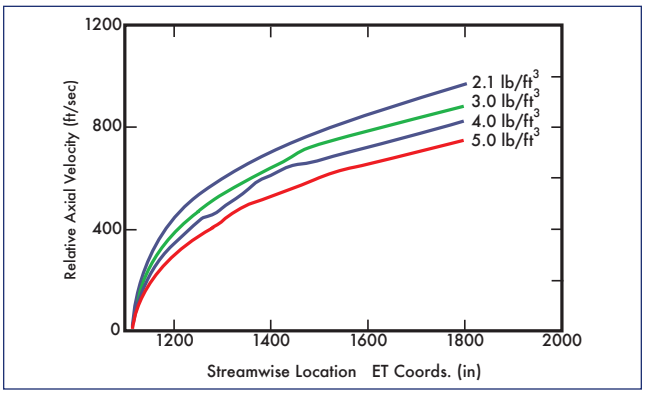


Figure 8-2. Impact velocity for various effective densities.

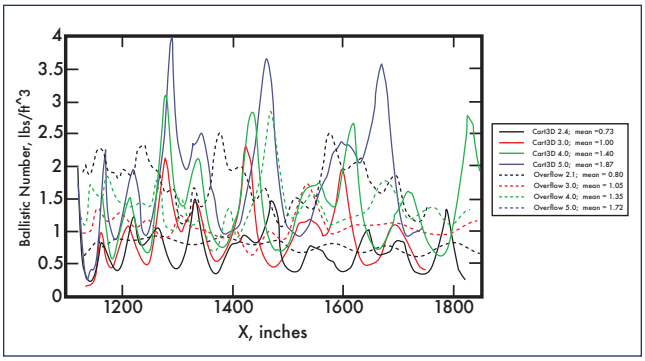


Figure 8-3. Ballistic number variation along trajectory (704 in^3 foam volume).

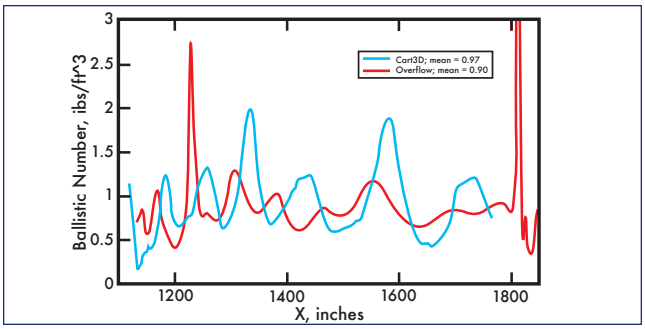


Figure 8-4. Ballistic number variation along trajectory (855 in^3 foam volume).

Axis	Rotation rate (Hz)
W1	38 ± 12
W2	[1] 1 ± 10
W3	12 ± 12

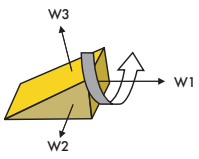


Figure 8-5. Rotation rates from unsteady CFD.

The effects of the debris on the surface pressures of the Shuttle were estimated by subtracting the steady state solution surface pressures from those computed during an unsteady trajectory computation. This analysis shows that the Orbiter leading edge pressure is lowered by approximately 0.4 psi just before the debris impact. This is shown in the following figure, which shows color contours of the difference in pressure on the surfaces.

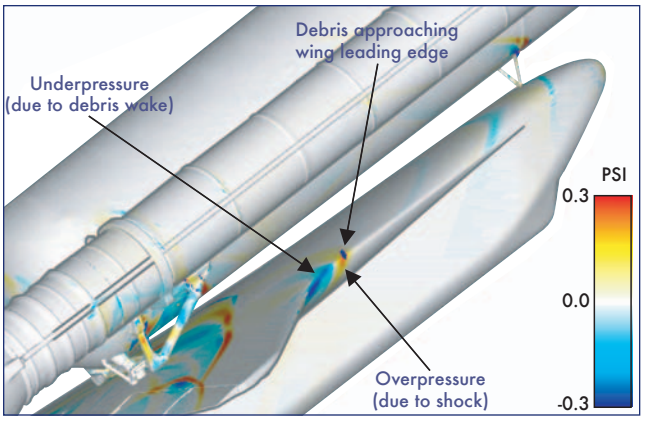


Figure 8-6. Delta pressure on vehicle surface caused by debris.

Red and yellow indicate increased pressures and cyan and blue indicate lowered local pressure. White or gray regions show small or no change in pressure. The lowered local wing surface pressure is caused by the wake of the debris piece that precedes the debris as it travels past a fixed point on the Orbiter wing. This change in local pressure may help explain the anomalous accelerations measured on the left wing outboard elevon accelerometer recorded during ascent and may explain the unusual acceleration signature seen shortly after the debris impact on the leading edge of the wing.

A similar trajectory that missed the wing leading edge and traveled near one of the two Orbiter pressure instruments that showed unusual behavior during the STS-107 launch is shown below. The debris velocity is probably somewhat higher than the debris cloud seen after the initial debris impact. The passage of the cloud of debris was too rapid for the 10 Hz pressure instrumentation to detect the effect of the debris passage but the 200 Hz accelerometer on the left wing outboard elevon could detect a pressure change of this duration. Review of the digitally enhanced launch video shows a number of large pieces of debris traveling outboard under the left wing elevon that may have caused a similar pressure change on the control surface.

The following figure shows the change in pressure near one of the anomalous taps caused by the simulated debris shape passing near the Orbiter wing without an impacting the wing leading edge. For this debris velocity the pressure oscillation occurs over approximately 0.01 seconds and realistically would not have been sensed by the 10 Hz sample rate of the pressure taps. The zero value on the x-axis is simply a reference time prior to the debris's passage near the pressure tap.

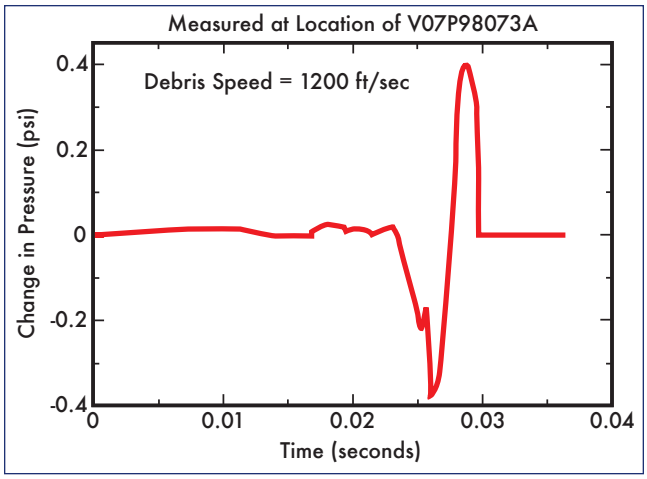


Figure 8-7. Delta pressure near orbiter lower surface pressure tap.

9.0 RCC Impact Testing Inputs

The primary goal of the impact testing on Orbiter RCC panels was to simulate, as closely as possible, the debris event on STS-107. Several aspects of this goal were difficult to achieve. Simulating the complete combined environment including external pressure loads and temperatures was not possible due to limitations in the testing setup and equipment. External pressures and temperatures from the static geometry CFD solutions were provided to the impact analysts for pre- and post test assessment purposes. Impact velocities from the trajectory analysis/ballistic number estimation were used but mass estimates and angle of incidence inputs required additional analysis.

9.1 Debris Mass Estimation

The debris mass estimates were based on the ballistic coefficient analysis results combined with the ADT program and unsteady CFD results for the 855 in^3 foam volume estimate from the External Tank Project. ADT and the unsteady CFD results predicted that the 855 in^3 foam would have a BN approximately equal to 1.0 with an impact velocity of 950 ft/sec.

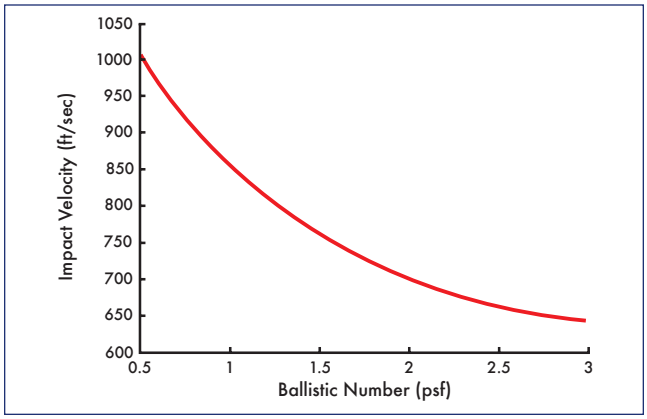


figure 9-1. impact velocity at 1,800 inches vs. ballistic number.

Ballistic number analysis of the Image Analysis trajectories estimated the most likely range of 1.2 < BN < 1.4. Due to the accelerated test schedule and lead times required to procure test article hardware a simple ratio of the predicted ballistic numbers to the baseline 855 in^3 geometry was used to predict the as tested foam weights.

Writing the ballistic number in terms of foam density results in the following equation:

$$BN = \frac{\rho_{foam}\, Volume}{C_D\, Area_{ref}}$$

Equation 9-1. Ballistic number as a function of density.

The increase in BN could have come from a number of different sources:

- Reduced drag coefficient (C_D)
- Higher effective mass
  - Due to larger volume
  - Due to embedded mass

Drag coefficient is a function of geometry and Mach number. Characterizing the drag coefficient for a tumbling object is a difficult undertaking. The best estimate of the average drag coefficient for this debris comes from the unsteady 6-DOF CFD results. These codes predicted a C_D of 1.67 for the baseline shape from the ET Project, using a reference area equal to one fifth of the foam surface area. Comparing this value to experimental data from a number of different sources, using consistent reference area definitions did not support a large reduction in this value that would account for the BN number increase.

The ET Project did not support any significant added mass scenarios involving ice or SLA embedded in the foam and the Project's largest estimated weight of the debris was 1.3 lb.

Considering these inputs, along with the larger potential volume of a smaller ramp angle discussed in Section 4, the judgment was made that a larger foam volume could have come from the bipod ramp.

9.2 Angle of Incidence Inputs

The angle of incidence inputs were provided relative to the impact test RCC test article. The data was provided in this format to simplify the aiming procedure in the test and to allow the structural analysts to choose any point on the RCC surface as their target. The curvature of the Orbiter wing leading edge and the size of the debris make specific angle of incidence estimates difficult. The following figure shows the intersection of a debris trajectory with the wing leading edge along with an estimated "footprint" due to the debris impact. This illustrates the range of impact angles that are possible for a specific impact predicted by one of the Image Analysis Team members.

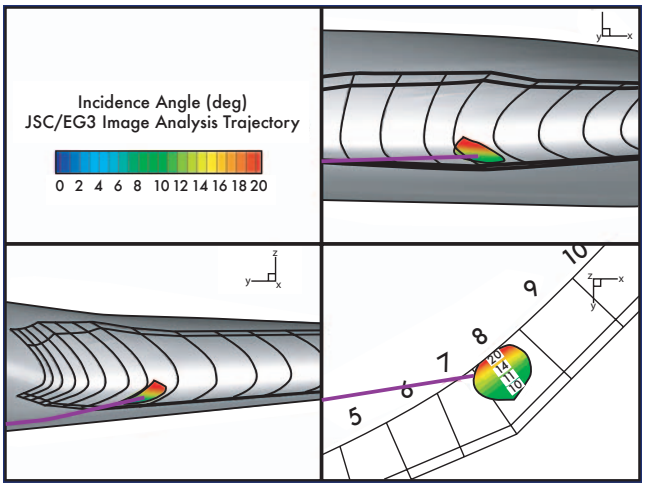


Figure 9-2. Angle of incidence on RCC panel (1 foot radius footprint).

The final incidence angle range was determined based the range predicted debris trajectory impacts on RCC Panel 8 from the trajectory analysis analysts. The terminal velocity vectors for these trajectories were extracted and the vector's angles relative to the test article coordinate system were calculated. The results are shown in the following two figures.

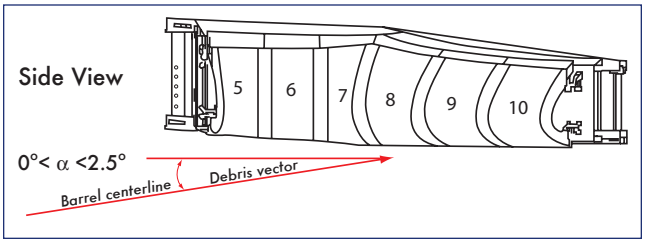


Figure 9-3. Impact test article rotation about Y-axis.

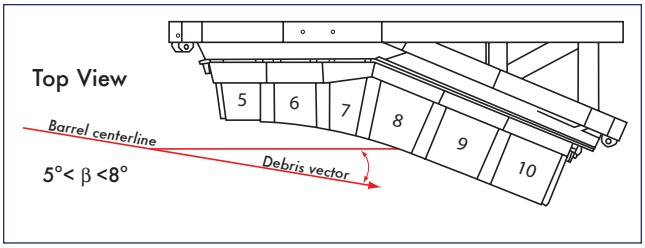


Figure 9-4. Impact test article rotation about Z-axis.

Bold values indicate more conservative angles that would result in higher energy normal to the test article.

10.0 Conclusions/Recommendations

10.1 Image Analysis

The Columbia Accident Investigation Board has made a number of recommendations in this area that are consistent with the recommendations made by the trajectory analysis/ ballistic number estimation analysts in Section 7.

The application of physics-based trajectory analysis techniques to the Image Analysis trajectories clearly showed their capability to improve the debris impact velocity estimates. Additionally these techniques can provide insight into the mass of observed debris and physics based trajectory extrapolations where multiple views are not available. A turnkey system including this capability could significantly reduce the uncertainty associated with determining ascent debris mass and trajectories.

Worst-case debris impacts occur in a flow regime that generates a number of strong shock waves. These shocks can cause optical distortions that might mislead image analysts. Portions of the STS-107 debris trajectory were probably distorted by the density gradients caused by these shock waves and resulted in higher uncertainties in these areas. Simulating these distortions using CFD tools could provide insight into the magnitude of these distortions and improve the quality of the Image Analysis products.

10.2 Debris Transport

The current Ascent Debris Trajectory Program provided estimates were very close to the final investigation recommendations for debris mass and impact velocity. However, due to inefficiencies in the code and errors in the code's implementation the Ascent Debris Transport code has been completely rewritten. The new code is currently undergoing verification and validation testing.

Unsteady 6-DOF CFD solutions provided valuable insight into aerodynamic and debris dynamics that would have been difficult or impossible to obtain by any other means. These tools are being utilized to better characterize tumbling debris aerodynamics and to assess the assumptions made in the current debris transport code. These results will be used to update the debris transport code and to improve the accuracy of its predictions.

11.0 Acknowledgements

The authors would like to acknowledge the outstanding support provided by the NASA Advanced Supercomputing Division and Silicon Graphics, Inc. Without the dedicated access and support they provided throughout the investigation many of the required analyses could not have been accomplished in a timely manner.

Additionally we would like to acknowledge all of the individuals and companies that volunteered their time and resources to support this effort.

Most of the NASA Ames Research Center members of this team were coworkers of Kalpana Chawla prior to her acceptance as an astronaut candidate. She will be missed.

12.0 References

1-1 G. J. Byrne and C. A. Evans, "STS-107 Image Analysis Team Final Report," NSTS-37384, June 30, 2003.

1-2 Joint Scenarios Report, July 8, 2003.

5-1 D.C. Jespersen, T.H. Pulliam, and P.G. Buning, "Recent Enhancements to OVERFLOW," AIAA-97-0644, AIAA 35th Aerospace Sciences Meeting, Reno, NV, Jan. 1997. http://science.nas.nasa.gov/~jesperse/papers/aiaa97-0644.ps.Z

2-2 P.G. Buning, D.C. Jespersen, T.H. Pulliam, G.H. Klopfer, W.M. Chan, J.P. Slotnick, S.E. Krist, and K.J. Renze, "OVERFLOW User's Manual, Version 1.8s," NASA Langley Research Center, Nov. 2000.

2-3 D. G. Pearce, et al, "Development of a Large Scale Chimera Grid System for the Space Shuttle Launch Vehicle," AIAA-93-0533-CP, January 1993.

2-4 J. P. Slotnick, et al, "Navier-Stokes Simulation of the Space Shuttle Launch Vehicle Flight Transonic Flowfield Using a Large Scale Chimera Grid System," AIAA-94-1860, June 1994.

2-5 R. J. Gomez, E. C. Ma, "Validation of a Large Scale Chimera Grid System for the Space Shuttle Launch Vehicle," AIAA 94-1859.

6-1 J.W. McClymonds, J.J. Baumbach, R.R. Cassas, L.B. Grassi, J. M. Kelleher, "Space Shuttle Debris Data Book," SSD95D0193-Rev A, November 2000.

6-2 Dr. Ing. S.F. Hoerner, "Fluid Dynamic Drag," Hoerner Fluid Dynamics, 1964.

13.0 Appendix A

13.1 Acronyms and Abbreviations

6-DOF	6 Degrees Of Freedom (3 forces + 3 moments)
ADTP	Ascent Debris Transport Program
CFD	Computational Fluid Dynamics
ET	External Tank
KSC	Kennedy Space Center
MET	Mission Elapsed Time
MSFC	Marshall Space Flight Center
NASA	National Aeronautics and Space Administration
RCC	Reinforced Carbon Carbon
SLA	Super-Lightweight Ablator
SRB	Solid Rocket Booster
SSLV	Space Shuttle Launch Vehicle
STS	Space Transportation System

14.0 Appendix B

14.1 Bipod Ramp Airloads

A key concern of the investigation was whether external air loads caused or contributed to the failure of the foam ramp resulting in the debris release. A number of static CFD runs were performed at STS-107 ascent conditions and compared to design certification loads and air loads at STS-107 conditions predicted using the engineering techniques used to design the bipod ramps. The engineering results consistently bounded the CFD analysis indicating that the design certification loads were conservative and did not under predict the actual load environments.

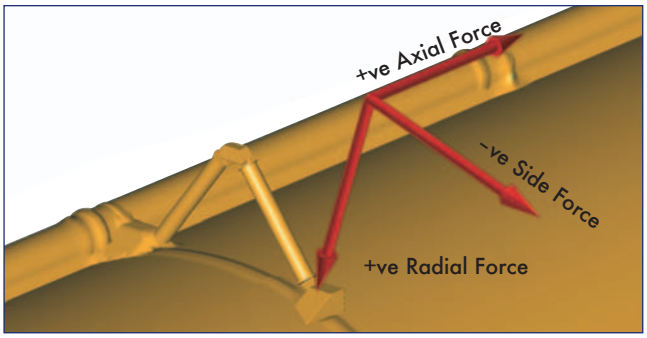


Figure 14-1. Bipod ramp force convention.

These calculations follow the engineering methodology used to predict airloads on the bipod ramps. This process integrates (pressure – freestream pressure) over the ramp surfaces to determine the aerodynamic forces acting on the ramp. The actual forces, for a perfectly bonded ramp without any venting, can be predicted by simply integrating pressures on the ramp exposed surfaces.

The following figures show the calculated loads on the –Y, or left-hand, bipod ramp. The design requirement curve is based on a high dynamic pressure trajectory designed to fly

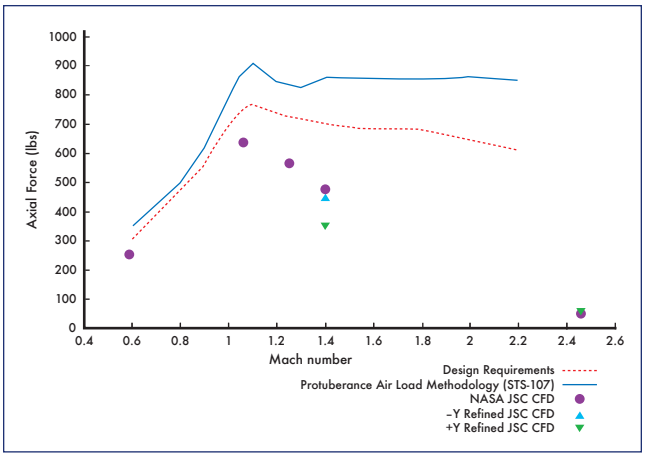


Figure 14-2. -Y Bipod ramp axial force vs. Mach number.

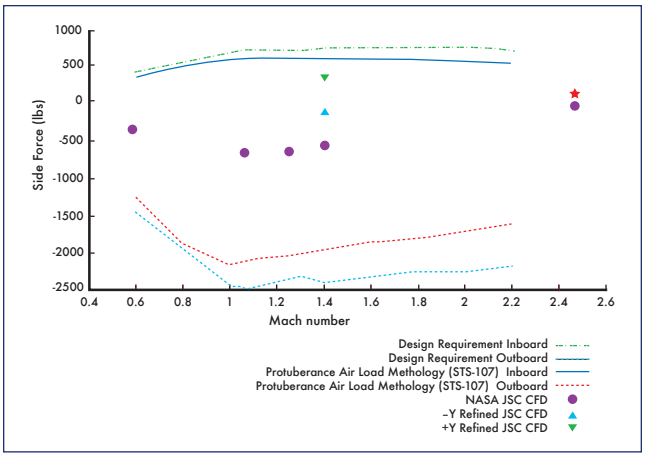


Figure 14-3. -Y bipod ramp side force vs. Mach number.

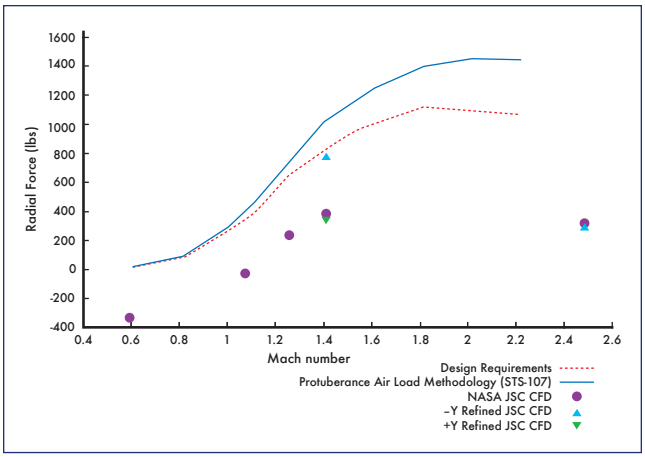


Figure 14-4. -Y Bipod ramp radial force vs. Mach number.

at the Shuttle structural design limits. The STS-107 curve uses the same analysis procedure but uses the STS-107 trajectory dynamic pressures to compute the various loads. The NASA JSC CFD symbols were computed using a simplified geometry that did not included the External Tank Intertank Stringers. The Refined JSC CFD symbols are for an updated CFD geometry that includes the stringers and refined +Y ramp geometry.

By definition positive radial force acts towards the External Tank centerline, which would tend to press the ramp down onto the External Tank surface. The bipod ramp deflects the oncoming air upward resulting in a net force that holds the ramp on to the ET.

This analysis shows that the air loads were within the design envelope and implies that a ramp with no flaws would not fail due to air loads alone. Internal voids could contain gas at atmospheric pressure that would results in local failures when the delta pressure between the gas voids and the external pressure exceeds the strength of the foam insulation. Information from the ET Project indicates that internal flaws could significantly reduce the foam strength and that cryogenic temperatures would cause a further reduction in strength.

[continued on next page]

15.0 Appendix C

15.1 Time-dependent position data sets from JSC/ES, JSC/SX, KSC and JSC/EG

JSC/ES Reference Data

Point	Elapsed Time	XET	YET	ZET	Rho	VelX	VelY	VelZ	Speed of Sound
	Sec	inches	inches	inches	slug/ft3	ft/sec	ft/sec	ft/sec	ft/sec
1	0	1115	-65	581	2.32387E-04	1375.187	-410.57	-137.074	1256.976
2	0.017	1125	-89	581	2.07126E-04	1737.851	-53.0254	-216.018	1169.928
3	0.033	1136	-117	581	2.68687E-04	1967.677	-160.848	16.28692	1088.297
4	0.05	1141	-139	585	2.73989E-04	1941.608	-245.992	40.81452	1094.212
5	0.066	1204	-170	597	2.39994E-04	2060.441	-294.194	-23.2117	1047.247
6	0.083	1259	-174	604	2.03557E-04	2138.5	-263.008	-26.0106	1017.069
7	0.1	1314	-175	611	1.91290E-04	2165.326	-277.616	-79.9681	1004.108
8	0.117	1439	-182	623	1.43675E-04	2288.054	-167.191	-91.8438	952.4276
9	0.133	1556	-190	625	1.42941E-04	2282.208	-195.35	-70.863	954.579
10	0.15	1668	-190	625	1.70959E-04	2202.615	-132.83	91.80206	993.5049
11	0.167	1787	-193	625	1.83534E-04	2148.811	-122.726	-0.39817	1021.162

JSC/SX Reference Data

Point	Elapsed Time	XET	YET	ZET	Rho	VelX	VelY	VelZ	Speed of Sound
	Sec	inches	inches	inches	slug/ft3	ft/sec	ft/sec	ft/sec	ft/sec
1	0	1112.5	-43.895	573.58	2.16640E-04	49.46285	-177.988	334.6481	1395.33
2	0.017	1127.2	-80.441	575.46	1.97820E-04	1334.217	-453.177	-444.755	1242.135
3	0.033	1125.3	-96.702	581.41	2.14074E-04	1887.878	94.9397	-74.6841	1120.574
4	0.05	1160.9	-138.38	581.03	2.54430E-04	1999.954	-216.817	-2.25609	1074.105
5	0.066	1187.7	-140.11	586.3	2.33491E-04	2050.208	-190.261	-26.3199	1056.017
6	0.083	1244.5	-133.37	597.91	2.17631E-04	2079.32	-243.409	-84.3914	1042.191
7	0.1	1308.1	-138.1	610.19	1.71978E-04	2197.666	-190.632	-82.8541	994.2547
8	0.117	1440.2	-165.52	614.38	1.41428E-04	2284.71	-183.007	-105.64	953.4332
9	0.133	1553.2	-181.13	617.4	1.40716E-04	2285.151	-202.576	-83.9461	952.8312
10	0.15	1684.1	-192.93	618.05	1.74800E-04	2202.278	-116.505	91.05107	994.2049
11	0.167	1814.2	-210.69	618.63	1.73565E-04	1882.989	-25.157	-278.549	1113.49

KSC Reference Data

Point	Elapsed Time	XET	YET	ZET	Rho	VelX	VelY	VelZ	Speed of Sound
	Sec	inches	inches	inches	slug/ft3	ft/sec	ft/sec	ft/sec	ft/sec
1	0	1133	-58	575.5	1.69402E-04	878.0123	-495.741	166.5922	1325.663
2	0.015	1139	-79	580.5	2.46196E-04	1802.137	-317.569	-321.847	1130.33
3	0.031	1149	-104	583.5	2.35645E-04	2037.209	24.80037	-91.2693	1066.995
4	0.047	1168	-126	585.5	2.37981E-04	2037.508	-131.667	-4.29115	1062.876
5	0.062	1198	-135	592.5	2.29344E-04	2053.935	-169.072	-25.681	1055.481
6	0.078	1244	-144	601.5	2.16592E-04	2083.916	-271.009	-48.178	1039.217
7	0.093	1323	-162	611.5	1.78214E-04	2192.271	-234.635	-84.5304	994.4348
8	0.109	1416	-173	620.5	1.47391E-04	2272.257	-178.868	-91.3495	959.7419
9	0.125	1524	-186	617.5	1.43629E-04	2281.069	-206.015	-86.8857	954.4202
10	0.14	1634	-194	620.5	1.63414E-04	2231.948	-127.52	45.20563	981.0337
11	0.166	1787	-207	620.5	2.37158E-04	2002.997	-301.408	-339.699	1058.553

JSC/EG Reference Data Set

Point	Elapsed Time	XET	YET	ZET	Rho	VelX	VelY	VelZ	Speed of Sound
	Sec	inches	inches	inches	slug/ft3	ft/sec	ft/sec	ft/sec	ft/sec
1	0.000	1130.7	-61.0	571.0	1.68679E-04	961.8044	-395.291	124.0708	1320.115
2	0.017	1123.9	-75.3	576.6	2.03591E-04	1220.147	-555.456	-366.008	1263.976
3	0.033	1145.7	-108.7	579.3	2.26083E-04	2023.392	29.45869	-17.7892	1072.062
4	0.050	1137.2	-116.3	586.6	2.61401E-04	1993.299	-127.235	16.73082	1079.331
5	0.066	1186.2	-128.4	593.1	2.33698E-04	2043.497	-144.773	-17.5247	1060.271
6	0.066	1186.2	-128.4	593.1	2.33698E-04	2043.497	-144.773	-17.5247	1060.271
7	0.100	1323.7	-144.2	608.9	1.67756E-04	2211.619	-187.739	-91.1938	987.9354
8	0.117	1481.6	-172.4	611.7	1.43627E-04	2275.56	-219.244	-100.71	956.3618
9	0.133	1570.6	-186.1	614.9	1.43774E-04	2282.363	-180.533	-72.9557	955.274
10	0.150	1674.5	-201.4	618.3	1.74779E-04	2210.775	-103.87	103.0063	990.4358
11	0.166	1806.8	-220.9	622.6	2.47921E-04	1936.095	-299.572	-425.604	1079.068

15.2 Time-dependent ground camera view vector data sets

Appendix E.2.a Composite data – Interleaved data for Camera 208 and 212 based on original view vector data obtained from MSFC. Included are anchor locations (x0, y0, z0, x1, y1, z1) for time dependent view vectors for cameras 208 and 212. Also included is the estimated error (in inches) associated with each view vector.

Index	Time (sec)	x0 (inches)	y0 (inches)	z0 (inches)	x1 (inches)	y1 (inches)	z1 (inches)	Camera	Error
1	0.000	2102.9500	-500.0130	671.9760	1125.8000	-61.2923	576.4040	212	8.2000
2	0.004	1774.2600	-499.9580	438.0427	1169.6900	-86.6527	552.9080	208	18.5962
3	0.016	2063.2600	-500.0000	668.3100	1128.8700	-80.6685	576.6020	212	8.2000
4	0.021	1733.1600	-499.9600	454.6232	1157.7400	-106.7230	563.7380	208	23.5915
5	0.032	2019.4000	-499.9870	669.1120	1140.0200	-105.4980	582.6850	212	8.2000
6	0.038	1703.1000	-499.9610	474.8298	1149.8500	-122.0140	579.5370	208	20.3733
7	0.047	1991.2600	-499.9910	664.9740	1148.8200	-122.2180	581.9860	212	8.2000
8	0.054	1691.7400	-499.9620	473.6517	1193.8200	-159.9260	567.7090	208	16.3291
9	0.063	1996.1300	-500.0000	667.8960	1177.6700	-133.1250	587.0760	212	8.2000
10	0.071	1721.4100	-499.9610	485.8514	1217.4800	-155.8150	581.0500	208	20.4872
11	0.078	2022.3800	-500.0000	676.9680	1194.0700	-128.7940	594.9300	212	8.2000
12	0.094	2062.1900	-499.9890	683.0460	1287.5000	-152.9570	606.1940	212	8.2000
13	0.110	2133.6600	-499.9950	686.6290	1355.0700	-151.3240	609.2000	212	8.2000
14	0.121	1881.0300	-499.9590	528.1820	1381.1200	-158.9790	621.9050	208	18.3798
15	0.125	2210.3600	-499.9910	685.3920	1483.8500	-174.7320	612.9710	212	8.2000
16	0.138	2000.6600	-499.9570	531.9460	1524.4400	-175.2120	621.0590	208	20.3733
17	0.141	2282.3900	-500.0110	690.6460	1576.7600	-184.1750	620.0830	212	8.2000
18	0.154	2128.0600	-499.9530	537.7890	1638.4800	-166.1720	629.2390	208	19.9629
19	0.171	2202.7100	-499.9520	553.5490	1817.9400	-237.7020	625.1690	208	19.6575

Appendix E.2.b Composite data – Interleaved data for camera 208 and 212 with camera 208 time data shifted up (earlier) by 6.75 millisecond. This data set is consistent with the time shift that MSFC claimed provided the best "triangulation" of the image data. Included are anchor locations (x0, y0, z0, x1, y1, z1) for time dependent view vectors for cameras 208 and 212. Also included is the estimated error (in inches) associated with each view vector.

Index	Time (sec)	x0 (inches)	y0 (inches)	z0 (inches)	x1 (inches)	y1 (inches)	z1 (inches)	Camera	Error
1	0.00000	1774.2600	-499.9580	438.0427	1169.6900	-86.6527	552.9080	208	18.5962
2	0.00275	2102.9500	-500.0130	671.9760	1125.8000	-61.2923	576.4040	212	8.2000
3	0.01700	1733.1600	-499.9600	454.6232	1157.7400	-106.7230	563.7380	208	23.5915
4	0.01875	2063.2600	-500.0000	668.3100	1128.8700	-80.6685	576.6020	212	8.2000
5	0.03400	1703.1000	-499.9610	474.8298	1149.8500	-122.0140	579.5370	208	20.3733
6	0.03475	2019.4000	-499.9870	669.1120	1140.0200	-105.4980	582.6850	212	8.2000
7	0.04975	1991.2600	-499.9910	664.9740	1148.8200	-122.2180	581.9860	212	8.2000
8	0.05000	1691.7400	-499.9620	473.6517	1193.8200	-159.9260	567.7090	208	16.3291
9	0.06575	1996.1300	-500.0000	667.8960	1177.6700	-133.1250	587.0760	212	8.2000
10	0.06700	1721.4100	-499.9610	485.8514	1217.4800	-155.8150	581.0500	208	20.4872
11	0.08075	2022.3800	-500.0000	676.9680	1194.0700	-128.7940	594.9300	212	8.2000
12	0.09675	2062.1900	-499.9890	683.0460	1287.5000	-152.9570	606.1940	212	8.2000
13	0.11275	2133.6600	-499.9950	686.6290	1355.0700	-151.3240	609.2000	212	8.2000
14	0.11700	1881.0300	-499.9590	528.1820	1381.1200	-158.9790	621.9050	208	18.3798
15	0.12775	2210.3600	-499.9910	685.3920	1483.8500	-174.7320	612.9710	212	8.2000
16	0.13400	2000.6600	-499.9570	531.9460	1524.4400	-175.2120	621.0590	208	20.3733
17	0.14375	2282.3900	-500.0110	690.6460	1576.7600	-184.1750	620.0830	212	8.2000
18	0.15000	2128.0600	-499.9530	537.7890	1638.4800	-166.1720	629.2390	208	19.9629
19	0.16700	2202.7100	-499.9520	553.5490	1817.9400	-237.7020	625.1690	208	19.6575

15.3 Time-dependent ground camera view vector data sets

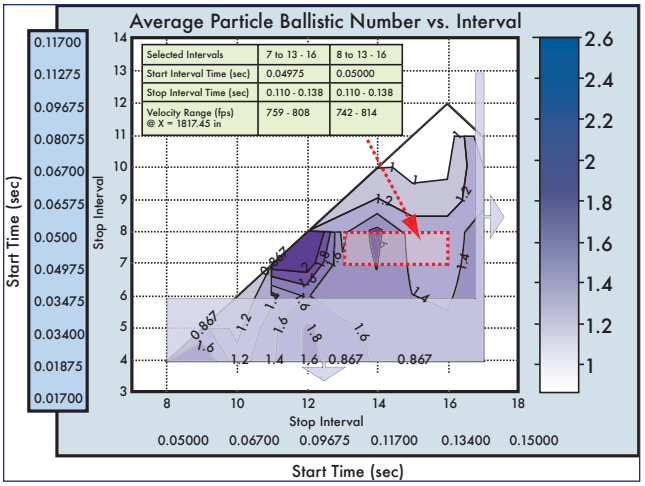


Figure 15-1. Contour plot of foam debris ballistic number vs. start and stop intervals, based on view vector data compare.

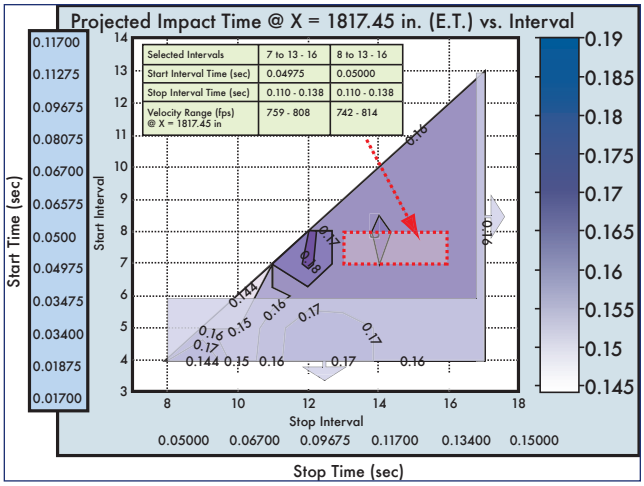


Figure 15-3. Contour plot of foam debris projected impact time at X = 1817.45 inches vs. start and stop intervals, based on view vector data compare.

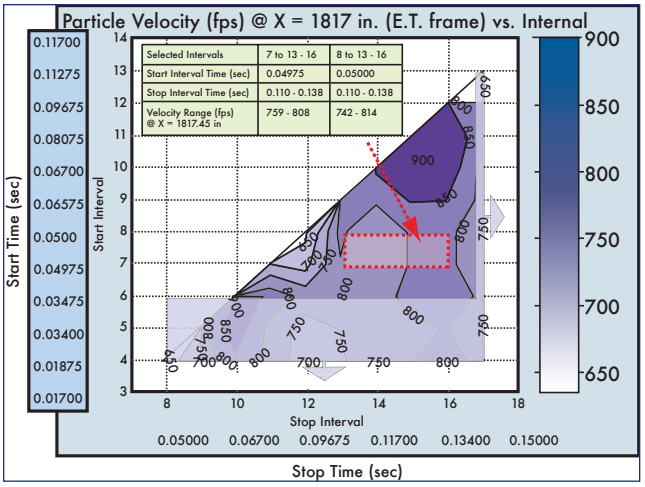


Figure 15-2. Contour plot of foam debris projected impact velocity at X = 1817.45 inches vs. start and stop intervals, based on view vector data compare.

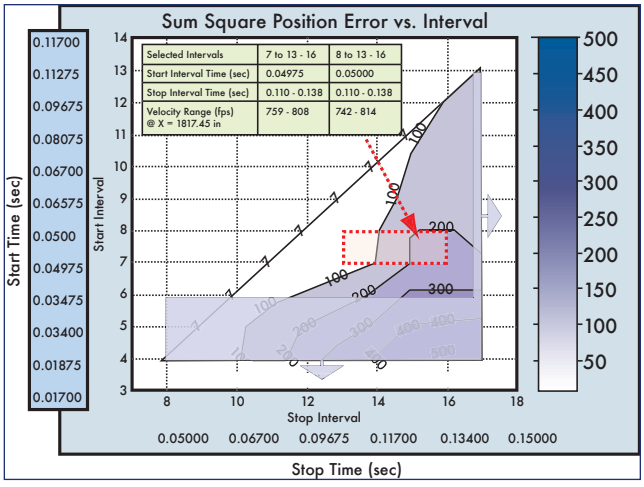


Figure 15-4. Contour plot of sum square position error between integrated trajectory and view vectors vs. start and stop intervals, based on view vector data compare.

Endnotes for Appendix D.8

1 Lee later performed trajectory analysis including the lift vector.

2 The trajectory is propagated beyond the optimized index interval to the Shuttle impact point using the local velocity flow grid provided by JSC/EG3. In one case (index range 8-13), the trajectory data was extrapolated about 10 inches beyond the 1817.45 X-position propagation target.

Volume II
Appendix D.9

Data Review and Timeline Reconstruction Report

This appendix contains the basic timeline data that was used to reconstruct the final minutes of *Columbia*'s re-entry on February 1, 2003. The version in this appendix contains all of the timeline events, but in condensed form.

The timeline organized the re-entry data. As such, this appendix contains no conclusions or recommendations. A visual presentation of the timeline has also been included on the CD that contains this appendix. It shows the timeline laid over a map of the United States along the ground track that *Columbia* flew during the re-entry.

THIS PAGE INTENTIONALLY LEFT BLANK

Data Review and Timeline Reconstruction Report

Don L. McCormack, Jr., NASA Team Leader, David W. Camp, Boeing Co-Team Leader,
and Joyce Seriale-Grush, NASA Co-Team Leader

NSTS 37376
June 3, 2003

Data Review and Timeline Reconstruction Team Final Report

in support of the *Columbia* Accident Investigation

June 3, 2003

Submitted by:

/s/ Don L. McCormack, Jr.
Don L McCormack, Jr., NASA
Team Leader

/s/ David W. Camp
David W. Camp, Boeing
Co-Team Leader

/s/ Joyce Seriale-Grush
Joyce Seriale-Grush, NASA
Co-Team Leader

This information is being distributed to aid in the investigation of the Columbia mishap and should only be distributed to personnel who are actively involved in this investigation.

Table of Contents

Executive Summary 3
1.0 Introduction 5
2.0 Purpose and Scope 5
3.0 Ground Rules and Assumptions 6
4.0 Process Definition 7
5.0 Results 8
6.0 Conclusions 9

Appendices
Appendix A STS-107 Timelines
A.1 Summary Entry Timeline
A.2 Master Entry Timeline
Appendix B STS-107 Master Entry Timeline Supporting Data
Appendix C Graphical Version of the STS-107 Entry Timeline
Appendix D Subsystem Data Review Summary Report
Appendix E Measurement Data for Timeline Events
Appendix F List of Contributors

This information is being distributed to aid in the investigation of the Columbia mishap and should only be distributed to personnel who are actively involved in this investigation.

EXECUTIVE SUMMARY

The Date Review and Timeline Reconstruction Team was one of many Technical Integration Team sub-teams created in support of the Orbiter Vehicle Engineering (OVE) Working Group (WG) investigation into the *Columbia* accident. The team's charter was to review the available telemetry and recorded data from *Columbia* and develop a timeline of events leading up to the loss of *Columbia* and its crew.

This report defines and documents the process that the Data Review and Timeline Reconstruction Team used to develop the STS-107 entry timeline. It also defines and documents the team's products and interfaces.

The scope of the data review included all available real-time telemetry from *Columbia* and all recorded data from the Orbiter experiments (OEX) recorder. Available data from all mission phases – ascent, on-orbit, and entry – were reviewed for the discovery of timeline events. The vast majority of the off-nominal events were discovered in the review of entry data and subsequently the entry timeline is the principle product. The few off-nominal events discovered during the ascent data review were delivered to personnel in the Space Shuttle Program (SSP) Systems Integration group who were responsible for ascent timeline reconstruction.

The primary ground rule established by the Data Review and Timeline Reconstruction team was that the team was to identify off-nominal performance from a review of the available flight data, describe that off-nominal performance as events on a timeline and make the timeline available to the pertinent Technical Integration Team sub-teams. Detailed analysis to determine the cause of the events was then performed by the pertinent sub-teams.

The timeline also included nominal Orbiter events, a time reference from entry interface (EI), and ground-track locations so that the off-nominal events could be more easily placed into the proper time and space reference.

The Data Review and Timeline Reconstruction Team consisted of a core group that were responsible for the generation of the timeline and conducting the data reviews. The data reviews were performed by the various Orbiter subsystem managers (SSMs) and/or subsystem engineers (SSEs). The data review and the reconstruction of the timeline began in the first hours following the *Columbia* accident. It began with quick look reviews of subsystem entry data conducted in the Mission Evaluation Room. From these reviews the initial versions of the entry timeline were developed. More formal data reviews were subsequently conducted at the Boeing Houston facility. These reviews were supported by personnel from Boeing (technical management and SSMs/SSEs), the Johnson Space Center (JSC) Engineering Directorate, the JSC Mission Operations Directorate (MOD),

This information is being distributed to aid in the investigation of the Columbia mishap and should only be distributed to personnel who are actively involved in this investigation.

the JSC and contractor Safety, Reliability and Quality Assurance (SR&QA) organizations, and the JSC Astronaut Office.

The timeline is documented in the Appendices. In Appendix A.1 is a summary entry timeline that groups events and shows only the more significant events to present the timeline in a more manageable form. Appendix A.2 is the master entry timeline that shows all of the entry events. Appendix B provides supporting data for the events on the entry timeline. Appendix C documents a graphical version of the entry timeline that is based on the summary entry timeline. The results of the subsystem data reviews are documented in Appendix D. Appendix E provides measurement data (description, source, type, location, range, sample rate) for each of the measurements associated with events on the timeline. Finally, Appendix F lists the names of many of the people who contributed in some way to this effort.

Utilizing the results of thorough reviews of all available flight data, as well as the review of videos of *Columbia's* entry and the results of the aerodynamic reconstruction, the Data Review and Timeline Reconstruction Team developed a thorough STS-107 entry timeline. This timeline provided a basis for the investigation and as such proved to be a valuable tool in the investigation of the *Columbia* accident.

This information is being distributed to aid in the investigation of the Columbia mishap and should only be distributed to personnel who are actively involved in this investigation.

1.0 INTRODUCTION

The Date Review and Timeline Reconstruction Team was one of many Technical Integration Team sub-teams created in support of the Orbiter Vehicle Engineering (OVE) Working Group (WG) investigation into the *Columbia* accident. The team's charter was to review the available telemetry and recorded data from *Columbia* and develop a timeline of events leading up to the loss of *Columbia* and its crew.

The primary source of data for the timeline reconstruction was real-time telemetry from *Columbia* and recorded data from the Orbiter experiments (OEX) recorder that was discovered during the search for debris. Individual subsystem teams reviewed the data for off-nominal events based on the team's knowledge of expected subsystem performance and the comparison of STS-107 flight data with previous flight data.

The review included flight data from throughout the mission; ascent, on-orbit and entry. Obviously, the vast majority of off-nominal events were discovered in the review of entry data and those events are documented in the entry timeline. This timeline was baselined and configuration controlled by the OVE WG. The few off-nominal events discovered during the ascent data review were delivered to personnel in the Systems Integration group who were responsible for ascent timeline reconstruction. There were no off-nominal events related to the *Columbia* accident discovered in the review of on-orbit data.

Another source of data included the evaluation of videos received from individuals across the western United States who had recorded *Columbia's* entry. From these videos, debris shedding events were characterized and documented in the entry timeline. Additionally, aerodynamic events derived by the analysis of the entry trajectory were included in the timeline. These events show the changes in aerodynamic coefficients during entry. Finally, the timeline also included nominal Orbiter events, a time reference from entry interface (EI), and ground-track locations so that the off-nominal events could be more easily placed into the proper time and space reference.

2.0 PURPOSE AND SCOPE

This report defines and documents the process that the Data Review and Timeline Reconstruction Team used to develop the STS-107 entry timeline. It also defines and documents the team's products and interfaces.

The scope of the data review included all available real-time telemetry from *Columbia* and all recorded data from the OEX recorder. Available data from all mission phases – ascent, on-orbit, and entry – were reviewed for the discovery of

This information is being distributed to aid in the investigation of the Columbia mishap and should only be distributed to personnel who are actively involved in this investigation.

timeline events. The vast majority of the off-nominal events were discovered in the review of entry data and subsequently the entry timeline is the principle product. The few off-nominal events discovered during the ascent data review were delivered to personnel in the Space Shuttle Program (SSP) Systems Integration group who were responsible for ascent timeline reconstruction. There were no off-nominal events related to the *Columbia* accident discovered in the review of on-orbit data.

In addition to the development of the timeline (Appendix A), a graphical version of the entry timeline was developed (Appendix B), a data package was compiled with data for each event on the timeline (Appendix C), a report summarizing the results of the subsystem data reviews was generated (Appendix D), and a table with measurement information for each measurement referenced on the entry timeline was generated (Appendix E).

3.0 GROUND RULES AND ASSUMPTIONS

The primary ground rule established by the Data Review and Timeline Reconstruction team was that the team was to identify off-nominal performance from a review of the available flight data, describe that off-nominal performance as events on a timeline and make the timeline available to the pertinent Technical Integration Team sub-teams. Detailed analysis to determine the cause of the events was then performed by the pertinent sub-teams.

There are exceptions to that ground rule in that two classes of events are actually the products of the analyses conducted by two of the sub-teams. The Image Analysis Team screened over 140 videos received from the public. Approximately 25 contained good records of debris emanating from *Columbia's* plasma envelope. The Image Analysis Team's emphasis was to obtain the most accurate times possible for the debris observations. A characterization of those observations and the times at which they occurred were included in the entry timeline.

Additionally, the Integrated Entry Environments team derived events for the timeline from entry trajectory reconstruction analyses. These events characterized changes in aerodynamic coefficients that occurred over the final 7-minutes of *Columbia's* entry.

Finally, the timeline also included nominal Orbiter events, a time reference from entry interface (EI), and ground-track locations so that the off-nominal events could be more easily placed into the proper time and space reference.

This information is being distributed to aid in the investigation of the Columbia mishap and should only be distributed to personnel who are actively involved in this investigation.

4.0 PROCESS DEFINITION

The Data Review and Timeline Reconstruction Team consisted of a core group that were responsible for the generation of the timeline and conducting the data reviews. The data reviews were performed by the various Orbiter subsystem managers (SSMs) and/or subsystem engineers (SSEs). The data review and the reconstruction of the timeline began in the first hours following the *Columbia* accident. It began with quick look reviews of subsystem entry data conducted in the Mission Evaluation Room. From these reviews the initial versions of the entry timeline were developed.

More formal data reviews were subsequently conducted at the Boeing Houston facility. These reviews were supported by personnel from Boeing (technical management and SSMs/SSEs), the Johnson Space Center (JSC) Engineering Directorate, the JSC Mission Operations Directorate (MOD), the JSC and contractor Safety, Reliability and Quality Assurance (SR&QA) organizations, and the JSC Astronaut Office. The initial focus of the review was on the entry data but it subsequently expanded to include ascent and on-orbit data. The review also included a 32-second period of real-time telemetry data that was not initially accepted by the Orbiter Data Reduction Complex (ODRC) due to the high bit error rate. This period of data was reconstructed so that it could be processed by the ODRC for review. The 32-second period consisted of approximately 5-seconds of data at the start of the period, an approximate 25-second data gap, and approximately 2-seconds of data at the end of the period.

The early revisions of entry timeline were considered preliminary as the events on the timeline matured through the process of more thorough and complete data reviews. Revision 12 of the timeline was subsequently baselined at the OVE WG on February 10, 2003, for configuration control. From that point on, changes could only be made to the timeline by re-baselining revisions at the OVE WG.

Timeline events were also received from two other sources, the Image Analysis Team and the Integrated Entry Environments Team. The Image Analysis Team screened videos received from the public, of which approximately 25 contained good records of debris emanating from *Columbia's* plasma envelope. From these videos, the team was able to characterize off-nominal events with a description of the events and the times at which they occurred. The Integrated Entry Environments team derived events for the timeline from entry trajectory reconstruction analyses that characterized changes in aerodynamic coefficients that occurred over the final 7-minutes of *Columbia's* entry.

In March, the OEX recorder was found and the data on the recorder was recovered. On the last weekend of March, the review of that data was begun. The process followed was that same as that established for the review of the real-

This information is being distributed to aid in the investigation of the Columbia mishap and should only be distributed to personnel who are actively involved in this investigation.

time telemetry data. Initially, a separate entry timeline was developed from the OEX data. As with the timeline developed with the real-time telemetry data, the early revisions of this timeline were considered preliminary as the events on the timeline matured through the process of more thorough and complete data reviews. Revision 17 of the entry timeline subsequently merged revision 16 of the entry timeline with the entry timeline developed from the OEX data. Revision 17 of the entry timeline was baselined at the OVE WG on May 7, 2003.

In the weeks leading up to the release of this final report, minor changes were made to the entry timeline. These changes were primarily editorial in nature but did include changes to debris event times just prior to breakup of the vehicle. Therefore the version of the timeline documented in Appendix A of this report is revision 19 of the entry timeline.

Throughout the process, a graphical version of the timeline was developed and maintained. Additionally, each revision of the timeline was distributed to each of the Technical Integration Team sub-teams and other groups involved in the Columbia investigation. The Vehicle Data Mapping Team developed several products to more graphically illustrate the events during entry. The timeline was also used by the Scenario and Fact Database Teams and was used for the development of integrated ground track/timeline charts generated by organizations in JSC Engineering and MOD.

5.0 RESULTS

The Data Review and Timeline Reconstruction Team conducted data reviews of all available data from all phases of the STS-107 mission. From the results of these reviews and inputs from the Image Analysis and the Integrated Entry Environments Teams, an entry timeline was developed.

Revision 19 of the entry timeline is documented in the Appendices. In Appendix A.1 is a summary version of the entry timeline that groups events and shows only the more significant events to present the timeline in a more manageable form. In Appendix A.2 is the master entry timeline that shows all of the entry events.

A great amount of data was compiled and reviewed in support of this effort. Although all of that data is not documented here, Appendix B provides a brief verbal description and supporting data for each of the events on the entry timeline.

Appendix C documents a graphical version of the entry timeline that is based on the summary entry timeline. Note that other graphical versions were developed by other teams/organizations. The Vehicle Data Mapping Team developed both 2D

This information is being distributed to aid in the investigation of the Columbia mishap and should only be distributed to personnel who are actively involved in this investigation.

and 3D products to visually show the events and organizations in JSC/Engineering and MOD integrated the entry timeline into ground track maps.

The results of the subsystem data reviews are documented in Appendix D. The reports summarize the results of the data reviews conducted by each of the subsystem teams. The reports cover all mission phases and indicate that although there was evidence of the impending catastrophic failure in the data, all of *Columbia's* active systems were performing nominally until the final minute prior to breakup.

Appendix E provides measurement data (description, source, type, location, range, sample rate) for each of the measurements associated with events on the timeline.

Finally, Appendix F lists the names of many of the people who contributed in some way to this effort.

6.0 CONCLUSIONS

Utilizing the results of thorough reviews of all available flight data, as well as the review of videos of *Columbia's* entry and the results of the aerodynamic reconstruction, the Data Review and Timeline Reconstruction Team developed a thorough STS-107 entry timeline. This timeline provided a basis for the investigation and as such proved to be a valuable tool in the investigation of the *Columbia* accident.

This information is being distributed to aid in the investigation of the Columbia mishap and should only be distributed to personnel who are actively involved in this investigation.

A.1-3
Integ Time Line Team - REV 19 BASELINE

Appendix A.1 - STS-107 Mishap Investigation - Summary Time Line

6/9/2003 1 PM

Note: Rev 19 BASELINE updates Rev 18 with the eastern most debris events (over Texas) and is the timeline used for the Final Report

Sum No.	GMT GMT Day 32	EI s:ec	OEX data	Milestone	Entry Event	Remarks	MSID
8.0	deleted					Rationale for deletion: inadvertently added to summary timeline	
9	deleted						
10	13:52:59	EI+5:30			Left INBD Elevon Lower Skin Temp (1) - OSL	Began trending down 3 secs earlier	V09T1006A
QBAR = ~25.5 psf (~1.18 psi); Mach 23.2					----- 32:13:53:00 -----	EI + 531 sec; WLE Stagnation Temp: ~2800 F	
10.3	deleted					Rationale for deletion: Merged with seq #10.75 after further analysis.	
10.6	13:53:03	EI+5:34	X		Left Outboard Elevon Wide Band Accelerometers - onset of signal saturation indicating likely measurement failure (approximately 10G peak-to-peak - off-scale)		V08D9729A
11	13:53:10 / 36	EI+5:41 / EI+6:07			Hydraulic System Left Outbd / Inbd Elevon Return Line Temps (4) - OSL	OSL was preceded by Nominal Temp rise.	V58T0394A V58T0193A V58T0157A V58T0257A
11.1	deleted					Rationale for deletion: alpha modulation time tag updated - moved to seq #11.25	
11.2	13:53:26	EI+5:57		Approx Veh Grd Location: 38.7 N / -123.5 W	Altitude 231600 ft / Mach 23.0 - Crossing the California Coastline	Data source: STS-107 GPS Trajectory Data	
11.21	13:53:29	EI+6:00	X		Left Fuselage Side Surface Temp BP3605T - start of off-nominal increasing temperature trend from ~180 deg F to ~400 deg F	Trend followed by temperature drop and rise	V07T9253A X1000.7 Y-105 Z354.5
11.22	13:53:29	EI+6:00	X		Left PLBD Surface TC BP3603T - Start of slightly off-nominal erratic temperature trend when compared to previous flights of same inclination		V07T9913A X1005.8 YLH Z441.3
11.23	13:53:29	EI+6:00	X		Left PLBD Surface TC BP3703T - start of off-nominal temperature rise, peaking at EI+625, followed by temperature drop and subsequent off-nominal higher-than-expected temperature signature		V07T9925A X1138.5 YLH Z441.4
11.24	13:53:29	EI+6:00	X		Left Fuselage Side Surface TC BP3604T - Start of slightly off-nominal erratic temperature trend when compared to previous flights of same inclination		V07T9903A X1000 Y-105 Z356.4
11.25	13:53:31	EI+6:02		Alpha Modulation	Angle of attack (alpha) modulation active		V90H0803C
11.3	13:53:32 / 54:22	EI+5:63 / EI+5:63			Two events of unexpected return link comm drop-out (Comm events 10-11)	On upper left aft antenna (TDRS 171W). Appears off-nominal based on previous flt data. Comm loss not continuous thru period indicated.	
11.35	13:53:37	EI+5:68	X		Xo 1040 Spar (MLG Forward Wall Spar) Strain Gage - Upper Cap - start of off-nominal increase in strain indication (over an approximate 115 second interval) followed by sudden decrease		V12G9049A X1040 Y-135 ZUPR
11.37	13:53:38	EI+5:69			Inertial sideslip angle (Beta) exceeds flight history.	The steady state navigation derived sideslip angle becomes out-of-family as compared to previous flight data at this point in the trajectory.	V90H2249C
11.4	13:53:44	EI+5:75	X		OMS-L Pod HRSI Surf T1-AFT - Start of off-nominal lower-than-expected temperature trend when compared to previous flights of same inclination	Sensor goes erratic at EI+940	V07T9219A X1007.1 Y-126.0 Z422.0
11.5	13:53:45 / 54:11	EI+5:76 / EI+6:02			1st reported debris (5) observed leaving the Orbiter just aft of Orbiter envelope (Debris # 1 thru 5)	EOC video # EOC2-4-0055, 0056, 0064, 00136 & 0201. No evidence of jet firings near events.	n/a
QBAR = ~29 psf (~1.20 psi); Mach 22.7					----- 32:13:54:00 -----	EI + 591 sec; WLE Stagnation Temp: ~2850 F	
12	deleted						
13	13:54:10 / 55:12	EI+6:01 / EI+6:63			Left Main Gear Brake Line Temp B (1) / Strut Actuator Temp (1) / Sys 3 LMG Brake Sw Vlv Ret Line Temp (FWD) (1) - start of off nominal trend	Unusual Temperature Increase	V58T1701A V58T0842A V58T0405A
13.5	13:54:11	EI+6:02			Reversal in growth trend of derived roll moment coefficient	Observed roll moment changed from a negative to positive slope (derived by analysis).	n/a

A.1-1
Integ Time Line Team - REV 19 BASELINE

Appendix A.1 - STS-107 Mishap Investigation - Summary Time Line

6/9/2003 1 PM

Note: Rev 19 BASELINE updates Rev 18 with the eastern most debris events (over Texas) and is the timeline used for the Final Report

Sum No.	GMT GMT Day 32	EI s:ec	OEX data	Milestone	Entry Event	Remarks	MSID
1	13:10:19	EI+2:03		TAS-5	APU 2 Start		
2	13:15:30	EI~1719		TIG	OMS TIG		
3	13:18:06	EI~1961			OMS End of Burn		
4	13:31:25	EI+764		EI-13	APU 1 Start		
5	13:31:29	EI+768			APU 3 Start		
5.5	13:39:28.959	EI~2804	X		Start of OEX PCM Data Block		
6	13:44:09	EI+0		EI	Entry Interface (400,000 ft)	Mach 24.57	
6.1	13:45:39 / 48:59	EI+90 / EI+290	X		16 Temperature Sensors on the lower surface to the left of or at the centerline experience off-nominal early temperature trends (warmer temperature rise rate compared to previous flights of OV-102 at the same inclination)		V09T9849A V07T9784A V07T9666A V07T9786A V07T9468A V07T9787A V07T9470A V07T9788A V07T971 1A V07T9478A V07T971 3A V07T9480A V07T9785A V09T9845A V09T9231A V07T9480A
6.15	13:48:39	EI+27.0	X		Left Wing Front Spar at RCC Panel 9 - initiation of off-nominal trend in strain (small increase) followed by a more significant off-nominal signature to failure at EI+495 secs	The measurement began to fail at approximately EI+495 sec	V12G9921A X1106.0 Y-229.0 ZMID
6.2	13:48:59	EI+29.0	X		Left Wing RCC Panel 9 Lower Attach Clevis (between RCC 9 and 10) - initiation of an off-nominal temperature trend (early temperature increase compared to previous flights of same inclination)	The measurement began to fail at approximately EI+492 sec	V09T9910A X1112.0 Y-239.0 Z389.0
6.3	13:49:32	EI+32.3			Start of initial roll		
6.4	~13:49:39*	~EI+330*	X		Left Wing Front Spar Caps Strain Gage shows early off nominal downward trend	*Note: PCM3 entry data is in snapshot format (not continuous). Time indicated is at start of data segment where off-nominal signature is first observed, therefore event may have started earlier than noted.	V12G9169A X1107 Y232 Z7
6.45	13:49:49 / 49:59	EI+340 / EI+350	X		4 Left OMS Pod Surface temps - Start of off-nominal temperature trend - cooler rise rate when compared to previous flights of same inclination	Followed by the start of a warmer-than-expected temperature trend beginning in the EI+510 to EI+540 sec range	V07T9976A V07T9978A V07T9220A V07T9972A
QBAR = ~15 psf (~0.10 psi); Mach 24.4					----- 32:13:50:00 -----	EI + 351 sec; WLE Stagnation Temp: ~2520 F; STS-107 Nom EOM Design Pred	
6.5	13:50:00 / 43	EI+351 / EI+394			Five events of unexpected return link comm drop-out (Comm events 1-5)	On upper left aft antenna (TDRS 171W). Appears off-nominal based on previous flt data. Comm loss not continuous thru period indicated.	
6.7	13:50:09	EI+36.0	X		Left PLBD Surface TC BP3703T - Start of off-nominal temperature trend - cooler rise rate when compared to previous flights of same inclination	Followed by large increase in temperature at EI + 570 seconds	V07T9925A X1138.5 YLH Z441.4
6.9	13:50:19	EI+37.0	X		Left Wing Lower Surface Thermocouple BP2510T begins off-nominal temp increase from ~2000 deg F to ~2200 deg F over approx 50 seconds followed by a momentary 100 deg F temperature spike	The measurement subsequently fails at approximately EI+496 sec	V07T9666A X1121.1 Y-235.5 ZLWR
7	13:50:53	EI+40.4		Start of Peak Heating		Determined by analysis	
QBAR = ~19 psf (~0.13 psi); Mach 24.1					----- 32:13:51:00 -----	EI + 411 sec; WLE Stagnation Temp: ~2650 F	
7.2	13:51:14	EI+42.5	X		Left Wing Front Spar at RCC Panel 9 - start of off-nominal increasing temperature trend	Increasing trend continues until the measurement starts to fail at approximately EI+520 sec	V09T9859A X1102.2 Y-239.0 Z-239.0
7.25	13:51:14	EI+42.5	X		Left Wing RCC Panel 9 Lower Attach Clevis (between RCC 9 and 10) - start of a more rapid off-nominal increasing temperature trend	Increases until the measurement starts to fail at approximately at EI + 492 secs	V09T9910A X1112.0 Y-239.0 Z389.0
7.3	deleted					Rationale for deletion: Upon further evaluation of the data, it was determined that the remote sensor signatures had been seen in previous flights and/or could be explained by known events	
7.35	deleted					Rationale for deletion: Moved to seq # 11.37 after further analysis.	
7.37	13:51:49	EI+46.0	X		OMS-L Pod HRS I Surf T3-AFT - Start of off-nominal higher-than-expected temperature trend when compared to previous flights of same inclination	Sensor sees a sharp temp increase at EI+910 and goes erratic at EI+940	V07T9223A X1437.2 Y-126 Z422

A.1-4
Integ Time Line Team - REV 19 BASELINE

Appendix A.1 - STS-107 Mishap Investigation - Summary Time Line

6/9/2003 1 PM

Note: Rev 19 BASELINE updates Rev 18 with the eastern most debris events (over Texas) and is the timeline used for the Final Report

Sum No.	GMT GMT Day 32	EI s:ec	OEX data	Milestone	Entry Event	Remarks	MSID
14	13:54:20	EI+6:11			Start of slow aileron trim change	The aileron trim setting observed in flight first deviates from the predicted trim setting at this pt in trajectory (GMT is approximate (+/- 10 sec) for aileron).	V90H1500C (aileron trim)
15	13:54:22	EI+6:13			Mid Fuselage LT BondLine Temp at x1215 (1) & LH Aft Fus Sidewall Temp at x1410 (1) - start of off nominal trend	Unusual increase in temperature rise rate	V54T1106A V09T1724A
15.2	13:54:29	EI+6:20	X		Left Fuselage Side Surface temp BP3605T peaks and starts downward trend		V07T9253A X1000.7 Y-105 Z354.5
15.3	13:54:33.3 / 54:37	EI+624.3 / EI+6:28			Flash #1 - Orbiter envelope suddenly brightened (duration 0.3 sec), leaving noticeably luminescent signature in plasma trail; plus Debris #6 - report of very bright debris observed leaving the Orbiter just aft of the Orbiter envelope.	EOC video # EOC2-4-0026, 0034, & 00099. R3R and R2R jet firings occurred near events. Debris events 6 & 14 are visually the biggest, brightest events & therefore may indicate the most significant changes to the Orbiter of the western debris events.	n/a
15.32	13:54:34	EI+6:25	X		Left Fuselage Side Surface temp BP3703T peaks and starts downward trend		V07T9925A X1138.5 YLH Z441.5
13.33	13:54:39	~EI+6:30	X		Strain Gages Centered on the Upper Surface of the Left MLG Wheel Wheel - Higher than-expected strain indications observed in these gages	Note: PCM3 entry data is in snapshot format (not continuous), therefore event may have occurred earlier than noted	V12G9156A, V12G9157A, V12G9158A
13.34	13:54:39	~EI+6:30	X		Left Wing X 1040 Spar Web - shows increase in strain	Note: Adjacent sensor V12G9165A did not show similar "off-nominal" signature at this time, also, PCM3 entry data is in snapshot format (not continuous), therefore event may have occurred earlier than noted	V12G9166A V12G9167A (V12G9165A-nominal)
QBAR = ~34.5 psf (~1.24 psi); Mach 22.1					----- 32:13:55:00 -----	EI + 651 sec; WLE Stagnation Temp: ~2800 F	
15.35	13:55:04 / 55:25	EI+6:55 / EI+6:80			Debris # 7, 7A, & 8 thru 10 observed leaving the Orbiter just aft of Orbiter envelope. Debris 8, 9, & 10 were seen aft of the Orbiter envelope inside Debris Shower A (next event listed).	EOC video # EOC2-4-0005, 0017, 0021, 0028, 0030, 0098 & 0161. No evidence of jet firings near events.	n/a
15.37	13:55:22 / 55:28	EI+6:73 / EI+6:79			Debris Shower A - Report of debris shower seen just aft of Orbiter envelope.	Seen just aft of Orbiter envelope. Over the course of these four seconds a luminescent section of plasma trail is observed which appears to contain a shower of indefinite particles and multiple, larger discrete debris that includes Debris 8, 9, and 10.	Saw debris: EOC2-4-0098, 0161, 0005, 0030 Saw shower: EOC2-4-0017, 0021, 0028
15.4	deleted					Rationale for deletion: Upon further evaluation of the data, it was determined that the remote sensor signatures had been seen in previous flights and/or could be explained by known events.	
15.43	13:55:33 / 56:03	EI+6:84 / EI+7:14			Two events of return link comm drop-outs (Comm events 12 & 13)	On upper right aft antenna (TDRS 171W). Uncertain if off-nominal based on previous flight data. Comm loss not continuous thru period indicated.	
15.44	deleted					Rationale for deletion: Moved to 15.46 after further review of the data	
15.45	13:55:35 / 56:12	EI+6:86 / EI+7:23			Debris # 11, 11A, 11B, 11C & 12 thru 15 observed leaving the Orbiter just aft of Orbiter envelope. Debris # 11B & #11C events were both seen at the head of a parallel plasma trail aft of the Orbiter envelope. Debris #12 event was preceded and followed by secondary plasma trails. Debris #13 event was followed by momentary brightening of plasma trail adjacent to debris. Debris #14 event consisted of very bright debris observed leaving the Orbiter.	EOC video # EOC2-4-0005, 0017, 0021, 0028, 0030, 0050, & 0098. No evidence of jet firings near events. (Nearest jet firings occur at 56:17.) Debris events 6 & 14 are visually the biggest, brightest events & therefore may indicate the most significant changes to the Orbiter of the western debris events.	n/a
15.46	13:55:36	EI+6:87	X		Xo 1040 Spar (MLG Forward Wall Spar) Strain Gage - Upper Cap - sudden drop in strain followed by gradual increase until erratic signature at approximately EI+930		V12G9049A X1040 Y-135 ZUPR

A.1-2
Integ Time Line Team - REV 19 BASELINE

Appendix A.1 - STS-107 Mishap Investigation - Summary Time Line

6/9/2003 1 PM

Note: Rev 19 BASELINE updates Rev 18 with the eastern most debris events (over Texas) and is the timeline used for the Final Report

Sum No.	GMT GMT Day 32	EI s:ec	OEX data	Milestone	Entry Event	Remarks	MSID
QBAR = ~22 psf (~0.16 psi); Mach 23.7					----- 32:13:52:00 -----	EI + 471 sec; WLE Stagnation Temp: ~2700 F	
7.4	deleted					Rationale for deletion: Moved to seq # 8.75 after further analysis.	
7.45	13:52:09 / 52:55	EI+4:80 / EI+4:86			Four events of unexpected return link comm drop-out (Comm events 6-9)	On upper left aft antenna (TDRS 171W). Appears off-nominal based on previous flt data. Comm loss not continuous thru period indicated.	
7.46	13:52:09 / 52:49	EI+4:80 / EI+5:20	X		Nose Cap RCC Attach OutBoard Clevis (Chin Panel) - Temporary change in slope, then returns to "nominal" Note: Adjacent sensor V09T9888 (on centerline) does not show this signature		V09T9869A X092.0 Y-23.0 LWR
7.47	13:52:16	EI+4:87	X		Two Left Wing and 1 Right Wing Surface Pressure measurements show signs of failure	First OEX data to show signs of failure	V07P8038A V07P8086A V07P8151A 18 of 18 measurements (Multiple measurements
7.48	13:52:16 / 53:17	EI+4:87 / EI+5:22	X		All of the active measurements (does not include PCM 3 data in snapshot mode) running in the wire bundles along the left wing leading edge show signs of failure - 16 measurements		
7.49	13:52:16 / 56:24	EI+4:87 / EI+7:30	X		The vast majority of left wing OEX measurements show signs of failure during this time period - this includes all left wing temperature and pressure measurements and all strain measurements aft of Xo 1040 with the exception of three strain measurements on the upper surface of the LMLG compartment Additionally, 30 right wing pressure measurements show signs of failure		
7.5	13:52:17	EI+4:88		Approx Vehicle Ground Location: 39.0 N / -129.2 W	Altitude 236,800 ft / Mach 23.6 - Over the Pacific Ocean, approx 300 miles West of California Coastline	Approx vehicle position when first off-nominal data was seen; Data source: STS-107 GPS Trajectory Data	
7.7	13:52:17	EI+4:88			LMG Brake Line Temps (D) - small increase in temperature ("bit lift up")	Initiation of temp rise ("bit lift up") - may be nominal based on rise rate comparison w/ flight experience	V58T1703A
7.75	13:52:18	EI+4:89	X		Left Wing Spar Cap Lwr L103 (Xo 1040 Spar - Lower Cap) - off-nominal increase in strain indication followed by gradual decrease over approx 330 seconds interval until measurement failure at ~EI+935		V12G9048A
7.77	13:52:24	EI+4:95	X		Left Wing Front Spar at RCC Panel 9 - strain gage goes erratic for approximatly 20 second - measurement appears to be failing	Subsequent data is suspect	V12G9921A X1106.0 Y-229.0 ZMID
7.8	13:52:25	EI+4:96	X		Left Outboard Elevon Wide Band Accelerometers - off-nominal vibration response (approximately 3G peak-to-peak) V08D9729A - L OB Elevon Z-Vib (MUX 18 Ch 2)		V08D9729A
7.85	13:52:29	EI+5:00	X		OMS-L Pod HRSI Surf T1-AFT - Start of slightly off-nominal erratic trend when compared to previous flights of same inclination	Followed by drop in temperature at EI + 570 seconds and subsequent erratic temperature changes	V07T9219A X1007.1 Y-126.0 Z422.0
7.9	13:52:31	EI+5:02	X		Left Outboard Elevon Wide Band Accelerometers - off-nominal vibration response (approximately 3G peak-to-peak) V08D9729A - L OB Elevon Z-Vib (MUX 18 Ch 2)		V08D9729A
8	deleted					Rationale for deletion: moved to seq #8.7	
8.5	13:52:32.55	EI+5:03			Supply H2O Dump Nozzle Temps (A, B) (2) and Vacuum Vent Temp (1) - transient 15 and 23 seconds, respectively) increase in typical rise rates.	GMT shown indicates initial rise duration. Supply H2O Dump Nozzle temps took additional 48 secs to return to nominal temp rise; vacuum vent temps took additional 40 secs to return to nominal rise.	V62T0440A V62T0439A V62T0551A
8.6	13:52:34	EI+5:05	X		OMS-L Pod HRS I Surf T2-AFT - Start of off-nominal lower-than-expected temperature trend (compared to previous flights of same inclination) until sensor sees a sharp temp increase at EI+910 and goes erratic at EI+940		V07T9222A X1486.9 Y-126 Z422.0
8.65	13:52:39 / 53:09	EI+5:10 / EI+5:40	X		4 Left OMS Pod Surface temps - Change in existing off-nominal temperature trend following a cooler rise rate than expected, the temperature trend that is significantly warmer when compared to previous flights of same inclination)		V07T9976A V07T9978A V07T9220A V07T9972A
8.7	13:52:41	EI+5:12			LMG Brake Line Temps (A, C) (2) - start of off nominal trend	Unusual Temperature Increase	V58T1700A V58T1702A
8.75	13:52:44 / 52:50	EI+5:15 / EI+5:21			First clear indication of off-nominal aero increments	Delta yawing and rolling moment coefficients indicate off-nominal trends. Derived by analysis.	n/a

A.1-7
Integ Time Line Team - REV 19 BASELINE

Appendix A.1 - STS-107 Mishap Investigation - Summary Time Line

6/5/2003 1 PM

Note: Rev 19 BASELINE updates Rev 18 with the eastern most debris events (over Texas) and is the timeline used for the Final Report

Sum No.	GMT GMT Day 32	EI sec	OEX data	Milestone	Entry Event	Remarks	MSID
QBAR = on pof; Mach nn					------ 32:14:00:00 ------	EI + 961 sec; WLE Stagnation Temp: ~2800 F	
42	deleted						
43	14:00:02.654	EI+953.654			PASS Fault Message annunciation - L RCS LJET		
44	14:00:02.660	EI+953.660		Beginning of 3 second period of reconstructed data	Start of last 2-seconds of the 32 second period of post-LOS data.		
					During this final 2 second period of reconstructed data, the data indicates the following systems were nominal: APUs were running and WSB cooling was evident. MPS integrity was still evident. Fuel cells were generating power and the PRSD tanks lines were intact. Comm and navaids systems in the forward fuselage were performing nominally. RSB, Body Flap, main engine, and right wing temps appeared active. ECLSS performance was nominal.		
					During this final 2 second period of reconstructed data, the data indicates the following systems were off-nominal: All three Hyd systems were lost. The left inbd/outbd elevon actuator temps were either OSL or no data exists. Majority of left OMS pod sensors were either OSH or OSL or no data exists. Elevated temps at bottom bondline centerline skin forward and aft of the wheel wells and at the port side structure over left wing were observed. EPDC shows general upward shift in Main Bus amps and downward shift in Main Bus volts. AC3 phase A inverter appeared disconnected from the AC Bus.		
					GNC data suggests vehicle was in an uncommanded attitude and was exhibiting uncontrolled rates. Yaw rate was at the sensor maximum of 20 deg/sec. The flight control mode was in AUTO. (Note that all Nav-derived parameters (e.g., alpha) are suspect due to high rates corrupting the IMU state.)		
45	14:00:03.470 / 14:00:03.637*	EI+954.470 / EI+954.637			BFS Fault Message annunciation - L OMS TK P BFS Fault Message annunciation - Indeterminant BFS Fault Message annunciation - SM1 AC VOLTS PASS Fault Message annunciation - L RCS PVT	* Time info corrupted on some of the events.	
46	14:00:03.637	EI+954.637			PASS Fault Message annunciation - DAP DOWNMODE RHC	The s/w process which logs the PASS message runs every 1.92 seconds, so this event could have occurred as early as 14:00:01.717 GMT. However, during the 2 sec period, available vehicle data indicates RHC was in detent and DAP was in AUTO.	
47	14:00:04.826	EI+955.826		End of 2-second period of reconstructed data	Last identifiable OI Downlink frame		n/a
47.5	14:00:13.439	EI+964.439	X		OEX PCM loss of sync		
48	deleted					Rationale for deletion: moved to 41. 5 after further review of the videos	n/a
48.3	14:00:17.8/18.8	EI+968.8 / EI+969.8			Catastrophic Event of an unknown nature (formally referred to as "Main Body Breakup) consisting of a sudden brightening of the Orbiter envelope followed by a definitive change in the character of the trail and disintegration of the main orbiter envelope into multiple pieces	EOC videos MIT-DVCAM-0001, EOC2-4-018, -0024, -0209-B, -0221-3 and -0221-4	
48.5	14:00:19.44	EI+970.44	X		FDM 1 A end of data		
49	deleted					Rationale for deletion: moved to 48. 3 after further review of the videos	n/a
50	14:00:53	EI+ 1004		End of Peak Heating		Determined by analysis	

= Nominal/Expected Event or Performance

A.1-8
Integ Time Line Team - REV 19 BASELINE

Appendix A.1 - STS-107 Mishap Investigation - Summary Time Line

6/5/2003 1 PM

Note: Rev 19 BASELINE updates Rev 18 with the eastern most debris events (over Texas) and is the timeline used for the Final Report

Sum No.	GMT GMT Day 32	EI sec	OEX data	Milestone	Entry Event	Remarks	MSID	
15.5	13:55:41	EI+692			Mid Fuselage Port (Left) Sill Longeron Temp at X 1215 - start of off-nominal trend	Unusual Temperature Increase	V54T1118A	
QBAR = >40 psf (~0.28 psi); Mach 21.4					------ 32:13:56:00 ------	EI + 711 sec; WLE Stagnation Temp: ~2800 F		
16	13:56:03 / 56:24	EI+714 / EI+736			Left Lower Upper Wing Skin Temps - Trending down (2)	Indication of potential measurement failures	V09T1002A	V09T1024A
16.5	13:56:16 / 56:53	EI+727 / EI+764			Hyd Sys 1 LMG Uplock Actuator Unlock Line Temp; Sys 3 LMG Brake Sw Vlv Ret Line Temp (FWD); LMG Brake Line Temp C; LMG Brake Line Temp B; Sys 3 Left Main Gear Strut Actuator Temp - all show a temp rise rate change.	Significant increase in temp rise rate on all four lines	V58T0125A V58T0842A V58T1702A	V58T1701A V58T0405A
16.55	13:56:30 / 56:58	EI+741 / EI+798			First Roll Reversal initiation / completion		V60H1044C	
16.6	deleted					Rationale for deletion: Comm dropout (event 14) is deleted since probably normal due to completion of roll reversal resulting in elevation angle nearing 60 deg's (vertical tail interference w/comm).		
QBAR = >42 psf (~0.29 psi); Mach 20.7					------ 32:13:57:00 ------	EI + 771 sec; WLE Stagnation Temp: ~2800 F		
16.65	13:57:09	EI+780	X		Fuselage Side Surf Thermocpl BP3976T - start of off-nominal trend (temp increase followed by temp drop / rise)		V07T9270A E1606.1 Y-124.8 Z307.1	
16.67	13:57:09	EI+780	X		Fuselage Lower Surface BF Thermocpl BP220T - start of off-nominal trend (shallow temp drop)		V07T9508A E1560Y-111.1 Z LWR	
16.7	13:57:19 / 24	EI+790 / EI+795			MLG LH Outbd Tire Pressures 1 & 2 - start of small increase in pressures	Not seen in previous flights	V51P0570A	V51P0572A
16.8	13:57:19 / 58:01.5	EI+790 / EI+832.5			Debris # 16 (very faint debris) observed leaving just aft of Orbiter followed by two events of assymmetrical brightening of the Orbiter shape (Flares 1 and 2). (Occurred over eastern AZ and NM.)	Debris #16 EOC video # EOC2-4-00148-2. Flares #1 & 2: EOC2-4-00148-4. Observations by personnel from the Starfire Optical Range (Kirtland Air Force Base, NM).	n/a	
17	13:57:28 / 57:43	EI+799 / EI+814			Left Lower Upper Wing Skin Temps (2) - OSL		V09T1002A	V09T1024A
18	deleted							
19	13:57:54				Sys 2 LH Brake Sw Vlv Return Temp (1)	Unusual Temperature Increase	V58T0841A	
QBAR = >52.5 psf (~0.36 psi); Mach 19.8					------ 32:13:58:00 ------	EI + 831 sec; WLE Stagnation Temp: ~2800 F		
20	13:58:03				Start of sharp aileron trim increase	GMT is approximate (+/- 10 sec)	V60H1500C	
20.3	13:58:04	EI+835	X		Left fuselage side surface temp BP3605T starts off-nominal temperature increase		V07T9253A E1007.7 Y105 Z354.5	
20.5	13:58:04 / 58:19	EI+835 / EI+850			Increase in off-nominal aero increments.	Substantial increase in rate of change of rolling and yawing moment increments and initial indication of off-nominal pitching moment increment. Derived by analysis.	n/a	
21	deleted							
22	deleted							
22.5	13:58:16	EI+847			LMG Brake Line Temp D - Temp rise rate change	Significant increase in temp rise rate.	V58T1703A	
23	13:58:32 / 58:54	EI+863 / EI+883			MLG LH Inbd / Outbd Tire Pressures (4) - Decay to OSL		V51P0570A V51P0571A	V51P0573A V51P0572A
24	deleted							
25	13:58:39 / 58:48	EI+870 / EI+878			MLG LH Inbd/Outbd Wheel Temps (2) - OSL		V51T0574A	V51T0575A
25.5	13:58:40	EI+871			BFS Fault Msg (4) - Tire Pressures - 1st Message			
26	13:58:56	EI+887			BFS Fault Msg (4) - Tire Pressures - Last Message			

A.2-1
Integ Time Line Team - REV 19 BASELINE

Appendix A.2 - STS-107 Mishap Investigation - Master Time Line

6/5/2003 1 PM

Note: Rev 19 BASELINE updates Rev 18 with the eastern most debris events (over Texas) and is the timeline used for the Final Report

Seq No.	Sum No.	OEX Data	GMT GMT Day 32	EI secs	Milestone	Entry Event	Remarks	MSID / ID	
1	1	--	13:10:39	EI-2010	TIG-5	APU 2 Start - Low Press			
2	2	--	13:15:30	EI-1719	TIG	OMS TIG			
3	3	--	13:18:08	EI-1561		OMS End of Burn			
4	--	--	13:26:09	EI-1080		FRCS Dump Start			
5	--	--	13:27:12	EI-1017		FRCS Dump Complete			
6	4	--	13:31:25	EI-764	EI-13	APU 1 Start - Low Press			
7	5	--	13:31:29	EI-760		APU 3 Start - Low Press			
8	--	--	13:31:57	EI-732		APU 1 Norm Press			
9	--	--	13:31:59	EI-730		APU 2 Norm Press			
10	--	--	13:32:01	EI-728		APU 3 Norm Press			
11	--	--	13:32:29	EI-700		SSME Engine Stow sequence start	Sequence was completed with closure of TVC iso Vlv 1 at 13:33:30 GMT.		
12	--	--	13:39:09	EI-300	EI-5	Entry Interface minus 5 minutes (304 PRO)	Aeroject DAP (entry FCS) and Entry Guidance are activated upon transition to OPS 304. Entry Guidance provides open-loop attitude commands (angle of attach = 40 deg, roll = 0 deg) to the entry FCS until sufficient drag is available to begin closed-loop guidance operations.	V60Q8001C	
13	--	--	13:39:11	EI-298		Speedbrake close & Rudder cmded to zero	The speedbrake is not used until below Mach 10.0, and the rudder until below Mach 5.0.		
13.5	5.5	X	13:39:28.559	EI-280.4		Start of OEX PCM Data Block			
14	6	--	13:44:09	EI+0	EI	Entry Interface (400,000 Ft)	Historical reference point to reflect initiation of atmospheric flight (Mach 24.6)		
15	--	--	deleted				Rationale for deletion: currently there is no relevant aero event at qbar=0.5 psf so not required for this timeline		
15.5	6.1	X	13:45:39 / 48:59	EI+ 90 / EI+290		16 Temperature Sensors on the lower surface to the left of or at the centerline experience off-nominal early temperature trends (warmer temperature rise rate compared to previous flights of OV-102 at the same inclination)		V09T9849A V07T9666A V07T9468A V07T9470A V07T9711A V07T9713A	V07T9784A V07T9786A V07T9787A V07T9788A V07T9789A V07T9480A
						V09T9849A-OB Elevon Gap LWR Surface Edge Temp V07T9666A-Wing Lower Surface TC BP2510T V07T9468A-Fuselage Lower Surface TC BP1300T V07T9470A-Fuselage Lower Surface TC BP1301T V07T9711A-Wing Lower Surface TC BP2667T V07T9713A-Wing Lower Surface TC BP2876T	X1429.1 Y-315.3 ZLWR X1121.1 Y-235.5 ZLWR X618 Y0 ZLWR X620 Y-51 ZLWR X1262.0 Y-369.3 ZLWR X1402.0 Y-375.3 ZLWR	V07T9785A V09T9231A	V09T9845A V07T9489A
						V07T9785A-LH Outboard Lwr Elevon Fwd Surface V09T9231A-Outboard Elevon, Mid Gap, Fwd Temp V07T9784A-LH LWR AFT Fuselage Surface Temp V07T9786A-Fuselage Pen Region TC BP3074-1 T V07T9787A-Aft Fuselage Lower Aft Surface Temp V07T9788A-Body Flap LH Lwr Outboard Fwd Temp	X1396.1 Y-372.2 ZLWR X1430.1 Y-316 ZLWR X1442.0 Y-117.0 ZLWR X1387.0 Y-229.0 ZLWR X1513 Y-113 ZLWR X1530.0 Y-119.4 ZLWR		
						V07T9478A-Fuselage Lower Surface TC BP1600T V07T9480A-Fuselage Lower Surface TC BP1602TR V09T9845A-Outboard Elevon, Mid Gap, FWD Temp V07T9489A-Fuselage LWR Surface TC BP1900T	X1003.8 Y0.0 ZLWR X1004.1 Y-99.8 ZLWR X1430.4 Y-316 ZLWR X1391.5 Y0.0 ZLWR		

A.1-6
Integ Time Line Team - REV 19 BASELINE

Appendix A.1 - STS-107 Mishap Investigation - Summary Time Line

6/5/2003 1 PM

Note: Rev 19 BASELINE updates Rev 18 with the eastern most debris events (over Texas) and is the timeline used for the Final Report

Sum No.	GMT GMT Day 32	EI sec	OEX data	Milestone	Entry Event	Remarks	MSID	
QBAR = ~83.5 psf (~0.44 psi); Mach 18.7					------ 32:13:59:00 ------	EI + 891 sec; WLE Stagnation Temp: ~2800 F		
27	13:59:06				Left Main Gear Downlocked Indication - Transferred ON		V51X0125E	
27.3	13:59:09 / 59:39	EI+900 / EI+931	X		Several left side temperature measurements show a rapid increase in temperature followed by erratic behavior and subsequent loss of the measurements at approximately EI+940		V07T9925A V07T9972A V07T9979A V07T9903A V07T9913A	V07T9976A V07T9978A V07T9922A V07T9923A
27.5	13:59:23	EI+914			Loss of MCC real-time data to the workstations in the FCR and MER			
27.7	13:59:26 / 59:28	EI+917 / EI+919			Abrupt increase in off-nominal aero increments.	Abrupt increase in rate of change of pitching, rolling, and yawing increments. Magnitude of aero increments starting to exceed ability of aileron to laterally trim the vehicle. Derived by analysis.	n/a	
28	13:59:30.66 / 59:30.68	EI+921.66 / EI+921.68			Start of two yaw jets firing (R2R and R3R)	Fired continuously until end of data at 13:59:37.4	V79X2634X	V79K2638X
29	13:59:31	EI+922			Observed elevon deflections at LOS	Left: -8.11 deg (up) Right: -1.15 deg (up)		
29.3	13:59:31.4 / 59:34.5	EI+922.4 / EI+925.5			Several events and PASS and BFS FSM messages during this time period all indicate the failure signature of ASA 4	ASA responded appropriately. However, signature is indicative of failure of ASA 4.	V57H0283A (5 Hz)	
29.5	13:59:32	EI+923			Observed aileron trim at LOS	-2.3 degrees		
30	deleted							
31	deleted							
32	deleted							
32.5	13:59:32	EI+923		Approx Veh Grd Location:	Altitude ~200700 ft / Mach ~18.1 - Near Dallas TX	Approximate Vehicle Ground Location at Loss of Signal based on GMT; Data source: STS-107 GPS Trajectory Data	n/a	
33	13:59:32.136	EI+923.136		32.9 N / -99.0 W LOS	Last valid downlink frame accepted by ODRC - OI / BFS / PASS. Start of reconstructed data.	Nominal loss of comm at this GMT (for ~15 sec max based on previous flt data)		
34	deleted							
35	13:59:35.56	EI+926 / EI+927			Sideslip on vehicle changes sign.	The event occurred between the two times listed. Aerodynamic forces due to sideslip are now reinforcing aerodynamic asymmetry.	n/a	
36	13:59:36	EI+927			Growth in Bank attitude error	Up until this time the flight control had been able to maintain the Bank error around 5 deg.		
37	13:59:36.8	EI+ 927.8			Aerojet DAP Requests Third Right Yaw RCS Jet (R4R)	This additional jet is required to counteract the increasing aerodynamic moments on the vehicle. Fired continuously until end of data at 13:59:37.4		
38	13:59:37.3	EI+ 928.3			Aerojet DAP Requests Fourth Right Yaw RCS Jet (R1R)	This additional jet is required to counteract the increasing aerodynamic moments on the vehicle. Fired continuously until end of data at 13:59:37.4		
39	13:59:37.n	EI+ 928.n			Last aileron data	The aileron position is now approx -5.2 deg with approx -2.5 deg of aileron trim. The rate of change of aileron trim had reached the maximum allowed by the flight control system.		
40	13:59:37.396	EI+928.396		End of 5-second period of reconstructed data	End of first 5-seconds of the 32-second period of post-LOS data. Start of approximately 25 seconds of no data available	GMT derived by MER data personnel	n/a	
40.5	13:59:39 / 14:00:19	EI+930 / EI+970	X		Beginning at EI+930 and continuing until the loss of sync on OEX data (EI+964.4 for PCM and EI+970.4 for FDM), essentially all of the OEX data for the entire vehicle becomes erratic and fails			
40.7	13:59:46 / 48	EI+937 / EI+939			Debris A observed leaving the Orbiter - Large debris seen falling away from the Orbiter envelope.	EOC videos # EOC2-4-0018, -0024, -0209-B, -0221-3 and -0221-4		
41	13:59:46.347 / 14:00:01.900*	EI+937.347 / EI+952.900			PASS Fault Message annunciation - ROLL REF PASS Fault Message annunciation - L RCS LEAK BFS Fault Message annunciations - L RCS LEAK (2)	*Time info corrupted on some of the events.		
41.5	14:00:01 / 04	EI+952 / EI+955			Debris B and C observed leaving the Orbiter	EOC video EOC2-4-0024 (for both B and C)		

A.2-4

Integ Time Line Team - REV 19 BASELINE — **Appendix A.2 - STS-107 Mishap Investigation - Master Time Line** — **6/5/2003 1 PM**

Note: Rev 19 BASELINE updates Rev 18 with the eastern most debris events (over Texas) and is the timeline used for the Final Report

Seq No.	Sum No.	OEX Data	GMT GMT Day 32	EI secs	Milestone	Entry Event	Remarks	MSID / ID
22.2	7.37	X	13:51:49	EI+460		OMS-L Pod HRSI Surf T3-AFT - Start of off-nominal higher-than-expected temperature trend when compared to previous flights of same inclination	Sensor sees a sharp temp increase at EI+910 and goes erratic at EI+940	V07T9223A X1437.2 Y-126 Z422
QBAR = ~22 psf (~0.15 psi); Mach 23.7			------ 32:13:52.00 ------					EI + 471 sec; WLE Stagnation Temp: ~2700 F
22.5		--	deleted				Rationale for Deletion: Moved to seq #26.3 (Accounted for wind effects in the aero increment derivation process).	
22.6	7.45	--	13:52:09 / 15	EI+480 / EI+486		Unexpected Return link comm drop-out (Event 6)	On upper left aft antenna (TDRS 171W). S Band comm drop-out considered out-of-family based on previous flt data (same remarks as seq # 20.3 above).	
22.8	7.46	X	13:52:09 / 49	EI+480 / EI+520		Nose Cap RCC Attach OutBoard Clevis (Chin Panel) - Temporary change in slope, then returns to "nominal" Note: Adjacent sensor V09T9888 (on centerline) does not show this signature		V09T9889A X283.2 Y-2.3 0 LWR
23			deleted					
23.3	--	--	13:52:15	EI+486	2nd Entry Heating Indication Noted in OI Telemetry	Nominal Rise in Center Line Bond Temps (2) due to Entry Heating	Mid Fus Lower "Mid" Skin Temp Mid Fus Bottom Center Bond Line Temp X1214	V34T1110A V34T1112A
23.35	7.47	X	13:52:16	EI+487		Two Left Wing and 1 Right Wing Surface Pressure measurements show signs of failure V07P8038A - L Wing Upper Surface Press (WB 3 to LE) V07P8086A - L Wing Lower Surface Press (WB 3) V07P8151A - R Wing Lower Surface Press	First OEX data to show signs of failure	V07P8038A V07P8086A V07P8151A
23.4	7.48	X	13:52:16 / 53:17	EI+487 / EI+522		All of the active measurements (does not include PCM 3 data in snapshot mode) running in ~~the~~ wire bundles along the left wing leading edge show signs of failure - 18 measurements	Note: Pressure measurement V07P8038A noted in seq 23.35 is included in this grouping	V07P8010A V07P8058A V07P8022A V07P8071A V07P8023A V07P8072A V07P8024A V07P8073A V07P8025A V07P8074A V07P8026A V09T9895A V07P8037A V09T9910A V07P8038A V07T9666A V07P8044A V12G9921A
23.45	7.49	X	13:52:16 / 56:24	EI+487 / EI+735		The vast majority of left wing OEX measurements show signs of failure during this time period - this includes all left wing temperature and pressure measurements and all strain measurements aft of Xo 1040 with the exception of three strain measurements on the upper surface of the LMLG compartment Additionally, 30 right wing pressure measurements show signs of failure	Note: The pressure measurements noted in seq 23.35 are included in this grouping	Multiple measurements
23.5	7.5	--	13:52:17	EI+488	Approx Vehicle Ground Location: 39.0 N / -129.2 W	Altitude 236,800 ft / Mach 23.6 - Over the Pacific Ocean, approx 300 miles West of California Coastline	Approx vehicle position when first off-nominal data was seen; Data source: STS-107 GPS Trajectory Data	

A.2-2

Integ Time Line Team - REV 19 BASELINE — **Appendix A.2 - STS-107 Mishap Investigation - Master Time Line** — **6/5/2003 1 PM**

Note: Rev 19 BASELINE updates Rev 18 with the eastern most debris events (over Texas) and is the timeline used for the Final Report

Seq No.	Sum No.	OEX Data	GMT GMT Day 32	EI secs	Milestone	Entry Event	Remarks	MSID / ID
16	--	--	13:47:52	EI+223	Qbar 2.0 psf	Elevon, BF active	The elevons (elevator and aileron) and body flap are first used for vehicle attitude control. Although the body flap is active at this time, actual motion does not occur until 4-seconds later due to time delays and hysteresis in the forward command path.	
16.3	6.15	X	13:48:39	EI+270		Left Wing Front Spar at RCC Panel 9 - Initiation of off-nominal trend in strain (small increase) followed by a more significant off-nominal signature to failure at EI+495 secs	The measurement began to fail at approximately EI+495 sec	V12G9921A X1106.0 Y-223.0 ZMID
16.6	6.2	X	13:48:59	EI+290		Left Wing RCC Panel 9 Lower Attach Clevis (between RCC 9 and 10) - initiation of an off-nominal temperature trend (early temperature increase compared to previous flights of same indination)	The measurement began to fail at approximately EI+492 sec	V09T9910A X11 12.0 Y-223.0 Z289.0
17	--	--	deleted					
17.5	--	--	13:49:07	EI+298	ISLECT = 2	Closed-Loop Guidance	Entry guidance initiates closed-loop roll commands to converge drag to the reference drag profile.	
17.7	--		deleted				Rationale for deletion: After further review of the data, it was concluded that this event was not off-nominal	
18	--	--	13:49:16	EI+307	Qbar 10 psf	Roll Jets Deactivated	Roll control is achieved solely through aileron and yaw jet commands from this point forward.	
19			deleted					
20	6.3	--	13:49:32	EI+323		Initial Roll	Entry guidance determines that a non-zero roll is required to achieve the targeted drag level. (Mach 24.5)	V90H1044C
20.1	6.4	X	~13:49:39*	~EI+330*		Left Wing Front Spar Caps Strain Gage shows early off nominal downward trend	*Note: PCM3 entry data is in snapshot format (not continuous). Time indicated is at start of data segment where off-nominal signature is first observed, therefore event may have started earlier than noted.	V12G9169A X1107 Y232 Z7
20.2	6.45	X	13:49:49 / 59	EI+340 / EI+350		4 Left OMS Pod Surface temps - Start of off-nominal temperature trend - cooler rise rate when compared to previous flights of same indination V07T9976A-Left OMS Pod TC BP0731T V07T9220A- OMS-L Pod LRSI Surface Temp-FWD V07T9978A- OMS-L Pod Thermocouple BP0732T V07T9972A-Left OMS Pod TC BP0749T	Followed by the start of a warmer-than-expected temperature trend beginning in the EI+510 to EI+540 sec range (seq 24.96) X1342.5 Y-128.5 Z462.6 X1321.0 YLH Z464.0 X1359.6 Y-135.1 Z463.1 X1324 Y-98 Z488	V07T9976A V07T9978A V07T9220A V07T9972A

A.2-5

Integ Time Line Team - REV 19 BASELINE — **Appendix A.2 - STS-107 Mishap Investigation - Master Time Line** — **6/5/2003 1 PM**

Note: Rev 19 BASELINE updates Rev 18 with the eastern most debris events (over Texas) and is the timeline used for the Final Report

Seq No.	Sum No.	OEX Data	GMT GMT Day 32	EI secs	Milestone	Entry Event	Remarks	MSID / ID
24	7.7	--	13:52:17	EI+488		LMG Brake Line Temp D - On wheel well inbd sidewall (aft of sw vlvs) - Small increase in temperature ("bit flip up")	Initiation of temp rise ("bit flip up") - may be nominal based on rise rate comparison with flight experience (similar temp response has been observed at this time frame on a small percentage of flights). Reference seq # 54.5 for next V58T1703A event.	V58T1703A
24.1	7.75	X	13:52:18	EI+489		Left Wing Spar Cap Lwr L103 (Xo 1040 Spar - Lower Cap) - off-nominal increase in strain indication followed by gradual decrease over approx 330 seconds interval until measurement failure at approximately EI+935		V12G9048A
24.12	--	X	13:52:21 / 24.8	EI+492 / EI+495.8		2 Left Wing temperature sensors begin an off-nominal response that appears to be an indication of the measurements (sensors/wiring) failing: V09T9910A - Wing LE 55 LWR attach clevis RCC10 V07T9666A - Wing LWR SURF TC	These measurements are included in the grouping of the event noted in seq 2.3.45 - all left wing temperature sensor failures are shown on the timeline X1112.0 Y-239.0 Z289.0 WB-Run 1 X1121.1 Y-235.5 ZLWR WB-Run 1	
24.14	--	X	13:52:22	EI+493		Unusual Upward Shift (in one sample) of 3 Thermocouples and Downward Shift (in one sample) of 2 Thermocouples Upward Shift: V07T9480A - Fuslg LWR Surf TC BP1602TR V07T9489A - Fuslg LWR Surf TC BP1900T V07T9492A - Fuslg LWR Surf TC BP1602TR Downward Shift: V07T9522A - Fuslg Aft Penetration Area TC BP3325T V07T9636A - Left Wing upper surface TC BP4860T	All sensors receive a common 5 V power excitation via Channel 89 of PCM MUX 1	V07T9480A X1094.1 Y-99.8 ZLWR V07T9489A X1391.5 Y0.0 ZLWR V07T9492A X1511.1 Y1.3 ZLWR	V07T9522A X849.3 Y-105.0 Z814.8 V07T9636A X1357.9 Y-398.0 ZUPR
24.16	7.77	X	13:52:24	EI+495		Left Wing Front Spar at RCC Panel 9 - strain gage goes erratic for approximatly 20 second - measurement appears to be failing	Subsequent data is suspect	V12G9921A X1106.0 Y-223.0 ZMID
24.18	7.8	X	13:52:25	EI+496		Left Outboard Elevon Wide Band Accelerometer - off-nominal vibration response (approximately 2G peak-to-peak) V08D9729A - L OB Elevon Z-Vib (MUX1B Ch 2)		V08D9729A
24.2	--	X	13:52:29	EI+500		Approx 10% of right wing strain gages shows small off-nominal data trend (flattening of signal followed by normal data increase or de increase in strain alone)		Multiple measurements
24.22	--	X	13:52:29	EI+500		Left Wing Lower Surface Thermocouple BP2570T - Start of approx 80 deg F drop in temperature over 20 seconds		V07T9674A X1353.1 Y-231.4 ZLWR
24.24	7.85	X	13:52:29	EI+500		OMS-L Pod HRSI Surf T1-AFT - Start of slightly off-nominal erratic trend when compared to previous flights of same inclination	Followed by drop in temperature at EI + 570 seconds and subsequent erratic temperature changes	V07T9219A X1501.1 Y-126.0 Z422.0

A.2-3

Integ Time Line Team - REV 19 BASELINE — **Appendix A.2 - STS-107 Mishap Investigation - Master Time Line** — **6/5/2003 1 PM**

Note: Rev 19 BASELINE updates Rev 18 with the eastern most debris events (over Texas) and is the timeline used for the Final Report

Seq No.	Sum No.	OEX Data	GMT GMT Day 32	EI secs	Milestone	Entry Event	Remarks	MSID / ID
QBAR = ~15 psf (~0.10 psi); Mach 24.4			------ 32:13:50.00 ------				EI + 391 sec; WLE Stagnation Temp: ~2520 F (STS-107 Nom EOM Design Pred	
20.3	6.5	--	13:50:00 / 43	EI+351 / EI+394		Five events of unexpected Return link comm drop-out. Event 1 - 13:50:00 (1 sec); Event 2 - 13:50:04 / 06; Event 3 - 13:50:16/22; Event 4 - 13:50:25/28; Event 5 - 13:50:42 (1 sec)	On upper left aft antenna (TDRS 171W). S Band comm drop-outs considered out-of-family based on comparison with previous 102 flight data at 39 degrees, into KSC, descending node and similar look angles to TDRS. Note: Observed Forward link (cmd link) dropout associated with events 3 and 4 (normal response due to switch to/from auxiliary oscillator instead of Fwd link frequency).	
20.35	6.7	X	13:50:09	EI+360		Left PLBD Surface TC BP3703T - Start of off-nominal temperature trend - cooler rise rate when compared to previous flights of same indination	Followed by large increase in temperature at EI + 570 seconds	V07T9925A X1138.5 YLH Z441.4
20.4	6.9	X	13:50:19	EI+370		Left Wing Lower Surface Thermocouple BP2510T begins off-nominal temp increase from ~ 2000 deg F to ~2200 deg F over approx 50 seconds followed by a momentary 100 deg F temperature spike	The measurement subsequently fails at approximately EI+496 sec	V07T9666A X11 21.1 Y-231.5 ZLWR
20.5	--	--	13:50:30	EI+381	1st Entry Heating Indication Noted in OI Telemetry	Nominal Rise in Center Line Bond Temp (1) due to Entry Heating	Aft fuselage center bottom bond line	V09T1702A
21	7	--	13:50:53	EI+404	Start of Peak Heating		Determined by analysis. The peak heating period represents the approximate time period during which the heating rate has flattened out at or near its maximum value.	
21.5			deleted				Rationale for deletion: The signatures of the STS-107 remote sensor events were very subtle. Upon further evaluation of the data, it was determined that the remote sensor signatures had been seen in previous flights and/or could be explained by in own events. The events are therefore not considered to be anomalous.	
QBAR = ~19 psf (~0.13 psi); Mach 24.1			------ 32:13:51.00 ------					EI + 411 sec; WLE Stagnation Temp: ~2650 F
21.7	7.2	X	13:51:14	EI+425		Left Wing Front Spar at RCC Panel 9 - start of off-nominal increasing temperature trend	Increasing trend continues until the measurement starts to fail at approximately EI+520 sec	V07T9895A X11 02.2 Y-239.0 Z-239.0
21.9	7.25	X	13:51:14	EI+425		Left Wing RCC Panel 9 Lower Attach Clevis (between RCC 9 and 10) - start of a more rapid off-nominal increasing temperature trend	Increases until the measurement starts to fail at approximately at EI + 492 secs (ref seq 16.6 for 1st off-nominal event and seq 24.12 for failure)	V09T9910A X11 12.0 Y-223.0 Z289.0
22		--	delete				Rationale for deletion: Moved to seq 31.3 (Due to wind effects, it is more appropriate to compare this parameter against previous flights for identification of off-nominal performance instead of simply referencing the point at which Beta goes and stays negative.)	

Note: Rev 19 BASELINE updates Rev 18 with the eastern most debris events (over Texas) and is the timeline used for the Final Report

Seq No.	Sum No.	OEX Data	GMT GMT Day 32	EI secs	Milestone	Entry Event	Remarks	MSID / ID
QBAR = ~25.5 psf (~0.18 psi); Mach 23.2			---------- 32:13:53:00 ----------				EI + 531 sec WLE Stagnation Temp: ~2800 F	
27.2		--	deleted				Rationale for deletion: This event moved merged with new sequence # 28.3 (Accounted for wind effects in aero increment derivation process).	
27.5	--	--	13:53:02	EI+533		Hyd Syst 1 LH INBD Elevon Actr Ret Ln Temp - start of off nominal trend	Temp trending down	V58T0157A
						Hyd Syst 3 LOE Ret LN Temp - start of off nominal trend	Temp trending down	V58T0394A
27.7	10.6	X	13:53:03	EI+534		Left Outboard Elevon Wide Band Accelerometer - onset of signal saturation indicating likely measurement failure (approximately 10G peak-to-peak - off-scale) V08D9729A - L OB Elevon Z-Vib (MUX1B Ch 2)		V08D9729A
28	11	--	13:53:10	EI+541		Hyd Syst 3 LOE Ret LN Temp - OSL	OSL was preceded by Nominal Temp rise	V58T0394A
29	11	--	13:53:11	EI+542		Hyd Syst 1LH INBD Elevon Actr Ret Ln Temp - OSL	OSL was preceded by Nominal Temp rise	V58T0157A
29.3			deleted				Rationale for deletion: alpha modulation time tag deleted - moved to seq #29.7	
29.5	11.2	--	13:53:26	EI+557	Approx Veh Grd Location: 36.7 N / -123.5 W	Altitude 231600 ft / Mach 23.0 - Crossing the California Coastline	Data source: STS-107 GPS Trajectory Data	
29.55	11.21	X	13:53:29	EI+560		Left Fuselage Side Surface Temp BP3605T - start of off-nominal increasing temperature trend from ~ 180 deg F to 400 deg F	Trend followed by temperature drop and rise (ref seq 36.2 for next event of this sensor)	V07T9253A X1018.7 Y-103 Z394.5
29.6	11.22	X	13:53:29	EI+560		Left PLBD Surface TC BP3603T - Start of slightly off-nominal erratic temperature trend when compared to previous flights of same indination		V07T9913A X1013.8 Y1.H Z441.3
29.63	11.23	X	13:53:29	EI+560		Left PLBD Surface TC BP3703T - start of off-nominal temperature rise, peaking at EI+625, followed by temperature drop and subsequent off-nominal higher-than-expected temperature signature		V07T9925A X1138.5 Y1.H Z441.4
29.66	11.24	X	13:53:29	EI+560		Left Fuselage Side Surface TC BP3604T - Start of slightly off-nominal erratic temperature trend when compared to previous flights of same indination		V07T9903A X1008 Y-105 Z398.4
29.7	11.25	--	13:53:31	EI+562	Alpha Modulation	Angle of attack (alpha) modulation active	Entry Guidance enables limited delta angle of attack commands from the reference angle of attack to promote improved convergence to the reference drag profile.	V90H0803C
30	11	--	13:53:31 / 53:34	EI+562 / EI+565		Hyd Syst 1 LOE Return Line Temp - OSL	OSL was preceded by Nom Temp rise plus data loss 3 sec's prior to event	V58T0193A
30.2	11.3	--	13:53:32 / 34	EI+563 / EI+565		Unexpected Return link comm drop-out (Comm event 10)	On upper left aft antennae (TDRS 171/W). S-Band comm drop-out considered out-of-family based on previous flt data (same remarks as seq # 20.3 above).	

Note: Rev 19 BASELINE updates Rev 18 with the eastern most debris events (over Texas) and is the timeline used for the Final Report

Seq No.	Sum No.	OEX Data	GMT GMT Day 32	EI secs	Milestone	Entry Event	Remarks	MSID / ID
24.26	7.9	X	13:52:31	EI+502		Left Outboard Elevon Wide Band Accelerometer - off-nominal vibration response (approximately 3G peak-to-peak) V08D9729A - L OB Elevon Z-Vib (MUX1B Ch 2)		V08D9729A
24.28	--	X	13:52:31.3 / 38.4	EI+502.3 / EI+509.4		5 Left Wing temperature sensors begin an off-nominal response that appears to be an indication of the measurements (sensors/wiring) failing:	These measurements are included in the grouping of the event noted in seq 23.45	V07T9786A V09T9860A V09T9893A V09T9231A V09T9894A
						V07T9786A - LH INBD LWR Elevon Fwd Surf V09T9893A - Wing Elevon Cove LWR Surf Temp V09T9894A - Wing Elevon Cove UPR Sur Temp V09T9860A - Elevon Cove Insul Surf 90 V09T9231A - Elevon LWR PLUG TEMP 1 (Surface)	X1387 Y-229 ZLWR WB-Run 3 X1383.8 Y-372.2 Z390.9 WB-Run 3 X1381.7 Y-372.2 Z393.9 WB-Run 3 X1379.4 Y-419.7 ZBOT WB-Run 1 X1443.5 Y-232.2 LWR WB-Run 1	
24.3	7.45	--	13:52:25 / 31	EI+496 / EI+502		Two events of unexpected Return link comm drop-out Event 7 - 13:52:25/26; Event 8 - 13:52:29/31	On upper left aft antenna (TDRS 171/W). S-Band comm drop-out considered out-of-family based on previous flt data (same remarks as seq # 20.3 above).	
24.5			deleted					
24.7			deleted					
24.8	8.5	--	13:52:32	EI+503		Supply H2O dump Nozzle temps A/B show temporary increase in temp rise rate (15 second duration of high rise rate).	High rise rate is bounded by data loss. Increase in rise rate not observed on previous flights. GMT shown indicates start of initial rise duration. Reference nce event seq no. 26.6 for termination of event.	V62T0440A V62T0439A
24.9	8.5	--	13:52:32	EI+503		Vacuum vent temp shows temporary increase in temp rise rate (23 second duration of high rise rate).	High rise rate is bounded by data loss. Increase in rise rate not observed on previous flights. GMT shown indicates start of initial rise duration. Reference event seq no. 26.65 for termination of event.	V62T0551A
24.93	8.6	X	13:52:34	EI+505		OMS-L Pod HRS1 Surf T2-AFT - Start of off-nominal lower-than-expected temperature trend (compared to previous flights of same inclination) until sensor sees a sharp temp increase at EI+910 and goes erratic at EI+940		V07T9222A X1496.9 Y-126 Z422.0
24.96	8.65	X	13:52:39 / 53:09	EI+510 / EI+540		4 Left OMS Pod Surface temps - Change in existing off-nominal temperature trend (following a cooler rise rate than expected, the temperature trend that is significantly warmer when compared to previous flights of same inclination)	Previous event seq 20.2	V07T9976A V07T9978A V07T9220A V07T9972A
						V07T9976A-Left OMS Pod TC BP0731T V07T9220A-OMS-L Pod LRSI Surface Temp-FWD V07T9978A-OMS-L Pod Thermocouple BP0732T V07T9972A-Left OMS Pod TC BP0749T	X1342.5 Y-128.5 Z462.6 X1321.0 YLH Z464.0 X1359.6 Y-135.1 Z463.1 X1324 Y-98 Z488	

Note: Rev 19 BASELINE updates Rev 18 with the eastern most debris events (over Texas) and is the timeline used for the Final Report

Seq No.	Sum No.	OEX Data	GMT GMT Day 32	EI secs	Milestone	Entry Event	Remarks	MSID / ID
30.3	--	--	13:53:34 / 55:57	EI+565 / EI+668	2nd Entry Heating Indication Noted in OI Telemetry	Nominal Rise in Center Line Bond Temps (3) due to Entry Heating	13:53:34 - V09T1016A (Mid Fus Bot Port BL T X 620); 13:54:00 - V09T1022A (Mid Fus Bot Port BL T X 777); 13:55:57 - V09T1624A (Fwd Fus Lwr Skin Bot CL T)	V09T1016A V09T1022A V09T1624A
30.5	--	--	13:53:34	EI+565		Hyd Sys 2 LIE Return Ln Temp - Start of Off Nominal Trend	Temp trending down	V58T0257A
31	11	--	13:53:36	EI+567		Hyd Sys 2 LIE Return Ln Temp - OSL		V58T0257A
31.25	11.35	X	13:53:37	EI+568		Xo 1040 Spar (MLG Forward Wall Spar) Strain Gage - Upper Cap - start of off-nominal increase in strain indication (over an approximate 115 second interval) followed by sudden decrease	Reference seq 41.2 for next event of this sensor	V12G9049A X1040 Y-135 ZUPR
31.3	11.37	--	13:53:38	EI+569		Inertial sideslip angle (Beta) exceeds flight history.	The steady state navigation derived sideslip angle becomes out-of-family as compared to previous flight data at this point in the trajectory.	V90H2249C
31.5			deleted					
31.7			deleted					
32			deleted					
32.05	11.4	X	13:53:44	EI+575		OMS-L Pod HRSI Surf T1-AFT - Start of off-nominal lower-than-expected temperature trend when compared to previous flights of same inclination	Sensor goes erratic at EI+940	V07T9219A X1507.1 Y-126.0 Z422.0
32.1	11.5	--	13:53:45 / 47	EI+576 / EI+578		Debris #1 - First report of debris observed leaving the Orbiter	Seen just aft of Orbiter envelope one second after a plasma anomaly which consisted of a noticeably luminescent section of the plasma trail. No evidence of RCS jet firings (ref Atlas data and plots).	EOC2-4-0064 EOC2-4-0056 EOC2-4-0201 Plasma anomaly: EOC2-4-0136
32.3	11.5	--	13:53:46 / 50	EI+577 / EI+581		Debris #2 - Second report of debris observed leaving the Orbiter	Seen just aft of Orbiter envelope. No evidence of RCS jet firings (ref Atlas data and plots).	EOC2-4-0064 EOC2-4-0056 EOC2-4-0201
32.5	--	--	13:53:46	EI+577		LMG Brake Line Temp A - On strut facing MLG door - Start of off nominal trend (temp rise rate change)	Temp rise rate change from 1.4 F/min to 5.5 F/min and increasing to LOS	V58T1700A
32.6	--	X	13:53:47.6	EI+578.6		1 temperature sensor begins an off-nominal response that appears to be an indication of the measurement (sensor/wiring) failing	This measurement is included in the grouping of the event noted in seq 23.45	V07T9674A
						V07T9674A - Wing LWR SURF TC	X1353.1 Y-236.4 ZLWR WB-Run 4	

Note: Rev 19 BASELINE updates Rev 18 with the eastern most debris events (over Texas) and is the timeline used for the Final Report

Seq No.	Sum No.	OEX Data	GMT GMT Day 32	EI secs	Milestone	Entry Event	Remarks	MSID / ID
25	8.7	--	13:52:41	EI+512		LMG Brake Line Temp A - On strut facing MLG door - start of off nominal trend	Initiation of temp rise - off nominal based on rise rate comparison with flight experience.	V58T1700A
25.5			deleted					
26	8.7	--	13:52:41	EI+512		Left Main Gear Brake Line Temp C - Start of off nominal trend	Unusual Temp Rise	V58T1702A
26.3	8.75	--	13:52:44 / 52:50	EI+515 / EI+521		First clear indication of off-nominal aero increments	Delta yawing moment coefficient indicates off-nominal trend at 13:52:44; delta rolling moment coefficient at 13:52:50. Derived by analysis.	n/a
26.5			deleted					
26.6	8.5	--	13:52:47	EI+518		Supply H2O dump Nozzle temps A/B return to typical rise rates.	High rise rate is bounded by data loss. GMT shown indicates end of initial rise duration. Temp took additional 48 seconds to return to nominal temp rise (53:35 GMT).	V62T0440A V62T0439A
26.63	7.45	--	13:52:49 / 55	EI+520 / EI+526		Unexpected Return link comm drop-out (Comm event 9)	On upper left aft antennae (TDRS 171/W). S-Band comm drop-out considered out-of-family based on previous flt data (same remarks as seq # 20.3 above).	
26.64	--	X	13:52:49.5 / 52:51.4	EI+520.5 / EI+522.4		2 Left Wing temperature sensors begin an off-nominal response that appears to be an indication of the measurements (sensors/wiring) failing:	These measurements are included in the grouping of the event noted in seq 23.45	V09T9895A V09T9849A
						V09T9895A - Wing Front Spar Panel 9 Temp V09T9849A - Outboard ELEVON, Lower Surface Edge	X1102.2 Y-239.0 Z-239.0 WB-Run 3 X1429.1 Y-315.3 ZLWR WB-Run 1	
26.65	8.5	--	13:52:55	EI+526		Vacuum vent temp returns to typical rise rate.	High rise rate is bounded by data loss. GMT shown indicates end of initial rise duration. Temp took additional 40 seconds to return to nominal temp rise (53:35 GMT).	V62T0551A
26.7	--	--	13:52:56	EI+527		Left INBD Elevon Lower Skin Temp - Start of off nominal trend	Temp trending down	V09T1006A
27	10		13:52:59	EI+530		Left INBD Elevon Lower Skin Temp - OSL		V09T1006A
27.1	--	X	13:52:59.4 / 53:07.4	EI+530.4 / EI+538.4		5 Left Wing temperature sensors begin an off-nominal response that appears to be an indication of the measurements (sensors/wiring) failing:	These measurements are included in the grouping of the event noted in seq 23.45	V07T9785A V09T9845A V07T9711A V07T9713A V07T9636A
						* V07T9785A - LH OTBD LWR Elevon Fwd Surf V07T9711A - Wing LWR SURF TC V07T9636A - Wing L Upper Surf Thermocouple V09T9845A - Outboard ELEVON, MID GAP, Fwd * V07T9713A - Wing LWR SURF TC	X1396.1 Y-372.2 ZLWR WB-Run 1 X1362.0 Y-369.3 ZLWR WB-Run 1 X1357.8 Y-358.0 ZUPR WB-Run 4 X1440.4 Y-316 ZLWR WB-Run 1 X1402.0 Y-375.3 ZLWR WB-Run 1	
						*Note: These measurements were observed off-nominal in the EI+48.5 / 488 period but it was inconclusive if the measurements were failing at that time		

A.2-12

Appendix A.2 - STS-107 Mishap Investigation - Master Time Line

Integ Time Line Team - REV 19 BASELINE — **6/5/2003 1 PM**

Note: Rev 19 BASELINE updates Rev 18 with the eastern most debris events (over Texas) and is the timeline used for the Final Report

Seq No.	Sum No.	OEX Data	GMT GMT Day 32	Ei secs	Milestone	Entry Event	Remarks	MSID / ID
40.02	15.35	–	13:55:21 / 25	Ei+672 / Ei+676		Debris #6 - Report of debris observed leaving the Orbiter.	Seen just aft of Orbiter envelope inside the aforementioned Debris Shower A. No evidence of RCS jet firings (ref Atlas data and plots).	Debris: EOC2-4-0030, 0098, & 0161
40.05	15.37	–	13:55:22 / 28	Ei+673 / Ei+679		Debris Shower A - Report of debris shower seen just aft of Orbiter envelope.	Seen just aft of Orbiter envelope. Over the course of these four seconds a luminescent section of plasma trail is observed which appears to contain a shower of indefinite particles and multiple, larger discrete debris that includes Debris 8, 9, and 10.	Saw debris: EOC2-4-0098, 0161, 0005, 0030 Saw shower: EOC2-4-0017, 0021, 0028
40.1			deleted				Rationale for deletion: moved to 40.02 after further review of the videos	
40.2	15.35	–	13:55:24 / 28	Ei+675 / Ei+679		Debris #9 - Report of debris observed leaving the Orbiter.	Seen just aft of Orbiter envelope inside the aforementioned Debris Shower A. No evidence of RCS jet firings (ref Atlas data and plots).	EOC2-4-0005, 0098
40.3	15.35	–	13:55:25 / 29	Ei+676 / Ei+680		Debris # 10 - Report of debris observed leaving the Orbiter	Seen well aft of Orbiter envelope inside the aforementioned Debris Shower A. No evidence of RCS jet firings (ref Atlas data and plots).	EOC2-4-0005
40.4			deleted				Rationale for deletion: The signatures of the STS-107 remote sensor events were very subtle. Upon further evaluation of the data, it was determined that the remote sensor signatures had been seen in previous flights and/or could be explained by known events. The events are therefore not considered to be anomalous.	
40.5	–	–	13:55:32	Ei+683	Approx Veh Grd Location: 37.4 N / -114.1 W	Altitude 223400 ft / Mach 21.8 - Crossing the Nevada / Utah State Line	Data source: STS-107 GPS Trajectory Data	
40.6	15.43	–	13:55:33 / 35	Ei+684 / Ei+686		Return link comm drop-out (Comm event 12)	First comm drop out after switched to upper right aft antennae (TDRS 171/W). While uncommon to have a drop out at this point, inconclusive if drop-out is off-nominal based on previous ft data.	
41			deleted					
41.2			deleted				Rationale for deletion: Moved to 41.55 after further review of the data	

A.2-13

Appendix A.2 - STS-107 Mishap Investigation - Master Time Line

Integ Time Line Team - REV 19 BASELINE — **6/5/2003 1 PM**

Note: Rev 19 BASELINE updates Rev 18 with the eastern most debris events (over Texas) and is the timeline used for the Final Report

Seq No.	Sum No.	OEX Data	GMT GMT Day 32	Ei secs	Milestone	Entry Event	Remarks	MSID / ID
41.5	15.45	–	13:55:35 / 39	Ei+686 / Ei+690		Debris #11 - Report of debris observed leaving the Orbiter	Appears at the head of a secondary parallel plasma trail well aft of Orbiter envelope. A second piece of debris is also seen in the secondary plasma trail. No evidence of RCS jet firings (ref Atlas data and plots).	EOC2-4-0050, EOC2-4-0098
41.55	15.46	X	13:55:36	Ei+687		Xo 1040 Spar (MLG Forward Wall Spar) Strain Gage - Upper Cap - sudden drop in strain followed by gradual increase until erratic signature at approximately Ei+930	Reference seq 31.25 for previous event of this sensor	V12G9049A X1040 Y-135 Z,RR
41.6	15.45	–	13:55:38 / 40	Ei+689 / Ei+691		Debris #11A - Report of debris observed leaving the Orbiter	Seen just aft of Orbiter envelope.	EOC2-4-0098
41.7	15.45	–	13:55:38 / 42	Ei+689 / Ei+693		Debris #11B - Report of debris observed leaving the Orbiter	Seen at head of a parallel plasma trail aft of the Orbiter envelope.	EOC2-4-0098
42	15.5	–	13:55:41	Ei+692		Mid Fus Port (Left) Sill Longn Temp at x1215 - start of off nominal trend	Unusually high temp rise with respect to STS-87 & 109. Went to 2.9 F/min from 0 F/min.	V34T1118A
42.2	15.45	–	13:55:42 / 46	Ei+693 / Ei+697		Debris #11C - Report of debris observed leaving the Orbiter	Seen at head of a parallel plasma trail well aft of the Orbiter envelope.	See debris & parallel trail: EOC-4-0098 See parallel plasma trail only: EOC2-4-0028, 0050
42.3	15.45	–	13:55:44 / 46	Ei+695 / Ei+697		Debris #12 - Report of debris observed leaving the Orbiter. Event was preceded and followed by secondary plasma trails.	Seen aft of Orbiter envelope. No evidence of RCS jet firings (ref Atlas data and plots).	EOC2-4-0028, 0050, 0098
42.5			deleted				Rationale for deletion: Moved to seq # 42.75 (misclocked in timeline based on GMT associated with event)	
42.7	15.45	–	13:55:54 / 58	Ei+705 / Ei+708		Debris #13 - Report of debris observed leaving the Orbiter. Event was followed by momentary brightening of plasma trail adjacent to debris.	Seen well aft of Orbiter envelope. No evidence of RCS jet firings (ref Atlas data and plots).	EOC2-4-0005, 0017, 0021, 0161
42.75	–	–	13:55:55	Ei+706	Approx Veh Grd Location: 37.0 N / -112.4 W	Altitude 222100 ft / Mach 21.5 - Crossing the Utah / Arizona State Line	Data source: STS-107 GPS Trajectory Data	
42.8	15.45	–	13:55:57 / 59	Ei+708 / Ei+710		Debris #14 - Very bright debris observed leaving the Orbiter.	Seen just aft of Orbiter envelope. Debris events 6 and 14 are visually the biggest, brightest events and therefore may indicate the most significant changes to the Orbiter of the western debris events.- No evidence of RCS jet firings (ref Atlas data and plots).	EOC2-4-0005, 0017, 0021, 0028, 0030

A.2-10

Appendix A.2 - STS-107 Mishap Investigation - Master Time Line

Integ Time Line Team - REV 19 BASELINE — **6/5/2003 1 PM**

Note: Rev 19 BASELINE updates Rev 18 with the eastern most debris events (over Texas) and is the timeline used for the Final Report

Seq No.	Sum No.	OEX Data	GMT GMT Day 32	Ei secs	Milestone	Entry Event	Remarks	MSID / ID
32.7	11.5	–	13:53:54 / 58	Ei+585 / Ei+589		Debris #3 - Third report of debris observed leaving the Orbiter. Event followed by momentary brightening of plasma trail.	Seen just aft of Orbiter envelope followed one second later by a plasma anomaly which consisted of a noticeably luminescent section of the plasma trail. No evidence of RCS jet firings (ref Atlas data and plots).	Debris: EOC2-4-0055, 0056 Plasma Anomaly: EOC2-4-0064, 0136
QBAR = ~29 psf (~0.20 psi); Mach 22.7			------- 32:13:54:00 -------					Ei = 591 sec; WLE Stagnation Temp: ~2850 F
32.8	11.5	–	13:54:00 / 04	Ei+591 / Ei+595		Debris #4 - Fourth report of debris observed leaving the Orbiter	Seen just aft of Orbiter envelope. No evidence of RCS jet firings (ref Atlas data and plots).	EOC2-4-0056 EOC2-4-0055
32.9	11.5	–	13:54:07 / 11	Ei+598 / Ei+602		Debris #5 - Fifth report of debris observed leaving the Orbiter	Seen just aft of Orbiter envelope at the head of a plasma anomaly. No evidence of RCS jet firings (ref Atlas data and plots).	EOC2-4-0056 EOC2-4-0055
33	13	–	13:54:10	Ei+601		LMG Brake Line Temp B - Start of off nominal trend	Temp Increase	V58T1701A
33.3	13.5	–	13:54:11	Ei+602		Reversal in growth trend of derived roll moment coefficient	Observed moment changed from a negative slope to positive slope. Derived by analysis.	n/a
33.5	11.3	–	13:54:14 / 22	Ei+605 / Ei+613		Unexpected Return link comm drop-out (Comm event 11)	On upper left aft antennae (TDRS 171/W). S-Band comm drop-out considered out-of-family based on previous ft data (same remarks as seq # 20.3 above).	
34	14	–	13:54:20	Ei+611		Start of slow aileron trim change	The aileron trim setting observed in flight first deviates from the predicted trim setting at this point in the trajectory, indicating that flight control is reacting to asymmetric aerodynamic conditions that are varying over time. (GMT is approximate (13:54:20 +/- 10 seconds))	V90H1500C
34.5			deleted				Rationale for deletion: Moved to seq #33.3, time tag updated	
35	15	–	13:54:22	Ei+613		M-FUS LT BL Temp at x1215 - start of off nominal trend (increased rise rate)	Unusual Temp Rise (Rise rate higher than STS-109 & 87). Rise rate increased from 1 F/min (typical) to 7.5 F/min.	V34T1106A
35.2	15	–	13:54:22	Ei+613		LH Aft Fus Sidewall Temp at x1410 - start of off nominal trend (increased rise rate)	Unusual Temp Rise (Rise rate higher than STS-109 & 87). Rise rate increased from 2.7 F/min (typical) to 5.4 F/min.	V09T1724A
35.5	13	–	13:54:24	Ei+615		Sys 3 Left Main Gear Strut Actuator Temp - start of off nominal trend	Unusual Temp Rise	V58T0405A
35.7	–	–	13:54:25	Ei+616	Approx Veh Grd Location: 38.3 N / -119.0 W	Altitude 227400 ft / Mach 22.5 - Crossing the California / Nevada State Line	Data source: STS-107 GPS Trajectory Data	
35.8	–	–	13:54:26	Ei+617		S-Band switched from upper left aft antennae to upper right aft antenna.	TDRS 171/W	

A.2-11

Appendix A.2 - STS-107 Mishap Investigation - Master Time Line

Integ Time Line Team - REV 19 BASELINE — **6/5/2003 1 PM**

Note: Rev 19 BASELINE updates Rev 18 with the eastern most debris events (over Texas) and is the timeline used for the Final Report

Seq No.	Sum No.	OEX Data	GMT GMT Day 32	Ei secs	Milestone	Entry Event	Remarks	MSID / ID
36			deleted					
36.2	15.2	X	13:54:29	Ei+620		Left Fuselage Side Surface temp BP3605T peaks and starts downward trend	Ref seq 29.55 for previous event of this sensor and seq 54.1 for next event of this sensor	V07T9253A X1000.7 Y-105 Z364.5
36.5	15.3	–	13:54:33.3 / 33.9	Ei+624.3 / Ei+624.9		Flash #1 - Orbiter envelope suddenly brightened (duration 0.3 sec) leaving noticeably luminescent signature in plasma trail	Note: R3R and R2R 0.24 sec jet firings occurred at 13:54:33.52 / 33.76 and 13:54:33.54 / 33.78 respectively (ref: RCS Atlas analysis and plots).	EOC2-4-0055 EOC2-4-0034 EOC2-4-0009B EOC2-4-0066 EOC2-4-0070
36.55	15.32	X	13:54:34	Ei+625		Left Fuselage Side Surface temp BP3703T peaks and starts downward trend	Ref seq 29.63 for previous event of this sensor and seq 70.1 for next event of this sensor	V07T9925A X1138.5 Y,LH Z441.5
36.6	15.3	–	13:54:35 / 37	Ei+626 / Ei+628		Debris #6 - Very bright debris seen leaving the Orbiter	Seen just aft of Orbiter envelope. Also, reference RCS jet firing note in item # 36.5 above. Debris events 6 and 14 are visually the biggest, brightest events and therefore may indicate the most significant changes to the Orbiter of the western debris events.	EOC2-4-0055 EOC2-4-0034 EOC2-4-0009B EOC2-4-0066 EOC2-4-0070
36.7	15.33	X	13:54:39	~Ei+630		Strain Gages Centered on the Upper Surface of the Left MLG Wheel Wheel - Higher-than-expected strain indications observed in these gages	Note: PCM3 entry data is in snapshot format (not continuous), therefore event may have occurred earlier than noted	V12G9156A, V12G9157A, V12G9158A
36.8	15.34	X	13:54:39	~Ei+630		Left Wing X1040 Spar Web - shows increase in strain	Note: Adjacent sensor V12G9165A did not show similar "off-nominal" signature at this time, also, PCM3 entry data is in snapshot format (not continuous), therefore event may have occurred earlier than noted	V12G9166A V12G9167A V12G9165A-nominal)
37			deleted					
37.5			deleted					
37.7	~	–	13:54:53	Ei+644		MLG LH Outbd Wheel Temp - start of off nominal trend	2 bit flips up (ref #56.5 when temp starts to trend down)	V51T0574A
QBAR = ~34.5 psf (~0.24 psi); Mach 22.1			------- 32:13:55:00 -------					Ei = 651 sec; WLE Stagnation Temp: ~2900 F
37.75	15.35	–	13:55:04 / 06	Ei+655 / Ei+657		Debris #7 - Seventh report of debris observed leaving the Orbiter	Seen just aft of Orbiter envelope. No evidence of RCS jet firings (ref Atlas data and plots).	EOC2-4-0030
37.8	13	–	13:55:12	Ei+663		Sys 3 LMG Brake Sw Vlv Ret Line Temp (FWD) - start of off nominal trend	Temp Increase	V58T0842A
37.9	15.35	–	13:55:17 / 19	Ei+668 / Ei+670		Debris #7A - Report of debris observed leaving the Orbiter	Seen just aft of Orbiter envelope	EOC2-4-0161
38			deleted					
39			deleted					
40	–	–	13:55:21	Ei+672	Drag 11 ft/sec^2	Drag Measurement Incorporation	Incorporation of drag-derived altitude into the vehicle navigation state.	

Note: Rev 19 BASELINE updates Rev 18 with the eastern most debris events (over Texas) and is the timeline used for the Final Report

Seq No.	Sum No.	OEX Data	GMT GMT Day 32	Ei secs	Milestone	Entry Event	Remarks	MSID / ID
53.5	16.8	--	13:57:53.5 / 55.5	Ei+824.5 / Ei+826.5		Flare 1: Assymmetrical brightening of Orbiter shape observed. (Occurred over eastern AZ and NM.)	Observations by personnel from the Starfire Optical Range (Kirtland Air Force Base, NM). Note: nearest jet firings: Same as seq no. 49.55 plus L2L at 032:13:58:00.50 / 01.46 & L3L at 032:13:58:00.48 / 01.44 (in both cases there was no start up data, but good tail-offs/shutdown) - 0.96 sec pulse each. Also, R2R at 032:13:58:03.18 / 09.16 & R3R at 032:13:58:03.18 / 09.16 - (in both cases firings occurred during data dropouts and were determined by injector temps). (Ref Atlas analysis and plots.)	EOC2-4-0148-4
53.7	16.8	--	13:57:59.5 / 58:01.5	Ei+830.5 / Ei+832.5		Flare 2: Assymmetrical brightening of Orbiter shape observed. (Occurred over eastern AZ and NM.)	Observations by personnel from the Starfire Optical Range (Kirtland Air Force Base, NM). Note: same jet firing information as for event seq no.s 49.55 & 53.5. (Ref Atlas analysis and plots.)	EOC2-4-0148-4
QBAR = ~52.5 psf (~0.36 psi); Mach 19.8				-------- 32:13:58:00 --------				Ei + 831 sec; WLE Stagnation Temp: ~2880 F
54	20	--	13:58:03	Ei+834		Start of "sharp" aileron trim increase	An abrupt increase in the rate of change in the aileron trim occurs near this time, indicating flight control is now compensating for increasingly asymmetric aero dynamics. This trend continues to LOS. (GMT is approximate (13:58:03+/-10 seconds).)	V60H1500C
54.1	20.3	X	13:58:04	Ei+835		Left fuselage side surface temp BP3605T starts off-nominal temperature increase	Ref seq 36.2 for previous event of this sensor	V07T9253A X1000.7 Y-1.05 Z354.5
54.3	20.5	--	13:58:04 / 58:19	Ei+835 / Ei+850		Increase in off-no minal aero increments.	Substantial increase in rate of change of rolling (13:58:04) and yawing (13:58:19) moment increments and initial indication of off-nominal pitching moment increment (13:58:05). Derived by analysis.	n/a
54.5 55	22.5	--	13:58:16 deleted	Ei+847		LMG Brake Line Temp D - Temp rise rate change	Temp rise rate change from 0.9 F /min to 11.7 F /min (stayed at this rate to LOS)	V58T1703A
55.5			13:58:20 deleted	Ei+851	Approx Veh Grd Location: 34.2 N / - 103.1 W	Altitude 209800 ft / Mach 19.5 - Crossing the New Mexico / Texas State Line	Data source: STS-107 GPS Trajectory Data	
57	23	--	13:58:32	Ei+863		MLG LH Outbd Tire Pressure 1 - pressure trending down (to OSL)	Trending to OSL following 7 sec LOS (initiation time not exact) - ref #60	V51P0570A
58	23	--	13:58:32	Ei+863		MLG LH Inbd Tire Pressure 1 - pressure trending down (to OSL)	Trending to OSL following 7 sec LOS (initiation time not exact) - ref #64	V51P0571A
58.5	--	--	13:58:32	Ei+863		MLG LH Outbd Wheel Temp - temperature trending down (to OSL)	Trending to OSL following 7 sec LOS (initiation time not exact) - ref #62	V51T0574A

Note: Rev 19 BASELINE updates Rev 18 with the eastern most debris events (over Texas) and is the timeline used for the Final Report

Seq No.	Sum No.	OEX Data	GMT GMT Day 32	Ei secs	Milestone	Entry Event	Remarks	MSID / ID
QBAR = ~40 psf (~0.28 psi); Mach 21.4				-------- 32:13:56:00 --------				Ei + 711 sec; WLE Stagnation Temp: ~2900 F
42.9	15.43	--	13:56:00 / 03	Ei+711 / Ei+714		Return link comm drop-out (Comm event 13)	On upper right aft antennae (TDRS 171/W). While uncommon to have a drop out at this point, inconclusive if drop-out is off-nominal based on previous flt data. Note: No further comm drop-out events are listed in the timeline thru LOS, since are not considered out-of-family at this time.	
43	--	--	13:56:02	Ei+713		Qbar 40 psf	Aft RCS Pitch Jets Deactivated	Pitch control is solely achieved through elevator and body flap commands from this point forward.	
44	16	--	13:56:03	Ei+714		Left Lower Wing Skin Temp - start of off nominal trend	Temp reading trending down (potential sensor/wire damage)	V09T1002A
44.2	15.45	--	13:56:08 / 12	Ei+719 / Ei+723		Debris #15 - Report of debris observed leaving the Orbiter.	Seen just aft of Orbiter envelope. Nearest jet firings: R2R jet firing at 032:13:56:17.30 / 56:17.54 for 0.24 seconds, & R3R jet firing at 032:13:56:17. 28 / 56:17.52 for 0.24 seconds. (Ref: RCS Atlas data analysis and plots.)	EOC2-4-0017
44.5	16.5	--	13:56:16	Ei+727		Hyd Sys 1 LMG UpLK Actr Unik Ln Temp - Temp rise rate change	Temp rise rate change from 0.7 F /min (nominal) to 3.9F/min and increasing to LOS	V58T0125A
44.6	16.5	--	13:56:17	Ei+728		Sys 3 LMG Brake Sw Vlv Ret Line Temp (FWD) - Temp rise rate change	Temp rise rate change from 1.5 F /min to 8.8 F /min (stayed at this rate to LOS)	V58T0842A
44.7	16.5	--	13:56:20	Ei+731		LMG Brake Line Temp C - Temp rise rate change	Temp rise rate change from 1.3 F /min to 9.9 F /min (stayed at this rate to LOS)	V58T1702A
44.8	16.5	--	13:56:22	Ei+733		LMG Brake Line Temp B - Temp rise rate change	Temp rise rate change from 2.1 F /min to 9.1 F /min increasing to LOS	V58T1701A
45	16	--	13:56:24	Ei+735		Left Upper Wing Skin Temp - start of off nominal trend	Temp reading trending down (potential sensor/wire damage)	V09T1024A
46	16.55	--	13:56:30	Ei+741		1st Roll Reversal Initiation	Entry guidance changes the sign of the roll command to redirect the vehicle back towards the center of the delta azimuth (heading error) corridor.	V90H1044C
46.5	--	--	13:56:45	Ei+756	Approx Veh Grd Location: 36.1 N / -109.0 W	Altitude 219000 ft / Mach 20.9 - Crossing the Arizona / New Mexico State Line	Data source: STS-107 GPS Trajectory Data	
46.7	16.5	--	13:56:53	Ei+764		Sys 3 Left Main Gear Strut Actuator Temp - Temp rise rate change	Temp rise rate change from 1.7 F /min to 12.9 F /min (stayed at this rate to LOS)	V58T0405A
47	16.55	--	13:56:55	Ei+766	Roll Reversal #1	1st Roll Reversal Complete	Actual roll achieves desired roll command.	V90H1044C

Note: Rev 19 BASELINE updates Rev 18 with the eastern most debris events (over Texas) and is the timeline used for the Final Report

Seq No.	Sum No.	OEX Data	GMT GMT Day 32	Ei secs	Milestone	Entry Event	Remarks	MSID / ID
58.7	--	--	13:58:32 / 59:22	Ei+863 / Ei+913		Sys 2 LH Brake Switching Vlv Return Temp (AFT) - temp rise rate change	Temp rise rate change from 2.5 F /min to 40.0 F /min until 13:59:22 (temp peak) - ref #70.5	V58T0841A
59	--	--	13:58:36	Ei+867		MLG LH Inbd Wheel Temp - start of temperature trending down (to OSL)	Start of trend to OSL - ref #66	V51T0575A
60 61	23	--	13:58:38 deleted	Ei+869		MLG LH Outbd Tire Pressure 1 - OSL	Rationale for deletion: Moved to seq no. 63.5 after further data review.	V51P0570A
62	25	--	13:58:39	Ei+870		MLG LH Outbd Wheel Temp - OSL		V51T0574A
63	23	--	13:58:39	Ei+870		MLG LH Outbd Tire Pressure 2 - start of pressure trending down (to OSL)	Start of trend to OSL - ref #68	V51P0572A
63.5	25.5	--	13:58:40	Ei+871		BFS Fault Msg (4) - Tire Pressures - First Message	32/13:58:39.94 - SM0 Tire P LOB 32/13:58:41.84 - SM0 Tire P LIB 32/13:58:49.54 - SM0 Tire P LIB 32/13:58:56.26 - SM0 Tire P LOB	
64	23	--	13:58:40	Ei+871		MLG LH Inbd Tire Pressure 1 - OSL		V51P0571A
65	--	--	13:58:41	Ei+872		MLG LH Inbd Tire Pressure 2 - start of off nominal trend	Press rose ~3.5 psia in 2 sec's	V51P0573A
65.5	23	--	13:58:43	Ei+874		MLG LH Inbd Tire Pressure 2 - start of pressure trending down		V51P0573A
66	25	--	13:58:48	Ei+879		MLG LH Inbd Wheel Temp - OSL		V51T0575A
67	23	--	13:58:48	Ei+879		MLG Inbd Tire Pressure 2 - OSL		V51P0573A
68	23	--	13:58:54	Ei+885		MLG LH Outbd Tire Pressure 2 - OSL		V51P0572A
69	26	--	13:58:56	Ei+887		BFS Fault Msg (4) - Tire Pressures - Last Message		
QBAR = ~63.5 psf (~0.44 psi); Mach 18.7				-------- 32:13:59:00 --------				Ei + 891 sec; WLE Stagnation Temp: ~2880 F
70	27	--	13:59:06	Ei+897		Left Main Gear Downlocked Indication - Transferred ON	Uplock indicated no change	V51X0125E
70.1	27.3	X	13:59:09 / 59:39	Ei+900 / Ei+930		Several left side temperature measurements show a rapid increase in temperature followed by erratic behavior and subsequent loss of the measurements at approximately Ei+940 V07T9925A - L Fus Side Surf TC BP7303T (on PLBD) V07T9972A - OMS-L Pod TC BP0749T V07T9976A - OMS-L Pod TC BP0731T V07T9903A - L Fus Side Surf TC BP3604T V07T9913A - L Fus Side Surf TC BP3603T (on PLBD) V07T9976A - OMS-L Pod Thermocouple BP0731T V07T9978A - OMS-L Pod Thermocouple BP0732T V07T9223A - OMS-L Pod HR S1 Surf T2-AFT V07T9223A - OMS-L Pod HR S1 Surf T3-AFT	V07T9925A V07T9976A X138.5 Y-1.4 Z441.4 X1342.5 Y-128.5 Z462.6 V07T9972A V07T9978A X1324 Y-98 Z468 X1359.6 Y-135.1 Z493.1 V07T9976A V07T9222A X1342.5 Y-128.5 Z462.6 X1466.6 Y-1.26 Z422.0 V07T9903A V07T9223A X1000 Y-105 Z398.4 X1437.2 Y-1.26 Z422.0 V07T9913A X1003.8 Y-1.4 Z441.3	
70.3	27.5	--	13:59:23	Ei+914		Loss of MCC real-time data to the workstations in the FCR and MER		
70.5	--	--	13:59:22	Ei+913		Sys 2 LH Brake Switching Vlv Return Temp (AFT) - start of sharp downward temperature trend	Temp trending down until loss of signal - ref #61	V58T0841A
70.7	27.7	--	13:59:26 / 59:28	Ei+917 / Ei+919		Abrupt increase in off-nominal aero increments.	Abrupt increase in rate of change of pitching (13:59:28), rolling (13:59:28) and yawing (13:59:26) increments. Magnitude of aero increments starting to exceed ability of aileron to laterally trim the vehicle. Derived by analysis.	n/a

Note: Rev 19 BASELINE updates Rev 18 with the eastern most debris events (over Texas) and is the timeline used for the Final Report

Seq No.	Sum No.	OEX Data	GMT GMT Day 32	Ei secs	Milestone	Entry Event	Remarks	MSID / ID
47.5 48			deleted deleted				Rationale for deletion: Comm drop-out (event 14) is deleted since probably nominal due to completion of roll reversal resulting in elevation angle nearing 60 degrees. Rationale for deletion: IMU Velocity increase reflects accelerations imparted during roll reversal. Same signature observed on STS-109. Nominal event.	
QBAR = ~42 psf (~0.29 psi); Mach 20.7				-------- 32:13:57:00 --------				Ei + 771 sec; WLE Stagnation Temp: ~2900 F
49 49.5	--	--	13:57:nn deleted			Body flap deflection up 3 degrees	Matches nominal aero simulation	V90H64 10C
49.51	16.65	X	13:57:09	Ei+780		Fuselage Side Surf Thermocpl BP3976T - start of off-nominal trend (temp increase followed by temp drop / rise)		V07T9270A X1486.1 Y-134.8 Z307.1
49.53	16.67	X	13:57:09	Ei+780		Fuselage Lower Surface BF Thermocpl BP220T - start of off-nominal trend (shallow temp drop)		V07T9508A X1160 Y-111.1 Z LWR
49.55	16.8	--	13:57:19 / 29	Ei+790 / Ei+800		Debris # 16 - Very faint debris observed leaving just aft of Orbiter. (Occurred over eastern AZ and NM.)	Observations by personnel from the Starfire Optical Range (Kirtland Air Force Base, NM). Note: nearest jet firings: L2L jet firing at 032:13:56:54.71 / 57:01.12 & 032:13:57:46.35 / 57:53.12 & L3L jet firing at 032:13:56:54.66 / 57:01.07 & 032:13:57:46.33 / 57:53.10 (all 4 occurred during data dropouts & were determined based on injector temps alone). Also, R2R at 032:13:57:43.94 / 57:44.42 & R3R at 032:13:57:43.92 / 57:44.4 0 for 0.48 secs ea. (Ref Atlas data analysis and plots.)	EOC2-4-0148-2
49.6	16.9	--	13:57:19	Ei+790		MLG LH Outbd Tire Pressure 1 - start of off nominal trend	Bit flip up - off nominal thru comparison with previous flights	V51P0570A
49.7	16.9	--	13:57:24	Ei+795		MLG LH Outbd Tire Pressure 2 - start of off nominal trend	Bit flip up - off nominal thru comparison with previous flights	V51P0572A
50 51	17	-- --	13:57:28 deleted	Ei+799		Left Lower Wing Skin Temp - OSL	Rationale for deletion: Originally indicated as "Start of Roll trim in elevons". Inserted independently early in the investigation, but is better defined by sequence no. 54. "Roll trim" is better indicated with aileron trim.	V09T1002A
52	17	--	13:57:43	Ei+814		Left Upper Wing Skin Temp - OSL		V09T1024A
53	19	--	13:57:54	Ei+825		Sys 2 LH Brake Switching Vlv Return Temp (AFT) - start of off nominal trend	Temp increase	V58T0841A

A.2-20

Appendix A.2 - STS-107 Mishap Investigation - Master Time Line

Integ Time Line Team - REV 19 BASELINE **6/5/2003 1 PM**

Note: Rev 19 BASELINE updates Rev 18 with the eastern most debris events (over Texas) and is the timeline used for the Final Report

Seq No.	Sum No.	OEX Data	GMT GMT Day 32	Ei secs	Milestone	Entry Event	Remarks	MSID / ID
91	36	--	13:59:36	EI+927		Growth in Bank attitude error	Up until this time the flight control had been able to maintain the Bank error around 5 deg. Aerojet DAP drops left wing to compensate for increasing aerodynamic moments, creating a bank attitude error.	
92	37	--	13:59:36.8	EI+927.8		Aerojet DAP Requests Third Right Yaw RCS Jet (R4R)	This additional jet is required to counteract the increasing aerodynamic moments on the vehicle. The RCS jet fired, as expected and stayed on to end of first 5-sec period of recon data at 032/13:59:37.4 GMT.	
93	38	--	13:59:37.3	EI+928.3		Aerojet DAP Requests Fourth Right Yaw RCS Jet (R1R)	This additional jet is required to counteract the increasing aerodynamic moments on the vehicle. The RCS jet fired, as expected and stayed on to end of first 5-sec period of recon data at 032/13:59:37.4 GMT.	
94	39		13:59:37.n	EI+928.n		Last aileron data	The aileron position is now approx -5.2 deg with approx -2.5 deg of aileron trim. The rate of change of aileron trim had reached the maximum allowed by the flight control system.	
95	40	--	13:59:37.396	EI+928.396	End of 5 second period of reconstructed data	End of first 5-seconds of the 32-second period of post-LOS data. Start of approximately 25 seconds of no data available	GMT derived by MER data personnel	
95.5	40.5	X	13:59:39 / 14:00.19	EI+930 / EI+970		Beginning at EI+930 and continuing until the loss of sync on OEX data (EI+964.4 for PCM and EI+970.4 for FDM), essentially all of the OEX data for the entire vehicle becomes erratic and fails		
95.8	40.7	--	13:59:46 / 4.8	EI+937 / EI+939		Debris A observed leaving the Orbiter - Large debris seen falling away from the Orbiter envelope.		EOC2-4-0018 EOC2-4-0024 EOC2-4-0209-B EOC2-4-0221-3 EOC2-4-0221-4
96	41	--	13:59:46.347	EI+937.347		PASS Fault Message annunciation - ROLL REF	Message retrieved from PASS "fault message buffer" received between 14:00:04 and 14:00:05. Data is potentially error prone. The ROLL REF message is triggered when Roll command req'd to fly reference profile falls below 37 degs. Message generation less than 10 secs (5 guidance cycles) after start of 4 yaw jets firing suggests unexpected reduction in Lift to Drag ratio.	

A.2-18

Appendix A.2 - STS-107 Mishap Investigation - Master Time Line

Integ Time Line Team - REV 19 BASELINE **6/5/2003 1 PM**

Note: Rev 19 BASELINE updates Rev 18 with the eastern most debris events (over Texas) and is the timeline used for the Final Report

Seq No.	Sum No.	OEX Data	GMT GMT Day 32	Ei secs	Milestone	Entry Event	Remarks	MSID / ID	
71	28	--	13:59:30.66	EI+921.66		Start of R2R yaw firing	Last pulse before LOS (stayed on to end of first 5-sec period of recon data at 032/13:59:37.4 GMT)	V79X2634X	
72	28	--	13:59:30.68	EI+921.68		Start of R3R yaw firing	Last pulse before LOS (stayed on to end of first 5-sec period of recon data at 032/13:59:37.4 GMT)	V79X2638X	
73	29	--	13:59:31	EI+922		Observed elevon deflections at LOS	Left: -8.1 1 deg (up); Right: -1.15 deg (up)	V90H7505C V90H7555C	
73.1	29.3	--	13:59:31.400	EI+922.4		FCS Channel 4 Aerosurface position measurements start trending towards their null values	Indicates worsening failure of transducer excitation via a wiring short conditions	V57H0253A (5 Hz)	
73.2	29.3	--	13:59:31.478	EI+922.5		All FCS Channel 4 Bypass valves close (indicating bypassed)	Leading indicator of ASA fail (high-rate data)	V58P0915A	
73.3	29.3	--	13:59:31.7	EI+922.7		Speedbrake channel 4 CII position measurement indicated successively 19, 20, 24 degrees over last three samples prior to LOS (should be closed / 0°).	Speedbrake was commanded to "overclose" (-10 degrees), position measurements for Channels 1 thru 3 were 0 degrees. Secondary delta pressure on CH 4 went to zero, which indicates that the channel was bypassed. This is real data and the ASAs were responding appropriately.	V57H0253A (5 Hz)	
73.5	29.5	--	13:59:32	EI+923		Observed aileron trim at LOS	Trim: -2.3 deg (V96H2045C - V90H1500C)		
74	--	--	13:59:32	EI+923		M-FUS LT BL Temp at x 1215 - LOS	LOS	V34T1106A	
74.5	--	--	13:59:32	EI+923		LH Aft Fus Sidewall Temp at x 1410 - LOS	LOS	V09T1724A	
75	--	--	13:59:32	EI+923		LMG Brake Line Temp A - LOS	LOS at 172.2 F	V58T1700A	
76	--	--	13:59:32	EI+923		LMG Brake Line Temp B - LOS	LOS at 154.2 F	V58T1701A	
77	--	--	13:59:32	EI+923		LMG Brake Line Temp C - LOS	LOS at 104.8 F	V58T1702A	
78	--	--	13:59:32	EI+923		LMG Brake Line Temp D - LOS	LOS at 88.3 F	V58T1703A	
79	--	--	13:59:32	EI+923		Left Main Gear Strut Actuator Temp - LOS	LOS at 76.3 F	V58T0405A	
80	--	--	13:59:32	EI+923		Hyd Sys 1 LMG Uplk Actr Unlk Ln Temp - LOS	LOS at 52.2 F	V58T0125A	
81	--	--	13:59:32	EI+923		Sys 2 LH Brake Sw Vlv Return Temp (AFT) - LOS	LOS at 62.8 F	V58T0841A	
82	--	--	13:59:32	EI+923		Sys 3 LMG Brake Sw Vlv Return Line Temp (FWD) - LOS	LOS at 67.3 F	V58T0842A	
82.7	32.5	--	31:59:32	EI+923	Approx Veh Grd Location: 32.9 N / -99.0 W	Altitude = 200700 ft / Mach ~18.1 - Near Dallas TX	Approximate Vehicle Ground Location at Loss of Signal based on GMT; Data sources: STS-107 GPS Trajectory Data		
82.8	29.3	--	13:59:32.130	EI+923.130		FCS Channel 4 fail flags raised (1 Hz) on all aerosurface actuators	Lagging indicator of ASA position measurement discrepancy	V79X3263X V79X3268X V79X3273X	V79X3278X V79X3334X V79X3339X
83	33	--	13:59:32.136	EI+923.136	LOS (Loss of Signal)	Last valid downlink frame accepted by ODRC - OI / BFS / PASS (This time has been referred to as "LOS" thoughout the investigation.) Start of reconstructed data	Upper Right Aft (URA) Quad Antenna was selected by BFS Antennae Manage S/W to communicate with TDRS-W. The pointing angle to TDRS-W was off the Orb tail at -65 degs and trending further into blockage. Prev experience / eng calcs predict probable loss of comm at elevation angles greater than -60 degrees. Loss of comm at this GMT is therefore considered nominal.		

A.2-21

Appendix A.2 - STS-107 Mishap Investigation - Master Time Line

Integ Time Line Team - REV 19 BASELINE **6/5/2003 1 PM**

Note: Rev 19 BASELINE updates Rev 18 with the eastern most debris events (over Texas) and is the timeline used for the Final Report

Seq No.	Sum No.	OEX Data	GMT GMT Day 32	Ei secs	Milestone	Entry Event	Remarks	MSID / ID
							Note: BFS does not have this message in the Fault message stack. It is likely that BFS annunciated this message during the 25 second gap of no data, but that if it was annunciated it was pushed out of the downlist stack by additional fault messages (at least 5) annunciated during the gap.	
97	41	--	13:59:52.114	EI+943.114		PASS Fault Message annunciation - L RCS LEAK	Data located in PASS fault message buffer. Data is potentially error prone. Generated when difference between left aft RCS oxidizer and fuel thermodynamically derived quantities is more than 9.5% PVT. Indicates a leak of either helium and/or propellant OR the temperature/pressure sensor readings used to compute the quantities are erroneous.	
97.3	41.5	--	14:00.01 / 03	EI+952 / EI+954		Debris B observed leaving the Orbiter	Time is for debris first seen well aft of Orbiter envelope.	EOC2-4-0024
QBAR = n psf, Mach nn						------ 32:14:00:00 ------		EI + 951 sec; WLE Stagnation Temp: ~2800 F
98	41	--	14:00:01.540*	EI+952.540		BFS Fault Message annunciation - L RCS LEAK	Data located in BFS fault message buffer. Data is potentially error prone. Generated when difference between left aft RCS oxidizer and fuel thermodynamically derived quantities is more than 9.5% PVT. Indicates a leak of either helium and/or propellant OR the temperature/pressure sensor readings used to compute the quantities are erroneous. *Time info corrupted.	
99	41	--	14:00:01.900*	EI+952.900		BFS Fault Message annunciation - L RCS LEAK	Data located in BFS fault message buffer. Data is potentially error prone. *Time info corrupted.	
99.5	41.5	--	14:00:02 / 04	EI+953 / EI+955		Debris C observed leaving the Orbiter	Time is for debris first seen well aft of Orbiter envelope.	EOC2-4-0024
100			deleted				Rationale for deletion: moved to 95.8 after further review of the videos	

A.2-19

Appendix A.2 - STS-107 Mishap Investigation - Master Time Line

Integ Time Line Team - REV 19 BASELINE **6/5/2003 1 PM**

Note: Rev 19 BASELINE updates Rev 18 with the eastern most debris events (over Texas) and is the timeline used for the Final Report

Seq No.	Sum No.	OEX Data	GMT GMT Day 32	Ei secs	Milestone	Entry Event	Remarks	MSID / ID
84	29.3	--	13:59:32.195	EI+923.195		ASA 4 RPC A&C Trip Indication	Lagging indicator of ASA transducer excitation short condition	V79X4210E V76X4211E
85			deleted				Rationale for deletion: moved to 85.6 after further data review.	
85.5	29.3	--	13:59:32.598	EI+923.598		Left Outboard bypass valve reopens. A force fight between channels 1/2/3 and channel 4 begins, resulting in a difference of up to 0.5 degrees observed between the left outboard and inboard elevons	Indicates a short in bypass valve has grown sufficient to drop below voltage threshold of valve. RPC B is current limiting.	V58P0865A
85.6	29.3	--	13:59:33.680	EI+924.680		BFS Fault Message annunciation (1) - FCS CH 4	TDRS-E Data. Error is detected by ATVC/ASA hardware when sensed delta pressure across actuator exceeds a limit indicating the FCS channel is no longer driving the actuator. FCS CH 4 failure will annunciate for any of the following: LIB / LOB / RIB / ROB elevon actutor 4, rudder actuator 4, speedbrake actuator 4, SSME 1/2/3 P/Y Actuator D, & L/R SRB R/T actuator D.	
86	29.3	--	13:59:33.863	EI+924.863		PASS Fault Message annunciation (1) - FCS CH 4	TDRS-E Data	
87			13:59:33.976	EI+924.976		Master Alarm noted		
88	29.3	--	13:59:34.518	EI+925.518		Left Outboard force fight ends, driver currents go to zero. (RPC B trip indication).	Leading indicator of RPC B trip / ASA power down. I.e., indicates opening of all bypass valves (due to RPC B trip removing power) on ASA 4. Force fight goes away since actuators are already at the last commanded position (so channel 4 has no hyd load on the servo asking for position change).	V58P0865A
89	29.3	--	13:59:34.561	EI+925.561		Speedbrake force fight begins (continues to LOS)	Indicates opening of all bypass valves (due to RPC B trip removing power) on ASA 4. Since the speedbrake is at zero but is being commanded to "over-close" position (-10), this results in a force fight between channels 1,2,3 and channel 4.	V57P0260A V57P0261A V57P0262A
90	35	--	13:59:35/36	EI+926 / EI+927		Sideslip on vehicle changes sign.	The event occurred between the two times listed. Just prior to initial LOS the magnitude of the negative Sideslip started to decrease and between 59:34 and 59:37 sideslip grew from -.6 to +.8 deg. With this change, the normal roll and yaw moments on the vehicle would change sign. Aerodynamic forces due to sideslip are now reinforcing aerodynamic asymmetry.	

A.2-24

Appendix A.2 - STS-107 Mishap Investigation - Master Time Line

Integ Time Line Team - REV 19 BASELINE — **6/5/2003 1 PM**

Note: Rev 19 BASELINE updates Rev 18 with the eastern most debris events (over Texas) and is the timeline used for the Final Report

Seq No.	Sum No.	OEX Data	GMT GMT Day 32	EI secs	Milestone	Entry Event	Remarks	MSID / ID
107.1	–	–	14:00:05.2 / 06.2	EI+956.2 / EI+957.2		Late Flash 1	Sudden brightening of the Orbiter envelope	EOC2-4-0018 EOC2-4-0024 EOC2-4-0209-B EOC2-4-0221-3 EOC2-4-0221-4
107.15	–	–	14:00:06.2 / 07.2	EI+957.2 / EI+958.2		Late Flash 2	Sudden brightening of the Orbiter envelope, followed by a shower of debris seen aft of the Orbiter envelop during the next 4 seconds (shower seen only in EOC2-4-0221-4)	EOC2-4-0018 EOC2-4-0024 EOC2-4-0209-B EOC2-4-0221-3 EOC2-4-0221-4
107.2	–	–	14:00:08 / 12	EI+959 / EI+963		Debris D	Debris first seen slightly aft of Orbiter envelope and begins generating its own trail	EOC2-4-0018 EOC2-4-0209-B EOC2-4-0221-3 EOC2-4-0221-4
107.25	–	–	14:00:09 / 13	EI+960 / EI+964		Debris E	Debris first seen aft of Debris "D"	EOC2-4-0209-B EOC2-4-0221-3 EOC2-4-0221-4
107.3	–	–	14:00:10 / 14	EI+961 / EI+965		Debris F	Debris first seen aft of Orbiter envelope, which for a short time begins generating its own trail	EOC2-4-0209-B EOC2-4-0221-4
107.4	–	–	14:00:13 / 17	EI+964 / EI+968		Debris Shower	Multiple debris seen immediately aft of the orbiter envelope over the next 2 seconds	EOC2-4-0209-B EOC2-4-0221-5
107.5 1.08	47.5	X	14:00:13.439 deleted	EI+964.439		OEX PCM loss of sync	Rationale for deletion: moved to 97.3 after further review of the videos	
109 1.09			deleted				Rationale for deletion: moved to 99.5 after further review of the videos	
109.3	48.3	–	14:00:17.8/18.8	EI+968.8 / EI+969.8		Catastrophic Event of an unknown nature (formally referred to as "Main Body Breakup) consisting of a sudden brightening of the Orbiter envelope followed by a definitive change in the character of the trail	Numerous debris seen aft of Orbiter envelope over the next 10 seconds, followed by disintegration of the main Orbiter envelope into multiple pieces	MIT-DVCAM-0001 EOC2-4-0018 EOC2-4-0024 EOC2-4-0209-B EOC2-4-0221-3 EOC2-4-0221-4
109.5 1.10	48.5	X	14:00:19.44 deleted	EI+970.44		FDM1 A end of data	Rationale for deletion: moved to 109.3 after further review of the videos	
111	50	–	14:00:53	EI+1004	End of Peak Heating		Determined by analysis. The peak heating period represents the approximate time period during which the heating rate has flattened out at or near its maximum value.	

= Expected/Nominal performance or event — nn = data still needed

A.2-22

Appendix A.2 - STS-107 Mishap Investigation - Master Time Line

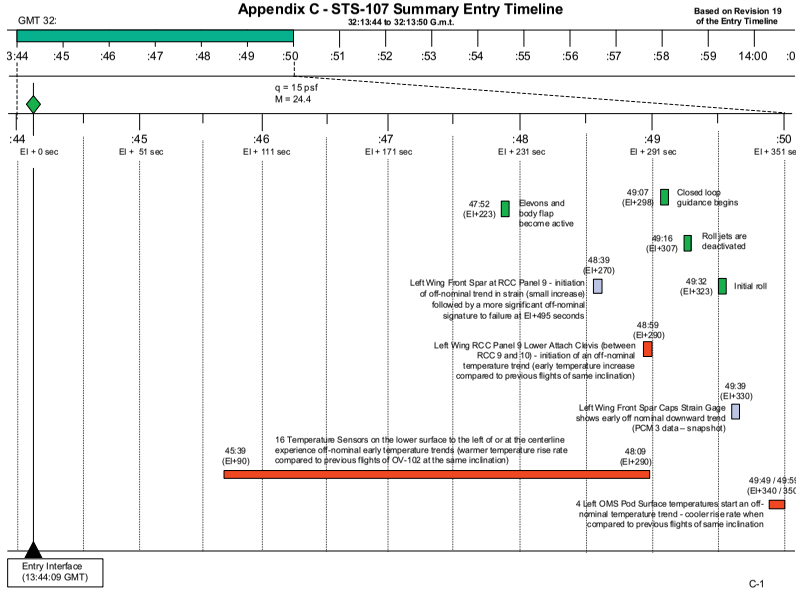
Integ Time Line Team - REV 19 BASELINE — **6/5/2003 1 PM**

Note: Rev 19 BASELINE updates Rev 18 with the eastern most debris events (over Texas) and is the timeline used for the Final Report

Seq No.	Sum No.	OEX Data	GMT GMT Day 32	EI secs	Milestone	Entry Event	Remarks	MSID / ID
101	43	–	14:00:02.654	EI+953.654		PASS Fault Message annunciation - L RCS LJET	Data is potentially error prone. Data located in PASS fault message. Generated when a left firing RCS jet on the left OMS pod has failed with a FAIL OFF, FAIL ON, or FAIL LEAK.	
102	44	–	14:00:02.660	EI+953.660	Beginning of 2 second period of reconstructed data	Start of last 2-seconds of the 32 second period of post-LOS data.	GMT derived by MER data personnel.	
						CAUTION: Data from this period is suspect because multiple bit errors were evident in this reconstructed data. Many of the parameters were 1 Hz data and therefore only one data sample was available. Where possible, high rate data and/or corroborating data were used to draw subsystem performance conclusions. However, some of the conclusions drawn below may be in error or misinterpreted.		
						During this final 2 second period of reconstructed data, the data indicates the following systems were nominal: APUs were running and WSB cooling was evident (although potentially overcooling). MPS integrity was still evident. Fuel cells were generating power and the PRSD tanks/lines were intact. Comm and navaids systems in the forward fuselage were performing nominally. RSB, Body Flap, main engine, and right wing temps appeared active. With the exception of an apparent FES shutdown, ECLSS performance was nominal.		
						During this final 2 second period of reconstructed data, the data indicates the following systems were off-nominal: All three Hyd systems were lost (zero pressure/zero rsvr qty's). The left inbd/outbd elevon actuator temps were either OBL or no data exists. WSB's appeared to be overcooling APU lube oil. The FES appeared to have shutdown. Majority of left OMS pod sensors were either OSH or OSL or no data exists. Multiple BFS and PASS fault message annunciations for left pod hardware were found in the buffer. (Note: All of the left RCS fault messages could be result of a real leak or loss of instrumentation. The OMS fault message could be a real loss of pressure or instrumentation problem. There is not enough data to determine the true cause of the messages associated with the left OMS pod.)		
						Elevated temps at bottom bondline centerline skin forward and aft of the wheel wells and at the port side structure over left wing were observed. EPDC shows general upward shift in Main Bus amps and downward shift in Main Bus volts. AC3 phase A inverter appeared disconnected from the AC Bus.		
						GNC data suggests vehicle was in an uncommanded attitude and was exhibiting uncontrolled rates. Yaw rate was at the sensor maximum of 20 deg/sec. The flight control mode was in AUTO. (Note that all Nav-derived parameters (e.g., alpha) are suspect due to high rates corrupting the IMU state.)		
						Based on the nominal and off-nominal system performance described above, it appears that the fwd/mid/aft fuselage, right wing, and right pod were still intact.		
103	45	–	14:00:03.470*	EI+954.470*		BFS Fault Message annunciation - L OMS TK P	Data located in BFS fault message buffer after acquisition of data. Data is potentially error prone. *Time info corrupted. Note: Error is annunciated when left OMS oxidizer tank ullage pressure (V43P4221C) or fuel tank ullage pressure (V43P4321C) is out of limits high or low. Oxidizer limits - High: 288 psi; Low 234 psi; Fuel limits - High: 288 psi; Low: 234 psi.	

Appendix C - STS-107 Summary Entry Timeline

Based on Revision 19 of the Entry Timeline



C-1

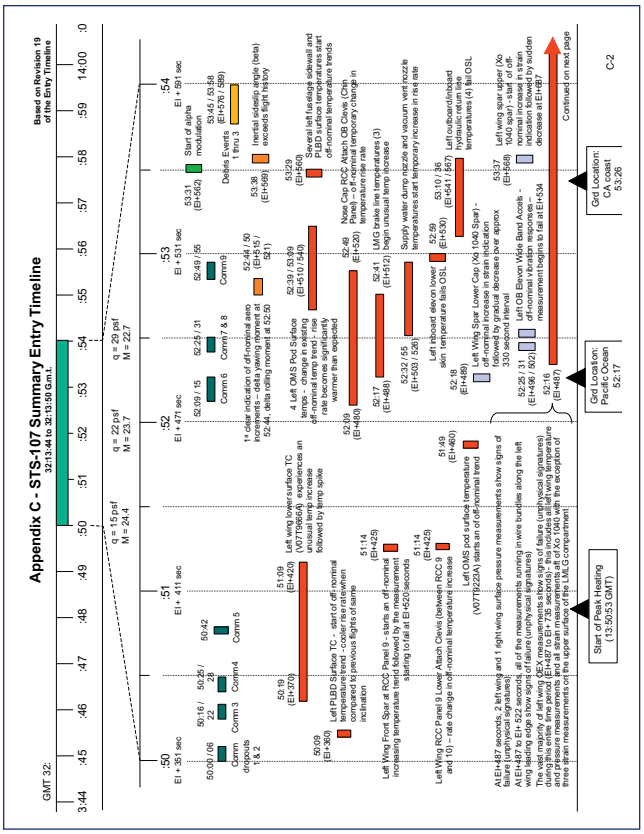
A.2-23

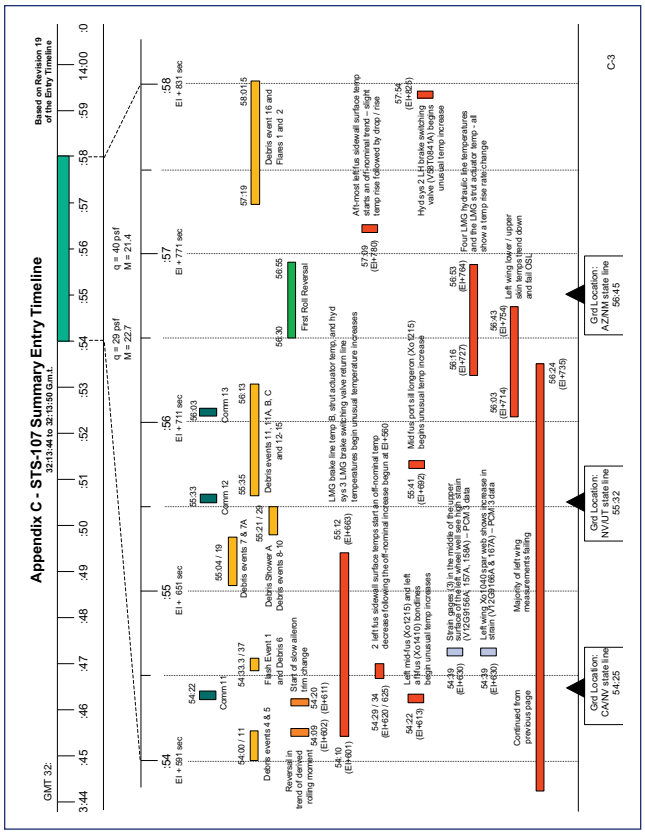
Appendix A.2 - STS-107 Mishap Investigation - Master Time Line

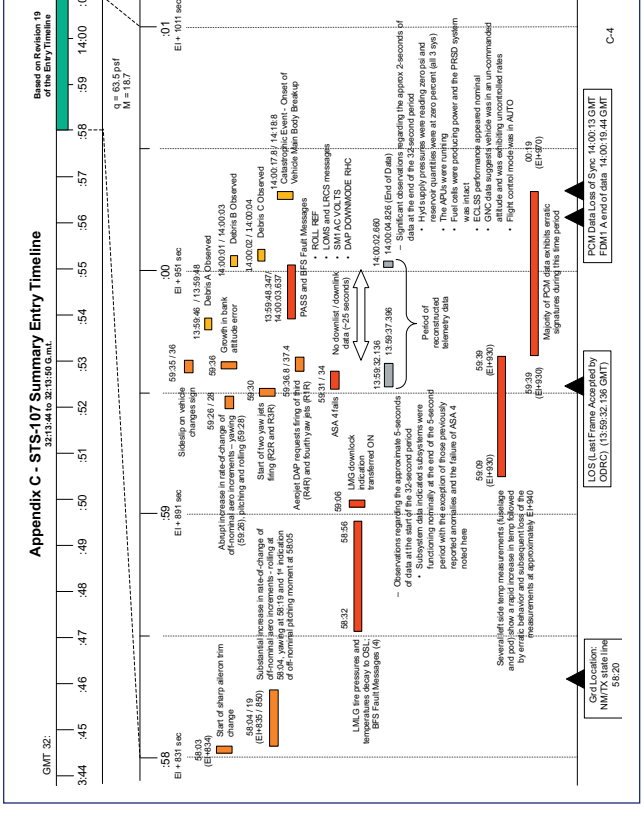
Integ Time Line Team - REV 19 BASELINE — **6/5/2003 1 PM**

Note: Rev 19 BASELINE updates Rev 18 with the eastern most debris events (over Texas) and is the timeline used for the Final Report

Seq No.	Sum No.	OEX Data	GMT GMT Day 32	EI secs	Milestone	Entry Event	Remarks	MSID / ID
103.5	45	–	14:00:0n.nnn			BFS Fault Message annunciation - Indeterminant		
104	45	–	14:00:0n.nnn*			BFS Fault Message annunciation - SM1 AC VOLTS	Occurred after L OMS TK P message. Data is potentially error prone. *Time info corrupted. Note: Error message indicates that AC Bus 3 phase A, B, or C voltage (V76V1700A, V75V1701A, V76V1702A) is out of limits high or low. Low limit for all 3 parameters is 108VAC; High limit is 123VAC.	
105	45	–	14:00:03.637	EI+954.637		PASS Fault Message annunciation - L RCS PVT	Data is potentially error prone. Data located in PASS fault message. Generated when RCS Quantity software does not have enough input data to calculate a quantity. At least one input and its backup are not within valid ranges.	
106	46	–	14:00:03.637	EI+954.637		PASS Fault Message annunciation - DAP DNMODE RHC	Data located in PASS fault message buffer. Generated when the Flight Control System (DAP) downmodes from AUTO to CSS via an RHC deflection passed a threshold. The software process which logs the PASS message runs every 1.92 seconds, so event could have occurred as early as 14:00:01.717 GMT. The fault message was corroborated by an initialization flag for the DAP CSS roll stick function indicating that CSS was entered during the data gap. However, during this final 2 sec period, available vehicle data indicates RHC was in detent & DAP was in AUTO. Data is potentially error prone. Note: BFS downlist bits indicating CSS mode are initialized to "ON" for entry because BFS does not have an "Auto" mode, is always CSS, and will drive the eyebrow panel lights ON if engaged. These bits are always on in BFS through all of OPS 3 until touchdown.	
107	47	–	14:00:04.826	EI+955.826	End of 2 second period of reconstructed data	Last identifiable OI Downlink frame	GMT derived by MER data personnel. Last recognizable Downlist frame (BFS & PASS) was approx 60 ms earlier.	







Appendix D
Subsystem Data Review Summary Report

Table of Contents

D.1 INTRODUCTION
D.2 AUXILIARY POWER UNIT SUBSYSTEM PERFORMANCE EVALUATION
D.3 HYDRAULICS/WATER SPRAY BOILER SUBSYSTEM PERFORMANCE EVALUATION
D.4 MAIN PROPULSION SUBSYSTEM PERFORMANCE EVALUATION
D.5 ORBITAL MANEUVERING SUBSYSTEM PERFORMANCE EVALUATION
D.6 REACTION CONTROL SUBSYSTEM PERFORMANCE EVALUATION
D.7 FUEL CELL POWERPLANT SUBSYSTEM PERFORMANCE EVALUATION
D.8 POWER REACTANT STORAGE AND DISTRIBUTION SUBSYSTEM PERFORMANCE EVALUATION
D.9 ATMOSPHERIC REVITALIZATION SUBSYSTEM PERFORMANCE EVALUATION
D.10 PRESSURE CONTROL SUBSYSTEM PERFORMANCE EVALUATION
D.11 ACTIVE THERMAL CONTROL SUBSYSTEM PERFORMANCE EVALUATION
D.12 SUPPLY AND WASTE WATER MANAGEMENT SUBSYSTEM PERFORMANCE EVALUATION
D.13 AIRLOCK SUBSYSTEM PERFORMANCE EVALUATION
D.14 SMOKE AND FIRE SUPPRESSION SUBSYSTEM PERFORMANCE EVALUATION
D.15 PASSIVE THERMAL CONTROL SUBSYSTEM PERFORMANCE EVALUATION
D.16 MECHANICAL SUBSYSTEM PERFORMANCE EVALUATION
D.17 LANDING AND DECELERATION SUBSYSTEM PERFORMANCE EVALUATION
D.18 PURGE, VENT AND DRAIN SUBSYSTEM PERFORMANCE EVALUATION
D.19 ELECTRICAL POWER DISTRIBUTION AND CONTROL SUBSYSTEM PERFORMANCE EVALUATION
D.20 DATA PROCESSING SYSTEM PERFORMANCE EVALUATION
D.21 FLIGHT CONTROL SYSTEM PERFORMANCE EVALUATION
D.22 INERTIAL MEASUREMENT UNIT PERFORMANCE EVALUATION
D.23 STAR TRACKER SUBSYSTEM PERFORMANCE EVALUATION
D.24 NAVIGATIONAL AIDS SUBSYSTEM PERFORMANCE EVALUATION
D.25 S-BAND SUBSYSTEM PERFORMANCE EVALUATION
D.26 KU-BAND SUBSYSTEM PERFORMANCE EVALUATION
D.27 INSTRUMENTATION SUBSYSTEM PERFORMANCE EVALUATION
D.28 DISPLAYS AND CONTROLS SUBSYSTEM PERFORMANCE EVALUATION
D.29 MULTIFUNCTION ELECTRONIC DISPLAY SUBSYSTEM PERFORMANCE EVALUATION

D-1

D.30 AIR DATA TRANSDUCER ASSEMBLY HARDWARE PERFORMANCE EVALUATION

D.1.0 INTRODUCTION

The results of the subsystem data reviews are documented in Appendix D. The report summarizes the results of the data reviews conducted by each of the subsystem teams. The report covers all mission phases and indicate that although there was evidence in the data of the impending catastrophic failure, all of the *Columbia* vehicle active systems were performing nominally until the final minute prior to breakup.

D2.0 AUXILIARY POWER UNIT PERFORMANCE EVALUATION

D2.1 Executive Summary

The auxiliary power unit (APU) subsystem performed nominally during all phases of the mission. During entry, all APU parameters were nominal at loss-of-data.

Data during entry through the initial Orbiter loss of signal (LOS), prior to the 32-second (LOS+32) period of reconstructed data, showed nothing off nominal except for one-bit data hits in nine measurements. Data obtained from the final 32-second period of reconstructed data were comprised of an initial 5-second period, followed by a 25-second period of no data, concluding with a final 2-second period of data. The 5-second and 2-second data periods contained many data hits, which required extensive evaluation to extract valid data. Evaluation concluded that all three APUs were operating properly at normal speed through the final loss of all data (LOS+32 seconds) with all three hydraulic systems having lost all hydraulic main-pump pressure.

The APU subsystem had no off-nominal events, deviations from nominal, or unusual data other than one-bit data hits through the initial LOS period. Analysis indicates that no APU subsystem hardware contributed directly or indirectly, or was in any way associated with the cause of the loss of the Orbiter.

D2.2 Pre-launch/Ascent Performance

APU subsystem performance was nominal during the pre-launch/ascent phase. Two minor observations are noted in the following paragraphs.

A small-temperature-drop in the APU 2 injector tube temperature, which was recorded at approximately 16:15:39 G.m.t., was initially reported as caused by a suspected loose spring clip. However, following an investigation of the hydraulic loads data during this period and a comparison with data from the previous mission (STS-109) of this vehicle, it has now been concluded that the temperature drop was a normal APU response to a drop in hydraulic load.

Movement of a small amount of hydrazine in the APU 2 fuel pump seal cavity drain line is suspected to have caused a small temperature rise and drop in the APU fuel pump drain line temperature 2 near main engine cutoff (MECO). This event is not considered to be anomalous.

D2.3 On-Orbit Performance

APU subsystem performance was nominal during the on-orbit phase. The APU heater systems maintained all APU systems within the nominal temperature

range. APU 1 operated satisfactorily during the flight control subsystem (FCS) checkout.

D2.4 Entry Performance

The APU subsystem had no off-nominal events, deviations from nominal, or unusual data other than one-bit data hits through the final loss of data at 32:14:00:04 G.m.t. (LOS +32 seconds). Analysis indicates that no APU subsystem hardware contributed directly or indirectly, or was in any way associated with the cause of the loss of the Orbiter.

The thrust vector control (TVC) isolation valves of two of the three hydraulic systems are opened during hydraulic normal pressure to stow the Space Shuttle main engine (SSME). These periods of load on the corresponding APUs are evidenced in the APU turbine-speed and chamber-pressure plots. APU performance was nominal during the stowing of the SSMEs on the STS-107 mission.

Subsystem performance during the final 32-second period (LOS+32) of reconstructed data was within specifications and was as expected except for lower APU lubrication oil and bearing temperatures in the final 2-second period. This may be attributed to loss of all hydraulic loads as a result of loss of all hydraulic main pump pressure in all three hydraulic systems and/or possibly to a hydraulic water spray boiler (WSB) overcooling condition.

The APU group performed a review of the APU 1 revolutions per minute (RPM) signature during the final 2-second segment of the 32 seconds period of reconstructed data. The latest version (07) of the 32-second period of reconstructed data was used, and all APU parameters were re-reviewed. The 5-second segment and final 2-second segment indicate that the three APUs were functioning nominally to the end of data (32:14:00:05 G.m.t.).

Specifically with regard to the last 2 seconds of the reconstructed data, the APU 1 RPM signature was somewhat different than normal, and warranted special review, including consultation with the vendor, Hamilton Sundstrand Corp. (HSC). The portion of the cycle obtained is only the ramp-down, or turbine wheel spin-down. It was different from other cycles in that it started at a higher speed (112.9-percent) and ramped down slower (105.5-percent at end of data and still decreasing).

From an operational viewpoint, the APU is speed-controlled by a digital controller operating an on-off valve that sends pulses of fuel to the APU at a frequency of approximately once per second. The actuation of an elevon or any other increase in hydraulic load will cause the valve-pulsing frequency as well as the valve-on time to increase because of the increased hydraulic load. The controller set points for normal-speed operation are 102-104 percent, which results in a

turbine-speed-band of about 102-110 percent, based on the designed valve response time and a programmed controller response time. When APU high-speed operation is selected in the cockpit, the controller set points are 112-114 percent, with resulting turbine-speed-band of about 112-117 percent.

The 112.9-percent data point is not indicative of high-speed operation, but is assessed as a data hit (bad data) for the following reasons:

1. The speed continues to ramp down below the high-speed set points and high-speed band;
2. The drop from 112.9 to 109.6 percent is 5 time-bit values, but would be only one or two for a real spin-down;
3. The remaining good data (109.6-105.5 percent) is a good, smooth, normal-speed signature, but at a slower spin-down rate, and it did not reach the lower set point by the end-of-data. This latter fact is the result of the loss of hydraulic fluid in the hydraulic system sometime during the 25-second gap in the period of reconstructed data. The APU is spinning an empty pump without load or pressure; this same effect was seen during an APU test at White Sands Test Facility June 5, 2001, when the hydraulic pump lost fluid and ran for 21 seconds before shutdown;
4. The 112.9-percent data point was extracted from a section of telemetry data for which a low-level of confidence exists for its accuracy;
5. The high-speed switch-scan data showed normal speed for APU 1. The switch-scan data were suspect for APU 2, and the switch-scan data were not available for APU 3; and,
6. No APU caution and warning indications occurred throughout the entry run, thus giving additional confirmation that the three APUs were operating nominally in normal speed and were not switched (commanded) to high speed.

However, in the remote possibility that the 112.9-percent data point were real data, it could possibly be explained by events in the Orbiter causing the controller set point to drift, degrading the valve response time, or perhaps causing a mechanical binding that could induce a shut off valve internal leak to the gas generator. It would not be indicative of high-speed operation.

In summary, the turbine speed was nominal for all three APUs up until loss of data at 32:14:00:04.7 G.m.t., and was indicative of normal speed. In addition, APU 2 exhibited a chamber pressure pulse that ended at this time; this pulse was typical of normal-speed pulses. Switch scans did not show a switch to high-speed. Although a switch position change could have been executed during the 25-second gap, the subsequent three RPM signatures and the one pulse signature indicate normal speed. The hydraulic system reservoirs were shown to have no oil at this time (last two seconds), with the APUs driving empty pumps, lubricated by residual hydraulic fluid.

D.3.0 HYDRAULICS/WATER SPRAY BOILER SUBSYSTEM PERFORMANCE EVALUATION

D3.1 Executive Summary

The hydraulics/water spray boiler (HYD/WSB) subsystem performed nominally during all phases of the mission. However, evidence of the event that led to the loss of the Orbiter was apparent in hydraulic subsystem parameters during the entry. Initially, this evidence was the loss of data from four left-hand elevon return-line temperature sensors and the anomalous temperature rise of eight temperature sensors in the left-hand wheel well. Finally, this evidence included the indication that the hydraulic subsystem had been breached and all three systems were lost.

All HYD/WSB subsystem parameters were functioning nominally and all subsystem parameters were within nominal ranges up until vehicle LOS. The HYD/WSB MER personnel were aware of the off-scale low (OSL) indication on the four left-hand elevon return line temperature sensors when the OSL indication occurred in flight. Post-flight analysis indicated that a total of 12 hydraulic subsystem thermal sensors had anomalous indications. These sensors included the four left-hand elevon return-line temperature sensors that went OSL and eight temperature sensors in the left-hand wheel well that indicated off-nominal increases in temperature. The off-nominal responses indicated by the 12 hydraulic subsystem temperature sensors is not indicative of any anomaly in the HYD/WSB subsystem operation but are an indication of an entry thermal event that led to the loss of the Orbiter.

The post-LOS reconstructed data covered a time period of 32 seconds and consisted of 5 seconds of data followed by a gap of 25 seconds followed by a final 2 seconds of data. Although both the 5- and 2-second data strings provided additional insightful data, both segments were characterized by, in some cases, multiple data hits. The final 2 seconds of data indicated that sometime in the previous 25-second data gap, the hydraulic subsystems were apparently breached. The final 2 seconds of data indicated hydraulic subsystem main pump (system) pressure at 0 psia on all three systems. The hydraulic reservoir pressures likewise indicated 0 psia and indicated reservoir quantities of 0 percent on all three systems.

D.3.2 Pre-launch/Ascent Performance

The hydraulics/water spray boiler (HYD/WSB) subsystem performed nominally during the pre-launch and ascent phases of the mission.

Circulation pump operation during pre-launch was nominal. Two bootstrap accumulator recharges occurred during the pre-launch operations. The first recharge occurred in system 1 (2192 to 2465 psia) and the second in system 3 (2143 to 2465 psia).

The three HYD/WSB systems were activated at T minus 5 minutes prior to launch. During ascent, the three thrust vector control (TVC) isolation valves were open. The three priority valves cracked within the required time limit of less than 1 second. The three hydraulic systems pressures were within the required range of 3050 - 3200 psia. The reseating of the priority valves at APU shutdown was nominal.

The water spray boiler system cores were loaded with approximately 5.0 lb of the additive mixture (53-percent water; 47-percent Propylene Glycol Monomethyl Ether (PGME). The WSB-ready indication was exhibited on all three WSB systems shortly after the water spray boiler gaseous nitrogen (GN_2) isolation valves were opened during pre-launch operations. Nominal WSB cooling performance was observed on all three HYD/WSB systems. System 3 initiated spray cooling approximately 6 seconds after MECO while systems 2 and 1 started approximately 32 seconds and 1 minute 32 seconds after MECO, respectively. No APU lubrication oil overcooling or undercooling conditions occurred. Water spray boiler water usage during ascent for spray cooling was within allowable limits.

D.3.3 On-Orbit Performance

The HYD/WSB subsystem performed nominally throughout the on-orbit phase of the mission. No deviations from the nominal were observed during the on-orbit operations.

D.3.4 Entry Performance

The HYD/WSB subsystem performed nominally throughout the entry phase of the mission until loss of data. The data review indicates that no HYD/WSB subsystem hardware contributed directly or indirectly, or was in any way associated with the cause of the loss of the Orbiter. However, evidence of the event that led to the loss of the Orbiter was apparent in hydraulic subsystem parameters and is discussed in this section.

Post-mission analysis of the HYD/WSB subsystem data involved plotting high-rate data for all system parameters and examining the high-rate data for any anomalous indications. The data analysis indicated a thermal effect in the Orbiter vehicle left-hand main landing gear (MLG) wheel well as indicated by eight hydraulic system thermal sensors. It was determined that all HYD/WSB entry/landing operations and thermal sensor responses appeared nominal up to 32:13:52:17 G.m.t. Analysis of the data indicated that the left MLG brake-line

temperature sensor D began an anomalous rise in temperature at 32:13:52:17 G.m.t. Within 24 seconds, at 32:13:52:41 G.m.t., the left MLG brake-line temperature sensors A and C also initiated a temperature rise.

Four Orbiter vehicle left-side elevon actuator hydraulic return-line thermal sensors indicated an off-scale low (OSL) temperature of –76 °F. The sensors indicating OSL were as follows:

1. System 3 left outboard elevon (LOE) actuator return line;
2. System 1 left inboard elevon (LIE) actuator return line;
3. System 1 LOE actuator return line; and
4. System 2 LIE actuator return line.

The hydraulic system reservoir fluid quantities and all HYD/WSB subsystem temperatures and pressures appeared stable, indicating no subsystem leaks or instability. At that time, the water spray boilers were operating and the spray cooling was nominal. Initial discussions of the situation led to the conclusion that the data dropout of the elevon actuator return lines was caused by a dedicated signal conditioner (DSC) card dropout. Continued monitoring of the in-flight data indicated nominal HYD/WSB subsystem operation, despite the four elevon return-line temperature-sensor dropouts. The data analysis indicated that the four elevon-actuator sensor dropouts were slightly staggered within a time span of approximately 26 seconds, beginning at 32:13:53:10 G.m.t. The system 3 LOE actuator return-line and the system 1 LIE actuator return-line went OSL within 1 second of each other followed by the system 1 LOE actuator return-line and the system 2 LIE actuator return-line going OSL within 2 seconds of each other beginning 24 seconds after the first sensor began going OSL (system 3 LOE actuator return line) and 1 minute, 19 seconds following the first indicated anomalous temperature sensor rise indication in the left MLG wheel well.

Within 10 seconds of the last elevon-actuator return-line sensor going OSL, the left MLG brake-line temperature sensor A began an increase in rise rate, 1 minute, 5 seconds following the initial temperature increase on this sensor. Within 23 seconds, at 32:13:54:10 G.m.t., the left MLG brake-line temperature-sensor B initiated a temperature increase, the first anomalous response indicated on this sensor. Within the next 1 minute, 2 seconds, the left MLG strut actuator sensor and the left MLG system 3 brake-line return line temperature also initiated an indicated rise in temperature. At this point, it was 2 minutes, 55 seconds elapsed time since the first anomalous thermal sensor temperature increase indicated in the left-hand wheel well.

At 32:13:56:16 G.m.t., 3 minutes and 59 seconds after the first anomalous condition was noted in the hydraulic subsystem, the left MLG uplock actuator sensor initiated an anomalous rise in temperature. Within the next 37 seconds, the following four thermal sensors exhibited a change to an increasing rate of rise in temperature:

1. Left MLG system 3 brake return line sensor; and
2. Left MLG brake-line temperature sensors C and B, and the left MLG strut actuator sensor.

At this point, it was 4 minutes, 36 seconds since the first anomalous thermal sensor temperature increase was indicated in the left-hand wheel well. Within 1 minute, 1 second, at 32:13:57:54 G.m.t., the system 2 left-hand brake switch valve return line initiated an anomalous rise in temperature. This was the last of the eight anomaly-affected sensors in the left-hand wheel well to indicate a rise in temperature. At 32:13:58:16 G.m.t., the left MLG brake-line temperature sensor D indicated a change to a rapid increase in the temperature. Sixteen seconds later, the system 2 left-hand brake switch valve return line also initiated a rapid increase in the temperature rise-rate. This sensor indicated the most rapid rise rate of all the left-hand wheel-well thermal sensors, indicating a rate of approximately 40 °F/min. This occurred at an elapsed time of 6 minutes, 15 seconds since the first hydraulic subsystem thermal sensor temperature increase was indicated in the left-hand wheel well.

Loss-of-signal from the vehicle occurred at 32:13:59:32 G.m.t., at which time all hydraulic subsystem sensor downlink data were lost. The elapsed time from the indication of the first sensor temperature indicating an anomalous temperature rise in the left-hand wheel well to LOS was 7 minutes, 15 seconds. At LOS, all of the thermal sensors within the left-hand wheel well, though rising, were all still below redline limits.

It should also be noted that, unlike other sensors that were still trending upward at LOS, the system 2 brake switching-valve return-line temperature sensor and the left MLG brake-line temperature sensor A, which had exhibited the greatest temperature rise rate, very briefly flattened and then exhibited a decrease (approximately 3 °F) prior to LOS. The reason for this is unknown.

The post-LOS period of reconstructed data covered a time period of 32 seconds and consisted of 5 seconds of data followed by a gap of 25 seconds followed by a final 2 seconds of data. Although both the 5- and 2-second data strings provided additional insightful data, both segments were characterized, in some cases, by multiple data hits. The initial 5 seconds of post-LOS reconstructed data indicated that all three hydraulic subsystem main pump pressures were still within nominal ranges (2700 - 3400 psia). All three hydraulic system reservoir volumes were within nominal range (46 - 90 percent) as were reservoir pressures (60 - 95 psia) and temperatures (less than 220 °F). All three hydraulic system bootstrap accumulator pressures were between 3050 psia and 3200 psia, which is within the nominal range. The eight left-hand wheel well thermal sensors discussed previously indicated relatively flat temperatures during the initial 5-second data period, and no data on any of these sensors were indicated in the

final 2 seconds of data. All water spray boiler data was within the nominal range during the initial 5 seconds of post-LOS data. The water spray boiler system 1, 2, and 3 GN_2 tank pressures indicated nominal pressures of 2537 psia, 2452 psia and 2506 psia, respectively, at LOS.

The final 2 seconds of data indicated that sometime in the previous 25-second data gap, the hydraulic subsystems were apparently breached. The final 2 seconds of data indicated hydraulic system main pump (system) pressure at 0 psia on all three systems. The hydraulic system reservoir pressures likewise indicated 0 psia and indicated reservoir quantities of 0 percent on all three systems. Each of the three hydraulic system bootstrap accumulators showed a pressure below 2000 psia on the liquid side of the bellows, indicating that a less-than-nominal pressure was still locked up downstream of each of the system priority valves. The nominal bootstrap accumulator reseat pressure following a nominal main pump shutdown is not less than 2675 psia and is controlled by the priority valve (system 1 - 1970 psia, system 2 - 1920 psia and system 3 - 1860 psia). The fact that the three bootstrap accumulator pressures was less than 2675 psia is consistent with the hydraulic system reservoir pressures being at 0 psia and reservoir quantities at 0 percent. The water spray boiler system 1, 2, and 3 GN_2 tank pressures still indicated pressure integrity during the final 2 seconds of post-LOS data, and the pressures were 2530 psia, 2450 psia, and 2510 psia, respectively, at the last salvaged data bit. The decreasing water spray boiler lubrication oil return line temperatures during the 32-second period of reconstructed data is attributed to reduced APU loads because of breached and depleted hydraulic systems. The APUs were spinning empty pumps without a load or pressure sometime during the 25-second period of LOS. The APU spin data are consistent with White Sands Test Facility test data for a depleted hydraulic pump. Depleted hydraulic systems and off-loading the APUs are consistent with decreasing APU bearing and lubrication oil outlet temperatures as well as water spray boiler lubrication oil return temperatures and increasing water spray boiler hydraulic heat exchanger temperatures. The data indicate that the water spray boilers did not experience a typical overshoot/overcool condition.

In summary, typical mission entry data in the timeframe of the observed anomaly indicates MLG wheel well thermal sensors leveling off to trending downward, not rising as occurred during the STS-107 event. Based on the data analysis, it is believed that the loss of the four elevon actuator return line thermal sensors to OSL was due to the destruction of the instrumentation wiring at some point in the wire routing. Discussions have led to the understanding that the wiring bundle carrying the left-hand elevon actuator instrumentation wiring is routed from the actuators to the vehicle left sidewall and around the outboard perimeter of the left-hand wheel well. The eight hydraulic subsystem sensors that indicated an anomalous temperature rise are located on hydraulic lines in the left-hand wheel well aft-portion inboard sidewall and on the left MLG strut and actuator. The maximum temperature change from the initiation of the temperature rise occurred on the left MLG brake-line temperature sensor A, indicating a rise from

approximately 124 °F to 172 °F (48 °F change). This was also the highest temperature recorded in the left-hand wheel well prior to LOS. The minimum temperature change occurred on the left MLG brake-line temperature D, indicating a rise from 88 °F to 100 °F (12 °F change). The left MLG strut actuator temperature indicated a temperature of 76 °F at LOS.

Although showing evidence of the event leading to the loss of the Orbiter, the HYD/WSB parameters were all within nominal ranges and maintained apparent nominal operation up until the final 2 seconds of reconstructed data that indicated all three hydraulic systems had been lost.

D4.0 MAIN PROPULSION SYSTEM PERFORMANCE EVALUATION

D4.1 Executive Summary

The main propulsion subsystem (MPS) performed nominally during all phases of the mission. During entry, all MPS parameters were nominal until loss of data.

D.4.2 Prelaunch/Ascent Performance

The MPS performed nominally during the pre-launch and ascent phases of the mission. No MPS anomalies or significant events were noted in the review of the ascent data.

D.4.3 On-Orbit Performance

The MPS performed nominally during the on-orbit phase of the mission. No MPS anomalies or significant events were noted during the review of the on-orbit data.

D.4.4 Entry Performance

The MPS performed nominally during the entry phase of the mission. No MPS anomalies or significant events were noted during the review of the entry data.

MPS helium system decay from reconfiguration until LOS was nominal. Some of the tanks for the helium systems for SSME 2 and 3 are located on the left side of the midbody. These systems did not indicate any temperature or associated pressure rise in the systems prior to LOS.

The LH_2 manifold was vented to vacuum for the duration of the flight prior to opening the return to launch site (RTLS) dump valves, so no pressure decay was noted upon opening the valves.

D.5.0 ORBITAL MANEUVERING SUBSYSTEM PERFORMANCE EVALUATION

D.5.1 Executive Summary

The orbital maneuvering subsystem (OMS) performed nominally during all phases of the mission. During entry, the OMS performance was nominal and without incident until the final 2 seconds of the 32-second period of reconstructed data. At that time, there was a significant loss of instrumentation on the left OMS pod.

D.5.2 Pre-launch/Ascent Performance

The OMS performed nominally during the pre-launch and ascent phases of the mission. No deviations or significant events related to the OMS were noted during the review of the ascent data.

D.5.3 On-Orbit Performance

The OMS performed nominally during the on-orbit phase of the mission. No deviations or significant events related to the OMS were noted during the review of the on-orbit data.

D.5.4 Entry Performance

During entry, the OMS performance was nominal and without incident until the final 2 seconds of the 32-second period of reconstructed data. At that time, there was a significant loss of instrumentation on the left OMS pod.

The overall performance of the left and right OMS was nominal, with no exceptions prior to LOS at 32:13:59:32 G.m.t. The left OMS experienced a loss of instrumentation when data came back for approximately 2 seconds before the final LOS at 32:14:00:05 G.m.t.

Starting at 32:13:59:30 G.m.t. (just prior to LOS), all the OMS parameters were reading nominal values and the values remained at nominal levels until 32:13:59:37.4 G.m.t. (end of the first 5-second period of reconstructed data). When data came back at 32:14:00:03 G.m.t., it was seen that most of the pressure and temperature measurements in the left OMS pod were reading an off-nominal value. In most cases, the data were at an off-scale low value, although some off-scale high measurements were observed. Some measurements were not available at all because of the intermittent nature of the data caused by data hits. However, there was one good reading of the left OMS engine GN_2 pressure that had the same reading as at 32:13:59:36 G.m.t. (during the first 5-second period of reconstructed data).

The data during this final 2-second period of reconstructed data can be interpreted as showing the left OMS as having been breached because the available pressure data show the systems at dramatically reduced pressures. This interpretation is also supported by three primary avionics software system (PASS) fault summary messages concerning the left RCS and one backup flight system (BFS) fault message concerning the left OMS that was not on the PASS summary. There were no fault messages, or at least none in the buffer, for the right OMS. The fault messages, the criteria the GPCs use to generate them, and possible causes/interpretations of the messages are detailed in the following paragraphs.

There was no PASS message in the Queue for the left OMS; however, the BFS had an L OMS TK P message that was time-tagged at 32:14:00:03.470 G.m.t. The time tag is suspect data because of data errors in the time-word. The PASS will annunciate this message when the propellant tank ullage pressures are either high (> 288 psia) or low (< 234 psia). The BFS will annunciate this message for the propellant tank ullage pressures being either high (> 288 psia) or low (approximately 234 psia), or if the helium or GN_2 tanks fall below 1500 psia or 1200 psia, respectively, or the GN_2 accumulator pressure falls below 299 psia or exceeds 434 psia.

The error code for this message showed it was either the oxidizer and/or fuel tank that caused this message to be generated. There were no BFS data for the helium or GN_2 system during the final 2 seconds of the reconstructed data before the final LOS. On the PASS, there was only one data sample for only one left OMS tank pressure during this time period that was the left OMS oxidizer ullage pressure of 37.6 psia at 32:14:00:03 G.m.t. If this value drove the BFS fault, however, the PASS should have also annunciated a fault message, but none was recorded.

Since there were no right OMS fault messages and no left OMS pod data were available immediately prior to the final LOS, it is clear that something occurred in the left OMS pod during the 25-second data gap prior to the final 2-second period of reconstructed data. Without more data, any further explanations are speculation.

D.6.0 REACTION CONTROL SUBSYSTEM PERFORMANCE EVALUATION

D.6.1 Executive Summary

The reaction control subsystem (RCS) performed nominally during all phases of the mission. During entry, the RCS performance was nominal and without incident until the final 2 seconds of the 32-second period of reconstructed data.

The overall performance of the forward RCS and the left and right RCS was nominal, with no exceptions prior to LOS at 032:13:59:32 G.m.t. The left RCS, housed in the left OMS pod, had experienced a significant loss of instrumentation, for some unknown reason, when data came back for approximately 2 seconds (reconstructed data period) before the final LOS at 032:14:00:05 G.m.t.

D.6.2 Pre-launch/Ascent Performance

No deviations or significant events related to the RCS were noted during the review of the pre-launch and ascent data.

D.6.3 On-Orbit Performance

No deviations or significant events related to the RCS were noted during the review of the on-orbit data.

D.6.4 Entry Performance

The overall performance of the forward RCS and the left and right RCS was nominal during entry, with no exceptions prior to LOS at 32:13:59:32 G.m.t. The left RCS, housed in the left OMS pod, had experienced a significant loss of instrumentation, for some unknown reason, when data came back for approximately 2 seconds before the final LOS at 32:14:00:05 G.m.t.

At 32:13:59:52.114 G.m.t., the PASS had a message that there was a leak in the left RCS. Subsequently at 32:14:00:01.54 G.m.t. and 32:14:00:03.47 G.m.t., the BFS had messages of a left RCS leak. A low-level of confidence exists for the time tags for the two BFS messages. This message is generated when the difference between the oxidizer and fuel quantities, as calculated by the RCS quantity monitor software, is greater than 9.5 percent based on pressure, volume and temperature (PVT) derived values. The unit percent-PVT is used to distinguish the quantity from percent gage where the latter implies a physical gage (found within the OMS tanks) and the former implies a thermodynamically derived value (in this case, the RCS quantity).

At 32:14:00:02.654 G.m.t., the PASS had a message that a thruster in the left RCS had failed (L RCS LJET). No similar message was received from the BFS. This message is generated when an RCS thruster on the left OMS pod has failed. This can be a fail off, fail on, or fail leak. The crew would use their computer to determine the failure mode.

At 32:14:00:03.637 G.m.t., the PASS had a message that the left RCS PVT was not operating correctly (L RCS PVT). The BFS does not generate this message. This message is generated when the RCS quantity monitor software does not have enough input data to process, and therefore cannot calculate a quantity for either the oxidizer or fuel tanks. This means that at least one input and its backup have fallen outside the reasonableness limits for those particular inputs, and the software has suspended the quantity calculation.

The obvious analysis of the RCS leak message is that there was a leak, either oxidizer or fuel or both. However, there are also other things that can generate the message because the quantity message is based on tank pressures and temperatures. If the temperatures and/or the pressures give erroneous readings that satisfy the reasonableness limits, then the software will treat the values as good and calculate a quantity. For the data from STS-107 at LOS (approximately 032:13:59:32 G.m.t.), if both the left RCS oxidizer and fuel tank temperatures gave erroneous readings of 120 °F instead of the actual 80 °F, then the quantity monitoring software would have computed quantities which differed from each other by 9.5 percent PVT and a leak message would have been generated. However, if an input falls outside the reasonableness limits for that particular input, then the software uses a backup input. This allows a less accurate quantity to be calculated. In the previous example, the 120 °F temperature for the propellant tank is still within the reasonableness limits.

During the review of entry data past the first LOS at 032:13:59:32 G.m.t., it was determined that the left RCS data were nominal until approximately 32:13:59:37 G.m.t. (end of the 5-second period of reconstructed data). When data returned for a brief time at approximately 32:14:00:03 G.m.t. (final 2-second period of reconstructed data), the analysis showed that most of the left RCS operational instrumentation (OI) data and the limited downlist data that was available had values of OSL, OSH (off-scale high) or an off-nominal value. The data from the right RCS and the forward RCS on the other hand had nominal values, with a limited number of exceptions.

The analysis indicates that something caused the loss of data from the left RCS. The LEAK and PVT messages could have been caused by a mere lack of data resulting from the wires being severed by some means. The messages could also have been caused by an actual leak either through thruster valves (a thruster valve that did not completely close), or because of a breach of the system (ruptured propellant tank, broken propellant line, ruptured helium tank,

broken helium line). Thus, the following two possible scenarios are provided and both are equally valid because of the paucity of data.

1. The first scenario is based on the premise that the left RCS had a leak that resulted in a quantity divergence of greater than 9.5-percent PVT between the fuel and oxidizer and, thus, generated the first message. This leak would be of such magnitude that the resulting propellant tank(s) would not be capable of supporting thruster firings causing the left thruster (LJET) message. Finally, enough propellant leaked out that the resulting propellant tank pressures fell outside the reasonableness limits and the PVT gaging calculation was suspended for the left RCS (the third message, L RCS PVT).

2. The second scenario is based on the premise that there was no leak. Instead, system instrumentation was being lost. In this scenario, some instrumentation loss caused a degradation of the PVT calculation and generated the first message. Then instrumentation for the thrusters themselves was lost and this loss resulted in the general purpose computer (GPC) being unable to confirm that the thrusters were firing in response to the reaction jet driver (RJD) outputs; thus the second message. Enough instrumentation was finally lost that the PVT gauging calculation was suspended for the left RCS, which resulted in the third message.

In response to questions that have been asked on the subject of calculating the amount of RCS propellant used, and therefore, gage the amount of thruster activity during the 25-second data gap before the final 2-second period of reconstructed data. Inadequate data exists from the left RCS oxidizer system to determine a final quantity. The left RCS fuel has one more measurement than the oxidizer, but that measurement is still not enough to accurately gage the propellant quantity. The gage readings are present just before final LOS (end of 2-second period of reconstructed data) and show the oxidizer and fuel quantities as 17.8 percent PVT and 31.8 percent PVT, respectively. This difference of more than 9.5-percent PVT shows that the left RCS leak message was generated, and the Master Alarm had been triggered. However, inadequate data exist from the telemetry to determine with any degree of certainty the cause the left RCS PVT message.

PASS data from the right RCS during the period from 32:13:59:36 G.m.t. to 32:14:00:03 G.m.t. shows that the quantities changed by an average value of 7.4-percent PVT. For the right RCS, there are no PASS pressure or temperature data for any tank during the final 2-second period of reconstructed data. The downlisted PASS quantities for the oxidizer and fuel tanks had values of 35.2-percent PVT and 31.2-percent PVT, respectively, while the BFS values were 33-percent PVT and 32-percent PVT, respectively. The cause of this

difference is that the BFS uses slightly different quantity equations and initial conditions than the PASS.

The BFS had values for the helium P2 and propellant tank outlet pressures and tank quantities for the right RCS during the final 2-second period of reconstructed data. Using the available BFS pressures and adding the bias seen earlier in the mission to estimate the redundant pressure measurement, and assuming the tank temperatures had not changed in the previous 30 seconds, the PASS algorithm computes values of 31.8-percent PVT and 30.2-percent PVT in the oxidizer and fuel tanks, respectively. These values are reasonably close to the BFS values. These results give some confidence in the data quality of the downlisted propellant quantities. Since STS-1, it has been observed that periods of heavy RCS propellant usage cause the PVT gaging program to show a lower-than-actual quantity, because the helium and propellant temperature readings are slow to show the actual average temperatures. Once the thruster usage ceases, these temperatures "move" toward the actual average temperature of the tank contents, and the calculated propellant quantities likewise change in the direction of the actual propellant quantities. This phenomenon is referred to as "bounce- back".

An estimate of the bounce-back effect can be made from the forward RCS quantity bounce-back ratio seen after the forward RCS dump on STS-107. For this case, it is seen that for every 1-percent of propellant used the gage indicates 1.2775-percent PVT used. The 2, 3, and 4 thruster flow-rates found in the Shuttle Operational Data Book (SODB) are also used. As there are no data available to show how many thrusters actually fired and for how long, an estimation of the total thruster-on time for the right RCS during the LOS before the final 2-second period of reconstructed data is shown in the following table. The estimate is bounded using different propellant flow rates both with and without the bounce back effect. The results are given for seconds of time beyond 32:13:59:36.6 G.m.t.

Number of Thrusters Firing	Without PVT Bounce-Back	With PVT Bounce-Back
2	26 seconds	20 seconds
3	18 seconds	14 seconds
4	13 seconds	10 seconds

As for the forward RCS, with the exception of the ullage pressures that appear to be data hits, the pressures and temperatures of all the forward RCS tanks were unchanged from their former values when data was acquired for the final 2 seconds of reconstructed data.

D.7.0 FUEL CELL POWERPLANT SUBSYSTEM PERFORMANCE EVALUATION

D.7.1 Executive Summary

The fuel cell powerplant (FCP) subsystem performed nominally during all phases of the mission. During entry, all FCP parameters were nominal until 2 seconds prior to the final loss-of-data. There were no gross system operation anomalies that could be confirmed in the final 2 seconds of reconstructed data. The changes seen appear to be a result of other events that were taking place on the vehicle.

D7.2 Pre-launch/Ascent Performance

The FCP subsystem performed nominally during the pre-launch and ascent phases of the mission.

During powered flight, the electrical load peaked to approximately 23 kW immediately prior to Solid Rocket Booster (SRB) separation. All fuel cell measurements (current, voltage, temperatures, pressure, flow rates, and sub-stack differential voltages) were nominal. The fuel cell water relief and purge system temperatures were nominal. There were nominal heater cycles on the fuel cell alternate water lines.

During vent door opening at approximately T-18 seconds during pre-launch operations, the fuel fell 2 hydrogen (H_2) motor status jumped for one data sample approximately 0.1 V from 0.59 to 0.69 V. This change did not violate the Launch Commit Criteria (LCC) limit of 1.0 V. The voltage returned to the normal level on the next data sample one second later. Fuel cell operation continued to be nominal. This indication appears to be associated with the suspected ac bus 2 B-phase anomaly.

D.7.3 On-Orbit Performance

The FCP subsystem performed nominally during the on-orbit phase of the mission.

The voltage change discussed in the previous paragraph was also observed during a seat adjustment as well as during the payload bay door opening. These indications appear to be associated with the suspected ac bus 2 phase-B anomaly.

D.7.4 Entry Performance

The fuel cell powerplant (FCP) subsystem performed nominally during the entry phase of the mission. During entry, all FCP parameters were nominal until 2 seconds prior to the final loss-of-data. The fuel cell subsystem performance during the period from 32:13:00 G.m.t. through LOS + 5 seconds of the reconstructed data were nominal. There are no direct or indirect findings or associations with the problem that caused the loss of the vehicle.

During the last 2 seconds of the 32-second period of reconstructed data, the fuel cell 3 hydrogen/water pump was operating on 2 phase ac current rather than the usual 3 phases, all loads on the fuel cells were increasing, the oxygen purge vent line temperature was experiencing an unexpected rise, and there were conflicting indications that manifold 1 had lost oxygen pressure (possibly instrumentation). No gross system operation anomaly is confirmable in the last 2 seconds of the reconstructed data. The changes of fuel cell parameters appear to be a result of other events that were taking place on the vehicle.

During the last 2 seconds of the 32-second period of reconstructed data, it was unreliable because of data hits with many fuel cell telemetry measurements missing from the "STS-107 EDIT" data. The basic conclusions derived are:

1. Fuel cell 3 hydrogen separator/water pump was operating on 2 phases based upon the pump motor status reading of about 4.5 Vdc;
2. All 3 fuel cells displayed load increases. Fuel cell 1 increased about 120 amps; fuel cell 2 increased about 44 amps; fuel cell 3 increased about 48 amps;
3. Fuel cell 3 and main bus C voltage both experienced a 0.5-Vdc drop during the last portion of the 2-second data before the final LOS;
4. Fuel cell oxygen purge-line temperature rose 84 °F from the LOS + 5 second data to the last 2 seconds of data. Only 1 sample of fuel cell telemetry was deemed to be of good quality by the Data Verification Team (DVT); and
5. PRSD oxygen manifold 1 pressure indicated off-scale low and fuel cell 1 coolant pressure (provides fuel cell indication of oxygen pressure) indicated OSL. No manifold-2 pressure indication was available to verify the readings. No other confirming cues were present to verify the loss of oxygen pressure in the manifold such as the fuel cell 1 oxygen reactant flow meter indicating good reactant flow; no other fuel cell coolant pressures had dropped; no tank pressures had dropped.

Nominal H_2 tank heater cycles in tanks 1 and 2 occurred to maintain nominal manifold pressure to support fuel cell operations. The O_2 manifold pressure was decaying at a nominal rate to support fuel cell operations and crew breathing. No oxygen tank heater cycles were required during entry up to the end of the 32-second period of reconstructed data, but nominal heater cycles were

occurring prior to the entry phase. All tank internal fluid and heater assembly temperatures were nominal.

The total Orbiter power produced by the three fuel cells was nominal for LOS + 5 second data at about 20.5 kW. All fuel cell measurements (current, voltage, temperatures, pressure, flow-rates, and substack voltages) were nominal. The fuel cell water relief nozzle temperature was increasing as expected after entry interface because of aerothermal heating. The fuel cell product water line temperatures were beginning to decrease in a nominal fashion due to convective cooling caused by entering the atmosphere.

During the last 2 seconds of the 32-second period of reconstructed data, the total Orbiter power level had increased to about 23 kW. Current on all 3 three fuel cells was increasing; fuel cell 3 had 2 phase ac operation on its hydrogen/water pump; an off-nominal 84 °F rise in the oxygen purge vent line temperature was noted; and fuel cell 1 coolant pressure and oxygen manifold pressure 1 were reading OSL.

D.8.0 POWER REACTANT STORAGE AND DISTRIBUTION SUBSYSTEM PERFORMANCE EVALUATION

D.8.1 Executive Summary

The power reactant storage and distribution (PRSD) subsystem performed nominally during all phases of the mission. During entry, all PRSD parameters were nominal at loss-of-data. The PRSD subsystem performance during the period from 32:13:00 G.m.t. through the LOS + 5-second period of reconstructed data were nominal. There are no direct or indirect findings or associations with the problem.

During the last 2 seconds of the 32-second period of reconstructed data, the fuel cell 3 hydrogen/water pump was operating on 2 phase AC current rather than the usual 3 phases, the oxygen purge vent line temperature was experiencing an unexpected rise, and conflicting indications were observed that manifold 1 had lost oxygen pressure (possibly instrumentation). No gross system operation anomaly is confirmable in the last 2 seconds of data. The changes of PRSD parameters appear to be a result of other events that were taking place on the vehicle.

D.8.2 Pre-launch/Ascent Performance

The PRSD subsystem oxygen (O_2) and hydrogen (H_2) tank sets 1 and 2 heater switches were in nominal ascent configuration. The O_2 and H_2 tanks 1 and 2 'A' heaters were in AUTO. All of the seven other tank set heater switches were configured to OFF. All four manifold isolation valves were open. The extended duration Orbiter (EDO) pallet, installed in the aft part of the payload bay with four tank sets, was deactivated. An O_2 offload was performed to reduce the nominal end-of-mission (EOM) landing weight. Oxygen tanks 1, 2 and 3 were offloaded by approximately 100 lb each and tanks 4 and 5 were offloaded by approximately 25 lb each for a total O_2 offload of approximately 350 lb.

The main buses were untied for ascent. The main bus B (MNB) to main bus C (MNC) crosstie was performed at 16:16:56:48 G.m.t., for nominal on-orbit SpaceHab load distribution. The water line heaters were on the A system.

The O_2 and H_2 manifold and tank pressure decay rates were nominal to support fuel cell operations and crew breathing. The oxygen manifold pressures reached the tank 1 and 2 control band and these tanks began nominal heater cycles at 16:16:28 G.m.t. The hydrogen manifold pressures did not reach their tank 1 and 2 control band during the ascent-data evaluated.

All tank internal fluid and heater assembly temperatures were nominal.

D.8.3 On-Orbit Performance

All of the PRSD system tank pressure cycles that were regulated by internal electrical heater operation were nominal, and were controlled by the heater AUTO function. All of the tank internal fluid and heater assembly temperatures were nominal for the entire on-orbit operation. The EDO pallet was activated throughout the on-orbit operations, and was deactivated during deorbit preparations.

A hydrogen manifold pressure spike occurred when manifold pressure control was switched to H_2 tank 3 after H_2 tanks 4 and 5 were depleted. This was a nominal signature seen previously in all orbiters when control is switched from low-quantity tanks to high-quantity tanks with colder, denser fluid. The manifold pressure did not reach the manifold relief valve crack pressure.

The Operations and Maintenance Requirements and Specification Document (OMRSD) in-flight checkout of the tank heater current sensors was performed. Nominal sensor operation was verified on all of the tank heaters except for O_2 tank 7. During this test, the O_2 tank 7 heater-A manual-command failed to energize the A heater. Later in the mission, however, the heater sensor for O_2 tank 7 was verified during tank heater operation in the AUTO mode.

D.8.4 Entry Performance

The overall entry performance of the PRSD subsystem was nominal, with the exception of several abnormalities seen in the last 2 seconds of the 32-second period of reconstructed data that was recovered. These abnormalities are the rise in temperature of the fuel cell purge line and the conflicting indications that O_2 manifold 1 had lost pressure. These abnormalities are discussed in section D.7.4. Events that occurred during the entry timeline period were evaluated. The 32:13:00 G.m.t. through LOS + 5-second data was confirmed to be nominal system operations and PRSD measurements experienced no data loss. Other than some telemetry parameters beginning to become unreliable because of data hits before the 25-second period on no data, all PRSD measurements were nominal.

D.9.0 ATMOSPHERIC REVITALIZATION SUBSYSTEM PERFORMANCE EVALUATION

D.9.1 Executive Summary

The atmospheric revitalization subsystem (ARS) performed nominally during all phases of the mission. During entry, all ARS parameters were nominal at loss-of-data.

D.9.2 Pre-launch/Ascent Performance

The ARS performed nominally during the pre-launch and ascent phases of the mission. No anomalous conditions were noted in the data during this phase of operations.

D.9.3 On-Orbit Performance

The ARS performed nominally during the nominally during the on-orbit phase of the mission.

D.9.4 Entry Performance

The ARS performed nominally during the entry phase of the mission. No anomalous conditions were noted in the data during this phase of operations.

D.10.0 PRESSURE CONTROL SUBSYSTEM PERFORMANCE EVALUATION

D.10.1 Executive Summary

The pressure control subsystem (PCS) performed nominally during all phases of the mission. During entry, all PCS parameters were nominal at loss-of-data.

D.10.2 Pre-launch/Ascent Performance

Review of the PCS pre-launch/ascent data indicated nominal system performance with no anomalous conditions observed.

D.10.3 On-Orbit Performance

Review of the PCS on-orbit data indicated nominal system performance with no anomalous conditions observed.

D.10.4 Entry Performance

The PCS operated nominally during the entry phase. Additionally, subsystem performance gave no indications of anomalous performance in other subsystems.

The 14.7-psia cabin pressure regulator inlet valves were closed and the pressure control system was inactive for nominal cabin pressurization for entry with the exception of oxygen supply to the Launch and Entry Helmets (LEH) and g-suits. Nominal activation and oxygen use by the crew for the g-suits was evident in the data evaluated.

There were no data for most of the 32-second period of reconstructed data following LOS. Based on the limited data for all measurements (PPO_2, O_2 percent, cabin pressure, cabin temperature and $PPCO_2$), the cabin parameters were nominal at the end of the first 5-second period of data and it appears that the cabin pressure integrity was intact throughout the 32-second period of reconstructed data.

D.11.0 ACTIVE THERMAL CONTROL SUBSYSTEM PERFORMANCE EVALUATION

D.11.1 Executive Summary

The active thermal control subsystem (ATCS) performed nominally during all phases of the mission. During entry, all ATCS parameters were nominal at loss-of-data.

D.11.2 Pre-launch/Ascent Performance

Review of the ATCS pre-launch and ascent data indicated nominal system performance with no anomalous conditions observed.

D.11.3 On-Orbit Performance

Review of the ATCS on-orbit data indicated nominal system performance with no anomalous conditions observed.

D.11.4 Entry Performance

The ATCS performed nominally during the entry phase of the mission. Normal flash evaporator water use was observed in the analysis of the data. No ATCS anomalous conditions were noted in the data.

D.12.0 SUPPLY AND WASTE WATER MANAGEMENT SUBSYSTEM PERFORMANCE EVALUATION

D.12.1 Executive Summary

The supply and wastewater management (SWWM) subsystem performed nominally during all phases of the mission. During entry, all SWWM parameters were nominal at loss-of-data.

D.12.2 Pre-launch/Ascent Performance

Review of the SWWM subsystem pre-launch and ascent data indicated nominal system performance with no anomalous conditions observed.

D.12.3 On-Orbit Performance

Review of the SWWM subsystem on-orbit data indicated nominal system performance with no anomalous conditions observed.

D.12.4 Entry Performance

The SWWM subsystem indicated nominal operation during the entry phase and no anomalous conditions were observed.

An out-of-family condition was observed in the supply water dump nozzle and vacuum vent nozzle temperatures during entry. Supply water dump nozzle entry heating rates on temperature sensors A and B increased from 33.5 °F per minute to 43.25 °F per minute. After 2 minutes and 17 seconds, the increase rate changed to 30.47 °F per minute. Vacuum vent nozzle entry heating rate increased from 0.88 °F per minute to 7.49 °F per minute in 26 seconds and then changed to 1.33 °F per minute. All past flight entry nozzle temperatures were reviewed, and there was no past flight with similar signatures to those observed on STS-107.

The wastewater dump nozzle temperature was nominal throughout this period. Due to the physical proximity of the wastewater dump nozzle to the other two nozzles, it might be expected that all three nozzles would behave similarly to the aerodynamics of entry. This inconsistency between the three nozzle temperatures may provide further clues as to the aerodynamic/aerothermal events and timing of those events during STS-107.

D.13.0 AIRLOCK SUBSYSTEM PERFORMANCE EVALUATION

D.13.1 Executive Summary

The airlock subsystem performed nominally during all phases of the mission. During entry, all airlock subsystem parameters were nominal at loss-of-data.

D.13-2 Pre-launch/Ascent Performance

Review of the airlock subsystem pre-launch and ascent data indicated nominal system performance with no anomalous conditions observed.

D.13.3 On-Orbit Performance

Review of the airlock subsystem on-orbit data indicated nominal system performance with no anomalous conditions observed.

D.13.4 Entry Performance

The airlock subsystem performed nominally during the entry phase of the mission. No in-flight anomalies were identified in the data analysis.

D.14.0 SMOKE AND FIRE SUPPRESSION SUBSYSTEM PERFORMANCE EVALUATION

D.14.1 Executive Summary

The smoke and fire suppression subsystem performed nominally during all phases of the mission. During entry, all smoke and fire suppression subsystem parameters were nominal at loss-of-data.

D.13-2 Pre-launch/Ascent Performance

Review of the smoke and fire suppression subsystem pre-launch and ascent data indicated nominal system performance with no anomalous conditions observed.

D.13.3 On-Orbit Performance

Review of the smoke and fire suppression subsystem on-orbit data indicated nominal system performance with no anomalous conditions observed.

D.13.4 Entry Performance

The smoke and fire suppression subsystem performed nominally during the entry phase of the mission. No in-flight anomalies were identified in the data analysis.

D.15.0 PASSIVE THERMAL CONTROL SUBSYSTEM PERFORMANCE EVALUATION

D.15.1 Executive Summary

The passive thermal control subsystem performed nominally during all phases of the mission. During entry, some passive thermal control subsystem parameter temperatures were off-nominal at loss-of-data.

From the real-time operational instrumentation (OI) data, it could be seen that abnormal temperature rises occurred in the left main landing gear compartment and left-side structure, and that sensors failed on the hydraulic actuator return-lines of the left inboard and outboard elevons, lower elevon bondline and left upper and lower wing bondlines. Also, an off-nominal signature (change in temperature rise rate) occurred in the supply water dump nozzle and vacuum vent nozzle.

From the operational experiment (OEX) recorder data, many off-nominal thermal responses were noted. These included off-nominal temperature-rises of the left wing front spar at reinforced carbon carbon (RCC) panel 9 and the left wing RCC panel 9 lower-outboard attachment clevis. Additionally, there were off-nominal temperature responses of several thermal protection subsystem (TPS) surface measurements on the left side of the vehicle and all of the left wing temperature measurements failed.

D.15.2 Pre-launch/Ascent Performance

The passive thermal control subsystem pre-launch and ascent temperature responses were nominal and compared favorably with those of previous missions. No in-flight anomalies were identified in the evaluation of the data for this phase of the mission.

D.15.3 On-Orbit Performance

The on-orbit performance of the passive thermal control subsystem was nominal and compared favorably with that of previous missions. The on-orbit temperature responses for the bottom bondline and main landing gear were nominal. Attitude adjustments were made for the nominal end-of-mission thermal conditioning for water production and radiator protection concerns. This attitude change had no adverse effect on the vehicle thermal performance. Heaters enabled for the deorbit phase of the mission operated nominally. No in-flight anomalies were identified in the evaluation of the data.

D.15.4 Entry Performance

The entry performance of the passive thermal control subsystem was nominal with the exception of abnormal temperature rises and temperature sensor failures.

During entry, the bondline structure OI data increases in temperature because of entry heating. From plots comparing the STS-107 bondline temperature response with selected flights, the right-hand side fuselage and bottom centerline temperature responses were nominal. However, the left-hand side fuselage temperature data responded nominally with three exceptions that were:

1. Mid fuselage compartment sidewall temperature at Xo1215;
2. Mid fuselage sill longeron temperature at Xo1215; and
3. Aft fuselage compartment sidewall temperature at X1410.

At 32:13:54:22 G.m.t., the temperature rise rates at these locations began faster than previously experienced on comparison flights. Also, uneven temperature responses occurred between port and starboard side at the same Xo location; symmetrical heating and temperature rise rates were expected.

The temperature rises on the portside fuselage structure measurements (mid sidewall, longeron, and aft sidewall) indicate higher-than-nominal environmental heating.

From the OEX data, off-nominal temperature responses were noted very early during entry. The left wing front spar at RCC panel 9 started an off-nominal increasing temperature trend at 32:13:48:59 G.m.t. [entry interface (EI) plus 270 seconds), and the left wing RCC panel 9 lower outboard attachment clevis started an off-nominal increasing temperature trend at 32:13:48:59 G.m.t. Within the next 70 seconds, the TPS surface temperatures on the left side of the vehicle and the left OMS pod began off-nominal responses when compared to previous flights. This response continued to LOS. Finally, during the period from 32:13:52:21 to 32:13:53:47 G.m.t., all of the left wing temperature measurements failed.

D.16.0 MECHANICAL SUBSYSTEM PERFORMANCE EVALUATION

D.16.1 Executive Summary

The mechanical subsystem performed nominally during all phases of the mission. During entry, all mechanical subsystem parameters were nominal at loss-of-data.

There were two unexplained occurrences of additional current draw on ac bus 1, but it is not believed that these were in any way related to the loss of the crew and vehicle.

D.16.2 Pre-launch/Ascent Performance

No anomalies were noted in the mechanical systems during the pre-launch and ascent phases of the mission. All mechanisms operated in nominal dual-motor time with all limit switches transferring properly.

D.16.3 On-Orbit Performance

The overall performance of the mechanical systems was nominal during the on-orbit phase of the mission and no anomalies were noted. The port radiator was deployed and stowed twice, and all involved mechanisms operated in nominal dual-motor time with all limit switches transferring properly.

During the vent-door opening, payload bay door (PLBD) opening and Ku-band antenna deployment, an intermittent signature occurred on ac bus 2, phase B where the current was slow to increase at motor startup. This anomaly is discussed in D.19.0 Electrical Power Distribution and Control subsystem section of this appendix.

D.16.4 Entry Performance

The overall performance of the mechanical systems was nominal during the entry phase up to the loss of the vehicle

There were two unexplained occurrences of additional current draw on ac bus 1, but it is not believed that they were in any way related to the loss of the crew and vehicle.

Motor control assembly (MCA) operational status (Op Stat) indications show that the appropriate MCA relays were operating to supply ac power to the motors. During deorbit preparation and entry, all mechanisms operated in nominal dual-motor time with all limit switches and op stats transferring properly.

During payload bay door (PLBD) closure, after starboard door closure had been stopped for the nominal alignment check, a 0.7-second period of additional current draw occurred on ac bus 1. The amplitude and signature of the trace appear to correspond to starboard door drive motor 1. However, a scenario could not be determined that would explain why one door drive motor would run without the bulkhead latches running as well. Because the sample rate for limit switch and op stat data is only 1 Hz, it is impossible to determine whether any changes occurred in these indications within the 0.7-second time period.

During vent door closure, a 0.1-second period of additional current draw was noted on ac bus 1 phases A and C. It is possible that a momentary limit switch failure could have caused a motor to drive for this short period. Because the ac current sample rate is 0.1 Hz and the op stat and limit switch data sample rate is only 1 Hz., this could have occurred without showing up in the phase B, op stat, or limit-witch data.

All data reviewed indicated nominal performance of mechanical systems hardware from deorbit preparations through entry and LOS+32. The two unexplained occurrences of additional current draw on ac bus 1 are not believed in any way related to the loss of the crew and vehicle.

D.17.0 LANDING AND DECELERATION SUBSYSTEM PERFORMANCE EVALUATION

D.17.1 Executive Summary

The landing and deceleration subsystem performed nominally during all phases of the mission. However, evidence of the event that led to the loss of the Orbiter was apparent in landing and deceleration parameters during the entry.

1. Left-hand MLG tire pressure measurements failed OSL prior to LOS;
2. Left-hand inboard and left-hand outboard wheel temperature measurements went OSL prior to LOS; and
3. Left MLG down-lock indication transferred and remained on through LOS.

D.17.2 Pre-launch/Ascent Performance

This system was not active throughout the pre-launch and ascent phases of the flight, and no anomalies were noted in the data that was reviewed.

D.17.3 On-Orbit Performance

This system was not active throughout the on-orbit phase of the flight, and no anomalies were noted in the data that was reviewed. All data reviewed indicated nominal performance of landing and deceleration hardware throughout the on-orbit phase.

D.17.4 Entry Performance

The overall performance of the landing/deceleration subsystem was nominal throughout entry and the LOS+32-second period of reconstructed data with the exceptions noted in the following paragraphs.

The left-hand main landing gear tire pressure measurements failed off-scale-low (OSL) prior to loss of signal (LOS). The data review showed that the loss of the primary measurements occurred prior to the loss of the secondary measurements. This appears to indicate an instrumentation failure as opposed to a loss of tire pressure.

The left-hand inboard (LHIB) and left-hand outboard (LHOB) wheel temperature measurements went OSL prior to LOS. There are no redundant measurements for wheel temperature. Prior to the failure of the instrumentation, all indications were in the nominal range for landing.

The left MLG down-lock indication transferred on at 32:13:59:05.877 G.m.t. and remained on through LOS. This appeared to be an erroneous output because all other available data indicated that the gear was up and locked during this time.

Based on redundant sensors and other indications; all observed anomalies appear to be due to instrumentation failures and not hardware. The following is a discussion of the instrumentation data of the landing system.

The left-hand inboard (LHIB) 1 and left-hand outboard (LHOB) 1 tire-pressure measurements went OSL (230 psia). The trend toward OSL started at 32:13:58:33.171 G.m.t. for both measurements. The LHOB 1 went OSL at 32:13:58:40.194 G.m.t. and LHIB 1 went OSL at 32:13:58:38.225 G.m.t. Prior to this event the pressures were at a nominal value of 350 to 355 psia, which is consistent with the expected pressures adjusted for wheel-well environmental conditions given the post top-off tire pressures and leak rates obtained prior to launch.

Both LHIB and LHOB wheel temperature measurements went OSL (-75 °F). The trend toward OSL started at 32:13:58:35.730 G.m.t. for the LHIB and at 32:13:58:33.201 G.m.t. for the LHOB. The LHIB went OSL at 32:13:58:44.219 G.m.t. and the LHOB went OSL at 32:13:58:39.783 G.m.t. Prior to this event, the temperatures were at a nominal 35 °F. The data were consistent with the on-orbit thermal conditioning performed to maintain minimum nominal end of mission (NEOM) tire pressures.

The right-hand inboard (RHIB) 1 and right-hand outboard (RHOB) 1 tire pressure measurements appeared to dip approximately 3 psi and then recover to a nominal 355 psia. The first pressure drop started at 32:13:58:37.316 G.m.t. for RHIB 1 and at 32:13:58:38:304 G.m.t. for the RHOB 1. This condition lasted for approximately 10 seconds after which the pressures recovered until LOS. Prior to this event, the pressures were at a nominal value of 350 to 355 psia, which is consistent with the expected pressures adjusted for wheel-well environmental conditions given the post top-off tire pressures and leak rates obtained prior to launch.

The LHIB 2 and LHOB 2 tire pressure measurements went OSL (230 psia). The trend toward OSL started at 32:13:58:33.171 G.m.t. for both of these measurements. The LHIB 2 went OSL at 32:13:58:44.192 G.m.t. and LHOB 2 went OSL at 32:13:58:54.189 G.m.t. Prior to this event, the pressures were at a nominal value of 350 to 355 psia, which is consistent with the expected pressures adjusted for wheel well environmental conditions given the post top-off tire pressures and leak rates obtained prior to launch.

The RHOB 2 tire-pressure measurement appeared to dip approximately 3 psi and then recovered to a nominal 355 psia. The pressure drop started at 32:13:58:45.199 G.m.t. This lasted for approximately 10 seconds after which the

pressure recovered until LOS. Prior to this event, the pressure was at a nominal 355 psia, which is consistent with the expected pressure adjusted for wheel well environmental conditions given the post top-off tire pressure and leak rate obtained prior to launch.

The left MLG down-lock indication transferred on at 32:13:59:05.877 G.m.t. and lasted through the LOS+32 period of reconstructed data. All other indications showed the gear was still up and locked during this time. Testing of the proximity sensor circuit has shown that it is possible for this indication to fail in this manner when wires are burned through.

At the beginning of the post-LOS 25-second data gap, the left MLG brake line temperature A measurement, located on the strut, indicated 103 ° F, while at the end of the gap it indicated 278 °F. Although the downlinked data has been verified to contain no errors, this is considered an erroneous measurement because the brake line B measurement, which is located beside the A measurement, indicated exactly the same value (118.6 °F) as before the gap. In addition, there is no significant change in the C and D measurements, which are located on the wheel-well wall near the hydraulic switching valve.

D.18.0 PURGE, VENT, AND DRAIN SUBSYSTEM PERFORMANCE EVALUATION

D.18.1 Executive Summary

The purge, vent and drain (PV&D) subsystem and hazardous gas detection subsystem (HGDS) performed nominally during all phases of the mission. During entry, all PV&D and HGDS parameters were nominal at loss-of-data. The vehicle drain system is passive; there is no telemetry to monitor or review.

D.17.2 Pre-launch/Ascent Performance

The PV&D subsystem and HGDS performed nominally during the pre-launch and ascent phases of the mission. The purge temperatures and flow rates were set to predetermined levels and stayed within nominal tolerances. Orbiter circuit 2 was supplied with a higher-than-normal flow rate (225 lb./min) because of the extended duration Orbiter (EDO) pallet requirement agreed to in the payload integration plan. The higher flow rate was within Orbiter purge system certification. During the T minus 9-minute hold, the circuit 2 flow-rate was reduced to 170 lb./min to alleviate the need for a post-flight inspection of the Orbiter T-0 purge-circuit quick-disconnect flappers. The inspection is required if separation occurs at a flow rate at or above 180 lb./min.

D.17.3 On-Orbit Performance

The PV&D subsystem and HGDS performed nominally during the on-orbit phase of the mission, as the subsystems are inactive during the on-orbit period.

D.17.4 Entry Performance

The PV&D subsystem and HGDS performed nominally during the entry phase of the mission.

D.19.0 ELECTRICAL POWER DISTRIBUTION AND CONTROL SUBSYSTEM PERFORMANCE EVALUATION

D.19.1 Executive Summary

The electrical power distribution and control (EPDC) subsystem performed nominally except for the sluggish ac 2 bus phase B current response initially noted post-ascent. During entry, all EPDC subsystem parameters were nominal at loss-of-data.

The ac 2 phase B sluggish current response (STS-107 MER Problem 1) was not present during PLBD closing or during entry, and had no effect on the Orbiter contingency. Prior to the last 2 seconds of reconstructed entry data, no EPDC measurements were lost, and there were no ac or dc bus shorts or losses.

D.19.2 Pre-launch/Ascent Performance

The EPDC subsystem pre-launch and ascent responses were nominal with the exception of the in-flight anomaly discussed in the following paragraph. This in-flight anomaly had no impact on mission accomplishment.

During vent-door opening, PLBD opening and Ku-band antenna deployment, the ac 2 bus phase B current exhibited a sluggish response. The phase B current increased to about one-half of the expected value, then increased to its nominal value within 0.5 to 1.5 seconds. During this time period, the ac 2 bus phases A and C current increased a similar amount. During steady-state periods, there were periodic occurrences of smaller magnitude signals of the same type (phase B dropping, phases A and C increasing). As before, most of these occurrences lasted between 0.5 and 1.5 seconds, and the phase B drop was between 0.2 and 0.3 ampere (between 3 and 4 telemetry counts). Water-loop pump cycling on the ac 2 bus sometimes triggered the described response. The occurrence of this condition was very sporadic and unpredictable. During a couple of 24-hour periods, no occurrences were noted. The cause of this anomaly was believed to be the ac 2 bus phase B inverter or the wiring between the ac 2 phase B inverter and panels L4 and MA73C.

D.19.3 On-Orbit Performance

The EPDC subsystem on-orbit operations were nominal with the exception of the anomaly discussed in the previous section. This in-flight anomaly had no impact on mission accomplishment.

D.19.4 Entry Performance

Off-nominal indications were identified in the last 32 seconds of reconstructed data. These are:

1. The 5-seconds of the reconstructed data had numerous data hits throughout the period. Based on the ASA 4 failure times during the 5 seconds of reconstructed data, three signatures were found on the aft main buses that could be 5-ampere remote power controller (RPC) trip signatures. The RPCs performed as designed.
2. In the 2-second period of reconstructed data, some of the EPDC data were missing, some data were available for only one data sample and some data were in conflict with confirming data. Three conclusions from the data are:

    a. There was a general upward shift in fuel cell and forward main bus amperes and a general downward shift in main bus voltages;
    b. Several confirming parameters indicate that the ac 3 phase A inverter was disconnected from its ac bus, and there was an increasingly high voltage and current load on ac 3 phases B and C.
    c. The fuel cell 1 amperes and single data samples indicate the possibility of a high load on ac 1 phase C.

D.20.0 DATA PROCESSING SYSTEM PERFORMANCE EVALUATION

D.20.1 Executive Summary

The data processing system (DPS) pre-launch, ascent and on-orbit operations were nominal. During entry, all DPS parameters were nominal at loss-of-data.

D.20.2 Pre-launch/Ascent Performance

No unexpected general-purpose computer (GPC) errors occurred during pre-launch or ascent operations. The mass memory unit (MMU) hardware was used successfully during the OPS 1 transition at T-20 minutes on launch day as the program was obtained from MMU 1 area 1 on the tape. Prior to launch, the Kennedy Space Center (KSC) performed a dump and compare of the entire software of GPC 1 with no miscompares identified. The multiplexer/demultiplexer (MDM) hardware performance was satisfactory as exhibited in the data review conducted after the contingency.

D.20.3 On-Orbit Performance

All DPS hardware performed satisfactorily during the on-orbit operations, and no in-flight anomalies were noted in the analysis of the data.

D/20.4 Entry Performance

The DPS entry operations were nominal. Fault messages were generated and are discussed in the appropriate sections of this appendix.

D.21.0 FLIGHT CONTROL SYSTEM HARDWARE PERFORMANCE EVALUATION

D. 21.1 Executive Summary

The flight control system (FCS) pre-launch, ascent and on-orbit operations were nominal. During entry, all FCS parameters were nominal at loss-of-data.

The 32-second period of reconstructed data indicate that there was an anomaly involving aerosurface actuator (ASA) 4. This condition has been evaluated and determined to be the result of a wiring short in the aft of the left wing.

D.21.2 Pre-launch/Ascent Performance

At all times, the Solid Rocket Booster (SRB) thrust vector controllers (TVC), MPS TVC, and aerosurface actuators were positioned exactly as the GPC commands were given with normal driver currents, secondary differential pressures, and elevon primary differential pressures. The reaction jet driver (RJD) operation was also normal with no thruster-fail indications or other anomalies noted. The rotational hand controller (RHC) and translation hand controller (THC) were both used and exhibited normal channel tracking.

At no time during the ascent of STS-107 did the flight controls fail to accomplish the task of implementing GPC commands. Actuator positions closely tracked GPC commands, and at no time did secondary differential pressures used in the fault detection mechanism approach the limits that would initiate a failure response.

D.21.3 On-Orbit Performance

The flight control hardware on-orbit performance was nominal. No anomalies were found in the data. The limited aerosurface data available also showed no anomalies. Flight control hardware performance during the on-orbit flight control system checkout was nominal. No anomalies were found in any of the tests or checkout prior to entry.

D.21.4 Entry Performance

The FCS performance during the entry phase was nominal until the final seconds before LOS.

The STS-107 aerosurface actuator performance was nominal until the final second before LOS, when the ASA 4 anomaly began to appear. Aerosurface position did follow GPC commands, even after the occurrence of the ASA 4 anomaly and until LOS + 5 seconds. Aerosurface actuator secondary differential

pressures were well below the bypass level and normal until the ASA 4 anomaly appeared.

At 32:13:59:31.7 G.m.t., aerosurface channel 4 positions either were at their null value or were transitioning toward their null value. Less than one second later at 32:13:59:32.396 G.m.t., the power was current-limiting and the voltage had dropped sufficiently for both remote power controllers (RPCs) for ASA 4 to drive the RPC trip measurement (1 Hz). Secondary differential pressure data indicates channel 4 on the right outboard elevon, right inboard elevon, left inboard elevon, left outboard elevon, rudder, and speedbrake were bypassed. The channel 4 fail flag was raised on the right outboard elevon, right inboard elevon, left inboard elevon, left outboard elevon, rudder, and speedbrake at 32:13:39:32.1 G.m.t. (1-Hertz measurement).

The channel 4 driver currents on the right outboard elevon, right inboard elevon, left inboard elevon, left outboard elevon, and speedbrake were non-zero (driving the channel 4 servo valve). A force fight occurred between channel 4 and the other 3 channels on the left outboard elevon from 32:13:59:32.597 G.m.t. to 32:13:59:34.318 G.m.t., as indicated by secondary differential pressure data. This force fight began when the bypass valve on channel 4 reopened (non-bypassed state) and allowed the servo valve to become active.

At 32:13:59:34.536 G.m.t., speedbrake channel 1, 2, and 3 secondary differential pressures indicate a force fight against channel 4. The secondary differential pressure on channel 4 was at null. The isolation valve power RPC was tripped at this point, removing power from the bypass valves on all actuators for channel 4. At 32:13:59:35.077 G.m.t., the actuator fail flags from ASA 4 had turned off.

At approximately 32:14:00:04 G.m.t., just prior to final LOS, aerosurface switching valves are indicated to be in their secondary positions, while the valves are expected to be in their primary positions with zero hydraulic pressure in all three hydraulic systems. In the same time period (32:14:00:04 G.m.t.), all aerosurface position indications read zero volts. Also in the same time period, ASA 1, 2 and 3 RPC indications show that they are off while the ASA 1, 2 and 3 power-on commands show on. In the same time period (32:14:00:04 G.m.t.), there are valid hydraulic reservoir temperatures, rudder/speedbrake actuator return line temperatures, right elevon actuator temperatures, body flap temperatures and MPS TVC return line temperatures, but no valid left elevon actuator temperatures or hydraulic return line temperatures.

D.22.0 INERTIAL MEASUREMENT UNIT PERFORMANCE EVALUATION

D.22.1 Executive Summary

The inertial measurement unit (IMU) pre-launch, ascent and on-orbit operations were nominal. During entry, all FCS parameters were nominal at loss-of-data.

D.22.2 Pre-launch/Ascent Performance

The IMU pre-launch and ascent performance was nominal. The IMUs measured and reflected the Orbiter changes in attitude and velocity due to the nominal ascent activities. Review of the IMU pre-launch and ascent data did not show any anomalous conditions.

D.22.3 On-Orbit Performance

The IMU on-orbit operations were nominal. The IMUs measured and reflected the Orbiter changes in attitude and velocity due to the nominal on-orbit operations. Review of the IMU on-orbit data did not show any anomalous conditions.

D.22.4 Entry Performance

The overall performance of the three IMUs during entry was nominal. The IMUs measured and reflected the Orbiter changes in attitude and velocity due to the nominal entry activities. The deorbit firing and energy reduction maneuvers were accurately tracked by all three IMUs. The post-LOS data indicated continued nominal velocity changes, but large attitude changes were noted between the first few seconds of data and the small sample of data at the end.

D.23.0 STAR TRACKER SUBSYSTEM PERFORMANCE EVALUATION

D.23.1 Executive Summary

The star tracker subsystem was powered off during ascent and no subsystem data are available. The star tracker subsystem performance on-orbit was nominal. The star tracker was powered off during entry.

D.23.2 Prelaunch/Ascent Performance

The star tracker subsystem was powered off during ascent and no subsystem data are available.

D.23.3 On-Orbit Performance

The star tracker subsystem performance on-orbit was nominal. Review of the star tracker subsystem data from the on-orbit period indicated no anomalous or off-nominal performance.

D.23.4 Entry Performance

The star tracker subsystem was powered off during entry and no subsystem data are available.

D.24.0 NAVIGATIONAL AIDS SUBSYSTEM PERFORMANCE EVALUATION

D.24.1 Executive Summary

All navigational aids subsystem (NAVAIDS) operations were nominal during the pre-launch, ascent and on-orbit operations. During entry, all NAVAIDS parameters were nominal at loss-of-data. Based on the analysis of the data, the conclusion is that the NAVAIDS were nominal and had no involvement in the catastrophic failure that preceded the loss of the *Columbia* during the entry phase of the STS-107 mission.

D.24.2 Pre-launch/Ascent Performance

The overall performance of the NAVAIDS was nominal during pre-launch and ascent operations. All three tactical air navigation (TACAN) systems remained locked on to KSC during the ascent and broke lock when the station was out of range. The NAVAIDS were powered off after the operational sequence (OPS) 2 transition.

D.24.3 On-Orbit Performance

The NAVAIDS are normally powered off during the on-orbit phase until the transition to OPS 8 for the FCS checkout approximately 24 hours prior to the predicted landing. All of the NAVAIDS successfully passed the self-test during the FCS checkout. The NAVAIDS were then powered off after the OPS 2 transition. No deviations or significant events were observed in the NAVAIDS performance.

D.24.4 Entry Performance

All NAVAIDS subsystems were powered on at 32:09:30:05 G.m.t., and were functioning nominally prior to loss of signal (LOS). The TACAN systems had locked on to various channel 111X ground stations during the pass over the United States just prior to the de-orbit maneuver and that was nominal operation. The TACAN systems were in the search mode, but were out-of-range of the KSC ground station when LOS occurred at 32:13:59:32:174 G.m.t. The TACAN systems remained in the search mode during the extra 32 seconds of telemetry data that were later recovered. At 32:13:47:37 G.m.t., radar altimeter 1 locked on to plasma. At 32:13:47:39 G.m.t., radar altimeter 2 locked on to plasma. At 32:13:48:53 G.m.t., radar altimeter 2 broke lock on the plasma and remained un-locked until 32:13:59:26:20 G.m.t., when one sample indicating 800 feet was observed. Radar altimeter 1 remained locked on to the plasma until 32:13:58:45:00 G.m.t., and then broke lock until 32:13:59:34:30 G.m.t., when one sample indicating 5200 feet was observed. The 800 feet and 5200 feet indications were proven to be invalid and were disregarded. The radar altimeter

data were compared with the data from previous OV-102 missions, including STS-109, STS-93 and STS-90. Similar radar altimeter signatures were observed for these flights when compared with the data from STS-107. The radar altimeter performance was determined to be nominal. The three microwave-scanning-beam landing systems (MSBLS) were powered on but were out-of-range of the KSC ground station and did not lock on. The MSBLS indications were nominal. The MSBLS were still out-of-range of the ground station during the extra 32 seconds of telemetry data that were later recovered.

D.25.0 S-BAND SUBSYSTEM PERFORMANCE EVALUATION

D.25.1 Executive Summary

All S-Band subsystems and processors including S-Band phase-modulated (PM) system 2 and S-Band frequency modulated (FM) system 1 performed nominally during the pre-launch, ascent and on-orbit phases of STS-107. During entry, all S-Band subsystem and processor parameters were nominal at loss-of-data.

D.25.2 Pre-launch/Ascent Performance

The overall performance of the communications and tracking (C&T) subsystems during the pre-launch and ascent phase was nominal. The payload signal processor (PSP) was configured and tested satisfactory during pre-launch and then powered off per procedures prior to launch. S-Band PM system string 1 and 2 and the S-Band FM system were powered on and a checkout of these systems was completed prior to-launch. The S-Band PM system string 2 provided nominal S-Band Orbiter telemetry and air-to-ground (A/G) voice communication overage during the pre-launch, launch, and ascent phases. There were no off-nominal telemetry indications from any S-Band subsystems or processors.

D.25.3 On-Orbit Performance

The overall performance of the C&T subsystems was nominal during the on-orbit phase. The PSP was powered on, configured for SpaceHab support, and operated nominally until powered off at SpaceHab de-activation prior to the deorbit maneuver. During on-orbit operations, the S-Band FM system was occasionally powered on for operations recorder dumps via ground stations and powered off again when not in use. The S-Band PM systems string 2 provided nominal S-Band Orbiter telemetry and A/G voice communication coverage in the Tracking and Data Relay Satellite (TDRS) mode during the majority of the on-orbit phase. There were no off-nominal telemetry indications from either of the S-Band PM subsystems in any operational mode and S-Band communication coverage was nominal throughout the on-orbit phase.

D.25.4 Entry Performance

The overall performance of the C&T subsystems hardware during entry was nominal. The S-band communications coverage via the TDRS was as good as anticipated and very comparable to previous Shuttle entries at the same orbital inclination of 39 degrees. There were several S-Band return-link data dropouts during entry from 32:13:50:00 G.m.t. to 32:13:56:00 G.m.t. that cannot be explained. The antenna look-angles to the TDRS during this period would not typically result in dropouts. Data dropouts after this period until the final LOS

were not unexpected based on the antenna look angles to the TDRS. There were no off-nominal telemetry indications from any C&T subsystem.

The recovered data after the 25-second LOS indicated the BFS software commanded a switch from the upper right aft (URA) antenna to upper right forward (URF) antenna at 32:14:00:04 G.m.t., and there were ins trumentation indications of the execution of the commanded switch. This conclusion was based on the two antenna switch discretes and the analog value of power amplifier (PA) reflected power, which were consistent with the performance characteristics the URF antenna.

D.26.0 Ku-BAND SUBSYSTEM PERFORMANCE EVALUATION

D.26.1 Executive Summary

The overall performance of the Ku-Band subsystem was nominal with no in-flight anomalies found during data analysis. During entry, all Ku-band subsystem parameters were nominal at loss-of-data.

D.26.2 Pre-launch/Ascent Performance

The overall performance of the Ku-Band subsystem during the pre-launch and ascent phases was nominal. The Ku-Band deployed assembly was stowed for ascent. Telemetry and operations indicate that the Ku-Band was still in its nominal ascent position prior to on-orbit deployment.

D.26.3 On-Orbit Performance

The overall performance of the Ku-Band subsystem during the on-orbit phase was nominal. The Ku-Band assembly was deployed at 16:17:54 G.m.t. in the expected dual motor time of 23 seconds. All telemetry measurements indicated the Ku-Band deployed assembly transitioned from the stowed to the deployed position. The Ku-Band system was activated at 16:17:58 G.m.t., passed the self-test, and functioned properly throughout the mission until it was nominally stowed and powered off at 32:01:47 G.m.t.

D.26.4 Entry Performance

The Ku-Band deployed assembly was stowed for entry. Telemetry indicates that the Ku-Band was still in its nominal position during entry.

D.27.0 INSTRUMENTATION SUBSYSTEM PERFORMANCE EVALUATION

D.27.1 Executive Summary

The overall performance of the instrumentation subsystem during the pre-launch, ascent and entry was nominal with no in-flight anomalies identified during the data analysis. During entry, all instrumentation subsystem parameters were nominal at loss-of-data.

D.27.2 Pre-launch/Ascent Performance

The OI and Orbiter experiments (OEX) recorder subsystems performed nominally throughout the STS-107 pre-launch and ascent phases. No significant events or findings were found during the data analysis.

D.27.3 On-Orbit Performance

The overall performance of the instrumentation subsystem during the on-orbit phase was nominal. Review of the OI subsystem on-orbit data indicated no in-flight anomalies or anomalous conditions in the subsystem performance.

D.27.4 Entry Performance

The overall performance of the instrumentation subsystem during the entry phase was nominal until loss of signal. There were no indications of any anomalous performance in any of the subsystem hardware. A number of individual measurements failed or had anomalous readings in the minutes immediately prior to loss of signal. All of these are apparently related to the accident.

During entry operations, several of the hydraulic measurements failed to off-scale-low. These were:

Hydraulic system 3 left outboard elevon return line temperature;
Hydraulic system 1 left-hand inboard elevon actuator return line temperature;
Hydraulic system 1 left outboard elevon return line temperature; and
Hydraulic system 2 left outboard elevon return line temperature.

All tire pressure and wheel temperature measurements for the left-hand MLG were then observed to have drifted lower and failed to OSL. The left-hand outboard tire pressure 1 began drifting lower at 32:13:58:34 G.m.t., and failed OSL at 32:13:58:38 G.m.t. The left-hand inboard tire pressure 1 began drifting lower at 32:13:58:33 G.m.t. and failed OSL at 32:13:58:40 G.m.t. The left-hand inboard wheel temperature began drifting lower at 32:13:58:35 G.m.t., and failed OSL at 32:13:58:45 G.m.t. The left-hand inboard tire pressure began drifting

lower at 32:13:58:41 G.m.t. and failed OSL at 32:13:58:48 G.m.t. The left-hand outboard wheel temperature began drifting lower at 32:13:58:35 G.m.t., and failed OSL at 32:13:59:40 G.m.t. The left-hand outboard tire pressure 2 began drifting lower at 32:13:58:39 G.m.t., and failed OSL at 32:13:58:54 G.m.t.

The failed measurements used multiple dedicated signal conditioners (DSC) with no more than one affected measurement using a single DSC card. Similarly multiple MDM cards in more than one MDM were used. The failed tire-pressure measurements used two different strain gage signal conditioners (SGSC).

Temperatures in the area of the midbody DSC's and SGSC remained nominal (50-55 °F) until loss of data. As the measurements utilized multiple DSC's, the source of the failures is not believed to be related to a signal conditioner. Temperatures at the wheel itself were increasing but not high enough to cause transducer failure. Furthermore, the staggered loss of the individual measurements suggests that the failures were measurement failures, rather than actual loss of tire pressure.

The source of the failures is consequently believed to be in the wire harnesses between the wheel area and the midbody. Since the measurements did not exhibit the characteristics observed with breakage of the wheel separation harness, it is more likely to be due to heat-related degradation of the wiring harnesses in the vicinity of the left-hand wheel well.

Review of the post-LOS data did not alter the conclusions reached, and no additional anomalies were identified.

The OEX recorder was recovered and the data were successfully retrieved indicating that the hardware performed nominally. These data were extremely helpful to the investigation as data were recorded until the breakup of the vehicle. The vast majority of the left-wing measurements failed apparently because of heat-related degradation of wiring harnesses in the left wing.

D.28.0 DISPLAYS AND CONTROLS SUBSYSTEM PERFORMANCE EVALUATION

D.28.1 Executive Summary

Review of the Displays and Controls (D&C) subsystem pre-launch, ascent and on-orbit data indicated nominal system performance with no anomalous conditions observed. During entry, all D&C subsystem parameters were nominal at loss-of-data.

D.28.2 Pre-launch/Ascent Performance

The D&C subsystem was in the normal configuration and exhibited nominal operation during the pre-launch and ascent phase. All pre-launch master alarm occurrences were attributable to expected operations.

D.28.3 On-Orbit Performance

The D&C subsystem performed nominally during the on-orbit phase of the mission.

D.28.3 Entry Performance

The D&C subsystem exhibited nominal operation during the entry phase, including the additional 32-second period of reconstructed data. During the entry phase up to the additional 32-second time frame, the master alarms annunciated were correlated to the individual subsystems that triggered the alarms.

The downlisted data for the caution and warning master alarm subsystem shows evidence of the master alarm annunciating continuously from 32:13:59.33.863 to 32:14:00:04.760 G.m.t., which includes the additional 32-second period of reconstructed data. The data review indicates several subsystems could have triggered the master alarm. Each individual subsystem with possible master alarm triggers has been evaluated for validity of the master alarm data relative to that subsystems performance. A review of the BFS data reveals a correlation of the events with the downlisted caution and warning master alarm telemetry data.

Appendix D
Subsystem Data Review Summary Report

D.29.0 MULTIFUNCTION ELECTRONIC DISPLAY SUBSYSTEM PERFORMANCE EVALUATION

D.29.1 Executive Summary

The overall performance of the MEDS was nominal during the pre-launch, ascent and on-orbit phases with no in-flight anomalies identified during the analysis of the data. During entry, all MEDS subsystem parameters were nominal at loss-of-data.

D.29.2 Pre-launch/Ascent Performance

The overall performance of the MEDS was nominal during the pre-launch and ascent phases. There were no significant deviations from the nominal/expected operation of the MEDS subsystem during the pre-launch/ascent period; all downlisted Edge Key inputs reflect those that would be expected during normal operations.

D.29.3 On-Orbit Performance

The overall performance of the MEDS was nominal during the on-orbit operations was nominal. There were no significant deviations from the nominal/expected operation of the MEDS subsystem during the on-orbit period; all downlisted Edge Key inputs reflect those that would be expected during normal operations.

D.29.4 Entry Performance

The MEDS subsystem operation was nominal during the entry until loss-of-data and LOS.

Appendix D
Subsystem Data Review Summary Report

D.30.0 AIR DATA TRANSDUCER ASSEMBLY HARDWARE PERFORMANCE EVALUATION

D30.1 Executive Summary

The air data transducer assembly (ADTA) hardware performed satisfactorily during the entry phase of the mission. The ADTA probes were not deployed so no data were received on that subsystem operation.

D.30.2 Pre-launch/Ascent Performance

The ADTA is not deployed during the ascent phase and no data were received.

D.30.3 On-Orbit Performance

The ADTA is not deployed during the on-orbit phase and no data were received.

D.30.4 Entry Performance

The ADTA performed nominally during FCS checkout and from power-on for deorbit through loss of signal. Pressure indications from all 16 ADTA transducers were well within redundancy management (RM) limits, and all mode/status word indications were satisfactory. Data also shows that the air data probes (ADPs) were not deployed during this phase of entry. Probe temperatures were in the normal range for stowed ADPs.

The ADTA data is not used by GN&C until the crew manually enables the data around Mach 3.5. The air data probes remain stowed until around Mach 5 during entry. At the time of LOS, the ADTA transducers were reading within ± 0.040 inch Hg between transducers connected to the same-side air data probe and ± 0.080 inch Hg between transducers connected to opposite-side air data probes. The ADTAs were reading the ambient pressure inside the forward RCS cavity and responding to very small changes in pressure due to vehicle motion and attitude. Pressures from the left probe were slightly higher than pressures from the right, but these differences are not atypical of ADTA performance during this phase of flight. Data during a similar portion of entry from STS-109 and STS-110 have been reviewed as comparisons.

ADTA data was not being used at the time of vehicle loss and could not have been a factor in the mishap. In addition, the ambient ADTA data shows no indication of abnormal vehicle GN&C.

Appendix E
STS-107 Mishap Investigation Timeline Instrumentation Data
Note: nm = no data

No.	MSID / ID No.	OEX	OI	Type	Title	Location X	Location Y	Location Z	Range OSL	Range OSH	Sample Rate	Units
1	V07P9036A	X		Press	L Wing Upper Surface Press (WB 3)	1334	-423.5	UPR	0	16	10 sps	PSIA
2	V07P9086A	X		Press	L Wing Lower Surface Press (WB 3)	1383.4	-419.1	LWR	0	16	10 sps	PSIA
3	V07P9181A	X		Press	Right Wing Lower Surface Press	1407.8	1917.8	LWR	0	16	10 sps	PSIA
4	V07T9213A	X		Temp	OMS-L Pod LRSI Surf 1-AFT	1321	LH	464	0	1740	1 sps	Deg F
5	V07T9222A	X		Temp	OMS-L Pod HRSI Surf 2-AFT	1321	LH	464	0	1740	1 sps	Deg F
6	V07T9222A	X		Temp	OMS-L Pod HRSI Surf 2-AFT	1486.9	-108	422	0	1740	1 sps	Deg F
7	V07T9223A	X		Temp	OMS-L Pod HRSI Surf 3-AFT	1437.2	-108	422	0	1740	1 sps	Deg F
8	V07T9065A	X		Temp	Left Fuselage Side Surface TC BP1965T	1009.7	-165	564.5	0	1740	1 sps	Deg F
9	V07T9270A	X		Temp	Fuselage Side Surface Thermocouple BP3976T	1560	-111.1	LWR	0	1740	1 sps	Deg F
10	V07T9468A	X		Temp	Fuselage Lower Surface Thermocouple X619	618.9	0	LWR	900	2700	10 sps	DegF
11	V07T9470A	X		Temp	Fuselage Lower Surface Thermocouple X620	620.1	-51.1	LWR	900	2700	10 sps	DegF
12	V07T9471A	X		Temp	Fuselage Lower Surface Thermocouple X1004	1003.8	0	LWR	900	2700	10 sps	DegF
13	V07T9469A	X		Temp	Fuselage Lower Surface TC BP1602TR	1004.1	-99.8	LWR	900	2700	10 sps	Deg F
14	V07T9469A	X		Temp	Fuselage Lower Surface TC BP1900T	1391.5	0	LWR	900	2700	10 sps	Deg F
15	V07T9469A	X		Temp	Fuselage Lower Surface TC BP1902TR	1511.1	1.3	LWR	900	2700	10 sps	Deg F
16	V07T9539A	X		Temp	Fuselage Lower Surface Thermocouple	1549.3	-111.1	LWR	0	2400	10 sps	Deg F
17	V07T9540A	X		Temp	Left Wing Lower Surface TC BP4801T	1446.3	1514.8	LWR	0	2400	10 sps	Deg F
18	V07T9539A	X		Temp	Left Wing Upper Surface TC BP4880T	1397.8	358	UPR	0	900	1 sps	Deg F
19	V07T9066A	X		Temp	WING LWR SURF THERMOCOUPLE BP2910T	1121.7	-236.5	LWR	0	2400	10 sps	Deg F
20	V07T9074A	X		Temp	Left Wing Lower Surface Thermocouples	1353.1	-236.4	LWR	800	2700	10 sps	Deg F
21	V07T9074A	X		Temp	Left Wing Lower Surface Thermocouples	1382.2	-236.4	LWR	0	2400	10 sps	Deg F
22	V07T9713A	X		Temp	WING LWR SURF ELEVON TC BP2870T	1402	-375.3	LWR	0	3000	1 sps	Deg F
23	V07T9704A	X		Temp	Left Half Lower Aft Fuselage Surface	1443	-117	LWR	0	2400	10 sps	Deg F
24	V07T9705A	X		Temp	Left Half OTBD Lower Elevon Forward Surface	1396.1	-372.2	LWR	0	3000	1 sps	Deg F
25	V07T9706A	X		Temp	Left Half OTBD Lower Elevon Aft Surface	1397.2	-372.2	LWR	0	3000	1 sps	Deg F
26	V07T9707A	X		Temp	AFT FUS LWR AFT SURFACE	1513	-116	LWR	0	2400	10 sps	Deg F
27	V07T9708A	X		Temp	BODY FLAP LH LWR OTBD FWD	1530	-119.4	LWR	0	2400	10 sps	DegF
28	V07T9603A	X		Temp	Left Fuselage Side Surface TC BP3604T	1006	-105	398.4	0	1300	1 sps	Deg F
29	V07T9613A	X		Temp	FUSLG SIDE SURFACE TC BP3605T	1103.8	LH	441.3	0	1740	1 sps	Deg F
30	V07T9607A	X		Temp	Left OMS Pod TC BP4790T	1104.4	LH	447.4	0	1740	1 sps	Deg F
31	V07T9972A	X		Temp	Left OMS Pod TC BP0740T	1324	-99	468	0	1300	1 sps	Deg F
32	V07T9975A	X		Temp	Left OMS Pod TC BP0731T	1342.5	-128.5	462.6	0	1740	1 sps	Deg F
33	V07T9979A	X		Temp	OMS-L Pod Thermocouple BP0732T	1359.6	-126.1	463.1	0	1300	1 sps	Deg F
34	V07T9980A	X		Temp	LEFT OMS POD THERMOCOUPLE BP0731R	1359.6	-126.1	463.1	0	1300	1 sps	Deg F
35	V09T1002A		X	Temp	Left Lower Wing Skin Temp	1250.1	240	LWR	-200	450	1 sps	Deg F
36	V09T1006A		X	Temp	Left INBD Elevon Lower Skin Temp	1441.9	-234.5	1019	-200	450	1 sps	Deg F
37	V09T1016A		X	Temp	Mid Fus Bot Port BL Temp X620 - Center Line	620	-52.4	BOT	-200	450	1 sps	Deg F
38	V09T1022A		X	Temp	Mid Fus Bot Port BL Temp X777 - Center Line	777	-52.5	BOT	-200	450	1 sps	Deg F
39	V09T1024A	X		Temp	Fwd Fus Lwr Skin Bot Center Line Temp	1280.7	240	LWR	-200	450	1 sps	Deg F
40	V09T1624A		X	Temp	Fwd Fus Lwr Skin Bot Center Line Temp	560	240	277	-200	450	1 sps	Deg F
41	V09T1724A		X	Temp	LH Aft Fus Sidewall Temp at x1410	1410	nm	340	-200	450	1 sps	Deg F
42	V09T9231A	X		Temp	Elevon LWR PLUG TEMP T (Surface) P171	1443.5	-232.2	LWR	0	3000	1 sps	Deg F
43	V09T9645A	X		Temp	Outboard ELEVON MID GAP Fwd	1446.4	-316	LWR	0	2400	10 sps	Deg F
44	V09T9648A	X		Temp	Outboard ELEVON Lower Surface Edge	1428.1	-315.3	LWR	0	2400	10 sps	Deg F
45	V09T9653A	X		Temp	Wing Elevon Cove LWR Surface Temp	1382.2	-372.2	LWR	-200	450	1 sps	Deg F
46	V09T9693A	X		Temp	Wing Elevon Cove LWR Surface Temp	1388.8	-372.2	260.9	0	2400	10 sps	Deg F
47	V09T9694A	X		Temp	Wing Elevon Cove UPR Surface Temp	1381.7	-372.2	260.9	0	2400	10 sps	Deg F
48	V09T9695A	X		Temp	Wing Front Spar Panel 9 Temp	1182.2	239	239	-200	450	1 sps	Deg F
49	V09T9696A	X		Temp	Wing Front Spar Panel 9 Temp	1182.2	239	239	-200	450	1 sps	Deg F
50	V12G9048A	X		Stain	L WING SPAR CAP LWR L 103	1040	-135	LWR	-1000	1000	10 sps	uin/n
51	V12G9049A	X		Stain	L WING SPAR CAP UPR L104	1040	-135	UPR	-1000	1000	10 sps	uin/n
52	V12G9156A	X		Stain	LEFT WING UPR SKIN STN X X1 115 Y136	1115	-136	UPR	-2000	1500	10 sps	uin/n
53	V12G9157A	X		Stain	LEFT WING UPR SKIN STN XY X1 115 Y136	1115	-136	UPR	-1500	1500	10 sps	uin/n
54	V12G9158A	X		Stain	LEFT WING UPR SKIN STN XY X1 115 Y136	1115	-136	UPR	-1200	1200	10 sps	uin/n
55	V12G9165A	X		Stain	LEFT WING SPAR WEB STN Z X1040 Y132	1040	-132	MID	-2000	2000	10 sps	uin/n
56	V12G9166A	X		Stain	LEFT WING SPAR WEB STN YZ X1040 Y132	1040	-132	MID	-2000	2000	10 sps	uin/n
57	V12G9167A	X		Stain	LEFT WING SPAR WEB STN Y X1040 Y132	1040	-132	MID	-2000	2000	10 sps	uin/n
58	V12G9168A	X		Stain	LEFT WING FRONT SPAR WEB OUTER L120	1106	-229	MID	-1500	1000	10 sps	uin/n
59	V12G9921A	X		Stain	LEFT WING FRONT SPAR WEB INNER L120	1106	-229	MID	-1500	1000	10 sps	uin/n
60	V34T1106A		X	Temp	M-FUS LT BL Temp at x1215	1215	-105	395	-200	450	1 sps	DegF
61	V34T1116A		X	Temp	Mid Fus Port (Left) Sill Longr Temp at x1215	1215	-97	410	-200	450	1 sps	DegF
62	V34T9508A	X		Press	MLG LH Inbd Tire Pressure 1	1074	-160	nm	230	401	1 sps	PSIA
63	V5P9057A	X		Press	MLG LH Inbd Tire Pressure 1	1074	-116	nm	230	401	1 sps	PSIA
64	V5P9059A	X		Press	MLG LH Outbd Tire Pressure 2	1074	-160	nm	230	401	1 sps	PSIA
65	V5P9059A	X		Press	MLG LH Inbd Tire Pressure 2	10747	-1607	nm	230	401	1 sps	PSIA
66	V61T0074A	X		Temp	MLG LH Outbd Wheel Temp	1074	-1607	nm	-75	175	1 sps	Deg F
67	V61T0075A	X		Temp	MLG LH Inbd Wheel Temp	1074	-116	nm	-75	175	1 sps	Deg F
68	V61T0077A	X	Derived	Temp	Left Main Gear Strut Actuator Temperature	1377	-1352	nm	0	300	1 sps	Deg F
69	V07T9023SA	X	Derived		SPEED BRAKE ACTR CHAN 4 PCSN	n/a	n/a	n/a	0	98.6	5 sps	DEG
70	V57P0080A	X		Press	SPEED BRAKE DELTA PRESS 1	(Below Vert Fin/Rudder areas)			-3000	3000	25 sps	PSID
71	V57P0081A	X		Press	SPEED BRAKE DELTA PRESS 2	(Below Vert Fin/Rudder areas)			-3000	3000	25 sps	PSID
72	V58P0082A	X		Press	RUDDER DELTA PRESS 3	(Below Vert Fin/Rudder areas)			-3000	3000	25 sps	PSID
73	V58P0083A	X		Press	LEFT OUTBD ELEVON SEC DELTA PRESS 4 (see Notes (*))	1365	387	108	-3000	3000	25 sps	PSID
74	V58P0091SA	X		Press	RIGHT INBD ELEVON SEC DELTA PRESS 4 (see Notes (*))	1365	387	108	-3000	3000	25 sps	PSID
75	V58T0135A	X	X	Temp	Hyd Sys 1 LMG Up Lk Actr Unlk Ln Temp	1159	-123.5	436	-75	300	1 sps	Deg F
76	V58T0137A	X	X	Temp	Hyd Sys 1 Lnd INBD Elevon Actr Ret Ln Temp	1360	-219	198	-75	300	1 sps	Deg F
77	V58T0225A	X	X	Temp	Left Main Gear Strut Actuator Temperature	1377	-2352	1438	-75	300	1 sps	Deg F
78	V58T0237A	X	X	Temp	Hyd Syst 2 LIE Return Line Temp	1348	-219	116	-75	300	1 sps	Deg F
79	V58T0394A	X	X	Temp	Hyd Syst 3 LOE Return Line Temp	1368	398	nm	-75	300	1 sps	Deg F
80	V58T0405A	X	X	Temp	LEFT MAIN GEAR STRUT ACTUATOR TEMP	1182.5	-116	315.5	-75	300	1 sps	Deg F
81	V58T0841A	X	X	Temp	HYD 2 LH AFT BRAKE SW VLV RTN LN TEMP	1173	-107	313	-75	300	1 sps	Deg F
82	V58T1702A	X	X	Temp	HYD 1 LH AFT BRAKE SW VLV RTN LN TEMP	1166.5	-109.5	313.7	-75	300	1 sps	Deg F
83	V58T1703A	X	X	Temp	LMG Brake Line Temp A (Sensor Near MLG Door)	1166	-140.4	282.8	-75	300	1 sps	Deg F
84	V58T1701A	X	X	Temp	LMG Brake Line Temp B	1116	-139.6	282.8	-75	300	1 sps	Deg F

Appendix E
STS-107 Mishap Investigation Timeline Instrumentation Data
Note: nm = no data

No.	MSID / ID No.	OEX	OI	Type	Title	Location X	Location Y	Location Z	Range OSL	Range OSH	Sample Rate	Units
44	V09T9648A	X		Temp	Outboard ELEVON Lower Surface Edge	1428.1	-315.3	LWR	0	2400	10 sps	Deg F
45	V09T9653A	X		Temp	Wing Elevon Cove LWR Surface Temp	1382.2	-372.2	LWR	-200	450	1 sps	Deg F
46	V09T9693A	X		Temp	Wing Elevon Cove LWR Surface Temp	1388.8	-372.2	260.9	0	2400	10 sps	Deg F
47	V09T9694A	X		Temp	Wing Elevon Cove UPR Surface Temp	1381.7	-372.2	260.9	0	2400	10 sps	Deg F
48	V09T9695A	X		Temp	Wing Front Spar Panel 9 Temp	1182.2	239	239	-200	450	1 sps	Deg F
49	V09T9696A	X		Temp	Wing Front Spar Panel 9 Temp	1182.2	239	239	-200	450	1 sps	Deg F
50	V12G9048A	X		Stain	L WING SPAR CAP LWR L 103	1040	-135	LWR	-1000	1000	10 sps	uin/n
51	V12G9049A	X		Stain	L WING SPAR CAP UPR L104	1040	-135	UPR	-1000	1000	10 sps	uin/n
52	V12G9156A	X		Stain	LEFT WING UPR SKIN STN X X1 115 Y136	1115	-136	UPR	-2000	1500	10 sps	uin/n
53	V12G9157A	X		Stain	LEFT WING UPR SKIN STN XY X1 115 Y136	1115	-136	UPR	-1500	1500	10 sps	uin/n
54	V12G9158A	X		Stain	LEFT WING UPR SKIN STN XY X1 115 Y136	1115	-136	UPR	-1200	1200	10 sps	uin/n
55	V12G9165A	X		Stain	LEFT WING SPAR WEB STN Z X1040 Y132	1040	-132	MID	-2000	2000	10 sps	uin/n
56	V12G9166A	X		Stain	LEFT WING SPAR WEB STN YZ X1040 Y132	1040	-132	MID	-2000	2000	10 sps	uin/n
57	V12G9167A	X		Stain	LEFT WING SPAR WEB STN Y X1040 Y132	1040	-132	MID	-2000	2000	10 sps	uin/n
58	V12G9168A	X		Stain	LEFT WING FRONT SPAR WEB OUTER L120	1106	-229	MID	-1500	1000	10 sps	uin/n
59	V12G9921A	X		Stain	LEFT WING FRONT SPAR WEB INNER L120	1106	-229	MID	-1500	1000	10 sps	uin/n
60	V34T1106A		X	Temp	M-FUS LT BL Temp at x1215	1215	-105	395	-200	450	1 sps	DegF
61	V34T1116A		X	Temp	Mid Fus Port (Left) Sill Longr Temp at x1215	1215	-97	410	-200	450	1 sps	DegF
62	V58T0082A	X	X	Press	RUDDER DELTA PRESS 3	(Below Vert Fin/Rudder areas)			-3000	3000	25 sps	PSID
63	V5P9057A	X		Press	MLG LH Inbd Tire Pressure 1	1074	-116	nm	230	401	1 sps	PSIA
64	V5P9059A	X		Press	MLG LH Outbd Tire Pressure 2	1074	-160	nm	230	401	1 sps	PSIA
65	V5P9059A	X		Press	MLG LH Inbd Tire Pressure 2	10747	-1607	nm	230	401	1 sps	PSIA
66	V61T0074A	X		Temp	MLG LH Outbd Wheel Temp	1074	-1607	nm	-75	175	1 sps	Deg F
67	V61T0075A	X		Temp	MLG LH Inbd Wheel Temp	1074	-116	nm	-75	175	1 sps	Deg F
68	V61T0077A	X	Derived	Temp	Left Main Gear Strut Actuator Temperature	1377	-1352	nm	0	300	1 sps	Deg F
69	V07T9023SA	X	Derived		SPEED BRAKE ACTR CHAN 4 PCSN	n/a	n/a	n/a	0	98.6	5 sps	DEG
70	V57P0080A	X		Press	SPEED BRAKE DELTA PRESS 1	(Below Vert Fin/Rudder areas)			-3000	3000	25 sps	PSID
71	V57P0081A	X		Press	SPEED BRAKE DELTA PRESS 2	(Below Vert Fin/Rudder areas)			-3000	3000	25 sps	PSID
72	V58P0082A	X		Press	RUDDER DELTA PRESS 3	(Below Vert Fin/Rudder areas)			-3000	3000	25 sps	PSID
73	V58P0083A	X		Press	LEFT OUTBD ELEVON SEC DELTA PRESS 4 (see Notes (*))	1365	387	108	-3000	3000	25 sps	PSID
74	V58P0091SA	X		Press	RIGHT INBD ELEVON SEC DELTA PRESS 4 (see Notes (*))	1365	387	108	-3000	3000	25 sps	PSID
75	V58T0135A	X	X	Temp	Hyd Sys 1 LMG Up Lk Actr Unlk Ln Temp	1159	-123.5	436	-75	300	1 sps	Deg F
76	V58T0137A	X	X	Temp	Hyd Sys 1 Lnd INBD Elevon Actr Ret Ln Temp	1360	-219	198	-75	300	1 sps	Deg F
77	V58T0225A	X	X	Temp	Left Main Gear Strut Actuator Temperature	1377	-2352	1438	-75	300	1 sps	Deg F
78	V58T0237A	X	X	Temp	Hyd Syst 2 LIE Return Line Temp	1348	-219	116	-75	300	1 sps	Deg F
79	V58T0394A	X	X	Temp	Hyd Syst 3 LOE Return Line Temp	1368	398	nm	-75	300	1 sps	Deg F
80	V58T0405A	X	X	Temp	LEFT MAIN GEAR STRUT ACTUATOR TEMP	1182.5	-116	315.5	-75	300	1 sps	Deg F
81	V58T0841A	X	X	Temp	HYD 2 LH AFT BRAKE SW VLV RTN LN TEMP	1173	-107	313	-75	300	1 sps	Deg F
82	V58T1702A	X	X	Temp	HYD 1 LH AFT BRAKE SW VLV RTN LN TEMP	1166.5	-109.5	313.7	-75	300	1 sps	Deg F
83	V58T1703A	X	X	Temp	LMG Brake Line Temp A (Sensor Near MLG Door)	1166	-140.4	282.8	-75	300	1 sps	Deg F
84	V58T1701A	X	X	Temp	LMG Brake Line Temp B	1116	-139.6	282.8	-75	300	1 sps	Deg F

Appendix E
STS-107 Mishap Investigation Timeline Instrumentation Data
Note: xxx = no data

No.	MSID / ID No.	OBX	OI	Type	Title	Location X	Location Y	Location Z	OSL	Range OSH	Sample Rate	Units
85	V58T1702A		X	Temp	Left Main Gear Brake Line Temp C	1140	-108	309	-75	300	1 sps	Deg F
86	V58T1703A		X	Temp	LMG Brake Line Temp D	1183	-108	312	-75	300	1 sps	Deg F
87	V62T0439A		X	Temp	SUPPLY H2O DUMP NOZZLE TEMP B	620	-105	342.46	0	400	1 sps	DegF
88	V62T0440A		X	Temp	SUPPLY H2O DUMP NOZZLE TEMP A	620	-105	342.46	0	400	1 sps	DegF
89	V62T0605A		X	Temp	WASTE H2O DUMP LINE TEMP	620	-105	342.46	-75	300	1 sps	DegF
90	V79X2683X		X	Position	RJDA 1 JET FQR DRIVER (see Note 1)	n/a	n/a	n/a		On	25 sps	Event
91	V79X2684X		X	Position	RJDA 2 JET FQR DRIVER (see Note 1)	n/a	n/a	n/a		On	25 sps	Event
92	V79X2683X		X	Position	LEFT INBOARD ELEVON ACTR 4 FAIL	(Located @ ASA4, Avionics Bay 6)				F-at	1 sps	Event
93	V79X2684X		X	Position	LEFT OUTBOARD ELEVON ACTR 4 FAIL	(Located @ ASA4, Avionics Bay 6)				F-at	1 sps	Event
94	V79X3273X		X	Position	RIGHT INBOARD ELEVON ACTR 4 FAIL	(Located @ ASA4, Avionics Bay 6)				F-at	1 sps	Event
95	V79X3274X		X	Position	RIGHT OTBOARD ELEVON ACTR 4 FAIL	(Located @ ASA4, Avionics Bay 6)				F-at	1 sps	Event
96	V79X3384X		X	Position	RUDDER ACTR 4 FAIL OUTPUT	(Located @ ASA4, Avionics Bay 6)				F-at	1 sps	Event
97	V79X4210E		X	Position	SPEED BRAKE ACTR 4 FAIL	(Located @ ASA4, Avionics Bay 6)				F-at	1 sps	Event
98	V79X4211E		X	Position	PCA FLT CONT ASA 4 RPC A ON	1320	55	372	Off	On	1 sps	Event
99	V79X4211E		X	Position	PCA FLT CONT ASA 4 RPC A ON	1320	55	372	Off	On	1 sps	Event
100	V00H0803C		X	Derived	COMMANDED ANGLE OF ATTACK (ALPCMD)	n/a	n/a	n/a	-45	45	1 sps	DEG
101	V00H1044C		X	Derived	COMMANDED ROLL ANGLE (ROLLC)	n/a	n/a	n/a	0	360	1 sps	Special
102	V00H1045C		X	Derived	FINAL ROLL COMMAND (ROLLCMD)	n/a	n/a	n/a			1 sps	DEG
103	V00H8410C		X	Derived	SELECTED BODY FLAP FDBK (BFP) (see Note 2)	n/a	n/a	n/a	-5	5	5 sps	VDC
104	V00H7505C		X	Derived	SELECTED L/B ELEVON (ELV/L) FDBK (see Note 3)	n/a	n/a	n/a	-5	5	5sps	VDC
105	V00H7505C		X	Derived	SELECTED R/B ELEVON (ELV/R) FDBK (see Note 3)	n/a	n/a	n/a	-5	5	5sps	VDC

Notes: sps = sample per second.
(*) = MSID is physically located on the Left/Right Elevon actuator.

Note 1 They are calling a Discrete=0 or Off as Off-Scale Low and Discrete=1 or On as Off-Scale High.

Note 2 While this is listed in the database as VDC, it is not downlisted as such. What is downlisted is the count value for the selected 16 bit MDM hardware word. A value of +5.00 VDC which is +500 counts in the sign +9 bits is a count value of +32,000 counts in the sign +15 bits. Dividing by 64 converts to the sign +9 bit value and dividing by 100 counts/VDC converts to VDC. Thus, we put a calibration Coefficient in the Calibration Data of 1/6400 (1.5625E-04). Back then we could not enter the number directly. Instead we had to put in data and let the computer calculate the Calibration Coefficients. Thus it came out as 1.561999E-04 or 1/6402.049065 (close enough). That is in the Shuttle Data Tape so it gets converted to VDC on the ground. With MCC Calibrations it is converted to percent.

Note 3 Same as Note 2 except with MCC Calibrations, Selected Elevon FDBK is converted to degrees (DEG).

Appendix F
List of Contributors

A great many people participated in the review and analysis of flight data from STS-107. The following is a list of some of the many people who contributed to the review of the STS-107 data and the generation of the entry timeline. The Data Review and Timeline Team thanks all of those who contributed to this effort and apologizes to those who have been inadvertently left of this list.

Core Team (conducted data reviews and represented their organizations at the data reviews, generated timeline, compiled supporting data, generated report, etc.)

Don L. McCormack, Jr.	NASA/MV
David W. Camp	Boeing
Joyce Seriale-Grush	NASA/EA
Tim Reith	Boeing
Don Peck	Boeing
Randy Moore	Boeing
Lonnie Jenkins	Boeing
Tony Leba	Boeing
Chuck Armstrong	Boeing
Tom Davies	Boeing/Cimarron
Walter Scott	Boeing/Cimarron
Joe Mechelay	Boeing/Cimarron
Scott Altman	NASA/CB
George Zamka	NASA/CB
Eric Boe	NASA/CB
David Moyer	NASA/MV
Bert Wagster	USA
Jon Olansen	NASA/NC
Al Arnold	GHG
Ross Engle	SAIC
Jeff Kling	NASA/DF
Howard Wagner	NASA/EP
Robert W. Fricke, Jr.	LMSO

Auxiliary Power Unit Subsystem

Ken Smith	Boeing
Paul Grout	Boeing
Mike Houle	Boeing
Tom Reuland	Boeing
Mel Friant	NASA/DF
Eddie Eskola	USA

Hydraulics Subsystem

Bob Rauch	Boeing
Jeff Goza	Boeing

Appendix F
List of Contributors

Charles Ritrivi	Boeing
David Beaugh	Boeing
Farzad Rezayat	Boeing
Francisco Hernandez	NASA/EP
Mike Snyder	USA

Main Propulsion Subsystem

David Rigby	Boeing
Jeff Stinnett	Boeing
Trina Martingano	Boeing
Mohammed Jebril	Boeing
John Chan	Boeing
Scott Baird	NASA/EP
John Melcher	NASA/DF
Thomas Arnold	NASA/DF

Orbital Maneuvering and Reaction Control Subsystems

Brian Werner	Boeing
Steven Arrieta	Boeing
James Garza	Boeing
Ed Fitzgerald	Boeing
Mickie Eguia	Boeing
Courtney Dorris	Boeing
Dean Lenort	USA/MOD

Fuel Cell and Power Reactant Storage and Distribution Subsystems

Danny Fitzgerald	Boeing
Ken Adams	Boeing
Johnny Wong	Boeing
Tim North	Boeing

Environmental Control and Life Support Subsystems

Jordan Metcalf	NASA/EC
Bruce Harkness	USA
Don Sandersfeld	Boeing
Chris Hoffman	Boeing
Isaac Andu	Boeing
Carmelo Ascunsion	Boeing
Menghis Hagos	Boeing
Thomas Londrigan	Boeing
Vince Reyes	Boeing
Marco Lorenzano	Boeing
Keith Mosall	NASA/EC
Chau Pham	NASA/EC
Darren Fasbender	USA/MOD

Appendix F
List of Contributors

Michael Fitzpatrick	USA/MOD

Passive Thermal Control Subsystem

Harry Chang	NASA/ES
Diana Coronado	Boeing
Shannon Belknap	Boeing
Tim Davies	Boeing
David Russell	Boeing
Dan Reynolds	Boeing
Guadalupe Gonzales	Boeing

Mechanical / Landing and Deceleration Subsystems

Robert Davis	NASA/ES
Bill Heitzman	USA
Tom Hoffman	Boeing
Link Salvador	Boeing
Ruben Smith	Boeing
Jeff Goodmark	Boeing
Chip Heinol	Boeing

Purge, Vent and Drain Subsystem

Doug Cline	Boeing

Electrical Power Distribution and Control Subsystem

Larry Minter	Boeing
Mark Fugitt	Boeing
Pete Peterson	Boeing
Kenneth Utley	Boeing
Mike Danielson	Boeing
Mark Welch	USA/MOD
Angela Bauer	NASA/DF

Flight Control Subsystem

Don McCorvey	Boeing
Rich Kawaga	Boeing
Vester Purkey	Boeing
Stephen Choi	Boeing
Jeff Wyrick	USA/MOD
Kyle Belton	USA/MOD
David Weiler	USA/MOD
Vic Untalan	NASA/DF

Inertial Measurement Unit Subsystem

Mike Reves	Boeing
Mike Rodgers	Boeing

Appendix F
List of Contributors

Star Tracker Subsystem	
Phil Perkins	Boeing
Avionics Subsystems	
Denise Romero	NASA
Kevin Dunn	NASA
John Hunt	USA
Data Processing Subsystem	
Jon Cummings	USA
James Cooley	Boeing
Vinh Nguyen	Boeing
Lynna Wood	Boeing
Jennifer Hagin	NASA/DF
Navigational Aids Subsystems	
Lance Borden	Boeing
Billy Cowan	Boeing
Communication Subsystems	
Jeff Stafford	Boeing
Ken McCrary	Boeing
Marty O'Hare	Boeing
Martha May	Boeing
Laura Hoppe	USA/MOD
Daryl Brown	NASA/DF
Cathy Sham	NASA/EV
Chip Kroll	NASA/EV
John Boster	Lockheed
Antha Atkins	Lockheed
Instrumentation / Recorders Subsystem	
Dwight Favors	Boeing
Steve Woods	Boeing
Rey Rivas	Boeing
Patrick Ngo	Boeing
Mike Garske	NASA/MV
Displays and Controls Subsystem	
Brian Kang	Boeing
Andy Farkas	Boeing
Multifunction Electronic Display Subsystem	
Jim Newsome	NASA

Appendix F
List of Contributors

Danny Siner	NASA
Brent Bynum	Boeing
Chris Gentz	Boeing
Debra Owen	Boeing
Entry Aerodynamics	
Jim Harder	Boeing
Olman Carvajal	Boeing
Brandon Redding	Boeing
Georgi Ushev	Boeing
Stress Analysis	
Mike Dunham	Boeing
Shawn Sorenson	Boeing
Image Analysis	
Greg Byrne	NASA/SX
Jon Disler	LM
Safety	
Alan Peterson	Boeing
Mike Dye	Boeing
Bruce Stewart	Boeing
Jeremy Verostko	SAIC
Meagan Bell	GHG
Michael Penney	SAIC



Volume II
Appendix D.10
Debris Recovery

The *Columbia* accident initiated the largest debris search in history. The evidence collected during the effort was instrumental in confirming the working hypothesis that had been developed by the Columbia Accident Investigation Board and the NASA Accident Investigation Team. The Board is very indebted to the thousands of individuals, companies, and organizations that responded to the call to service. We sincerely apologize to anybody inadvertently omitted from this appendix.

THIS PAGE INTENTIONALLY LEFT BLANK

Debris Recovery

Submitted by NASA Mishap Investigation Team, June 2003
David W. Whittle, Chair

The Shuttle Program activated the Mishap Investigation Team (MIT) on February 1, 2003. The MIT membership, processes and procedures are outlined in the Shuttle Program document NSTS 07700 Volume VIII. The MIT is initially composed of 10 members from various disciplines but was soon supplemented by hundreds of support personnel from several NASA centers. The specific MIT membership is published by way of memo six weeks prior to launch. The MIT assumed the responsibility for debris recovery, protection, and impoundment. The Columbia Accident Investigation Board had the prerogative to alter the debris collection process, but chose to retain the MIT in this role.

Organizational Structure and Responsibilities

Declaring Texas and Louisiana as federal disaster areas brought the Federal Emergency Management Agency (FEMA) and all their resources into the recovery picture. For the first three weeks there were two parallel recovery activities in place. One activity was for the recovery of the human remains and the second for the recovery of the Columbia debris. NASA had the lead responsibility for each activity with supporting roles by other state, federal, and local agencies. NASA, FEMA, Environmental Protection Agency (EPA), and the Forest Service were the primary players in the debris recovery activity. NASA identified the areas to be searched; the Forest Service provided the people and equipment to search the identified areas. EPA provided experts in decontamination of the debris and also tagged, photographed, and identified location of the debris. They then picked the debris up for transport. FEMA provided the money for most of the activity but of equal importance, FEMA had the authority and agreements to activate assistance from federal and state agencies.

Initially Barksdale AFB was the location of the recovery coordination activity. As the magnitude of the debris area became evident a sub group of the MIT was deployed to Carswell field in Ft. Worth, Texas and to Lufkin, Texas. The Carswell group was responsible for responding to debris reports between Corsicana, Texas and areas west of Ft. Worth, Texas. Based on reported debris items, small self-initiated searches were done by the Carswell operation, but none to the level done by the Forest Service between Corsicana and Toledo Bend Reservoir. The Lufkin representatives of the MIT worked debris recovery in the area from Corsicana, Texas to Ft. Polk, Louisiana. They identified the initial search corridor and coordinated with the Federal Emergency Management Agency (FEMA) and the Forest Service for the resources to search these areas. All MIT search activity was coordinated with daily teleconferences involving all locations.

There were a great many people across NASA that volunteered to assist. NASA centers developed a list of volunteers and coordinated the rotating in of new people through points of contact at the task level. In most cases there was a time overlap between volunteers to insure that the task and philosophy was understood before the new volunteer was left alone. In some instances there was a rotation between a fixed set people, thus requiring minimal overlap. Those volunteering in the search areas received briefs and directions in the same way that the forest service searchers did. The Forest Service rotated crews on a 14, 21, or 30-day basis. This required a continuous indoctrination program for the new searchers.

Debris Distribution

One thousand four hundred fifty nine debris reports came in from 42 states, Canada, Jamaica, and the Bahamas. Teams representing the MIT addressed all reports. Using video, radar analysis, telemetry analysis, and public reports, the debris trail was identified. Video from a variety of sources as well as telemetry indicated that *Columbia* was loosing pieces significantly west of Texas, even west of California. The greatest density of debris began south of Ft. Worth, Texas and ended in Ft. Polk, Louisiana. Although there is significant evidence that debris fell in Nevada, Utah, and New Mexico, the most westerly piece found was located in Littlefield, Texas. As expected, heavier pieces, with their

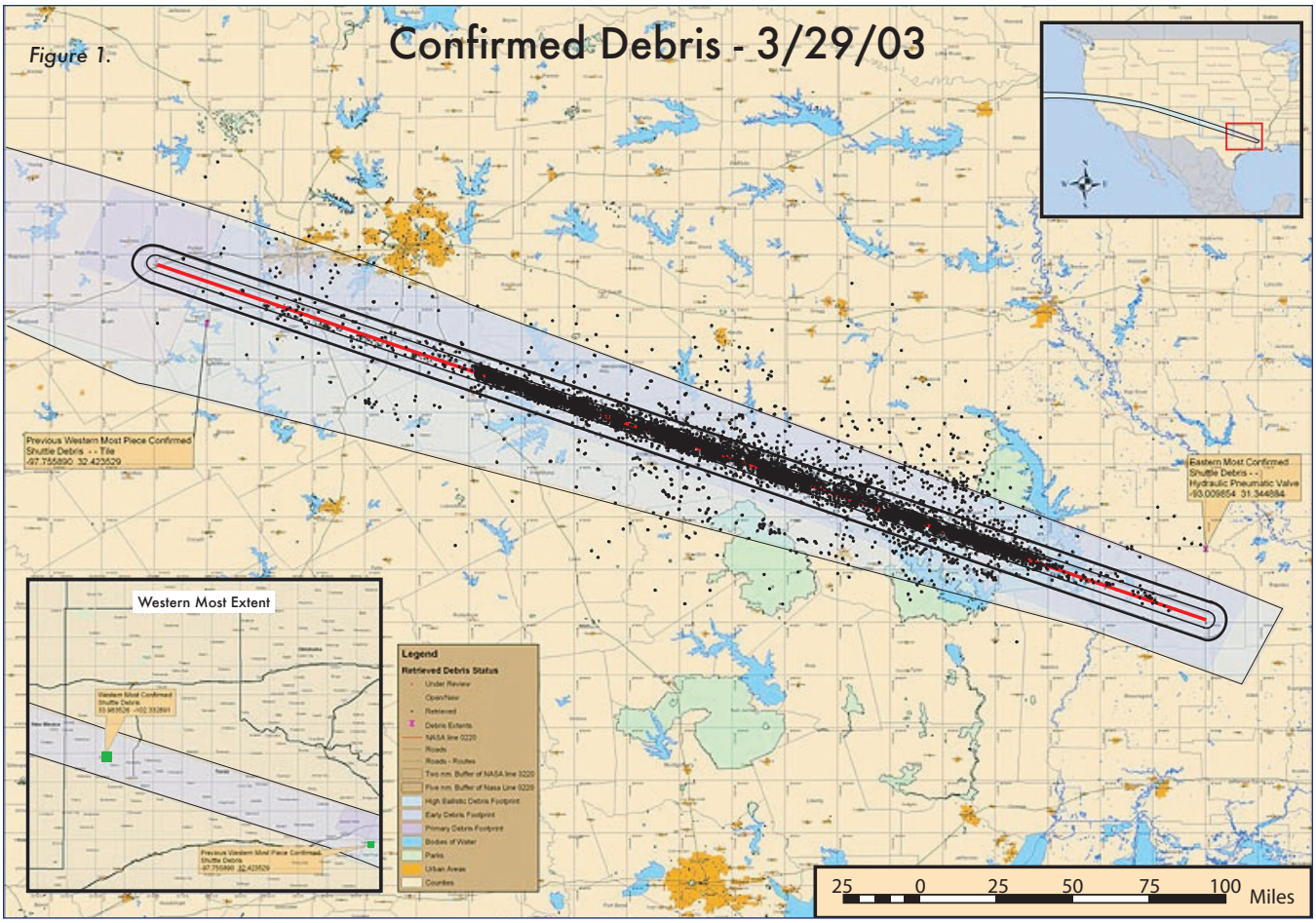


Figure 1.

higher ballistic coefficients, were found towards the end of the debris trail closer to Louisiana while light objects were found earlier in the path in north central and west Texas. Figure 1 gives a sense of the magnitude of the debris that was located. Each dot represents a piece of debris. There are some outlying points where errors were made in the recorded position.

Search Process and Procedures

The process and procedures for debris recovery was different depending on the debris location. The states of Louisiana and Texas were handled differently than the search for debris in the rest of the United States. Texas had the largest concentrations of debris spread along a well-defined line. Louisiana had several large engine pieces, which had the highest ballistic coefficients, and a small scattering of smaller items in several parishes.

Along the *Columbia* flight path from Texas to the California coast, there were radar and visual evidence of debris leaving the Shuttle vehicle and perhaps hitting the ground. Radar, video analysis, and trajectory analysis were used to define high probability areas for ground search in New Mexico, Utah, and Nevada. Working through FEMA, local resources were activated to search these high probability areas for Shuttle debris. Notices were published and broadcast asking that any debris or sighting information be forwarded to the NASA toll free number. Public notices via flyers and news media pieces were used several times during the recovery process.

At the Lufkin Disaster Field Office (DFO) search responsibilities were divided into five areas or responsibility each with a designated leader. These areas were:

1. All States outside Texas and Louisiana
2. Ground search within Texas and Louisiana
3. Air Search within Texas and Louisiana
4. Water search
5. Strategic search activities

The area leader coordinated search activities in each of the identified areas. Overall coordination was done at the daily planning and coordination meeting with the MIT.

Search Activities

Deployment

The MIT initially deployed to Barksdale AFB, Louisiana. Barksdale was chosen because it provided the facilities to handle large aircraft, had capabilities to accommodate a large contingent of people, had the appropriate facilities to accommodate human remains processing and transportation, and provided the security needed.

Active search was started on February 1, 2003. Within 2 weeks the number of ground searchers per day was in excess of 3,000. All search activity was coordinated through the Lufkin DFO, Barksdale MIT Operations Area, or Carswell Field MIT Office. After one month all search coordination was centered at the Lufkin DFO, this included the air, ground, and water search activities. Water search concluded on April 15, air search was completed on April 20. Ground search activity continued at full strength until April 25 and then gradually tapered off as the search of the identified areas was completed. Search of areas to the west of Texas were continued after the closure of the Lufkin DFO and managed from the Columbia Recovery Office (CRO).

Land Search

Initial priorities were to recover human remains. Because of the sensitivity and time importance of human remains recovery, it initially took priority over vehicle debris. The Texas Department of Public Safety (DPS), Texas National Guard, FBI, and NASA played significant roles in human remains recovery. Of equal importance was public safety. There was a concern that certain tanks from the orbiter might contain hazardous materials such as propellants. Public safety included clearing debris from schools and schoolyards as well as public areas. The EPA accomplished this task with the assistance of various local agencies. Early warnings about touching debris significantly slowed the recovery process. A change in policy to allow certain officials to evaluate and retrieve debris significantly sped up the early recovery. Once the Forest Service workers were employed, retrieval rates jumped to over 1,000 pieces a day.

Search of the larger debris areas used a variety of assets and techniques. In Texas alone, debris was spread over an area exceeding 2,000 square miles. The large area required a combination of ground and airborne search techniques (Figures 2 and 3). The heaviest debris corridor between Corsicana and Ft. Polk was the initial focus of attention. One hundred recovered items were used to define a debris distribution line. Analysis indicated this line represented the center of the debris distribution in east Texas. A +/- 2-mile corridor was defined around the centerline, which represented the 1-sigma lateral distribution of the debris. A second +/- 5-mile corridor was defined which represented the 2-sigma lateral debris distribution. It was decided that the center 4-mile wide corridor would be hand searched while the area outside the +/- 2-mile corridor to the +/- 5-mile corridor would be searched by air.


Figure 2.


Figure 3.

Most of the ground search was conducted by fire fighters from the US Forest Service assisted by representatives from Environmental Protection Agency (EPA) and NASA. For the ground search, a probability of detection (POD) of 75% for a 6" X 6" object was selected. The 75% POD determined the search techniques to be used by the field searchers. For the air search the POD was 50% for a 12" X 12" piece of debris. Over 3,000 US Forest Service wild land firefighters were used in the search activities. These searchers were staged out of four US Forest Service managed camps located in Corsicana, Palestine, Nacogdoches, and Hemphill, Texas. The area along the corridor from Granbury, Texas to Ft. Polk, Louisiana was divided into 2 nautical miles by 2 nautical mile grids. Grids were assigned to the Forest Service for search by the fire fighters.

Air Search

Over 37 helicopters and 7 fixed wing aircraft were assigned to search areas outside of the center 4-mile corridor to the edge of the 10-mile corridor.

Several other airborne assets were used to search for debris. These include hyper spectral scanners, forest penetration radar, photography from a U-2 reconnaissance aircraft, forward looking infrared, and images from two satellite platforms. Other search attempts included powered parachutes and civil air patrol searches. Use of these high tech devices proved of little value. Either the sensors could not penetrate the vegetation or the required resolution was beyond sensor capabilities. Hyperspectral scanning offered some potential, but data analysis was extremely time consuming and cumbersome so it was terminated.

Water Search

The debris area also included several bodies of water. Toledo Bend reservoir and Lake Nacogdoches were deemed to have the highest probability of containing shuttle debris. The US Navy Supervisor of Salvage (SUPVSAL) organized the efforts of 8 dive teams to search these bodies of water. Over 31 square miles these water bodies were bottom mapped using sonar devices. The mapping identified 3,100 potential targets in Toledo Bend and 326 targets in Lake Nacogdoches. Divers visited all identified targets. Only one piece of shuttle debris was located in Toledo Bend and nothing was found in Lake Nacogdoches. Figure 4 shows representative lake dive activity.



Figure 4.

NTSB Boxes

Several areas in Texas, New Mexico, Nevada, and Utah were identified as having high potential of containing shuttle debris. These areas were identified using radar, trajectory analysis, and video analysis. These search areas were called NTSB boxes due to the analysis provided by the National Transportation Safety Board (NTSB) in identifying these areas. Four areas were identified in west Texas, one in New Mexico, two in Nevada and two in Utah. All these boxes were searched either by people on the ground or air. To date nothing has been found west of Littlefield, Texas (Figures 5 and 6).

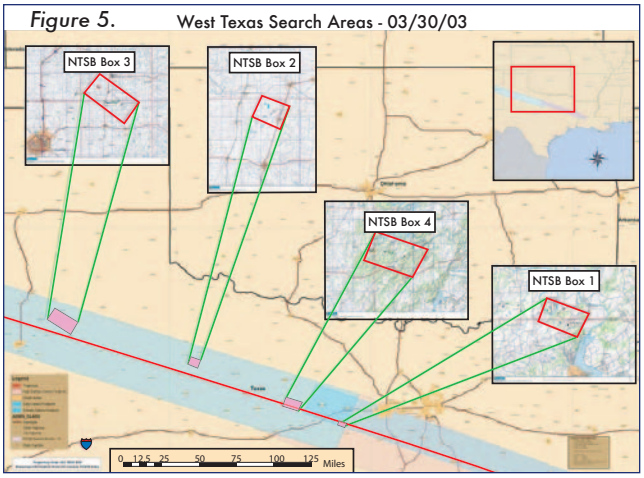


Figure 5. West Texas Search Areas - 03/30/03

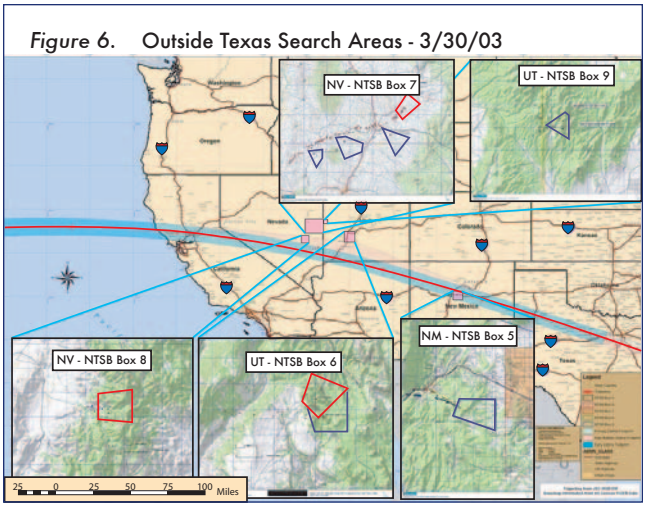


Figure 6. Outside Texas Search Areas - 3/30/03

California Coast

If the initial breakup occurred over the Pacific Ocean then there is a high likelihood that some *Columbia* debris fell into the ocean. Oceanographic data indicated three counties along the California coast, which had the highest probability of debris washing up on the beach. An organized search of the beach area was conducted using local law enforcement and local volunteer organizations. Figure 7 shows the shuttle crossing point on the California coast and the three counties involved in coastline searches. No debris was found.



Figure 7. California Coastal Search - 3/30/03

Statistics

By the time the search was ended the following assets were used:

- Over 30,000 people, over 1.5 million man-hours
- Over 130 federal, state, and local agencies
- 37+ helicopters
- 7+ fixed wing aircraft
- 84,000 pieces of *Columbia* were recovered
- 84,900 pounds were recovered
- By weight 39% of *Columbia* was recovered

The search covered the following:

- 700,000 acres was searched on foot
- 1.6 million acres were searched with aircraft.

The total search area is equivalent to a 1.25 mile wide track across the U.S. from Boston to Seattle.

Debris Handling

Debris from the Columbia was decontaminated if necessary and then tagged with information concerning its location. Pictures were taken of the debris in its found location. Collection centers were opened at Corsicana, Palestine, Nacogdoches, and Hemphill, Texas (Figure 8). All collection sites shipped debris to Barksdale AFB, Louisiana. Barksdale AFB was the location of most debris packaging and shipping to Kennedy Space Center. Debris going to Barksdale AFB was entered into the database, photographed, packaged for protection, and shipped to the Kennedy Space Center (KSC) Shuttle Landing Facility (SLF) hangar.

Twenty to thirty items were identified as "hot items" and were shipped to other locations. These too were entered into the database. Examples of these items are General Purpose Computers, film, cameras, MAGER GPS, OEX (MADS) recorder, and OPS recorders. All these items had information, which could potentially impact the search and the investigation. In some cases battery life times could limit access to potentially important information.


Figure 8.

Columbia Recovery Office

On April 28, as the field search was winding down, the Columbia Recovery Office (CRO) was opened at Johnson Space Center in Houston. This office will remain open to respond to calls from the general public and to retrieve any debris reported by the public. When required a contractor will be dispatched to decontaminate and recover reported items. Items will be shipped to KSC to be included with other debris. It is expected that the CRO will be in place until fall 2003 after which time the responsibility for call response will transfer to KSC.

MIT Reported Lessons Learned and Recommendations

1. It is important to get a good database as early as possible. A good database administrator should be named immediately. Database functionality, hosting, changes, etc should be coordinated through a single point. NASA should consider developing a database that could serve as a starting point for similar activities.
2. Significant administrative support should be identified early in the process. Large amounts of data need to be organized and accessed throughout the field activity. There is also the need for records retention and archiving. Planning for records retention and archival needs to start early.
3. Leaving decision making at the field level made for a more efficient operation. This activity was a perfect example of letting the field operations be managed in the field.
4. The mapping capability provided by the Geographic Information System (GIS) was a significant asset. It provided a good communications tool between the field and management and between the DFO and remote locations.
5. Having dual top NASA management representatives in the field with overlapping responsibilities was confusing to many people including the other agencies that worked with the MIT. Due to the cooperative nature of the specific individuals in this particular case, there were no conflicts that affected the work at hand.
6. Having the leadership operate from a central location helps interagency and team communications significantly.
7. FEMA provided access to significant people resources. The declaration of a disaster by the President made this possible. NASA should consider how to accomplish debris retrieval if a disaster were not declared or if a similar accident were to happen outside the US.
8. Remote sensing provided little assistance identifying debris locations.
9. Communications support is a must. Cell phones, telephones, and computers are absolute requirements. These resources were provided by FEMA. NASA should have a plan to provide similar capabilities in cases where FEMA is not involved.
10. Mobility of management is important for a search area of this magnitude. Face-to-face meeting with leaders at the remote locations is very important. FEMA provided fixed wing aircraft and helicopter support for management visits to remote locations.
11. Planning for a major Shuttle event on foreign soil needs attention. The fact that the NASA and NTSB had previously coordinated responsibilities was significant in determining lines of responsibility. Similar coordination needs to take place with host countries of Transoceanic Abort Landing (TAL) sites.

MIT Reported Contingency Action Plan Comments

The contingency action plans published by the Shuttle program and the NASA centers worked very well. They provided directions for the initial notification and coordination. The program has conducted contingency simulations at least every 18 months. These simulations play a key part in making the process familiar to the key players. As is often the case, the *Columbia* accident was not exactly the scenario simulated or expected. The *Columbia* scenario did not impact the contingency declaration, MIT activation, or management process. The impoundment of evidence and key documentation began immediately and had few problems throughout the entire search process. The Contingency plan did not take into consideration the disaster declaration made by the president. This made significant additional resources available to the MIT. These additional resources were easily incorporated into the recovery plan and were key in the success of the effort.

Cost

FEMA spent over $305 million to fund the search activity. NASA funds were also used for SLF and aircraft support. Not included in the cost figures are the wages of the hundreds of civil servants employed at the recovery area and in analysis roles at various centers.

Summary

This search activity is probably the largest search ever carried out in the history of the United States and likely in the world. Its success is a tribute to those agencies and individuals who participated in this unparalleled cooperative effort.

Most significantly, the recovered debris has been an essential component in our understanding of the important details of the accident scenario. It has corroborated other key data in the investigation. Without it there would be significant uncertainty in the cause and the location of the initial damage to *Columbia*.

Acknowledgements

Acme Electric Company of Texas
Air Conditioning Unlimited
Air Line Pilots Association
Alabama Forestry Commission
The Alabama Coushatta Tribe of Texas
Alaska Division of Forestry – Tok Area Office
Alaska Fire Service
Alaska Interagency Coordination Center
Alpine Rescue Team
Alvarado Fire Department
American Red Cross
Analytical Spectral Devices
Anderson County Courthouse
Angelina & Neches River Authority
Angelina County Precinct 3 Constable
Angelina County Precinct 5 Constable
Angelina County Sheriff Office
Appleby Volunteer Fire Department
Arcada Associates
Arizona State Land Department
Arizona Task Force 1
Arkansas Forestry Commission
Arkansas-oklahoma Interagency Fire Center
Ark-La-Tex Narcotics
Arlington Police Department
Armed Forces Institute of Pathology
Artel Inc
At&t World Service
Austin/Travis County Mhmr
Ball Aerospace
Beckville Volunteer Fire Department
Betty Hardwick Center
Big County of Abilene
Blue Bell
Bluebonnet Critical Incident Stress Management Team
Boeing
Boise Interagency Dispatch Center
Booz Allen Hamilton
Brandom Elementary School
Brookshires
Broward County Sheriffs Office
Bureau of Alcohol Tobacco Firearms and Explosives
Bureau of Indian Affairs – Albuquerque Area Office
Bureau of Indian Affairs – Blackfeet Agency
Bureau of Indian Affairs – Cheyenne River Agency
Bureau of Indian Affairs – Crow Agency
Bureau of Indian Affairs – Eastern Cherokee Agency
Bureau of Indian Affairs – Eastern Nevada Agency
Bureau of Indian Affairs – Flathead Agency
Bureau of Indian Affairs – Fort Apache Agency
Bureau of Indian Affairs – Fort Belknap Agency
Bureau of Indian Affairs – Fort Berthold Agency
Bureau of Indian Affairs – Fort Hall Agency
Bureau of Indian Affairs – Fort Peck Agency
Bureau of Indian Affairs – Fort Totten Agency
Bureau of Indian Affairs – Jicarilla Agency
Bureau of Indian Affairs – Laguna Area Agency
Bureau of Indian Affairs – Lower Brule Agency
Bureau of Indian Affairs – Mescalero Agency
Bureau of Indian Affairs – Navajo Area Office
Bureau of Indian Affairs – Northern Cheyenne Agency
Bureau of Indian Affairs – Northern Idaho Agency
Bureau of Indian Affairs – Northern Pueblos Agency
Bureau of Indian Affairs – Phoenix Area Office
Bureau of Indian Affairs – Pine Ridge Agency
Bureau of Indian Affairs – Puget Sound Agency
Bureau of Indian Affairs – Quinault Nation
Bureau of Indian Affairs – Ramah Navajo Agency
Bureau of Indian Affairs – Rocky Boys Agency
Bureau of Indian Affairs – Rosebud Agency
Bureau of Indian Affairs – San Carlos Agency
Bureau of Indian Affairs – Southern California Agency
Bureau of Indian Affairs – Southern Pueblos Agency
Bureau of Indian Affairs – Standing Rock Agency
Bureau of Indian Affairs – Talihina Field Office
Bureau of Indian Affairs – Turtle Mountain Agency
Bureau of Indian Affairs – Western Nevada Agency
Bureau of Indian Affairs – Wind River Agency
Bureau of Indian Affairs – Winnebago Agency
Bureau of Indian Affairs – Ute Mountain Agency
Bureau of Indian Affairs – Uintah And Ouray Agency
Bureau of Indian Affairs – Yakima Agency
Bureau of Indian Affairs – Zuni Agency
Bureau of Indian Affairs – Bureau of Land Management
Bureau of Indian Affairs – Alaska State Office
Bureau of Indian Affairs – Bakersfield District
Bureau of Indian Affairs – Battle Mountain District
Bureau of Indian Affairs – Burns District
Bureau of Indian Affairs – California State Office
Bureau of Indian Affairs – Carson City District
Bureau of Indian Affairs – Casper Field Office
Bureau of Indian Affairs – Cedar City District
Bureau of Indian Affairs – Elko Field Office
Bureau of Indian Affairs – Ely District
Bureau of Indian Affairs – Eugene District
Bureau of Indian Affairs – Galena Zone
Bureau of Indian Affairs – Grand Junction Field Office
Bureau of Indian Affairs – Idaho Falls District
Bureau of Indian Affairs – Lakwview District
Bureau of Indian Affairs – Lewistown Field Office
Bureau of Indian Affairs – Las Cruces District
Bureau of Indian Affairs – Las Vegas Field Office
Bureau of Indian Affairs – Lower Snake River District
Bureau of Indian Affairs – Medford District
Bureau of Indian Affairs – Miles City District
Bureau of Indian Affairs – Montana State Office
Bureau of Indian Affairs – Montrose District
Bureau of Indian Affairs – Nevada State Office

Bureau of Indian Affairs – New Mexico State Office
Bureau of Indian Affairs – Oregon State Office
Bureau of Indian Affairs – Phoenix Field Office
Bureau of Indian Affairs – Rawlins District
Bureau of Indian Affairs – Roswell District
Bureau of Indian Affairs – Richfield Field Office
Bureau of Indian Affairs – Rock Springs District
Bureau of Indian Affairs – Roseburg District
Bureau of Indian Affairs – Royal Gorge Field Office
Bureau of Indian Affairs – Safford Field Office
Bureau of Indian Affairs – Salem District
Bureau of Indian Affairs – Salt Lake Field Office
Bureau of Indian Affairs – Taos Field Office
Bureau of Indian Affairs – Upper Columbia Salmon Clearwater District
Bureau of Indian Affairs – Upper Snake River District
Bureau of Indian Affairs – Utah State Office
Bureau of Indian Affairs – Vale District
Bureau of Indian Affairs – Vernal Field Office
Bureau of Indian Affairs – Yuma Field Office
Bureau of Indian Affairs – Winnemucca Field Office
Bureau of Indian Affairs – White River Field Office
Bureau of Reclamation
Burnet County Sheriffs Office
C & C Technologies Survey Services
C. A. Richards
California Task Force 2
California Task Force 3
California Task Force 5
California Task Force 7
California Task Force 8
Cameron County Sheriffs Office
Casper Interagency Dispatch Center
Carthage Fire Department
Center for Disease Control & Prevention
Center Independent School District
Central Heights Volunteer Fire Department
Central Idaho Interagency Fire Center
Cherokee County
Cherokee County Sheriffs Office
Chevron
Chireno Independent School District
Chireno Volunteer Fire Department
City of Alto
City of Alvarado
City of Diboll
City of Euless
City of Fort Worth
City of Garland
City of Hemphill
City of Henderson
City of Joshua
City of Lufkin
City of Many
City of Maypearl
City of Mesquite
City of Mount Vernon
City of Nacodoches
City of Nederalnd
City of Orange
City of Palestine
City of Plano
City of Port Arthur
City of Rowlett
City of San Antonio
City of San Augustine
City of The Colony
Civil Air Patrol Texas Wing
Clarksville Warren City Volunteer Fire Department
Clayton Volunteer Fire Department
Coca-Cola
College Station Police Department
Collin County
Collin County Commissioners Court
Collin County Sheriffs Office
Colorado Forest Service
Colorado Task Force 1
Community Coffee
Community Four Volunteer Fire Department
Conagra Foods
Coppell Fire Department
Corrigan Consulting Inc.
Coserv
Cox Communications
Crandall Volunteer Fire Department
Crims Chapel Volunteer Fire Department
Cushing Fire Department
D & B Security
Dallas County
Dallas Fire Department
Dallas Fort Worth Fire Department
Dallas Fort Worth International Airport
David Wade Correctional Center
Deep East Texas Workforce Development Center
Deer Park Fire Department
Defense Criminal Investigative Service
Defense Intelligence Agency
Department of Defense
Department of Health And Human Services
Department of Interior
Department of Transportation
Dewberry & Davis
Diboll Fire Department
Diboll Police Department
Digitalnet Government Solutions
Diversified Technology LLC
Douglas County
Douglas Fire Department
Douglas Independent School District
Dow Chemical Emergency Response
Durango Interagency Dispatch Center
Dyncorp
East Texas Copy Systems
Eastern Area Coordination Center
Eastex Maintenance Service Inc
Ellis County
Ellis Environmental Group
El Paso County Search & Rescue
El Paso County Woodland Park
Emergency Corp
Envirinmental Restoration LLC
Environmental Protection Agency – EPA/START/WESTON
Environmental Systems Research Institute
Etoile Volunteer Fire Department

Eugene Interagency Communications Center
Evergreen Helicopter
Fairmount Volunteer Fire Department
Farm Service Agency
Farmington Construction Office
Federal Bureau of Investigation – Beaumont
Federal Bureau of Investigation – Dallas
Federal Bureau of Investigation – Houston
Federal Bureau of Investigation – Laredo
Federal Bureau of Investigation – Lufkin
Federal Bureau of Investigation – New York
Federal Bureau of Investigation – Tyler
Federal Aviation Administration – Southern Region
Federal Aviation Administration – Southwest Region
Federal Emergency Management Agency
Federal Highway Administration
Firefighters National Trust
Firecom Llc
Flathead Interagency Dispatch Center
Flatwoods Job Corps Center
Flatwoods Volunteer Fire Department
Florida Division of Forestry
Florida Interagency Coordination Center
Florida Task Force 1
Florida Task Force 2
Foremost
Fort Collins Interagency Dispatch Center
Fort Worth Fire Department
Fort Worth Independent School District
Franklin County Fire Department
Franklin County Sheriffs Office
Fremont County
Frito Lays
Fuller Springs Volunteer Fire Departmenet
Galveston Sheriffs Department
Gary Volunteer Fire Department
Grayson County
Grayson County Sheriffs Office
General Services Administration
Georgia Forestry Commission
Georgia Interagency Coordination Center
Global Aerospace
Go Jo Company
Goldstar Ems
Good Samaritan Hospital
Goodyear
Grand Junction Interagency Dispatch Center
Gregg County
Gregg County Office of Emergency Management
Gulf Engineers And Consultants
Harris County
Harris County Sheriffs Department
Harrison County
Harrison County Sheriffs Office
Hardin County
Haynes Construction
Heart of Texas
Henderson County
Henderson County Sheriffs Office
Henderson Police Department
Hill County Mental Health And Mental Retardation
Hopkins County Sheriffs Office
Houston County
Houston County Office of Emergency Management
Houston Police Department
Huntington Police Department
Indiana Division of Forestry
Indiana Task Force 1
Intercommunity Volunteer Fire Department
Jasper County Sheriffs Office
Jasper/newton/sabine County Oem
Jefferson County
Johnson County
Joshua Volunteer Fire Department
Kaufman City Volunteer Fire Department
Kaufman County
Kaufman County Office of Emergency Management
Kaufman County Sheriffs Office
Keltys Baptist Church
Kemp Volunteer Fire Department
Kentucky Airmotive
Kentucky Division of Forestry
Kentucky Interagency Coordination Center
Kern County Fire Department
Kevric Company
Kgas Radio Station
Kingtown Volunteer Fire Department
Klamath Falls Interagency Fire Center
Kongsberg Maritime
Lake Nacogdoches Volunteer Fire Department
Lamar County Sheriffs Office
Land o' Pines
Larimer County Search & Rescue
LBJ Job Corp Center
Leesville County Sheriffs Office
Leon County Sheriffs Department
Lilbert Looneyville Volunteer Fire Department
Lincoln Zone Coordination Center
Linn Flat Fire Department
Livingston Fire Department
Livingston Police Department
Lockheed Martin
Lonestar Police Department
Longview Fire Department
Lopez Garcia Group
Los Angeles County Fire Department
Louisiana Office of Forestry
Louisiana Department of Health & Hospitals
Louisiana Department of Public Safety & Corrections
Louisiana Department of Wildlife & Fisheries
Louisiana Military Department
Louisiana National Guard
Louisiana Office of Emergency Preparedness
Louisiana State Police
Lufkin Chamber of Commerce
Lufkin Fire Department
Lufkin Police Department
Maness Scientific Inc
Marshall Fire Department
Marshall Police Department
Maryland Task Force 1
Massachusetts Task Force 1
Maypearl Volunteer Fire Department
McDonald's

Media Services Group
Melrose Volunteer Fire Department
Memorial Health Systems
Menlo Park Fire Department
Mesquite Fire Department
Minnesota Department of Natural Resources
Minnesota Interagency Fire Center
Missouri Task Force 1
Moffat Volunteer Fire Department
Montgomery County Sheriffs Office
Mri Technologies
Murray Biscuit Company
Nacogdoches County
Nacogdoches Chamber of Commerce
Nacogdoches County Auditors Office
Nacogdoches County Sheriffs Department
Nacogdoches Police Department
Nacogdoches Westside Volunteer Fire Department
NASA – Ames Research Center
NASA – Dryden Flight Research Center
NASA – Glenn Research Center
NASA – Goddard Space Flight Center
NASA – Johnson Space Center
NASA – Kennedy Space Center
NASA – Langley Research Center
NASA – Marshall Space Flight Center
NASA – Office of The Inspector General
NASA – Stennis Space Center
Natchitoches Police Jury
National Ground Intelligence Center
National Imagery and Mapping Agency – Ft. Mcpherson
National Imagery and Mapping Agency – Arnold
National Imagery and Mapping Agency – Reston
National Interagency Coordination Center
National Interagency Fire Center
National Park Service – Abraham Lincoln Birthplace National Historical Park
National Park Service – Acadia National Park
National Park Service – Alaska Area Region
National Park Service – Amistad National Recreation Area
National Park Service – Arches National Park
National Park Service – Bandelier National Monument
National Park Service – Big Ben National Park
National Park Service – Big Cypress National Preserve
National Park Service – Big Thicket National Preserve
National Park Service – Blueridge Parkway
National Park Service – Buffalo National River
National Park Service – Carlsbad Caverns National Park
National Park Service – Chickasaw National Recreation Area
National Park Service – Chiricahua National Monumnt
National Park Service – Cuyahoga Valley National Park
National Park Service – Delaware Water Gap National Recreation Area
National Park Service – Everglades National Park
National Park Service – Fort Laramie National Historic Site
National Park Service – Fort Smith National Historic Site
National Park Service – Fredericksburg/Spotsylvania National Military Park
National Park Service – Gettysburg National Military Park
National Park Service – Glacier National Park
National Park Service – Grand Canyon National Park
National Park Service – Grand Teton National Park
National Park Service – Great Sand Dunes National Monument and Preserve
National Park Service – Great Smokey Mountains National Park
National Park Service – Harpers Ferry National Historic Park
National Park Service – Jean Lafitte National Historic Park and Preserve
National Park Service – Lake Meade National Recreation Area
National Park Service – Lake Meredith National Recreation Area
National Park Service – Lyndon B Johnson National Historic Park
National Park Service – New River Gorge National River
National Park Service – North Cascades National Park
National Park Service – Mesa Verde National Park
National Park Service – Padre Island National Seashore
National Park Service – San Juan Island National Historic Park
National Park Service – Shenandoah National Park
National Park Service – Sleeping Bear Dunes National Lakeshore
National Park Service – Yellowstone National Park
National Park Service – Zion National Park
National Park Service – Yosemite National Park
National Park Service – National Processing Service Center
National Property Management Association
National Transportation Safety Board – Dallas South Central Regional
National Weather Service
National Weather Service – Los Angeles Office
Navarro County
Navarro County Office of Emergency Management
Nebraska Task Force 1
Nederland Police Department
New Mexico National Guard
New Mexico Task Force 1
New York Fire Department
New York Office of Emergency Management
Nevada Division of Forestry
North Carolina Division of Forest Resources Region 1
North Carolina Division of Forest Resources Region 3
North Carolina Interagency Coordination Center
Northwestern Land Office
Nueces County Mental Health and Mental Retardation Center
Ohio Division of Forestry
Ohio Task Force 1
Oklahoma Division of Forestry
Oklahoma Emergency Management
Orange County Sheriffs Office
Oregon Department of Forestry
Omni Glow
Ozarka Water
Panola County
Panola County Constable
Panola County Sheriffs Office
Papillon Grand Canyon Helicopters
Paris Police Department
Parker County
Parker County Office of Emergency Management
Pepsi
Perry's Victory & International Peace Memorial
Phoenix International Inc
Phoenix Kingman Zone
Polk County
Polk County Sheriffs Office
Private
Raytheon

Railroad Retirement Board
Richfield Interagency Fire Center
Rockwall County
Rockwall County Sheriffs Department
Rockwall Police Department
Rocky Mountain Interagency Helitack
Rocky Mountain Rescue Group
Roh, Inc.
Rosser Volunteer Fire Department
Rusk County
Rusk County Fire Department
Rusk County Office of Emergency Management
Rusk County Sheriffs Office
Rusk County Volunteer Fire Department
Sabine County Firefighters
Sabine County Sheriffs Office
Sabine Parish Sheriffs Department
Sabine River Authority
Salado Volunteer Fire Department
Salvation Army
San Augustine County
San Augustine Independent School District
San Luis Obispo Fire Department
Santa Barbara County Fire Department
Science Applications International Corp
Scurry Volunteer Fire Department
Shelby County
Shelby County Sheriffs Department
Shreveport Fire Department
Shreveport Police Department
Sierra Fron Interagency Dispatch Center
Skylane Helicopters
Skywarn
Smith County
Smith County Office of Emergency Management
Smith County Sheriffs Office
South Carolina Forestry Commission
South Channel Bay Area Stress Management
South Dakota Division of Resource Conservation And Forestry
Southwest Texas Debriefing Team
Southwestern Land Office
Spacelab, Inc.
Spokane County Fire District 4
State of Utah
Stephen F. Austin State University – Arthur Temple College of Forestry
Stephen F. Austin State University – Hues Gis Lab
Stewarts Catering
Sulphur Springs Police Department
Susan Ramares
Sweetwater County
Swift Shady Grove Volunteer Fire Department
Temple Fire And Rescue
Temple Fire Department
Tennessee Task Force 1
Tennessee Interagency Coordination Center
Tennessee Southern Research Station
Tetra Tech
Texas A & M
Texas A & M at Corpus Christi
Texas Alcoholic Beverage Commission
Texas Animal Health Commission
Texas CISM Network
Texas Commission on Environmental Quality
Texas Department of Criminal Justice
Texas Division of Emergency Management
Texas Department of Health And Human Services
Texas Department of MHMR
Texas Department of Public Safety
Texas Department of Transportation
Texas Forest Serivce
Texas Interagency Coordination Center
Texas National Guard
Texas Natural Resources Information System
Texas Parks and Wildlife Department
Texas Rangers
Texas State Senate
Texas Task Force 1
Texas Water Development Board
Titus County
Tomball Fire Department
Tawakoni Fire Department
Travis County Sheriff's Office CISM Team
Txu Communiations
Tyler Fire Department
Tyler Volunteer Fire Department
Uma Fire Managemnent
Uneeda Ice
Unita County
United Space Alliance
University of Texas Center For Space Research
Upshur County Sheriffs Office
Urban Search And Rescue
URS Corp.
U.S. Air Force – Barksdale Air Force Base
U.S. Air Force – U.S. Air Force Bomb Squad
U.S. Air Force – National Air Intelligence Center
U.S. Air Force – National Security Emergency Preparedness
U.S. Air Force – Patrick Airforce Base
U.S. Army
U.S. Army Corps of Engineers
U.S. Attorney's Office
U.S. Coast Guard – 13th Coast Guard District
U.S. Coast Guard – Atlantic Strike Team
U.S. Coast Guard – Auxillary
U.S. Coast Guard – Gulf Strike Team
U.S. Coast Guard – National Strike Force Coordination Center
U.S. Coast Guard – Pacific Strike Team
U.S. Fish & Wildlife Service – Anahuac National Wildlife Refuge
U.S. Fish & Wildlife Service – Aransas National Wildlife Refuge
U.S. Fish & Wildlife Service – Arizona Ecological Services Field Office
U.S. Fish & Wildlife Service – Attwater Prarie Chicken National Wildlife Refuge
U.S. Fish & Wildlife Service – Balcones Canyonlands National Wildlife Refuge
U.S. Fish & Wildlife Service – Blackwater National Wildlife Refuge
U.S. Fish & Wildlife Service – Brazoia National Wildlife Refuge
U.S. Fish & Wildlife Service – Buenos Aires National Wildlife Refuge
U.S. Fish & Wildlife Service – Charles M Russell National Wildlife Refuge
U.S. Fish & Wildlife Service – Chenier Plains National Wildlife

Refuge
U.S. Fish & Wildlife Service – Kenai National Wildlife Refuge
U.S. Fish & Wildlife Service – Northeast Regional offce
U.S. Fish & Wildlife Service – Okefenokee National Wildlife Refuge
U.S. Fish & Wildlife Service – Sandhill Crane National Wildlife Refuge
U.S. Fish & Wildlife Service – Santa Ana National Wildlife Refuge
U.S. Fish & Wildlife Service – Southwest Regional Office
U.S. Fish & Wildlife Service – Texas Point National Wildlife Refuge
U.S. Fish & Wildlife Service – Texas Mid-coast National Wildlife Refuge
U.S. Forest Service – Angeles National Forest
U.S. Forest Service – Apache-Sitgreaves National Forest
U.S. Forest Service – Arapaho & Roosevelt National Forest
U.S. Forest Service – Ashley National Forest
U.S. Forest Service – Beaverhead/deerlodge National Forest
U.S. Forest Service – Big Horn National Forest
U.S. Forest Service – Bitterroot National Forest
U.S. Forest Service – Black Hills National Forest
U.S. Forest Service – Boise National Forest
U.S. Forest Service – Bridger-Teton National Forest
U.S. Forest Service – Caddo-LBJ National Grasslands
U.S. Forest Service – Caribbean Natioinal Forest
U.S. Forest Service – Caribou-Targhee National Forest
U.S. Forest Service – Carson National Forest
U.S. Forest Service – Chattahoochee-Oconee National Forest
U.S. Forest Service – Chequamegon-Nicolet National Forest
U.S. Forest Service – Cherokee National Forest
U.S. Forest Service – Chippewa National Forest
U.S. Forest Service – Chugach National Forest
U.S. Forest Service – Cibola National Forest
U.S. Forest Service – Clearwater National Forest
U.S. Forest Service – Cleveland National Forest
U.S. Forest Service – Coconino National Forest
U.S. Forest Service – Columbia River Gorge National Scenic Area
U.S. Forest Service – Colville National Forest
U.S. Forest Service – Coronado National Forest
U.S. Forest Service – Custer National Forest
U.S. Forest Service – Dakota Prairie Grasslands
U.S. Forest Service – Daniel Boone National Forest
U.S. Forest Service – Davy Crockett National Forest
U.S. Forest Service – Deschutes National Forest
U.S. Forest Service – Dixie National Forest
U.S. Forest Service – Eldorado National Forest
U.S. Forest Service – Fishlake National Forest
U.S. Forest Service – Flathead National Forest
U.S. Forest Service – Francis Marion-sumter National Forest
U.S. Forest Service – Fremont National Forest
U.S. Forest Service – Gallatin National Forest
U.S. Forest Service – Grand Mesa, Uncompahgre & Gunnision National Forests
U.S. Forest Service – George Washington and Jefferson National Forests
U.S. Forest Service – Gifford Pinchot National Forest
U.S. Forest Service – Gila National Forest
U.S. Forest Service – Helena National Forest
U.S. Forest Service – Hoosier National Forest
U.S. Forest Service – Humboldt-Toiyabe National Forests
U.S. Forest Service – Huron-Manistee National Forests
U.S. Forest Service – Idaho Panhandle National Forest
U.S. Forest Service – Inyo National Forest
U.S. Forest Service – Kaibab National Forest
U.S. Forest Service – Kisatchie National Forest
U.S. Forest Service – Klamath National Forest
U.S. Forest Service – Kootenai National Forest
U.S. Forest Service – Lake Tahoe Basin Management Unit
U.S. Forest Service – Land Between the Lakes National Recreation Area
U.S. Forest Service – Lassen National Forest
U.S. Forest Service – Lewis & Clark National Forest
U.S. Forest Service – Lincoln National Forest
U.S. Forest Service – Lolo National Forest
U.S. Forest Service – Los Padres National Forest
U.S. Forest Service – Malheur National Forest
U.S. Forest Service – Manti-Lasal National Forest
U.S. Forest Service – Mark Twain National Forest
U.S. Forest Service – Mendocino National Forest
U.S. Forest Service – Modoc National Forest
U.S. Forest Service – Monongahela National Forest
U.S. Forest Service – Mt. Baker-Snoquaimie National Forest
U.S. Forest Service – Mount Hood National Forest
U.S. Forest Service – National Forests in Alabama
U.S. Forest Service – National Forests in Florida
U.S. Forest Service – National Forests in Mississippi
U.S. Forest Service – National Forests in North Carolina
U.S. Forest Service – National Forests and Grasslands in Texas
U.S. Forest Service – Nebraska National Forest
U.S. Forest Service – Nez Perce National Forest
U.S. Forest Service – Ochoca National Forest
U.S. Forest Service – Okanogan National Forest
U.S. Forest Service – Olympic National Forest
U.S. Forest Service – Ouachita National Forest
U.S. Forest Service – Ozark and St. Francis National Forests
U.S. Forest Service – Payette National Forest
U.S. Forest Service – Pike and San Isabel National Forests
U.S. Forest Service – Plumas National Forest
U.S. Forest Service – Prescott National Forest
U.S. Forest Service – Region 1 Northern Regional Office
U.S. Forest Service – Region 2 Rocky Mountain Regional Office
U.S. Forest Service – Region 3 Southwestern Regional Office
U.S. Forest Service – Region 4 Intermountain Regional Office
U.S. Forest Service – Region 5 Pacific Southwest Regional Office
U.S. Forest Service – Region 6 Pacific Northwest Regional Office
U.S. Forest Service – Region 8 Southern Area Regional Office
U.S. Forest Service – Region 9 Eastern Regional Office
U.S. Forest Service – Rio Grande National Forest
U.S. Forest Service – Rogue River National Forest
U.S. Forest Service – Sabine National Forest
U.S. Forest Service – Salmon-Challis Natioinal Forest
U.S. Forest Service – Sam Houston National Forest
U.S. Forest Service – San Bernardino National Forest
U.S. Forest Service – San Juan National Forest
U.S. Forest Service – Santa Fe National Forest
U.S. Forest Service – Savannah River Project
U.S. Forest Service – Sawtooth National Forest
U.S. Forest Service – Sequoia National Forest
U.S. Forest Service – Shasta-Trinity National Forest
U.S. Forest Service – Shawnee National Forest
U.S. Forest Service – Shoshone National Forest
U.S. Forest Service – Sierra National Forest

U.S. Forest Service – Siskiyou National Forest
U.S. Forest Service – Siuslaw National Forest
U.S. Forest Service – Six Rivers National Forest
U.S. Forest Service – Stanislaus National Forest
U.S. Forest Service – Superior National Forest
U.S. Forest Service – Tahoe National Forest
U.S. Forest Service – Targhee National Forest
U.S. Forest Service – Tongass National Forest
U.S. Forest Service – Tonto National Forest
U.S. Forest Service – Uinta National Forest
U.S. Forest Service – Umitilla National Forest
U.S. Forest Service – Umpqua National Forest
U.S. Forest Service – Wallowa-Whitman National Forest
U.S. Forest Service – Wasatch-cache National Forest
U.S. Forest Service – Wayne National Forest
U.S. Forest Service – Wenatchee National Forest
U.S. Forest Service – White Mountain National Forest
U.S. Forest Service – White River National Forest
U.S. Forest Service – Winema National Forest
U.S. Forest Service – Willamette National Forest
U.S. Marshals Service
U.S. Navy – Combat Camera
U.S. Navy – Coastal Systems Station
U.S. Navy – EODTraining and Evaluation Unit Two
U.S. Navy – Mobile Diving and Salvage Unit Two
U.S. Navy – Mobile Diving and Salvage Unit Two Det 101
U.S. Navy – Mobile Diving and Salvage Unit Two Det 409
U.S. Navy – Mobile Diving and Salvage Unit Two Det 608
U.S. Navy – Naval Research Laboratory
U.S. Navy – Naval Air Station Joint Reserve Base Fort Worth
U.S. Navy – Naval Media Center
U.S. Navy – Naval Safety Center
U.S. Navy – Naval Sea Systems Command
U.S. Navy – Pearl Harbor Naval Shipyard
U.S. Navy – Shore Intermediate Maintenance Activity Mayport
Utah Task Force 1
Uvalde County
Uvalde County Sheriffs Department
Van Zandt County Sheriffs Office
Veridian
Vernon Parish Sheriffs Office
Virginia Department of Forestry
Virginia Task Force 1
Virginia Task Force 2
Volunteers
Washington Task Force 1
Waxahachie Independent School District
Weston Solutions
Woden Fire Department
Woods Volunteer Fire Department
Woodville Volunteer Fire Department
Wyle Life Sciences

Volume II
Appendix D.11

STS-107 *Columbia* Reconstruction Report

This appendix contains the STS-107 Columbia Reconstruction Report – reproduced at smaller than normal size – written by NASA during the investigation. While the Board investigation eventually focused on the left wing and the forensics evidence from that area, this report looked at Orbiter damage over the entire vehicle.

The Board's conclusions about debris evidence in Chapter 3 of Volume I were based on this report and independent analysis and investigation by Board investigators.

This is a NASA document and is published here as written, without editing by the Columbia Accident Investigation Board. The conclusions drawn in this report do not necessarily reflect the opinion of the Board; when there is a conflict, the statements in Volume I of the Columbia Accident Investigation Board Report take precedence. While the report contains many recommendations to improve the data used in this type of analysis for future missions, the Board did not adopt every recommendation into the Columbia Accident Investigation Board Report.

THIS PAGE INTENTIONALLY LEFT BLANK

STS-107 *Columbia* Reconstruction Report

Submitted by Columbia Reconstruction Team
Steven J. Altemus, Jon N. Cowart, Warren H. Woodworth





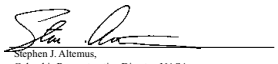


STS-107 Columbia Reconstruction Report

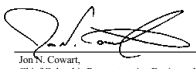
NSTS-60501

JUNE 30, 2003

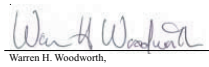
STS-107 Columbia Reconstruction Report



Stephen J. Altemus,
Columbia Reconstruction Director, NASA



Jon N. Cowart,
Chief Columbia Reconstruction Engineer, NASA



Warren H. Woodworth,
Chief Columbia Reconstruction Engineer, USA



Table of Contents

Executive Summary 1
Introduction 3
- Accident Background 3
- Purpose of Reconstruction 3

Organizational Structure 5
- Staffing the Reconstruction Effort 5
  - Floor Support 6
  - Technical Disciplines 6
  - Crew Module Area Staffing 7
  - Payloads 7
  - Materials & Processes (M&P) Engineering 8
  - Data Management Staffing 8
- External Interfaces 9
  - Mishap Response Team 9
  - Columbia Accident Investigation Board 9
  - Columbia Task Force 10
  - NASA Accident Investigation Team 10
  - Technical Support 10

Facilities of Reconstruction 11
- Columbia Hangar 11
- Clamshell 11
- Midfield Park Site Decontamination Area 12

Tools and Techniques 13
- Columbia Reconstruction Database System 13
  - Architecture 13
  - User Interface 13
  - Access Controls 13
- Two-Dimensional Grid 14
- Crew Module Reconstruction 16
- M&P Sampling and Analysis 17
  - Sampling 17
  - Analysis 17
- Three-Dimensional Physical Reconstruction 18
  - Left Wing Leading Edge 18
  - Right Wing Leading Edge 19
  - Left Wing Lower Tile 19
- Virtual Reconstruction 20
- Identification Tools 21
  - Electronic Maps 21
  - Thermal Information Processing System 21
  - Tile Thickness Maps and Sidewall Angle Charts 23
  - Configuration Verification Accounting System 23
  - Shuttle Drawing System 23

Debris Handling and Management 25
- Receiving and Process Flow 25
  - Shipping and Transportation 25
  - Uncrating 27
  - Quality Receiving 27
  - Movement and Release of Debris 28
- Debris Requiring Special Receiving 29
  - Crew Module Debris Receiving 29
  - Biological Debris 29
  - Pyrotechnic Devices 30
- Engineering Identification Process 30
  - Cleaning 31
  - Tile Identification 31
  - Crew Module 32
  - Payloads 32
- Search and Recovery Coordination 32
  - Significant Recovered Items List 33
  - Fast Track Process 33
  - Debris Plotting Capability 33
- Engineering Assessment Process 34
  - Disassembly 34
  - Reconstruction Documentation Sheet 34
  - Work Authorization 34
  - Fact Sheets 34
  - Debris Assessment Working Group 35

Supporting Processes 37
- Environmental Safety and Health 37
  - Personal Safety 37
  - Component Monitoring 38
  - Decontamination Operations 38
  - Waste Streams 38
- Security 39
  - Area Security 39
  - Physical Control 39
  - Personnel Control 39
  - Security Procedures 40
- Public Affairs/Media Support 40
- Photography/Video Imaging Operations 41
- Document Control 42

Debris Assessment 43
- General Observations 43

Forward 53
- Forward Fuselage 53
- Forward Reaction Control System 54

Mid 55
Mid Fuselage 55
Payload Bay Doors 58
Wings 59
General Observations 59
Wing Glove 60
Intermediate Wing 62
Main Landing Gear Door 64
Torque Box 64
Trailing Edge/Cove 68
Elevons 70
Thermal Protection System - Wings 73
Left Wing 73
Right Wing 76
Wing Leading Edge Sub-System 79
Glove Region 85
Transition Region 88
Torque Box Region 94
Aft 97
Aft Fuselage 97
Orbital Maneuvering System Pods 99
Vertical Stabilizer and Rudder Speed Brakes 99
Body Flap 100
Payloads 101
Sub-Systems 103
Crew Module 103
Electrical Power Distribution and Instrumentation 104
Flight Controls and Hydraulics Systems 105
Landing Gear Systems 106
Life Support Systems 109
Mechanical Systems 110
Orbital Maneuvering, Reaction Control, and Auxiliary Power Unit Systems 110
Payload Mechanical System 111
Power Reactant Supply and Distribution and Fuel Cell Systems 112
Space Shuttle Main Engines and Main Propulsion Systems 113
Conclusions 117
Materials & Failure Analysis 119
Samples and Items Analyzed 119
Initial M&P Engineering Support 119
Midbody Panel 119
Main Landing Gear Door Uplock Roller 120
Landing Gear 120
Main Landing Gear Tires 120
Carrier Panel Attach Fasteners 120
Forward Outboard LH MLGD Corner Tile 121

Littlefield Tile 121
Pathfinder Debris Analysis 122
Analysis of Wing Leading Edge Debris and Attach Hardware 122
Radiography of Carrier Panels and RCC 122
Thermal Effects of LESS Carrier Panel Tiles 122
Evaluation of Deposits on RCC Panels 126
Summary of RCC Analysis 134
Summary and Conclusions 134
Critical Success Factors 137
Organization and Communication 137
Facilities and Infrastructure 138
Tools and Techniques 138
Search and Recovery Coordination 143
Supporting Processes 141
Debris Handling and Management 143
Appendix A - Definitions 147
Appendix B - RCC Sampling 147
Appendix C - Acronyms 147

EXECUTIVE SUMMARY

The Columbia search and recovery effort began February 1st, 2003. Expectations anticipated debris collected in east Texas and Louisiana would provide evidence critical to the Columbia accident investigation and aid in the development of the most probable failure scenario. In the first several days following the Columbia accident, a team formed and planning began for the reconstruction of Columbia. The Space Shuttle Program selected Kennedy Space Center's Shuttle Landing Facility Reusable Launch Vehicle hangar as the optimal reconstruction facility, based on its size, available technical workforce, access to the vehicle ground-processing infrastructure, and its proximity to materials science laboratories. This became known simply as the Columbia hangar.

In the planning phase, the Reconstruction Team established several critical processes for safe handling and management of the debris. These processes included receiving, handling, decontamination, tracking, identification, cleaning and assessment of the debris, each with an emphasis on evidence preservation. The team was comprised of engineers, technicians, inspectors and managers from the National Aeronautics and Space Administration, United Space Alliance, Boeing, and the National Transportation Safety Board.

The reconstruction effort spanned a period of five months in which 27 tractor-trailer loads of Columbia debris were shipped from Barksdale Air Force Base in Louisiana to KSC. As of June 30, 2003, the recovery forces collected an estimated 38 percent of the Orbiter's dry weight. The amount of debris received weighed approximately 84,900 pounds and comprised 83,900 items. The majority of items were no larger than one half square foot. More than 40,000 items could not be positively identified and were placed in the category of unknown metal, tile, electrical, tubing, structure, composite, plastic or fabric. The remaining balance of debris was instrumental in steering the investigation toward a root cause —with the 876 pieces associated with the left wing being the most critical.

Initially, a two-dimensional reconstruction of the Orbiter outer mold line was developed to facilitate assessment of the debris. As debris was positively identified, the left wing leading edge became the investigation's main focus area. This initiated a three dimensional reconstruction of the left wing leading edge panels 1 through 13. In addition, a virtual reconstruction of the Orbiter left wing leading edge was performed. A full-scale left hand wing was also built on tables to display lower surface thermal protection tiles and structure. These reconstruction techniques used in conjunction with material sampling and failure analysis, allowed the investigators to extract the greatest amount of information possible from the debris.

In general, most recovered debris exhibited a combination of thermal damage and mechanical overload failure. Items with high ballistic coefficients showed much greater levels of ablation, while others failed because of aerodynamic forces or ground impact. Specifically, the condition of the left hand wing leading edge provides compelling evidence of an initial breach in the transition region that resulted in catastrophic damage.

The Columbia Reconstruction Team concludes that the initial breach occurred in the lower surface of left hand Reinforced Carbon Carbon wing leading edge panel eight. The breach allowed plasma flow into the wing leading edge cavity, which melted the insulation and structural members in the transition region. The upper leading edge access panels were likely lost due to hot gas venting. Shrapnel from the disintegrating left wing impacted the vertical tail and left Orbital Maneuvering System pod. The plasma penetrated the left wing with one of the exit points being

through the trailing edge. The wing's structural capability was diminished to the point where it failed aerodynamically allowing the wing tip and elevons to break off. This resulted in vehicle instability thus increasing aerodynamic and thermal loads on the Orbiter's left side, which caused vertical tail and payload bay door failure. The vehicle orientation rotated to allow thermal flow to penetrate the left mid and aft fuselage sidewall at the wing footprint. In the right wing, the hot gas flow is from the inboard side. Internal thermal loading combined with increased aerodynamic load caused dynamic break up and separation of the upper and lower right wing skin panels. The breakup of the remaining fuselage continued from aft to forward until aerodynamic loads caused final disintegration of Columbia.

As with any undertaking of this magnitude, critical success factors and lessons learned can be gleaned from the organization and execution of such an effort. The goal in documenting this information is to positively influence the organization and execution of future accident investigations. With this intent, the critical success factors that were accumulated over the entire recovery and reconstruction efforts are discussed at the end of this report.

Introduction

Accident Background

On February 1, 2003 at approximately 0800 Central Standard Time the Orbiter Columbia broke up over east central Texas during re-entry into the earth's atmosphere. The Orbiter was returning to Kennedy Space Center (KSC) at the completion of mission STS-107. At the time of breakup, the Orbiter was traveling at about Mach 18 at an altitude of approximately 208,000 feet. The debris field was scattered over an area of eastern Texas and western Louisiana and measured approximately 645 miles long by 10 miles wide. The debris was recovered and shipped to KSC for examination in the Columbia hangar. It is estimated that approximately 38% (comprised of over 83,900 individual items) of the Orbiter, by weight, has been recovered to date. The debris field is depicted in figure 2.1 – Debris Field.

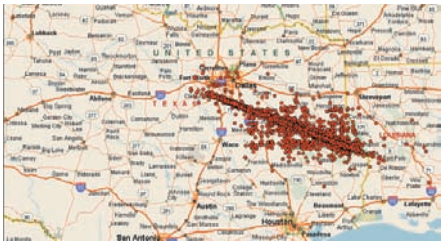


Figure 2.1 – Debris Field

Purpose of Reconstruction

Aircraft accident investigators typically perform a partial or total vehicle reconstruction to trace damage patterns and failure clues to aid in determining the accident's probable cause. This is especially useful when the recorded vehicle data does not provide significant insight into the causes and contributing factors or when an in-flight structural breakup occurs scattering parts over a large geographical area.

Reconstruction may take on many forms, but essentially involves placing the recovered debris into its original position prior to the occurrence of the structural failure. In some cases the reconstruction is performed in a two-dimensional (2-D) representation, and in other cases the debris is reconstructed three-dimensionally (3-D) in custom designed fixtures.

In virtually all aircraft accident investigations, a 2-D layout of at least a section of the vehicle is performed and only when enough information cannot be obtained through this method is a more costly 3-D reconstruction performed. Thus, the 2-D reconstruction planning must begin before the debris arrives at the reconstruction site. Planning for the 3-D reconstruction can be done months or even years later if required.

An essential decision to make before performing a 2-D layout is how to best utilize the available reconstruction space and how to intelligently represent a 3-D vehicle on a 2-D layout grid. Usually, the initial accident reports and preliminary data dictate the reconstruction scheme.

In most aircraft reconstructions, the fuselage layout is split at either the upper or lower centerline then opened up to show either the internal or the external surface. The 2-D layout grid has an expansion factor, usually set at 10 percent to 25 percent, allowing sufficient room for investigators to examine each piece of debris from all angles.

Damage patterns can be discerned as the reconstruction grid is populated. It becomes possible to study the damage's continuity or lack of continuity on associated pieces. As an example, if a wrinkle in one skin panel section continues across a break or tear, it is possible to conclude that the forces necessary to cause the wrinkle were applied prior to the break or tear. The continuity of smears and score marks across breaks provides additional evidence and aids in differentiating between in-flight, post-breakup, and ground impact damage.

Overall, relating the damage between individual debris pieces determines failure patterns, including directional indications of force application (for example, the manner and direction in which rivets, screws and bolts were sheared).

Many times differences between adjacent or symmetric (i.e., left vs. right) debris pieces provide valuable clues that lead to determining the initiating event. All significant debris pieces are documented and the most relevant are further analyzed by various sampling and forensic techniques. Because the failure modes and signatures of typical aerospace construction materials are known, an accurate assessment of the overall failure scenario can be made based upon the debris and material assessment results.

ORGANIZATIONAL STRUCTURE

The National Aeronautics and Space Administration (NASA) Deputy Administrator gave direction to perform the reconstruction at the KSC. This was the triggering decision for the creation of the Reconstruction Team and the activation of the Reusable Launch Vehicle (RLV) Hangar at the Shuttle Landing Facility (SLF) as the Columbia reconstruction site. Initially based on plans contained in SFOC-GO0014, KSC, Space Shuttle Program, Salvage Operations Plan, the Reconstruction Team structure was adapted for the Columbia contingency and debris reconstruction effort. NASA maintained primary responsibility for the Columbia reconstruction effort with support from United Space Alliance (USA), Boeing, the National Transportation Safety Board (NTSB), and other various support contractors. The team organization chart is shown in Figure 3.1 - Mishap Investigation Team (MIT) - Reconstruction.

Staffing the Reconstruction Effort

For the majority of the reconstruction period, approximately 75 personnel supported operations on each of two 8-hour shifts, 6 days a week. Technical experts from KSC and Johnson Space Center (JSC) were deployed to the Columbia hangar and assigned to staff the Floor Support, Technical Disciplines, Crew Module Support, Payload Support, Material and Process Engineering, or Data Management processes.

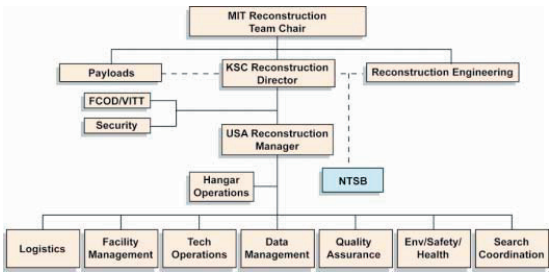


Figure 3.1 - Mishap Investigation Team (MIT) - Reconstruction

FLOOR SUPPORT

Floor Support consisted of Environmental Safety and Health personnel, Logistics Specialists, Receiving Technicians, Quality Inspectors, Material Handling Technicians, and Industrial Engineers. All were employees from the USA Integrated Logistics, and USA Orbiter/Launch Operations directorates. These personnel constituted approximately 60% of the daily workforce.

Environmental Safety and Health personnel were responsible for determining if detectible levels of hazardous propellant residue were present on the debris. This group verified each truck and box was safe for handling before entering the Columbia hangar. NASA, USA Safety and Health, and Space Gateway Services (SGS)/CHS Environmental Health and Services employed these personnel.

Logistics Specialists, under the supervision of a first line manager, controlled the truck off-loading and the uncrating of all materials received at the Columbia hanger. Orbiter technicians were used in the receiving areas to unpack and clean debris. Quality Inspectors verified debris associated field notes, separated multiple items under one tracking number into individual tracking numbered items and photographed each item.

Material Handler Technicians facilitated the movement of all material from one location to another. All items moved to the reconstruction grid, or material storage bins and shelves, were inventoried and recorded by material handlers.

Periodic audits of debris location within the Columbia hangar were performed to verify process integrity and accuracy. Industrial Engineers performed these independent assessments of debris handling and storage. In addition, a Grid Manager was utilized to control all movement of items to and from the reconstruction grid.

TECHNICAL DISCIPLINES

USA, Boeing, Rocketdyne, and NASA supplied the engineering support for the Columbia reconstruction effort. The engineering team leadership was comprised of NASA JSC Resident Office, USA Orbiter Element and USA Ground Operations. NASA/JSRO manager and USA Orbiter Sub-System Area Managers (SAMs) provided technical and processing leadership, including 3-D laser imaging and debris assessment respectively. USA Ground Operations provided administrative leadership. Engineering personnel made up approximately 30% of the total Reconstruction Team and consisted of the following disciplines:

- Structure Engineer - responsible for vehicle airframe debris
- Mechanisms Engineer - responsible for landing gear hatches and mechanisms
- Thermal Protection System (TPS)/ Thermal Control System (TCS) Engineer - responsible for Orbiter thermal protection debris such as tile, thermal blankets, gap fillers, etc.
- Hypergolic Engineer - responsible for Orbiter Orbital Maneuvering/Reaction Control System (OMS/RCS) components and safing of hypergolic contaminated debris
- Fluids Engineer - responsible for evaluation of non-hypergolic fluid systems debris such as main fuel cells, engines, radiators, etc.
- Electrical Engineer - responsible for evaluation of Electrical Power and Distribution, Instrumentation, and Avionics debris such as black boxes,

wiring, etc.
- APU /HYD Engineer - responsible for Auxiliary Power Unit (APU) and Hydraulic (HYD) Orbiter systems
- Flight Crew Systems (FCS) Engineer - responsible for processing & identification of items with which the crew directly interfaced
- SpaceHab/Payload - responsible for SpaceHab and STS-107 Payload related debris

An Engineering triage team was established and consisted of one engineer per shift for each discipline. Engineers were chosen to be members of this team based upon their multi-system experience and expertise. The triage team members were given the leadership responsibilities for processing and identification of the debris. Other system engineers, experienced senior technicians and quality personnel supported the engineering identification effort. The structures and thermal protection systems required the largest support groups.

A subset of specific engineers performed assessments of key identified items on the grid in support of the scenario teams at JSC. This group created fact sheets with detailed descriptions of the items and significant characteristics for each. Presentations were made to the Orbiter Vehicle Engineering Working Group (OVEWG) for these items on a weekly basis.

After the bulk of debris was processed into the Columbia hangar, the Debris Assessment Working Group (DAWG) was established. This team began a system wide engineering analysis of the debris to determine how the major structure and TPS elements failed. The DAWG was comprised of Boeing sub-system engineers, USA SAMs, USA system specialists, senior NASA system engineers and NTSB investigators.

CREW MODULE AREA STAFFING

The crew module organizational structure was dictated by a combination of the work force available at the Columbia hangar, the need for privacy for crew sensitive items, and the engineering experience needed for assessment.

KSC FCS technicians and KSC Vehicle Integration Test Office (VITO) personnel performed the first line of engineering assessment and held primary responsibility for conducting audits to verify debris was correctly handled.

The formal engineering assessment team consisted of engineers from the KSC FCS division (both USA and NASA) and members from the VITO (both KSC and JSC). Specialist engineers were brought in as required from JSC and Boeing Huntington Beach, CA for unique sub-system assessments.

The Flight Crew Operations Directorate (FCOD) at JSC assigned astronauts to the reconstruction effort, with them responsible for overall management of the crew module workforce. They provided a continuous on-site astronaut presence at the Columbia hangar. Other astronauts rotated to KSC for help in debris identification and determining stowage locations.

The crew module lead was responsible for working with Columbia hangar management, agency management, FCOD and the Crew Module Investigation Team to ensure appropriate handling of the debris while maintaining privacy and security.

PAYLOADS

KSC, Goddard Space Flight Center (GSFC), Boeing, and SpaceHab personnel supported payload recovery efforts. The core group consisted of two NASA Payload Management representatives, one NASA Operations Engineer, and NASA and Boeing engineers with extensive payload experiment backgrounds. This core group coordinated activities with the NASA Accident Investigation Team (NAIT), the KSC Reconstruction Team, the Shuttle

Payload Integration Office, and the payload developers. The engineers led the payload debris identification efforts.

SpaceHab provided several personnel on a rotational schedule that allowed debris to be analyzed by various disciplines. Initially two to four SpaceHab personnel supported first shift daily. In April, as the debris flow slowed down, SpaceHab was able to reduce this support to two days a week.

A team of three to five GSFC engineers traveled to KSC as needed to identify items from the Fast Reaction Experiment Enabling Science, Technology, Applications and Research (FREESTAR) payload. This small team visited approximately once each month for several days at a time.

MATERIALS & PROCESSES (M&P) ENGINEERING

The M&P team was formed to support the reconstruction effort with representatives from USA, NASA, and Boeing from JSC, KSC, MSFC, and Huntington Beach, CA. In addition to supporting the reconstruction engineering team, the M&P team supported the Hardware Forensics Team (HFT), the DAWG and the OVEWG.

Areas of responsibility included the following:
- Development of cleaning procedures and the actual cleaning of debris
- Submitting requests for disassembly of debris
- Development and execution of sampling procedures
- Performing nondestructive testing in the Columbia hangar and writing the test procedures and reports
- Performing analysis of debris items, or deposits on debris items, including writing the test procedures and related reports
- Performing failure analysis and writing related test plans, requests and reports

The team used laboratory resources from KSC (NASA, USA and Boeing NASA Shuttle Logistics Depot (NSLD)), Marshal Space Flight Center (MSFC), JSC, Glenn Research Center (GRC), Langley Research Center (LaRC) and Boeing Huntington Beach to support analytical activities. In a few select cases, laboratories outside the NASA community were used to perform unique analysis.

DATA MANAGEMENT STAFFING

The Columbia Reconstruction Data System (CRDS) development team consisted of multiple USA organizations. There was a core group that worked on-site, full-time while the remainder of the team worked remotely on an as-needed basis. The team consisted of a project leader, web page curators, web administrators, a database administrator and the Documentum support team.

The project leader's role was to act as an interface to the management team. By being intimately involved with the overall reconstruction process development, the project leader was able to define and prioritize software requirements to meet users needs. After software development, the project leader also validated the software to ensure it performed as expected prior to promoting to a production environment. The project leader was the overall system administrator and Responsible Data Manager (RDM) and approved all data access permissions after coordinating with the appropriate disciplines.

The web page curator team initially consisted of two fulltime, on-site, programmers from the Corrective Action Engineering group. These individuals were chosen due to their expertise and familiarity with Orbiter hardware. This background enabled them to perform rapid code development. In April, the web page curator's responsibility transitioned from Corrective Action Engineering to Applications Engineering Services.

The web administrators handled the

web server support. Their responsibility was to ensure the web servers were up and running, promote web software to the production environment, and provide access permissions when requested by the CRDS Project Leader/System Administrator. They also assisted in troubleshooting.

The DataBase Administrator (DBA) was responsible for overall maintenance and supportability of the Structured Query Language (SQL) Server database. The DBA was also the point of contact and responsible for all the interfaces with external databases, such as the Shuttle Interagency Debris Database System (SIDDS).

The Documentum Support Team was responsible for the storage and retrieval of all photographs and supporting debris documentation. User interfaces were developed by this team to easily load photos and documents into the proper folder structure. In addition, web pages were developed by this team to quickly and easily retrieve the photos and documents.

External Interfaces

MISHAP RESPONSE TEAM

The initial NASA response to the loss of Columbia was the establishment of the Mishap Response Telecon chaired by the Mission Management Team. The Mishap Response Telecon managed and coordinated all activities for the first 24 hours. The telecon became the Mishap Response Team (MRT) the day after the accident. Representatives from all program elements, as well as other federal agencies, departments, and military units participated in assisting with the recovery efforts and supported the MRT.

The KSC Rapid Response Team (RRT) consisting of 40 people, under the auspices of the MRT, arrived at Barksdale Air Force Base (BAFB) within 12 hours of the accident. KSC's initial support was two-fold; First, the senior leadership in Texas and Louisiana presented plans for the debris recovery in the field and second, KSC leadership presented their status on supplying personnel for that effort. The RRT evolved into two distinct teams; one responsible to continue the planning and recovery of the Orbiter debris, and one established to begin the reconstruction of the Orbiter debris itself. Planning for the formation of the Reconstruction Team began at this point. The Reconstruction Team at KSC was formed less than 1 week after the Columbia accident upon the decision of the NASA Deputy Administrator.

The chain of command that initially had the Reconstruction Team reporting to the MIT evolved over time, given the geographic separation of the Recovery Team in Texas and the Reconstruction Team at the Columbia hangar. The Reconstruction Team was recognized as a distinct and separate entity and began reporting directly to the MRT. This was also necessary because the ground search ended and the MIT was phased out two months before the reconstruction effort concluded. The Reconstruction Team provided its status to and received direction from the MRT for the remainder of the reconstruction/investigation.

COLUMBIA ACCIDENT INVESTIGATION BOARD

Concurrent with the above, the NASA Administrator activated an independent investigative body, the Columbia Accident Investigation Board (CAIB). By policy, the Board controlled the debris and began to assemble the members and support staff required to conduct an investigation into the accident.

The MRT received direction from the CAIB and continued the NASA investigation into the accident using all of the functional elements and organizations normally reporting to the Space Shuttle Program (SSP).

COLUMBIA TASK FORCE

Recognizing the need for a formal interface, the Columbia Task Force (CTF) was established shortly after the CAIB and became the forum for resolving all matters between the Board and the MRT. The CTF had no specific investigative responsibilities, but was an administrative body that controlled a number of work tasks and ensured appropriate managers were aware of their tasks and priorities.

NASA ACCIDENT INVESTIGATION TEAM

After approximately 7 weeks, the MRT was reformulated into the NAIT to reflect the same three-team structure and responsibilities the CAIB had adopted. The NAIT Team 1 (Materials) lead was the Deputy Center Director of KSC. The Team 2 (Operations) lead was the Deputy Center Director of JSC, who also acted as the overall NASA lead. The Team 3 lead (Engineering) was the Director of Engineering at JSC.

Representatives of the CAIB, NAIT, OVEWG, NTSB, and the Astronaut Office were co-located with the Reconstruction Team to facilitate communication and expedite all necessary paperwork.

TECHNICAL SUPPORT

Many companies and government organizations were called upon to provide special expertise to the Reconstruction Team. These included:
- Michelin: Tire identification
- Goodrich: Landing gear identification
- Aerospace Corporation: Re-entry science
- NASA Glenn Research Center: Wiring
- NASA Langley Research Center: High temperature materials
- Federal Bureau of Investigation: Tile identification
- Honeywell: Avionics identification
- SpaceHab: SpaceHab item identification

Other teams active in the investigation called upon the Reconstruction Team for their knowledge of the debris and what it showed. These included:
- OVEWG
- Failure Scenario Teams
  STS-107 Unexplained Anomaly Closure Team

FACILITIES OF RECONSTRUCTION

Columbia Hangar

The hangar located on the south end of the SLF runway adjacent to the Orbiter tow way was used as the primary facility for the receipt, processing, and investigation of the Columbia debris recovered from the field. Originally built for the RLV, this 50,000 square foot facility allowed ample room for a 2-D, 110 percent scale layout of the Orbiter airframe outer mold line (OML) and TPS. Forty thousand square feet of the available hangar space was dedicated to the 2-D grid, while the remaining 10,000 square feet was used to accommodate storage and processing areas. The hangar is pictured in figure 4.1 – Columbia Hangar.

The east wall of the Columbia hanger provided staging for items associated with TPS, Internal Structure, and Reinforced Carbon Carbon (RCC), as well as the sub-system personnel. The west wall of the hanger provided areas for the following sub-system personnel and hardware:

- Avionics
- Main Propulsion System (MPS)
- Purge, Vent & Drain (PVD)
- APU
- Orbiter Electrical (OEL)
- OMS
- Environment Controls and Life Support Systems (ECLSS)
- Payloads and SpaceHab

One bay along this wall, plus the southwest corner of the facility, was used for the 3-D laser scanning effort. Large storage boxes lined the south end of the hanger providing storage for unknown materials made of metal, fabric, plastic, or related to electrical, and payload bay door (PLBD) debris items.

A separate area was constructed within the facility for recovered crew module debris and served as a visible barrier allowing the debris to be handled with discretion.

Clamshell

A 13,000 square foot facility termed Clamshell 4 was chosen to provide auxiliary storage in addition to the Columbia hangar. The purpose of this facility was to store large system components not directly relevant to the





Figure 4.1 – Columbia Hangar





Figure 4.2-Clamshell Auxiliary Storage

investigation. This additional storage capacity allowed for growth in the main facility processes and work areas. The Clamshell is pictured in figure 4.2 – Clamshell Auxiliary Storage.

Certain debris items were selected for storage at the Clamshell including:

- Space Shuttle Main Engine (SSME) items
- Power Reactant Storage and Distribution (PRSD) tanks
- MPS helium Tanks
- APU tanks
- SpaceHab/FREESTAR items
- Unknown TPS items

Midfield Park Site Decontamination Area

It was determined that a facility separate from the Columbia hangar was required to cope with any debris contaminated with hypergolic fluids. This facility, known as the SLF Midfield Park Site Decontamination Area, was capable of handling this type of debris. The decontamination facility included waste and rinsate drums, hard-line breathing air, protective equipment, and an impound storage cage. The decontamination area is pictured in figure 4.3 - SLF Midfield Park Site Decontamination Area.

The SLF Midfield Park Site Decontamination Area was set up in accordance with current KSC requirements (FSOP 6100 USA Florida Safety Operating Plan and KHB1710.2 KSC Safety Practices Handbook) and approved for use by both NASA and USA.

All hazardous waste was processed and removed from the area in accordance with current KSC requirements when the recovery effort was completed and the SLF Midfield Park Site Decontamination Area was no longer required. The site was then disassembled.





Figure 4.3-SLF Midfield Park Site Decontamination

TOOLS & TECHNIQUES

Columbia Reconstruction Database System

Prior to the database team being formally chartered, a preliminary database application was already being developed. It was deployed to the BAFB recovery site to begin the task of tracking recovered items.

Within 4 days of the accident, the official database team was established. This team was given the monumental task of having a fully operational database system designed, developed, tested and deployed within 1 week of being formally chartered. When the debris began arriving at the Columbia hangar 1 week later, the Columbia Reconstruction Database System (CRDS) was online and ready to support.

ARCHITECTURE

The CRDS architecture consisted of an SQL Server database with a Cold Fusion web page user interface. Documentum, USA's enterprise document management system, was used to store digital photographs, 3-D images, and various documentation files. Documentation files consisted of various Word documents such as fact sheets, .pdf files, and scanned-in files. Both the SQL Server database and Documentum systems were backed up daily. This architecture provided a robust and secure backbone for the CRDS. It also allowed remote sites at BAFB and other NASA facilities the ability to access the data as needed to aid the recovery and investigation operations.

In parallel with the development of the CRDS, numerous other databases were developed to support recovery operations. The CRDS team remained in constant communication with these other teams to ensure seamless data flow between systems. These other databases were later consolidated into what became SIDDS.

All CRDS data with the exception of photos, documents and secure crew module item data, was replicated real-time to the SIDDS. Some SIDDS data was also replicated to the CRDS such as the Environmental Protection Agency (EPA) tracking numbers, field descriptions, and latitude/longitude information.

USER INTERFACE

The CRDS web pages were designed to provide all users with a common look and feel. This provided users changing from one job to another an easy transition with a minimum of training. All users' screens provided access to common information such as engineering assessment and current item location. In addition, all screens provided a complete history of where the item had been, who performed various functions on the item, and date/time stamps of when the function was completed.

The CRDS provided straightforward user access to a variety of information via a standard set of hyperlinks on all web pages. Using this standard set of hyperlinks, any user could view photographs or open related supporting documents. Additionally, items that had a 3-D image rendered could be viewed directly from the CRDS web page.

The CRDS user interface also provided hyperlinks back to the EPA database that was used by the recovery operation. With the proper access permissions, a CRDS user could gain access to additional recovery data, such as photos taken at the recovery sites, along with any other descriptive data contained in the EPA database.

ACCESS CONTROLS

Read access of the CRDS was made generally available to the NASA centers and to contractors involved in the Columbia investigation, provided they were within trusted domains.

The CRDS had controls to assign data entry permissions to authorized personnel. The system administrator granted the

permissions upon receiving a written request from the process owners. Personnel with data entry permissions were restricted to the screens pertinent to their job functions. As an example, only users with engineering permissions could access the data entry screens for engineering assessment. Users with FCOD permissions had additional access to view and update secure crew module engineering assessment fields.

In addition to data entry controls, the CRDS provided data access controls for the viewing of information relating to crew module items and Flight Crew personal items. Engineering assessments, crew module photos and documents were considered sensitive and viewing access controls for secure information were established both by network login and Documentum user authentication. Network login user authentication provided viewing access control to the secure database entries and Documentum provided an additional layer of security for secure photos and documentation. Only personnel with the FCOD or CAIB permission level could access secure data.

The CRDS team continually addressed issues by adding new functionality to the system. These enhancements were made throughout the entire life of the reconstruction project. The team continually supported the user community by providing custom reports for data not readily available from the standard query reports provided via the web page. CRDS is continuing to evolve with the addition of archival requirements used to support the long-term storage and study of the Columbia debris.

Two-Dimensional Grid

With guidance from the NTSB, a grid layout was chosen which maximized the amount of Orbiter OML that could be reassembled in the space available in the Columbia hangar. A 2-D layout was chosen over a 3-D layout for reconstruction. This was due to the limitations a 3-D layout would place on accessing each of the items after placement on the grid, as well as the supposition that only a very small percentage of the Orbiter would be recovered.

The outline of the Orbiter airframe sections that were to be reconstructed were laid out on the hanger floor. To aid in placing items in their proper location on the grid, each airframe section was annotated with Orbiter X_o, Y_o and Z_o coordinates. Another feature of the grid was that it was laid out at 110% of the actual size, which provided access between the recovered items. This allowed for detailed evaluations of each item for fracture matching and accounted for the deformed condition of the items. Only items with a higher probability of contributing to the Orbiter break up were chosen for reconstruction on the 2-D grid. The OMS pods, the Forward Reaction Control System (FRCS) and most internal system components were not placed on the grid; however, they were placed in storage around the perimeter of the grid for easy access if required. The grid is depicted in Figure 5.1 – Columbia Reconstruction Grid.

The Orbiter layout for the forward, mid and aft fuselage was split along the upper centerline, splayed open, inverted, and then laid on the floor with the TPS surface facing up. A separate grid area was set-aside for any individual lower surface tiles that were no longer attached to the airframe.

Each wing was divided into three separate regions; the lower TPS, the lower structure and the upper structure combined with TPS. The wing sections were positioned adjacent to the perimeter of the forward, mid and aft fuselage grid but not contiguous to the mating surfaces. As the focus of the investigation narrowed

to the left wing leading edge, a separate area was added to the left and right hand wing grid that represented the wing Leading Edge Sub-System (LESS) hardware.

Each elevon was assigned a region on the grid separate from its physical location on a wing. The body flap was positioned in its general location with respect to the aft fuselage. The elevons and the body flap components were oriented with the lower TPS surface facing up.

The vertical tail section and the rudder speed brakes were split into a left and right hand region. Each region was placed on the grid with the exterior surface facing up. These two regions were placed at the north end of the hanger near the forward fuselage section.

When the evaluation process of reconstruction began, the mid body lower surface items that mated with the left wing were temporarily relocated to their proper orientation on the left hand wing lower surface grid or to the tile tables. The tile tables were platforms built up off the floor in the left wing lower surface TPS region of the grid. This allowed engineers to safely place tiles out in the open for evaluation without concern for damage by personnel walking the grid.

After the focus for TPS identification was narrowed to the left hand wing, the lower fuselage TPS region of the grid was partially used for the left and right Main Landing Gear (MLG) hardware and the Wing Leading Edge (WLE) 3-D fixtures.

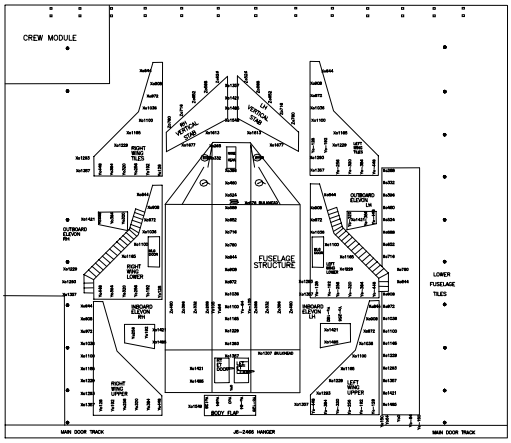
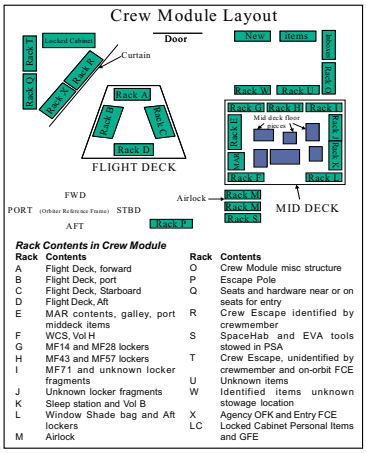


Figure 5.1. Columbia Reconstruction Grid

Figure 5.2. Crew Module Grid



Rack Contents in Crew Module

Rack	Contents	Rack	Contents
A	Flight Deck, forward	O	Crew Module misc structure
B	Flight Deck, port	P	Escape Pole
C	Flight Deck, Starboard	Q	Seats and hardware near or on seats for entry
D	Flight Deck, Aft	R	Crew Escape identified by crewmember
E	MAR contents, galley, port middeck items	S	SpaceHab and EVA tools stowed in PSA
F	WCS, Vol H	T	Crew Escape, unidentified by crewmember and on-orbit FCE
G	MF14 and MF28 lockers	U	Unknown items
H	MF43 and MF57 lockers	W	Identified items unknown stowage location
I	MF71 and unknown locker fragments	X	Agency OFK and Entry FCE
J	Unknown locker fragments	LC	Locked Cabinet Personal Items and GFE
K	Sleep station and Vol B		
L	Window Shade bag and Aft lockers		
M	Airlock		

Crew Module Reconstruction

The crew module was set up as a 3-D grid upon recommendations from the NTSB. The 3-D aspect was provided by the use of bread racks to store items in bins. One area of the crew module was set up as the flight deck and another as the middeck. Racks were labeled both with their physical location identification on the Orbiter and also with a simple rack identification. The crew module grid is depicted in Figure 5.2 - Crew Module Grid.

Crew personal and sensitive items were kept segregated even within the crew module area because of their potential emotional impact and also their potential financial value. Personal items and agency Official Flight Kit (OFK) items were kept in a locked cabinet in the segregated area as an extra measure of security.

The initial decision was made to only manage debris that was interfaced by the crew inside the crew module area. The significant structure inside the crew module included the Middeck Access Rack (MAR), panels from the flight deck and the airlock, and middeck floor. Structural floor items set up in the middeck area inside the crew module. As the crew module investigation developed, more structural information was needed. The condition of the water tanks under the middeck floor, the black boxes in the avionics bays, and the physical pressure vessel structure were all collected for analysis. Ultimately the pressure vessel structures were brought into the crew module area of control. As there was insufficient room in the crew module area to store all items, items that were pulled off the structures racks were stored first in large boxes and eventually on bread racks. Bulkheads were reconstructed for short periods of time so that photos could be taken and to allow the investigators to evaluate them; for space reasons they were piled up on pallets between evaluations.

M&P Sampling and Analysis

SAMPLING

A sampling plan was developed to ensure that samples obtained from the Orbiter debris yielded the most data possible while maintaining the integrity of the debris. This plan defined sampling type by criticality, destructive and nondestructive debris sampling, and preservation of samples.

Sampling criticality was divided into two classifications. Type II sampling was defined as sampling conducted on a critical surface, such as a fracture surface, a uniquely damaged area, or a single point source of contamination. By default, Type I sampling was defined as those that did not meet the Type II criteria. The level of approval required for sampling depended upon the classification.

Several destructive and non-destructive sampling techniques were developed. These included coring for debris which was either on or embedded in tile, removal of metal deposits from the structure or RCC surface by a clean laboratory scalpel or forceps, and removal of a small portion of the debris item by cutting with a diamond blade.

Preservation of debris samples was an important aspect of sampling. Photos of the debris item were taken prior to taking a sample. The sample orientation relative to the original item was maintained and documented. Also, work instructions defined packaging requirements to prevent sample contamination.

Various techniques were used in determining a location for sampling on a debris item. The prevalent methods used throughout the reconstruction effort were stereomicroscopy and real-time x-ray analysis.

Stereomicroscopy was used to locate areas of interest on a debris item and to determine if further analysis was required. It was also used during actual removal of samples from the debris item and in conjunction with photo documentation. This sampling technique aided in the identification of part numbers or serial numbers that were not visible to the naked eye.

Also in support of sampling, a real-time x-ray technique was established. This technique used a standard x-ray source and an amorphous silicon plate for detection. X-ray images were collected real-time on a computer and enhanced to provide an aid in selecting debris items for sampling and the sample location. This technique was calibrated using aluminum and Inconel of various thicknesses allowing the team to locate contaminants in or on a debris item composed of either high or low atomic mass.

Debris items sampled included RCC, tile, and metallic components. As the investigation progressed, the majority of the sampling was done in support of analysis for left WLE items.

ANALYSIS

The M&P team employed standard forensic analysis techniques in both the Columbia hangar and laboratories. Some non-destructive testing was conducted within the hangar using stereomicroscopic examination, x-ray, and eddy current. Analytical techniques developed and evolved throughout the investigation as results from previous analyses gave the team insight into the types of information that could be gleaned from the debris. Initial analyses consisted of the following:

- Optical macroscopic and microscopic examination
- Polarized light microscopy-crystalline characterization
- Scanning Electron Microscopy (including low-vacuum) with Energy Dispersive X-Ray Spectroscopy (SEM w/ EDS) including semi quantification and dot mapping
- X-Ray Photoelectron Spectroscopy or Electron Spectroscopy for Chemical Analysis (XPS or ESCA)

- Metallographic sectioning, mounting, polishing
- X-Ray Diffraction (XRD)
- Fourier Transform Infrared Spectroscopy (FTIR)

As the investigation progressed the following techniques were included:

- Exemplar technique
- Neutron activation
- Microprobe with Wavelength Dispersive Spectroscopy (WDS)
- Auger spectroscopy

A number of laboratories were used for the various analyses. These included NASA laboratories at KSC, MSFC, JSC, LaRC and GRC, USA laboratories and Boeing Huntington Beach laboratories. In addition to these locations, several industry and university laboratories were used during the investigation including Batelle, Caltech, and North Carolina State University.

Forensic analysis techniques played a significant role in the analysis of left hand MLG components, WLE structure and selected left wing tiles.

Three-Dimensional Physical Reconstruction

LEFT WING LEADING EDGE

The evaluation of the WLE hardware, as it was laid out on the grid, quickly reached a point where no further useful information could be ascertained. It was decided to reconstruct this region in 3-D and a local prototype lab was tasked with fabrication of 3-D support fixtures for the WLE hardware. These fixtures consisted of a transparent Lexan sheet that was shaped to the contour of the RCC panel and Tee OML. Metal braces supported the Lexan and connected it to a support sub-frame. This connection was made with quick disconnection pins allowing the Lexan and bracing portion of the fixture to be rotated for access to the interior of the RCC panel. The sub-frame was attached to a heavy metal stand through a pivoting arm that allowed the RCC items to be viewed either right side up or inverted like the grid orientation. The stand was mounted on castors to make the fixtures as mobile as possible. Each fixture contained two or three adjacent RCC panels.

The RCC panel items were attached to the contoured Lexan sheets using several different methods that ensured no damage to the RCC material resulted. The spar fittings were also attached to the fixtures to maintain continuity for the evaluation of the RCC hardware. A picture of these fixtures is depicted in figure 5.3 - Left Wing Leading Edge Physical 3-D Fixtures.

A complete 360-degree evaluation of each item was possible for the WLE hardware using the fixtures. This allowed the investigators to clearly visualize each RCC panel/tee and their relationship with adjacent panel items, which was nearly impossible in the 2-D layout. The 3-D fixtures allowed an accurate assessment of the percentage of recovered RCC material for each location to be made. Direct comparisons between related areas on different panels were also possible.



Figure 5.3. Left Wing Leading Edge Physical 3-D Fixtures

Due to the cost and manpower required to fabricate the fixtures and the emphasis placed on merely a small portion of the WLE, only RCC panels 1 through 13 were built-up into 3-D fixtures. For the remainder of the RCC panels, foam blocks, plastic backing material and tape were used to cobble the items together into a facsimile of an RCC panel and Tee.

RIGHT WING LEADING EDGE

To support the comparison of the right hand WLE to the left, the right side was also reconstructed in 3-D. However, due to the same limitations noted above, no right hand WLE panels were placed in fixtures. The same materials and techniques used on the left hand WLE panels 14 through 22 were used for all the panels on the right side. An example of this technique is depicted in figure 5.4 - Right Wing Leading Edge Physical 3-D Reconstruction.

LEFT WING LOWER TILE

Initially, when a tile was positively identified or identified to an approximate Orbiter location, the tile was placed in a tote box on the grid at the corresponding X_0 and Y_0 location. This method however failed to provide a visual trend of the overall wing TPS. Additional tools were required to assist TPS engineers with the debris assessment process and to allow investigators to visualize the entire lower surface. Thus, 22 moveable tables, sized to allow for easy access and handling, were built to replicate the lower left hand wing surface. A picture of the tile tables is shown in figure 5.5 – Left Wing Lower Tile Tables.

The tables were covered with a full-scale tile map that displayed the part number and cavity size of each tile. The tables were covered with Lexan to prevent degradation of the maps. Troughs were added to the WLE to hold the lower LESS carrier panels. Structural seams were added to the table to establish visual indicators for screed and rivet patterns.

These tools allowed each positively identified tile to be correctly placed on the table and provided visual data to help with the evaluation of scenarios. Placing the positively identified tiles on the table also assisted in the identification of other tiles by matching their damage characteristics to the characte-ristics of the previously identified tiles.



Figure 5.4 - Right Wing Leading Edge Physical 3-D Reconstruction



Figure 5.5 – Left Wing Lower Tile Tables

Virtual Reconstruction

At the time of the Columbia accident, NASA was engaged in the Digital Shuttle Project to document the as-built configuration of the Orbiter using scanning devices. After a demonstration of Digital Shuttle's capabilities, scanning was adopted as a Reconstruction Team technique. The initial purpose was to provide a 3-D virtual reconstruction visualizing Columbia debris items in their proper location on the Orbiter. Later it was also used for debris identification.

Two scanning methods were utilized during the reconstruction effort depending upon the complexity of the debris to be scanned. The MENSI Corporation scanner used a tripod-mounted laser scanning head that projected a focused laser beam to image the object and was primarily used to scan skin panels and TPS carrier panels. The Advanced Topometric Optical Scanner (ATOS) used a digital white light to scan the object and was used for debris with complex shapes requiring higher definition. Examples of debris item placement can be seen in figures 5.6 - Left Wing Leading Edge Virtual 3-D Lower View and 5.7 - Left Wing Leading Edge Virtual 3-D Upper View.

After scanning each item, post processing was required. Post processing is the manual process used to refine the scan results into usable solid body Computer Aided Drafting (CAD) rendering of an object. A key result of post processing was that the specific location for each debris model was determined within the Orbiter X_0, Y_0 and Z_0 coordinate system. These coordinates were then used to properly locate objects in the CAD environment in order to achieve a 3-D virtual reconstruction of the Orbiter. DELMIA Corporation CAD software was used to accomplish this task.

While the combined processing produced the 3-D model of a scanned object, the object's surface was monochrome. Texture mapping provided a means to capture the true colors of an object and place them on the scanned image. Texture mapping was achieved by taking a series of digital photographs from various look angles around the perimeter of the object and electronically mapping the photographs onto the scanned image.

The scope of the scanning effort evolved as the investigation matured. At one time the scope included scanning of both wings, the leading edges, and the mid-body. However, the final product featured only the left wing and its leading edge with the items in RCC panels 5 through 10 texture mapped. Several factors influenced the content of the final product:

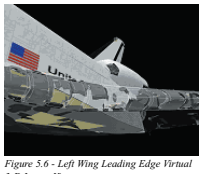


Figure 5.6 - Left Wing Leading Edge Virtual 3-D Lower View

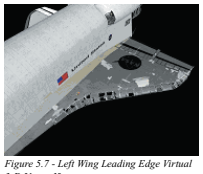


Figure 5.7 - Left Wing Leading Edge Virtual 3-D Upper View

- The focus of the investigation upon the left wing
- The intensive time and effort to scan, post-process, and rig
- The desire to texture map key items
- The addition of debris identification

The first debris identification effort was for "The Littlefield Tile", a small triangular tile fragment that was the western most piece of debris recovered. Geometric matching determined it was a left wing upper surface tile located about 24 inches behind RCC panel 9. Over the course of the investigation, no additional tile identifications were made using this process, however 20 RCC items were scanned to aid in the identification process. The identification effort eventually yielded positive identification of four RCC items and narrowed the possible locations of the other 16 RCC items.

The visualization objectives of scanning were achieved by producing a movie on CD-ROM and DVD with fly around scenes of the left WLE, left wing upper and lower surfaces, and interior views of the left wing including phantom displays of the unrecovered internal structure. The movie also had views of the left WLE RCC panels' interior surfaces.

Identification Tools

ELECTRONIC MAPS

Electronic Maps (E-Maps) is a 3-D computer model originally designed for tracking tile waterproofing and TPS inspection status. However, the tool was used during reconstruction to visualize the OML of the debris recovered. The 3-D model could be rotated or zoomed in or out to accommodate any view angle or level of detail desired.

E-Maps was modified for the reconstruction effort to allow tracking of positively identified RCC and OML structural components placed on the grid. Using color codes, the Reconstruction Team was able to designate three categories of debris; structure with tile, structure only, and tile only. Technicians used a laptop computer to collect the data from the grid. The lap top data was later downloaded to a data collection server. As the tools matured, downloading was accomplished using a wireless network that had been installed in the Columbia hangar.

Another modification made to the E-Maps tool provided a visual indication of where the items were recovered. By importing recovery latitude and longitude data from the CRDS, the E-Maps system showed where the debris was found in comparison to the Orbiter flight path. An example of this is depicted in figure 5.8 - Columbia Reconstruction E-Maps Computer Model.

THERMAL INFORMATION PROCESSING SYSTEM

The Thermal Information Processing System (TIPS) database tracks all TPS component installation and repair information. The following tools were programs controlled by TIPS, used

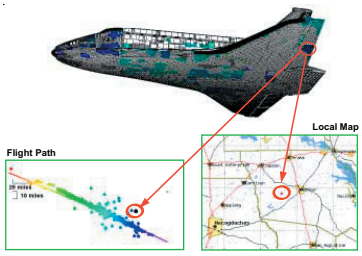


Figure 5.8. Columbia Reconstruction E-Maps Computer Model

essentially for TPS identification purposes:

Multiple Document Interface for Gap Fillers (MDIGAP95)

MDIGAP95 is a graphics program that provided information on tiles and gap fillers installed on all Orbiters. The database is updated each day during Orbiter processing for all configuration changes to tiles and gap fillers. The database that tracked Columbia's components was preserved immediately following the accident. This allowed the system to be used for the reconstruction efforts.

MDIGAP95 data consisted of Order Control Numbers (OCNs), and unique part tile part numbers, tile thickness at the center of the tile and Strain Isolation Pad (SIP) thickness. All of the above data allowed engineering to perform a data search on a partially identified OCN or part number, and then match it with the corresponding tiles that had similar SIP and tile thickness. This provided a list of tile part numbers that the item could represent.

To further support the tile identification effort, the MDIGAP95 database was modified to provide information relating to corner thickness and sidewall angles. Since many lower surface tiles have similar thicknesses, distinctive sidewall angles provided another path in which engineering could isolate a distinct tile characteristic, thus narrowing the possibilities of potential tile numbers.

Shuttle Configuration & Information Display (SCIDS95)

SCIDS95 allowed the capability to enter a tile part number to view 3-D graphics with Orbiter X_0, Y_0 and Z_0 coordinate information for all points. From the X_0, Y_0 and Z_0 point data, engineering could calculate any of the tile sidewall lengths as designed per drawing. This design length was then compared to the item being evaluated. SCIDS95 data combined with the information from MDIGAP95, efficiently narrowed the search for a potential positive identification of a tile.

SCIDS95 also provided the location of structural seams and spar locations in relationship to a tile. Since the majority of tiles recovered were from the lower surface of the vehicle, some structural seams and spar lines provided a distinguishing footprint on the bottom of a tile. SCIDS95 allowed engineering to narrow the location of a tile by the seam or spar line and the tile's thickness.

Columbia Reconstruction Identification Database

During standard vehicle processing, the TPS community does not have access to the master TIPS database. This database contains information pertaining to tiles such as tile thickness, material type, a inner mold line (IML) footprint, specific repair types and screed installations. The standard method used to gain access to this information is to call or e-mail TIPS personnel. However, with the reconstruction efforts and the Columbia portion of the database preserved, it was possible to provide read only access to engineering for some portions of the database. This provided another tool for the tile identification team to perform data searches on key characteristics of an unidentified tile to narrow the search for potential part numbers.

Automated Work Control System

Automated Work Control System (AWCS) is the system used by the Thermal Protection System Facility (TPSF) to track the fabrication of TPS components. The

system was used during the reconstruction effort to find a gap filler part number when only the OCN was known. MDIGAP95 was then used to find the exact location on the Orbiter.

TILE THICKNESS MAPS AND SIDEWALL ANGLE CHARTS

Tile thickness maps are items that are used during standard vehicle processing. The maps are color coded with the tiles' thickness for each Orbiter. With the reconstruction effort, the maps were used to see trends in tile thickness for identification purposes.

The ability to identify the wing tiles became crucial once it was determined that the lower left wing was the critical area of investigation. Since lower wing tiles have distinctive sidewall angles, charts depicting actual design sidewall angles were created. This was used when a tile was determined to belong to the lower wing region. The sidewall angle of the debris item was compared to the sidewall angles charts. This was essential in facilitating the tile's potential location. The TPSF supplied the sidewall angle charts and thickness maps.

CONFIGURATION VERIFICATION ACCOUNTING SYSTEM

The Configuration Verification Accounting System (CVAS) was developed to track all configuration changes to hardware on the Orbiters. After the accident, Columbia's database was also preserved. This allowed the reconstruction effort to utilize the database in the identification of both TPS and non-TPS components. CVAS aided in the identification process by providing any necessary information from part numbers to document numbers.

SHUTTLE DRAWING SYSTEM

The Shuttle Drawing System (SDS) is a system that provides on-line access to all Boeing controlled engineering drawings and Engineering Orders (EOs). During the reconstruction effort, SDS was utilized to help identify components with distinct design features such as rivet, rib or seam patterns, screed, or instrumentation.

DEBRIS HANDLING AND MANAGEMENT

Receiving and Process Flow

A receiving and processing flow was developed prior to arrival of the first debris truck at the Columbia hangar. An overview of the Receipt & Processing Flow activities is depicted by figure 6.1 – Receipt and Processing Flowchart and the flow of debris items within the hangar is shown in figure 6.2 – Hangar Work Area Debris Flow.

SHIPPING AND TRANSPORTATION

Barksdale AFB in Louisiana served as the central collection facility for all debris being collected at the various field recovery sites in east Texas and Louisiana. As debris was received at the BAFB hangar facility, a data record for each item was entered into the CRDS and assigned a KSC tracking item number. A paper traveler that included the KSC item number, associated bar-code and descriptive information was then printed and attached to the item.

Some items were not entered into the CRDS during times when there was a significant backlog at BAFB in order to expedite items to KSC. Instead, the shipping box containing multiple items was entered into the CRDS and assigned an item number for tracking purposes.

Debris items were packaged for shipment at the Barksdale collection site. Typical packaging of debris involved bagging or bubble wrapping individual items before boxing or crating. Larger items were palletized for shipment.

As debris was collected at BAFB, a delivery schedule was established for shipment of the debris to KSC. Lone Star Trucking Company performed the transport of the debris from BAFB to KSC. At first, two trucks departed Barksdale every Monday and Thursday

RECEIPT & PROCESSING FLOW

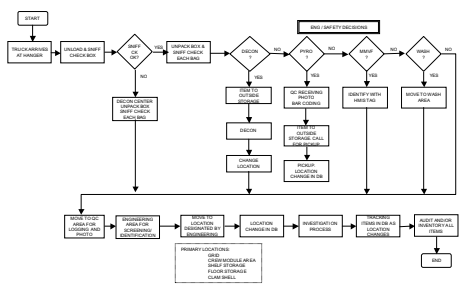


Figure 6.1 – Receipt and Processing Flowchart

with arrival scheduled at KSC every Tuesday and Friday. Several months into the recovery effort, as the amount of debris collected began to taper off, the frequency of shipments was reduced to one truck twice a week, then eventually to an as needed basis.

As items were loaded onto the trucks for shipment to KSC, shipping reports were generated from the CRDS to inventory what was on the truck. Each truck arrived with a shipping manifest.

Crew module debris items required special handling due to their sensitive nature. These crew module items included crew personal items, valuable items such as mission patches, and generally most crew escape items. Therefore, a process was set up in the field to segregate and protect those types of debris to ensure they were not exposed to public or media viewing and to prevent theft. Items identified in the field as sensitive were packed in boxes and labeled. These boxes were carried in the cab of the transport truck from Barksdale AFB to KSC.

There were some debris items that were thought to be biologically hazardous, thus these items were sent directly from the field to JSC. After being cleared as safe to handle, these items were boxed up separately, labeled and sent to KSC.

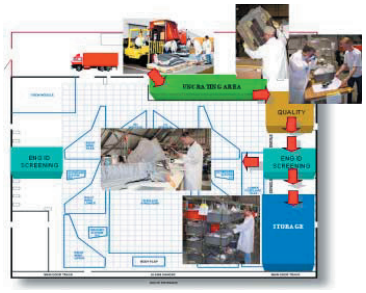


Figure 6.2 – Hangar Work Area Debris Flow

Weighing of Debris

After the arrival and processing of the first shipment of debris at KSC, the program levied a requirement to determine the weight of the recovered hardware. To avoid having to weigh each item individually, a statistical analysis was performed on the next several shipments of debris to determine the weight of the shipping pallets, storage boxes and packaging material. Using the inventory list of the first shipment, a close approximation of the total weight of non-debris items was established. A detailed review of photos of all the items in the first shipment was performed and several specific items were weighed. The approximate total debris weight was calculated using this data.

For all subsequent shipments, the loaded weight of each truck was determined at the Logistics Facility prior to unloading at the Columbia hangar. The weight of each shipping container, standard pallet, and truck trailer was subtracted from this value. All non-standard pallets were individually weighed and the weight of all packing materials for each shipment was determined. The weight of these items was also subtracted from the total.

The combined weight of all the debris shipments was calculated to be approximately 84,900 pounds. This represents 38 percent of Columbia's 223,900 pound dry weight.

UNCRATING

After the debris arrived at the Columbia hangar, all containers and items were screened in the unloading/unpacking zone for hazards or contaminates. Toxic Vapor Checks (TVCs) were performed on all boxes and containers down to and including zip lock bags before processing any items. All items deemed safe to handle were unpacked and unwrapped. Any items identified as pyrotechnics or crew module received special handling.

Debris suspected of containing Man Made Vitreous Fibers (MMVF) was sealed in plastic bags or wrapped in plastic wrap to contain any hazardous particulates. The term friable was also used to describe these items, which refers to any item that is easily broken into small fragments or reduced to powder. Hazardous Material Inventory System (HMIS) tags were then affixed to notify personnel of the possible hazards involved, all items deemed safe to handle were unpacked and unwrapped. All items were then checked against the manifest/shipping document to assure receipt of all items. External packaging and wrapping materials were then broken down and weighed. The weight was used for the final calculation of received materials.

QUALITY RECEIVING

Database Entry

After the debris was uncrated, it was transferred to the quality receiving area where it was photographed and appropriately tagged. A data record was generated or updated for each debris item using the CRDS. Items previously entered in the CRDS at Barksdale were checked in at the hangar with minimal data entry. New records for items not previously entered into CRDS at Barksdale were created at this point in the process. When multiple items contained in the same box or bag were identified with a single tracking number, the items were separated and assigned individual item numbers referenced to the parent item number. This was referred to as the parent/child relationship.

Data records included item description, time and date of arrival, location of recovery area (longitude and latitude), and date and time of recovery. EPA and SIDDS tracking numbers that were generated at the field recovery sites were entered when available.

Bar-coding

A bar-code was generated for each piece of debris. The bar-code label was attached directly to the debris item or affixed to the packaging containing the item. The bar-code labeling system improved efficiency throughout the process when accessing CRDS screens.

Both pen and gun type scanners were used in the reconstruction process. Personal Digital Assistants (PDAs) with bar-code scanning capability were also used in the reconstruction process. The PDAs were used primarily for audit and inventory purposes.

Photographing

All debris items were photographed as part of the receiving process with 4 mega-pixel digital cameras. The photos were linked to the debris item data record using the CRDS. Photos of items related to the crew module were uploaded to a password-protected partition in the database. Additional photos were added upon request of any Reconstruction Team member.

Because of the secure photo requirement, crew module debris was not photographed at the quality receiving area like all other debris. It was routed to the crew module area and verified as either crew personal or non-personal. Once it was identified as not personal, a photograph was taken within the crew module and the photo was uploaded to the secure area of the CRDS. The number of quality receiving personnel asked to

perform this function within the crew module area was kept to a minimum to maintain the appropriate level of sensitivity.

MOVEMENT AND RELEASE OF DEBRIS

As the debris items moved through the process, their location was tracked using the CRDS. In addition, when a part left the Columbia hangar, the quality assurance personnel made an entry in the CRDS to record authorization for item removal. Upon debris return, an additional entry was made.

The CRDS was utilized to track the current locations of all items and the complete running history of all item locations. Using the CRDS, the handlers assigned items to a grid location, storage location, or sent them to engineering or quality assurance for further disposition.

Grid Management

A method of tracking the movement of debris on and off the grid was required. Flags were the tools developed to help manage the movement of the debris. When a flag was used as a placeholder for an item temporarily removed from the grid, the item number and name of the person removing the item were recorded on the back of the flag and the item location in the database was left unchanged. The following flags were used:



NEW - This flag was placed with new items on the grid that had not been entered into the E-Maps program. This flag was removed when E-Maps personnel began evaluating an item.



EMAPS - This flag was placed with items on the grid that were being evaluated by E-Maps personnel. The flag was removed when E-Maps had been updated to show the inclusion of the noted item.



HOT PINK - This flag was placed with items on the grid that had been evaluated by E-Maps but the location could not be positively identified.



LASER - 3-D Laser Imaging personnel used this flag as a grid placeholder when an item was temporarily removed for 3-D image processing.



CAIB - CAIB team members used this flag as a grid placeholder when an item was removed from its original grid location as part of the investigation process.



ENG - Engineering personnel used this flag as a grid placeholder when an item was temporarily removed for further evaluation.



PROCESS EVAL - This flag was placed with items on the grid that were being audited as part of Process Evaluation. This flag was removed when Process Evaluation for the item in question was complete.

The Grid Manager and the Industrial Engineering group performed periodic audits of the debris location within the Columbia hangar to verify system integrity. Using the CRDS, a material handler compared the location of the debris in storage to the location stored in the database, correctly relocated any debris found in the wrong location, and then updated the database accordingly.

A quality function was developed to ensure database entries were truly standardized. The VITO had developed a cue card for 'Level 1 Audit' procedures for the crew module to check for standardization. These procedures were adopted for the broader hangar operation. The audit ensured entries were standardized, that accurate latitudes and longitudes were entered, that items were logged in and that photographs were in the proper part of the database. After the audit began, new items that came in were audited before placement on the 2-D grid. This method ensured that at least two individuals looked at the database entry; the original data entry personnel and then the auditor.

Debris Release Process

Any time a debris item or sample of a debris item was removed from the Columbia hangar premises, a sample release form (SRF) or impound release form (IRF) was required. A SRF required the approval of Quality and the Reconstruction Engineering Lead while Quality and the NASA Reconstruction Director approved an IRF.

Contaminated debris was either entered into the CRDS and temporarily stored outside the Columbia hangar until pick up, or was moved directly to the decontamination site with accountability recorded down to the major package level (i.e., box).

As the engineering teams identified debris items for transfer to the clamshell for storage, the database was updated to indicate that the debris had been relocated. Quality personnel issued a release form before a material handler moved the item to the truck. This process was repeated for each item being transferred. Once at the clamshell, the items were offloaded with their new location recorded for later entry into the CRDS.

Debris Requiring Special Receiving

CREW MODULE DEBRIS RECEIVING

Boxes of debris labeled "Crew Module" were segregated as soon as the truck arrived. Members of the crew module team were on hand as a designated receiving technician opened each bag to check for hazardous contents. Once the TVC was complete, the box was taken to a cordoned area with quality and handling personnel. Quality would print out bar-code labels and enter the description based on guidance from the crew module person. This was to ensure that field descriptions did not contain sensitive information that could identify the item in the public part of the database. The handler would then check out the item directly to the crew module.

The field recovery process did not capture all personal or sensitive items; therefore these items would sometimes arrive mixed in with the other debris. Receiving technicians would immediately contact crew module personnel and ensure that those items were expedited to the crew module area. Non-sensitive items followed the standard process through receiving.

BIOLOGICAL DEBRIS

Initially, biological debris was screened by medical personnel in the field or sent to JSC for medical screening. Upon arrival at KSC, this debris had already been verified safe for handling and was routed through the normal receiving process and then stored along with the other systems debris. This debris did not require any special provisions other than the use of normal Personal Protective Equipment (PPE) during handling.

Toward the end of the recovery effort, medical screening at JSC and in the field was suspended. KSC then adapted the

receiving process to have resident medical personnel screen the biological debris as it arrived in the receiving area before it continued through the normal hangar processes. This was done to ensure that no biological hazards existed and that no incidental remains entered the process.

PYROTECHNIC DEVICES

Pyrotechnic devices were identified and segregated from other items, placed in ammo cans, then relocated to the pyrotechnic storage Conex outside of the hangar until they could be transported to an impound area within the Ordnance Storage Facility. Pyrotechnic engineering was notified for pick up and safing of the items. Expended pyrotechnic items were then returned to the Columbia hangar.

KSC work authorization documents controlled traceability and all work associated with the identification, transport, impounding and disposition of pyrotechnic components. Proper authorization was obtained from the Prevention/Resolution Team (PRT) representative prior to disposition of pyrotechnic components.

Engineering Identification Process

After the debris receiving process was completed, items were routed to the engineering identification area of the hangar. Items initially identified by the Engineering Triage Team as Orbiter debris were further categorized as either airframe (Tile, RCC or Airframe skin) or non-airframe. Duplicate engineering identification areas were established on the east and west sides of the hangar.

All non-airframe debris items were routed to the west identification area with a non-airframe traveler attached to facilitate movement of the items through all sub-systems. After determining an item did not belong to a specific system, engineers put a check in the box by their system and passed the item on to another system. When ownership of an item was established, the component was identified with the appropriate system and the CRDS was updated. The item was then placed in storage in the appropriate system bin.

When ownership of an item could not be determined, as evidenced by a check in all boxes on the traveler, a material handler put the item in the 'Unidentified' storage area. The traveler was retained with the item for future verification that the component had been evaluated by all systems.

Airframe items were routed to the east identification area of the hangar and evaluated by engineering to determine their exact location on the Orbiter. Items positively identified (using drawings, maps, etc.) were entered in the CRDS and routed to their final location on the grid (wing, mid fuselage, body flap, etc.) and updated by E-Maps personnel. A red tag was placed on an item if it was identified only to a particular section of the grid and not to a final, positive location. The red tag clearly distinguished these items from positively identified items and allowed items to be maneuvered on the grid until final placement was determined. Airframe components not readily identified were placed in a staging area until they could be placed on the grid and/or additional expertise could be contacted to assist with the identification. Red tagged, staging area, and positively identified debris items were all updated in the CRDS.

The remaining items that could not be identified were updated in CRDS as belonging to one of the following unknown categories and routed to storage:

- Metals
- Tubing
- Electrical
- Fabric/Composite
- Non-Orbiter
- Structures
- TPS
- Plastics

Database entries throughout the

process reflected the effort to identify items and their stowage locations. Part and serial numbers were used when known. The concept of key words for search functions was understood early and was incorporated into a standardized entry format. The standard format for an item was established by each engineering discipline. Keywords that were meaningful to each sub-system were used consistently in the engineering description field, which would allow for database searches of like items.

CLEANING

M&P Engineering provided cleaning procedures and instructions to support the reconstruction triage and engineering efforts. Triage procedures for the cleaning of tiles, blankets, RCC, composite structure, metals, non-metals and electrical components were provided. Specific procedures to aid in part identification were written for tile, printed circuit boards, and MLG components.

Cleaning procedures were documented in a procedure titled 'Detailed Cleaning Methods to Aid Identification and Engineering Analysis'. A one-page summary of triage cleaning instructions was also prepared and posted in the hangar.

TILE IDENTIFICATION

Approximately 7,000 tile items were recovered. Due to the varying degree of damage, several different methods were used during the tile identification process. First, identifiable tiles were sorted in triage by longitude. 96 degrees longitude was chosen to segregate the tiles that may have initially come off the lower left wing, which was the critical area of focus for the investigation. Any tiles found west of 96 degrees longitude were retained in the engineering area for evaluation. These tiles were then sorted by vehicle locations. All tiles, except the wing and tiles west of 96 degrees longitude, were routed to storage. Material handlers entered the possible vehicle location, as identified by engineering, in the CRDS and then routed the tile to the appropriate storage bin. If an unidentifiable tile fragment was received, it was routed directly to unknown tile storage.

The potential wing tiles found west of 96 degrees longitude were first evaluated to determine if a part number could be read. Part numbers were visible on some tiles or could be retrieved by a simple cleaning of the part using Isopropyl Alcohol (IPA). Black lights used with IPA sometimes allowed faded impressions of the part number to be read. When part numbers were not detectible, distinct tile features such as thickness, sidewall angles and repairs were used to aid with the identification process. Engineering drawings were used when there was a distinct design feature on the tile, such as a rivet or seam pattern on the IML, instrumentation, or insert holes. The TIPS database provided a history of each tile that included most repairs and bond and removal dates. Documented repairs often provided enough of a signature to use as an identifier. The TIPS database allowed engineering to perform a data run of a particular repair of the tile within a specific thickness and footprint. This information would then aid in reducing the number of potential part numbers for a specific tile.

Initially, when a tile was positively identified or identified to an approximate location (distinguished by a red tag), the tile was placed in a tote box on the grid at the corresponding X_0 and Y_0 location. This method however failed to provide a visual trend of the overall wing TPS. Full-scale TPS tile tables were used to allow each positively identified tile to be placed in its exact location, therefore trends became more apparent. Placing the positively identified tiles on the table assisted in the identification of other tiles by matching

their damage characteristics to the characteristics of the previously identified tiles.

CREW MODULE

Once an item was identified as possible crew module debris and routed to that area of the hangar, various sub-system engineers familiar with the equipment in the cabin reviewed the debris. A series of inboxes were used for each sub-system and items for review were placed there. If an item did not belong to a sub-system that engineer marked the part accordingly and passed it to the next inbox. If a part completed this process and remained unidentified it was placed on a rack for unidentified parts. Frequently, identification was not possible beyond the type of material used (i.e. metal, fabric, foam, etc.). The crew module team also examined the hangar unknown part bins looking for any additional crew module items.

When an item was positively identified, an effort was made to identify its stowage location within the cabin in the event that information proved useful to the investigation. Positive identification proved challenging because some payloads were stowed on the middeck and some Government Furnished Equipment (GFE) was stowed in SpaceHab. In some cases, items with multiple onboard copies, like Payload and General Support Computers (PGSC) or Photo TV equipment, had more than one possible stowage location.

PAYLOADS

The initial MRT direction to the payloads identification team was to simply separate payload debris from Orbiter debris to better facilitate the prime Orbiter structural focus of the investigation. However, the identification effort quickly grew to identifying specific payload assemblies where possible. This positive identification not only provided a certainty that the item was not to be included in the Orbiter investigation, it ultimately led to unexpected recovery of science.

Positively linking payload debris to one of 80 experiments flown on STS-107 was challenging and complicated. Due to the diversity of experiment owners, experiment configuration information was not located in centralized drawing systems or databases. The recovery team called on payload integration offices and payload developers to provide drawings or photos documenting the original configuration of the experiments. Hardware developers provided photos that included the assembly stage through final closeouts. SpaceHab provided their module drawing and payload closeouts photos. Payload identification was aided by the Boeing Engineering Action Center, especially when part numbers or other identifications were visible on debris.

In addition, payload developers were brought in, when appropriate, to help identify their unique internal hardware items. In some cases, when specific experiment debris was positively identified, payload developers were able to facilitate science recovery efforts. KSC initiated global CAIB/NAIT approval for researchers to access their hardware debris for science recovery.

Search and Recovery Coordination

The accurate and prompt relay of engineering assessments of the significant recovered items from KSC back to the recovery command center at Lufkin was crucial to the debris search effort. The reconstruction effort provided daily updates to the recovery team in an attempt to assist in search prioritization. The accuracy of data published in Lufkin depended heavily on the prompt relay of engineering assessments from KSC for the significant parts recovered in Texas and Louisiana. By working closely with

Weston, EPA's contractor, KSC supported the recovery team by investigating, verifying, and correcting inconsistencies in the recovery location data. Comparing the results from data mining in both the EPA/Weston and the KSC databases allowed KSC to find and correct any errors or mismatches located in either database. By tracing actual field data sheets on the recovered items in the hangar, KSC was able to correct hundreds of data entry errors in both databases. Correcting latitude and longitude inconsistencies was vital to the success of planning the search and recovery efforts.

SIGNIFICANT RECOVERED ITEMS LIST

The product used to facilitate the exchange of information between reconstruction and recovery was the Significant Recovered Items List (SRIL). This product was used by the Lufkin Command Center to methodically and continuously refine plot strategies for further air and ground searches. The SRIL became the single source of accurate recovery information and engineering assessments for the majority of the left wing recovered debris. The search areas were extended beyond the initial corridor as a result of daily engineering assessment updates to the SRIL.

KSC supported the recovery efforts of the Columbia Recovery Office (CRO) for the western states with a separate list of recovered items, named CRO SRIL. This list closed the feedback loop to the CRO for items found in California, Nevada, Utah, and New Mexico. As items were received and assessed, the list was updated and distributed via email to the CRO at JSC.

FAST TRACK PROCESS

The fast track process was initiated to prioritize the handling and assessment of significant recovered items, particularly left wing components and items found outside the main debris field. This process was also used to expedite the identification of items from the same areas on the vehicle as cameras, film, and recording devices. By tracking this debris, search teams could extrapolate the most probable location of these critical recording devices.

When an item was assessed in the field as possibly fitting the description, the item was tagged as "Fast Track" and sent to KSC on a priority basis. These parts were segregated on the transportation trucks to ease identification upon arrival at the Columbia hangar. Fast tracked items received priority processing through the receiving and engineering assessment processes in order to expedite a final description of the item and relay that information back to the recovery team.

DEBRIS PLOTTING CAPABILITY

Unique maps were used daily by the air, ground, and water search groups in Texas to triangulate locations of key components and successfully locate related items. These plots were created using updated assessments supplied by the Reconstruction Team via the SRIL.

At the Columbia hangar, debris plots were developed upon request by the search or investigation teams. These maps were used to verify and correct latitude and longitude data for recovered items. Plotting the pick-up points and times of certain EPA/Weston field teams helped correct possible latitude and longitude debris errors.

Plots based on item type were developed for engineers performing analysis on initial vehicle break-up scenarios. Other plots of particular recovered items helped engineers in the hangar identify and assess individual items based on their proximity to each other or by where they landed in the search corridor.

Recovery locations located outside the search corridor required verification

due to the inconsistencies in the Global Positioning Satellite (GPS) latitude and longitude formats initially entered in the EPA/Weston Database. The plotting enabled a quick determination of which points required investigating. Although a great deal of effort was spent on trying to decipher the correct location, the daily plots were not 100 percent accurate.

Engineering Assessment Process

The engineering team personnelused a variety of assessment methods. The majority of engineering assessment was accomplished in the hangar. Offsite testing and M&P analysis was performed when required.

In most cases, an engineering assessment of the debris could be performed via visual examination. When necessary, stereomicroscopic (30-500X) examination was performed for part identification or to analyze fracture surfaces or heat-damaged features. A variety of traditional Non-Destructive Evaluation (NDE) techniques were also available in the Columbia hangar. Sampling of numerous debris items was performed and the samples were analyzed at offsite laboratories. In a few select cases, failure analysis was performed at offsite laboratories on debris items or extractions from debris items.

DISASSEMBLY

When required for debris identification, sampling or failure analysis disassembly instructions were provided via a Reconstruction Documentation Sheet (RDS). The debris configuration was recorded and photographed prior to disassembly. Detailed steps annotated disassembly and assembly procedures. Where applicable, the debris was returned to a pre-disassembly configuration.

RECONSTRUCTION DOCUMENTATION SHEET

An RDS was a form used to document any work that was performed on a debris item. The RDS included instructions to properly perform any activity from simple disassembly through destructive testing. The RDS was titled and identified by the KSC assigned item number.

As steps in the RDS were worked, personnel performing the work either signed or initialed the step indicating completion of the step. After completion of the final step in an RDS, it was returned to the library for record retention.

Approvals for working an RDS were:

- Systems Engineer
- MIT representative
- CAIB representative

WORK AUTHORIZATION

Work authorization approval guidelines were established early in the reconstruction process. For non-intrusive tasks such as NDE, disassembly for identification purposes, and non-destructive sampling, a RDS approved by the system engineer, MIT local representative and CAIB resident were sufficient. In all other cases, approval of the OVEWG, MIT, MRT and CAIB was required. A Test Approval Request (TAR) was utilized to document this authorization. When the NAIT was formed as the replacement for the MIT/MRT, it became the authority.

FACT SHEETS

Engineering generated fact sheets on key or critical debris items without supposition of cause. Fact sheets documented physical observations and laboratory results of a debris item. All fact sheets were posted in the CRDS and were available to all investigators. For example, fact sheets contained the following

information:
- Zone and item number
- Part number and nomenclature
- Associated items
- Location drawing
- Physical observation
- General condition
- Materials (design & foreign)
- Deformation
- Fracture features
- Thermal effects
- Environmental effects
- Photos or critical sketches/drawings
- Sampling or NDE Results

DEBRIS ASSESSMENT WORKING GROUP

The DAWG, with guidance from the NTSB, was a team comprised of airframe engineers from NASA, USA and Boeing, and M&P engineers. The charter of the DAWG was to determine what the hardware revealed independent of telemetry, photographic and video data, derived hypothetical scenarios, and timeline evaluations. The DAWG compiled system summaries from all Orbiter sub-systems and generated airframe and TPS reports of all the major regions of the Orbiter. From these evaluations, a failure scenario based solely upon the debris evidence was developed.

SUPPORTING PROCESSES

Environmental Safety and Health

NASA and USA Safety and Health reviewed the Columbia reconstruction process and assessed the hazards associated with the Orbiter and the handling of its components. Plans were put in place to mitigate both physical and health hazards to an acceptable level. Where applicable, engineering controls were incorporated into the process and the appropriate PPE was identified and required for use.

The health hazards identified included, but were not limited to, the handling of hypergolic contaminated items, contacting liquid chemicals and handling friable materials. Hypergolic propellants are fuels and oxidizers which ignite on contact with each other and need no ignition source. For Orbiter systems the fuel is Mono-Methyl Hydrazine (MMH) and the oxidizer is nitrogen tetroxide (N2O4). Friable materials are those that are easily broken into small fragments or reduced to powder.

The physical hazards identified included, but were not limited to, the handling of non-contaminated debris, handling of ordnance and handling high pressure systems. Special procedures were established for each of these hazards.

The NASA Environmental Program Branch and USA Environmental Management reviewed all processes and walked down the reconstruction impoundment areas to identify potential environmental compliance concerns in an effort to limit liability with state and federal regulations.

The USA Environmental, Safety & Health organizations supplied the reconstruction engineering team with a checklist to review when writing debris handling work steps so that all potential safety or environmental issues could be addressed prior to the process being implemented.

PERSONAL SAFETY

Training

The KSC workforce is required to maintain a mandatory level of safety training for normal vehicle processing. In addition to this mandatory training, all personnel obtaining access to the Columbia hangar, with either a permanent or temporary badge, were required to review a safety briefing. This briefing described all potential safety and environmental hazards within the hangar and the individual's responsibilities upon entering the hangar. After the briefing, individuals were required to sign a course attendance roster verifying their understanding of safety requirements. Only then was a hangar access badge issued.

Personal Protective Equipment

PPE was identified for each process and posted throughout the hangar. All PPE requirements were defined in the component handling PPE matrix, which was part of the safety training briefing.

Typical PPE requirements for performing TVCs on trucks prior to unloading and for unloading trucks included the use of Pylox or Kevlar gloves, Tyvek coats, safety glasses, hydrazine dosimeters, and steel-toe shoes. Similarly, the PPE required for personnel opening bagged components, handling friable materials, handling components with liquid, handling non-contaminated components, or using less than or equal to 4 oz of chemical for cleaning purposes consisted of the use of Kevlar gloves, Nitrile gloves, goggles and aprons, safety glasses and Tyvek coats.

Additional PPE requirements were established for personnel emptying the High Efficiency Particle Air (HEPA) filter vacuum or for personnel cutting RCC or TPS material. Typical PPE requirements consisted of the use of Nitrile gloves, safety goggles, Tyvek coats, and air purifying respirators.

COMPONENT MONITORING

Toxic Vapor Checks

TVCs are performed using a meter which can detect trace levels of hazardous chemicals. TVCs performed at the Columbia hangar by Environmental Health personnel were to determine if debris was contaminated with fuel and/or oxidizer residue.

Any items that were identified as having detectable levels of hypergolic propellant residue were immediately routed to either a fuel or oxidizer cabinet located outside of the hangar and transported to the SLF Midfield Park Site Decontamination Area for further evaluation.

Particulates

All debris items that were determined to contain MMVF (i.e. glass fibers) were clearly marked with the hazard and contained in a tote tray or wrapped in plastic when appropriate. All areas where MMVF items were handled or stored were routinely cleaned with approved HEPA vacuums to keep the particle count to a minimum.

Sample monitoring of the hangar and the various personnel identified to be in Similar Exposure Groups (SEGs) was performed by Environmental Health Services. The personal sampling plan for fibers, respirable particulate and silica was set up to perform four personal samples per SEG per shift. Sampling of various SEGs continued throughout the reconstruction effort.

It is policy at KSC to use the most stringent guidelines of the Occupational Safety and Health (OSHA) Permissible Exposure Limit-Time Weighted Average (PEL-TWA) and the American Conference of Governmental Industrial Hygienists (ACGIH) Threshold Limit Value-Time Weighted Average (TLV-TWA). The area monitoring of the hangar and the personal monitoring of the employees did not reveal any violation of the exposure limits for the criteria stated above.

DECONTAMINATION OPERATIONS

All items identified as possibly hazardous or contaminated were routed to the SLF Midfield Park Site Decontamination Area for further evaluation. There, technicians performed more detailed toxic vapor checks to determine if the suspect parts were truly contaminated or just off-gassing residual vapors that may have been trapped in the plastic bags during transportation.

The SLF Midfield Park Site Decontamination Area was set up to handle decontamination operations for both fuel and oxidizer contaminated debris. Detailed procedures to decontaminate the debris were developed, which reflected operations routinely performed during flight processing. Safety and Environmental Health closely monitored all SLF Midfield Park Site Decontamination Area operations.

The SLF Midfield Park Site was chosen as a decontamination area due to its remote location and ease of modification to an impoundment site. NASA Environmental requested that the area around the site be sampled prior to and at the completion of the decontamination activities to ensure that the Columbia reconstruction process caused no ground contamination.

Although no actual decontamination operations were performed at the SLF Midfield Park Site Decontamination Area, some wastewater was generated by the removal of mud from the debris. The final ground sampling after deactivation of the site indicated no contamination.

WASTE STREAMS

An Environmental Phase I Site Assessment of the Columbia hangar was performed prior to the beginning of

reconstruction operations and a closeout assessment was performed when all reconstruction operations were completed.

Waste Containment

USA Environmental Management evaluated all processes that occurred inside the Columbia hangar and at the SLF Midfield Park Site Decontamination Area for possible waste generation. All possible waste streams were collected and sampled prior to disposal. Processes were reviewed for waste minimization practices before receiving Environmental Management approval. One drum of waste water was generated during reconstruction operations and was treated as hazardous waste.

Wash Down Area

A wash down area was set up on the north side of the Columbia hangar to allow mud to be washed from some of the larger debris using water. A wash down area was established and approved by the Florida Department of Environment Protection (FDEP) prior to use. The wash down area consisted of a heavy-duty plastic tarp laid on the ground and surrounded by petroleum absorbing booms and a turbidity barrier. A third layer of protection at the wash area was provided by placing hay bales around the perimeter of the turbidity barrier for support.

Chemical Usage

Prior to use, all chemicals were approved by the CAIB through coordination with USA M&P Engineering, Environmental Management, and Safety & Health. Cleaners were limited to water, Spirit 126, and IPA. No aerosols or other cleaners were allowed inside the hangar without prior approval from the above organizations. Limiting the chemicals used during the reconstruction process prevented incompatibility issues with the debris, minimized the type of PPE required for the operations, and mitigated the waste streams to non-hazardous waste only.

Security

AREA SECURITY

The designated debris impound areas included the Columbia hangar, the north facility apron area adjacent to the hangar, the recovery/salvage related temporary storage buildings and containers required to support the reconstruction effort. Additional controlled areas included the SLF Midfield Park Site Decontamination Area, Landing Aids Control Building (LACB) and the clamshell.

PHYSICAL CONTROL

Physical security measures included secure core locks, deadbolts, security seal eyelets, a designated key custodian, and an eight-foot chain link fence at the north side of the hangar. The fence controlled both personnel and vehicle access to the hangar. Entrances outside the fenced area were locked and sealed. Security Officers provided armed access control to this area.

All Conex trailers and dumpsters were located within the secured area. The on-site Security Officer and the Access Control Monitors (ACMs) conducted periodic checks of the security seals.

Six Closed Circuit Television (CCTV) cameras were installed in various locations inside the Columbia hangar. Videotapes were routinely collected by a NASA Special Agent and stored in a combination safe. Additionally, a video monitor capable of displaying all camera angles was installed in the guard shack at the personnel access point to the Columbia hangar.

PERSONNEL CONTROL

Personnel requiring access were properly badged for KSC and were also placed on a hangar access list. An additional badge, approved by NASA KSC Security, was issued for personnel on the list. Three badge designations were used: "Permanent", "Temporary", or "CAIB".

For personnel who would be at the hangar nearly full time, a "Permanent" badge was issued with their name written on it. Permanent badges were kept until the work at the hangar was completed. Personnel at the hangar three days or less a week were issued a "Temporary" badge. This badge allowed the same access as the permanent, however was surrendered at the end of the day. The third designation was a "CAIB" badge, which was a brightly colored full-access permanent badge that allowed for quick identification of CAIB members.

SGS Security Officers provided 24/7 access control and security to the Columbia hangar and surrounding fenced area. One officer ensured all personnel requiring entry to the hangar were in possession of the proper badge or under the control of a properly designated escort. The officer also verified appropriate hand receipts were obtained prior to removing debris and other controlled equipment from the hangar and that no prohibited items were brought into the hangar.

In addition, USA provided three ACMs to control access and provide security inside the LACB and Columbia hangar. The ACMs issued permanent and temporary badges and conducted badge exchanges for temporary personnel from the Action Center inside the LACB. They logged temporary badged personnel in and out of the hangar, and ensured appropriate hand receipts were used when necessary. ACMs also checked all interior hangar security seals and assisted with the opening and closing of the hangar.

SECURITY PROCEDURES

Designated debris areas were established as NASA Limited Areas and were controlled as such. Limited area signs were posted conspicuously around facility perimeters and on fences in accordance with KHB 1610.1 (as revised), KSC Security Handbook.

Introduction and removal of material or packages into or out of the designated area, or sub-component areas, of this operation was controlled by a system that identified the individual(s) moving the item(s), and accountability/ tracking of the item(s) moved. This system was determined and managed by designated authority specified in SFOC-GO0014, KSC, Space Shuttle Program, Salvage Operations Plan.

Unless approved by the Reconstruction Director, the following items were prohibited inside the Columbia hangar:

- Briefcases, backpacks, lunch boxes, or other such containers
- Cameras and laptop computers
- Food and drink items
- Flammable devices

Media events inside the Columbia hangar were supported with one SGS Security Officer and/or a NASA Special Agent. Mutually agreed upon media areas were cordoned off with ropes and stanchions. These areas provided the media access to the debris without compromising security and safety requirements.

Public Affairs/Media Support

As the Columbia debris began arriving at KSC, the Center's Public Affairs Office (PAO) was asked to coordinate with the Reconstruction Team concerning all media requests concerning the reconstruction effort.

While the debris grid was being populated, KSC PAO worked closely with managers to organize media tours through the hangar, assist with interviews with designated managers, and respond to numerous media questions concerning reconstruction. The NASA News Chief at KSC was assigned to be the single point of contact to coordinate media interview and hangar tour requests.

Working under CAIB guidelines, PAO

and the Reconstruction Team held weekly media events in the hangar and hosted reporters and photographers who desired access. Every other week, the Reconstruction Chairman met with the press and during this event provided them with details, on the record, regarding the progress of reconstruction efforts.

PAO also supported routine events involving reconstruction efforts by providing extensive photographic and TV coverage of the activities for release to the media and the general public. The images were provided to the media via PAO dissemination methods (i.e., web, NASA TV uplink, press releases, etc.).

Events routinely photographed and documented included the weekly truck deliveries of debris and the eventual placement in the hangar, workers in the hangar, CAIB tours, elected representatives and other VIP tours, and media activities in the hangar.

Photography/Video Imaging Operations

Aside from the photo documentation done for the PAO, the reconstruction personnel needed their own photographic support to complete their work. The photographs were used to provide visual documentation of hardware at check in to the CRDS, to support the hangar status briefing to the NAIT and OVEWG, for engineering identification of hardware through electronic transmission to system experts, on-site and off-site engineering routine uses, unique initiatives such as the virtual scanning or the spectral imaging, and the CAIB's investigations.

Initially, the quality receiving personnel within the hangar were capable of supporting the required needs. However, the engineering need for additional support with images for their interim reports and to share information with off-center investigators quickly overwhelmed the process.

Since access to the debris needed to be controlled, any requirement for outside photography or other imaging operations needed to be coordinated through the NASA operations office. Specific requests that could not be handled in house were assigned to KSC contract photographers. Photographic tasks requiring contractor support were overall grid photos, tile table photos, WLE 3-D reconstruction fixture photos and unique engineering request photos.

Contractor photographers became accustomed to taking photographs of the overall grid view, detail shots of each wing, and hangar operational improvements intended to be shared with the entire investigative management team. The support of high-rangers and other personnel lifts were used to get the best image possible. The photographer and the personnel needed to operate the heavy equipment were scheduled twice per week. The same photographer and personnel lifts were also used to take the final report images of each grid area in the hangar.

Additionally some unique initiatives required that engineers take photos. The NASA operations office authorized theses requests on as as-needed basis. An example was the spectral imaging to capture the spectrum reflected by debris excited by lasers. This was in an attempt to aid the debris identification and recovery effort in the field. Another requirement was to support the texture mapping of the laser scanned debris so that a visible image could be overlaid onto the virtual image taken. These images were transported outside the hangar to specialized facilities across the country for processing, but remained protected and impounded due to information technology security requirements levied on the process.

The HFT also required highly detailed images using special equipment. M&P personnel provided dedicated camera

equipment to the hangar. This equipment remained secured within the hangar for the length of the investigation.

The CAIB investigators were authorized to use their own photographic equipment within the hangar. To discern and control who was allowed to have personal equipment, all CAIB members were issued orange badges from the reconstruction action center.

Document Control

As additional documentation requirements evolved during the reconstruction process, it became apparent there was a need to establish some form of paperwork storage and control in the hangar. A library was set up to house all paperwork that was not directly attached to the debris.

Team Leaders were authorized to publish plans and procedures in support of the overall Orbiter Reconstruction Plan. All documents were revision controlled and a hardcopy was provided to the librarian. The Quality Assurance Manager was responsible for the librarian function.

The librarian maintained the Orbiter Reconstruction Plan and any supporting documents, as well as the RDS used for testing, sampling, or other activities involved with the investigation of the debris. The library contained hardware debris reports, fact sheets and tile paperwork. The librarian maintained an index of those documents, which provided the title and revision information. Additionally, the librarian verified the minimum signature requirements were satisfied prior to release of the work documents.

DEBRIS ASSESSMENT

General Observations

There were more recovered and identified OML debris items in the forward fuselage area of the orbiter with a bias in favor of the starboard side. Almost every piece of OML debris showed some of heat damage as evidenced by charred filler bar or Strain Isolation Pad (SIP), discoloration of the exposed primer, slag, and/or thermal erosion (ablation) of the fracture edges of structural pieces. Significantly less molten metal and aluminum oxide were present on the debris from the forward end of the vehicle. Very little (<1%) of the Fibrous Insulation Blanket (FIB) survived the break up and even less of the Felt Reusable Surface Insulation (FRSI) was recovered. The High Temperature Reusable Surface Insulation (HRSI) and Low Reusable Surface Insulation (LRSI) tiles are either missing or substantially damaged on all items due to either heating or aero loading or both. Recovered OML structural items were at least partially protected by their TPS during re-entry.

Honeycomb skin panels are notable in their complete absence or in the severity of facesheet loss and core erosion. The recovered pieces were typically skin material that was attached to internal structure or were otherwise shielded during re-entry. Skin panel stringers, located in the forward fuselage, mid fuselage and wings, typically failed due to a combination of thermal and aerodynamic loads as evidenced by either fracture along the upper or lower bend radius or the chemical milling lines. .

Items of relatively high ballistic coefficient show substantial ablation. Examples of this condition include payload longeron fittings, Orbiter/External Tank (ET) attach fitting, Space Shuttle Main Engines (SSME), Main Landing Gear (MLG), and thrust structure components.

With few exceptions, Reinforced Carbon-Carbon (RCC) components (both nose and wing) and their attach hardware appear to have failed as a result of mechanical overload, either in flight or due to ground impact. For those exceptions, thermal damage was a significant factor in the component failure and will be addressed in detail later.

Cumulative tracking of recovered debris by OML location was accomplished graphically with an electronic mapping system. Figures 8.1 through 8.4 show the recovered OML debris as viewed from above, below, and both sides.

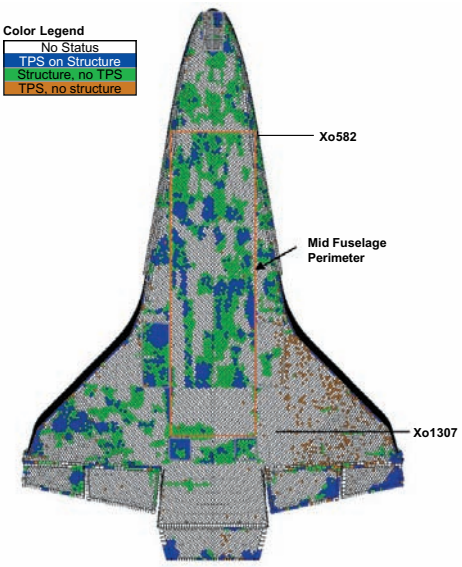


Figure 8.1 Recovered Orbiter Debris - Lower Surface

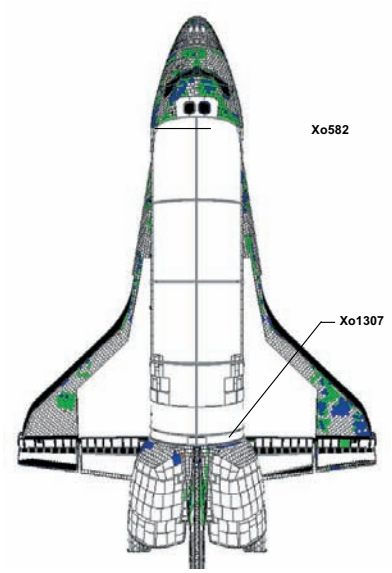


Figure 8.2 Recovered Orbiter Debris - Upper Surface

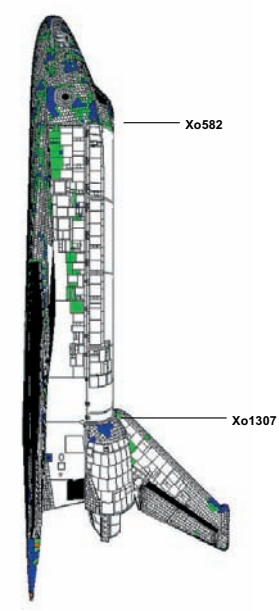


Figure 8.3 Recovered Orbiter Debris - LH Side

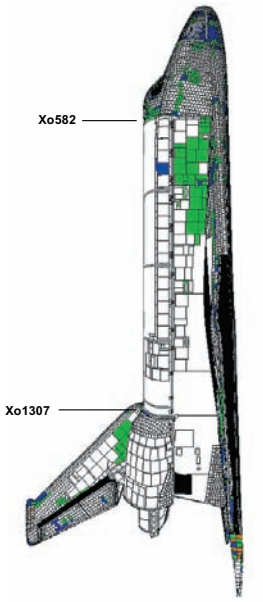


Figure 8.4 Recovered Orbiter Debris - RH Side



Figure 8.5 Forward Fuselage

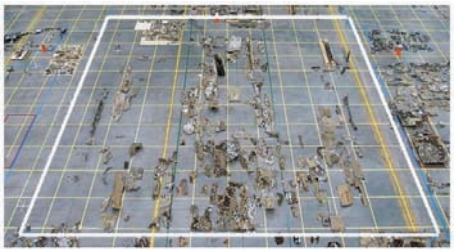


Figure 8.6 Mid Fuselage



Figure 8.7 Aft Fuselage

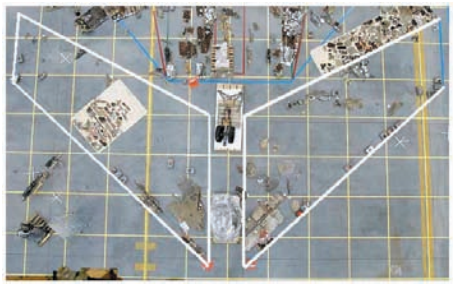


Figure 8.8 Vertical Stabilizer



Figure 8.9 Body Flap



Figure 8.10 Left Wing Lower



Figure 8.11 Right Wing Lower



Figure 8.12 Left Wing Leading Edge

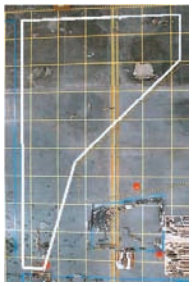


Figure 8.13 Left Wing Upper



Figure 8.14 Right Wing Upper



Figure 8.15 Left Wing Lower Tile



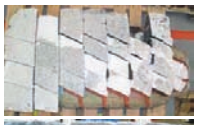
Figure 8.16 Right Wing Lower Tile

FORWARD

Forward Fuselage

The recovered forward fuselage components are predominantly skin/stringer segments and include a few noteworthy subsystem components. The component size ranges from less than one square foot to approximately ten square feet. All observed components exhibit evidence of mechanical overload as the primary failure mechanism. With very few exceptions, heating plays an insignificant role in the component degradation and appears to be during or subsequent to the mechanical breakup. Roughly 40% of the forward fuselage has been recovered with no difference in damage levels comparing left to right or upper to lower. Two recovered RCC components, nosecap and chin panel (1114), show evidence of mechanical breakup with no thermal damage.

Other OML components include the forward Orbiter/ET attach fitting with RCC arrowhead (37046) and the forward half of the left hand nose landing gear door (Item 284).





Item 284

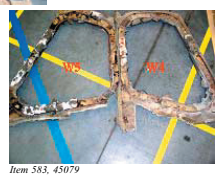
The left hand and right hand thermal window assemblies (1269, 63978, 583, and 45079) were recovered.

The right hand overhead thermal window assembly (1175) was also recovered.

The overhead window carrier panel (1175) tile damage is unique in that the perimeter carrier panel tiles show outward slumping and glassification on all four edges



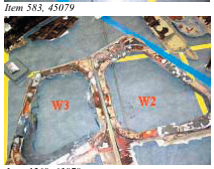
Item 1114



Item 583, 45079



Item 37046



Item 1269, 63978

Item 1175



Three of the four crew module attach links (1678, 1765 and 2171) were recovered. Three of the four attach lugs for the links were intact, while the left hand lug was fractured.

Several lower surface and sidewall antennas were also recovered. Most OML surfaces show substantial damage to bonded (TPS) components including: particle impacts (nose landing gear door tiles), erosion, ground impact damage, and in-plane failures. Items of high ballistic coefficient (egress hatch window ring frame and crew module link fittings) show evidence of ablation. Very few tile cavities show evidence of failure/loss due to backside heating. In most cases where the cavity is exposed, the failure mode appears to be erosion, in-plane fracture, or lifting/peeling due to aerodynamic loads. In the latter case, the remaining SIP layer shows light charring. There is no evidence of ablation on any of the RCC fracture surfaces. A few metallic fracture locations show broomstrawing. One exposed metal chin panel attach fitting exhibits no discoloration, even though it is located in a high heat region.

Forward Reaction Control System

Twelve primary structural components and all of the forward reaction control system (FRCS) thrusters were recovered. Each of those components exhibits evidence of mechanical overload as the primary failure mechanism. Heating did not appear to play a significant role in the component degradation and appears to be during or subsequent to the mechanical breakup. The recovered FRCS structure items include six internal stringers and six sections of the shell with internal structural members attached. The internal stringers appear to have been torn away from the skin, retaining their attach rivets. The skin sections (792, 82061) typically have fracture edges that follow fastener rows and are not thermally eroded. Approximately 25% of the outer mold line was recovered. In only one location, the





Item 792



Item 2171



Item 82061

backside primer is substantially blistered with the corresponding outer surface TPS showing evidence of failure due to backside heating.

Mid Fuselage

Recovered mid fuselage components are predominantly skin panel segments with a few noteworthy structural or subsystem components as well. Roughly 30% of the mid fuselage has been recovered, biased towards the floor area and the front of the vehicle. The component size ranges from less than one square foot to approximately thirty square feet. With very few exceptions, heating played an insignificant role in the component degradation and appears to be during or subsequent to the mechanical breakup.

Most mid fuselage OML components show evidence of mechanical overload as the primary failure mechanism. Out-of-plane deflection is noted on numerous pieces, indicating exposure to high aerodynamic loads both during and after breakup. The midbody floor segments extend all the way to the forward mating plane at Xo582 for nearly the width of the floor. Fracture edges of the sidewall skin segments are generally less heat affected than those of the floor segments. For those locations where skins connect to the midbody main frames, the majority of failures occurred between skin and frame rather than within the frame itself. Very few frame segments have been recovered. Noteworthy components include heavily eroded titanium longeron bridge fittings (266).


Item 32038

The left hand forward (32038) and right hand aft (49366) hoist fittings are significant due to ablation of the titanium.

Three sections (1 left hand and 2 right hand) of the sill longerons were recovered. The mid fuselage sill longerons (105, 266, 54117) are significant as they provide primary mid fuselage stiffness.


Item 49366


Item 266


Item 105




Item 283

The eroded skin panel (283) just inboard of the left hand wheel well, has outward plasma flow from the wheel well region. The point of erosion is located at the forward-inboard corner of the wheel well.

The close-up shows outward flow region at Yo105 and Xo104

Most OML surfaces show substantial damage to bonded TPS components. Damage includes particle impacts, erosion, ground impact damage, in-plane failures, and three locations with glassified tile. Greater amounts of TPS tile remnants are present closer to the vehicle centerline. Almost no tile cavities show evidence of failure/loss due to backside heating. In most cases where the cavity is exposed,

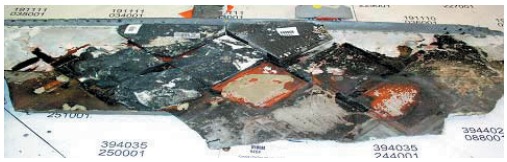
the failure mode appears to be erosion, in-plane failure,

primer-to-primer failure, or lifting/peeling due to aerodynamic load. Several metallic fractures have broomstrawing.

A few mid fuselage items have significant TPS slumping or glassification. An example is the lower wing root to fuselage attachment at Xo1249 (53827), and the inboard edge of the left hand MLG wheel well (9464) at Yo105.

A few lower surface skin segments (52240, 1193) show heavy edge erosion. The aft inboard corner of the left hand wheel well where the Yo105 sidewall and the Xo1191 spar join, are two examples of this condition.


Item 53827



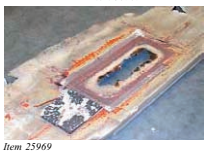
Item 9464


Item 52240


Item 1193


Item 38767




Item 25969

A typical fuselage sidewall segment (38767) has TPS erosion on the outer surface and fractured stringers on the inner surface.

One item which shows localized heating damage is the vent door blanking plate (25969), which is part of the left hand midbody sidewall.

Payload Bay Doors

The recovered and identified payload bay doors (PLBD) items are predominantly skin or skin/rib segments of the door itself, but include a few noteworthy subsystem components as well. The component size ranges from mostly less than one square foot to approximately sixteen square feet (53993). All observed components exhibit evidence of mechanical overload as the primary failure mechanism. Heating plays an insignificant role in the component degradation and appears to be during or subsequent to the mechanical breakup. It is estimated that 1300 lbs. of PLBD hardware was recovered, which equates to approximately 25% of the entire PLBD structure.


Item 53993

The representative sample of PLBD segments that was evaluated exhibits mechanical failure and falls into three major categories. The most prominent category (approximately 80% of all items) consists of small (under one square foot) skin fragments, with or without honeycomb core, that show fracture and ply delamination around the entire perimeter of the item. In many cases, one facesheet is missing and various amounts (up to all) of the honeycomb core is eroded. The second category includes segments of primary PLBD structure, either partial frames or partial torque box, with small fragments of skin attached. Frames are typically fractured into segments of approximately 1/4 to 1/3 of their original length. The least populated category (approximately 10 items) includes multiple partial frames with connecting skin. Typical to all fracture edges, the laminates are degraded/unwoven to individual fabric strands. Numerous subsystem components such as handhold brackets, wiring clamps, latch fittings, hooks, rollers, and linkages remain attached. The subsystem components, which were observed with the representative samples, did not show obvious deformation.

There is very little evidence of thermal degradation. RTV adhesive applications (bondlines, conformal coating) do not show charring or loss of resilience on most items. No thermal erosion of aluminum fastener collars was observed, as noted on numerous other structural items. On most items there is either partial or total erosion of the bonded TPS tiles or blankets. In some cases, only the inner blanket fabric remains installed. A few items have portions of wire harnesses installed with partially melted insulation. The polyurethane coating, which was applied to some inner surface locations, is blistered or has peeled away in some of these locations.

Wings

The wing OML assessments were performed by breaking down the wings into smaller zones using main spar locations/ skin splices as the dividing line. The smaller zones help to distinguish between different skin types in the different zones. The wing glove (Xw807 to Xw1009) is aluminum skin stringer assembly combined with a honeycomb leading edge and the intermediate wing and elevons are aluminum honeycomb (Xw1009 to Xw1191). The wheel well (Xw1040 to Xw1191, Yw105 to Yw167), torque box (Xw1191 to Xw1365), and lower trailing edge/ cove (Xw1365 to Xw1387) are aluminum skin stringer assemblies.

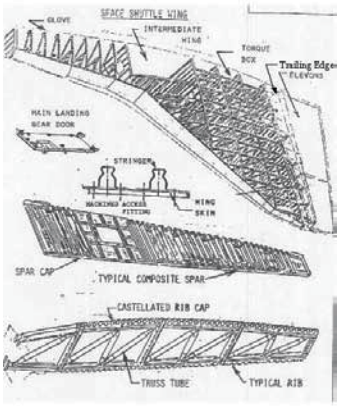
General Observations

Significantly less surface area of the left hand upper and lower skin was recovered compared to the right hand upper and lower skin surface area. Significantly less of the upper than lower skins were recovered for both wings. The intermediate section has less upper and lower skins recovered than either the glove or torque box sections for both wings. A large portion of both wing tips consisting of skin/leading edge spar was also recovered.

The recovered upper and lower right hand skin pieces are generally larger when compared to the left hand skin pieces. The left hand skin pieces are attached to a reinforced splice plate at main spar locations. Internal wing structure such as truss tubes, frames and composite spars were not recovered, except for two large pieces of aluminum right hand wing spar. A significant portion of the upper wing-to-fuselage attach at the right hand wing root (Xw1249 to Xw1365) was recovered compared to one small left hand wing root piece at Xw1191. Almost the entire right hand MLG door (95%) was recovered compared to less than 5% of the left hand MLG door.

Based upon visual inspection of the inner mold line (IML) and OML, the overall condition of recovered left hand skin pieces indicates more thermal damage than right hand skin pieces. Slag is most prevalent in the intermediate and trailing edge/cove areas for both wings.

The left hand wing inboard actuator and the right hand wing outboard actuator were recovered. The amount of recovered skin surface areas of all four elevons was generally the same with most pieces concentrated on the lower side located along the inboard, outboard and aft edges. The right hand elevons have more pieces recovered on the aft-inboard corners compared to the left hand elevons that have more pieces recovered on the aft-outboard corners.

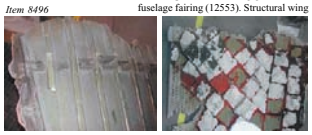


Wing Glove

Right Hand Glove - Fifteen percent of the right hand glove upper and lower surface area was recovered. The upper pieces were mostly one to three square feet and located near the leading edge in the area where tile was installed compared to the lower glove area, which included one large skin piece (8496) that is approximately fifteen square feet. One upper skin piece included a portion of the Xw807 splice for the wing glove to mid fuselage fairing (12553). Structural wing skin doublers in the glove area were still attached to the skin pieces and have numerous areas of local buckling and cracking between the attach rivet rows.

The hat stringers on the IML of the upper and lower glove skin pieces were fractured except in the areas of the splice fittings and ribs. Although only a few smaller items were available for comparison, the lower glove pieces aft of Xw900 show more heat effects on both the OML and IML surfaces, correlating to the proximity of the forward edge (starting point) of the RCC panels.

Item 8496



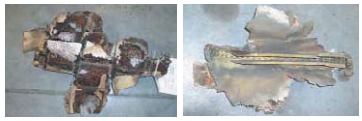
Item 12553



Item 734



Item 1632



Left Hand Glove - Twenty-five percent of the left hand glove upper and lower surface area was recovered. The left hand and right hand glove were comparable in that the pieces were located primarily in the same areas with typical failures of the hat stringers on the IML and the wing skin doublers on the OML.

Only four items of upper glove skin were recovered, a portion of the Xw807 glove to fairing splice, a piece of glove honeycomb leading edge, a piece of upper glove skin and the glove bulkhead at RCC panel 1. The left hand Xw807 upper glove to fairing splice piece (734) showed similar thermal damage and slag as a comparable item on the right hand side (12553). Very little honeycomb skin was recovered in the wing areas except a piece of glove honeycomb leading edge (1632) skin, which was approximately two square feet. The OML side of the piece has tile fragments and charring of exposed filler bar. Both the upper and lower facesheets

were completely delaminated from the core, and the IML side of the piece has no discoloration of the primer on the fwd side of the rib.

A piece of upper wing glove skin at Xw949 and Yw140 (33611) has overload fractures on the inboard and outboard edges and unique molten fracture surfaces on the forward and aft edges. The molten fracture edges are very porous, and there are tiny impact craters covering the entire part's IML and OML surfaces.

The OML surface has only a slight tile/filler bar footprint and the primer was missing on the IML and OML of this part. The location of this piece is inboard of a recovered left hand leading edge spar piece (83323) with RCC panel 2 upper-fwd attachment, which has medium slag on the IML side.

The glove honeycomb bulkhead piece (24709), which is forward of RCC panel 1, has more thermal damage on the aft side than the forward side. The four internal tiles on the aft side are missing and the FRSI in the four internal cavities is charred black. The forward side has more

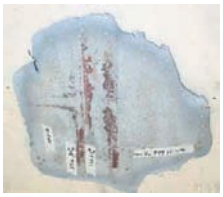


Item 24709

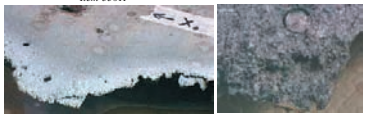


thermal erosion and slag than the aft side and the honeycomb bulkhead is thermally eroded everywhere except where the structure is reinforced.

The lower glove area was comprised of four large skin pieces greater than one square foot, a piece that included a portion of the Xw807 glove to fairing splice (272) which was approximately six square feet, two smaller pieces of the Xw1009 glove to intermediate section splice (62708, 41798), and one piece located in the



Item 33611



lower wing glove skin acreage (2113). This skin piece (2113) was comparable to a right hand piece that was approximately the same size and in approximately the same location with the left hand piece having more heat effects than the right hand piece (8496) on the IML and OML surfaces.





Item 2113

Intermediate Wing

Right Hand Intermediate Wing – Ten percent of the right hand intermediate wing upper and lower surface area was recovered. Recovered pieces were less than one square foot and consist of pieces of honeycomb skin splices at intersections of main spars and ribs.

A portion of the upper Xw1040 spar, Yw198 rib intersection with attached wing skin (68801) was recovered. This area was structurally reinforced because it is one of the wing assembly hoist points, consisting of a four-bolt pattern centered on the intersection. On this item there is medium slag build up, thermal erosion and broomstraw fractures. The entire surrounding upper honeycomb skin is completely eroded away on the edges with heavy thermal erosion on the aft-inboard hoist point fastener.

A lower skin to fuselage splice piece (14880) also shows thermal damage on the fracture edges, including broomstraw fractures and thermal erosion. A rib located at Xw1113 and Yw174 (75613) has medium slag build up and the exposed fasteners are eroded more on the inboard side. The upper and lower intermediate wing have medium slag build up between the Xw1040 to Xw1113 stations, both outboard in the RCC panels 7 and 8, and inboard in the main landing gear door (MLGD) (658).

Item 68801



Item 14880



Item 75613



Left Hand Intermediate Wing – Less than one percent of the right hand intermediate wing upper and lower surface area was recovered. The upper intermediate wing has only two items identified to a location on the grid. The two small items are honeycomb skin splices at intersections of main spars and ribs less than one square foot in surface area. A lower Xw1040 spar, Yw167 rib intersection with attached wing skin (67091) is a structurally reinforced assembly hoist point and the entire surrounding upper honeycomb skin is completely eroded away on the edges.

Item 67091



Although slightly smaller compared to a corresponding piece on the right hand wing (68801) there is very similar thermal erosion on the IML side with the left hand piece showing a heavier slag build up than the right hand. Additionally, both pieces have some shadowing effects on the forward side of the IML. The OML sides of the left hand and right hand pieces were similar with charred filler bar and/or tile fragments fractured at the densification layer.

The other piece is the upper wing skin at Xw1160 and Yw282 rib at its intersection with the wing leading edge spar (36264) adjacent to RCC panel 13. The lower facesheet is missing and the exposed honeycomb core is thermally eroded down to the potting adhesive used around the string of fasteners where the rib attached on the IML side.





Item 36264

Item 43698





Item 24812





The lower intermediate wing is comprised of seven smaller items of honeycomb skin splices at intersections of main spars and ribs. Four pieces are located forward of the MLGD and three pieces are located along the outboard side of the MLGD. No other pieces were recovered in this area. The four pieces forward of the MLGD (74416, 43698, 40982, 41089) and the three pieces outboard of the MLGD (50345, 49482, 24812) all have honeycomb facesheet and core erosion except for the areas along fastener rows where a potting compound was used.

The three pieces outboard of the MLGD were more structurally reinforced than the four located forward of the MLGD and have more thermal erosion and slag deposits on the IML side. One of the pieces outboard of the MLGD is a small portion of the Xw1191 splice plate (24812) located outboard near the wing leading edge at Yw254, which has thermal erosion, and heavy slag deposits on the IML side.





Item 658

Item 260









Item 32013

Main Landing Gear Door

Right Hand Main Landing Gear Door – Ninety five percent of the MLGD structure was recovered in two small pieces and two large pieces. The large pieces were nearly intact with OML skin/ stringers, and IML skin/ stringers still attached forming the basic box section of the door.

The aft side of the forward piece of MLGD (658) has fracture edges in the lower skin immediately aft of the center hinges, which are deflected out-of-plane. The edge of this door piece has slag uniformly distributed across the entire surface, which is not present on any other edges of this piece or on any other edges of the aft door piece (260). The forward and center hinge fittings are fractured two thirds of the way along the fitting arc length and there are two intact up-lock rollers along the inboard edge, and one intact along the forward edge. The forward side of the aft piece of MLGD (260) has edges in the lower skin thirty-one inches forward of the aft hinge, which are in plane. The aft hinge fitting tore out at the hinge attach point on the wing side, leaving nearly the full length of the aft hinge fitting attached to this piece of MLGD. There is one intact up-lock roller on the inboard edge.

Left Hand MLGD - Five percent of the MLGD was recovered in four smaller pieces of OML skin each less than two square feet in surface area. The pieces are from the center area of the door with the forward fracture edge of the largest piece (32013) located just aft of the center hinge point. Only one of four uplock rollers was recovered.

Torque Box

Right Hand Torque Box – Forty-five percent of the torque box upper and lower surface area was recovered with a majority of the skin pieces belonging to the lower surface. The recovered upper skin pieces are from two main areas; outboard near the wing tip and inboard at the reinforced wing-to-mid fuselage carry-through structure. Structural wing skin doublers in this area are still attached to the skin pieces and displayed numerous areas of local buckling and cracking in between the attach rivet rows. All of the recovered skin have typical failures of the hat stringers on the IML except for two upper skin pieces and three lower skin pieces

between Xw1249 to Xw1307, outboard of Yw312. The upper pieces (12213, 78275) and lower pieces (2071, 1446 and 16556) have stringers fully intact with no failures of the hat sections and little discoloration of the primer on the IML side of the skin. The OML of these five skin pieces has more tile remaining and less in plane fractures than the surrounding skin pieces.

Only two identified pieces of internal wing spar at Xw1307 were recovered; the inboard (1421) and the outboard (41670)





Item 16556

spar personnel pass through locations with attached structural doublers and small pieces of the upper wing skin splice plates.

Additional primary structure recovered in this area included several pieces from the torque box at the wing root and a large piece of right hand wing honeycomb leading edge spar from Xw1307 to Xw1365 including pieces of the lower skin. The seven pieces of wing root between Yw105 and Yw123 (1165, 59401, 1550, 77707, 73025, 67930, 37309) include main spar attach bolts between Xw1191 to Xw1249 (59401), main spar attach bolts at Xw1307, and reinforced upper wing skin panels with stringer carry-through fittings (1165). All of these parts have broomstraw fractures and localized heavy thermal erosion.

The piece of honeycomb leading edge spar (59409) is from the tip area forward approximately six feet and has lower skin pieces attached. Many leading edge components are attached to the





Item 12213

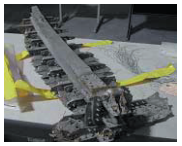
Item 1421



Item 41670



Item 1165







Item 59409

Item 59401



outboard/forward side including RCC fittings, spar insulators and access panels. There are localized areas of heavy slag build up and thermal erosion on the IML side.

Each internal main spar location contains a corresponding splice plate along the upper wing skin OML. Seventy percent and 10% of the Xw1191 splice, 50% and 50% of the Xw1249, 5% and 75% of the Xw1307, and 50% and 70% of the Xw1365 splice plates were recovered for the upper and lower wing respectively. The splice plates are thicker than the adjacent skin and were recovered either still attached to the skin on the forward side, aft side or all by itself with many of the fractures occurring along fastener rows.

Left Hand Torque Box – Less than five percent of each of the upper and lower torque box surface areas were recovered. The pieces are less than one square foot in surface area except for two large skin pieces greater than five square feet. One of the large skin pieces located at Xw1220 and Yw147 to Yw183 (76275) is comparable to a right hand piece (71706)

Item 76275





Item 71706 (RH Wing)





Item 4493





that is in approximately the same location and has approximately the same size. The right hand piece remains relatively flat as compared to the left hand piece, which is bent out of plane in several locations. Although the left hand and the right hand pieces have similar thermal effects based on coloration and slag, the left hand hat stringers have more thermal erosion on the IML. The other large skin piece is from Xw1249, Yw312 to Yw372 (49443) and is comparable to a right hand piece (2287) that is smaller in size and in approximately the same location. In this case the left hand piece also exhibits more heat effects than the right hand when based on coloration, slag, and thermal erosion of the hat stringers on the IML. The remaining smaller items are pieces of upper wing skin splice plates at main spar locations. The recovered pieces of left hand Xw1365 splice plates have a much larger slag build up than the right hand Xw1365 splice plate pieces.

The lower skin pieces recovered in the torque box were located outboard of Yw256, except for one, and attached to wing skin splice plates at main spar locations. The piece inboard of Yw256, the Xw1249 splice plate at Yw167 (16647), has medium slag on the IML.

Further outboard along the Xw1249 spar at Yw357 to Yw372 another piece (52816) was recovered that has a medium slag build up on the IML. This piece, although smaller in size, is comparable in location to a piece on the right hand side (2071) which has no slag present, and little primer discoloration. A total of five pieces of the Xw1307 splice plate were recovered. One piece at Yw372 (71799) Item 71799 includes a reinforced hoist point area and

Item 52816



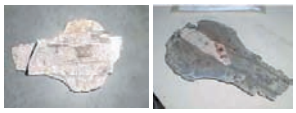
Item 2287 (RH Wing)



Item 16647



Item 71799



Item 2071 (RH Wing)





has heavy slag on the IML side and is comparable to a right hand piece (33194) that is larger but from the same location. The left hand piece has more heat effects than the right hand piece when based on coloration, slag, and thermal erosion on the IML.

Two pieces of the Xw1365 splice plate were recovered that had medium slag on the OML. One located at Yw335 (73945)

Item 33194



Item 73945





Item 780







Item 67481



Item 37739



and the other was attached to the recovered wing tip piece. Ten percent and 5% of the Xw1191 splice, 15% and 30% of the Xw1249, 1% and 10% of the Xw1307, and 10% and 20% of the Xw1365 splice plates were recovered for the upper and lower wing respectively. Similar to the right hand side the splice plates were recovered with skin pieces attached to either the forward or aft sides, or both, with many skin fractures occurring along the fastener rows.

The largest recovered piece was the left hand wing tip (780), which contained several elements including the outboard section of the primary seal tube, lower wing skin sections, wing tip installation, wing trailing edge beam, and a small portion of the wing leading edge honeycomb spar. The OML surfaces of the wing tip piece are less affected by heat than the IML surfaces, which have heavy slag deposits on the forward facing surfaces.

Trailing Edge/ Cove

Right Hand Trailing Edge/ Cove – Thirty percent of the wing trailing edge lower surface area was recovered with most skin pieces attached to the Xw1365 splice plates. The area outboard of the Yw312 wing stub had fewer recovered pieces than inboard of Yw312. Approximately 70% of the wing trailing edge carrier panels were recovered and in every case the wing trailing edge beam structure fracture edges were approximately equivalent to the footprint of the carrier panel (67481).

A section of the primary seal tube (37739) was recovered that was forty-six inches long between Yw212 to Yw258. Additional pieces of primary seal tube

splices were found attached to the wing hinge fittings at Yw435, Yw342, Yw312, Yw282, and Yw212.

The Yw312 wing stub between the inboard and outboard elevon, the Yw212 hinge point for the inboard elevon, and the Yw387.5 hinge point for the outboard elevon were recovered. The Yw312 wing stub (44937) has a fracture edge approximately fifteen inches forward of the hinge point. The fracture edges are out-of-plane with broomstraw fractures. The outboard surface of this piece of wing stub has heavier slag than the inboard surface. The Yw212 hinge rib piece (56265) is seventy inches long and runs fwd from the hinge point with the fwd fracture edge forward of the hinge point. At the actuator forward attach point there is severe gouging in the top surface of the clevis that matches the footprint of the upper surface of the actuator rod end. Additionally the hinge rib has thermal erosion exposing the full length of the fastener, which has erosion of the exposed shank.

Left Hand Trailing Edge/ Cove – Five

Item 56265







Item 44937

Item 36076



Item 59522



corresponding to the area where the integrally machined castellated rib attaches to the upper and lower skin. The lower rib cap appears to have the original contour but the upper rib cap is bent ninety degrees upward at a location eighteen inches forward of the hinge point.

The rib melted all along the neutral axis in the center of the web and the rib caps have broomstraw fractures and thermal erosion. The Yw387.5 hinge rib piece (36076) is sixty-four inches long with the hydraulic actuator assembly attached. The forward fracture edges of this piece have out of plane tearing with broomstraw fractures occurring in the integrally machined castellated rib forty-three inches percent of the wing trailing edge lower surface area was recovered with most skin pieces less than one square foot and attached to the Xw1365 splice plates (ref 7.4 Torque Box). Approximately 5% of the wing trailing edge carrier panels were recovered and in every case the carrier panel failed at the attach fittings, one at Yw312 (59522), one at Yw255 (58088), and one at Yw201 (66765), this is in contrast to the right hand failures, which occurred in the wing trailing edge beam structure (67481). The carrier panels on the left hand wing have medium slag on the fwd facing side compared to the right hand carrier panels, which have no slag.

One section of the primary seal tube was recovered along with the wing tip (ref





Item 1204

7.4 Torque Box) from Yw435 to Yw465. Additional pieces of the primary seal tube splices were attached to the wing hinge fittings at Yw342, Yw312, and Yw212. The Yw342 wing hinge fitting (1204) has heavy slag and thermal erosion on the lower surface directly through the splice tube. This thermal erosion also was also present on a recovered Yw435 right hand wing hinge fitting (1151).

The Yw312 wing stub (44446) has a fracture edge approximately fifteen inches forward of the hinge point. The fracture edge is out of plane with broomstraw effects. The outboard surface of this piece of wing stub has heavier slag than the inboard surface. The thermal effects on this piece were of the same magnitude as a comparable right hand piece (44937), which also has the heaviest slag on the outboard side. The Yw212 actuator (7327) was recovered and had a hole through the outer casing on the upper fwd surface caused by thermal erosion. Its corresponding hinge rib piece (279) is forty inches long and runs forward from the hinge point has a forward fracture edge where the rib attaches to the lower skin. The lower rib cap appears to have the original contour and the upper rib cap is fractured eight inches forward of the hinge point. The web and rib caps have thermal erosion and broomstraw fractures.

Item 1151 (RH Wing)





Item 44446



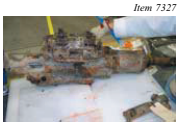


Elevons

Right Hand Inboard Elevon – Fifteen percent of the upper surface OML and 10% of the lower surface OML were recovered. The two largest items are the lower surface inboard edge (38891) and the upper surface inboard edge (26197).

The other recovered pieces consist of narrow pieces of honeycomb skins that are attached to a rib on the IML side with a minor presence of slag. A piece of the Yw212 elevon hinge rib (56265, 7.5 Trailing Edge/ Cove) is attached and fractured approximately eighteen inches aft of the

Item 7327



Item 279



hinge point. Six elevon cove carrier panels (all or in part), 40% of the primary seal panel, and 15% of the flipper door rub panels were recovered. One of the six carrier panels tore out at the boss on the inboard side and the outboard side was only slightly deformed. The remaining five carrier panels have only slight deformation at either hole location.

Right Hand Outboard Elevon – Thirty five percent of the upper and lower surface OML was recovered. The largest item was approximately eighteen square feet and was located along the inboard edge (75987) and included a portion of the lower elevon skin, inboard sidewall, outboard closure rib, and upper elevon skin. The IML surfaces have no discoloration of the primer and the lower OML surfaces have severely heat damaged honeycomb facesheets consisting of fractured/ missing pieces of outer facesheet and thermal erosion of the core to the inner facesheet. The upper OML surface has less thermal effects than the lower surface that includes the only area of FRSI recovered from anywhere on the wings. The outer room temperature vulcanizing (RTV) adhesive membrane is charred black and the residual Nomex felt is pliable.

Item 26197





The other recovered pieces consist of narrow pieces of honeycomb skins that are attached to a rib on the IML side with a minor presence of slag similar to those on the inboard elevon. A piece of the Yw387.5 elevon hinge rib is attached to the wing hinge rib (36076, 7.5 Trailing Edge/ Cove) and fractured approximately six inches aft of the hinge point. One elevon cove carrier panel, 10% of the primary seal panel, and 15% of the flipper door rub panels were recovered. The elevon cove carrier panel tore out at the boss on the inboard side and the outboard side was only slightly deformed.

Left Hand Inboard Elevon – Five percent of the upper surface OML and 35% of the lower surface OML were located along the aft edge, including the aft-inboard and aft-outboard corners. The other smaller recovered pieces consist of narrow pieces of honeycomb skins that are attached to a rib on the IML side. The twenty square foot aft outboard corner (20583), the adjacent outboard sidewall honeycomb closeout (87) and the aft inboard corner (71626) were recovered. On the two corner pieces the upper OML TPS was missing, except in the trailing edge

Item 87



Item 71626





Item 38891



Item 20583





area, and there is thermal erosion of the honeycomb facesheet and core with broomstraw fractures. The lower OML tile has many tile or tile fragments attached. A piece of the Yw212 elevon hinge rib is attached to the wing hinge rib (279, 7.5 Trailing Edge/ Cove) and fractured approximately fourteen inches aft of the hinge point.

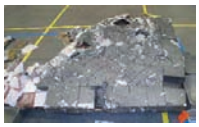
Five elevon cove carrier panels (all or in part), 5% of the primary seal panel, and 10% of the flipper door rub panels were recovered. Three of the five carrier panels tore out at the boss on the inboard side and two had the threaded insert pulled out of the structure at the inboard side. In either case the outboard side appeared only slightly deformed.

Left Hand Outboard Elevon – Twenty five percent of the upper surface OML and 35% of the lower surface OML were recovered. The larger recovered items were located along the aft edge, including the aft-inboard and aft-outboard corners. The other smaller recovered pieces consist of narrow pieces of honeycomb skins that are attached to a rib on the IML side.

The largest piece was the aft outboard corner (35) that is forty square feet and has medium slag on IML fittings and ribs with broomstraw fractures. The upper OML TPS was missing, except in the trailing edge area, and there is thermal erosion of the honeycomb facesheet and core with broomstraw fractures. The lower OML tile has debris peppering and light gray discoloration compared to the inboard elevon piece (20583), and has many tile or tile fragments attached.

Three elevon cove carrier panels (all or in part), 5% of the primary seal panel, and 40% of the flipper door rub panels were recovered. One of the three carrier panels tore out at the boss on the inboard side and two had the threaded insert pulled out of the structure at the inboard side. In either case the outboard side appeared only slightly deformed.

Item 35





THERMAL PROTECTION SYSTEM WINGS

Left Wing

Of the tiles that have been recovered, seven percent are identified to the left wing, with the majority belonging on the lower wing section. The lower wing tiles and structure are placed on a full-scale model of the wing, which provides a method of seeing trends. The predominant tile failure mode was from internal wing heating that caused the primer layer between the structure and tile bond line to fail.

There are a greater number of structural pieces with tile remains forward of the MLGD than aft. The tile remnants, resulting from in-plane fractures, consist of silica, charred filler bar, and RTV adhesive. Individual tiles identified in this region do not have signs of slumping or glassification damages, but do have debris impact damages.

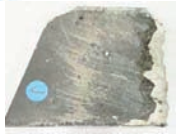
The majority of tiles identified in the MLGD region are concentrated around the perimeter of the outboard edge of the gear door. One tile, (33590), located on the outboard forward corner of the door has excessive heating. The erosion patterns



Forward of the MLGD

show the flow direction starting from the IML to OML, moving inboard. The midbody structure side, inboard of the MLGD, has 6 tiles (283) with black deposits on the OML. The silica and Reaction Cured Glass (RCG) coating erosion patterns have a thermal erosion signature of an inboard flow direction. The remaining tiles on the gear door have minimal thermal degradation or contamination, with less backside heating effects as compared to the rest of the lower wing.

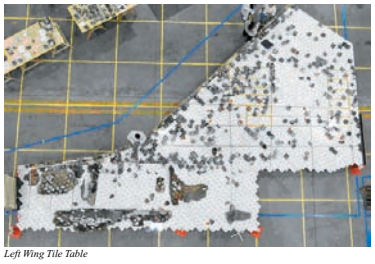
From the leading edge of the MLGD



Item 33590



Item 283



Left Wing Tile Table



Forward of Xo-1191



Aft of Xo-1191

progressing aft, all tiles, except fifteen, failed due to backside heating. The fifteen tiles, which are located on the leading edge of the wing aft of LESS access panel 13, failed by in-plane fractures.

Tiles aft of Xo1191 between Yo198 and Yo254 exhibited minimal signs of thermal degradation compared to those forward of Xo1191. The forward facing sidewalls of these tiles, do however have slumped RCG coating that indicates direct airflow impingement. Tiles from Xo1091 and Xo1191, aft of LESS access panel number 9, have significant thermal related damages, which consist of glassification and erosion.

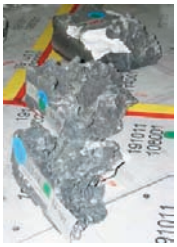
Adjacent to LESS access panel 9, two leading edge wing tiles (23553 and 15523) have severely slumped RCG OML and sidewall coating. Black deposits are embedded into both slumped regions. The flow patterns are approximately twenty-five degrees outboard of the normal airflow direction. On LESS access panel 9, the two tiles (57754 and 22571) have similar slumping and flow patterns as the two leading edge wing tiles.

Three tiles (43820, 13001, 1858) located inboard of LESS access panel 13 have very unique erosion patterns. These patterns indicate RCG coating was damaged due to a debris impact, which not only exposed the underlying silica but also removed an entire portion of the tile. The remaining silica is severely glassified, but shows a normal reentry directional flow pattern. These features indicate the tile remained bonded to the structure for a substantial period of time during reentry. The remaining silica has embedded aluminum oxide, which is black in appearance.

The tile (85472) is located inboard and aft from LESS access panel number 9 is the third most western tile found in the debris field. The design thickness was



Items 23553, 15523, 57754, 22571



Items 43820, 13001, 1858

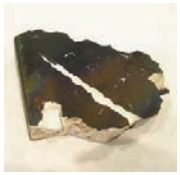


Item 85472

color in appearance.

There are two open areas on the lower wing that are bounded by three densely populated tiles regions. The open areas, which consist of 40 tile locations, are inboard of Yo-198 and outboard of Yo-226, and forward of Xo1191. Items 1858, 43820, 13001, also border this region.

The most western recovered tile (14768) found in the debris field was a piece of upper wing LRSI tile, with black deposits covering the OML. The tile piece was not positively identified, however 3D evaluation and lab analysis indicated the tile could be placed in one of two locations. Both possible locations on the left and right wing are inboard of Leading Edge Structural Subsystem (LESS) upper wing access panels 8 and 9.


Item 14768

2.1 inches, however a debris impact with subsequent heating and thermal erosion resulted in a loss of 70% of the RCG coating and silica material. The remaining portion of the tile consists of white silica, with slight glassification. The tile failed due to backside heating, with no evidence of aluminum oxide deposits, but the remaining OML coating has light brown


Voids on Left Wing Table

Right Wing

With the focus belonging to the left wing, less than 1% of the recovered tiles have been positively identified to the right wing. The overall right wing tile failure mode indicated less backside heating and more in-plane fracture, in comparison with the left wing.

On the lower wing, from Xo1040 to Xo1191, the MLGD had the majority of bonded tiles and tile remnants. Thirty percent of the MLGD tiles (658) were still bonded and show some shallow OML debris and heating damages. Tiles in this location typically showed a light brown discoloration. The remaining exposed structure has primer slightly charred and peeling with RTV adhesive attached.

There is no evidence of silica remnants on the structure aft of the MLGD, from Xo1191 to approximately Xo 1250. Residual RTV remains on the structure but is charred in some locations. From Xo1250 to Xo1300 and including the wing tip, the tiles failed by in-plane fracture with the remaining silica and SIP adhered to the structure. However, several individual tiles in the


Lower Right Wing Tile Grid


Lower Right Wing Structure


Item 658

identified, with 10% of the OML coating intact and the exposed silica having black deposits. Backside heating was the cause of the tile failure.

On the lower inboard and outboard elevons, unusual tile heating occurred on the outboard elevon, inboard edge. The OML Reaction Cured Glass (RCG) coating was separated from the underlying silica (75968). The remaining RCG coating was pooled indicating airflow direction. The color of the RCG coating and silica are unusually discolored exhibiting a light brown gray appearance. The upper surface of the elevons are covered FRSI per design, of which the only recovered portion was on the upper outboard elevon.


Item 75968

region do show evidence of backside heating failures.

Tile failures on the upper wing were a combination of backside heating and in-plane fractures, however, no FRSI was recovered. Structure pieces with tiles still installed (28421 and 1412) are primarily located from Xo1191 aft, inboard from the spar edge. Tiles in this region are less that one-inch thick and were recovered with black deposits on the OML. One instrumentation tile (43000) was positively


Item 28421


Item 1412

WLE SUB-SYSTEM

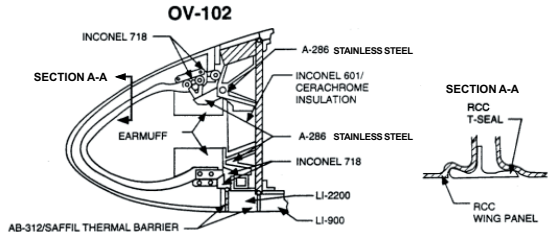
Wing Leading Edge Sub-System

The Wing Leading Edge Sub-System (WLE) consists of 22 Reinforced Carbon Carbon (RCC) panel assemblies per wing, which provides thermal protection to the aluminum wing spar. Each assembly, except panel 22, pairs a panel with an associated gap "tee" seal. The gap seal attaches to its mating panel with two A286 bolts and bushings at clevis attach fittings and mechanically locks on the panel periphery. The gap between installed panels is referred to as a rib splice, which is closed by a gap seal. The gap seals install to the outboard end of the RCC panels, with the exception of gap seal 1, which installs to the spar fittings, using two bolts/sleeves. The rib splice between panel 1, the forward-most location, and the glove is closed by gap seal 1 "L" angle seal, whereas panel 22 does not have a gap seal and adjoins the wing tip.

The larger panels (5-19) contain Inconel 718 spanner beams to carry moment loads on the panels. The spanner beams, Inconel 718 clevis fittings and aluminum honeycomb wing spar are thermally protected with insulators made of Cerachrome batting encased in Inconel-Dynaflex 601 foil.

The panels are installed onto the wing leading edge spar via A286 spar fittings (mounting brackets). Each upper and lower spar fitting is installed to the wing spar with four A286 bolts. Each spar fitting has attach points for adjacent RCC panels, with the exception of rib splice 1 and 23. Each RCC panel attaches to four spar fittings, two lower and two upper, by means of A286 bolts and bushings, which allow panels to slide inboard and outboard along the wing. Adjustable shear pins (two each per panel) located on the upper and lower spar fittings insert into fittings on the outboard/aft heel of the panels to retain the panel's position in the inboard and outboard direction.

Upper and lower access panels attach to the spar to seal the gap between the RCC panel and wing spar/tile. The upper LESS access panels are 2024 aluminum honeycomb and install with four (two inboard and two outboard) A286 bolts. The lower panels are extruded boxes made of either 2024 or 6061 aluminum and installed with two (one inboard and one outboard) A286 bolts.



General Observations
RCC material recovered
- Left Wing – Panels 65 %, Gap Seals 45%
- Right Wing – Panels 70%, Gap Seals 70%

Spar Fittings (or portions) recovered – 23 possible
- Left Wing Upper – 16 Lower – 15
- Right Wing Upper – 17 Lower – 18

Access Panels (or portions or individual tiles) recovered – 22 possible
- Left Wing Upper – 17 Lower – 19
- Right Wing Upper – 18 Lower – 21

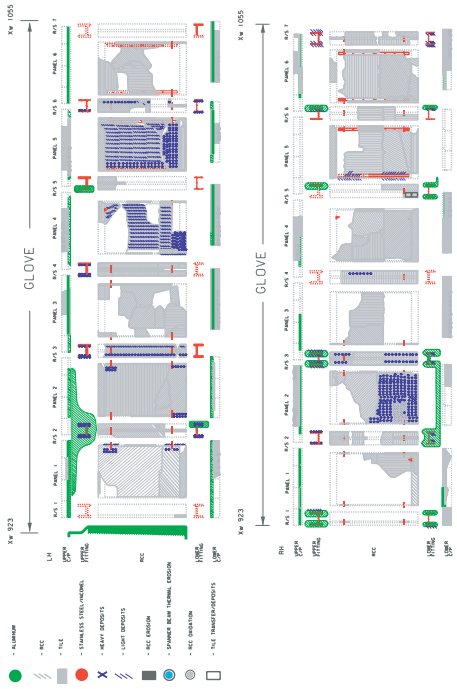
The majority of the RCC panels/seals have fracture surfaces without thermal erosion. The WLE has been categorized into three different regions for evaluation based on the heat damage.
- Glove region (Rib Splice 1-7 / Xw 923-1055) medium heating
- Transition region (Rib Splice 7-12 / Xw 1055-1152) high heating
  - LH Panel 8 & 9 severe heating
- Torque box region (Rib Splice 12-22 / Xw 1152-1365) light heating

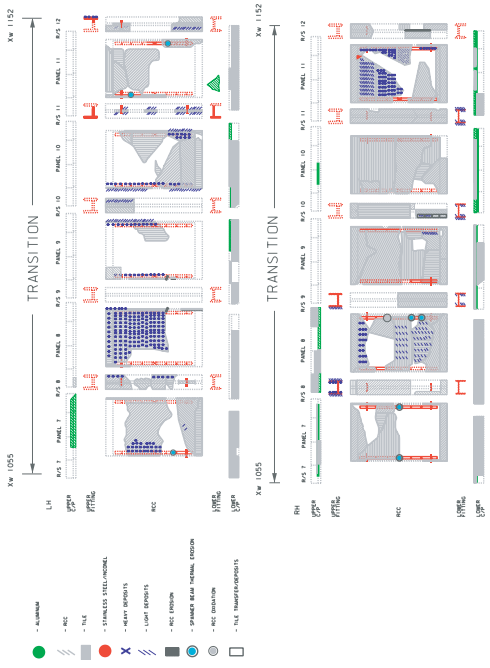
This observation is supported by the quantity, size and condition of metal hardware, including wing spar sections. More hardware from the torque box region was recovered than from glove and transition regions, with the least amount found for the transition.

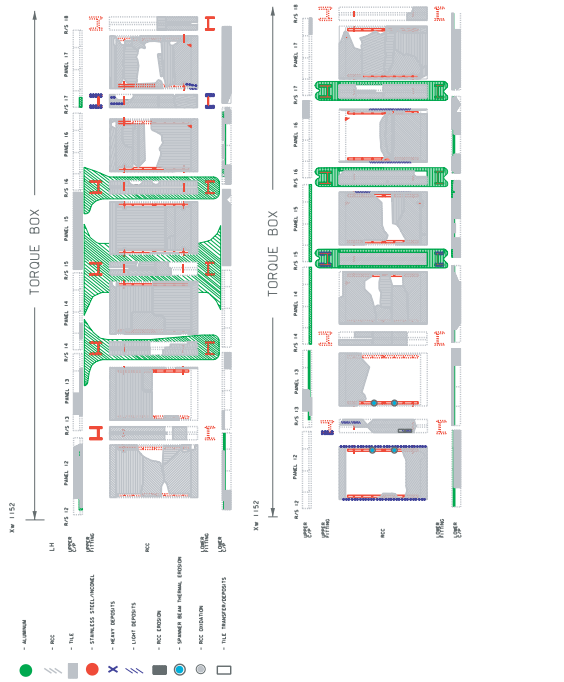
Fewer upper than lower LESS access panels and/or tile were recovered and had more damage. Inspection of the LESS access panels attaching hardware shows thread engagement met design requirements. The primary failure mode for the lower panel attach is bolt pull through whereas the upper is honeycomb core pull through (36).

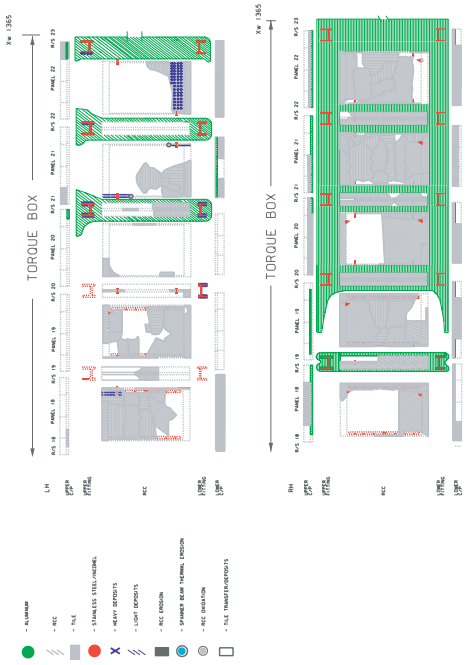
The maps on the following pages depict the identified recovered wing leading edge components and their condition (left hand, top; right hand, bottom).











Glove Region (Rib Splice 1-7)

All of the left hand and right hand LESS access panels for the glove region were recovered with the exception of the right hand 5 upper and lower panels. The damage to the upper panels varied from relatively intact panels with tile to only portions of aluminum facesheet, as depicted with left hand panels 5 and 6 (21066 and 22510).

The unusual finding in this area is right hand lower panel 4 (68729, 75915, 80558) with slumped tile similar to left hand lower panel 9 tile.

There are fourteen spar fittings per side in the glove region. Ten fittings, five upper and five lower, were found for the left hand side. Twelve fittings, six upper and six lower, were found for the right hand side. Upper and lower 1, upper 7 and lower 4 left hand spar fittings were not recovered. The right hand upper and lower spar fittings for rib splice 4 were not recovered. There are pieces of the aluminum wing spar attached to the spar fittings. The fittings and outer facesheet of wing spar have a non-uniform splattering of molten aluminum deposits



Item 21066, 22510



Item 68729, 75915, 80558



Item 75915, 80558

though the remaining pieces of silicone barrier on the spar are still pliable. The inner spar facesheet is virtually free of metallic deposits.

Per design, in the glove region only panels 5 and 6 have spanner beams, two per panel. Entire or partial spanner beams were recovered for each location on the right hand panels. Panel 5 outboard and 6 inboard spanner beams for the left hand side were recovered. The inboard spanner beams for panel 6 on both left hand and right hand sides along with left hand 5 were free of deposits or thermal erosion. The spanner beam for right hand 5 exhibits deposits consistent with the deposits found on RCC panel 5. Right hand panel 6 spanner beam has spar side thermal erosion. Pieces of Inconel foil from the insulators are scattered throughout the glove region.

All the RCC pieces in the glove region have fracture surfaces without signs of thermal erosion, though some of the fracture edges have substrate oxidation. The majority of the RCC lug clevis attach fittings were recovered. Uniform thin deposits on the interior of the panels contain Inconel, Ceracrhrome and aluminum at all deposition layers. The largest source of aluminum is the wing



Item 83323
LH Splice 2





Left Hand RCC Panels 1, 2, and 3



Left Hand RCC Panels 4, 5, and 6

spar, with the aluminum access panel providing a secondary source.

The highest concentration of deposits on the panels is the lower portion of right hand RCC panel 2, which coincides with a missing lower access panel 2. Fracture sequencing can be determined based on deposit levels. Panel 2 and its associated gap seal have a heavy concentration of metallic deposits on one side of a fracture while the mating fracture surface is completely free of deposits. This condition is found on the gap seal (64823, 58575, 18474) where the middle



Items 64823, 58575, 18474



Items 58575, 18474



Item 64725



Item 50336

section is free of deposits and the upper and lower portions have a heavy coating of deposits.

Gap seal 5 lower portion has tile coating transferred to the outer surface of the seal (64725). Similar tile deposition is also found on right hand gap seal 10 and 13.

A gap seal rotation test confirmed that a de-pinned (not fastened) upper attach point will allow the seal to pivot about the lower attach point. An apex region through crack in a gap seal is required to allow a portion of the gap seal to pivot about the upper attach point. This pivoting could allow contact with tile, thus transferring material.

Transition Region (Panels 7-11)

There are ten LESS access panels, five upper and five lower, per side in this region. The condition of the right hand panels is consistent with the panels in the other regions. Each lower access panel location for left hand and right hand side is represented either by tile, panel or combination of the two. Three right hand upper access panels are represented, of which panel 10 is facesheet only. The upper left hand transition area is void of access panels and tiles with the exception of the inboard interior tile for panel 8 (50336). The tile exhibits radiant heating and has deposits of Inconel, aluminum, carbon and Cerachrome.

There is no heat damage on any of the right hand panels. The only heat damage to the lower panels is to the tiles for left hand panel 9 (16692, 50338, 22571, 57754) on the surface adjacent to the RCC. Though the tiles exhibit severe heating, a portion of the aluminum access panel, as well as panel 8 and 10, survived with minimal heat effects.



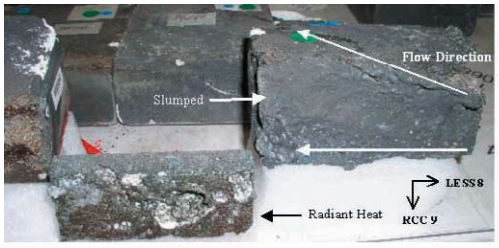
Panel 8 - Lower Access Panel Tile



Panel 9 - Items 16692, 50338, 22571, 57754



Panel 10 - Lower Access Panel Tile



The slumping and erosion of the tiles for panel 9 originates in the inboard forward corner, which aligns directly with the design notch in the heel of RCC panel 8 as shown above.

There are ten spar fittings per side, five upper and five lower. Six of ten right hand fittings were recovered, upper 8, 9 and lower 8, 9, 10 and 11. The right hand fittings have minor splattering of metallic deposits. No left hand spar fittings were recovered for rib splice 8 through 10 and only portions of the fittings for rib splice 11 and upper 12 were recovered.

Nine of the ten spanner beams on the right hand side were recovered, six of which are complete assemblies. Only portions of three spanner beams were recovered for the left hand side, none in panels 8, 9 or 10. Spar-side thermal erosion occurred on several of the recovered spanner beams as shown below:

- Right hand 7 inboard & outboard (55085 & 32087)
- Right hand 8 outboard, two locations (66897)
- Left hand 7 inboard upper (83639)
- Left hand 11 inboard (70376)

The only insulation material found is a piece of Inconel foil for the outboard



Item 55085



Item 83639



Item 70376



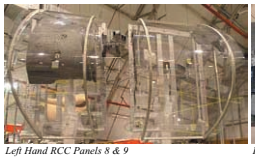
Left Hand RCC Panels 7, 8 & 9

spanner beam insulator on right hand panel 9. There wasn't any insulation recovered in the transition region for the left hand side.

There is significantly less RCC material and internal components on the left hand side than the right hand side, particularly in the transition region.

The lower acreage of left hand panels 8 and 9 are completely void of RCC material.

Per design there are twenty-four lug clevis fittings for panel and gap seals per side. Fifteen fittings are represented for



Left Hand RCC Panels 8 & 9



Right Hand RCC Panels 9 & 8



Left Hand RCC Panels 10 & 11



Right Hand RCC Panels 11 & 10

the right hand side and only eight fittings for left hand side, plus a bolt without clevis fittings for panel 10. The split bushing from the lug is fused to the bolt.

A failure unique to the left hand transition region is the absence of hardware for the upper lugs. All other location failures consisted of lug break up or clevis fitting to spar fitting overload. For the locations listed in the table to the right, the lugs were recovered with varying degrees of missing hardware.

The heaviest concentration of deposits for the left hand and right hand wings is on the internal surface of RCC panel 8. On the left hand side the heaviest concentration of deposits in this region is on panels 7, 8 and 9, with panel 8 being the most dense overall for both wings.

Deposit samples were analyzed to determine composition and the layering effect. The deposit layers indicate internal component melting timeline and can be used to determine the breakdown sequence of the leading edge. Deposits on all four panels consist of Inconel, Cerachrome and aluminum. Right hand panel 8 and left hand panels 7 and 9 have

Panel	Lug Location	Item	Hardware Condition
7	Outboard	26014	Missing all hardware, except split bushings
8	Inboard	17957	Partial clevis, split bushing, aft bushing, no bolts
8	Outboard	61143	Missing all hardware, slag deposits in holes
9	Inboard	N/A	Lug was not recovered
9	Outboard	29741	Missing all hardware, including gap seal hardware
10	Inboard	34713	Missing all hardware, except one bolt with split bushing



Item 26014



Deposits on Item 2200

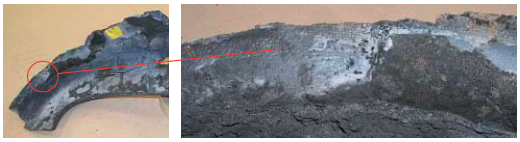


Panel 8

traces of aluminum on the initial deposit layers. There is no evidence of aluminum in the initial layer for left hand panel 8, with some aluminum deposits in the secondary layer and significant levels in the last deposit layer. Though not on the first layer, A286 deposits were found on left hand panel 9, however no A286 deposits were found in left hand panel 8.

No RCC erosion was found on the right hand wing. There is oxidation of RCC material on both wings. The outboard rib on right hand panel 8 has oxidation on the spar side of the panel (1419). The only erosion found on any of the RCC panels is the outboard rib and heel of left hand panel 8 and the inboard rib of left hand panel 9.

Item 82423, does not have sufficient geometry or remaining surfaces to



Item 1419



Panel 8



Panel 9

positively confirm its location. The piece of RCC rib has been located on panel 9 based on a fit that matches the drawing profile and erosion pattern. The erosion on 82423 is identical to the erosion on 52018. The edges of the piece have been eroded down to a knife edge.

The erosion is on the upstream side of the ribs, indicating a downstream flow direction. The rib on each piece is eroded down to a knife edge. The lug holes, to accommodate clevis attach fittings for panel 8, are oversized by means of erosion. The bolts and split bushings were not recovered.



There are two pieces of left hand lower gap seal (35201, 17943) that still need location confirmation. Comparing wear, deposits, near fracture match and upstream erosion the pieces appear to be related. The pieces dimensionally fits in several locations, most eliminated due to recovered items. The remaining locations







Items 17943, 35201



Items 1616, 5338

are rib splice 9 and 10. The best fit based on surroundings is rib splice 10. The erosion on the gap seal does not match the erosion on the ribs of the RCC panels at rib splice 9. The deposits on the seal pieces, does match the deposits on panel 11 at rib splice 10.

Right hand gap Seal 10 and panel 9 lower portion have tile material on the outer surfaces (1616, 5338) similar to gap seal 5 in the glove (64725) and 13 in the torque box (59454) regions.

Torque Box Region (Rib Splice 12-23)

The torque box region of the wing leading edge has less thermal damage than the other regions. There are eleven each upper and lower LESS access panels per side. Twenty-one of the twenty-two panels for the right hand side and eighteen of the left hand panels are represented. Left hand panel locations 16-22 are completely void of panels or are represented by a single tile or small piece of honeycomb. The right hand panels outboard of rib splice 17 have virtually no discernable heat damage.

There are twenty-two spar fittings in the torque box region per side. Seventeen (nine upper and eight lower) fittings were found for the right hand side. Eighteen (nine upper and nine lower) fittings for the left hand side were found. Compared to the glove and transition regions, larger pieces of aluminum wing spar were recovered in this region. On the left hand side metallic deposits are on the spar fittings (68) whereas on the right hand side the deposits are on the wing spar inner facesheet (59409, 9544). The silicone barrier on the outer facesheet of the right hand wing spar is free of metallic deposits and remains pliable.



Item 68 LH Spar Splice 15




Items 59409, 9544 RH Spar Splice 22 & 23

Per design, there are sixteen spanner beams for panels 12 through 19. Panels 20, 21 and 22 do not have spanner beams. Thirteen of the sixteen beams for the right hand side have been recovered, with panel 13 inboard beam exhibiting spar-side thermal erosion (65539). Nine of sixteen beams (some partial) were recovered with some showing overload damage. The majority of the insulators found on the wing leading edge were in the torque box region, particularly on the right hand side. Right hand insulators found inboard of rib splice 17 experienced minor heating and aero damage, whereas insulators outboard have no heat damage and only ground impact damage.

Right hand gap Seal 13 lower portion has tile material on the outer surface of the seal (59454).

The RCC in the torque box regions do not exhibit any thermal erosion however do have some areas of oxidation as shown on left hand panel 21 (6024).



Item 59454



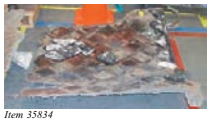
Item 6024

AFT

Aft Fuselage

The total percentage of the aft fuselage OML surface area recovered was approximately fifteen percent, with tile/tile fragments present only on the largest pieces. More right hand than left hand pieces were recovered. The skin pieces have fracture edges that are minimally affected by heat, except for the large ballistic coefficient items that have severe heat erosion. Many of the skin panels located in the aft fuselage were smaller and could not be specifically located within the grid. These items are waffle pattern aluminum structure with fracture edges all around and some light slag on the IML side. The largest items from the aft floor area were located fwd of Xo1365.

These items included the right hand and left hand ET door, two large skin pieces (35834, 76544) on each side of the vehicle centerline, and a portion of the lower Xo1307 bulkhead. The recovered pieces of structure on the left hand side have more heat related effects than those on the right hand side, except for the internal thrust structure items of high ballistic coefficient. Numerous tiles were identified as possible aft tiles; however, their final location was not determined due established priorities. The only tiles that were assessed were on the largest of the recovered pieces. The exposed filler bar/remnants were more charred on the left hand recovered pieces than the right hand.



Item 35834



Item 76544

No flow directionality could be discerned from any of the assessed tile.

The right hand ET door (53830) is fully intact with fracture edges at each of the two hinge points. Approximately sixty percent of the tile is still bonded. The OML surface and the primer on the IML of the door is not discolored. In comparison, seventy-five percent of the left hand ET door was recovered, in seven pieces, and has only five percent of the tile fragments attached. Two large floor skin pieces recovered accounted for nearly the entire area between the left hand and right hand ET doors. The right hand piece (76544) included the aft ET door latch mechanism. The forward ET door latch mechanism was also recovered in a much smaller skin piece.



LH ET Door



Item 53830



1307 Bulkhead



Item 1181

The large portion of the right hand Xo1307 bulkhead was recovered, which included wing-fuselage attach structure, mid-aft fuselage attach structure, a portion of the sidewall, a portion of the Xo1307 bulkhead, ET socket structure, and the LO2 blast can assembly attached with separation hardware contained within. This item has heavy slag deposits and heat effects on the aft facing surfaces. The forward facing surfaces were shadowed, evidenced by minimal slag deposits and no discolored primer.



Item 36055, 42928, 24846

The corresponding part on the left hand side is much smaller in size and consisted primarily of just the ET socket structure (31154) itself. The left hand item has extreme thermal erosion on all edges of the piece.

Two additional recovered primary structural items were the right hand (49596) and left hand structure (63994) surrounding the aft outboard corner of the ET door. The right hand piece has less overall heat effects than the corresponding left hand piece.

The titanium thrust box beam (2485) is an example of extreme heat exposure, characterized by splaying into a flat piece as compared to the intact titanium box beam (36072).

Four additional recovered pieces of primary structure each having heavy thermal erosion and melting on the edges are a thrust structure strut, beam, and strut attach points (36055, 42928, 1181, 24846).

The RH sidewall hoist point (49366) includes a portion of the mid-to-aft fuselage and attach fittings. This piece has heavy thermal erosion from the aft side evidenced by missing and melted collars



Item 49366

Item 63994



Item 31154

Item 2485





Item 49596



for the doors. Only minimal evidence of thermal exposure is present. A large portion of the upper and lower drag brace assembly (2540 and 2218) was recovered. Both parts have broomstrawing and overload failures.

Several pieces of the wheel well box structure were recovered and only superficial heat discoloration of the koropon is present. Parts of the uplock assembly were attached to these box parts and predominantly show evidence of overload failure. An example is item 561.

With the exception of the upper cylinder and the lower piston, only a small percentage of the left hand MLG was recovered. Most of the hardware shows signs of high temperature exposure. The lower piston assembly (1257) exhibited melting and thermal damage on the lower end. The outboard axle threads are gone with melted surfaces where they begin on the axle. There are burn through areas just aft of the jack pad and at the lower scissors mount. Both ends of the scissors mounting pin are melted. More than 95% of the bronze/aluminum portion of the upper end of the piston is missing. Sawtooth fractures and melting are visible. The piston barrel is in relatively good condition. The forward side of the piston barrel has much less chrome damage and less evidence of melting (bronze/aluminum material) than the aft side.

On the upper cylinder (12697), the gland nut threads are melted for two-thirds of the circumference and the uplock lug is melted away. The lower lug of the downlock link is attached and melted. One leg of the clevis is more than 80% melted away. The upper portion of the cylinder has extensive melting and distortion. The upper scissors pin and fitting are intact. The aft side of the upper cylinder is in better condition than the forward side, which shows more chrome damage and more overall heat damage.



Item 1257



Item 12697

The lower drag/lock brace (24823) has minimal thermal damage. The upper pin and outboard mating clevis are still attached. The attached clevis piece, and the adjacent clevis piece (81992) recovered separately, are both thermally damaged. These two are the only aluminum parts recovered for the left hand MLG that is not protected by other hardware during flight. The lower end of the brace demonstrates a typical over-stress condition.

Several brake assembly rotor and stator components were recovered with



Item 24823

conditions ranging from intact to fractured small pieces. The left hand outboard brake body (1805) was recovered and has extensive thermal damaged.

The tires were recovered separated from any other structure. The left hand outboard tire (197 and 210) is split into two pieces around the circumference and directed heat is evident on the inboard side of the tire. The inboard tire (2168 most probable location) is in good condition with only minor thermal damage to the entire outer surface and a split in the body.

Very little of the right hand MLG was recovered, in stark contrast to the recovery of almost the entire right hand MLG door, mostly intact. The tires were recovered separate from any other structure. Both tires are in good condition with only minor thermal damage to the entire outer surface and are in very similar condition to the inboard tire on the left hand side. The right hand outboard tire (31168 most probable location) does have a circumferential split in the body, while the inboard tire (71814) has no splits. Several brake rotor and stator parts have been recovered along with the upstop pad (8559), the down lock spring bungee housing (16548), and the uplock mechanism drive shaft (41425). This hardware has minimal thermal damage.

The right hand outboard wheel (567) has a melted fracture surface on the inboard side of the wheel and the center portion of the wheel is missing.

The gear retract actuator (27323) is intact and is attached to the upper portion of the landing gear. The gear portion has evidence of high temperature exposure. The down lock brace clevis fitting (45724) that attaches to the upper cylinder was



Item 1805



Item 197



Item 210



Item 2168





Item 567



Item 84265



Item 27323

also recovered with similar thermal damage.

The MLG door retract actuator beam (84265) has some thermal damage as well, however, it is also mostly intact.

Life Support Systems

Environmental Control and Life Support System (ECLSS) – Multiple components of the ECLSS were recovered and identified from the forward, midbody, and aft areas. All items have been exposed to thermal degradation with the majority items identified to the crew module.

In the forward section, the stainless steel cold plates from the water cooling loops, both humidity separators (53764), the avionics bay heat exchangers, the cooling air ducts and miscellaneous water cooling lines were identified. The humidity separators survived with the foam insulation intact, which helped in differentiating them from the SpaceHab humidity separators, which do not have the same foam insulation. Twenty percent of the ECL items had sections of part numbers remaining, but drawing dimensions and/or bolt patterns were used to identify most items. All three fire bottle Halon containers were identified.

In the midbody, items recovered include Freon cooling loop hardware, aluminum cold plates (6800), accumulator parts (2029), and some cooling lines. The Orbiter has five gaseous nitrogen (GN2) tanks, all of which were recovered and identified. Most of the stainless steel vacuum vent and radiator Freon cooling lines were identified.

In the aft, aluminum cold plates were identified either in pieces or in conjunction with avionics boxes. Most of the flash evaporator system was not found.



Item 53764



Item 6800



Item 2029

Ammonia tank B was found intact but thermal erosion had removed the insulating paint. Most of the titanium ammonia tank A was recovered as three large items.

Purge, Vent and Drain (PVD) - system employs ducts that are made of composite material, which is susceptible to damage from off-nominal loading. Most duct debris recovered are end pieces or short fragments. A barrier check valve assembly from the area near the crew hatch, assorted tubing from the window cavity conditioning system, the star tracker vent screen, and payload bay vent liner filter frames were also identified.



Item 751



Item 84241



Item 585



Item 74844

Mechanical Systems

The condition of the recovered mechanical system components varied both with respect to the quantity of items per system as well as the degree of degradation. For example, except for the semi-circular housing cover missing from the left hand air data probe (ADP), both the left hand and right hand ADP's were recovered intact, with little significant physical or thermal damage. Likewise, the NLG strut, it's associated axle, and both nose wheel assemblies (NWAs) were recovered as a complete assembly with some physical damage but relatively minor thermal damage. In contrast, nothing has yet been recovered from the -Z star tracker door mechanism.

ADP -Both right hand and left hand ADP's (751) were recovered with little damage except for missing cover on left hand side.

Star Tracker: The -Y star tracker door was recovered with minor physical and thermal damage. Nothing was recovered from the -Z star tracker door.

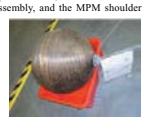
PLBD - Several bulkhead rollers were recovered such as right hand forward #1, right hand aft #2 and #3 and left hand aft #4. Also recovered were a rotary actuator, one of twelve PLBD drive bellcranks (814), and the right hand forward #2 bulkhead latch bellcrank.

Manipulator Positioning Mechanism (MPM) - An extensive portion of the port sill containing the forward pedestal base and section of the drive shaft was recovered, along with the mid MPM pedestal base, the MPM shoulder base assembly, and the MPM shoulder drive mechanism.

Radiators - Six outboard radiator latch assemblies (428), two inboard radiator latch assemblies, three radiator latch rotary actuators, and one radiator drive rotary actuator were recovered.

ET Doors - The right hand ET door was recovered as a unit (84241). Eight sections representing about 85% of the left hand ET door was also recovered, as were the forward and aft ET door centerline latch mechanisms, and portions of the left hand ET door drive assembly and right hand ET door drive assembly (59003).

Hatches - Hatch interface collars for the A and B hatch (no hatch flown at this location), tunnel adapter C hatch, and tunnel adapter D hatch were all recovered. A hatch (585) was recovered as a unit with some burn through, but all six latches and bellcranks were attached. D hatch (74844) was recovered also, with burn through, and all seventeen latches and most of the drive linkage were intact. Fifteen of eighteen internal/external hatch latches were recovered; latches 1 through 6 and 16 through 18, latches 11 and 12, latches 8 and 9, latch 10, and latch 13. Five latch sections of C hatch were also recovered.



Item 38913

Orbiter Maneuvering Reaction Control and Auxiliary Power Unit Systems

The OMS/reaction control system (RCS) components were damaged more severely than those of the FRCS module. Seventy-five percent of the FRCS internal components were recovered, while 60% of the left pod internal components and 40% of the right pod internal components were recovered. Forty percent of the APU system has been recovered.

OMS/RCS - A significant percentage of FRCS internal components are intact, including the fuel and oxidizer helium tanks, the fuel and oxidizer propellant tanks, all primary thrusters, and both vernier thrusters. Seventy-five percent of the A/C motor valves, various sizes and

lengths of stainless steal tubing runs, and several area heater panels were identified. The FRCS components, though damaged, were easily identified. The entire right side of the module was intact with thrusters installed (792).

Recovered aft pod internal components:

- Both OMS helium tanks (38913), intact
- All four RCS helium tanks, intact
- 90% of the left OMS fuel propellant tank
- 5% of the right OMS fuel propellant tank
- 10% of the left OMS oxidizer propellant tank
- 90% of the right OMS oxidizer propellant tank
- 33% of the left RCS fuel propellant tank
- Right RCS fuel propellant tank (53835), intact
- Left RCS oxidizer propellant tank, intact

A significant number of aft pod thrusters were recovered. However, most have no unique characteristics due to heavy thermal erosion and therefore have not been identified to an exact location. Several A/C motor valves and tubing runs were identified, but were too badly damaged to verify the exact location. Very little of the Orbiter maneuvering engine (OME) components were recovered. Two of the items recovered are the right OMS pneumatic pack and the right OMS engine chamber.

Auxilary power unit (APU) – The APU propellant/GN2 tanks from systems 1, 2, and 3 (59623) were recovered. The tanks have moderate damage and all of the diaphragms are torn or detached from their mounting surfaces. One system 3 pump and another undetermined fuel pump were recovered. One APU catch bottle was recovered, while none of the APU assemblies themselves were recovered. A small piece of lubricant oil line tubing with a transducer attached was the only other recovered APU system component.



Item 53835



Item 266



Item 76452



Item 59623

Payload Mechanical System

Major components - Nine of the ten titanium longeron bridges (266) have been recovered and identified. Damage ranges from mechanical overload fractures, melted holes penetrating thinner flange areas, mounting hole galling, slag, and thermal damage. No damage trends are evident based on the location of this hardware in Orbiter. Eleven of the fourteen sill latches have been recovered, and have heavy damage similar to the longeron bridges. Two of the missing sill latches are secondary latches, and the third missing sill latch is part of the missing longeron bridge. All four of the keel bridges have been recovered, but only three of the keel latches were returned. The missing keel latch is torn off of the bay 3 keel latch.

EVA components - Due to their aluminum or composite construction, and



Item 264

the heat encountered, very little of the Orbiter EVA handholds survived, although many smaller handhold support fittings and linkages were found and identified. None of the slidewire linkage structure was recovered. Several port stowage assembly (PSA) tools were recovered. None of the four payload bay cameras were found, and only one camera shelf structure was recovered. Two camera lenses were found.

Payload components - The only recovered sections of the tunnel adapter (264) and forward extension were the main structural rings and small sections of interior panels. The rings are distorted, have slag, and show heavy melting from exposure to intense heat.

Power Reactant Supply and Distribution and Fuel Cells Systems

PRSD System - A hydrogen (H2) T-0 valve and a fuel cell 1 (FC1) reactant valve (16130) were identified, both of which came from H2 manifold 2. The left hand fuel cell oxygen (O2) purge port was identified. Power reactant supply and distribution (PRSD) hydrogen relief 2 port was identified. The PRSD servicing panel (74847) behind door 45 was recovered. A few sections of PRSD plumbing remnants were identified through part marking or unique line insulation. Four Belleville washers, from two O2 tank relief valves, were identified and have minor damage (internal to the relief valve).



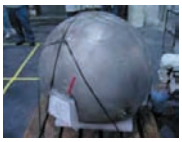
Item 16130



Item 69490



Item 10257



Item 1122

PRSD Tanks - All nine PRSD and external duration Orbiter (EDO) tank sets (each containing one O2 and one H2 tank) were recovered except H2 tanks 1 and 4. Tank pressure vessels were recovered with various degrees of damage, some intact and some as fragments. All tanks lost their outer aluminum shell. Many sections of the outer shell trunnion support rings were recovered and were severely degraded.

Several tank quantity probes and heater assemblies were identified. Several tank vacuum-ion pump converters (10257) were recovered, and some of them have thermal damage. The outer metal shell is removed from some of the recovered vacuum-ion pump converters exposing the internal components. One vacuum-ion pump (69490) was recovered with an intact magnet and exposed internal portion of the cathode.

The following is a summary of PRSD tanks recovered:

- O2 tank 1, (1575)
- O2 tank 2, (41040)
- O2 tank 3, (36989)
- O2 tank 4
- O2 tank 5, (2087)
- O2 tank 6 (EDO), (67814)
- O2 tank 7 (EDO), (1122)
- O2 tank 8 (EDO), (43558)
- O2 tank 9 (EDO), (24316)
- H2 tank 2, (1194)

- H2 tank 3, (9279)
- H2 tank 5, (217)
- H2 tank 6 (EDO), (206)
- H2 tank 7 (EDO), (219)
- H2 tank 8 (EDO), (214)
- H2 tank 9 (EDO), (209)

EDO Pallet - All of the PRSD tanks which were mounted to the EDO pallet were recovered and are listed above. The only identified pallet structural components are the port longeron and support, the keel trunnion, and the payload keel. Some of the unidentified plumbing may be from the EDO pallet. A recovered bus current sensor, which was not identified to an exact location, may have also been from the pallet.

Potable & Waste Water Components - Portions of the potable water tanks (52023) and the waste tank (12055) were recovered. Some tank outer skin sections were also recovered. The internal bellows were separated from the outer vessel container. One supply water valve was found but was not identified to an exact location. The waste dump nozzle (8118) was recovered with part of the skin panel.

Fuel Cells - Fuel cell (FC) components were recovered with varying thermal damage. Approximately twenty of 288 internal cell reactant plates (8767) were identified and traced to their original FC. Several plates are nearly intact. Hundreds of small pieces of cell plates were also recovered but could not be identified.

Two hydrogen separator pumps were recovered. The FC1 pump is still attached



Item 214



Item 52023



Item 12055



Item 8767

to the hydrogen condenser housing. All three cell end plates, all three coolant accumulators, and one coolant filter were recovered.

Space Shuttle Main Engines and Main Propulsion Systems

Ten percent of the main propulsion system (MPS) was recovered. The MPS hardware exhibits common characteristics. Items with high ballistic coefficients were able to survive. Also, titanium tanks, which were covered with epoxy-impregnated Kevlar-49 fiber strands, were able to withstand the high tenperatures and the off-nominal dynamic forces.

MPS components - The helium supply tanks (49386), which are made from two, forged hemispheres of titanium 6AL-4V alloy and covered with epoxy-impregnated Kevlar-49 fiber strands remained fully intact. The three 17.3 cubic feet and seven 4.7 cubic feet helium supply tanks were recovered and



Item 49386



Item 56643



Item 16931

are charred and unraveled. No MPS valves, neither mono-stable nor bi-stable were recovered intact. All four of the fill and drain valve actuators, less the gear racks, were recovered, with the two LO2 valve (16931) visor blades still being attached to the actuators. Prevalve (56643) pieces were limited to housing flanges, anti-slam mechanisms, detent rollers/covers/belleville washers, visor/ shaft assemblies, and actuator clutch/ bearing assemblies. Mono-stable valve actuator internals such as pinion gears and gear racks along with housing flanges were recovered.

The Orbiter-to-external tank 17-inch disconnect housings (22229) were both recovered, but the associated ancillary tubing, drive arms, flapper valves, and latches are either missing or in various stages of thermal degradation. LH2 4-inch recirculation return system and gaseous oxygen/ gaseous hydrogen (GO2/GH2) 2-inch pressurization disconnect primary and secondary belleville springs along with the 4-inch belleville spring retainer were recovered. Also recovered were one partial 8-inch fill and drain line T-0 disconnect and one 1½-inch liquid oxygen (LO2) bleed T-0 quick disconnects. Small segments of the engine mounted heat shield (EMHS) were recovered ranging from complete cross sections with clips and doubler plates attached to just the inner or outer Inconel 625 sheeting.

Other miscellaneous components identified by MPS are:

- Partial vibration isolators
- Recirculation pump cover plates, rotor, stator, and inducer
- GH2 filter assembly and element (7010)
- LO2 engine cut-off sensor MT2
- LH2 flame arrestor
- 1-inch relief valve SOV bellows/poppet assembly
- Curtain attach plate segments and retainer brackets

Absent from the MPS recovered valves were pneumatic system solenoid valves, check valves, relief mechanisms, and GO2/GH2 Flow Control Valves.



Item 7010



Item 22229

MPS Pressure Carriers - Less than 5% of the MPS system lines/tubing was/were recovered. None of the propellant system vacuum jacketed lines were recovered intact. Small segments of Inconel internal pressure carrier lines and multiple pieces of bellows convolutes (75590) were recovered along with the more robust line flanges, ball strut tie rod assembly (BSTRA) joints and gimbal/gimbar joints. Four LH2 12-inch engine feedline, two LO2 12-inch engine feedline, and two LO2 17-inch BSTRA (1540) joints were recovered.

In addition, three 12-inch feedline gimbal rings (19520) were located and identified. Some of the vacuum jacketed line structural annulus stiffeners, standoff rings, burst disc assemblies, test ports and spacers were also recovered. The small, uninsulated tubing was generally charred beyond recognition and could not, in most cases, be specifically linked to a certain system. A small percentage of MPS pneumatic and GO2/GH2 pressurization tubing was identified by specific fittings, bend configuration, brazes and/or welds.



Item 1540



Item 19520

CONCLUSION

The Columbia search, recovery and reconstruction effort provided evidence critical to the Columbia accident investigation to develop the most probable failure scenario. In general, most recovered debris exhibits a combination of thermal damage and mechanical overload failure. Items with high ballistic coefficients show much greater levels of ablation, while others failed as the result of aerodynamic forces or ground impact. Specifically, the condition of the left hand wing leading edge provides compelling evidence of an initial breach in the transition region that resulted in catastrophic damage.

The transition region of the left hand wing leading edge from RCC panel 7 through panel 11 has unique characteristics compared to the rest of the wing. The upper access panels for RCC panel 8 through panel 11 were not recovered, with the exception of one inboard/interior tile of access panel 8. From the inboard lower rib on panel 8 through panel 10, the absence of all metal hardware (spanner beams, spar fittings, clevis fittings and insulators), with the exception of a single clevis-mounting bolt, suggests that this region experienced temperatures high enough to melt the structural members.

Panel 8 has the heaviest concentration of deposits, followed by panels 7 and 9. The forensic analysis of the deposits on RCC hardware in this area provides key sequencing data. All three panel locations have aluminum, Inconel and Cerachrome deposits. The initial layers of deposits on the interior surface of RCC panels 7 and 9 have aluminum. Panel 8 is free of aluminum deposits in the initial layer, which indicates the spanner beams and insulators melted prior to the wing spar.

The panel 8 outboard rib and panel 9 inboard rib are the only positively identified pieces to have thermal erosion. This erosion is in the downstream direction. Arc jet testing at Johnson Space Center demonstrated that prolonged exposure to plasma is required to obtain thermal erosion of RCC. All the lower access panel 9 tiles have erosion, with the upstream tiles having the most damage. Lower access panel 8 tiles are not eroded.

The missing hardware, analysis of the deposits, damage to the access panel tiles and the directional erosion on the rib pieces bound the breach to panel 8. None of the lower acreage of panel 8 was recovered. The upper portion was recovered and does not have a penetration point, therefore, the initial breach occurred in the lower portion of left hand RCC panel 8.

The condition of the left hand wing hardware strongly indicates it was exposed to initial heating caused by the breach in the wing leading edge. The erosion pattern on the left hand MLGD perimeter indicates off-nominal port to starboard aerothermal flow. In contrast to the right hand wing, a small percentage of the left hand wing debris was recovered and is dimensionally smaller with greater thermal degradation. Aerodynamic failures were predominant on the right hand wing, as indicated by the condition of the fracture surfaces. In addition, the inner surface of the right hand wing skin has inboard to outboard flow, as evident by erosion of the interior rib surfaces and the evaluation of deposits on the wing leading edge. The leading edge spar pieces have deposit build-up on the inner surface of the spar (wing side) but not the outer surface (RCC side). Forensic analysis detected aluminum in the first layer of slag sampled from the right hand wing RCC panel 8, indicating that melting of the spar occurred concurrent with the melting of the leading edge components.

The elevons and body flap are comprised mostly of honeycomb sandwich panel assemblies that are susceptible to failures due to thermal exposure. The larger recovered body flap items were along the outboard and trailing

edges. Slumped tiles on the body flap trailing edge indicates flow in the port to starboard direction. The elevon debris was recovered with a bias to the port side with minimal thermal degradation.

Tile damage to the outboard forward corner of the left hand OMS pod and the disparity of damage between the right and left hand side of three upper vertical tail pieces indicates the tiles were impacted by left wing debris prior to vehicle breakup. Forensic analysis of samples taken from the OMS pod tiles determined the imbedded deposits to be the same materials as the wing leading edge spar fittings and spanner beams.

The small amount of aft fuselage hardware recovered provides some evidence to how it failed. The right hand lower Xo1307 bulkhead has heavier slag on the aft side near the right hand ET attach fitting than the forward side of the bulkhead indicating a flow in the forward direction. The left hand ET attach fitting has significantly more thermal erosion than the right hand fitting. The structure recovered forward of the Xo 1365 bulkhead consists of skin pieces larger than those aft of the bulkhead. The pieces aft of Xo 1365 were exposed to internal heating, which resulted in backside heating tile failures. This indicates that the aft fuselage failed at the Xo1365 spar plane after the initial breakup of the orbiter.

The mid fuselage structure was recovered in decreasing percentage from forward to aft. The primary failure for most of the mid fuselage structure was mechanical overload with subsequent thermal damage. Some mid fuselage items have substantial thermal damage evident by broomstraw fractures. The absence of mid fuselage sidewall skin at both wing interfaces coincides with the absence of internal wing components. A large percentage of the recovered payload bay door debris was broken into relatively small pieces. The payload bay doors, constructed of a lightweight graphite/epoxy composite, most likely broke up earlier than the rest of the fuselage due to off-nominal loads.

A greater percentage of the forward fuselage structure was recovered than mid or aft fuselage. The recovered forward fuselage structure and TPS items have very little thermal damage when compared to the rest of the vehicle. This suggests that the forward fuselage remained thermally protected for a longer period of time after the initial breach. Separation of the crew module and forward fuselage assembly together from the rest of the vehicle likely occurred at the interface between the Xo576 and Xo582 bulkheads.

The Columbia Debris Assessment Working Group concludes that the initial breach occurred in the lower surface of left hand RCC panel 8. The breach allowed plasma flow into the wing leading edge cavity, which melted the insulation and structural members in the transition region. The upper leading edge access panels were likely lost due to hot gas venting. Shrapnel from the disintegrating left hand wing impacted the vertical tail and left OMS pod. The plasma penetrated the left hand wing with one of the exit points being through the trailing edge. The structural capability of the wing was diminished to the point where it failed aerodynamically allowing the wing tip and elevons to break off. This resulted in vehicle instability thus increasing aerodynamic and thermal loads on the left side of the orbiter, which caused vertical tail and PLBD failure. The vehicle orientation rotated to allow thermal flow to penetrate the left mid and aft fuselage sidewall at the wing footprint. In the right hand wing, the hot gas flow is from the inboard side. Internal thermal loading combined with increased aerodynamic load caused dynamic break up and separation of the upper and lower right hand wing skin panels. The breakup of the remaining fuselage continued from aft to forward until aerodynamic loads caused final disintegration of Columbia.

Samples and Items Analyzed

The M&P Team processed 176 Reconstruction Documentation Sheets (RDS's) for disassembly, identification, NDE, sampling, and analysis of Columbia debris. Each RDS defined specific techniques used to perform Type I (non-destructive) or Type II (destructive) sampling and engineering evaluations of selected debris from RCC pieces, structure, tile, wing leading edge components, and unknown metallic pieces. A summary of the RDS matrix for NDE and Analysis is shown below in Table 9.1.

Initial M&P Engineering Support

The M&P Team supported early assessments of left hand airframe components believed to be possibly associated with the breach and breakup of the Orbiter. The Team also assisted the HFT in selecting Pathfinder debris samples that exhibited similar characteristics like that of damaged components from the left wing. Factual observations of suspect left wing components and tiles including the Midbody Panel, Uplock Roller, Main Landing Gear (MLG) Strut, Tire pieces, A286 Carrier Panel Fasteners, and Left Wing Tiles were recorded into the reconstruction database. Additionally, the Team also recorded extensive photo documentation, radiographic images, and Fact Sheets of debris items in the database, and detailed procedures and sampling techniques were developed to preserve hardware and critical evidence. Much effort was expended into developing the the M&P process and developing the best Type I techniques (CT scan, real time X-ray, etc.) so that limited sampling could be performed.

During the early stages of the investigation, a number of left wing component locations were seriously considered as a possible breach location. Many left wing components exhibited varying degrees of thermal effects, and the M&P Team was tasked to evaluate the significance of the damage and their possible relation to the breakup.

This section reviews the early analyses conducted by the M&P Team prior to the recovery of on-board sensor data. The Team analyzed debris to understand the characteristics of the damage and to qualify early Type I and Type II sampling techniques. Additional knowledge of secondary events that occurred during the breakup was gained from the early analysis. Debris assessments recorded by the M&P Team later appeared to correlate well with the sensor data obtained from Shuttle Modular Auxiliary Data System/ Orbiter Experiments (MADS/OEX) Recorder.

RDS Type	RCC	Structure	Tile	Leading Edge Components	Unknown	Total
Disassembly	2	0	0	0	0	2
NDE	46	6	22	0	0	74
Sampling & Analysis	49	2	14	2	0	67
Failure Analysis	4	8	1	10	0	23
Identification	0	3	0	0	7	10

Table 9.1: Summary of M&P RDS Matrix

MIDBODY PANEL

Unique flow patterns were observed on portions of the left midbody panel (Item 283) tiles, and there was evidence of localized heat erosion at the OML along the panel's edge. The surface of the tiles eroded by the flow patterns was glazed and hardened, and some metallic deposits were observed on the tile surface. The patterns observed in the tile were approximately ninety degrees from the nominal reentry flow pattern. The corners of the tiles near the inboard corner of the gear door were cratered and eroded, however there were no visible deposits on the tiles.

The edge of the panel at the inboard corner was also cratered, and a small hemispherical erosion pattern was observed at the panel's edge. The flow patterns observed in the tile near the forward inboard corner of the panel were approximately ninety degrees from the nominal reentry flow pattern. Additionally, the OML of the panel opposite the midbody panel (forward outboard corner) (Item 24704), and the OML of the saw-tooth doubler (aft inboard corner) (Item 1193) showed very localized heating and erosion at the corners.

MAIN LANDING GEAR DOOR UPLOCK ROLLER

The M&P Team evaluated additional landing gear door and wheel well hardware believed to be relevant to the investigation. One of four left landing gear uplock rollers (Item 9618) was recovered, and several metallic deposits were observed on the frame and roller portions. A thin, uniform, metallic coating was observed on all surfaces of the inner and outer titanium flanges and approximately the lower third of the cylindrical shaft. Additionally, some discoloration/heat tinting was observed on the cylindrical shaft adjacent to the metallic deposits. Analysis of the coating showed large amounts of metallic aluminum with lesser amounts of copper, titanium, manganese, and iron. No surface features or markings could be identified that would aid in identifying the location of the roller within the wheel well.

LANDING GEAR

A portion of a landing gear strut was recovered during search operations and identified by the Mechanical PRT as a left MLG component (Item 1257). The backside and bottom of the cylindrical strut had very localized regions of erosion and burning, and they were heavily coated with metallic slag. The front side (faces forward when deployed) showed no signs of burning or erosion, and some of the chrome plating was still intact. The outboard axle showed uniform thin slag deposits while approximately 3.5 to 4 inches of the inboard axle was heavily eroded.

MAIN LANDING GEAR TIRES

Early visual assessments were also made of thermal effects on two tire pieces (Items 197 & 201) believed to have been installed on the LH MLG. The placement of two balance patches on the internal surface of Item 201 later confirmed it to be the LH MLG Outboard Tire. Physical evidence was not available from the vendor to confirm the location of Item 197, however the fracture surfaces of Item 201 and 197 were visually overlaid and compared. Both tire sections showed significant thermal damage relative to two other unidentified intact tires (Items 2168 & 31168), and their carcasses were heavily deformed. Sections of the rubber and nylon reinforcements in Items 197 and 201 showed signs of high temperature exposure due to their increased hardness and stiffness.

CARRIER PANEL ATTACH FASTENERS

During the debris assessment it was discovered that several steel fasteners that attach the upper and lower aluminum access panels to the wing spar appeared to have brittle fracture characteristics. The aluminum 2024 panels were protected with tile and secured to the RCC spar attach fittings with two A286 stainless steel fasteners. The lower panels had an aluminum 2219 box beam as a spacer between the access panel and the spar fitting.

Nine failed and four unfailed fasteners were delivered to Boeing Huntington Beach for failure analysis. Seven of the nine failed fasteners were determined to be high temperature failures, and the remaining two were lower temperature failures. Of the seven high temperature failures, four were melted at the head end, indicating localized temperatures in excess of 1315°C (2400°F). The remaining three failures exhibited intergranular fractures on a large grained structure, indicating temperatures between 1038°C (1900°F) and 1204°C (2200°F) prior to fracture.

The two lower temperature failures were ductile bending, and the grain sizes of these indicated moderate temperature exposure between 704°C (1300°F) and 927°C (1700°F). Because these were not intergranular fractures, a time of failure could not be correlated to the period of exposure.

FORWARD OUTBOARD LH MLGD CORNER TILE

The LH main landing gear door tile on the forward outboard corner (identified as item 33590, P/N V070-191101-031) demonstrated a similar flow pattern as the left midbody panel (Item 283). Visual evaluation of the OML of the tile revealed apparent thermal flow erosion (melting, flowing and lifting of the RCG coating) of the outboard edge (directly adjacent to the outboard thermal barrier), with the flow direction inboard and slightly forward (Figure 9.1). This flow pattern was oriented approximately ninety degrees from the nominal flow direction expected in this area. In addition, the IML showed similar evidence of thermal flow erosion, but indicated the flow direction to be from inside the forward outboard corner of the main landing gear cavity, outward and forward. X-ray radiography did not detect any notable features aside from the surface features noted above; therefore, no sampling or chemical analysis was performed.

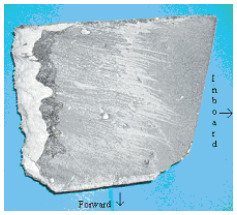


Figure 9.1. Left landing gear door perimeter tile, forward corner, item 33590

LITTLEFIELD TILE

One of the western-most items recovered in the debris field was a tile fragment (Item#14768), commonly referred to as "the Littlefield tile" because it was named after the town in which it was discovered. A high degree of interest was generated in determining where the tile had been located on the vehicle. Although the tile's surface coating was black in appearance, thickness measurements and a small area of visible white RCG coating beneath the black layer indicated it was most likely from the upper wing or canopy areas. Visual examination alone was not sufficient to determine if the black appearance was paint, which is applied to some of the upper surface tile per drawing, or metallic deposition, which occurred during structural heating/vehicle break-up.

Initial sample analysis on a sample taken from the fragment was inconclusive. Further comparative laboratory analysis with LRSI tile from both painted and unpainted regions of the vehicle indicated the black "coating" was most likely aluminum deposition. In parallel, extrapolation of data obtained through 3-D mapping of the fragment identified three potential LRSI candidate locations, all of which were not painted per drawing, further confirming the hypothesis of the laboratory analyses. Based on the results, a "best fit" candidate location was identified as V070-195003-150/154 (LH/RH), located directly inboard of RCC panels 8 & 9 on the upper wing. Information regarding the analysis was documented in Boeing Report 03-064 and NASA report KSC-MSL-2003-0115.

PATHFINDER DEBRIS ANALYSIS

The M&P Team also assisted the HFT in selecting structural debris that exhibited similar thermal and mechanical damage like that of the left wing areas of interest. Some structural pieces were selected by the HFT to develop a failure analysis process for debris hardware and to obtain exploratory laboratory data. Because of the extreme heating involved with the hardware, the laboratory investigations required exploratory test methods, analyses, and interpretations.

To facilitate and expedite the failure analysis process, six debris items remote from the high interest areas of the left wing were selected as exemplars for failure analysis. A description of the hardware selected for analysis and its analysis location is listed below in Table 9.2

Item	Description	Analysis Location
33767	R/H ET Door Cavity	Boeing – Huntington Beach
24521	R/H Vertical Tail Structure	NASA - JSC
797	R/H Lower Wing Glove Fairing Skin	NASA - Langley
36758	R/H Forward Fuselage Upper Skin Splice	NASA - Langley
37696	Midbody Fuselage / Sidewall	NASA - Langley
41372	R/H Lower Wing Glove Fairing Skin	NASA - Langley

Table 9.2. Pathfinder Parts Selected for Failure Analysis

The Pathfinder areas of interest included fracture surfaces, high temperature erosion and melting of fractures and other protrusions, various metal deposits, and various degrees of tile discoloration and deposits. The results of the tests and analyses were intended to provide guidance of future failure analyses and provide a basis for debris damage interpretation.

Analysis of Wing Leading Edge Debris and Attach Hardware

The M&P Team's analysis of wing leading edge debris was consistent with assessments made by the HFT regarding Columbia's breakup scenario. The HFT identified potential sites for a breach in the wing leading edge and entry points for plasma flow. Damage patterns observed on select wing leading edge component debris suggested that major thermal events occurred in the left wing leading edge near RCC Panels #8 - 9. These observations were strongly supported by data obtained from the (MADS/OEX) Recorder and physical evidence at the left wing leading edge.

Several left wing leading edge components exhibited unique indications of heat damage relative to other wing leading edge parts, and they were identified by the HFT and CAIB as focus areas for materials analysis. These focus areas included:

- Excessive overheating and slumping of LESS carrier panel tiles
- Eroded and knife-edged RCC rib sections
- Heavy deposits on select pieces of RCC panels

Samples of deposits from these areas were chosen from extensive examinations of radiographic images to minimize the quantity of sampling. Samples of interest were removed from the affected areas where permitted and analyzed by the M&P Team.

RADIOGRAPHY OF CARRIER PANELS AND RCC

Non-destructive Type I sampling included real time radiography of carrier panel tiles and RCC materials. A major objective of this type of sampling was to

perform a macro-examination to determine ideal regions to conduct more destructive Type II sampling and limit costly and time consuming analyses requiring special labs. Radiography of tiles and RCC panel pieces showed that x-rays were an excellent method of characterizing the following attributes:
- Location and shape of metallic deposits
- Melt flow patterns on tile
- Imbedded debris not visible on the surface.

The M&P Team used the radiographic data to develop Type II analysis procedures that carefully characterized all important features on critical tile and RCC surfaces.

THERMAL EFFECTS OF LESS CARRIER PANEL TILES

Surface Deposits and Slumping

Evidence of overheating and slumping was observed on three LI-2200 Lower Left Carrier Panel 9 tiles adjacent to left hand RCC panel 9. The item numbers of tiles are: 16692 (V070-199716-048), 22571 (V070-199716-052) and 57754 (V070-199716-054). Figure 9.2 shows the simulated configuration of the carrier panel tiles. Depressed/slumped and eroded regions were observed in two of the three tiles (Items 16692, 22571). For

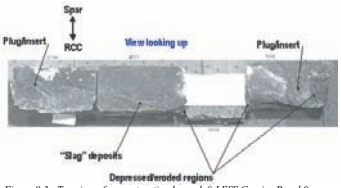
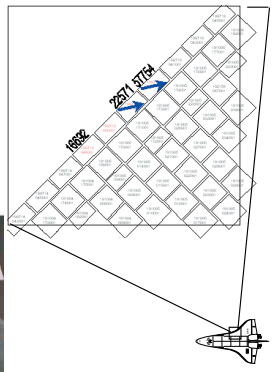


Figure 9.3. Top view of reconstruction lower left LESS Carrier Panel 9.

Figure 9.4. Apparent flow direction of surface deposits on Carrier Panel 9tiles.



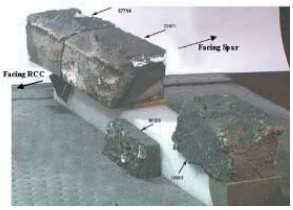


Figure 9.2. Reconstruction of recovered left hand lower LESS Carrier Panel 9 tiles.

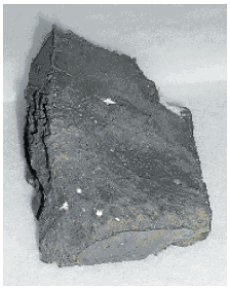


Figure 9.5. Upper left hand LESS Carrier Panel 8 internal tile (Item 50336)

example, the forward-facing sidewalls of Items 16692 and 22571 that nominally seal against the lower RCC panel 9 heel were severely slumped and eroded.

Dark-colored deposits were observed on all three outer mold line (OML) tiles (Items 16692, 22571, 57754). The thickness of the deposits varied across the tile surfaces. In the case of 22571 and 57754, the deposits produced visually apparent flow-like patterns oriented in the aft/outboard direction (Figures 9.3 and 9.4). Visual evaluation showed evidence that in some locations on the tile sidewalls, the deposits had built up over adjacent soft goods. This was supported by the presence of entrapped ceramic fibers in the deposits.

One internal LI-900 tile originally located on Lower Left LESS Carrier Panel 9 was recovered. This tile (Item 50338, V070-194205-004) exhibited a heavily slumped and cratered appearance (Figure 9.2). An additional internal LI-900 tile was recovered from upper Left LESS Carrier Panel 8. This tile exhibited a greenish coloration and heavy slumping (Figure 9.5). The surface deposits on internal tiles 50336 and 50338 were not as thick as those observed on the Lower Left LESS Carrier Panel 9 OML tiles.

X-ray radiography of the carrier panel tiles did not detect any notable features aside from the surface deposits noted above. A typical example is shown in Figure 9.6. Sampling and chemical analysis were therefore initiated for surface deposits only.

Chemical Analysis of Deposits

Samples of the surface deposits were removed and chemical analysis was performed using Scanning Electron Microscopy/Energy Dispersive Spectroscopy (SEM/EDS) and Electron Spectroscopy for Chemical Analysis (ESCA). The results indicated that the elemental components of the deposits were primarily aluminum, nickel, niobium and carbon (references provided in Table 9.3). Although the precise composition of the source alloys/compounds cannot be identified with certainty, the elements found are consistent with the compositions of 2000 series aluminum alloy, Inconel 601, Inconel 718 and Incoflex batting (e.g. Cerachrome). ESCA results indicated that the outermost layer was highly carbonaceous. This indicates that the carbonaceous outer layer was deposited after the metallic layer, which had in some cases fluxed into the RCG coating.

Tile item 57754 remained bonded to a section of underlying carrier panel 9 (Figure 9.7). Tile items 22571, 16692, 50338



Figure 9.6. X-ray radiograph of tile Item 22571; front view (left) and side view (right)

Item #	Date	Title
16692	5/7/03	Boeing NSLD FA Report 03-079, "SEM/EDS Analysis of STS-107 Debris Samples
	N/A	*Xray*
	5/13/03	Boeing HB Case Report 301974, " ESCA of STS-107 Debris Samples"
22571	5/6/03	Boeing NSLD FA Report 03-079, "SEM/EDS Analysis of STS-107 Debris Samples
	N/A	*Xray*
50336	5/6/03	Boeing NSLD FA Report 03-079, "SEM/EDS Analysis of STS-107 Debris Samples
	N/A	*Xray*
	5/13/03	Boeing HB Case Report 301974, "ESCA of STS-107 Debris Samples"
50338	4/18/03	Boeing NSLD FA Report 03-071, "SEM/EDS Analysis of STS-107 Debris Samples"
	N/A	*Xray*
57754	*N/A*	*Xray*

Table 9.3. Index of Laboratory Reports for Tile Sampling/Analysis

and 50336 had all been detached from underlying structure.

Deposits were found on the threaded internal surface of the ceramic insert in tile item 16692. The fused silica plug and lock cord were observed to be intact at the OML end of the insert. This indicated that the deposits were introduced from the IML side of the tile. The elemental composition of the deposits was essentially the same as that of the deposits found on the OML of the tile. The deposits may have occurred after the SIP had been partially eroded away or debonded.

Summary of Thermal Effects
- Tile slumping and surface deposits on the left lower LESS carrier panel tiles are consistent with flow occurring from inside the RCC cavity out through the upper and lower carrier panel locations in that vicinity
- The surface deposits on lower left hand carrier panel 9 tiles are consistent with a flow direction exiting from RCC panel 8.
- The thermal degradation of the internal tiles recovered from upper carrier panel 8 and lower carrier panel 9 suggests that the flow was in excess of 1649°C (3000°F)
- The composition of the tile surface



Figure 9.7. Tile Item 57754 bonded to section of carrier panel

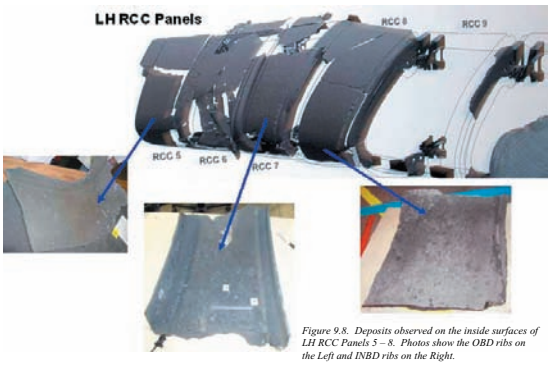


Figure 9.8. Deposits observed on the inside surfaces of LH RCC Panels 5 – 8. Photos show the OBD ribs on the Left and INBD ribs on the Right.

deposits suggests that the flow contained molten/vaporized materials from the LESS internal insulators, attachments, carrier panels, and/or wing spar.

EVALUATION OF DEPOSITS ON RCC PANELS

Visual Assessments of RCC Deposits

Deposits similar to those observed on the LESS carrier panel tiles were also observed on the inner surfaces of several LH RCC panels (Figure 9.8). The deposits resembled solidified metallic slag, and were strongly adhered to the internal surfaces of the panel segments. The quantity and thickness of the deposits also varied according to the RCC panel number.

The M&P Team noted marked differences in the appearance and quantity of deposits between the LH and RH RCC surfaces. Table 9.3 summarizes the visual surface condition observations for left wing RCC panel pieces, ribs and T-seals 1- 12.

Table 9.4 and Figure 9.8 show the relative severity of the left wing leading edge deposits approached a maximum at RCC Panel 8 and decreased on either side. Heavy deposits were also observed on the inner surfaces of the Outboard Ribs of Panels 4, 5, and 7, however very few deposits were observed on the inboard ribs of these panels.

Very few deposits were observed on RCC Panels past Panel 12, and there was more evidence of mechanical damage than thermal effects on the remaining panels outboard of Panel 12. Although the

quantity of deposits was considerably greater on the LH leading edge panels than the RH panel sections, Medium grade deposits were also observed on an upper panel portion and outboard rib section of RH RCC Panel 8.

Metallurgical Analysis of RCC Deposits

The relative differences observed between the amount of slag deposits on the LH and RH RCC panels prompted a metallurgical analysis. The analysis included the following: (A) review of the chemistry of high temperature reactions associated with the wing materials, (B) non-destructive radiography of the RCC panel surfaces, and (C) a metallurgical evaluation of samples removed from the RCC panels. Cross sections of deposits from LH and RH RCC panels were analyzed to identify and characterize their composition, composition gradients, and any layering effects on the inner surfaces.

The high level objectives of the analysis were the following:

- Can evidence of plasma flow direction and thermal damage be correlated withs lag deposition?
- Can the sequence of deposition be identified and correlated with relative altitude/time and temperature?
- Do slag deposits reveal information about the location of a breach in the wing leading edge?

Initial Phase I samples were analyzed to validate process flows within the labs and analytical techniques that would be used to meet the high level objectives. Later in the investigation, visual assessments made by the HFT and data from the MADS/OEX Recorder narrowed the analytical focus to LH RCC Panels 5 – 10, precipitating Phase II & III sampling and analysis of wing leading edge materials. Some RH RCC panel segments were also analyzed for comparison with LH RCC deposits. Details of each phase of RCC sampling and the analytical techniques used to characterize the samples are described in Appendix A.

RCC Panel	No. of Parts Assessed	Observations
1	3	Good Condition; No Deposits
2	5	Good Condition; No Deposits
3	5	Light Deposits – gray, red discolorations (2 of 5)
4	5	Light Deposits (3 of 5); Slag on IML of OBD rib on T-Seal facing 5
5	9	Light Deposits (4) ; Medium Deposits(1); Slag on IML of OBD rib on T-Seal facing 6
6	0 (Missing)	
7	3	Heavy (1); Very Heavy (1); Heavy slag on IML of OBD rib; No deposits on inner surface of INBD rib
8	**5**	**Medium (T-seal); Very Heavy (3); Heavy (1)**
9	3	Heavy (3)
10	3	Light – Heavy (1); Medium (3)
11	1	Light
12	1	No Deposits

Table 9.4. Left wing RCC panel deposits

(A) Chemistry of Reactions

Prior to the metallurgical analysis of debris samples from the RCC panel surfaces, experts from NASA-WSTF and Glenn Research Center (GRC) reviewed the chemistry of high temperature reactions associated with wing leading edge materials. Atmospheric conditions expected during reentry and during Orbiter breakup were reviewed, and high temperature reactions associated with the Aluminum spar material were discussed. Key points determined from the discussions were as follows:

- The atmosphere during peak heating was significantly less dense than sea level conditions but still contained elemental nitrogen and oxygen
- High temperature compounds may have formed from the reaction of aluminum spar materials in the upper atmosphere (GRC Report CT-050103-10).
- Aluminum oxide (Al_2O_3) was the most stable oxide formed
  - Other oxides (AlO, Al_2O, etc.) may form at high temperatures and lower partial pressures of oxygen
  - Upon lowering of the temperature, in presence of abundant oxygen, oxides immediately convert to Al_2O_3
  - Nitrides are only stable if the temperature is immediately quenched to less than 1200°C (2192°F) (not expected)

Based on the expected air reaction products with Al, it was hypothesized that Al_2O_3 was the primary oxide compound formed. Therefore, Al_2O_3 was chosen as one of the trend marker for the chemical analysis of debris, and the amount of Al_2O_3 formed would also depend on the time that Al metal was exposed to air at high temperature.

Identification of the compound Mullite (crystalline $2Al_2O_3+1SiO_2$) from preliminary x-ray diffraction of a sample containing Cerachrome prompted the M&P Team to study high temperature transformations. In laboratory experiments at GRC, Cerachrome formed Mullite at around 1100°C (2012°F) and Cristobalite at 1300°C (2372°F). With higher temperature, their amounts increased. Cerachrome melted between temperatures of 1800-1900°C (3272-3452°F). These results were summarized in GRC reports CT-051203-7C, -7D.

The identification of nickel-aluminides in preliminary x-ray diffraction experiments also prompted some studies of mixing effects between Ni and Al at high temperature. High purity Ni and Al pellets were exposed to temperatures from 1100-1500°C (2012-2732°F) in a vacuum furnace. Various forms of stable nickel-aluminides were formed (identified by x-ray diffraction) and summarized in GRC report CT-051203-6C, -6D. In the presence of air, despite molten aluminum, no nickel aluminides were formed until Ni melted. The formation of aluminum oxide appears to have prevented formation of the aluminides.

(B) Radiography of RCC Panels

The M&P Team collaborated with Langley Research Center for the use of real time radiography to assist in destructively sampling and evaluating RCC deposits. Large density differences between the deposits of LH and RH RCC panels were detected, and possible deposition patterns on the RCC panels were interpreted from the images. The initial radiographic images of calibration samples clearly identified locations, shapes, sizes, and distributions of deposits on the RCC panels having large density differences. Details of the measurement method and the images obtained were described in a NASALARC Report.

Key findings from the radiography of both calibration and RCC panel samples were:

- The inverse radiographic response of heavier materials compared well with that of an IN718 standard
- Darker areas in the inverse radiographic images compared with the Inconel standard
- Aluminum and Cerachrome gave a similar radiographic response despite their diverse material characteristics
- Four types of deposit patterns were identified from LH RCC Panel 8 (Fig. 9.9)
  - Uniform thickness
  - Spheroids
  - Tear-shaped
  - Globular-shaped
- Other RCC panels imaged had Uniform thickness deposits

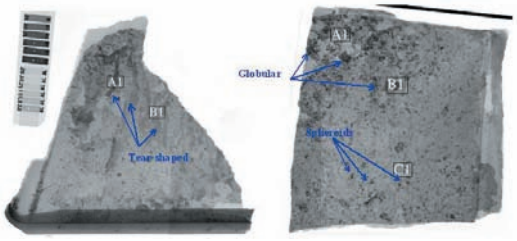


Figure 9.9. Types of deposition patterns observed on radiographic images of LH RCC Panel 8 pieces.

(C) Metallurgical Evaluation of RCC Deposits

Interpretation Criteria

Due to the presence of different materials in the wing leading edge, it was also expected that other high temperature reactions would take place resulting in formation of many other products. Therefore, prior to rigorous analysis, some criteria for the interpretation of results from chemical analyses of the deposits were established from preliminary microprobe analyses. Examples of those criteria are summarized below. They are all listed in report MSFC-ED33-2003-066.

1. Alloys containing high amounts of Ni and Fe such as A286, IN718, IN625, and IN601 could be identified and distinguished based on a Ni/Fe ratio and the presence of secondary elements such as Mo, Nb, Co, and Ti
2. Aluminum 2024 wing spar material could be identified from the presence of Cu with Al and Cu with Al_2O_3.
3. Cerachrome could be identified by the presence of Cr within a mixture of Al_2O_3 and SiO_2.
5. The presence of a pure metal, such as Iron that is surrounded by Al_2O_3 with no other elements nearby, is indicative of a thermite reaction
6. SiO_2 from tile may be identified by physical nature and the absence of other accompanying elements and compounds. However, SiO_2 may also form from the erosion and oxidation of SiC in RCC.

Guided by radiography, samples of deposits from LH RCC Panels 4-5, 7-9, and RH RCC Panel 8 were removed and analyzed using SEM/EDS, microprobe, and x-ray diffraction. A description of the techniques used for all phases of the analysis is provided in Appendix A, and the results are summarized in Reports: MSFC-ED33-2003: 067 - 098 and GRC reports CT-050903-4: C-D, and CT-060203-9: C-D.

Key findings from each metallurgical analysis were as follows:

LH RCC Panel 4:

1. Aluminum was detected in all layers of the deposits on the RCC Panels (Figure 9.10)

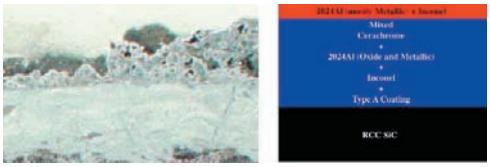


Figure 9.10. Cross-section of LH Panel 4 Lower Inboard (Item 80632)

2. Aluminum was not detected in the first deposited layer on the RCC Rib (Figure 9.11). This is unlike the observations of LH RCC panel 8 and is similar to LH RCC panels 5 & 7.

LH RCC Panel 5:

1. Aluminum was detected in all layers on the RCC Panels (similar to Panel 4)
2. Aluminum was detected in the first deposited layer, which is similar to LH RCC panels 4 & 7 but unlike LH RCC panel 8
3. Deposits on the RCC panels were uniform and thinner than those on LH RCC panel 8

LH RCC Panel 7:

1. Aluminum was detected in the first deposited layer, which is similar to LH RCC panels 4 & 5 but unlike LH RCC panel 8 (Figure 9.12)
2. Deposit thickness was thinner than that of LH RCC panel 8

LH RCC Panel 8:

1. Samples contained large amounts of molten Cerachrome mixed with metallic deposits of Inconel 718 and Inconel 601 (Figure 9.13)
   - Initially believed to be molten aluminum due to low density radiographic indications
   - Deposition temperatures exceeded 1760°C (3200°F), which is the melting point of Cerachrome)
2. Samples contained large spheroids of both Inconel 601 and 718
   - Consistent with melting of RCC

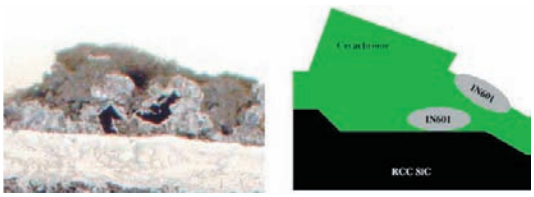


Figure 9.11. Cross-section of RCC Panel 4 Lower Inboard Rib (Item 80632)

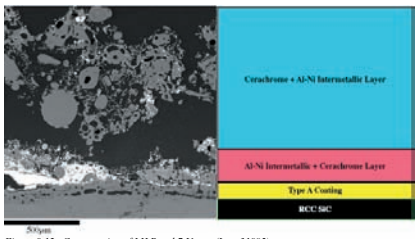


Figure 9.12. Cross-section of LH Panel 7 Upper (Item 31985)

spanner beam, insulator foils, and other RCC fitting materials

3. The first deposited layer contained both Cerachrome and Inconel but not aluminum
4. The final deposited layers contained heavy amounts of aluminum
   - Elemental composition was consistent with Al 2024 alloy
   - Aluminum was in either metallic or oxidized form
5. Deposits on the OML apex of Item 2200's fracture surface were molten Cerachrome with significant porosity, and some sodium and minor amounts of copper were observed
   - Indicates that the deposited Cerachrome was mixed in with Type

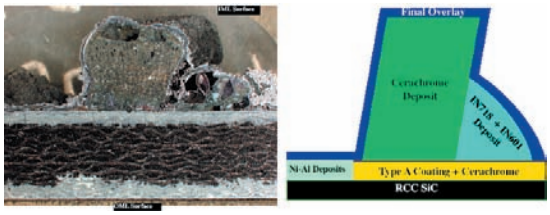


Figure 9.13. Cross-section of LH Panel 8 Upper (Item 43709)

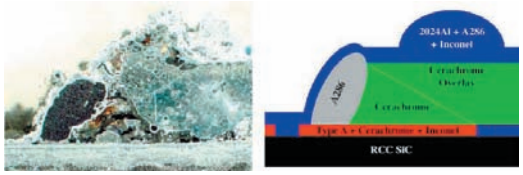


Figure 9.14. Cross section of LH Panel 8 Upper (Item 18477). The sample was removed near the inside of the panel's heel.

A coating and Al 2024 spar material
- No metallic components were detected, suggesting it either evaporated or flowed away with the plasma

6. A286 alloy was only detected in samples from Item 18477 at a location close to the spar fitting (Figure 9.14)
   - A286 was not detected in the first layers of the deposit
   - A286 was mixed with molten Cerachrome and coated with aluminum deposits
7. Heavy erosion was detected on Item 24724, LH RCC Panel 8 outboard heel rib, on the OML side (Figure 9.15)
   - The silicon carbide layer on the OML of the RCC was missing
   - Silicon carbide on the IML was partially missing in some locations
   - Where SiC remained on the IML, it was infiltrated by IN718 and then overlaid by aluminum.
   - The exposed carbon on the OML was also infiltrated by IN718 and overlaid by aluminum

LH RCC Panel 9:

Although very small pieces of RCC Panel 9 were identified, the deposits on LH RCC Panel 9 parts 7025, 29741, and

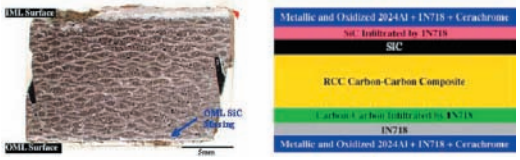


Figure 9.15. Cross section of Panel 8 Outboard Rib (Item 24724)

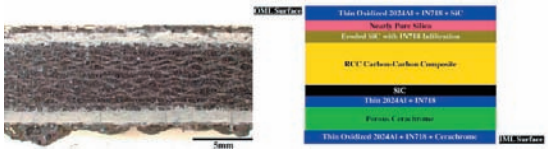


Figure 9.16. Cross section of Panel 9 Upper Rib (Item 7025)

38223 suggested the following:

1. Aluminum was detected in the first deposited layer
   - The amount of initially deposited aluminum was less than that of LH RCC 5, 7 and RH RCC 8
   - Elemental composition was consistent with Al 2024 alloy
2. Aluminum deposits on the outer layers of the samples were thinner and more oxidized than that of LH RCC 8 deposits
3. No erosion was detected on the IML of Items 29741 and 38223
   - Erosion only detected on the OML of Item 7025 (Panel 9 Inboard Rib) (Figure 9.16)
4. Smaller quantities of molten Cerachrome were detected in the deposits relative to LH RCC Panel 8
   - Cerachrome was porous and contained less amounts of aluminum
   - Outer layers had less amounts of aluminum as a top layer
5. Samples contained spheroids of A286, IN718, and IN625 alloys (Figures 9.17-9.18)
   - A286 alloy was not detected in the first layers
6. There were less deposits on the IML of the Outboard Rib (Item 29741) than that of the IML of RCC Panel 8 (Item 61143)

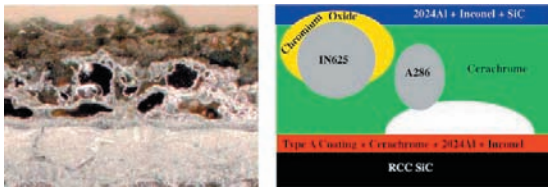


Figure 9.17. Cross section of Panel 9 Upper Outboard (Item 38223)

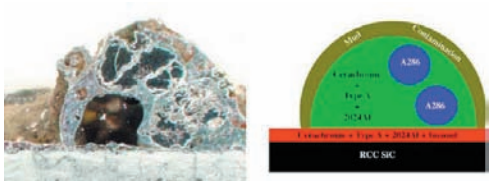


Figure 9.18. Cross section of Panel 9 Rib (Item 29741)

RH RCC Panel 8:

1. Samples from Item 16523 and 1419 contained mixtures of aluminum alloy, Inconel 718, and Cerachrome
   - Deposits were more uniform and thinner than LH RCC deposits; no concentrated regions of melting detected
   - Aluminum was found in all deposited layers.
   - Leading edge RCC surfaces contained very little deposits; fracture surfaces were not eroded

SUMMARY OF RCC ANALYSIS

- LH RCC Panel 8 surfaces contained larger quantities of IN718 and Cerachrome deposits when compared to other LH and RH RCC panels.
- A286 alloy, used mainly in the spar attachment fittings, was only detected on RCC Panel 8, upper, near the spar attach fitting location, while IN718, used in side spanner supports, was found in almost all samples.
- Most of the initial deposits on LH RCC panel 8 were composed of IN718, IN601, and Cerachrome.
- Metallic aluminum and aluminum oxide mixed with Cerachrome were detected in most of the first deposited layers of the other remaining RCC panels.
- The deposit analysis could not provide exact duration time but did shed some light on possible plasma flow directions.

SUMMARY AND CONCLUSIONS

Results obtained from the materials analyses of Columbia debris were consistent with the visual assessments and interpretations presented by the Reconstruction Team. Analytical data collected by the M&P Team showed that a significant thermal event occurred at the left wing leading edge in the proximity of LH RCC Panels 8-9, and a correlation was formed between the deposits and overheating in these areas to the wing leading edge components. Additionally, the finding of molten Cerachrome deposits showed that temperatures in excess of 1649°C (3200°F) were present which could severely slump and erode support structure, tiles, and lead to eroded RCC panel materials.

Analysis of lower and upper carrier panel tiles showed leading edge material-containing deposits on the outside surfaces, suggesting flow of plasma from the inside of the RCC panel to the outside.

Referring to Figure 9.19 and data collected from the analysis of both carrier panel tiles and RCC materials, several conclusions can be made regarding the observed thermal effects:

- The composition of deposits near LH Panels 8-9 and the deposition patterns revealed from radiography suggested that flow occurred from inside the RCC cavity out through the upper and lower

carrier panel locations.

- The presence of Inconel 601 and 718 deposits as first layers on the surface of LH Panel 8 suggested that plasma entered through a breach on the lower side of the panel.
- Initial materials possibly exposed to the plasma were the insulators (Inconel 601, Cerachrome), spanner beams (Inconel 718); the A286 fittings were not exposed
- Evidence of plasma flow and deposits near the carrier panel tile vents were consistent with the deposits observed on the upper tile surfaces
- Evidence of molten Cerachrome within the RCC deposits suggested that temperatures were in excess of 1649°C (3000°F) that melted all leading edge materials except RCC
- Melting of the wing spar section was a secondary event due to the lack of aluminum detected at the RCC surface and protection of the spar by insulator materials

The integrated failure analysis of wing leading edge debris and deposits strongly supported the hypothesis of a breach that occurred at LH RCC Panel 8, however there was insufficient evidence to preclude additional damage near the T-Seal 8 or RCC Panel 9.

Due to the absence of wing leading edge debris adjacent to LH RCC Panels 8-9, the duration of exposure and direction of plasma flow could not be determined. Additionally, sufficient material evidence near LH RCC Panels 8-9 was not available to correlate the configuration and geometry of the breach to the observed thermal effects.

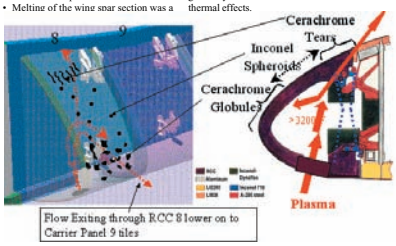


Figure 9.19. Schematic of deposition patterns analyzed near LH RCC Panels 8-9

CRITICAL SUCCESS FACTORS

Organization and Communication

...Build a well-defined, co-located, and focused team...

The success of the reconstruction effort was attributable to a well defined, co-located, and focused team of knowledgeable people with a common mission. The team, with no regards to company affiliations, was willing to cross functional lines and overcome any obstacle encountered. This cohesive attitude, along with the persistence to prevail even when facing an overwhelming task under unpleasant circumstances, allowed this initiative to exceed expectations.

This broad and diverse team of experts gathered from essentially every NASA Center and Shuttle prime contractor. In addition, resident experts assigned by the CAIB and NTSB were co-located at the Columbia hangar. As a direct result of this resident support, the reconstruction team was able to address the needs of all the various investigative bodies directly.

...Write flexible contingency plans...

Initially, the organization of the recovery and reconstruction effort was based upon KSC's salvage plan. The good intentions of this approach cannot be overlooked and adaptation of these plans to the specifics of the situation is the key to success. Using plans in contingency situations as guidelines and not as specific situational mapping and implementation tools is appropriate.

...Clearly define and empower the chain of command...

By necessity, NASA is a very process oriented organization in order to accomplish the complex mission of human space flight. This procedural hierarchy actually hindered the investigation in some instances. A prime example encountered during the early phases of debris receiving was when on-site personnel made a recommendation regarding whether it was acceptable to wash mud off of the debris or disassemble a part to aid in identification. There were multiple management forums that had to render a decision before work could proceed. This slowed the pace of debris processing. More autonomy and approval authority should be given to the on-site team, which was specifically staffed with appropriate expertise to make these types of on site decisions.

The reconstruction team reported to both the MIT Chair and the OVEWG Chair. Both recognized the need for the preservation of evidence and both took leadership roles in reconstruction. However, the relationship between these two entities was not well defined. The impact of this to the Reconstruction Team was conflicting requirements and priorities. It remained unclear to some as to who was ultimately in charge of the reconstruction activity at the Program level. Therefore, the role of reconstruction engineering and their chain of command remained fuzzy for the duration of the effort.

There was also strain induced in the M&P PRT due to multiple and often times conflicting priorities levied on the team by differing CAIB teams, OVEWG, and the HFT. Requests for sampling and failure analysis should go through one individual to prioritize multiple or conflicting requests for analysis and information.

...Promote trust and a free flow of information...

There is a lesson to learn in the evolution of the team from independent elements to a synergistic unit. The initial charge to the CAIB was for an independent investigation. However, a teaming approach from the start would have been more effective. Though the reconstruction participants eventually melded into a team, early on in the investigation the information flow to and from CAIB was very slow. The duality of the investigation by the CAIB and NASA during the first few weeks caused some tension and competition for resources.

There appeared to be a fear of giving raw data to on-site CAIB personnel before

NASA had a chance to review and validate it. Part of the reservations exhibited by the NASA team was due to the legitimate fear that the data would be released prematurely or misinterpreted by the CAIB. Communications improved when the CAIB personnel were permitted to share any factual reports with NASA. Once the teams began two-way sharing of data and analyses, real investigation and technical exchange of ideas could occur.

The ability of the Reconstruction Team Chair to communicate directly with the CAIB Chair for certain issues and the ability to work particularly sensitive issues outside the normal, public forums was valuable. These specific issues were associated with flight crew, security, and those of a time critical nature.

...Create a "badge less" environment...

The Reconstruction Team had many unique characteristics that distinguished it from a classic organization, but the single most significant trait was its "badge less" operation. While there was a team structure, the corporate or governmental affiliation of its members and leaders was largely inconsequential. This altruistic attitude, along with a common purpose, contributed more to team success than anything else. It was apparent which teams adopted this attitude and those whose members looked to the organizational charts or contractual hierarchy. The experience of the Reconstruction Team bears out a lesson that has been timelessly learned and taught in every class on successful management: The best teams are those with a truly common purpose and membership dedicated to that purpose and no other.

Facilities and Infrastructure

...Select a site with broad and available infrastructure...

The decision to reconstruct the Orbiter at KSC was the correct one. As a reconstruction site, KSC was ideal because the other Orbiters were within close proximity, the hangar space was available, and technicians and engineers that worked with the hardware during day-to-day processing were available to provide their expertise.

The KSC engineering team was able to provide technical expertise while examining the recovered vehicle hardware. The technical experts in particular systems efficiently identified and performed assessments on the debris, as well as educated the multiple investigation team members on the fundamentals of their systems.

Having the other Orbiters in close proximity to the reconstruction site allowed for first hand comparisons of the debris with the flight vehicles. This aided in the overall debris identification process.

One of the other benefits of KSC reconstruction was the availability of the KSC infrastructure. KSC is home to three world-class material science laboratories that were available to perform the majority of the forensic analysis of the debris. The availability of KSC's prototype lab and resident carpentry shop filled an unexpected need for the construction of jigs, fixtures, and enclosures for the debris. KSC was also able to provide other resources used during vehicle processing; namely Safety, Environmental Health, security services, photographic support, heavy equipment, office space, and Information Technology (IT) support.

...Overestimate information technology requirements...

IT support in particular was critical to communications among and between investigative entities. Both NASA and USA were able to make their service contractors and network infrastructure available to support the investigation.

Satisfying the IT requirements necessary for the reconstruction effort proved to be more difficult than originally anticipated, as computers were extensively used in all areas of the effort. The entire process of tracking, identification, assessment, and analysis

of debris was performed and documented electronically. Based on the multitude of tasks being performed electronically, and the volume of data being developed and exchanged, it quickly became apparent that the initial set of requirements would not be sufficient. Upgraded computer systems and increased network bandwidth resolved the issues. Computer resources were essentially tripled to support the investigation.

With a team as broad and diverse as the Reconstruction Team, the IT team faced challenges associated with connecting users from various contractors, agencies, and geographic locations, while maintaining security. In order to overcome this issue, trust agreements were negotiated between centers to allow users to access any computer regardless of their domain. However, one integrated network for information exchange that all teams, and sub-teams could access would have eased communications.

The size of the Columbia hangar (50,000 square feet) limited the mobility of engineers, technicians, and handlers working to identify and locate debris via networked desktop computers. To optimize productivity, the IT team implemented a wireless network with wireless laptop computers. Even though it took many weeks to get the wireless network approved and implemented, it was an extremely effective tool. It provided hangar personnel the mobility to move about the grid while performing their assessments with all the available identification resources at their fingertips.

Tools and Techniques

...Provide high-fidelity identification tools in a timely manner...

Reference material to aid in debris identification was essential to successful reconstruction. The dependency on these reference tools was apparent when the initial effort to identify flight crew equipment debris was delayed by the unavailability of a quality library of digital photos. Bench review and other photos tended to show items all together in their packed and stowed configuration, as opposed to individual photos of equipment. Eventually a library of CDs and hard copy drawings of these items was built up, but in many cases no photos existed at all. The effort to identify orbiter structure was much easier because the SDS and KSC closeout photos were readily available.

Initially, the payload reconstruction team did not have access to the available payload photos and drawings. While payload developers provided extensive information to the Program Payload Integration Office within days of the accident, that information was not transferred to the reconstruction team until a month and a half later. The lack of this information delayed the identification and assessment of the debris.

...Create a powerful yet flexible database...

The CRDS was an immensely powerful and useful tool to organize and track items throughout the reconstruction process. The programmers are commended for such a rapid and successful deployment. The CRDS was routinely enhanced to meet changing requirements. The ability to see the photos and reports associated with a piece of debris and the ability to search and export results was very helpful.

The CRDS Team was very receptive to the user's needs by continually addressing issues and by adding new functionality to the system. Enhancements were made throughout the entire life of the reconstruction project, and were normally incorporated within a day or two of the request. The team stayed in constant communications with the user community to ensure any issues that arose were addressed as quickly as possible. The team also consistently supported the user community by providing custom reports for data not readily available from the standard query reports provided via the web page.

However, as helpful as the database was, it was only as good as the data being entered into it. A standard vocabulary list and structured description fields could have been created and applied to every debris item. These key words and descriptions would have aided in database searches. In addition, the initial field identifications were only valuable until a more exact identification could be made. Once made, the initial field identification should have been overwritten with the correct assessment.

...Consider innovative technologies...

The potential of 3-D scanning was demonstrated in the scope of the virtual 3D reconstruction product. This pathfinder project demonstrated the concept of virtually reconstructing large sections of a vehicle without requiring a large amount of floor space to do it. The team was able to successfully visualize in 3D most of the left wing, left WLE panels 1 through 22, several pieces of the left mid-fuselage sidewall, the left OMS pod leading edge and the vertical stabilizer leading edge. Virtual reconstruction was also able to identify six significant debris items: The "Littlefield Tile" and five RCC pieces. Another feature was the ability to reproduce a scanned item in a plastic form. Virtual reconstruction was successful in all of these regards, though its practical application to this investigation was limited.

Texture mapping proved to be very labor intensive. The workload depended heavily on the complexity of the surface shapes of the debris item. Familiarity with the tasks greatly affected the production rate. An outside company had to be hired to produce the majority of the texture-mapped files due to the backlog of work and the available schedule.

Two-way data transfer was a significant obstacle to completing virtual reconstruction due to large file sizes and network bandwidth limitations. Most file transfers were accomplished by hand carried or shipped CD ROM. These files had to be transferred back to KSC for implementation in the visualization applications then stored for back-up and archiving purposes. Eventually the facility network capabilities were enhanced and electronic transfer became possible between two different on-site facilities at KSC only. However, secure cross-country data transfer of large data files from KSC was never consistently accomplished during reconstruction.

The Reconstruction Team recognizes the two tremendous potentials for 3-D scanning. The first potential is reverse engineering to identify parts. The second one gives people who cannot travel to see the items in person the ability to visualize debris (in either individual items or in a reconstructed section). The 3-D scanning effort realized the first potential to some extent and the second one late in the investigation. If 3-D scanning can be made cost effective and quickly provide those two things, then the true potential can be realized.

...Let the debris tell its story...

Immediately following the accident, it appeared that the investigation would have to depend solely on analytical methods and most probable scenarios. The assumption was that a significant amount of debris would not be recovered. This initial assumption was due to the altitude of the breakup, reentry heating, and the magnitude of the debris field. However, after one of the most extensive ground searches in history, 38 percent of the orbiter was recovered. In fact, many critical pieces were recovered, identified, and became compelling evidence. Facts began to emerge from the debris regarding the initiation point, damage progression, and severity. This evidence was used to refute or confirm scenarios developed by other branches of the investigation. In the end, the reconstructed debris provided tangible evidence about the initial breach to the orbiter, and proved to be a significant factor in understanding the failure.

...Address the medium for technical information exchange...

As hardware began to arrive at KSC and identification was underway, a process was developed to assess debris items and provide some level of documentation (fact sheet) on their condition. Fact sheets are a fairly standard tool in aircraft accident investigations and are normally just quick notes and sketches of individual items. Investigators use the fact sheets as the basis for their final reports. However, for this accident, fact sheets very quickly mushroomed into an unmanageable task when the Technical Integration Team/OVEWG required briefings and top quality, exacting reports complete with color photos on every item that was of interest. This left no time for individual evaluation of the mass majority of items. As a result the investigation began to outpace the team's ability to prepare fact sheets. The technique was therefore suspended in lieu of broader sub-system or zonal reports. The final report had to be generated without the benefit of a large number of fact sheets as back-up material. Fact sheets would have continued to serve their purpose if an appropriate statusing tool was made available to facilitate technical information exchange among teams.

...Develop survivable part marking...

Most of the system components on the orbiter were identified per drawing with decals, metal tags, or ink stamped over coated surfaces. This made identification very difficult unless the appropriate area on the item was shielded from aerodynamic and thermal effects. Items that had etched part numbers usually required only minimal cleaning to raise the number and were therefore much easier to identify. With respect to TPS, today's convention is to print part numbers on the OML only. Most tile part numbers on the OML were ablated and unreadable. However, many recovered Columbia tiles were identified by the stamped part numbers on the IML; a technique used in the past for array SIP bonds. This duplicate part marking of tile was useful in the identification process.

Search and Recovery Coordination

...Foster communication between recovery and reconstruction...

Communications between the recovery and reconstruction teams was imperative to operations. Initially, during the planning phase of reconstruction as processes were being established, the recovery team provided insight into the condition and hazard level of debris to be shipped to KSC. The day-to-day operations of the two efforts required a constant exchange of information concerning truck delivery schedules, hazardous debris handling, sensitive shipments, fast track items, and equipment exchanges.

During the continuing debris collection effort, a search coordination function was established to serve as a liaison between the two teams. This function was the conduit for sharing debris identification data with the field recovery teams in an effort to direct search patterns for critical debris. The search coordinators actually rotated assignments between recovery and reconstruction for continuity throughout the process. By coupling the engineering expertise at KSC with the search recovery forces that established air and ground search priorities, emphasis could be placed on recovering much more critical left wing debris and recording devices. It was through these efforts that the OEX recorder was found.

The communication exchange had to continue for the extended collection effort even after the main thrust of recovery was completed. Communications on the transition of authority and coordination of continuing small shipments had to be established.

...Prioritize recovered debris carefully...

The process of labeling items in the field as "Fast Track" to increase their priority and speed their identification because of their suspected criticality was useful in

assisting grid search priorities. However, it was only useful when it was used for a limited number of items. Fast track was to be an exception process. It lost its significance when the majority of parts received were labeled as such, therefore overwhelming the identification pipeline. The recovery forces must have clear guidelines on what to identify as fast track.

Other factors contributed to the success and limitations of the fast track process. Changes in the process were not always communicated immediately between the collection sites, Barksdale, and KSC. Notification of process evolution or changes must be provided to all teams so that a consistent process with consistent tags. Physically attaching visual identifiers to the debris, and then packing all items together on the delivery trucks worked well. Ensure individual items are labeled "Fast Track" in lieu of just labeling the box containing multiple items. As items within these boxes were removed for processing, they were separated and lost their fast track designation.

...Standardize data entry forms for field items...

Accuracy of data entry is the key to database success and is important at all levels of the process, from the initial formation of the record in the field through engineering assessments and storage at the reconstruction site. Consistent data format, particularly GPS coordinates, is vital to a search and recovery effort.

Field recovery teams adopted a variety of formats when entering GPS location data for each recovered piece of debris. This inconsistency was the source of data entry errors as the information was transferred to the EPA and CRDS databases. The actual field data proved to be the best method to resolve latitude/longitude miscompares between in the EPA/Weston database and the CRDS. The further removed the data was from the point of origin the more suspect it became. Field data must always remain with the item or should be properly placed in a library.

The other source of data discrepancy was in the EPA number. CRDS provided a link to the SIDDS via the EPA Field ID number. Due to inconsistent formats and typos of the EPA Field ID, this link was often broken. If the link was broken, CRDS did not have access to critical latitude/longitude information needed for the investigation. CRDS was modified to aid data entry personnel by providing a drop down list of valid EPA Field ID numbers. Although this helped, it did not completely alleviate the problem. There were still multiple items with the same EPA Field ID number and the data entry personnel had to make a 'best effort' choice on which one to select. In some cases, items found outside of Texas did not have an EPA Field ID so the link between CRDS and SIDDS did not exist.

...Consider science recovery from the start...

The initial focus, plans, and implementation of the investigation were geared towards Columbia debris recovery and reconstruction. Though STS-107 was a science mission, there were no initial plans or consideration given to implement the return of payload debris to payload investigators for the purpose of science recovery. Although researchers eventually were given access to their science, recognition and a higher priority for the possibility of science recovery may have yielded faster results and possibly even more science recovery opportunities.

Early on, the SSP Payload Integration Office attempted to insulate the reconstruction effort from an onslaught of payload developers to avoid impeding investigation progress. In the end, payload developers that did participate in the reconstruction proved effective in identifying payload components and science recovery. In hindsight, earlier controlled and locally managed developer access to the debris would have expedited payload identification and science recovery.

Because of biological material presence, several science items were held at JSC for up to two months without identification or tracking, and therefore their recovery remained unknown. Once these items were shipped from JSC to KSC, they were immediately identified, and in the case of Biological Research in Canisters (BRIC), some science was recovered.

In addition to delays due to traceability issues, the debris release process delayed possible science recovery. The TAR process and approval loop was laborious and not geared to expedite the rapid return of payload debris to the payload developer. To overcome this delay, a generic TAR was proposed, drafted, and initiated to accommodate the return and science recovery for payloads.

Supporting Processes

...Emphasize security controls...

The entire security process was well organized. The Action Center worked well for badging, especially requiring another photo identification to be exchanged for the temporary hangar badge. Personnel manning the guard gate did a good job of controlling hangar access and of checking for cameras and other items entering the hangar. They also did a good job looking for items leaving the hangar. Finally, the access control monitor process for logging visitors in and out of the hangar and ensuring no debris was removed without proper paperwork worked well.

...Generate a realistic safety plan...

One safety issue that was never adequately resolved was the monitoring of personnel and air within the hangar for hazardous particulates generated from the collection and handling of debris. Safety and Health representatives imposed requirements for daily personnel and area air monitoring of operations inside the Columbia hangar. The original plan was designed around the potential for worst-case friable materials and by-products because of the unknown condition of the debris arriving from the field collection sites.

The Reconstruction Team established an air-monitoring program to gain baseline data on air quality in the hangar. Once some baseline monitoring was performed and the results of the samples showed that particulate counts remained at ambient levels, the Reconstruction Team requested that the Safety and Health organization revisit the plan to see if some of the more stringent requirements for personnel monitoring could be lifted.

Although a revised sampling plan was eventually put in place, there was a great deal of debate within the Safety and Health organization with no clear ruling authority among parties involved to make the appropriate revisions. There remained some confusion over the requirements and the team never did come to consensus on the plan. It is recommended that any future Safety Plan that is geared to address the worst-case scenario also have provisions to allow for modification of the requirements to fit the needs of the operations when warranted.

Debris Handling and Management

...Plan, execute, and adapt the process flow...

The process flow of debris through the hangar was excellent. From unloading off the truck, safety checks, logging in and photographing the debris, assessing the debris, and finally placing it on the grid, the process worked extremely well. The process was robust enough to handle over 83,900 pieces during the three months of debris collection.

Identification of the debris was a meticulous, often tedious and time-consuming process. Material handlers and technicians were brought into the identification process

to help reduce the engineering workload. With their specific hands-on vehicle experience, they proved very effective at providing initial assessments and placement of debris.

Other methods used to adapt to the increasing backlog of items in engineering assessment included splitting the process flow so that the identification area was duplicated on the west side of the hangar and all non-airframe debris was routed to the west identification area. This cleared the way for priority processing of airframe and TPS debris.

Based on requirements for safe handling of MMVF, several encapsulation techniques were proposed and tested early in the debris receiving effort. During the course of this testing, protective sealants were sprayed on some recovered debris. This approach was quickly altered to not compromise evidence. This encapsulation technique had the potential for contaminating the surface of debris that would need to be analyzed for chemical composition later in the investigation. The primary and most effective means of encapsulating friable items was by wrapping them in plastic wrap.

General debris cleaning guidelines and guidelines for the handling of friable material should be established in GO0014 – Space Shuttle Salvage Operation Plan. Perhaps the cleaning policy that was finally adopted for the Columbia reconstruction can be made the standard. This would reduce the excessive time required to get approval for cleaning procedures.

...Keep photographs to a minimum, but take the right photographs...

To keep from accumulating a large volume of extraneous photographs, the NTSB cautioned the Reconstruction Team to minimize the number of photographs taken. However, many photos were missing scales/rulers and a significant percentage of the time only one side of the object was photographed. To be more useful items, should be photographed in perspective view, out of bags, with registration marks, preferably in an area with proper lighting, and background. Furthermore, at a minimum, both top and bottom views of a part should be photographed as well as other unique features.

...Adopt a flexible approach to fit the phases of reconstruction...

The approach adopted for Columbia reconstruction called for a 2-D grid of the OML of the vehicle. This approach allowed engineers to view the debris close-up, and made the debris accessible for sampling and forensic analysis. The 2-D grid approach was extremely successful and appropriate up to the point where determining the orientation of the many pieces of debris on the grid became difficult for investigators, especially in the leading edge area of the wings. Therefore, the LH and RH wing grids were modified to highlight the leading edge components. Eventually, critical sections of the LH wing were reconstructed in 3-D using uniquely designed fixtures. The RH wing was reconstructed in 3-D on the floor without the use of fixtures. While not as glamorous, this technique was also useful as a visualization aid, though it hindered viewing the backside of the assembled debris.

The use of 3-D fixtures to integrate debris of the left wing leading edge subsystem in a see-through lexan cover was an excellent idea that quickly led to an improved forensic understanding of the debris evidence. In addition, the development of tables to elevate, and accurately place recovered left wing tiles aided in the evaluation of plasma flow and associated damage to tiles, also enhancing the forensic analysis of the debris. The approach to adapt the reconstruction techniques to accommodate the shape, size, and characteristics of the debris allowed the team to extract the greatest amount of information from the recovered debris.

As population of the grid increased, it became more difficult for some to visualize the debris in its 2-D layout. At this point, members of the CAIB proposed major

alterations to the grid. Keeping to the approach to evolve the grid slowly as we gained a better understanding of the debris and not make midstream wholesale changes to the layout saved time, energy, money, and shortened the time required to identify a likely failure mode and cause.

The originally selected 2-D layout was not without its limitations however. First, due to the limits on space, the wing lower surfaces were not placed contiguous with the mating mid-body and aft fuselages. Secondly, the mid-body sidewalls were positioned adjacent to the mid-body lower surface, which further complicated the reconstruction effort. Additionally, this placed the left hand wing at the complete opposite side of the hangar from the right wing, thereby eliminating any potential for easy comparison between the two. It would have been easier to place right wing RCC parts if the right wing and left wing RCC parts were in closer proximity to the unidentified RCC parts racks and RCC identification area. However, several subsequent evaluations of the grid layout failed to produce a better design that could eliminate all the deficiencies without creating other problems.

...Streamline the paper process...

No paper process is without flaws or limitations. The Columbia investigation and the reconstruction effort in particular generated large volumes of paperwork to assure proper tracking and investigation integrity. The reconstruction documentation process was established with the best intentions, but did not result in as streamlined a process as planned or desired. The process turned out to be burdensome, requiring unique procedures (RDS) for the analysis of each component. Each RDS required multiple reviews and signatures before implementation. Generically grouped procedures, or "Bucket RDS's", could have been used for non-destructive, generic failure analyses.

The overarching investigation documentation process - involving Test Approval Requests (TAR) and Hardware Release Requests (HRR) - was usually the cause for delays in accomplishing tasks that had some urgency. Delays of several days were not uncommon throughout the investigation. The Reconstruction Team acknowledges the responsibility of the CAIB to oversee the reconstruction and suggests that more local authority by CAIB resident members would have greatly increased the speed of many test and analysis efforts.

...Develop a standard for handling crew sensitive debris...

The overall handling and management of crew module related debris and items of personnel or sensitive nature was exceptional and accommodated the appropriate level of discretion to protect the interests of NASA and the families. At the outset of the reconstruction, the team developed guidelines for dealing with crew module related debris and items of a personal or sensitive nature. The team used its best judgment in establishing the processes and protocols in the absence of prescribed standards. The team's recommendation is to craft a NASA standard for future investigations dealing with legal status and handling of crew personal effects, handling of sensitive items like crew helmets, physical access to the crew module related debris, and accessibility of data records and photographs. Discussed below are some of the issues encountered during the effort.

It was decided early on that the crew module debris would be reconstructed separate from the rest of the Orbiter behind closed doors and by a select group of people. Most of the investigators examining the general Orbiter structure were not allowed access to the crew module area and those working on the crew module did not spend much time working with the rest of the vehicle. Understandably, there were some sensitivity issues that had to be taken into consideration when dealing with the human aspect of

space flight, but it was very difficult to determine failure scenarios when only looking at a fraction of the debris for the forward section of the vehicle. Strictly from an investigative perspective, it was burdensome having the interior crew module structure segregated from the rest of the structure and only observable to a select few.

Initially, the CAIB and MRT/NAIT provided little direction concerning the level of investigation to be performed on the crew module. Much later in the overall investigation, NASA chartered an official crew module investigation without disclosing the initiative to Reconstruction Team management. Up until this point, the Reconstruction Team had begun a "grass roots" investigation, adopting the processes, knowledge, and techniques of the broader reconstruction effort. An earlier understanding of the crew module reconstruction initiative could have facilitated the investigation.

A critical issue to the crew module team became the wide access to the database enjoyed by NASA employees and contractors. This access was useful because it enhanced the identification and investigation process, but it also created the potential for inappropriate levels of information to be available to people without a need to know.

In order to address this concern, there were a few database features provided. First, a secure text field called "Crew Module Description" was provided. Also, all pictures of items inside the crew module were put into a secure bin called "Crew Module Photos". Approximately 30 people, including the crew module team and the crew module investigation team, were allowed access to both the text field and the photos. Although this did limit the ability of engineers at JSC to evaluate hardware from a distance, the benefits far outweighed the disadvantages. There were always a few people with access at JSC who could access the pictures if needed, and pictures were emailed when needed for identification. Personal items photographs were not entered into the database at all; they were stored on a secure JSC server.

APPENDIX A

Definitions

Ablation – Melting of material due to heat and airflow generated by atmospheric friction during re-entry.

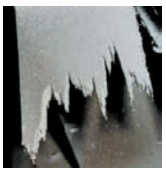
Backside Heating - Separation of tile from structure that occurs at the primer interface due to internal vehicle heating. Item 57481 shown



Backside Heating

Ballistic Coefficient - Ratio of mass to surface area that governs the re-entry trajectory, velocity and heating of an object.

Broomstraw - Type of aluminum alloy fracture due to a high temperature failure of the material where there is incipient melting along the grain boundaries. At high temperatures very little applied stress is needed to fracture the material. Item 105 shown.



Broomstraw

Erosion - Gradual loss of material by aerodynamic abrasion.

Friable - Material that can be easily broken down into small particles or powder.

Glassification - Melting of the base silica material of a tile forming glass when subjected to temperatures over 3000 degrees Fahrenheit. The RCG must be damaged or missing for this to occure.



Glassification

Ground Impact Damage – 1. Damaged surface of tile where the exposed silica is soft and has no glassification, normally associated with ground impact.
2. Deformation of non-TPS components associated with ground impact.

Inner Mold Line – 1. The bottom surface of TPS that is bonded to the structure.
2. Internal structural surface that comprises the outer shell of the vehicle.

In-Plane TPS Fracture - Tile fracture



In-Plane TPS Fracture



Overload Fracture



Primer-to-Primer Failure



Sawtooth Fracture



Slumping

occurring about 0.10 inches above the IML just above the densified portion of the tile. Also known as densification layer failure.

Liquification - Melting and separation of RCG from the tile base material that pools onto the OML .
(See glassification image item 33590)

Outer Mold Line –
1. The TPS outer surface exposed to the airflow
2. The structure surface in which TPS is bonded.
3. Structure with TPS bonded which makes up the outer shell of the vehicle.

Overload Fracture - Failure when the applied stress exceeds the material allowable, typically in ductile materials, with a fracture face on a 45-degree shear plane and associated with crisp (unablated) fracture surfaces, tearing of machined stringers, or skin fracture along fastener rows. Item 2436 shown.

Primer-to-Primer Failure - Separation between two coats of epoxy primer, normally associated with back side heating. Item 283 shown.

Sawtooth Fracture – Fracture characterized by a saw blade appearance. May or may not be associated with a fastener row. Item 52981 shown.

Slag - Deposits of molten material present on the debris

Slumping - Melting of the RCG coating combined with substrate collapse when the tile is subjected to temperatures above 3100 degrees fahrenheit. Item 76761 shown.

APPENDIX B

RCC Sampling

PHASE I SAMPLING

Phase I sampling involved the extraction of only Type I samples to preserve critical hardware and establish trend markers through various analytical techniques. This activity served as a benchmark for identifying techniques that could be used to obtain meaningful results for future sampling and analysis.

A total of 8 RCC pieces were sampled and 53 samples were taken. They are summarized in Table I.

Analytical Techniques – Phase I

The analysis techniques and the information it would provide are summarized below. Alternative techniques where feasible are also identified.

1. Optical photography of top and bottom surfaces of the sample. Purpose of this technique was to document unique features of the sample.
2. Scanning Electron Microscopy/Energy Dispersive Spectroscopy (SEM/EDS) of top and bottom surface of deposit. Initial elemental analysis on top and bottom surface may suggest layering through thickness based on the differences in the analysis. This technique uses electrons for imaging and resultant x-rays for chemical analysis. The beam penetrates to shallow depths on the surface. It is well known that an EDS spectrum is sensitive to many external parameters and quantitative reproducibility is not the greatest asset. The method is more efficient in identifying the elements present and their ranges of composition in categories of "major", "minor", and "trace". However, quantification of the spectra was the
3. only way of representing and effectively communicating the data to a larger audience. It was accepted that the Analysis results in only semi-quantitative elemental composition of the area analyzed.
4. Electron Spectroscopy for Chemical Analysis (ESCA) or X-ray Photo-electron spectroscopy (XPS). The purpose of this technique is to identify compounds on the surface. This technique essentially establishes the shift in elemental binding energy. Upon

Item #	RDS #	Sample ID	Part	Current Location
2200	2200-3	A1-A3, B1,B2,D1	RCC	Left Panel 8 Upper
18477	18477-1	A1-A3, B1, C1, C2, D1, E1-E4	RCC	Left Panel 8
1419	1419-1	A1-A4	RCC	Right Panel 8
16523	16523-1	A1-A4	RCC	Right Panel 8
24732	24732-1	A1-A5	RCC	Left Panel 5
853	853-1	A1,A2,B1,C1,D1-D3, E1-E3, F1	Fitting	Left Upper Spar Attach Fitting Panel 3
24543	24543-1	A1-A5	LESS Carrier Panel	Lower Left #2
24086	24086-1	A1-A4	LESS Carrier Panel	Lower Left #1

Appendix B Table 1 - Phase I Sampling Matrix

comparing this shift with known compounds, compound identification can be made. In this technique the beam only penetrates the first few layers of atoms on the surface. It is not a through-thickness technique. An alternative technique is powder X-ray diffraction where crystalline compounds can be identified directly. Moreover, XRD is a bulk technique that is destructive to the sample.

4. Fourier Transformation Infra-red (FTIR) Spectroscopy was identified as a technique for analysis of organic deposits. This technique was not required in any analysis.
5. Destructive cross sectioning combined with SEM/EDS dot maps can help identify layering of compounds through thickness. However, this technique is also subject to the limitations of SEM/EDS. It was known that microprobe analysis provides more accurate local compositions and could be effectively used in combination with SEM/EDS to determine distribution of material in the cross-section. The limitations of microprobe analysis are that it requires a polished sample, the analysis is more accurate at higher magnifications, and is not the best tool for imaging. None of the local labs had an operational microprobe. Therefore, as the analysis approached this step, a decision was made to send it to another NASA lab that had the right facility.
5. Another destructive technique was the bulk chemical analysis of samples. All other techniques listed above are surface analysis techniques. This technique was considered as a last technique because in its destructive nature, it consumed the sample. A significant limitation of this technique for the application is that the slag deposit could not be standardized. It was also important prior to using these techniques to find out what elements and compounds are present by above analysis. Thus, this technique was the last resort.

Phase I Results

1. SEM/EDS analysis of metallic slag provided information on the types of elements present, including oxygen. Their semi-quantitative analysis suggested the levels of each element present. It was immediately clear that there were differences between the top and bottom surfaces of the slag suggesting cross-sections to obtain through-thickness information. It was also clear that the elements identified in the slag were consistent with the elements present in leading edge materials. However, due to limitations of the information this technique provides, it was recommended not to carry forward in Phase II analysis. KSC reports that summarize Phase I results are KSC-MSL-2003-0137, KSC-MSL-2003-0143, KSC-MSL-2003-0144, KSC-MSL-2003-0145, KSC-MSL-2003-0148, KSC-MSL-2003-0149, KSC-MSL-2003-0150, KSC-MSL-2003-0167.
2. ESCA analysis suggested the presence of compounds. In addition to metallic elements, compounds identified were oxides such as Al_2O_3, Fe_2O_3, Cr_2O_3, and Ni-Aluminides. No nitrides were identified. Once again the results are summarized in individual reports and are consistent with leading edge materials and their possible reaction products. For verification of results, parts of the samples were sent to GRC for reproduction where a powder diffractometer was utilized as an alternative technique. ESCA results at GRC matched in principle with results obtained at KSC. However, the powder diffraction method was more successful in identifying bulk crystalline compounds. It identified the presence of crystalline mullite, Ni-aluminides and other compounds. It was decided that powder diffraction technique was more powerful and sensitive and will be

utilized for the phase II analysis. ESCA was chosen not to be utilized for phase II analysis. KSC reports that summarize phase I results are KSC-MSL-2003-0137, KSC-MSL-2003-0143, KSC-MSL-2003-0144, KSC-MSL-2003-0145, KSC-MSL-2003-0148, KSC-MSL-2003-0149, KSC-MSL-2003-0150, KSC-MSL-2003-0167.

3. The FTIR technique was not utilized because no organic compounds appeared to be present.
4. Cross-sectioning and dot mapping of elements clearly showed distribution and layering of elements (and possibly compounds). However, the technique lacked the detail that would be necessary to identify the source of the deposits and exact content of layering. Accurate compositional analysis by microprobe was required. Several cross-ectioned and mounted samples were sent to NASA MSFC and NASA GRC for microprobe analysis. The results were conclusive and solidified the position that cross sectioning with SEM/EDS dot maps, followed by point microprobe analysis will provide the best content and layering information. The interpretative findings from GRC analysis were very similar to those at MSFC despite different samples. This further attested to the reproducibility aspect of the technique. The relevant reports that summarize Phase I results are KSC-MSL-2003-0137, KSC-MSL-2003-0143, KSC-MSL-2003-0144, KSC-MSL-2003-0145, KSC-MSL-2003-0148, KSC-MSL-2003-0149, KSC-MSL-2003-0150, KSC-MSL-2003-0167, MSFC-ED33-2003-063, MSFC-ED33-2003-064, GRC (CT-050103-2C, -2D, CT-050903-3C, 3D, CT-051203-5C, -5D).
5. No bulk chemical analysis was done because of technical hurdles of standardizing the sample and the ability to get point information from the above techniques.

Standards Verification of Techniques Selected

An important aspect of using an analysis technique is its verification by known standards. This underscores the emphasis on accurate interpretation due to confidence in results. Once it was decided that electron microprobe analysis would be used for more accurate local compositional analysis, selected standards were purchased and the equipment calibrated. Metallic analyses were compared against pure metal and IN718 standards. A 100-point average statistical method was used for calibration. Oxide analysis was compared with mainly oxide standards. The analysis indicates that the results varied from standards from 0.5% to 25% depending on the amount of element present. For greater than 1% by weight element composition in standard, the analysis error was maximum of 5%. For less than 1% by weight element composition in standard, the analysis error could be as high as 25%. The variations in oxide standards and analysis results were in similar ranges. The details are presented in MSFC-ED33-2003-065 and GRC reports CT-051203-8C, -8D.

PHASE II SAMPLING PLAN

Phase II sampling plan was generated based on the success of radiography in identifying "heavy material". The decision was made to sample with RCC intact. It was also agreed that two samples in close proximity could be taken for X-ray diffraction and cross sectioning. This will help save time.

The sampling procedure that worked successfully was a diamond cutter wheel on a Dremel tool. The Dremel tool operated at 20,000 rpm and took about 15 minutes of cutting per sample. There was minimal heating of the part, and the part was warm to the touch after cutting. A vacuum was operated to collect the dust generated. A1"X1.25" sample was taken and a 0.25"

Part #	RDS #	Sample ID	Part	Deposit Features
55083	55083-2	A1, A2, B1, B2, C1, C2	LH RCC #5 upper	Uniform deposit with some small globular nature at the apex of the panel. Sample A was taken in region of globular deposit. Other samples were taken in areas of thin sketchy deposits.
31985	31985-2	A1, A2, B1, B2, C1, C2	LH RCC #7 Upper panel	Sample A and B were taken from the panel with more uniform deposit. Sample C was taken from the inboard rib with thicker deposit indicating some directionality to the deposit.
2200	2200-6	A1, A2, B1, B2, C1, C2	LH RCC #8, Upper panel	Samples A and B were taken from the apex area which show globular deposits. Sample C was taken in location having spheroids as seen in the radiograph.
18477	18477-5	A1, A2, B1, B2	LH RCC #8, Upper panel	Sample A was taken in region of uniform deposit not having any other unique features. Sample B was taken in a region with more spheroids in an effort to take more specimens with spheroids
43709	43709-2	A1, A2, B1, B2	LH RCC #8, Upper panel	Sample A was taken in a very thick "Tear" region. Sample B was taken in a thin "Tear" region.
61143	61143-2	A1, A2	LH RCC #8 Upper Rib	Deposits exist on inbd and otbd side. Both surfaces will be analyzed. The deposit shows uniform nature and spheroid features.
1419	1419-3	A1, A2, B1, B2	RH RCC #8 Upper Rib	Uniform deposit. No special feature to deposit identified in radiographs.
16523	16523-4	A1, A2	RH RCC #8 Upper panel	Uniform deposit. No special feature to deposit identified in radiographs.

Appendix B Table 2 - Phase II Sampling Matrix

X 0.25" piece was cut for x-ray diffraction. The samples were photographed at every step and documented in the reconstruction database. They were boxed in a petri dish and held down with Kapton tape for transportation. They were also radiographed post-cutting. These radiographs were used as a guide to decide where exactly to take the cross-section.

Table 2 details the number of samples taken. Sample "1" will be cross-sectioned and sample "2" will be x-ray diffraction tested.

PHASE III SAMPLING PLAN:

Based on the additional questions, additional parts were sampled. Their samples taken are described in Table 3 below.

Part #	RDS #	Sample ID	Part	Comments
2200	2200-XY	A1	LH RCC #8 Apex	Bluish green deposit on the outer surface of the apex.
18477	18477-XY	A1,A2	LH RCC #8 Upper panel	Sample is being taken close to spar fitting attachment location. Objective is to look for A286.
24724	24724-XY	A1, A2, B1	LH RCC #8, Lower heel	Sample A was taken to find evidence of A286 and study the RCC degradation. Sample B is flaked off deposit from rib surface.
7025	7025-XY	A1, A2	LH RCC #9, Upper inbd rib	The rib has deposits on inside and outside surfaces and is located on previously un-analyzed RCC 9. The sample shows some spheroids.
29741	29741-XY	A1, A2	LH RCC #9, Upper obd rib	Sampling of RCC Panel 9 for slag content and layering.
38223	38223-XY	A1, A2, B1, B2	LH RCC #9 Upper panel	Sampling of RCC Panel 9 for slag content and layering.
80632	80632-XY	A1, A2, B1, B2	LH RCC #4 Upper	Sampling of RCC Panel 4 for slag content and layering. Compare analysis with LH RCC Panels 5,7.
1860	1860-XY	A1, A2	Unknown	Sample has spheroids and hole in RCC through which material is seen coming out. Can slag sampling help locate it to LH RCC 9.

Appendix B Table 3 - Phase III Sampling Matrix

APPENDIX C

Acronyms

ACGIH	American Conference of Governmental Industrial Hygienists
ACM	Access Control Monitor
ADP	Air Data Probe
AMEC	Advanced Master Events Controller
APU	Auxiliary Power Unit
ARC	Ames Research Center
ASA	Aero-surface Amplifier
ATOS	Advanced Topometric Optical Scanner
ATVC	Ascent Thrust Vector Control
AWCS	Automated Work Control System
BAFB	Barksdale Air Force Base
BRIC	Biological Research in Canisters
BSTRA	Ball Strut Tie Rod Assembly
CAD	Computer Aided Drafting
CAIB	Columbia Accident Investigation Board
CBX-2	Critical Viscosity of Xenon
CCCD	Crew Compartment Configuration Drawing
CCTV	Closed Circuit Television
CM	Combustion Module
CRDS	Columbia Reconstruction Data System
CRO	Columbia Recovery Office
CT	Computed Tomography
CTF	Columbia Task Force
CVAS	Configuration Verification Accounting System
DAWG	Debris Assessment Working Group
DBA	Database Administrator
DHCP	Dynamic Host Configuration Protocol
EA	Electronic Assembly
ECLSS	Environmental Controls and Life Support Systems

EDO	Extended Duration Orbiter
EMS	Experiment Module
EMU	Extravehicular Mobility Unit
EPA	Environmental Protection Agency
ESCA	Electron Spectroscopy for Chemical Analysis
ET	External Tank
EVA	Extravehicular Activity
FC	Fuel Cell
FCOD	Flight Crew Operations Directorate
FCPA	Fluid Control and Pump Assembly
FCS	Flight Crew Systems
FDEP	Florida Department of Environment Protection
FDF	Flight Data File
FDM	Frequency Division Multiplexer
FIB	Fibrous Insulation Blanket
FRCS	Forward Reaction Control System
FREESTAR	Fast Reaction Experiment Enabling Science, Technology, Applications and Research
FRSI	Felt Reusable Surface Insulation
FTE	Full Time Equivalent
FTIR	Fourier Transform Infrared Spectroscopy
GAS	Get-Away Special
GFE	Government Furnished Equipment
GH2	Gaseous Hydrogen
GIS	Geographical Information Systems
GN2	Gaseous Nitrogen
GNC	Guidance, Navigation and Controls
GO2	Gaseous Oxygen
GPC	General Purpose Computer
GPS	Global Positioning Satellite
GRC	Glenn Research Center

GSFC	Goddard Space Flight Center
HEPA	High Efficiency Particle Air (filter)
HFT	Hardware Forensics Team
HMIS	Hazardous Material Inventory System
HRSI	High Temperature Reusable Surface Insulation
HUDE	Heads Up Display Electronics
HYD	Hydraulics
IML	Inner Mold Line
IP	Internet Protocol
IPA	Isopropyl Alcohol
IRF	Item Release Form
IT	Information Technology
JSC	Johnson Space Center
KSC	Kennedy Space Center
LACB	Landing Aids Control Building
LAN	Local Area Network
LaRC	Langley Research Center
LESS	Leading Edge Sub-System
LH	Left Hand
LH2	Liquid Hydrogen
LO2	Liquid Oxygen
LRSI	Low Temperature Reusable Surface Installation
M&P	Materials and Processes
MAC	Machine Address Code
MADS	Measurement and Acquisition Data Systems
MAR	Middeck Access Rack
MDM	Multiplexer De-Mulitiplexer
MESS	Large Stowage Rack
MIT	Mishap Investigation Team
MLG	Main Landing Gear
MLGD	Main Landing Gear Door

MMT	Mission Management Team
MMVF	Man Made Vitreous Fibers
MPM	Manipulator Positioning Mechanism
MPS	Main Propulsion System
MRT	Mishap Response Team
MSFC	Marshall Space Flight Center
NAIT	NASA Accident Investigation Team
NASA	National Aeronautics and Space Administration
NDE	Non-Destructive Evaluation
NHA	Next Higher Assembly
NSLD	NASA Shuttle Logistics Depot
NTSB	National Transportation Safety Board
NWA	Nose Wheel Assembly
OCN	Order Control Number
ODIN	Outsourcing Desktop Initiative
OEL	Orbiter Electrical
OEX	Orbiter Experiment Recorder
OFK	Official Flight Kit
OML	Outer Mold Line
OMS	Orbital Maneuvering System
OPF	Orbiter Processing Facility
ORB	Orbiter
OSHA	Occupational Safety and Health
OVEWG	Orbiter Vehicle Engineering Working Group
PAO	Public Affairs Office
PCM	Pulse Code Multiplexer
PCPA	Pressure Control and Pump Assembly
PDA	Personal Digital Assistant
PEL	Permissible Exposure Limit
PGSC	Payload and General Support Computers
PIM	Payload Integration Management

PLBD	Payload Bay Door
PPE	Personal Protective Equipment
PPK	Personal Preference Kit
PRSD	Power Reactant Storage and Distribution
PRT	Prevention/Resolution Team
PSA	Port Stowage Assembly
PVD	Purge, Vent and Drain Systems
QA	Quality Assurance
QC	Quality Control
RCC	Reinforced Carbon Carbon
RCG	Reaction Cured Glass
RCS	Reaction Control System
RDM	Responsible Data Manager
RDM	Research Double Module
RDS	Reconstruction Documentation Sheet
RH	Right Hand
RLV	Reusable Launch Vehicle
RMT	Recovery Management Team
RRT	Rapid Response Team
RSB	Rudder Speed Brake
RTV	Room Temperature Vulcanizing
SAM	Sub-system Area Manager
SDS	Shuttle Drawing System
SEG	Similar Exposure Group
SFOC	Space Flight Operations Contract
SGS	Space Gateway Services
SIDDS	Shuttle Interagency Debris Database System
SILTS	Shuttle Infra-red Leeside Temperature Sensor
SIMS	Still Image Management System
SIP	Strain Isolation Pad

SLF	Shuttle Landing Facility
SOFBALL	Structure of Flame Balls at Low Lewis-Number
SPA	Signal Processing Assembly
SQL	Structured Query Language
SRF	Sample Release Form
SRIL	Significant Recovered Items List
SSME	Space Shuttle Main Engine
SSP	Space Shuttle Program
STS	Space Transportation System
TAR	Test Approval Request
TCS	Thermal Control System
TIPS	Thermal Information Processing System
TLV	Threshold Limit Value
TPS	Thermal Protection System
TPSF	Thermal Protection System Facility
TVC	Toxic Vapor Check
TWA	Time Weighted Average
USA	United Space Alliance
VAB	Vehicle Assembly Building
VCD	Vapor condensation Distillation
VITO	Vehicle Integration Test Office
VPN	Virtual Private Network
VRML	Virtual Reality Modeling Language
WDS	Wavelength Dispersive Spectroscopy
WLE	Wing Leading Edge
XPS	X-Ray Photoelectron Spectroscopy
XRD	X-ray Diffraction
ZCG	Zeolite Crystal Growth

Great hearts, hands, and minds devoted their talents to this reconstruction in honor of Columbia, her crew, and their loved ones.



THIS PAGE INTENTIONALLY LEFT BLANK

Volume II
Appendix D.12
Impact Modeling

This appendix contains the independent analysis of the foam impact with the left wing conducted by Southwest Research Institute in support of the Columbia Accident Investigation Board. In addition to the analysis performed by NASA during the investigation, the Board called for a second independent analysis of the foam impact data. This report examines the foam impact data as it might have affected both thermal tiles and the RCC. The results of this analysis were used to predict damage to the RCC and tile and to set conditions for the foam impact testing program.

The conclusions drawn in this report do not necessarily reflect the conclusions of the Board; when there is a conflict, the statements in Volume I of the Columbia Accident Investigation Board Report take precedence.

Section 3.8 of CAIB Report Volume I, published in August 2003, states that details of impact tests performed during the investigation would be documented in Volume II, Appendix D.12. Due to the quantity of information required to describe this critical task, these details could not be included in this Volume. NASA Technical Publication TP-2003-212066, "Impact Testing of the Orbiter Thermal Protection System: Final Report in Support of the Columbia Accident Investigation," to be released in December 2003, documents in detail the activities conducted by the Orbiter TPS Impact Test Team for the OVE Office, the NASA Accident Investigation Team, and the CAIB. The report is divided into six sections: (1) introduction, (2) test facility design and development, (3) test article and projectile fabrication, (4) test program descriptions, (5) results, and (6) future work. The report fully documents the test program development, methodology, results, analysis, and conclusions to the degree that future investigators can reproduce the tests and understand the basis for decisions made during the development of the tests. Furthermore, it will serve to communicate the results of the test program to decision makers, the engineering and scientific communities, and the public.

THIS PAGE INTENTIONALLY LEFT BLANK

Impact Modeling

Submitted by James D. Walker
Southwest Research Institute

EXECUTIVE SUMMARY

After the loss of the Orbiter *Columbia* during reentry on February 1, 2003, Southwest Research Institute (SwRI) was contracted by the Columbia Accident Investigation Board (CAIB) to perform impact modeling in support of the investigation. At the SwRI site, the CAIB in conjunction with the NASA Accident Investigation Team (NAIT) was performing impact tests against thermal protection system structures, including thermal tiles and fiberglass and reinforced carbon carbon (RCC) leading edges. To complement the extensive modeling work being carried out by the NAIT, the CAIB wished to support an independent analysis of the impact event.

Through the course of the work, SwRI developed a detailed analytic and numerical model of foam insulation impact on thermal tiles. This model provided a damage/no damage transition curve in the impact speed-impact angle plane. In particular, it was shown that the component of the foam impactor velocity that is normal to the impact surface determined whether there is tile damage. Thus, given an impact speed and an impact angle for an incoming piece of foam insulation, the model determined whether tile material would be damaged. This model agrees extremely well with previously performed tile impact work conducted at SwRI as well as with the tests performed during the Columbia accident investigation of foam insulation impacting tiles placed on the main landing gear door of Enterprise.

Computations were performed to examine the role of foam rotational velocity on the impact. Foam impactor rotational velocity can increase the damage done to tiles since it can increase the impact velocity component that is normal to the surface of the tile. An angle and impactor shape were determined that would produce similar damage to tile material as would the rectangular impactor with a given rotational velocity striking at the expected impact angle.

In addition to the modeling of tile, the impact of foam insulation on RCC panels was also modeled. Here, a numerical model was developed to model the panel and an analytic boundary condition was developed to model the pressure load supplied by the impacting foam. Once again, central to the load delivered and the stresses calculated is the normal component of the foam impact velocity. Comparison with the two tests performed against RCC panels led to estimates of failure stresses within the panel material. Parametric studies were performed with the model to investigate the question of impact location and to investigate the effect of foam impactors with rotational velocity. It was shown that a nonzero rotation velocity for the foam impactor nearly always increased the stresses on both the panel face and the rib of the panel. Computations were performed to determine the most severe loads within the framework of impact location and rotational velocities. Also, an estimate of an angle adjustment for a rotational velocity was determined, as actual tests did not include a rotating foam impactor.

In all, the modeling work was extremely successful and led to a greater physical understanding of the impact of foam insulation against the Orbiter's thermal protection system. In particular, it was shown that the most important piece of information is the velocity component of the foam that is normal to the surface being impacted. This velocity determines the loading stress on that surface. Given the stress, in the case of tiles, stresses above the crush-up stress lead to tile damage, while stresses below the crush-up stress lead to no damage. In the case of the RCC panel, the loading stress combined with the loading area gives rise to the loads seen by the panel and by the rib. These loads lead to stresses in both the panel and rib that subsequently can fail the rib or panel face. Though the geometry and deformation modes of the RCC panel do not produce a simple theory for damage as was found in the tile impact model, still the physical understanding of the impact is that stresses arise from normal velocities over a footprint of the impact to give loads that can then fail the panel.

SwRI appreciates the opportunity to participate in the Columbia investigation, and this report presents the work performed in the modeling effort.

Thermal Tile and Foam Insulation Models

To correctly model the impact of materials, it is essential to correctly model the materials involved. In order to do this, work began with the experimental testing of foam cubes left over from the 1999 SwRI testing program of foam against tile [1] and the testing of a thermal tile supplied by NASA.

The important information about both the foam and the tile that was lacking in the available data from NASA and the shuttle contractors was crush-up data for the material in compression. To address this lack of information, two 1" (2.54 cm)* cubes of tile left over from the 1999 SwRI testing program were crushed in an MTS test machine. The foam material is identified as NCFI 24-124 [1]. Two tests were performed. In the first, the foam was crushed till a large stress was reached, and in the second, three unload/reloads were performed during the crush up. Results are shown in Figs. 1 and 2. Strain rates were roughly 7×10^{-3}/s. The initial knee in the compression curve, where the slope of the stress-strain curve greatly diminishes, will be referred to as the "initial crush-up" and the corresponding stress will be referred to as the crush-up stress σ_{crush} in this report.

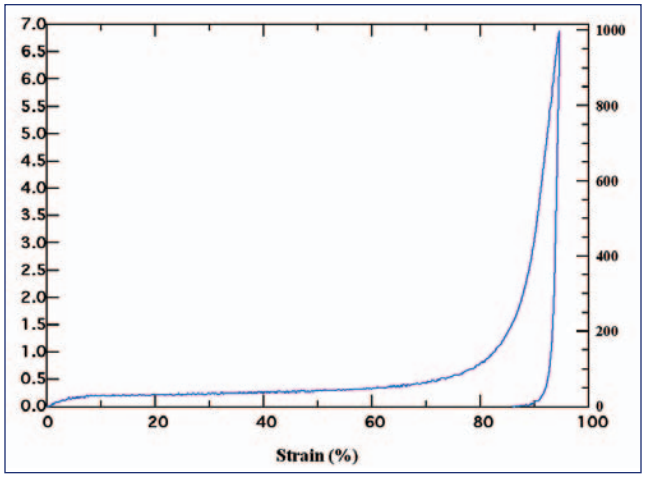


Figure 1. Results of test of foam cube.

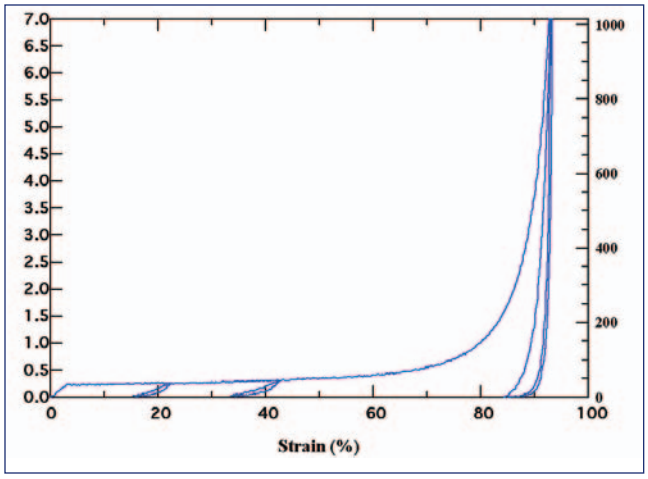


Figure 2. Test of second foam sample. Note the three unload/reloads.

Visual observation of the tests revealed two important facts about the foam during loading: first, there was virtually no lateral expansion; and second, when compressed the foam stayed intact and compressed (i.e., there was a permanent crush-up). The second observation on crush-up is confirmed in Figure 2 by the unloading curves that clearly indicate a permanent deformation.

However, in the tests that were being performed at SwRI under the NAIT/CAIB program with foam impacts against aluminum panels, it was clear that at the higher rates the foam was not permanently crushing up. It was undergoing large deformations, but after the impact it was releasing to its original shape.

Based on these observations, it was decided to model the foam as a nonlinear elastic material. Since impact computations were to be performed in the Eulerian hydrocode CTH from Sandia National Laboratories [2], it was important to develop the model in the context of CTH's computational algorithm. Within CTH, as with many hydrocodes, the material response is divided into a spherical response (i.e., a pressure-volume response) and a shear response. To correctly model the material, the fact that there was no lateral expansion of the material was caused by setting Poisson's ration ν equal to zero:

$$\nu = 0 \qquad (1)$$

Within CTH, the local value of the shear modulus is computed from the current value of the bulk modulus and the constant Poisson's ratio. Thus, to model the material as a nonlinear elastic material with no lateral expansion, all that is required is determining the bulk response, that is, the bulk modulus as a function of pressure.

For a linear elastic material with a Poisson's ratio of zero, the bulk modulus K is simply 1/3rd the Young's modulus E, and the shear modulus G is simply 1/2 the Young's modulus:

$$K = E/3,\ G = E/2 \qquad (2)$$

The initial values that were measured for the foam insulation at SwRI from the weight and dimensions of the samples and the stress-strain curves are given in Table 1. For a nonlinear elastic material with a Poisson's ratio of zero, corresponding differential relations between the local bulk modulus, shear modulus and Young's modulus apply. Thus, specifying one of the moduli as a function of pressure and energy completely determines the elastic response.

	ρ_0	E_0	σ_{crush}	ν
Foam Insulation	0.03844 g/cm³ 2.4 lb/ft³	8.0 MPa 1160 psi	220 kPa 31.9 psi	0
Tile	0.18 g/cm³ 11.2 lb/ft³	27.0 MPa 3916 psi	345 kPa 50 psi	0

Table 1. Measured Properties of the Foam Insulation and the Thermal Tile.

Within CTH, new subroutines were written to model the foam insulation and thermal tile material response. Some details of these routines are described in another portion of the Columbia Accident report since CTH is an Export Controlled code. The model essentially returned the pressure and bulk modulus given a density. The table of values from which the subroutine linearly interpolated to produce pressures and moduli (in particular, the local bulk sound speed) for the foam insulation is given in Table 2. Since these are axial stress values, they correspond to the Young's modulus, and the corresponding bulk modulus was found by dividing by 3. Also, no thermal component to the stress was included in the EOS. Thus, given the density of the material, its pressure state was determined. The final values with very large stresses are to provide robustness to the computational scheme so that, if large compressions did occur, the EOS would be able to provide corresponding pressures.

Density	*Axial Stress*	*Density (g/cm^3)*	*Axial Stress (kPa)*
0 g/cm3	0 Pa	0.	0
$0.3\times\rho_0$	$-2\sigma_{crush\text{-}f}$	0.015320	-440
$(1-\sigma_{crush\text{-}f}/E_{0f})\rho_0$	$-\sigma_{crush\text{-}f}$	0.037383	-220
ρ_0	0 Pa	0.038440	0
$(1+\sigma_{crush\text{-}f}/E_{0f})\rho_0$	$\sigma_{crush\text{-}f}$	0.039497	220
$\rho_0/0.3$	$2\sigma_{crush\text{-}f}$	0.128133	440
$\rho_0/0.15$	1.31 MPa	0.256267	1.31×10^3
$\rho_0/0.05$	7 MPa	0.768800	7.00×10^3
$\rho_0/0.04$	7 GPa	0.961000	7.00×10^6

Table 2. Tabular Foam Insulation Values in EOS.

Due to the tests with the foam showing no permanent crush-up during the dynamic tests, the foam was modeled as purely elastic by 1) setting a flag within the new EOS to say that the pressure response was elastic (i.e., there was no permanent crush-up) and 2) setting the yield stress in the elastic-plastic portion of the code to 7 MPa (~1 ksi). It is unlikely this stress level will be reached, so this stress is viewed as a large stress to maintain elastic behavior in the foam. Also required within CTH is a tensile failure stress which was set to 230 kPa (33.4 psi).

For the foam insulation, Figure 3 compares the model to the data from the two tests, and Figure 4 is an enlargement of the low pressure region. The agreement is excellent.

Similar material characterization work was performed on a shuttle thermal tile. SwRI was mailed a tile (MISC-794-400-120) from which were cut roughly 2" (5.08 cm) cube samples. Two cubes were then crushed in an MTS machine. The results of the crushing are shown in Figs. 5 and 6. Strain rates were roughly 3×10^{-3}/s.

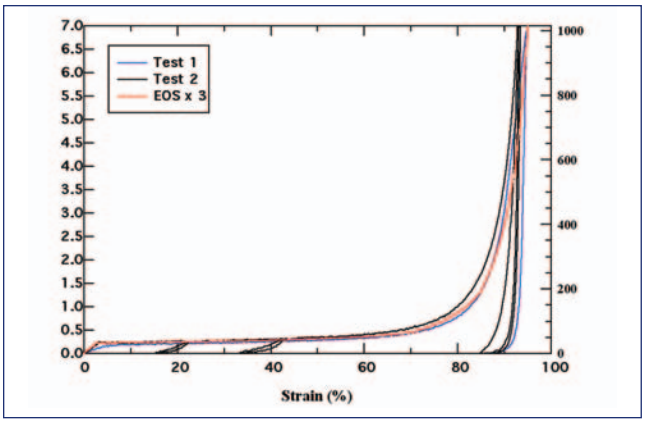


Figure 3. Stress-strain curve for foam: blue and black from tests, red from model.

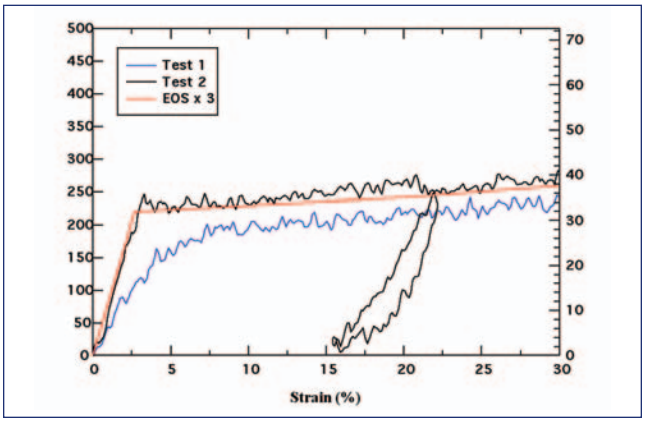


Figure 4. Enlargement of stress-strain curve for foam in Figure 3: blue and black from tests, red from model.

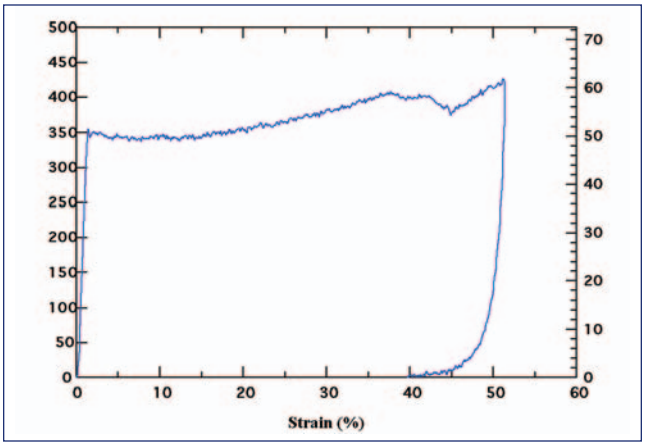


Figure 5. Stress-strain curve for shuttle thermal tile.

The initial values (i.e., near zero stress) that were measured for the thermal tile at SwRI from the weight and dimensions of the samples and the stress-strain curves are given in Table 1. Though it is clearly an LI-900 tile, the measured density was larger than the stated 9 lb/ft^3. As throughout this report, the values measured at SwRI will be used in the modeling and analysis.

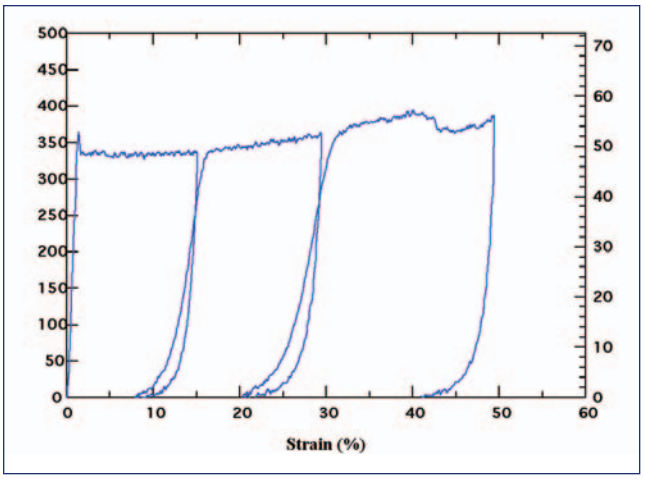


Figure 6. Stress-strain curve for shuttle thermal tile, including unload/reloads.

Upon loading, the initial crush-up point in the curve occurs at 345 kPa (50 psi). After this point, there is a slowly increasing stress as strains increase. A difference between the foam crush-up and the tile crush-up is that the tile breaks apart. Visual observation during the compression test indicated that failure begins when the stress-strain curve begins to dip in the 40% strain region. Fractures form in the tile material and the cube of tile subsequently disintegrates as loading progresses. To model this behavior, the elastic-plastic yield stress was set to 400 kPa (58 psi). The elastic-plastic yield is an important part of the crush-up behavior of the tile (see Figure 8, where the solid curve is without the yield stress while the dot-dash curve is with the yield stress in the formulation). Also, a failure model was invoked, namely that the material would fail at 50% equivalent plastic strain (this failure model was invoked by using constants D2=0.5, D1=D3=D4=D5=0 in the Johnson-Cook fracture model). The tensile failure stress was set at 360 kPa (52.2 psi). Also important in the computations that included both foam and tile was setting certain parameters in the CTH fracture input: pfvoid=pffrac=-50 kPa and setting nface1 and nface2 equal to the material numbers of the foam and tile. Though the tensile behavior is not well modeled (a general problem for Eulerian codes), it is an important part of the model and does affect results. Fortunately, the most interest for these models is when the materials are under compression.

For the tile model, permanent crush up was assumed to occur. Thus, once compressed beyond the crush-up stress, a permanent set occurs and the unloading curve is different than the loading curve. This behavior was accomplished by setting the appropriate flag in the new EOS model in CTH.

The model for the thermal tile material is shown in comparison to test data in Figs. 7 and 8. The behavior beyond the failure of the tile material is extrapolated based on the foam's properties. Table 3 displays the values of axial stress versus the density, similar to Table 2 for foam. This table, with the Poisson's ratio equal to zero and the yield stress and fracture model as defined above, completely defines the material response.

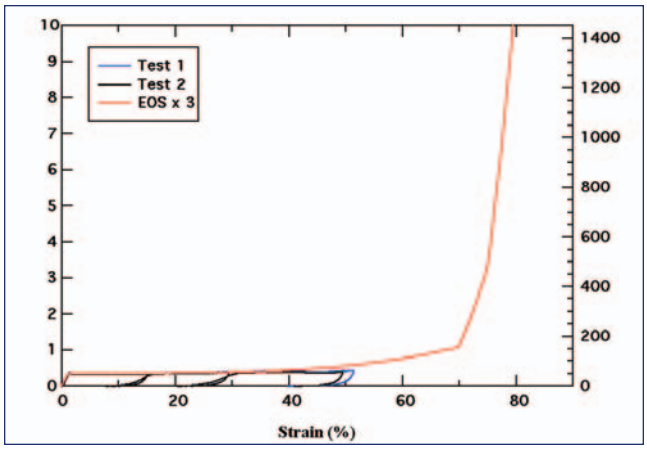


Figure 7. Stress-strain curve for thermal tile: blue and black are data, red is model.

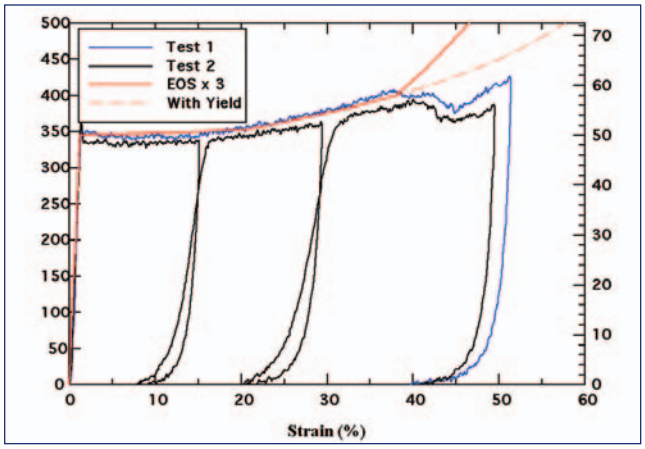


Figure 8. Enlargement of tress-strain curve for thermal tile: blue and black are data, red is model (solid curve is without yield; dashed curve is behavior with yield).

Density	*Axial Stress*	*Density (g/cm³)*	*Axial Stress (kPa)*
0 g/cm³	0 Pa	0.	0
$0.3\times\rho_0$	$-2\sigma_{crush\text{-}t}$	0.0540	-690
$(1-\sigma_{crush\text{-}t}/E_{0t})\rho_0$	$-\sigma_{crush\text{-}t}$	0.1777	-345
ρ_0	0 Pa	0.1800	0
$(1+\sigma_{crush\text{-}t}/E_{0t})\rho_0$	$\sigma_{crush\text{-}t}$	0.1823	345
$\rho_0/0.8$	352 kPa	0.2250	352
$\rho_0/0.62$	400 kPa	0.2903	400
$\rho_0/0.50$	550 kPa	0.3600	550
$\rho_0/0.30$	1.10 MPa	0.6000	1.10×10^3
$\rho_0/0.25$	3.30 MPa	0.7200	3.30×10^3
$\rho_0/0.20$	11.0 MPa	0.9000	1.10×10^4
$\rho_0/0.18$	11.0 GPa	1.0000	1.10×10^7

Table 3. Tabular Tile Values Used in EOS.

Foam Impact on Tile Computations

The models developed above were then exercised by examining the impact tests reported in [1]. These tests included 1" (2.54 cm) cubes of foam insulation impacting individual thermal tiles at various angles and velocities. The experiments included impacts ranging from no-damage to significant damage to and cratering in the tiles, and were thus viewed as a good range of data to compare against.

Most of the computations were performed in 2-dimensional plane strain. It turned out that due to the physics involved (and as was explicitly shown for one case), there was excellent agreement between 3-dimensional and 2-dimensional calculations for the impact parameters considered. Computations were performed with CTH for a variety of striking angles and velocities. Information extracted from the computations primarily focused on the normal stress at the surface of the tile; the histories of these stresses were examined at locations spaced 0.5 cm apart on the tile surface.

As a first example, the comparison between a 2D and 3D computation will be considered. Figure 9 shows the initial geometry for both the 2D and 3D computation. The thermal tiles are 6" × 6" × 2" in 3D, and 6" × 2" in 2D. The impact velocity was chosen to be 800 ft/s (244 m/s) at a striking angle of 30°. The cell size in the computations was 1 mm cube or square, depending on the dimension, with 160 × 100 × 40 cells used in 3D (a plane of symmetry was assumed at the center, and only 1.5" width of the half tile was included), and 160 × 100 cells used in 2D. The computations were carried out to 500 μs. The figure also shows frames of each computation at 200 and 500 μs. The outlines of the materials show that the deformation in these cases is quite similar. The colors in the figures show σ_{yy}, where *y* is the vertical axis. Though similar, it can be seen that the stresses away from the impact region are lower in the 3D computation as the extra dimension has stress-free boundaries that supply rarefaction waves reducing the stress beneath the impact site.

As a quantitative measure, results from the experiment as well as the computations are shown in Table 4. The final crater dimensions agree very well for the three cases. In addition to considering the final crater dimensions, the normal stress (σ_{yy}) histories at 0.5 cm interval locations were compared (Figure 10). As can be seen, the normal stress histories agree very well for the two computations. Due to the agreement, further calculations to explore the behavior of the impact event were carried out in 2D plane strain.

	Crater Depth	*Crater Length*	*Crater Width*
Experiment [1]	0.64 cm (0.25")	5.1 cm (2")	3.2 cm (1.25")
3D computation	0.8 cm (0.3")	6.4 cm (2.5")	2.9 cm (1.15")
2D computation	0.8 cm (0.3")	5.4 cm (2.1")	n/a

Table 4. Comparison Between Experiment and 3D and 2D-Plane-Strain Computations.

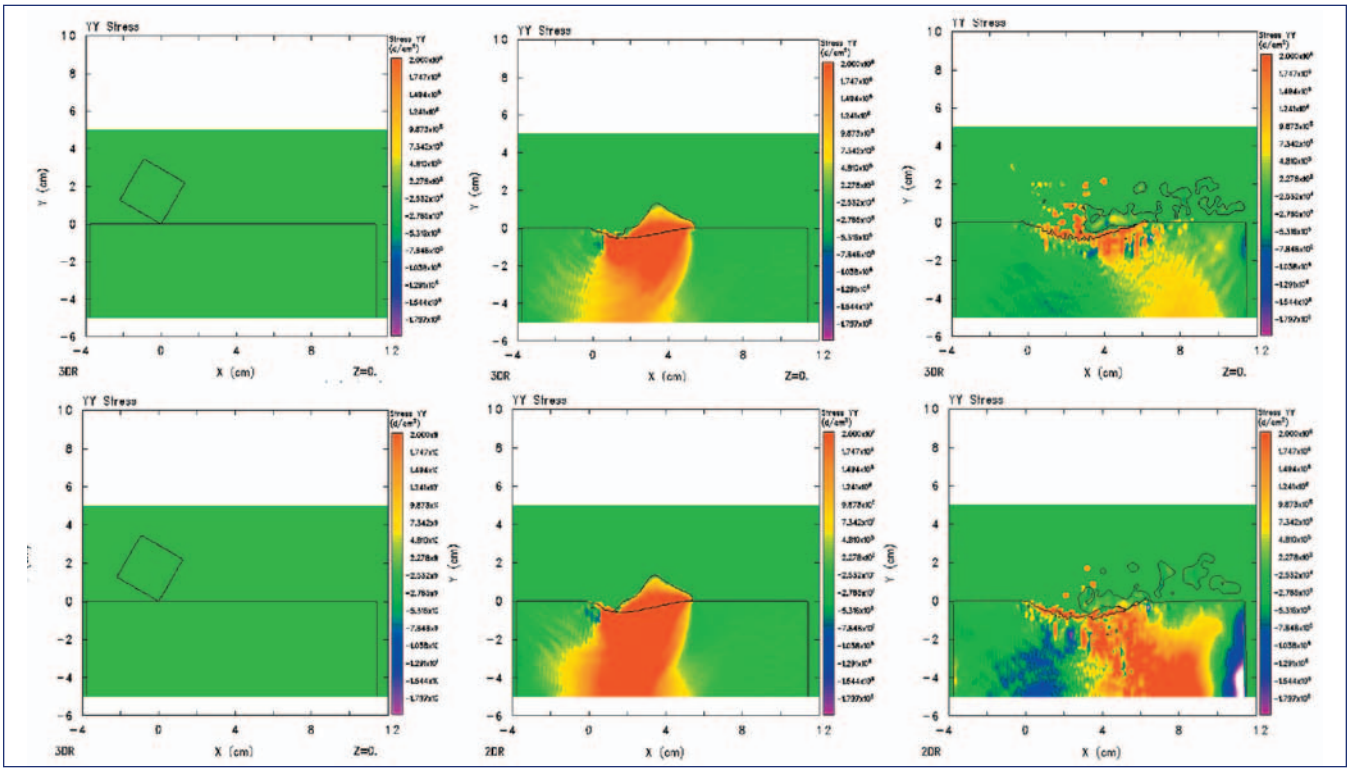


Figure 9. CTH computations with new foam insulation and thermal tile models. Top is 3D computation, bottom is 2D plane strain of 1" cube of foam insulation material impacting thermal tile at 800 ft/s at 30° impact angle. Times are 0, 200 and 500 μs. Colors mark σ_{yy}, ranging from –200 kPa (-29 psi, purple) to 200 kPa (red); green is 0 kPa.

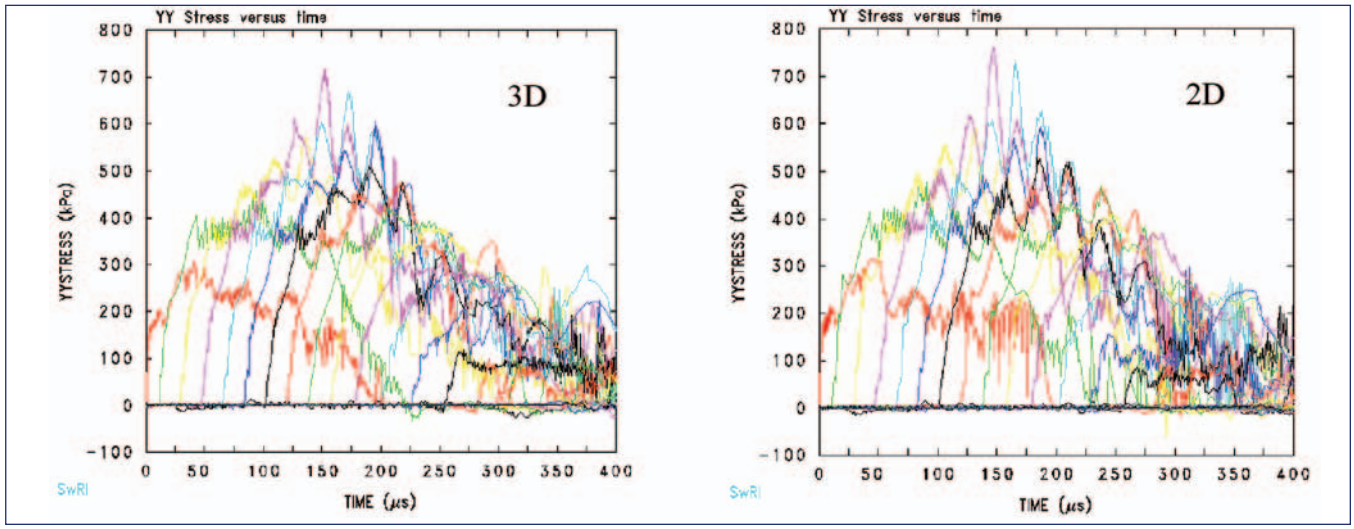


Figure 10. Normal stress histories for 3D (left) and 2D-plane-strain (right) computations of 1" cube of foam insulation impacting thermal tile at 800 ft/s at 30° impact angle.

Damage/No Damage Criteria

Given that the material models and impact simulations were behaving well and reproducing experimental results, it was decided to pursue a damage/no damage transition curve through computation. In particular, a sequence of computations was performed with the intent of determining whether an impacting 1" cube of foam insulation material would damage the thermal tile. The damage/no damage decision was based on an examination of both the final state of the tile surface and the normal stress history at the gage locations along the tile surface. For example, the computation at 700 ft/s at 15° impact angle was decided to have no damage since there was little deformation at the surface of the tile (what deformation is seen there is typical of numerical anomalies in interfaces in Eulerian codes) and the stresses remain below the 345 kPa (50 psi) crush-up stress determined above for the thermal tiles. The results are shown in Figure 11.

However, for an impact at the same velocity but a larger impact angle, damage does occur. Figure 12 shows the results for 1" cube of foam insulation impacting a thermal tile at 700 ft/s at a 23° impact angle. In this case there is damage: a crater is seen when the surface of the tile is examined and the normal stresses at the interface exceed 345 kPa by a significant amount and for a significant time duration.

Mapping Out the Damage/ No Damage Transition Curve

A series of computations were performed to determine the damage/no damage transition curve in the impact speed-impact angle plane. In each case a given impact speed and impact angle computation was performed with the new model in CTH, and based on the arguments presented above either "damage" or "no damage" (or in some in-between cases, "slight damage") was assigned to the results. These

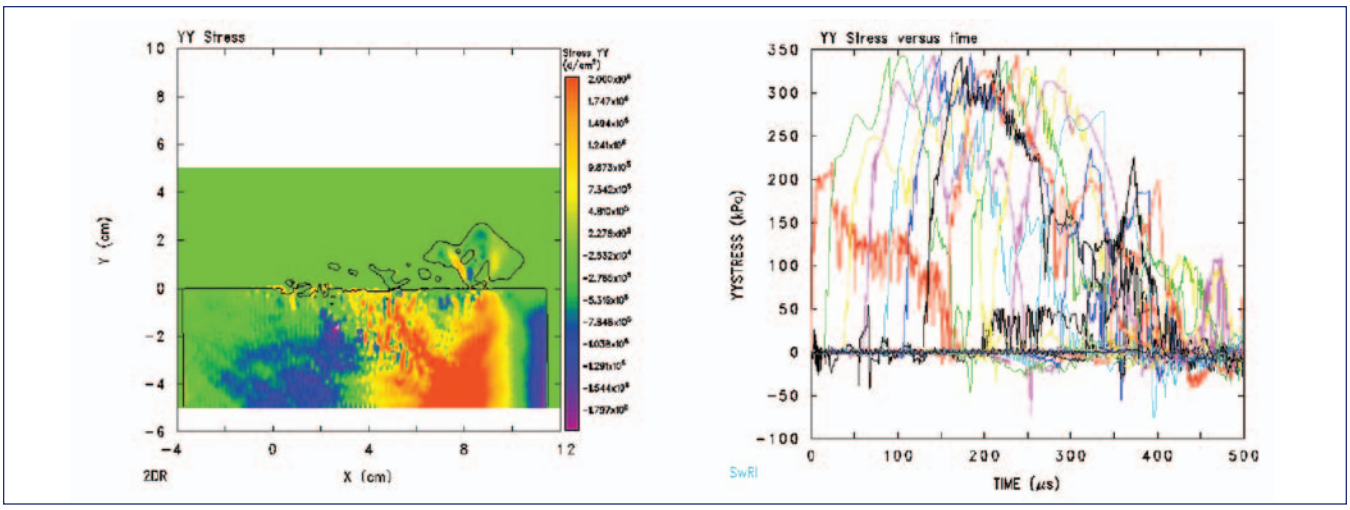


Figure 11. σ_{yy} (left) and normal stress (σ_{yy}) histories (right) for 1" cube of foam insulation impacting thermal tile at 700 ft/s at 15° impact angle; no damage occurs to the tile.

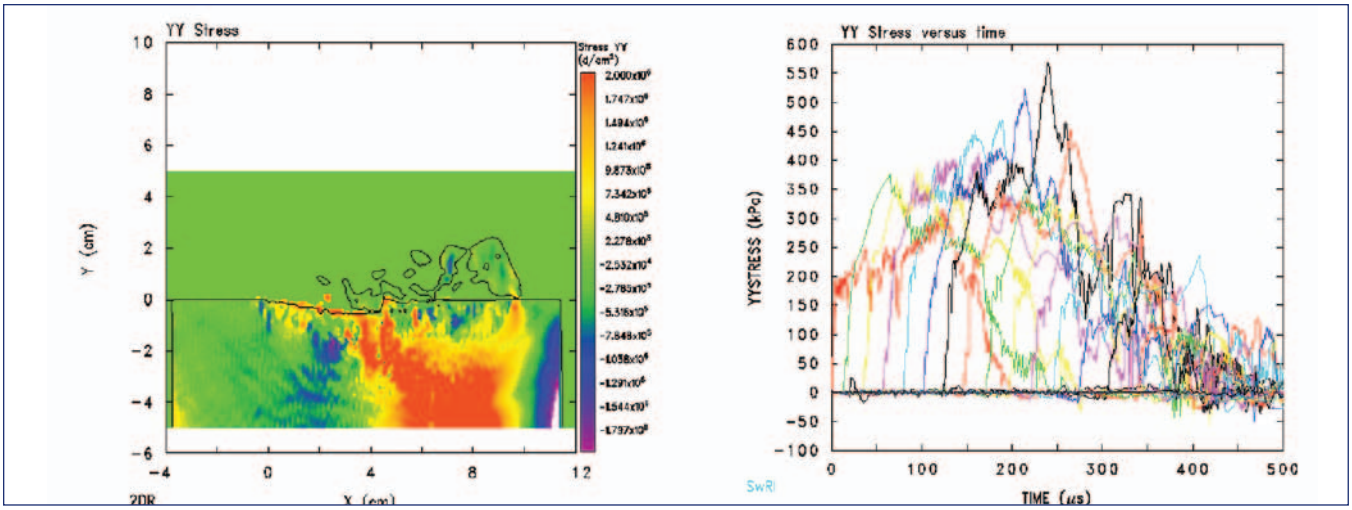


Figure 12. σ_{yy} (left) and normal stress (σ_{yy}) histories (right) for 1" cube of foam insulation impacting thermal tile at 700 ft/s at 23° impact angle; damage occurs to the tile.

computations were then plotted in the impact speed-impact angle plane. After each computation, the decision was made on what case to run next, thus allowing the curve to be followed. Table 5 shows the results of the computations. When plotted on a graph, these results give indication of a fairly well defined damage/no damage transition curve in the plane (Figure 13).

Velocity (ft/s)	*No Damage*	*Slight Damage*	*Damage*
175	40°, 50°, 70°		
200	90°	40°, 50°, 70°	
225		50°	
250		50°, 90°	
300	30°		90°
400	20°, 25°		30°
500	20°	25°	30°
600	17°	20°, 23°	25°
700	10°, 15°		20°, 23°, 30°
800	13°	17°	20°
900	12°		17°
1000	10°	15°	20°
1100	10°		15°
1200	10°		15°
1400	10°		13°
1600	7°	10°	12°

Table 5. Results of Computations of 1" Cube of Foam Insulation Impacting a Thermal Tile. Each Angle Entry Represents a CTH Calculation.

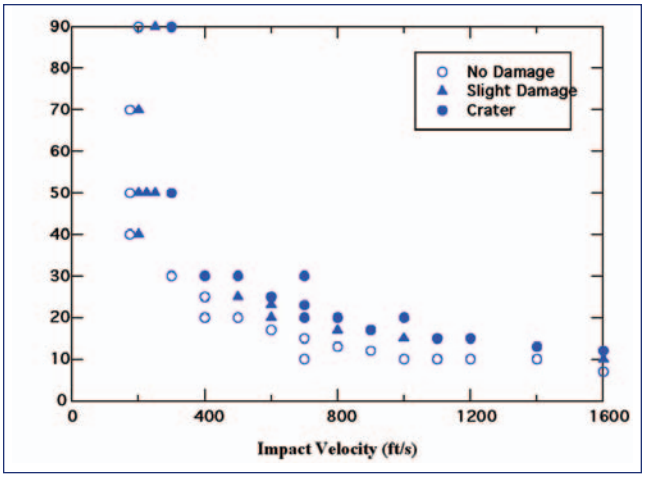


Figure 13. Damage/no damage results from numerical calculations.

Analytical Model for Damage/ No Damage Transition Curve

When the foam insulation material impacts the tile surface at an angle, it appears it is possible to separate the velocity of the foam material into two parts: tangential to the surface and normal to the surface. As there is no Poisson's effect for the foam, the two behaviors seem to separate nearly completely. Thus, the question arises as to what normal velocity leads to the crush-up of the thermal tile. The Hugoniot jump conditions for mass and momentum conservation for a shock moving to the right state

$$\rho_2 = \frac{\rho_1}{1 - \frac{u_2 - u_1}{U - u_1}} \tag{3}$$

$$\sigma_2 - \sigma_1 = \rho_1 (U - u_1)(u_2 - u_1) \tag{4}$$

where subscript 1 refers to the region in front of the shock (before passage) and subscript 2 refers to the region behind the shock, U is the shock velocity, ρ is density, σ is stress and u is particle velocity. For the impact situation here, the crush-up stress of the foam insulation is less than that of the tile and therefore the foam will achieve its crush-up stress and then continue loading into its relatively flat stress-response region (Figure 4). The thermal tile, on the other hand, will be responding in its initial elastic regime up to the crush-up stress. In equations for each material, with the subscript e referring to elastic, the material states after the passage of the initial elastic wave are

$$\rho_e = \frac{\rho_0}{1 - \frac{u_e}{c_0}} \tag{5}$$

$$c_0 = \frac{\sigma_{crush}}{\rho_0 c_0} \tag{6}$$

where subscript 0 refers to the initial state and $c_0 = \sqrt{(E_0/\rho_0)}$ (the Young's modulus is used in this expression for the longitudinal sound speed since Poisson's ratio is zero). At the crush-up stress of the thermal tile, the material velocity in the tile is u_{et} and the stress is $\sigma_{crush\text{-}t}$ (where the subscript t stands for tile). The Hugoniot jump conditions are now applied to the foam insulation to give

$$\sigma_{crush\text{-}t} - \sigma_{crush\text{-}f} = \rho_{ef}(c_{1f} + u_{ef})(V_{crush} - u_{ef} - u_{et}) \tag{7}$$

Solving for the impact velocity at which the tile crush stress is reached yields

$$V_{crush} = u_{et} + u_{ef} + \frac{\sigma_{crush\text{-}t} - \sigma_{crush\text{-}f}}{\rho_{ef} = (c_{1f} - u_{ef})} \tag{8}$$

This equation for the crush velocity can be evaluated using the properties of the foam insulation and thermal tile material determined above. The values obtained are

c_{0f} = 456 m/s
c_{0t} = 387 m/s
c_{1f} = 49.8 m/s
ρ_{ef} = 0.03953 g/cm^3
ρ_{et} = 0.18233 g/cm^3
u_{ef} = 12.5 m/s
u_{et} = 4.95 m/s
V_{crush} = 68.2 m/s (224 ft/s)

Thus, for a normal impact of foam insulation against a thermal tile, crush-up of the thermal tile begins at an impact velocity of 68.2 m/s. This derivation was for one-dimensional response. In the situation where the piece of foam is impacting at an angle θ, the normal velocity (the velocity into the tile) is given by

$$V_y - V\sin(\theta) \tag{9}$$

Thus, for foam insulation impacting thermal tile at a velocity V and angle θ, the thermal tile will begin to crush at

$$V - V_{crush}/V\sin(\theta) \tag{10}$$

For the value of V_{crush} computed for the foam insulation impact into tile, this damage/no damage transition curve is plotted in Figure 14 along with the results from the computations. It is seen that there is excellent agreement.

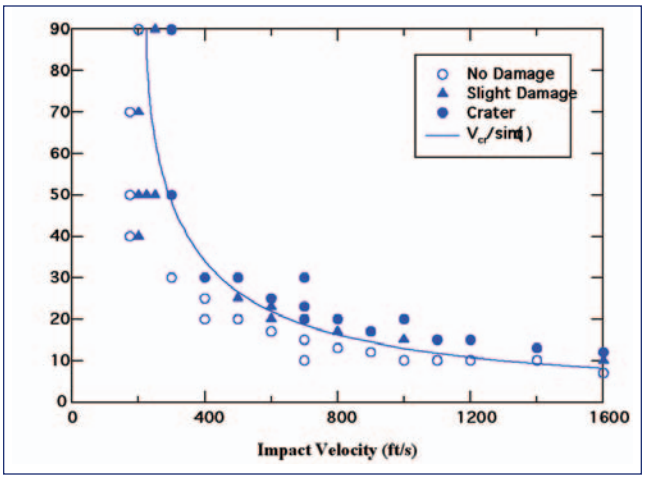


Figure 14. Theoretical damage/no damage transition curve with computational results.

Returning to the reports of previous work performed at SwRI [1,3], all the experimental results of foam insulation impact into single thermal tiles were categorized with the same damage/slight damage/no damage designation. Figure 15 breaks out these various impact cases. Figures 15a-c are for NCFI 24-124 [1]. The material in Figure 15d from [3] is an ablator material with a higher density (around 0.3 g/cm^3, 19 lb/ft^3) and unknown crush strength.* Rough dimensions of the impactors are shown in the figure captions. Of most interest are the foam insulation impactors with leading cross section 1" × 1" (Figure 15a). Though of two different lengths, the agreement is remarkable. In this case, the tile is fully loaded by the foam, and the length of the impactor does not affect whether damage occurred (it does affect crater size [1]). In other cases with much smaller cross sections, it is likely the projectile buckled before fully loading the tile, thus leading to less damage to the tile. Figure 15e shows results of tests performed during the Columbia investigation (discussed below). Finally, Figure 15f shows all the data points plotted with the theoretical curve. The agreement is excellent.

A strong case can be made that the foam insulation impacting thermal tiles is well understood. Good agreement has been shown between the large-scale numerical computations, the theoretical model, and experimental results. Thus, it is clear that loading from the foam arises from the component of the velocity normal to the surface being struck. If the resulting normal stress exceeds the crush-up stress of the tile, then the thermal tile crushes and a crater is formed. Otherwise, there is minimal or no damage to the tile. Figure 16 puts all three (CTH calculations, theoretical curve, experimental results) on one plot.

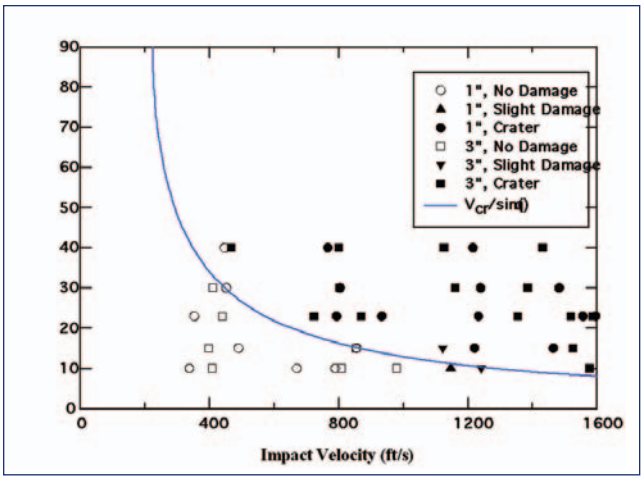


Figure 15a. 2.54 × 2.54 × 2.54/7.62 cm.

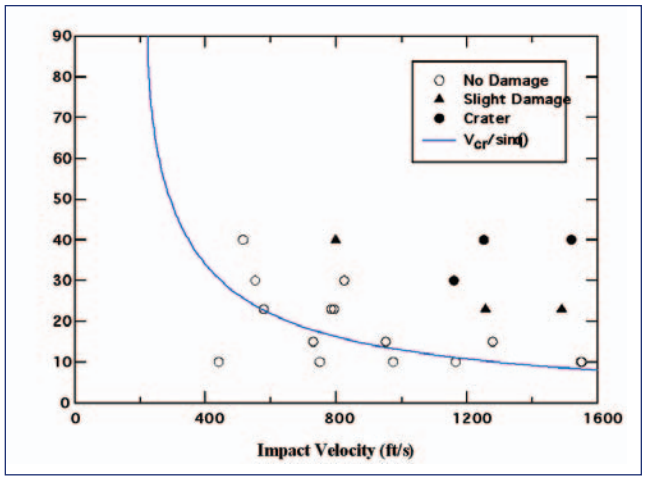


Figure 15b. 0.64 x 2.3 x 2.3 cm.

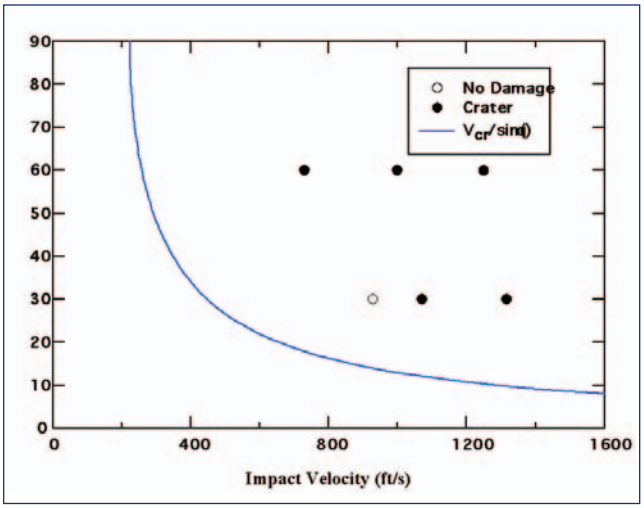


Figure 15c. 0.95 diameter x 7.62 cm.

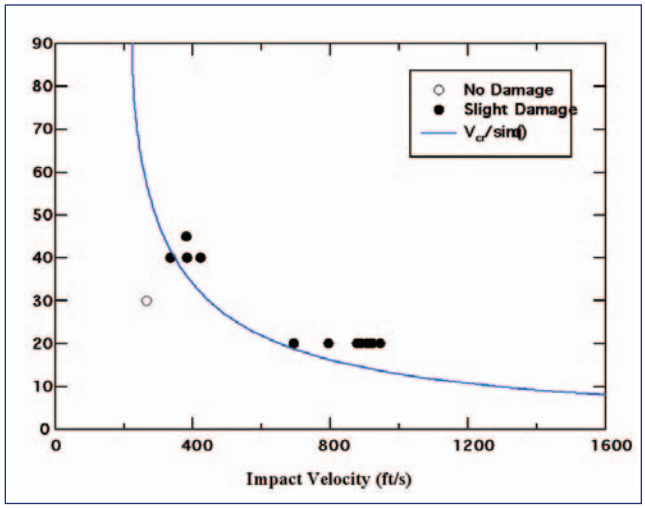


Figure 15d. 0.5 x 0.5 x 5.1 cm (ablator) [3].

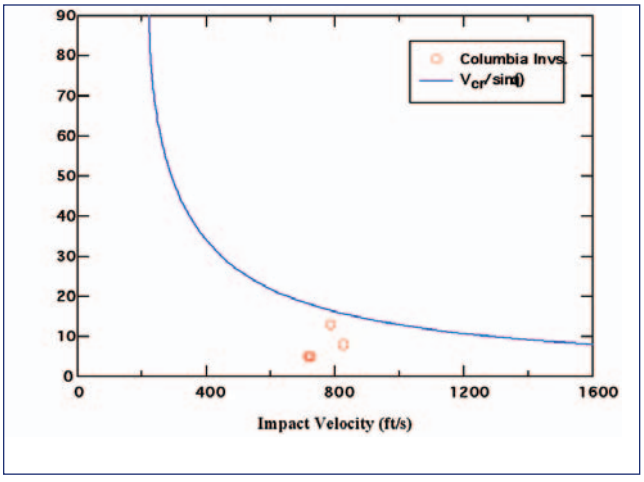


Figure 15e. Columbia *investigation tests.*

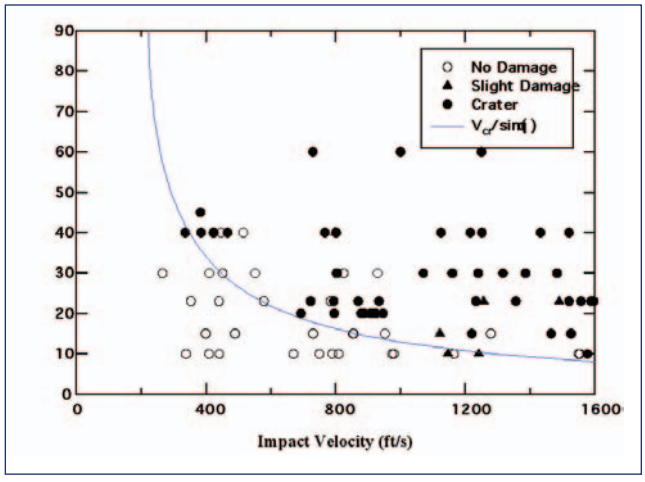


Figure 15f. All data from [1] and [3].

Figures 15a – 15f. Theoretical damage/no damage transition curve with results of all impacts into thermal tiles contained in [1,3] and Columbia *investigation tests.*

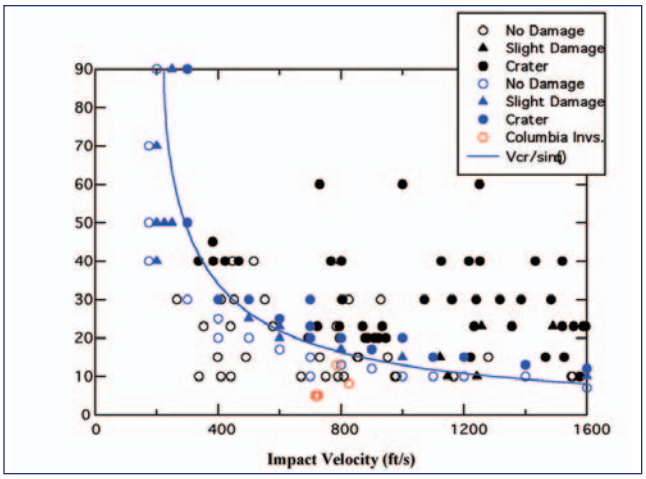


Figure 16. Theoretical damage/no damage transition curve with results of computations (blue) and all impacts into thermal tiles contained in [1,3] (black) and the Columbia investigation tests (red).

Impact into Tiled Surface of Orbiter

So far, the discussion has focused on the impact of a single tile by a piece of foam. From a theoretical viewpoint, the tile and foam can be of arbitrary size, so if a tiled surface behaved like a "large" tile, the above damage/no damage transition curve would carry over to the tiled surface of the Orbiter.

There are three differences between the tiled surface and a "large" tile:

1) On the Orbiter the tiles are attached to an aluminum substructure through a strain isolation pad. Both the pad and aluminum substructure introduce less stiffness to the problem, making it easier for the tiles to move. Per se, that is not a difference. The difference arises when the aluminum substructure stops moving. Then, due to the load being produced by the impacting tile, the aluminum structure flexes and, in some areas, increases the angle of incidence and thus increases the normal component of the velocity, thus increasing the stress on the surface. Thus, surface motion can lead to higher stresses which may crush the tile. In practice, it is unlikely the structure will flex very much, and so this is not a great concern.
2) The aluminum substructure could fail due to the load. This would not be a failure of the thermal protection system. As such, it is not considered here.
3) In the Orbiter configuration, the tiles are separated and a gap-filler is placed between the tiles. On impact with foam, the edges of the tiles are essentially being struck at a much higher incident angle and are therefore undergoing larger stresses than the flat top of the tile. Crush-up of the tile could begin at the edges and then propagate across the tile surface causing more damage.

In practice, for foam insulation impacts on tile, only "3" is a concern.

The testing performed by NAIT/CAIB during the Columbia investigation included the impact of a main landing gear door from Enterprise to which thermal tiles had been added. Five tests were performed (Table 6). All these tests were with velocities and angles that were well below the damage/no damage transition curve. The critical angle is the angle obtained from Eq. (10) for the given impact velocity and V_{crush} = 68.2 m/s. Thus, no crush-up of the tile is to be expected, and none was observed. There was minor damage done to the tiles, but all of it appeared to be due to edge damage due to the foam hitting or catching on an edge of the tile. Thus, the impact testing for the Columbia investigation agrees with the theoretical damage/no damage transition curve presented here.

Effect of Changes in Material Properties

One of the benefits of a good theoretical model is that it is possible to explore the role of material properties. For example, material properties could lie outside the expected ranges, and it is desirable to know how such variation affects the results.

In this vein, two variables were considered. First, the question of what would be the effect of doubling the foam density is addressed. If the foam density is doubled from the value of 2.4 lb/ft^3 (0.03844 g/cm^3) to 4.8 lb/ft^3 (0.07688 g/cm^3), Eq. (8) gives that the new crush-up velocity is V_{crush} = 49.7 m/s (163 ft/s), or a reduction of 27%. When plotted on the previous graph, the result of such an increase in density is clear: it reduces the allowable angle for a given speed by about 25% for speeds above 400 ft/s (Figure 17).

In a similar fashion, the question of what would occur if the thermal tile crush-up strength was reduced by 20%, from 345 kPa (50 psi) to 275 kPa (40 psi), was considered. Such a reduction has a much more severe effect on the damage/no damage transition curve: V_{crush} = 39.2 m/s (129 ft/s), and the allowable angle is reduced about 40% for a given impact ve-

Impact Speed (ft/s)	Impact Angle	Critical Angle	Damage
723	5°	18.0°	Small gouges initiating at edges
717	5°	18.2°	None
725	5°	18.0°	None
827	8°	15.7°	Small gouges initiating at edges
787	13°	16.5°	Small gouges initiating at edges

Table 6. Test Summary from Main Landing Gear Door Impact Tests.

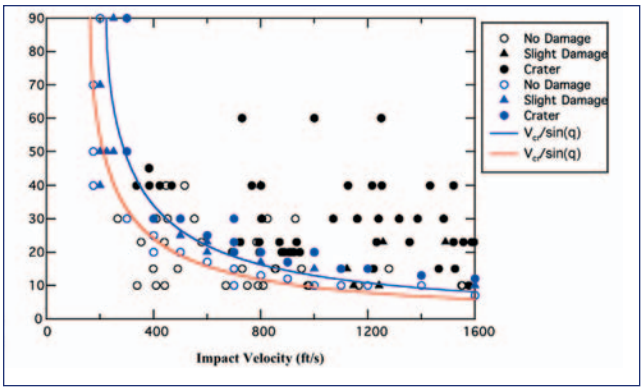


Figure 17. Effect of doubling the foam insulation density on the damage/no damage transition curve (red).

locity for velocities above 400 ft/s. Thus, tile failure is more sensitive to tile crush-up strength than relatively large variations in foam density. The condition of the tile is therefore of more concern than variations in foam properties.

Effect of Rotation of the Foam Impactor

The video footage of the foam insulation debris traversing the path from the external tank to the Orbiter wing shows a flickering that is likely due to rapid rotation of the foam insulation debris. Initial estimates put the rotation rate at 30 Hz, though by the time the RCC panel impact work was performed the rotation rate estimate had been lowered to 18 Hz. Since it is difficult to have controlled rotation during a ballistic test, the effect of rotation was examined computationally and then an equivalent non-rotating-impactor impact scenario was determined. The equivalent scenario involved an impactor of smaller size but a greater impact angle.

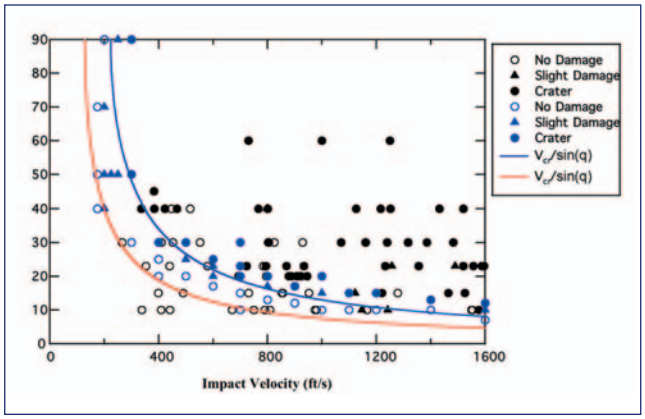


Figure 18. Effect of reducing tile strength 20% (red).

At first it may seem that rotation could not affect the impact a great deal. However, since it is normal velocities that matter, the rotational velocity can have a large effect. The maximum velocity due to rotation is given by the distance from the center of the rotation times the angular velocity:

$$v = \omega r \qquad (11)$$

For a piece of foam 19" long rotating at 30Hz about its center, the tangential velocity at the outer edge is 150 ft/s (45 m/s). Thus, since the crush velocity is 224 ft/s (68.2 m/s), it is clear that if the rotating foam impacts the surface in such a way that the rotational velocity is normal to the surface, then the rotational velocity can provide a significant percentage of the velocity required to reach the crush-up threshold.

The particular case of a 775 ft/s impact at 8° impact angle was considered. The theoretical damage/no damage transition curve above (Eq. 10) gives a critical angle of 16.8°, and therefore, no damage would be expected from the impact. In this case the impactor has assumed dimensions of 19" × 11.5" × 5.5" (though the latter dimension will not enter in, as the computations will be 2D plane strain). The normal component of velocity is 108 ft/s. The 30 Hz rotation rate at 9.5" gives a speed of 150 ft/s. Thus, the sum of these speeds exceeds the 224 ft/s crush-up velocity. That means that given the right orientation at impact, the rotation of the foam impactor can change what would otherwise be a non-damaging impact against the thermal tile to a damaging one.

Computations were performed for the above impact geometry for a counterclockwise rotation, no rotation, and a clockwise rotation. Lacking a full model for a tiled surface, a single "large" tile was used to represent the thermal tile. Figure 19 shows the results of the CTH computations for the three cases. The figure shows the σ_{yy} stress. The images in the left column are for the impactor rotating counterclockwise, the center column is the non-rotating case, and the right column is the clockwise rotation. As time progresses (0, 1, 2 and 5 ms) it can be seen that the counterclockwise rotation prevents an impact on the front end of the impactor, and rather for this case the back end impacts first. For the counterclockwise case, little damage is done to the tile. As predicted, there is no crater formed for the non-rotating case. For the clockwise rotation case, however, the leading edge impacts with a normal velocity above the crush-up velocity and a crater is formed in the tile. Thus, for the clockwise case, rotation leads to damage of the thermal tile. Figure 20 shows the normal stresses at the tracer locations for the three cases; these normal stresses confirm the damage seen from the previous figure, namely that the stresses are below the 345 kPa (50 psi) tile crush stress for the counterclockwise and non-rotating cases and are well above the tile crush stress for the clockwise rotation case.

Computations were then performed to determine an equivalent non-rotating impactor to mimic the clockwise rotating case. It was assumed that the impact velocity would be the same – 775 ft/s. As a first step, it is clear that to achieve the same result seen in the clockwise rotating case it is necessary to exceed the critical angle of 16.8° degrees, because unless that angle is exceeded, no damage will occur in the tile. Thus, computations were performed at impact angles of 17° and 18°. In order to obtain a loading time similar to that produced by the rotating impactor, it was necessary to reduce the length of the foam impactor. A similar loading time is necessary because the loading time determines the depth and extent of the crater; using the same size impactor results in too long and too deep a crater. An impactor length that produced a similar crater in the tile was 9.5" (half the original length). Figure 21

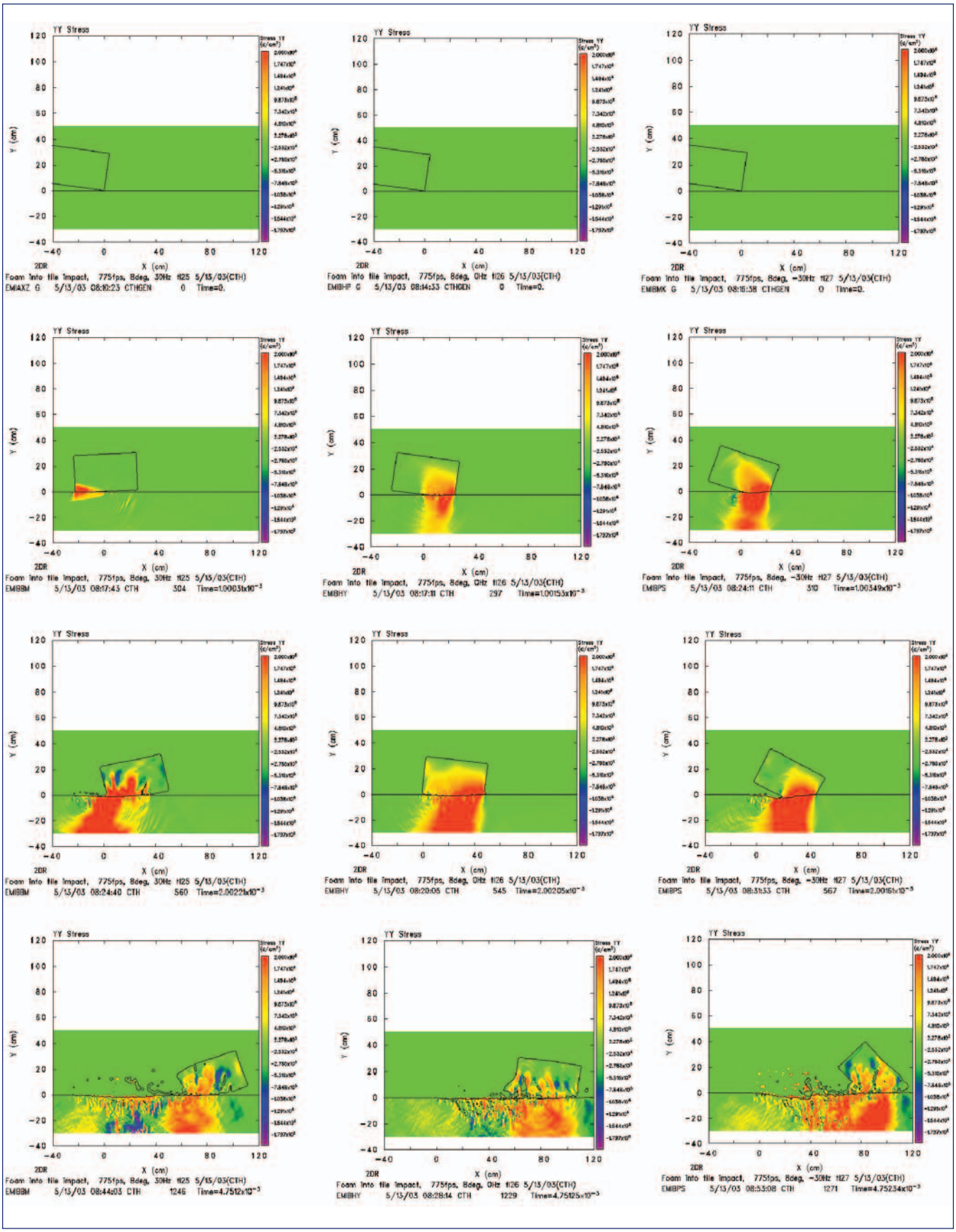


Figure 19. Comparison of rotation cases for 775 ft/s impact at 8° angle, 30 Hz counterclockwise in left column, no rotation in center column, 30 Hz clockwise rotation in right column. Times are 0, 1, 2 and 5 ms.

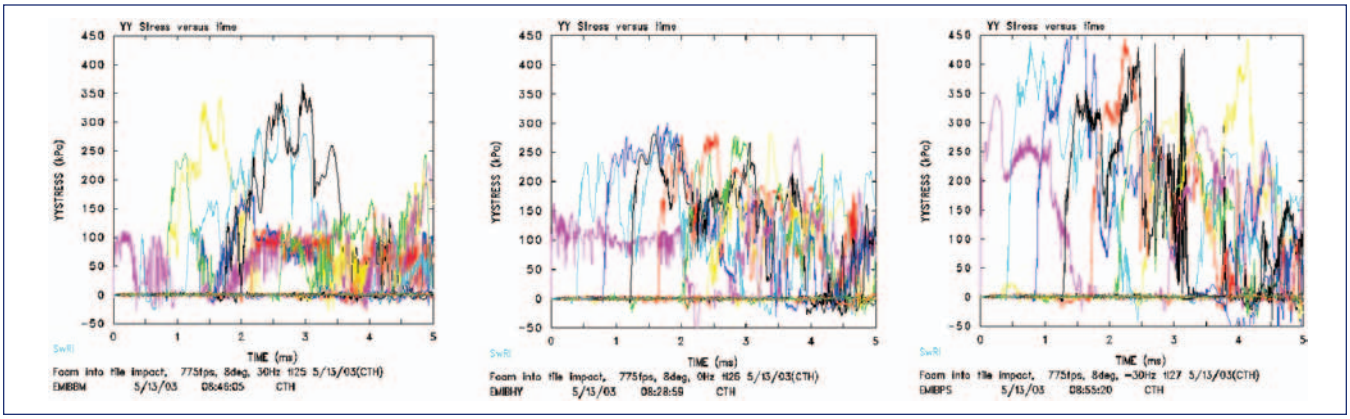


Figure 20. Normal stresses from rotation case comparison, left is 30 Hz counterclockwise, center is no rotation, right is 30 Hz clockwise. For the clockwise case, the stresses clearly exceed the 345 kPa (50 psi) crush-up stress of the tile, and damage is expected.

shows the σ_{yy} stress from three impact cases: 8° with 30 Hz clockwise rotation with the original sized impactor (left column), and 17° (center column) and 18° (right column) non-rotating impactors of half the length, or dimensions of 9.5" × 11.5" × 5.5" (though again the last dimension doesn't enter in as the computation is 2D plane strain). It can be seen that all three impacts are producing similar stresses and craters in the tile. Figure 22 shows the normal stresses at the tracer locations. The tracers for the three cases are similar. Thus, to replicate the influence of 30 Hz clockwise rotation rate of the 8°-impact-angle impact one would use a non-rotating half-length projectile at a considerably higher impact angle of 17° or 18°. This equivalent impactor is determined based on how the tile crushes up and, in particular, that damage depends on the load delivered at the surface.

Though it is not considered here, another way to obtain similar damage would be increase the velocity of the foam impactor, rather than the impact angle, since increasing the impact speed while keeping the impact angle the same also increases the normal velocity. Using Eq. (10), if the impact angle of 8° were to be kept the same, then the impact velocity would need to be increased to at least 1610 ft/s (491 m/s) to begin damaging the tile. Calculations would need to be performed at these higher velocities to determine the new size of the impactor to produce similar damage. The approach is the same as that done above for the equivalent impactor at the higher impact angle.

RCC Impact Modeling

During the course of the investigation, attention moved away from the thermal tiles towards the leading edge. The leading edges are made of panels of reinforced carbon carbon (RCC).

Modeling of the impacts of RCC Panels performed during this investigation involved two major assumptions:

1) The RCC material was modeled as an isotropic elastic solid;
2) The foam impact on the outer face of the RCC Panel was handled through an analytic boundary condition.

These assumptions will be discussed below. A consequence of assumption #1 is that there is no damage model and thus no failure: stresses in various parts of the panel assembly were computed and conclusions about damage to panels will be based on the two experiments performed. In general, though, the stress levels are used to compare the results of various parameter studies for the impact event. Assumption #2 will be discussed in detail below; one of its consequences is that load calculations are an upper bound to the loads that would be delivered by the foam impactor to the panel.

Due to lack of detailed damage information as well as material properties, it was decided to model the RCC material as a purely isotropic elastic solid and to examine the history of the stress in various regions of the RCC panels during impact to study the impact event. The properties from the Rockwell International Materials and Processes Report "Shuttle Orbiter Leading Edge RCC T-Seal Cracking Investigation" (M. R. Leifeste, A. R. Murphy and S. V. Christensen, LTR 4088-2401, November 1991) give Young's moduli of 4 to 10 Msi. Experimental work performed by Sandia National Laboratories Livermore as part of the Columbia investigation (W-Y Lu, B. Antoun, J. Korellis and S. Scheffel) gave Young's moduli of 0.6 to 2.5 Msi. (Part of the reason for ranges in value is due to tests in different orientations and differences in tension and compression results.) For the computations performed here, the value of 20 GPa (2.90 Msi) was used. The density was taken to be 1.6 g/cm^3 and the Poisson's ratio was taken to be 0.27. These three values completely specify the behavior of RCC material in the modeling. Within the code other values were computed from these values for use, such as the bulk modulus K = 14.5 GPa, the bulk wave speed $\sqrt{(K/\rho)}$ = 3009 m/s and the shear modulus 7.87 GPa. The material properties for the RCC are summarized in Table 7.

ρ	*E*	*Poisson's Ratio*
1.6 g/cm^3 *100 lb/ft^3*	*20 GPa* *2.9 Msi*	*0.27*

Table 7. RCC Material Properties Used in the Modeling.

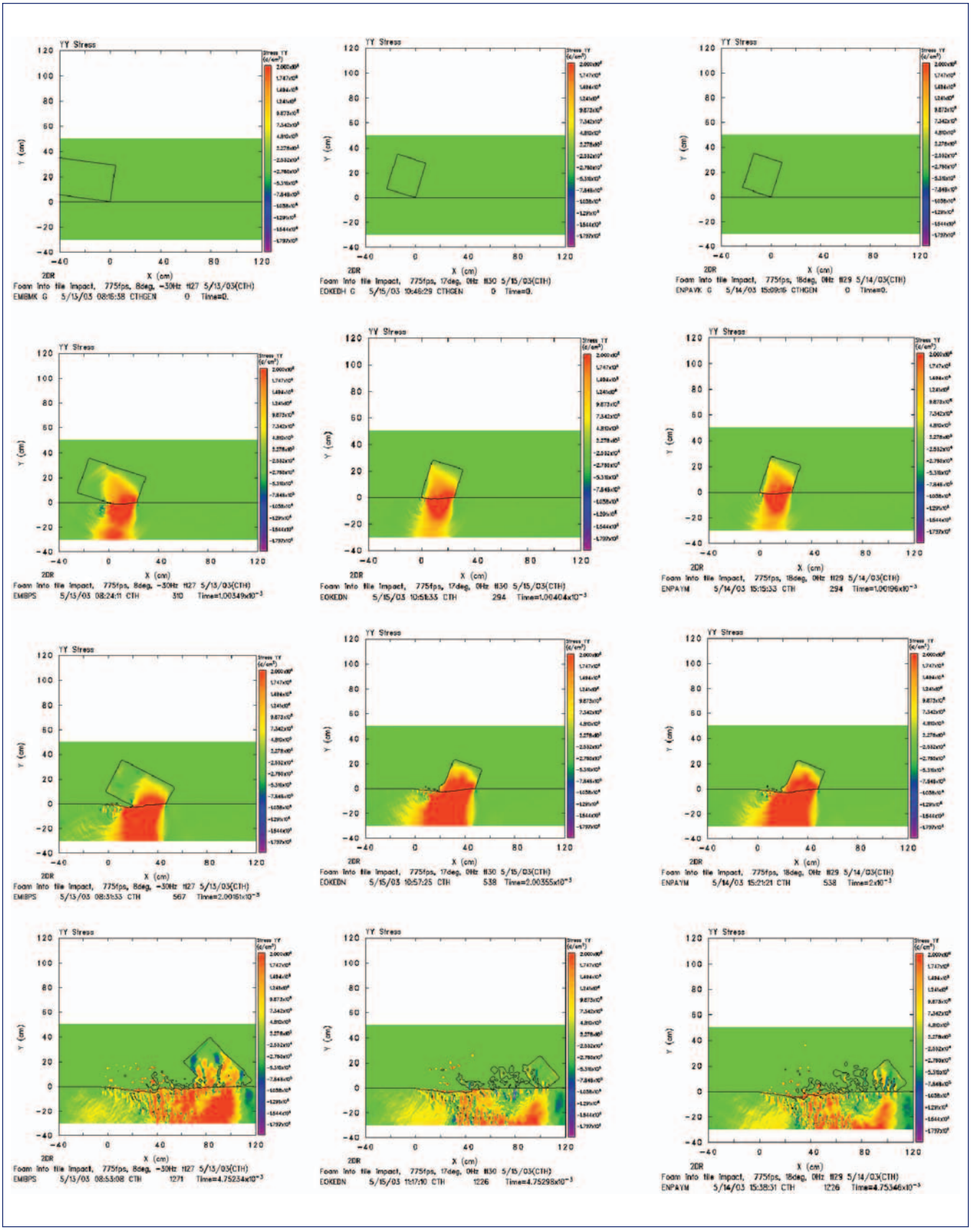


Figure 21. Nonrotating impactor to produce similar damage as 30 Hz clockwise rotating impactor. 30 Hz clockwise rotating impactor at 8° angle in left column, 17° degree nonrotating impactor in center column and 18° nonrotating impactor in right column. All impacts at 775 ft/s. Figures show σ_{yy} stress. Times are 0, 1, 2 and 5 ms.

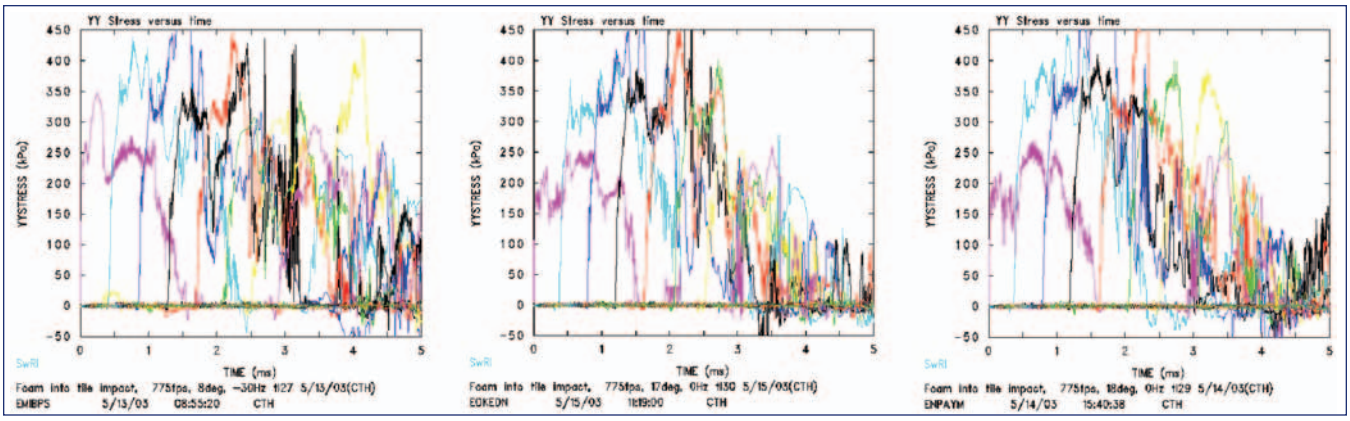


Figure 22. Nonrotating impactor to produce similar damage as 30 Hz clockwise rotating impactor. 30 Hz clockwise rotating impactor at 8° angle in left column, 17° degree nonrotating impactor in center column and 18° nonrotating impactor in right column. All impacts at 775 ft/s. Graphs show normal stress at tracer locations versus time.

Early attempts to model the problem with CTH, as done above for the tile impact, were unsuccessful. In the past, SwRI has had difficulty modeling thin plates with CTH, as the tensile states lead to void insertion and failure of the plates. Attempts to perform impact calculations against thin plates, even with 10 cells across the thickness of the plate, were unsuccessful, and so it was decided to pursue a Lagrangian model of the RCC panel.

To model the RCC panel in the Lagrangian frame, new software was written. The coding was based on the finite difference/finite volume algorithms used in HEMP 3D and detailed in [4]. The mathematics of these algorithms is similar to that of explicit finite element codes (for example, DYNA) and it allows for large deformation and large deflection. The written software's implementation was verified by computations involving wave propagation at arbitrary angles and plate vibration at arbitrary angles. The solutions from the new code produced the correct wave propagation speeds and magnitudes and the correct vibrational frequencies. Performing the test cases at arbitrary angles with respect to the coordinate system ensured that the whole stress tensor was being engaged and that the implementation was correct, hence verified.

To simplify and speed up the computations, it was decided to handle the foam insulation impact through an analytic boundary condition based upon the results of the work detailed above. The stress at the boundary was written as a function of the foam velocity, the local material velocity, and the angle of impact. In particular,

$$p = \begin{cases} \rho_{0f} c_{0f} (V - u_{RCC}) & V \le u_{RCC} + u_{ef} \\ \sigma_{crush\text{-}f} + \rho_{ef} (c_{1f} - u_{ef})(V - u_{ef} - u_{RCC}) & V > u_{RCC} + u_{ef} \end{cases} \quad (12)$$

where V is the velocity of the foam normal to the surface and u_{RCC} is the velocity of the RCC material normal to the surface. Thus, an explicit analytic expression for the pressure has been obtained from Hugoniot jump condition considerations outlined above, and shown to agree with the CTH computations performed during the tile impact study. Figure 23 shows the dependence of loading pressure on velocity (in particular, on V-u_{RCC}). The impacts during the testing program were at 775 ft/s with the local impact angles typically between 10° and 25°, the angle varying since the leading edge panels have curvature. Thus, the normal velocities were between 135 and 330 ft/s, with pressures between 40 and 65 psi. These values give some idea of the expected loads. Two impacts of foam insulations against RCC were performed. The modeling will be discussed below, but for now the footprints of the impacts are shown in Figure 24. For the RCC Panel #6 impact (to the left), the maximum loading footprint has an area of 110 in^2 (712 cm^2) roughly corresponding to a triangle of base 20" and height 11". If the panel doesn't move, there is an average pressure of 55.6 psi (384 kPa) for a 768 ft/s impact at the appropriate impact orientation. Thus, the expected maximum load is 6140 lb (2.73×10^9 dynes). (The actual load during the impact will be less due to panel material motion since $u_{RCC} > 0$.) The area-averaged impact angle is 19.7° (that is, this angle is the average interaction angle based on the foam impactor's velocity vector and the surface normals of the surface cells). For the RCC Panel #8 impact (to the right), the quadrilateral footprint has an area of 193 in^2 (1246 cm^2) and is roughly 17" across and 11.5" high. If there is no panel motion the average pressure would be 52.9 psi (364 kPa) for a maximum load of 10,200 lb (4.55×10^9 dynes). The area-averaged impact angle is 17.5°. In both cases the foam impactor delivers a substantial load to the panels. Errors from the analytic load approximation are reduced by the fact that the loading occurs in the region of the pressure-velocity curve with the shallower slope: thus, when rarefactions tend to reduce the loading pressure, the change in pressure is less than if the loading response of the foam were such that it did not have the relatively level stress portion after the crush-up point is reached (Figs. 23 and 24). In any event, loads computed from the analytic expression (Eq. 12) are upper bounds for those that would be observed in an actual impact event.

Based on the properties of the RCC used in this analysis, the longitudinal wave speed in the RCC material is 3950 m/s, and so the particle velocity in the RCC at the foam's crush stress is 3.5 cm/s. Thus, relative to the foam, the RCC mate-

rial is a rigid surface. Thus, the material velocity of the RCC material due to elastic waves in a thick material resulting the impact with the foam is not large, and is in fact negligible compared to the structure motion of the plate. However, as will be seen, the velocities associated with the structural motion of the plate are large enough that they must be included. The u_{RCC} term in the above equation includes all motion of the RCC panel, including small elastic motions due to elastic wave transit and the larger structure motions that the panel undergoes during the impact event.

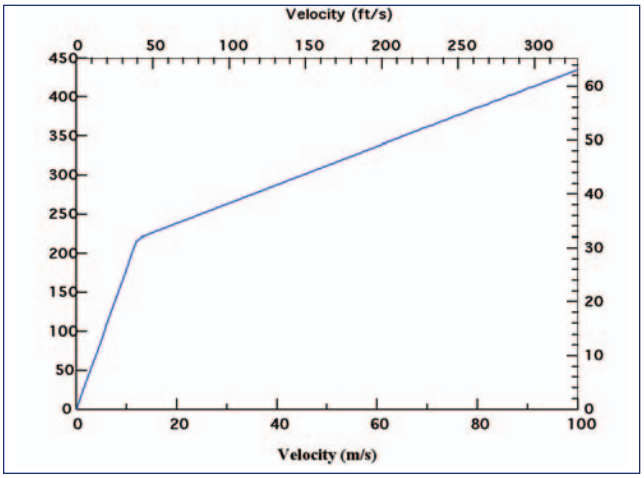


Figure 23. Pressure vs. velocity for the analytic boundary condition.

The only failing of the analytical pressure boundary condition as presented in Eq. (12) is that it does not include the reduction in pressure that can occur from relief waves returning from the free surfaces of the foam (note that the waves propagating outward from the impact point are correctly included, as is the material motion of the RCC panel material and the free surface on the interior of the panel) and the reduction in pressure that can occur from the fracture of the foam impactor. Due to not including these relief waves, the computed load will be greater than the actual load and can be viewed as an upper bound. Though there is some unloading from the elastic wave, unloading that causes the foam impactor to lift away from the panel face is controlled by the wave speed $c_{1f} = 49.8$ m/s. Thus, with the thickness of the foam impactor being 5.6", and assuming a compressive strain of 50% (so that the total travel distance for the wave is 5.6"), the time of unloading is on the order of 2.9 ms.

CTH computations with this impactor also showed that the loading for impact velocities on the order of 775 ft/s and angles of on the order of 20° and less produced unloading times on the order of 2 ms and greater. The time it takes to travel 20", roughly the furthest distance along the panel face the impactor travels (see Figure 24), is 2.3 ms. Thus, the geometry and impact conditions are fortuitous in that for the foam impactor considered here (with a thickness of 5.6") and with the impact angles and velocities considered here (leading to a 20" long or less loading path), the unloading from the free surface of the foam impactor occurs as the foam impactor is extending beyond the panel face. Thus, the unloading behavior does not need to be included in the boundary condition for these computations. As will be seen, the maximum load is typically achieved by 2 ms during the foam impacts on the RCC panels. Breakup of the foam insulation impactor can occur due to the way the impactor flexes when striking the curved panel surface or by catching on a sharp edge; in the tests, impactor breakup was observed later in the impact event (later than 2 ms) either due to impacting the T-seal, twisting of the foam impactor, or impact with the sharp edge of a hole. Thus, the lack of including unloading effects due to relief waves and fracture in the foam is not detrimental. (The lower corner of the foam impactor can be seen to leave the panel face in the test against RCC Panel #8, but this departure is as the foam is leaving the panel face and does not greatly affect the load).

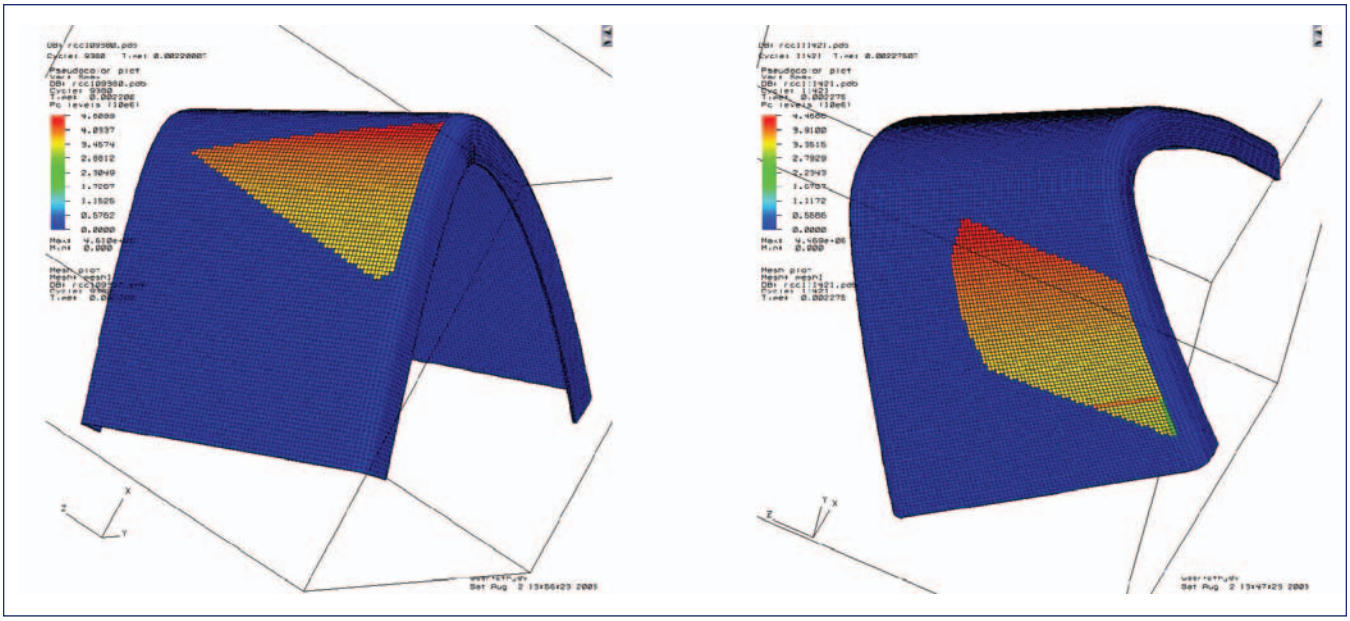


Figure 24. Footprints of impacts against RCC Panel #6 (left) and RCC Panel #8 (right).

Two panels were modeled, Panel #6 and Panel #8. Both were modeled in a similar fashion. The zoning was 4 zones through the thickness of the panel, 100 zones from side to side, including ribs, and 200 zones from bottom to top. In addition, the bottom flange was modeled for both, with 4 zones through the flange and the appropriate connections with the panel. For the connection of the panel with the ribs, a smooth transition from panel to rib was made with a radius of curvature of 0.8" for Panel #6 and 1.0" for Panel #8.

As to geometric details of the two panels, both were constructed taking two curves from the Pro-E model delivered to SwRI by Jim Hyde in May, 2003. The coordinate system in the file is what was used in the computations, which the author is told are in the "Wing Coordinate" system. The curves defined the inboard and outboard edges of the panel geometry. Measurements were then taken from the panels when they were on hand at SwRI to determine the various thicknesses, and these thicknesses were then used in the model. In particular, the thickness of the panel, ribs, and flange for Panel #6 was 6.7 mm, as measured from RCC Panel #6. This value compares to the stated value of 0.233" (5.9 mm) according to Boeing supplied information. For RCC Panel #8, the thickness of the principal part of the panel was again 6.7 mm, with the ribs after the curve 9.5 mm and the flange 8.0 mm. Also, for the lower portion of Panel #8 there is a doubler that increased the thickness of panel on the lower panel face from 6.7 mm to 8.0 mm. Again, these values are based upon measurements taken from RCC Panel #8 while at SwRI.

To approximate the boundary conditions, the bottom of the rib on both the upwind side and the downwind side and above the wing and below the wing were pinned so that they could not move.

Diagnostics taken from each computation were the maximum principal stress in the panel face, the maximum principal stress in the rib, the total load, and the maximum displacement anywhere on the whole panel and the maximum velocity anywhere on the panel (though these tended to be near the center of loading on the panel face). All the stresses through the thickness of the panel were included; for example, the maximum principal stress on the panel face was typically on the back face (wing interior) of the panel. In computing the maximum principal stress for the panel face, the region considered did not include the flange connection, as large stresses sometimes arose there due to boundary condition behavior that is not representative of the panel face. Also, the maximum principal stress in the rib was measured away from the pinned ends, since large stresses arose at the connections that are not representative of the actual boundary conditions at the rib. The actual boundary condition in the test fixture and on the Orbiter has more slop.

The reference frame of the panel was taken to be the same as that supplied in the initial Pro-E file. Thus, the angles discussed below should be the same as those used during the testing program. The z-axis goes from the front to back of the Orbiter, the y-axis from the bottom to top of the Orbiter, and the x-axis is perpendicular to the y- and z-axes and runs in the lateral direction. The direction of travel of the foam impactor when it impacts the RCC panel is determined by the angles α and β: α is the angle between the z-axis and the foam impactor velocity vector in the y-z plane (or the difference from a right angle between the velocity vector and the y-axis in the y-z plane) and β is the angle between the foam impactor velocity vector and the z-axis in the x-z plane (or the difference from a right angle between the velocity vector and the x-axis in the x-z plane). Thus, the direction α=0, β=0 is the negative z-axis direction: that is, the foam impactor is traveling directly along the main Orbiter axis from the front of the vehicle to the back. β positive means the velocity vector is pointing away from the center of the vehicle and α positive means the velocity vector is pointing from the bottom to the top of the vehicle (these qualitative statements are for small angles). Thus, positive α means that the foam impactor is hitting the underside of the leading edge at a steeper angle, and positive β means that the foam is traveling away from the centerline of the Orbiter when it impacts the leading edge. Increasing α increases the impact angle. Unfortunately, the angle β's influence is more complicated and ties into the impact geometry, the shape and orientation of the foam, where the foam impacts with regard to the curved leading edge and the path the foam takes (needed for computing an "average" impact angle). In general, increasing β tends to increase (in an integrated average sense) the impact angle.

Overview of RCC Panel Impact Computations

Results of twenty-one computations of impacts of foam against RCC panels will be presented. For discussion purposes, it seems that presenting the modeling of the two tests allows the best explanation of the results of the computations and their interpretation. After the comparisons with the two test cases are presented, calculations will be described that examined the role of impact location, impactor rotational velocity, and impact angle.

Impact on Panel #6 for Test Impact Condition

During the testing program, one impact was performed on RCC Panel #6. The impact conditions were a foam impactor of dimensions 21.4" × 11.6" × 5.6" (all impact computations into RCC panels in this report have these dimensions), flying at 768 ft/s and impacting at an angle of α=5.5°, β=2.5°. The impact location was 18.7" from the bottom of the panel at the carrier panel interface and 0.83" aft of the 5-6 T-seal. These impact conditions were replicated in a computation in the model that was run to 5 ms after impact.

Figure 25 shows some stills from the computation. In the figure, the outline of the foam impactor as if it did not deform is shown (though the boundary pressures are provided analytically, as described above). All figures of the panel computations were made with Lawrence Livermore National Laboratory's MeshTV software. The panel is shaded to show the maximum principal stress at the given surface – that is, when looking on the outer panel face, the maximum principal stress in the outer layer of cells will be used, while looking at the inner surface of the panel face, the stresses from the innermost layer of cells will be used. The scale changes for each frame in the figure.

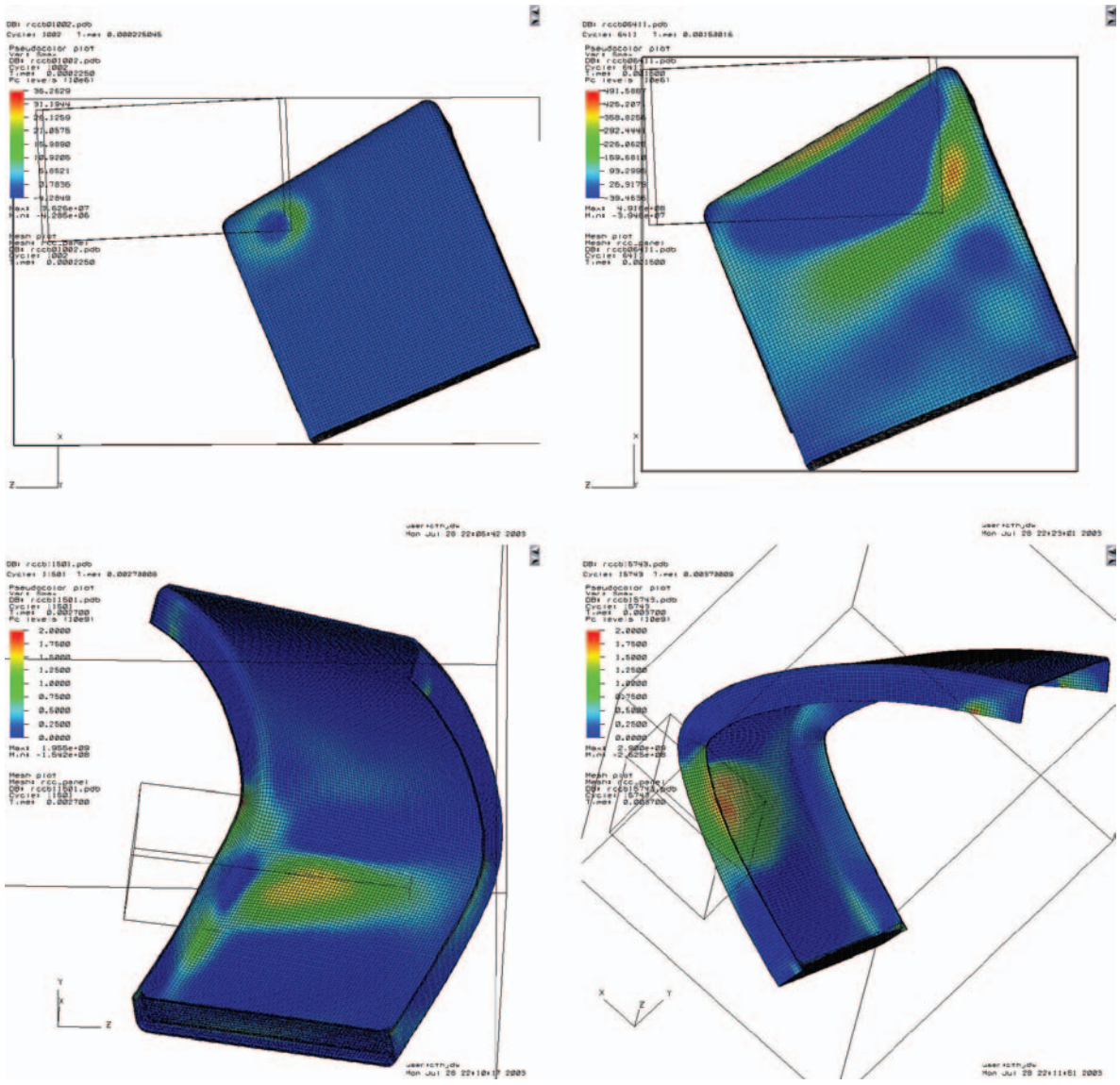


Figure 25. Four frames of the RCC Panel #6 test condition calculation (α=5.5°, β=2.5°, 768 ft/s), at 0.225, 1.5, 2.7 and 3.7 ms. The 2.7 ms frame is where the peak rib stress is achieved near the greatest curvature of the rib; the 3.7 ms frame is where the outward flexing of the rib achieves the greatest stress.

RCC Panel #6 768 ft/s (234 m/s) α=5.5°, β=2.5° 18.7" up from carrier panel 0.83" from 5-6 T-seal 0° clocking angle	Load: 5850 lb (2.60×10⁹ dynes) Panel stress: 26.8 ksi (185 MPa) Rib stress: 29.2 ksi (201 MPa) Displacement: 1.2 in (30 mm) Velocity: 102 ft/s (31.2 m/s)
RCC Panel #8 777 ft/s (237 m/s) α=5.5°, β=5.0° 25.5" up from carrier panel 7.3" from 7-8 T-seal 30° clocking angle	Load: 9150 lb (4.07×10⁹ dynes) Panel stress: 43.2 ksi (298 MPa) Rib stress: 33.4 ksi (230 MPa) Displacement: 2.5 in (63 mm) Velocity: 137 ft/s (41.8 m/s)
(Option #3 – test condition)	

Table 8. Summary of Results of Test Conditions' Calculations.

Figure 26 shows the maximum principal stress seen in both the panel and the rib as a function of time as well as the load as a function of time. The left hand scale is in metric units for both the load and stresses. The right hand scale is in English units and applies to the stresses. The undulating behavior seen in the maximum principal stress curves is due to the fact that these curves are the maximum of many curves, one for each computational cell. Thus, as one maximum principal stress curve decreases, another increases and overtakes the original maximum principal stress cell, thus becoming the maximum principle stress cell itself. It can be seen that both the maximum principal stress in the rib and in the panel face are still increasing when the load decreases, thus showing that inertia plays an important role in the impact event. Finally, Figure 27 shows the maximum displacement and the maximum velocity seen on the panel during the impact event. Table 8 summarizes the historical maximums.

As was mentioned above, panel deformation affects panel loading. The panel is both deformed in shaped and is in motion, both aspects of which affect the local impact velocity, hence loading pressure, due to the foam impactor. The maximum average surface-normal component of the panel velocity over the loading area was 29 ft/s (8.9 m/s). This local velocity decreases the impact speed since the panel is being moved in the direction of travel of the foam impactor, thus decreasing the pressure load. However, the deformation of the panel led to an area-averaged angle of 20.1°, an increase over the 19.7° as would have been the case for the rigid panel. Because of the panel's deformed shape and higher angle than the rigid panel, the relative impact velocity increases (in average) to 264 ft/s (80.5 m/s) over the 259 ft/s (78.9 m/s) for the rigid panel, or an average increase of 5 ft/s. The deformed shape of the panel tends to increase the impact angle and thus increase the local pressure and the load delivered by the foam. However, since the area-averaged surface-normal velocity component at which the panel is moving away from the impactor is 29 ft/s, this overcomes the 5 ft/s increase in impact velocity due to increase in angle. Thus, overall, the load is less for the deforming panel than it would be for a rigid panel. On average, the pressure load (at maximum) for

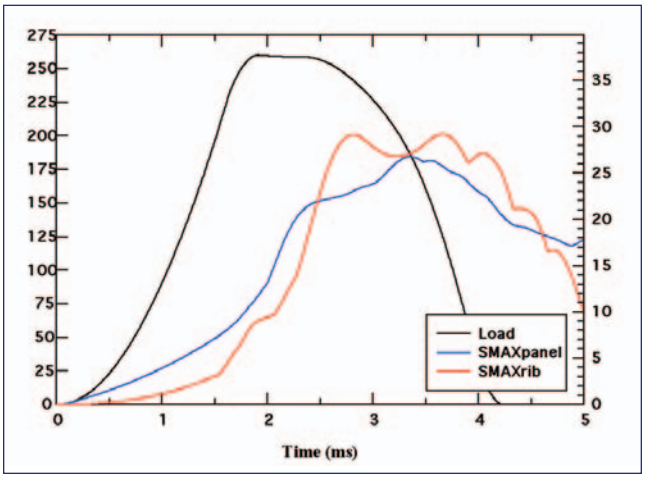


Figure 26. Load and maximum principal stress for panel face and rib vs. time for RCC Panel #6 test condition computation (α=5.5°, β=2.5°, 768 ft/s).

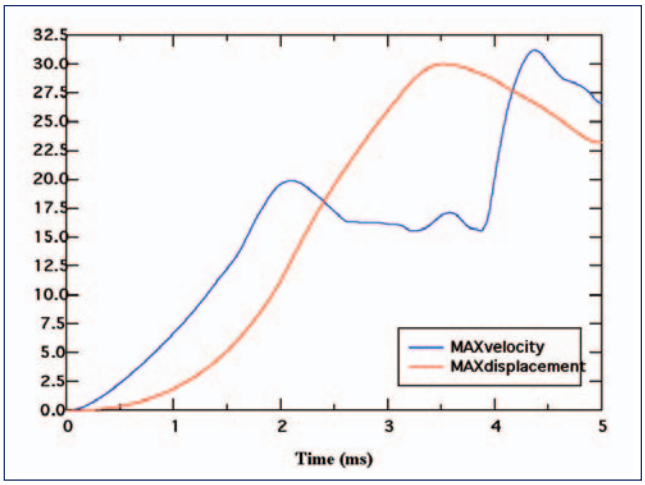


Figure 27. Maximum velocity and maximum displacement vs. time for RCC Panel #6 test condition computation (α=5.5°, β=2.5°, 768 ft/s).

the deforming panel is 53.0 psi (366 kPa) while for the rigid panel it would have been 55.6 psi (384 kPa). This reduction is reflected in the maximum load in Table 8 versus the number given above for the rigid panel – a reduction of about 5%.

As has been described, these computations are purely elastic, with no failure criteria. Thus, now it becomes necessary to interpret this computation in the context of the failure that occurred. Once failure occurs, the history of the stresses will change, and thus it is not possible to draw conclusions based on the behavior of the elastic calculations after the failure. As the RCC material is quite brittle, the use of the maximum principal tensile stress seems an appropriate failure measure.

In the test, the downwind rib broke, approximately 50 cm from the carrier panel. The crack ran, turning the corner slightly so that a small crack could be seen on the panel face.

If one reasons that a higher failure stress is expected in the panel (since there are no boundaries) than in the rib (since the rib has an edge where presumably there are many fracture initiation sites), then no rigorous information can be obtained from Figure 26. (If it were assumed that the maximum failure stress is the same in the panel face and the rib, then it could be concluded that the minimum maximum principal stress the RCC material can support is 21.9 ksi (151 MPa), the value of the maximum principal stress when the two curves of Figure 26 cross at 2.47 ms). However, we know that at some time the rib broke, and that this point was after some load had accrued. Looking at the curves, at early time the maximum principal stress in the panel is significantly above the maximum principal stress in the rib. Thus, it is likely that the failure occurred at a later time, probably in the vicinity of the larger stress observed, 2.7-3.7 ms. The mechanics of the larger stresses are as follows. As the foam impact loads the panels, a large tensile stress is created near the largest curvature of the outer edge of the rib (see Figure 25 at 2.7 ms). The location of this large maximum principal stress is approximately 55 cm from the carrier panel. The maximum principal stress in the rib is at

this location from roughly 2.3 to 3.9 ms. Though the load reaches its maximum and then decreases, the stresses in the panel face and rib are still high or increasing. The loading becomes such that it causes an elastic buckling motion of the rib, so that the downwind rib (the rib next to the 6-7 T-seal) flexes outward (downwind). The flexing motion leads to large tensile stresses on the outside of the rib (Figure 25 at 3.7 ms), and for the period of 3.9 to 4.3 ms these are the large tensile stresses in the rib. The maximum value of the stress occurs about 42 cm from the carrier panel. As the load continues to drop while the foam impactor leaves the panel face, the buckling motion ceases, the rib straightens out and the region of the maximum tensile stresses return to the area near the largest curvature of the rib.

The interpretation now focuses on the time in this loading history that the rib broke. It is likely that it happened later in the loading process, perhaps at 3.7 ms, since the crack does not propagate very far in the face of the panel. The lack of crack propagation in the face of the panel implies that the load to the panel was decreasing when the fracture occurred. This reasoning implies that the rib fails at a maximum principal stress in the vicinity of 29 ksi (200 MPa), perhaps after some loading time (some damage theories hold that a tensile stress state must exceed a given value for a given length of time before failure occurs). This reasoning also implies that the panel face can support a 27 ksi (185 MPa) maximum principal stress.

Impact on Panel #8 for Test Impact Condition

A computation was performed for the impact test conditions on the Panel #8 impact, where the angles were α=5.5°, β=5.0°, with an impact speed of 777 ft/s (237 m/s). The geometry of Panel #8 is more complicated, as there are various thicknesses of RCC in the panel as described above.

In the test, the panel face failed, and a large hole was produced. An additional conclusion from the test is that it is likely the failure occurred at 2.7 ms or later due to the fact that half the foam impactor survived the impact. In the fiberglass tests and the RCC Panel #6 test, the foam impactor completely disintegrated, apparently due to the foam catching on the 6-7 T-seal. In the RCC Panel #8 test, the foam impactor is lifting off the panel (ricocheting due to the arrival of rarefaction waves) just before the 8-9 T-seal, but when the panel breaks the foam catches on the hole edge that is formed. Thus, examining the time sequence of impact from the computation, it is conjectured that the failure probably occurred (assuming it started near the 8-9 T-seal or near the downwind rib) around 2.7 ms.

Figure 28 shows the maximum principal stress in the panel interior versus time, as well as the maximum stress observed in the thick portion of the rib (the dotted portion of the maximum principal stress for the rib includes only the thicker part of the rib). In this test, the thick portion of the rib did not fail, whereas the panel face did. At 2.7 ms, the maximum principal stress in the panel face was 30.0 ksi (207 MPa) and in the panel rib was 25.4 ksi (175 MPa). Based on the results of the RCC Panel #6 test, these seem to be reasonable stresses for the failure. Once a crack forms, it runs quickly leading to extensive failure. Such failure was seen in the panel face. With failure of the face occurring around 2.7 ms, the load being transferred to the rib would reduce, and the stresses in the rib would decrease. This last statement is qualitative: there are inertial effects still, and so the stress could increase for a while. To quantitatively examine the histories beyond failure requires a failure model.

As with the RCC Panel #6 test conditions computation, panel deformation affected panel loading. The maximum average surface-normal component of the panel velocity over the loading area was 74 ft/s (23 m/s). This local velocity decreases the impact speed since the panel is being moved in the direction of travel of the foam impactor, thus decreasing the pressure load. However, the deformation of the panel led to an area-averaged angle of 19.9°, an increase over the 17.5° as would have been the case for the rigid panel. Because of the panel's deformed shape and higher angle than the rigid panel, the relative impact velocity increases (in average) to 264 ft/s (80.5 m/s) over the 234 ft/s (71.2 m/s) for the rigid panel, or an average increase of 30 ft/s. Since the area-averaged surface-normal velocity component at which the panel is moving away from the impactor is 74 ft/s, this overcomes the 30 ft/s increase in impact velocity due to increase in angle. Thus, overall, the load for the deforming panel is less

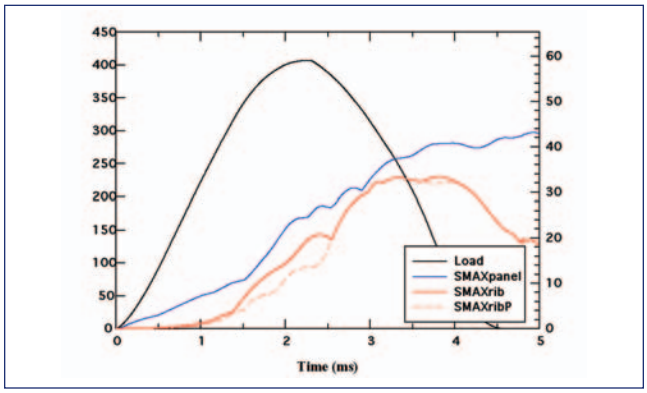


Figure 28. Load and maximum principal stress for panel face and rib vs. time for RCC Panel #8 test condition computation (α=5.5°, β=5.0°, 777 ft/s).

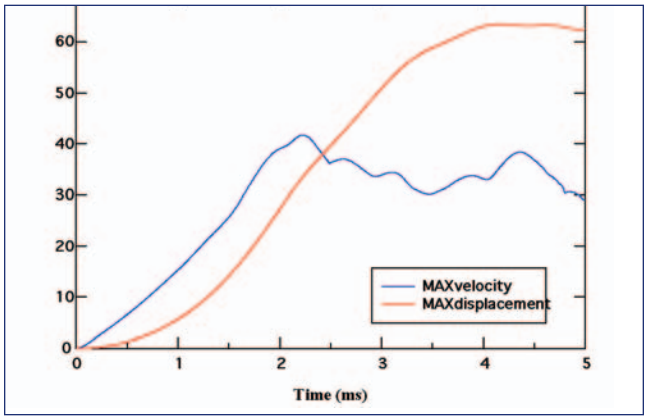


Figure 29. Maximum velocity and maximum displacement vs. time for RCC Panel #8 test condition computation (α=5.5°, β=5.0°, 777 ft/s).

than it would be for a rigid panel. On average, the pressure load (at maximum) for the deforming panel is 47.7 psi (329 kPa) while for the rigid panel it would have been 52.9 psi (365 kPa). (These pressures are lower than they were for the corresponding RCC Panel #6 test condition case above because the average impact angle is less.) This reduction is reflected in the maximum load in Table 8 versus the number given above for the rigid panel – a reduction of about 10%.

In summary, for the two impact tests performed, for the numerical model developed here, large cracks form in the vicinity of 28 to 30 ksi for the panel face and for the rib. These stresses correspond to roughly 1% strain in the material. These tensile stresses leading to cracks are viewed as being consistent within this model for analyzing the additional cases to be run. They are understood in the context of the two main assumptions made for this modeling: the isotropic elastic constitutive model and the analytic boundary condition, which is an upper bound.

Impact Location Study

One topic of interest was the effect of impact location on the load and stress seen by the panel. To explore this effect with the numerical model, a study of nine impact locations on RCC Panel #6 was performed with the impact velocity vector aligning itself with the Orbiter's z-axis (i.e., α=0°, β=0°). The impact speed was 768 ft/s. The nine impact locations considered were variations of the impact location used in the RCC Panel #6 test with combinations of 3" and 6" down from the original impact point and 3" and 6" across from the original impact point.

Table 9 shows the maximum stresses seen in the panel interior and the rib for each impact case as well as the maximum load. The largest stresses are seen for the lowest and most upwind location on the panel. It can be seen that these values are large enough to assume the rib would fracture. It is interesting to note that the largest loads did not produce the

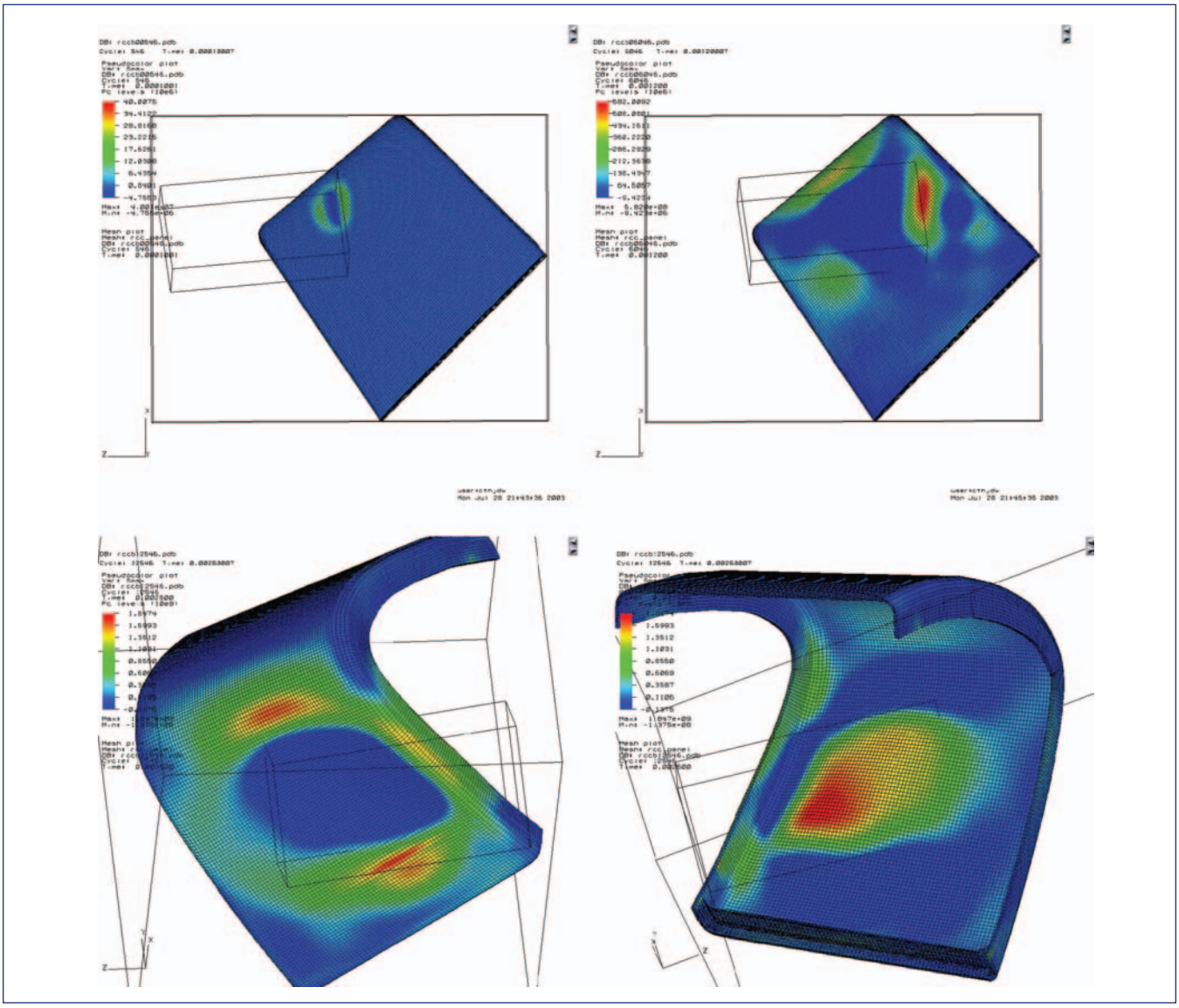


Figure 30. Four frames of the RCC Panel #8 test condition calculation (α=5.5°, β=5.0°, 777 ft/s), at 0.1, 1.2, 2.5 (front face) and 2.5 (back face) ms (the last two frames are probably near the failure time of the panel).

	0.83″ from T-seal	*3.83″ from T-seal*	*6.83″ from T-seal*
18.7″ from carrier panel	Load: 4680 lb Panel stress: 24.5 ksi Rib stress: 24.4 ksi	Load: 3330 lb Panel stress: 18.3 ksi Rib stress: 19.8 ksi	Load: 2150 lb Panel stress: 9.6 ksi Rib stress: 14.0 ksi
15.7″ from carrier panel	Load: 4320 lb Panel stress: 25.8 ksi Rib stress: 27.5 ksi	Load: 3090 lb Panel stress: 21.9 ksi Rib stress: 20.6 ksi	Load: 2030 lb Panel stress: 15.5 ksi Rib stress: 13.6 ksi
12.7″ from carrier panel	Load: 4290 lb Panel stress: 26.9 ksi Rib stress: 30.1 ksi	Load: 3040 lb Panel stress: 22.9 ksi Rib stress: 21.7 ksi	Load: 2000 lb Panel stress: 18.3 ksi Rib stress: 15.3 ksi

Table 9. Maximum Values for Load, Panel Stress and Rib Stress for Various Hit Locations (RCC Panel #6, α=0°, β=0°, 768 ft/s).

largest maximum principal stresses in the rib or panel face. This result is due to the fact that the largest loads occur when the foam impactor has the largest angle where it is impacting the panel. However, the large angle is on the curved portion of the panel, where the curvature of the panel allows the membrane stresses to support some of the load. (This support behavior is the cause of the surprising load supporting ability of shells, such as domes.) The higher loading pressures are occurring in a region of the panel where the geometry has curvature and is thus more able to support the load. As the impact point moves down the panel face into the flatter region of the panel, the loads decrease because the angle is decreasing and thus the loading pressure is decreasing. However, the ability of the panel to support the loads through curved (shell) geometry decreases as the flatter region of the panel is now being impacted, and the net result is larger stresses in both the panel face and the rib.

As a reference, results from the baseline impact (the same impact location as the RCC Panel #6 test but with α=0°, β=0°) are presented. Figure 31 shows stills of maximum principal stress at four times: 0.2, 1.2, 2.5 and 3.5 ms. Figure 32 shows the stress history of the panel, and Figure 33 the maximum velocity and displacement. The same three-hump behavior can be seen in the rib stress as was observed in the actual test condition calculation, due to loading near the maximum curvature and then a downwind buckling type flexure of the rib. As the impact continues, the load from the foam projectile decreases as the loading area decreases as the foam continues to travel, and the buckling motion is relieved, and the rib straightens out. This places high stresses at the top of the arch, which are the high stresses seen in the 4 to 4.5 ms time frame in the stress history plot. The stress upon release of the buckling is especially high for the maximum stress case (impact point at 0.83" from 5-6 T-seal, 12.7" up from carrier panel) and is shown in Figs. 34 and 35. Though the maximum stress in the rib is a little higher in the earlier impact times (2-4 ms), it is the large peak upon the straightening of the rib between 4 and 5 ms that puts the maximum principal stress over 30 ksi (207 MPa). The impact location with the most severe stresses increased the maximum panel face stress by 10% and the maximum rib stress by 23% over the baseline.

Similarly, two impact conditions for RCC Panel #8 were considered, referred to as "Option #3" and "Option #2" during the RCC Panel #8 test design. "Option #3" was chosen for the actual test that was performed. "Option #2" is essentially a 3" shift towards the 7-8 T-seal. Based on the results outlined above for Panel #6 it is expected that "Option #2" would have higher loads due to the larger loading footprint and larger stresses. Table 10 shows the results: as expected, shifting upwind does increase the load on the panel as well as the maximum principal stresses seen in the panel face and in the rib. Thus, the impact point chosen ("Option #3) was less severe than Option #2. In both cases fracture of the panel face would be expected. Figures 36-37 show the various results from the "Option #2" RCC Panel #8 calculation. Based on the stress histories, the panel face would be expected to fail.

Effect of Rotation of Foam Impactor Study

As with the foam insulation impact on tile, there was concern about the effect of the foam impactor having a rotational velocity and how that might affect the impact. To explore the effect of rotation, a series of six computations were performed where the foam impactor had a rotational velocity about one of its major axes, either clockwise or counterclockwise, with a frequency of 18 Hz. Figure 38 shows the various foam orientations and defines the clockwise/counter-clockwise orientation for the results table: the axis of rotation is in the center of the foam and is coming directly out of the page. Clockwise and counterclockwise is defined according to these figures.

The computations were performed with the initial alignment of the Orbiter's *z*-axis (i.e., α=0°, β=0°). The impact speed was 768 ft/s. The impact location was the same as the baseline case in the impact location study, namely the upper left corner case, with the point be 18.7" up from the carrier panel and 0.83" from the 5-6 T-seal. Table 11 shows the maximum values of the load, the maximum principal

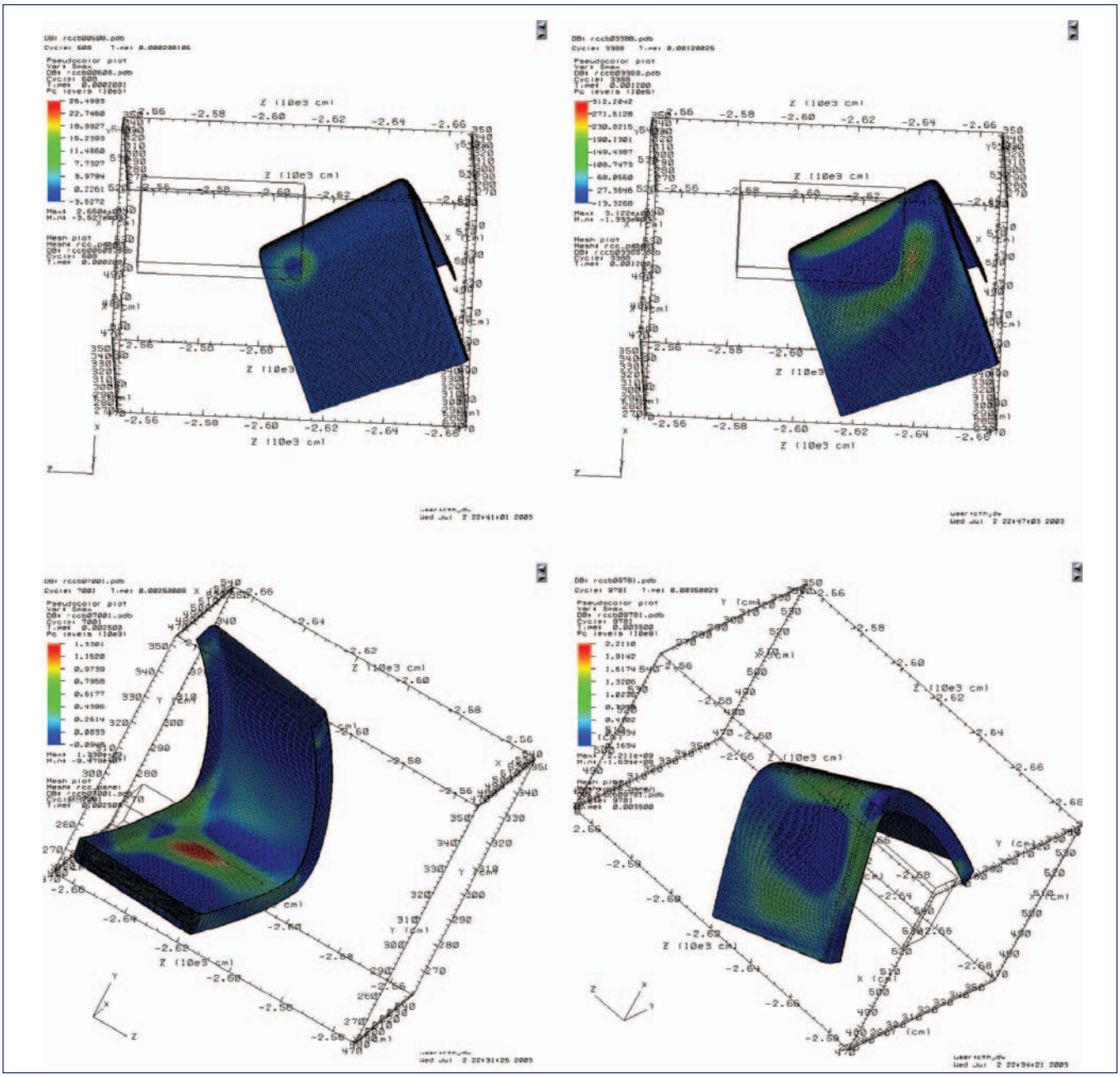


Figure 31. Four frames of the RCC Panel #6 baseline case computation (α=0°, β=0°, 768 ft/s), at 0.2, 1.2, 2.5 and 3.5 ms.

"Option #3" – test condition 25.5" up from carrier panel 7.3" from 7-8 T-seal	Load: 9150 lb (4.07×10⁹ dynes) Panel stress: 43.2 ksi (298 MPa) Rib stress: 33.4 ksi (230 MPa) Displacement: 2.5 in (63 mm) Velocity: 137 ft/s (41.8 m/s)
"Option #2" – not used 25.2" up from carrier panel 4.3" from 7-8 T-seal	Load: 9760 lb (4.34×10⁹ dynes) Panel stress: 48.8 ksi (336 MPa) Rib stress: 35.7 ksi (246 MPa) Displacement: 2.8 in (72 mm) Velocity: 150 ft/s (45.6 m/s)

Table 10. Impact Location Study for RCC Panel #8 (α=5.5°, β=5.0°, 777 ft/s, 30° Clocking Angle).

stress in the panel and the maximum principal stress in the rib over the time from 0 to 5 ms. An immediate conclusion of the computations is that almost all rotational cases lead to larger stresses: only the counterclockwise rotation around the *z*-axis had less load and less stress, but even there, it was not significantly less. Thus, rotation does increase the load delivered to the panel and it increases the stress seen in the panel face and in the rib. The largest load and stresses are seen with the clockwise rotation about the *x*-axis. Stills from this impact are shown in Figure 39, and the various histories are shown in Figs. 40 and 41. The load is increased over the baseline by 32%, the maximum stress in the panel interior by 8% and the maximum principal stress in the rib by 25%. Based on the results of the tests, the rib would be expected to break during this impact.

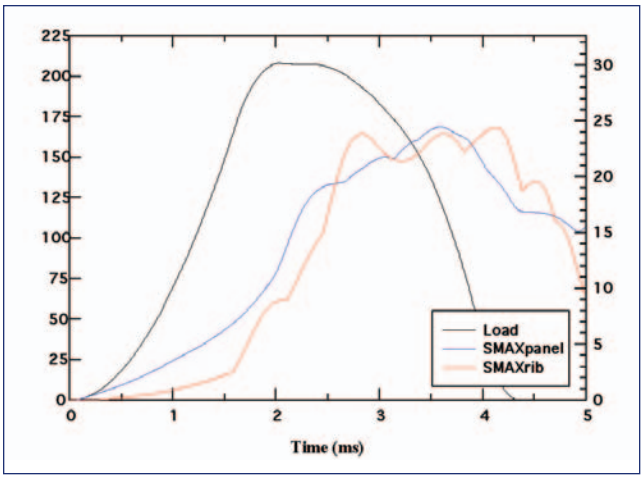


Figure 32. Load and maximum principal stress for panel face and rib vs. time for RCC Panel #6 baseline case computation (α=0°, β=0°, 768 ft/s, 0.83" from 5-6 T-seal, 18.7" up from carrier panel).

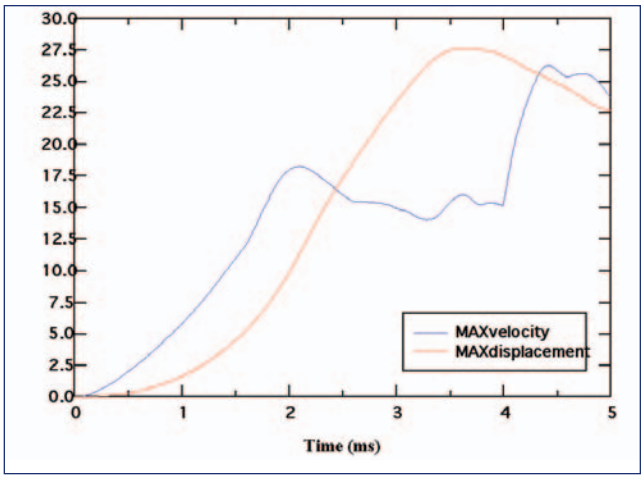


Figure 33. Maximum velocity and maximum displacement vs. time for RCC Panel #6 baseline case computation (α=0°, β=0°, 768 ft/s, 0.83" from 5-6 T-seal, 18.7" up from carrier panel).

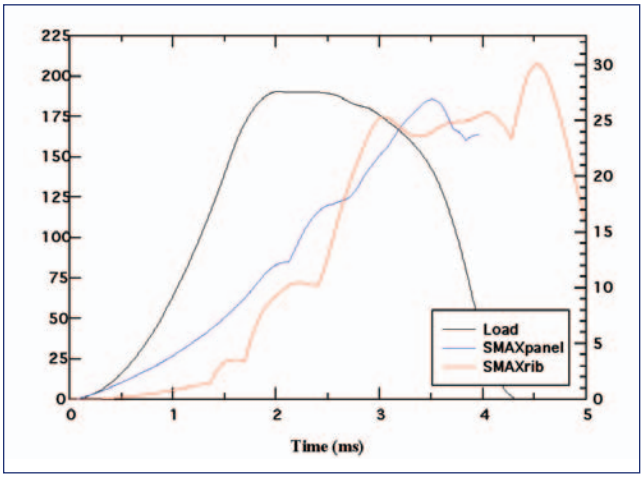


Figure 34. Load and maximum principal stress for panel face and rib vs. time for RCC Panel #6 hit location study maximum stress case (α=0°, β=0°, 768 ft/s, 0.83" from 5-6 T-seal, 12.7" from carrier panel).

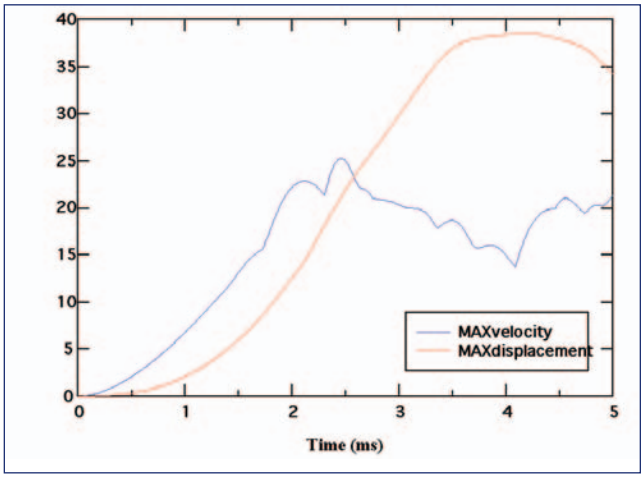


Figure 35. Maximum velocity and displacement vs. time for RCC Panel #6 hit location study maximum stress case (α=0°, β=0°, 768 ft/s, 0.83" from 5-6 T-seal, 12.7" up from carrier panel).

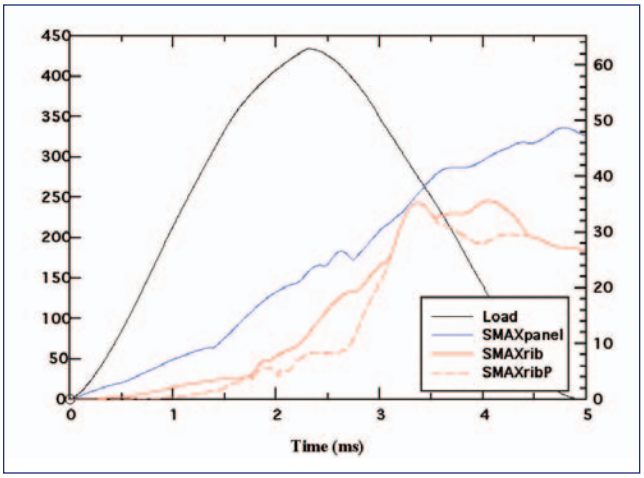


Figure 36. Load and maximum principal stress for panel face and rib vs. time for RCC Panel #8 "Option #2" (α=5.5°, β=5.0°, 777 ft/s).

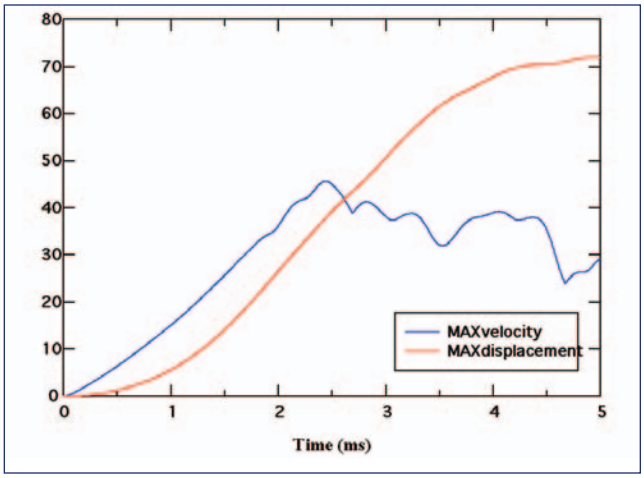
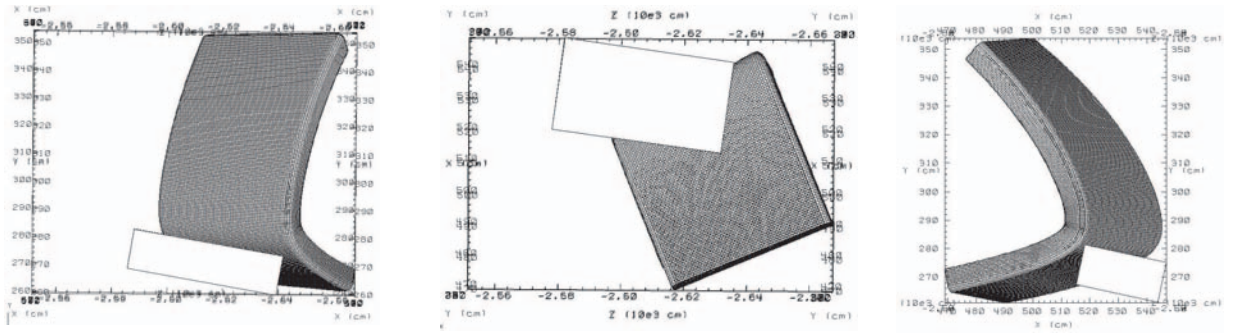


Figure 37. Maximum velocity and displacement vs. time for RCC Panel #8 "Option #2" (α=5.5°, β=5.0°, 777 ft/s).



x-axis (from side of Orbiter, looking directly into center). *y-axis (from bottom to top of Orbiter).* *z-axis (from front of Orbiter to back).*

Figure 38. The three major axes of the foam impactor in Wing Coordinates. The rotational axis is in the geometric center of the presented face of the foam impactor and is coming out of the page. Rotation direction, clockwise and counterclockwise, are defined by these figures (looking down).

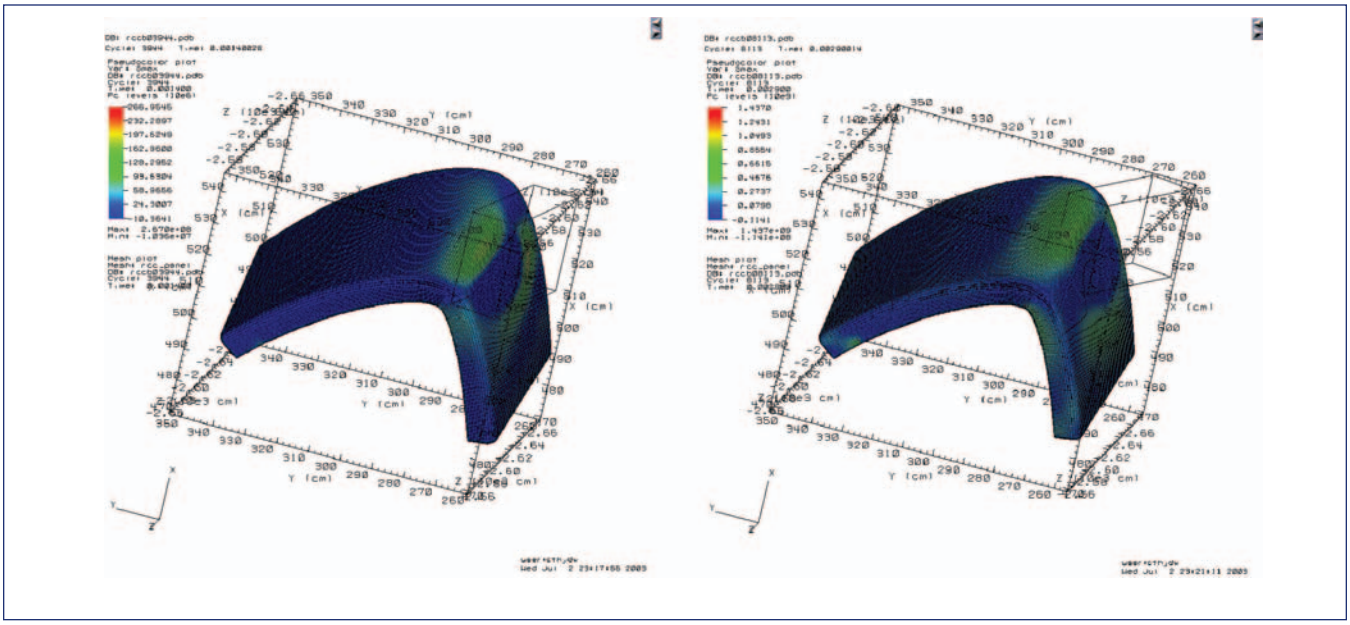


Figure 39. Two frames of the RCC Panel #6 clockwise rotation about x-axis case computation (α=0°, β=0°, 768 ft/s, 18 Hz), at 1.6 (left) and 2.9 (right) ms.

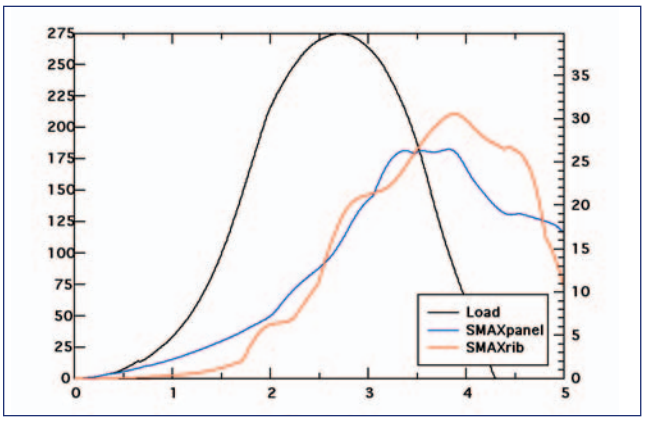


Figure 40. Load and maximum principal stress for panel face and rib vs. time for RCC Panel #6 clockwise rotation about x-axis case (α=0°, β=0°, 768 ft/s, 18 Hz).

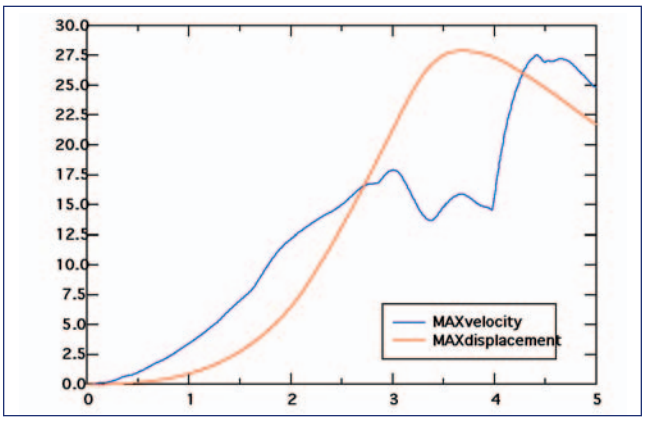


Figure 41. Maximum velocity and displacement vs. time for RCC Panel #6 clockwise rotation about x-axis case (α=0°, β=0°, 768 ft/s, 18 Hz).

Combination of Impactor Rotation and Impact Location

What would be the result of combining the lower impact location with the foam impactor rotation that led to the highest stresses (clockwise about the x-axis)? When these two states were combined, the resulting impact produced even larger loads and stresses as is seen in Table 12 (all save the lower right hand corner have appeared in previous tables). The increase in load over the baseline is 39% and the increase in the stress in the panel face is 36% and in the rib is 61%. Figure 42 shows two stills from the computation, and Figs. 43 and 44 show the various histories. Based on the stress history, it is expected that the panel face would fail.

Axis	*Clockwise*	*Counterclockwise*
x	Load: 6180 lb Panel stress: 26.5 ksi Rib stress: 30.6 ksi	Load: 5380 lb Panel stress: 24.0 ksi Rib stress: 27.6 ksi
y	Load: 4730 lb Panel stress: 24.6 ksi Rib stress: 26.1 ksi	Load: 4890 lb Panel stress: 26.0 ksi Rib stress: 28.8 ksi
z	Load: 5080 lb Panel stress: 26.3 ksi Rib stress: 26.0 ksi	Load: 4250 lb Panel stress: 21.6 ksi Rib stress: 24.4 ksi

Table 11. Results for Rotations about Various Axes. (RCC Panel #6, Baseline Impact Location, α=0°, β=0°, 768 ft/s, 18 Hz Rotation Rate).

Influence of Impact Angle: Increasing α

To study the effect of increasing the impact angle, two additional computations were performed where the angle α was altered. Increasing α increases the angle at which the foam impact strikes the underside of the leading edge: thus, increasing α increases the load delivered to the panel. The results of these computations are shown in Table 13. The table also includes two previous computations for comparison, namely the α=0°, β=0° case that is the baseline for the parameter studies above as well as the actual impact test condition case, where α=5.5°, β=2.5°. All impacts were at 768 ft/s. The impact point for all four was 18.7" above the carrier panel and 0.83" downwind from the 5-6 T-seal. As can be seen from the table, increasing α from 0° to 5.5° increased the load by 35%, increased the panel face stress by 17% and increased the rib stress by 26%. These changes are similar to those produced by the *x*-axis clockwise rotation case, which was the worst case in terms of increasing maximum principal stress in the rib and panel interior. Though not everything is the same, it appears that increasing the impact angle by increasing α on the order of 5° is a reasonable approach to experimentally adjusting for the rotating impactor. A detailed match as was produced for the rotating impact against tile would require a damage model for the RCC, so that the failure process could be matched, as loads are affected by failure, when it occurs and how it progresses.

	No Rotation	*18 Hz Rotation – Clockwise about x-axis*
Baseline impact location 18.7" up from carrier panel 0.83" right of 5-6 T-seal	Load: 4680 lb Panel stress: 24.5 ksi Rib stress: 24.4 ksi	Load: 6180 lb Panel stress: 26.5 ksi Rib stress: 30.6 ksi
Lower impact location 12.7" up from carrier panel 0.83" right of 5-6 T-seal	Load: 4290 lb Panel stress: 26.9 ksi Rib stress: 30.1 ksi	Load: 6510 lb Panel stress: 33.3 ksi Rib stress: 39.3 ksi

Table 12. Combining Most Severe Impact Location and Impactor Rotation (RCC Panel #6, α=0°, β=0°, 768 ft/s).

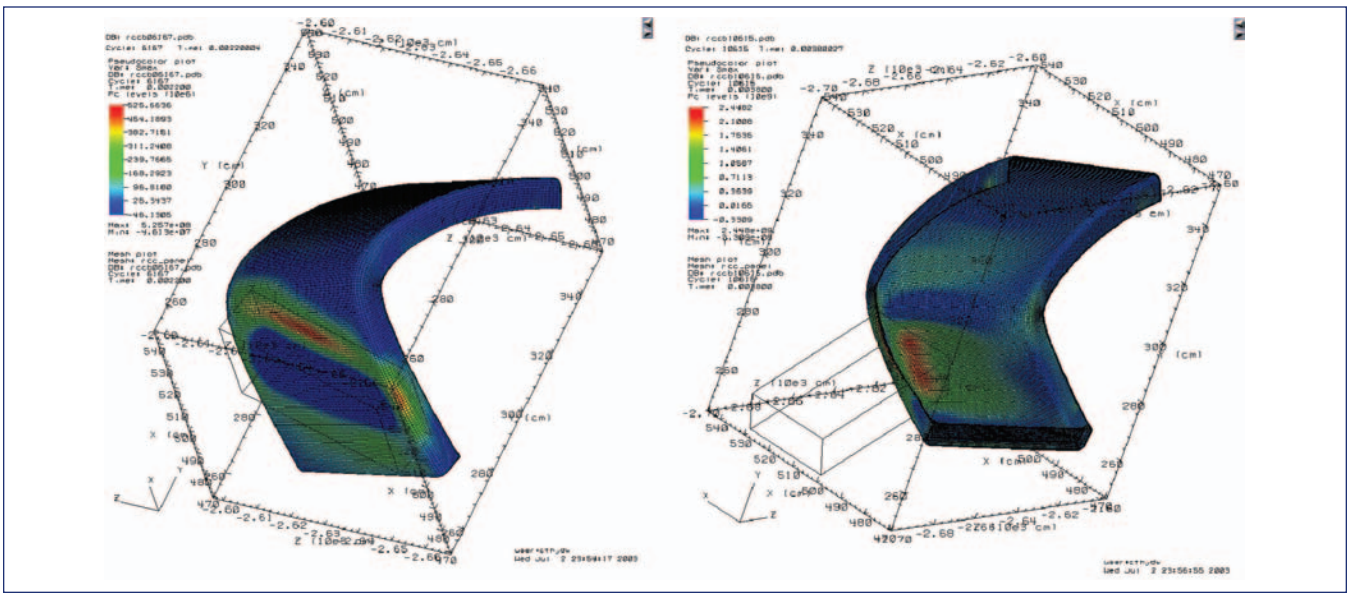


Figure 42. 18 Hz clockwise rotation about x-axis with lower impact point, maximum principal stress at 2.2 (left) and 3.8 (right) ms.

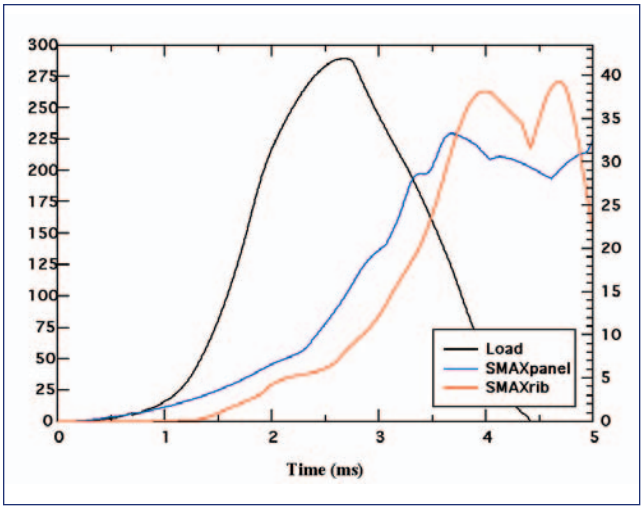


Figure 43. Load and maximum principal stress for panel face and rib vs. time for RCC Panel #6 lower impact point with clockwise rotation about x-axis case (α=0°, β=0°, 768 ft/s, 18 Hz).

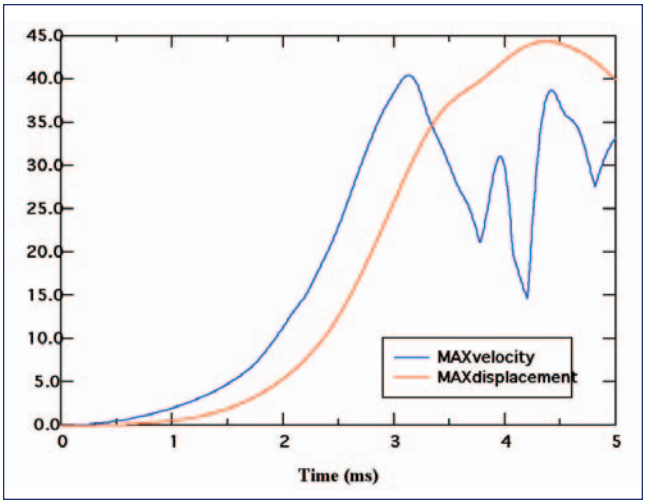


Figure 44. Maximum velocity and displacement vs. time for RCC Panel #6 lower impact point with clockwise rotation about x-axis case (α=0°, β=0°, 768 ft/s, 18 Hz).

α	β	
0°	0°	Load: 4680 lb Panel stress: 24.5 ksi Rib stress: 24.4 ksi
2.25°	0°	Load: 5340 lb Panel stress: 25.9 ksi Rib stress: 26.8 ksi
5.5°	0°	Load: 6300 lb Panel stress: 28.6 ksi Rib stress: 30.7 ksi
5.5°	2.5°	Load: 5850 lb Panel stress: 26.8 ksi Rib stress: 29.2 ksi

Table 13. Results of Various Impact Angle Calculations (RCC Panel #6, Baseline Impact Location, 768 ft/s).

Summary of RCC Computations

Table 14 on the next page summarizes the RCC Panel computations.

Summary

Impact modeling in support of the Columbia Accident Investigation has been performed. It has been shown that for foam insulation impacts, the most important parameter is the component of the velocity vector that is normal to the surface being impacted. This realization allowed the development of a theoretical damage/no damage transition curve for foam insulation impacts against thermal tile. This theoretical curve agreed extremely well with large-scale numerical simulations and with experimental results. During the course of the modeling an equation of state for both the foam insulation and the thermal tiles was developed for the hydrocde CTH. These models gave excellent agreement with data and allowed computations of impacts and calculations of craters with the CTH code. The model was used to analyze the role of impactor rotational velocity, and to arrive at an equivalent impactor that could be more easily launched from the gas gun.

Foam insulation impacts on two of the RCC panels were also modeled (#6 and #8). An analytic boundary condition was developed for the foam impact on the panel. The panels were modeled as elastic, and interpretation of the stress histories was obtained by analyzing the two test cases. Further, parameter studies were carried out on RCC Panel #6 that showed that the upwind, lower on the panel face impacts were the most severe. Impact of foam impactors with rotational velocity against RCC panels was computationally analyzed. Almost all rotational states led to larger stresses in the panel face and rib. It was shown that the most severe 18 Hz rotation could be approximately modeled by increasing the α angle by roughly 5°. Thus result depends strongly on the specific impact geometry.

All in all the modeling was very successful and gave insight into the damage and failure process of thermal tiles and RCC panels under impact by foam insulation.

Acknowledgments

The author wishes to thank Art Nicholls (SwRI) for performing the compression tests on the foam and tile specimens, Erick Sagebiel and Doug McKee (both SwRI) for their assistance with the Pro-E and IGS files for the production of the RCC panel meshes, Don Grosch (SwRI) and Justin Kerr (NASA JSC) for comments, answering questions and providing information about the test geometries and conditions, and Paul Wilde (CAIB) for support and assistance.

Run #	Panel #	Impact Velocity (ft/s)	α	β	Clocking Angle	Rotation Rate (Hz)	Rotation Axis	Impact Point from Carrier Panel	Impact Point from T-seal
4	6	768	0°	0°				18.7″	0.83″
5	6	768	0°	0°				15.7″	0.83″
6	6	768	0°	0°				12.7″	0.83″
7	6	768	0°	0°				18.7″	3.83″
8	6	768	0°	0°				15.7″	3.83″
9	6	768	0°	0°				12.7″	3.83″
10	6	768	0°	0°				18.7″	6.83″
11	6	768	0°	0°				15.7″	6.83″
12	6	768	0°	0°				12.7″	6.83″
13	6	768	0°	0°		+18 (-)	x-axis	18.7″	0.83″
14	6	768	0°	0°		+18 (+)	y-axis	18.7″	0.83″
15	6	768	0°	0°		+18 (-)	z-axis	18.7″	0.83″
16	6	768	0°	0°		-18 (+)	x-axis	18.7″	0.83″
17	6	768	0°	0°		-18 (-)	y-axis	18.7″	0.83″
18	6	768	0°	0°		-18 (+)	z-axis	18.7″	0.83″
19	6	768	0°	0°		-18 (+)	x-axis	12.7″	0.83″
23	6	768	5.5°	2.5°				18.7″	0.83″
25	6	768	2.25°	0°				18.7″	0.83″
26	6	768	5.5°	0°				18.7″	0.83″
24	8	777	5.5°	5°	30°			25.2″	4.3″
27	8	777	5.5°	5°	30°			25.5″	7.3″

Table 14. Summary of RCC Panel Computations Discussed in This Report. For Rotation Rate, the leading sign is the actual sign of the component of the rotation vector; a parenthetical + sign means clockwise with respect to Figure 38 and a parenthetical - sign means counterclockwise with respect to Figure 38.

References For Appendix D.12

1. Drew L. Goodlin, "Orbiter Tile Impact Testing," Southwest Research Institute Final Report #18-7503-005 prepared for NASA JSC, San Antonio, Texas, March 5, 1999.
2. J. M. McGlaun, S. L. Thompson and M. G. Elrick, "CTH: A Three-Dimensional Shock Wave Physics Code," *International Journal Impact Engineering*, Vol. 10, pp. 351-360, 1990.
3. D. J. Grosch and J. P. Riegel, III, "Ballistic Testing of Orbiter Tiles," Southwest Research Institute Final Report #06-2720 prepared for Rockwell International, San Antonio, Texas, February 10, 1989.
4. Mark L. Wilkins, *Computer Simulation of Dynamic Phenomena*, Springer-Verlag, Berlin, 1999.

Footnotes For Appendix D.12

* All computations in this report were carried out in the metric system, in cgs. However, due to the prevalent use of English units in the Shuttle program, many of the results will be presented in English units or both systems.

* This data is included for completeness; the damage/no damage transition curve would be different for this material – see the discussion below on the effects of increasing foam density.

Volume II
Appendix D.13

STS-107 In-Flight Options Assessment

During the course of the investigation, the Board heard several NASA officials say there was nothing that could have been done to save *Columbia*'s crew, even if they had known about the damage. The Board therefore directed NASA to determine whether that opinion was valid. NASA was to design hypothetical on-orbit repair and rescue scenarios based on the premise that the wing damage events during launch were recognized early during the mission. The scenarios were to assume that a decision to repair or rescue the *Columbia* crew would be made quickly, with no regard to risk. These ground rules were not necessarily "real world," but allowed the analysis to proceed without regard to political or managerial considerations. This report is the full result of that analysis; a summary was presented in Volume I of the report.

This is a NASA document and is published here as written, without editing by the Columbia Accident Investigation Board. The conclusions drawn in this report do not necessarily reflect the conclusions of the Board; when there is a conflict, the statements in Volume I of the Columbia Accident Investigation Board Report take precedence.

Executive Summary 395

Major assumptions / Initial conditions 396

Section 1.0 Columbia Consumables (available time in orbit) 397
. 1.1 Lithium Hydroxide / CO2 removal / Crew Health 397
1.2 Oxygen 398
1.3 Food / water 398
1.4 Propellant 398

Section 2.0 Decision Path Timeline 398
2.1 Powerdown Requirements 399
2.2 Description of Leading Edge Inspection via EVA 399

Section 3.0 Rescue Mission 400
3.1 Success Criteria 400
3.2 *Atlantis* configuration on STS-107 FD 4 400
3.3 Launch Vehicle Processing Timeline 400
3.4 Flight Software 400
3.5 Mission Control Center Software 401
3.6 Crew Size / Skills 401
3.7 Crew equipment 401
3.8 Launch Window / ET disposal 401
3.9 Rendezvous / Proximity Operations 402
3.10 Rescue EVA 403
3.11 *Atlantis* Return 404
3.12 *Columbia* Disposal 404
13.13 Aggregate Risk 404
13.14 Mission Firsts 404
13.15 The Launch Decision 405

Section 4.0 Columbia repair 405
4.1 Success Criteria 405
4.2 Materials Available 405
4.3 Options Considered 405
4.4 Best Option 406
4.5 EVA Techniques 406
4.6 Wing Coldsoak 407
4.7 Additional Entry Options – the "Cain Report" 407
4.8 Uncertified Options - Increased Alpha /Low drag profile 407
4.9 Thermal Analysis 407
4.10 Bailout 408
4.10.1 *Crew cabin configuration* 408
4.10.2 *Maximum Altitude* 408

Section 5.0 Other Considerations 408
5.1 LiOH Regeneration 408
5.2 Other vehicles (Soyuz, Ariane 4) 408
5.3 ISS Safe Haven 408

APPENDIX

Appendix A Timeline of Events 408

Appendix B EVA Inspection Procedure 408

Appendix C EVA Transfer Procedure 410

Appendix D EVA Repair Procedure 410

Appendix E Rendezvous Burn Plans 411

List of Figures

Figure 1 ppCO2 plot with 8 Hours of Crew Sleep 397
Figure 2 ppCO2 plot with 8 Hours of Crew Sleep 398
Figure 3 Decision Path Timeline 398
Figure 4 Mission Electrical Power Level 399
Figure 5 EV-1 Position Between Payload Bay Door and Wing Leading Edge 400
Figure 6 *Atlantis* Launch Windows 401
Figure 7 ET Disposal Area for 39 Degree Inclination Rendezvous Mission 402
Figure 8 Rendezvous Approach 403
Figure 9 Orbiter Orientation During Proximity Operations / Rescue EVA 403
Figure 10 Rescue EVA 404
Figure 11 Repair EVA 406
Figure 12 Relative Wing Leading Edge Temperature (No Boundary Layer Trip) 407

THIS PAGE INTENTIONALLY LEFT BLANK

STS-107 In-Flight Options Assessment

Submitted by the NASA Accident Investigation Team, Houston, Texas
May 22, 2003

EXECUTIVE SUMMARY

The NASA team was asked by the Columbia Accident Investigation Board (CAIB) to determine whether there were any options available to return the STS-107 crew. The one significant initial condition in this request was that engineers were aware that there was damage to the leading edge of the left wing that could be ascertained either through the use of national assets or through EVA inspection. Whether this was the actual condition on STS-107 is not known.

Two different options were studied: a rescue mission with the Space Shuttle *Atlantis*, and a repair by the STS-107 astronauts, using materials available onboard *Columbia*.

To determine the amount of on-orbit time available for each of these options, significant effort was spent in the analysis of how on-orbit consumables could be preserved. It was determined that the limiting consumable was lithium hydroxide (LiOH), which is used to remove carbon dioxide from the crew compartment atmosphere. Using real crew metabolic rates and an estimate of acceptable CO2 concentration levels, it was determined that the maximum on-orbit lifetime was 30 days total Mission Elapsed Time (MET), or until the morning of February 15. Other consumables, such as oxygen, hydrogen, nitrogen, food, water, and propellant were assessed and determined to provide support beyond 30 days MET (*Columbia* Flight Day 30).

Several different timelines were then built and assessed against the consumable resources. The following timeline was used for the study:

On Flight Day (FD) 2 the NASA team would be notified that the left wing had been struck by debris. On FD 3 NASA would make an expedited request for national assets to inspect *Columbia*. To be conservative, it was assumed that this inspection was inconclusive and that an "inspection EVA" would be required. NASA would spend FD 4 developing procedures for the inspection EVA, which would be performed on FD 5. This EVA consists of one crewmember translating down the port payload bay door and being a "human bridge" between the edge of the door and the wing. The second EVA crewmember would translate down the first EVA crewmember and inspect the lower half of the leading edge. It was assumed at this point that the damage was visible and a clear threat to the vehicle, although whether this was really the case with STS-107 is not known. The risk associated with this EVA was assessed to be low and the likelihood of success high. At this point, the crew would be instructed to power-down *Columbia*, begin conserving LiOH, and the ground teams would begin working two parallel paths: one to process *Atlantis* and develop rescue procedures, the other to develop possible repair techniques and test them for effectiveness.

For the rescue mission, the following processes were assessed: Launch vehicle processing, modification of flight software, Mission Control Center software and facility capability, systems integration requirements, crew size and skill mix, availability of required crew equipment, launch window availability, external tank disposal, rendezvous and proximity operations, EVA crew transfer procedures, weight and c.g. of *Atlantis* for the return, and *Columbia* disposal requirements. All of these areas were determined to be low to moderate risk with some significant schedule pressure. The team also assessed the "aggregate risk" of decreasing the preparation time for all of the required areas. While each of the individual areas could have supported a launch attempt, it was recognized that this was a "best-case" analysis, with very little margin, and it deviated greatly from the standard mission planning and preparation cycle.

It was determined that by accelerating the schedule for the above areas, a launch of *Atlantis* on February 10, 11, or 12 was possible. All three launch dates could have provided a rendezvous and EVA transfer of the crew prior to the depletion of consumables. Two major assumptions, apart from the already stated assumption that the damage had to be visible, have to be recognized – the first is that there were no prob-

lems during the preparation and rollout of *Atlantis*, and the second is the question of whether NASA and the government would have deemed it acceptable to launch *Atlantis* with exposure to the same events that had damaged *Columbia*. At this point, at least two of the last three flights (STS-112 and STS-107) had bipod ramp foam problems, and the flight in-between these two, STS-113, was a night launch without adequate imaging of the External Tank during ascent. This new risk to the Orbiter would weigh heavily in the decision process on launching another shuttle and crew. Based on CAIB direction, it was assumed that the *Atlantis* would have been launched without processing time added to modify the External Tank.

For the repair option, all of the materials onboard *Columbia* were considered for their usefulness in repairing leading edge damage. To bound the problem, a certain level of damage had to be assumed. After consulting with the aerothermal analysts, it was determined that two different damage conditions would be assessed for potential repair options: a six-inch diameter hole in the lower part of RCC panel #8, and a ten-inch long missing piece of T-seal between RCC panels #8 and #9. Whether these were the actual conditions on *Columbia* is not known.

The best repair options were determined to be the following:

Six-inch diameter hole in RCC panel 8: An EVA crew member would insert a stowage bag through the hole into the leading edge cavity and place as much metal as possible (tools, etc.) into it, he would then insert two or three Contingency Water Containers (CWC) into the hole in front of the bag of metal. A hose would be run from the airlock water supply to the EVA astronaut; this hose would be used to fill the CWCs with water. Insulation blankets removed from the top of the payload bay door would be used to fill the remaining hole and a Teflon foot loop would be placed over the hole to ensure that the insulation stays in place during subsequent vehicle maneuvers. The wing would then be "coldsoaked" to freeze the water and reduce the overall structural temperature of the wing. The theory behind this repair is that the insulation would burn away fairly quickly, but the thermal mass of the ice and metal, if it could block the plasma flow from reaching the spar, may extend the time until the spar burns through.

Missing T-seal: The gap between the RCC panels would be filled with tile fragments harvested from non-critical locations on *Columbia*. The tile fragments would be shaped by the crew IVA and then pushed into the gap during a second EVA. There are a number of uncertainties with this approach. Ground demonstrations indicate that a tight fit could be achieved. However, the fit achieved on orbit would be dependent of many variables and would be very difficult for the crew to assess or control. It would require a number of tile fragments to seal the gap. The crew would leave the smallest possible gap between the tile pieces. No testing has been done to determine how much friction is required to hold the tile in place or how large a gap between tiles would be acceptable.

The applicable repair would be used with other options, such as reducing the vehicle weight, lowering perigee, and increasing the angle of attack during entry to lower the overall heat on the leading edge of the vehicle and potentially provide structural integrity long enough to allow a bailout at 34,000 feet altitude.

Limited thermal analyses of the repair and entry modification options were inconclusive, as there are too many unknowns concerning the flow path of the plasma and the resulting structural effects. It is thought that the EVA procedures to execute this repair would be extremely difficult due to access problems and trying to work within the enclosed space of the leading edge. Therefore it is thought that the likelihood of success of this option would be low.

The best option for the return of the crew was to attempt to transfer them to *Atlantis*. Both of these plans however, rely on the assumption that the RCC problem would have been found and be unambiguous, and that it would be acceptable to launch *Atlantis* with exposure to the same condition.

Major assumptions/Initial conditions

To determine whether there were any options available to return the STS-107 *Columbia* crew safely to Earth, two significant assumptions were directed by the CAIB:

Assumption #1: Damage Characteristics: The actual damage to the leading edge of *Columbia* is not known, nor is it likely to be known with a great deal of accuracy. However, NASA aerothermal modeling has demonstrated that the most likely damage size and locations are a six inch diameter hole in the lower surface of RCC panel #8 or a ten-inch piece of T-seal missing between RCC Panels #8 and #9. Both damage scenarios will be addressed in the "*Columbia* Repair" section of this study. Additionally, for the purposes of this assessment, it is assumed that the damage to the leading edge of the wing can be determined to be catastrophic by either national assets or astronaut inspection. This assumption rules out damage consisting of a crack, an intact deformation of the panel, or damage to the attachment structure of a leading-edge component.

The timing of discovering the damage is critical to this study. It is assumed that the Intercenter Imagery Working Group notified NASA management of the foam debris strike on Flight Day (FD) 2 and that national assets were requested on FD 3. Depending upon the size of the damage, these national assets may or may not have been conclusive in determining that the damage is potentially catastrophic. To address this uncertainty, two timelines have been developed. The first timeline assumes that the information provided by the national assets is conclusive. In this case, a powerdown is started immediately on *Columbia*, consumable assets are strictly conserved, and the ground teams begin working on the rescue and repair options. A second timeline has been developed for the case in which the information from the national assets is inconclusive; in this case the *Columbia* crew would begin a partial power-down of the vehicle while

the Mission Control Center developed procedures for an "inspection EVA" on FD 5. This visual inspection of the damage by the astronauts is assumed to be conclusive, and the powerdown and conservation of consumables would begin at the end of FD 5. In both cases, the ground activity to develop rescue and repair options would be identical, but for the case where the EVA astronaut inspection is required, the crew would lose consumables equivalent to approximately 30 hours and one EVA.

Assumption #2: Willingness to Launch *Atlantis* with Exposure to Bipod Ramp Debris: It is an important point in the discussion of a rescue mission to assume that it would be acceptable to launch *Atlantis* without a redesign to the ET bipod foam, even though this component is suspected to have caused the damage to *Columbia*. Undoubtedly, there would have been significant discussions on the risk trades of various modifications to the –Y bipod ramp. For the purpose of this study, the CAIB directed that *Atlantis* would be launched without any modification to the external tank. However, an inspection of *Atlantis*' leading edge was inserted into the "Rescue EVA" timeline.

1.0 *Columbia* Consumables (Available Time In Orbit)

"Consumables" is defined as non-replaceable resources that are required to keep the crew alive and to operate the Shuttle systems.

1.1 Lithium Hydroxide/CO2 Removal/Crew Health

The limiting consumable on *Columbia* was lithium hydroxide (LiOH). LiOH is used for CO2 removal in the crew compartment. There were 69 cans of LiOH available on *Columbia*. To determine how much time on-orbit was available from these cans, several assumptions have to be made about the crew's CO2 production levels and the highest percentage of CO2 that could be tolerated by the crew over an extended period of time.

To determine CO2 production, a metabolic rate halfway between the STS-107 actual sleep and wake levels was used. Two cases were run, one with the crewmembers awake for 16 hours and asleep for 8 hours, and the other with a 12-hour awake, 12 hour asleep cycle. It was assumed that there was no crew exercise, minimal activities planned, and no payload experiments. The live animals in the SPACEHAB would be euthanized.

The determination of the maximum allowable CO2 percentage would have been more difficult. The mission rules require that a flight be terminated if the CO2 level gets above 15 mmHg (~2.0%). For levels between 7.6 mmHg and 15 mmHg (~1.0%-2.0%), all crew activities are evaluated by the Flight Surgeon.

There are few relevant experiments to date on long-term exposure of humans to elevated CO2 levels with a limited amount of activity in microgravity. However, the flight surgeons believe that a CO2 percentage of 26.6 mmHg (3.5%) would not produce any long-term effects on the health of the crewmembers. Shortness of breath, fatigue, and headaches may have occurred. However, the crew did have access to pure-oxygen masks if symptoms became acute. It is also believed that the body would adapt over time to these elevated levels.

The plots show the relationship of metabolic rate and LiOH changeout level. If the metabolic rate could be kept to the equivalent of a 12 hour sleep, 12 hour awake rate, the onboard LiOH could be stretched to 30 days Mission Elapsed Time (MET) without violating the 15 mmHg Mission Rule limit. If the crew metabolic rate could not be reduced (by sleep, inactivity, or by medication), accepting the increased limit of 25 mmHg would also provide 30 days of on-orbit lifetime. Thirty days MET is equivalent to the morning of February 15.

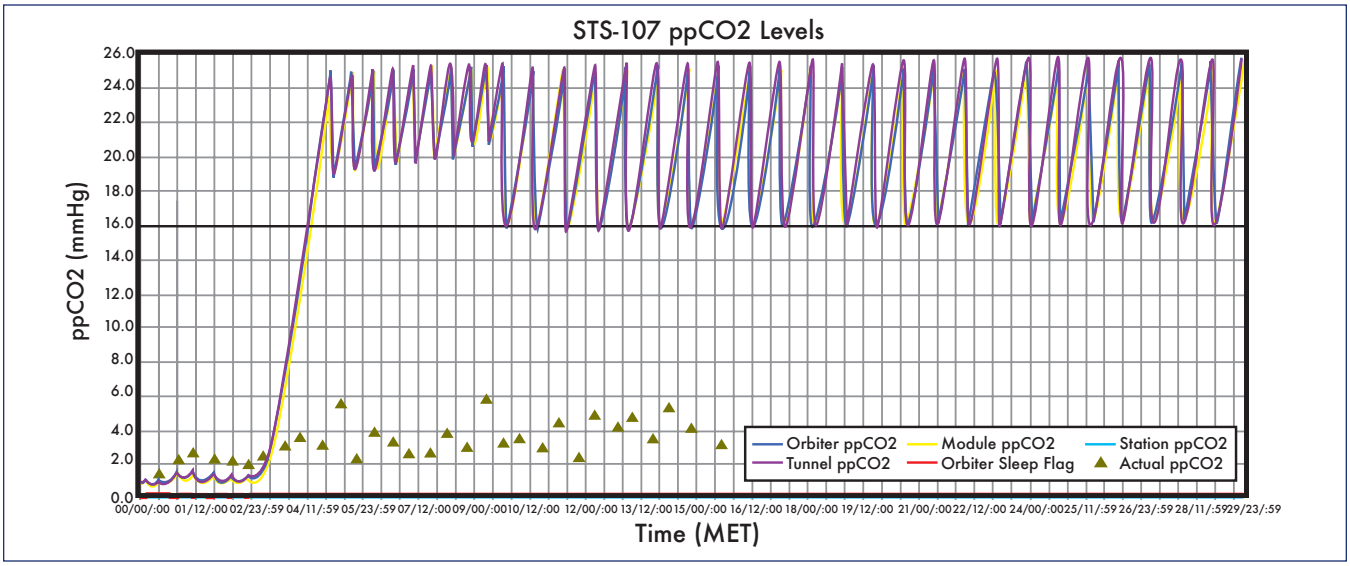


Figure 1. ppCO2 plot with 8 hours of Crew Sleep.

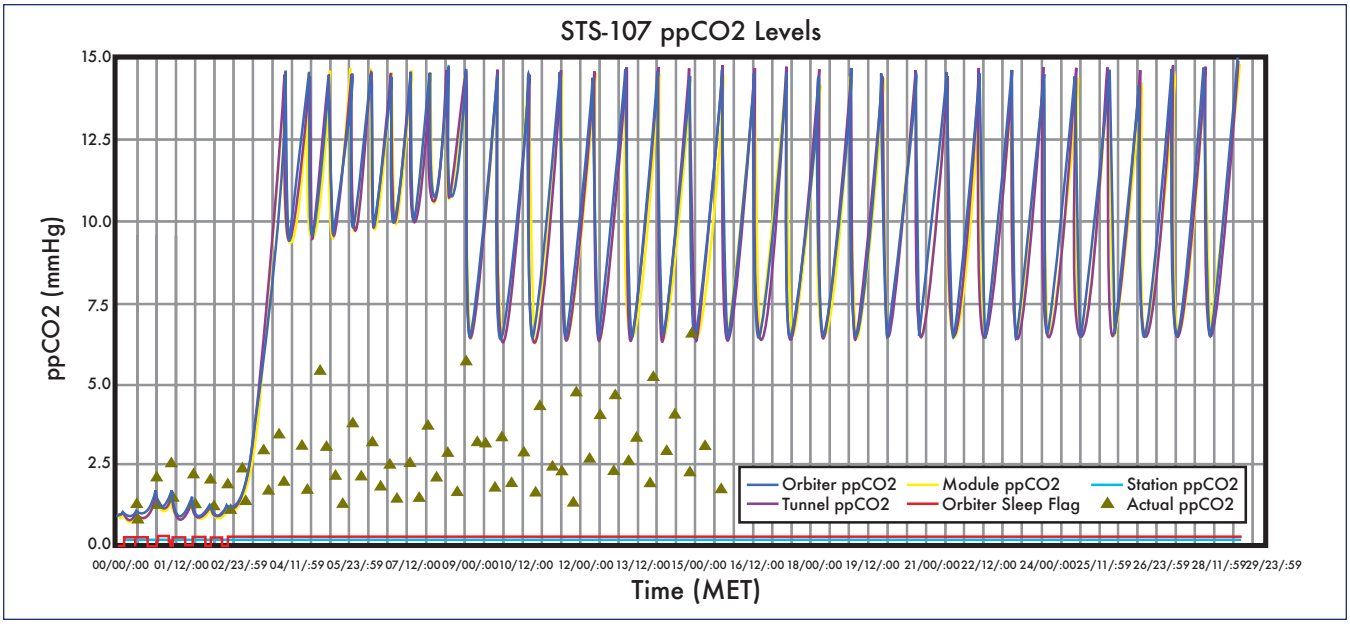


Figure 2. ppCO2 plot with 12 hours of Crew Sleep.

1.2 Oxygen

Oxygen is the next most limited consumable. The oxygen onboard *Columbia* is used to replenish the crew atmosphere, to power fuel cells that provide electricity, and to provide potable water to the crew as a byproduct of the fuel cell reaction.

Columbia had an Extended Duration Orbiter (EDO) pallet located in the aft part of the payload bay that provided extra storage for cryogenic oxygen and hydrogen. Following the *Discovery* of critical damage to the leading edge of the wing, a power-down (Section 2.1) would have been performed to preserve the available oxygen and hydrogen. This power-down would have supported only the most basic vehicle control and crew support and communication equipment. The O2 margin above 30 days (limited by LiOH) could have been used to power additional equipment or breathed by the crew through emergency masks periodically to offset the deleterious effects of the elevated CO2 levels.

1.3 Food / Water

There were no significant impacts to the timeline for food or water. At a low metabolic rate, sufficient food was available for more than 30 days. The minimal power level was sufficient to supply 3 gallons of potable water per crewmember per day as a byproduct of the fuel cell power reaction.

1.4 Propellant

When the damage to the leading edge of the wing was discovered, in addition to performing the powerdown and modifying the LiOH changeout schedule, the orbiter would have been placed in a tail-down gravity gradient attitude that would require very little propellant. Sufficient propellant would have then been available to perform joint-rendezvous maneuvers, hold attitude for proximity operations or a cold-soak of the left wing, and eventual deorbit/disposal.

2.0 Decision Path Timeline

Figure 3 shows the anticipated decision timeline.

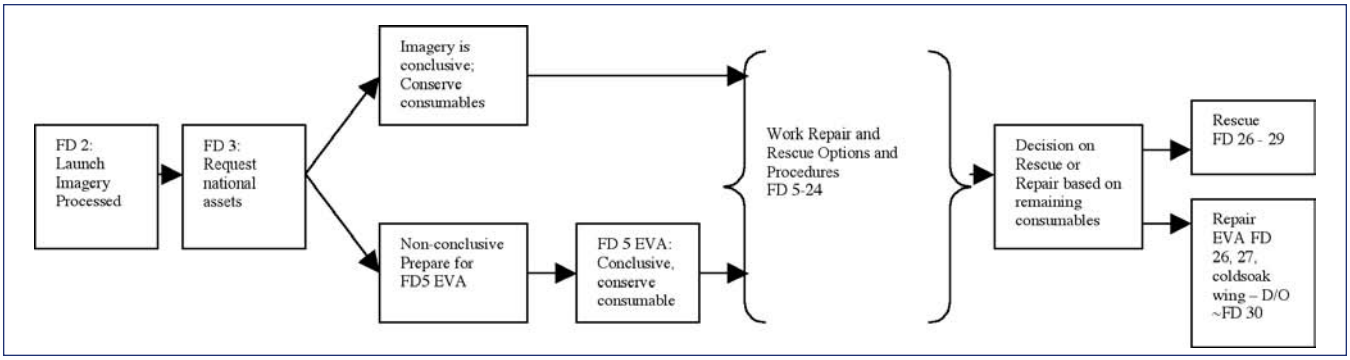


Figure 3. Decision path timeline.

2.1 Powerdown Requirements

It was the opinion of the team that the launch video would be received on FD 2, national assets would be requested and delivered on FD 3. At this point, if the data was conclusive the following powerdown would be performed by the crew:

- All payload and related equipment is powered off
- A "Group C" systems power down is performed
- All camera's, camera heaters, TV monitors, and video equipment off
- One General Purpose Computer (GPC) powered for vehicle control, one GPC running 25% for systems monitoring, GPC 5 in sleep mode, GPC's 2 and 4 OFF.
- One crew monitor (IDP and MDU) on 50% of time
- 1 personal laptop computer powered 25% of time
- Inertial Measurement Unit (IMU) 1 is left ON, 2 and 3 are off
- The crew galley is off
- Avionics bay instrumentation is off
- KU Band antenna is stowed
- The Orbiter Cabin Air Cleaner (OCAC) fan is running at medium speed
- FWD and AFT Motor Controller are unpowered until deorbit day.
- Fuel Cell 3 and Freon Loop 2 are unpowered until deorbit day.

This powerdown would reduce the average mission power level to 9.4 kW. Protecting for 1 deorbit opportunity on the final day would result in a total oxygen capability of 34 days 10 hours.

If the data from the national assets were inconclusive, no power-down beyond the normal on-orbit configuration would be performed until the inspection EVA was completed. Not performing a power down would have preserved the science mission if the inspection EVA determined that there was no significant damage. For this case, the additional powered day plus one EVA from 14.7 psi cabin pressure would result in a total oxygen margin of 32 days, 11 hours.

Performing the above case plus four airlock depresses and three airlock represses for a rescue EVA, results in a total O2 margin of 31 days, 6 hours.

2.2 Description of Leading Edge Inspection via EVA

The inspection EVA procedures would have been developed on FD 4 and executed on FD 5. It is anticipated that this would have been a maximum two-hour EVA, using a four-hour prebreathe protocol based on 14.7 psi cabin pressure. The first EVA crewmember (EV-1) would tape towels to his boots to protect the Orbiter wing. Upon egress from the airlock, EV-1 would translate out along the edge of the port payload bay door until above the wing leading edge area (approximate position of RCC panel 8). The upper surface of the wing leading edge would be inspected from this position. If no damage is observed on the upper surface, EV1 would gently place his right foot on the upper surface of the wing and his left foot in front of the leading edge, while holding onto the payload bay door. The upper surface of the wing is approximately four feet from the edge of the door. The second EVA crewmember (EV-2) would follow EV1 along the edge of the payload bay door and translate down EV-1 to visually inspect the lower surface of the leading edge structure. STS-107 did not have any EVA-compatible video cameras or digital cameras to record damage, so the inspection report would be verbal from EV-2. Because of the sharp edge hazard potential, and concern about further damaging the impact site, the EVA crew would make every effort not to contact the suspected damaged area.

A consideration in the planning for this task was the EVA training level of the *Columbia* crew. Although the two EVA crewmembers were fully trained for a standard set of Orbiter contingency tasks, none of these were specific to this inspection activity. There were no scheduled EVAs during the STS 107 mission. Additionally, *Columbia* was only equipped with a minimal set of EVA tools (i.e. no SAFERs, no EVA cameras, etc.).

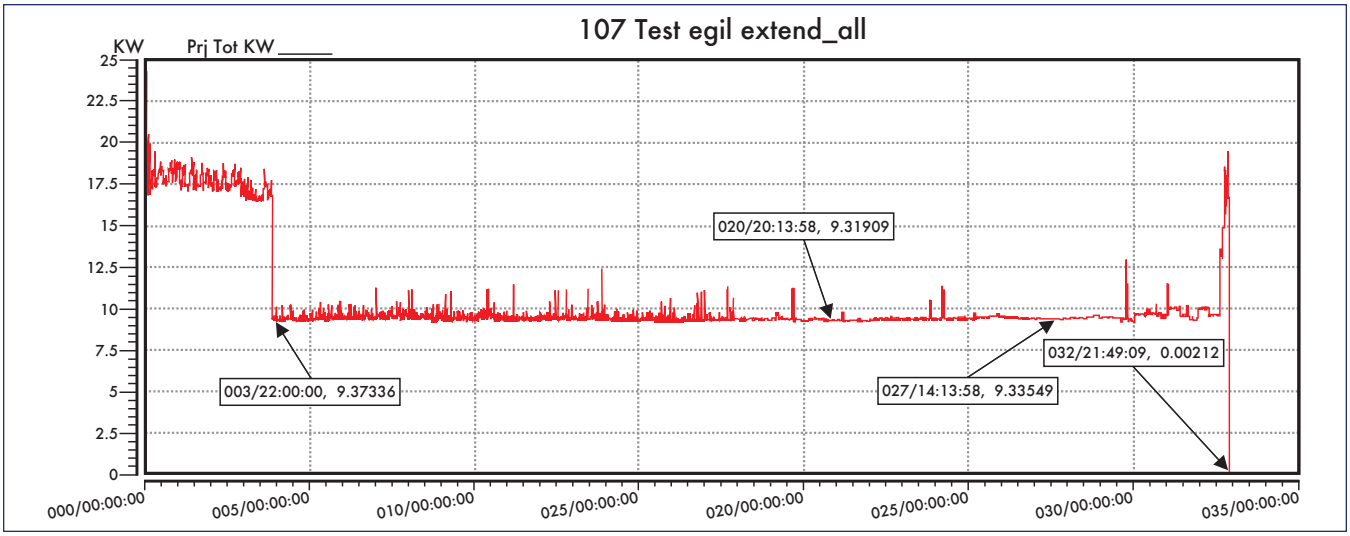


Figure 4. Mission Electrical Power level.

Two experienced EVA astronauts and two EVA flight controllers assessed this task in the Johnson Space Center virtual reality lab. The level of difficulty of the EVA inspection procedure is moderate. The risk of injury to crew is low and of further damage to the site is low to moderate. The expectation of mission success (providing conclusive information regarding damage severity) is judged to be high.

A detailed synopsis of the wing leading edge inspection procedure is included in Appendix B.

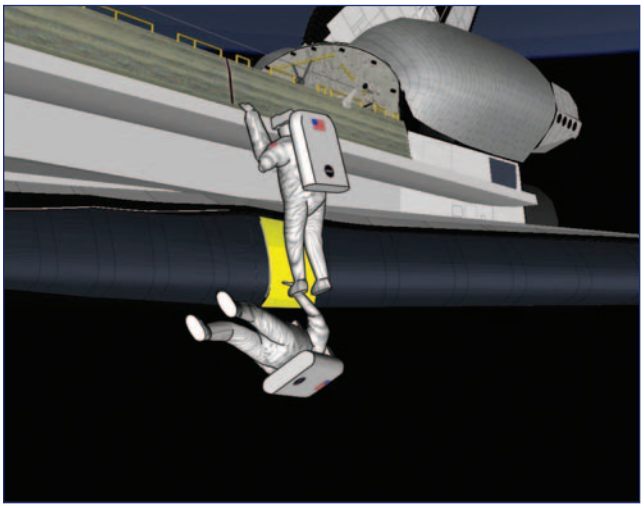


Figure 5. EV-1 position between payload bay door and wing leading edge.

3.0 Rescue Mission

3.1 Success Criteria

The safe return of the rescue vehicle (*Atlantis*) and both crews.

3.2 Atlantis configuration on STS-107 FD 4

On STS-107 Flight Day 4 (January 19th), the Space Shuttle *Atlantis* was in the Orbiter Processing Facility (OPF), being prepared for a launch to the International Space Station on March 1, 2003. The Space Shuttle Main Engines were installed and there were approximately ten days of routine orbiter processing required before the rollover to the Vertical Assembly Building (VAB). No payload elements or Remote Manipulator System were installed in the cargo bay. In the VAB, the External Tank (ET) and the Solid Rocket Boosters (SRB) had been mated on January 7th. The template for STS-114 processing called for the ET/SRB and *Atlantis* to undergo parallel processing until January 29th, when *Atlantis* would be rolled to the VAB and mated to the integrated stack. The cargo elements for the ISS were planned to be installed at the launch pad on February 17.

3.3 Launch Vehicle Processing Timeline

The minimum time necessary to safely prepare *Atlantis* to be launched on a rescue mission were assessed by senior government and contractor management at Kennedy Space Center (KSC). If notified on *Columbia* FD 5 (Monday, January 20th), KSC would begin 24/7 processing on the vehicle in the OPF. All standard vehicle checks would have been performed, including structural leakage tests, final closeouts of different areas of the vehicle, and a weight and c.g. assessment. An expedited schedule would have resulted in rollout to the VAB on January 26 (*Columbia* FD 11). The VAB flow would have been shortened from the standard five days to four days based on 24/7 support. Tests not performed at the pad, and the risk associated with this non-performance, are as follows;

- S0017 – Terminal Countdown Demonstration Test (TCDT) – no risk to eliminate. This is a practice countdown to allow new astronauts to get a feel for launch day activities.
- S0044 – Launch Countdown Simulation – low risk to eliminate. This is a practice for the Launch Control Team. The team is likely to be the same launch team that launched *Columbia* three weeks earlier.
- S0056 – Cryogenics Load Sim – low risk – Same rationale as the S0044
- V1202 – Helium Signature Test – no to low risk. This test checks for leaks in the Main Propulsion System (MPS). If there were a leak, it would be caught in the launch countdown. If a leak were found during this test, there would be insufficient time to fix it.
- S0007 – Launch Countdown – low risk – Planned launch holds would be reduced to the minimum and tailored to meet the desired rendezvous launch window.
- No Flight Readiness Review or Certification of Flight Readiness

A review of the weather conditions during the major milestones in this timeline show that there did not appear to be any violations of established criteria.

This flow results in a launch capability of approximately February 10 (*Columbia* FD 26).

3.4 Flight Software

The impact of changing the STS-114 Flight software was assessed and determined to be within the launch vehicle processing timeline. The STS-114 flight software load would be used, since this flight has the appropriate rendezvous information and STS-107 did not. The changes to the flight design: inclination, altitude, launch window and rendezvous information, and External Tank disposal criteria were assessed and could be developed and uplinked in the Day of Launch I-Load Update process (DOLILU). While these DOLILU I-Load updates are certified, this would be the largest DOLILU uplink ever performed. One additional patch to the software would have been required to change the main engine cutoff altitude to meet external tank heating constraints.

Additionally, time was available to perform prelaunch testing of the flight software and proposed uplinks in the Shuttle Avionics Integration Laboratory to verify launch, rendezvous and deorbit software integrity. Boeing Flight Software would provide an independent assessment. The overall risk level was assessed to be low.

3.5 Mission Control Center Software

Mission Control Center software includes all of the vehicle control and monitoring data specific for a Shuttle mission. The STS-114 mission had a complete software load built and ready for the planned launch on March 1st. Flight Controllers had performed seven integrated simulations on this software load, including two ascents, prior to the launch of STS-107. The vehicle monitoring software would not be affected by a change in the mission content.

From a Mission Control Center facility standpoint, sufficient hardware capability was available to control the International Space Station, *Columbia*, and an *Atlantis* rescue mission.

3.6 Crew Size / Skills

Based on the unresolved launch debris risk and the constraints for crew seating during entry, *Atlantis* would be launched with the minimum required crew. Minimum crew size for the rescue mission, based on the rendezvous/ proximity operations and EVA tasks, would be four astronauts – Commander (CDR), Pilot (PLT), and two EVA crewmembers (EV1 and EV2). Two EVA astronauts are required to perform the "Rescue EVA" transfer tasks. Two additional astronauts are required to simultaneously perform the rendezvous and extended proximity operations (8-9 hours of manual flying) and perform the EVA assist functions. These tasks would be performed by the CDR and PLT.

With a planned FD1 rendezvous and EVA, it would be important to have a high degree of confidence in the astronauts' ability to quickly adapt to the micro-gravity environment. This factor, in combination with the minimum time available for training, would dictate the selection of EVA and rendezvous experienced astronauts with a high level of proficiency at the time of the STS-107 mission. There were 9 EVA astronauts, 7 CDRs, and 7 PLTs available in January 2003 who would have met these requirements.

3.7 Crew Equipment

Four EMUs would be launched on *Atlantis*; two for the *Atlantis* EVA crew and two for use in transferring *Columbia* crewmembers. Two SAFERS (Simplified Aid for EVA Rescue) and two wireless video helmet units would be included as well, for *Atlantis* EVA crew only. Two portable foot restraints would be launched on each side of the *Atlantis* payload bay. An EVA telescoping boom would be stowed on the forward bulkhead. The standard complement of notebook computers required for rendezvous and proximity operations would be stowed on *Atlantis*. Additional "core" stowage of habitability equipment would be stored in the middeck along with extra LiOH canisters for transfer to *Columbia*.

3.8 Launch Window / ET Disposal

Three days prior to the anticipated launch of *Atlantis*, *Columbia* would execute a 74 feet per second translation maneuver

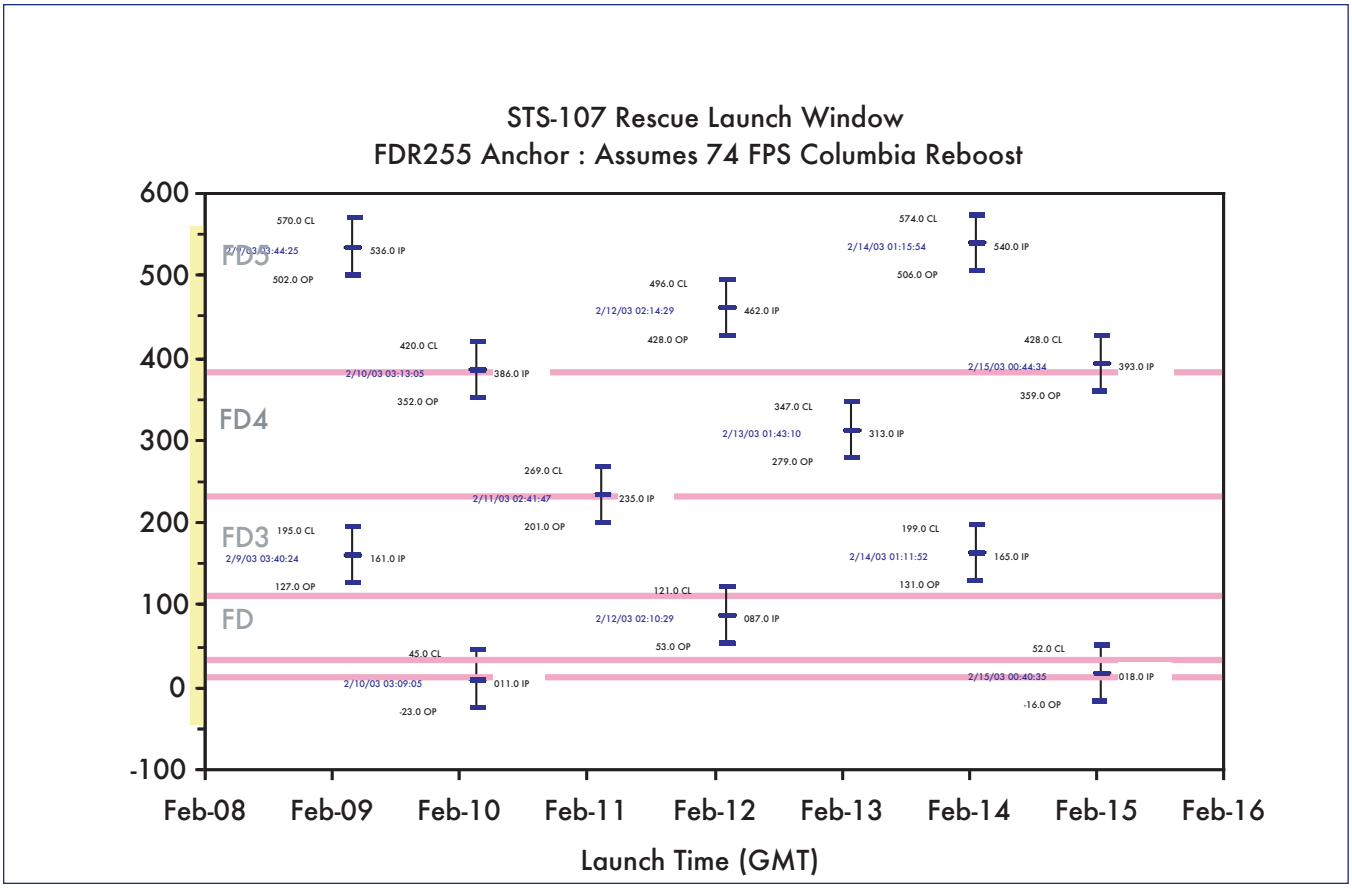


Figure 6. Atlantis *Launch Windows.*

to raise the orbit to 185 nautical miles by 139 nautical miles. This maneuver would increase the rendezvous windows available for the *Atlantis* launch. Assuming that the vehicle processing could support on or around February 10, the following rendezvous launch windows would be available:

- Launch February 10, 03:05:09 GMT (February 9, 10:05 p.m. EST) for rendezvous on February 10
- Launch February 11, 02:40:07 GMT (February 10, 9:40 p.m. EST) for rendezvous on February 13
- Launch February 12, 02:10:29 GMT (February 11, 9:05 p.m. EST) for rendezvous on February 13

The most desirable option would be to make the launch date of February 9, as it provides the earliest rendezvous option with *Columbia*. However, if vehicle processing could not support this date, the launch times for February 11 and 12 would both support a rendezvous on February 13, with an estimated 36 hours of margin available before depletion of the LiOH.

ET Disposal:

To provide adequate clearance of the ET impact point from landmasses, an uplink to change the Main Engine Cut-Off (MECO) velocity would be required. This is a certified capability that could be used on any mission. Additionally, a flight software patch would be implemented to change the MECO altitude target to 54 nautical miles, vice the planned STS-114 MECO altitude of 52 nautical miles, to maintain flight conditions within the certification envelope and provide ET impact point clearance from landmasses.

3.9 Rendezvous / Proximity Operations

The *Atlantis* would follow a standard rendezvous profile that would result in an approach from below *Columbia* (+Rbar approach). This approach is the easiest to fly for maintaining long duration proximity operations as orbital mechanics tend to slowly cause separation between the vehicles. This approach was used for all of the MIR docking missions and all of the ISS assembly missions up to STS-102. There would be minimal training required for a rendezvous experienced CDR.

Proximity operations are also straightforward, but of an unprecedented duration. The *Columbia* would be positioned wing-forward, payload bay to Earth under active attitude control. The *Atlantis* would approach nose forward with the payload bay facing *Columbia*. This ninety-degree "clocking" of the Orbiters allows a close approach without concerns over the vertical tail impacting the other vehicle. It

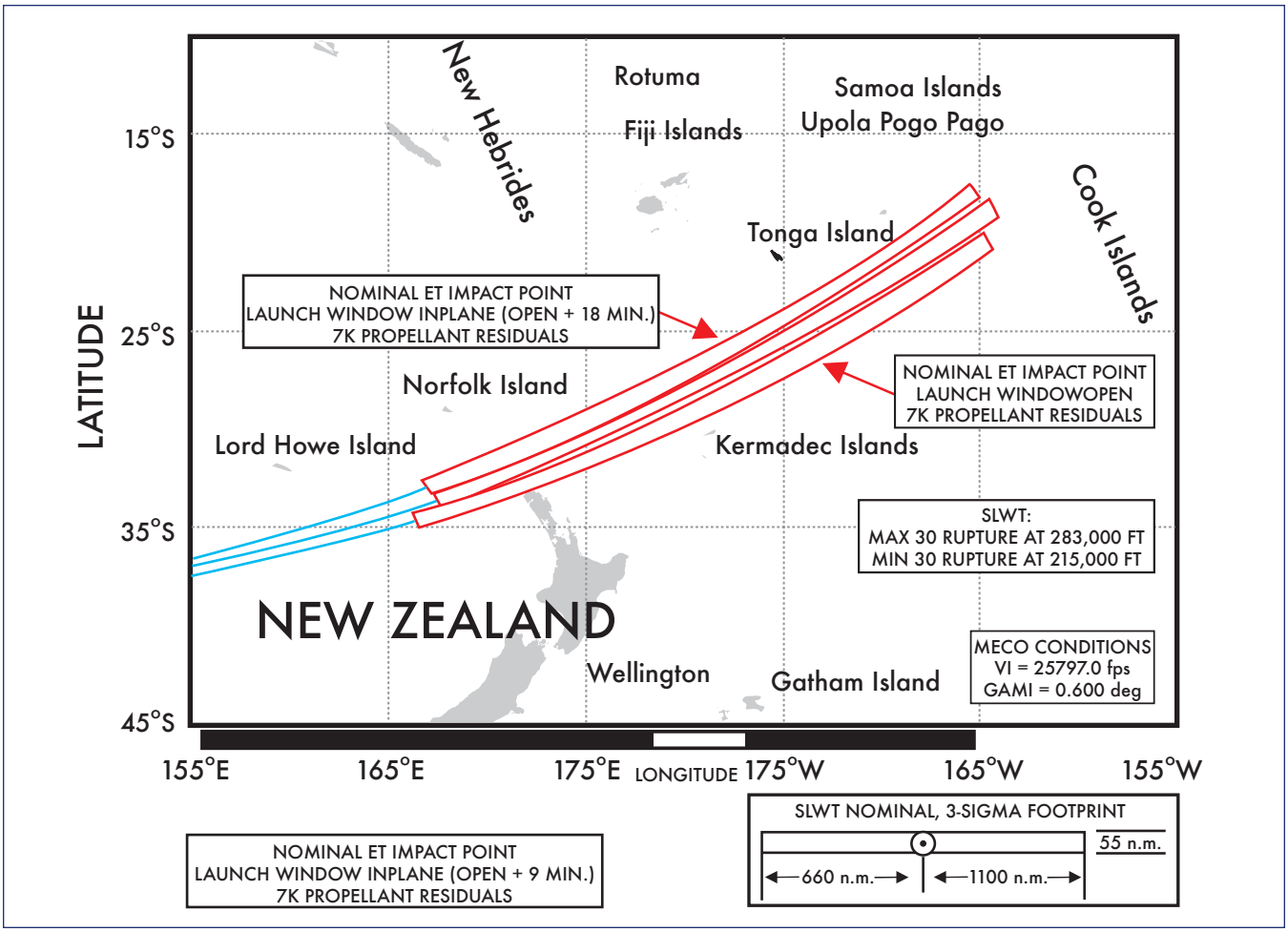


Figure 7. ET disposal area for 39 Degree Inclination Rendezvous Mission.

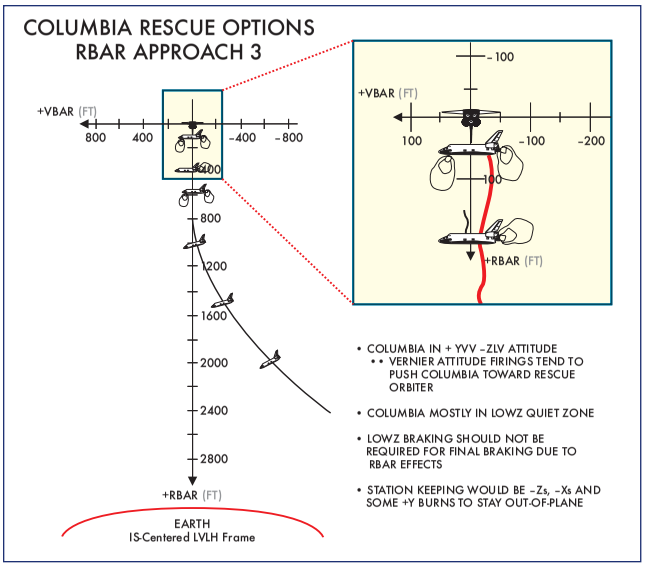


Figure 8. Rendezvous approach.

is believed, based on flight experience, that the two vehicles could be flown very close to each other (tens of feet). During ISS assembly missions, the Orbiter is typically held 30 feet from the ISS docking port in order for the CDR to manually fly out any rotational or position errors. Also, there have been at least two cases in which a payload has been "flown" into the reach of the EVA crewmember and several instances where a retrieved payload was flown to a point where the robotic arm could grapple it.

One concern would be the length of time in proximity operations (8-9 hours), which drives the crew requirement on *Atlantis* to four. To help mitigate this concern, a retro-reflector would be taken to *Columbia* on the first EVA and placed on top of the SPACEHAB module. The Trajectory Control System was installed on *Atlantis*, and could be used with the suite of rendezvous tools to assist in the proximity operations through the day/night cycles. Additionally, it is thought that *Columbia* crewmembers that are transferred early could assist in the station-keeping task.

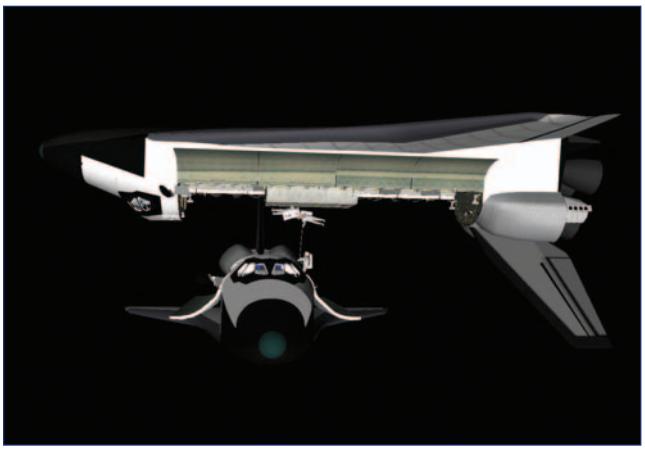


Figure 9. Orbiter Orientation during Proximity Operations / Rescue EVA.

3.10 Rescue EVA

The EVA crewmembers on *Atlantis* would use a 10.2 psi cabin pressure EVA prebreathe protocol. If a FD1 rendezvous and EVA were attempted, the *Atlantis* EVA crew would need to prebreathe O2, possibly beginning as early as Orbiter ingress on the pad, and *Atlantis* would be depressed to a 10.2 psi cabin pressure during post-insertion activities. The crew on *Columbia* would maintain a 14.7psi cabin pressure to minimize CO2 percentage. The EMUs on *Columbia* would be approximately sized for the first two *Columbia* crewmembers (CM1 and CM2) to be transferred. CM1 and CM2 would don the EMUs in the *Columbia* airlock and be ready for depress upon the arrival of *Atlantis*. At the completion of the rendezvous, *Atlantis* and *Columbia* would be "clocked" 90 degrees with the payload bays facing each other at a distance of 20 feet from payload bay sill to payload bay sill.

EVA Overview:

The initial priority for the rescue EVA would be the transfer of replacement LiOH to *Columbia*. Both *Columbia* and *Atlantis* airlocks would be depressed to start the EVA. *Atlantis*' EV2, using a portable foot restraint on the payload bay sill and the EVA boom to extend his reach, would transfer EV1, extra LiOH canisters, and two EMUs to *Columbia*. EV1 would assist CM1 and CM2 from the *Columbia* airlock,place the two spare EMUs and extra LiOH canisters in the airlock, and close the outer hatch. After repressing the *Columbia* airlock, the next two *Columbia* crewmembers (CM3 and 4) would don these EMUs.

CM1 and 2 would transfer to *Atlantis* (using the EVA boom and assisted by EV1), for airlock ingress and repress. Once inside *Atlantis*, the EMUs would be doffed and prepared for transfer back to *Columbia*.

This process would be repeated until all seven *Columbia* crewmembers were rescued. On the third transfer, only one *Columbia* crewmember is rescued, leaving two remaining to assist each other in donning the EMU's.

Two additional tasks would be performed by the *Atlantis* EVA crew after the first transfer operation (while waiting for suit doffing and prep to be completed). EV1 and 2 would conduct a SAFER inspection of the *Atlantis* TPS, and install a portable TCS laser reflector onto *Columbia*.

Although a standard EVA prebreathe protocol could be used by the *Columbia* astronauts, a modified protocol that would minimize prebreathe duration could be approved by the flight surgeons and would expedite *Columbia* crew transfers substantially. EMUs that are transferred from *Atlantis* to *Columbia* empty, would need to be transferred powered up and pressurized to prevent water freeze up. It should be noted that not all of the *Columbia* crewmembers were EVA-trained so the *Atlantis* crew would be prime for all aspects of the EVA rescue. The complete transfer activity would require two EVAs unless all suit donning/doffing and transfers went exceptionally well and prebreathe times were minimized, in which case EVA duration for *Atlantis* EV crew would be 8.5-9 hours.

A detailed synopsis of the Rescue EVA procedure is included in Appendix C.

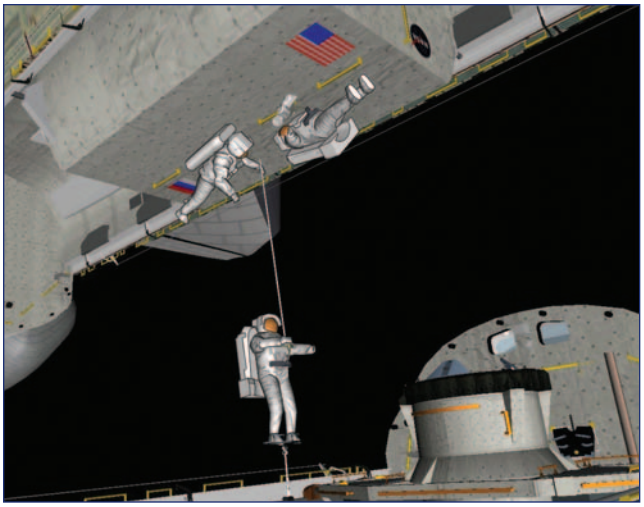


Figure 10. Rescue EVA.

3.11 Atlantis Return

An assessment was made concerning the resultant weight and center of gravity (c.g.) of *Atlantis* carrying 11 crewmembers, "core" middeck stowage, and six EMUs. The weight was 209,157 pounds and the c.g. was 1081.2 inches, within the certified requirements. No OMS or RCS ballasting would be required. Sufficient propellant would be available to allow normal deorbit targeting methods to be used.

3.12 Columbia Disposal

Prior to the last crewmember departing *Atlantis*, there would be a small number of switch configurations required to allow the Mission Control Center (MCC) to command the deorbit of *Columbia*. The OMS and RCS systems would be pressurized for a burn, the OMS engines would be armed, and the onboard computer system would be configured to allow ground command of the necessary actions.

The MCC has the capability to autonomously command the required maneuvers. There would be no possibility of recovering *Columbia* however, as the ground does not have the capability to start auxiliary power units, deploy air data probes, or extend the landing gear. It is thought that the *Columbia* would be deorbited into the South Pacific.

3.13 "Aggregate Risk"

It should be noted that although each of the individual elements could be completed in a best-case scenario to allow a rescue mission to be attempted, the total risk of shortening training and preparation time is higher than the individual elements.

3.14 Mission "Firsts"

There would be a number of activities that would be attempted for the first time during this conceptual inspection and rescue mission. Among these are:

- Inspection EVA
  - EVA in the wing area of the Orbiter – unknown comm issues, tether routing around freon panels
  - Translation along the PLBD – no sharp edge inspection
- Rescue EVA
  - Crew members fully isolated outside of the ship (both airlock hatches sealed)
  - Translation using boom
- Mission profile
  - Full use of DOLILU for major configuration

Mission Task	*Normal Template*	*Rescue Template*	*Risk Assessment*
Orbiter Processing	10 days to VAB	7 days to VAB	Moderate, requires no failures
VAB Flow	5 days	4 days	Moderate, requires no failures
Pad Flow	Previous record – 14 days	11 days	Moderate, requires no failures
Flight S/W	6 months, but 114 work already completed	7-8 days for deltas and verification	Low
Systems Integration	6 months for loads 4-5 months for thermal Drawings –10 months 114 work completed	8 days for deltas and verification	Low
MCC S/W	N/A	Already developed	Low
Training CDR/PLT	48-54 weeks	2 weeks	Moderate
Training EVA Crew	40-50 weeks	2 weeks	Moderate to High
COFR Process	12 – 15 weeks	2 weeks	Moderate

changes
- 11 person return, not all in seats
- Ground command of deorbit burn for *Columbia*
- Extended Proximity Operations (9-10 hours) between Orbiters (safe separation)

3.15 The Launch Decision

Additional considerations in making the decision to launch a rescue mission would be:

- The mission would launch at night
- The bipod foam problem was not well understood (what had changed?)
- The flow required many activities to be done faster than normal, demonstrated templates
- Several techniques would have their first use during the mission
- Risk to the second crew and vehicle must be considered fully.
- The timing of decisions and the information for their basis is critical and highly optimistic

4.0 Columbia Repair

4.1 Success Criteria

Repair of the damage to the wing leading edge would be considered successful if spar burn through is delayed to allow the orbiter to reach an altitude in a sufficiently intact and controllable configuration to allow the crew to bail out.

4.2 Materials Available

There are three categories of material considered for repair:

First are materials capable of surviving the reentry environment that could be used to seal the damaged area of the wing. The only available material identified was tile harvested from less critical portions of the orbiter. While there is RCC located in less critical areas that might have been used for repair, these areas were not accessible to the crew. The other TPS components could not survive the reentry environment at the wing leading edge.

The second category is high thermal mass materials that could be used to temporarily interrupt the flow of hot gasses to the wing spar. There were a number of materials available. TPS materials like tile fragments and AFRSI blankets were considered and rejected due to their low thermal mass. Metals have the appropriate material properties. There were sufficient quantities of aluminum components that could have been inserted into the RCC cavity.

The third class of materials is sacrificial materials that could be used to temporarily seal the damage in the wing.

A final class of materials is materials to provide restraint. None of the adhesive materials on *Columbia* would have survived the reentry environment heating.

The following materials were considered as candidates:

Crew Compartment	*Orbiter*	*Payload*
Light Weight MAR Carbon Fiber Shell	Blanket Material AFRSI (1,500 °F) FRSI (9,00 °F)	SHAB - Titanium Shell
Teflon Sheet (contingency Kit)	Payload Bay Door Seal	PTCU Insulation
Silver Shield Gloves (contingency Kit) Norfoil – Al Foil	P/L Bay Thermal Liner	EOR/F or TEHM Doors
LiOH/Li Carbonate		Payload Thermal Mittens
CWC w/water – ICE		
Thermal Mittens		
ATCO Canister		
Charcoal Canister		
Tapes (Duct, Al, Kapton)		
Foam		

Material Thermal Limits
Titanium – 3,000 F
Inconel – 2,400 F
Stainless – 2,000 – 2,400 F
Aluminum – 1,000 F
Carbon Fibers < 1,000 F

4.3 Options Considered

The preferred option would be to seal the damaged area with a material capable of surviving reentry conditions. This option requires a repair material capable of surviving the reentry environment and a method of restraining that material in a manner that completely or nearly completely seals the damaged area. To seal the damage the material would have to be restrained in the hole. This might be accomplished by either a press or friction fit or by using an adhesive capable of surviving reentry conditions. There were no adhesives identified on board *Columbia* that could survive reentry conditions for any significant period of time. No friction fit method could be identified for restraining tile or in a hole in an RCC panel. However, a friction fit in the gap between panels could restrain shaped tile.

The other family of options focused on interrupting the flow of hot gasses to the spar. A number of options were identified for filling the cavity between the wing spar and RCC panel. The factors considered in choosing a material were 1) the material properties, 2) the ability to restrain the material between the hole in the RCC and the spar, and 3) the ability to insert the material through a small hole in the RCC panel. There are spanner beams at the edge of each RCC panel, which would tend to restrain large items or bags. Solid items could be placed in a jettison stowage bag installed in the hole, leaving the mouth of the bag outside the hole.

One of the desirable materials would be small pieces of titanium or other metal scavenged from the orbiter crew cabin. Because the cavity between the spar and RCC is open the length of the wing, the metal would have to be contained inside panel 8. This could be accomplished by inserting the bag that could then be filled with metal. This would keep the metal in place at least until the bag burned through.

There are several options for using ice to disrupt the flow of hot gases. There was enough hose on the vehicle to construct a hose that would reach from a test port in the airlock to RCC panel 8. The hose could either be used to fill a Contingency Water Container (CWC) or to spray free water into the RCC cavity. There were four CWCs on *Columbia*. Some or all could have been inserted empty through the hole in the RCC panel and then filled inside the wing. The water inside would have formed solid ice after 3-6 days. Free water could also be sprayed into the wing. The ice formed would be much less dense and would have to be restrained in some manner to keep it inside panel 8.

4.4 Best Option

For a missing portion of T-seal, the best option would have been to fill the resulting gap between the RCC panels with tile fragments harvested by the EVA crew. The tile fragments would be shaped by the crew IVA and then pushed into the gap by the EVA crew. There are a number of uncertainties with this approach. Ground demonstrations indicate that a tight fit could be achieved. However, the fit achieved on orbit would be dependent of many variables and would be very difficult for the crew to assess or control. It would require a number of tile fragments to seal the gap. The crew would leave the smallest possible gap between the tile pieces. No testing has been done to determine how much friction is required to hold the tile in place or how large a gap between tiles would be acceptable.

For a six-inch hole in the RCC panel, the cavity between the RCC panel and spar would be filled with a combination of titanium and water (ice) and the hole would be sealed with AFRSI.

These repair techniques would delay spar heating and burn through. However, it is not possible to accurately determine whether the delay would be sufficient to allow the vehicle to successfully reach a bailout altitude. This is due to uncertainties inherent in the identified repair techniques, including but not limited to the following: Gaps between the inserted tiles; Securing the tiles in place; Distribution of materials in the RCC cavity; Shifting of materials once hot gas enters the cavity and melts the ice.

4.5 EVA Techniques

An attempt to repair damage to the wing leading edge would require two EVAs. The objectives of the first EVA would be to harvest the materials to the used in the repair (tiles, AFRSI, etc) and to retrieve the EVA tools / equipment from the payload bay stowage assembly (if not retrieved on the inspection EVA). The objective of the second EVA would be to execute the repair of the wing leading edge.

The EVA to harvest repair materials has been assessed to have a moderate to high level of difficulty. The degree of difficulty is directly dependent on the type and location of the materials to be harvested.

Prior to the second repair EVA, the crew would remove and modify the Orbiter middeck ladder for use as an on-site EVA restraint aid. The crew would wrap towels or foam near the top of the ladder to protect the Orbiter wing from direct contact. The crew would also securely attach EV1's mini-workstation (MWS) to the ladder on the upper rung.

Other required hardware for the repair is TBD (see 4.2 above), but might include CWCs, jettison stowage bags, hose/valve/nozzle assembly, metal, AFRSI, tiles, etc.

At the start of the EVA, the EV crew would egress the airlock, retrieve the required EVA tools from the payload bay and translate with the middeck ladder along the port payload bay door. The first activity would be to restrain the middeck ladder at the worksite. The ladder would be inverted with the foam-protected portion against the wing leading edge. The ladder would be secured to the payload bay door using EVA retention devices and would be carefully tensioned to pull the ladder against the wing leading edge. EV1 and 2 would then transfer the repair hardware to the worksite. EV1 would translate down the middeck ladder and, with assistance from EV2, attach the preintegrated MWS to the EMU fittings (thus restraining himself to the ladder near the worksite). EV2 would then help to stabilize EV1 and assist with repair materials and hardware as required.

The assessment of the level of difficulty of the repair operation is high. The level of risk to the crew is moderate and the risk of doing additional damage to the Orbiter is high (i.e. enlarging the wing leading edge breach). The overall assessment of the expectation of task success is moderate to low, depending on damage site characteristics and the required repair technique.

A detailed synopsis of the EVA repair procedure is included in Appendix D.

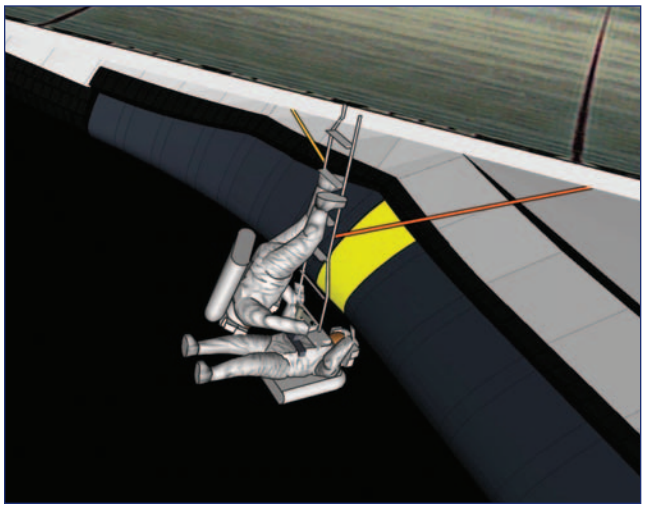


Figure 11. Repair EVA.

4.6 Wing Coldsoak

To freeze the water that was pumped into the CWC(s) in the left wing leading edge repair procedure, the left wing would have to be "coldsoaked" for three to six days. This coldsoak would result in a temperature decrease of the wing structure. In a typical flight, this type of coldsoak would not be performed, due to the impact on other systems like the main landing tires and wheels and the payload bay doors. However, for a known bailout case, tire and wheel temperature are not important and the thermal distortions of the payload bay doors may be acceptable. From the "Cain report" on entry options, it was determined that the maximum coldsoak would result in a 65 degree Fahrenheit decrease in the structural temperature at entry interface. This alone would not have been sufficient to maintain wing structural integrity, but coupled with the repair technique, weight jettison, and flying a 45-degree alpha profile, the structural heating may have been delayed sufficiently to allow a bailout.

4.7 Additional Entry Options – The "Cain Report"

NASA Flight Director Leroy Cain presented the report from the "Entry Options Tiger Team" to the Orbiter Vehicle Engineering Working Group (OVEWG) on April 22. This report was a very complete analysis of the results of jettisoning most of the payload bay cargo and coldsoaking the wing. Although this report looked at options within the certified entry design envelope, the options presented required some very difficult EVA tasks like cutting power and fluid cables, cutting through a tunnel, and large mass handling. This study does not assess the feasibility of these tasks, but it simply notes that whatever jettison tasks that could be accomplished in any remaining time during the two "repair" EVAs would be performed, as this would decrease the entry heating by a small amount. As there is a very large uncertainty band in the thermal analysis of a wing leading edge repair, it is sufficient to say that jettison of equipment would have occurred during any remaining EVA time, and this may have helped the overall total heat load.

4.8 Uncertified Options - Increased Angle of Attack /Low Drag Profile

The Entry Options Tiger Team was requested to look at certified options only. The only uncertified entry flight design options that could significantly reduce the wing leading edge temperature would be to change guidance to fly a lower drag profile during entry or to raise the angle of attack (alpha) to a reference of 45 degrees, vice the standard 40 degrees. However, it should be noted that while flying either one of these entry profiles would reduce heating on the leading edge, the heat load would increase on another part of the TPS structure. A simplified analysis that does not account for heating effects due to boundary layer tripping from a damaged area shows that a wing leading edge peak temperature could be decreased from a reference of 2,900 degrees F to 2,578 degrees F. This would be considered as an additional tool in attempting to maintain the spar structural integrity. It should be noted that changing the reference alpha would require a significant software patch to entry guidance.

4.9 Thermal Analysis

As previously stated, the team does not believe that an accurate thermal analysis can be performed to determine the effectiveness of any repair option. Rather, this is the best option relative to the other candidates, and it is possible that the combination of the repair, coldsoaking the wing, deorbiting from the minimum perigee, jettisoning available cargo bay hardware, and flying a 45 degree angle of attack could potentially provide enough relief to reach an acceptable bailout altitude. Limited thermal analysis was done on the option,

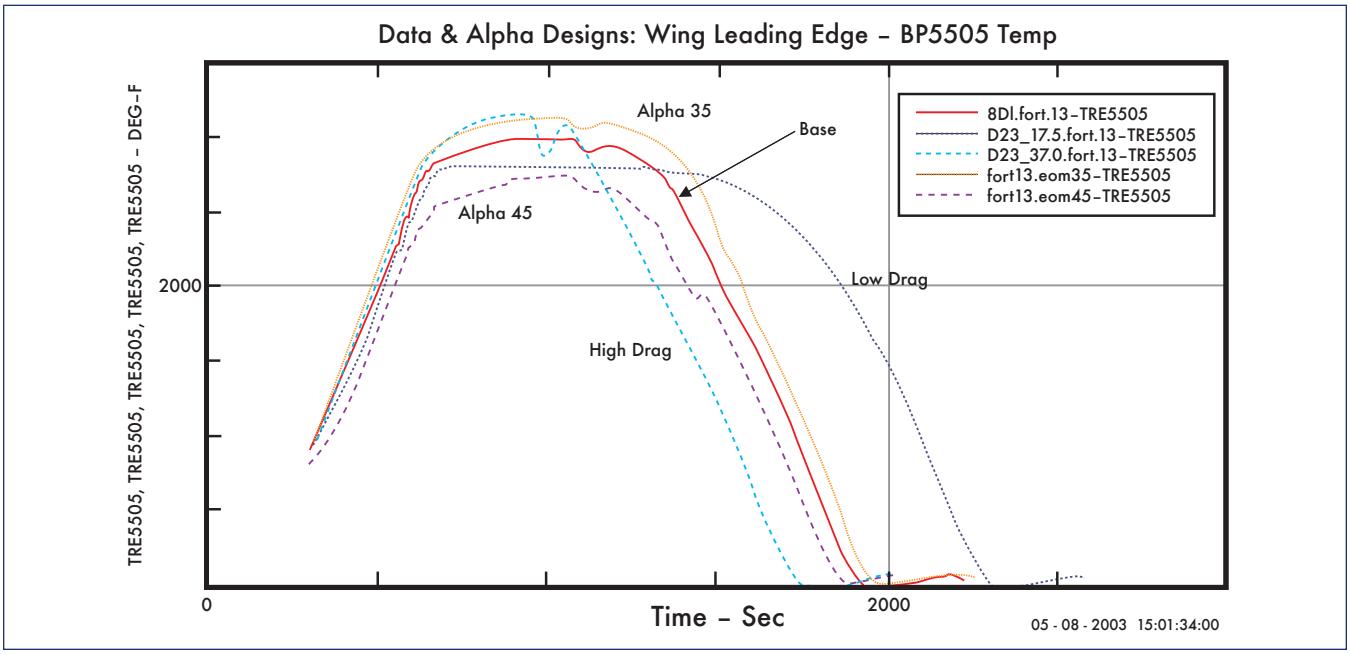


Figure 12. Relative Wing Leading Edge Temperature (No Boundary layer trip).

which assumed a flat plate of metal behind a flat plate of ice, behind a layer of AFRSI. The results while inconclusive, do not indicate this option was likely to succeed. However, the team believes it is sufficient to say that this would have been the best option to try, given the limited time and materials.

4.10 Bailout

4.10.1 Crew cabin configuration

For any repair option, it was the consensus of the team that the crew would be directed to bailout using standard procedures, due to the unknowns concerning structural damage to the wing and the landing gear. If the wing is damaged, the most probable time for failure is during final approach and landing. The dynamic pressure at landing is approximately 325 psf, while at bailout altitude (30K ft.) it is 225 psf.

For a planned bailout, or a potential vehicle breakup at an altitude higher than 30K feet, the following is the recommended procedure:

During D/O Prep, crewmembers would install seats and the escape pole as normal, and crewmembers would be strapped into seats as normal for entry. This would protect the crew in the event there is a loss of control or vehicle break-up. If there is a vehicle break-up (and the crew module survives intact), the crew could egress the crew module per the Break-up/LOC Cue Card.

During Entry, when the vehicle is at roughly 50k feet, the crew would start working the bailout portion of the emergency egress cue card. At 40k feet, they would vent the cabin. Working this step earlier, in the event of a vehicle breakup, would not be a good idea. If they started venting the cabin any earlier, it is likely that the cabin pressure would go low enough that their suits would begin to pressurize, making activity difficult. Venting at 40k feet keeps the cabin pressure high enough that the suits do not pressurize. At roughly 32k – 30k feet (as soon cabin pressure equalizes with ambient), they would jettison the hatch and bailout. Assuming the orbiter remains in controlled flight, there would be about 4 minutes from hatch jettison (~30k feet) to orbiter impact. In training, we typically see crews get out in about 2 minutes.

4.10.2 Maximum Altitude

Using the current Shuttle escape system, bailout (with the escape pole) must be done subsonic, and below 200 KEAS. Otherwise it is possible the pole may fail, crewmembers may contact the vehicle, crewmembers may experience flail injuries, or the suit and/or parachute may experience failures due to the wind speed. For a break-up scenario where the crewmember is egressing the separated crew module, it is still recommended to egress below 35K feet to reduce the possibility of flail injuries or suit/parachute failures. Also, bailing out at a higher altitude would be difficult. The suit will pressurize above 34K feet, limiting mobility and making it extremely difficult, if not impossible to get out the side hatch.

5.0 Other Considerations

5.1 LiOH Regeneration

LiOH that has been exposed to CO2 turns into lithium carbonate (Li2CO3). Research was performed at Ames Research Center to demonstrate that Li2CO3 could be converted to LiO using high temperature (1,250 degrees F) and a vacuum. The same researchers are now looking at the feasibility of conversion at lower temperatures. The maximum temperature for any part of the Orbiter payload bay environment is 250 degrees F. There is a potential that extended vacuum exposure could convert some of the Li2CO3 to LiO, which could then be hydrated to form LiOH. If it is determined that lower temperatures in a vacuum produce some conversion, the option of taking LiOH canisters into a hot part of the payload bay may provide additional LiOH capability. These tests are ongoing at this time.

5.2 Other vehicles (Soyuz, Ariane 4)

There has been some discussion regarding the possibility of sending supplies to *Columbia* using an expendable launch vehicle – to lengthen the amount of time available to execute a rescue mission. Because of *Columbia*'s 39-degree orbital inclination, an expendable launch from a launch site with a latitude greater than 39 degrees would not be able to reach *Columbia*. This rules out a Soyuz/Progress launch. There was an Ariane 4 in French Guiana that successfully launched an Intelsat satellite on February 15. The challenge with developing a supply kit, building an appropriate housing and separation system, and reprogramming the Ariane seems very difficult in three weeks, although this option is still in work.

5.3 ISS Safe Haven

The *Columbia*'s 39 degree orbital inclination could not have been altered to the ISS 51.6 degree inclination without approximately 12,600 ft/sec of translational capability. *Columbia* had 448 ft/sec of propellant available.

Appendix

Appendix A – Table of Events

(*Next page*)

Appendix B: EVA Inspection Procedure

- Pre-EVA, modify EV1 EMU to include an adjustable equipment tether (AET) secured around left EMU ankle (stabilization aid for EV2 at the inspection site), and towels gray-taped to right EMU boot (to protect the wing leading edge).
- EV1 egress airlock and transfer EV2's safety tether to port slidewire.
- EV1 and EV2 translate out and down the port Orbiter payload bay door (PLBD), first along the forward edge then aft along the outboard edge.
- Prior to reaching the wing leading edge, EV1 and 2 practice inspection technique with EV1 holding PLBD

Calendar Date	*Columbia – Mission Elapsed Time (MET) at 10:39 a.m.*	Columbia *Flight Day*	*Events*
Jan. 16	00/00:00	1	Columbia launch –10:39 a.m. EST
Jan. 17	01/00:00	2	Notification of foam strike on left wing
Jan. 18	02/00:00	3	Request National Assets
Jan. 19	03/00:00	4	Plan Inspection EVA – notify KSC to begin processing Atlantis
Jan. 20	04/00:00	5	Perform Inspection EVA. Major powerdown begins, LiOH conservation
Jan. 21	05/00:00	6	
Jan. 22	06/00:00	7	Last day to notify KSC for vehicle processing (to make 2/14 7:40 p.m. FD 1 rendezvous window)
Jan. 23	07/00:00	8	
Jan. 24	08/00:00	9	
Jan. 25	09/00:00	10	
Jan. 26	10/00:00	11	Atlantis Rollover – OPF to VAB
Jan. 27	11/00:00	12	
Jan. 28	12/00:00	13	
Jan. 29	13/00:00	14	
Jan. 30	14/00:00	15	Atlantis Rollout – VAB to Pad
Jan. 31	15/00:00	16	
Feb. 1	16/00:00	17	
Feb. 2	17/00:00	18	
Feb. 3	18/00:00	19	
Feb. 4	19/00:00	20	
Feb. 5	20/00:00	21	
Feb. 6	21/00:00	22	
Feb. 7	22/00:00	23	
Feb. 8	23/00:00	24	
Feb. 9	24/00:00	25	First launch window – 11:09 p.m. EST, rendezvous on Feb. 10
Feb. 10	25/00:00	26	Second launch window – 10:40 p.m. EST, rendezvous on Feb. 13
Feb. 11	26/00:00	27	Third launch window – 10:05 p.m. EST, rendezvous on Feb. 13
Feb. 12	27/00:00	28	
Feb. 13	28/00:00	29	
Feb. 14	29/00:00	30	Last FD 1 rndz Window 8:40 p.m. EST
Feb. 15	30/00:00	31	LiOH depleted – morning

edge while EV2 translates down EV1.
- Complete the translation to wing leading edge near RCC panel 8, and visually survey the upper surface of the wing.
- EV1 remain holding on to PLBD using the passive centerline latch mechanism for primary stabilization (body orientation facing inboard, head toward Orbiter –Z. If no damage noted on the upper surface, gently place right foot on the top of wing with left foot near wing leading edge.
- Using EV1 as translation aid, EV2 translate down EV1 to inspect panel (using AET on left leg as handling aid). EV2 provide verbal assessment of damage.
  - Note: If adequate stability achieved during practice

inspection, contact with the upper surface of the wing would not be required.

Appendix C: EVA Transfer Procedure

EVA Transfer Procedure:

- Both *Columbia* and *Atlantis* airlocks are depressed at the start of EVA.
- *Atlantis* EV2, using PFR sill stack and EVA boom (to extend reach), transfers other *Atlantis* EV1, and then extra LiOH canisters and two spare EMUs to *Columbia*.
- EV1 assists the first *Columbia* crewmembers (CM1 and 2) from the *Columbia* airlock.
- EV1 puts spare EMUs and LiOH canisters in the airlock, which is then repressed. CM3 and 4 don these EMUs.
- CM1 and 2 transfer to *Atlantis* (accompanied by *Atlantis* EV1), repress the airlock, doff their EMUs and prepare them for transfer back to *Columbia*.
- *Atlantis* EV1 and 2 conduct SAFER inspection of *Atlantis* TPS, and when convenient, EV1 installs a TCS reflector on *Columbia* for subsequent rendezvous.
- The same general process for CM transfer is used to transfer the remaining *Columbia* crewmembers to *Atlantis*. On the third transfer, only one *Columbia* crewmember is rescued, leaving two remaining (CM6 and 7).
- EMU donning for CM6 and 7 will be difficult since no IV will be available to assist. *Columbia*'s contingency EVA CMs would be best suited for this task. Consideration would be made to using EMU donning techniques developed for the first four Shuttle flights, while taking into account the recent ISS Expedition 7 EMU self-donning exercise.

Appendix D: EVA Repair Procedures

Damaged RCC Panel

Pre-EVA:

- Remove Orbiter middeck ladder and wrap towels or foam near the top of the ladder (to protect Orbiter wing from direct contact).
- Required hardware for repair:
  1. 2-3 empty CWCs
  2. 2 empty jettison stowage bags
  3. Jettison stowage bag filled with various metal parts
  4. Hose/valve/nozzle assembly attached to water port on Airlock panel
- Prior EVA required to retrieve mini-workstations (MWS) from PSA.
- Attach EV1 MWS securely to ladder. (EV2 will begin EVA with MWS, EV1 without.)

EVA Repair Procedure:

- EVA crew egress airlock and retrieve required EVA tools from PSA.
- EVA crew harvest AFRSI from aft fuselage of Orbiter; stow in bag
- EVA crew, with middeck ladder, translate out and down port Orbiter PLBD using same translation route used during inspection.
- Restrain middeck ladder at worksite:
  - Note: ladder is inverted with foam-protected top portion against wing leading edge.
  - Attach ladder to PLBD passive centerline latch mechanism using tethers.
  - Use aft bulkhead winch (or rope reel) and PRD routed from aft hinge of PLBD (under opened PLBD) to ladder close to the top of the wing and gently pull ladder against wing leading edge.
- Transfer repair hardware to worksite.
- EV1 translate down middeck ladder and, with assistance from EV2, attach MWS to EMU (thus restraining self to ladder and near worksite).
- EV2 help to stabilize EV1, and assist with repair materials and hardware as required.
- EV1 repair damaged panel:
  - Stuff empty jettison stowage bag in hole.
  - Fill jettison stowage bag with various metal parts (from other bag).
  - Stuff empty CWC in hole and fill with water.
  - Stuff additional CWC in hole and fill with water.
  - Seal hole with AFRSI.

Note: The assessment of the level of difficulty is high, level of risk to crew is moderate and the risk of doing additional damage to Orbiter is high (i.e. enlarging the wing leading edge breach). Overall assessment of the expectation of task success is moderate to low, depending on damage site characteristics.

Damaged T-seal

Pre-EVA:

- Remove Orbiter middeck ladder and wrap towels or foam near the top of the ladder (to protect Orbiter wing from direct contact).
- Required hardware for repair:
  1. Harvested tile sculpted to fit in T-seal
- Prior EVA required to retrieve mini-workstations (MWS) from PSA and harvest tile from canopy of Orbiter.
- Attach EV1 MWS securely to ladder. (EV2 will begin EVA with MWS, EV1 without.)

EVA Repair Procedure:

- EVA crew egress airlock and retrieve required EVA tools from PSA.
- EVA crew, with middeck ladder, translate out and down port Orbiter PLBD using same translation route used during inspection.
- Restrain middeck ladder at worksite:
  - Note: ladder is inverted with foam-protected top portion against wing leading edge.
  - Attach ladder to PLBD passive centerline latch mechanism using tethers.
  - Use aft bulkhead winch (or rope reel) and PRD

routed from aft hinge of PLBD (under opened PLBD) to ladder close to the top of the wing and gently pull ladder against wing leading edge.
- Transfer repair hardware (jettison stowage bag) to worksite.
- EV1 translate down middeck ladder and, with assistance from EV2, attach MWS to EMU (thus restraining self to ladder and near worksite).
- EV2 help to stabilize EV1, and assist with repair materials and hardware as required.
- EV1 repair damaged T-seal:
  - Insert tile into T-seal gap minimizing spaces between tile

Note: The assessment of the level of difficulty is high, level of risk to crew is moderate and the risk of doing additional damage to Orbiter is high (i.e. enlarging the wing leading edge breach). Overall assessment of the expectation of task success is moderate to low, depending on damage site characteristics.

Appendix E: Rendezvous Burn Plans

February 9th:

Launch Window Inplane Launch GMT: 40/03:40:24
Second window pane available (will require FD4 rndz)

Phase angle: 161 degrees (FD3 rndz)

OMS-2:	0/00:38 07 MET	150.4 fps
NC-1:	0/03:35:52 MET	6.0 fps
NC-2:	0/15:27:21 MET	3.0 fps
NPC:	0/19:04:29 MET	1.5 fps
NC-3:	0/22:52:01 MET	3.0 fps
NH:	1/13:24:45 MET	103.5 fps
NC-4:	1/13:57:09 MET	37.1 fps
Ti:	1/15:27:33 MET	9.0 fps

Total Cost (OMS-2 to Ti) = 313.5 fps

February 10th:

Launch Window Inplane Launch GMT: 41/03:09:05
Second window pane available (may require FD4 rndz)

FD1, 2, or 3 rndz available on this day.

Delay launch until a phase angle of 30 degrees was achieved (phase angle at the IP time was only 11 degrees)

Phase angle: 30 degrees (this plan reflects a FD3 rndz)

OMS-2:	0/00:38:08 MET	229.4 fps
NH (NC-1):	0/03:14:25 MET	50.9 fps
NC-2:	0/18:16:58 MET	6.0 fps
NPC:	0/21:39:48 MET	1.3 fps
NC-3:	1/03:18:48 MET	3.0 fps
NC-4:	1/16:02:24 MET	6.1 fps
Ti:	1/17:32:48 MET	9.0 fps

Total Cost (OMS-2 to Ti) = 305.7 fps
Note: For a FD2 or FD1 rndz, costs increase approximately 10 fps total.

February 11th:

Launch window Inplane Launch GMT: 42/02:41:47
Single pane day, FD3 rndz only.

Phase angle: 235 degrees

OMS-2:	0/00:38:07 MET	97.4 fps
NC-1:	0/03:34:46 MET	6.0 fps
NC-2:	0/15:21:41 MET	3.0 fps
NPC:	0/18:47:53 MET	1.3 fps
NC-3:	1/03:20:00 MET	3.0 fps
NH:	1/14:40:45 MET	145.7 fps
NC-4:	1/15:12:20 MET	68.8 fps
Ti:	1/16:42:43 MET	9.0 fps

Total Cost (OMS-2 to Ti) = 334.2 fps

February 12th:

Launch Window Inplane Launch GMT: 43/02:10:29
Second window pane available (FD4 rndz required)

Phase angle: 87 degrees (FD3 rndz)

OMS-2:	0/00:38:35 MET	165.8 fps
NC-1:	0/03:36:11 MET	6.0 fps
NC-2:	0/15:17:45 MET	89.0 fps
NPC:	0/18:22:15 MET	0.8 fps
NC-3:	1/01:47:52 MET	3.0 fps
NC-4:	1/14:21:06 MET	32.3 fps
Ti:	1/15:51:28 MET	9.1 fps

Total Cost (OMS-2 to Ti) = 305.9 fps

February 13th:

Launch window Inplane Launch GMT: 44/01:43:10
FD4 rndz only
However, we chose to phase from above (go higher than the target) and launch near the end of the window. This costs more propellant but preserves FD3 rndz.
FD1 or FD2 rndz not possible.
Richard, this case would involve some fancy IY generation.

Phase angle: -28 degrees

OMS-2:	0/00:38:35 MET	212.4 fps
NC-1:	0/03:29:00 MET	118.8 fps
NC-2:	0/15:36:01 MET	3.0 fps
NPC:	0/19:13:01 MET	1.0 fps
NC-3:	1/01:47:00 MET	3.0 fps
NH:	1/14:25:45 MET	81.38 fps (retrograde)
NC-4:	1/14:45:00 MET	29.7 fps
Ti:	1/16:21:47 MET	9.0 fps

Total Cost (OMS-2 to Ti) = 458.3 fps
Note: FD4 rndz would be more in line with the other plans (cost ~330 fps)

February 14th:

Launch Window Inplane Launch GMT: 45/01:11:52

Plan virtually identical to February 9th. No significant deltas.

THIS PAGE INTENTIONALLY LEFT BLANK



Volume II

Appendix D.14

Orbiter Major Modification Review

Investigation Group I of the Columbia Accident Investigation Board conducted a review of the policies and procedures used by NASA during Orbiter Major Modifications (OMM) and Orbiter Maintenance Down Periods (OMPD). As part of this effort, the U.S. Air Force was invited to conduct an independent review. The results of these efforts are documented in this appendix.

The investigators who conducted this review proposed a number of recommendations, several of which were adopted by the Board for inclusion in the final report. The conclusions drawn in this review do not necessarily reflect the conclusions of the Board; when there is a conflict, the statements in Volume I of the Columbia Accident Investigation Board Report take precedence.

THIS PAGE INTENTIONALLY LEFT BLANK

Orbiter Major Modification Review

Submitted by Group I
Major General John L. Barry, Brigadier General Duane W. Deal, Rear Admiral Stephen A. Turcotte
Colonel Timothy D. Bair, John F. Lehman, Colonel David T. Nakayama

1.0 ISSUE

Review/assess past OMM performance, the movement of OMMs from Palmdale to Kennedy Space Center (KSC), and OV-102's most recent OMM; identify significant issues and/or concerns.

2.0 BACKGROUND

The Space Shuttle Program Requirements, NSTS 07700, Volume III, establishes the requirement for each Orbiter to undergo an OMM every 8 flights or 3 years. Orbiters are removed from service for varying amounts of time to accomplish OMMs, depending on the amount and type of work to be performed. This work includes baseline requirements, such as component changes based on time and/or cycles; routine inspections, such as structural components; special inspections, such as the wiring work performed on OV-102 in the aftermath of the short circuit on STS-93; modifications, deferred work, and correcting "stumble ons" (estimated to be at least 40 percent of the total work performed). Besides OMMs, two other opportunities to perform Orbiter inspection and maintenance occur during the "standard flow" that is part of every mission. An OMM is a subset of an OMDP, although OMMs are not part of every OMDP. There are vastly more inspection and maintenance requirements during an OMDP; a recent comparison showed 8,702 OMDP/OMM requirements (STS-109) versus 3,826 for a standard flow (STS-111), or 127 percent more. OMMs typically involve the most intrusive inspections, maintenance, and modifications compared to a flow.

3.0 FINDINGS

OMM History – Wide Variations in Duration

Ten OMMs have been performed in the history of the Space Shuttle Program (SSP): eight at Air Force Plant 42 in Palmdale, California, by Boeing (formerly Rockwell, the shuttle's original manufacturer), and two at Kennedy Space Center (KSC). Figure 1 shows the OMM history.

The eight at Palmdale include OV-102's "AA" OMM, which was a demodification from a test/development to an operational configuration. Both OMMs at KSC were OV-103, first for its J1 OMM (February to August 1992), and again for its J3 (in progress since Sep 02). The durations of each OMM has varied widely, ranging anywhere from 5.7 months (OV-102/J1) to 19.5 months (OV-104/J1); the OV-102/J3 OMM, at 17 months, was the second longest in program history. The time duration of an OMM is driven more by the number of modifications than by recurring inspections and maintenance, and the wide variation is the result of differences in OMM content.

OMM Intervals – Should They Be Extended?

Over the history of the Space shuttle Program, the challenge with scheduling Orbiters for OMM has been accomplishing interval/periodic requirements as close to the specified interval as possible without exceeding them, while simultaneously supporting the launch schedule (manifest) and having no more than one Orbiter undergoing OMDP at a time. Because of these scheduling complexities, some latitude in the 8-flight/ 3-year interval is allowed, as long as requirements are met through actions during flows. This can be seen in the number of Orbiters that have exceeded the 8 flight/3 year interval: OV-102 had 9 flights and 4 years between its J2 and J3 OMMs; OV-103 had 9 flights and 4.5 years between its J2 and J3; OV-105 currently has 8 flights and over 5 years and, by the time of its next OMM, would have had 11 flights and over 6 years if the schedule prior to the *Columbia* accident was still in effect; finally, OV-104 would have 12 flights and 6 years by its October 2005 OMM if the pre-*Columbia* manifest was still in effect. Studies/analyses have been conducted since 1999 on how intervals might be extended to as much as 12 flights and 6 years, but there has been no decision to date. A general rule

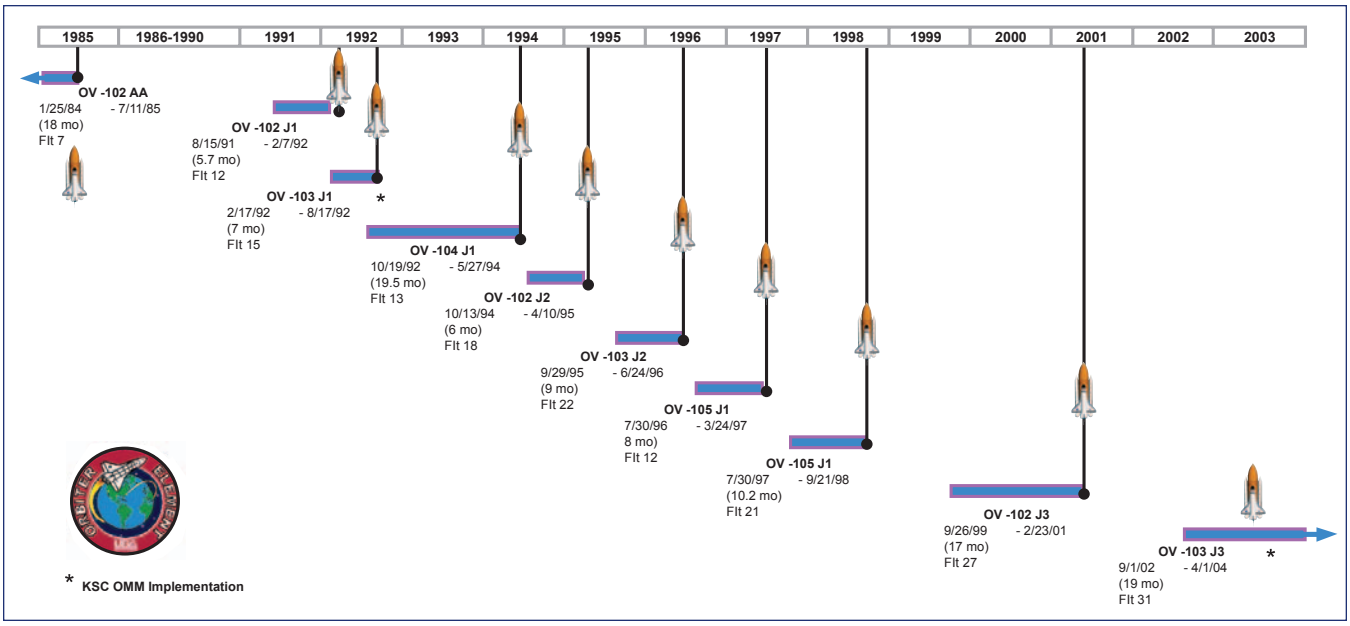


Figure 1. Orbiter Major Modification (OMM) history.

in industry, however, is that time-based inspections become more frequent as vehicles age. This seems to run counter to the Space Shuttle Program's initiative of increasing the OMM interval.

OMM Content – Where Are Modifications Really Performed?

More modifications are performed during flows than during OMM. Thirty-six percent, or 2,177 of the 5,985 total modifications across the fleet were done in OMMs, whereas 3,808, or 64 percent, were accomplished during flows. While these numbers alone do not indicate the relative simplicity or complexity of each mod, they do reflect a philosophy of scheduling simpler, less intrusive mods during flow rather than deferring them to OMM. This leaves OMMs with increased flexibility for more complex mods and unexpected problems. Figure 2 shows the numbers of mods performed in OMMs/flows.

ORBITER	MODS IN OMM	MODS IN FLOW	TOTAL MODS
OV-102	608	1,058	1,666
OV-103	675	936	1,611
OV-104	691	725	1,416
OV-105	203	1,089	1,292
TOTAL	2,177	3,808	5,985

Figure 2. Modifications performed in OMM vs. flow.

OMM Location – Palmdale or KSC?

A major change in location occurred with the move of OMMs from Palmdale, the Orbiters' birthplace, to KSC, starting with OV-103 in September 2002. Since Palmdale completed the last Orbiter (*Endeavour*, OV-105) there has been discussions of moving major maintenace from Palmdale to another site. During the late 1980s these discussions took the form of moving OMDPs to the Orbiter Maintenance and Checkout Facility at Vandenberg Air Force Base in California since it was a state-of-the-art facility. This concept was discarded on cost grounds, and the equipment from the VLS OMCF was later moved to KSC to equip OPF-3. Discussion then turned to moving major maintenance to KSC. While Palmdale had the advantage of being the manufacturing site, there were a large number of disadvantages, such as the high labor rate, the higher cost of basics such as utilities, and a "migrant" workforce that ebbed and flowed with each OMM. A 1995 NASA Inspector General (IG) report acknowledged a move to KSC would result in cost savings, but due to the complexity of scheduled work (including an aggressive launch schedule - eight were launched in 1996 and another eight in 1997), recommended leaving the next two OMMs at Palmdale. A second look by the NASA IG in 1998 reconfirmed that OMMs at Palmdale were costlier, but also stated risk was greatly reduced by performing them there, and that the risk of moving them to KSC outweighed potential cost savings. The report recommended reevaluating the feasibility of moving when significant changes occur (there were only four launches annually in 1998, 1999, and 2000, but no OMM movement). In the summer and fall of 2001, the JSC Systems Management Office (SMO) and the Space Shuttle Program conducted more reviews. The JSC SMO concluded that significant savings could be realized even comparing the worst case at KSC with the best case at Palmdale. Meanwhile, the launch rate rose to seven in 2001 and six in 2002, levels of activity nearing those when the NASA IG had recommended not moving OMMs from Palmdale. Nevertheless, in February 2002, the NASA Administrator approved performing OV-103's OMM at KSC, beginning in September 2002. The staffing package specifically cited FY 03 budget shortfalls and their impact on FY02

as short-term factors, and overall life cycle cost reduction as a long-term factor weighing on the decision. Though a reduced launch rate is reported to have been a consideration, the decision packages only mention budgetary concerns and, given the increasing number of launches in 2001 and 2002, the reduced launch rate appears to have been a secondary consideration, at best.

Palmdale/KSC Infrastructure Comparison

A comparison of the infrastructure at both locations shows them to roughly be on par. KSC has three processing bays, whereas Palmdale has two. KSC became "maxed out" after the move, with four Orbiters and only three bays. One illustration of the impact of this Orbiter overpopulation is OV-103's movement at least 6 times in 9-months while awaiting an OMM location decision. These moves unnecessarily consume manpower, take time, can be disruptive if maintenance is in progress, and creates opportunities for mistakes; when OMMs were performed at Palmdale, this was typically not an issue. The loss of *Columbia* alleviated this situation since there are only three remaining Orbiters.



Figure 3. OV-102 undergoing OMM at Boeing's Palmdale facility.

Support equipment capabilities are comparable, with a slight advantage at Palmdale when it comes to large component removal and installation. This is the result of Palmdale being the original manufacturing site and having, among other assets, large overhead hoists. Other pieces of support equipment were shared/shipped between KSC and Palmdale. Figure 3. shows OV-102 in OMM at Palmdale.

Palmdale/KSC Logistics Comparison

In terms of logistics, the steady improvement of the NASA Shuttle Logistics Depot (NSLD) in Florida over the years has reduced the need for expensive, duplicate capabilities on the West Coast. Even prior to the OMM move, support to Orbiters in OMM at Palmdale was increasingly coming from NSLD. For the last OMM at Palmdale (OV-102), 2,663 orders comprising 76,894 pieces were shipped from NSLD; these included hardware, line replacement units (LRU), and consumables. For the OMM prior to OV-102 (OV-104), 1,538 orders comprised of 47,487 pieces were shipped from the NSLD. The majority of Palmdale's industrial shops (Thermal Protection Systems, Avionics, and Wiring, just to mention a few) have generally atrophied due to the lack of activity. There are a few exceptions where Boeing is currently the sole source provider of services to the Space Shuttle Program (manufacture of 17 inch disconnects and cold plates). The Palmdale machine shop is another capability that has not atrophied, not because it is a sole source supplier, but primarily due to its support of other non-Space Shuttle Program requirements; what *is* important is that it is used by NSLD for reserve/overflow capacity.

Workforce Efficiency, Flexibility, and Capacity

Work force/labor expenditures appear more efficient at KSC, but differences in tracking methodology and the newness of OMMs at KSC make it too early for any definitive conclusions. The last four Palmdale OMMs ranged anywhere from 324 to 448 equivalent personnel (EP), with an average of 383. OV-102 required 394 EP and took 17 months, whereas its predecessor, OV-104 required 448 EP but only took 10.2 months. KSC augmentation of the Palmdale work force with 30 to 40 technicians, inspectors, and engineers also occurred on a regular basis; some of this was due to KSC's familiarity/proficiency with "power-on" requirements. During the first 9 months (Sepember 2002 – May 2003) of OV-103's OMM at KSC, an average of 307 EP have been required, compared with a projection of 235. While the number of EP is higher than forecasted, this is probably due to increasing requirements (discussed later in this chapter) and is still lower than the EP required for OV-102 at Palmdale. There are several potential reasons favoring more efficient work force utilization at KSC, and these factored heavily in the decision to move OMMs to KSC. When all Orbiter work (OMDPs and standard flows) is considered, there is a larger amount at KSC. This requires a larger overall workforce, which, in turn, allows management the flexibility to reallocate manpower to match specific peaks and valleys associated with each Orbiter. While workers may not always be working on an OMM, they are more likely to be consistently doing Orbiter work at KSC. This contrasts with the "nomadic" work force at Palmdale, which, after an OMM was complete, moved to other jobs (not necessarily on Orbiters or in aviation) until the next OMM. The steadier overall Orbiter workload at KSC thus serves to keep worker proficiency at a higher level and, more importantly, preserves Orbiter-related proficiency (a much higher standard compared to general aviation). It is important to note that the larger, more versatile work force and improved efficiency at KSC are not limited to technicians; it also applies to management and staff (planners, schedulers, engineers, etc). However, one concern voiced by senior managers is the ability of the work force to focus because of their increased "fluidity" (i.e., moving between OMM and down-/up-mission processing); this may apply even more to management and staff personnel (given that technician workload is very structured), and needs to be carefully monitored.

Workforce Experience and Training

Workforce inexperience can also be handled with less impact in a large workforce, as at KSC. For the OMM relocation to KSC, 176 additional workers were hired. These new hires were dispersed throughout the entire workforce

of 1,900 to minimize their training load/impact; the larger workforce, compared to Palmdale, was better able to absorb inexperienced technicians. By comparison, the OV-102 OMM at Palmdale shows how a smaller workforce is less able to deal with this kind of challenge. Palmdale's initial workforce of 342 had an 85 percent experience level (either previous OMM work or Orbiter manufacturing). Key personnel had been strategically placed in other Boeing organizations to keep them employed when there was no OMM work and have them available for recall as OMMs were scheduled. However, as OV-102's OMM workload increased (with new, post roll-in requirements), the workforce had to be expanded to 500; in this expansion, experienced personnel were "tapped out" and the experience level dropped to 58 percent; simultaneously, the time spent training new/inexperienced workers increased, including on-the-job training.

Palmdale's Last OMM – OV-102

The last OMM at Palmdale, OV-102, requires comment because problems encountered should serve as valuable "lessons learned" for future work, regardless of location. It was the first OMM completely managed by United States Alliance with Boeing subcontracted to do the work. OV-102 rolled into OMM at Palmdale on 26 September 1999 and rolled out on 24 February 2001. The contractor initially forecast OMM duration at 331 days, but the Space Shuttle Program Office directed it downward to 293 days based on "considerations of repeat modifications and a lesser workload." Its actual duration was 517 days, a 76 percent growth. Despite this, it rolled out with 98 percent of all work complete. Major modifications included, but were not limited to MEDS (Multifunction Electronic Display System, aka glass cockpit), GPS (Global Positioning System), and wireless video. There was a large growth in requirements (see Figure 4.) – 103-percent since the preplanning baseline 10 months prior to roll-in.

When OV-102's requirements growth is compared with the three previous OMMs, Columbia exceeds all three, with the next highest being approximately 20 percent less; with wiring inspection requirements removed from the comparison, OV-102 still has the second largest rate of increase, but only by 4 percent.

ORBITER	INITIAL PLANNING	CCB BASELINE	PERCENT INCREASE
OV-103 J2 9/95 – 6/96	383	532	39%
OV-105 J1 7/96 – 3/97	278	405	46%
OV-104 J2 11/97 – 9/98	461	844	83%
OV-102 J3 9/99 – 2/01	330	671	103%
OV-102 J3 w/o Wire Insp	330	591	79%

Figure 5. Comparison of OMM Requirements Growth.

More important than the increasing numbers of requirements or the percent growth is the manner in which the changing requirements were managed. An independent assessment of the OV-102 OMM by HEDS, the Human Exploration and Development of Space office, summarized the OV-102 OMM in terms of cost and schedule slippage as "poor performance on the parts of NASA, USA, and Boeing." The same report noted, however, that "Work quality was very good to excellent."

More specific examples of these general comments follow. Palmdale had an adequate workforce, both in numbers and skill, to perform OV-102's OMM as originally planned, but unforeseen problems and added requirements quickly exceeded Palmdale's capabilities. The number of requirements established at the Modification Site Requirements Review grew by 103 percent, although this was the planning baseline for resource allocation; additionally, it grew by 82 percent after roll-in. An extremely invasive wiring inspection, based on identifying and correcting the root cause of an anomaly during STS-93, was added 1-month after roll-in; 8 additional weeks were estimated for this add-on, based on the expectation of 500 to 700 anomalies; in reality, over 4,600 were found; as anomalies were identified and analyzed, the CHIT directing the inspection was revised six times, adding further turmoil. Other technical surprises such as the accidental discovery of cold plate corrosion, and

	Preplanning Baseline (11/06/98)	Initial Baseline (04/01/99)	Baseline Wire Insp (10/13/99)	CCB Baseline (10/25/00)	CCB Baseline (01/31/01)	Percent Growth (since 1998)
MCRs	66	70	75	99	102	85%
Mod Kits	62	68	80	142	152	145%
Tech Orders	28	36	42	56	58	107%
TCTIs & NSW	55	58	68	100	110	100%
Deferred WADs	105	150	194	204	206	96%
Chits	14	17	20	37	43	207%
Total	330	399	479	638	671	103%

Figure 4. Ov-102 OMM Requirements Growth.

procedural problems such as payload door rigging taking twice as long as expected, stretched the schedule out and, combined with the wiring inspections, slipped the all-critical power-on testing phase. The contractor's OMM flow manager was inexperienced and messages to the Space Shuttle Program regarding key milestones were regularly optimistic. The contractor used a new, unproven scheduling tool that was eventually assessed as inadequate; management returned to the previously used tool 12-months into the OMM. The rapidly increasing number of non-conformances made integration of the workload increasingly difficult. Integrated scheduling meetings were held weekly (vice daily) and were not frequent enough to stay abreast of the rapidly changing scope of work; it was not until 12 months into the OMM that daily meetings were held. The Space Shuttle Program Office exacerbated the situation by turning the OMM management process over to the contractor without a structured insight function in place.

It is important to reiterate that, despite these problems, a commitment to excellence prevailed and OV-102 was rolled out with 98 percent of all scheduled work complete. "Traveled work", the work carried forward to KSC and completed there, amounted to 9,071 hours, or 0.66 percent of the total work. By comparison, traveled work following OV-102's J2 OMM was 0.89 percent (7,886 hours), and OV-103's J2 was 0.38 percent (2,252 hours). All traveled work was fully coordinated and there were no surprises at KSC.

OV-103's OMM – Were Lessons Learned From OV-102?

It appears lessons learned from the OV-102 J3 experience are being applied to the OV-103 J3 OMM, currently in progress at KSC. For example, efforts at better communication include scheduling meetings three times a week, reviews by Ground Operations managers twice weekly, and monthly Project Management Reviews (PMR) chaired by the JSC Orbiter Project Manager, all with close attention to critical path. There also appears to be a healthy "give and take" at the PMRs, and capabilities assessments for resource-constrained areas are presented at PMRs. However, the OV-103 OMM still demonstrates room for improvement. For example, the problem of requirements growth continues, to a greater extent than OV-102; there were originally 20 scheduled modifications for OV-103, reportedly due to budget constraints and also due to a conservative approach since this was the first OMM at KSC in 10 years; hence, many planned mods were "shelved"; however, 9-months (75 percent) through the OMM, the number of mods being performed has increased to 84 (320 percent growth, far worse than OV-102's 103 percent growth) as mods are being "pulled off the shelf" and added; while the OMM critical path is closely monitored and workload is being relatively well-managed (e.g., another 24 mods are being held), the added work again introduces turmoil and increased potential for mistakes. Despite this requirements growth, OMM flow managers seem to be coping fairly well. However, the requirements growth adds an unnecessary unplanned/ unscheduled dimension to the OMM requirements. An independent Air Force Programmed Depot Maintenance benchmarking team made the same observation with the same concerns.

Air Force Programmed Depot Maintenance (Palmdale) Benchmarking Visit

In June 2003, an Air Force Depot Maintenance Team conducted an OMDP/OMM benchmarking visit for 4-days at the invitation of NASA Code M. The team was led by an Air Force program manager and comprised of five civil servants with extensive experience in the Air Force's Programmed Depot Maintenance system; specific areas of expertise included requirements/sustainment engineering, planning, scheduling, quality assurance, safety, training, and industrial production. Areas worthy of benchmarking from an Air Forceperspective included the painstakingly meticulous documentation (WADs, or Work Authorization Documents), adherence to policy and procedures (traceability of inspection/maintenance requirements from source documents), logistics support (NASA Shuttle Logistics Depot), "ship side" engineering support (engineers in the Orbiter Processing Facility), safety ("time out" policy), and communication (numerous meetings to stay abreast of OMM progress). Areas requiring review/ increased attention on NASA's part included instituting a better closed loop feedback process for requirements definition (e.g., the Master Verification Plan, the Operations and Maintenance Requirements Specification Document, and the Quality Planning Requirements Document) to keep them updated as changes occur, increased planning and scheduling stability, incorporating Orbiter sustainment roadmap requirements into OMMs, and reviewing government/contractor relationships to ensure the right contractor "behavior" is being encouraged/incentivized. The issue of closed loop feedback is extensively addressed in this report under Safety and Mission Assurance (S&MA), but is equally applicable to inspection and maintenance requirements (MVP and OMRSD). Increased planning and scheduling stability were previously addressed as a "lesson learned" from the OV-102/J3 OMM, and also from the current OV-103/J3 OMM. Sustainment roadmap issues are addressed separately in this report under Service Life Extension Program (SLEP) and Mid-Life Certification (MLC), just as government/contractor relationships are. In summary, the Air Force OMM Benchmarking Visit duplicated/validated issues already being examined by the Columbia Accident Investigation Board and was an excellent second look.

4.0 Conclusions

While there are specific baseline elements to every OMM, no two are alike; variations in content will occur, and should be expected to continue to occur, based on aging requirements (wiring inspections, cold plate corrosion), on mission requirements (reconfiguration for *Mir*), and in some cases due to fluctuating resources (budget). However, improving planning/scheduling stability, to include factors for the "unknown-unknowns", and instituting increased consistency is needed to reduce the wide variations in OMM duration and make the flow more manageable.

Increasing OMM intervals as the Orbiters age is counter to industry norms and, for high performance systems, raises even greater questions. While no decision has yet been made, NASA must carefully study the implications of such a decision.

Relocating OMMs from Palmdale to KSC, while heavily driven by cost and budget, was a sound decision from an overall program perspective. However, it creates new challenges that must be readily recognized and quickly addressed. For example, even KSC's increased capabilities can be overwhelmed if not carefully managed. Additionally, several NASA, USA, and Boeing senior managers have expressed concern over the ability of a fluid workforce (i.e., one that is being shifted between different Orbiters to respond to workload peaks and valleys) to focus on the task at hand.

The wiring inspection CHIT and its timing, 1-month after OV-102's roll-in, played a major role in OV-102's schedule slippage and cost growth. It is representative of "technical surprises" that will likely continue, particularly as the Orbiters age, with no option other than "must do".

The overall OV-102/J3 OMM experience presents a multitude of lessons learned that have fleet implications because, as the Orbiters age, workload will likely increase; so will technical surprises, as mentioned above; and a significant return-to-flight workload is also probable. All of these factors will combine to generate new challenges for both managers and the workforce.

5.0 Proposed Recommendations

The Space Shuttle Program Office must work to achieve greater stability, consistency, and predictability in OMM planning, scheduling, and work standards, particularly the number of modifications. Continually changing schedules, predominantly because of requirements growth, create unnecessary turmoil and can be detrimental to product quality. Templates for "standard work" must be developed and refined through use in planning and scheduling.

Both NASA and United Space Alliance managers must understand workforce and facilities capabilities, match them against requirements, and take action to avoid exceeding thresholds.

NASA and USA Space Shuttle Program managers should continue to benchmark with the Air Force in the areas of program management, coping with aging systems, life extension programs, mid-life certification, workload planning and scheduling, work force management and training, quality assurance, etc; the initial Air Force visit in Jun 03 was only the beginning of a potentially great exchange of ideas and practices. As much as possible, both Air Forceand NASA personnel involved in these benchmarking events should remain the same to overcome initial learning curves.

The SSP Office must determine how it will effectively meet the challenges of inspecting and maintaining an aging Orbiter fleet Prior to lengthening the OMM interval.

References

1. Air Force Assistance Visit briefing, "NASA Orbiter Maintenance Down Period/Orbiter Major Modification, 17 Jun 03
2. USA briefing, "OV-103 J3 OMDP Project Management Review", 12 Jun 03
3. NASA "OMDP/OMM Requirements Overview" briefing, 9 Jun 03
4. NASA "Orbiter Maintenance Down Period (OMDP) Overview – Implementation" briefing, 9 Jun 03
5. Shuttle Ground Operations OMM Quality briefing, 9 Jun 03
6. Boeing/Palmdale OMM briefings/tours, 14 May 03
7. USA briefing, "OV-103 J3 OMDP Project Management Review", 1 May 03
8. USA briefing, "Delta MSFR OV-103 J3 OMM", 17 Apr 03
9. USA briefing, "KSC and Palmdale OMDP Comparison", 26 Feb 03
10. USA briefing, "Orbiter Modifications", 8 Feb 03
11. GAO response to Senator Boxer, "Relocation of Space Shuttle Major Modification Work", 2 Dec 02
12. JSC/AC5 memo to JSC/MA (SSP) et al, "Trip Report: Orbiter Processing Facility, Bay 3, Orbiter OV-103 Maintenance Down Period (OMDP) Inspections and Upgrades, 8 Oct 02
13. USA briefing to PRB & PRCB, "OV-103 OMDP-3 Mod Site Flow Review (MSFR)", 13/15 Aug 02
14. JSC Systems Management Office briefing, "Response to the GAO Audit of the Decision to Move the Orbiter OV-103 OMM to KSC", 18 Jul 02
15. Code M briefing to Senator Feinstein's staff, "Orbiter Major Modifications (OMM), 26 Jun 02
16. JSC/AC5 memo to JSC/MA (SSP) et al, "OV-103, Discovery, Maintenance Upgrades", 18 Apr 02
17. NASA Code M memo to NASA Administrator, "Should OMMs be moved from Palmdale to Florida?", 16 Jan 02
18. USA briefing, "OV-103 J3 Pre-Decision Package Summary", 19 Dec 01
19. Space Shuttle Program (MA-01) memo to NASA Code M, "Orbiter Vehicle –103 (OV-103) Orbiter Major Down Period (OMDP), 21 Nov 01
20. HEDS/IA briefing, "OV-103 J3 OMM Assessment", 14 Nov 01
21. HEDS/IA Report KS-0003, "Evaluation of the Current (OV-102) Orbiter major Modification (OMM) Flow, Mar 01
22. NASA/IG Report, "Followup Audit on Orbiter Maintenance Down Periods at KSC", 12 Jun 98
23. NASA/IG memo to Code M, "Final Rapid Action Report [on] Impacts of Performing Orbiter Maintenance Down Periods (OMDPs) at KSC versus Palmdale", 24 Oct 95.

Volume II
Appendix D.15

Maintenance, Material, and Management Inputs

Group I of the Columbia Accident Investigation Board was directed to examine maintenance procedures and sustainment issues as they related to the investigation, returning the Shuttle fleet to active service, and sustaining it for the foreseeable program lifespan. Specific areas of emphasis included: 1) Vehicle and subsystem analysis relating to the investigation, 2) Maintenance requirements determination including safety, quality assurance, scheduling and documentation, 3) Fleet sustainment issues including aging infrastructure and service life extension, and 4) logistics support issues including manpower, contract and financial management. This group's charter extended into management and sustainment issues and the final report includes proposed recommendations for the continuation of safe flight operations for the remaining Shuttles, *Discovery*, *Endeavour*, and *Atlantis*. The objectives of this report were to highlight, support, and present potential recommendations pertaining to key issues concerning the Shuttle fleet, its sustainment and support in the interest of preventing the next accident.

Various recommendations were made by the authors of this report and reviewed by the Board. Several were adopted into the final report. The conclusions drawn in the report do not necessarily reflect the conclusions of the Board; when there is a conflict, the information in Volume I of the Columbia Accident Investigation Board final report takes precedence.

Introduction

Section 1 Vehicle and Subsystem Analysis 423
1.1 Orbiter Wiring 423
1.2 Hypergolic Fuel Spill Documentation 427
1.3 Ov-102 Exposure to Elements/Increasing Corrosion 428
1.4 Premature Firing of Pyrotechnic Devices 430
1.5 SRB Bolt Catcher 431
1.6 Separation Bolt 434
1.7 Leading Edge Support System (LESS) Hardware Use 435
1.8 *Columbia* Hard Landing 436

Section 2 Maintenance Requirements Determination 436
2.1 Technical Data/Specifications 436
2.2 Safety and Mission Assurance 439
2.3 Maintenance Documentation (WAD Accuracy) 444
2.4 Capabilities Analysis 446

Section 3 Fleet Sustainment 448
3.1 Service Life Extension Program 448
3.2 Sustainment of Aging NASA Infrastructure 452

Section 4 Logistics Support 457
4.1 Workforce 457
4.2 Production Support 457
4.3 Shuttle Systems Depot Support 458
4.4 Budgets and Financial 459
4.5 Contracting Issues 459
4.6 SFOC Award Fee 462
4.7 Non-SFOC Contracts 464
4.8 Contractually Required Documents Applicable to External Tank Thermal Protection System (TPS) Foam Application 466
4.9 Contractual Penalties for External Tank Failure 467
4.10 Workforce: Size and Aging 467

Maintenance, Material, and Management Inputs

Submitted by Group I
Major General John L. Barry, Brigadier General Duane W. Deal, Rear Admiral Stephen A. Turcotte
Colonel Timothy D. Bair, John F. Lehman, Colonel David T. Nakayama

1.0 Vehicle and Subsystem Analysis

1.1. Orbiter wiring

Issue:

Proper inspection and maintenance of Kapton insulated wiring (MIL-W-81381) is an important factor as the Space Shuttle continues to age.

Background:

Kapton refers to a type of insulation (technical name: aromatic polyimide) developed by DuPont during the 1960s. It has many positive attributes: lightweight, less bulk/volume, excellent damage resistance, high dielectric strength, a wide operating temperature range, and inflammability (will not melt, drip, or propagate flame). Based on these attributes, it was widely used in the aviation industry in the 1970s through the 1990s, with applications in both military and civil aircraft, as well as the Space Shuttle. It has also revealed some disadvantages, the most notable being a breakdown of the insulation, leading to a phenomenon known as arc-tracking. Other disadvantages include "ringing" (circular cracks initiated by nicks in the Kapton) and hydrolytic degradation (moisture intrusion). Arc-tracking is the leading concern in the aviation community, though the level of concern and what actions should be taken vary widely, even among experts.

Findings:

Arc-tracking is the propagation of carbonization/insulation damage along the length of wire and to adjacent wires. When Kapton wiring experiences arc tracking, the insulation carbonizes at temperatures ranging from 1,100 to 1,200 degrees Fahrenheit. An important distinction must be made between carbonization and flammability. During tests (not related to the *Columbia* accident), Kapton wiring subjected to an open flame did not continue to burn when removed from the flame. However, carbonized Kapton becomes a conductor, leading to what is referred to as a "soft short." Systems with a "soft short," as a result of carbonized wiring, do not necessarily drop off line in a clear, abrupt, or obvious manner, but may continue to operate in a degraded fashion. Figure 1.1.1 displays arc-tracking.

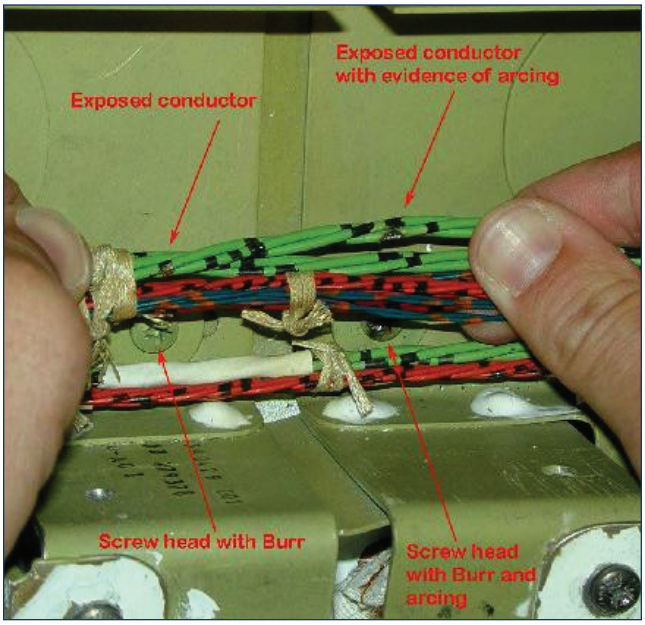


Figure 1.1.1. Picture of Kapton damage.

Kapton insulation breakdown manifests itself in the form of splitting, cracking, and flaking. The major causes of insulation breakdown are improper installation (at time of manufacture) and handling/mishandling during inspection and maintenance over the life of the vehicle. Examples of improper installation include routing wires with overly tight bends, clamping wires too tightly or with improper clamp insulation, and positioning wires against burred screw heads, rivet tails, or sharp edges. Subsequent to installation,

and over the life of the system, wiring stress is introduced through inspections and maintenance as technicians reposition wires, either to gain access to the wire bundle itself or to adjacent areas. Other disturbances contributing to insulation degradation include stepping on, laying equipment/tools on, or dropping tools on wiring. Conditions that degrade Kapton insulation, whether introduced during manufacture or during subsequent inspections and maintenance, are exacerbated by age of the vehicle and wiring, continued use (e.g., vibration), and environmental factors such as fluid spills and moisture intrusion.

Each Orbiter contains between 740,000 and 830,000 feet (140-157 miles) of wire. Over 570,000 feet of these totals are Kapton-insulated wire, with the remaining 169,000 feet being shielded wire with Kapton insulation. Over 1,700 feet of wiring is inaccessible without removing the crew compartment.

During STS-93 (*Columbia*, July 1999), a short-circuit five seconds after liftoff caused the loss of power to two of the six Main Engine Controller computers. This short circuit was later traced to a damaged wire in the left mid-body wire tray and prompted an examination of previous wiring problems. The results showed only two documented events related to arc-tracking in the Space Shuttle's history: a humidity separator wire on OV-099 during STS-6 in November 1982 and a teleprinter cable on OV-102 during STS-28 in July 1989. In efforts to identify and correct wiring problems, a partial inspection was initially conducted on all Orbiters during a fleet stand-down in 1999, with plans to perform more extensive inspections during Orbiter Major Modification (OMM) periods. OV-102 was the first to go through the more extensive wiring inspection during its J3 OMM at the Boeing facility in Palmdale, California (September 1999 – February 2001), shortly after STS-93.

Inspection of OV-102 during its J3 OMM provided the first "hard look" at Kapton wiring for any of the Orbiters. Areas not normally accessed during flow (down-mission, up-mission) processing were inspected. This extensive inspection revealed 4,884 wire anomalies: 1,890 were categorized as a "high level" nonconformances and reported under Problem Reporting procedures; of these, Kapton insulation accounted for 70 percent (1,324), or 27 percent of the total nonconformances. Finally, 2,123 were categorized as minor, or fair wear and tear. There was a strong correlation between the vehicle areas that experience the most personnel traffic during inspections and maintenance and wire damage.[1] The Boeing Inspection Report stated, "These findings demonstrate a real need for detailed wire inspection during modification periods, as it is doubtful that OMRS type inspections would have been as effective in detecting all of these anomalies."[2] Finally, redundant system wiring in the same bundles was separated to prevent damage from arc tracking propagation.

OV-103 is currently undergoing its J3 OMM (September 2002 – April 2004) at Kennedy Space Center. This OMM includes wiring inspections not conducted during the initial fleet stand down and, upon completion, OV-103 will be only the second Orbiter to have completed a full wiring inspection. As of the end of May 2003, the combined total of nonconformances was 3,822 (1,677 during initial stand down inspection and 2,145 to date in OMM). The remaining Orbiters (OV-104 and OV-105) will complete their full wiring inspections in conjunction with their scheduled OMM completions (2004 for OV-105 and 2006 for OV-104, based on the recent decision to accelerate OV-105). A new and significant development presented at the 14 June 03 OMM Project Management Review (PMR) involved surprise/concern that the number of nonconformances on OV-103 is as high as on OV-102 and includes many in areas not previously regarded as susceptible, such as low traffic areas. This has led to a change from the earlier opinion of "Where there's traffic, there's wire damage" to "Where there's wire, there can be damage" and, in turn, concerns that delayed implementation of the wiring inspection and corrective action leads to an unquantifiable level of program risk. With OV-103 nearing completion of its OMM, and OV-105's accelerated OMM input, the only Orbiter in question is OV-104, based on its 2005 OMM input. As of publication, this situation continues to be evaluated by NASA with focus on what additional actions are necessary, and how soon must they be undertaken, to ensure continued safe operations.

Wiring nonconformances can be corrected several ways: rerouting, reclamping, or installation of additional insulation (convoluted tubing, insulating tape, insulating sheets, heat shrink sleeving, abrasion pads, and so forth). (See Figure 1.1.2) Additionally, testing of Orbiter wiring under normal operating loads has shown arc tracking in bundles usually stops due to wire separation (as opposed to circuit protection devices tripping). Further testing under conditions approximating the Shuttle wiring environment also showed that, after separation, arc tracking did not progress beyond six inches. Based on these results, Boeing recommended NASA separate all critical paths from larger wire bundles and individually protects them. This protection should extend a minimum of six inches beyond the confluence of critical paths.[3] This is being implemented during OMMs.

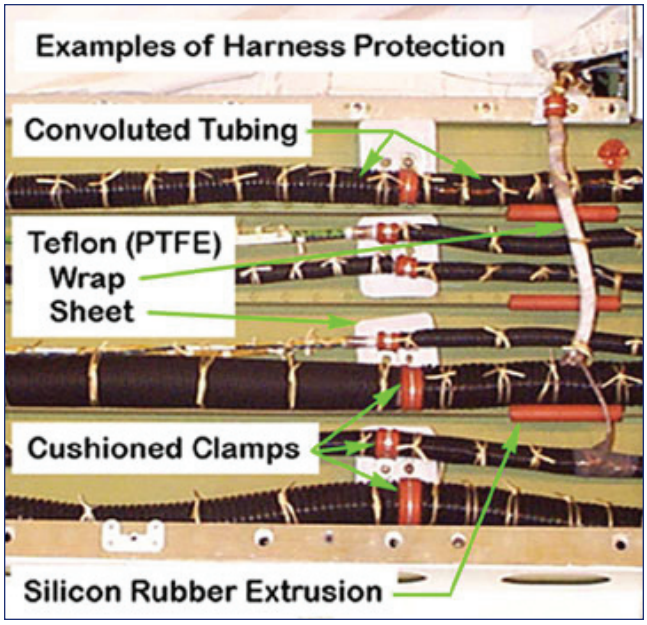


Figure 1.1.2. Examples of Harness Protection.

There have been a number of initiatives, over and above the inspections during OMM, directed at eliminating Kapton related problems. Databases used to record and trend nonconformances have been revised to allow for more precise reporting, to include the specific nature and location. Training to enable technicians and inspectors to better identify wiring nonconformances has been created with initial and recurring (every two years) requirements. Additionally, there is mandatory "Wiring Awareness" training for all personnel working on the Orbiter (not just electrical technicians) with a two-year recurring refresher. This training includes a video and is tailored to individual sections of the Orbiter: Cert 800 for forward and mid-body access, and Cert 801 for aft access. Another measure requires recurring wiring inspections whenever work is performed in an area; the type of inspection (Type 1 involves opening a wire bundle and "fanning out" the individual wires for inspection, Type 2 requires an area inspection without intruding into the bundle) depends on the type of work performed. Yet another measure requires technicians working on the Orbiter to tether their tools to avoid damage, should they inadvertently drop them. Finally, wire crimpers are now calibrated and controlled as calibrated devices, and work authorization documents stipulate specific crimping values and require technician documentation ascertaining compliance.

Inadequate inspection and maintenance practices have been recognized as contributing to Kapton-related problems in the military and commercial aviation communities. There has been increased recognition that wiring is not something to "install and forget about," but must be treated as a "system" that requires ongoing inspection and maintenance. Similar actions are being implemented to varying degrees in the Space Shuttle Program. While new types of composite/hybrid insulations have recently replaced Kapton as the wire of choice in "new builds," there are no plans for wholesale removal and replacement of Kapton wiring in existing inventories in the aviation community, though specific problem areas have been replaced. Since 1989, the Air Force has discouraged the use of Kapton by requiring System Program Office approval; the Air Force reviewed/revalidated this position in 1998. The Navy has followed a similar practice since 1985. Air Force Research Lab wiring experts (Wright-Patterson Air Force Base) have participated in a number of joint studies on Kapton with NASA and have provided inputs to the Shuttle Independent Assessment Team (SIAT) and played a role in expanding wiring inspections during OMM.

Care must be exercised in drawing parallels between the aviation community and the Space Shuttle Program. Many of the new composite insulations commercially available have been tested as potential replacements for Shuttle wiring, and no viable/improved alternatives to Kapton have been found. Two examples: TKT, a Teflon/Kapton/Teflon composite, lacks the robustness of Kapton; XL-ETFE, or cross-linked Tefzel, also lacks the robustness of Kapton as well as increased weight and a smaller temperature operating range. As with the years following Kapton introduction, it is still too early to know if the new insulations have any, as yet undetermined disadvantages, though one area of increasing criticism is their tendency to "scuff." Finally, the Shuttle spends much less time, compared with military and civil aircraft, exposed to the weather. Most of its ground time is spent in the controlled environment of the Orbiter Processing Facility.

As a whole, the aviation community has not been able to develop better test equipment to detect degradation of wiring prior to failure. Efforts in this area continue, with one being led by the Air Force Research Lab with participation and funding from NASA.

The Shuttle's operating environment is the basis of two unique concerns: exposure of wiring to atomic oxygen (AO) and ultra-violet (UV) radiation. During a mission, the Orbiter's payload bay doors are opened to expose cooling radiators. AO acts as an oxidizing agent and can lead to mass loss and surface property changes as a result of both chemical reactions and physical erosion. While laboratory tests have shown significant degradation due to AO, actual exposure has been significantly less than lab conditions and inspections have shown that degradation is minimal. UV radiation is known to enhance the degradation of organic insulations. Laboratory tests with Kapton have confirmed the incidence of delamination, shrinkage, and wrinkling.

There were wiring variations between the first Orbiter (OV-102) and subsequent vehicles. The wiring routed through the wing cavities outboard of the main landing gear wheel well wall of OV-102 were gathered in four bundles, while the wiring in other Orbiters was secured in seven bundles. (See Figure 1.1.3) This variation resulted from design changes to the wire bundle securing method. Clamps were used on OV-102, and metalized tape (MBO 135-050) straps were used on the remaining vehicles. Although effective, metalized tape is incapable of securing a bundle containing a large quantity of wires as configured in OV-102, hence the increased number of smaller bundles in subsequent Orbiters. Nearly 90 percent of wires routed through OV-102's left wing forward of the main landing gear belonged either to systems gathering thermal, strain load, acoustic and other data for the Orbiter Experiment (OEX) instrumentation package (similar to the Modular Auxiliary Data System – MADS – on other Orbiters) or to disconnected systems. OEX data was recorded on magnetic tape that was downloaded after landing and not relayed via telemetry. The typical wire harness routing passes within 8-10 inches of the forward wing spar at the forward corner pass-through, immediately aft of the Reinforced Carbon-Carbon (RCC) panel 6. All temperature sensors in the main landing gear well were located within a four-foot radius with the main landing gear retracted. Fifty percent of all electrical drawings for the Orbiter fleet were unique to OV-102, due to first-production unit anomalies/changes, and additional wiring for the Developmental Flight Instrumentation (DFI, later OEX).

Analysis of telemetered data from 14 of *Columbia*'s left wing sensors (hydraulic line/wing skin/wheel temperatures, tire pressure, and landing gear downlock position indication) in the final minutes prior to the Orbiter's breakup provided failure signatures supporting the leading causal scenario of left wing thermal intrusion, as opposed to a catastrophic failure (extensive arc tracking) of Kapton wiring. Actual NASA testing in the months following the *Columbia* tragedy, during which wiring bundles were subjected to intense heat (hot



Figure 1.1.3. Wire Bundle Comparison.

oven, blowtorch, and arc jet), verified these failure signature analyses. Finally, extensive testing and analysis for years prior to STS-107 showed that, given the low voltages and low currents associated with the Orbiter's instrumentation system (such as those in the left wing), the probability of arc tracking is commensurately low.

Based on the extensive wiring inspections, pre-STS-107 maintenance and modifications, analysis of sensor/wiring failure signatures, and the lack of alignment of catastrophic wiring failure with any of the likely failure modes, the presence of Kapton wiring in *Columbia* is highly unlikely to be causal.

Still of concern is the 0.2 percent of inaccessible wiring (over 1,700 feet) which NASA has no plans to inspect, based on the absence of any Criticality 1 wiring. While the absence of "Crit 1" wiring reduces concern over the necessity of immediate inspection, based on findings during OV-103's OMM (that all wiring, including low traffic areas is susceptible to damage), and on projections to operate the Space Shuttle until 2020 (a service life approaching 40 years), this position needs to be reevaluated.

Proposed Recommendations:

NASA must make every effort to fully inspect every Orbiter in the fleet for wiring anomalies as soon as possible and incorporate arc-tracking redundancy separation.

Based on wiring inspection findings during OV-103's OMM, and on projected Space Shuttle operations until 2020, NASA should develop a plan to inspect the over 1,700 feet of inaccessible Orbiter wiring.

While NASA's actions to address wiring issues are highly commendable, they MUST continue to treat wiring as a "system," collecting and analyzing data as the Orbiters age and this system evolves. This includes:

Assessing the effectiveness of all of the actions taken to date to minimize wiring problems.

Continuing to assess the impact of unknowns, such as AO and UV exposure as the Orbiter ages.

Assessing the cumulative effects of aging, to include moisture intrusion.

References:

1. USA briefing, "OV-103 J3 OMDP Project Management Review," 12 June 2003
2. NASA JSC Energy Systems Division (JSC/EP5) Test Report, "Cable Bundle Testing in the Arc Jet For the STS-107 *Columbia* Investigation," 6 June 2003
3. USA Orbiter Operations Requirements (Matthew Warren) e-mail, 30 May 2003, with attachments (MCR 23167, MCR 19596, MCR 19527)
4. USA briefing, "OV-103 J3 OMDP Project Management Review," 1 May 2003
5. NASA/JSC/EP briefing, "STS-107 Aero-Thermal/ Cable Testing to Support Failure Scenario Team," 27 Mar 2003
6. NASA/JSC/EP briefing, "Brad's test results on single cable with voltage applied," undated but estimated around March 2003
7. Vehicle Data Mapping Team Report VDM-P10, "Sensor Signal Characterization For Failure Scenarios," 28 February 2003
8. NASA/JSC/EP briefing, "VDM Team Testing to Un-

derstand Sensor Failure Modes," 27 February 2003
9. Lockheed Martin Space Operations/Energy Systems Department report, "Preliminary Summary of the STS-107 Wire Bundle Burn Through Characterization Testing," Contract NAS 9-19100, 18 February 2003
10. NASA Vehicle Data Mapping Team briefing, Gene Grush, 15 February 03
11. Report, "Wire Insulation Deterioration Analysis System Survey for Boeing Reusable Space
Systems - Revised NASA Orbiter Sampling Test Results and Analysis," Lectromechanical Design Company, 14 November 2001
12. Boeing briefing, "Orbiter Avionics Damage Database Issues," November 2001
13. Paper, "Aircraft Wiring System Integrity Initiatives – A Government and Industry Partnership," George Slenski and Joseph Kuzniar, Oct 2001
14. Boeing report, "OV-102 Wire Inspection Report, September 1999 – February 2001," July 2001
15. "Summary Report on the Orbiter Kapton Insulated Wire Arc Track Investigation," Lectromechanical Design Company, 16 July 2001
16. Boeing briefing, "Arc Track Separation of Critical Wiring Redundancy Violations," Joe Daileda, Jr., and Bill Crawford, 18 April 2001
17. Boeing report, "OV-102 J3 V30/V31 Inspection Report," March 2001
18. Boeing briefing, "Wire Inspection Requirements for Future OMMs," J. Daileda, 19 March 2001
19. USAF/AFRL/MLSA briefing, "Aircraft Wiring System Integrity Initiatives," George Slenski, 1 March 2001
20. Boeing Workmanship Manual, "Flown and Used Orbiter Wiring Conditions," 5 September 00
21. Boeing briefing, "Orbiter Kapton Insulated Wire Age Test Results," Joe Daileda, Jr., 27 June 2000
22. Boeing briefing, "New Wire Insulation Study For Potential Orbiter Use," Joe Daileda, Jr., 5 June 2000
23. Boeing Training Course Presentation, "Orbiter Wiring Discrepancy & Repair," April 2000
24. NASA report, "Space Shuttle Independent Assessment Team," 7 March 2000
25. Briefing, "Space Shuttle Independent Assessment Team Sub-Team on Wiring," George Slenski, 8 November 1999
26. USA briefing, "Fleet Wire Inspection & Repair Summary," Doug White, 2 November 1999
27. Paper, "Managing Electrical Connection Systems and Wire Integrity on Legacy Aerospace Vehicles," Steven J. Sullivan (NASA/KSCARRIER PANELK-F) and George Slenski (USAF/AFMC/AFRL/MLSA), September 1999
28. Testimony of Bernard Loeb, Director Office of Aviation Safety, National Transportation Safety Board, on "Aging Aircraft Wiring" before the Subcommittee on Oversight, Investigations, and Emergency Management Committee on Transportation and Infrastructure, House of Representatives, 15 September 1999
29. "Electronic Failure Analysis Handbook, Chapter 15: Wires and Cables," George Slenski, 1999
30. Final Report, "Study and Recommend New Wire Insulation Task," Gary Troeger, undated (est. 1998)
31. International Conference for the Promotion of Advanced Fire Resistant Aircraft Interior Materials paper, "Development and Analysis of Insulating Constructions for Aerospace Wiring Applications," George A. Slenski, 10 February 1993
32. NASA Conference Publication 10145, "First NASA Workshop on Wiring for Space Applications," 23-24 July 1991
33. Lewis Research Center Space Application Wiring Workshop briefing, "Orbiter Kapton Wire Operational Requirements and Experience," R.V. Peterson (Rockwell International), 23 July 1991
34. Air Force Wright Aeronautical Laboratory briefing, "Understanding Flashover – Wet Arc Tracking Material Properties Arc Propogation," 1 September 1987
35. Article, "Pyrolytic Polyimide Is Semiconductor," C&EN, 26 July 1965

1.2 Hypergolic Fuel Spill Documentation

Issue:

Spill of hypergolic fuel on OV-102 during maintenance could have damaged Orbiter Thermal Protection System (TPS) and/or structure.

Background:

OV-102 experienced a hypergolic fuel spill on August 20, 1999 at KSC during preparation for shipment to Palmdale. A maintenance technician had disconnected a hydrazine line without capping off the line, and laid it down on a maintenance platform, enabling 2.25 ounces of the volatile and corrosive fuel to drip onto the trailing edge of the left inboard elevon. After the spill was cleaned up, two tiles were removed for inspection, with no damage found to the control surface skin or structure. The tiles were replaced, with no further maintenance action taken.[4]

Engineers from United Space Alliance (USA) briefed the Shuttle Operations Advisory Group on November 1, 1999 of the corrective action taken, which consisted of briefing all USA employees working with these systems on procedures to prevent recurrence. All briefing recipients signed and stamped off a roster acknowledging receipt of the briefing. Improvements to the ground support equipment were recommended. Plan also included permanent installation of the de-servicing panel, interconnects, and flexible hoses.

Findings:

The subject event was investigated and corrective actions were implemented by the Shuttle Operations Assessment Group (SOAG) and are tracked in the Safety Reporting Database as SOAG 99-069. This event was closed in the database on 2-9-01: "Expedite implementation of Engineering Support Request ESR K16460 for installation of permanent APU panels in Orbiter Processing Facilities (OPF) 1, 2 and 3 that will eliminate use of temporary Ground Support Equipment for major hazardous propellant transfer operations."[5] Engineering Support Request (ESR) K16460 was implemented to install permanent APU panels in OPF 1, 2, and 3

that will eliminate use of temporary GSE for major hazardous propellant transfer operations. In checking the status of the completion of ESR K16460 with the Program Office Configuration Control group, investigators found that the ESR has not been completely closed. It appears that the work in all three OPFs has been completed and changes made to the engineering. The ESR is being held open until the engineering is changed to agree with the as-installed configuration. There is also one Problem Report (PR) open pending engineering on work to be done in-house that must be completed before the ESR is finally closed. There is no expected completion date for these details.

There is no reason to believe the actions taken were anything less than adequate. The hypergolic spill is not believed to have been a factor in the accident. The spill is believed to have had no effect on the wiring, the TPS, or the underlying structure.

Proposed Recommendations:

None. Immediate corrective action taken was appropriate given the small quantity of fuel spilled. Follow-on permanent corrective actions implemented by USA are adequate and in place.

1.3 OV-102 Exposure to Elements/Increasing Corrosion

Issue:

Review/assess Orbiter exposure to environmental elements, including OV-102. Determine what actions are necessary, if any.

Background:

OV-102 had a cumulative launch pad exposure of approximately 3.3 years, and the fleet of four Orbiters had a total of 11.8 years at the time of *Columbia*'s loss. Exposure anywhere, but especially in the highly corrosive environment at Kennedy Space Center (KSC), has a negative impact due to corrosion/oxidation/damage/deterioration of materials such as structure, wiring, and insulation. This is a significant concern, given the fleet's age of nearly 20 years and the possibility of continued service for another 20 years.

Findings:

Individual Orbiter exposure time (excluding OV-102) varies from 2.1 to 2.9 years. OV-102 led the fleet in total exposure time at 3.3 years. When exposure time is averaged over the number of launches, OV-102, with 28, averages 43.1 days per launch. OV-103 (Discovery), with 30 launches, averages 35.0 days. There is nearly a seven-day difference between OV-102's average and that of the rest of the fleet. See Figure 1.3.1 for a comparison by Orbiter.

Exposure is measured from the time an Orbiter rolls-out of the Vehicle Assembly Building (VAB) until it is either launched or rolled-back to the VAB. Other events, notably ferry flights and stays at Edwards Air Force Base, also count toward exposure. Exposure time is due to a number of factors: normal launch preparations, including servicing; troubleshooting and repairing maintenance problems; deservicing prior to rollback to the VAB, whether for hurricane "safe havening" or for maintenance; and pad functional checks. OV-102 holds the record for the longest exposure associated with a launch: 164 days for STS-35; OV-103 holds the record for shortest exposure: eight days for STS-96.

The 164-day exposure for STS-35 occurred over eight months and four launch attempts, from April to December 1990, and illustrates the complexities associated with launching Shuttles. OV-102's initial rollout was on April 22; a Freon system repair added 14 days, but the launch was scrubbed on May 30 due to a Main Propulsion System (MPS) liquid hydrogen (LH2) leak. After troubleshooting and maintenance preparations, OV-102 was rolled back to the VAB on June 12. It was rolled out a second time on August 9, but required a 6-day stand down for telemetry repair. Its September 1 launch was scrubbed on 5 September due to another hydrogen leak. Following maintenance at the pad, the next launch attempt was scrubbed on September 18, due to another MPS LH2 leak. After further troubleshooting and maintenance preps, it was rolled back on October 9. Rollout next occurred on October 14, followed by special LH2 tanking tests for two additional days; however, Auxiliary Power Unit water valve problems and follow-on maintenance and servicing took another 16 days. OV-102 finally launched successfully on December 2. It should be noted that STS-35 is an outlier when compared with all other Shuttle launches. Figure 1.3.2 shows a comparison of exposure time by mission.

Besides pad exposure, an Orbiter's most notable vulnerability to environmental exposure is during mate/demate and ferry operations. Three events were noted, all related to mate/demate/ferry ops, in which Orbiters accumulated significant rainwater internally; two involved OV-102. In September 1999, as OV-102 was being mated to the 747 Shuttle Carrier

	Challenger	Endeavour	Atlantis	Discovery	Columbia	*Total Fleet*	*Fleet minus* Columbia
Total Days Exposed	361	749	948	1,050	1,208	4,316	3,108
# of Launches	10	19	26	30	28	113	85
Avg. Days per Launch	36.1	39.4	36.5	35.0	43.1	38.2	36.6

Figure 1.3.1. Orbiter Environmental Exposure at Launch Complex 39.

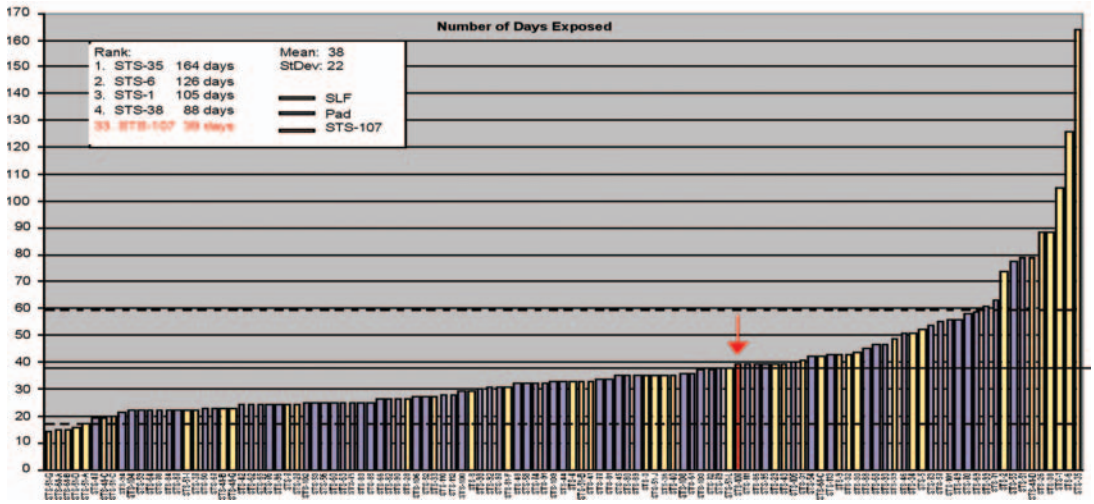


Figure 1.3.2. Exposure by Mission: red arrow depicts STS-107, STS-35 is at far right.

Aircraft (SCA) for a ferry flight to Palmdale, California, it was caught in the rain; 128 pounds/16 gallons of water were removed after its arrival at Palmdale. In February 01, after OV-102 had been mated to the SCA for its return from Palmdale to KSC, it was again caught in a downpour. The mated Orbiter/SCA were partially sheltered in a hangar but, due to vertical clearance limits, the tails of both craft remained exposed (See Figure 1.3.4). After arrival at KSC, 112 pounds/14 gallons of water were removed. The same February 2001 rainstorm at Palmdale also affected OV-104, which had recently landed (February 20/STS-98) and was being prepared for its ferry flight to KSC. OV-104's "aft fuselage under bay 6 [was] full of standing water" and water was "five inches deep along [the] back of 1307 bulkhead;" 1,600 pounds (200 gallons) were removed after its arrival at KSC.



Figure 1.3.4. An Orbiter and SCA partially inside a hangar in Palmdale.

Environmental exposure constraints are clearly outlined in RTOMI S0018.100, Adverse Environmental and Lightning Monitoring at LC39. This publication includes guidance on actions to minimize exposure to rain, hail, winds, freezing temperatures, or tornados. In spite of this existing guidance, circumstances such as those related above, both on the launch pad and during ferry operations, contribute to more exposure than is desirable. Figure 1.3.5 shows rain exposure data by launch, with STS-35 again being the worst case.

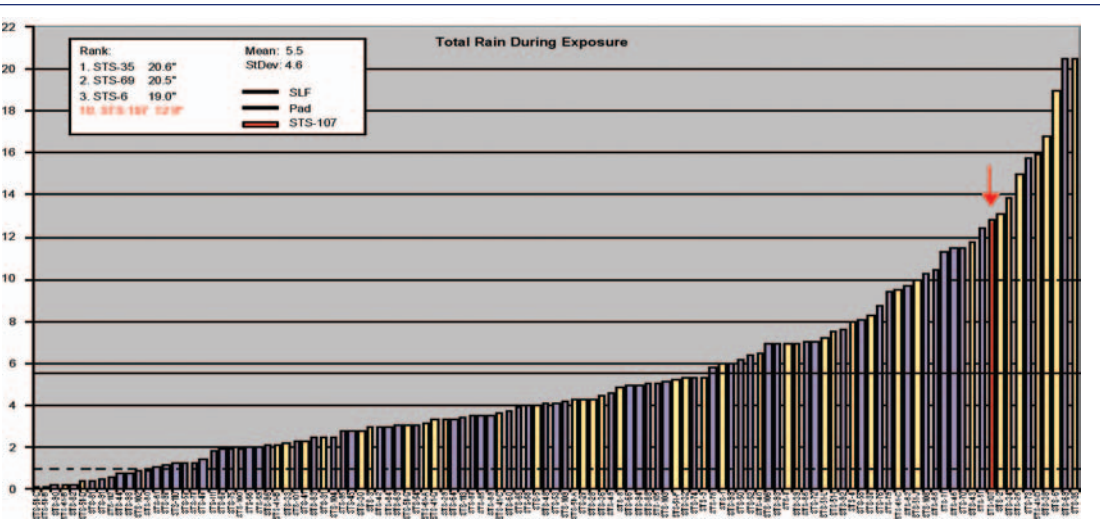


Figure 1.3.5. Total rain exposure by launch (arrow denotes STS-107; STS-35 at far right).

The environment at KSC is about as challenging, from a corrosion perspective, as exists. The necessity to control exposure is reflected in the amount of work needed to keep the Orbiters in a mission-ready condition. Corrosion, in general, is trending upward for the Orbiter fleet by 10 percent annually, and there is a marked increase in corrosion in areas such as the body flap cove (one of the lowest points when the Orbiter is in a vertical orientation). Figures 1.3.6 and 1.3.7 show these corrosion increases, one classic symptom of aging aircraft.

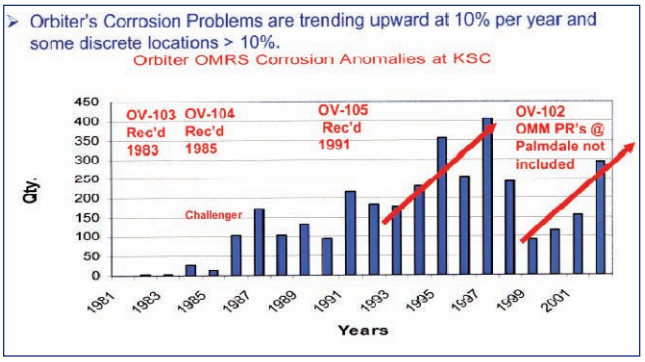


Figure 1.3.6. Increasing orbiter corrosion trends.

While corrosion is symptomatic of normal aging, in the Orbiter's case, its location at the aft (lowest point in its launch configuration) shows the effect of launch pad exposure. The body flap cove and surrounding area, as well as associated hardware, are showing significant growth in man-hour consumption to grind out corrosion pits. Components, such as the body flap actuator, illustrate the increasing challenge posed by corrosion and the impact on logistics and spare parts availability. Over the last several years, body flap actuators have been removed for corrosion. During repair, internal corrosion has also been discovered, with some piece parts being beyond repair. Manufacturing new piece parts entails extensive lead times, in some cases years. Status of body flap actuators at the end of April 2003 was seven in inventory, with four installed; two had been removed and were in the repair cycle, along with the only spare; the first serviceable spare was projected to be available in June 2003.

Proposed Recommendations:

Corrosion is a problem in both military and commercial aviation. Due to the Shuttle's critical mission and limited design life (originally projected to be between10 and 20 years), as well as its now projected use for as much as another 20 years, strict adherence to existing guidance must be reemphasized on an ongoing basis. Furthermore, every opportunity to avoid/minimize/reduce exposure must be taken. Ground Operations should review launches where exposure was more than one standard deviation above or below the mean (Figure 1.3.5.) for lessons that may be applied to reduce exposure. Finally, as some amount of exposure is unavoidable, the Space Shuttle Program must have an intensive corrosion program of inspection, treatment, and prevention. Such a program will factor into the fledgling Service Life Extension Program.

References:

1. Applied Meteorology Unit Memorandum, "Analysis of Rain Measurements in Support of the STS-107 Investigation," Dr. Francis Merceret, April 2003, with attachments
2. KSC Weather Office (John Madura) e-mail, "Orbiter Pad Exposure Days," 4 April 2003, with attachments
3. Boeing/Palmdale Director of Assembly and Test Operations (Al Hoffman) e-mail, "Water Damage On Board *Columbia* – Palmdale," 26 March 2003, with attachments
4. 45th Weather Squadron/Shuttle Launch Weather Office memo, "Shuttle Ops Weather Constraints," Katharine Winters, July 2002
5. NASA/JSC/Orbiter Engineering Office meeting minutes of Orbiter Structures Telecon, 19 June 2001

1.4 Premature Firing of Pyrotechnic Devices

Action/Issue:

Determine the temperature necessary for auto-ignition of the pyrotechnic devices in the main landing gear wheel well and their possible role in the loss of *Columbia*.

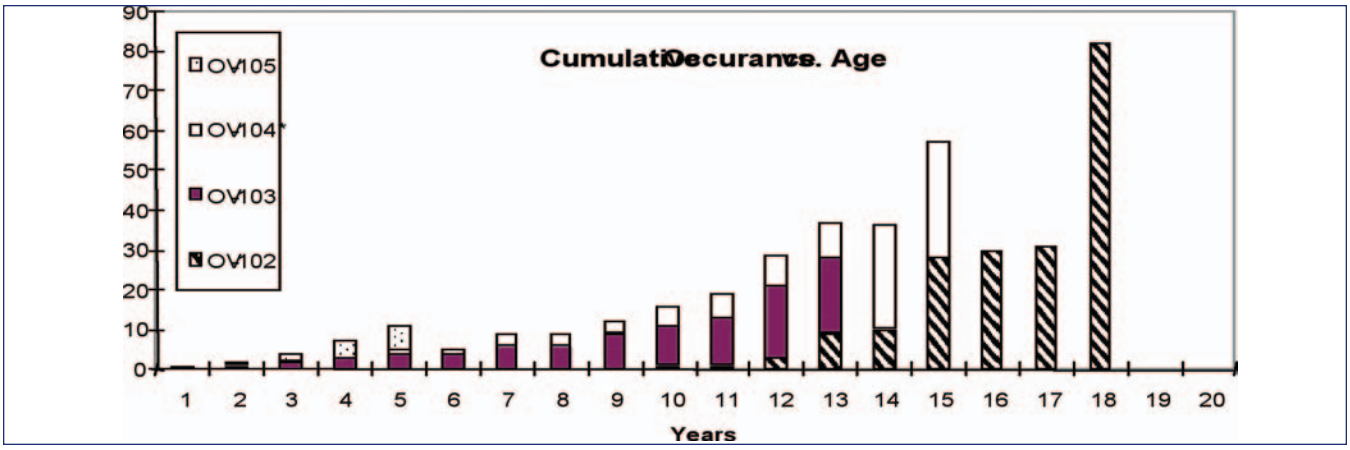


Figure 1.3.7. Fleet corrosion in body flap cove area.

Background:

The only pyrotechnic device in the main landing gear well is the gear uplock release thruster pressure cartridge. This cartridge, when activated by a NASA Standard Initiator (NSI), produces a pressure output that activates the main gear uplock thruster to lower the main landing gear. In the event of hydraulic system failure, a fire command is sent to the NSI/cartridge one second after the gear deployment command if there is no gear movement, as detected by a proximity sensor.

Findings:

There are 137 NSIs used to activate cartridges throughout the shuttle: 102 are fired during a nominal mission and 35 are for emergency applications, including main landing gear extension. The cartridges on STS-107 were from lot HTN, manufactured and accepted in 1994 based on successful acceptance testing.

Qualification requirements for cartridges specify an operating temperature range of –80 to 350 degrees Fahrenheit and no ignition when thermally soaked at 425 degrees for one hour. Tests on February 1, 2003, using cartridges from lot HTE, subjected units to external heating at a rate of 25 to 35 degrees per minute, with ignition occurring at 598 degrees Fahrenheit.

NASA engineers believe actual auto-ignition of these cartridges would require a temperature far exceeding 598 degrees Fahrenheit, based on insulation/ shielding in their installed configuration. The actual temperature would be difficult to determine, as tests in an installed configuration have not been conducted. However, the condition of the recovered left and right landing gear and associated components does not support a premature landing gear deployment scenario.

Conclusions:

Auto ignition of pyrotechnic cartridges will not occur below 598 degrees Fahrenheit; however, exactly what temperature this will occur at is unknown and difficult to determine. The condition of recovered main landing gear debris and associated components does not support premature main landing gear deployment.

Proposed Recommendations:

None. Any failure scenario cannot exclude pyrotechnic auto ignition as a factor.

1.5 SRB Bolt Catcher

Issue:

The Solid Rocket Booster (SRB) forward attachment separation bolt catcher was considered as a potential cause of damage to the Orbiter during SRB separation.

Background:

The External Tank (ET) is attached to the SRB Forward Skirt with one pyrotechnic separation bolt. At SRB separation, this bolt is pyrotechnically separated into two halves. On the ET side of the interface, a "bolt catcher" (see Figure 1.5.1) is mounted to catch the upper half of the fired separation bolt following NASA Standard Initiator (NSI) firing. The bolt catcher consists of a domed aluminum cover containing an aluminum honeycomb matrix to deform and absorb the bolt's energy as it is "caught." The bolt catcher is designed to prevent liberated objects from hitting the Orbiter after firing.

Early in the investigation process a fault tree of potential causes was developed that included the SRB and the bolt catcher system as a potential causal factor in the accident. In an effort to eliminate the bolt catcher a records review revealed some confusion regarding which two serial controlled catcher units were used in the STS-107 stack: 1, 19, or 41. There was a discrepancy between the USA and the Michoud Assembly Facility (MAF) serial numbers on the bolt catchers used on STS-107. During buildup of a Shuttle ET, the bolt catchers (two manufacturers, Summa and Harris) are furnished by USA and each is stamped with a USA serial number. When the unit is prepared for shipment with the ET, the old (USA) number is chemically removed, and then the catcher is coated with super lightweight ablative (SLA) material. At this point, the MAF assigns each bolt catcher a new serial number. Apparently the paperwork documenting which two Summa bolt catchers were used was unclear and does not positively identify which original USA numbered unit was used. MSFC system officials believe they have eliminated number 41 leaving numbers 1 and 19 as the Summa catchers used on STS-107. Harris bolt catchers have never been used on a Space Shuttle mission. The stated reason is that the Summa catchers are older and NASA/USA is using them up first.

Findings:

The configuration of the current bolt catcher flight hardware differs significantly from the original qualification test configuration.[6] First, the attachment of the bolt catcher used in the original test fixture was qualified using through-bolts into a metal that was dissimilar to the ET/SRB attach point. The mounting method used for flight hardware (including STS-107) is bolts threaded into inserts. Second, original catcher testing did not have the SLA applied. Third, the original design load expected during bolt separation was determined to be 29,800 pounds in the 1979 timeframe. During initial tests the bolt catcher failed at the weld. The reason for this failure was determined to be overly rigid honeycomb, which led to the redesign of the honeycomb to reduce its static pressure capability from 1400 to 1000 psi. Finally, during the original test, temperature and pressure data were not recorded for the bolt firing. Instead of conducting additional tests, the flight design configuration was accepted by analysis (of extrapolated test data and the redesign specifications) and similarity. Consequently, predictive failure analysis, in the absence of post-flight evidence for examination (the bolt catcher and upper half of the separation bolt remain with the external tank and are therefore lost on reentry), must also be

based on analysis of limited data from testing 24 years ago or a new round of testing in order to remove the bolt catcher from investigative consideration. The current bolt catcher design was certified on the basis of analysis and similarity after limited testing. A new round of testing is underway to support the investigation.

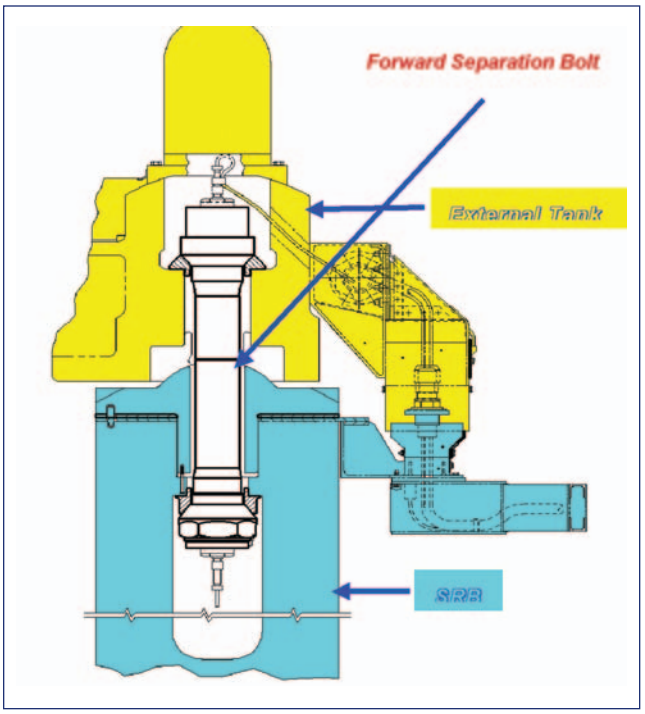


Figure 1.5.1. Diagram of a bolt catcher.

In the absence of physical evidence and adequate test data to measure bolt catcher performance against, it must be assumed that the bolt catcher could have played a role in damaging the left wing LESS of *Columbia*. Specifically, the dome could have catastrophically failed at the weld, SLA coating could have come off (in adequately large quantity to damage the shuttle), or a bolt/insert could have failed to hold. Review of radar imaging data reveals objects were liberated from the STS-107 stack at the time of SRB separation (approximately 126 seconds).[7] Much of this debris is from known sources aft of the Orbiter, and do not present a threat to the vehicle. However, the radar data has been inconclusive, to date, as to whether the bolt catcher could have been a part of the separation debris. Several other methods will be used to investigate the bolt catcher's potential as a source of damage to the LESS Thermal Protection System on *Columbia*. First, review of existing, but limited, data from STS-107. Second, a new set of tests of the as-flown configuration is being performed to better characterize the bolt catcher performance parameters.

Radar tracking and imaging is routinely done for every Space Shuttle launch and follows the vehicle well beyond SRB separation. The Board requested that the radar data from STS-107 be reviewed to determine if any objects came off the vehicle around the time of SRB separation. One event, (called debris item #33) at approximately 126 seconds after launch, produced a radar return consistent with the radar cross section of a bolt catcher.[8] The NASA team reviewing this data pulled the radar launch data from previous Shuttle missions to determine if this event was unusual. They discovered five previous missions with a similarly sized radar image liberated from the Shuttle stack at about the same time. Most missions have ascent pictures taken of the vehicle that show the (apparently) intact bolt catcher dome. Pictures of these same five missions showed all but one bolt catcher (STS-110) of the 10 intact and in place. The STS-107 pictures (taken from the ground) are indiscernible (see Figure 1.5.2). Video, taken by the STS-107 crew, of the ET as it floated away from the Orbiter does not show bolt catcher detail either. The review of MADS data did not show any off nominal events at the 126-second point (SRB separation) or immediately afterward as would be expected if a large enough item hit the wing. Consequently, there are no conclusive data points that would include or exclude the bolt catcher from consideration in this investigation.

Mission	*LH Vehicle*	*RH Vehicle*
STS-113	Not in FOV	Not in FOV
STS-112	Visible	Visible
STS-111	Visible	Visible
STS-110	Visible	Not in FOV
STS-109	Visible	Visible
STS-108	Dark Exposure	Dark Exposure
STS-106	Visible	Visible
STS-105	Visible	Visible
STS-104	Visible	Not in FOV
STS-103	Dark Exposure	Dark Exposure
STS-102	Not in FOV	Visible
STS-101	Visible	Visible
STS-100	Visible	Visible
STS-099	Visible	Visible
STS-098	No Film	No Film
STS-097	Poor Quality	Poor Quality
STS-096	Visible	Visible
STS-095	Visible	Visible
STS-093	Dark Exposure	Dark Exposure
STS-092	No Film	No Film
STS-091	Visible	Visible
STS-090	Visible	Visible
STS-088	Dark Exposure	Dark Exposure

FOV = Field of View
"Visible" indicates that the bolt catcher was identifiable in its installed position in post-SRB separation photographs.

Figure 1.5.2. Ascent photography of bolt catchers.

Testing was conducted to baseline the bolt catcher performance in the "as-flown" configuration. Testing began on May 27 and was completed in June 2003. These tests were done using various parameters and configurations, consistent with the system's history and current configuration. Intent of the tests is to "characterize loads with NSI ejection and nominal firing, qualification of SLA structural integrity, verify analytical models for safety factor determination, provide closure for the STS-107 accident fault tree and provide return to flight rationale."[9] Analysis of early results shows some interesting and somewhat alarming results. During the first three separation bolt tests the dynamic test peak loads were 22, 46, and 36 KIPs (thousand pounds), respectively. Those values were derived from strain gage measurements, and are believed to be accurate to approximately +/–10 percent. The peak load the bolt catcher was predicted to absorb during separation bolt firing was 29.8 KIPs. The lower number seen in the live fire separation bolt test was believed to be the result of a test-induced failure of one of the two bolt initiators. During the static tests (to date, 10 tests using a Harris and 1 using a Summa bolt catcher), load measurements at the point of catcher failure ranged from 44 - 59.7 KIPs. Those load measurements are direct readings from a load cell and accurate to + or – 2 percent. All of the bolt catchers failed well under the expected range of 68 KIPs and at the heat affected zone of the weld (instead of the expected failure of one of the mount bolts). The first test was designed to simulate the increased internal pressure (75 psid) seen when an NSI fires and is subsequently ejected from the bolt into the honeycomb ahead of the bolt half, as happened in about 20 percent of the missions. This test demonstrated that ejection of the NSI does not increase the load on the bolt catcher.

The first two Harris bolt catchers failed at an equivalent static load of 54 KIPs (+/– 2 percent), and 57 KIPs (+/– 2 percent), respectively. The third static test (using a Summa manufactured catcher) produced the most alarming results. This catcher failed at 44 KIPs (+/- 2 percent). The second dynamic test of a separation bolt firing produced a derived load on the bolt catcher of 46 KIPs (+/- 10 percent). If these results are consistent with the remaining tests, the factor of safety would be 0.956 for the bolt catcher and is significantly under the NASA design requirement of 1.4. The results of this test do not eliminate the bolt catcher from fault tree consideration and may imply a significant weakness in NASA's method of certification of critical systems by analysis and similarity.

The substandard performance of the Summa catcher used in this test led the test officials at Marshall to review its historical records that remain with each catcher. Every bolt catcher must be inspected (via x-ray) as a final step in the manufacturing process to ensure specification compliance. There are specific requirements for film type/quality to allow sufficient visibility of weld quality (where the dome is mated to the mounting flange) and reveal any flaws. There is also a requirement to archive the film for several years after the hardware has been used. The manufacturer is required to evaluate the film and a Defense Contract Management Agency (DCMA) representative certifies that requirements have been met. The substandard performance of the Summa Bolt Catchers tested by NASA at MSFC and subsequent investigation revealed the contractor's use of film failing to meet quality requirements and, because of this questionable quality, "probable" weld defects in most of the archived film. Film of STS-107's bolt catchers (serial numbers 1 and 19, both Summa manufactured), was also determined to be substandard with "probable" weld defects (cracks, porosity, lack of penetration) on number 1 (left SRB/ET attach point); number 19 appeared adequate, though the substandard film quality leaves some doubt.

Further investigation revealed a lack of qualified non-destructive inspection (NDI) technicians and differing interpretations of inspection requirements as contributing to this oversight. USA, NASA's agent in procuring bolt catchers, exercises limited process oversight, delegating actual contract compliance verification to DCMA. DCMA interpreted its responsibility as limited to certifying compliance with the requirement for x-ray inspections. Since neither DCMA nor USA had a resident NDI specialist they could not read the x-ray film or certify the weld. Consequently, the required inspections of weld quality and end-item certification were not properly performed. Inadequate oversight and confusion over the requirement on the parts of NASA, USA, and DCMA all contributed to this problem.

The x-ray testing (done as final step in manufacture to certify it as flight ready) film was reviewed by NASA NDE technicians after the test and clearly shows substandard film quality and possible weld problems. These test results and the potential weld issues of the STS-107 bolt catchers lead to the conclusion that this system (in conjunction with a radar event at the 126 second point) may have contributed to the causal chain of events that lead up to the loss of *Columbia*.

Transport analysis of the possible trajectory of a liberated bolt catcher (with and without the bolt upper half) was initiated by the NASA led Working Scenario group. The results of this study show several paths for the catcher to have traveled based on seven different velocities at departure. In summary, the zero velocity departure path can be traced to a point approximately 161 inches forward of the leading edge of the left wing. This is considered to be within the margin of error considering the numerous factors that are required to perform transport analysis. Consequently, the bolt catcher cannot be eliminated from the fault tree as a potential source of the damage to *Columbia*'s leading edge.

In addition, STS-107 radar data from the Eastern Range tracking system identified an object departing the stack at the time of Solid Rocket Booster separation that had a radar cross-section consistent with a bolt catcher. The resolution of the radar return was not sufficient to definitively identify the object. However, an object that has about the same radar signature as a bolt catcher was seen on at least five other Shuttle missions. Debris shedding during SRB separation is not an unusual event. However, the size of this object could be a potential threat if it came close to the Orbiter after coming off the stack.

Though bolt catchers can be neither definitively excluded nor included as a potential cause of left wing damage in STS-107, the impact of such a large object would likely have registered on *Columbia*'s sensors, which measure forces on

the vehicle. The "out of family" but indefinite data at the time of Solid Rocket Booster separation, in tandem with overwhelming evidence related to the foam debris strike, lead the Board to conclude that bolt catchers are unlikely to have been involved in the *Columbia* accident.

Proposed Recommendations:

Radar cross-section analysis of the bolt catcher minus SLA has been done, but has been inconclusive when compared to radar imagery. NASA should redo this comparison with SLA if launch radar data accuracy is adequate to draw conclusions.

Remove all remaining Summa and Harris catchers from service until testing is complete (including x-ray evaluation of all welds). Attempt to determine the Factor Of Safety on the Summa bolt catcher and the likelihood that STS-107 experienced an in flight failure of the Summa bolt catchers. Complete design upgrades to the SRB Bolt Catcher and perform qualification testing to certify the new configuration for flight use.

The investigative review of this system has revealed a number of errors in the methodology used for certification of the bolt catcher. The approach relied on incomplete testing, analysis, and similarity. The original testing and certification for this system was done in a configuration that did not adequately resemble the final flight configuration. Certification of flight critical systems by analysis and similarity, at least in the case of the bolt catcher was inadequate. Recommend NASA seek to identify other systems that were qualified inadequately, and re-perform certification.

Initiate an investigation into the nature of the object tracked on STS-107 at approximately the 126 second point to determine its nature and origin and whether or not it represents a threat to future Shuttle missions.

1.6 Separation Bolt

Issue:

The separation bolts procured from a new contractor were not adequately inspected before flight on STS-107.

Background:

USA replaced Hi-Shear as the prime contractor for separation bolts in May 2000. Certification of new bolts may have been done without adequate NDI (magnetic particle) of the internal bore. (See Figures 1.6.1 and 1.6.2.)

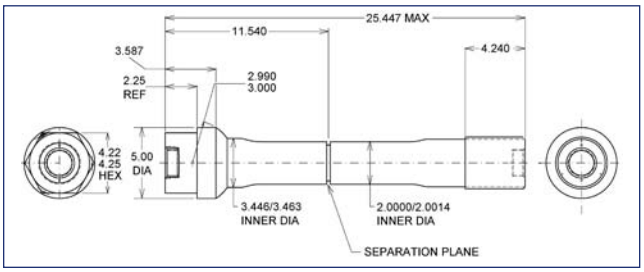


Figure 1.6.1. Separation Bolt.

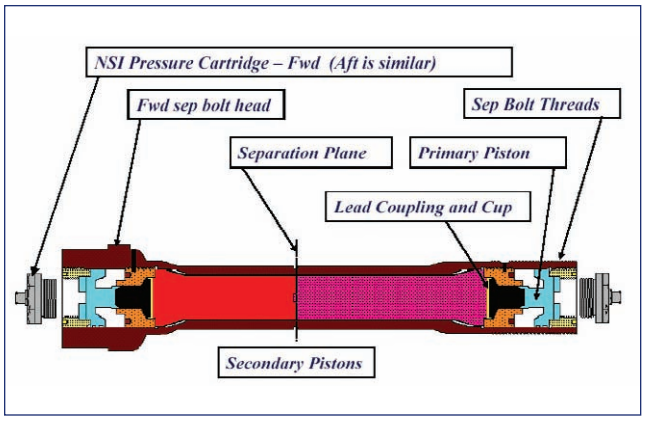


Figure 1.6.2. Separation bolt cross section.

Facts:

Hi-Shear manufactured all of the explosive bolts procured by NASA for the SSP up to approximately three years ago. Escalating price and problems meeting delivery schedules drove NASA to seek a second source. Pacific-Scientific Energetic Materials Company (PS/EMC) of Chandler, Arizona won the down select competition and was qualified as a manufacturing source using the same configuration and specifications as Hi-Shear. Approximately 40 separation bolts were produced for certification testing and (after approval) use on future Space Shuttle missions. After bolt housings are machined, grooved and proof loaded, PS/EMC sends housings to Pacific Magnetic & Penetrant (PMP) Inc., in North Hollywood, California to perform inspection of the inside diameter (ID) of the bolt housings using magnetic particle inspection.

STS-107 was the first flight of the new PS/EMC bolts. They were installed on both of the forward (upper) SRB/ET attach points. Previous flights used the remaining stock of Hi-Shear bolts. Shortly after the *Columbia* accident it was discovered (source unknown) that the new bolts may not have been correctly Non-Destructive Inspected (NDI) during the manufacturing process. On January 28, 2003, Forward Separation Bolt housings, Lot AAP, were tested at PMP with USA PQAR, PS/EMC Quality, and DCMA in attendance.

Investigation by the DCMA NDI 3 level (certified expert in specific NDI technology) of the second lot of PS/EMC produced bolts, revealed that the Magnetic Particle Inspection (MT) of the ID of the bore of the hollow bolt had not been done with a borescope, thereby making adequate observation of the test area for machine-created flaws impossible, in his opinion. According to the DCMA expert, the NDI requires use of borescope in order to adequately see inside the narrow (around two inches) bore. The Purchase Order imposes a Magnetic Particle inspection per ASTM E-1444-01 for the Forward Bolt Housings. His assessment referenced MCD2-502470-01 Rev. (N/C), paragraph 4.11, which states in part all internal and external surfaces, shall be inspected by con-

tinuous wet method. Each bolt housing shall be subjected to Magnetic Particle Inspection and, under ASTM E 1444, Paragraph 5.7.3 "Restricted Area Examination" states in part: "where lamps are physically too large to directly illuminate the examination surface, special lighting, such as UV pencil lights or UV light guides or Borescopes shall be used."[10]

The PMP borescope was not operational and was not used to inspect the ID of Lot AAP. USA had verbally instructed PMP to deviate from the Pac-Sci purchase order, providing that the borescope need not be used but a more stringent rejection criteria be applied (any indication). Due to the MT process concerns on Lot AAP, Lot AAN is also in question. Lot AAN bolt housings were used on STS-107, as well as, in the assembly of STS-114.

A process demonstration was conducted at PMP on March 5, 2003 using a test housing with simulated, intentionally induced, machining flaws. A Joint USA/DCMA team agreed to this NDI flaw standard (bolt with known and induced failures) test as means to validate the PMP process. The PMP Level II NDI technician used the same procedures as were used on the production lot and discovered 12 of 17 defects. This was consistent with the test dry run done previously at Wiley Labs using a similar Magnetic Particle Technique. All defects consistently found were 0.25 inches and above which is in compliance with MSFC STD 1249 established for this contract. Initial critical flaw size was re-baselined in 1988 to allow a flaw of 0.258 inches. Armed with these test results and consultation with other NDI experts, USA concluded that a borescope is not required and a dental mirror will provide adequate range of visibility.

Without photographic or physical evidence from the External Tank, an alternative method was needed to verify function of the new bolts used in STS-107. The STS-107 recovered bolts (bottom halves) from the SRB side of the attachment fixture were examined and found to be within design parameters. They were not inspected but rather evaluated for function. The remaining 10 bolts have been sequestered and will not be flown. USA intends to use these bolts in test only. PS/EMC and their NDI subcontractor are being requalified for explosive bolt production.

Proposed Recommendations:

Inspection of the inside diameter without a borescope may be adequate (arguably) but more thorough analysis would improve the confidence margin for success. NASA/USA should consider more stringent inspection criteria in accordance with ASTM E 1444, par. 5.7.3, Restricted Area Examination using a borescope or a different NDE technique.

The investigation determined that the Lot AAN forward bolts flown on STS-107 functioned per design and were consistent with performance of previous lots of forward bolts. The separation bolt is not believed to be a contributor to the STS-107 accident. Implications for the Space Shuttle Program are minimal; however, process and configuration controls may be inadequate if the process of changing manufacturing sources results in product deficiency or specification compromise.

1.7 Leading Edge Support System (LESS) Hardware Use

Action/Issue:

Review and assess Orbiter LESS maintenance practices regarding hardware use.

Background:

The Orbiter's wing leading edges are subjected to thermal and aerodynamic stresses during reentry. Proper inspection and maintenance of the LESS components, including attaching hardware, are essential to the system performing as designed/intended. The LESS consists of: 22 Reinforced Carbon-Carbon (RCC) panels on each wing; 44 carrier panels (22 on each wing's upper and lower surface); numerous other components (such as spar insulators, clevis insulators, spanner beam insulators, spar attach fittings, and brackets); and hardware (including bolts, pins, and sleeves). See Figure 1.7.1 for details.

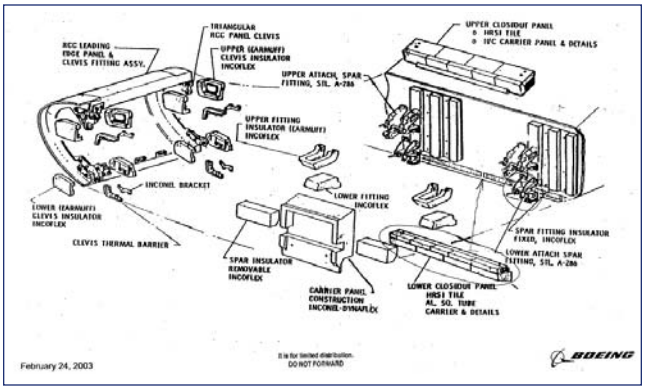


Figure 1.7.1. Details of the wing Leading Edge Support System.

Findings:

Reviewed Work Authorization Documents (WAD) covering carrier panel removal and installation for both lower and upper carrier panels. Also reviewed WADS for removal and installation of RCC panels. WADs are very specific on most tasks with one exception: carrier panel hardware (A-286 bolt) inspection and reuse.

Each upper carrier panel is secured with four bolts, and each lower carrier panel with two bolts. Upon visiting Orbiter Processing Facility (OPF) 3, where *Discovery* was undergoing Orbiter Major Modification (OMM), engineers initially stated these bolts are cleaned using isopropyl alcohol, inspected, and reused. Technicians stated they typically discard the hardware following carrier panel removal and replace it upon installation. Inspection of multiple carrier panel storage containers revealed carrier panels and associated paperwork, but no hardware. After further discussion, engineers restated bolts "can be reused" at the technician's discretion, based on cleaning and visual inspection.

Review of the WADs associated with carrier panel removal

and installation showed no requirement to clean, inspect, reuse, or replace hardware. In contrast, the WADs covering RCC panel removal clearly state "…identify, bag and retain hardware for future use" with respect to four separate, associated components. Physical inspection of removed RCC panels verified associated hardware properly bagged and identified.

Conclusions:

Inconsistent/lacking guidance allows for different interpretations and creates the potential for process variation(s).

Proposed Recommendations:

Eliminate the potential for varying interpretations of carrier panel bolt use by making WADs more specific.

1.8 Columbia Hard Landing

Action/Issue:

Review NASA's assessment of *Columbia*'s hard landing on STS-90.

Background:

Columbia made a hard landing during STS-90 (May 1998). Based on the combination of a 231,342 pound landing weight, 11 knot crosswind, and 6.7 feet per second (fps) sink rate, the established design criteria impact of 5.97 fps was exceeded by 12 percent.

Findings:

The main gear impact of 6.7 fps was estimated by using camera data and several techniques with reasonably close agreement. Crosswinds at the time of landing ranged from 4 to 11 knots and, for the assessment, the worst case (11 knots) was used.

Based on a 6.7 fps sink rate and 11 knot crosswind, reconstructed gear loads were determined to be less than half of design limit load. Figure 1.8.1 shows how energy levels decrease with lower sink rates and landing weights and explains how design criteria can be exceeded without exceeding structural capability. This was verified using MADS accelerometer and strain gage data.

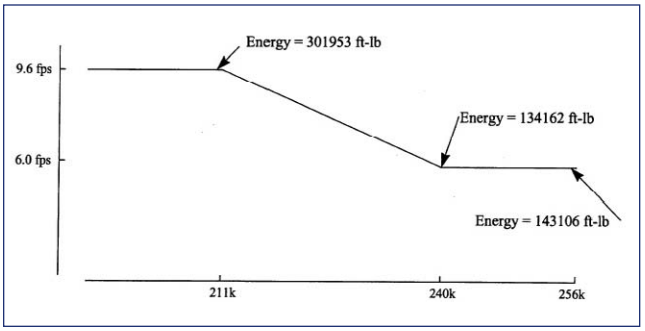


Figure 1.8.1. Energy Levels Based on Sink Rate/Landing Weight.

These results were reviewed and approved by the Orbiter Structures Team on July 14, 1998.

Conclusions:

Based on further study and analysis, including reconstructed main landing gear loads and energy comparisons, *Columbia*'s landing during STS-90, while exceeding the design criteria, was determined to be well within structural capability.

Recommendations:

None. Eliminate as a causal factor.

Source: Boeing briefing, STS-90 Hard Landing Follow-up Actions, ORB, July 28, 1998.

2.0 Maintenance Requirements Determination

2.1 Technical Data/Specifications

Action/Issue:

The backlog of Engineering Order (EO) updates is excessive and NASA's action to address prior independent assessments is inadequate.

Background:

NASA uses engineering drawings as the basic source document for all of its maintenance and engineering work on the Orbiters and Space Shuttle components. System engineers use these drawings to develop specific instructions (called Work Authorization Document, or WAD) for every repair or maintenance action. Updates to the drawings (required when a system is added or modified) are called Engineering Orders until they are incorporated into the drawing. The backlog of unincorporated Engineering Orders is a well-documented concern that has plagued Orbiter processing and maintenance for several years. Admiral Cantrell, in his briefing to the Board on the NASA-Navy Benchmarking Exchange, recommended NASA use the Navy SUBSAFE program's zero level as a baseline for technical data currency. This issue has been repeatedly presented as a finding in the Aerospace Safety Advisory Panel (ASAP) reports for 2001 and 2002. The 2002 ASAP report states:

"Previously, the Panel has been concerned with the large number of Orbiter drawings that are out of date. Many EO changes have not been incorporated into the drawings. Although they are noted on the drawings, engineers must refer to additional paperwork to understand the state of the hardware systems. Over 1600 drawings have more than 10 unincorporated EOs. The Orbiter program will update and incorporate all EOs on 59 of the most frequently used drawings by the end of 2003. Also during the year, an effort to address the 589 drawings referenced most frequently after those 59 will begin. Orbiter program management has committed to maintaining the upgraded drawings at no more than 10 unincorporated EOs. The Orbiter Project is now

reviewing the possibility of identifying the safety-critical drawings that should always be kept current. Recommendation 02-8: Identify drawings that are critical to flight safety, update them to include all EOs, and keep them current."[11] (See Figures 2.1.1 and 2.1.2.)

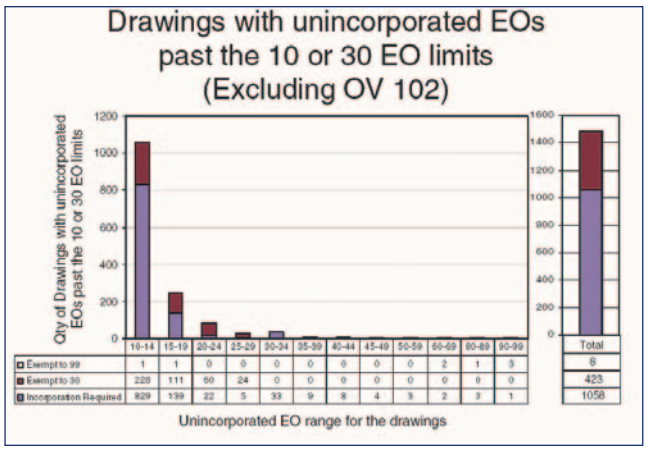
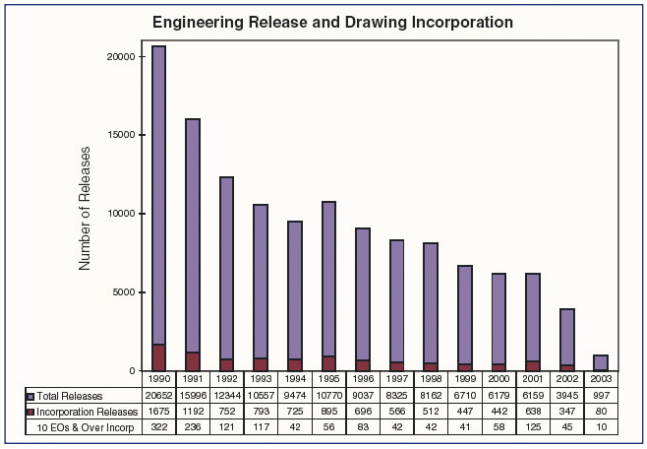


Figure 2.1.1. Unincorporated Engineering Order statistics.



	1990	1991	1992	1993	1994	1995	1996	1997	1998	1999	2000	2001	2002	2003
Total Releases	20652	15996	12344	10557	9474	10770	9037	8325	8162	6710	6179	6159	3945	997
Incorporation Releases	1675	1192	752	793	725	895	696	566	512	447	442	638	347	80
10 EOs & Over Incorp	322	236	121	117	42	56	83	42	42	41	58	125	45	10

Figure 2.1.2. Engineering Release and Drawing incorporation statistics.

Findings:

The Navy's SUBSAFE program identified 1,600 technical drawings, out of approximately 33,000, that are critical to a boat's ability to surface in an emergency. All of this technical data must be current before a sub is approved to sail. The approval process is run very much like a Shuttle CoFR and includes maintenance, operations, program and engineering input to certify the boat for the next sortie. Out of date drawings are criteria to withhold the certification.

The Navy's SUBSAFE program is not an isolated example of successfully maintaining technical data integrity. Boeing-Rocketdyne, the original equipment manufacturer, manages the Space Shuttle Program's main engines as well as contract maintenance and logistics. The drawings and source specifications for the SSME are maintained in their legacy system called the Engineering, Manufacturing, and Planning Log. In 1996 Boeing began a program to digitize all of their technical data, which is now complete. Master documents have been developed for most predictable tasks performed on the engine such as remove, replace, or inspect. Any changes to the specifications or master documents, by virtue of a program or configuration change, are logged into the system and automatic tags or lock outs prevent use of all related technical instructions until that change has been incorporated or digital "red line" data is approved by the engineer. Red line data (edits normally used temporarily for unique tasks) are not used more than three times before the program locks it out for mandatory update to the master document. Updates to the technical data are rigorously reviewed and approved but relatively easy to enact in digital format.

Members of the Board staff visited with USA managers at both the NASA Shuttle Logistics Depot and OPF 3 (J3 OMM in progress on OV-103) to evaluate the impact of unincorporated EO changes on Shuttle maintenance. Observations of the EO system, in use, revealed the difficulties of navigating the technical data with multiple unincorporated EO changes and the potential for human error. This observation was also documented in an April 2001 independent study. "The high quantity of EOs on some engineering drawings is causing confusion, slowing the workflow and providing a potential error source for technicians who must comply with the drawing specifications on the shop floor… Compared to airplane manufacturers or government military programs, the current Space Shuttle system… is very liberal."[12] NASA has built a noteworthy plan to incorporate the most important changes to drawings, for Orbiter, on basis of highest use and complexity (2002-2004). This program, as discussed above, will cover a small number of the drawings and does not address the process that NASA will adopt to maintain them at that level.

Delays in work progress are routinely experienced due to the necessity to review all unincorporated changes before proceeding with a maintenance action. According to the technicians, there are routinely many unincorporated changes and it is not unusual for one change to be "unchanged" or nullified by a follow-on EO change. Frequently, significant delays are created when inconsistencies between the EO, unincorporated changes, and the actual component or vehicle do not correlate to one another. This complexity delays maintenance and creates another vulnerability in the system for human error due to interpretation or oversight. When engineers are drafting WADs for use on the OPF floor, they must navigate through the drawings as well as all of the engineering orders. This process is labor intensive and open to human error as well. During the Board's paper review of STS-107, one of the findings in the SSME area was an incorrect torque specification taken directly from the drawings and EOs (even after three layers of review in the office prior to being issued as a WAD). Every Space Shuttle mission may result in a large number of changes to the drawings. In most many cases, the pace of new changes is significantly greater than the pace of updates.

During the Board's investigation of *Columbia*'s wreckage, progress was significantly hampered by a lack of accurate and up to date drawings of OV-102. Data acquired from the

OEX recorder referenced sensor readings that did not exist in *Columbia*'s engineering drawings or the engineering orders. Fortunately, photos taken at the conclusion of *Columbia*'s J3 OMM (called close-out photos) showed the cables and their location inside the wing. These closeout photos are a part of NASA's routine documentation of ground processing at KSC. The Operating Procedure for Hardware Photographic Documentation provides guidance for when these photos are required: "1. Closeout photos are to be taken to document the as-assembled condition of flight hardware. 2. Closeout photos are to be taken of normally closed areas (areas not visible due to the installation of panels, trays, fairings, blankets, etc.) only when planned or unplanned work or problems result in the removal and reinstallation of functional system components."[13] During the investigation these photos helped pinpoint the sequence of events as the hot gases spread throughout *Columbia*'s left wing. However, there were a few problems discovered that delayed progress further. First, the effort to recover these photos from NASA's database was extensive, taking up to six weeks. Photos are kept in different databases (manual and digital) for the various Shuttle components (Orbiter, Space Shuttle Main Engines, Solid Rocket Boosters, and External Tank). Kennedy Space Center files the close out photos in the Still Image Management System (SIMS) and is referenced in the database that the WADs are stored in (Shuttle Processing Electronic Archival and Retrieval System, SPEARS). It took up to 6 weeks to recover the internal wing photography for *Columbia*. Second, the photos documented the closeout of the particular WAD but did not adequately show all of the wiring that deviated from the engineering drawings. A systematic method to photographically document (panoramic or sequential pictures showing the entire wire bundle or system) all of the divergent system is not specified in the guiding Operating Procedure.

The problems with out-of-date engineering drawings and the time delay to retrieve close-out photos led investigators to the conclusion that NASA may not be able to rapidly or accurately respond to a future in-flight emergency. In such a scenario there may only be a few hours to reference source documents and pass instructions to the crew. Analog systems, filed in various locations, with potential inaccuracies based on unincorporated (or missing as in the case of sensor wiring on *Columbia*) engineering orders may make rapid response impossible or lead ground controllers to provide erroneous direction. NASA/USA has identified and prioritized the backlog using a most-used/most-critical methodology. NASA responded to a Board request for information regarding the status of the unincorporated EOs with the following answer:

At the present time, 1,489 drawings (1600, excluding OV102 only drawings) have more than 10 Engineering Orders (EO). Orbiter drawings have a requirement to be updated after 10 EOs, but exemptions have been allowed on some drawings to have up to 30 and 99 EOs. Of the 1489 drawings, 431 drawings have exemptions to go beyond the 10 EO requirements, which leave 1,058 drawings that do not have exemptions. The Vehicle Engineering office and KSC Operations office have prioritized these drawings with outstanding EOs and determined that 325 drawings (of the 1,058) have significant KSC interaction. The Vehicle Engineering is currently incorporating the outstanding EOs on these 325 drawings. Incorporating the remainder of the 1,058 is not prudent because these drawings are rarely used.

In 2002 the Space Shuttle Vehicle Engineering Office (SSVEO) started allocating money for EOs incorporation. This task is funded to incorporate 20 to 30 drawings worth of EOs per year (depending on the number of EOs open against a drawing). In addition to the scheduled planned EO incorporation, EO incorporation is also performed through updates to drawings due to other modifications affecting those drawings. At this rate, approximately 8 to 10 years will be required to update all 325 drawings.[14]

Figures 2.1.1 and 2.1.2 show the status of the Shuttle Program's technical data in two graphics. The first shows the number of drawings that have greater than 10 unincorporated EOs each. The total figure, as mentioned above is 1,058. However, the significance of this number is further emphasized in the columns that have larger numbers of unincorporated changes but are supposed to be limited to no more than 10 unincorporated changes. Specifically, 90 have more than 20 EOs and 21 have over 40 unincorporated changes. The second graphic shows the number of total releases (new or updated technical drawings or specifications) by year. Over the last 10 years there has been a steady decrease in the number of new releases but incorporations have remained at a significantly lower level and at a relatively slow pace. In 2001 NASA accelerated this pace and has continued at this rate since then.

This process only addresses the most commonly used drawings, and their EOs, and therefore leaves hundreds of EOs remaining. The process to update analog drawings is expensive and time consuming. This backlog will continue to grow with return-to-flight recommendations and the pace at which engineers make systems changes for mission and safety. Until NASA funds a digitally based engineering and technical data system this process will continue to be labor and capital intensive. The repeat nature of this issue and NASA's response to the Board leads to the conclusion that NASA considers this issue to be problematic. In other words, there has been a corporate decision to accept this level of backlog and its not considered to be an issue. NASA should take immediate action to significantly reduce the backlog of unincorporated engineering orders and accelerate the time to update them. Using a digital system to update the commonly used or highly critical technical data will be initially more expensive but significantly more flexible for future updates.

Proposed Recommendations:

The current status of engineering drawings and engineering orders is inadequate to support the Shuttle Program for another 20 years. NASA should significantly accelerate the update of critical EOs and build a plan for the remaining majority of EO updates to minimize vulnerability to human error and improve maintenance efficiency. Highly recommend they consider digitizing the data to streamline the process to facilitate more rapid updates and retrieval in an emergency.

The current status of engineering drawings, engineering orders, and closeout photos will not support rapid crisis resolution such as an on-orbit event. NASA must, before returning to flight, develop a system(s) that ensures engineering drawings, unincorporated EOs, and closeout photos, (processing and manufacturing, where applicable, for all Shuttle systems) are readily accessible to support crisis resolution.

2.2 Safety & Mission Assurance

Issue:

The adaptation of NASA's Safety & Mission Assurance (S&MA) under the changing environment with several contractors raises concerns over scope and depth of program insight and oversight.

Background:

NASA and contractors' assurance programs have undergone considerable change over the past five years. The transition to the Space Flight Operations Contract (SFOC) significantly changed the role of NASA S&MA inspectors as well as the relationship between NASA's other centers and their contractors. Much attention has been paid to the adequacy of government oversight in validating USA's work, the Safety, Quality, and Mission Assurance (SQ&MA) verification of work performed and the number of government mandated inspection points (GMIP). NASA's Shuttle Processing Surveillance Plan employs surveillance in accordance with KDP-P-1693, Surveillance of SFOC Activities at KSC. The KSC Shuttle Processing Directorate's Engineering, Logistics, and S&MA Divisions and the Shuttle Project Office perform a dual insight/oversight role and are responsible for evaluating contractor performance and verification of maintenance for flight readiness. Ultimately this (and many other factors emanating from the various subsystems and centers) is considered in the flight readiness review process and culminates with the signing of the Certification of Flight Readiness (CoFR).

The NASA quality program has significantly evolved in scope and depth, with a transition from an intensive, comprehensive inspection regimen, to one based on risk-analysis. At Kennedy, in 1989, 300,000 inspections were accomplished by contractors, with an additional 44,000 performed by NASA inspectors. Today, an estimated 140,000 inspections are accomplished by USA, with approximately 8,500 inspections conducted by KSC S&MA. MSFC went through a similar process that reduced their inspection workload (1990: 49,000 GMIPs, 821,000 contractor inspections, 2000: 13,300 GMIPs, 444,000 contractor inspections, 2002: 13,700 GMIPs, 461,000 contractor inspections) as did most of the NASA centers. Inspection requirements are specified in the Quality Planning Requirements Document (QPRD). For a single Shuttle maintenance flow, an estimated total of 730,000 tasks require "T-stamp" documentation by USA technicians. Of those tasks, approximately 140,000 tasks require "Q-stamp" verification by USA SQ&MA, with 8,500 of those tasks requiring "N-stamp" by NASA S&MA inspectors (GMIP). All tasks assessed as Criticality Code 1, 1R (redundant), or 2 are inspected 100 percent of the time, as are any systems not verifiable by operational check or test prior to close out.

Findings:

The NASA/USA quality assurance processes are not fully integrated with each other or the Safety, Health & Independent Assessment and engineering surveillance programs. Each one, separately, plays a vital role in the control and assessment of the product as it comes together in the OPF or shop. The four together represent a nearly comprehensive quality control process but require integration and additional sampling-based inspections to flesh out the assurance process. MSFC has a similar challenge. They are responsible for the management of several different Space Shuttle systems through contractors that maintain data in various (mostly proprietary) databases. Integration between the systems is limited with the exception of the Space Shuttle Main Engine (SSME), which uses PRACA to document nonconformances as well as a proprietary database. However, they overcome a lot of this challenge by being centrally organized under a single S&MA division chief that reports to the center director. KSC has a separate S&MA office working directly for each program, a separate SH&IA office under the center director, and separate quality engineers under each program. Integration of the quality program would be better served if this were consolidated under one S&MA office reporting to the center director.

Application of industry standard quality sampling and analysis techniques is inconsistent. SQ&MA (and other NASA contractors) sample a large amount of their workload. S&MA samples USA work informally (but is officially discouraged) and results are only documented in the S&MA Safety & Mission Assurance Reporting Tool (SMART) database. SMART is used by NASA S&MA as a quality problem-tracking tool to help them identify trends in findings and focus their approach to oversight and insight. Problems revealed by the sampling inspections or from the informal SMART database can be communicated to USA through the USA QCAT system but there is no contractual requirement for USA to respond or even take corrective action. MSFC samples contractor work but does not use any preplanned, statistically based approach or analysis. The Space Shuttle Processing Independent Assessment Report of 2001 documented this succinctly; "Process surveillance as it exists today is not accomplishing its desired goals nor is it a true measure of the health of the work processes, as was its original stated objective. "[15] Sample-based inspections should include all aspects of production, including training records, worker certification, etc., as well as FOD prevention. NASA should also add all process inspection findings to its metrics program, including processing debris. Emphasis should go beyond "command performance" formal inspection events to validate USA quality inspection results.

The engineering assessment of work paper, which is accomplished without use of structured sampling methodology or consistency across the various systems/subsystems, is another example. Every work assignment document is reviewed by up to three additional engineers. Additionally, the Technical Accuracy Measurement system outlines

a review of WADs at the system or subsystem level but does not specify frequency or quantity using statistically representative methodology or use of this information for trend analysis. This is just one system example of a review process used by one subsystem. This very issue was addressed in an independent assessment report; "The goal of USA's work procedure improvement programs need to be continued and expanded to remove inconsistencies and inaccuracies, incorporate deviations and clarify procedural steps. The better the work documentation is, the greater the procedural compliance, and the less chance for error. USA should investigate the consolidation of the many separate initiatives for improving work documentation into one cohesive, integrated program."[16]

The list of NASA S&MA oversight inspections (GMIP) was based on engineering risk assessment with limited application of quality analysis and sampling techniques in determining the scope and frequency of inspections. Tasks were retained for government oversight on the basis of criticality, not process or quality assurance. Marshall S&MA retained government oversight options during their GMIPs reduction; by moving all the former GMIPs into a new category they call Surveillance Opportunities (SO). These "opportunities" are no longer mandatory oversight inspection points but remain as an optional area for S&MA inspection. Thiokol actually calls the S&MA shop with 15 minutes warning when a SO is occurring, but will not (by agreement) wait for the inspector in order to maintain job flow. These inspections are not statistically driven. USA inspectors accomplish additional assessments by sampling 40 different production processes such as personal protective equipment (PPE) use and clean as you go, in addition to planned task inspections. The contractor cited an 80 percent confidence level in the sampling's effectiveness in evaluating daily compliance per established processes and practices. The MSFC S&MA system includes feedback and closed loop systems to use in trend analysis and in developing future S&MA tasks to improve oversight and quality. S&MA observed events that result in a Verbal Corrective Action Report are included in this tracking system and used to tailor surveillance or GMIPs.

Several reports have documented organizational inconsistency within the NASA quality assurance construct. The October to December 1999 Space Shuttle Independent Assessment Team report echoed the Rogers Commission Report by including a lengthy discussion of the need for organizational independence and a strong S&MA presence.[17] "The SIAT believes strongly that an independent, visible Safety and Mission Assurance function is vital to the safe operation and maintenance of the Shuttle. The Shuttle Program in its 'one strike and you're out' environment is unlike most other defense or commercial industries. As a consequence, it is believed the industry trend toward reducing Safety & Mission Assurance oversight and functions is inappropriate for the Shuttle."[18] Among their recommendations was a strong mandate to restore surveillance.[19] This is consistent with the testimony of several S&MA inspectors to members of the Board.

NASA's S&MA quality assurance organization has experienced some challenges with its quality assurance inspector workforce as leadership works to evolve the business relationship with the contractor and the inspector culture. Some inspectors, who assert that more GMIPs are necessary, tend toward an adversarial approach, which may discourage the contractor from disclosing problems or noncompliance issues. One senior manager suggested that GMIPs may not be "all in the right place," and should be reviewed/selected by application of statistical sampling techniques in addition to the current practice of risk assessment. This same individual proposed that the engineering sampling of work paper should be statistically based, to ensure that the data gathered is representative.

The significant reduction of GMIPs tasks over the last 14 years (in 1989, 300,000 inspections were accomplished by contractors, 44,000 by NASA inspectors, today, an estimated 140,000 inspections are accomplished by USA, approximately 8,500, at NASA-KSC) was accomplished by a rigorous review of all Category 1, 1R and 2 tasks and areas of concern that would be impossible to observe later. Many of the inspectors interviewed by Board members felt strongly that this number is inadequate and that the process to adjust the level is intentionally inflexible. One example cited was a request to add a main engine final review prior to transport from the shop to the OPF for installation. Their rationale is that the engine is on a rotary stand and in the best position to inspect. The effort to add this task as a GMIP started approximately two years ago and has repeatedly been denied on the basis of inadequate staffing. S&MA's response has been to continue doing it informally. The process to adjust GMIPs tasks is constrained by the belief that the level was set on strong engineering logic and should need no adjustment. This may be predominately true but leaves out any options for quality assurance to respond to a changing environment in terms of an aging system, workforce dynamics, or process improvement initiative.

The Marshall GMIP process is overseen by the quality engineer in charge and has proven over the last two years to be significantly more flexible than KSC. They, like KSC, do not have a regular process to review either GMIPs or surveillance inspections. However, Marshall's use of former GMIPs (SO) to ensure adequate government oversight relieves their concern about too few GMIPs. NASA should build a regular (at least annual) process to review S&MA, contractor, and PRACA databases to adjust GMIPs and sampling goals to assure mission success, contractor compliance and provide more accurate insight/oversight.

Feedback to members of the Board reflected that NASA QA inspectors feel they do not have authority (or are discouraged from doing so) to reject USA work. Consequently, NASA S&MA does not track reject rates (hexagonal-shaped stamps applied to WADs by S&MA inspectors) for occurrences in which a NASA QA inspector might reject a job closed out by a USA quality inspector. They also assert that inspectors are only authorized to use their Hex stamp to notify the contractor to "stop work." Use of the Hex stamp is apparently rare, presumably due in part to overall inspector reluctance or potentially NASA's lack of metrics to track hex stamp issuance. The following data was retrieved for use in this report. Total inspections conducted from FY2001 through

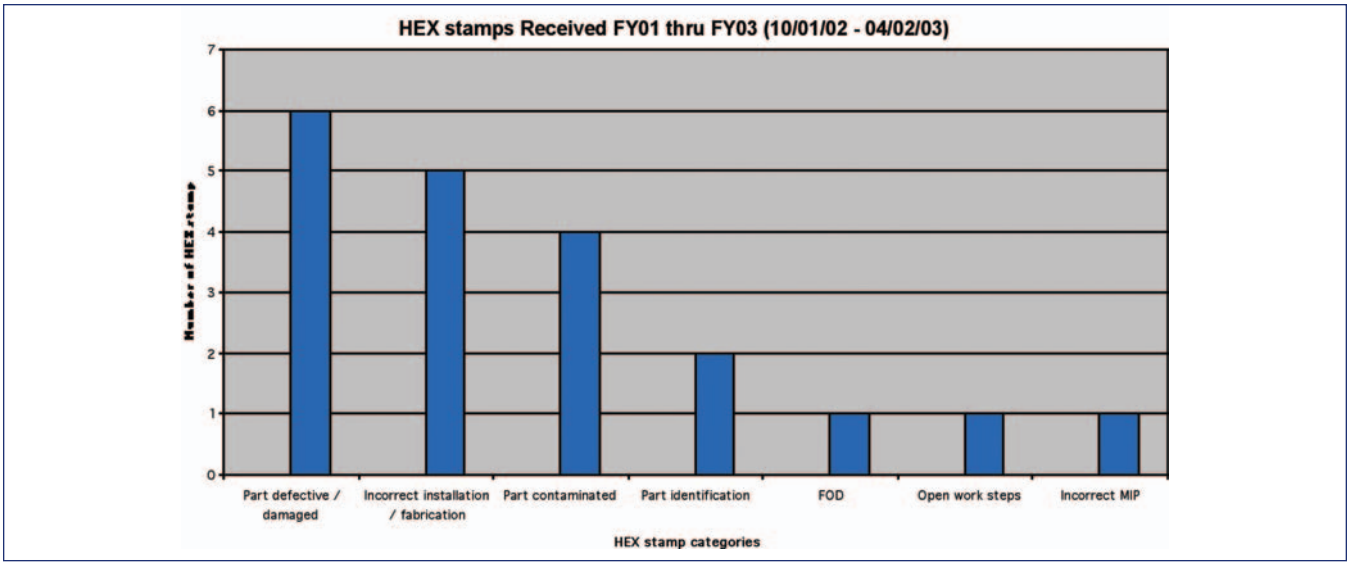


Figure 2.2.1. HEX stamps received between October 1, 2002 and April 2, 2003.

March 2003 that would have been subject to potential hex stamp use were 141,247. During that same period only 20 hex stamps were issued for various operations. (See Figure 2.2.1) HEX stamps received in FY2001, FY2002, and current FY2003 have been reviewed and the conclusion drawn is that the number of HEX stamps received compared to the number of inspection opportunities and hardware items completed/shipped provided too few data points for extensive analysis. According to several sources, this practice has been curtailed due to previous practices of using the stamps as a "hammer" against the contractor. The more common practice is for the inspector to refuse to buy the discrepant job, and offer to come back later once corrective action is taken. Such instances are not tracked by any measurement.

Use of metrics appears to be of inconsistent effectiveness. NASA staff offered the following quotes:

> "Collection of metrics is rampant; but the utility and the analysis of that data is questionable and lacking."
>
> "A lot of metrics are kept, some with no value added, little true management using metrics."
>
> "The CAIB could help NASA understand how they can use metrics more effectively."
>
> "Assessment of contractor performance is largely anecdotal."
>
> "Very few leading metrics are used; predictive metrics are very hard to develop/use"[20]

When asked if people were their most constrained resource, NASA S&MA leadership cited that while the number of quality assurance people may be adequate, if they had more people, they could be more responsive during workload peaks to avoid workers having to wait for an inspector to close out a job. One member stated that the situation was much improved since 2000, when the organization had zero quality engineers and many issues had to be deferred to system engineers. The USA representative stated that the staffing situation had improved considerably since the program's transition from California. Additionally, while USA may have enough people in SQ&MA, the organization would benefit with more personnel to be used in industrial and human factors engineering to accomplish more process assessments and analyses. One of the more common reasons quality engineers declined to add GMIPs was cited as inadequate manpower. The 1999 SIAT[21] report documented its concern with the declining manpower pool and approximately 35 new inspectors were added at KSC. Since then most of that increase has been eroded through retirements and promotions. Marshall's S&MA staff is also short approximately 10 people. In both cases the replacement manpower is on hold due to budgetary considerations. We highly recommend that NASA review its S&MA manning.

The NASA S&MA chiefs are at a lower grade position relative to the Chief Engineer or Launch Director. This organizational structure may be problematic with respect to potential pressure in resolving conflicting priorities between respective organizations. NASA should review the position description and adjust to establish parity in leadership and influence.

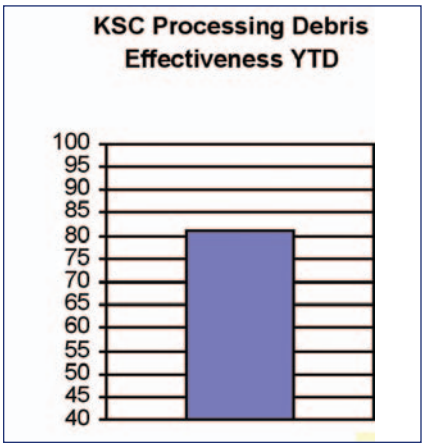
USA's Safety, Quality and Mission Assurance (SQ&MA) team has implemented a robust program to verify that work accomplished is in compliance with the OMRSD. USA has invested much effort in building a culture focused on quality and safety. Its "Time Out" program authorizes any worker to call a halt to operations, report problems/defects (even if only suspected), and is encouraged, even rewarded, by management. The NASA Shuttle Logistics Depot's (NSLD) effort in building a safety focus has been recognized as an OSHA "Star Site" for its participation in this voluntary protection program. Recently re-certified in 2002, its workforce has gone 750 days (as of April 2003) without a lost-time mishap.

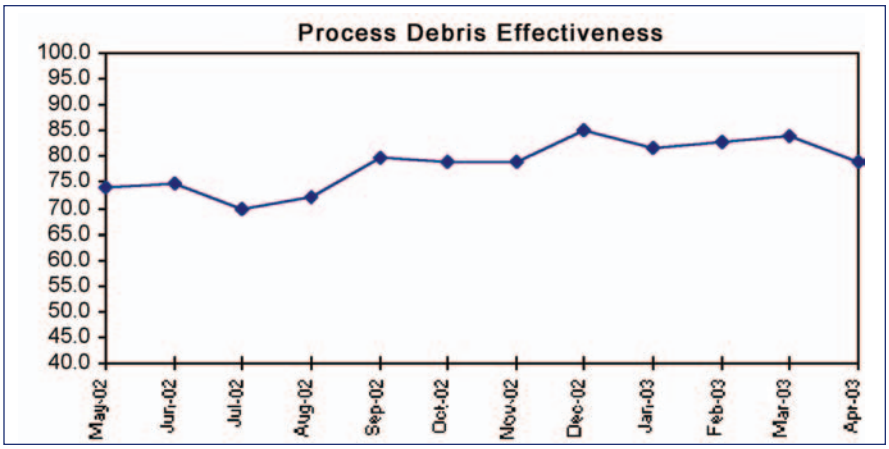
The NASA and USA Foreign Object Debris (FOD) prevention program should be reconsidered. FOD prevention programs typically fall under the auspices of Quality Assurance programs in the DoD and aviation industries. After the publication of the National Aerospace FOD Prevention, Inc (NAFTI) FOD Prevention Guideline in July of 2000, the FOD program was changed (took effect during the Award Fee Rating Period from March 1 through September 1, 2001) with FOD re-categorized into "process debris" and "FOD." Processing debris is defined as "Any material, product, substance, tool or aid generally used during the processing of flight hardware that remains in the work area when not directly in use, or that is left unattended in the work area for any length of time during the processing of tasks, or that is left remaining or forgotten in the work area after the completion of a task or at the end of a work shift. Also any item, material or substance in the work area that should be found and removed as part of standard housekeeping, Hazard Recognition and Inspection Program (HRIP) walkdowns, or as part of "Clean As You Go" practices."[22] Foreign object debris or FOD, is defined as "Processing debris becomes FOD when it poses a potential risk to the Shuttle or any of its components, and only occurs when the debris is found during or subsequent to a final/flight Closeout Inspection, or subsequent to OMI S0007 ET Load SAF/FAC walkdown."[23] The rationale for including this step as a mandatory inspection point was that the area was put into use at the closeout; therefore, any debris found at that time was no longer "potential FOD" but was FOD.

This FOD program redefinition was a result of a National Aerospace FOD Prevention, Inc. (NAFPI) conference that resulted in some new industry-wide initiatives. NAFPI is a "nonprofit, educational organization developed to standardize terms and methods for the prevention of foreign object damage to aircraft and aerospace vehicles. The objective is to make the aerospace industry aware of the need to eliminate foreign object debris and provide information about current proven practices and technological advancements that prevent FOD.... An effective FOD prevention program identifies potential problems, corrects negative factors, provides awareness, effective employee training, and uses industry "lessons learned" for continued improvement."[24] There is no mention of Process Debris but it does talk to potential foreign object debris. NASA has done a good job of complying with almost every area of this guideline. However, the document addresses FOD investigations in a singular sense. "All incidents of actual or potential FOD should be reported and investigated. These reports should be directed to the FOD Focal Point who should perform tracking and trending analysis. The focal point should also assure all affected personnel are aware of all potential (near mishap) /actual FOD reports to facilitate feedback ("lessons learned")."[25]

The NASA FOD program does have some outstanding aspects. The USA FOD program includes daily debris walk downs by management to ensure workers comply with the "clean as you go" USA policy. This program is noteworthy but statistics kept by USA show its success rate varies between 70 and 86 percent.[26] (See Figures 2.2.2 and 2.2.3.) The danger of migrating debris begins while the job is in work. FOD prevention must be considered as critical as clean up, regardless of timing and division of labor between USA and NASA quality responsibilities.

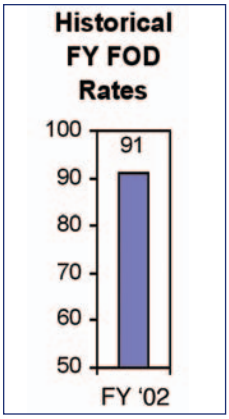
NASA inspectors may inspect areas prior to closeout but cannot take formal action (categorize debris found as FOD) for those observations made before closeout. The consensus among inspectors is that this program re-categorization was to decrease the impact of NASA SM&A-found FOD on the USA awards fee. This may be anecdotal but indicates a

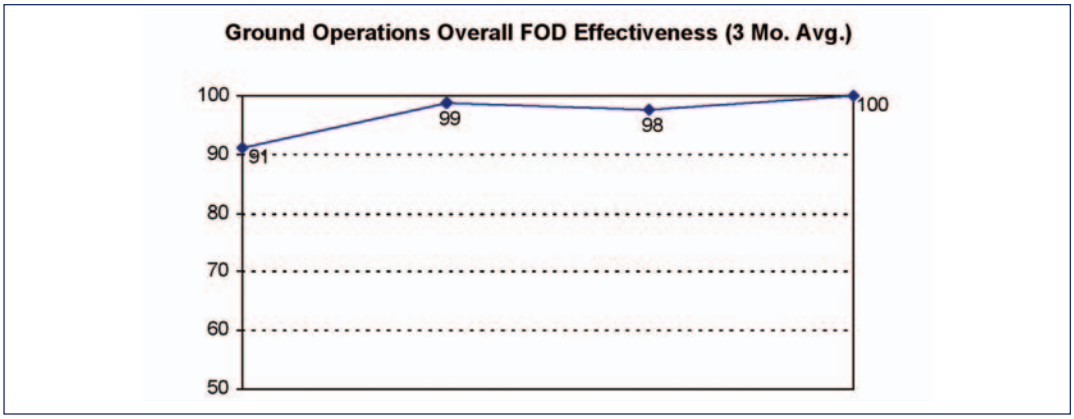




	####	####	Jul-02	####	####	####	####	####	Jan-03	Feb-03	Mar-03	Apr-03
# of Reports	660	486	546	556	427	487	427	331	424	345	367	373
# Debris Free Reports	489	363	382	400	340	385	337	282	347	286	308	295
# of Debris Findings	171	123	164	156	87	102	90	49	77	59	59	78
% effectiveness	74	75	70	72	80	79	79	85	82	83	84	79
Process Debris Rate	25.9%	25.3%	30.0%	28.1%	20.4%	20.9%	21.1%	14.8%	18.2%	17.1%	16.1%	20.9%

Figure 2.2.2. Process debris performance metrics.





		FY '02						FY '03					
		APR - JUN			JLY - SEP			OCT - DEC			JAN - MAR		
# of Closeout Inspections		205			172			83			60		
# FOD Free Closeouts		187			170			81			60		
		APR	MAY	JUN	JLY	AUG	SEP	OCT	NOV	DEC	JAN	FEB	MAR
STS 107	# INSPECTIONS	21	45	48	1	1	0	3	8	9	6	0	
	# FOD FREE	18	36	42	1	1	0	3	8	9	6	0	
STS 114	# INSPECTIONS	0	1	4	0	0	0	0	1	10	38	1	
	# FOD FREE	0	1	4	0	0	0	0	1	10	38	1	
OTHER	# INSPECTIONS	34	23	29	52	42	76	28	21	3	2	13	
	# FOD FREE	34	23	29	52	41	75	27	20	3	2	13	

Figure 2.2.3. NASA FOD Metrics.

broad misunderstanding brought on by the recategorization and potentially a need for recurring (not presently required) training to reemphasize FOD prevention. Process debris statistics do not directly impact award fee. The award fee calculation for the last half of FY2002 resulted in the highest award in the history of the SFOC relationship. FOD rates for that period were at 91 percent and the process debris metric in the low 70s. This delineation of FOD is unique to the SFOC. NASA should recombine their FOD prevention program and increase its impact in the contract award fee. Since processing debris (or Potential FOD as it is called in the NAFTI guideline) and FOD are verifications, recommend the inspections be sequential (i.e., contractor inspects and then NASA inspects).

FOD prevention practices at the launch pads consist of 23 separate checks, from pre- to post-launch, accomplished in varying levels of detail by a broad range of personnel from different organizations. Implementing FOD prevention requirements for subcontractors accomplishing major maintenance on launch pad structures is a significant challenge. USA personnel cited a recent incident in which a bolt estimated to be of 2 inch length was observed blown about during launch. USA has established excellent FOD prevention standards by which they hold subcontractors responsible for compliance. The Statements of Work define subcontractor requirements for FOD prevention, and USA FOD prevention training is provided to subcontractors for their work crews. Subcontractors are required to sign a "Statement of Commitment for Prevention of Foreign Object Debris" accepting that FOD prevention will be enforced during implementation of all tasks associated with that contract. Work crews are required to "clean as you go." USA field monitors, focusing on routine debris clean up and control accomplish work site inspections, and inspection for FOD is included in the Quality Planning and Verification Sheets. Finally, FOD prevention compliance is among the requirements for final inspection and acceptance of subcontractor work. FOD discovered on the launch pad prior to a mission has a direct impact on the USA award fee as a safety factor.

Proposed Recommendations:

Re-evaluate the Space Shuttle Program's S&MA inspection program and implement changes to enhance its effectiveness, including the following:

Perform a risk evaluation of the current FMEA/CIL (including GMIPs), while assessing other tasks for possible GMIPs inclusion or exclusion as appropriate.

NASA S&MA establish a process inspection program to provide oversight into contractor daily operations, while in process, using statistically driven sampling. Inspections should include all aspects of production, including training records, worker certification, etc., as well as FOD preven-

tion. NASA should also add all process inspection findings to its metrics program, including processing debris. Finally, inspections should be designed to evaluate all areas of production through concurrent and sequential evaluations as well as GMIPs, surveillance, and sampling based inspection events.

Develop a regular (at least annual) process to evaluate the quality assurance program. As a minimum it should consider inputs from engineering, technicians, PRACA, contractors and quality metrics to adapt the following year's program. This will make the quality program more adaptive to the changing environment of an aging vehicle/infrastructure and concentrate inspections on developing problems to ensure quality. Highly recommend benchmarking the airline industry and DoD.

Engineering review of work documents should be accomplished according to statistical sampling methods, to ensure a representative sample is evaluated and adequate feedback into the process is communicated to resolve documentation problems.

Designate NASA S&MA as the singular focal point for development and oversight of all quality assurance programs to ensure a fully integrated program across all divisions. Elevate the role of NASA's S&MA senior leaders to a position of parity with the key decision makers involved in launch and critical operations. Commensurate with this recommendation is the need to organize coherently within NASA to eliminate center and program options and provide adequate independence. Centralized control of S&MA at the Center Director level should be enforced.

Revise NASA's role in the FOD program to expand inspector involvement and number of inspections. These revisions should include the addition of random process surveillance including FOD prevention requirements. Such inspections will provide a better means of crosschecking contractors' oversight.

The FOD program should be revised to eliminate any alternative definitions of FOD, such as "processing debris." "FOD" is an industry-accepted term, and the use of any other definition could be interpreted as diminishing the significance of items left behind during maintenance, irrespective of job signoff status.

The seriousness of FOD in the Space Shuttle Program must be communicated in fiscal terms allowing very little room for marginal performance. Changing the impact of FOD as a safety program in the award fee calculation will communicate this clearly.

Finally, NASA should re-evaluate their manning posture to accomplish the S&MA mission as it is currently defined and as a result of the above recommended improvements after a QPRD program review. Manning should be adjusted to a level commensurate with the effort required to support revised GMIP and surveillance levels.

2.3 Maintenance Documentation (WAD Accuracy)

Issue:

Assess accountability/traceability of work papers/ maintenance actions from the source to the technician accomplishing the specific task to proper documentation analysis/archiving.

Background:

Accountability/traceability of every action is critical to safe operation of the Shuttle. Members of the Board toured the TAIR (Test and Inspection Records) station in OPF-3, where OV-103 has been undergoing OMM (since August 2002). During the tour inspection, maintenance, and modification requirements in paper form were observed being distributed to various work groups: TPS, electrical-mechanical, structural, etc. Engineers were observed at the TAIR station reviewing paperwork and forwarding requests for Problem Reports (PR) to systems engineers located elsewhere at KSC. Additionally, the team observed Work Authorizing Documents (WAD) in a specific work center (electrical-mechanical) being reviewed prior to work commencing and tools/equipment determination by assigned technicians.

Quality Data Center is responsible for tracking all paperwork from job completion in the OPF through each coordination function. All papers end up in this organization, where they are scanned, electronically archived, and physically archived. On an average day, 15,000 pages are archived; 4,500,000 pages annually. This database forms the basis for PRACA, SPEARS and SIMS, all of which are used for trend analysis, metrics, historical research, and so forth. Typically, all documentation is archived prior to launch.

Findings:

The engineering assessment of work paper, which is accomplished with very limited use of structured sampling methodology, is inconsistently used across the various systems/subsystems. Every WAD is reviewed by up to three additional engineers in the USA SSME division. Additionally, the Technical Accuracy Measurement system outlines a review of WADs at the system or subsystem level but does not specify frequency or quantity using statistically representative methodology or use of this information for trend analysis. This is just one example of a review process used by one system. This very issue was addressed in an independent assessment report; "The goal of USA's work procedure improvement programs needs to be continued and expanded to remove inconsistencies and inaccuracies, incorporate deviations and clarify procedural steps. The better the work documentation is, the greater the procedural compliance, and the less chance for error. USA should investigate the consolidation of the many separate initiatives for improving work documentation into one cohesive, integrated program."[27] USA does limited sampling of WAD completion during process quality sampling but NASA S&MA apparently does little to none.

The Board asked KSC NASA/USA to review documentation for STS-107, STS-109, and OV-102's J3 OMM paper work with specific interest in gleaning any information,

relevant to the investigation, which may have been causal or may reveal areas of weakness to be considered for return to flight recommendations. NASA built a team (Process Review Team…PRT) of 445 NASA and contractor engineers and quality personnel, divided into eight system teams and two special purpose teams. The KSC PRT activities involved three separate analyses of as-run procedures. The System Engineering Work Authorizing Document (WAD) Review focused on the technical aspects of WADs, (i.e., the quality of the work paper and the performance to the work paper); the Assurance Engineering Review[28] *provided an independent, assurance review of the as-run WADs, and the Systemic Analysis*[29] *focused on categories of observations and technical observations derived from analysis of the System Engineering WAD Review results. The result of their work was a list of Findings (potential relationship to the mishap), Technical Observations (technical concerns or process issues), and Documentation Observations (minor errors). The team reviewed approximately 16,500 WADs with an estimated sheet count in excess of 600,000 pages over a three-month period. The team only generated one Finding, related to the bipod ramp, and no observations that may have contributed to the accident.*

The PRTs sampling plan resulted in an excellent database of observations and was documented in their report.[30] The general results of this review are included in Figure 2.3.1. The number of observations is relatively low compared to the total amount of WADs reviewed and give an apparent 99.75 percent accuracy rate. While this number is high, a closer review of the data shows some of the weakness in the system. The total Technical Observations of 2,847 out of the samples taken from the STS-107, STS-109 and OMM reviews are delineated into 17 categories. Five of these categories, E, F, G, H, and M are of particular concern for mishap prevention and reinforce the need for process improvement. Category E, entitled "System configuration could damage hardware" was observed 112 times. Categories, F, G, and H, which deal with poor incorporation of technical guidance, are of particular interest due to the Board's concern over the backlog of unincorporated engineering orders. Finally, category M, entitled "paper has open work steps," indicates that the review system failed to catch a potentially significant oversight 310 times in this sample. Figures 2.3.2, 2.3.3, and 2.3.4 give list the results in detail.

The USA review of this data resulted in 10 recommendations for remedial action to reduce the potential for recurrence of this problem. It is noteworthy that they recognize a need for action and have outlined a get-well plan to accomplish it. Their enumerated list of actions is provided below.

- Operations and Quality review all closed paper for unworked steps
- OEL, INS & TPS Engineering review all their documents for correct specification callout
- ET, SRB, Payloads review all their documents for application of critical skills
- GNC, PVD, MEQ review their closed documents for "Not Performed Options" incorrectly worked
- Engineering review closed paper for Data Not Recorded within Specific Limits
- INS, ETM & OEL review documents for Drawing Requirements Incorporation
- OEL review documents for System Configuration and OMRSD deficiencies
- INS review documents for System Configuration deficiencies
- OMS review documents for correct OMRS application.
- All Engineering teams review their paper for correct hardware callouts[31]

	STS-107	STS-109	OMM
Findings	1	0	0
Technical Observations	1222	1304	321
Documentation Observations	3406	3419	Not Required
WADS Reviewed	6751	6946	2866

Figure 2.3.1. Database review results.

Total Technical Observations Summary Count

Team - Report Count	STS: 107 All Tech. Obs. Type/Code
19	A - MR Rationale incorrect or missing
32	B - Summary/Conclusion incorrect or missing
2	C - System cleanliness level compromised
9	D - System config. could compromise data integrity or accuracy
38	E - System configuration could damage hardware
59	F - Drawing Reqts incorrectly incorporated, incomplete or missing
32	G - OMRSD Reqts incorrectly incorporated, incomplete or missing
222	H - Other specification incorrectly incorporated, incomplete or
9	I - Troubleshooting data analysis incomplete, incorrect or missing
7	J - Troubleshooting leads to incorrect conclusion
7	K - Retest incomplete, incorrect or missing.
93	L - Data recorded not within specified limits
200	M - Paper has open work steps (steps not bought complete)
97	N - Wrong steps worked (NP options incorrectly selected)
188	O - Critical skill requirements incomplete, incorrect or missing
177	X - Other
21	Z - Missing Document - Process Review Incomplete
1222	*Total Tech. Observations*

Figure 2.3.2.

Total Technical Observations Summary Count

Team - Report Count	STS: OMM A - Struc/Mech & C - Electrical Tech. Obs. Type/Code
23	A - MR Rationale incorrect or missing
33	B - Summary/Conclusion incorrect or missing
7	D - System config. could compromise data integrity or accuracy
24	E - System configuration could damage hardware
19	F - Drawing Reqts incorrectly incorporated, incomplete or missing
34	H - Other specification incorrectly incorporated, incomplete or
1	I - Troubleshooting data analysis incomplete, incorrect or missing
2	J - Troubleshooting leads to incorrect conclusion
4	K - Retest incomplete, incorrect or missing.
7	L - Data recorded not within specified limits
42	M - Paper has open work steps (steps not bought complete)
9	N - Wrong steps worked (NP options incorrectly selected)
39	O - Critical skill requirements incomplete, incorrect or missing
74	X - Other
3	Z - Missing Document - Process Review Incomplete
321	*Total Tech. Observations*

Figure 2.3.3.

Total Technical Observations Summary Count

STS:	109
Team - Report	All
Count	Tech. Obs. Type/Code
17	A - MR Rationale incorrect or missing
43	B - Summary/Conclusion incorrect or missing
9	C - System cleanliness level compromised
11	D - System config. could compromise data integrity or accuracy
50	E - System configuration could damage hardware
94	F - Drawing Reqts incorrectly incorporated, incomplete or missing
54	G - OMRSD Reqts incorrectly incorporated, incomplete or missing
152	H - Other specification incorrectly incorporated, incomplete or
16	I - Troubleshooting data analysis incomplete, incorrect or missing
4	J - Troubleshooting leads to incorrect conclusion
9	K - Retest incomplete, incorrect or missing.
85	L - Data recorded not within specified limits
258	M - Paper has open work steps (steps not bought complete)
158	N - Wrong steps worked (NP options incorrectly selected)
110	O - Critical skill requirements incomplete, incorrect or missing
184	X - Other
20	Z - Missing Document - Process Review Incomplete
1304	Total Tech. Observations

Figure 2.3.4.

This review pointed out two weaknesses that NASA/USA must correct. The engineering review of paperwork should have been done, as an aspect of the quality assurance program, all along. More oversight may not be necessary. Current process provides three or more layers over paperwork review prior to being scanned into the database. However, if review authorities in the work section, S&MA, SQ&MA, TAIR, or engineering are not aware of the most common problems to look for corrections cannot be made. Routine sampling will help refine this process and cut the error significantly. Finally, the process of paperwork review must be standardized among the various Space Shuttle systems for both quality assurance functions and engineering. Some of the system engineering offices have processes that sample WADs for accuracy prior to being published. Applying a statistically based process control system for sampling of WADs before and after the fact is highly recommended.

Existing paperwork trail, auditing accountability/traceability system is excellent. The extent of documentation required and the sheer volume of paperwork involved are phenomenal and appear very well managed. The monumental task of cataloguing and preserving Space Shuttle documentation is well organized and commendable.

Proposed Recommendations:

Quality and Engineering review of work documents for STS-114 should be accomplished according to statistical sampling methods, to ensure a representative sample is evaluated and adequate feedback into the process is communicated to resolve documentation problems.

Implement USA's suggested remedial actions for process improvement to include a statistically based recurring sampling (by SQ&MA) of all future paper work to identify recurring problems and implement corrective actions.

Develop a NASA S&MA oversight process to statistically sample the work performed and documented by USA technicians to ensure process control, compliance and consistency with SQ&MA sampling results.

2.4 Capabilities Analysis

Issue:

Do NASA and contractor ground operations managers routinely assess their capability to support workload requirements? Do they have the tools to identify when they are approaching (or exceeding) the "ragged edge"; i.e., the point at which requirements exceed capabilities? At what point does the production/launch schedule become unsupportable without adding resources or delaying milestones? What actions are taken to add resources or slip milestones?

Background:

NASA's resources have been trimmed and processes streamlined in efforts to control/reduce the cost of operations (see Figure 2.4.1). While this has happened in many areas, one of the most obvious examples is the reduction of the combined NASA/USA workforce at Kennedy Space Center (KSC), which totaled over 8,800 in 1991. By 2002, this workforce had been downsized by slightly more than 50 percent to approximately 4,400. Shuttle launches over the same period had decreased disproportionately by only 25 percent, from eight to six. Another example of efforts to improve efficiency and lower costs was the relocation of Orbiter Major Modifications (OMM) from Palmdale, California, to KSC, starting with OV-103 (*Discovery*) in September 2002. Although the last four OMMs at Palmdale had required anywhere from 324 to 448 equivalent personnel, it was estimated that that OMMs could be supported at KSC with only 235 additional equivalent personnel due to more effective utilization of the existing KSC workforce. However, during the first 9 months of OV-103's OMM, an average of 307 EP have been required, a 31 percent overrun of the initial estimate.

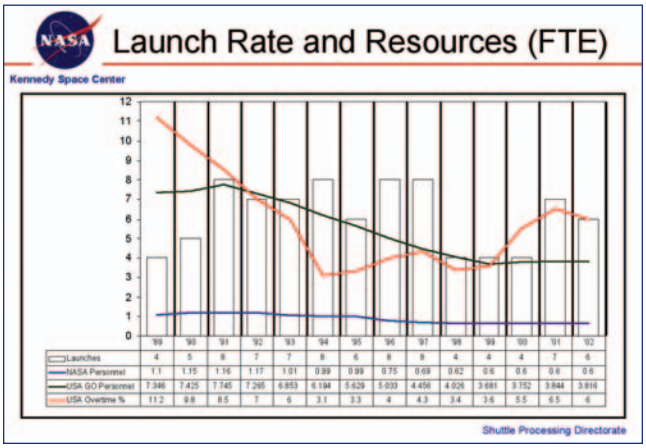


Figure 2.4.1. Space Shuttle launch rate versus Full Time Employee resources.

While the drive toward increased efficiency and controlling costs is commendable, it is vitally important that managers have the tools necessary to determine, as far in advance as possible and preferably during workload planning and scheduling, when resources and capabilities will be exceeded. Such knowledge would allow them to take mitigating

actions well in advance of the forecasted shortfalls. This is particularly critical, given the many opportunities for unforeseen requirements that can result from limited experience operating and maintaining this unique, reusable space vehicle. These unknowns can manifest themselves in many different and valid forms including technical surprises requiring additional, unplanned inspections, maintenance, and modifications. These requirements must be accomplished over and above a production schedule built to balance efficiency with timeliness, and one in which milestone slippages leading to delayed launches are seen as negatives to be avoided as much as possible. These unanticipated requirements almost always equate to more inspections and/or maintenance that, in turn, either drives increased overtime labor or a need to increase the size of the workforce by hiring more employees. Each course of action carries inherent disadvantages. Prolonged use of overtime increases the potential for mistakes and hiring more personnel to perform highly technical, painstakingly meticulous work brings other challenges, such as finding qualified people, training them, and ensuring their lower levels of experience do not cause mistakes.

An example of a technical surprise that drove an unanticipated workload occurred in the aftermath of STS-93 (July 1999), when a short circuit five seconds after *Columbia*'s liftoff caused a loss of power to two of the six main engine controller computers. The ensuing investigation determined the root cause to be a damaged wire and led to extensive fleet-wide inspections and modifications, starting with *Columbia* in October 1999, only one month after it began its OMM. None of this additional workload was anticipated, planned, scheduled, or resourced. Compounding the surprise, engineers and planners expected 500 to 700 wiring anomalies, but were shocked by over 4,600 actual discoveries; each and every one of these required engineering evaluation and disposition, and in the majority of cases, correction by maintenance personnel. The vast number of wiring anomalies necessitated revising the inspection "chit" no less than six times in the course of the OMM, further exacerbating the growing workload. The initial workforce resourced to perform *Columbia*'s OMM was determined based on the original OMM requirement, which excluded the wiring inspections and modifications. This workforce numbered 342 and had an 85 percent experience level, with experience being defined as either manufacturing the Orbiter or working on a previous OMM. However, as the workload steadily grew, personnel worked longer hours and more personnel had to be hired, increasing the workforce by 46 percent to 500 personnel. This dropped the experience level to approximately 58 percent, which, in turn, drove increased training requirements, including on-the-job training, at the expense of production. Yet another example of a technical surprise during *Columbia*'s OMM was the chance discovery of cold plate corrosion.

As the Orbiter fleet ages, technical surprises such as those cited above will also likely continue and may even increase. Additionally, there will be great pressure to return to flight once the *Columbia* accident investigation has concluded. Given these kinds of surprises and production pressures, capabilities assessments will grow increasingly important to safe Shuttle operations.

Findings:

During the May 1, 2003 OV-103 J3 OMDP (Orbiter Maintenance Down Period) Project Management Review (PMR), the Orbiter Processing Facility (OPF) tile technician workload was briefed as a concern. Tile replacement requirements had grown 28 percent over original projections, and tile technician labor requirements had grown by 11.5 percent. Potential additional tile technician labor growth ranged from a low of another seven percent to a high of 24 percent (82,522 to 111,892 labor hours). No mitigating actions were proposed, and the briefing was treated as informational (rather than actionable) at that point.

During the same PMR, the "tile backstop" also briefed similar concerns. Test tile production in support of the *Columbia* Accident Investigation had driven a 473 percent requirements increase, from 128 to 606 tiles, not to mention the previously mentioned higher projections related to *Discovery*'s OMM. Tile backshop management offered several mitigation options, including working more overtime, augmenting the workforce with additional manpower, reactivating the Palmdale tile shop to produce test tiles, or bringing skilled tile technicians from Palmdale to KSC on a temporary basis. The approved action was to hire additional personnel, specifically machinists, to open up one of the production bottlenecks.

What's important in both of these examples is that two production areas were attempting to project their capabilities and assess them against projected/potential requirements.

Discussions with both NASA and USA managers revealed that baselines and templates were being developed for both OMM and down-/up-mission processing; these, in turn would enable better requirements projections. They have also used various capability assessment models over the past several years, such as "equivalent flow" which showed, prior to the *Columbia* tragedy, that the FY2003 and FY2004 launch schedule would drive a workload that would exceed capability by as much as 64 percent. These same managers were adamant that they would do everything in their power to mitigate situations such as this 64 percent overload, to include production/launch schedule slippages. However, they also commented that the launch schedule was driven by direction from the very top levels of NASA, and their launch slippage requests often fell on unreceptive ears.

Conclusions:

As the Orbiter fleet ages, technical surprises will likely continue and may even increase. Additionally, there will be great pressure to return to flight once the *Columbia* Accident Investigation has concluded.

Unanticipated requirements, such as those caused by technical surprises, combined with production pressures, can quickly outstrip resources and capabilities. Under these circumstances, capability assessments that enable mitigating actions as far in advance as possible will grow increasingly important to safe Shuttle operations.

Some work centers have performed capability assessments and used them to advise managers of various options to mitigate existing or potential requirements overload situations. NASA/USA managers have been working with capability assessment models for several years at a macro-level but do not feel they have a tool with sufficient fidelity and confidence to advise when launch (manifest) schedule slippages are necessary.

Proposed Recommendations:

NASA/USA managers should expedite efforts that have been ongoing for several years to develop accurate, credible capability assessment models and use the results to take action as far in advance as possible whenever requirements exceed capabilities.

NASA/USA managers should develop sufficient confidence in capability assessments to use them in manifest (launch) and ground operations resource planning.

References:

1. USA briefing, "OV-103 J3 OMDP Project Management Review," 12 June 03
2. Boeing/Palmdale OMM briefings/tours, 14 May 03
3. USA briefing, "OV-103 J3 OMDP Project Management Review," 1 May 03
4. USA Ground Operations briefing, "Equivalent Flow Model," Apr 03
5. HEDS/IA briefing, "OV-103 J3 OMM Assessment," 14 November 01
6. Boeing report, "OV-102 Wire Inspection Report, September 99 – February 01," Jul 01
7. HEDS/IA report KS-0003, "Evaluation of the Current (OV-102) Orbiter Major Modification (OMM) Flow," Mar 01
8. KSC Shuttle Processing Directorate chart, "Launch Rate and Resources (FTE)," undated
9. USA Ground Operations chart, "Orbiter Power Capability," undated

3.0 Fleet Sustainment

3.1 Service Life Extension Program (SLEP)

Issue:

Evaluate NASA plans for the SLEP of the Space Shuttle to provide for safe and efficient operations beyond the 2012 timeframe.

Background:

Shuttle Program retirement, until recently, was planned for the early 21st century. Early Program expectations for the service life of the Shuttle system were based on 100 flights per vehicle over a 10-year period. The original certification of some of the structures and subsystems was done to 2 or 2.5 times the life expectancy at that time, specifically 10 years, starting 1981. Some destructive testing was done on partial or subscale structures at the beginning of the program but follow-on sustainment research has been done at subsystem level primarily. The Orbiter was originally designed for a minimum of 10 years useful age life; i.e., static age life plus operating life (100 missions); static life is defined as storage life plus installed life in a non-operating mode in an ambient environment. In preparation for return to flight (RTF) following *Challenger*, it was recognized that some materials were already in excess of 10 years static age life. This led to concerted efforts by Materials and Processes and Design Engineers to identify age/life problems. In 1987, a review of 330 non-metallic materials used in the Payload Integration Hardware program (324 common to the Orbiter) was done; 291 were extended to 20 years; 38 were deemed "probably" acceptable for 20 years, but lacked sufficient data, with the recommendation of periodic inspection; one remained limited to 10 years.[32]

In preparation for STS-26 (September 29, 1988), approximately 2,500 Orbiter parts that exceeded 10 years of life, were assessed by their respective subsystem design groups using the results of the above referenced non-metallic materials assessment. These subgroups reached the conclusion that there were no age life concerns in the program at that time. For STS-29, STS-30, and STS-28, similar assessments were performed for the "delta" items; i.e., new items exceeding 10 years. Based on the absence of age/life concerns in four consecutive pre-launch reviews and the "inherent stability of nonmetallic materials,"[33] NASA and Rockwell agreed in May 1989 to discontinue flight-by-flight assessments relying on CoFR processes to validate aging issues when surfaced by the subsystem managers. This historical approach to extend the 10-year certification to 20-years, while including materials and subsystems assessments, fell short in integrating these efforts at an overall Space Shuttle Program level. Apparently individual materials and components were requalified, rather than an overall systems approach to recertifying the Shuttle system. The recertification that was done to extend the Shuttle fleet beyond ten years was a rudimentary tabletop drill and review of subsystems and materials. While this drill resulted in the identification of some obsolescence issues and created some preventative maintenance programs, it lacked the rigor necessary to predictively build longer-term sustainment programs or extend the Shuttle system beyond the second 10 years.

The Integrated Space Transportation Plan states a requirement for the Space Shuttle "through the middle of the next decade and possibly beyond." Consequently, the SLEP program was initiated by Headquarters Code M in December 2002 and established at Johnson Space Center under the Space Shuttle Program Development Office. The SLEP office consists of four people. DAA-SSP/ISS set the program goal for sustainment at 2022 to accommodate the budget cycle. Their mission is to identify the investments required to fly the Space Shuttle safely and effectively through 2022 and then build a budget requirement timeline to support this plan. This new office has built a straw man budget plan through the out years with funding lines for four different prioritized categories: Should Do, Current Commitments, Foundational Activities, and Projects and Studies. Program development is still in the seminal stages and program definition, including lines of responsibility, is stated in broad terms.

Findings:

The overall goal of the Service Life Extension Program is to identify, prioritize and advocate programs that will extend the service life of the Orbiter vehicle and associated Shuttle systems. Several goals have been expressed within NASA for the programmed life extension of the Shuttle ranging from "middle of the next decade" to 2020, 2022 and as long as 2030.[34] Definitive planning needs a target date to set its course. In the absence of a target date, the Shuttle Program Office is unofficially using the 2022 date as a planning horizon but is not limiting itself to that specific date. NASA should identify a target date to base SLEP plans on and, eventually, budget support.

Development of a prioritized list of SLEP championed projects has been done using an Analytical Hierarchy Process (AHP) tool that will help compare dissimilar projects on the basis of total impact to service life extension as well as safety, urgency, and cost. (See Figure 3.1.1) A team of eight program managers developed the weights for the AHP to evaluate and define sustainment projects. The Shuttle Program Manager approved their recommendations with some adjustment to add weight to safety related issues. The "Should Start" priority items are defined as sustainment projects that must be initiated in FY2004 due to an urgent requirement such as Diminishing Manufacturing Source (DMS) or obsolescence. Examples include sustaining test equipment tasks for SSME and case hardware availability for RSRM. Priority 2, "Current Commitments," includes projects that are already committed to a budget timeline. Examples include the Cockpit Avionics Upgrade, SSME Advanced Health Management System (phase 1), infrastructure, and Industrial Engineering for Safety. Priority 3 "Foundational Activities" includes Aging vehicle studies, Mid-Life Certification and NDE upgrades. Priority 4, "Projects and Studies," includes obsolescence issues and vehicle health monitoring. This matrix is employed to derive the priority for candidate SLEP programs.[35]

The methodology used to begin populating the SLEP candidate list was a simple data call to all Space Shuttle project, system, and subsystem managers. During the March 19-20, 2003 SLEP conference this list grew to over 100 candidates ranging from direct Shuttle serviceability impacts to industrial safety and infrastructure. The well-defined projects were run through the AHP algorithm yielding a prioritized list. This list was then built into a straw-man budget plan. Figures 3.1.2 and 3.1.3 show the budget plan by year and project.[36]

The SSP SLEP is in the infancy stages of requirements development and needs some definitive bounds. It currently includes classic sustainment of aging aircraft projects in the same priority analysis with safety (ground and flight), infrastructure (tooling, buildings and equipment), capability upgrades, and basic research projects for the program, not necessarily limited to Shuttle service life. Funding lines for classic sustainment issues (such as obsolescence and tasks revealed by the mid-life recertification process) are limited to the next two years due to the lack of project definition beyond FY2005. Under normal federal financial and budgeting processes this lack of definitive bounds may leave the SLEP open to budget cuts and priority confusion resulting in selection of non-direct sustainment projects and dilution of NASA's ability to resolve sustainment issues.

At this stage in the program's development there does not appear to be much reliance on the existing databases, such as PRACA, that could be used to help identify SLEP opportunities as individual subsystem project management. The first summit meeting held last March resulted in a list of over 100 new project recommendations collected from the

	A. Sustainability	B. Safety Improvement	C. Efficiency Improvement	D. Customer Driven Capability
1. Should Start	• RSRM Case Vendor • PRSD Tank Vendor • SSME STE Equipment			
2. Existing Commitments	• LLAFC • Infrastructure	• Cockpit Avionics • AHMS I • MLG Tire/wheel • Industrial Safety		

3. Foundational Activities	• Aging Vehicle
	  • Mid Life Cert
	  • Fleet Leader
	  • Corrosion Ctrl...
	• RSRM Ground Test
	• Sustain Health
		• PRA Development		• Performance Trades
				  • Lift
				  • Power
				  • Stay Time
				• SS Utilization Reinvent

4. Projects and Studies	• Vehicle Hlth Mon. • STE Obsolesc • Material obsolesc • Component obsolesc • Supply Chain Viability • Spares Augment	• New Start: AHMS II • Study: Hydrazine • Study: SSME Nozzle • Study: Orbiter Hardening • Study: Enhanced C/W • Study: Crew Surviv		

Figure 3.1.1. SLEP prioritization structure.

various program/project managers. This is encouraging in that it indicates broad acceptance of the program; however, it also indicates that there isn't much rigor in the qualification process.

The Mid-Life Certification (MLC) is a necessary process that will require NASA and Shuttle Program managers to review all the basic vehicle design and certification criteria and revalidate them. This recertification will uncover design and manufacturing assumptions that were made using the limited 10-year/100-launch life span of the system. Shuttle Program management has delegated the development of MLC to the individual elements and subsystem managers. Approximately 80 percent of the effort will reside in the Orbiter itself. The Orbiter element is beginning its MLC program development using a three-step process, an expanded Certification of Flight Readiness (called CoFR Plus), certification verification, and certification extension.

CoFR Plus is the first step for Orbiter return to fly as well as MLC. This more rigorous certification will begin in summer 2003 in preparation for the anticipated first flight after *Columbia*. In addition to the normal subsystem-by-subsystem review of flight certification, reported up-channel to the program management, the Orbiter MLC office wants to add a horizontal check to verify certification between subsystems. Essentially, they want to look at known problem areas in one system and determine if there's a risk to other systems. An example of this horizontal review is the integrated approach used to alert other systems of the problem with the flex hoses. This will facilitate an integrated approach to certification of all the subsystems as part of the overall system as well as their interaction. The intent is to integrate this process improvement into all future certifications.

The Space Shuttle Program's extended life raises several questions about the vehicle and component's original certification. The verification of certification step is envisioned to be a review of the CoFR process with intent to verify that the program is reviewing the right areas, prior to flight approval, with regard to the current operating environment (as compared to the anticipated operating environment in the late 1970s). The long-term exposure to salt air and the high wear induced by maintenance are two examples of environments that the original certification did not anticipate. The flex hoses, mentioned previously, failed under low frequency vibration induced stress that was not anticipated in the original certification. This MLC process is expected to be a one-time review. The Orbiter Project is planning to complete this verification for all CRIT 1.1 systems in time for the next CoFR. The remaining CRIT systems will be accomplished thereafter.

The extension of the SSP certification beyond 2020 is the final step. This data intensive process will include a review of the NASA and contractors' databases with intent to identify all the original certification criteria and assumptions that may not be valid today. Their intent is to do this archival review as well as current trend analysis using UA, PRACA, CARS data, and other relevant databases. This information will then be used to build new certification criteria and maintenance or modification programs to sustain the Shuttle Program. Additionally, this review will build a database to be used in future certifications and provide training for younger engineers in the program invaluable experience relating to system certification processes. The extension program will be designed as a one-time review as well.

The MLC is currently ranked in the third tier of SLEP projects, at the top of a list of undefined projects. This list, which includes Mid-Life Certification, Fleet Leader, and Corrosion Control, are the core of a service life extension for this system. Funds to start MLC are programmed to begin in 2004 and include adding 50 to 100 additional personnel to get this program started. The MLC is expected to increase certification confidence and build a sustainment program complete with maintenance, inspection, and modifications that will extend the life of the Shuttle Program. The key to success will be in its funding and rigor as the program office integrates the various systems toward one goal.

The Shuttle's next certification and the SLEP program should be founded on the basis of a thorough Mid-Life Certification. The SLEP management recognized this problem at the May 2003 program review: "We need a focused effort to move these activities from the undefinitized to the definitized portion of the budget. Progress should be targeted to support the 2004 Summit."[37] The Orbiter Program is starting out with some outstanding ideas on how to organize this tremendous MLC task. The Program Office should standardize the approach between the systems to ensure rigor and accuracy of the final product. NASA has most of the necessary ingredients for a successful sustainment program for the Shuttle Program. The only impediment to building it is a centrally organized sustainment office with authority to integrate the various Space Shuttle systems and sites.

NASA Langley was invited to brief the Board on the status of their research in the area of aging aircraft on May 12, 2003. Their briefing included information on the various structures, crack growth predictive techniques and non-destructive examination techniques. The briefing ended with their recommendations for a service life extension program that will help identify the projects for the Shuttle fleet:

NASA Langley has learned critical lessons from the aging aircraft commercial and military fleet experiences:

- Update the design flight loads spectrum.
- Update the original durability and damage tolerance analyses and include environmental effects.
- Search for the emergence of new fracture critical structure.
- Evaluate the necessity for a new full-scale fatigue test to support the life extension goal.[38]

Proposed Recommendations:

NASA needs to identify a definitive target date for SLEP planning. The current goal(s) leaves confusion and may not result in an adequate solution set.

Build a Space Shuttle Program sustainment office with authority to integrate between systems.

NASA needs to more restrictively define the SLEP mission. The current construct apparently establishes this program as the central repository for nearly any Shuttle and age/life related project. The result of this loose mission definition will more likely be budget cuts and priority confusion resulting in selection of non-direct sustainment projects and dilution of NASA's ability to resolve sustainment issues. NASA must restrict this program's mission to direct sustainment of the Space Shuttle Program and its associated infrastructure.

NASA should build this program, first, on the basis of a rigorous and comprehensive mid-life recertification of the SSP and second, on the data collected through OMDP and aging aircraft studies that should identify the priority areas

	FY03	FY04	FY05	FY06	FY07	FY08	FY09	Total FY04-FY08
Total POP 03 SLEP Recommendation	28	41	42	347	24	23	21	1,668
1 Should Start In Fiscal Year 2004	0	15	16	14	9	13	13	66
RSRM - Case Hardware	0	5	5	5	5	5	5	25
Orbiter - Certify PRSD Tank Supplier & Procure Spares	0	4	8	8	4	8	8	31
SSME - Sustaining Test	0	6	3	1	0	0	0	10
2 Commitment	26	27	23	156	13	12	12	926
Vehicle Cockpit Avionics	8	9	7	1	0	0	0	182
Vehicle Main Landing Gear Tire &	3	3	0	0	0	0	0	3
SSME Adv'd Health Mgmt System (AHMS Phase 1)	8	4	3	2	1	0	0	10
Industrial Engineering for	8	1	1	1	1	1	1	75
RSRM	1	1	1	2	2	2	2	98
Infrastruct	9	9	7	7	7	8	8	406
Other	5	5	4	2	2	1	8	152
3 Foundational	3	23	31	23	12	24	12	113
Aging Vehicle	2	1	1					24
Mid-Life Certification Assessment & Issue Mitigation								
Fleet Leader								
Corrosion								
STE Survey /								
Non-Destructive Evaluation Upgrades								
Ground Test	0	4	1	2	9	2	9	64
Performance Trade Studies / Lift,	1	2	2					4
Improved Tools /	1	7	5	3	3	3	3	21
Probabilistic Risk Assessment								
Sustainability Health Metrics								
Analytical Hierarchy Tool System								

Real Year Dollars in Millions - Not in Full Cost

	FY03	FY04	FY05	FY06	FY07	FY08	FY09	Total FY04-FY08
4a Sustainability	2	40	62	73	47	38	40	259
New Start: Vehicle Health	1	4	4					8
New Start: ET 3rd Generation	0	3	7	8				
STE Obsolescence	1	1	1	1	7	7	5	59
Material	0	2						2
Component	0	6	2	2	1	1	9	85
Supply Chain	0	4	0	1	1			5
Spares Augmentation for	0	5	1	2	2	1	2	82
4 Improvement	16	45	62	62	23	12	5	204
New Start: SSME Adv'd Health Mgmt System Phase 2b	7	3	4	4	2	1	5	160
Study: Hydrazine	3	3	3	1				7
Study: Orbiter	2	2	2					4
Study: SSME Channel Wall	3	4	1	1				32
Study: Orbiter Enhanced Caution and								
Study: Crew Survivability	1	1						1
4c New Capabilities	0	0	0	0	0	0	0	0
Reserves	0	20	20	20	20	20	20	100

Figures 3.1.2 and 3.1.3. SLEP Budget Plan.

of concern for this aging system. This MLC should be thorough enough to build a sustainment plan based on analytical condition inspections, service extending modifications and maintenance and inspection programs to keep close vigilance of aging systems and component structures.

Finally, NASA Shuttle Program management should significantly accelerate plans for the Mid-Life Certification in advance of the 2004-2005 study period and rank it highest in the SLEP hierarchy.

3.2 Sustainment of Aging NASA Infrastructure

Issue:

Assess aging NASA infrastructure (facilities and equipment), to include planning and programming of sustainment/replacement actions.

Background:

Much of NASA's infrastructure was built in two eras: the Apollo era of the 1960s and the Space Shuttle era of the mid- to late-1970s. In many cases, the forecasted life of the program was not much more than 10 years, and facilities and equipment have been rehabilitated or modified numerous times to keep them "launch ready" as the program was "extended to the right." Primary focus has been on infrastructure deemed critical to the mission, such as launch pads and crawler-transporters (CT). The further removed from the immediate mission, the less the attention it received, explaining the lack of shelters for ground support equipment. Infrastructure funding has varied in parallel with expectations of how much longer the Space Shuttle Program (SSP) would continue; in the mid-1990s, it could have been characterized as "life support until imminent retirement," which later changed to "sustainment until 2020" after the X-33 program was terminated. By the time SSP managers received guidance to invest in infrastructure due to the X-33's demise, construction of facility (CoF) and facility maintenance budgets had already been consistently reduced for six years, from 1994 to 1999. This was the result of heavy NASA budget cuts, starting in 1994 and resulting in a strategy to absorb many of the reductions from infrastructure. Much of today's "bow wave" or "catch up" is the result of these years of under-funding in particular, and overall short budgets in general. Finally, at Kennedy Space Center, keeping the infrastructure in serviceable condition is problematized by one of the most corrosive environments known: a combination of the highly corrosive natural environment along the Atlantic Ocean and acidic deposits from the Solid Rocket Motor (SRM) exhaust.

Findings:

Following are three examples of a deteriorating infrastructure.

Example 1: KSC launch pads 39A and 39B are continual challenges to maintain in launch ready condition due to corrosion and the forces associated with launches. The original structure, which serves as the core of the Fixed Service Structure (FSS), was designed and built in the Apollo era and incorporates older designs which trap fluids, including corrosives, even after post-launch wash downs, as well as precipitation. To their credit, ground systems support personnel and engineers recognized these design problems a long time ago, and newer modifications/replacements, such as the Rotating Service Structure (RSS), are better designed, without fluid traps. As the pads have aged and modifications/upgrades have been incorporated, many of the older systems have been abandoned in place; there is evidence of old clamps, conduits, mounting brackets, and other hardware that continue to corrode. This can be problematic, as continued degradation of these abandoned systems can contribute to loose debris during launch, posing a hazard to the shuttle. Again, to the ground support systems management's credit, they have recognized this and have lobbied for/received funding to remove formerly abandoned-in-place hardware; while much has been done, much remains and efforts are continuing. On each pad's RSS, the Payload Changeout Room's walls of foam core sandwich construction are deteriorating due to acoustic loads during launch. While repairs have been accomplished using a multitude of through-bolts, these are at best temporary and add needless weight to the movable structure. A more permanent repair will require serious consideration of an alternative design to ensure durability. There is also extensive concrete deterioration at the pad base and blast deflector areas; these are repaired from launch to launch. KSC has 83 railroad boxcars at pads 39A and 39B. These were procured for their durability and are used as offices and work centers for support personnel. Unfortunately, they are extensively corroded and ceiling leaks/buckled floors can be seen in various locations. To KSC's credit, they are correcting this situation with the construction of new facilities at each launch pad that will completely replace the boxcars; move-in is scheduled for FY2003.



Figure 3.2.1. Launch Pad Corrosion and Boxcar Facilities.

Past upgrades of wiring in the Pad Terminal Control Room are another example of attention to the sustainment of a launch critical system, with a progressive approach incorporating modernization as demanded by system requirements. One specific area requiring attention is the theory (suggested in the early- to mid-1990s) that the lack of top-coating over inorganic zinc primer on launch pad areas was leading to zinc leaching through rainwater runoff onto Orbiter wing

leading edges; this, in turn, was causing the formation of pinholes in the RCC panels and possibly decreasing the service life of these critical Orbiter components. Launch pad rain sampling in 1994 confirmed zinc oxide contamination. Despite improved corrosion control management and execution since then, follow-on rain sampling in July 2003 showed that zinc oxide contamination persists and illustrates how infrastructure maintenance can have a direct impact, not just on immediate Shuttle operations, but also on service life. NASA Standard 5008, "Protective Coating of Carbon Steel, Stainless Steel, and Aluminum on Launch Structures, Facilities, and Ground Support Equipment "requires a top-coating on all new and repaired surfaces, with the exception of Mobile Launch Platform (MLP) 0-level deck surfaces and lower levels of the FSS (95- and 75-foot levels), as these are in the direct blast impingement area during liftoff. Despite these requirements, launch pad corrosion control measures need to be examined with the objective of further reducing or completely eliminating zinc fallout.

Example 2: The Vehicle Assembly Building (VAB) is the only facility of its kind in the world and a critical element of the Space Shuttle Program. It is where the Orbiter, External Tank, and Solid Rocket Boosters are mated and demated. It was constructed in the 1960s for Saturn V buildup. Like the launch pads, it serves as an example of both the problems faced by the SSP and NASA in maintaining aging infrastructure, as well as ongoing efforts to meet these challenges. The 5-acres of roof from its original 1964 construction are comprised of 6 inches of foam and vinyl layers added over the concrete slab through the years. Regular repairs are accomplished on the roof's outer surface using sealant and asphalt paper. Roof leaks over the years have led to deterioration (spalling) of the concrete ceiling on the interior of the roof slab, with concrete fragments occasionally falling loose from a height of over 500 feet. This FOD hazard has been mitigated by the installation of a subdeck five feet below the ceiling to catch debris and safety nets at lower levels. A comprehensive repair effort has been funded for FY2004 to remove all roof outer layers down to the original slab and recover with sloped roofing boards and a synthetic membrane, as well as repairs to the interior concrete ceiling. Significant portions of the VAB's 1.1 million square feet of siding also require repair due to corrosion; this is especially critical due exposure of this vast surface area to hurricane-force winds; repairs are scheduled for FY2006. Several of the VAB's massive multi-panel doors require extensive corrosion repair. The structure's overhead bridge cranes are a mix of 1960s and 1990s vintage equipment, but are effectively sustained through regular maintenance due to their critical role in mating/demating operations.

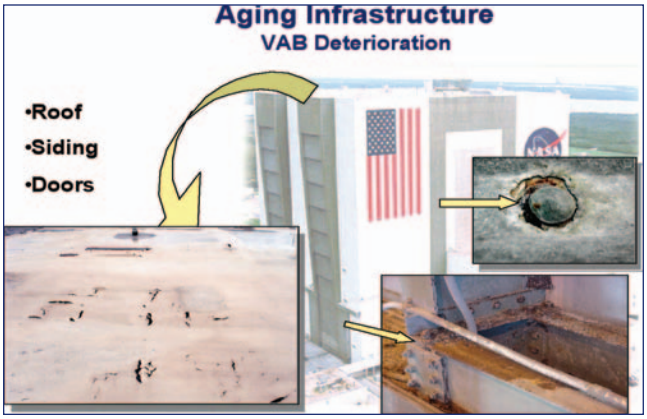


Figure 3.2.2. Vehicle Assembly Building.

Example 3: Two of the Shuttle Program's most critical pieces of equipment, the Crawler/Transporter (CT) systems, pose a significant technical sustainment challenge. (See Figure 3.2.3) These unique vehicles are necessary to move the stacked Space Shuttle to and from the launch pads. During hurricane season – roughly half of the year starting in early summer – both must be up and running in the event Shuttles must be moved from the pad back to the VAB for "safe haven." This precludes extensive maintenance during this entire period. Built in 1965, the CTs each average over 1,700 miles. They have received incremental capability upgrades over the years, including a laser docking system, computerized control stations, and replacement control cabs. The massive hydraulic actuators used to jack, level, and carry the Mobile Launch Platform (MLP) and Shuttle Stack were recently refurbished for the first time. Obsolescence of purpose-built components poses a major challenge, and will continue to need correction through upgrades. Corrosion is a significant problem due to no sheltered storage, and maintenance is frequently suspended due to severe weather. As support costs rise due to aging and obsolescence, it was noted that managers track resources expended (costs of modifications/parts/labor) over time, but do not do so per unit of output (miles driven or operating hours). While costs over time will always increase, a more valuable metric is cost per unit of output, as this can be used for analysis and trending and can help in more clearly comparing the cost/benefit tradeoffs of inaction, modification, or replacement.



Figure 3.2.3. Crawler Transporter (CT).

Benchmarking With Industry/Adopting Best Practices at KSC

The GSS contractor has implemented an effective program to manage its facilities' corrosion problems. In 1995, Lockheed Space Operations (now part of USA) contracted Corrpro (formerly Consulex) to develop a comprehensive software package to gather, archive and present a wide range of data concerning assessment, programming and execution of the facility corrosion control program. Corrpro took a tool developed for the offshore oil industry and adapted it to KSC. The system, known as Basecoat, is in its third year of use. (See Figure 3.2.4) It integrates the corrosion protection

requirement, type of material, estimated cost, photos and video of actual structure for condition trending, life cycle costing, and so forth. Efficiencies realized by this software enable all facility condition data to be gathered by two inspectors, as opposed to the former method of file cabinets populated with files of paper that were labor-intensive to compile, review, trend, and prioritize. Basecoat can be efficiently used to prioritize requirements, determine/program budget requests, and schedule maintenance. It also has the ability to divide structures, such as the launch pads, into subcategories (levels) and components on each level; this, in turn, enables prioritization at the subcategory or component levels if resources (such as money or system availability) are not available for the entire system. Another feature identifies "hot spots" where multiple problem areas cluster together, and rank orders them according to criticality for immediate programming. This exceptionally effective package is worthy of benchmarking.

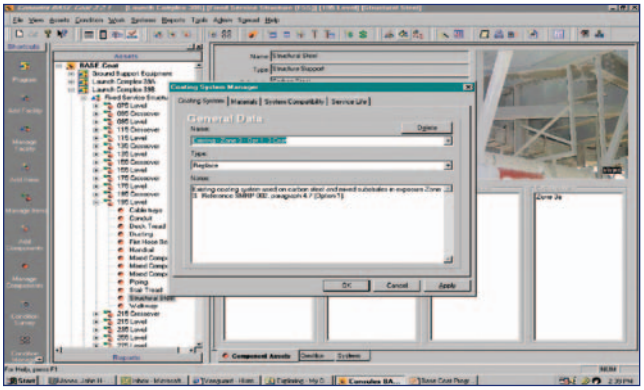


Figure 3.2.4. CorrPro Basecoat Software Example.

KSC Facility Sustainment Management

NASA's Facility Project Budget and Management strategy has undergone several major changes over the past decade. Prior to 1994, a single Construction of Facilities (CoF) appropriation for NASA was allocated; in 1994, the process was changed, with CoF funds now appropriated per program. The annual budget development and coordination process involves both the contractor and KSC management in requirements determination, with the budget forwarded through NASA hierarchy. Development of programs to replace and refurbish systems is accomplished by the Ground Systems Working Team (GSWT). The GWST is jointly staffed by USA, Shuttle Gateway Services (SGS), and NASA personnel and uses a risk assessment process to prioritize requirements.

The portion of SFOC pertaining to infrastructure maintenance (generically falls under "ground operations") includes a cost savings incentive for cost under run: NASA gets 65 percent, USA 35 percent of savings. NASA retains its provisioning role under SFOC, including Construction of Facilities (CoF). USA is an active participant in the requirements development process. The Facility Management Plan is a contract deliverable, under SFOC contract DRD 1.5.5.2, and includes the long range plan, annual work plan, preventive maintenance, predictive test and inspection, corrective/programmed maintenance, backlog of maintenance and repair (BMAR), and facility condition assessment program (FCAP). The Facility and Equipment Maintenance Plan, Part II - KSC Ground Operations, is a contract deliverable, under SFOC contract DRD 1.5.5.2, and includes an annual submittal of metrics reflecting Facility/System Availability During Operations, Condition Assessment Program, CM/Total Maintenance Ratio, and Actual Cost Trends by General Classification. According to a senior manager, "The three hardest aspects of our job are getting the funding, the resources, and the proper window in the operations schedule to line up. Based on my 30 years experience, infrastructure support has always been budget-driven, not requirements-driven."

Recently, in efforts to better align the "windows" of opportunity mentioned above, USA has established master planner positions for GSS (fall 2002) and Orbiter horizontal processing (early 2003). These two personnel coordinate on a regular basis with the vertical processing master planner to better synchronize their respective schedules. The expectations are, through better synchronization of schedules, windows of opportunity can be maximized and more GSS maintenance can be performed with existing resources; another benefit will be fewer work time deviations and violations.

The most significant finding is that these program metrics only reflect performance with respect to contract deliverables. Until recently, USA has not tracked maintenance hours or materiel expenditures required to achieve program performance objectives. As a result, this limited management perspective compromises NASA's and USA's ability to properly characterize the magnitude of deteriorating infrastructure and equipment, limiting their ability to substantiate the requirement to NASA Headquarters and Congress

Management personnel involved in infrastructure support were reluctant to make the case that they are under funded. They maintained the opinion that they typically get enough to "get by" with no mission jeopardy. If no one is tracking resources expended to keep infrastructure in adequate condition (such as operating hours for the crawler-transporter), then management is unable to make fact-based assessments of when support costs are reaching unacceptable levels and when alternate/replacement actions should be programmed.

Michoud Assembly Facility (MAF)

MAF, which falls under the Marshall Space Flight Center (MSFC), is a government owned, contractor operated facility (GOCO). Some of its infrastructure dates back to the 1940s, with add-ons for Apollo and the Space Shuttle. It is where the ET is built and shipped by barge to KSC. Compared with KSC, it is a much smaller installation, has the advantage of being more single-mission focused, and has a much less corrosive environment. Starting in 1997, MAF managers developed all infrastructure and equipment requirements into comprehensive, 15-year strategic plans that address every requirement in a "big picture" context. MAF has been successful in assessing, prioritizing, and articulating their infrastructure requirements, in large part due

to this disciplined, structured approach. The result has been funding support: CoF funding has increased by 371 percent from FY1997 to FY2003 ($7.9 million to $37.2 million). Successful projects include the repair of a 43-acre roof over their Main Manufacturing Building and upgrade of their 1940s-vintage 480 volt electrical system. MAF's 15-year facilities and equipment strategic plans are a benchmark practice for all of NASA.

Stennis Space Center (SSC)

SSC, as the National Space Transportation Laboratory, was built during the mid-1960s as part of the Apollo ramp up. Its primary mission is liquid fueled rocket engine testing, including the Shuttle's main engines. Every engine must be tested here after modification and/or overhaul. It has three tests stands, designated A1, A2, and B1/2, which, like much of NASA's infrastructure, are considered national assets. The A1 stand is the only one capable of testing gimbaling. However, it is also scheduled to be mothballed in FY2003 based on no known future requirements. The retirement of the A1 test stand will help conserve scarce infrastructure funding and allow it to be applied elsewhere, as long as the assessment of no future need remains valid.

Boeing/Palmdale (Air Force Plant 42)

These facilities are leased by NASA from the Air Force and appeared in good condition due to the dry, non-corrosive environment. Equipment degradation was evident, primarily due to the recent decrease of Shuttle support.

The NASA "Big Picture"

It is important to examine all of the foregoing observations in the context of the overall NASA program, managed by Code JX at Headquarters. NASA owns over 2,600 buildings and an equally large number of other major structures with an average age of nearly 40 years. The current replacement value of this infrastructure is $21.9 billion; for Code M is just over $10 billion. NASA's current replacement value is approximately 40 percent higher than the Department of Defense's and reflects the unique, specialized nature of many NASA facilities, such as the VAB and launch pads.

A NASA-wide infrastructure assessment was conducted in FY2002 to address the growing Backlog of Maintenance and Repair (BMAR), estimated at $1 billion. The steady BMAR increase and concern over its safety implications were addressed in the Aerospace Safety Advisory Panel's 2002 report, as well as prior reports. However, because previous BMAR assessments were not consistent or auditable, difficult to "roll up," and were subject to "spin," the FY2002 assessment established a new category designated Deferred Maintenance (DM) and set clear guidelines to be applied consistently across NASA. The result: DM totaled over $2 billion, double the previously assessed BMAR, primarily because it took into account all facilities, but there is greater fidelity in this figure. This $2 billion DM figure represents 10 percent of NASA's CRV (an industry rule of thumb is for annual spending of two to four percent of CRV); this high percentage reflects the unique nature and small numbers of much of NASA's infrastructure which, in turn, leads to a "must fix" approach in many cases, as well as a need to catch up due to years of under funding. What's important is Code JX now has a consistent, NASA-wide DM database and is working to apply it to future planning and programming of infrastructure requirements.

Simultaneous with the DM assessment, another "yardstick" known as the Facility Condition Index (FCI) was applied across NASA. Under FCI, facility condition was assessed on a five-point scale, with five being "excellent" and one being "bad." The average FCI was 3.6; for Code M, 3.5; for JSC, 3.6; for KSC, 3.3; for MSFC, 3.9; for SSC, 3.1. Figure 3.2.5 shows the relative FCIs of each center. These FCIs

NASA Sites	Total CRV ($B)	Total '01 BMAR ($B)	Total '02 DM ($B)	Total FCI (Wgtd)	Active Facilities '02 DM ($B)	Active Facilities FCI (Avg)	Inactive Facilities '02 DM ($B)	Inactive Facilities FCI (Avg)
Ames Research Center Total	3.48	0.07	0.23	3.6	0.14	3.3	0.09	2.9
Dryden Flight Research Center Total	0.26	0.01	0.01	4.1	0.01	3.2	na	na
Glenn Research Center Total	2.44	0.05	0.27	3.6	0.14	3.6	0.13	2.5
Langley Research Center Total	2.55	0.03	0.29	3.7	0.24	3.4	0.04	2.2
Code R(Aerospace Technology)	8.73	0.16	0.80	3.7	0.53	3.4	0.27	2.3
Goddard Space Flight Center Total	1.55	0.18	0.10	3.9	0.06	3.7	0.03	1.7
Code Y (Earth Science)	1.55	0.18	0.10	3.9	0.06	3.7	0.03	1.7
Jet Propulsion Laboratory Total	1.01	0.03	0.05	4.1	0.05	3.8	0.01	3.3
Code S (Astrobiology and Space Research/ Science)	1.01	0.03	0.05	4.1	0.05	3.8	0.01	3.3
Johnson Space Center Total	1.71	0.20	0.12	3.6	0.12	3.6	0.00	1.0
Kennedy Space Center Total	4.36	0.08	0.51	3.3	0.48	3.8	0.03	2.4
Marshall Space Flight Center Total	2.45	0.23	0.17	3.9	0.13	3.9	0.05	3.4
Stennis Space Center Total	1.57	0.08	0.28	3.1	0.28	3.6	0.00	1.9
Code M (Human Exploration and Development of Space)	10.09	0.59	1.06	3.5	1.00	3.7	0.08	2.5
NASA Total ($B)	21.4	.95	2.03	3.6	1.64	3.6	0.39	2.5

Figure 3.2.5. Comparison of NASA Sites.

"peel back" to individual assessment areas such as structure, roof, exterior, interior, electric, plumbing, and equipment, and assign varying weights to each area depending on the primary function of the facility. KSC's lower overall rating reflects the large amount of infrastructure dedicated to the Space Shuttle Program, as well as to its harsh environment. Center ratings can be skewed depending on the value of certain infrastructure relative to the total value; for example, SSC's rating of 3.1 is based on their engine test stands' rating of 2.2; since these stands make up 37 percent of SSC's total CRV, their removal from the overall FCI raises it to 3.6. The NASA goal is to improve the overall average FCI to 4.2 by FY2009, which requires an annual investment of $312 million.

In efforts to assess the impact of infrastructure investment, Code JX has adopted DoD's Facility Sustainment Model (FSM) and is refining it for NASA use. This tool estimates the amount of maintenance investment required as a percentage of CRV. For example, NASA has determined that $333 million of annual facility maintenance funding is required to arrest deterioration. By contrast, $224M (actual), or 67 percent, was spent in FY2002, and in FY2005, $273 million, or 82 percent, is planned. Based on past and current funding, NASA's Facility Revitalization Rate (FRR), or the rate at which a facility will be replaced or revitalized based on funding, is slightly over 100 years. This is down from a high exceeding 200 years, but is still far from the DoD goal of 67 years and the industry goal of 55 years. NASA has determined it can reach the DoD goal of 67 years by FY2009 based on an annual investment of $302M over five years. Figure 3.2.6 shows past and targeted NASA FRRs. This amount can be reduced by reducing infrastructure, such as the retirement of the A1 test stand at SSC.

NASA has outlined its road ahead for infrastructure improvement. It includes identifying and disposing of excess facilities, making better use of existing facilities through consolidations, and sustaining remaining infrastructure by reducing BMAR/DM (which, in turn, will lower the revitalization rate from over 100 years toward the DoD goal of 67 years), advocating "repair by replacement" where it makes sense, and successfully securing funding support.

A 1996 GAO audit cited NASA problems identifying, assessing, and implementing infrastructure cost reduction opportunities. Initiatives such as last year's NASA-wide DM and FCI assessments, combined with determinations of facility maintenance and revitalization requirements, indicate a much improved, structured approach to addressing infrastructure from a NASA-wide perspective. While many of these initiatives are in their infancy, this further development will increase the level of fidelity in stated requirements and hopefully result in improved infrastructure funding.

Proposed Recommendations:

While there is a need for much "catch up" funding in Space Shuttle-related infrastructure, NASA's structured approach to assess the entire organization using a uniform assessment scale is the right approach. This structured methodology, coupled with a long-term view of each facility's role – such as that taken by Michoud in their 15-year strategic planning – is a sound path to assessing and prioritizing funding requirements. Michoud's 15-year strategic plans, both for infrastructure and equipment, should be benchmarks for all of NASA; these plans examine and prioritize requirements in a larger, longer term context compared to the five-year Program Operating Plan and are part of the reason for their funding success. Infrastructure requirements can also be reduced by consolidating facilities, or by retiring unnecessary or redundant facilities such as the A1 engine test stand at Stennis; the practice of identifying opportunities for consolidations and retirements needs to continue.

At the tactical level, KSC's approach toward better schedule integration through the recent establishment of master planners for horizontal and GSS operations holds great promise. Their adoption of commercial practices, such as CorrPro's Basecoat database, is also highly noteworthy, and they should explore further application beyond corrosion. KSC should do a cost/benefit analysis of building additional shel-

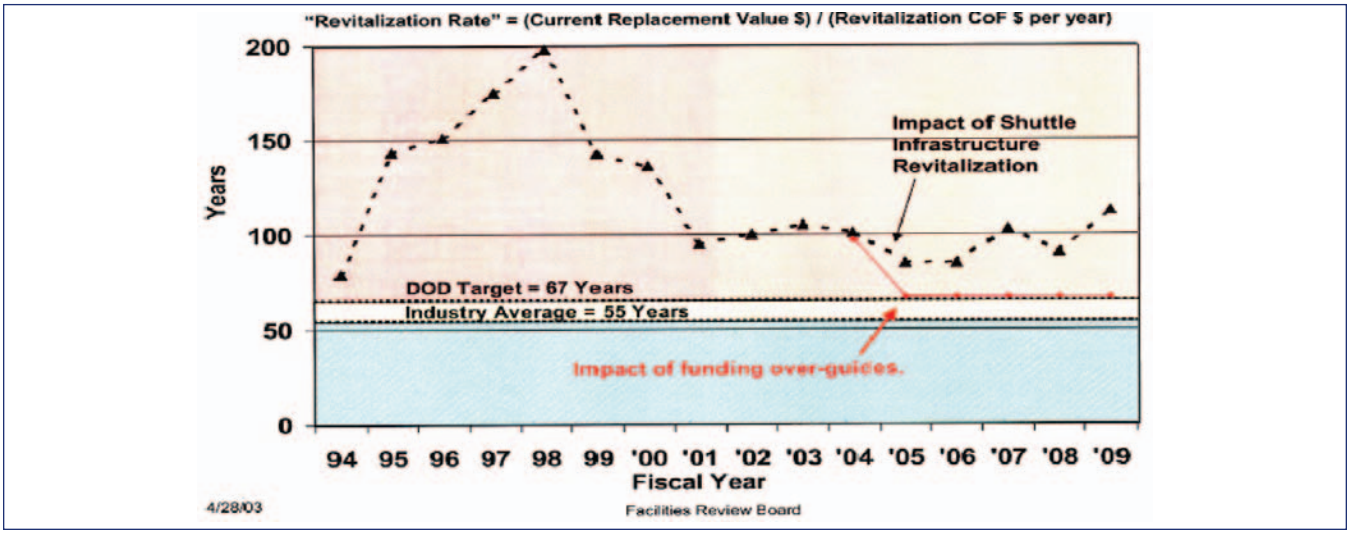


Figure 3.2.6. NASA Facility Revitalization Rates.

ters for its ground support equipment, much of which is left outdoors. They should also perform trending and analysis of infrastructure/ equipment support costs factored over unit of output wherever possible, rather than simply tracking costs, as rate comparisons will facilitate tradeoff/investment decisions. Finally, KSC should examine current launch pad maintenance practices and make every effort to reduce or, better yet, eliminate zinc fallout.

References:

1. NASA report KSC-5600-6256, "Launch Pad Zinc Sampling at LC-39B," June 03
2. Michoud Assembly Facility "Infrastructure Overview" briefing, May 03
3. Michoud Assembly Facility "External Tank Tooling Overview" briefing, May 03
4. NASA "Facilities Review Board/POP-03" briefing, 29 Apr 03
5. "CAIB VAB Group Tour – Cranes/Doors/Platforms" briefing, 14 Apr 03
6. "Ground System Survivability Assessment/Assured Shuttle Availability (GSSA/ASA)" briefing, 14 Apr 03
7. Aerospace Safety Advisory Panel Annual Report for 2002, Mar 03
8. NASA HQ Code JX briefing, "Infrastructure Panel – Service Life Extension Program – 'Returning to Flight'," Mar 03
9. Report on the FY 02 NASA-Wide Standardized Deferred Maintenance Assessment, 10 Mar 03, NASW-02010
10. KSCARRIER PANELH-J e-mail, "Crawler Transporter Information" with attachments, 21 Mar 03
11. Analysis of FY 03 Agency-Wide Facilities Phase-Down Data (Part 3), Oct 02, Contract Number NASW-00008
12. "Welcome to the NASA Master Planning Workshop" briefing, 21 May 02
13. "Review of LC39, Pad A and Pad B Infrastructure" briefing, 10 May 02
14. Aerospace Safety Advisory Panel Annual Report for 2001, Mar 02
15. "Facilities Maintenance History, Issues & Strategy" briefing, February 02 NASA Facilities Maintenance Workshop
16. USA "Facilities Maintenance" briefing, 7 November 01
17. NASA Facilities Engineering Report, Mar 01
18. "Alternate Trajectories - Options for Competitive Sourcing of the Space Shuttle Program," Dec 02, RAND
19. "Facilities Maintenance in NASA – 2000" briefing, February 00 Facilities Maintenance Workshop
20. "Space Shuttle Program Infrastructure Revitalization to Space Flight Advisory Committee" briefing, November 00
21. Space Shuttle Program's Infrastructure Upgrade Initiative to ASAP briefing, Mar 00
22. Boeing report KLO-98-009, "Launch Pad Zinc Fallout Determination," 22 Dec 98
23. GAO report, "NASA Infrastructure – Challenges to Achieving Reductions and Efficiencies," September 96

4.0 Logistics Support

4.1 Workforce

Issue:

United Space Alliance (USA) has established a multi-skilled workforce to accomplish maintenance requirements on the Orbiter fleet. Observations were made of work procedures and practices.

Background:

Despite the unique requirements of such a technically advanced vehicle such as the Orbiter, the fundamental principles upon which aerospace maintenance practices and policies are based should be applicable to any such maintenance operation.

Findings:

USA technicians work at a grade structure commensurate with experience and proficiency, and are certified at skill levels. An entry-level worker starts out as "B-Tech," which, until recently, was eligible for upgrade after one year of experience. This standard has recently been changed to three years. Next experience level is "A-Tech," who can perform work alone. The senior most technician is the "AS-Tech" (Advanced System), who works closely with engineers, and are authorized to write basic work paper. These workers are limited in number, with approximately 50 among a workforce of over 4,000, typically one to two per system.

Effective tool control was observed in OPF 3 through inspection of toolboxes and discussing accountability procedures with workers. The toolboxes were professional quality, with tool locations shadowed with contoured foam, and the tools were laser etched. A common requirement was the use of tethers on ratchets to prevent Orbiter damage resulting from a dropped tool. Issue/turn-in procedures provide positive accountability with toolbox keys signed out by worker at beginning of shift, and supervisory inspection at shift's end.

The USA workforce demonstrates good teamwork, with effective interchange between technicians and engineers. Dedicated engineers are readily available to provide technicians assistance when necessary. When asked if engineering support was a problem on second shift, a tile technician worker cited that he did have to wait on occasion for assistance – "up to an hour." Time spent awaiting disposition is minimal.

Proposed Recommendations:

None.

4.2 Production Support

Issue:

USA Integrated Logistics is effectively postured to support production with delivery of material just in time to the work site.

Background:

Over the course of three visits to KSC by team members, including tours of the NASA Shuttle Logistics Depot and production facilities such as the OPFs, observations were made of kitting practices and repair processes for components. The goal of these visits was to gain understanding of the logistics processes and organizations supporting the Space Shuttle Program.

Findings:

Much of the pre-planned jobs are supported with pre-packaged, kitted hardware delivered by the support section/tool crib. Technicians order materiel for unplanned jobs as specified by engineer disposition or drawings. Accountability for work residue (hardware left over from a job) is based on an honor system, with the worker expected to turn in unused hardware and material to Logistics. Any lost hardware left in the Orbiter is to be reported for recovery under "Lost and Found" procedures for tracking lost tools and material. USA procedures call for a formal parts and tool inventory requirement to be accomplished prior to or following work on the vehicle, with documentation on a check sheet. This policy was not observed in practice during OMM and flow at KSC.

The Logistics tool room is also being equipped with an automated tracking system to monitor benchstock issues, which will facilitate requisition of bench stock at the appropriate order point. There is a distinct possibility that leftover hardware not returned to benchstock may be retained at the worksite for future use. If not positively identified, the risk exists that the wrong hardware may be used in a future job. While two pieces of hardware may look the same, specific characteristics (material, heat treatment, hardening, and so forth) may not be readily apparent. Unaccounted hardware also poses a potential foreign object damage hazard.

The team observed a demonstration of an automated unit (resembling a sandwich vending machine) for issue and turn-in of precision tools such as torque wrenches and gages, scheduled for implementation mid-March 2003. This system interfaces with computer tracking software to monitor issue, turn-in, and calibration date, automatically flagging noncompliant tools to the user's supervisor, and preventing the issue of tools that are overdue or immediately due for calibration.

Proposed Recommendations:

NASA/USA have policies in place to control materiel being used for Orbiter maintenance that is not adequately adhered to. NASA should enforce procedures for more positive accounting of hardware, tools and materials used in end-item (such as Orbiter and External Tank) maintenance. NASA's Focus should be to minimize likelihood of items left behind in the worksite, eliminate the potential for technicians building a personal benchstock, and better facilitate the reporting of "lost-and-found" items in a timely manner. Possible options could involve the use of inventory sheets to account for quantity of hardware issued/used, rags, etc. In addition, USA should develop and implement procedures to return unused hardware to issue point to ensure proper sorting of work residue for reutilization.

4.3 Shuttle Systems Depot Support

Issue:

USA Integrated Logistics operates an effective repair depot at the NASA Shuttle Logistics Depot (NSLD) in supporting the Space Flight Operations Contract (SFOC) to accomplish repair and overhaul of Shuttle system components.

Background:

A unique vehicle such as the Shuttle has very limited support available from the private sector. A viable alternative is to establish a robust self-supporting capability for fabrication, repair, and manufacturing of Shuttle-unique components and materials.

Findings:

The NSLD facility has eight buildings housing shops for avionics and mechanical repair, cryo testing, component/materials storage, and administrative space. The depot repairs and manufactures hardware and components for the Orbiter, and holds 250 certifications to repair 6,000 Orbiter line items, 70 percent of Orbiter line replaceable units, including analog, digital, and RF avionics, and wire harness buildup and repair. The shops also have in-house capability for thermal and vibration environmental testing. Its extensive fabrication capability is certified to manufacture 90 percent of Orbiter spares hardware. Repair capability of mechanical components includes hydraulics and structural repair such as welding, brazing, and composite/adhesive repair. The NSLD shops also have several computer numerically controlled machines capable of manufacturing a broad range of replacement fittings and mechanical devices.

USA Integrated Logistics also operates the Thermal Protection System Facility (TPSF), which manufactures Orbiter tile and thermal protective soft goods to support KSC production on a real-time basis. In addition to its manufacture capability, the TPSF accomplishes repair and fitting of TPS blankets, seals, miscellaneous protective blankets, and similar items. USA Integrated Logistics has extensive laboratory materials and processing capabilities for failure analysis of mechanical, electrical, and electronic components. Testing methodologies include spectroscopy, scanning electron microscopy, x-ray, metalography, and fractography. The Materials and Processes lab also has a broad range of inspection capabilities using a variety of technologies.

Obsolescence of test equipment will continue to pose a growing risk. NASA and Integrated Logistics are escalating their collective efforts to develop a service life extension program for all test equipment facing supportability risk due to Diminishing Manufacturing Sources (DMS).

Proposed Recommendations:

None.

4.4 Budgets and Financial

Issue:

NASA planned work has been resource-constrained, leading to a cost saving emphasis in contract activities with possible bearing on program performance. Full cost accounting if implemented as intended, will better identify the cost of work and allow more flexibility in focusing resources.

Background:

Human Spaceflight Programs, including the Space Shuttle and the International Space Station, have been subject to unpredictable cost growth for a variety of reasons, including the lack of a full cost accounting system.[39] These budget pressures have had a profound influence on contract activities. Concern over the International Space Station (ISS) costs was a major factor in awarding the SFOC to USA.

Findings:

The Space Flight Advisory Committee (SFAC) reports from 2000 through 2002[40] indicated a general concern over extensive cost growth on the ISS while Space Shuttle costs were reflecting a decreasing trend. The cost growth was recently addressed in Congress's NASA Authorization Act of 2000 (P.L. 106-391), which provided that the Space Shuttle flights supporting the ISS must be within an overall $17.7 billion cost limitation.

NASA is putting in place the full cost accounting[41] approach as a methodology to better track current and future costs associated with the ISS and Space Shuttle programs. Basically, managers are provided with more accurate historical budget and expenditure information to support decision-making. In its simplest terms, the full cost concept ties all direct and indirect costs (including civil service personnel costs) to benefiting programs and projects. With full cost accounting, there are no "free" resources for program managers. This is in contrast to the prior approach, in which institutional infrastructure costs, such as civil service salaries and the use of facilities and support services, were treated separately from benefiting programs and projects. See Figure 4.4.1 for a graphic representation of the NASA full cost accounting system.

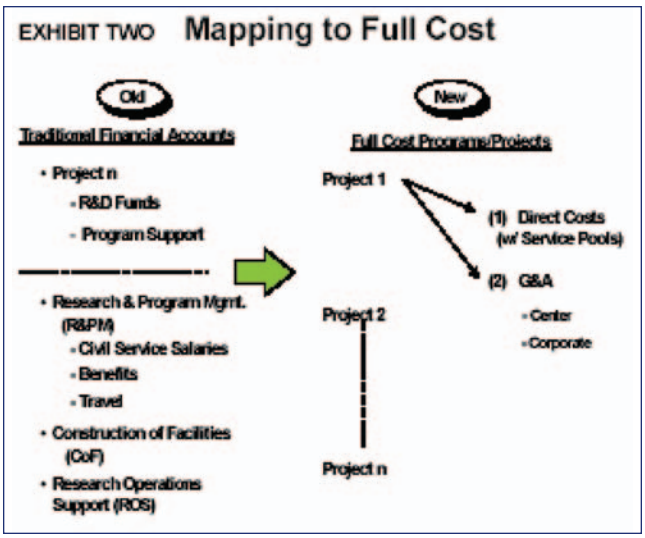


Figure 4.4.1.

NASA's annual budget history reflects considerable decline in Space Shuttle Program budgets in the recent past. In 1994 NASA, requested $4.05 billion. This decreased to $3.1 billion in 2002.

The Program Operating Plan (POP) is the agency-wide budget process in which NASA validates budget requirements and submissions. The POP is reviewed, consolidated, and approved at Division, Directorate, Lead Center, Program, Headquarters, Capital Investment Council, and NASA Administrator/ Comptroller levels. The POP process is iterative reflecting work and cost estimate inputs at the bottom, and high-level budget guidelines and work priorities at the top.

NASA conducts only one major POP cycle per year, but the high-risk programs, such as the ISS, may have more budget reviews. Historically, the Space Shuttle program has not been considered high risk from a budget perspective. Human space flight is contractor-driven, while many other NASA programs and projects are more closely related to civil service labor costs.

Proposed Recommendations:

The conversion to full cost accounting should be beneficial to NASA management, and provide better visibility to NASA overseers. However, the full benefit will only result if NASA, as planned, ensures program managers receive the authority to use resources identified to their programs as they see fit. This will be difficult or impossible to do without significant organizational changes and probably changes in Civil Service rules.

4.5 Contracting Issues

Issue:

SFOC contains a complex fee formula that combines award fees, incentive fees, and performance fees. The structure of the contract award fee plan may not reward the desired performance.

Background:

NASA has historically been highly reliant on commercial sector contractors to accomplish its mission. This includes contracts with educational institutions, government labs, and the private sector, made up primarily of the aerospace-defense industry. These contracts become the vehicles in which NASA conveys its mission priorities to the commercial sector. Contract type and structure are determined on the basis of the appropriate degree of risk sharing between the government and the contractor. A wide selection of contract types is available to the government and contractors in order to provide needed flexibility in acquiring the large variety and volume of supplies and services required by NASA.

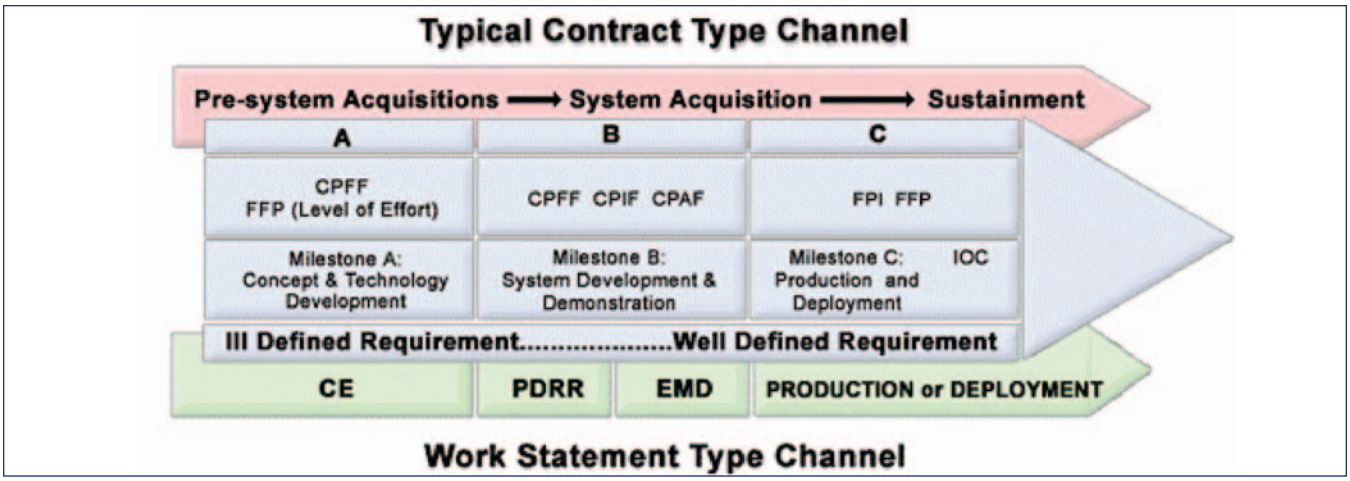


Figure 4.5.1. Typical Contract type channel.

Contract types vary according to: (1) the degree and timing of the responsibility assumed by the contractor for the costs of performance; and (2) the amount and nature of the profit incentive offered to the contractor for achieving or exceeding specified standards or goals. (See Figure 4.5.1) In general, NASA's Space Shuttle Program element uses the cost-plus-award-fee contract format, with additional incentive fees and performance fees.

The SFOC is a combination contract containing aspects of the cost-plus-incentive-fee cost-plus-award-fee and cost-plus-performance-fee contracts. (See Figure 4.5.2) The cost-plus-incentive-fee is a cost-reimbursement contract that provides for an initially negotiated fee to be adjusted later by a formula based on the relationship of total allowable costs to total target costs.

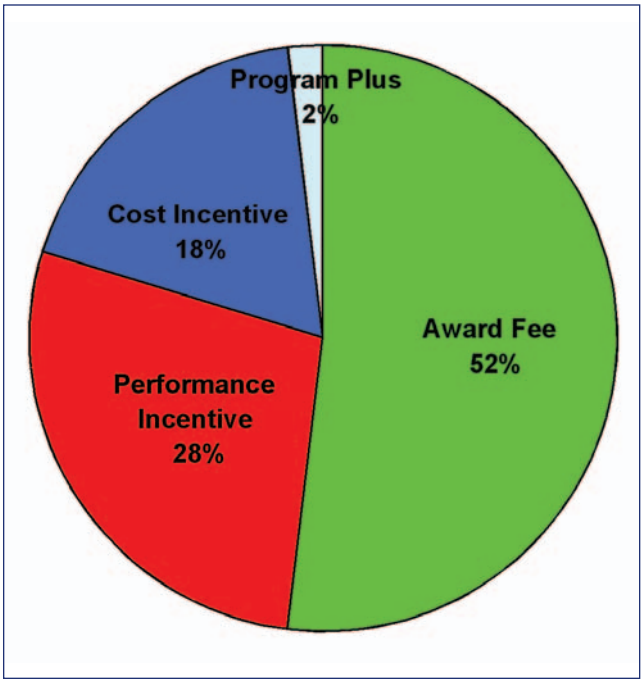


Figure 4.5.2. Available fee percentages.

A cost-plus-award-fee contract is a cost-reimbursement contract that provides for a fee consisting of a base amount fixed at inception of the contract and an award amount that the contractor may earn in whole or in part during performance and that is sufficient to provide motivation for excellence in such areas as quality, timeliness, technical ingenuity, and cost-effective management. The amount of the award fee to be paid is determined by the government's evaluation of the contractor's performance in terms of the criteria stated in the contract. This determination is made unilaterally by the government and is not subject to the disputes clause.

Initiatives under the Government Performance and Results Act (GPRA) encouraged agencies, including NASA, to explore better methods to accomplish agency missions through the use of commercial sector contract support. Opportunities to "contract-out" what had been historically considered inherently governmental action could potentially produce results by both decreasing contract costs and by reducing the headcount of NASA employees engaged in contract compliance.

The Kraft Report (Report of the Space Shuttle Independent Review Team) became a major impetus in moving the Shuttle Program to a contractor-managed activity. The committee made recommendations that NASA and the Space Shuttle Program should:

(1) Establish a clear set of program goals, placing a greater emphasis on cost-efficient operations and user-friendly payload integration.
(2) Redefine the management structure, separating development and operations and disengaging NASA from the daily operation of the Space Shuttle.
(3) Provide the necessary environment and conditions within the program to pursue these goals.

The report further stated that, given the maturity of the vehicle, a change to a new mode of management with considerably less NASA oversight is possible at this time. In addition, the bureaucracy that has developed over the program's lifetime – and particularly since the Challenger accident

– will be difficult to overcome and the optimum operational effectiveness of the system will be difficult to achieve unless a new management system is provided. [42]

The Kraft review team found that NASA needed to freeze the configuration of the Shuttle and then continue to disengage from the daily operations functions of the program. The intent was to keep NASA in the development activities where the scientific expertise was most beneficial. This plan was based on the opinion that the Shuttle is a mature operational vehicle. A contract structure was to be developed that incentivized the contractor to reduce cost while maintaining safety of flight and mission success. Though NASA's narrow focus on cost reduction was criticized in the *Challenger* investigation, the committee and NASA considered much of the expense of the program to be tied up in redundant activity and excess overhead.

United Space Alliance (USA) was created by the partners, Lockheed Martin and Rockwell (Rockwell was later purchased by Boeing), to provide efficiency in managing the effort of existing Space Shuttle contractors. Prior to the formation of USA, NASA expended significant effort in the formation of a Source Evaluation Board (SEB) chartered to select a single supplier for the Space Shuttle Program. The SEB published a "sources sought synopsis" for the Space Fight Operations Contract in the Commerce Business Daily (CBD) in August 1995. This action requested that potential offerers submit statements of interest, as the prime contractor, along with specific information to support evaluation.[43] The Shuttle Program Director at the Johnson Spacer Center also presented a formal industry brief in August 1995. Four contractors (BAMSI, USA, Boeing, and McDonnell Douglas) submitted responses indicating interest. The SEB chairman recommended an award to USA based primarily on the determination that only USA had the necessary experience base and existing operational structure to minimize schedule and safety risks. The partners of the alliance already held 69 percent of the Shuttle-related contracts, which would simplify contract consolidation for NASA. After selection, NASA and the USA jointly developed incentives that would provide an appropriate reward for desired performance.

Findings:

The various fees available to USA on the SFOC could total approximately $900 million, or approximately 10 percent of the target contract value at the negotiated target cost.[44] Award fees are the largest portions of contract fee pool. They are determined semi-annually and could total over $500 million for the first contract period and $165 million for the first option. The contract award fee criteria stipulate that USA must exceed the minimum "gate" score of 61 or above to earn any fee. The award fee plan criteria are broken down into ratings in seven areas. Management Effectiveness (including costs control) is the largest segment of the award fee formula at 25 percent and is closely followed by Operational Safety 20 percent, which is most heavily weighted. The remaining graded areas are Quality at 20 percent, Small Business Utilization (mandated by Agency rules) at 15 percent, Schedule at 5 percent, Manifest Effectiveness at 5 percent, Supportability at 5 percent and Cost (only level of effort and program provisioning) at 5 percent. The structure of the SFOC Award Fee plan required a deviation from the NASA mandated attention to cost control. The NASA FAR Supplement provides that when explicit evaluation factor weightings are used, cost control shall be no less than 25 percent of the total weighted evaluation factors.[45] [46] Because of the unusual consolidation of effort included in the SFOC, the Award Fee Plan includes a provision for twelve to thirteen separate Technical Management Representatives (TMR) who rate the contractor's performance on sections of the Statement of Work, carried forward from preceding Shuttle contracts. Each TMR rates the contractor's performance, using a rating of 0-100 for all award fee ratings, other than Cost and Small Business ratings. The award fee earned is determined by applying the numerical score to the award fee pool. For example, a score of 85 yields an award fee of 85 percent of the award fee pool. No award fee shall be paid unless the total score is 61 or greater.

The NASA FAR Supplement and the SFOC contract provides the following standard adjectival ratings for the associated numerical scores:

(1) **Excellent** (100-91): Of exceptional merit; exemplary performance in a timely, efficient, and economical manner; very minor (if any) deficiencies with no adverse effect on overall performance.
(2) **Very good** (90-81): Very effective performance, fully responsive to contract requirements; contract requirements accomplished in a timely, efficient, and economical manner for the most part; only minor deficiencies.
(3) **Good** (80-71): Effective performance; fully responsive to contract requirements; reportable deficiencies, but with little identifiable effect on overall performance.
(4) **Satisfactory** (70-61): Meets or slightly exceeds minimum acceptable standards; adequate results; reportable deficiencies with identifiable, but not substantial, effects on overall performance.
(5) **Poor/Unsatisfactory** (less than 61): Does not meet minimum acceptable standards in one or more areas; remedial action required in one or more areas; deficiencies in one or more areas, which adversely affect overall performance. [47]

Weights are then assigned to the scores based upon the share of the budget. One of the most noticeable trends is that the ratings are generally very good or higher, although USA has forfeited over $44 million in potential award fee dollars.

Overall scores for the six month periods beginning October 1996 and ending September 2002: 1) 84, Very Good; 2) 86, Very Good; 3) 81, Very Good; 4) 84, Very Good; 5) 85, Very Good; 6) 85, Very Good; 7) 83, Very Good; 8) 80, Very Good; 9) 87, Very Good; 10) 88, Very Good; 11) 88, Very Good; and 12) 91, Excellent. (See Figure 4.5.3.)

USA has earned over $207 million in performance fees so far. USA forfeited $1 million on STS-80 (OV-102), January 1997 (challenged by USA, resolved September 1997). This was attributed to an in-flight anomaly (IFA) that resulted

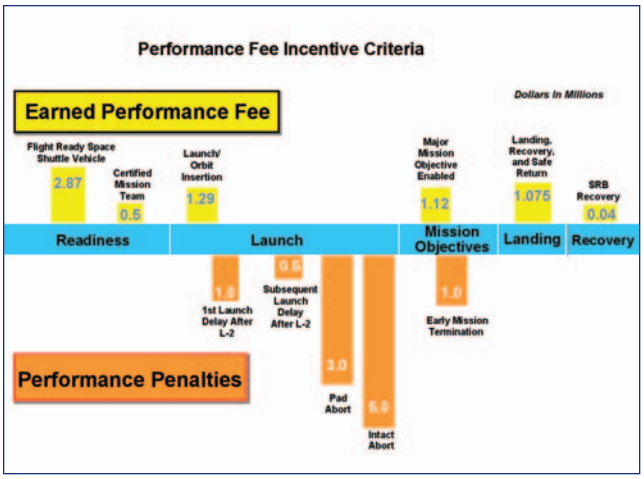


Figure 4.5.3. Amount of fee earned versus available fee.

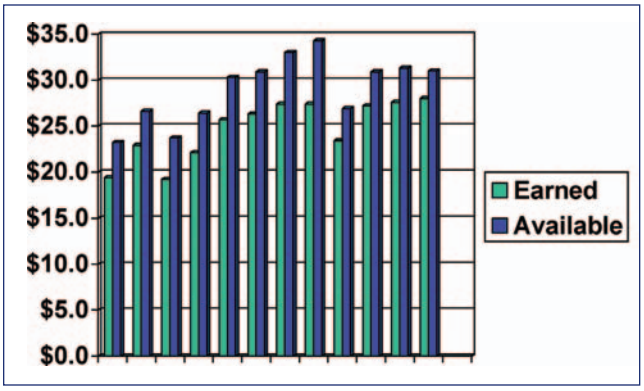


Figure 4.5.4. Performance fee incentive criteria.

in the inability to accomplish a major mission objective. Additionally, USA forfeited $1 million on STS-92 (OV-103), September 2000, for a 24-hour launch delay and $2.9 million on STS-103 (OV-103), January 2000, for a missed manifest launch date by more than seven days. This was attributed to workmanship damage to wiring. They forfeited $2,87M on STS-99 (OV-105), March 2000, and $2.9 million on STS-101 (OV-104), June 2000, both for workmanship damage to wiring. Finally, $1.4 million was lost on STS-109 (OV-102), May 2002, due to a missed manifest date, ready for launch criteria not met.

The contract includes a unique Program Plus fee, totaling up to $199 million, which is available at the discretion of the Program Manager. The intent of this is to provision for accomplishing or accelerating priority tasks, which were unforeseen at the start of the contract. A Cost Incentive Fee, $178 million at target, is available to reward under-run of the estimated contract value over the entire period of the six-year contract. This has significant potential for increase if the contractor can find ways to cut the overall cost of the contract. This fee is not actually calculated until the end of the contract period when audited and negotiated costs are available. The share line allows USA to retain $0.35 of each dollar under target cost. USA has declared an under run and has received provisional payment.

Finally, the Value Engineering Change Fee (VECP), estimated at $4 million is to reward the contractor for recommending engineering improvements that save money. USA would get a share of any cost savings that come about because of an engineering change developed by the contractor. This is awarded on a case-by-case basis and is not aligned with a specific period.

Proposed Recommendations:

While it is extremely difficult to assign any causal relationship to the contract structure, bundling contract activities, as in the case of the SFOC, may contribute to conflicting priorities for the contractor, given the incentive to maximize the financial return associated with a contract.

4.6 SFOC Award Fee

Issue:

Weighting of the SFOC Award Fee may mask substandard performance in one area with higher scores in other areas.

Background:

The SFOC consolidated the work previously under 13 (originally 12) separate contracts. A formula was developed to weight award fee balloting in order to more accurately reflect the budget performance of each area. The NASA FAR Supplement discusses the weighting methodology to be used in most award fee determinations. Under this system, each evaluation factor (e.g., technical, schedule, cost control) is assigned a specific percentage weighting with the cumulative weightings of all factors totaling 100. (See Figure 4.6.1) During the award fee evaluation, each factor is scored from 0-100 according to the ratings scale. The numerical score for each factor is then multiplied by the weighting for that factor to determine the weighted score. For example, if the technical factor has a weighting of 60 percent and the numerical score for that factor is 80, the weighted technical score is 48 (80 x 60 percent). The weighted scores for each evaluation factor are then added to determine the total award fee score.

However, because the contract content of the SFOC includes divergent activities, a methodology was developed to assemble ratings of each Technical Management Representative (TMR) based on their share of the contract budget. The TMR rating is then presented to the Performance Evaluation Board, chaired by the Contracting Officer's Technical Representative (COTR). The COTR then forwards a recommendation to the Fee Determining Official (FDO). The contracting officer authorizes the payment of the Award Fee based on input from the FDO. In the case of the SFOC the delegation to the COTR includes additional delegations to the TMRs "to assist you in your delegated authorities and responsibilities.[48] Prior to the formal review process, the Johnson Space Center budget office provides the COTR with the budget share assigned to each area of the Statement of Work. These range from less than 1 percent to over 30 percent. The TMR assigns scores to the appropriate rating categories (Operational Safety and Quality, Management Effectiveness, Cost Control, Small Business, Sub-Contract Management, Manifest,

and Ground Operations). These ratings are then weighted by the assigned budget percentage. The weighted scores are then totaled to produce a total weighted score that serves as the Performance Evaluation Board recommendation.

Finding:

The effect of the weighting on the award fee process produces a series of budget drivers that become the determinants of the assigned score. The final score will be close to the score given by the TMRs rating the budget drivers (segments of the budget with a higher overall percentage of the total).

Over the course of the SFOC, there are cases when individual TMRs assigned scores of 60, which would have precluded award fee payment under the individual contracts. For example, during the eighth award fee period, April-September 2000, the TMR responsible for vehicle engineering rated USA's performance at 60 or poor. The reason for this low score in period eight was lack of management oversight on OV-102 OMDP and missed corrosion during inspection. However, because of the weighting the overall score given to USA was higher, the composite score (and recommendation to the FDO by the board) averaged up to 79, which earned USA over $21 million in award fees. In that case, weighting on vehicle engineering was at 22 percent, which was significant enough to reduce the score, but not below the award threshold. In another example, period nine, October 2000-March 2001, SSP Systems Integration was rated at 60 for ineffective management by SFOC over a subcontractor and cost oversight on the remotely operated fluid umbilical cited. Because it was weighted at 7.33 percent, the final score recommended to the PEB became 84, earning $23.4 million for USA. Through the first 12 evaluation periods, there were 24 instances when the individual TMRs gave ratings below 80. However, in no cases was the final award determination by the FDO less than 80.

TMR Weighted scoring

• KSC Launch and	27.96
• SSP vehicle	17.67
•	14.47
• Integrated	12.03
• Solid Rocket	9.26
• SSP SYS	6.99
• Avionics andbftwar	5.48
• Station Ops and	2.69
• SP	.89
• SSP	1.09
• Management	0.39
•	0.27

Figure 4.6.1. Award fee weighted scores.

Proposed Recommendations:

The budget-based weighting formula, while a seemingly correct mathematical construct, may not put the proper emphasis on desired performance within each area. If each SOW area were a separate contract, the strengths and weaknesses of USA's performance would be more obvious and the TMR, COTR, and FDO would have greater leverage in rewarding above average performance. While it is recognized that the management of separate fee pools would require additional effort by the COTR and FDO, it may be appropriate to distribute the Award Fee dollars to each TMR. The dollars actually assigned to USA may end up the same in the aggregate, but high or low ratings would stand out with appropriate fee losses and gains.

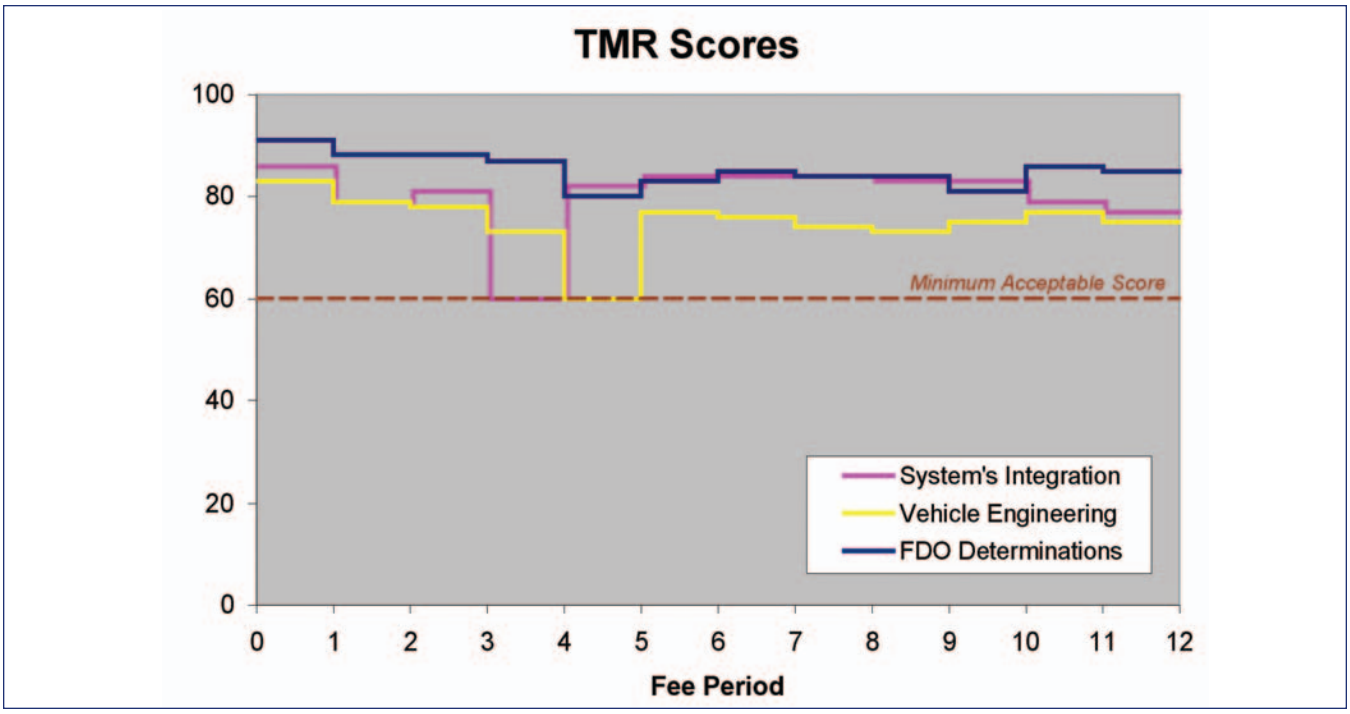


Figure 4.6.2. TMR scores.

4.7 Non-SFOC Contracts

Issue:

Over time, non-SFOC contracts have "evolved" to shift emphasis away from cost savings.

Background:

Marshall Space Flight Center (MSFC) has contract cognizance over Space Shuttle Program element contracts that are not within the SFOC. These include the Space Shuttle Main Engine (SSME), External Tank (ET), and the Reusable Solid Rocket Motor (RSRM). MSFC also had contract cognizance over the Solid Rocket Booster, until 1998. That element has since been transitioned to USA, originally as a directed subcontract to USBI. All other element contracts were "on the table" to be included in the SFOC as part of future phases, but those decisions have not yet been implemented.

Findings:

Boeing Rocketdyne manufactures the SSME. Rocketdyne has been the supplier since 1972,[49] when it was awarded the SSME development. The current contract, awarded in 2002 is for $1.2 billion and requires the effort necessary to meet six flights per year, with continued availability of 12 flight ready engines.[50] The contract includes incentives of over 11 percent – 5 percent for award fee and 5.5 percent in performance fees. (See Figure 4.7.1.)

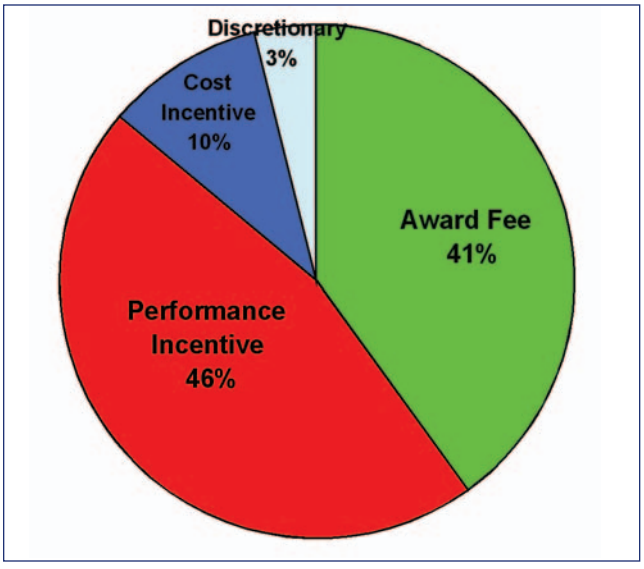


Figure 4.7.1.

Award fees are based on the following evaluation criteria: Management 30 percent; Flight Support 40-60 percent; Safety and Mission Assurance less than 30 percent. The weights of each criterion are determined at the beginning of each fee period and are conveyed to the contactor. As with other Space Shuttle contracts, the award fee is determined in six month periods, with the Performance Evaluation Board (PEB) recommending the score to the Fee Determining Official. The PEB at Marshall is comprised of the center's senior management, intended to provide an independent review of the COTR evaluation.[51] (See Figure 4.7.2)

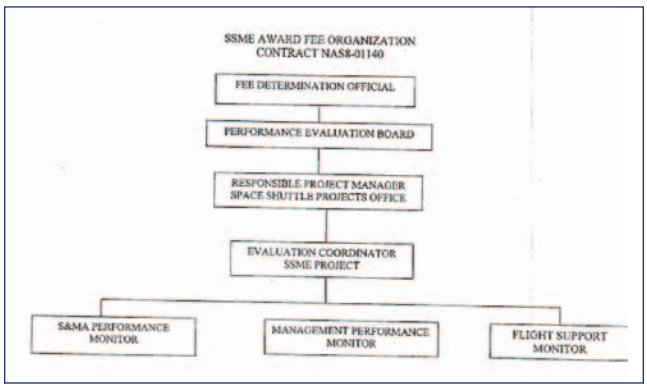


Figure 4.7.2 Performance Evaluation Board.

The SSME contract does not permit "rollover" of any unearned fee. Rollover provisions place unearned award fee funds into a virtual suspense account that could be earned by the contractor in the future for tasks not identified in the original fee plan. The award fee also serves as a cost incentive "gate" in that the incentives earned for cost reduction will not be paid unless the award fee score average is above 70. Additionally, for score averages below 85, there are caps applied to overrun earnings. During the current contract period, Boeing has earned fees of over $8.6 million with scores of 81.2 and 91.4. (See Figures 4.7.3 and 4.7.4)

The SSME contract places more potential fee dollars, and

Evaluation Period	Start Date	End Date	Avail. Award Fee Dollars	Dollars Earned	Dollars Not Earned	Overall Score
1	1/1/02	6/30/02	$4,823,679	$3,916,827	$906,852	81.20%
2	7/1/02	12/31/02	$5,222,203	$4,773,094	$449,109	91.40%
3	1/1/03	6/30/03	$5,370,488			
4	7/1/03	12/31/03	$5,261,730			
5	1/1/04	6/30/04	$5,111,443			
6	7/1/04	12/31/04	$5,051,295			
7	1/1/05	6/30/05	$5,118,927			
8	7/1/05	12/31/05	$4,950,116			
9	1/1/06	6/30/06	$5,182,323			
10	7/1/06	12/31/06	$4,906,367			
			$50,998,571			

Figure 4.7.3. SSME Fees Earned.

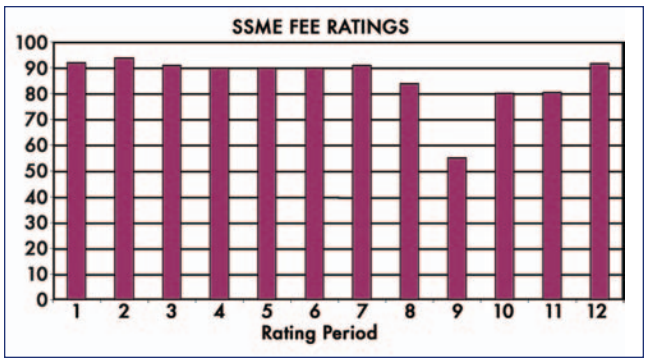


Figure 4.7.4. Boeing's ratings for the previous contract.

therefore more contract emphasis, on the performance success of the SSME. Each engine delivered on-time earned $1.5 million plus an additional $1.2 million paid for each successful launch.

MSFC has placed a more balanced emphasis on cost control on the External Tank procurement in contrast to the performance emphasis on the SSME contract. (See Figure 4.7.5) The ET contract was awarded to Martin Marietta (now Lockheed Martin) in 1973 for production of the first seven tanks.[52] The current contract, awarded in 1999, calls for the delivery of 35 tanks and 60 ship sets of flight hardware. The additional flight hardware is then used for the production of the next ET order. The contract also provides for the operation and maintenance of the Michoud Assembly Facility (MAF). Within this single contract, MFSC has included four separate fee plans, each with differing emphasis. The cost incentive is greatest on the long lead procurement portion and least on the friction stir weld upgrade (a product technology improvement). The award fee weights assigned are different for the contract portions as well. Production quality on the ET is weighted at 70 percent and management performance is weighted at 30 percent. In MAF operations, operations and maintenance is weighted at 20-30 percent, production support at 20percent, construction of facilities at 30 percent, and environmental compliance at 30-40 percent. The history of Lockheed Martin's earnings of fees is displayed on Figure 4.7.6.

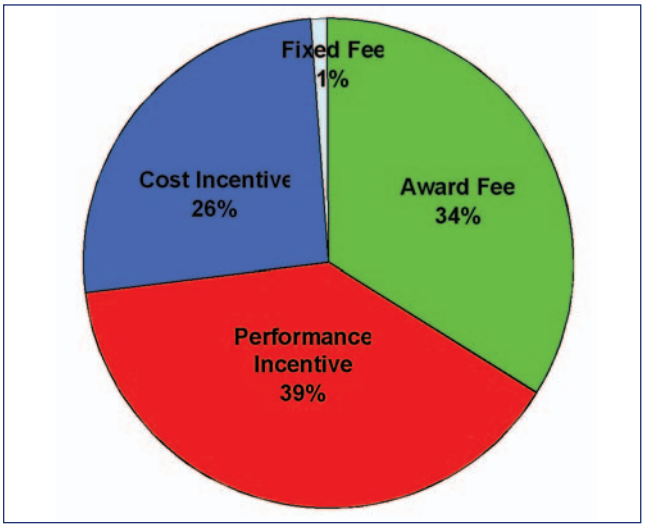


Figure 4.7.5. External Tank Contract Fee Distribution.

The ET contract also include performance incentives fee of 3.8 percent. This is distributed to safety (accidents/incidents), 1.14 percent; on-time delivery, 1.14 percent; launch success, 0.38 percent; and flight success, 1.14 percent. The dollar amount of these incentives are: delivery of approximately $347 thousand; launch success of approximately $115 thousand and flight success of $233 thousand. The safety incentive is based on hours worked over an annual period. One unique aspect of the ET performance award is that the flight success awards are granted after the Tank remains unused for twelve months. This is because NASA accepts the ET at the Michoud facility and the tank may remain unused for long periods, awaiting the flight schedule. Lockheed Martin also has included an employee motivation award that rewards each employee based on the contractor's earned fees. As the only major non-reusable Shuttle element, the design of the

Production Award Fee Pools

Period	Amount Available		Earned Amount	Earned Percent
October 1, 2000 - March 31, 2001	$1,499,664		$1,370,693	91.40%
April 1, 2001 - September 30, 2001	$2,493,361		$2,202,136	88.32%
October 1, 2001 - March 31, 2002	$3,273,186		$3,070,903	93.82%
April 1, 2002 - September 30, 2002	$2,498,684		$2,296,290	91.90%
Total	$9,764,895		$8,940,022	91.55%

MAF Operations & Maintenance Award Fee Pools

Period	Amount Available		Earned Amount	Earned Percent
October 1, 2000 - March 31, 2001	$345,327		$334,622	96.90%
April 1, 2001 - September 30, 2001	$485,448		$461,661	95.10%
October 1, 2001 - March 31, 2002	$658,718		$645,544	98.00%
April 1, 2002 - September 30, 2002	$761,736		$717,555	94.20%
Total	$2,251,229		$2,159,382	95.92%

B02063 – "Implementation of Friction Stir Welding" Award Fee Pools

Period	Amount Available		Earned Amount	Earned Percent
May 1, 2000 - March 31, 2001	$ 343,218-		$314,044	91.50%
April 1, 2001 - September 30, 2001	$297,000		$268,785	90.50%
October 1, 2001 - March 31, 2002	$128,000		$114,278	89.28%
April 1, 2002 - September 30, 2002	$84,687		$83,840	99.00%
Total	$852,905		$780,947	91.56%

Figure 4.7.6. Lockheed Martin Michoud Fees Earned.

Tank has been relatively stable. The ET contract has been considered for a fixed price contract transferring much of the financial risk of accomplishment to the contractor. The ET was being considered for a competition in the next award.[53]

The NASA contract system was criticized in an October 29, 1986, report by the House Committee on Science and Technology that stated: "Existing contract incentives do not adequately address or promote safety and quality concerns. Most emphasis is placed on meeting cost and schedule requirements."[54] Today, Marshall places much less emphasis on cost savings, than cost control, as budget management is a significant award fee criterion. [55]

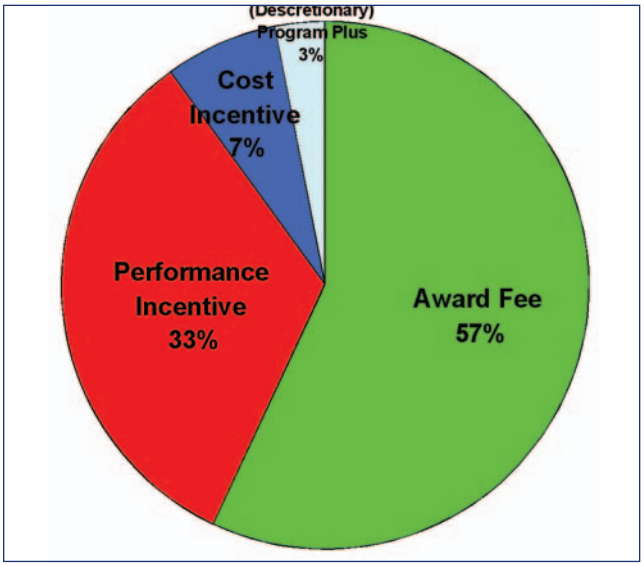


Figure 4.7.7. Reusable Solid Rocket Motor Fee Distributions.

The RSRM is the only major element contract that includes no incentive for cost under-run. While there is a one percent incentive in the contract to meet the target cost, the fee does not increase for cost under-run. (See Figure 4.6 7) Discussions with the Program offices revealed that it was a conscious decision not to add incentives for further cost reductions by the contractor. Concern was raised that the headcount had been reduced to the lowest level while maintaining safe operations and that further reductions would increase the risk to the program.

The award fee can total up to a potential fee of 8.5 percent. The fee plan is weighted 50 percent for performance management and 50percent for safety and mission assurance. The contract was changed in Buy 4 to eliminate the provision for rollover of unearned award fee (see above). On the previous RSRM contracts (Buy 3), there was a reallocation of the unearned award fees through the rollover provision.[56] The performance incentive portions of the fee structure amount to a potential 5percent of the available fee. These fees are earned for; on-time delivery - 2percent or approximately $1.2 million; per ship set assembly - 0.5 percent or approximately $300 thousand; launch/flight performance – 2.5 percent or approximately $1.5 million flight. (See Figure 4.6.8 for RSRM history)

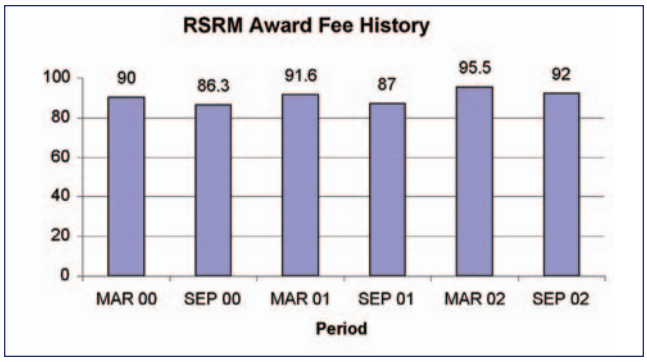


Figure 4.7.8. RSRM fee history.

In summary, the various treatments of fees on the Marshall managed program illustrate that the government can use several techniques to convey program emphasis through contract incentives. In the case of the External Tank, multiple incentive fee plans are used to appropriately reward different types of effort on the same contract. In the case of the SSME, the contract reflects that the element is still considered high risk and performance success is paramount. Finally, in the case of the RSRM, the government recognizes that while cost control is important, continued cutting of program costs may increase risk and therefore should not be rewarded.

Proposed Recommendations:

MSFC has demonstrated that the contract can be used to recognize the evolved state of the contractual performance while recognizing that the SFOC statement of work differs greatly in the contracts for the ET, SSME, and RSRM. NASA should consider subdividing the SFOC, to reflect differing emphasis on cost savings or performance, rather than the averaging of performance now present in the contract. When and if the element contracts are bundled into the SFOC, NASA should consider the history at MSFC and maintain the best practices in terms of contract incentives.

4.8 Contractually Required Documents Applicable to External Tank Thermal Protection System (TPS) Foam Application

Issue:

Foam application process is not specified as a contractual requirement.

Background / Facts:

Marshall Space Flight Center contract number NAS8-00016 covers the period from September 27, 1999 through December 1, 2008 for the production of External Tanks numbered ET-121 through ET-156. Contract number NAS8-36200 includes the effort for the production of external tanks 61-120.[57] Lockheed Martin's manufacturing and process plans (MPP) specify the application processes currently in use at the MAF for the external tank production. The statement of

work (SOW) (Figure 4.8.1) included in the contracts contains the Index of Compliance Specification, Documents and Deviations. This index lists the Type 1 documents applicable to the contract. Document Number MMC-ET-CM02a provides the Prime Equipment Detail Specification. CMO2 identifies all the technical requirements that are pertinent to the ET. This document contains a cross-referenced matrix to identify the NSTS 07700 Volume X, which specifies Space Shuttle Program requirements. The ET Project Manager and Contracting Office must approve all changes to CM02 (as is a Type 1 document) prior to implementation. A Preliminary Specification Change Notice (PSCN) is drafted and submitted to NASA as part of a Change Summary. This requirement further flows to MMC-ET-SE16, the Materials and Processes Control Plan that specifies the materials and the processes for the ET including the thermal protection system (TPS). Since this is also a Type 1 document, all changes must be processed through the NASA ET project office as well. A preliminary drawing change notice (PALMDALECN) is drafted as part of a change summary. However, at a specification level below SE16, NASA initially approves Engineering Material Specifications (STM) and Engineering Process Specifications (STP), and coordinates changes.

Manufacturing Process Plans (MPP) provides the fabrication instructions. They may include processes describing all manufacturing operations, operational buy offs and data recording, or may provide general instruction referencing specific processes with limited data recording and minimal buy off. Buy offs include production, production assurance, or government inspection agency (GIA) and may include inspections of critical items list (CIL) items. The MPPs are under the control of Lockheed Martin. Changes to the MPPs are not required to be coordinated with the government unless they affect form, fit, or function. NASA and DCMA are to review any contractor implemented changes that affect form, fit, or function.

Proposed Recommendations:

None.

4.9 Contractual Penalties for Eternal Tank Failure

Action:

The external tank used on STS-107 was not subject to a catastrophic loss penalty clause.

Background / Facts:

After the *Challenger* accident, NASA contracting officers began to include catastrophic loss clauses in the Space Shuttle Program ET contract.[58] The last Marshal Space Flight Center ET contract included the production of External Tank 93, which was delivered in 2000 and used on STS-107.The government accepted delivery of this tank and held it until needed. The catastrophic failure clause (included in the current contract, section B5) provides that Lockheed Martin is assessed a fee reduction in the event of any critical category I or category II failures on a Space Shuttle mission using ET-121 through ET-156. A category I failure is an incident directly caused by external tank hardware that results in death of a Shuttle crewmember or "total loss of the Shuttle Orbiter Vehicle."[59] A category II failure is an incident directly caused by external tank hardware that results in a mission failure. The fee reduction for a category I failure is $5 million or $10 million for a category II failure. The category II or I failure determination will be made by a Failure Investigation Board (convened and conducted in accordance with the requirements of NASA Management Instruction NMI 8621.1).

Similar contract clauses are include in the Space Shuttle Operations Contract (SFOC) and contracts for the Space Shuttle Main Engine (SSME) and Reusable Solid Rocket Motor (RSRM). Some contracts include forfeiture of any fees earned during the period in which a catastrophic loss occurs. However, the ET used on STS-107 was delivered under the previous contract, NAS8-36200. Lockheed Martin had requested, in negotiation discussions incident to that contract, that the available fees be raised considerably if NASA were to request inclusion of a catastrophic loss clause.[60] The Marshall negotiators considered the potential increase in the contract price and determined that the benefits of the clause did not justify the cost.

Findings:

The absence of a specific catastrophic loss clause does not necessarily mean that the contractor is exempt from financial penalties, should responsibility be determined.

Proposed Recommendations:

Should the Board determine that the External Tank was a causal factor to the accident and further determine that the contractor is culpable, complete contract review should be accomplished to identify whether other provisions exist in prior contracts to assign penalties or fee forfeitures

4.10 Workforce: Size and Aging

Action/Issue:

The NASA/contractor workforce is aging and may not be adequate to do its assigned mission.

Background:

Since NASA was established in 1958, its civil service workforce has fluctuated widely. In 1967, at the height of the Apollo program, the workforce reached approximately 35,900 personnel. In the mid-70s an involuntary separation program decreased the workforce by several thousand employees. By 1980, the workforce had stabilized near 21,000. It remained close to that level until 1986, when the Space Shuttle *Challenger* accident forced a reexamination of NASA, adding significant man-hours to Safety and Quality Assurance processes.

NASA began some ambitious new programs in the late 1980s and its workforce began to grow again peaking in

1992 at more than 25,000. When the Clinton administration took office in 1993, it initiated steps to reduce the size of the overall federal workforce. Total NASA headcount went from approximately 25,000 civil servants in FY1993 to slightly more than 18,000 (full-time permanents) by the end of 2002. As the NASA workforce declined, the continuing strategy was to lose junior personnel first, resulting in an experienced but aging workforce. In November 1995, NASA selected United Space Alliance – a Rockwell International and Lockheed Martin partnership – as the prime contractor for space flight operations. Thus, fewer civil servants were required to manage the program. NASA estimated that it would be able to make personnel reductions in the range of 700 to 1,100 full-time equivalent personnel (FTE) at the Kennedy Space Center alone. The challenge to Space Shuttle contractors, including United Space Alliance, was to address the aging workforce concerns through a continual influx of inexperienced personnel who could stay with the industry for many years. Contractors have much more flexibility in their personnel decisions than does the federal government. Compensation packages, including both wages and benefits, are tailor made to address the shortages that face the industry while correcting oversupply in some skills. All SSP contractors, including United Space Alliance, have been given financial incentives to reduce the cost of performing the contract. Personnel costs can be reduced by eliminating personnel in overhead support or management functions, or by encouraging efficiencies in the direct labor elements. United Space Alliance, through the Space Flight Operations Contract, is accountable for professional, managerial, and technical workforce support to the Space Shuttle Program. Jobs range from maintenance personnel at Kennedy Space Center to subsystem managers within the Mission Control structure. USA recognized its obligation to maintain a balanced workforce in professional skills, and that there must be a flow of personnel through the "pipeline" to guard against future shortfalls in critical skills.

United Space Alliance stated that while they accepted the challenge to reduce the headcount on the Space Shuttle Program, they intended to do so without reducing the direct headcount. They would do this primarily through efficiencies achieved by consolidations. USA did not place the same emphasis on the retention of the non-professional, technician workforce. USA has stated that it does not suffer from the same concerns as with engineers and has never faced a shortage of applicants for these jobs.

United Space Alliance closely tracks personnel trends, especially with respect to engineering manpower. USA has a nearly bimodal distribution with respect to age or experience. There are a significant number of personnel over 40 years of age as well as a significant number in the under-30 age group. This illustrates a pipeline from which the workforce of the future will be drawn. Other Space Shuttle contractors may not have had the flexibility to make these kinds of "overhead only" process gains, as elimination of direct as well as indirect personnel was necessary. While reducing the cost of labor through lay-offs, the contractor must continually guard against creating an impression of the company as an unattractive workplace. Contrast the United Space Alliance distribution with ATK Thiokol Propulsion in Utah, the supplier of the Reusable Solid Rocket Motor (RSRM) since the 1970s.

During the peak production of the RSRM in the 1980s Thiokol employed over 4,000 personnel. Today, with production of the RSRM at less than 30 units annually, their personnel count is stable at 1,350. Demographics at the Utah plant show a spike in the 45-49 age group, with the majority of the workforce being over 45 years old. This trend is true for engineering as well as plant personnel. ATK Thiokol has identified their aging workforce as a significant issue in relation to the Service Life Extension Program (SLEP). ATK Thiokol recognizes that they must "pump significant new energy into recruiting new talent and retaining/training the younger ones currently in our workforce now."[61] The contracting community at Marshall Space Flight Center recognized the risk associated with downsizing and has eliminated incentives associated with cost cutting in the latest RSRM contract.

The Michoud Assembly Facility workforce has been declining over the past five years. In 1998, there was some increase in hiring as a result of the RLV and X-33 programs. However, after that, hiring was limited to budget-driven replacements only. Budget challenges have led to involuntary separations, which approached 10 percent in 2002. One of the risks of multiple periods of downsizing is that it may lead to a perception among the workforce of limited potential for both growth and reliable employment. This has been highlighted as one of the most significant reasons for the voluntary attrition over the past three years. The average age of the employee at Michoud is now 47.8 years, but the skilled labor (represented) employees average 48.2 years.

In conclusion, the issues associated with aging workforce present formidable challenges to the future of the Shuttle Program, especially if the vehicle is expected to serve until 2020 and beyond. Of the major contractors, only USA has a recruiting effort with significant numbers.

Additionally, while USA's benefit packages have been considered by some to be below the industry standard, we have reviewed DCAA documentation that reflects that the packages are among the best in the industry and may actually be considered excessive.

Proposed Recommendation:

It is essential that NASA take actions to ensure a stable experienced base of support for the Shuttle programs. This may require modifications to the way contract incentives are used or other contractual arrangements or changes. It may benefit NASA to continue the bundling of Space Shuttle element contracts, ET, SSME, and RSRM under the SFOC and USA in order to maximize the return on leverage of personnel recruitment efforts.

ENDNOTES

[1] Boeing Inspection Report, OV-102, Wire Inspection Report, September 1999-February 2001.
[2] Boeing Inspection Report, OV-102 J3 V30/V31, September 1999-February 2001, p. 13.
[3] Boeing briefing, "Arc Tracking Separation of Critical Wiring Redundancy Violations," present to NASA April 18, 2001, Joe Daileda, Bill Crawford.
[4] Minutes of Orbiter Structures Telecon meeting, June 19, 2001, held with NASA, KSC, USA, JSC, BNA-Downey, Huntington Beach, and Palmdale
[5] Shuttle Operations Assessment Group (SOAG), Safety Reporting Database-SOAG 99-069, Aug, 25, 1999, Engineering Support Request ESR K16460
[6] SRB Forward Separation Bolt Test Plan, Doc Number 90ENG-00XX, 2 Apr 2003
[7] Contract F08650-00-C-0005: CSR Technical Report –Debris, Analysis Report For Operation F1120, Shuttle STS-107, 16 January 2003, Revision 1 (Cdr A205), pg 29
[8] Contract F08650-00-C-0005: CSR Technical Note –Bolt Catcher Debris Analysis For Shuttle STS-107 (CDR A205), 25 June 2003, pg 29
[9] Marshal SFC briefing on Bolt Catcher Test Plan, Joe Gentry, 5 April 2003
[10] "Non-Destructive Test Evaluation Assessment of Pacific Magnetic & Penetrant Inc., Bellringer #03-0-W/14, March 2003, DCMA Phoenix, DCMA-GPOZD.
[11] Aerospace Safety Advisory Panel, Annual report for 2002, 32.
[12] Space Shuttle Processing Independent Assessment Report for USA, April 23, 2001, 30.
[13] USA Operating Procedure: Hardware Photographic Documentation. No. USA 004663, 11/27/02, p 1.
[14] CAIB request for information #B1-001178
[15] Space Shuttle Independent Assessment Report for United Space Alliance, April 23, 2001, page 46.
[16] Space Shuttle Processing Independent Assessment Report for USA, April 23, 2001, pg 22.
[17] Report of the Presidential Commission on the Space Shuttle Challenger Accident (In compliance with Executive Order 12546 of February 3, 1986)
[18] Space Shuttle Independent Assessment Team, Report to Associate Administrator, October-December 1999, March 7, 2000, pg 51
[19] Ibid.
[20] Various informal testimony gathered by Board members and staff while traveling to NASA sites.
[21] Space Shuttle Independent Assessment Team, Report to Associate Administrator, October-December 1999, March 7, 2000, pg 53
[22] Standard Operating Procedure, Foreign Object Debris (FOD) Reporting, Revision A, Document Number: SOP-O-0801-035, October 01, 2002, United Space Alliance, KSC, 3.
[23] Ibid, pg 2.
[24] National Aerospace FOD Prevention, Inc., Rev E July 2000, 1.
[25] Ibid.
[26] SFOC, Performance Measurement System Reports for January 2003, February 25, 2003, USA004840, issue 014, contract NAS9-20000.
[27] Space Shuttle Processing Independent Assessment Report for USA, April 23, 2001, 22.
[28] Kennedy Space Center Processing Review Team Assurance Engineering Final Report, April 2003: Safety, Quality, Industrial Engineering, Corrective Action Human Factors, and Reliability
[29] STS-107 and STS-109 Engineering Process Review Team (PRT) Systemic Analysis (Assurance Engineering Review), May 23, 2003
[30] KSC Processing Review Team Final Summary, USA, June 10, 2003
[31] KSC Processing Review Team Final Summary, USA, June 10, 2003
[32] NASA brief, "CAIB Informal Action: Orbiter Life Extension- History/ Current Status," 6/02/03.
[33] Ibid.
[34] Followup Audit on Orbiter Maintenance Down Periods at KSC, June 12, 1998, NASA Office of the Inspector General, pg 2 et al.
[35] NASA Briefing, presented 7 May, 2003, by the SLEP program manager during a SLEP video telecom.
[36] NASA briefing, presented 7 May, 2003, by the SLEP program manager during a SLEP video telecom.
[37] NASA briefing, presented 7 May, 2003, by the SLEP program manager during a SLEP video telecom.
NASA briefing, presented 7 May, 2003, by the SLEP program manager during a SLEP video telecom.
[38] NASA-Langley Briefing to the CAIB, Presented 12 May 2003, by Mark J. Shuart, et al.
[39] Statement of Russell A. Rau, Assistant Inspector General for Auditing National Aeronautics and Space Administration before the House Committee on Science, April 4, 2001
[40] Minutes of the Space Flight Advisory Committee, May 3, 2002, 1.
[41] Full Cost Management: Background, Purpose, Legislative Proposals, January 1998.
[42] Report of the Space Shuttle Management Independent Review Team, February 1995, Dr. Christopher Kraft, pg 12.
[43] Statement of Daniel Goldin to the Subcommittee on Space and Aeronautics Committee on Science U.S. House of Representatives, November 30, 1995.
[44] SFOC Briefing and discussion with the CAIB, March 17, 2003.
[45] SFOC Post Negotiation memorandum, September 23, 1996
[46] NASA FAR Supplement 1816.405-274
[47] NASA FAR Supplement 1816.405-275
[48] The Contracting Officer Technical Delegation, July 18, 2001, form 1634.
[49] SSME CAIB Briefing and discussion April 30, 2003
[50] Contract Number NAS8-01140
[51] Award Fee Plan for Contract Number NAS8-01140
[52] CAIB External Tank Contacrt Briefing, April 30, 2003
[53] ET Program Discussions, April 30, 2003
[54] Thiokol got `flight success' bonus a week before disaster, Houston Chronicle, November 20, 1986
[55] Ibid.
[56] CAIB ET Contract Briefing, April 30, 2003
[57] NASA External Tank Contract Briefing to the CAIB, April 30, 2003
[58] "NASA ponders $10 Million Thiokol Fine," Houston Chronicle, November 19, 1986
[59] NASA contract with Lockheed Martin for ET production, NAS8-00016.
[60] CAIB discussion with ET contracting and program office, April 30, 2003.

THIS PAGE INTENTIONALLY LEFT BLANK



Volume II
Appendix D.16

Determination of Debris Risk to the Public Due to the *Columbia* Breakup During Reentry

Acknowledgements 475

Summary 475

Section 1. Introduction 476

Section 2. Derivation Of The Breakup Debris Model 476
2.1 Overall Procedure 476
2.2 Mechanics of Debris Fall and Dispersion 477
2.3 Analysis of Gathered Debris 478
2.4 Development of Reference Trajectories 479
2.5 Development of Breakup State Vectors and Associated Debris Groups 480

Section 3. Debris Dispersion 483
3.1 Basics of Impact Dispersion of Debris 483
3.2 Description of CRTF and RRAT 483
3.3 Computed Dispersion of Debris Using the Breakup Model 483

Section 4. Casualty Model Due To Debris Impacting On People In The Open 487
4.1 Basic Impact Casualty Model 487
4.2 Casualty Areas for Representative Debris 488

Section 5. Exposure And Sheltering Model 490
5.1 Ground Exposure Methodology 490
5.2 Sheltering Categories 491
5.3 Data 492
5.4 Resulting Ground Exposure Model 495
5.5 Aircraft Exposure Model 495

Section 6. Risk Analysis Due To Columbia Debris 496
6.1 General Procedure 496
6.2 Computed Risks Using the Breakup Model, the Casualty Model and CRTF/RRAT 497
6.3 Risk to Aircraft 498
6.4 Validation of Computed Risks Using a Simplified Model 499
6.5 Sensitivity of Results to Model Parameters 500

Section 7. Study Conclusions And Recommendations 500

References 500

Appendix A

Reprint of CRTF Paper Presented to JANNAF 501

List of Figures

2-1 Locations of Recovered Debris 477
2-2 Free-Body Diagram of a Piece of Debris 478
2-3 The Influence of the Ballistic Coefficient, β, and Wind upon Debris Impact Points 478
2-4 Size Histogram of Measured Fragments 479
2-5 Rule Based β (Ballistic Coefficient) Approximation 479
2-6 Debris List Extracted from Records with at Least Two Dimensions 479
2-7 Reference Trajectories 479
2-8 Relationship between Downrange Impact Distance and Downrange Time for each Ballistic Coefficient Group (Measured from Loss of Signal) 480
2-9 Distribution of Debris with Dimension Data as a Function of Impact Range 480
2-10 Group 1 Debris List 481
2-11 Group 2 Debris List 481
2-12 Group 3 Debris List 482
2-13 Group 4 Debris List 482
2-14 Estimated Breakup Model as a Function of Time by Ballistic Coefficient Category 483

3-1 Contributions to Debris Dispersion Models 483
3-2 Comparison of Gathered Data with Modeled Dispersion (Group 1) 484
3-3 Comparison of Gathered Data with Modeled Dispersion (Group 2) 484
3-4 Comparison of Gathered Data with Modeled Dispersion (Group 3) 485
3-5 Comparison of Gathered Data with Modeled Dispersion (Group 4) 485
3-6 Comparison of Gathered Data with Modeled Dispersion (All Groups) 486
3-7 Modeled Debris Density in Three Dimensions 486
3-8 Comparison of the Actual Fragment Count (Green) in the Downrange Direction with the Fragment Count in the Reconstructed Model (Blue) 487
3-9 Comparison of the Actual Fragment Count (Green) in the Crossrange Direction with the Fragment Count in the Reconstructed Model (Blue) 487

4-1 Relationship between Casualty (AIS 3) and Fragment Impact Conditions 488
4-2 General Logic for Computing Casualty Area 488
4-3 Distribution of Total Hazard, Casualty and Fatality Area among the Debris Classes 488

5-1 Population / Sheltering Modeling Overview 490
5-2 Example Casualty Areas for Steel Debris Impacting at Terminal Velocity 492
5-3 Population Model and Impact Area Defined by Recovered Debris 496

6-1 Integration of the Bivariate Normal Debris Impact Distribution Over the Area of the Population Center to Determine the Probability of Impact Upon the Population Center 497
6-2 Debris Risk Profiles for Different Percentages of Surviving Debris 498

List Of Tables

2-1. Material Densities 479

4-1. Abbreviated Injury Scale (AIS) 487
4-2. Hazard, Casualty and Fatality Areas for People in the Open Based on Recovered Columbia Debris 489

5-1. Variables for Modeling Sheltering 491
5-2. Roof Penetration Models 492
5-3. Translation Table for Houses/Apartments 493
5-4. Translation Table for Occupations 494
5-5. Translation Table for Schools and Group Quarters 495
5-6. Average Sheltering Distribution 495
5-7. Aircraft Parameters for Impact Analysis 496
5-8. Aircraft Density 496

6-1. Ground Risk Results Based on Gathered Debris (Model) 497
6-2. Ground Risk Results as a Function of Amount of Debris Assumed to Survive 497
6-3. E_{Haz}, E_C and E_F from the Approximate Analysis 499
6-4. Sensitivity of the Final E_C Results to the Assumption of the Percentage of the People at Home who are Outside . 500

THIS PAGE INTENTIONALLY LEFT BLANK

Determination of Debris Risk to the Public Due to the *Columbia* Breakup During Reentry

Technical Report No. 03-517-01
Prepared for the Columbia Accident Investigation Board
Under Subcontract to Valador, by Mark Y. Y. Lin, Erik W. F. Larson, and Jon D. Collins: ACTA Inc.
September 2003

ACKNOWLEDGEMENTS

This work was performed under subcontract to Valador, Inc. for the Columbia Accident Investigation Board. The work was awarded as the result of a competitive procurement. Dr. Daniel Heimerdinger monitored and was administrator for the contract.

The project manager for the work by ACTA was Dr. Jon D. Collins. Dr. Mark Lin developed the debris model and performed the ground risk analysis. Dr. Erik Larson developed the population model and performed the aircraft risk analysis. In addition, Dr. Keng Yap performed the simplified casualty area computations, Bud Parks provided the meteorological data and Dr. Steven Carbon modified the CRTF program to be able to compute P(≥ 1 casualties).

ACTA acknowledges Dr. Paul Wilde of the Federal Aviation Administration and Elizabeth Fountain of the Columbia Task Force in furnishing the field data used in this study. Dr. Wilde also monitored the progress of the work and provided very helpful direction.

SUMMARY

This report provides the findings from a study initiated by the Columbia Accident Investigation Board to determine if the lack of casualties from the large number of Columbia fragments would have been the expected. The study was based upon the last reported position of the vehicle, the impact locations (latitude and longitude) of all of the recovered debris, the total weight (sum) of the recovered debris and some data (material, two dimensions) on some of the pieces of debris. The study was performed before any more detailed evaluation of the debris was available. The process used in the study involved the following steps:

1. Create a mathematical model of the Columbia (STS-107) breakup debris in terms of size, weights, numbers, aerodynamic characteristics and origins (initial time, position). This model is based on the best available information at the time the study was started, which was in late May of 2003. Ground search activity for the debris recovery effort continued at full strength until April 25, and then gradually tapered off as the search was completed. Therefore, the data needed for this study was not available until late May.
2. Develop a "population library" that describes where people were most likely to be located and whether and how they were sheltered. The population study assumed that about 18% of the people were probably outdoors and the remaining in various levels of sheltering.
3. Simulate the debris cloud and develop probabilistic impact dispersions for the debris impacts. The paths of the fall of the debris fragments take into consideration the best estimate of the wind conditions (measured in terms of speed and direction and as a function of altitude) at the time of the event. Wind data was available from the Dallas Fort Worth Airport and the airport at Shreveport, Louisiana.
4. Determine the expected number of casualties, E_C, considering the debris impact distributions, estimated locations of people, sheltering of people and the vulnerability of people to inert debris impacts.
5. Estimate the probability of any impact to aircraft in the vicinity of the debris cloud.

The CRTF (Common Real-Time Debris Footprint) program operating inside the RRAT (Range Risk Analysis Tool) was used to perform the risk analysis. The results are summarized in the table at the top of the next page.

There is no certainty as to the amount of debris that survived. The range of possibilities is from the gathered debris being all of the debris that survived to all of the Columbia debris surviving, but not having been located. The table presents that range with the assumption that the mix of the gathered debris is representative of the mix at every other survival percentage. The column containing P(≥1 Casual-

Debris Case	*Percentage of Total Orbiter and Payload Weight*	*E_C (Including sheltering)*	*P(≥1 Cas.)[1] (Including sheltering)*
Model (gathered debris)	38%	0.14	0.13
60% of total wt. survived	60%	0.21	0.19
80% of total wt. survived	80%	0.29	0.25
100% of total wt. survived	100%	0.37	0.30

ties) provides an estimate of the probability of one or more casualties. It is a probability with range of $0 \leq P \leq 1$ whereas the E_C is an average that can have a value that exceeds 1.

Individual risk was also computed. The highest probability of any particular person exposed to the recovered debris becoming a casualty was determined to be 7.6×10^{-5}.

A preliminary study of the risk to aircraft indicated that the expected number of planes impacted by the Columbia breakup was approximately 3×10^{-2}. This is primarily due to possible impacts with general aviation (>80%). The numbers were based on estimates of the aircraft density for similar conditions to those in another study, but not on actual statistics at the time of the accident.

The general conclusion is that the lack of casualties was the expected consequence, but not overwhelmingly so. Sheltering played an important role as well as the lower density of population in the region where the debris was recovered in reducing the likelihood of injuries among the general public. This study should be revisited when the debris data are cataloged more completely to determine if the model assumptions and results shift due to the finer debris resolution.

1. Introduction

There were no reported casualties due to debris from the breakup of the Columbia. *The primary purpose of the analysis in this report is to confirm whether the lack of casualties is the expected consequence, or whether this happened to be good fortune for the people on the ground exposed to the debris.*

The Columbia Accident Investigation Board (CAIB) contracted with ACTA Inc. to accomplish this task using the debris data available at the time. The process used in the study involved the following steps:

1. Create a mathematical model of the Columbia (STS-107) breakup debris in terms of size, weights, numbers, aerodynamic characteristics and origins (initial time, position). This model is based on the best available information at the time the study was started.
2. Develop a "population library" that describes where people are located and whether and how they are sheltered. This is to take into consideration as to where people would most likely be at the time of the event.
3. Simulate the debris cloud and develop probabilistic impact dispersions for the debris impacts. The fall of the debris takes into consideration the best estimate of the wind conditions (measured in terms of speed and direction and as a function of altitude) at the time of the event.
4. Use casualty models for people in the open and in structures, based on computed vulnerabilities of people and specific structure types, combined with the locations and numbers of people and probability of impact, to determine the expected number of casualties.
5. Make an estimate of the risks to aircraft in the vicinity of the debris cloud.
6. Use an alternate simplified model to estimate the risk to provide some logical validity to the risks computed by the more elaborate model.
7. Evaluate the sensitivity of the results to model parameters.

ACTA used the CRTF (Common Real-Time Debris Footprint) program [1] operating inside the RRAT (Range Risk Analysis Tool) [2] to perform the risk analysis. The CRTF program, described briefly in Appendix A, was originally developed to support the range safety work at the Air Force Eastern and Western Ranges.

The risk posed to people on the ground from launch vehicle flight is typically quantified in terms of expected casualties, which is the mean value from a statistical analysis of the probability and consequence of all foreseen outcomes of flight [3, 4]. A casualty is generally defined as a serious injury or worse, including death. A typical risk estimate for accidental debris impacts during ascent of an expendable rocket is about 0.00002 expected casualties for all members of the public, including over flight of Africa. The typical total of 0.00002 expected casualties for an expendable rocket ascent predicts an average of two seriously injured individuals located on the ground after 100,000 launches. The expected casualties is equal to the probability of at least one casualty times one casualty, plus the probability of two casualties times two casualties, plus the probability of three casualties times three casualties, etc.

2. Derivation Of The Breakup Debris Model

2.1 Overall Procedure

The CAIB provided the coordinates of 75,440 pieces of gathered debris in an EXCEL spreadsheet. No individual weights were provided as that information had not yet been developed at the time of this study, only the total weight of the gathered pieces (84,900 lbs). The spreadsheet also contained some useful descriptive information, including material and some dimensions, for about 15,470 pieces of

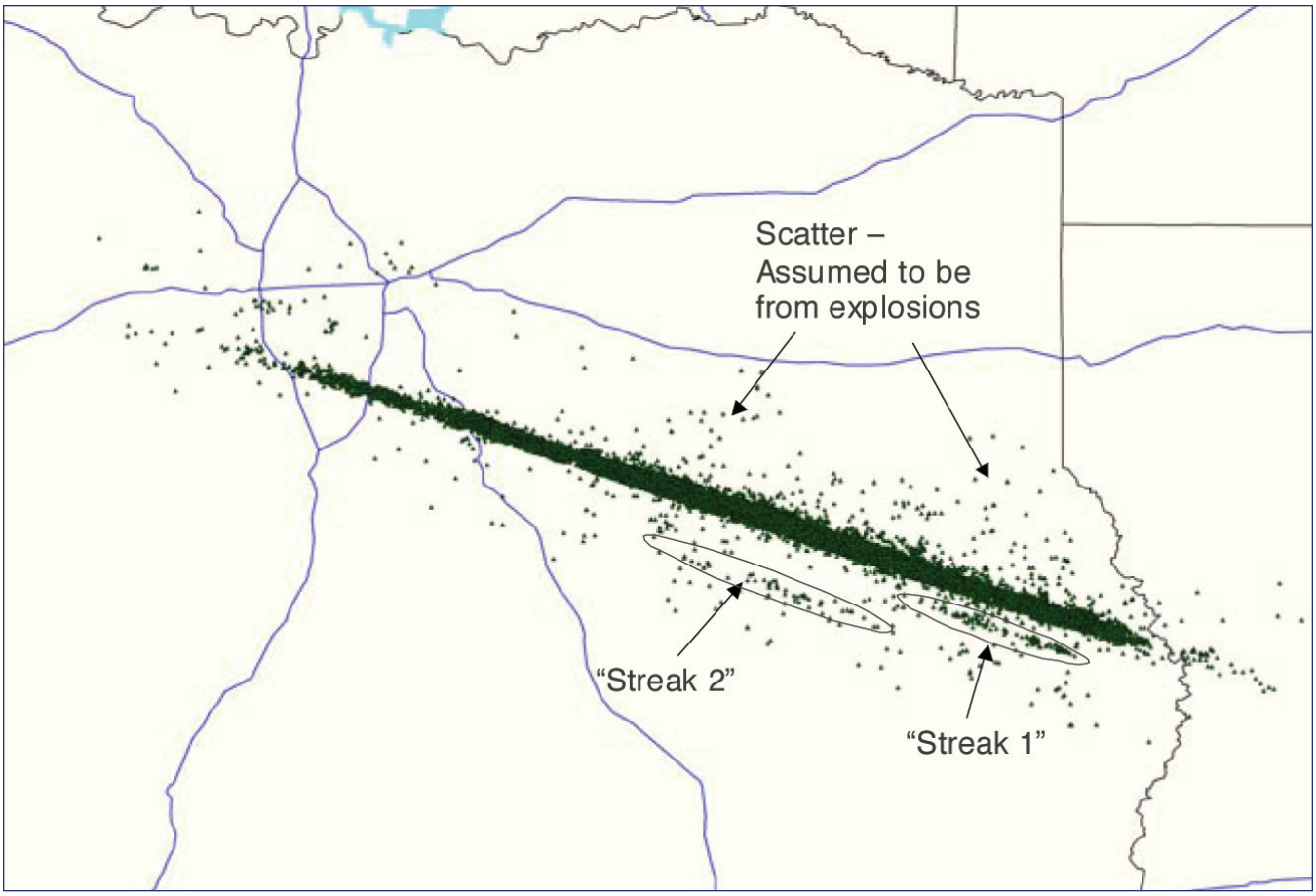


Figure 2-1. Locations of Recovered Debris.

debris. In addition, the CAIB provided the last state vector (position and velocity) communicated from the Columbia and a time-line of events.

The debris list developed for the study was extracted from the raw data in the EXCEL spreadsheet with a computer algorithm implemented to identify each fragment's composition, dimensions and shape. While errors were unavoidable in the processing of individual records, the overall weight of the constructed debris model and histogram of debris sizes and ballistic coefficients correlate well with observed data. It should be possible in later studies to remove more erroneous data by additional manual processing of the field records.

Figure 2-1 contains a map showing where the debris was recovered. A primary data grouping, Group 1, was used to account for the main debris field. Two secondary debris groups, Group 2 and Group 3 (identified as Streak 1 and Streak 2 in the figure) were created with separately fitted trajectories. Group 4 accounted for the widely scattered debris recovered outside of Group 1. The scatter observed in Group 4 debris seemed beyond the range that could be explained by lift, and thus it was assumed that a large velocity impulse of unknown source (an explosion?) was responsible. A standard deviation of 333 ft/sec in the velocity impulse produced a scatter that proved to be the best fit to the gathered Group 4 debris. There is no current explanation for the high velocities in Group 4, but the velocity impulse assumption enables the mathematical model to match the observed scatter. It will be shown later that the risks contributed by Groups 2, 3 and 4 are very small compared to Group 1 because of the relatively small numbers of pieces of debris in these groups. Therefore they do not contribute materially to the final result, and no further effort was put forth to model and explain the phenomenon.

2.2 Mechanics of Debris Fall and Dispersion

Before proceeding further, it is worthwhile to discuss the basic physics of falling debris. A piece of debris has an initial state vector that is defined by a position and velocity vector (six total components). The initial state vector may be perturbed from by an explosion that imparts a velocity and a consequential adjustment to the velocity vector. There is no adjustment to the initial position because the velocity is added impulsively. The gravity and aerodynamic forces affect the fall of the debris. Figure 2-2 shows a free-body diagram of a piece of debris. The dominant parameter in the trajectory computation is the ballistic coefficient represented by the Greek letter β. The formula for ballistic coefficient is

$$\beta = \frac{W}{C_D A}$$

where W is the weight of the fragment, C_D is the drag coefficient and A is a characteristic area associated with the drag coefficient. In this study the units for are lb/ft^2. This formula represents the ratio between inertial effects (W) and drag effects (C_DA). Objects with low weight to drag ratio fall much more slowly than objects with a high weight to drag ratio, e.g. a feather vs. a bowling ball.

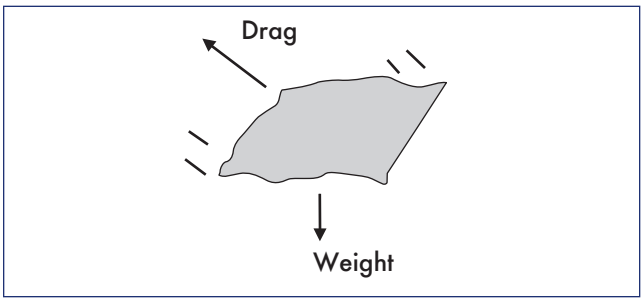


Figure 2-2. Free-Body Diagram of a Piece of Debris.

A fragment having an initial velocity with a horizontal component will travel further if it has a higher ballistic coefficient. As the debris falls it may come into equilibrium between the weight and the drag, resulting in falling at terminal velocity. At terminal velocity, and without the presence of wind, the fragment is falling vertically. At terminal velocity, the drag force, $1/2\ \rho V^2 C_D A$, equals the weight, W. This yields the equation,

$$V_{term} = \sqrt{\frac{2W}{\rho C_D A}} = \sqrt{\frac{2\beta}{\rho}}$$

which is equivalent to $V_{term} = 30\sqrt{\beta}$ at sea level, if β is expressed in lb/ft^2 and velocity in ft/s.

Wind is the other major factor affecting the fall of the debris. The effect, without explanation here, is proportional to $1/\sqrt{\beta}$. Thus, in summary, debris with smaller ballistic coefficients will fall closer to their initiation point, in the absence of winds, but will be moved more due to the wind (and in the direction of the wind). This is demonstrated in Figure 2-3.

The term Vacuum IP in the figure represents the impact point when there is no atmosphere, i.e. no drag. Note how the wind effect diminishes with increasing β.

2.3 Analysis of Gathered Debris

Data on 84,000 pieces of recovered debris were provided in EXCEL files. Data on 75,440 pieces of recovered debris included impact coordinates. The total recovered weight was 84,900 lbs., approximately 38% of expected orbiter and payload landing weight. For 15,470 pieces of recovered debris at least two dimensions were provided. Most measurements did not include a third dimension. A histogram of estimated fragment areas is shown in Figure 2-4. The histogram exhibits the characteristics of an exponential distribution. In addition, an 800 lb turbo pump impacted with an estimated kinetic energy equivalent to 2 lb TNT (β = 300 lbs/ft^2 at terminal velocity $\approx$ 500 ft/sec). It will be seen later that the risk contributed by the turbo pump was very small compared to the risk from the large number of smaller fragments.

NASA provided material descriptions that allowed categorization of debris into material types: tile, tile & metal, metal, composite and fabric. This process was keyword driven. For example, "HRSI" and "FRCI" would identify a fragment as "High-Temperature Reusable Surface Insulation" or "Fibrous Refractory Composite Insulation Tiles" respectively [5]. Note, if it was both composite and metal, it was categorized as metal.

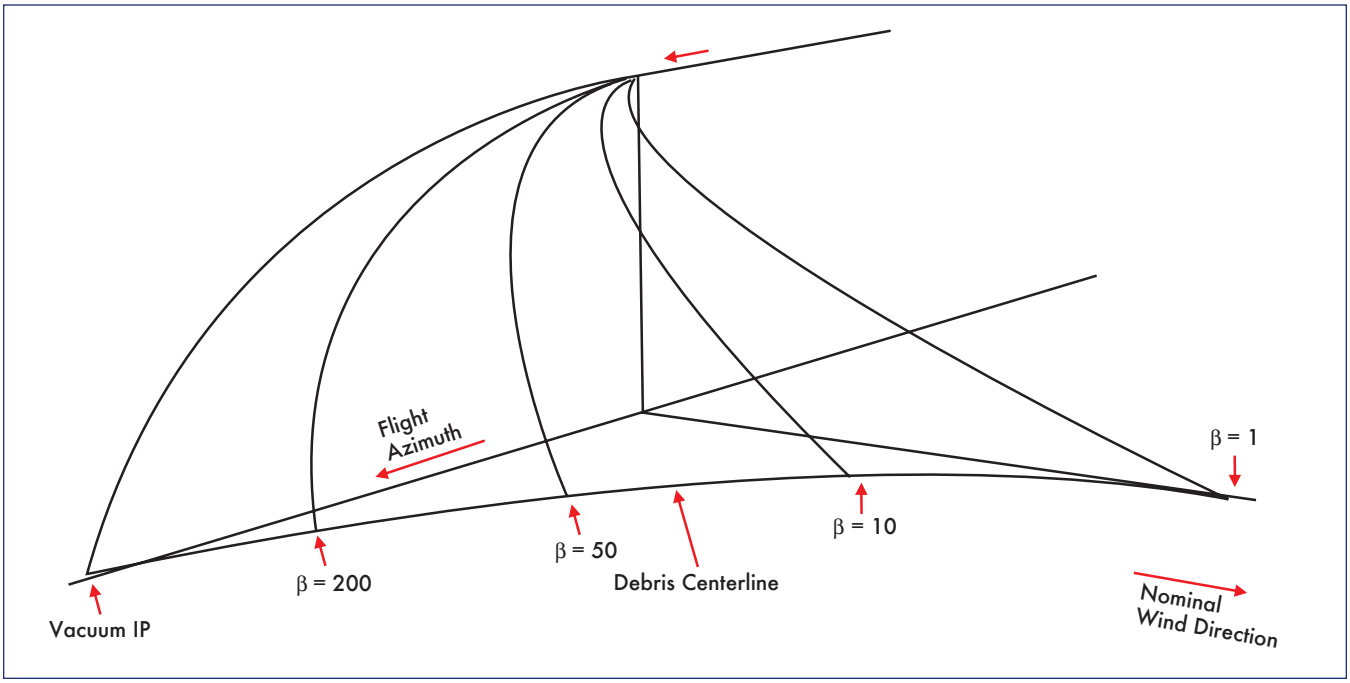


Figure 2-3. The Influence of the Ballistic Coefficient, β, and Wind upon Debris Impact Points.

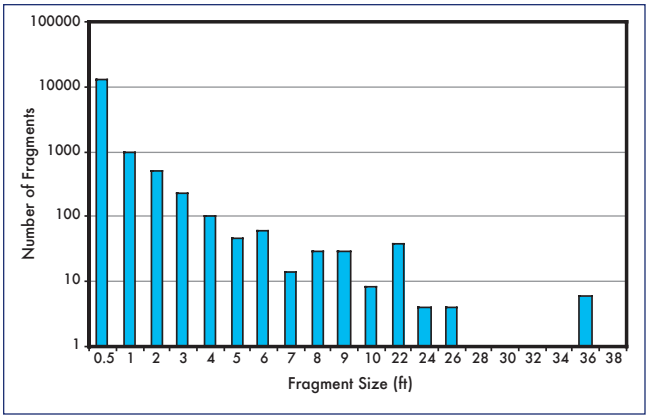


Figure 2-4. Size Histogram of Measured Fragments.

Figure 2-5 contains a flow chart of the rule-based algorithm used to estimate the dimensions and weight of each fragment. Table 2-1 contains the material densities. Several parameters used in these rules were varied to meet the constraint of overall weight. These parameters are the minimum and maximum plate thickness, and empty volume ratios F_1, F_2. (F_1 and F_2 are fractions of the volume defined by the exterior boundaries that contains no material).[2] Although the final values for the minimum and maximum plate thickness may seem unrealistically thin, it can be justified in part by the assumption that many plate fragments may be triangular instead of rectangular in shape and thus have a smaller mass

Material	*Density (lb/ft³)*
Steel	502
Aluminum	168
Graphite/Epoxy	124
HRSI Tiles	22
FRCI Tiles	12
LRSI Tiles	9
Insulation Fabric	9

Table 2-1. Material Densities.

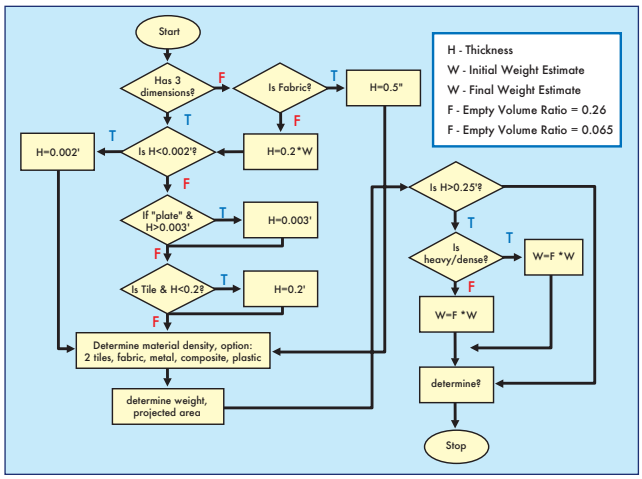


Figure 2-5. Rule Based β (Ballistic Coefficient) Approximation.

that would lead to a smaller thickness for an equivalent rectangular plate having the same length-width dimensions. A plate fragment may also have holes and non-uniform thickness. Furthermore, weight accuracy for individual fragments can be relaxed provided a reasonable weight distribution is found and the overall weight constraint is satisfied.[3] Figure 2-6 shows the β distribution of measured fragments. The distribution appears to be similar to a lognormal distribution with the mean located in the $1 < \beta < 3$ lb/ft^2 category.

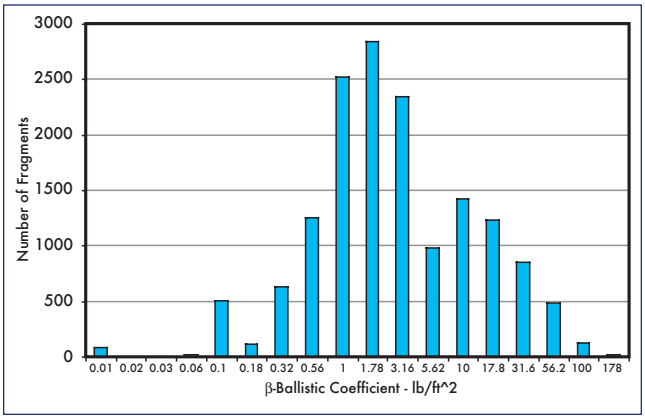


Figure 2-6. Debris List Extracted from Records with at Least Two Dimensions.

2.4 Development of Reference Trajectories

Initial positions and velocities for the reference trajectories were first based on the orbiter's last known state vector at loss of signal. A computer program, TAOS, was used to generate the base trajectories [6]. Each trajectory is configured to have the longest impact range for its debris. Some of the initial positions were subsequently modified to align the footprints with gathered data. For Group 1, the initial position was moved south by 3.2 miles. For Group 3 the initial position was moved south by 11 miles. Final trajectories for all four major fragment groups are plotted in Figure 2-7.

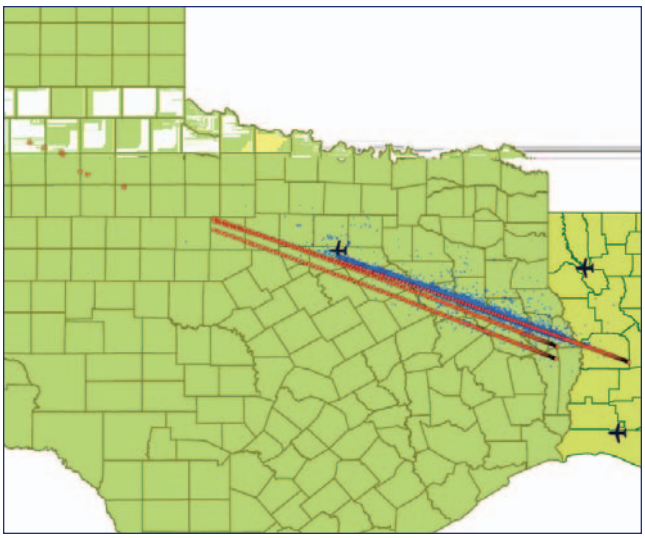


Figure 2-7. Reference Trajectories.

2.5 Development of Breakup State Vectors and Associated Debris Groups

The breakup state vectors are based on a progressive breakup model that initiated at 13:59:30 GMT and spans 120 seconds. 24 debris lists are created for each five-second interval. 5 state vectors are used to cover each five-second interval. Each state vector was assigned a failure probability of 0.2. In other words, each debris group is distributed evenly over a five-second span.

To populate the debris list, a trial run was used to determine the relationship of downrange distance and failure time for each ballistic coefficient, β class (see Figure 2-8). In this study, the Loss of Signal (LOS) point at -99.0413 °E, 32.956 °N is used as the point of origin. Next, the downrange impact distance for each fragment is measured from the same point of origin.

If the approximate size and dimension of a piece of debris were available, a ballistic coefficient is assigned and the relationship shown in Figure 2-8 is used to interpolate for the breakup (shedding) time for the fragment. Fragments without dimensions are assigned ballistic coefficients such that the ballistic coefficient distribution matches that of the fragments with dimensions at a similar downrange distance, and from this a breakup/shedding time. If there is not sufficient information to determine the breakup/shedding time by either of these two means, a low (i.e. 1.7 psf) ballistic coefficient is assigned with the condition that the final total weight of all fragment groups must be equivalent to the recovered weight of debris. Less than 10 percent of all the fragments belong in this category.

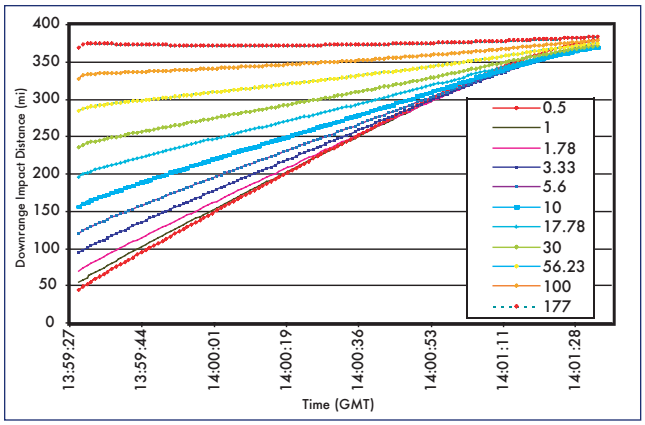


Figure 2-8. Relationship between Downrange Impact Distance and Downrange Time for each Ballistic Coefficient Group (Measured from Loss of Signal).

Figure 2-10 shows the debris model for group 1 for each ballistic coefficient class and breakup time. The ballistic coefficients used start at 0.5 lbs/ft^2 and increase logarithmically in quarter power increments up to 333 lbs/ft^2. Figure 2-11, Figure 2-12, and Figure 2-13 show the debris models for fragment groups 2, 3 and 4 respectively. When compared to other groups, group 4 fragments broke off earlier in the time frame.

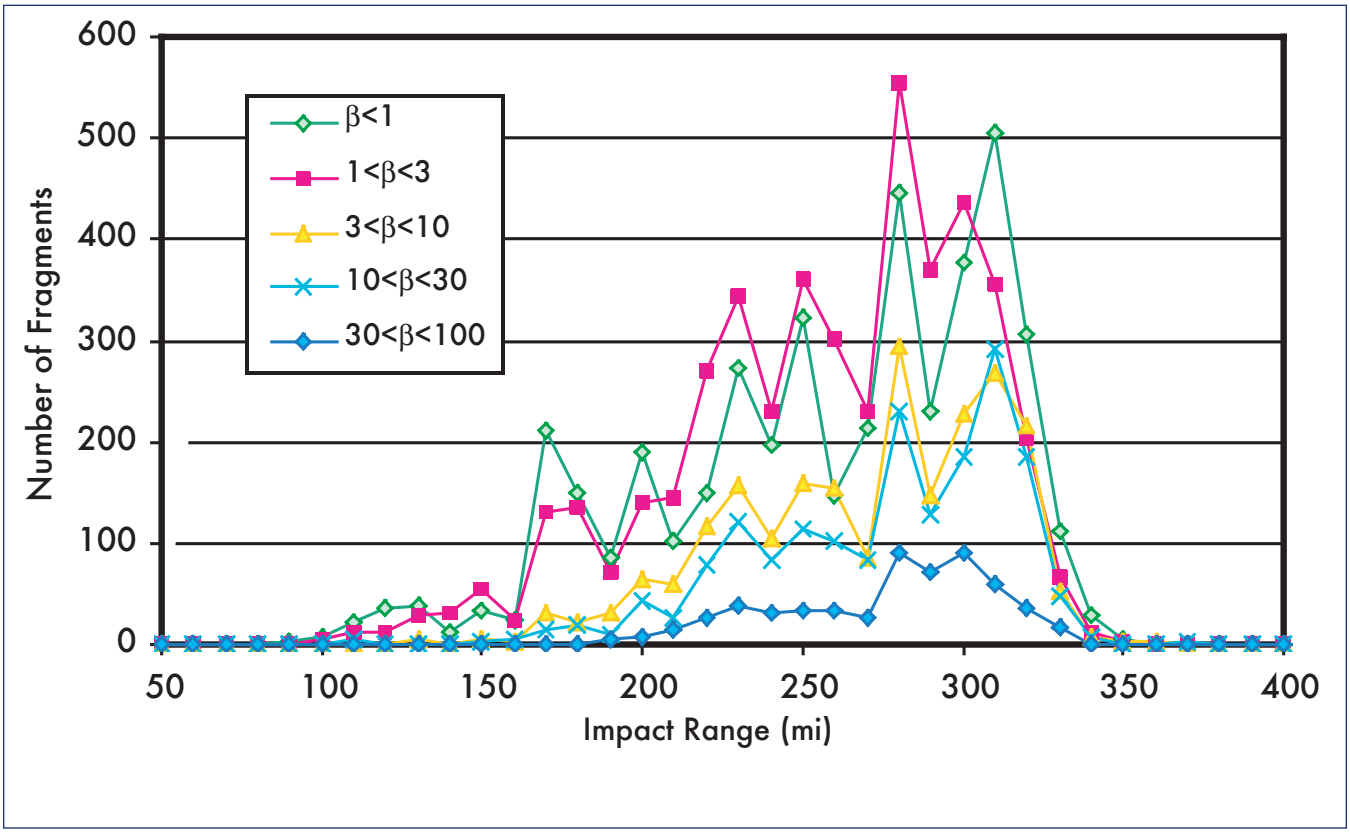


Figure 2-9. Distribution of Debris with Dimension Data as a Function of Impact Range.

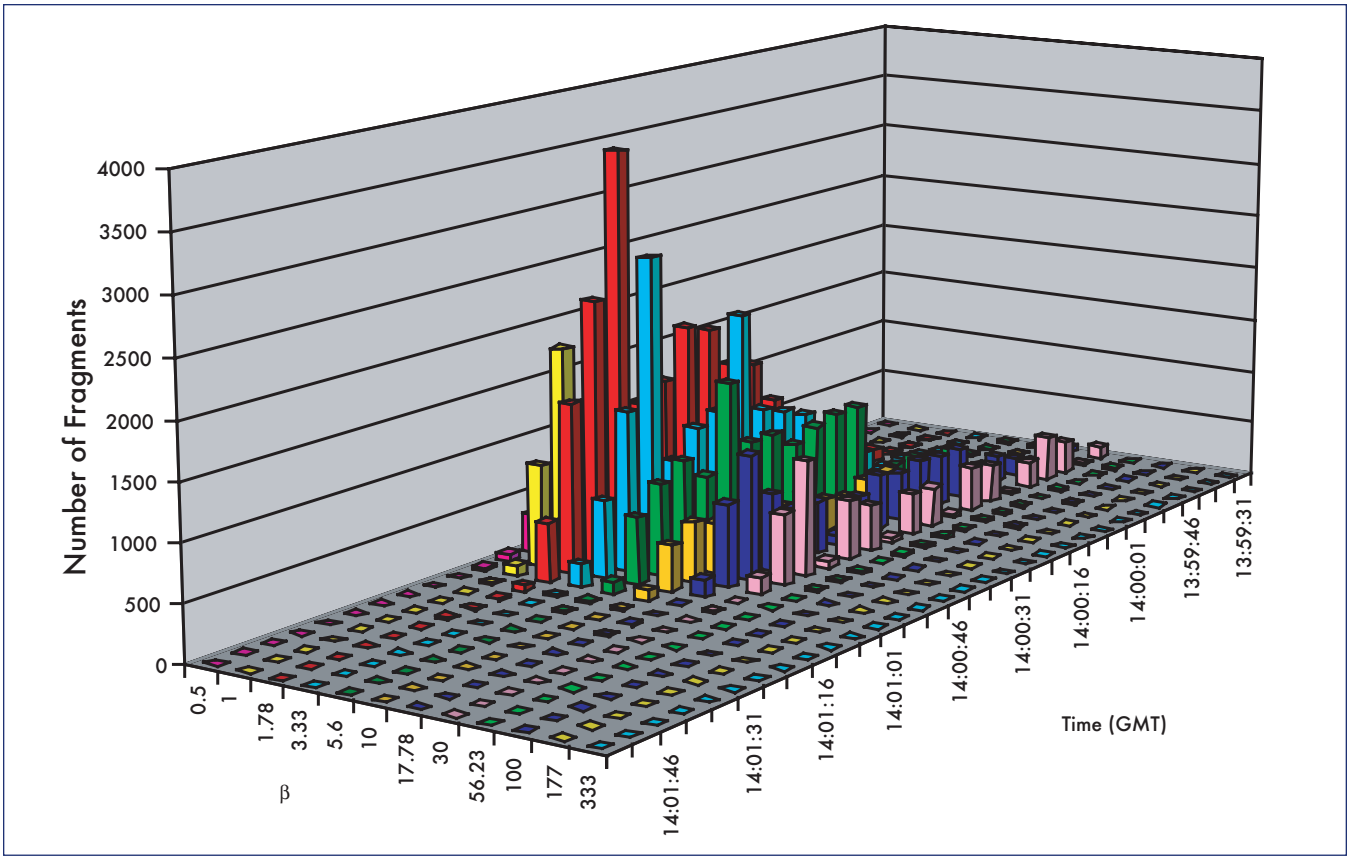


Figure 2-10. Group 1 Debris List.

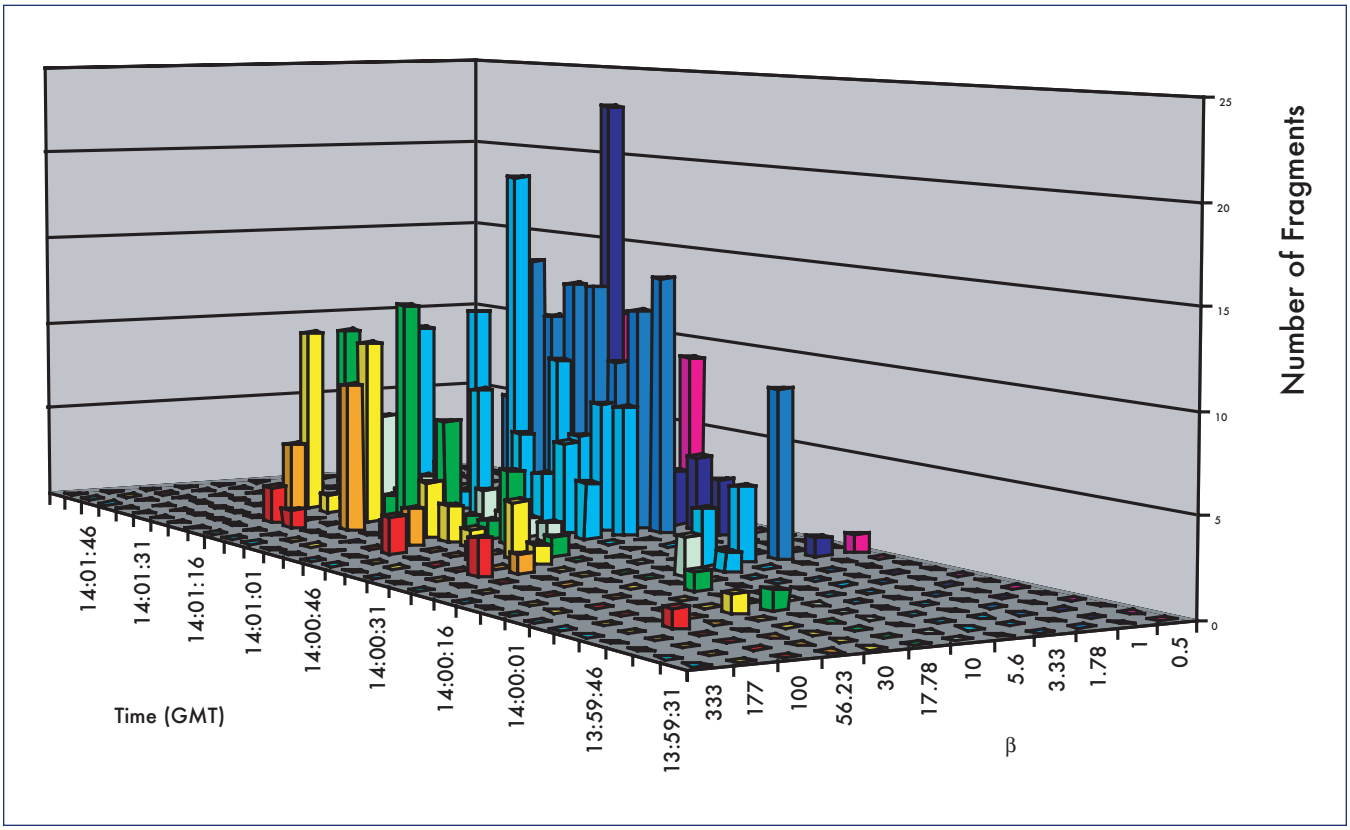


Figure 2-11. Group 2 Debris List.

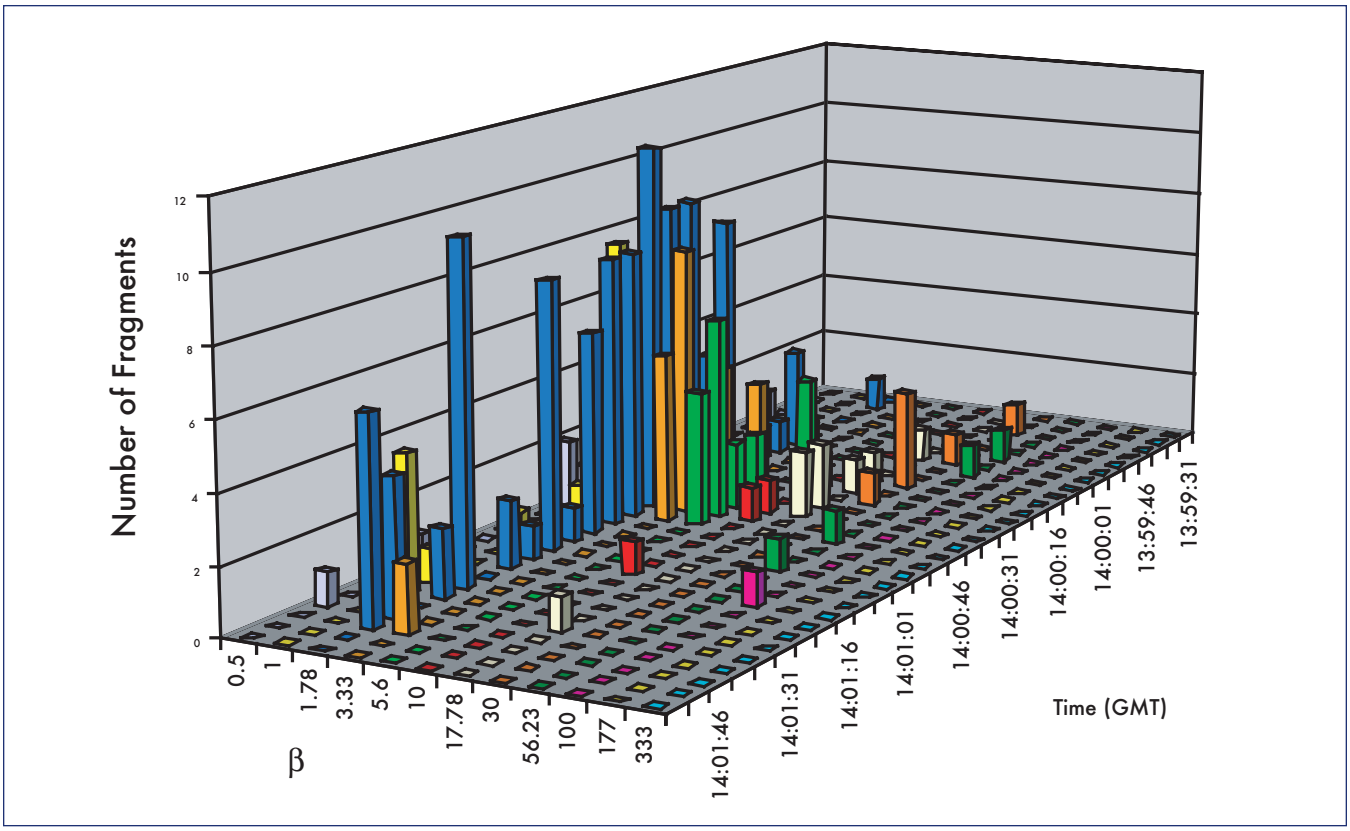


Figure 2-12. Group 3 Debris List.

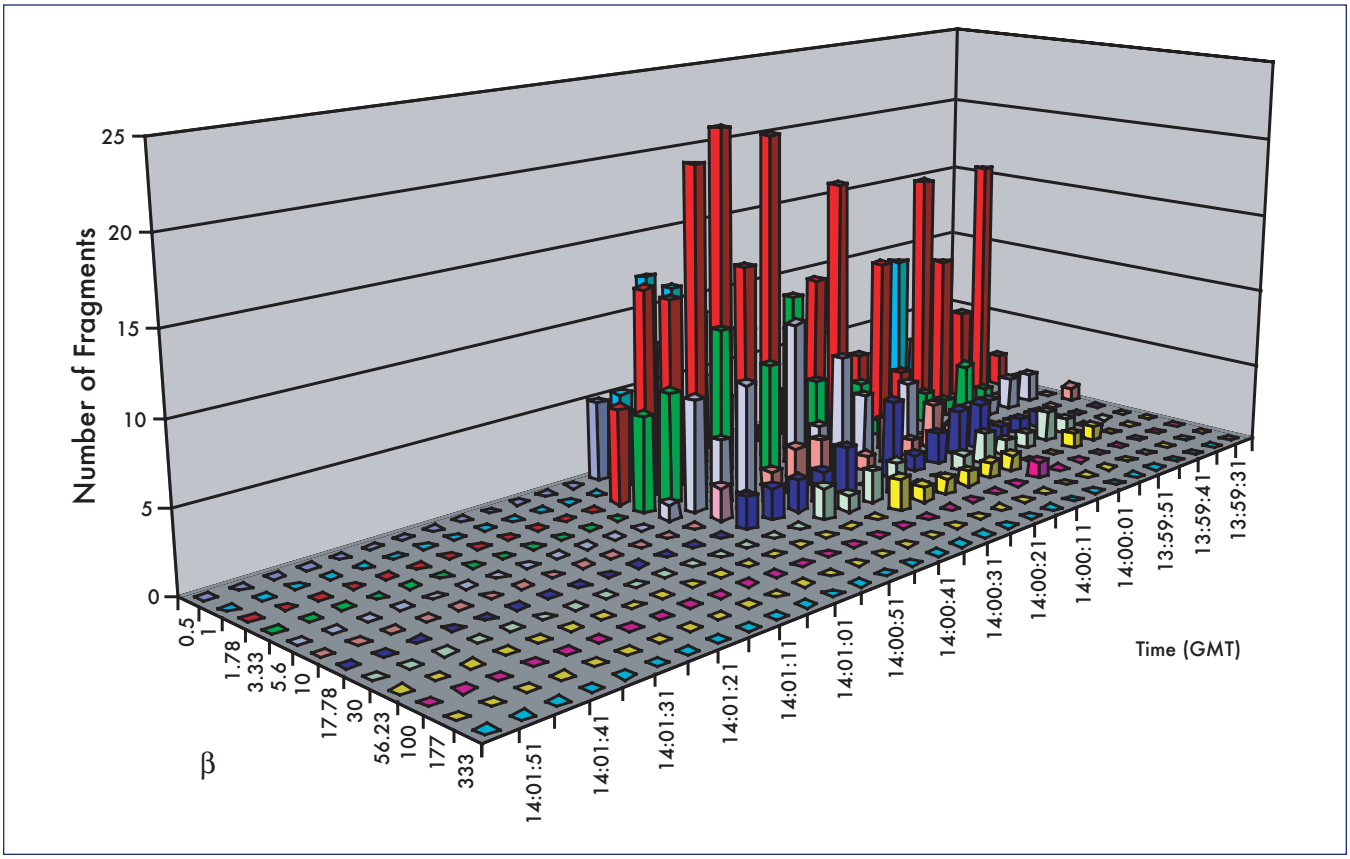


Figure 2-13. Group 4 Debris List.

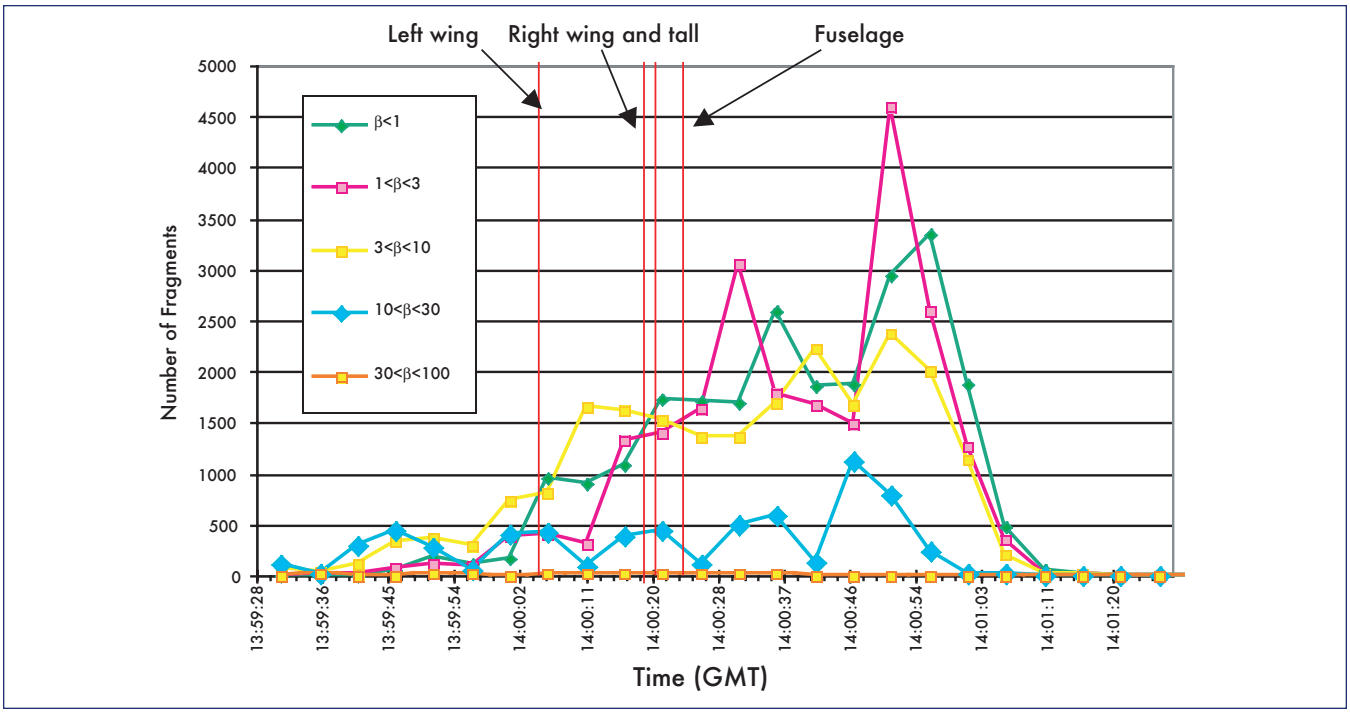


Figure 2-14. Estimated Breakup Model as a Function of Time by Ballistic Coefficient Category.

The breakup model developed to account for the total weight of the recovered debris is plotted in Figure 2-14. The fraction of the highest ballistic coefficient group $30<\beta<100$ lbs/ft^2 is much less prominent when compared to the impact range distribution shown in Figure 2-9 because the fragments without dimensions were not assigned to large weight debris groups in order to meet the overall weight constraint. Because the breakup model would vary if the reference trajectory is varied, it does not reflect the actual time when a fragment separated from the orbiter. It does, however, illustrate the progressive nature of the breakup process, and matches the available data as presented in Section 3.

3. Debris Dispersion

3.1 Basics of Impact Dispersion of Debris

The dispersion of debris impact location associated with a given initial state vector is illustrated in Figure 3-1. The primary sources in the case of the Columbia breakup are the ballistic coefficient, wind and velocity perturbation. The development of these uncertainties is explained in the technical paper describing CRTF included as Appendix A.

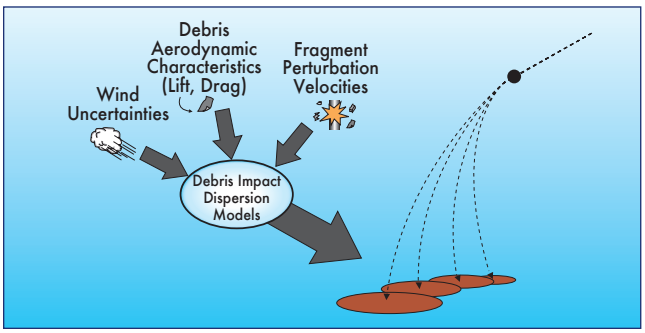


Figure 3-1. Contributions to Debris Dispersion Models.

3.2 Description of CRTF and RRAT

CRTF was developed to estimate the range of free-fall, the mean impact locations and impact dispersions of fragments resulting from a vehicle breakup. Either CRTF's dispersion footprints or the impact probability (P_I) contours can be used to define the hazard areas. CRTF can also define hazard areas as a moving volume in space, thereby providing means for assessing risks to aircraft.

3.3 Computed Dispersion of Debris Using the Breakup Model

Wind data for Feb 1, 2003 was obtained from both the Dallas/Fort Worth and the Shreveport airports. A monthly averaged model was used for atmospheric temperature and density, and for upper atmospheric winds. Probability of impact, P_I, per 1000 square feet for each of the debris group was contoured and is presented in Figures 3-2, 3-3, 3-4 and 3-5 for four debris groups. The combined contours are plotted in Figure 3-6. Figure 3-7 provides a three-dimensional view of the reference trajectories and combined P_I contours. Figures 3-8 and 3-9 compare the dispersion of the gathered debris and the model results in both the downrange and cross-range directions. The standard deviation used for the lift-to-drag ratio was 0.04 for all debris groups. This value produced the best fit to the cross-range dispersion of the debris in Group1. The standard deviation of velocity impulse in Groups 1 to 3 was assumed to be zero and in Group 4 was assumed to be 333 ft/sec respectively.

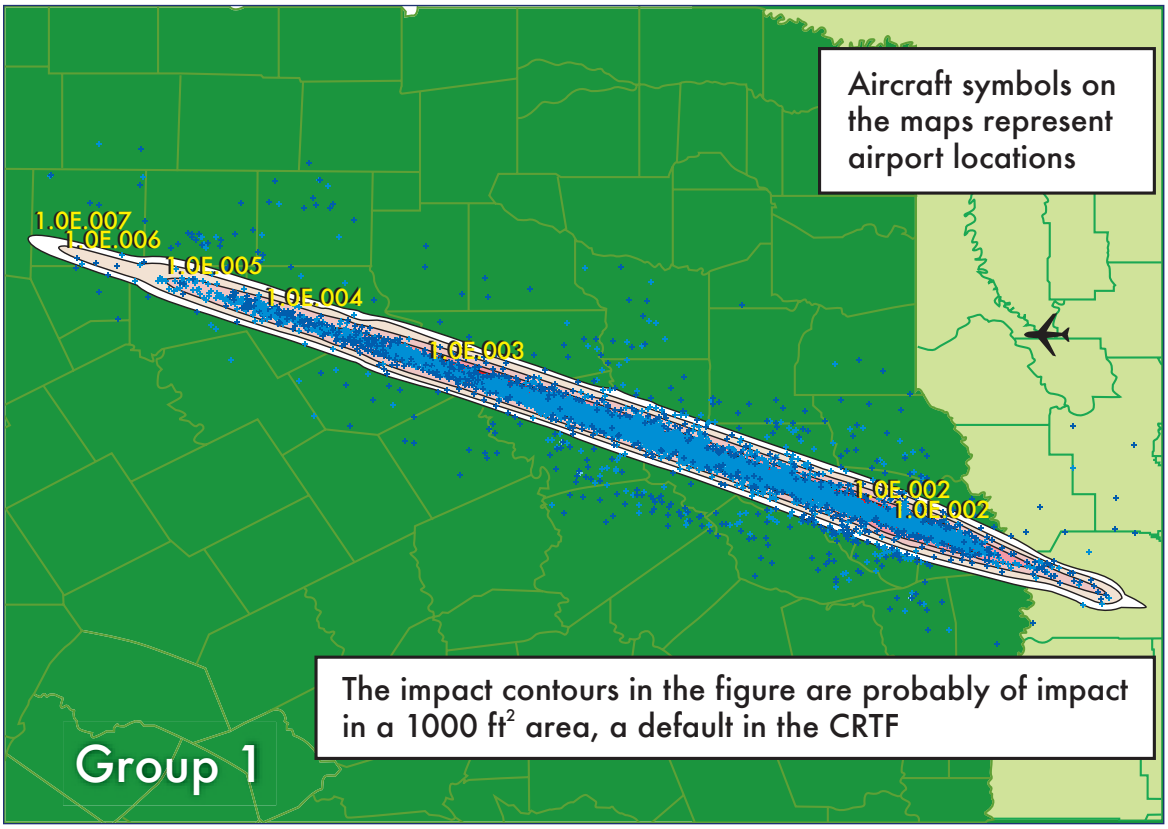


Figure 3-2. Comparison of Gathered Data with Modeled Dispersion (Group 1).

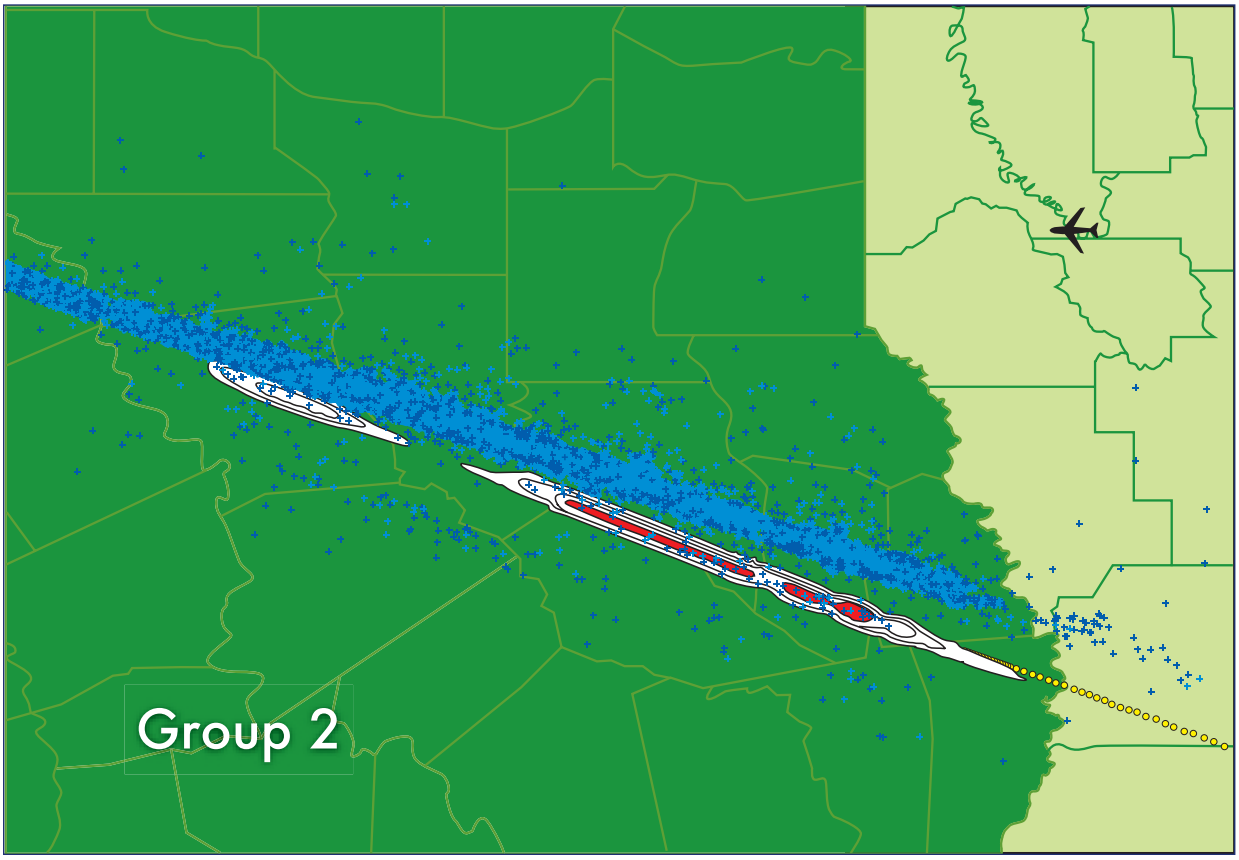


Figure 3-3. Comparison of Gathered Data with Modeled Dispersion (Group 2).

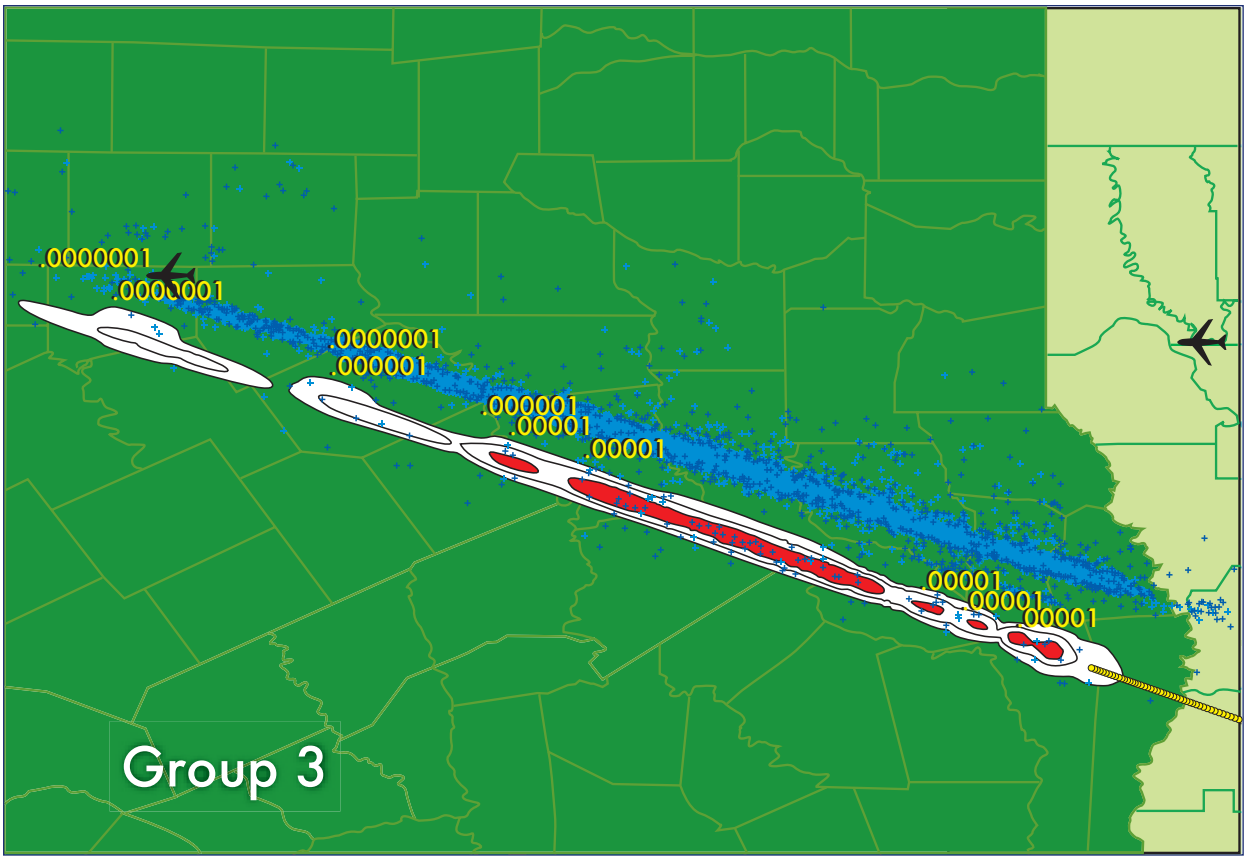


Figure 3-4. Comparison of Gathered Data with Modeled Dispersion (Group 3).

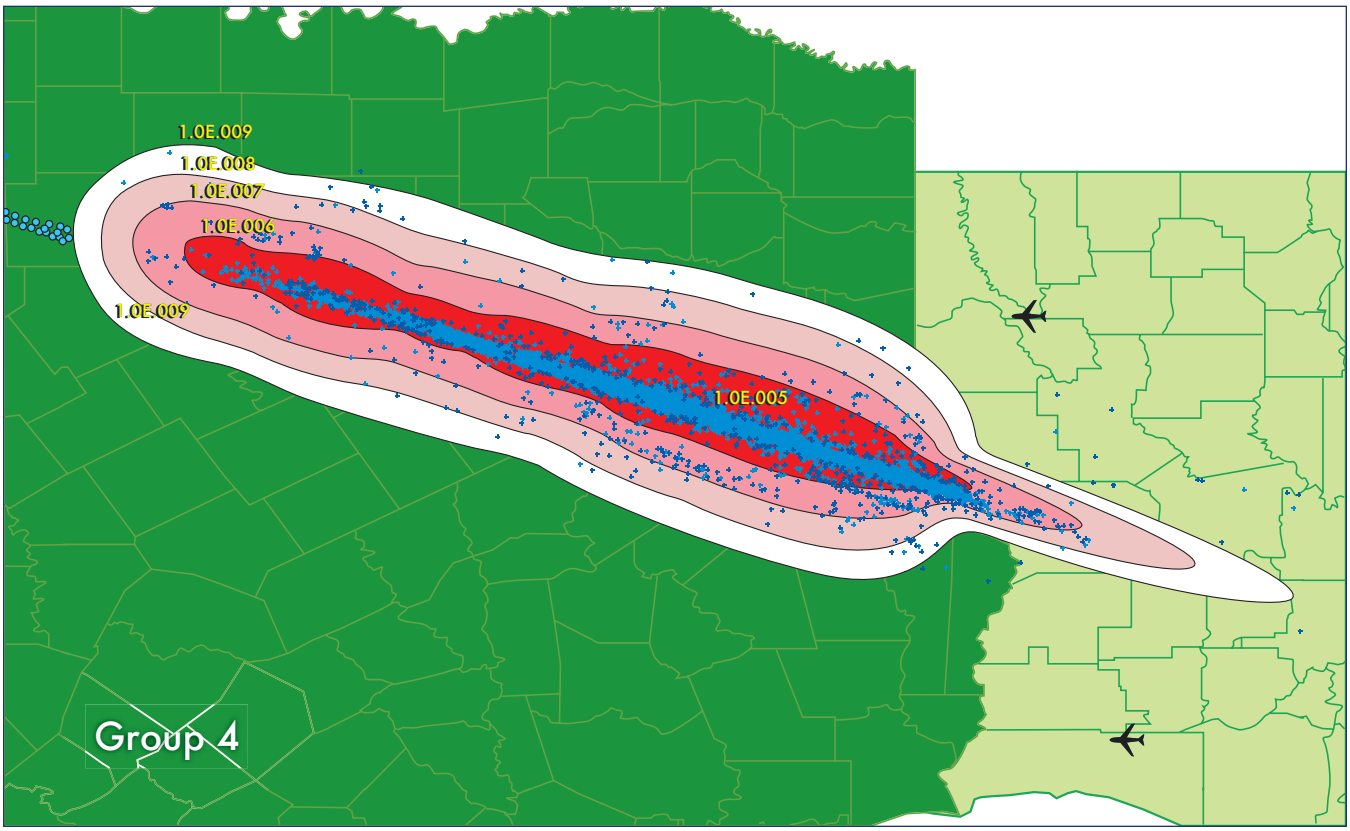


Figure 3-5. Comparison of Gathered Data with Modeled Dispersion (Group 4).

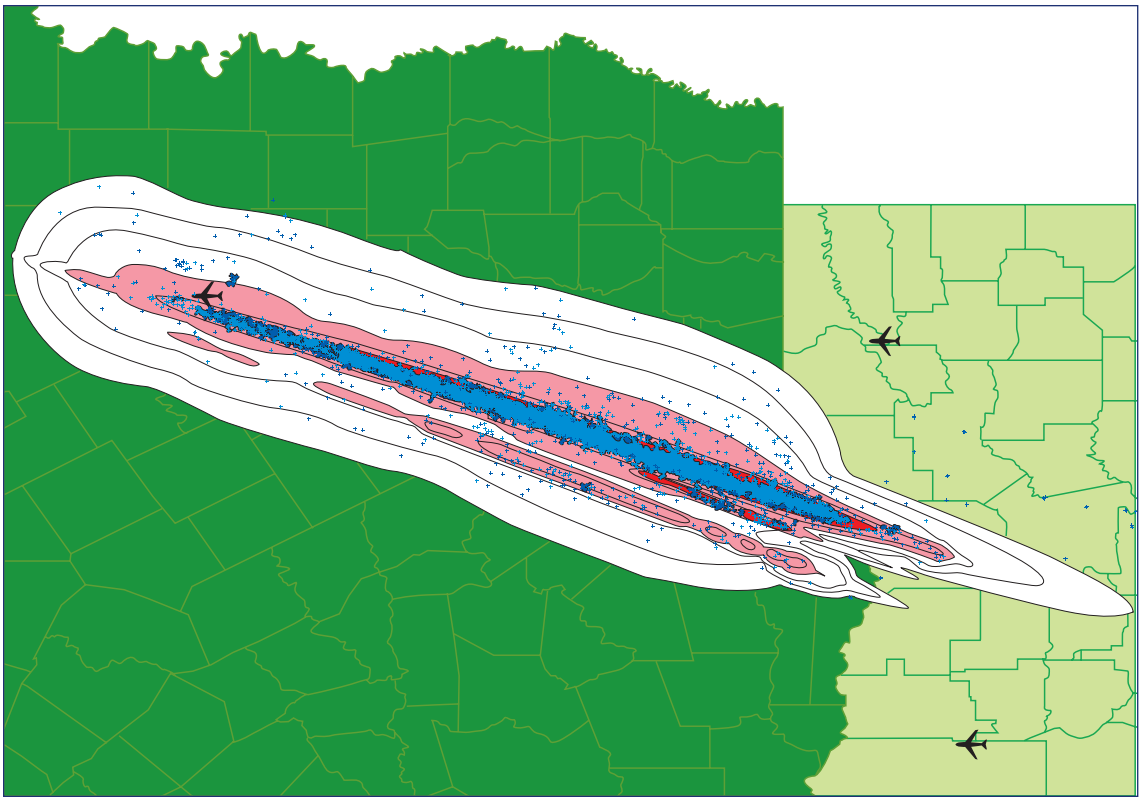


Figure 3-6. Comparison of Gathered Data with Modeled Dispersion (All Groups).

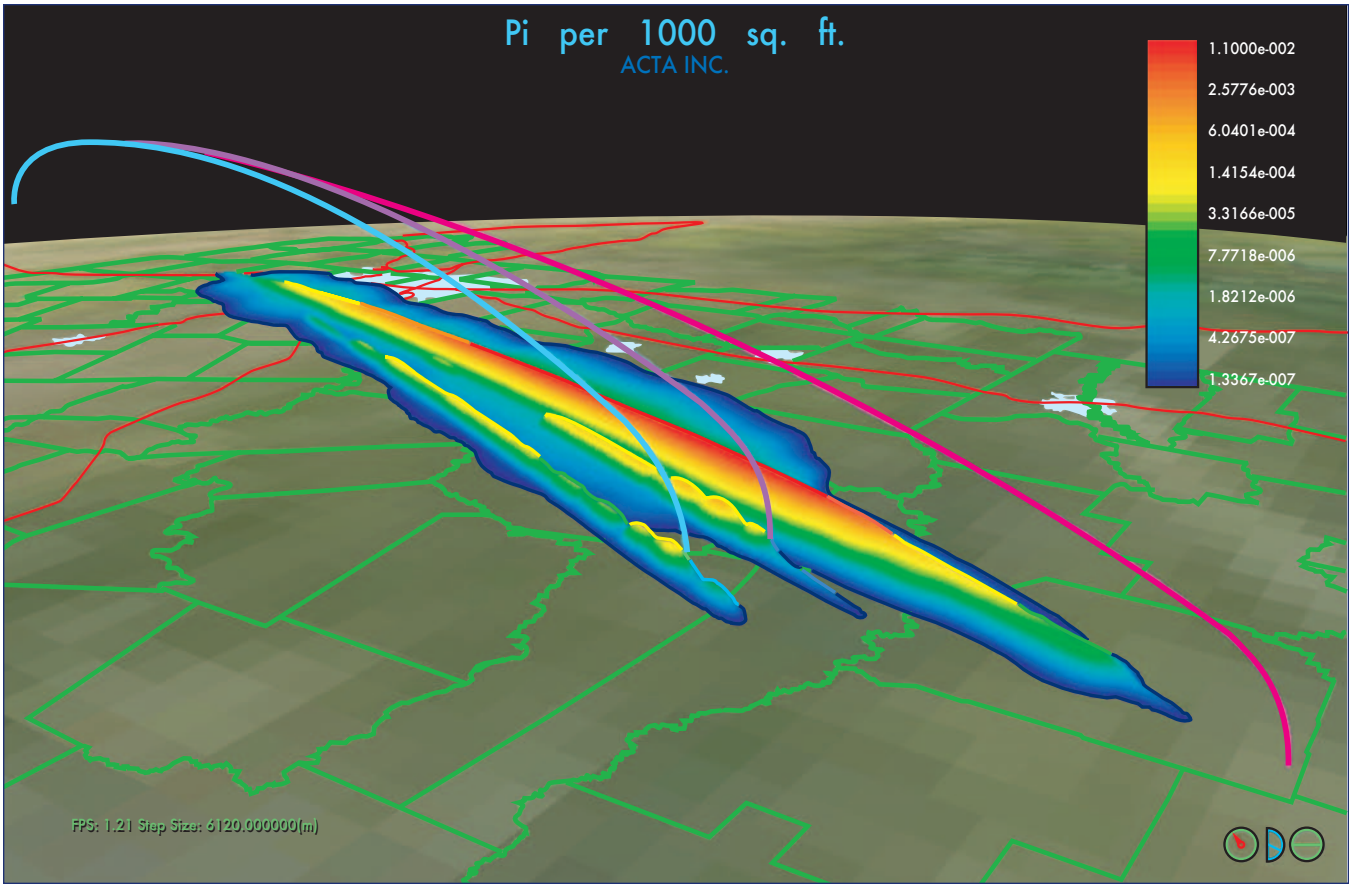


Figure 3-7. Modeled Debris Density in Three Dimensions .

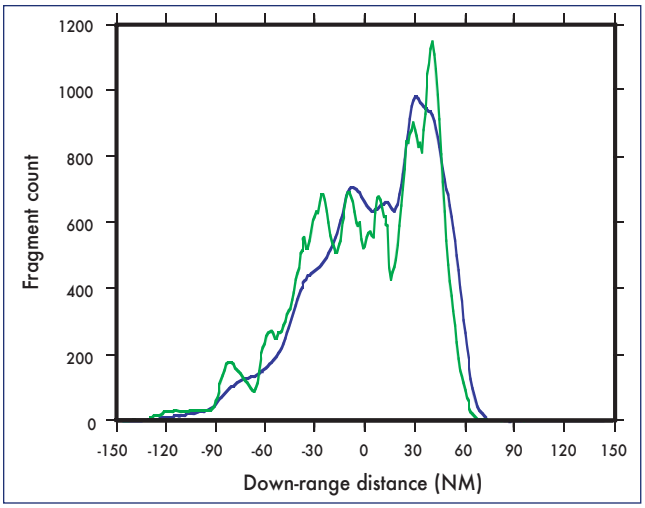


Figure 3-8. Comparison of the Actual Fragment Count (Green) in the Downrange Direction with the Fragment Count in the Reconstructed Model (Blue).

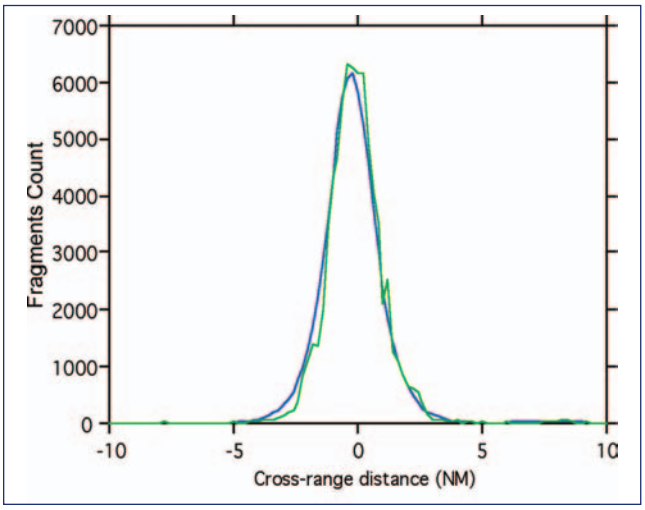


Figure 3-9. Comparison of the Actual Fragment Count (Green) in the Crossrange Direction with the Fragment Count in the Reconstructed Model (Blue).

4. Casualty Model Due To Debris Impacting On People In The Open

4.1 Basic Impact Casualty Model

The estimated threat to people in the open from Columbia debris impacts took into consideration:

1. the angle of impact and of the debris (it is not vertical if there is a ground wind),
2. the possible effect of bounce, roll or secondary breakup,
3. the vulnerability of the body to debris impact.

Table 4-1 gives a summary of the six Abbreviated Injury Scale (AIS) levels from minor to virtually unsurvivable. The AIS scale is used as a measure of severity of injury for individuals arriving at hospital emergency rooms. The term casualty in this study applies to all individuals predicted to sustain an injury that is at AIS level 3 or higher (including fatality). The serious injury level was chosen because it is consistent with the severity levels used by the FAA and the Air Force Eastern and Western Ranges for launch vehicle risk assessments.

AIS Level	Severity	Type of injury
0	None	None
1	Minor	Superficial
2	Moderate	Reversible injuries; medical attention required
3	Serious	Reversible Injuries; hospitalization required
4	Severe	Life threatening; not fully recoverable without care
5	Critical	Non-reversible injury; not fully recoverable even with medical care
6	Virtually Unsurvivable	Fatal

Table 4-1. Abbreviated Injury Scale (AIS).

Figure 4-1 presents the median delineating the region of casualty producing impacts as a function of fragment weight and impact velocity. Note the three injury mechanisms that depend on weight and impact velocity. There is considerable inherent uncertainty in any casualty estimate because the level of injury produced by an impact depends on a variety of factors including the body part impacted, the weight, age and health of the person impacted, as well as the characteristics of the fragment. Thus, in the model, the line separating casualty from non-casualty has an uncertainty represented by a probability density function. These uncertainties are included in the CRTF casualty model used here. The models are based on simulations of actual impacts on dummies with the dummy responses being numerically modeled by a biomechanical computer program to compute different AIS levels.

The casualty area is a primary parameter in the risk computation. The casualty area is the equivalent impact area that will lead to a casualty if a person is struck by a piece of debris with sufficient weight and velocity to cause the person to become a casualty. If the debris is falling vertically, the casualty area is estimated by first taking the maximum projected area of the piece of debris, finding the equivalent radius of the piece and then adding a foot to the radius to represent the radius of the equivalent human. The basic casualty area, A_c, in square feet, for vertical impact is then expressed as

$$A_c = \pi \left(\sqrt{\frac{A_f}{\pi}} + 1 \right)^2 \qquad (4\text{-}1)$$

where A_f is the maximum projected area of the fragment in

square feet.

If a fragment has a horizontal component of velocity, then the velocity and weight must also be evaluated to determine if a person can become a casualty due to being hit horizontally in the head, thorax, abdomen or legs. A vulnerability model is necessary for each of these cases such as that in Figure 4-1. Currently CRTF contains models for the head, thorax and abdomen but not for legs. The abdomen model was extended down to the ankles in this study. As will be seen, the horizontal velocity component does not contribute much in this study because the combined weights and horizontal velocities are rarely sufficient to produce a casualty.

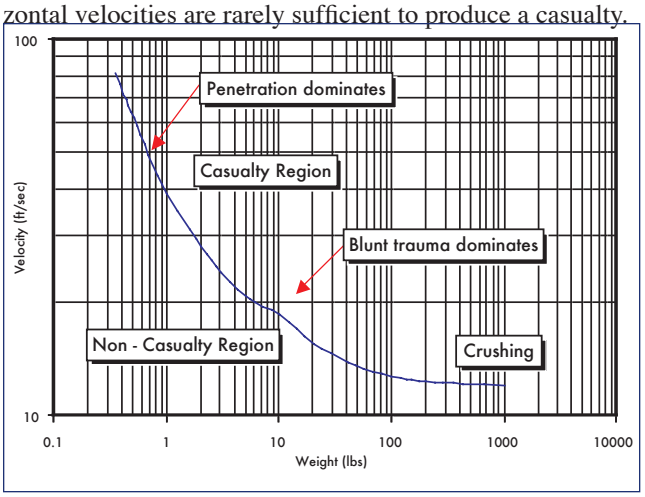


Figure 4-1. Relationship between Casualty (AIS 3) and Fragment Impact Conditions.

If the fragment has a horizontal velocity, and does not directly strike the person, it can bounce, skid or roll and then strike the person. These aspects are also in the CRTF casualty model with the logical treatment illustrated in Figure 4-2. The casualty area for the horizontal component of velocity now uses the height and width of a person with the effective radius of the fragment, $\sqrt{(A_f/\pi)}$, added to the dimensions on three sides. The expanded casualty area accounts for potential hits on the head, thorax and abdomen with separate vulnerability models for each of these body parts. The potential for bounce, skid and roll is strongly dependent upon the firmness of the ground and on the material properties and shape of the impacting fragment. In addition, casualties can result from breakup of the fragment upon impact, especially for high velocity fragments. Because very few fragments from Columbia appeared capable of significant breakup after impact, this effect was not considered in this study.

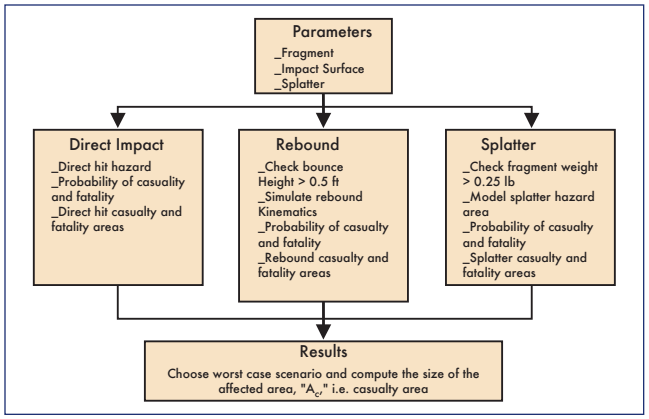


Figure 4-2. General Logic for Computing Casualty Area.

This study assumes that everyone in the open is standing. At eight o'clock in the morning, few are expected to be lying down or sitting, outside. If these positions must be considered, then the CRTF casualty model can be adjusted accordingly.

4.2 Casualty Areas for Representative Debris

Casualty areas, using the logic described in Section 4.1, were computed for all of the debris classes in Figure 2-4. These are presented in Table 4-2 on the next page. Hazard area and fatality area are computed as well. The hazard area covers all cases of impact without injury, non-fatal injury and fatal injury. In addition, the numbers of fragments in each category are included, enabling the computation of total hazard area, casualty area and fatality area.

Notes:

1. The debris list used here is the result of the process of scaling up and adjustment of the debris described in Section 2. This is the same debris list as the one used in the more detailed analysis.
2. Assumed 10 ft/s surface wind, drag coefficient = 0.6, coefficient of restitution = 0.25, kinetic friction coefficient = 0.6, rolling friction coefficient = 0.06.
3. Fragment Category 11 had one high velocity fragment that reportedly did not break on impact (splatter). For purposes of the study, it was assumed that the mechanical energy of impact was converted to TNT (2 lb) and used the overpressure and impulse on the human body to determine equivalent hazard, casualty and fatality areas. The effect of this assumption does not influence the final result because there was only one fragment in this category.

Figure 4-3 contains a histogram showing the distribution of total hazard, casualty and fatality areas among the debris classes.

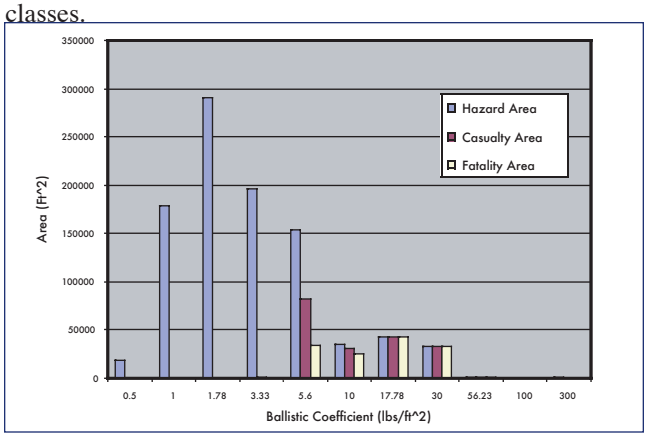


Figure 4-3. Distribution of Total Hazard, Casualty and Fatality Area among the Debris Classes.

	Wf	Af	Beta f	Vf	Theta f	KE f	N		A haz	A cas	A fat	A haz	A cas	A fat
	(lb)	(ft^2)	(lb/ft^2)		(deg.)	(lb-ft)			(ft^2)	(ft^2)	(ft^2)	(ft^2)	(ft^2)	(ft^2)
Frag. Cat.	Ave. Frag. Wt.	Ave. Frag. Area	Ballistic Coeff.	Impact Velocity	Impact Angle	Kinetic Energy	No. of Frags.	Total Wt.	Hazard Area	Casualty Area	Fatality Area	Total Hazard Area	Total Casualty Area	Total Fatality Area
1	0.04	0.143	0.50	22.9	25.9	0.3	1860	80	10.3	0.0	0.0	19160	0	0
2	0.19	0.312	1.00	30.8	19.0	3	11260	2106	15.9	0.0	0.0	179348	0	1
3	0.22	0.204	1.78	40.1	14.4	5	19541	4260	14.9	0.0	0.0	290452	6	8
4	0.37	0.185	3.33	54.0	10.7	17	13846	5109	14.1	0.1	0.0	195888	692	68
5	1.32	0.392	5.60	69.6	8.3	99	10901	14357	14.1	7.6	3.1	154141	82779	33765
6	1.77	0.295	10.00	92.6	6.2	236	4597	8146	7.7	6.8	5.5	35318	31148	25453
7	2.63	0.247	17.78	123.1	4.7	620	6969	18356	6.1	6.1	6.1	42758	42758	42758
8	5.04	0.280	30.00	159.7	3.6	1995	5387	27140	6.1	6.1	6.1	32665	32665	32665
9	9.67	0.287	56.23	218.4	2.6	7166	246	2379	5.9	5.9	5.9	1448	1448	1448
10	4.29	0.072	100.00	291.2	2.0	5648	33	142	4.5	4.5	4.5	150	150	150
11	800	4.444	300.00	504.1	1.1	3157056	1	800	1017.9	113.1	15.4	1018	113	15
Total for all fragments							74641	82874				952346	191760	136332

Table 4-2. Hazard, Casualty and Fatality Areas for People in the Open Based on Recovered Columbia Debris.

5. Exposure And Sheltering Model

The exposure model provides numbers and locations of people at risk on the ground to the impacting debris, and location and density of flying aircraft in the vicinity of the debris during descent. The model of people on the ground considers those both inside and outside of structures and vehicles. In addition, it provides the degree of sheltering offered by roofs and upper floors for categories of structures most likely in the region of debris impact. This is typically called a "population model with sheltering," and this study provides a population model with sheltering for all of Texas and Louisiana, encompassing the area where debris from the *Columbia* was recovered. The probability of impact to aircraft is typically much smaller than the risk to people on the ground, as found in the study of the risks of a return from orbit of a generic lifting entry vehicle [7]. To make an initial approximate estimate of the effects of the debris on aircraft in flight due to this event, an aircraft model was used that is based on the work in a previous unrelated study. This section discusses the details of both the ground and the aircraft model.

5.1 Ground Exposure Methodology

Census data typically provides a reasonably high resolution model of the location of residences. However, it does not provide direct information about structure types needed to estimate sheltering characteristics. It is not cost-effective to survey a large region to determine the types of buildings present. One solution has been to arbitrarily assume a distribution of building types (typically only a couple of types) that applies across the whole region. This type of model usually has little justification, and is obviously not very reliable. Instead, we developed a modeling method that uses "proxy" data, and allows for variation among different places on a very fine scale.

The sheltering model development used four types of data: people counts (i.e. census), demographic/economic statistics, structural/engineering reports or knowledge, and georeferencing information (association of coordinates with named places). For a risk analysis, the resulting database must include three components: a quantitative geographic description of where people are located, a description of the structure types that provide protection to the population, and an allocation of how many people are in each structure type. These all must be in a format and a resolution convenient for risk analysis.

As intermediate steps, a population model (without sheltering), a model of sheltering percentages for each demographic group, and a model of sheltering percentages for each geographic region are developed. The model assumes that a more accurate model of structure types can be developed for a specific demographic category than for everyone at once. The process is outlined in Figure 5-1, where arrows indicate data flow, and double lines indicate linked data elements.

The primary challenge is to develop translations of the demographic information into distributions of people among

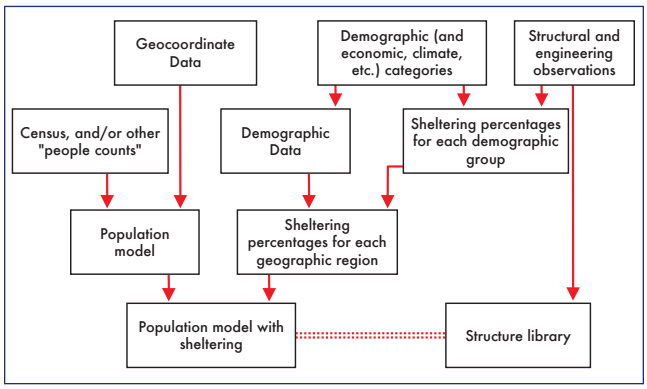


Figure 5-1. Population / Sheltering Modeling Overview.

sheltering types. At a top level, it is assumed that people are always in one of four locations: home, school, in transit [i.e. in cars], or work. The demographic data defines how many people are in each location. In addition, the demographic data for each category typically has some additional information regarding people in each location. For example, typical data for people at work is their occupation. The sheltering percentages are then modeled for each of these data items. For example, it might be assumed that people who are "gardeners" are outside 80% of the time and inside a one-story wood-roof structure 20% of the time during daylight hours. Other occupations have different sheltering distributions. A key assumption of the method is that better estimates of sheltering can be determined by occupation than for generic "working people".

Next, the percentage of people in each occupation is multiplied by the structure distribution for the occupation, and these percentages are summed over structure types. Mathematically, this is a matrix multiplication,

$$\begin{pmatrix} c_1 \\ c_2 \\ \vdots \\ c_m \end{pmatrix} = \begin{pmatrix} O_{11} & \cdots & O_{1n} \\ \vdots & \ddots & \vdots \\ O_{m1} & \cdots & O_{mn} \end{pmatrix} \begin{pmatrix} o_1 \\ o_2 \\ \vdots \\ o_m \end{pmatrix} \qquad (5\text{-}1)$$

where the vector **o** is the percentage of people in each occupation, each row of the matrix **O** has the distribution of structures for an occupation, and the vector **f** is the percentage of people in each structure class. A similar operation is performed for people at home and at school.

Estimating the number of people who are home, work, or school is complicated somewhat because these numbers change with time of day and season. For example, people are usually at work during the day and at home at night. In addition to the day/night difference, two factors differentially locate people: the time of year (especially for students) and weekday/weekend differences. There is little information available regarding these parameters, but reasonable assumptions can be applied to determine how these variations affect the resulting population model with sheltering. For this study, a model appropriate for daytime during a

winter weekend is appropriate. The scenario is implemented in the method by adding four parameters: the percentage of employed people who are actually at work, the percentage of students who are at school, and the percentage of people who are at home but instead are outside, and the percentage of people in transit.

The full method can be summarized by a matrix equation. The sheltering in a population center, **c** (a vector whose elements are the number of people in the sheltering categories), is calculated by:

$$\mathbf{c} = p\{e\mathbf{Oo} + s\mathbf{s} + (1-e-s)[(1-d)\mathbf{Hh} + (0 \quad 0 \quad \cdots \quad d)^T]\}, \tag{5-2}$$

where the "people in the open" structure category is the last element of vector c, and the variables are listed in Table 5-1.

The shelter types for people at work and school are distinguished from those at home. Census data provides detailed information about the prevalence of various types of residential structures, but this detailed data is not provided for non-residential structures.

Variable name	*Description*
p	Population in a given population center
d	Percentage of people at home who are outside (1-d is the percentage of people at home who are inside)
s	Percentage of people in school
e	Percentage of people at work
o, a vector elements o_{ij}	Percentage of people who are at work who are in each occupation category
O, a matrix elements O_{ij}	Percentage of people in each occupation category who are assigned to each sheltering type
s, a vector elements s_{ij}	Percentage of students in school who are assigned to each sheltering type
h, a vector elements h_i	Percentage of housing units in each housing structure category
H, a matrix elements H_{ij}	Percentage of each housing structure category which are assigned to each sheltering type

Table 5-1. Variables for Modeling Sheltering.

For clarity, the equation can be written with expanded notation as:
where there are *i* sheltering categories, *j* occupational categories, and *k* housing structure categories.

Consider a simple example: assume that all people at risk are working and that there are only two occupation categories, office workers and farmers. Also, assume that office workers are always in buildings, and may be in light, medium or heavy sheltering with equal probability (33% in each). Farmers, on the other hand, are usually outside, say 75 percent of the time, and in light structures the remaining 25 percent of the time. If there are 1,000 people in the population center, and 40 percent of the people are farmers and 60 percent are office workers, then the following equation characterizes the sheltering distribution:

$$\begin{pmatrix} c_{Light} \\ c_{Medium} \\ c_{Heavy} \\ c_{Open} \end{pmatrix} = \underset{\text{people}}{1000} \left\{ \begin{pmatrix} 100\% \\ \text{at work} \end{pmatrix} \begin{array}{c|cc} & \textit{Office} & \textit{Office} \\ \hline \textit{Light} & 33\% & 25\% \\ \textit{Med} & 33\% & 0\% \\ \textit{Heavy} & 33\% & 0\% \\ \textit{Open} & 0\% & 75\% \end{array} \begin{pmatrix} 60\% \text{ office} \\ 40\% \text{ farmers} \end{pmatrix} \right\} \tag{5-4}$$

which results in:

c_{Light} = 1,000 * 100% * (33% * 60% + 25% * 40%) = 300 people in light structures,
c_{Medium} = 1,000 * 100% * (33% * 60% + 0% * 40%) = 200 people in medium structures,
c_{Heavy} = 1,000 * 100% * (33% * 60% + 0% * 40%) = 200 people in heavy structures, and
c_{Open} = 1,000 * 100% * (0% * 60% + 75% * 40%) = 300 people in the open.

In this study, there are many more occupations and structure categories than in the example.

5.2 Sheltering Categories

The sheltering model allocates people to buildings, vehicles or to being in the open. Building/ vehicle roofs and building sub-floors provide some level of protection to their occupants from inert debris. ACTA previously developed inert debris roof/floor penetration models [8,9,and 10]. Table 5-2 shows the inert debris roof categories. For most roof types, there are three levels or protection: one for people on the top floor, one for people one floor lower, and one for everyone farther from the roof.

Figure 5-2 shows an example of the level of protection provided by several roof classes. The figure depicts the casualty area of a cubic steel fragment impacting face-on at terminal velocity as a function of fragment weight. The casualty area is the statistically expected area within which

$$\begin{pmatrix} c_1 \\ c_2 \\ \vdots \\ c_i \end{pmatrix} = p\left\{ e \begin{pmatrix} O_{11} & O_{12} & O_{1j} \\ O_{21} & O_{22} \cdots & O_{2j} \\ \vdots & \vdots \ddots & \vdots \\ O_{i1} & O_{i2} \cdots & O_{ij} \end{pmatrix} \begin{pmatrix} o_1 \\ o_2 \\ \vdots \\ o_j \end{pmatrix} + s \begin{pmatrix} s_1 \\ s_2 \\ \vdots \\ s_i \end{pmatrix} + (1-e-s) \left[(1-d) \begin{pmatrix} H_{11} & H_{12} & H_{1k} \\ H_{21} & H_{22} \cdots & H_{2k} \\ \vdots & \vdots \ddots & \vdots \\ H_{i1} & H_{i2} \cdots & H_{ik} \end{pmatrix} \begin{pmatrix} h_1 \\ h_2 \\ \vdots \\ h_k \end{pmatrix} \begin{pmatrix} 0 \\ 0 \\ \vdots \\ d \end{pmatrix} \right] \right\} \tag{5-3}$$

Index	Name	Building Description
0	Open	Exposed people without benefit of an overhead roof
1	Wood-Roof	Wood roof
2	Wood-1st	1st floor beneath roof of wood-framed structure
3	Wood-2nd	2nd floor beneath roof of wood-framed structure
4	Steel-Roof	Steel roof
5	Steel-1st	1st floor beneath steel roof structure
6	Steel-2nd	2nd floor beneath steel roof structure
7	Concrete-Roof	Reinforced concrete roof
8	Concrete-1st	1st floor beneath concrete roof
9	Concrete-2nd	2nd floor beneath concrete roof
10	Light-Metal	Roof of pre-engineered metal structure (or vehicle)
11	Composite	Layered roof made up of light-weight, non-metallic materials
12	Tile-Roof	Tile roof
13	Tile-1st	1st floor beneath tile roof of wood-framed structure
14	Tile-2nd	2nd floor beneath tile roof of wood-framed structure

Table 5-2. Roof Penetration Models.

a person would be seriously injured by a single impacting fragment. In the simplest case, this is the area of a person plus a region around the person to account for the size of the fragment. The casualty area calculation for people within structures must also consider the possibility that the fragment does not penetrate the roof of the structure (i.e., some probability of zero casualty area) and the possibility that when the fragment penetrates the roof, failure of roof elements causes additional debris to fall through increasing the effective casualty area. The casualty area can be less than the area of a person when averaged over all of the impacts of the particular fragment weight because the fragment may only occasionally be able to penetrate the roof and cause an injury. Note that the casualty area is basically zero for fragments that weigh less than one pound at impact with any of these roof types.

The figure depicts casualty areas as a function of fragment weights for six construction types. Both casualty area and

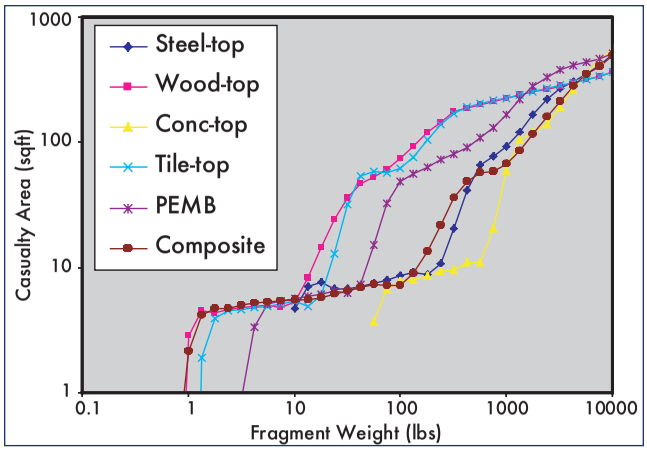


Figure 5-2. Example Casualty Areas for Steel Debris Impacting at Terminal Velocity.

fragment weight are plotted on a logarithmic scale. The "stair step" appearance results from multiple roof failure modes. The lowest "step", smallest fragment weight, results from fragments "punching through" the roof, generating little additional debris. The second "step" results from failures of joists causing a larger amount of roof structure to impact the floor below. The final "step" results from more massive structural failure in which the impacting fragment brings down substantial amounts of roof debris.

The figure illustrates the difficulty in answering the question of which roof provides the most protection without specifying the particular fragment characteristics. For fragments weighing up to a few thousand pounds, concrete offers the greatest amount of protection, followed by steel, pre-engineered metal (PEMB), tile, and finally wood. By contrast, for the more massive fragments, the order is altered because the impacting fragments cause partial or total roof collapse. The collateral damage of roof debris increases the casualty area according to the weight of the roof materials; concrete debris creates much larger casualty areas than the corresponding wood debris.

5.3 Data

The 2000 U.S. Census [11] provides a great wealth of data applicable to this study. It is complete (covers the entire area), detailed (small geographic regions), and has many data items that can be used to estimate sheltering. The Census "Summary File 3" (SF3) contains the demographic data useful for this work; and data is indexed by a unique table number (such as P31) and element number (such as P031001). There are several steps involved in making use of the data:

- Determining the demographic data items that will be useful for determining sheltering for homes, occupations, and/or schools, and the data used to calculating the percentages of people at school and at work.
- Developing translation tables (matrices **O** and **H** above) based on the demographic data items retrieved.
- Retrieving and geo-referencing all the necessary data.

This section details each of these topics.

5.3.1 Choosing Census Data Items

First, the choice of census data items must be made. There are many tables in the U.S. census, but for only a few is there a likely correlation with structure type. Based on a review of all the census tables, those most helpful to determine building distributions for people in different activities were selected. This section details which census tables were chosen, and how they are used to compute the values for sheltering. The tables which are used to translate from census category to structure type are discussed in the next section.

The census table "Units in Structure" (SF3, table H30) can be used to infer structure type for people at home. Building size is typically correlated with a structure type. For example, most single-family residences are wood frame buildings with wood or tile roofs. The data item "1 unit in structure" would correspond to a single-family residence. Likewise, large apartment complexes are likely to be multi-story structures. For the "50+ units in structure," most buildings have steel or concrete roofs and have many stories. The number of people at home is computed by subtracting the number of people at work and at school from the total population, and it can vary by scenario. The percentage of people who are outside while they are at home varies is assumed to be 20% for daytime on a weekend in the winter.

Estimating the total number of people at work is somewhat complicated. However, only a small percentage people are likely at work on a Saturday morning—2% of the working population is assumed for this study. Therefore, risk estimates are not very sensitive to the building distribution of people at work. A detailed algorithm was used to determine the allocation of working people to structure categories based on occupation [7], but is not described here. Similarly, only a small percentage of people are in school on a Saturday morning. In this study, 2% of the enrolled school population is assumed to be at school.

In addition, in the 2000 Census, there is a category of people in "Group Quarters" (SF3, table P9, item P009025). This population includes institutionalized and non-institutionalized people. For this study, these people tallied separately from people in other categories. They are always counted as being protected by the "group quarters" structure distribution (i.e. it is assumed they are never in an occupation or in school).

5.3.2 Translation to Building Types

Engineering judgment was applied in order to develop translations from demographic data to building distributions. Using their experience from looking at buildings and developing sheltering models, several experts independently estimated building distributions for each census category. In order to simplify the process, each expert chose several roof types and a height distribution for each roof type. These estimates were compared, and discrepancies discussed. The resulting translation from demographic data item to structure distribution is shown in Table 5-3 for people at home, Table 5-4 for people at work, and Table 5-5 for people at school

	Roof Type														
Census Category	1	2	3	4	5	6	7	8	9	10	11	12	13	14	Car
Group quarters	29.8	12.9	2.3	4.3	2.8	3.0	6.4	4.1	4.5			16.6	7.2	1.3	5.0
1-detached	57.0	3.0	0.0									28.5	1.5	0.0	10.0
1-attached	57.0	3.0	0.0									28.5	1.5	0.0	10.0
2 units	54.8	5.3	0.0									27.4	2.6	0.0	10.0
3 or 4 units	48.6	9.6	1.8									24.3	4.8	0.9	10.0
5 to 9 units	29.8	12.9	2.3	5.4	2.8	1.7	5.4	2.8	1.7			16.6	7.2	1.3	10.0
10 to 19 units	26.5	11.5	2.0	8.2	4.2	2.6	8.2	4.2	2.6			13.3	5.8	1.0	10.0
20 to 49 units	20.2	8.2	1.6	11.1	6.9	7.0	11.1	6.9	7.0			6.7	2.7	0.5	10.0
50 + units	12.6	6.6	0.8	7.3	6.7	15.9	9.2	7.5	13.3			6.3	3.3	0.4	10.0
Mobile home	42.8	2.3	0.0							45.0					10.0
Boat, RV, van, etc.	42.8	2.3	0.0							45.0					10.0

Table 5-3. Translation Table for Houses/Apartments

	Roof Type															
Census Category	0	1	2	3	4	5	6	7	8	9	10	11	12	13	14	Car
Management occupations, except farmers and farm managers		11.7	6.5	1.8	7.7	6.4	10.9	9.0	7.0	9.0		20.0	5.6	3.0	0.3	1.0
Farmers and farm managers		28.5	1.5	0.0							25.0	20.0				25.0
Business operations specialists		11.7	6.5	1.8	7.7	6.4	10.9	9.0	7.0	9.0		20.0	5.6	3.0	0.3	1.0
Financial specialists		11.7	6.5	1.8	7.7	6.4	10.9	9.0	7.0	9.0		20.0	5.6	3.0	0.3	1.0
Computer and mathematical occupations		11.7	6.5	1.8	7.7	6.4	10.9	9.0	7.0	9.0		20.0	5.6	3.0	0.3	1.0
Architects, surveyors, cartographers, and engineers		11.7	6.5	1.8	7.7	6.4	10.9	9.0	7.0	9.0		20.0	5.6	3.0	0.3	1.0
Drafters, engineering, and mapping technicians		11.7	6.5	1.8	7.7	6.4	10.9	9.0	7.0	9.0		20.0	5.6	3.0	0.3	1.0
Life, physical, and social science occupations		11.7	6.5	1.8	7.7	6.4	10.9	9.0	7.0	9.0		20.0	5.6	3.0	0.3	1.0
Community and social services occupations		11.7	6.5	1.8	7.7	6.4	10.9	9.0	7.0	9.0		20.0	5.6	3.0	0.3	1.0
Legal occupations		11.7	6.5	1.8	7.7	6.4	10.9	9.0	7.0	9.0		20.0	5.6	3.0	0.3	1.0
Education, training, and library occupations		20.9	5.3	3.8	16.3	8.4	5.2	16.3	8.4	5.2		5.0	2.7	1.2	0.2	1.0
Arts, design, entertainment, sports, and media occupations	20.0	17.7	2.4	0.0	8.7	7.0	9.3	8.7	7.0	9.3						10.0
Health diagnosing and treating practitioners and technical occupations		12.0	6.8	1.3	8.6	7.4	13.9	8.7	7.0	9.3		15.0	5.6	3.1	0.3	1.0
Health technologists and technicians		12.0	6.8	1.3	8.6	7.4	13.9	8.7	7.0	9.3		15.0	5.6	3.1	0.3	1.0
Healthcare support occupations		12.0	6.8	1.3	8.6	7.4	13.9	8.7	7.0	9.3		15.0	5.6	3.1	0.3	1.0
Fire fighting, prevention, and law enforcement workers, including supervisors	20.0	1.3	0.6	0.1	9.9	4.3	0.8	16.6	7.2	1.3		2.0	0.7	0.3	0.1	35.0
Other protective service workers, including supervisors	10.0	1.3	0.6	0.1	16.6	7.2	1.3	26.5	11.5	2.0		2.0	0.7	0.3	0.1	20.0
Food preparation and serving related occupations		34.6	4.2	0.2	8.5	5.5	6.0	8.5	5.5	6.0		5.0	13.2	1.7	0.1	1.0
Building and grounds cleaning and maintenance occupations	20.0	24.4	2.6	0.1	7.7	5.0	5.4	7.7	5.0	5.4		1.0	0.7	0.3	0.1	15.0
Personal care and service occupations		34.6	4.2	0.2	8.5	5.5	6.0	8.5	5.5	6.0		5.0	13.2	1.7	0.1	1.0
Sales and related occupations		33.8	5.0	0.2	7.6	5.6	6.9	7.6	5.6	6.9		5.0	12.9	2.0	0.1	1.0
Office and administrative support occupations		12.7	6.0	1.4	10.3	7.8	11.9	10.2	6.9	7.9		15.0	5.9	2.7	0.4	1.0
Farming, fishing, and forestry occupations	50.0	4.8	0.3	0.0	0.5	0.0	0.0	0.5	0.0	0.0	5.0	5.0	4.8	0.3	0.0	29.0
Supervisors, construction and extraction workers		12.7	6.0	1.4	10.3	7.8	11.9	10.2	6.9	7.9		15.0	5.9	2.7	0.4	1.0
Construction trades workers	40.0										20.0					40.0
Extraction workers	40.0										20.0					40.0
Installation, maintenance, and repair occupations	20.0	24.9	4.6	0.5	7.2	4.7	5.1	6.8	4.4	4.8		1.0	0.7	0.3	0.1	15.0
Production occupations		3.2	1.6	0.2	10.8	2.9	0.3	15.4	4.2	0.4	50.0	5.0	3.2	1.6	0.2	1.0
Supervisors, transportation and material moving workers	30.0										50.0					20.0
Aircraft and traffic control occupations	10.0				23.6	5.6	0.8	23.6	5.6	0.8						30.0
Motor vehicle operators	10.0															90.0
Rail, water and other transportation occupations	25.0										25.0					50.0
Material moving workers	33.3										33.4					33.3

Table 5-4. Translation Table for Occupations.

	Roof Type															
Census Category	0	1	2	3	4	5	6	7	8	9	10	11	12	13	14	Car
Group Quarters	varies	29.8	12.9	2.3	4.3	2.8	3.0	6.4	4.1	4.5			16.6	7.2	1.3	5.0
Schools	15.0	34.2	3.3	0.0	9.3	4.8	3.0	9.3	4.8	3.0	0.0	4.3	7.7	0.8	0.0	0.9

Table 5-5. Translation Table for Schools and Group Quarters

and in group quarters. These tables are used in Equation (5-2) to calculate the overall building distribution.

5.3.3 Retrieving and Correlating Data

Two other census elements are necessary: the geographic coordinates and the population counts. The census data is organized by records, with each record specifying some geographic area. The records are organized by summary level, which describes the type of geographic entity. For example, one summary level is "county" and another is "state". Each record can be correlated to a particular geographic region by matching the appropriate data fields with the attributes in the census cartographic boundary files for the correct summary level.

For a population model, it is important to choose the geographic region size appropriately. Once the regions are small compared to the debris dispersions, it is not cost-effective to choose smaller regions. In addition, there is inherent uncertainty in applying the census data, due to commuting, visitors, etc. The smallest geographic entity in the U.S. Census is the "block group", and a population model composed of all block groups is the highest resolution. However, block group size is based on population, so higher density regions (cities) have very small block groups. This is unnecessary detail for a risk analysis. A dual solution is used in this study. The "census designated places" (CDPs, with summary level=160) account for higher density locations, and these are also convenient because they correspond uniquely to named places. However, rural areas are not included within summary level 160 (since they are not CDPs). Outside of CDPs, block groups are used (level 090/091). These are selected by selecting only records with level 090/091 which have the field Place=99999, which indicates they are outside of a CDP. This solution offers a good balance between the number and size of population regions.

The census summary files include also the "GEO" table, which provides some data used to develop the population model. This includes an interior point (latitude/longitude, which is the approximate geographic center), a name, and the area (excluding water) for each geographic entity. While this data is also in the cartographic files, it requires more processing to extract, so therefore the data from the GEO table is used when creating the model. The GEO table also provides the total population for each entity (POP100) field, and this value is used to multiply by the sheltering percentages determined for each region (value p in Equation (5-2)).

5.4 Resulting Ground Exposure Model

The resulting population model with sheltering is shown in Figure 5-2, along with polygons to show the major debris regions. The blue region shows the main debris field where over 97% of all recovered debris was found. The green region shows a region where all credible Columbia debris was found—a few obvious erroneous coordinates have been excluded. The population map represents each population center as a square, with the size corresponding to the area of the population center, and the color the density of people in the region. Some population centers overlap others, as some census regions completely encircle others. Dallas/Ft. Worth can be easily seen just above the left edge of the blue region, and Houston is at the bottom center of the region.

The population model with sheltering includes all of the population and all of the area of Texas and Louisiana. It includes nearly 10,000 population centers, accounting for over 25 million people. The population is allocated to 16 sheltering categories in each population center. The average distribution of the population to the sheltering categories is shown in Table 5-6. A total of 18.7% of the people are in the open, and 70% are sheltered only by light structures (cars, wood/tile roofs, composite roofs).

Structure Type	*Percentage*	*Structure Type*	*Percentage*
Wood-Roof	39.9%	*Concrete-Roof*	1.5%
Wood-1st	3.1%	*Concrete-1st*	1.0%
Wood-2nd	0.3%	*Concrete-2nd*	1.1%
Steel-Roof	1.4%	*Tile-Roof*	18.1%
Steel-1st	0.9%	*Tile-1st*	1.5%
Steel-2nd	1.3%	*Tile-2nd*	0.1%
Light Metal	3.2%	*Car*	7.1%
Composite	0.8%	*Open*	18.7%

Table 5-6. Average Sheltering Distribution.

5.5 Aircraft Exposure Model

In order to determine the risks to aircraft, the probability of debris hitting a particular size aircraft at a particular speed must be calculated. Just as for population on the ground, the type of structure is important for determining risks. However, for aircraft, the strength is not the relevant parameter, because in this study, all parts of all aircraft are vulnerable to all potential debris. However, the probability of a debris impact with aircraft increases with aircraft size and with speed. Therefore, a large commercial aircraft (i.e. a Boeing 747) is the most likely to be impacted by debris. However, there are typically many fewer larger aircraft than small in any given

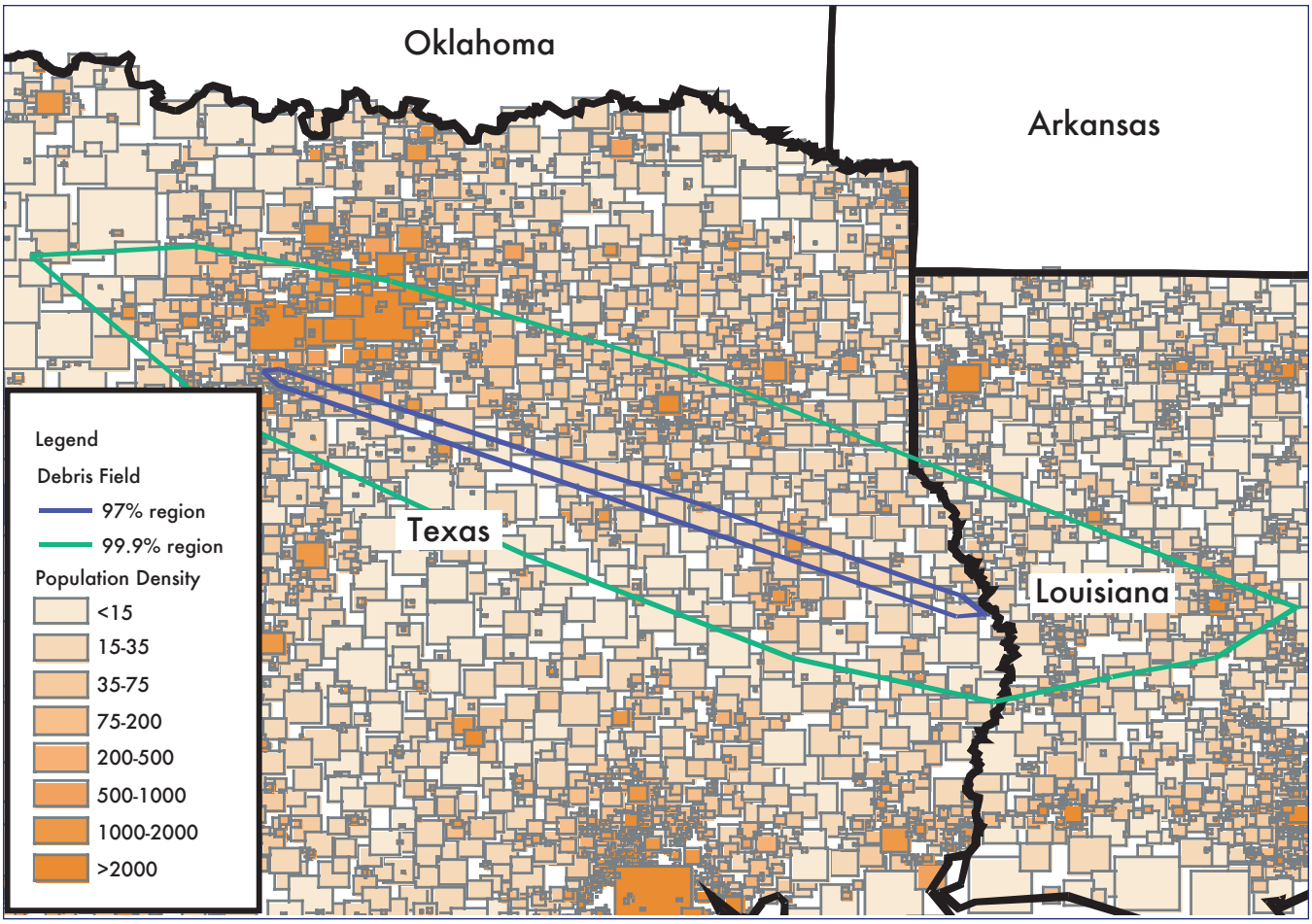


Figure 5-3. Population Model and Impact Area Defined by Recovered Debris.

region. Therefore, it is also instructive to determine the risks to a small private aircraft (such as a Cessna 172). The parameters used for the impact analyses with these two types of aircraft are shown in Table 5-7.

The density of aircraft is determined from the results of a previous study [7]. A complex procedure with data from all airports was used to determine density of aircraft in California as a function of location and altitude. For this study, it was assumed that the aircraft density in the debris field would be similar to the Central Valley of California. Like this region, the region of the debris field is relatively rural. Also, the Central Valley is near to a large metropolitan area (Los Angeles & San Francisco Bay Area), and the debris field is near to Dallas/Ft. Worth. For simplicity, the density of large planes was assumed to be the calculated density at 25,000 feet, while the density of small planes was assumed to be the density at 5,000 feet. The following table shows the density of the two types of planes in several ways.

	Boeing 747	*Cessna 172*
Altitude (feet)	38,000	7200
Speed (knots)	500	120
Front area (square feet)	480	52
Top area (square feet)	3000	281

Table 5-7. Aircraft Parameters for Impact Analysis.

	Boeing 747	*Cessna 172*
Areal density (planes per square nautical mile)	8×10^{-4}	3×10^{-2}
Average horizontal separation (nautical mile)	60	10
Volumetric density (planes per cubic nautical mile)	2×10^{-4}	1×10^{-2}

Table 5-8. Aircraft Density.

6. Risk Analysis Due To Columbia Debris

6.1 General Procedure

The risk analysis process in CRTF evaluates each footprint for each debris category and each initial state vector and computes a probability of impact in each of the population centers in the population library. The impact probability on a population center is computed based on a bivariate normal distribution and represents the volume over the area of the

population center. This is demonstrated in Figure 6-1. The methods used by CRFT to estimate bivariate normal impact probability distributions are described in Appendix A.

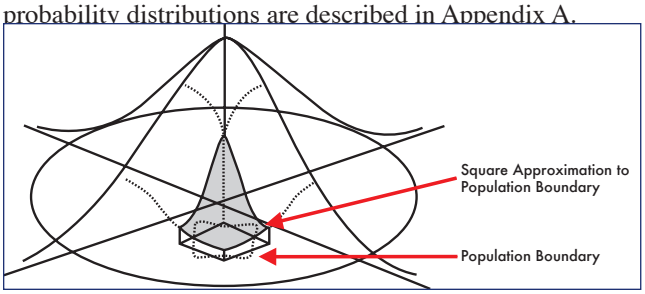


Figure 6-1. Integration of the Bivariate Normal Debris Impact Distribution Over the Area of the Population Center to Determine the Probability of Impact Upon the Population Center.

The equation for casualty expectation, given an initial state vector for debris group "i" that could impact on population center "j" is

$$E_{Cij} = P_{Iij} A_{Ci} N_{Fi} \frac{N_{Pj}}{A_{Pj}} \quad (6\text{-}1)$$

Where P_{Iij} is the impact probability of debris group "i" in that particular class (ballistic coefficient and state vector) on population center "j", A_{Ci} is the casualty area for that fragment class "i" on that population center considering whether the person is outside or sheltered and in what shelter category, N_{Fi} is the number of fragments in that category, N_{Pj} is the number of people in population center "j" and A_{Pj} is the area of the population center. (Note this equation is simplified, since in general there may be another summation over various shelter categories, since each fragment group may have a different casualty area for each shelter category.)

To obtain the total casualty expectation, sum over all cases of fragments classes "i" and population centers "j", i. e.

$$E_{C-Total} = \sum_i \sum_j E_{Cij} \quad (6\text{-}2)$$

If the $E_{C\text{-}Total}$ computed in this study is greater than 0.5, then a casualty would be the expected consequence. If it is less than 0.5, then casualties are not the expected consequence of a single event, but casualties are still possible.

6.2 Computed Risks Using the Breakup Model, the Casualty Model and CRTF/RRAT

Table 6-1 summarizes the risks from the model developed using the gathered and processed fragments. The population model for the day and time of day assumes that 18% of the people are outdoors and 82% are inside with various levels of sheltering. The four groups identified in the table are from the groupings identified in Section 2. Note that Group 1 totally dominates the risk and the effects of the two streaks identified as Groups 2 and 3 and the scatter identified as Group 4 are totally inconsequential. If we assume that there is no other debris that survived, then the model indicates that the total casualty expectation is 0.111 (considering sheltering) which is a number less than 0.5. Therefore, the lack of seriously injured people on the ground was the most likely (i.e. expected) result of this accident.

	Number of Fragments	Weight (lb)	Ec
Group 1	73319	82287	0.11
Group 2	537	942	0.0002
Group 3	316	1239	0.0003
Group 4	540	1801	0.0003
Total	74712	86269	0.111

Table 6-1. Ground Risk Results Based on Gathered Debris (Model).

If we assume that the Columbia broke up, but all fragments survived, and assume the recovered debris is representative of the "un-recovered debris," then the E_C due to all debris surviving is 0.29. These assumptions are considered quite conservative because (1) it is almost certain that some debris burned up during re-entry, and (2) much of the un-recovered debris is likely to be smaller than the recovered fragments, and thus not potentially casualty producing. Table 6-2 shows that the E_C ranging from recovered debris, to 60, 80 and 100% surviving. Table 6-2 also contains the probability that there will be one or more casualties.

Debris Case	Percentage of total Orbiter/ Payload weight	E_C - Sheltered	P [≥ 1 casualty]
Model (recovered debris)	38%	0.14	0.13
60% of total wt. survived	60%	0.21	0.19
80% of total wt. survived	80%	0.29	0.25
100% of total wt. survived	100%	0.36	0.30

Table 6-2. Ground Risk Results as a Function of Amount of Debris Assumed to Survive.

Figure 6-2 shows the risk profile, P(≥ n casualties) as a function of n, for each of the debris cases.

Individual risk was also computed. Looking at the case where only recovered debris is considered, the highest

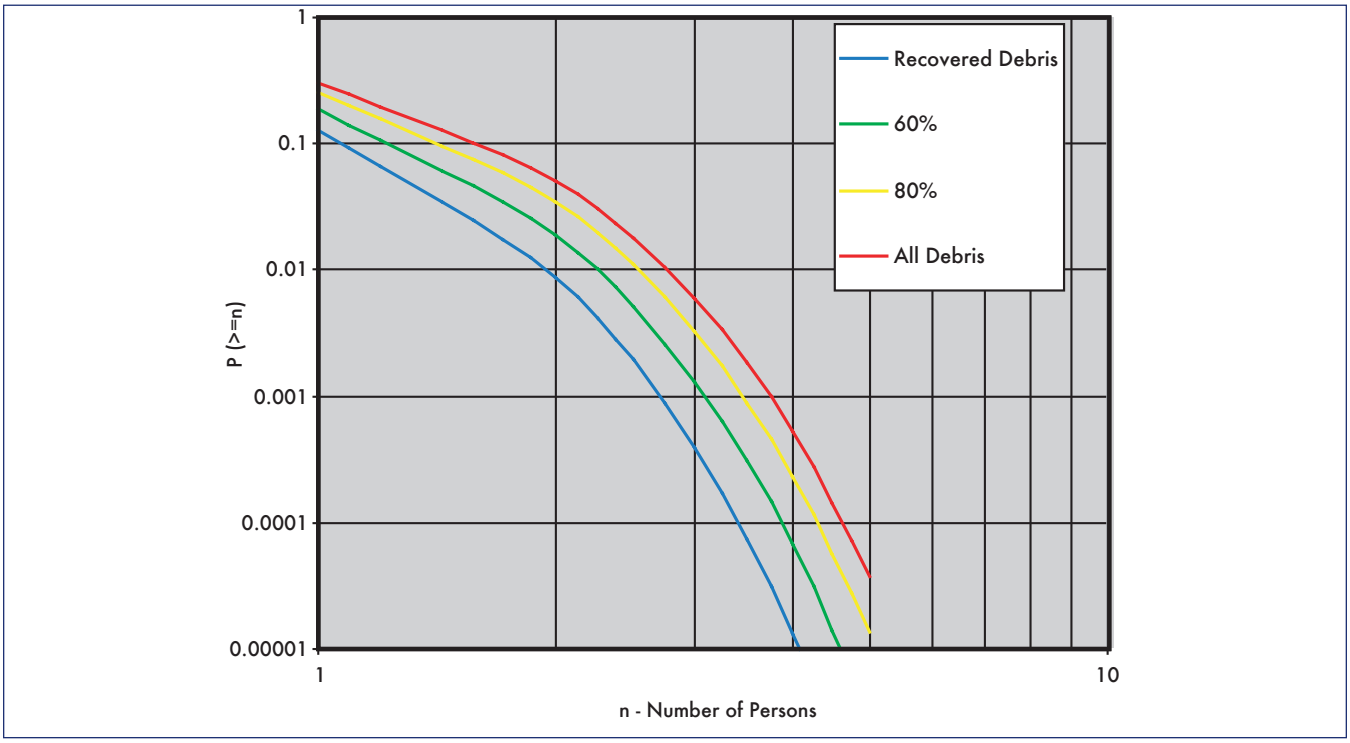


Figure 6-2. Debris Risk Profiles for Different Percentages of Surviving Debris.

computed risk to any individual exposed to the debris field was determined to be 7.6×10^{-5}. The number increased proportionately for those cases where more debris was assumed to survive. The largest number after examining all the population centers was the largest individual E_C. Since the E_C for one person is equivalent to the probability of the person becoming a casualty, the statement in terms of probability is "the highest probability of any particular person exposed to the recovered debris becoming a casualty was 7.6×10^{-5}."

6.3 Risk to Aircraft

The collision between two moving bodies depends on the velocities and dimensions of the two bodies. We define the velocity of the aircraft as $\mathbf{v}_a$, the velocity of the debris as $\mathbf{v}_d$, the characteristic length of the debris as x_d, and the length, width, and height of the airplane as l, w, and h, respectively. It is useful to define the angle φ as the orientation of the relative velocity vector of the debris and aircraft with respect to the local vertical. This angle is given by

$$\varphi = \tan^{-1}\frac{|\mathbf{v}_a|}{|\mathbf{v}_d|}$$

For simplicity, it is assumed that the debris falls vertically and the aircraft flies horizontally. This is a good approximation for the Columbia accident; except for a few fragments with large ballistic coefficients, the horizontal velocity component is relatively small by the time the debris reaches altitudes where aircraft may be present.

For a single aircraft, the volume in which a collision occurs is the volume of space swept out by the aircraft in the time

$$t_{fall} = \frac{x_d + h}{|\mathbf{v}_d|}$$

it takes the debris to fall the height of the aircraft. The time of the fall is

The volume swept out by the aircraft must be determined from area of the aircraft as viewed from the fragment. An area of collision for plan view is

$$A_{PLAN} = (l + x_d)(w + x_d)$$

The front area of collision is

$$A_{FRONT} = (w + x_d)(h + x_d)$$

For an airplane, which is not a simple box, the plan and front areas can be defined more carefully based on the actual areas of the airplane. The area of the aircraft from the perspective of the debris is

$$A_{sweep} = A_{FRONT}\cos\varphi + A_{PLAN}\sin\varphi.$$

The collision volume is the volume of the airplane plus the volume swept out by the aircraft moving for time t_{fall},

$$V_{collision} = l\,w\,h + A_{sweep}\,|\mathbf{v}_a|\,t_{fall}\,.$$

The probability of debris impacting a single hypothetical airplane assumed to fly through a particular space at a given time is the collision volume multiplied by the probability density of debris at that point:

$P_I = (x,y,z) = V_{collision} d_{debris}(x,y,z)$.

CRTF can compute the density of fragments as a function of time and position while the debris is descending. It uses trivariate normal distributions to model dispersions about the nominal descent trajectory for each fragment group originating from each state vector. CRTF computes the characteristics of each distribution from release to impact at small time steps. These 3-dimensional distributions are used to compute $d_{debris}(x,y,z,t)$ in the aircraft risk computation.

The probability density of debris was calculated by CRTF from the sum of all the distributions of debris from each breakup time. By calculating the probability of impact with airplanes for many combinations of breakup times and aircraft different positions and altitudes, $P_I(x,y,z)$ can be determined for each type of airplane.

The plot of impact probability density has a similar shape for all classes of airplanes at all altitudes; only the magnitude of the impact probability density varies. This plot is visually indistinguishable, except in absolute magnitude, with a probability of impact chart on the ground.

The worst case probability of a debris impact on any single plane can be determined by finding the maximum $P_I(x,y,z)$ from the breakup analysis. For a commercial aircraft, the worst case was 0.08, and for general aviation for a single plane, it was 0.0037.

For each class of aircraft, the expected number of impacts with debris per mission, E_I, can be calculated by integrating over all space the probability of impact multiplied by the density of airplanes, as

$$E_I^j = \iiint_{all\ space} E_{3D}^j(x,y,z) P_I^j(x,y,x)\, dx\, dy\, dz$$

$$E_I^{total} = \sum_{j=1}^{N_{classes}} E_I^j$$

where j is the airplane class. For this study, the density of planes is assumed to be a constant for each airplane class, as discussed in the previous section on the aircraft exposure model. The total E_I for a trajectory is the sum of the E_I's of each airplane class,

The expected number of planes impacted by the Columbia breakup was approximately 3×10^{-2}. This is primarily due to possible impacts with general aviation (>80%).

6.4 Validation of Computed Risks Using a Simplified Model

This section compares the CRTF computed risks with an alternate simplified model that assumed the exposed population had a uniform density and that only people without shelter are vulnerable to serious injuries due to *Columbia* debris impacts. The average population density over the region at risk was approximately 85 people / per square nautical mile. The total casualty area for people in the open was determined in Section 4 and presented in Table 5-2. Table 5-6 presented an estimate of the percentage of people without shelter. The product of these three values are given in Table 6-3 along with the results from the CRTF analysis that accounted for the potential casualties indoors as well as the distributions of population and debris impacts. Since Table 5-2 also contains hazard and fatality areas, these can also be used in estimating the expected hazard and the expected number of fatalities. These results are also included in Table 6-3.

The results of the simplified analysis in Table 6-3 give an estimate of the casualty expectation that is 60% of the values in the detailed analysis. Since the approximate analysis is quite intuitive, these results provide support to the results from the detailed analysis. The fact that the detailed analysis produced higher risk estimates than the simplified analysis also suggests that the population density was also relatively high where the debris impact density was also relatively high. Examination of Figures 3-7 and 5-3 indicates that, indeed this appears to be the case. Furthermore, the debris recovery effort seemed to show that Nacogdoches, TX, which was the most significant concentrated population center in the vicinity of the debris impacts, was in an area of relatively high debris impact density. This result may be influenced by the fact that more debris is likely to be seen and recovered in highly populated areas compared to areas away from roads, buildings, and tended property. However, ACTA found no statistically significant correlation between the location of recovered debris and population density.

The E_{Haz} in Table 6-3 includes all of those cases where debris can hit someone and not result in an injury. A large number of the collected Columbia fragments are in this category. The E_{Haz} in Table 6-3 is typically five times the E_C. In addition,

Debris Case	Percentage of Total Orbiter and Payload Weight	E_{Haz}	E_C	E_F
Model (gathered debris)	38%	0.41	0.08 (0.14)	0.06
60% of total wt. survived	60%	0.66	0.13 (0.21)	0.10
80% of total wt. survived	80%	0.88	0.18 (0.29)	0.13
100% of total wt. survived	100%	1.11	0.22 (0.36)	0.16

Note: All results based on the assumption of a ground wind of 10 ft/s and a population density of 85 people/per square nautical mile).
Numbers in parentheses represent the numbers computed in the detailed analysis.

Table 6-3. E_{Haz}, E_C and E_F from the Approximate Analysis.

the ratios between the E_C's and the E_f's indicate that 75% of the casualties will be fatalities. Note that the absolute values of the numbers in the table are considered less accurate than those from the detailed analysis, but the relative values in the table are considered quite representative.

6.5 Sensitivity of Results to Model Parameters

A formal uncertainty analysis was not performed due to the limited time available for this study. However, sensitivity studies were performed to determine the sensitivity of the computed risks to the following critical model parameters.

1) Sensitivity to the amount of debris that survives reentry to impact the ground.

   The computed risk to the public shifts up and down directly proportional to the percentage of the debris that survives. This was demonstrated in Table 6-2:

2) Sensitivity to the assignment of numbers of fragments to each ballistic coefficient group.

   The model, based on the recovered fragment data, has a large number of fragments with low ballistic coefficients. One test of the stability of the answer is to shift the numbers of fragments to cells with higher ballistic coefficient to see if higher numbers of fragments in the higher ballistic coefficient cells would increase the risk. This test was accomplished in two steps:

   a) All of the fragment counts were shifted one ballistic coefficient category, i.e. fragments that were in the β=0.5 category were shifted to β=1.0 category, β=1.0 to the β=1.78 category, etc. Compute the total E_C using the approximate method in Section 6.4 and compare with the E_C for the unshifted case.

   b) Repeat the Step 1 process by shifting all of the fragment counts one more ballistic coefficient category. Again, compute the E_C and compare with the unshifted case.

      The results of this exercise indicate an increase of E_C of 50% for a one-cell shift of fragment count and 125% for a two-cell shift of fragment count. However, each higher β cell also has a higher average fragment weight. If the total fragment count is adjusted downward after the shift, to maintain the total fragment weight, the risk actually decreases by about 29% for a one-cell shift and 53% for a two-cell shift.

      This latter test is not really valid because the total number of fragments cannot be decreased from the actual gathered count. However, the important result from this test is that shifts in the cells will not make major shifts (i.e. order of magnitude) in the final result.

3) Sensitivity to a shift in the initial breakup point of the Orbiter.

   One test was made where the breakup point was shifted to 50 seconds earlier, moving the footprint approximately 100 nm uprange along the reentry path. The breakup state vectors were recomputed for this condition and the risk analysis was performed again using these state vectors. The result, in this case, was an increase in the calculated risk to the public by about 36%. The increased population density south of Dallas was responsible for the increased risk.

4) Sensitivity of the public risk to a shift in the assumption of 20% of the people at home at 8:00AM on Saturday morning being outside.

% Debris Surviving	*People at home 10% in the open*	*People at home 20% in the open*	*People at home 30% in the open*
Model – 38% of total wt.	0.08	0.14	0.21
60% of total wt. survived	0.11	0.21	0.32
80% of total wt. survived	0.15	0.29	0.44
100% of total wt. survived	0.18	0.36	0.54

Table 6-4. Sensitivity of the Final E_C Results to the Assumption of the Percentage of the People at Home who are Outside.

   The public risk was computed using CRFT for 30% of the people at home being outside and 10% of the people at home being outside. The results are presented in Table 6-4.

   The results in Table 6.4 shows that the public risk estimate given the Columbia accident is linearly related to the percentage of people without sheltering. This result indicates that public risk from the Columbia accident would have been substantially mitigated by landing during the middle of the night, when almost everyone is inside a shelter and few aircraft are in flight.

5) Sensitivity of the public risk due to shift of orbit such that the debris field falls over Houston.

   The risk, in terms of E_C, is increased by a factor of 10.5. The higher E_C and probability of casualty are due to the debris field lying over Houston. Houston is a little closer to the landing point of the Shuttle at KSC and thus lines up under the debris pattern when the orbit is shifted. The actual debris field from *Columbia* missed most of Dallas and fell in an area of much

lower population density.

For this case, the probability of one or more casualties is increased from a range of 0.13 to 0.30 For the actual *Columbia* debris impact to a range of 0.89 to 0.98 for the same debris field falling over Houston.

7. Study Conclusions And Recommendations

The following are the conclusions and recommendations for this study.

1) The results of the risk analysis indicate that the lack of casualties was the expected event, but there was a reasonable probability (less than 0.5 but greater than 0.05) that casualties could have occurred.

2) A preliminary evaluation of aircraft risk indicates that there was a lower likelihood of debris impact on commercial or general aviation aircraft than impact on people on the ground. However, the estimated probability of aircraft hit levels were higher than would be allowed for unrestricted aircraft operations.

3) Detailed fragment data were not available for the study (the details had not been developed yet) and therefore some engineering judgment was necessary to develop models of individual weights, dimensions, aerodynamic characteristics and conditions of impact. This lack of information increases the uncertainty in the accuracy of the final results. The study should be revisited after the fragment data has been fully processed.

4) A more detailed aircraft risk analysis should be performed using the actual records of aircraft activity at the time of the accident. This additional study should also take into consideration the vulnerability of the aircraft.

5) The risk to people on the ground due to the Columbia accident was predominately due to people in the open. To the extent that future Orbiter re-entry accidents are likely to produce similar debris impacts, public risk from Shuttle re-entry may be mitigated by landing during the middle of the night, when almost everyone is inside a shelter and few aircraft are in flight.

References

[1] Carbon, S., Common Real-Time Debris Footprint, Program CRTF7 User's Manuel, ACTA Report No. 01-451/23.1-01, Sept 2001

[2] Haber, Jerold M., Liquin Cao and John O. Morris, "Range Risk Analysis Tool (RRAT)," *Proceedings of the JANNAF 30th Propellant Development and Characteristics Subcommittee and 19th Safety and Environmental Protection Subcommittee Joint Meeting*, Colorado Springs, Colorado, March 2003

[3] Code of Federal Regulations (CFR) 14 CFR Part 415 Launch License, Federal Register / Vol. 64, No. 76 / April 21, 1999 /

[4] Range Commanders Council Standard 321-02, Common Risk Criteria for National Test Ranges, published by the Secretariat of the RCC US Army White Sands Missile Range, NM 88002-5110, June 2002

[5] Orbiter Thermal Protection System, NASA Facts, FS-2000-06-29-KSC, March 1997

[6] Salguero, D., Trajectory Analysis and Optimization Software (TAOS), Sandia National Laboratories, SAND99-0811, June 2001

[7] Larson, Erik and Jerold M. Haber. Final Quantitative Risk Analysis for Generic Lifting Entry Vehicle Landing at Edwards Air Force Base. Report No 01-474-04, ACTA Inc., Torrance, CA, October 2001. Also available from http://www.ealev.com/pdf/QRA.pdf.

[8] Hasselman, Timothy K., Mark R. Legg, and Mark C. Anderson. Casualty and Fatality Risk Models for Roof Penetration by Inert Debris. Technical Report 99-400/11.4-03, ACTA Inc., Torrance CA, September 1999

[9] Hasselman, Timothy K. and Mark R. Legg. Update of Casualty and Fatality Risk Models for Roof Penetration by Inert Debris. Technical Report 00-430/16.4-02, ACTA Inc., Torrance CA, September 2000

[10] Larson, Erik, and Jon Chrostowski. *Population Library with Sheltering for Overflight of Europe and the Middle East*. Report No. 02-481/4-04, ACTA Inc., Torrance, CA, September 2002

[11] United States Census Bureau. *2000 Census*. http://www.census.gov/main/www/cen2000.html

Appendix A

Reprint of Paper Describing CRTF[4]

Real-Time Debris Footprint

Steven L. Carbon and Jon D. Collins
ACTA, Inc.
2790 Skypark Drive Suite 310
Torrance, CA 90505

Abstract

During the launch of a rocket, range safety typically has used the track/locus of the vacuum instantaneous impact point (VIIP) as the indicator of vehicle position. When this track crosses pre-established abort lines, the Mission Flight Control Officer (MFCO) issues a command to abort the launch. The problem with the use of the IIP is that it does not actually show where the debris will impact. Thus decisions to abort are not based on a realistic depiction of the consequences, but rather the crossing of a point and a line, where the position of the line is adjusted to protect the public. There are situations where a more accurate display of the instantaneous debris impact dispersion will permit the MFCO more latitude. This is particularly important with manned launches such as the Space Shuttle and, in fact, a debris footprint has been used by the safety office at the Eastern Range to control the launch for some time.

This paper describes a new footprint program, CRTF (Common Real-Time Footprint) that was developed under the joint sponsorship of the Eastern and Western Ranges. The footprint differs in that it is probabilistically based and develops all of the dispersion data in real-time so that it can use the actual state vector as the starting point for the dispersion analysis. The resulting footprint can provide a statistical basis for the MFCO decision. Instead of an abort line, an Impact Limit Line (ILL) can be used for the abort decision, with probabilistic statements such as "99% sure that no fragment will land on the opposite side of the Impact Limit line if abort is initiated when the footprint touches the Impact Limit Line." The program is designed to compute very quickly and, as part of the RSA real-time system, it will update ten times/second.

The method uses a series of bi-variate normal distributions, with each representing the impact distribution for a different debris category. These distributions provide the basis of the probabilistic model. These same bi-variate normal distributions are also used in a risk model in the program to compute risk in real-time. CRTF also has a number of other features that can be used for various vehicle and tracking system failure modes.

Program Overview

CRTF is designed to compute the dispersions that define an instantaneous scenario of a vehicle breakup and dispersion of debris. It can be used in real-time to show instantaneously the statistical dispersion of debris impacts if the vehicle is destroyed at that instant, or it can be used as a subroutine in a risk analysis program that generates a large number of state vectors describing all of the potential accident/failure conditions along with their corresponding probabilities. Most of the dispersion models in CRTF originated in the LARA launch risk analysis program,[5] but their implementation is somewhat different in several cases because of the need to make the program run very fast in real-time.

The two most dominant effects on footprint length and shape are ballistic coefficient of the debris and the wind. The debris with very low ballistic coefficient decelerates very quickly and if the wind is light, it falls to the ground close to the sub-missile point at the time of breakup. If the wind is strong, the debris will move with the wind and land in the direction of the wind relative to the breakup point. If the debris has a very high ballistic coefficient, it moves with little effect of the wind and lands in the direction of the vacuum impact point. Figure 1 illustrates the effects of ballistic coefficient and wind on the "centerline" of debris footprint.

The dispersion relative to the debris centerline is the result of impulses and uncertainties from a number of sources. These are illustrated in Figure 2. The "disks" around the impact points in Figure 2 represent the impact uncertainty of debris due to the uncertainty sources. Four pieces of debris are shown, but actually there can be thousands. To simplify the modeling process, debris pieces are grouped into classes. There may be 50 or more classes, each containing debris

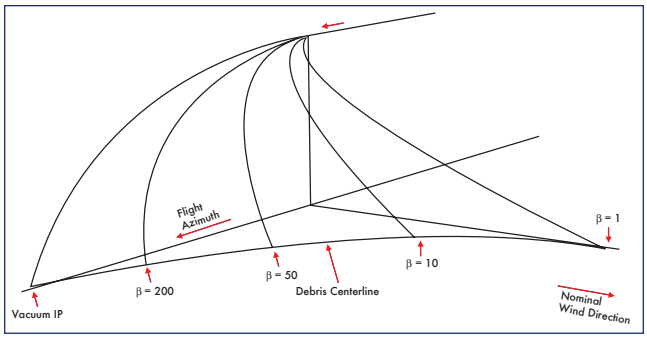


Figure 1. The influence of the ballistic coefficient.

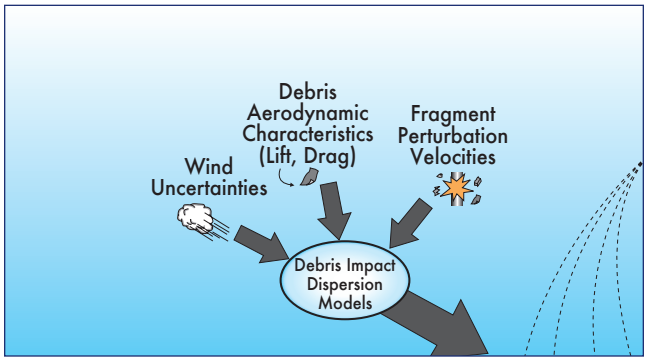


Figure 2. Contributions to debris dispersion models.

pieces that have similar ballistic coefficients, explosive characteristics or velocity perturbation characteristics. The CRTF process is to simulate the behavior and impact dispersions of each of these groups and then, in the final step, adjust the statistical results to account for the number of fragments in the group.

CRTF was designed to operate in real-time with an update rate of 10 times per second. Another specification of the program was that it must operate off the actual state vector and no tables were permitted that were developed before launch and used in a look-up mode. Previous programs developed for the Western and Eastern Ranges used look up tables based on vehicle altitude or velocity at the time of destruct. This requirement was difficult but became workable as the capability of computers improved. The speed requirement required considerable innovation in the program design. The impact predictor, for example, could not use a typical Runge Kutta algorithm, but had to use a faster three and a half order Taylor series concept (non-corrective) that, after adjustment, proved to be quite accurate.

CRTF contains a set of models that estimate the range of free-fall and impact locations of the fragments that result from vehicle breakup. The initiating event is assumed to be the activation of on-board destruct charges due to a command destruct signal, leading to total vehicle destruction into a fixed set of fragments. There are other breakup conditions (e.g. aerodynamic) but the intent of the program is to provide the impact dispersions if there is a destruct, thus providing the Mission Flight Control Officer with the probabilistic extent of the debris resulting from destruct action. The CRTF models attempt to quantify the uncertainties that exist in the

vehicle location at the moment of breakup, in the characteristics of the generated fragment debris, and in the external conditions during fragment free-fall. There are six uncertainty models in CRTF, four of which employ a Monte Carlo technique. The Monte Carlo routines are used to handle some of the uncertainties and develop impact distributions that contribute to the total uncertainty. The other impact uncertainties are developed using linear equations and covariance propagation, thus the program is a hybrid, taking advantages of the best of both statistical modeling methods.

Through judicious choice of input, one can isolate the execution of each individual uncertainty model. In the following paragraphs, each of the models is described.

(1) The real-time vehicle state vector, passed to CRTF, is generated from an estimation routine (Kalman filter) that utilizes tracking data from one or more sources. Each individual data source contains measurement error, which is implicit in the composite filter solution and is represented by the filter's covariance matrix.

$$\Sigma\,(x,y,z,\dot{x},\dot{y},\dot{z}) = \begin{bmatrix} \sigma_x^2 & \rho_{xy}\sigma_x\sigma_y & \rho_{xz}\sigma_x\sigma_z & \rho_{x\dot{x}}\sigma_x\sigma_{\dot{x}} & \rho_{x\dot{y}}\sigma_x\sigma_{\dot{y}} & \rho_{x\dot{z}}\sigma_x\sigma_{\dot{z}} \\ \rho_{yx}\sigma_y\sigma_x & \sigma_y^2 & \rho_{yz}\sigma_y\sigma_z & \rho_{y\dot{x}}\sigma_y\sigma_{\dot{x}} & \rho_{y\dot{y}}\sigma_y\sigma_{\dot{y}} & \rho_{y\dot{z}}\sigma_y\sigma_{\dot{z}} \\ \rho_{zx}\sigma_z\sigma_x & \rho_{zy}\sigma_z\sigma_y & \sigma_z^2 & \rho_{z\dot{x}}\sigma_z\sigma_{\dot{x}} & \rho_{z\dot{y}}\sigma_z\sigma_{\dot{y}} & \rho_{z\dot{z}}\sigma_z\sigma_{\dot{z}} \\ \rho_{\dot{x}x}\sigma_{\dot{x}}\sigma_x & \rho_{\dot{x}y}\sigma_{\dot{x}}\sigma_y & \rho_{\dot{x}z}\sigma_{\dot{x}}\sigma_z & \sigma_{\dot{x}}^2 & \rho_{\dot{x}\dot{y}}\sigma_{\dot{x}}\sigma_{\dot{y}} & \rho_{\dot{x}\dot{z}}\sigma_{\dot{x}}\sigma_{\dot{z}} \\ \rho_{\dot{y}x}\sigma_{\dot{y}}\sigma_x & \rho_{\dot{y}y}\sigma_{\dot{y}}\sigma_y & \rho_{\dot{y}z}\sigma_{\dot{y}}\sigma_z & \rho_{\dot{y}\dot{x}}\sigma_{\dot{y}}\sigma_{\dot{x}} & \sigma_{\dot{y}}^2 & \rho_{\dot{y}\dot{z}}\sigma_{\dot{y}}\sigma_{\dot{z}} \\ \rho_{\dot{z}x}\sigma_{\dot{z}}\sigma_x & \rho_{\dot{z}y}\sigma_{\dot{z}}\sigma_y & \rho_{\dot{z}z}\sigma_{\dot{z}}\sigma_z & \rho_{\dot{z}\dot{x}}\sigma_{\dot{z}}\sigma_{\dot{x}} & \rho_{\dot{z}\dot{y}}\sigma_{\dot{z}}\sigma_{\dot{y}} & \sigma_{\dot{z}}^2 \end{bmatrix}$$

This matrix contains both position and velocity uncertainty along each of three orthogonal axes. The model in CRTF assumes a normal distribution in each direction, and generates Monte Carlo samples for each of the six degrees of freedom.

where σ_x is the standard deviation of x, σ_y is the standard deviation of y, etc. and ρ_{xy} is the correlation coefficient of between the two variables, x and y. The x, y, z coordinate system is Cartesian in whatever frame used by the real-time system.

(2) There is a time delay between the moment of decision to send command destruct, and the time at which the charges on the vehicle respond. During this time delay, which is typically between three and five seconds, the vehicle may experience a failure and start to tumble or deviate from its trajectory. This course change is computed using malfunction tumble turn curves supplied by the vehicle's manufacturer. At each state time, there is a range of possible tumble rates depending upon the degree of offset of the thrust vector. The offset is due to a nozzle deflection or engine burn-through. Since the vehicle manufacturer is required to provide a series of tumble turn curves (velocity perturbation from nominal velocity and perturbed direction in velocity) for discrete engine offsets, these curves are considered as the discrete possibilities for a tumble turn (in any direction relative to the state vector). Each of these discrete thrust offsets is assigned a relative probability. Currently, in most applications, the program treats each of the tumble turns as equally likely, but the capability is there to vary the probability of each offset if the data is available from the manufacturer. Thus the program randomly selects the turn curve, randomly selects the direction away from the velocity vector and randomly selects the delay time before destruct.

(3) When fragments are produced at breakup, they are given an impulse away from the main explosion. This leads to both an imparted speed and direction for each fragment. Since the orientation of the vehicle is not known to the estimation generator, no preferred direction can be assigned to the fragments. Further, the fragment data input to CRTF only contains the maximum explosion speed that each fragment category may expect. To handle this explosion velocity uncertainty the CRTF model assumes that, along each of the three orthogonal axes, the speed obeys a normal distribution with a standard deviation given by one-third the maximum explosion speed. The full three-dimensional velocity then fits a Maxwellian distribution. Monte Carlo samples are obtained for each of the three speed components and are used to augment the state velocity.

(4) The size and shape of each fragment determines the drag effect during free-fall. The parameter that quantifies this atmospheric influence is the ballistic coefficient of the fragment. Due to the uncertain nature of the breakup of the vehicle, each fragment can only be assigned a range of ballistic coefficients. The values in this span are taken to obey a Gaussian distribution (it can be different, e.g. lognormal, triangular, etc.), where the two extremes and nominal value are specified by input to CRTF. The ballistic coefficient uncertainty model in CRTF generates Monte Carlo samples for each fragment category just prior to initiating the free-fall propagator. The ballistic coefficient may change during free-fall if the fragment contains burning propellant.

(5) During free-fall, the fragments experience a lift effect where the piece is subjected to a force perpendicular to its direction of motion. The lift force is largest for flat plates (as an aircraft wing), and at lower altitudes where the air density is greatest. The magnitude of the lift force fluctuates as the fragment tumbles since the surface along the direction of motion changes. The lift model in CRTF computes two impact points, starting from the initial state position. One location is for a fragment that sees no lift, and the second for a fragment that is given a constant lift. The lift is computed using a lift-to-drag coefficient that relates the relative effect compared to drag, and which is specified in the CRTF input for each fragment category.

(6) An external source of uncertainty applied to each fragment during free-fall is the strength of the wind. Several hours prior to vehicle launch, empirical wind measurements are obtained. The accuracy of these wind measurements decreases as the time since data acquisition increases. CRTF handles the aging wind

data, not by adjusting the wind used in the fragment propagator, but by computing separate wind uncertainty impact dispersions. The input to this calculation uses uncertainty data acquired over a period of years, which quantifies how much the wind speed and direction are in error for a given age of wind, a given season, and a given altitude. A wind covariance matrix is shown below. The wind dispersion effect is determined by computing the time a fragment traveling at terminal velocity passes through an altitude band and, assuming that the fragment is embedded in the wind, the fragment while falling through the band moves laterally at the velocity of the wind. This assumption is

$$\Sigma_{\text{Wind}} = \left[\begin{array}{cccc|cccc} \sigma^2_{E_1} & \sigma_{E_1E_2} & \cdots & \sigma_{E_1E_n} & \sigma_{E_1N_1} & \sigma_{E_1N_2} & \cdots & \sigma_{E_1N_n} \\ \sigma_{E_2E_1} & \sigma^2_{E_2} & \cdots & \sigma_{E_2E_n} & \sigma_{E_2N_1} & \sigma_{E_2N_2} & \cdots & \sigma_{E_2N_n} \\ \cdots & \cdots & \cdots & \cdots & \cdots & \cdots & \cdots & \cdots \\ \sigma_{E_nE_1} & \sigma_{E_nE_2} & \cdots & \sigma^2_{E_n} & \sigma_{E_nN_1} & \sigma_{E_nN_2} & \cdots & \sigma_{E_nN_n} \\ \hline \sigma_{N_1E_1} & \sigma_{N_1E_2} & \cdots & \sigma_{N_1E_n} & \sigma^2_{N} & \sigma^2_{N_2} & \cdots & \sigma_{N_1N_n} \\ \sigma_{N_2E_1} & \sigma_{N_2E_2} & \cdots & \sigma_{N_2E_n} & \sigma_{N_2N_1} & \sigma_{N_2N_1} & \cdots & \sigma_{N_2N_n} \\ \cdots & \cdots & \cdots & \cdots & \cdots & \cdots & \cdots & \cdots \\ \sigma_{N_nE_1} & \cdots & \cdots & \sigma_{N_nE_n} & \sigma_{N_nN_1} & \sigma_{N_nN_2} & \cdots & \sigma^2_{N_n} \end{array}\right]$$

$$\left[\Sigma^{\text{EN}}_{\text{Wind}}\right]_h = ????????????????????????????????$$

quite accurate for low ballistic coefficient debris (β=1 to 10 psf) and less so as β increases. Fortunately, the effect of ballistic coefficient on drift decreases as $1/\sqrt{\beta}$. The wind covariance matrix and the matrix product to obtain impact dispersions due to wind. Note, $\sigma_{EiEj} \equiv \rho_{EiEj}\,\sigma_{Ei}\,\sigma_{Ej}$, = etc.

For each active fragment group, the above six sources of uncertainty are combined by building three impact covariance matrices as follows. A set of N Monte Carlo simulations are set up to represent selections of random conditions. The number of simulations is specified by the user, and for real-time, N should be at least 100 cycles. For each simulation, CRTF determines the post-malfunction tumble turn position and velocity state vector and adds in the measurement error vectors and explosion velocity vectors. Next, the ballistic coefficient of the fragment group is sampled. The fragment is then propagated to the ground, leading to N impact points from which the first impact covariance matrix is computed. For lift, the second impact covariance is defined by treating the separation of the two impact points (lift and no-lift) as standard deviations. The third impact covariance matrix, due to wind, is constructed by a more technical procedure that we omit here. The total impact covariance is the sum of the three matrices. The procedure is shown in the flow diagram

$$\Sigma_{EN} = \begin{bmatrix} \sigma^2_E & \rho_{EN}\sigma_E\sigma_N \\ \rho_{EN}\sigma_E\sigma_N & \sigma^2_N \end{bmatrix}$$

in Figure 4.

At the end of the dispersion analysis, each debris group has

$$\Sigma_{EN}\begin{bmatrix} E \\ N \end{bmatrix} = \lambda^2 \begin{bmatrix} E \\ N \end{bmatrix} \Rightarrow \left(\quad _{EN} - \lambda^2 \right)\begin{bmatrix} E \\ N \end{bmatrix} = 0$$

$$\det \begin{bmatrix} \sigma^2_E - \lambda^2 & \sigma_{EN} \\ \sigma_{EN} & \sigma^2_N - \lambda^2 \end{bmatrix} = 0$$

a mean impact point and a covariance matrix defining the impact uncertainties. The covariance matrix (in East-North coordinates) contains the information for finding the size and orientation of the impact ellipse.
The eigenvalues and eigenvectors of Σ_{EN} provide the magnitudes of the major and minor axes and the orientation of the axes.

$$\tan\alpha = \frac{\sigma_N{}^2 - \sigma_E{}^2}{\rho_{EN}\sigma_E - \sigma_N}$$

The two values for λ, solved from the above determinant, are the equivalent values of the standard deviation along the two orthogonal axes rotated by the angle α as shown below. The angle α is determined by the ratios of E/N computed in the above matrix equation after the computed values of λ^2 have been substituted into the equation.

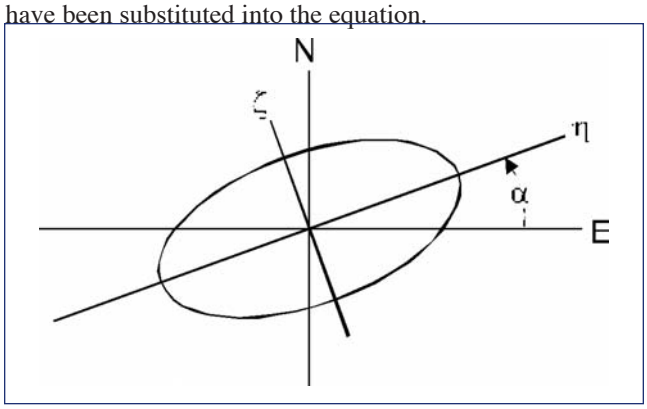


Figure 3. Rotation to a coordinate system withno off-diagonal terms in the covariance matrix.

Figure 4 (facing page). Computation procedure used by CRTF.

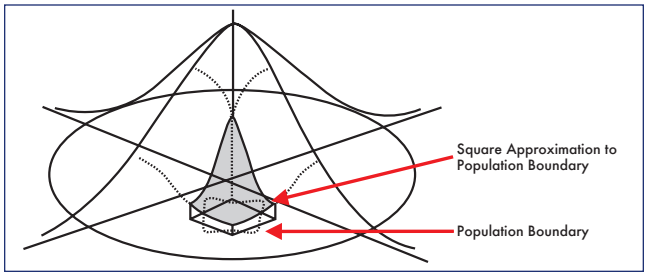
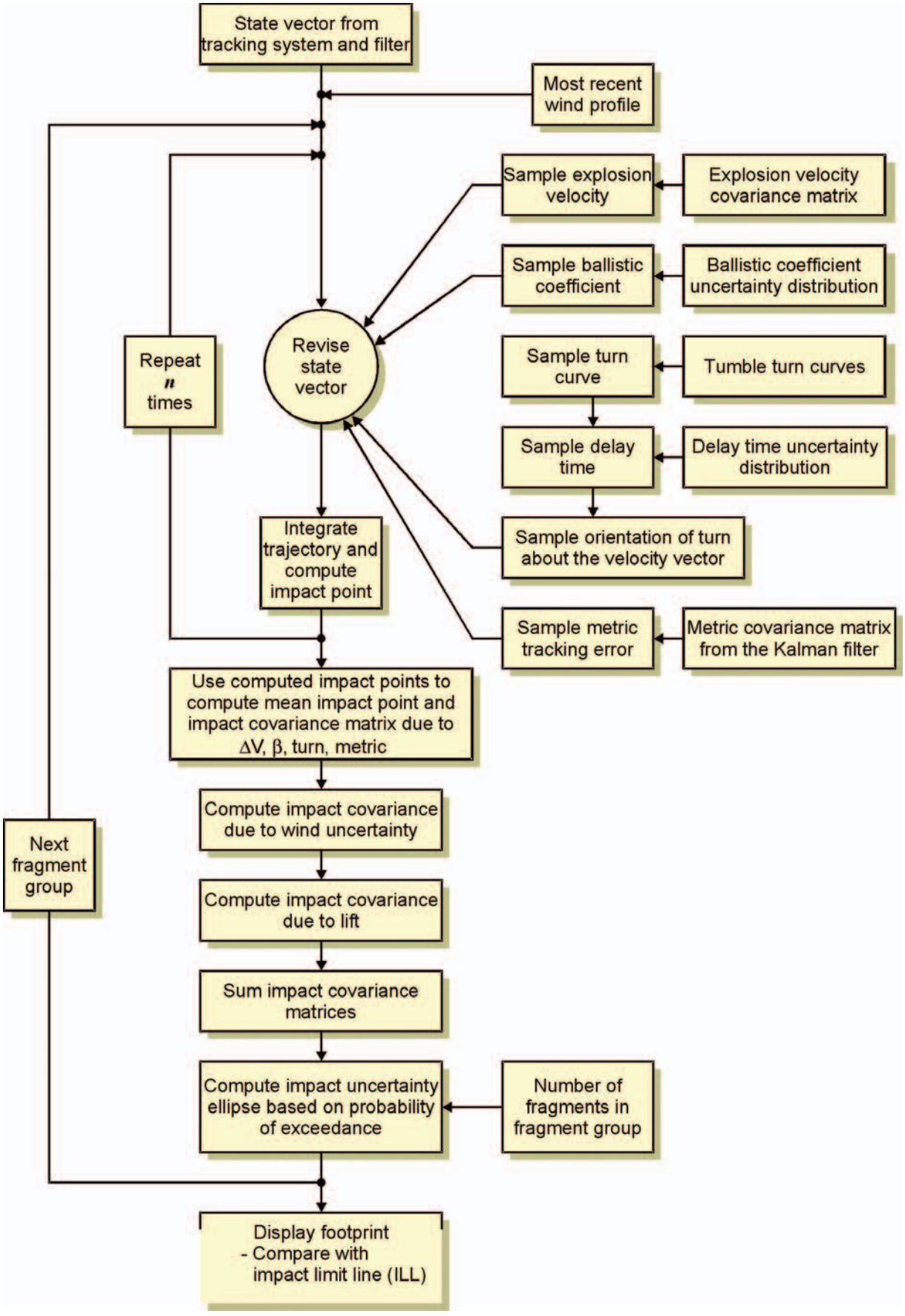


Figure 5. Determination of the equi-density contours.

The ellipse showing the rotation and the relative lengths of the major and minor axes is shown in Figure 3. The two standard deviations ($\sigma_\eta = \lambda_1$ and $\sigma_\xi = \lambda_2$) define a bivariate


State vector from tracking system and filter
Most recent wind profile
Sample explosion velocity
Explosion velocity covariance matrix
Sample ballistic coefficient
Ballistic coefficient uncertainty distribution
Repeat n times
Revise state vector
Sample turn curve
Tumble turn curves
Sample delay time
Delay time uncertainty distribution
Integrate trajectory and compute impact point
Sample orientation of turn about the velocity vector
Sample metric tracking error
Metric covariance matrix from the Kalman filter
Use computed impact points to compute mean impact point and impact covariance matrix due to ΔV, β, turn, metric
Compute impact covariance due to wind uncertainty
Next fragment group
Compute impact covariance due to lift
Sum impact covariance matrices
Compute impact uncertainty ellipse based on probability of exceedance
Number of fragments in fragment group
Display footprint
- Compare with impact limit line (ILL)

normal distribution that is used to develop isopleths (equi-density contours) of constant impact probability as shown in Figure 5.

The bivariate distribution is also the distribution used to compute impact probability on population centers if the program is to be used for risk analysis.
One option of the program is to surround all of the impact dispersion ellipses with a convex "hull" and use only the hull for display in real-time. A geometrical hull is a curve that bounds a compact set of points.

To give the ellipses and hull a statistical meaning when they reach an impact limit line (ILL), a confidence level C is specified by the user. The ellipses and hull are then resized based on the value of C and on the number of fragments in the group, which in some cases may be in the thousands. The interpretation of the ellipse drawn is that there is a probability C that no fragment from the corresponding fragment group crosses the boundary of the ellipse (such as the ILL). For the hull, C is the probability that no fragment from any fragment group crosses the ILL. The formulas for C for the two cases of debris falling outside of the ellipses and for the debris crossing the tangent to the ellipse (the ILL) are shown below.

The two standard deviations along the major and minor axes are multiplied by a factor z to establish the ellipse size that corresponds to the appropriate probability statement. For "C" probability that no fragment out of N fragments falls

$$z = t - \frac{c_0 + c_1 t + c_2 t^2}{1 + d_1 t + d_2 t^2 + d_3 t^3},$$

outside the ellipse, the formula for z is

$$z = \sqrt{(-2\ln(1 - C^{1/N}))}$$

For "C" probability that no fragment out of N fragments falls beyond a line tangent to the ellipse (such as an ILL), the formula for z is
where $t = \sqrt{(-2\ln(1 - C^{1/N}))}$ and $c_0 = 2.515517$, $c_1 = 0.802853$, $c_2 = 0.010328$, $d_1 = 1.432788$, $d_2 = 0.189269$, $d_3 = 0.001308$.

An additional feature had to be added for explosive debris. When the fragments contain solid propellants that explode on impact, the ellipse radii and the hull are increased by the blast radius corresponding to an overpressure threshold value specified by the user.

The characteristics of some of the debris in free fall may change as a function of time. Solid propellant fragments that burn during descent see a change in both ballistic coefficient and weight. If the propellant fragment completely burns up before impact, this piece will not be included in the impact dispersion set. This results in a reduction in size of the displayed ellipse, or its complete elimination if all the fragments in the group are exhausted. If vehicle breakup occurs in thin or no atmosphere, the solid propellants will be assumed to snuff out before their descent begins.

Figures 6 and 7 show debris footprints for the Space Shuttle and the Titan IV launched from Kennedy Space Center and Vandenberg Air Force Criteria. The ellipses are based on a 95% probability that no fragment will cross any line tangent to any ellipse.

Conclusion

CRTF should provide a valuable tool for range safety at both the Eastern and Western Ranges. It provides an alternate criterion to the traditional vacuum IIP crossing a predetermined abort line as the basis for an abort decision. This approach has been in place for the Space Shuttle for a number of years. CRTF will eventually replace the footprint that is currently in place.

The impact distributions used by CRTF to determine the contours, are the same distributions needed to determine impact probabilities and risks (casualty expectations). Consequently, all of the necessary models to compute risk have also been incorporated into CRTF. One of the program's risk capabilities is to compute contours of constant risk (e.g. 1×10^{-6} conditional probability of casualty) in real time.

Acknowledgement

The authors are particularly grateful for the guidance and support provided by Martin Kinna at the U. S. Air Force Space Command 30th Space Wing and the late Ronald Stout at the 45th Space Wing.

Distribution Statement: Approved for public release, distribution unlimited.

This work was sponsored by the US Air Force Space Command 30th Space Wing at Vandenberg Air Force Base and 45th Space Wing at Patrick Air Force Base under contract number FO4703-91-C-0112.

Footnotes

[1] The numbers given here for casualty probability are somewhat higher than the 0.09 to 0.24 quoted in Section 10.1, Page 21-3 of the CAIB Report, Vol. 1. This is due to an improvement in the probability model made after publication of Vol. 1.
[2] The discrete nature of the model rules out the use of conventional

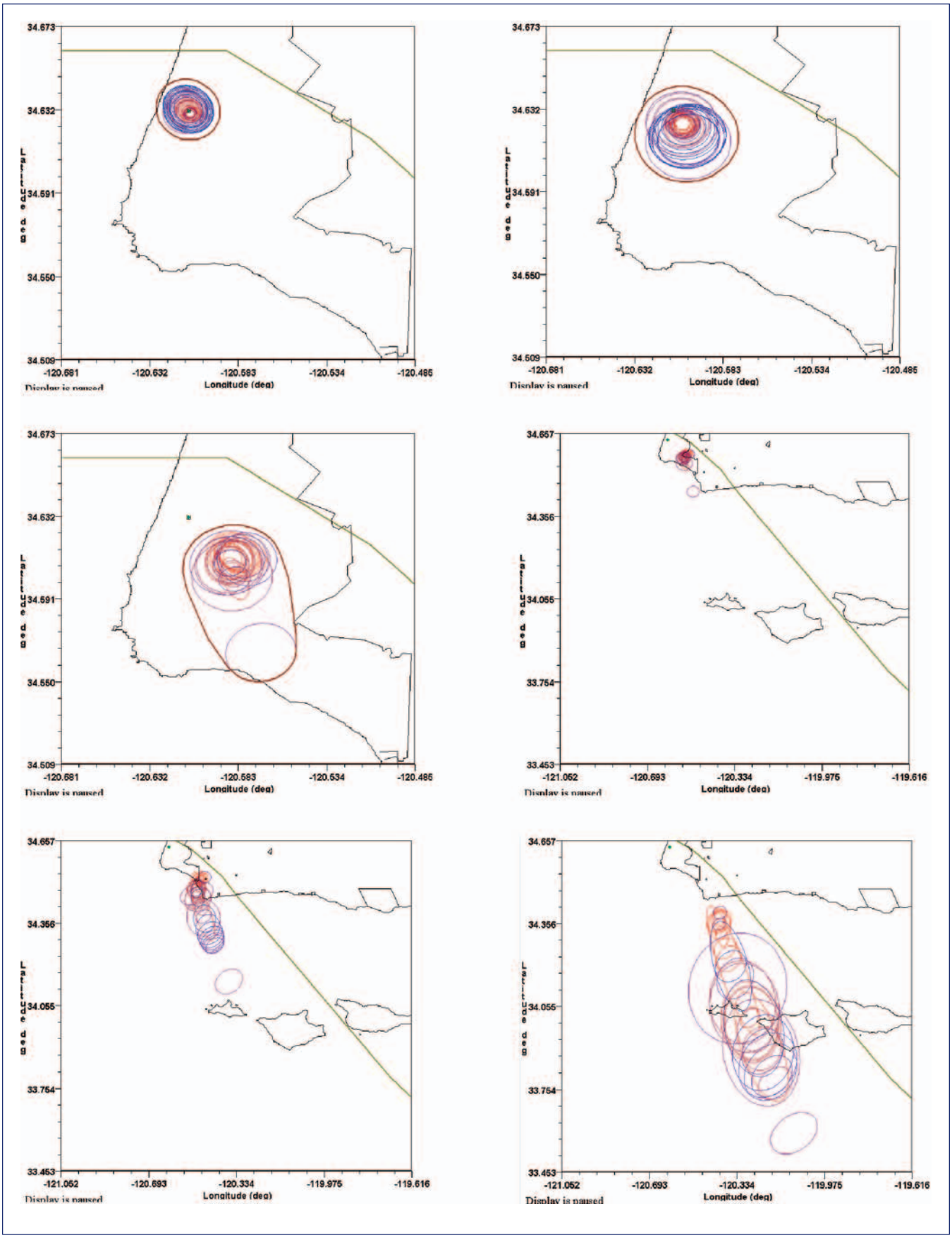


Figure 6. Titan IV Debris Footprints at 15, 30, 45, 60, 75 and 90 seconds after lift-off from Vandenberg Air Force Base (with hull before 60 seconds)).

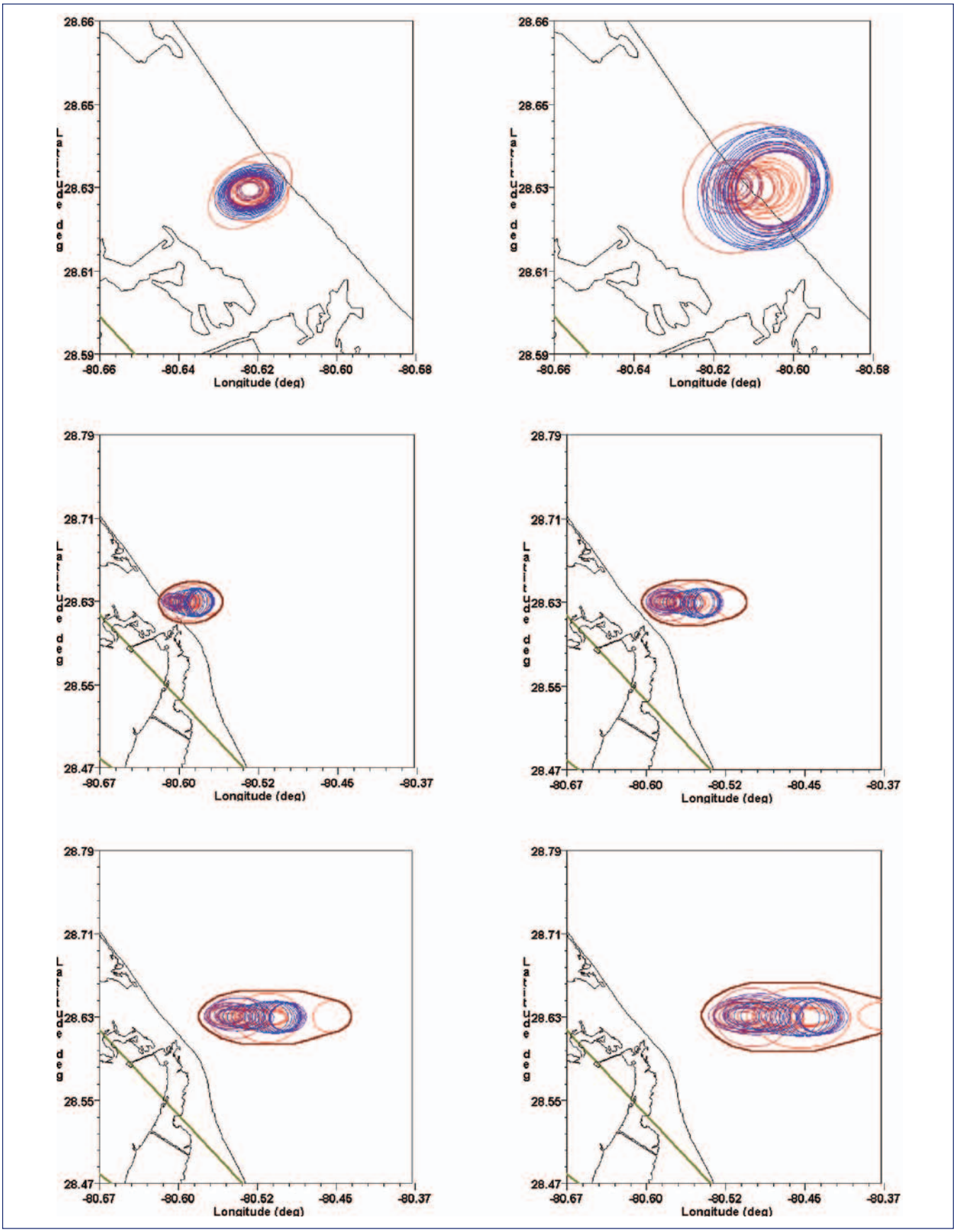


Figure 7. Space Shuttle Debris Footprints at 10, 20, 30, 40, 50 and 60 seconds after lift-off from Kennedy Space Center (with hull after 20 seconds)).

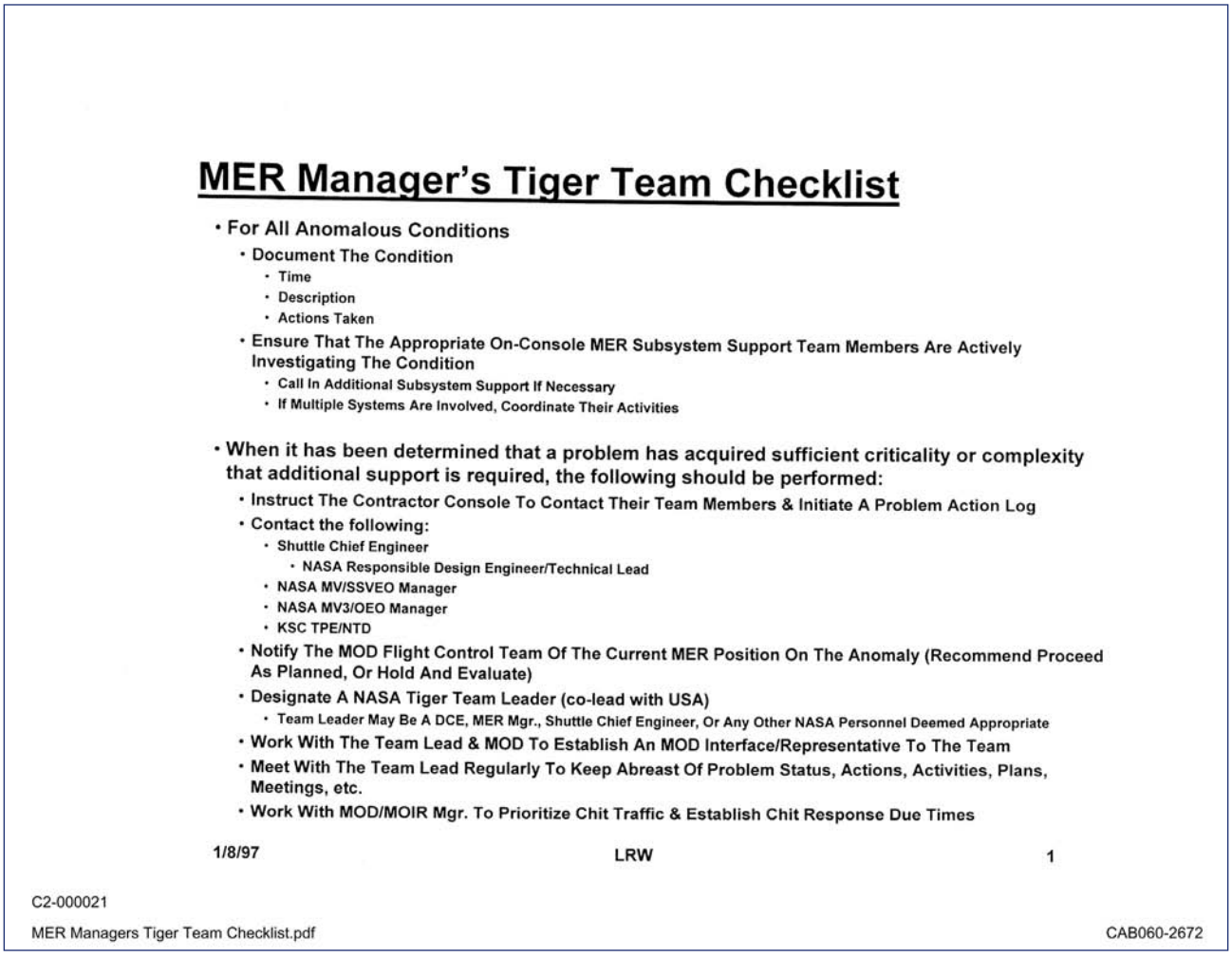
Volume II
Appendix D.17

MER Manager's Tiger Team Checklist

This appendix contains the Mission Evaluation Room Manager's Tiger Team Checklist referenced in Volume I, Chapter 6. The checklist is reproduced at smaller than normal page size.

THIS PAGE INTENTIONALLY LEFT BLANK

MER Manager's Tiger Team Checklist



MER Manager's Tiger Team Checklist

- For All Anomalous Conditions
  - Document The Condition
    - Time
    - Description
    - Actions Taken
  - Ensure That The Appropriate On-Console MER Subsystem Support Team Members Are Actively Investigating The Condition
    - Call In Additional Subsystem Support If Necessary
    - If Multiple Systems Are Involved, Coordinate Their Activities

- When it has been determined that a problem has acquired sufficient criticality or complexity that additional support is required, the following should be performed:
  - Instruct The Contractor Console To Contact Their Team Members & Initiate A Problem Action Log
  - Contact the following:
    - Shuttle Chief Engineer
      - NASA Responsible Design Engineer/Technical Lead
    - NASA MV/SSVEO Manager
    - NASA MV3/OEO Manager
    - KSC TPE/NTD
  - Notify The MOD Flight Control Team Of The Current MER Position On The Anomaly (Recommend Proceed As Planned, Or Hold And Evaluate)
  - Designate A NASA Tiger Team Leader (co-lead with USA)
    - Team Leader May Be A DCE, MER Mgr., Shuttle Chief Engineer, Or Any Other NASA Personnel Deemed Appropriate
  - Work With The Team Lead & MOD To Establish An MOD Interface/Representative To The Team
  - Meet With The Team Lead Regularly To Keep Abreast Of Problem Status, Actions, Activities, Plans, Meetings, etc.
  - Work With MOD/MOIR Mgr. To Prioritize Chit Traffic & Establish Chit Response Due Times

1/8/97 LRW 1

C2-000021

MER Managers Tiger Team Checklist.pdf CAB060-2672

MER Contractor Console Tiger Team Checklist

- For All Anomalous Conditions
  - Document The Condition
    - Time
    - Description
    - Actions Taken
  - Assist The MER Manager Console With The Call-in Of Additional Subsystem Support Personnel (If Requested)

- When the MER Manager has informed the Contractor console that a problem has acquired sufficient criticality or complexity that additional support is required, the following should be performed:
  - Contact The Following:
    - Houston BNA Mission Engineering Support Operations Director
    - Downey MSR On-Call Lead
    - Downey BNA Vehicle Project Office Personnel On Travel To Houston
    - USA Operations Requirements Project Director
    - Appropriate BNA Houston Subsystem Engineers (As Required)
    - Appropriate BNA SSM As Required
  - Create An Action Tracking List For The Anomaly
  - Organize A Hard Copy File For All Documents Associated With The Anomaly
  - Set Up A Directory On The Contractor Console Laptop (or in an appropriate file server) For All Electronic Documents Associated With The Anomaly

1/8/97 LRW 2

C2-000021
MER Managers Tiger Team Checklist.pdf CAB060-2673

Shuttle Chief Engineer's Tiger Team Checklist

When notified by the MER Manager that a problem has acquired sufficient criticality or complexity that additional support is required, the following should be performed:

- Ensure That The Appropriate Engineering Team Members Are Actively Investigating The Condition
- Work With MER Mgr. & Team Leaders To Assess The Anomaly & Plan An Initial Course Of Action
  - Call In Additional Engineering Support If Necessary
  - If Multiple Systems Are Involved, Coordinate Their Activities
  - Inform The MER Contractor Console Of The Status Of All Actions Assigned (for tracking purposes)

- Contact the following:
  - Affected NASA Division Chief Engineer(s) (DCE)
  - Affected NASA Responsible Design Engineer/Technical Lead

- Routinely Discuss/Status The Engineering Position On The Anomaly With The MER Manager And The Team Leaders

1/8/97 LRW 3

C2-000021
MER Managers Tiger Team Checklist.pdf CAB060-2674

USA Ops Requirements Project Director's Tiger Team Checklist

When notified by the Contractor Console that a problem has acquired sufficient criticality or complexity that additional support is required, the following should be performed:

- Ensure That The Appropriate Engineering Team Members Are Actively Investigating The Condition
- Designate A USA Tiger Team Leader (co-lead with NASA)
- Work With The Team Leaders To Assess The Anomaly And Plan An Initial Course Of Action
  - Call In Additional Engineering Support If Necessary
  - Inform The MER Contractor Console Of The Status Of All Actions Assigned (for tracking purposes)
- Contact the following:
  - Affected USA Subsystem Area Manager(s) (SAM)
  - Downey BNA Orbiter Program Manager
  - USA Orbiter Program Management (as required)
  - KSC NSLD On-call Personnel
  - KSC USA Vehicle Manager
  - KSC USA On-call Personnel
- Routinely Discuss/Status The Engineering Position On The Anomaly With The MER Manager And The Team Leaders

1/8/97 LRW 4

C2-000021

MER Managers Tiger Team Checklist.pdf CAB060-2675

Tiger Team Leader's Checklist

- Work With NASA & Contractor Management To Establish The Tiger Team Membership
- Work With The Shuttle Chief Engineer, The USA And Contractor Management, And The Tiger Team Members To Assess The Anomaly And Plan A Course Of Action
  - Request Additional Engineering Support If Necessary
  - Keep The MER Contractor Console Informed Of The Status Of All Actions Assigned (for tracking purposes)
  - Coordinate All Meetings Involving The Tiger Team
- Ensure That The Tiger Team Members Have Clearly Defined Actions To Perform
- Serve As The Focal Point To Ensure That The MER Manager And The NASA And Contractor Management Are Kept Informed Of The Team Position And Activities Associated With The Anomaly
  - Provide Recommendations Concerning All In-Flight Activities Involving The Anomaly
  - Coordinate The Plan Of Action
  - Coordinate Team Activities, Meeting Schedules, Personnel, And MER Facility/Administrative Support Requirements
  - Coordinate Requests For Information From The Flight Crew, Crew Actions, And Crew Troubleshooting
  - Coordinate The Generation Of, And The Responses To, Flight Chits

1/8/97 LRW 5

C2-000021

MER Managers Tiger Team Checklist.pdf CAB060-2676

THIS PAGE INTENTIONALLY LEFT BLANK

Volume II
Appendix D.18
Past Reports Review

Appendix D.18 is a summary of previous reports submitted to NASA by other independent review boards. This appendix is referenced in Volume I of the Columbia Accident Investigation Board's report; however, due to size limitations, the entirety of Appendix D.18 has been included in Volume V, Appendix G.11.

THIS PAGE INTENTIONALLY LEFT BLANK

Volume II
Appendix D.19

Qualification and Interpretation of Sensor Data from STS-107

This appendix provides a thorough review of the Modular Auxiliary Data System (MADS) recorder and sensor operation and an analysis of the data that was gathered from the MADS system and used during the investigation.

This appendix also contains several draft recommendations that were reviewed by the Board. Several of these were adopted and are included in their final form in Volume I. The conclusions drawn in this report do not necessarily reflect the conclusions of the Board; when there is a conflict, the statements in Volume I of the Columbia Accident Investigation Board Report take precedence.

THIS PAGE INTENTIONALLY LEFT BLANK

Qualification and Interpretation of Sensor Data from STS-107

Submitted by Prof. R. B. Darling, Ph.D., P.E.,
University of Washington, Department of Electrical Engineering, June 26, 2003

INTRODUCTION

The first indications of problems with the space shuttle orbiter *Columbia*, flight mission STS-107, during its re-entry on February 1, 2003, were provided by telemetry data that revealed numerous sensors on board the spacecraft had either malfunctioned or recorded a path of propagating destruction through the left wing areas. In the aftermath of the accident, during the ground search over Northern Texas, the OEX flight data recorder was recovered, miraculously intact, and it provided a wealth of additional sensor readings which have proven invaluable to reconstructing the events of the accident. In order to better understand the information provided by these two sources of data, and to provide practical working limits on the extent to which events can be inferred from them, an analysis of the sensor instrumentation systems on the *Columbia* and of the telemetry and recorded data that they provided was undertaken. This work was carried out under the direction of the independent Columbia Accident Investigation Board (CAIB) over the period of March 15 through June 15, 2003. Close support for this work was provided by the *Columbia* Task Force (CTF) at NASA which provided access to raw data, databases, briefings, technical specifications, and specific requests for information.

This report is organized into two main sections: first, an analytical description of the instrumentation system and its operational behavior, and second, an analysis of the unusual events and time correlations on the STS-107 mission. The description of the instrumentation systems follows the same order as the signal flow, starting with the various sensors themselves, proceeding though the wiring to the data acquisition hardware, onward to the data recorder or the telemetry communication links, and finally to the ground where the raw data is extracted and calibrated. The analysis of the anomalous events and time correlations first examines various groups of sensors within the telemetry data and then groups of sensors within the data that came from the OEX recorder. Finally, the report closes with some overall conclusions and recommendations.

As with all efforts to reconstruct a past series of events, numerous hypotheses are put forward to explain the circumstances. This report does not attempt to present any such hypothesis, nor to judge one as being more plausible than any other. Rather, the purpose of this report is to provide a factual basis upon which specific hypotheses can be anchored, and of equal importance, to limit the degree to which conclusions can be logically drawn. It is a natural tendency of human nature to find one minor fact and to over extend its implications. In the present case, there may be a tendency to take a one bit change from one sensor at one point in time and proclaim an entirely new scenario from it. While the one bit may support a new hypothesis, the remaining hundreds of sensors and thousands of time slices may not. In assessing the worth of various hypothetical scenarios for the *Columbia* accident, it is important to not use isolated fragments of the sensor data to support one or more pet hypotheses, but rather to use all of the sensor data collectively to uniformly critique all of the hypotheses. A single instrument does not convey the music of an orchestra, and the same is true for the sensor systems of the *Columbia*.

LINK-WISE ANALYSIS

SENSORS

Resistance-Temperature Detector (RTD) Temperature Sensors

These temperature sensors are described in drawing no. ME449-0160, which can be found in the Shuttle Drawing System (SDS) database. Ten different dash numbers are in use, -0001 through -0010, each comprising a chemically pure platinum (Pt) sensing element that is bonded onto an insulating carrier substrate. These sensors are designed to operate under normal conditions from –320°F to +500°F or up to +2000°F, depending upon the dash number. Each is configured with #30 gauge solid copper leads that are nickel plated and Teflon insulated. Higher temperature sensors have fiberglass insulation on the lead wires. The sensors are connected

by three leads, brown on one end for the (+) lead, and two white leads on the other end for (–) and ground. The sensors are designed to measure surface temperatures and are typically adhesively bonded onto the mechanical component to be measured, using either tape or RTV-560, a silicone rubber adhesive and potting compound. The lead wires from the sensor are connected to the main general purpose instrumentation wiring harnesses by means of crimp-type splices.

Platinum is a near-refractory metal and has a melting point of 1769°C (3216°F). Cold-drawn copper lead wires have a melting point of 1083°C (1981°F). Failure modes for the sensor would thus be most likely associated with debonding or adhesive release, rather than direct melting of the metallic electrical components. This depends greatly upon the specifics of each sensor installation, but should be consistent with their highest temperature of intended use.

Each sensor has a nominal resistance of 100±0.25 Ω at 0°C (32°F), except for a few which have nominal resistances of 500 and 1380 Ω. Self heating effects with up to 5 mW of electrical power produce less than 0.5°F rise in temperature. The thermal time constant for each of these sensors is less than 0.5 seconds due to their small thermal mass. A two-lead plus ground configuration is used to connect each RTD to the data acquisition system. Thus, the series resistance of the wiring harnesses does add directly to the net measured resistance of the RTD. However, 100 ft. of #24 gauge solid copper wire has a series resistance of only 2.567 Ω, and any fixed offset in nominal resistance is removed using the 0^{th} polynomial coefficient of the calibration curve. The temperature rise of the Pt sensing element produces an increase in its electrical resistance, given by the temperature coefficient of resistivity (TCR) of Pt that is $\alpha = 0.0039\ °C^{-1}$. Platinum is used for RTDs because its TCR remains fairly linear and stable over a wide temperature range. A temperature rise of 900°F = 500°C would thus change the resistance of a nominal 100 Ω Pt RTD to 295 Ω. The slight nonlinearity in the TCR versus temperature of Pt is modeled by the Callendar-Van Dusen equation. When this nonlinearity is taken in account, laboratory grade Pt RTDs can readily measure temperatures to an absolute accuracy of 0.01°C. This type of RTD and this type of nonlinear correction are not used on the Space Shuttle Orbiter (SSO) instrumentation. The inherent accuracy of the SSO Pt RTD systems is estimated to be 2-3°F. The RTD sensors were supplied by Rosemount, Minneapolis, MN, and by RdF Corporation, Hudson, NH. Rosemount has since been bought by BF Goodrich Aircraft Sensors Division. Both vendors supplied parts with serial number traceability.

Thermocouple (TC) Temperature Sensors

Thermocouple temperature sensors are described in drawing no. ME449-0204, and two different dash numbers are used. Type I (dash no. -0001) are chromel-alumel thermocouples, known in industry as Type-K, and are used to measure temperatures in the range of –250°F to +2300°F. Type II (dash no. -0002) are platinum alloy (87% Pt, 13% Rh)-platinum thermocouples, known in industry as Type-R, and are used to measure temperatures in the range of –65°F to +3000°F. Both types are welded beads between two wires of the different materials. The wire diameter is specified to be 0.010", which equivalent to #30 gauge. The two wires do not have any insulation, only short colored tape bands to indicate the lead polarity; yellow(+)/red(–) for type K; black(+)/red(–) for type R. The higher temperature capable Type-II (Type R) thermocouples are used for all temperature measurements on the lower outer skin of the wings and fuselage, the outer surface of the heat tiles. Bond line temperature measurements on the inner side of the heat tiles typically use the lower temperature capable Type-I (Type K) thermocouples. The total weight of each sensor is specified to be less than 0.2 ounces, so this will give the thermocouples a thermal time constant of less than one second. Thermocouples were supplied by Templine Co., Torrance, CA, and later by Tayco Engineering, Inc., Long Beach, CA. Both vendors supplied lot traceable calibration.

Chromel is a 80% Ni, 20% Cr alloy, also commonly known as nichrome, and has a melting point of 1400°C (2552°F). Alumel is a 96% Ni, 2% Mn, 2% Al alloy that is produced by the Hastelloy Company. Its melting point is approximately the same as for chromel. Both pure platinum and its rhodium alloy (87% Pt, 13% Rh) have approximately the same melting point of 1769°C (3216°F). All of the thermocouple metals have sufficiently high melting points that they should not have been destroyed by direct heating of the orbiter during re-entry. Each of the materials is also fairly inert so that chemical reactions with the hot gases impacting on the orbiter surfaces should not have caused any unusual etching or corrosion. Failure modes for the thermocouples would more likely arise from mechanical stresses which either broke the welds, wires, or splices, or which pinched the leads together to cause them to short at a location below the weld bead. If thermocouple wires short together downstream of the weld bead sensing point, the effect is simply to move the sensing point to the location of the short. If the short opens at a later time, the sensing point returns to the original weld bead.

The installation of the thermocouple temperature sensors on the outer surfaces of the heat tiles is a complex procedure. A chosen heat tile has an approximately 2" long slot cut into its center and the thermocouple lead wires are fed through with a needle such that the thermocouple weld bead lies coincident with the outer surface. The heat tile is then glazed in its usual manner, and the glazing seals the slot and encapsulates the thermocouple weld bead into the outer surface. On the underside of the heat tile, two small wells are cut into the tile in which insulated thermocouple extension wire is crimp spliced, and the two wells are then back filled with RTV-560. The tile is then mounted onto the orbiter surface in the usual manner with the two thermocouple extension wires running along the vehicle bond line, and out from the bottom edge of the heat tile. An adjacent heat tile is used as the location where the thermocouple extension wires are fed through a grommet into the interior of the vehicle. After the wires have been spliced together, the adjacent heat tile is mounted in the usual manner to close up the connections. About 12" of thermocouple wire runs directly along the bond line of the vehicle, sandwiched between the heat tile and the metal surface paneling. Once inside the vehicle, the thermocouple extension wire is crimp spliced to the thermocouple reference junction (TRJ). Although the grommet through the

metal surface paneling provides a smoothed edge, severe mechanical trauma to this point could cause the insulation on the thermocouple extension wire to be cut, shorting the thermocouple wires to the aluminum metal panel, the grommet, or to each other. Another failure mode is through direct mechanical abrasion or impact to the outer surface of the heat tile where the thermocouple weld bead is located. Past flight history on the OV-102 has indicated that these thermocouple installations have been quite robust with no direct failures from mechanical sources having been reported.

Direct heating of the thermocouple wires will increase their series resistance, similar to the effects in an RTD; however, the thermocouple has a low impedance of 25 Ω or less which works into a high impedance bridge circuit. Hence, heating effects which change the resistance of the wires have an insignificant effect on the measured reading. Thermocouples directly measure the temperature difference between two junctions, the sensing junction and the reference junction. For this reason, thermocouple extension wires are made of the same metals as the original wires themselves. The transition from these special metals to the copper of the wiring harnesses occurs at the thermocouple reference junction (TRJ). The signal voltage that appears between the two copper wires is termed the Seebeck voltage, and it is roughly proportional to the temperature difference between the two junctions and the Seebeck coefficient for the thermocouple pair. For Type K thermocouples, this relationship is fairly linear over a wide range; however, for Type R thermocouples, the relationship has a significant parabolic bow. Calibration for the Type K thermocouples is essentially first order (linear), while calibration for the Type R thermocouples is necessarily second order (parabolic). With this level of calibration, the temperature measurements produced by the thermocouple systems should have 5-7°F accuracy.

Thermocouple temperature transducers refer to a prepackaged thermocouple probe in which a bead-type thermocouple junction and its leads are encased in either a stainless steel or inconel sheath. The interior of the probe is filled with a MgO insulation. These are described in drawing no. ME449-0169. Ten different dash numbers are listed and correspond to different probe lengths (12, 20, and 36 inches), thermocouple types (K or R), sheath material (inconel, stainless steel, or Pt-Rh alloy), and connector fitting (none, pipe thread, or strain relief plate with Teflon sleeve). Type VI covering dash numbers -0008, -0009, and -0010, are assemblies with 3, 2, and 1 sheathed probes, respectively. The probes are collected together into a common connector shell, and each has pre-attached inconel mounting lugs welded to the probe sheath. All of the probes are ungrounded. Type K are specified for ±2°F accuracy; type R are specified for ±10°F accuracy. The fast responding types have thermal time constants of less than 0.1 seconds, while the others have thermal time constants of less than 5.0 seconds. Sensor resistance is specified to be less than 25 Ω with an insulation resistance of greater than 50 MΩ. Operating lifetime is specified to be greater than 5000 hours. These probes appear to be used rather infrequently in the orbiter and only for a few single-point specialized applications, such as the TPS and ambient gas temperature sensing in potentially explosive environments.

Standard Pressure Sensors

Standard low, medium, and high pressure sensors are described in drawing no. ME449-0177. A total of 129 different dash numbers are detailed; however, only two of these, -2101 and -2108 are absolute pressure sensors with a range of 0-15 psia, of the type that were used for OEX aerodynamic measurements on the wing outer surfaces. Both of these are rated as having a 25 psia proof pressure and a 45 psia burst pressure. All of the pressure sensors in this family are strain-gauge diaphragm types and consist of cylindrical metal housing with a threaded tubulation to connect to the pressure sensing port and a multi-pin connector on the other end from which the strain gauge bridge leads are connected into the instrumentation wiring harness. The great majority of all 129 of these sensors are absolute pressure sensors and have a sealed reference vacuum chamber on one side of the diaphragm. For a 0-15 psi absolute pressure sensor, the diaphragm is maximally deflected at sea level pressure of about 14.7 psi, and then becomes neutral (undeflected) as the absolute pressure drops to zero to match the sealed vacuum reference chamber. Each of the strain gauge bridges is excited by a +10.000±0.001 VDC regulated power supply and outputs a maximum signal of 30 mV at full scale deflection. The output impedance of the strain gauge bridge is nominally 2000 Ω. Most of these sensors were manufactured by Schlumberger, Statham Transducer Division, Oxnard, CA.

The pressure measurements recorded in the OEX data were aerodynamic measurements of absolute pressure on the R and L wings. The sensors for these measurements were installed according to six installation drawings: V070-192151, V070-192146, V070-192145, V070-192131, V070-192130, and V070-192134. All of these are 0-15 psia measurements, except for V070-192146 locations which are 0-16 psia measurements that are taken by miniature pressure sensors, described below. The pressure sensing ports were all located on either the center of a specific heat tile, or within the upper wing surface FRSI material. The installation of the pressure ports into the heat tiles was, like the thermocouple installations, rather complex. Each tile with a pressure measurement had a hole drilled through it and Pyrex or Vycor tube was press fitted into the tile to provide a sealed bore. The backside of the tile was milled out to provide a cavity for sealing the backside of the glass tube to a grommet in the metal bond-line skin. The tile was mounted using the usual RTV-560 and a special ring of RTV was created to form the gasket between the glass tube in the tile and the grommet in the metal bond line skin. On the inside of the wing metal skin, a port fitting block was installed into the wing at the time of the wing's manufacture that provided a connection point between the wing grommet and the tubulation of the pressure sensor that was screwed into the port block. The ports were arranged typically along constant Y planes of both wings to provide lateral pressure profiles across the wing versus time.

Of the 181 total aerodynamic absolute pressure measurements recorded in the MADS/OEX data, 55 of these were sensors that were known to be bad prior to the launch. These bad sensors were most likely the result of age and continued stress on the sealed vacuum reference chamber which would

introduce first an offset into the data, and later a permanent OSL condition, since the sensor was designed to measure diaphragm deflections in only one direction. The specifications for the pressure sensors note that they only have a 10 year shelf life, and the orbiter was over 22 years old. The age of the vehicle and the continual one atmosphere of static pressure against the diaphragm is probably responsible for the high fraction of these which went bad prior to the launch of STS-107. Failure modes for absolute pressure sensors are either a slow, gradual leak rate over time into the reference vacuum chamber, or a catastrophic leak which may immediately add a one atmosphere offset to the reading. In all cases, the sensor reads lower pressures as the reference vacuum chamber pressure increases due to leaks.

Miniature Pressure Sensors

The miniature pressure sensors are described in drawing no. ME449-0219. They consist of two types, a Type-I in which the pressure sensing port lies parallel to the body of the sensor, and a Type-II in which the pressure port is the axial end of a nozzle coming out of the body. There are 12 dash numbers, -0001 through -0006 are 0-15 through 0-20 psia range sensors of Type-I, and -0007 through -0012 are 0-15 through 0-20 psia range sensors of Type-II, respectively. All of these devices are excited by a +5.000±0.001 VDC regulated power supply and produce 15 mV full scale output from the strain gauge bridge. All four legs of the strain gauge bridge are contained within the body of the sensor and a temperature compensation module is also included, usually within the overall sensor body. These sensors are probably micromachined silicon strain gauges and diaphragms, due to their size, and were manufactured by Kulite Semiconductor Products, Ridgefield, NJ. These miniature pressure sensors were used mainly for the smaller installation areas within the FRSI material on the upper surface of each wing. All of these devices were 0-16 psia range sensors and are shown in installation drawing no. V070-192146. These devices were also absolute pressure sensors, so all of the preceding comments on the standard pressure sensors also apply to these. The Kulite pressure sensors are generally remarked to be more fragile than the larger Statham types.

Strain Gauge Sensors

The strain gauge sensors are described in drawing no. ME449-0141, and 40 different dash numbers are used to enumerate the many different geometrical permutations that are used. The strain gauges can be configured as single, double, or triple sensors, involving two, three, four, or six leads. Single devices measure uniaxial strain along only one direction. Double devices measure either coarse and fine uniaxial strain along one direction, or more commonly, biaxial strain along two orthogonal directions. Triple devices, sometimes known as strain gauge rosettes, have three devices oriented at 0°, 45°, and 90°, through which the two uniaxial strains can be directly measured, e.g. ε_x and ε_y, and the in-plane shear strain can then also be computed from the set of all three readings, e.g. τ_{xy}. Double and triple strain gauges can be recognized by their different measurement system IDs (MSID) having identical (X, Y, Z) coordinate locations on the vehicle, and are usually denoted by A,B or A,B,C suffixes.

The strain gauge itself is a thin-film metal serpentine pattern composed of either a nickel or copper alloy. The strain effectively changes only the geometrical aspect ratio of the equivalent resistor, not the resistivity of the thin film metal, so each strain gauge has a gauge factor that is very close to the theoretical ideal of 2.00, or equivalently, $\Delta R/R = 2.00*\varepsilon$. The great majority of the various dash numbers have a nominal resistance of R = 1000±0.8% Ω. The thin film metal serpentine pattern is printed onto a carrier material of either glass fiber reinforced epoxy-phenolic resin, or Q or E grades of polyimide film. Wires from each strain gauge element are crimp spliced into the instrumentation wiring harnesses and then run back to the central data acquisition system at which point they are handled by a special strain gauge signal conditioner (SGSC).

All of the strain gauges are specified to be self-temperature compensated (STC) types. This means that the strain gauge is configured for each measurement point so that the entire bridge circuit is located at the sensing site. Each resistor in the bridge is constructed in a similar manner and has the same nominal resistance; thus, each leg of the bridge will experience close to the same variations in temperature with resistance. The thin-film metal serpentine resistors will have, taken by themselves, TCRs in the range of 3500 to 4300 ppm/°C, similar to most metals. Balancing four of these together in a bridge reduces the overall TCR of the bridge to typically a few ppm/°C. The strain gauges are specified to be temperature compensated to better than 13 ppm/°F, 6 ppm/°F, and 0 ppm/°F. The "0 ppm/°F" is most likely interpreted to mean less than 0.5 ppm/°F. The Wheatstone bridge resistances are thus temperature compensated very closely; however, like any strain gauge, the gauge factor itself is not temperature compensated. Unlike a silicon resistor strain gauge, the metal film resistor strain gauges produce a gauge factor that is due to only geometrical changes rather than a combination of geometry and resistivity changes that a silicon resistor strain gauge would respond to. The gauge factor is specified to vary not more than 0.85% per 100°F over a temperature range of –200 to +500°F. For a metal film resistor strain gauge, the gauge factor is extremely temperature independent, and usually not a significant influence on the measurement. Due to the high heat that most of these sensors would have experienced during normal operation and during the accident, the effects of temperature on the strain gauges are of great importance to understanding and correctly interpreting the sensor data. The design of the strain gauge sensors appears to have reduced the temperature sensitivity to a negligible level, and the output from the strain gauges can safely be interpreted as actual mechanical strain, as opposed to a combination of strain and temperature effects on the sensor itself.

In terms of environmental ruggedness and reliability, the strain gauges are quite hearty. They are specified to have a shelf life of 5 years, isolation resistances of greater than 300 MΩ, specified operation over 10^{-10} torr to 15 psia, and remain capable of indicating strains over the range of ±10,000 μin/in (±1% elongation) over their full lifespan. Most measurements are designed to record over a range of ±1000 μin/in, and are thus well within the mechanical elasticity of the strain gauge itself. The specified temperature range for operation is –250 to +350°F. The strain gauges were originally

procured from Micro-Measurements, Raleigh, NC, but the vendor was later changed to Vishay, Measurements Group, Wendell, NC. Gauges are tracked by lot number, and each is supplied with a calibration curve of apparent strain over a temperature range of –300 to +500°F and gauge factor versus temperature over a temperature range of –200 to +500°F.

Piezoelectric and Low Frequency Accelerometers

Piezoelectric accelerometers are described in drawing no. ME449-0150. Six different dash numbers are described, -0001 for Type I, up through -0006 for Type VI. Types I, III, and V are compression types of nominally 2000 pF capacitance, while Types II, IV, and VI are ring shear types with nominal capacitances of 900 pF, 400 pF, and 770 pF. Types I, III, and V are packaged as a 5/8" hexagonal body that mounts on a #10-32 threaded stud. The bodies are roughly an inch tall. Type II have a 0.600" dia. × 0.350" tall cylindrical body. Type IV are a smaller 3/8" hexagonal body, and Type VI are 0.375" dia. × 0.220" tall cylindrical body. Each had a proprietary Endevco coaxial connector fitted to the body. The charge sensitivity for each of the six types is 11.5±0.4, 10.5±1.0, 11.5±0.4, 2.8±0.2, 11.5±0.5, and 3.071±0.180 pC/g at 100 Hz. The frequency response range of each of the six types is 20-2000, 2-50, 20-2000, 20-2000, 1.5-50, and 1.5-10 Hz. Transverse sensitivity is typically limited to 2-3% of the primary axis sensitivity. The response is linear with acceleration to within 1 % error. Each of the six types is specified to have a shelf life of 5 years and an operating service life of at least 2000 hours. These accelerometers were supplied by Endevco, San Juan Capistrano, CA, and were supplied with serial number traceability.

Linear, low-frequency accelerometers are described in drawing no. ME449-0163. Two dash numbers are described, -0001 and -0002; Type I have a temperature range of –65 to +250°F, and Type II have a temperature range of –400 to +350°F. The body is a 0.750" hex, 1.000" tall, and mounts with a ¼"-28/#10-32 threaded stud. A proprietary coaxial connector is fitted to one face of the hexagon base. These devices measure accelerations of 2 to 10 g over a frequency range of 1.5 to 50 Hz. The capacitance is nominally 1000 pF. Charge sensitivity is 11.5±0.2 pC/g at 50 Hz and an amplitude of ±10 g at 70±10°F. These accelerometers are also specified to have a shelf life of 5 years and an operational service life of at least 2000 hours. These accelerometers were supplied by Gulton Industries, Inc., Costa Mesa, CA, and were supplied with serial number traceability.

Both of these accelerometer types are used with a FDM signal conditioner to supply wide-band data measurements. Coaxial cable is run all the way from the sensor at its measurement location back to the FDM units which are housed in midbody bay 8, roughly bottom center in the fuselage, underneath the payload bay. These sensors do not share any power feeds with other sensors since they do not use a DC bias.

Proximity Switches

Proximity switches are described in drawing no. MC452-0124 and consist of three parts: a target piece, the sensor, and an electronics unit. The target is a thin piece of high permeability alloy, usually Hi-Mu 80, Moly Permalloy, or equivalent, typically about 1.0" × 0.5" × 0.05" in size, and mounted on the moving part of the mechanism whose position is to be sensed. The sensor is a small metal box with mounting lugs that contains two legs of a half bridge. The mating half bridge is contained inside the electronics unit and forms a reluctance bridge whose balance point is perturbed by the position of the target relative to the sensor. The electronics unit contains the mating half bridge, a differential amplifier which serves as a detector, a trigger and output driver circuit, a power supply and oscillator to excite the bridge, and several built-in test equipment (BITE) circuits to verify the operation of the system. The output is a discrete logic voltage, ON = +5.0±1.0 VDC and OFF = 0.0±0.5 VDC, with less than 20 μs rise and fall times. The electronics unit is powered by 115 VAC, single phase. The discrete output goes ON when the target enters the actuation envelope of the sensor, and the discrete output then goes OFF when the target leaves the deactuation envelope of the sensor. The deactuation envelope surrounds the actuation envelope to produce hysteresis in the operation of the proximity switch. The two legs of the bridge inside the sensor, Z_x and Z_a, are both inductors, whose mutual inductance is altered by the position of the target. The operation of this bridge circuit is similar to a linear variable differential transducer (LVDT).

Wiring

Wires

General purpose insulated electrical wire is described in drawing no. MP571-0086. Ten different dash numbers are listed which correspond to even wire gauges, -0001 being #26, and -0010 being #8. The greater majority of the wire used in the sensor instrumentation is -0002, #24 gauge, and is a stranded wire comprised of 19 strands of #36 gauge nickel plated copper wire. It is listed as having 30.10 Ω per 1000 ft. and a weight of 2.0 lbs. per 1000 ft. Each wire is wrapped with two oppositely spun layers of polyimide tape, each 1 mil thick with 0.1 mil coatings of FEP Teflon resin on both sides for lubrication during flexure. The outer insulation coating is 1 mil thick pigmented polyimide resin. For the -0002 #24 gauge wires, the insulation pigment is blue.

Each orbiter contains over 852,000 feet of wire with a weight of over 5,369 lbs. The OV-102 instrumentation load was heavier still, due to the extensive OEX sensor suite that was installed. Kapton insulation was used primarily because of its light weight (25% savings over conventional PVC insulation), size (50% smaller with no thick plastic jacket present), good chemical resistance, and thermal tolerance. However, Kapton has the disadvantage of being susceptible to splitting, cracking, and fraying when handled roughly or abraded. Most of the wiring damage recorded on the orbiter repair logs has been due to the wiring insulation getting mashed, cracked or split, or torn to cause a fault with the internal wires.

Cables

General purpose shielded and jacketed electrical cables are described in drawing nos. MP572-0310 through MP572-0316, for 1 to 7 conductors, respectively. Dash numbers

-0001 through -0006 correspond to wire gauges of #26 through #16, respectively, and match to the same dash numbers of the wire used for creating the cable. Each bundle of wires is wrapped in a braided shield composed of #38 gauge nickel plated copper strands providing at least 85% coverage of the wires contained inside. The shield is then jacketed with two wraps of oppositely spun polyimide tape, 1 mil thick with 0.1 mil of FEP Teflon resin on each side to provide flexure lubrication. Thermocouple extension cables are created using the same construction practice, except that the conductor metal is chosen to match that of the thermocouple being extended. For example, a MP572-0329-0001 thermocouple extension cable is the same as a MP572-0311-0002 wiring cable (2 conductor, #24 gauge), except that one of the wires is copper (MP571-0088-0001) and the other is copper alloy (MP571-0089-0001).

Cables of this type comprise the greater majority of the orbiter wiring. The long length runs from the sensors far out in the orbiter extremities to their signal conditioners in the central fuselage avionics bays add greatly to this sum. The RTD temperature sensors each used a shielded three-wire cable, MP572-0312, while the pressure sensors, strain gauges, and cables from the remotely placed thermocouple reference junctions (TRJs) each used a shielded four-wire cable, MP572-0313.

Splices

All splices are achieved using crimp type sleeves of four basic types: parallel splices (ME416-0030), butt splices (ME416-0031), solder sleeves (ME416-0032), and shielded cable splices (ME416-0034). Two dash numbers are used: -100X for the crew compartment and equipment bays, which are blue Kynar, and -200X for general use everywhere else, which are white Teflon. The shielded cable splices are used primarily for data buses and firing wires on pyrotechnic actuators. Installation practices are described in ML0303-0031 for splice and lug crimping, and in MA0113-304 for wire stripping.

The crimp sleeves appear to be constructed of a nickel alloy, and each is insulated with what appears to be a heat shrinkable polyolefin tubing. Splices are usually left free floating from the wiring harness with no tie wraps or other mechanical hold downs. Apparently, no solder is used anywhere within the wiring systems. The melting points of any solder joints are thus not a concern for the sensor instrumentation.

Connectors, Terminal Boards and Interface Panels

The large number of sensor cables are interconnected via high density multi-pin connectors, usually grouped together on specific interface panels which separate structural sections of the orbiter. The most commonly used are NLS connectors and are used for high density interconnections of 6, 13, 22, 37, 55, 66, 79, 100, or 128 contacts. These are described in NASA MSFC specification 40M38277. These are rated for use over the temperature range of –150°C to +200°C, although the hermetically sealed versions are derated to –100°C to +150°C. These connectors are circular, bayonet coupled, and designed for low outgassing. All of the contacts are size 22D. Smaller numbers of connections, from 3 to 61, with contacts of sizes 12 to 20, are handled by the NB connectors, described in 40M39569. A special version of these, the NBS connectors, have 2, 3, or 4 contacts, are used for pyrotechnic firing circuits, and are described in 40M38298. Another special version, the NC connectors, described in 40M38294, are used on cryogenic systems. All of these connectors have the same temperature ratings as the NLS connectors. Bayonet couplings are typically used for signals, while threaded couplings are used for power. Typical power connectors are described in drawing nos. ME414-0234 (receptacles) and ME414-0235 (plugs).

Grounding straps are used to interconnect frame components together into a low impedance ground network at most junctions between panels. This is achieved with uninsulated braid between crimped frame lugs. The Koropon paint is scraped away below each ground lug and a self-tapping screw is used to bite into the aluminum frame components. Each grounding lug is then coated with RTV-560 to exclude corrosion agents. Central point grounding is achieved though a network of terminal boards where ground leads and cable shields are collected. The terminal boards are described in drawing nos. ME417-0010, -0013, -0014, and -0015.

Multiple bulkhead mounted connectors are collected into interface panels between structural sections of the orbiter. The two most relevant ones are the LH wing interface panel #65, and the LH wheel well interface panel #67. Inside the LH wing box, panel #65 has 14 connectors feeding 5 cable harnesses, four running aft and one running forward. The harnesses are composed primarily of sensor instrumentation on the following connectors: run#1 aft: 65P107, 65P101, 65P113, and 65P115; run#2 aft: 65P123 and 65P121 (a dummy); run#3 aft: 65P109, 65P115, 65P119, 65P117, and 65P143; run#4 aft: 65P107, 65P141, 65P105, 65P103, and 65P111; and run#1 forward; 65P105 and 65P111. Inside the LH wheel well, panel #67 has 18 connectors feeding a large number of short harnesses that service the LH wheel hydraulic system. Panel #67 connectors include: P1, P3, P5, P7, P9, P11, P13, P15, P17, P19, P57, P63, P65, P79, P85, P87, and P89.

The insulating resin materials used in most mil-spec connectors, usually phenolics, provide good stability up to temperatures of 450-500°F, and sometimes higher. The insulating material and the connector pins are both protected by metal shells, making the electrical integrity of the connector typically much higher than that of its cable. Indeed, many electrical connectors were found in the orbiter ground debris, and most were still functional with the internal connectors intact.

Harnesses, Installation and Routing

Wires and cables are grouped together in a parallel lay fashion (without twisting or braiding) and bundled together into harnesses with spot ties. This is described in specifications MLO303-0013 and MLO303-0014. The spot ties are a waxed, woven lacing material that is hand tied around the harness bundle at each point and the ends clipped off short.

The harnesses are secured to the vehicle frame by PTFE Teflon tape, PTFE Teflon adhesive sheet, or TFE Teflon tape. Convoluted tubing and rubber extrusions are used to provide protection of the harnesses around sharp edges and turns. Harnesses involving only a few wires or cables are typically held in place with Teflon tape which is sometimes strengthened with a layer of red RTV-560. The heavy harnesses on OV-102 that contained hundreds of sensor wires were supported by metal cable clamps with rubber linings of up to a few inches in diameter. Close-out photographs of the wing box interior show this construction clearly.

Probable high temperature failure modes for the harness materials are release of the adhesive tapes, allowing the harness itself to wander, or burn-through of the spot ties, allowing individual wires or cables to move about. The metal cable clamps used on the more extensive sensor wiring of OV-102 should have in principle provided better high temperature survivability than the tape and string approach used in the later model orbiters.

Cable Burn Through Patterns

Analysis by the NASA *Columbia* Task Force (CTF) identified the failure mechanisms of many sensors as being a "propagating soft short," that is essentially a zone of insulation breakdown between two conductors of the cable that expands in both directions along its length, traveling away from the heat source along the temperature gradient caused by the thermal conductivity of the wires. Blow torch and oven testing of sample cable bundles showed that the conductor-to-conductor insulation resistance began to fall when the cable temperature rose to 1000°F, and then fell precipitously when the cable temperature rose to 1200°F. This testing also showed that shorting between conductors as a result of oven or torch heating was much more prevalent than the creation of open circuits. This is no great surprise since the melting point for the copper conductors is 1980°F, almost 1000°F higher, as would be required to simply melt away a conductor to create an open circuit. Most organic insulation materials degrade at elevated temperatures by reaction with available oxygen, and ultimately this leads to a black, carbonized composition which can become somewhat conductive and lead to gradual shorting of adjacent conductors. Simple heating, taken by itself, is generally far less of a degradation mechanism than the chemical reactions which can be brought into play by the available reactive compounds in the presence of that same heat.

It should be noted that the initial CTF cable testing was performed with a blow torch in air at atmospheric pressure (nominally 14.7 psia at sea level), and at the time for which the wiring in the orbiter appeared to be damaged, the atmospheric pressure surrounding the orbiter was just rising to less than 0.5 psia. With much less available oxygen, the degradation mechanism of the cables was undoubtedly different from what these sea-level blow torch tests attempted to reproduce. A reduced oxygen environment would tend to restrict the rate of the chemical process and extend the degradation time of a given cable. Some sensors exhibited decay times to off-scale low (OSL) that were over 200 seconds long, and this rather long time could possibly be caused by a restricted oxygen concentration. On the other hand, the momentum transfer of the impacting hot gas stream within the wing box could have acted to accelerate the breakdown of the insulation by direct mechanical erosion, somewhat counteracting the rate limiting by available oxygen. While the blow torch tests do produce some gas velocity, this is only a meager subsonic flow caused by the combustion pressure, and no where near the Mach 15-20 speeds of the air molecules impacting against the leading surfaces of the orbiter. The subsequent arc-jet testing of the cable harnesses much more closely approximated the conditions on the orbiter, although the arc-jet testing was still performed at atmospheric pressure.

Many of the sensor data, particularly those from the OEX/MADS recorder, also showed significant chatter and erratic readings, in many cases transitioning between off-scale high (OSH) and off-scale low (OSL) over an extended period. It was suggested that this might be caused by the hot gases entering the wing box having some degree of ionization, and the impact of these charged ions against the bare or partially insulated cables might create a significant electric current which would saturate the sensitive input amplifiers of the signal conditioners. However, Fig. 4.12 on p. 114 of W. L. Hankley, Re-Entry Aerodynamics, AIAA Education Series, 1988, shows that at an altitude of 200,000 ft and a velocity of 15,000 ft/sec, oxygen is well over 90% dissociated, nitrogen is slightly less than 10% dissociated, and the overall degree of ionization is less than a few percent at most. Hence, ionization related effects such as conductor charging are not likely to be very substantive under these conditions.

What is of perhaps greater importance, is the noted high fraction of dissociated oxygen. Free monoatomic oxygen (O) is an extremely reactive species, far more combustive and reactive than molecular oxygen (O_2). It is very probable that the monoatomic oxygen would cause a much faster degradation of the Kapton insulation for a given temperature, or equivalently, would produce the same damage at much lower temperature. The drastically increased erosion rates of Kapton insulation by monoatomic oxygen are well documented, and were first studied in detail following shuttle mission STS-03 (L. J. Leger, AIAA paper no. AIAA-83-0073, 1983). Typical erosion rates for a low Earth orbit (LEO) environment are $0.01\text{-}0.09 \times 10^{-24}$ cm^3 per incident oxygen atom for aluminum coated Kapton. The best data on monoatomic oxygen exposure is probably that taken from the NASA long duration exposure facility (LDEF) which spent 5.8 years in LEO and which was retrieved in 1990.

Thus, there is great deal of uncertainty about the specific conditions within the wing box that surrounded the burn through of the sensor cabling. In particular, one important question is the degree to which the incoming hot gas was focused into a directional jet, broadly dispersed, or somewhere in between. Some conditions could be pointed to as ones which would increase the burn through time, while there are others that would just as easily have shortened it. The particulars of where a specific cable resided within the harness would also have a significant effect on its burn through speed, with those directly exposed on the periphery going quickly and those concealed within the center holding out for lon-

ger. While the sensor instrumentation system of the orbiter provides an extremely precise time referenced recording of the electrical anomalies, there still exists quite a bit of time uncertainty associated with the physical events which may have prompted the electrical ones when a cabling fault is at cause. A sensor reading may show a wire burn through signature that abruptly transitions to an off-scale limit at a clearly delineated moment in time, but the burn through process of that particular pair of wires could have begun anywhere from 2 to 200 seconds prior, to cite the extremes.

Nonetheless, with the degradation temperature of Kapton insulation in the range of 1000 to 1200°F and the melting point of copper at 1980°F, the failure mode of a cable will involve first a loss of insulation resistance and then a loss of conductor integrity. Simply put, a cable that is subjected to heating or combustion should first develop short circuits between the conductors at roughly 1000°F, and then open circuits only after the individual conductors melt away at roughly 2000°F. This ordering of "shorts before opens" is also true for a bundle of wires that is mechanically mashed, torn, or sheared, and one of the largely unwritten rules of electrical engineering. Temperatures of only 1000-1200°F are all that is required to produce shorting cable faults, and these would be largely indistinguishable from purely mechanical insults which would produce the same electrical effects. So why is there the nearly universal presumption that all of the sensor cables burned through, rather than being mechanically torn apart? For many the justification is quite clear, since there was a temperature sensor in the immediate vicinity which recorded rapidly increasing temperatures. This was clearly the case for the four key sensors behind the damaged leading edge area of the left wing.

Wiring Faults and Failure Modes for Bridge Type Transducers

One of the most distinctive features of the instrumentation vintage used on the space shuttle orbiters is the prevalent use of Wheatstone bridge transducer circuits. A four-resistor Wheatstone bridge is used with each pressure sensor, with each strain gauge, with each thermocouple reference junction, and with each RTD temperature sensor. In the case of the pressure sensors and strain gauges, all four legs of the bridge are within the sensor itself. The thermocouple reference junction contains all four legs of the bridge to which the thermocouple Seebeck voltage is added. The RTD temperature sensors are one leg of a bridge and the remaining three legs are contained in the bridge completion circuit which is part of the central data acquisition system.

The four resistor legs of a Wheatstone bridge form a square, and the bridge is excited by a DC voltage that is applied across two opposite corners of the square, labeled EXC+ and EXC–. The signal output from the bridge is taken from the other two opposite corners of the square and labeled SIG+ and SIG–. Any bundle of N independent wires will produce N possible open circuit and (N – 1)! possible short circuit single wiring faults. Discounting the shield, the four wire cables used for most of the bridge type transducers create 4 open circuit and 6 short circuit single wiring faults. Multiple wiring faults, those involving multiple combinations of shorts and opens, are increasingly complicated to diagnose, but by in large, most cable faults begin with a single wiring fault and then progress from there.

When the resistance ratios on both sides of the bridge are equal, the SIG+ and SIG– nodes will be at the same potential, and the difference between these two nodes, which is what is measured by each of the various signal conditioners, is zero. The physical quantity that each sensor measures causes a deviation away from this balanced condition of the bridge and a difference in potential is produced between the SIG+ and SIG– nodes, which is amplified by the signal conditioners and passed on for digital processing, recording, and transmission by the remainder of the instrumentation avionics.

Various wiring faults can create specific trends in the recorded data, depending upon how the specific signal conditioner reacts to them. For example, if the EXC+ wire happens to short to the SIG+ wire, the SIG+ node is immediately pulled up to the positive DC power supply voltage and the large positive difference between the SIG+ and SIG– nodes creates an off-scale high (OSH) output, essentially saturating at the highest possible value within the input range of the signal conditioner. Similarly, shorting the EXC– wire to the SIG– wire would pull the SIG– node down to the negative power supply voltage and produce the same effect of an OSH. The opposite pairings of a short between EXC+ and SIG– and between EXC– and SIG+ would both produce the opposite off-scale low (OSL) reading from the signal conditioner. These four shorts between adjacent wires of the Wheatstone bridge produce the same patterns of OSH and OSL for all of the different signal conditioners, since the voltages remain well-defined on all four nodes of the bridge.

A symmetrical short between the SIG+ and SIG– nodes clearly produces zero potential difference between the nodes, but this does not necessarily produce a zero reading for the sensor. If the 4-wire cable went to a strain gauge signal conditioner (SGSC), then the input differential amplifier of this unit would have an input of zero and the output would be taken to the level set by the adjusted offset level of the differential amplifier. Each SGSC has a potentiometer screw adjustment to zero out its own offset against that of its sensor, but when the input is shorted, only the adjusted offset of the differential amplifier remains. The recorded output of the shorted sensor is then just the offset level of the differential amplifier, which can be quite some distance away from zero. However, for other signal conditioners, most notably those in the MADS PCM units, to be described shortly, there is no offset adjustment on the differential amplifier and for them, a shorted input creates a off-scale low (OSL) condition, due to the required bias currents of the differential amplifier being no longer supplied by the sensor.

The situation for open circuit wiring faults is more complex still and highly dependent upon the particular characteristics of the differential amplifier of the signal conditioner. When an open circuit occurs, that particular node then floats and the potential that it comes to rest at depends upon the resulting voltage division between whatever internal components are left on the high impedance nodes of the differential amplifier. Without detailed knowledge about the input dif-

ferential amplifier of each signal conditioner, it is nearly impossible to determine with certainty what will happen to the resulting sensor reading. The NASA CTF performed a matrix of tests on each of the sensor types and their possible configurations to determine what would happen for each of the possible single wiring faults. The results ended up being quite different for the different types of signal conditioners and sensor configurations.

Interestingly, the rather important case of a short between EXC+ and EXC– was omitted for all but the thermocouple reference junction (TRJ). For the TRJ, a short between EXC+ and EXC– resulted in simply an offset output, since for the thermocouple, turning off the TRJ simply feeds the un-referenced Seebeck voltage directly to the differential amplifier input. The importance of the case of a EXC+ to EXC– short is that it is central to the common coupling that can exist between several sensors that are each fed by a single DC power supply, as will be discussed later. The design of the instrumentation suggests that the response to a short between EXC+ and EXC– will also vary with the type of signal conditioner and sensor configuration. The lack of complete testing of this wiring fault makes the arguments regarding power supply coupling between simultaneously failing sensors somewhat less conclusive, but certainly not invalid.

One important conclusion from the analysis of the wiring faults for these bridge circuit transducers is that a short circuit can produce any of the three most often seen failure signatures, a jump to OSH, a jump to OSL, or a simple jump up or down to the offset level adjustment of the differential amplifier of the signal conditioner, depending upon which specific pair of wires the short circuit connects. The converse of this is also true, if a sensor reading shows none of the above failure tends, then none of the possible 4 opens or 6 shorts could have occurred. All wiring faults create an abrupt and clearly defined jump in the associated sensor reading.

Data Acquisition

Block Diagram Overview of Instrumentation Avionics

The orbiter flight instrumentation (OFI) is designed to monitor those sensors and systems which are involved with the real-time operational command of the vehicle and its mission. The OFI system collects the analog signals from a variety of physical sensors as well as digital logic signals which give the status of various vehicle functions. This diversity of input signals is put into a common format by the dedicated signal conditioners (DSCs) which are distributed throughout the vehicle's fuselage. Some sensors require more specialized signal conditioning, such as the strain gauges, and strain gauge signal conditioners (SGSCs) are also distributed within the vehicle avionics bays to accomplish this. The conditioned signals from the DSC and SGSC units are collected by seven multiplexer-demultiplexers (MDMs) which perform analog-to-digital conversion, buffer the converted data, and respond to transactions on the orbiter instrumentation (OI) data bus. The MDMs can also route commands from the OI bus to various subsystems in the vehicle. All of the OFI data is centrally handled by the pulse-code-modulation master unit (PCMMU), which converts the raw binary data into a digital pulse code modulated (PCM) format, and combines and organizes the digital data from all of the sensors into a one-second long major data frame, using time division multiplexing (TDM). Time stamps generated by the master timing unit (MTU) are also added to each data frame by the PCMMU. The network signal processor (NSP) routes the data frame to either the S-band or Ku-band communications transceivers for transmission back to the mission control center (MCC) back on the ground, or to a reel-to-reel tape recorder for permanent storage. The communications transceivers also receive commands from the MCC on the ground and pass them to the general purpose computers (GPCs) on the orbiter for processing and execution. A simplified block diagram of the OFI system is shown in Figure 1.

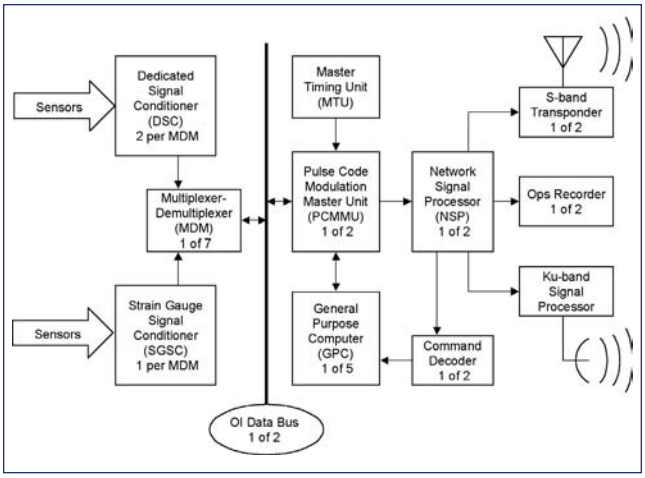


Figure 1. Operational Flight Instrumentation (OFI).

The modular auxiliary data system (MADS) is a supplemental instrumentation system that gathers vehicle flight data for processing after the mission is completed. Sensor inputs to the MADS system are almost exclusively physical sensor readings of temperature, pressure, mechanical strain, acceleration, or vibration. Sensors whose outputs vary comparatively slowly with time, such as temperature, pressure, and strain, are first signal conditioned by either thermocouple reference junctions (TRJs), strain gauge signal conditioners (SGSCs), or by the input circuits of one of the three pulse-code modulation (PCM) units. The PCM units perform analogous functions to what the MDMs and PCMMU do for the OFI system, performing analog-to-digital conversion of each sensor input, converting the raw binary data to pulse code modulation format, and combining all of the sensor readings into a time-stamped time-division-multiplexed frame of data. Sensors whose outputs vary rapidly with time, such as acceleration and vibration, are signal conditioned by wide band signal conditioners (WBSGs), and their data is collected by one of two frequency division multiplexers (FDMs). The FDMs modulate each input channel at different frequencies to combine the data into a single high-bandwidth track. Finally, the outputs from the three PCMs and two FDMs are routed to the appropriate tracks on a reel-to-reel tape recorder for playback once the vehicle is back on the ground. The MADS system is itself controlled by commands sent to it through the OFI system.

The orbiter experiment instrumentation (OEX) is an expanded suite of sensors for the MADS that was installed on the *Columbia* expressly for the purpose of engineering development. Since the *Columbia* was the first space shuttle orbiter to be launched, the engineering teams needed a means to gather more detailed flight data to validate their calculations of the conditions that the vehicle would experience during the critical flight phases of the mission. The voluminous data generated by the OEX suite required the installation of a particularly high capacity reel-to-reel tape recorder, known as the OEX recorder. The three flight phases of ascent, de-orbit, and re-entry are each recorded on chosen tracks of the OEX recorder. A simplified block diagram of the MADS/OEX system is shown in Figure 2.

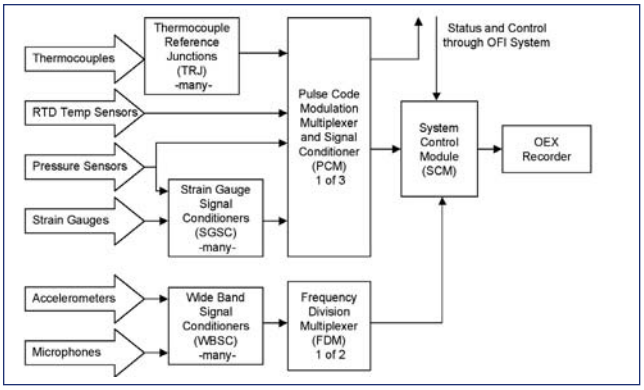


Figure 2. Modular Auxiliary Data System (MADS) and Orbiter Experimental Instrumentation (OEX).

Dedicated Signal Conditioners (DSC)

Fourteen DSC units were on *Columbia*, two for each of the seven multiplexer-demultiplexer (MDM) units, and all located within the fuselage. These were designated as follows: OF1, OF2, and OF3 were located in forward bays 1, 2, and 3, respectively. OF4 was a half-box located forward to support the Reaction Control System (RCS). OM1, OM2, and OM3 were located mid-body. OA1, OA2, and OA3 were located in aft bays 4, 5, and 6. OL1 and OL2 were both half boxes supporting the left Orbital Maneuvering System (OMS), and OR1 and OR2 were similarly half boxes supporting the right OMS. The DSC units could be configured with a variety of plug-in boards to support the measurements that they handled. The DSC units provided the majority of the front-end sensor signal conditioning for the OFI systems, serving much the same role as what the PCM units played for the OEX/MADS systems.

Each DSC consists of a chassis-mother interconnect board (CMIB) or backplane, which is described in drawing no. MC476-0147, a power supply module, a built-in test equipment (BITE) module, and up to 10, 15, or 30 plug-in cards that handle 3 or 4 measurement channels, each with a common power supply for the amplifiers and transducer excitation. The various types of plug-in cards include: a 3-channel pulse to DC converter for variable pulse rate transducers, a 4-channel resistance to DC converter for temperature transducers, a 4-channel AC to DC converter for AC signal transducers, a 4-channel discrete AC voltage converter for AC event voltages, a 4-channel 5 VDC discrete buffer for DC event voltages, a 4-channel DC amplifier-buffer-attenuator for internal DC signal transducers (such as potentiometers), and a 4-channel DC amplifier-buffer-attenuator for external DC signal transducers. The overall organization of the DSC units is best described in the Space Shuttle Systems Handbook, Section 17 (Instrumentation), drawing no. 17.1. The "channelization" of a particular measurement refers to which channel of a particular plug-in card, which card of the DSC, and which DSC through which a certain measurement is routed.

Strain Gauge Signal Conditioners (SGSC)

The Strain Gauge Signal Conditioners (SGSC) are described in drawing no. MC476-0134, and were manufactured by Rockwell International Space Division. The SGSCs are used in both the OFI and MADS/OEX instrumentation systems. There are 47 different dash numbers corresponding to different nominal bridge resistances (350 Ω or 1000 Ω), bridge types (full or half), excitation voltage (+10 VDC or +20 VDC), and gain range. Gain ranges vary from 10-50 up to 150-625. Each unit operates on +28 VDC power, and returns a conditioned signal in the range of 0 to +5 Volts. Typically, four strain gauge channels are combined into a single unit with a common power supply feed and overall dimensions of 3.000" wide × 3.500" long × 1.620" high. Each channel has potentiometer adjustments for gain, coarse offset, and fine offset. For half-bridge strain gauges, the remaining two resistors (R3 and R4) are contained within the SGSC along with a differential amplifier. For full-bridge strain gauges, the SGSC contains only the differential amplifier. A quarter-bridge system was also added in which the SGSC contains the three resistors (R1, R2, & R3) for the Bridge Completion Network (BCN) and the differential amplifier. Quarter-bridge strain gauges are set up with three leads (signal high, signal low, and power low) to balance the voltage drop of the excitation return current. The frequency response of the differential amplifier is flat from DC to 7 kHz and rolls off at –40 dB/decade, although only a 50-200 Hz –3 dB bandwidth is required for the application. Typical input signals range from 8 to 500 mV. Input impedance to the differential amplifier is specified to be greater than 9000 Ω, with an output impedance of less than 500 Ω. The Common-Mode Rejection Ratio (CMRR) is specified to be at least 70 dB at a voltage gain of 20 and at least 90 dB at a voltage gain of 200. Electrical isolation is specified to be at least 50 MΩ for power to signal and for circuit to case. Overall linearity, repeatability, and hysteresis is specified to be better than 0.1% from the best straight line. The specified minimum operating life of the SGSC is 5000 hours.

Inside each SGSC is a regulated power supply on a printed circuit board (#600356) that takes the +28 VDC input, passes it through an EMI filter, then a preregulator module, and then a DC-to-DC (buck) converter to provide a raw stepped-down DC voltage for two different linear regulators. One of these linear regulators provides the DC power supply for each of the four-channel differential amplifiers, and the other provides the DC excitation voltage for the strain gauge bridges. The preregulator module is actually a

separate printed circuit board (#600383). Each channel of the four-channel differential amplifier modules (#600355) takes the strain gauge input signal, completes the bridge if necessary with additional bridge resistors, and then amplifies the signal through a differential amplifier, rejecting the common-mode signal. The output is passed through an active filter and then a clipper to limit its amplitude. Most commonly, a given strain gauge is excited and amplified by the same SGSC unit, so that the excitation power supply and the differential amplifier module remain paired. There are a few exceptions where the excitation power supply is used to power the strain gauge bridge inside a pressure sensor.

Thermocouple Reference Junctions (TRJ)

The Thermocouple Reference Junctions (TRJ) are described in drawing no. MC476-0133 and were manufactured by Rockwell International Space Division. The thermocouple extension wires which are used to connect the thermocouple leads to the TRJs are described in drawing nos. MP572-0278 for Type K and MP572-0329 for Type SX. As a side note, Type SX is copper and a copper alloy known as Constantan (55% Cu, 45% Ni) which provides the same thermoelectric properties as a Type R Pt/Pt:Rh thermocouple, but with greater flexibility for wire routing and less high temperature capability. The thermocouple reference junctions are either a Type-I single channel or a Type-II 10-channel, and are small rectangular metal packages with mounting lugs which are fastened to the inner structural surface of the wing or fuselage, usually within a few feet of the thermocouple sensing junction. The TRJ utilize a Wheatstone bridge arrangement in which the thermocouple is balanced against an adjustable leg to establish the reference temperature for the measurement. There are six classes of the TRJs: class-1 is a chromel/alumel reference junction at 0°F; class-2 is a chromel/alumel reference junction at 500°F; class-3 is a Pt/Pt:Rh reference junction at 0°F; class-4 is a W:Re/W reference junction at –100°F; class-5 is a Pt/Pt:Rh reference junction at 500°F; and class-6 contains both a class-2 and class-3 reference junction in the same package. Different combinations of type and class produce 11 different dash numbers. The bridge is powered by +5.0 VDC power and ground wires that are routed from the data acquisition system (DAQ). Two wires connect the thermocouple to the TRJ, and then four wires connect the TRJ back to the DAQ. While thermocouple junctions generate their own thermoelectric voltage, the TRJ in this instance runs off of +5.0 VDC power. A drop in the power to the TRJ will have the effect of setting the output signal voltage to zero, resulting in a recorded temperature at the off-scale low (OSL) level. Because of the presence of the +5.0 VDC voltage in the same cable, a short between the +5.0 VDC wire and one signal return wire will create an OSL, while a short between the +5.0 VDC wire and the other signal return wire will create an off-scale high (OSH) reading. This latter situation is less probable, since it can occur in only the manner described, whereas an OSL reading can be created by roughly 15 other types of wiring faults. The response time for the TRJs is specified to be no more than 10 milliseconds. Each TRJ is factory calibrated; there are no adjustments on the units themselves. The TRJs are interconnected to the thermocouple extension wires and the general purpose instrumentation harness wiring with crimp splices.

Wide-Band Signal Conditioners (WBSC)

The Wide-Band Signal Conditioners (WBSC) are described in drawing no. MC476-0132 and were manufactured by Rockwell International Space Division. There are 57 different dash numbers of 6 types, corresponding to different frequency ranges, input vibration levels, transducer sensitivities, and amplifier gain ranges. Each are designed to work with piezoelectric transducers and consist of charge amplifiers with overall gains in the ranges of 0.4-2.4 to 50-150 mV/pC (millivolts per picocoulomb). Transducer sensitivities are typically 2.8, 8.0, 11.5, and 12.0 pC/G. Input vibration levels range from ±2 G to ±100 G, and frequency response varies from 2-50 Hz up to 20-8000 Hz. Each is powered by +28 VDC. The inputs from several WBSCs are combined in a Frequency Division Multiplexer (FDM) unit. The WBSCs consist of a small rectangular metal box with mounting lugs, 2.300" wide × 2.250" long × 1.250" high. Coax is used to connect the transducer to the WBSC.

OFI Multiplexer-Demultiplexer (MDM) Units and Instrumentation Data Buses

The Multiplexer-Demultiplexer (MDM) units collect the conditioned analog sensor signals from the Dedicated Signal Conditioners (DSCs), perform an analog-to-digital conversion, and create a Pulse Code Modulated (PCM) digital output that can be sent to the Pulse Code Modulation Master Unit (PCMMU) by way of the Operational Instrumentation (OI) data bus. Analog inputs to the analog-to-digital converters (ADCs) are always signal conditioned to lie within the range of –5.12 V to +5.11 V. A 10-bit conversion is performed so that the digital output is always 10 mV per count. A 10-bit twos complement digital output is produced for each measurement. This assigns a digital output of 0000000000 to a 0.00 V input, 0111111111 to a +5.11 V input, 1000000000 to a –5.12 V input, and 1111111111 to a –0.01 V input. The leading bit is thus interpreted as a sign bit, and the nine following bits give the magnitude in PCM counts, starting from 0.00 V for positive values and –5.12 V for negative values. Six zero bits are padded to the end to create a 16-bit word that is sent out onto the OI data bus.

Each MDM is fed by two Dedicated Signal Conditioners (DSC) and, optionally, a Strain Gauge Signal Conditioner (SGSC) and/or Wide-Band Signal Conditioner (WBSC). A total of 7 MDMs are installed, 4 front and 3 aft in the fuselage. In addition to conditioned analog signal inputs, each MDM can also process three different types of discrete digital inputs: a 28 V DC bi-level, a switch-closure isolated bi-level, and a 5 V DC bi-level. Like the DSCs, the MDMs are organized around a number of plug-in cards, and each measurement is "channelized" by specifying its MDM unit, the card number within the MDM unit, and the channel number within that card.

Two redundant Operational Instrumentation (OI) data buses interconnect each of the MDM units with the two redundant PCMMUs. Each of the OI data buses are 16 bits wide, bi-directional, and support data flow from each MDM to each PCMMU as well as command flow from each PCMMU to each MDM. Only one of the OI data buses is active at a time,

with the secondary being recruited from reserve only in the case of a recognized failure on the primary.

OFI Pulse Code Modulation Master Units (PCMMUs)

The Pulse Code Modulation Master Units (PCMMUs) are the backbone data processor for the Operational Flight Instrumentation (OFI) system. The PCMMUs are directly controlled by the network of five General Purpose Computers (GPCs), and act much like appendage special purpose hardware co-processors that free the GPCs from the chores of repetitive sensor data processing and formatting. The GPCs are the primary on-board computers for the orbiter. Four of the GPCs contain identical software and operate in a voting mode to insure data validity. The fifth GPC is set up in a bare-bones mode with a different and more basic software for emergency use. The flight crew can look at a conspicuous indicator panel in the cockpit to see which GPCs are in agreement at any moment. Well-defined protocols exist for when to switch over to the fifth GPC during emergencies, since once done, the switch back to the four main GPCs is neither easy nor quick. The PCMMUs run more or less unattended by the GPCs, but the GPCs do issue commands to the PCMMUs to program them to select the right sensor data and to organize it properly into the chosen telemetry data format.

Formatted telemetry data is sent from the PCMMUs to the Network Signal Processors (NSPs) which provide a final level of signal aggregation before sending the data to either the S-band transponder, the Ku-band signal processor, or the Operations (Ops) reel-to-reel data recorders. The NSPs combine voice communications channels with the telemetry data for the downlinks in either a High Data Rate (HDR) or Low Data Rate (LDR) mode. In the HDR mode, which is most frequently used, the 128 kbps telemetry data frames are combined with two 32 kbps air-to-ground voice channels for a total of 196 kbps. In the LDR mode, the 64 kbps telemetry data frames are combined with one 32 kbps air-to-ground voice channel for a total of 96 kbps. The NSPs also perform the reverse function of separating the ground-to-air voice channels from the received ground command data.

There are two PCMMUs, two NSPs, and two Ops recorders, but only one of each is used at any given time. Interconnections exist between both OI data buses and both PCMMUs, between both PCMMUs and both NSPs, and between both NSPs and both Ops recorders. This provides complete two-fold redundancy, if needed, so that a failure of either OI data bus, PCMMU, NSP, and Ops recorder can occur and a functional OFI system will still remain. When communications outages cause gaps in the telemetry data, one of the Ops data recorders can be used to downlink the missing data while the other continues to record the real-time data. Payload data is sent to a separate payload data recorder. All three recorders, Ops1, Ops2, and Payload, can send their data to only the Ku-band signal processor, since the S-band transponder does not have sufficient data capacity to handle this type of download. In addition, the *Columbia* (OV-102) utilized an OEX recorder, which does not have any means to transmit its data through a telemetry channel. When the orbiter is on the ground and connected to the Ground Support Equipment (GSE) through its T-0 umbilical, data from either PCMMU, either Ops recorder, the payload recorder, or the OEX recorder can be read out at the normal transfer rate of either 64 or 128 kbps.

All data acquisition and command operations are synchronized by a Master Timing Unit (MTU) which is a double oven-stabilized 4.608 MHz oscillator that provides a uniform frequency reference for all of the electronic systems within the vehicle. The oscillator is divided down to provide clock signals and referenced to a timing mark to provide Greenwich Mean Time (GMT) and Mission Elapsed Time (MET) stamps that are stored in both the Orbiter Timing Buffer (OTB) and Payload Timing Buffer (PTB). The 4.608 MHz oscillator reference is distributed directly to both of the PCMMUs. The PCMMUs in turn each provide 1.152 MHz and 100 Hz clock signals to both of the NSPs.

After each analog-to-digital conversion is completed by any of the MDMs, the 16-bit data is sent through the OI data bus to the PCMMU and stored in its Random Access Memory (RAM). The primary function of the PCMMU is to read out the contents of its RAM at the right times and compose overall, one second long formatted frames of data for telemetry or recording. The process of sequentially stringing together different serial data segments from different sources is termed commutation, and is essentially a word-by-word version of time division multiplexing. The specific set of sensors and other data to be included in the data frame, and their proper sequence and formatting, is specified by the Telemetry Format Load (TFL) instructions. The TFL is supplied to the PCMMU by the GPCs and covers several classes of analog sensor and digital system status data, including: Guidance, Navigation and Control (GNC) data, Systems Management (SM) data, Backup Flight System (BFS) data, Operational Instrumentation (OI) data, and data from the Payload Data Interleaver (PDI). The GNC, SM, and BFS data are collectively termed the GPC downlist data. The TFL is obtained from the Shuttle Data Tape (SDT) which is loaded into the orbiter's Mass Memory Unit (MMU) prior to launch. The SDT is created in two versions at the Johnson Space Center: an engineering version and a flight version. When instructed by commands from the GPCs, the TFL is read out from the MMU and transferred over to the PCMMU, where it then provides the instructions for formatting the next segment of telemetry data.

For each analog sensor measurement, the PCMMU only outputs a single 8-bit data word that is truncated from the original 10-bit analog-to-digital converter data. For bipolar measurements, only the sign bit and the first 7 most significant bits are retained, giving a PCM count in the range of –128 to +127. For unipolar measurements, the sign bit is dropped and the 8 most significant magnitude bits are retained, giving a PCM count in the range of 0 to +255. Each OI sensor measurement is thus only a simple 8-bit word, and these are concatenated to create the overall frame of data that represents a sampling of each of the sensors either once every second, or in some cases ten times per second.

MADS/OEX Pulse Code Modulator (PCM) Units

The Modular Auxiliary Data System (MADS) exists on all

of the orbiter vehicles, but the configuration on *Columbia* (OV-102) was different to support the larger number of sensors in the OEX system. For OV-102, the MADS consisted of 3 Pulse Code Modulator (PCM) units, 2 Frequency Division Multiplex (FDM) units, various Strain Gauge Signal Conditioners (SGSC) and WideBand Signal Conditioners (WBSC), a Remote Manipulator Digitizer Unit (RMDU), and a System Control Module (SCM). All of these avionics boxes were located on shelves 7 and 8 of mid-body bay 8. Sensor inputs were fed into the PCM units either directly or through a SGSC, into the FDM units through the WBSCs, and into the RMDU. The outputs of the PCM, FDM, and RMD units are each fed into the SCM which fed the overall data into the OEX recorder. Timing information from the Orbiter Timing Buffer (OTB) is fed into the PCM and FDM units. Control and monitoring of the MADS is achieved through the standard OFI instrumentation suite. Health and status information of the MADS system is generated by the PCM units and fed via a MDM into a PCMMU of the OFI system. Commands to the MADS system are directed from a MDM unit to the SCM of the MADS. The MADS and its subsystem components are described in detail in Section 35 of the Shuttle Operations document.

Three PCM units are installed in midbody bay 8, shelves 7 and 8, to support the MADS/OEX instrumentation. Each PCM unit contains a power supply, a selection of signal conditioners, an analog signal multiplexer, a sample-and-hold, an analog-to-digital converter (ADC), a reference voltage generator, a timing receiver and decoder, a format PROM, and finally a word generator. The PCM units which are part of the MADS are different from the PCMMUs which are part of the OFI subsystem. The PCM units were originally manufactured by Rockwell International Space Division and are described in drawing no. MC476-0251. Goodrich Data Systems is the present vendor for the PCM units. PCM-1 is operated as a master unit, controlled by command signals from the OFI system, and PCM-2 and PCM-3 are daisy-chained to operate as slave units from PCM-1.

Specification drawing MC476-0251 describes each PCM unit as containing 128 high level analog (HLA) inputs of 0-5.1 V range (#s 1-46 and 77-94 on J8, #s 47-76 and 94-128 on J10), a total of 188 low level analog differential (LLAD) inputs of 0-10 mV (#s 125-159, 35 ea., J7), 0-20 mV (#s 1-40, 40 ea., J6), 0-30 mV (#s 160-188, 29 ea., J7), 0-40 mV (#s 41-56, 16 ea., J6), 0-60 mV (#s 57-60, 4 ea., J6), and 0-15 mV (48 with PPS, #s 77-100 on J13, #s 101-124 on J15, and 16 without PPS, #s 61-76 on J13), 16 bipolar analog (BPA) inputs of ±5.1 V range (J5), 168 bridge completion (BC) inputs (#s 1-42 of −75° to +300°F range on J9, #s 43-84 of various temperature ranges on J11, #s 85-126 of various temperature ranges on J12, #s 127-168 of −200° to +450°F range on J14), 14 low level discrete (LLD) 5 V logic inputs (J4), 16 high level discrete (HLD) 28 V logic inputs (J4), and 112 precision power supply (PPS) outputs of 5.000±0.007 VDC (#s 1-24 on J5, #s 25-48 on J13, #s 49-72 on J15, and #s 73-112 on J3). Connectors J1-J15 on the box provide the interconnections of the inputs and outputs to the vehicle cable harnesses. Input 28 V and 5 V power are supplied to J1 and control and IRIG-B signals to J2.

The PCM units contain differential amplifiers which accept low level analog signals ranging from 0-10 mV to 0-60 mV from various transducer bridges. These have input protection and will indefinitely handle input voltages in the range of ±15 VDC without any damage. Other inputs are designed to handle over-voltages in the range of ±40 VDC. Each of the measurement channels are isolated, so that failure of one will not impact any of the other channels. Each channel is also protected against shorted input lines.

Each of the three PCM units on OV-102 internally contains 36 independent Precision Power Supplies (PPS). These, along with the power supplies in the SGSCs, are used to excite the pressure sensors, strain gauges, and temperature sensor bridges. Each PPS output is specified to produce +5.000±0.007 VDC to a 350 Ω load, recover from a short circuit within 100 ms, and be internally protected to voltages in the range of −1.0 to +10.0 VDC. The 36 outputs are internally connected to 112 PPS output terminals as 20 groups of four terminals and 16 groups of two terminals on J5, J13, and J15. The precision power supplies on each PCM unit are fully independent of the precision power supplies on the other two PCM units. All of the input pins of the PCM unit are designed to tolerate an indefinitely long short to any power supply line or chassis ground. Low-level analog inputs of 60 mV or less are rated to withstand overvoltages in the range of ±15 VDC, and all of the rest are rated to withstand overvoltages of ±40 VDC. All of the PCM unit outputs, including the PPS outputs, are designed to withstand short circuit conditions indefinitely. The outputs are specified to recover after the short circuit condition is removed, implying that no fuses or circuit breakers are used to provide this withstand capability.

Since several sensors are each supplied by a common PPS output group, a disturbance in the power supply excitation to these sensors will propagate through all of the sensors and show up as either a common failure or as an artifact in each of their outputs, such as an abrupt offset. PPS commonality can be either internal to the PCM unit, since a given precision power supply feeds two or four output terminals on the connector, or external, with the power feed going to a terminal board or splice where it branches to feed several sensors at different locations. PPS commonality is an important consideration in reviewing all of the sensor data, because a disturbance in the power feed to one sensor, for example a short between power and ground, can then cause other sensors on the same power feed to react to this disturbance, even though the sensors themselves may not be physically or geometrically related. However, if the short is removed, the design of the PCM PPS circuits should quickly recover (within 100 ms), and the unharmed sensors should also return to their normal, operational state. An important case of this on STS-107 is the abrupt jump that was recorded in the outputs of fuselage lower surface temperatures V07T9480A, V07T9489A, V07T9492A, V07T9522A, and V07T9636A at a time of GMT 13:52:22 (EI + 493 sec). All five of these thermocouple temperature sensors were fed from the same terminal board that was supplied +5.0 VDC from PCM-1 PPS 89. Another temperature sensor, V07T9666A, was also fed power from the same PCM-1 PPS, but not through the terminal board. NASA attributed the common fault point to the terminal board, as all five thermocouple temperature

sensors produced invalid data past the time of this fault. As will be discussed later, this sensor V07T9666A was one of the first to fail at GMT 13:52:24 (EI + 495 sec), and this failure could have also been responsible for these other five lower fuselage surface temperatures to have an abrupt jump in their readings at a few seconds prior.

The status and health of the PCM units themselves are recorded by means of several internal diagnostic voltages which are given MSIDs of V78V96xxD (17 ea.), V78V98xxD (17 ea.), and V78V99xxD (17 ea.) for PCM-1, PCM-2, and PCM-3, respectively. These measure low limit and high limit analog signal levels for the ADCs, typically at the 20% and 80% levels. In addition, V78V9638A and V78V9639A are internal diagnostics in which a +5.0 VDC output from PCM-1 and PCM-2 is wrapped around to a bipolar signal input to monitor the output excitation voltage. In addition, each PCM has 2 ea. internal diagnostic status flags which are given MSIDs of V78X9655D, V78X9656D, V78X9855D, V78X9856D, V78X9955D, V78X9956D for PCM-1, PCM-2, and PCM-3, respectively. These indicate the calibration settings for high and low level thresholds of the LLDs. These are each recorded on the OEX recorder tape.

PCM-1 internal diagnostic voltage V78V9638A fell from +5.0 VDC (254 counts) at GMT 13:53:09 (EI + 540 sec) to 0.0 VDC (129 counts) at GMT 13:53:18 (EI + 549 sec). This voltage is the output of PCM-1 PPS 83, and it wraps around to a bipolar signal input (BPA1) by means of a jumper wire located on the PCM1 connector. PPS 11, 12, 83, and 84 are tied together and supply +5.0 VDC to sensors V07T9713A, V07P8114A, V07P8162A on PCM-1. V07T9713A is a left wing lower surface elevon temperature sensor that went to OSL at EI + 540 sec. However, V07P8114A and V07P8162A remained functional up through EI + 940 sec.

In another instance, PCM-1 PPS 27 and 28 are tied together to supply +5.0 VDC to pressure sensors V07P8004A and V07P8005A (left wing upper surface pressures) and V07P8158A and V07P8176A (right wing lower surface pressures). The four pressure sensors on PCM-1 all go abruptly OSL at GMT 13:52:52 (EI + 523 sec). Due to the simultaneous timing, one or the other (or both) of the left wing sensors must have failed when the associated cable harness on the outside top of the left wheel well burnt through. The simultaneous failure of the other left wing sensor and both right wing sensors can be attributed to a loss of the common power supply lines that feed them from PCM-1. The wiring burn-through cause and effect appears very clear cut for this set of four sensors.

Besides the diagnostics which were recorded on tape, there were several diagnostic MSIDs which were downlinked through the OFI telemetry. Each PCM unit contains built-in test equipment (BITE), and the BITE status for the MUX components of PCM-1, PCM-2, and PCM-3 is downlinked as MSID V78X9611E, V78X9614E, and V78X9615E, respectively. The telemetry data showed that the master BITE was a logical 1, indicating good, for all three PCM units from Entry Interface (EI) up until the Loss Of Signal (LOS).

The internal diagnostics indicated that all three PCM units were for the most part functional throughout the re-entry flight, aside from disturbances resulting from the propagating left wing damage. PCM-1 and PCM-2 were fully functional through to the end of the OEX data at GMT 14:00:19 (EI + 970 sec), except that PCM-1 lost output signal amplitude during GMT 13:51:37 to 13:51:39 (EI + 448 to 450 sec), and PCM-2 lost output signal amplitude during GMT 13:54:52 to 13:54:55 (EI + 643 to 646 sec). PCM-3 also began snapshot acquisition of its data at GMT 13:39:30 (pre-EI). Several +5.0 VDC PPS outputs were lost at approximately GMT 13:53:00 (EI + 531 sec), and this would be most likely associated with the shorting of power supply feeds to sensors whose wiring was burnt through at around this time.

There also exist three temperature sensors which monitor the conditions surrounding the OEX and OFI avionics boxes in mid-body bay 8. All three of these are surface mounted RTDs which monitor temperatures over a range of –75°F to +175°F, and are sampled once per second. V78T9606A is located next to PCM-1 on the upper part of shelf 8; V78T9607A is located next to the FDM on the lower part of shelf 8; and V78T9608A is located near the FASCOS heat sink on the top of shelf 7. Since the FASCOS unit was not present on STS-107, only the two temperature measurements V78T9606A and V78T9607A on the upper and lower side of shelf 8 were recorded in the telemetry data. Sensor V78T9606A recorded a temperature of 50.2°F at the Entry Interface (EI) of GMT 13:44:09, which rose smoothly upward by 4 bits to a final value of 54.2°F at GMT 13:59:32 (EI + 923 sec) where the telemetry signal was lost. Similarly, sensor V78T9607A recorded a temperature of 49.2°F at EI which rose smoothly upward by 3 bits to a final value of 52.2°F at the point where the telemetry signal was lost. Both of these temperature sensor readings are completely consistent with the behavior of prior flights and indicate that there was no abnormal heating within these avionics bays which might have contributed to faulty telemetry data.

NASA staff indicated that on prior flights of OV-102, several sensors (V07T9253A, V07T9270A, V07T9468A, V07T9470A, and V07T9478A, all fuselage surface temperatures) showed "step function" behavior, similar to what was recorded for STS-107. These prior flights were STS-73, STS-75, and STS-78. This prompted PCM-1 (S/N 304) to be shipped back to the vendor, Goodrich Data Systems, for thermal testing and evaluation. No failures were found during these tests and the unit was shipped back and reinstalled in OV-102. Similar "step function" failures were then observed on STS-80, STS-94, and STS-87. It was felt that the problem was not within PCM-1, but the ultimate source of the problem was never identified.

MADS/OEX Frequency Division Multiplex (FDM) Units

Two FDM units are installed in midbody bay 8, shelves 7 and 8, to support the OEX instrumentation. Each FDM unit takes wideband signal data from accelerometers, vibrometers, and microphones, heterodynes each signal up to a higher center frequency, and combines up to fifteen of the signals into each of four separate channels that are routed to specific

tracks on the OEX recorder. A 16th constant frequency 240 kHz signal is combined into each channel to provide a reference signal for compensation of tape speed variations (wow and flutter). FDM unit 1 creates output channels designated M1A, M1B, M1C, and M1D; while FDM unit 2 similarly creates the M2A, M2B, M2C, and M2D channels. Each input signal is input to a voltage-controlled oscillator (VCO) to produce frequency modulation (FM). For each FDM unit, the first 7 VCO channels have center frequencies of 12, 16, 20, 24, 28, 32, and 36 kHz, and each of these channels has a response bandwidth of 500 Hz. The next 7 VCO channels have center frequencies of 48, 64, 80, 96, 112, 128, and 144 kHz, and each of these channels has a response bandwidth of 2.0 kHz. The 15th VCO channel has a center frequency of 184 kHz and supports a response bandwidth of 8.0 kHz. Specific OEX recorder tracks are assigned to each of the four channels from each FDM unit for the three mission phases of ascent, de-orbit, and re-entry. The lowest VCO frequency (12 kHz) of the first channel of each FDM unit (M1A and M2A) is used for recording the FDM time reference. These timing references are also given MSIDs: V75W9006D for M1A, and V75W9016D for M2A. The remaining sensor inputs can be arbitrarily assigned to various channels, frequencies, and units to accommodate the needed bandwidth of the measurements. These measurements can be any combination of vehicle strains, engine strains, vehicle accelerations, vehicle vibrations, engine vibrations, and vehicle acoustics. Because of the more complex method of combining, FDM data requires more time and effort to extract from the OEX recorder tape. This data extraction is normally performed by the Boeing Company, Huntington Beach, under contract to NASA. Under normal circumstances, both time and frequency representations of the data are created. Power Spectral Density (PSD) plots are also created to provide a mixed time-frequency representation of the data.

Like the PCM units, the FDM units also contain built-in test equipment (BITE) and the BITE status of the four MUX units is downlinked as MSIDs V78X9380E – V78X9383E for FDM-1 and as V78X9390E – V78X9393E for FDM-2. The telemetry data showed all four of these bits for both FDM-1 and FDM-2 remained in the logical "1" state from EI to LOS, indicating that all four MUX channels of both FDM units were operating properly. The data mode for FDM-1 and FDM-2 is also downlinked as MSID V78X9309E and V78X9310E, respectively, indicating if these units were operating in their wideband mode or not. The telemetry data showed that both FDM-1 and FDM-2 were indeed operating in their wideband modes.

Data Formatting

OFI data is exchanged in a common format to allow it to be either transmitted or recorded. The format consists of a major frame which is produced each second, and each major frame is composed of 100 minor frames, produced every 10 ms. There are two data rates: a high data rate at 128 kbps and a low data rate at 64 kbps. At the high data rate, 160 words compose each minor frame, and at the low data rate, 80 words compose a minor frame. Each word is 8 bits long. For both the high and low data rates, the first three words of each minor frame (24 bits) comprise a sync pattern for which 76571440 octal (FAF320 hex) is used for all shuttle telemetry systems. The 4th word in each minor frame gives the minor frame count in binary format with the first minor frame being number "0". Minor frames are error checked and the number of perfectly received minor frames is known as the frame count for each major frame of telemetry data. The 5th word of only the 1st minor frame contains the format ID. The MADS/OEX data is exchanged in an identical format, with the exception that each of the three PCM units outputs data at half of the OFI rate: a high data rate of 64 kbps and a low data rate of 32 kbps, with each major frame containing only 50 minor frames. Two MADS/OEX PCM units could thus be interleaved to produce the equivalent data throughput of one of the OFI PCMMUs.

Following after the sync pattern and the frame number, each minor frame then contains from 2 to 7 subcommutated windows of varying length. Each of these begins with a specific header that announces its beginning and then a sequence of 8-bit data words, one for each sensor reading within that subcommutated window. Each minor frame will contain exactly one OI sensor data window, 0 to 4 Payload Data Interleaver (PDI) data formats, and from 1 to 5 GPC downlist formats which may include GNC, SM, or BFS data. The first three minor frames usually contain the TFL ID, the GMT time stamp, and the MET time stamp in words 5-12.

Both Non-Return to Zero (NRZ) and Bi-Phase (Bi-ϕ), also known as Return to Zero (RZ), digital signaling formats are used within the orbiter data processing, recording, and telemetry hardware. NRZ data assigns a specific level (high or low) to a binary 0 or 1. Bi-ϕ data assigns a transition (up or down) to a binary 0 or 1. Both Level (L), Mark (M), and Space (S) subformats are also used. A binary 0 is represented as a low level in NRZ-L, no change in level in NRZ-M, a change in level for NRZ-S, a midperiod low to high transition in Bi-ϕ-L, no midperiod change in level for Bi-ϕ-M, and a midperiod change in level for Bi-ϕ-S. A binary 1 is represented by the opposite in each case. Bi-ϕ-L is also known as Manchester II coding and is used frequently within the orbiter avionics systems. OFI, OEX, and command data frames each use NRZ-L formatting, while Bi-ϕ-L formatting is used for radio transmission of the same data.

Command data that is sent to the space shuttle orbiter (SSO) is encoded to provide error checking capability. The 48-bit command words at 50 words/sec, 2.4 kbps, are padded with 2 leading zero bits and fed into a BCH(127,50) encoder. This appends 77 check bits to the incoming 50 bits, and finally, another leading zero bit is added to create the 128-bit encoded command word, still at 50 words/sec, but now 6.4 kbps. The BCH(127,50) command encoder is implemented as a 50-stage shift register with appropriate feedback coefficients. Once received by the SSO, the first 50 bits after the zero padding bit are passed through an identical BCH(127,50) encoder circuit to create the 77 check bits. If these generated check bits do not agree with those that were sent, the command is discarded. Encoded commands are also authenticated by being sent in a permuted form by modulo-2 addition with a 128-bit timing word that is created as an IRIG-B format GMT time stamp. Once received by the SSO, the encoded and permuted command word is retrieved

by another modulo-2 addition with the same 128-bit timing word that is generated independently within the SSO. After the command has been authenticated, by successful de-permuting and decoding, it is finally accepted as valid and allowed to perform its function within the SSO systems. Telemetry data that is sent back from the SSO is neither encoded in this manner, nor permuted with a time stamp.

Data Time Stamping

GMT time stamps are formatted according to the International Radio Instrumentation Group (IRIG) -B standard to 10 ms resolution. This formatting standard for time stamps is fully defined in IRIG Standard 200-95. These are produced by the Orbiter Timing Buffer (OTB) that runs from the Master Timing Unit (MTU) 4.608 MHz oscillator. A Payload Timing Buffer (PTB) performs the same function for the payload instrumentation. The most significant bit (MSB) and digits are sent first. Bits 1-10 contain days 1-365 in BCD format with the bit weightings being 200, 100, 80, 40, 20, 10, 8, 4, 2, and 1 days. Bits 11-16 contain hours 0-23 in BCD format with bit weightings of 20, 10, 8, 4, 2, and 1 hours. Bits 17-23 contain minutes 0-55 in BCD format with bit weightings of 40, 20, 10, 8, 4, 2, and 1 minute. Bits 24-30 contain seconds 0-55 in BCD format with bit weightings of 40, 20, 10, 8, 4, 2, and 1 second. Bits 31-38 contain tens of milliseconds 0-99 in binary format with bit weightings of 1280, 640, 320, 160, 80, 40, 20, and 10 milliseconds. MET time stamps are created from a simple, continuously running BCD counter. Both GMT and MET time stamps are usually inserted into words 5-12 of the first three minor frames of each one second long major frame, each occupying four words, or 32 bits.

For telemetry command authentication, the IRIG-B formatted GMT time stamp has its transmission order reversed and the milliseconds field replaced by 4 leading zeros to give a resolution of 1 second. Two more trailing zero bits are padded at the end following the days field to give a 32-bit command authentication timing byte. Uplink commands consist of 4 such 32-bit bytes, the first byte always being the IRIG-B time stamp, and each command is thus a 128-bit timing word that occupies sixteen 8-bit words within a minor frame.

Recording

MADS/OEX Recorder

The data recorder for the OEX sensor suite is a mostly standard Bell and Howell Modular Recording System (MARS) that has been only slightly modified for use on OV-102. It is a 28-track, wideband, reel-to-reel magnetic tape recorder of coaxial design, so that the two reels sit over top of one another and share the same spindle axis. It contains 9000 feet of tape, which at the usual tape speed of 15 ips provides about 2 hours of recording time. It contains both record and playback heads, but only electronics for recording. Playback is accomplished via a separate Driver Amplifier Module (DAM) which can dump the data to the Ground Support Equipment (GSE) through the T-O umbilical after the orbiter has landed. There is no means by which to take data off of the recorder while the orbiter is in flight. The tape transport is capable of speeds of 1-7/8, 3-3/4, 7-1/2, 15, 30, and 60 ips. At the nominal tape speed of 15 ips, analog frequencies in the range of 400 Hz to 250 kHz can be recorded, or digital biphase-L data at rates of 8 to 128 kbps. The recorder weighs 58 lbs and runs from +28 VDC. On OV-102, it was located in section G of the Environmental Control and Life Support System (ECLSS) bay, essentially lowest down in the belly of the fuselage along the midline, approximately midway along the length of the fuselage. MADS shelves 7 and 8 are located adjacent to this, underneath the floor of the payload bay. A detailed description of the MADS and OEX recorder can be found in Section 35 of the Space Shuttle Operations document. The OEX recorder, like the rest of the MADS, is rated to operate over a temperature range of 35°F to 120°F. The tape transport has hardware sensing for beginning of tape (BOT) and end of tape (EOT) that are implemented by optical sensors and a 15 ft. cut out window that exists 15 ft. from both ends of the tape. An analog voltage output is used to indicate the percent of tape remaining and is implemented as a 1850-turn, 1 kΩ potentiometer, of which only 92 turns and 50 Ω are used, with +10 V indicating a full tape at BOT, and 0.0 V indicating an empty tape at EOT. The OEX recorder can record in either tape direction, and typically for a given flight three passes are used to record the three different phases of ascent, de-orbit, and re-entry. Different recording tracks are assigned to different sets of data during each pass.

The OEX recorder operates nearly autonomously of the crew of the orbiter. The only crew controls on the system are for master OEX power on panel C3A5 and OEX power on panel A7L. There was also a switch for the Shuttle Infrared Left Temperature System (SILTS) pod, but this instrumentation was removed in 1991. The switch remains on the panel but is inactive. Interestingly, the SILTS pod, which is located on the forward tip of the vertical stabilizer, previously contained an IR camera that took images of the left wing thermal profile during re-entry. If this camera had been in place on STS-107, a telemetry movie of the thermal profile and break up of the left wing would have been available. The OEX recorder operates primarily through uplinked commands that are passed to it through the System Control Module (SCM). The SCM responds to 66 different ground commands which are detailed in Section 36 of the Shuttle Operations document. The real-time commands (RTC) are a sequence of opcodes which are concatenated to form a command sequence for either the SCM itself, the PCM units, the FDM units, or the OEX recorder. The commands are sent from the ground by the Mission Operations Computer (MOC). Eight-character hexadecimal commands either set or reset the 66 different command functions. Many of the command functions are actually arguments, that is, numerical values which are uplinked for a given opcode to act upon. Since many opcodes may be needed to trigger given functions, macros (MRTC) can be pre-programmed into the PROM for a given mission and then called with a single “continue at label” command. When the SCM receives a command string of opcodes that it recognizes, it then echoes them back on the downlink. If the command string is not recognized, an error code is downlinked instead.

Housekeeping data from the OEX recorder is also downlinked to the ground via OFI telemetry. These are given MSIDs like any other vehicle measurement. The status of

the OEX recorder built-in test equipment (BITE) is given on V78X9511E, which the telemetry data showed to remain in the logical "1" state, indicating a properly functioning system, from EI up until LOS. Recording on and tape motion bits are given on V78X9512E and V78X9513E, and the telemetry data showed both of these to be in the logical "1" state from EI up until LOS. Tape speed is given by three bits on V78X9548E – V78X9550E, which were in the "100" state from EI up until LOS, indicating the normal 15 ips speed. Tape position (analog) and tape direction (digital) are given on V78Q9551A and V78X9552E. The reading from V78Q9551A rose smoothly and continuously from EI up until LOS, and V78X9552E gave a logical "0" from EI up until LOS. The highest track recording is given by 5 bits on V78X9553E – V78X9557E, which gave a logical "11100" state from EI up until LOS. Because all of the built-in telemetry diagnostics indicated a normal and properly functioning OEX recording system, which was verified by the excellent quality of the retrieved data itself, there is no reason to suspect that the OEX recorder was suffering from any of the effects occurring in the left wing area prior to break up of the overall vehicle. The break up of the vehicle should in principle cause all of the avionics systems to halt their functions as the power supply feeds to them become interrupted. The final position of the tape in the OEX recorder also gives a useful timing point for this, indicating that the main fuselage of the vehicle was still largely intact at a time of GMT 14:00: 19 (EI + 970 sec). This is 47 seconds beyond the MCC LOS point at GMT 13:59:32 (EI + 923 sec).

A combination of extremely fortuitous circumstances allowed the data that was recorded on the OEX recorder to be retrieved and added into the engineering analysis of the accident investigation. First, the shuttle broke apart over the continental Southwest United States, allowing the debris to fall into a largely uninhabited and controllable area in which it could be methodically searched and collected. Second, the OEX recorder was located within this debris. Third, the OEX recorder fell through the atmosphere to the ground without even a scratch. Virtually all of the other avionics boxes aboard the *Columbia* were so severely burnt upon re-entry as to be barely recognizable and certainly not functional. Fourth, the OEX recorder managed to land right side up, like a pancake, so that the weight of the motors did not crush the tape spools that were sitting above them. If the OEX recorder had landed upside down, the data on the magnetic tape would almost certainly have been irretrievable. Fifth, the OEX recorder landed in a dry spot, so that its several days out in the weather did not cause any deterioration of its working parts or magnetic tape. The recorder suffered only a slightly broken case and electrical connectors, and the internal silica gel dessicant cartridge spilled open. Other than these effects, the OEX recorder was miraculously in perfect condition.

The Boeing Integrated Part and Component Locator (IPCL) 77BT listing details all of the 993 different sensor MSIDs for the MADS which were ever installed on *Columbia*. The first four characters of the MSID identifies the measurement type and system. The 993 MSIDs include: 24 main engine vibrations E41D, 12 main engine strains E41G, 8 ACIP accelerations V07A, 1 unknown ACIP measurement V07M, 35 left wing upper surface pressures V07P, 46 left wing lower surface pressures V07P, 36 right wing upper surface pressures V07P, 48 right wing lower surface pressures V07P, 22 vertical stabilizer surface pressures V07P, 25 unspecified wing surface pressures V07P, 22 fuselage side surface pressures V07P, (234 aerodynamic pressures V07P total), 3 ACIP axis rate gyros V07R, 9 OMS pod temperatures V07T, 70 fuselage surface temperatures V07T, 19 wing upper surface temperatures V07T, 4 wing lower surface temperatures V07T, 2 left elevon lower surface temperatures V07T, 2 vertical stabilizer surface temperatures V07T (106 temperatures V07T total), 2 ACIP calibration voltages V07U, 6 pressure range switches V07X, 19 vibrations V08D, 2 heat shield strains V08G, 4 payload acoustic pressures V08Y, 22 structural temperatures V09T, 121 left wing strains V12G, 126 right wing strains, 26 right elevon hinge strains V13G, 26 left elevon hinge strains V13G, 38 vertical stabilizer strains V22G, 12 rudder hinge moment strains V23G, 9 mid-fuselage accelerations V34A, 40 mid-fuselage strains V34G, 20 aft fuselage OMS deck strains V35G, 15 payload bay door hinge line strains V37G, 11 RCS thrust chamber pressures V42P, 1 ACIP rudder position V57H, 4 ACIP elevon positions V58H, 12 MADS PCM status measurements V75M, 21 PCM MUX IRIG-B time stamps V75M, 6 OTB IRIG-B time stamps V75W, 3 MADS PCM frame counters V78J, 53 MADS PCM test voltages V78V, and 6 MADS PCM calibration switches V78X.

Only a subset of the 993 MSIDs in the Boeing IPCL-77BT listing were actually active measurements on flight STS-107. This is a result of certain sensors failing over time and simply being disconnected from the data acquisition systems. Of the 128 temperature sensors, only 49 remained as active measurements on flight STS-107, and one of these, a door temperature, was known to be a failed sensor. Out of the 234 original pressure sensors, only 181 were active measurements, and of these, 55 were known to be broken or producing unreliable readings, leaving 126 valid pressure measurements. Out of the 426 strain measurements, 422 were remaining as active measurements. There were a total of 36 main engine sensors and 25 Aerodynamic Coefficient Instrumentation Package (ACIP) sensors that were not relevant for the re-entry phase of the flight. The MADS system also used 101 MSIDs for recording the health status of the instrumentation package (V75M, V75W, V78J, V78V, V78X). All totaled, there were 719 active measurements in the MADS system. One of these, a heat sink temperature on the MADS instrumentation shelf, was sent back as telemetry data, leaving 718 active measurements that were sent to the OEX recorder. This total excludes the 11 RCS pressures, 25 ACIP sensors, and 101 MADS diagnostics. One strain gauge, V12G9653A, recorded ascent data, but failed sometime thereafter, and thus did not provide data for the re-entry flight.

Ops Recorders

The operational flight instrumentation (OFI) data that is sent back from the orbiter's telemetry system is also recorded on a reel-to-reel data recorder, known as the ops recorder. Like most critical components of the OFI instrumentation system, two ops recorders are installed in a redundant fashion. Under normal conditions only one of the two is used, but a failure in one can be dealt with by switching over to the other. Unlike the MADS/OEX recorder, both of the ops recorders can

be played back during flight and their data transmitted back to Earth. When the orbiter is back on the ground, the data from the ops recorders can also be played back and downloaded through the T-0 umbilical. An instance of when this becomes used is during a normal re-entry flight, during the first half of which the telemetry data becomes broken up by various randomly timed communications drop outs, and during the second half when the telemetry data drops out almost entirely. The same data that is sent through the S-band radio telemetry is also recorded on the ops recorders. After the orbiter has safely landed, the entire, unbroken telemetry data stream can be retrieved to fill in the missing segments that the communications drop outs obliterated.

Neither of the ops recorders were recovered from the *Columbia*. Only one of the two would have contained the telemetry data that was being transmitted back from the orbiter during the re-entry flight. Because the telemetry data was fairly complete up until the loss of signal, in spite of the various anomalous, but brief, communications drop outs, the retrieval of the missing ops recorder would not have added that much new data. A payload data recorder also exists, but it does not contain much in the way of re-entry flight information. It was not recovered from the wreckage debris, either.

Telemetry and Radio Communication Links

Signal Formatting

The Space Shuttle Orbiter (SSO) can communicate with the Mission Control Center (MCC) via the ground station at the White Sands Complex (WSC) through several different systems operating at primarily S-band (2.1 GHz) and Ku-band (13.8 GHz). Only the S-band system will be described in detail, since that was the one operating during the time at which the SSO broke up during re-entry. Communication between the SSO and MCC can be either direct to the ground from the SSO to the WSC, or via a geosynchronous Telemetry and Data Relay Satellite (TDRS). Only the TDRS linked communications will be described in detail, again because that was the system in use during the re-entry phase of flight STS-107. The four links of this system are referred to as follows: MCC to TDRS is the up link, TDRS to SSO is the forward link, SSO to TDRS is the return link, and TDRS to MCC is the down link. The TDRS satellites do not perform any data manipulation; they only amplify the received signal power and then retransmit the signal, acting as a simple repeater. The signal format and content is thus unchanged passing through the TDRS satellite. The up and forward links use the same signal format as the return and down links, although the transmission frequency differs to allow full duplex communication (signals can be going both ways at once without interfering). The up and forward links are used to transmit command data from MCC to the SSO, while the return and down links are used to transmit telemetry data from the SSO to MCC. This organization reflects the fact that the SSO is under the control of the MCC and not vice-versa. An extremely large number of operations aboard the SSO are commanded directly from the MCC ground station without any astronaut intervention or direct awareness. The telemetry and communication interface specifications are found in the Space Shuttle Interface Control Document ICD-2-0D004.

Two data rates are used for command data sent on the up and forward link. A low 32 kbps data rate is created with a single 32 kbps voice channel. Alternatively, a high 76 kbps data rate is created by time division multiplex (TDM) of two 32 kbps voice channels, 6.4 kbps permuted and encoded command data, and a 1.6 kbps synchronization signal, all in non-return-to-zero, level (NRZ-L) format. The raw command data at 2.4 kbps is permuted and encoded prior to TDM to create the 6.4 kbps stream. Following the TDM formatting of the command and voice signals, a NSA-grade data encryptor is used prior to transmitting the signal from MCC to the White Sands Complex (WSC) ground station. This is set up to implement the 128-bit Data Encryption Standard (DES) that was established by NSA. The data encryption process does not change the bit rate. Under normal circumstances the high data rate is used; the low data rate is essentially a back up system for when the bit error rate (BER) of the channel becomes too large to support the higher data rate. At the White Sands Complex (WSC) ground station the received encrypted command data is then encoded to improve the BER of the links. A (V = 3, K = 7) convolutional encoder is used to create a 216/96 kbps NRZ-L stream from the incoming 72/32 kbps NRZ-L command data. The NRZ-L data is then converted to Bi-ϕ-L data and fed into a Phase-Shift Keying (PSK) spread spectrum transmitter which uses a 11.232 Mbps pseudo-noise sequence generator. Transmission is then sent out over a 2.041947900 GHz or 2.106406300 GHz carrier frequency. The pseudo-noise sequence generator consists of a 10-stage shift register with feedback coefficients set according to 2201_8 (octal) which produces a code length of 1023 chips. The (V = 3, K = 7) convolutional encoder consists of a 7-stage shift register, 3 modulo-2 adders with weightings 1111001, 1011011, 1100101, and a 3-position commutator that operates with a generator sequence of 7588127_H (hex). Upon reaching the SSO after passing through a TDRS, the up and forward link signal is amplified and detected by a PSK spread spectrum receiver. Bit synchronization is then performed, and a Viterbi decoder is used to extract the effects of the convolutional encoding. The data stream is then decrypted and command authenticated and finally passed through a TDM demultiplexer to separate the voice channels and command data.

The return and down link operates in a very similar manner but at two higher data rates. A low 96 kbps data stream is created from TDM of one 32 kbps voice channel and 64 kbps telemetry data. A high 192 kbps data stream is created from TDM of two 32 kbps voice channels and 128 kbps telemetry data. Both of these are formatted as NRZ-L data streams, and the higher data rate is the normally used one; the lower data rate is again a back-up for when the BER precludes the use of the higher rate of operation. From the TDM multiplexer, the data passes through an encryptor, a (V = 3, K = 7) convolutional encoder, a Bi-ϕ-L converter, and then the PSK spread spectrum transmitter. The (V = 3, K = 7) convolutional encoder works the same as in the reverse link, but converts the 192/96 kbps data into a 576/288 kbps output stream. The spread spectrum transmitter also uses a 10-stage shift register pseudo-noise sequence generator to create encoded words of 1023 chips. These are sent out on a 2.2175 GHz or 2.2875 GHz carrier frequency, passing through a TDRS, and picked up by the White Sands ground

station receiving antenna. The PSK spread spectrum receiver at the White Sands Complex detects the signal and also extracts a Doppler signal that can be used for ranging and tracking purposes. After bit synchronization, an 8-level soft-decision output at 576/288 kbps is fed into a Viterbi decoder to produce the hard-decision output at 192/96 kbps. After decryption, the telemetry data stream is passed through a TDM demultiplexer to separate out the voice channels and telemetry data at 128/64 kbps. The transponder in the SSO operates in a coherent mode which allows the Doppler ranging functions. The return link transmission carrier frequency is obtained by multiplying the received S-band carrier frequency by a factor of 240/221. If the forward link carrier frequency is not available for some reason, the transponder then uses its own free-running oscillator to provide a non-coherent replacement.

S-band (2.1 GHz) Telemetry and Data Relay Satellite (TDRS) Links

Two NASA geosynchronous orbit satellites (33,579 km circular geodetic altitude at 0° inclination) were programmed to be active during the STS-107 re-entry mission phase. TDRS-171, also know as TDRS-West, and stationed roughly over Guam, relayed the majority of the radio communication during re-entry. TDRS-047, also known as TDRS-East, picked up partial data frames toward the last few remaining seconds of the re-entry before STS-107 broke apart. The last three digits of each TDRS identifier give the geostationary longitude in degrees West from the Prime Meridian in Greenwich, England.

The S-band antennas are located on the front of the orbiter, directly above and below the crew cabin. Two antennas are used for frequency modulation (FM) transmission, and both are located on the vehicle centerline, one on the top and one on the bottom. Each of these have a hemispherical radiation pattern and are referred to as "hemis." These provide essentially the same gain as an isotropic radiator, i.e. 0 dB. Eight antennas make up the higher gain, more directional system that uses phase modulation (PM). Pairs of two are located in four locations around the crew cabin: upper left, upper right, lower left, and lower right. Each pair contains a forward pointing antenna and an aft pointing antenna. The eight antennas are thus designated ULF for upper left forward, ULA for upper left aft, and so on for the URF, URA, LLF, LLA, LRF, and LRA. Each of the antennas is constructed as a pair of crossed dipoles which are fed in quadrature to create a right hand circularly (RHC) polarized wave. The circularly polarized pattern makes each antenna insensitive to rotation about its normal axis. Each of these antennas are known as "quads" even though each is pointed into a specific octant of space. The forward quads cover an elevation angle of approximately +10° to +70°, while the aft quads cover elevation angles of approximately –50° to 0°. The azimuth angles of each quad (LL, UL, UR, LR) are approximately 90° wide. Note that elevation and azimuth in this context are with respect to vehicle pointing nose up, as if on the launch pad. Each of the antenna pairs is installed with a slight angle in toward the nose to match the vehicle's exterior contour. This and the presence of the vertical tail structure makes the coverage looking directly forward better than that looking directly aft. This coverage at the 2041.9 MHz receive frequency is generally better optimized than at the transmit frequency of 2217.5 MHz. The peak gain of each of the quads is approximately 6-7 dB above that for an isotropic radiator.

Switching of the S-band quad antennas is accomplished electronically. Switching between each of the four quad antenna pairs (LL, UL, UR, LR) is performed by an S-band antenna switch module which accepts commands either manually from the orbiter cockpit or from the telemetry ground command signals processed through the multiplexer – demultiplexer (MDM) units. The selection of the particular antenna is based upon calculations of the orbiter's position and attitude relative to either the White Sands Complex ground station or the TDRS satellites. Antenna selection is not based upon received signal strength. Transmit signals are fed into the antenna switch module from one of two redundant traveling wave tube (TWT) power amplifiers, each capable of producing 135 Watts of RF power. Received signals are taken from the antenna switch module and fed into one of two redundant preamplifier modules. The transmit and receive functions are isolated by a dual diplexer which handles both the low range (2217.5 MHz transmit, 2041.9 MHz receive) and high range (2287.5 MHz transmit, 2106.4 MHz receive) operating frequencies. After the transmit and receive signals are switched to one of the four selected quads, the forward versus aft antenna is selected by a relay switch on each of the quads that is energized by a switch beam control electronics module. The relay switch controls the phasing of a pair of –3 dB hybrid directional couplers which are in turn fed in quadrature by a third –3 dB hybrid coupler. One of the two antennas is made active by feeding the crossed dipoles in quadrature to create the RHC polarized beam. The other antenna is made inactive by feeding the crossed dipoles in opposite phase, for which the signals interfere destructively and cancel out. The overall insertion loss of the combined system of switches, circulators, diplexers, and transmission cable is estimated to be 4.6 dB.

The performance of the communication link can be monitored by several measures. The automatic gain control (AGC) level of the received forward link signal from TDRS to the SSO is monitored within the shuttle and then transmitted back as a measurement on the return link. When the forward link carrier signal is being received by the shuttle, several different status flag bits record the state of the carrier frequency lock, and these are also sent back as measurements on the return link. On the return link from the orbiter to TDRS, the minor frame count lock is monitored. If less than 95 of the 100 minor frames are not received correctly on at least one of the two integrated receivers, the entire major frame is discarded as invalid data by the MCC. This is what constitutes a formal communications drop out of the type that was observed during the early re-entry flight of STS-107. The signal-to-noise ratio of the integrated receiver for the return link is also monitored, although this is performed in the context of a digital data stream. The actual signal-to-noise ratio (SNR) of the received signal is equal to twice the ratio E_s/N_o, where E_s is the symbol energy and N_o is the noise density. The integrated receiver only samples the digital data stream and thus creates only an estimate

of the ratio E_s/N_o. 1024 samples are used each second for normal 192 kbps data rates. Because the 192 kbps digital data is convolutionally encoded as a 576 ksps symbol rate (three times the data rate), the ratio of energy per data bit to noise density is $E_b/N_o = 3\ E_s/N_o = 1.5$ SNR. The E_b/N_o value is computed every 100 ms from the sampled received data signal, and the reported value of E_b/N_o is constructed as a sliding (boxcar) average of the last 40 of the computed E_b/N_o values. Normal values of E_b/N_o during the re-entry flight are in the range of +13 to +19 dB.

Because the return link carrier signal is obtained by coherently multiplying the received forward link carrier by a factor of 240/221, the shift in the carrier signal frequency received back by TDRS can be used as a Doppler signal that reveals the relative speed between the orbiter and TDRS. Because TDRS is geostationary, there is no additional Doppler shift between it and the ground station. For example, the 2041.9 MHz signal transmitted from TDRS to the shuttle would be down shifted by a factor of $f'/f = (1 - v/c)$, where v is the relative velocity of separation between the TDRS and the shuttle and c is the speed of light, or as in this case radio wave propagation. The carrier frequency received by the shuttle would be down shifted by this factor, and this would be multiplied by the transponder factor of 240/221 to produce the return carrier frequency of nominally 2217.5 MHz. The return link carrier signal would also experience a Doppler shift in propagating back to the TDRS, so the overall round trip shift would be $f''/f = 2(1 - v/c) * (240/221)$. For typical shuttle re-entry velocities in the range of 5000 m/s, this produces Doppler shifts of approximately –70 kHz at S-band. It should be noted that the Doppler shift arises from the relative motion between the shuttle and TDRS, and that this is in general smaller than the re-entry velocity of the shuttle (as measured against a geostationary reference frame) by a factor which is the cosine of the angle between the shuttle's forward trajectory and its line of sight vector to TDRS.

If the forward link from TDRS to the shuttle were to drop, the transponder would shift over to its own internal local oscillator and continue to transmit telemetry back to TDRS on this frequency. This switch over of the carrier frequency oscillator would normally result in a brief 5 ms or less loss of carrier lock and this would cause up to one entire one second frame of telemetry data to be rejected as invalid by the MCC. The forward link AGC signal in the telemetry data would then show the forward link to have been lost during this time. When the forward link is restored, the transponder oscillator then switches back to a frequency lock on the forward link carrier which is multiplied by the 240/221 factor and used as the return link carrier frequency again. This switch over would once more cause a brief loss of carrier lock and the rejection of up to one full frame of telemetry data by MCC. The loss of a forward link carrier would also cause the Doppler frequency shift to show a jump when the original carrier frequency was restored.

If the return link from the shuttle to TDRS were to drop, no information would be received by MCC during this time, and all of the data displays would show an idle condition, with the last valid data remaining on each display. When the return link comes back after a dropout, the telemetry would indicate the state of the forward link lock flags and the forward link AGC level that existed at the one second frame prior to that instant. This is because there is a one second delay between when the communication receiver creates the lock flags and AGC signal level measurements and when these are interleaved into the telemetry data stream for transmission. If the dropout was brief and the forward link lock flags still show a locked forward carrier signal, then in all probability the forward link was not disturbed during this time. Similarly, because the return carrier signal frequency was not disturbed by a loss of forward lock, the Doppler signal would not show any jumps when the link was restored. For most of the communications drop outs that were observed during the early re-entry flight of STS-107, the Doppler signal did not jump and the forward link lock flags indicated a continued state of lock immediately after the link was restored. This indicates that these communications drop outs were associated with the return link, rather than the forward link.

Ku-band (13.8 GHz) Telemetry

A Ku-band dish antenna is located on a steerable mount within the payload bay. When the shuttle is in its normal orbit about the Earth with the payload bay doors open and the cargo hold facing the Earth, the Ku-band antenna can be used for data telemetry back to the Mission Control Center (MCC) using essentially the same formatting as for the S-band links. The Ku-band dish antenna is considerably more directional and must be accurately pointed to the ground station receiver to establish this link. The Ku-band antenna system also provides a much higher data throughput that is typically used for multiple video signals. However, since the orbiter had its belly to the Earth and the payload bay doors closed during the re-entry flight, the Ku-band antenna system was not in operation.

Calibration

Calibration of the sensor systems on the Space Shuttle Orbiter was designed in principle to be "potentiometer-free," so that there would be no manual adjustments to be made anywhere on the vehicle itself. However, each of the signal conditioners contain some combination of gain, span, offset, and balance adjustments. Some of these potentiometers are accessible through a screwdriver hole; others are potted over after being set to the proper adjustment by the vendor, usually Rockwell. Technicians sometimes adjust these potentiometer settings to bring readings on scale. It is unknown if the overall system is recalibrated after such adjustments.

All raw 8-bit PCM data must be manipulated through software computations on a digital computer, either on board or on the ground, to implement the proper calibration curve for each sensor. The calibration takes the general form of a polynomial of up to 5th order, $f(x) = a_o + a_1x^1 + a_2x^2 + a_3x^3 + a_4x^4 + a_5x^5$, where x is the raw digitized voltage signal from any sensor channel (8 bits), and f(x) is the final calibrated measurement. This system can thus be adjusted to correct for systematic offsets, nonlinearities, and unit scaling in any of the individual sensor measurements. Data from both the orbiter flight instrumentation (OFI) and orbiter experiment

instrumentation (OEX) are handled in this manner. The polynomial coefficients can, in principle, be different for each measurement system ID (MSID), and can, in principle, be different for each of the four Space Shuttle Orbiter vehicles. However, the majority of the sensor MSIDs are calibrated using generic data from the vendor, using transfer function values listed in the specification drawings for each sensor type. These produce calibration curve numbers that can be applied uniformly to a family of sensors. For example, calibration curve number N0432 is used to set the polynomial coefficients for strain gauge V12G9921A, and calibration curve number N1305 is used to calibrate temperature sensor V09T9895A. Calibration curve numbers and their specific polynomial coefficients are maintained in the Boeing MSID database, which is part of the "MML (Master Measurements List) Notebook" and is maintained on the Boeing NASA Systems FSSO database server.

While these calibration coefficients are stored as digital data, and thus do not drift over time, the sensors that they correspond to certainly do. It appears that the orbiter vehicle does not get any periodic recalibration of its sensor polynomial coefficients, nor of the adjustments to the signal conditioners. The specifications for each sensor are in general phrased to have the sensor remain within tight performance bounds for a period of 10 years. Many other sensors, such as pressure and strain, are only guaranteed by the manufacturer to have a 10 year shelf life. Many of these same sensors were installed on the vehicle when it was originally built in 1981 and along with the vehicle's airframe are 22 or more years old. The OEX sensor suite was originally installed for development purposes, and was not intended to be a long-life-span system, although it has produced reliable data up through the present.

Anomalous Events and Time Correlations

Orbiter Flight Instrumentation (OFI) – Telemetry Data

Fuselage Nozzle Temperatures

The fuselage nozzle temperatures were some of the earliest sensors to register anomalous readings among the OFI telemetry data. There are two nozzles on the left side of the fuselage, located just aft of the main bulkhead separating the crew cabin from the payload bay, which are used to discharge waste and supply water. A third nozzle located about 18 inches forward of these two is a vacuum vent. Each of the water nozzles consists of an approximately 2-inch diameter stainless steel plug with a single, approximately 1 mm diameter hole for discharging water. The outer surfaces of the nozzles are nominally flush with the finished surface of the vehicle. The vacuum vent nozzle is slightly smaller, about 1 inch in diameter, and also consists of a single small hole in a stainless steel flush mounted plug. Both the waste and supply water dump nozzles have built-in heaters to raise the nozzle temperatures above 32°F for which the water would otherwise be frozen into ice. Each of the nozzles have two redundant temperature sensors, named A and B, to measure the nozzle temperatures and provide feedback control to the nozzle heaters. The temperature sensors on the water dump nozzles and on the vacuum vent are each RTD type sensors with a range of 0 to 450°F. The supply water dump nozzle is located about 6 inches higher on the side of the fuselage than the waste water dump nozzle. While this difference might seem minor, visual inspection of the orbiter (the Discovery at KSC) showed that the lower waste water dump nozzle is actually much more protected by the leading chine of the left wing. As a result, the waste water dump nozzle typically does not heat up as much as the supply water dump nozzle during re-entry.

Like all of the OFI telemetry data, the readings from these sensors are discontinuous because of the communications drop outs that occurred. For these nozzle temperatures in particular, the anomalous part of the readings consists of a noticeable increase in the rate of the temperature rise for the vacuum vent and the supply water dump nozzle, but not for the waste water dump nozzle. Both the beginning and end of these increased rates of temperature rise happen to occur simultaneously with a communications drop out, and thus, the exact timing of their start and end is imprecise. The communications drop out which precedes the increased rate of temperature rise occurred over GMT 13:52:25 to 13:52:26 (EI + 496 to 497 sec), and then again over GMT 13:52:29 to 13:52:31 (EI + 500 to 502 sec). While the communications were restored briefly over GMT 13:52:27 to 13:52:28 (EI + 498 to 499 sec), the data in this period is not considered valid by the MCC, and thus no data is plotted during these two frames. This communications drop thus appears as a blank spot in the data from GMT 13:52:25 to 13:52:31, corresponding to EI + 496 to 502 seconds. Another communications drop out from GMT 13:52:49 to 13:52:55, corresponding to EI + 520 to 526 seconds, produced a blank spot in the data at about the same time at which the temperature returned to its more normal rate of rise.

Sensor V62T0439A is the supply water dump nozzle temperature B and the data from this sensor followed the normal trends of past vehicle flights up until a communications drop out at GMT 13:52:24 (EI + 495 sec). After the communications link was restored at GMT 13:52:32 (EI + 503 sec), the rate of temperature rise was approximately double and continued up to the next communications drop out at GMT 13:52:48 (EI + 519 sec). After the communications link was restored again at GMT 13:52:56 (EI + 527 sec), the rate of temperature rise had returned to its normal value, although the additional higher temperature did not return to its lower values. Sensor V62T0440A is the supply water dump nozzle temperature A, and the data from this sensor is virtually identical in value and trend as that from V62T039A. This indicates that the anomalous temperature rise is most likely not an artifact from some instrumentation system problem, and that both of these sensors were most likely recording the real temperature of the supply water dump nozzle. This seems to clearly indicate that a higher rate of heating occurred on the supply water dump nozzle in between the two communications drop out periods. Past flight data for these sensors show an increasing rate of temperature rise over EI + 150 to 300 seconds, and then this rate becomes fairly constant over EI + 300 to 800 seconds. The family of past flights bounds this temperature rise rate from (400°F

– 150°F)/(800 sec – 300 sec) = 0.500°F/sec for STS-050 to (400°F – 100°F)/(885 sec – 380 sec) = 0.594°F/sec for STS-087. For STS-107, the nominal rate of rise prior to the anomaly was (200°F – 100°F)/(485 sec – 310 sec) = 0.571°F/sec. In between the two communications drop outs, the anomalous rate of rise was (230°F – 210°F)/(519 sec – 503 sec) = 1.250°F/sec, more than double the rate of rise prior to the loss of communications.

Sensors V62T0519A and V62T0520A are the waste water dump nozzle temperatures, B and A, respectively, and the telemetry data from both of these was virtually identical, indicating a properly functioning measurement system, and also completely in keeping with the values and trends of past flights. As noted, the waste water dump nozzle is somewhat more protected by the leading chine of the left wing, and this nozzle does not experience as much heating during re-entry as the supply water dump nozzle. For STS-107 as well as all past flights, these sensors show an increasing temperature and rate of temperature rise over EI + 150 to 300 seconds. From EI + 300 to 900 seconds, the temperature still steadily increases but the rate of rise slows down. For STS-107, the maximum rate of temperature rise was (125°F – 65°F)/(420 sec – 300 sec) = 0.500°F/sec, which then fell back to (315°F – 280°F)/(900 sec – 780 sec) = 0.292°F/sec just prior to the breakup of the vehicle.

Sensor V62T0551A is the vacuum vent temperature. The re-entry heating that this vent experiences is much less than the water dump nozzles, in spite of its location being farther forward. This is probably due to the vent being physically much smaller than the water dump nozzles, and it may have better conductive heat dissipation from the plumbing immediately behind it. Over the re-entry flight period from EI to EI + 900 seconds this sensor typically records a temperature going from only 62°F to 85°F with the same quantization of approximately 1.4°F per bit as the water dump nozzles. Thus, this telemetry data from this sensor appears coarse because of the much smaller changes in its temperature during the re-entry period. Immediately after the communications link was restored at GMT 13:52:32 (EI + 503 sec), this sensor showed a much higher rate of temperature rise than just before the communications drop out. A normal rate of rise during this period of time would be (55°F – 52°F)/(585 sec – 465 sec) = 0.025°F/sec for STS-087, for example. For STS-107, the anomalous rate of temperature rise was (70°F – 67°F)/(538 sec – 503 sec) = 0.086°F/sec, over three times as great. All prior flights show this vacuum vent temperature as steadily rising with an increasing rate up through EI + 1000 seconds and beyond. Toward the end of this period, the rate of rise reaches values as high as (84°F – 70°F)/(1020 sec – 900 sec) = 0.117°F/sec. However, around the time period of EI + 503 to 519 seconds, none of the prior flights showed any rate of temperature rise near to that recorded by STS-107. Since the vacuum vent is essentially along the line of sight between the waste water dump nozzle and the most forward part of the left wing chine, any abnormal aerothermal vortex spinning off of the nose of the vehicle would affect both of these sensors in similar ways. Because of the similarity in their signatures and their identical timing, such a circumstance is most probably the physical situation which led to their anomalous readings. However, the manner in which this ties into the overall failure scenario for the orbiter is still unclear, and somewhat difficult to understand because these sensors were all located well forward of any of the supposed damaged area of the left wing leading edge.

Main Landing Gear (MLG) Proximity Switches

Four proximity switches are located within each of the main landing gear wheel wells to sense the mechanical position of the main landing gear and door latch moving parts. The sensors are mounted within the wheel well at various places to sense the position of the main landing gear door lock linkage, the main landing gear uplock, the main landing gear strut, and if the main landing gear is compressed with the weight of the vehicle. The wires from the sensors run outside of the wheel well to the electronics packages which convert the analog distance signal to a binary logic level indicating whether the magnetic target piece is near or far from the sensor. The electronics package which performs this operation is known as the "prox box." The prox box can be wired for either standard logic, in which a near target causes the digital output to be a logical "1" (nominally +5.0 Volts), or reverse logic, in which a near target causes the digital output to be a logical "0" (nominally 0.0 Volts).

Sensor V51X0116X, "left main gear door uplocked," is located at the front of the left wheel well on the main landing gear door latch linkage. When the door is closed and locked, so that all of the uplock rollers are captured by their hooks, the target which is attached to the most forward uplock hook is rotated to be in front of the sensor. This sensor is the one of the four which is wired for reverse logic, so that the normal door closed state which puts the target near to the sensor creates a logical "0" output. This sensor remained in the "0" state for the entire time that the telemetry signal was available.

Sensor V51X0100X, "left main gear uplocked," is located on the large inconel uplock arm that retains the left main landing gear strut in the up or stowed position. This sensor is wired for standard logic, and when the left main landing gear strut is captured in the uplock position by this assembly, the target is near to the sensor and the output of the prox box is a logical "1." The output of this sensor remained in a logical "1" state for the entire time of the re-entry flight telemetry.

Sensor V51X0130X, "left main gear no weight on wheels," is located on the left main landing gear strut itself and its wiring is routed along the backside of the strut, along with the wiring for several other sensors. When the vehicle is above the ground, the landing gear is not compressed, and the target remains in front of the sensor. This sensor is wired for standard logic, so that the near condition produces a logical "1" which is interpreted to mean "no weight on wheels" or no-WOW. This sensor also remained in the logical "1" state for the entire duration of the re-entry flight telemetry.
Sensor V51X0125E, "left main gear downlocked," is located on the folding linkage that locks the wheels down when they deploy. This sensor is different from the other three in that when the main landing gear is up and stowed position and the door is closed, the targets are near to the other three sensors, whereas for this sensor, the target is normally far

and then becomes near when the gear locks down. When the main landing gear fully deploys, the target then rotates to be in front of the sensor. The V51X0125E sensor is wired for standard logic, so that when the gear is up and target is far from the sensor, the output is a logical "0." The OFI telemetry data shows that at GMT 13:59:06 (EI + 897 sec), the output from this sensor abruptly transitioned from a "0" to a "1" state. This occurred only 26 seconds prior to the loss of signal (LOS) at GMT 13:59:32 (EI + 932 sec). This is physically inconsistent with the outputs from the V51X0116X sensor which indicated that the door was still locked closed and the V51X0100X sensor which indicated that the main landing gear was still locked in the up position. The wreckage debris showed clearly that the left main landing gear had not deployed and the wheel well door had not opened at anytime prior to the break up and loss of signal (LOS). Burn-through testing of the wires to this sensor showed that a burn-induced short in the wiring between the sensor and the prox box could produce the same transition from a logical "0" to a logical "1" state. The anomalous output transition for this sensor is thus interpreted almost conclusively as being caused by a burn through in the wiring which then caused an electrical short. Normally, a burn-induced soft short in the Kapton wiring would produce a slowly increasing insulation conductance which would be seen over several seconds. However, in the case of the proximity switches, the prox box electronics produce a hard binary decision output, and this threshold level masks any gradual changes in the wiring insulation conductance. All four of the corresponding proximity switch sensors for the right main landing gear remained at their normal values through out the re-entry flight up until the point where the telemetry was lost.

Tire Pressures and Wheel Temperatures

Because of the combination of high vehicle weight (233,995 lbs. on re-entry for STS-107), the comparatively hard landing, and the small number of main landing gear wheels to support the overall vehicle weight and landing forces, each of the four main landing gear tires were designed for and operated at high pressures of nominally 360 psia. Because tire pressure becomes such a critical issue in a safe landing of the vehicle, each of the four main landing gear tires had two redundant pressure sensors which provided continuous telemetry data to the ground. Each of these eight main landing gear tire pressure sensors were part number ME449-0177-1011 and were calibrated to measure absolute pressure over a range of 230 to 401 psia. The eight bit telemetry signal thus produced a bit quantization of 171 psia / 256 = 0.668 psia. The wiring for each of these pressure sensors runs down along the backside of each wheel strut to a break-away harness. The break-away harness consists mainly of a smaller diameter wire which connects the pressure sensors on each wheel to the cable on the strut. As soon as the main landing gear wheels touch the pavement, the wheels begin to spin, and the smaller diameter wire of the break-away harness is severed. Thus, tire pressures can only be monitored up until the point of touch-down. New break-away harnesses are replaced for each flight.

Each of the four tire pressure sensors on the left side of the vehicle showed a wiring burn-through signature in its telemetry data that began around GMT 13:58:27 to 13:58:41 (EI + 858 to 872 sec). An important feature is that the starting and ending times of these burn-through signatures differ, not between individual wheels, but between individual measurement channels. Sensor V51P0571A, the left-hand in-board tire channel 1, showed the first observable abnormality at GMT 13:58:27 (EI + 858 sec), which was a characteristic initially slow and then rapid decrease in signal that reached the off-scale low (OSL) value of 232 psia at GMT 13:58:39 (EI + 870 sec). This signature is characteristic of a wire burn-through in which the Kapton insulation resistance slowly degrades until it produces a "soft short" across the sensor wires, usually over the span of 10-15 seconds. Over nearly the same exact time span, sensor V51P0570A, the left-hand out-board tire channel 1, showed a similar soft short wire burn through pattern, beginning at GMT 13:58:29 (EI + 860 sec) and ending at an OSL value of 232 psia at GMT 13:58:39 (EI + 870 sec). The channel 2 sensors showed a similar trend but were delayed by approximately 10 seconds. Sensor V51P0572A, the left-hand out-board tire channel 2, began its decrease at GMT 13:58:39 (EI + 870 sec) and reached the OSL value of 232 psia at GMT 13:58:51 (EI + 882 sec). Sensor V51P0573A, the left-hand in-board tire channel 2, began its decrease at GMT 13:58:41 (EI + 872 sec), but fell abruptly to an OSL value of 232 psia at the next data point. All four of these tire pressure measurements read a normal value of 354-355 psia prior to the start of the failure signature.

Because of the high tire pressure and large volume of the tires as well, there was initial speculation that a rupture of one of the tires in the left wheel well could have been either a root or contributory cause of the demise of the vehicle. The tire pressure sensor data clearly rules this out, however. If a tire were to have ruptured, either spontaneously or as a result of some other event in the break-up, both pressure sensors on that one tire, i.e. channel 1 and channel 2, would have simultaneously recorded at least the first instant of such an event. However, the channel 1 and channel 2 sensors on the same tire, both for the in-board and out-board tires, show an approximately 10 second delay between their failure signatures. Furthermore, the channel 1 failure signatures on both tires (left in-board and left out-board) are nearly simultaneous and approximately 10 seconds earlier than the channel 2 failure signatures for the same two tires. Thus, it is fairly certain that the recorded failure signatures are those of a soft-short wiring burn through that affected channel 1 slightly before channel 2. There is no evidence in the sensor data that either tire experienced a rupture or even a slight depressurization prior to the failure modes of these tire pressure sensors.

Further confirmation of this conclusion exists in the tire pressure sensor data for the right main landing gear. While each of these four tire pressure sensors recorded an essentially nominal pressure up until the loss of the telemetry signal, upon close examination, all four of these pressure sensors show an unusual momentary 3-bit drop over the same time span of GMT 13:58:34 to 13:58:49 (EI + 865 to 880 sec). Prior flights show some single bit toggling as a normal occurrence for all of the tire pressure sensors, but the three bit drop is not seen in any of these prior flights. Sensor V51P0471A, right-hand in-board tire channel 1, and sensor V51P0470A,

right-hand out-board tire channel 1, both showed a continuous and nominal pressure of 356 psia prior to the three bit drop which began at GMT 13:58:37 (EI + 868 sec), and then returned to this nominal value afterwards. Similarly, sensor V51P0472A, right-hand out-board tire channel 2, and sensor V51P0473A, right-hand in-board tire channel 2, both showed a continuous and nominal pressure of 360-361 psia before and after the three bit drop that started at GMT 13:58:41 (EI + 872 sec). While each of the four three bit drops involves a slightly different shape, the channel 1 drops occur several seconds earlier than the channel 2 drops, again indicating that the anomaly is associated with the common instrumentation wiring of channel 1 versus channel 2, rather than with a particular tire. Because none of the other sensors within the right-hand wheel well give any indication of anomalous events, the simultaneous timing of these three bit drops with the wire burn-through signatures of the left-hand tire pressure sensors indicate that the common instrumentation aspects of the channel 1 versus channel 2 sensors are responsible for the anomalies seen in the right-hand tire pressures.

The temperatures of each wheel of the main landing gear are also measured, primarily to monitor the health of the braking system upon landing. Each sensor is an RTD temperature sensor of part number ME449-0160-0008, and is calibrated to measure temperatures over a range of −75°F to +175°F. The eight bit telemetry signal thus produces a single bit quantization of 250°F / 256 = 0.9766°F. The telemetry data from these four sensors yields a very similar story. Sensor V51T0574A, the left-hand out-board wheel temperature, showed a normal 34°F from EI up to GMT 13:58:27 (EI + 858 sec), after which it showed a characteristic soft short burn through pattern that reach an OSL value of −75°F at GMT 13:58:39 (EI + 870 sec). Sensor V51T0575A, the left-hand in-board wheel temperature, also showed a nominal 34°F from EI up to GMT 13:58:34 (EI + 865 sec), then a soft short burn through signature that reached an OSL of −75°F at GMT 13:58:49 (EI + 880 sec). The pattern between the two temperature measurements was virtually identical, but with the out-board wheel sensor failure occurring several seconds earlier. Sensor V51T0474A, the right-hand out-board wheel temperature, recorded a nominal 42-43°F from EI up until LOS, and sensor V51T0475A, the right-hand in-board wheel temperature, recorded a nominal 39°F from EI up until LOS, also. There were no observable anomalies in the right-hand wheel temperatures.

All of the left-hand tire pressure and wheel temperature failure signatures, as well as the three-bit momentary drops in the right-hand tire pressures, physically fit the circumstances of a Kapton wiring burn-through that produced a soft short in the sensor cabling. This burn-through process was most likely caused by the wiring to one tire or wheel sensor, but the commonality of the wiring and instrumentation channels caused the other measurements in the left-hand wheel well to fail, along with causing a minor perturbation of a few of the sensors in the right-hand wheel well which were also connected to that instrumentation channel. None of the instrumentation telemetry data indicates any rupture of the main landing gear tires, nor of any associated types of events, such as an induced leak which would cause a slower depressurization.

Main Landing Gear (MLG) Hydraulic System Temperatures

Within the left main landing gear wheel well there are also eight hydraulic system temperature sensors that recorded anomalous readings during the re-entry flight. All eight of these are RTD temperature sensors measuring hydraulic line temperatures over the range of −75°F to +300°F. In each case, the RTD sensor was adhesively attached to the stainless steel brake line tubing and covered with a combination of aluminum foil and red RTV-560. Sensors V58T1700A, V58T1701A, V58T1702A, and V58T1703A are sequentially placed along the left main landing gear brake line, designated A, B, C, and D, respectively. A and B are located on the main landing gear strut itself, while C and D are located toward the rear of the inboard wall of the wheel well within a cluster of hydraulic plumbing. Sensors V58T0841A and V58T0842A measure the aft and forward brake switch valve return line temperatures, respectively, and are also located within the inboard rear cluster of hydraulic plumbing. Sensor V58T0405A is located on and measures the temperature of the left main landing gear strut actuator, the large hydraulic cylinder located toward the inboard rear of the wheel well, which is used to hydraulically damp the deployment of the main landing gear, and also to hoist the gear back up into the stowed position. Sensor V58T0125A is located on the main landing gear uplock actuator and measures the hydraulic line temperature to this actuator which holds the main landing gear in the up and stowed position. All eight of these sensors exhibited an off nominal temperature rise at various times during the re-entry flight. Only one appears to have failed outright due to a wire burn through before the loss of signal (LOS) at GMT 13:59:32.

The four brake line temperature sensors exhibited the off normal trends first. Sensor V58T1703A measuring the left brake line temperature D was the first sensor of this group to record an off nominal temperature rise at GMT 13:52:17 (EI + 488 sec). It recorded a nominal 84°F temperature up to this time, after which the temperature rose abnormally to 100°F at the time of the LOS. Similarly, but slightly delayed, sensor V58T1702A measuring the left brake line temperature C recorded an off nominal temperature rise at GMT 13:52:41 (EI + 512 sec), beginning at a value of 70°F and rising ultimately up to 104°F at LOS. At the same moment, sensor V58T1700A measuring the left brake line temperature A recorded an off nominal temperature rise from a nominal value of 125°F that ultimately climbed to 172°F at LOS. Likewise, sensor V58T1701A measuring the left brake line temperature B recorded an off nominal temperature rise at GMT 13:54:10 (EI + 610 sec) that began at a nominal value of 110°F and rose to 154°F at LOS. Each of the corresponding sensors for the right main landing gear brake line temperatures A, B, C, and D, that is, V58T1750A, V58T1751A, V58T1752A, and V58T1753A, respectively, showed essentially a constant and normal temperature over the entire time span of the telemetry data.

The remaining hydraulic system temperature sensors then sequentially recorded similar off normal temperature rises. Sensor V58T0405A measuring the temperature of the left main gear strut actuator body showed an off nominal tem-

perature rise at GMT 13:54:24 (EI + 615 sec) that began at 37°F and ultimately rose to a value of 76°F at LOS. Sensor V58T0842A that measured the temperature of the forward brake switch valve return line showed an off nominal temperature rise at GMT 13:55:12 (EI + 663 sec) that began at 40°F and rose to 67°F at LOS. Sensor V58T0125A measuring the temperature of the left main gear uplock actuator hydraulic line showed an off nominal temperature rise at GMT 13:56:16 (EI + 727 sec) that began at 30°F and rose to 53°F at LOS. Sensor V58T0841A that measured the temperature of the aft brake switch valve return line showed an off nominal temperature rise at GMT 13:57:54 (EI + 825 sec) that began at 45°F and rose to 66°F at LOS. Each of the corresponding temperature sensors for the right main landing gear, V58T0406A, V58T0846A, V58T0128A, and V58T0845A, showed completely normal behavior over the period from EI to LOS.

Only one of these eight sensors showed any evidence of a complete failure mode. Sensor V58T0841A measuring the temperature of the aft brake switch valve return line showed the beginnings of a soft short wire burn through failure mode at GMT 13:59:22 (EI + 913 sec), just 10 seconds prior to LOS. This amounted to only a few bit changes in a downward trend at this point. NASA categorized this as a wire damage trend, but the few bit changes are not fully conclusive of this, since an OSL or OSH condition was never reached.

The primary conclusion to be drawn from this set of eight sensors is that there was a clear source of abnormal heating within the left wheel well as early as GMT 13:52:17 (EI + 488 sec) when the first of these, V58T1703A, started showing a rapid rise in temperature in the brake line. The heating appears to have been distributed throughout the back and inboard side of the wheel well, because of the varied locations of the temperature sensors and the difference in timing in their abnormal rise rates. Because of the heat dissipation capacity of the large metal masses in the wheel well, none of these abnormal temperature rises exceeded 50°F, but all of the temperature sensors showed a significant rise of at least 15°F.

Sensor V58T1700A measuring the left brake line temperature A, in addition to its more drastic abnormal behavior at GMT 13:52:41 (EI + 512 sec), showed a 3-bit (4.5°F), short duration rise at a very early time of GMT 13:47:56 (EI + 227 sec). This short rise, while clearly discernable, was thought to be an even earlier indication of some heating process taking place within the left wheel well. However, past flight data shows that similar short duration rises have occurred over the course of the re-entry flights. Thus, this 3-bit early rise in V58T1700A cannot be conclusively associated with an early breach of the left wheel well area. The sensor V58T1753A measuring the right main gear brake line temperature D also exhibited a few unexplained short duration, small amplitude rises during the re-entry flight. It rose and fell by 4 bits (6°F) over GMT 13:47:54 to 13:48:39 (EI + 225 to 270 sec), and then it rose and fell by 3 bits (4.5°F) over GMT 13:56:14 to 13:57:04 (EI + 725 to 775 sec). The other three right main gear brake line temperature sensors were completely quiet during the same time periods.
NASA has provided some explanation for these small-amplitude, small-duration temperature pulses as originating from a transfer of the hydraulic fluid from a reservoir at one temperature to the line which was at a different temperature, as the temperature pulse then represents the heat transfer associated with the fluid and the line reaching an equilibrium. While no parts of the main landing gear hydraulic system were being actuated during this phase of the re-entry flight, the circulation of neutral pressure hydraulic fluid does provide a reasonable explanation for these temperature variations. The only unexplainable feature of the behavior of these sensors is that they did not appear to completely fail with a wire burn through signature. The wiring for V58T1700A and V58T1701A was routed along the back of the left main landing gear strut, the same as for the tire pressures and wheel temperatures discussed previously. However, all of the tire pressures and wheel temperature sensors did show a wire burn through failure signature, while none of the hydraulic line temperature sensors did so. It is not clear why the soft short burn through process would favor the wires of one type of system over another.

Elevon Hydraulic System Temperatures

The four control surfaces on the shuttle wings, termed "elevons" as a dual purpose combination of elevator and aileron, are hydraulically actuated, and the hydraulic fluid return line temperatures are measured for each, along with the body temperature of the actuator cylinder. Each actuator can be driven by any one of three redundant hydraulic systems, numbered 1, 2, and 3. Each of the three hydraulic system return line temperatures and actuator body temperature for each of the four elevons is measured using an RTD temperature sensor, part number ME449-0160-0001, which are calibrated to measure temperatures over the range of –75°F to +300°F. The 8-bit telemetry data thus gives a quantization of 1.46°F per bit.

The elevon hydraulic system temperatures reveal a wiring burn through pattern within the left wing quite distinctly, because half of the sensors had their wiring routed forward along the wheel well while the other half of the sensors had their wiring routed inboard into the fuselage through an aft interconnect panel. Those with their wiring routed forward along the left wheel well showed a clear burn through failure mode, while those with their wiring routed inboard and aft stayed on-line and responded normally all the way up to the loss of signal (LOS) at GMT 13:59:32.

At GMT 13:53:02 (EI + 533 sec), sensor V58T0394A, the left outboard elevon hydraulic system 3 return line temperature, showed the beginning of a burn-through failure mode which took the measurement to OSL at GMT 13:53:10 (EI + 541 sec). Prior to this, the sensor had been responding normally, following a gentle rise up from 95°F at EI to 125°F when the failure mode began. Simultaneously, sensor V58T0157A, the left inboard elevon hydraulic system 1 return line temperature, which started out at 67°F at EI, showed a burn through failure mode that began at 100°F at GMT 13:53:02 (EI + 533 sec) and which went to OSL at GMT 13:53:11 (EI + 542 sec). Shortly thereafter at GMT 13:53:34 (EI + 565 sec), sensor V58T0257A, the left inboard elevon hydraulic system 2 return line temperature, began a burn

through failure mode which went to OSL at GMT 13:53:36 (EI + 567 sec). This sensor had been following a gentle rise from 135°F at EI up to 160°F when the failure mode began. Simultaneously, sensor V58T0193A, the left outboard elevon hydraulic system 1 return line temperature, which had been constant at 42°F since EI, showed an abrupt drop to OSL at GMT 13:53:34 (EI + 565 sec). All four of these sensors had their cables routed first inboard along the cross spar and then forward, following the service access ports in the cross spars until the harness ran along the upper outside wall of the left wheel well, finally crossing inboard along the 1040 spar to the interconnect panel P65 on the fuselage. This routing took all four of these sensor wires directly in front of the supposed breach area of the leading edge spar behind RCC panel # 9, along side many other sensor cables which also appear to have failed during this same general time period.

In contrast, sensor V58T0883A, the left outboard elevon hydraulic system 2 return line temperature, remained nearly constant from 72°F at EI to 74°F at LOS. Sensor V58T0833A, the left inboard elevon hydraulic system 3 return line temperature, followed a smooth and normal rise from 50°F at EI up to 100°F at LOS. Sensor V58T0880A, the left outboard elevon actuator body temperature, showed a smooth and normal rise from 63°F at EI up to 108°F at LOS. And similarly, sensor V58T0830A, the left inboard elevon actuator body temperature, showed a smooth and normal rise from 86°F up to 141°F at LOS. Even though these four sensors were physically located in essentially the same places as the preceding four, none of these showed any burn through failure modes, all remained on-line all the way up until the LOS, and all of their readings were normal as compared to prior flights of the vehicle. The difference is that their wiring cables were routed all the way inboard, aft of the left wheel well, and entered the fuselage at an aft interconnect panel. These sensor's cables thus did not pass anywhere near to the supposed breach area farther forward on the left wing leading edge.

All eight of the corresponding temperature sensors on the right wing showed perfectly normal responses over the entire time from EI up until the LOS. These included: V58T0359A, the right inboard elevon hydraulic system 3 temperature which went from 125°F to 156°F; V58T0159A, the right inboard elevon hydraulic system 1 temperature which went from 62°F to 82°F; V58T0933A, the right inboard elevon hydraulic system 2 temperature which went from 80°F to 84°F; V58T0930A, the right inboard elevon actuator body temperature which went from 72°F to 120°F; V58T0294A, the right outboard elevon hydraulic system 2 temperature which went from 127°F to 171°F; V58T0194A, the right outboard elevon hydraulic system 1 temperature which remained at a constant 28°F; V58T0983A, the right outboard elevon hydraulic system 3 temperature which went from 42°F to 70°F; and V58T0980A, the right outboard elevon actuator body temperature which went from 82°F to 134°F. All eight of these temperature measurements followed a smooth and uniform rise from EI to LOS and were completely within the expected patterns of prior flights of the vehicle.

While each of the elevons can be actuated by any one of the three redundant hydraulic systems, during normal flight, these hydraulic systems are selected in mixed sets. The primary system, which was operating during the re-entry flight, consists of hydraulic system 3, V58T0394A, for the left outboard elevon, hydraulic system 2, V58T0257A, for the left inboard elevon; hydraulic system 3, V58T0359A, for the right inboard elevon; and hydraulic system 2, V58T0294A, for the right outboard elevon. During the re-entry flight, there are two principal time periods when the elevons are being actuated to effect rolls of the vehicle. The first of these occurs over GMT 13:48:09 to 13:50:09 (EI + 240 to 360 sec), and each of these four hydraulic return line temperatures for the primary system showed some slightly erratic temperature readings during this period. The second period occurs over GMT 13:56:09 to 13:57:09 (EI + 720 to 780 sec), and both of the right hydraulic return line temperatures for the primary system showed similar erratic behavior. By this time, both of the cables to the other two primary hydraulic return line temperature sensors had burned through and were off line. For completeness, the secondary hydraulic system is composed of all four of the hydraulic system 1 lines, V58T0193A, V58T0157A, V58T0159A, and V58T0194A. The tertiary hydraulic system is composed of hydraulic system 2, V58T0883A, for the left outboard elevon; hydraulic system 3, V58T0833A, for the left inboard elevon; hydraulic system 2, V58T0933A, for the right inboard elevon; and hydraulic system 3, V58T0983A, for the right outboard elevon.

The temperatures of the three hydraulic system fluid reservoirs that are located inside the aft fuselage are also included with the OFI telemetry data. Each of these three sensors are RTD temperature sensors, part number ME449-0156-0003, and are calibrated to measure temperatures over the range of –75°F to +300°F. Sensor V58T0101A, on hydraulic system reservoir 1, showed a perfectly normal and smooth rise from 94°F at EI up to 178°F at the LOS. Sensor V58T0201A, on hydraulic system reservoir 2, measured a normal and smooth rise from 127°F at EI up to 169°F at LOS. Similarly, sensor V58T0301A, on hydraulic system reservoir 3, also showed a normal and smooth rise from 84°F at EI up to 141°F at LOS. All three of these temperature measurements were completely consistent with the expected patterns of past flights.

Skin Temperatures

The OFI telemetry data included a number of measurements of the orbiter skin temperatures. The V09T set included 23 temperature measurements over the wing and fuselage skin, the V34T set included 18 temperature measurements over the fuselage, primarily the mid-body section, and the V37T set included 4 temperature measurements over the payload bay doors. In each of these cases, a "skin" temperature refers to the temperature at the bond line where the heat tiles are bonded to the aluminum vehicle skin, and not the actual surface temperature of the heat tiles or friable surface insulation. Because of the lower temperatures experienced along the bond line, RTD temperature sensors were used for each of these measurements, using either part number ME449-0160-0001 or ME449-0160-0008. All of these were calibrated for the temperature range of –200°F to +450°F. The 8-bit telemetry data gave a bit quantization of 650°F / 256 = 2.45°F. From all of these temperature measurements, only six appeared to show any anomalous behavior from the trends of prior flights of the vehicle. There were also a total of 47 temperature mea-

surements within the engine compartments of the left and right OMS pods, set V43T, but all of these measurements, being inside the OMS pods, were completely consistent with the trends of prior flights of the vehicle.

Three of the skin temperature sensor readings involved clearly defined wiring burn through failure modes. Sensor V09T1006A, the left inboard elevon lower skin temperature, started at a reading of 11°F at EI, and then dropped by 1 bit to 8°F at GMT 13:52:56 (EI + 527 sec), at which point it exhibited a wire burn through failure mode which took it to an OSL value of –200°F at GMT 13:52:59 (EI + 530 sec). This burn through process took only 3 seconds and was thus comparatively quick. Sensor V09T1002A, the left lower wing skin temperature, began by reading 6°F at EI which increased slowly to 10°F at GMT 13:56:03 (EI + 714 sec), when it began to show a wire burn through failure mode. This was a very slow burn through process which finally reached an OSL value of –200°F at GMT 13:57:28 (EI + 799 sec). Similarly, the corresponding sensor at the same X-Y location on the left wing but on the upper surface, V09T1024A, the left upper wing skin temperature, began with a reading of 0°F at EI which then increased slowly to a value of 20°F at GMT 13:56:24 (EI + 735 sec), when it also began to show a wire burn through failure mode. This burn through process was also rather long in duration, with the reading finally going to an OSL value of –200°F at GMT 13:57:43 (EI + 814 sec). It is noteworthy that the wiring from each of these three temperature sensors was routed within the same harness which passed along the upper outside wall of the left wheel well, the point at which most of the sensor wiring burn throughs are thought to have taken place.

The other three anomalous skin temperature sensor readings each involved a change in the rate of the temperature rise, one of which was clear and drastic, while the other two were more subtle. Sensor V09T1724A, the left aft fuselage sidewall temperature, measured at section X1410, began at a reading of 31.5°F at EI and then started a normal rise at GMT 13:50:34 (EI + 385 sec). At GMT 13:54:22 (EI + 613 sec), the reading was 42°F and the rate of temperature rise approximately doubled, reaching a final value of 71.5°F at LOS, which was about 10-15°F hotter than what it would have reached if the original slope would have continued. Sensor V34T1106A, the left mid fuselage bond line side temperature at section X1215, started with a value of 20°F at EI and at GMT 13:54:22 (EI + 613 sec), the same timing as the preceding sensor, the reading increased rapidly from 20°F to 90°F at LOS. This was a 25 bit increase over this time period which was quite different from past flights in which the reading only increased by 6-7 bits. This V34T1106A sensor also exhibited an anomalous and abrupt spike up to 280°F over GMT 13:50:07 to 13:50:09 (EI + 358 to 360 sec), after which it appeared to react normally. This may have been a transient within the instrumentation or telemetry system, as there were a few other sensors which showed a similar abrupt spiking over the precise same three second time interval. Sensor V34T1118A, the mid fuselage left sill longeron temperature at section X1215, started at a value of 21.2°F at EI and at GMT 13:55:41 (EI + 692 sec), began a more rapid rise up to a value of 29.0°F at LOS. This was a fairly subtle off nominal rate of temperature rise, producing a 3 bit rise, whereas prior flights only produced 1-2 bits over the same period.

None of the other V09T, V34T, or V37T temperature measurements showed any anomalous behavior in comparison to prior flight data. Corresponding to V09T1002A and V09T1024A on the lower and upper left wing, were V09T1000A and V09T1004A on the lower and upper right wing, respectively. Sensor V09T1000A chattered between 1.0-3.5°F at EI and then at EI + 720 seconds started a smooth rise from 1.0°F to 7.5°F at LOS. Similarly, sensor V09T1004A also chattered between –2.0°F and –4.0°F at EI and then at EI + 300 seconds began a smooth rise from –2.0°F to +21°F at LOS. This was normal behavior for both sensors.

A variety of temperature measurements were made along the forward and mid sections of the fuselage, all of which also appeared to be completely consistent with prior flight data. These included V09T1008A, lower centerline front web temperature at X582; V09T1010A, front side cap temperature at X582; V09T1012A, forward fuselage left bond line temperature at X480; V09T1016A, mid fuselage bottom left bond line temperature at X620; V09T1018A, upper fuselage cap temperature at X576; V09T1020A, forward RCS upper skin temperature; V09T1022A, mid fuselage bottom left bond line temperature at X777; V09T1026A, lower center skin temperature; V09T1028A, right OMS pod skin temperature; V09T1030A, left OMS pod skin temperature; V09T1510A, right forward fuselage RCS skin temperature; V09T1514A, left forward fuselage RCS skin temperature; V09T1524A, forward fuselage upper skin centerline temperature; V09T1624A, forward fuselage lower skin bottom centerline temperature; V09T1702A, aft fuselage floor bottom centerline temperature; and V09T1720A, right aft fuselage sidewall temperature. The last of these, V09T1720A, is the right side equivalent of V09T1724A, which showed an anomalous rate of temperature rise. Sensor V09T1720A started at a reading of 19°F at EI and then rose smoothly to a value of 52°F over EI + 210 seconds to LOS. This pattern was also nominal for most of the sensors in the V09T set, that is, beginning at a fairly low temperature of 10-35°F at EI, staying constant for several minutes, and then slowly and smoothly climbing up to their peak value which occurred at LOS. Overall temperature rises were in the range of 10-30°F.

Similar behavior was found for most of the V34T set. These included: V34T1100A, lower right web temperature at X582; V34T1102A, mid fuselage left bond line temperature at X650; V34T1104A, mid fuselage right bond line temperature at X650; V34T1108A, mid fuselage right bond line temperature at X1215; V34T1110A, mid fuselage lower aft skin temperature; and V34T1112A, mid fuselage bottom center bond line temperature. Sensor V34T1108A is the right hand mate to sensor V34T1106A which exhibited an anomalous rate of temperature rise. Sensor V34T1108A recorded an initial temperature of 11°F at EI and this then rose to a value of 24°F over the period of EI + 420 seconds through LOS, all of which was completely nominal behavior.

Six temperature sensors were placed on the mid fuselage sill longerons: V34T1114A, on the left at X650; V34T1116A,

on the left at X1030; V34T1118A, on the left at X1215; V34T1120A, on the right at X650; V34T1122A, on the right at X1030; and V34T1124A, on the right at X1215. Except for V34T1118A, which showed the anomalous rate of temperature rise that resulted in an overall 3 bit rise, each of these other five showed a perfectly normal behavior in comparison to past flights, starting out in the range of 8-15°F, and rising up to a final value of 13-18°F at LOS. Sensor V34T1114A increased by 2 bits, while the other four increased by only 1 bit over the period from EI to LOS.

Five sensors were placed around the circumference of the fuselage structural frame at the X582 cross section. These included: V34T1126A, left side temperature; V34T1128A, left upper mid temperature; V34T1130A, right side temperature; V34T1132A, right upper mid temperature; and V34T1134A, right upper off center temperature. Because all five of these sensors were inside the skin of the fuselage, they only experienced an overall temperature increase of 1-2 bits over the period from EI to LOS. All five exhibited normal behavior.

Four sensors were placed on the payload bay doors on the top of the vehicle. These included: V37T1000A, payload left forward skin temperature; V37T1002A, payload right aft skin temperature; V37T1004A, payload left aft skin temperature; and V37T1006A, payload right forward skin temperature. Each of these exhibited normal behavior, starting out at –20°F to 0°F and rising by approximately 10°F to final values in the range of –10°F to +10°F at LOS.

Communications Drop Outs

One of the earliest indications of abnormal conditions during the re-entry, prior to the recovery of the OEX recorder data, was the series of communication drop outs that occurred while the orbiter was still over the Pacific Ocean. Many of these occurred close to the timing of various observed debris shedding events, suggesting that the shed debris could have blocked, attenuated, or scattered the S-band telemetry signal between the SSO and the TDRS. It is known, for example, that the fine metal particles in the plume from the solid rocket boosters (SRBs) strongly scatter and attenuate RF signals. Similarly, chaff that is used by the military consists of fine metal particles that are used to confuse enemy radars. An obvious speculation is that the vaporized aluminum spar materials might cause a similar effect on the communications links between the SSO and TDRS.

There are, however, numerous other physical mechanisms which could contribute to causing the communication links to drop out. First, the overall link margins during the re-entry flight are rather low to begin with. The received signal power is typically –112 to –114 dBm, and when the signal power falls to –122 to –124 dBm, bit errors in the transmission become frequent enough that valid data flow becomes interrupted. During the first six minutes past EI, the received bit energy to noise density ratio E_b/N_o for the SSO to TDRS-171 link typically varies from +13 to +19 dB, and then decays to +10 to +16 dB over the next ten minutes. After that, the link margins become sufficiently degraded that numerous communication link dropouts are commonplace. Angling off of the high gain direction of a given antenna can cause a reduction of 4 to 6 dB, and this in general occurs for look angles that have elevations greater than +80° (pointing straight ahead toward the nose of the vehicle would be +90°), or less than –70° (pointing directly aft toward the tail of the vehicle would be –90°). The plasma flow around the orbiter during re-entry is also a factor. This plasma sheath raises the ambient noise floor around the vehicle and thus reduces both the forward and return link margins. The much higher plasma density under the belly of the orbiter also renders the lower four antennas unusable during the re-entry flight. Since the orbiter flies through most of the re-entry path with a pitch of approximately 40°, the nose is pointed high into space and the best look angles for any of the S-band antennas are toward the rear which provides high gain looking toward the West horizon. This direction is also in the draft zone of the orbiter for which plasma accumulation is minimal. Radio frequency interference (RFI) arising from either ground or space sources can also corrupt the communication links. On the positive side, however, the S-band frequency of around 2.1 GHz incurs a particularly low atmospheric attenuation. Signal transmission from the surface of the Earth into low Earth orbit (LEO, typically 100 to 200 km altitudes, and farther out than what the shuttle ever reaches) incurs a signal loss of only 5 to 10 percent at frequencies in the range of 2.0-2.4 GHz, hence the popularity of this frequency range for satellite communications.

For a normal re-entry flight, as the orbiter executes various roll maneuvers, there are several switches that occur between different S-band antennas to maintain high gain signal reception from TDRS-171 which would be seen looking aft of the vehicle toward the West horizon. From entry interface (EI) up to about EI + 100 seconds, the upper right forward (URF) S-band antenna is active. From about EI + 100 seconds to EI + 350 seconds, the link is switched to the upper right aft (URA) antenna. From about EI + 350 seconds to EI + 650 seconds, the upper left aft (ULA) antenna is used, and then the upper right aft (URA) antenna again up until about EI + 800 seconds. Beyond this time, the link margins have degraded to the point where communication drop outs are frequent and actual two-way communication with the vehicle becomes spotty at best. For most of the prior flights, continuous communications were maintained up until this point where the link margins degraded. For STS-62, continuous communications remained up until EI + 840 seconds. For STS-73, communications remained up until EI + 940 seconds, although this flight did experience some 20 second long drop outs at approximately EI + 720 and EI + 840 seconds. For STS-78, communications were continuous up until EI + 830 seconds, and for STS-90, communications did not drop out until EI + 920 seconds. The orbiter's initial attitude at EI is a pitch up of approximately 40° with zero roll and zero yaw. Over approximately EI + 320 to EI + 350 seconds the orbiter executes a right roll to about +70° while maintaining the same pitch and yaw. This roll forces a switch over from the URA to the ULA antenna. After descending for several minutes, the orbiter then, over approximately EI + 740 to EI + 770 seconds, executes a reverse roll from right +70° to left –70° while still maintaining the same pitch and yaw. Just prior to initiating this roll reversal, the communications link is switched back from the ULA to the URA antenna for the duration of the re-entry. Several

minutes later, the communications links usually drop out as the link margin has degraded too far by that point.

For flight STS-107, the first 350 seconds past EI showed normal communications link behavior. The switch from the URF to the URA antenna occurred at GMT 13:46:16 (EI + 127 sec). Prior to and following this antenna switchover, the received signal strength of the forward link AGC showed a healthy signal, the return link frame counts were reading 100/100, and the return link E_b/N_o showed a healthy and nearly constant signal to noise ratio.

The anomalous communication drop outs began immediately after the completion of the first rightward roll when the S-band antenna was switched from URA to ULA at GMT 13:50:00 (EI + 351 sec). At this moment, the orbiter was a distance of 38,082 km away from TDRS-171 to the West. The major telemetry frame at this second had only 81 of its 100 minor frames lock on the primary integrated receiver (IR-A), and only 28/100 minor frames lock on the secondary integrated receiver (IR-B). The frame synchronization signal was present throughout on IR-A, but was lost on IR-B. This can be interpreted to mean that 81% of the telemetry data of that major frame was received on the primary receiver, and only 28% of the telemetry data was received on the secondary receiver. The MCC front end processor (FEP) rejects the entire frame of telemetry data as invalid whenever the frame lock count falls below 95/100 on either receiver. This is the definition of a communications drop out in this context. The antenna switchover is normally accomplished in only 5 ms, however this switching is not timed to match to any convenient point in the framed data. The antenna switchover should in principle corrupt only one minor frame, but if the switching took significantly longer, several minor frames could be corrupted. If more than five minor frames were to have been corrupted, implying an antenna switchover that took more than 50 ms to settle, then an official communication drop out would be declared by the MCC FEP. The antenna switching is accomplished using mechanical relays, and switch closure and opening times of 50 ms or longer could certainly be possible, particularly if the relay mechanism is old, dirty, or the solenoid pulser has become weak. On this basis NASA has explained this first communications drop out as being a direct result of the antenna switchover. However, in this instance, the two integrated receivers behaved quite differently, with IR-A losing only a few minor frames and IR-B losing most of them. An antenna switching issue would be thought to affect both integrated receivers in the same manner, while a decaying signal strength or increasing noise level could produce different effects within the two receivers.

The second communications drop out occurred over GMT 13:50:04 through 13:50:06 (EI + 355 through 357 sec). During the middle of this three second outage, both integrated receivers lost frame synchronization and the minor frame counts dropped to 9/100 and 5/100. Since the outage was greater than one second, the Doppler signal was lost for the last two of the three seconds, but it recovered without any noticeable jump in frequency. Similarly, the E_b/N_o estimators for both integrated receivers also fell to zero for the last two of the three second outage. NASA suggested that this second communications drop out could have been caused by a loss of the forward link which they say dropped out over GMT 13:50:03 through 13:50:06. However, if the forward link were to have been lost over this period, the transponder in the shuttle would have switched over to its local oscillator and then when the forward link returned, switched back to a frequency locked carrier at 240/221 times the received forward link frequency. This switchover in return carrier frequency would have created a jump in the Doppler signal which was not observed.

Communications drop out #3 occurred over GMT 13:50:16 through 13:50:22 (EI + 367 through 373 sec). Both receivers showed an immediate loss of frame synchronization and both showed minor frame counts that went essentially to zero for the middle 5 seconds of the seven second drop out. In this instance and in all subsequent ones, the responses of both integrated receivers were essentially identical.

Communications drop out #4 occurred over GMT 13:50:25 through 13:50:28 (EI + 376 through 379 sec). Both integrated receivers recorded exactly the same behavior, with zero minor frame counts and no frame synchronization over the middle two of the four second drop out.

Communications drop out #5 seems hardly a drop out at all. At GMT 13:50:42 (EI + 393 sec), both integrated receivers recorded a minor frame count of 94/100; one minor frame short of the 95 needed to constitute a valid frame. Neither receiver lost frame synchronization, nor had the E_b/N_o estimator fall. As minor as this drop out was in nature, there is very little of any consequence that can be associated with it.

Communications drop out #6 occurred over GMT 13:52:09 through 13:52:15 (EI + 480 through 486 sec). Both integrated receivers recorded exactly the same behavior, with the minor frame count dropping to zero over the middle five seconds, and the frame synchronization being lost over EI + 480 through 485 seconds. Doppler data and the E_b/N_o estimator also fell to zero for both receivers over EI + 480 through 485 seconds. Doppler data returned at EI + 487 seconds, without any major deviation from its prior readings, as would be expected if the forward link were to have remained intact over this drop out period.

Communications drop out #7 was by formal definition only two seconds in length and occurred over GMT 13:52:25 through 13:52:26 (EI + 496 through 497 sec). In this case, the primary integrated receiver IR-A lost the frame synchronization over EI + 496 through 498 seconds, while the secondary integrated receiver IR-B only lost the frame synchronization over the EI + 496 second alone. The IR-A thus lost Doppler data at EI + 497 while the IR-B kept continuous Doppler data. Both integrated receivers had their minor frame count fall to 32/100 at EI + 496, but at EI + 497, the IR-A frame count fell to zero while the IR-B frame count climbed back up to 79/100. At GMT 13:52:27 (EI + 498 sec), the IR-A frame synchronization and minor frame count were still both zero, but the IR-B frame synchronization was locked and a full 100/100 minor frames were counted, yielding a valid telemetry signal for the secondary (IR-B) receiver. Thus, this communication drop formally ended when the telemetry signal returned on the secondary integrated receiver, even

though the signal from the primary integrated receiver was completely dead. At GMT 13:52:28 (EI + 499 sec), the IR-A frame synchronization returned and it had a minor frame count of 25/100, an improving signal, although not yet good enough to produce valid telemetry.

Communications drop out #8 was only three seconds in duration and occurred over GMT 13:52:29 through 13:52:31 (EI + 500 through 502 sec). At EI + 500 seconds, both integrated receivers lost frame synchronization and both of their minor frame counts fell to 22/100. At EI + 501 seconds, both frame synchronizations and minor frame counts were zero. At EI + 502 seconds, the IR-B frame synchronization returned and its minor frame count went up to 25/100, while the IR-A was still zero on both scores. At EI + 503 seconds, both integrated receivers had frame synchronization, the IR-B minor frame count was back up to 100/100, but the IR-A minor frame count had only returned to 25/100. At EI + 504 seconds, both integrated receivers had frame synchronization and 100/100 minor frame counts. The period from GMT 13:52:25 through 13:52:31 (EI + 496 through 502 sec) is thus formally defined to be two communications drop outs, but clearly this period constitutes one overall event expressing the same effects on the communications links. The unusual feature of this particular pair of drop outs (#7 & #8) is that the two integrated receivers behaved quite differently, with the IR-A performance being significantly poorer than that of the IR-B. In so far as the IR-A receiver was concerned, this event would have been one continuous drop out from EI + 496 through 503 seconds. In nearly all of the other communications drop outs, the performance of both integrated receivers was nearly identical, with the only other slight exception being within drop out #2, where for one second the IR-A appeared to out perform the IR-B. This could be explainable by the two integrated receivers simply having closely matched, but slightly different, levels of signal lock range, whereby a small drop in the overall signal to noise ratio would loose lock and frame count in one receiver but not the other. The E_b/N_o estimators provide some evidence of this, with a fairly sharp threshold for which the frame synchronization is lost, typically between an E_b/N_o value of +10 to +11 dB. The minor frame counts begin to drop from 100/100 at E_b/N_o values in the range of +13 to +14 dB.

Communications drop out #9 occurred over GMT 13:52:49 through 13:52:55 (EI + 520 through 526 sec). At EI + 520 seconds, IR-A lost frame synchronization and its minor frame count fell to 42/100, while IR-B retained frame synchronization and recorded a minor frame count of 41/100. At EI + 521 seconds, both integrated receivers lost frame synchronization, IR-A counted zero minor frames and IR-B counted only 1/100. Over the next four second periods, both receivers have no frame synchronization and no minor frame counts. Then at EI + 526 seconds, both receivers regained frame synchronization and both had frame counts of 25/100. At GMT 13:52:56 (EI + 527 sec), the communications link was fully restored with both receivers in full frame synchronization and recording 100/100 minor frames. Although the secondary integrated receiver (IR-B) held on to the signal just slightly longer than the primary (IR-A), the two receivers were in large part tracking each other very closely over this drop out. At GMT 13:53:28 (EI + 559 sec), the ground track of the orbiter passed from over the Pacific Ocean into California.

Communications drop out #10 was only three seconds long and occurred over GMT 13:53:32 through 13:53:34 (EI + 563 through 565 sec). Both integrated receivers behaved exactly the same over this period, losing frame synchronization over EI + 563 to 564 seconds, and having their minor frame counts fall to 9/100 at EI + 563 sec, zero at EI + 564 sec, and the climb back up to 25/100 at EI + 565 seconds. Both the Doppler signal and the E_b/N_o estimator fell to zero over the last two seconds of the drop out, but returned immediately thereafter to nearly their original values without any noticeable jumps.

It is of note that following communications drop out #10, visual ground observations of debris shedding from the orbiter were made. Debris event #1 was sited at GMT 13:53:46 (EI + 577 sec); debris event #2 occurred at GMT 13:53:48 (EI + 579 sec); debris event #3 occurred at GMT 13:53:56 (EI + 587 sec); debris event #4 occurred at GMT 13:54:02 (EI + 593 sec); and debris event #5 occurred at GMT 13:54:09 (EI + 600 sec).

Communications drop out #11 was the longest at nine seconds and occurred over GMT 13:54:14 through 13:54:22 (EI + 605 through 613 sec). Both integrated receivers behaved in an identical fashion over this period. At EI + 605 seconds, the minor frame counts went to zero, although frame synchronization remained. At EI + 606 seconds, the frame synchronization was lost, and only one minor frame was counted on both receivers. Both frame synchronization and minor frame counts remained completely dead until EI + 613 seconds when the frame synchronization was restored and the minor frame count came back up to 25/100 on IR-A and 24/100 on IR-B. Communications were fully functional again at GMT 13:54:23 (EI + 614 sec). All eleven of these communications drop outs had thus far occurred while the upper left aft (ULA) S-band quad antenna was active. At GMT 13:54:26 (EI + 617) the antenna was switched from the ULA to the URA, coincident with the ground track of the vehicle passing from California into Nevada. While there might have been some question as to whether the ULA quad antenna might have been injured to cause these communications drop outs over the already fading re-entry link, the subsequent drops of precisely the same pattern in the URA antenna appear to rule out this possibility. There is no indication that either of the ULA or URA antennas were damaged. Damage to the antennas from any impacts during flight is also a remote possibility, as none of the S-band antennas are actually exposed to the outer surface. Each antenna is covered by heat tiles, and the RF signal propagates through the heat tiles with little attenuation. Foreign matter striking the orbiter over one of the antenna areas might damage the associated heat tiles, but would most likely not damage the antenna quad underneath.

At GMT 13:54:33 (EI + 624 sec), the first of the flashes around the envelope of the vehicle was observed from the ground. Following shortly thereafter, additional debris shedding was also observed. Debris #6 was sited at GMT 13:54:36 (EI + 627 sec); debris #7 occurred at GMT 13:55:07 (EI

+ 658 sec); debris #8 occurred at GMT 13:55:24 (EI + 675 sec); debris #9 occurred at GMT 13:55:27 (EI + 678 sec); and immediately following, debris #10 occurred at GMT 13:55:28 (EI + 679 sec).

Communications drop out #12 occurred 5 seconds after debris #10, and lasted for three seconds over GMT 13:55:33 through 13:55:35 (EI + 684 through 686 sec). This occurred just after the orbiter's ground track crossed into Utah at GMT 13:55:30 (EI + 681 sec). The second before the formal drop out at EI + 683 sec, the IR-A minor frame count fell to 97/100 and the IR-B minor frame count fell to 98/100. At EI + 684 sec, IR-A had lost frame synchronization and had a minor frame count of only 1/100, while IR-B still retained frame synchronization but had a zero minor frame count. At EI + 685 sec, both integrated receivers had lost frame synchronization, IR-A had a zero minor frame count, and IR-B had a minor frame count of only 1/100. At EI + 686 sec, both integrated receivers had reacquired frame synchronization and their minor frame counts had climbed back up to 25/100 and 24/100. At EI + 687 sec, full communications were restored on both integrated receivers. Although this drop out was now while the URA antenna quad was in use, it had precisely the same behavior as the drop outs from the ULA antenna quad.

In between communications drop outs #12 and #13, several more debris shedding events were observed from the ground. Debris #11 was observed at GMT 13:55:39 (EI + 690 sec); debris #12 occurred at GMT 13:55:47 (EI + 698 sec); debris #13 occurred at GMT 13:55:57 (EI + 708 sec), one second after the ground track crossed into Arizona; and debris #14 occurred two seconds later at GMT 13:55:59 (EI + 710 sec).

Communications drop out #13 occurred immediately following debris #14 and was four seconds long, occurring over GMT 13:56:00 through 13:56:03 (EI + 711 through 714 sec). Both integrated receivers behaved in an identical fashion, to within a minor frame count of one another. At EI + 711 sec, frame synchronization was lost and minor frame counts fell to 34/100 and 35/100. The frame synchronization and minor frame counts were zero for both integrated receivers for the middle two seconds of the drop out, and then at EI + 714 sec, frame synchronization was restored and the minor frame counts climbed back up to 26/100 and 24/100. At EI + 715 sec, both integrated receivers had fully restored communications links.

Shortly following communications drop out #13, debris shedding event #15 was seen from the ground at GMT 13:56:11 (EI + 722 sec).

Communications drop out #14 was three seconds in duration and occurred over GMT 13:56:55 through 13:56:57 (EI + 766 through 768 sec). Just prior to this drop out, the orbiter executed a roll reversal from the right to the left over GMT 13:56:30 through 13:56:55 (EI + 741 through 766 sec) which caused the URA quad antenna look angle to become slightly closer to the vertical stabilizer with an elevation of less than –60°. This is known to reduce the communication link margins and could be a contributing cause to communications drop out #14.

At this point, immediately following drop out #14, the forward link AGC signal strength level dropped out for an extended period of 30-40 seconds and then only returned sporadically for the remainder of the recorded re-entry flight. At this phase of the re-entry flight, the communication link margins have degraded to the point where further communication drop outs are common and considered normal in comparison to prior flight history. Between approximately GMT 13:57:30 to the formal loss of signal (LOS) at 13:59:32, another ten distinct communications drop outs were recorded as a period where one or the other of the integrated receivers recorded less than 95/100 valid minor frames. NASA categorized all ten of the communications drop outs within this time frame as "in family."

Over the period of GMT 13:59:31 through 13:59:38 (EI + 922 through 929 sec), just following the formal LOS, a brief and weak S-band communication signal was picked up through TDRS-047 to the East. The minor frame count on IR-A only climbed up to a maximum of 91/100 at GMT 13:59:36 (EI + 927 sec), and this was close, but still not sufficient, for any data validation by the MCC. This at first appeared unexpected, because the URA quad antenna was active during this time, and thus looking aft, not forward to where TDRS-047 would have been located. However, the radiation patterns of the upper aft S-band quad antennas do exhibit a side lobe towards the nose of the vehicle. The line of sight to TDRS-047 at this time would have been an elevation of +55° (pointing straight ahead toward the nose of the vehicle would be +90°), and an azimuth of 140° (pointing to the right of the vehicle would be +90° and pointing straight up out of the payload bay would be 0°). The calculated antenna gain for the URA quad would be only –6.00 dB or less, as this particular orientation does not catch much if any of the forward looking side lobe. The maximum gain of the side lobe is between –2.00 and 0.00 dB, and occurs at an elevation of +85° and an azimuth of 35° to 105°. Thus, the side lobe gain itself cannot account for pulling in the TDRS-047 signal. NASA calculations on the antenna gain to TDRS-047 show that it began at –14.8 dB at GMT 13:58:00 and steadily rose to approximately –7.5 dB at GMT 13:59:35. NASA also calculated that the required antenna gain to produce the measured frame synchronization values would be –6.9 dB. It is thus quite possible that the necessary link margin was present to have produced the observed minor frame counts via TDRS-047 over this period. These calculations did not include any attenuation from the plasma sheath, but this effect would seem likely since the pointing angle would have been forward. The plasma attenuation is known to behave in an unsteady fashion, so it still remains quite possible that a brief opening in the plasma sheath could have allowed the TDRS-047 link to be marginally connected. Regardless, the computed link margins and antenna gains are very close to fully explaining this event.

Shortly following the official LOS point, the orbiter S-band antenna was switched from the URA to the URF quad antenna. Within the period of GMT 14:00:05 through 14:00:10 (EI + 956 through 961 sec), the minor frame count climbed up to approximately 60/100, but this was insufficient to provide valid telemetry data to the MCC, so the LOS signal represents the last point of any valid data, although not actu-

ally the point of no signal whatsoever. Only one second of any data was received, by way of TDRS-171 to the West, and this was only sufficient to validate the OI talk-back, part of which indicated that the orbiter had in fact made this antenna switchover. Due to the diminishing information at this point in the re-entry flight, very little can be concluded from this brief communications reconnection. The antenna pattern from the URF quad would have given a lower gain of –6.00 dB or less for look angles to TDRS-171 to the West, and this could have occurred over a very wide range of possible orientations. Analysis of the communications margins shows that only –6.9 dB of antenna gain would be needed to account for the measured minor frame counts. In this instance like the previous one, the event can be fairly well explained by the computed link margins and antenna gains present at that point in the re-entry flight.

Although not discussed by NASA, there were a few other trends in the communication link performance measures which indicated a gradual degradation of the links over time into the re-entry flight. The formal communication drop outs are defined as where both of the integrated receiver minor frame counts fall to less than 95/100. However, there are several other occasions in which these minor frame counts fall, but not below the 95/100 threshold that would invalidate their data and define an additional communications drop out. Following drop out #4, over GMT 13:50:34 to 13:50:35 (EI + 385 to 386 sec), the IR-A first counts an anomalous 101/100 minor frames, and then immediately afterward 99/100 frames. While the running total number of minor frames remained correct, one minor frame apparently was counted amongst the wrong major frame. This type of major/minor frame lock count mishap occurred in several, but differently timed, groupings for the two integrated receivers. Over GMT 13:50:34 to 13:51:22 (EI + 385 to 433 sec), the IR-A recorded four of these frame mis-registrations at widely spaced times, while the IR-B saw none. After several minutes of none of this behavior, then over GMT 13:54:52 to 13:55:55 (EI + 613 to 706 sec), the IR-B recorded sixteen of these frame mis-registrations of the pattern 99-100-101, or 101-99. Finally, over GMT 13:56:21 to 13:56:47, both integrated receivers began acting up, with IR-A recording five and IR-B recording seven frame mis-registrations. Because these events only affected one of the 100 minor frames, they did not have any impact on the validity of the data used by the MCC. However, their increase in frequency toward the final moments of the re-entry flight further suggests a continuing degradation of the communication link margins.

At GMT 13:54:27 (EI + 618 sec), both integrated receivers recorded a minor frame count of only 97/100. This small drop is insufficient to be classified as a formal communication drop by the MCC. However, this event occurred immediately after the switch from the ULA to the URA quad antennas, and a drop in the minor frame count of this magnitude is completely consistent with the antenna switchover time. This small drop in the minor frame count over this one second of telemetry appears completely consistent with the expected behavior of a fully functioning communications system.

In summary, over the period from GMT 13:50:00 to 13:56:57 (EI + 351 to 768 sec), there were 14 distinct and formally defined communications drop outs which NASA considers to be out-of-family (OOF). Of these, #1 appears to clearly be associated with an antenna switchover at the end of the first roll maneuver, #5 was too minor to have had any consequence, #7 and #8 were really part of the same drop out event, and #14 simply marked the beginning of the time period for which communications drop outs were expected and considered "in-family" for the re-entry flight. The drop outs of a long duration and significant interruption were #3 (7 seconds long), #6 (7 seconds long), #9 (7 seconds long), and #11 (9 seconds long). While the one second sampling period for the minor frame counts does not provide any detail on a finer time scale than this, in each of these four major outages, both the frame synchronization and minor frame counts fell to zero within the span of approximately one second (and perhaps faster), indicating a rather abrupt loss of the signal. While the communications drop outs cannot be conclusively linked to the specific shedding of orbiter hardware, their timing does support the hypotheses drawn from other sensor and debris data. The hypothesized loss of the upper part of a leading edge T-seal at GMT 13:49:59 would have just preceded drop out #1. The hypothesized loss of the lower part of RCC panel #9 at GMT 13:52:21 would have occurred in between drop outs #6 and #7-8. The fairly well substantiated breach of the left wing leading edge spar at 5-15 seconds prior to the sensor wiring failure window of GMT 13:52:16 to 13:52:26 (EI + 487 to 497 sec) is simultaneous with the start of drop outs #7 and #8. The structural integrity of the wing spar was hypothesized to have been lost at GMT 13:52:54 (EI + 525 sec), and this is just at the end of the rather significant drop out #9. RCC panel #10 is hypothesized to have been lost at GMT 13:54:20 (EI + 611 sec), and this would have occurred toward the end of drop out #11. The longest duration drop out #11 also occurred only a few seconds after the first wave of debris shedding events (debris #1 through #5), and just prior the first observed flash around the orbiter's envelope. The shedding of RCC panel #10 could have thus accounted for the observed debris #6.

Orbiter Experimental Instrumentation (OEX) – Recorded Data

Four Key Sensors Behind RCC Panel #9

The four key sensors that were located behind RCC panel #9 were: V12G9921A, a strain gauge on the inside of the spar; V09T9895A, an RTD temperature sensor on the inside of the spar; V09T9910A, a high temperature RTD temperature sensor attached to the RCC clevis between RCC panels #9 and #10; and V07T9666A, a thermal protection system (TPS) thermocouple mounted on the outer surface of a heat tile, located two heat tiles aft of the closure panels and directly behind RCC panel #9. These sensors have turned out to be of greatest importance, because of their location on the aluminum honeycomb spar immediately behind RCC panel #9, and because their signals indicate clearly when the breach in the left wing leading edge broke through, breaching the spar and allowing hot gas to begin entering the interior of the wing box. These sensors also signaled unusual conditions far earlier than any of the OFI (telemetry) data, when the orbiter was out over the Pacific Ocean. Not only the response of the sensors themselves, but also the wiring

burn through patterns evident in the recorded signals help to identify both the time and location of the burn through of the left wing leading edge spar. This event is important, since it represents the time mark at which the destruction process of the left wing reached the interior frame of the wing box, and the fate of the orbiter was, at that point, irreversible.

The MSID # V12G9921A strain gauge has reference designation 65V12M331 and is installed as sensor part number ME449-0141-022 according to installation drawing M072-756106. The wiring is shown in installation drawing V070-786651 and appears in harness number (wire list) V070-776807. Wire lists were obtained from the Boeing Electronic Wire List of their P51 KSC on-line database. The strain gauge is taped down against the inside wall of the aluminum honeycomb left wing leading edge spar, immediately behind RCC panel #9, at coordinates (X1106.0, Y–231.5, ZMS), midway up on the spar. The type ME449-0141-0022 strain gauge contains two serpentine metal patterns, each with their sensitive axes at 45° to the edges of the substrate. The substrate is adhesively mounted to the spar surface and oriented so that the two sensitive axes point forward and down, and forward and up. The four contacts on the substrate are brought back to a connector strip, V070-780221, which ties the common center point of the half bridge together and reduce the wiring to three leads that get routed to a SGSC. From the connector strip, the sensor is spliced into harness V070-776807 which runs to interconnect panel 65P, connector P119. The three wires are named EXC, SIG, and RTN, and are wired as pins 69, 80, and 81, respectively, on connector 65V77W107P119. Integrated schematic V428-780122 shows the EXC+, SIG+, and SIG– leads as coming from pins 1, 2, and 3 (B, C, and A) of the strain gauge and going to pins 69, 80, and 81 of P119, with the shield connected to pin 114. J119 carries these same pin numbers to J503. P503 takes these three leads to P892 on the strain gauge signal conditioner (SGSC) 40V78A208A20 that is located on shelf 7, with the shield connected to the connector shell. The output SIG and RTN leads from P891 of the SGSC then go to pins 56 and 45 on J10 (channel 109) of PCM-2, 40V78A200, with the shield connected to the case. The interconnections and power feed to this strain gauge were handled entirely by its own dedicated SGSC that was located well within the protected part of the fuselage; thus, any failure of this sensor would not have had any effect on any other sensors in the vehicle.

The MSID # V09T9895A RTD temperature sensor has reference designation 65V09MT423 and is installed as sensor part number ME449-0160-0008 according to installation drawing V070-756114. The wiring is shown on installation drawing V070-786611 as harness number V070-776807. The sensor is adhesively fixed to the inside wall of the spar, halfway up, and behind RCC #9 where the strut line intersects it. The sensor is located at coordinates (X1102.2, Y–239.0, Z310.0). Drawing V070-786611 shows the wiring as running up and then forward along the spar, while drawing V070-756114 show the same wiring as running down and then forward along the spar. Close-out photographs show that the latter case is correct, with the wiring running down and then forward along the spar. Following splices, the three leads from the RTD sensor are routed into harness V070-776807 which leads forward along the spar to interconnect panel 65P. The EXC, COMMON, and SIG leads are connected to pins 111, 112, and 114, respectively, of connector 65V77W107P117. Integrated schematic V428-780082 shows the EXC, COM, and SIG leads coming from pins 1, 3, and 2 of the RTD temperature sensor and going to pins 111, 112, and 114 of P119/J119, with the cable shield is connected to pin 115. The leads are then routed to pins 117, 115, and 119 of J504/P504 with the shield connected to pin 120. On shelf 8, the leads then go pins 105, 115, and 1?6 on J9 (channel ?) of PCM-1, 40V78A199, with the shield connected to the case. Since this sensor was wired directly and independently to PCM1, any failure mode it may have taken would not have affected any other sensors in the vehicle.

The MSID # V09T9910A high temperature RTD temperature sensor has reference designation 65V09MT371 and is installed as sensor part number ME449-0160-0006 according to installation drawing V070-786142. The wiring is shown on installation drawing V070-786611 as harness number V070-776807. This sensor installation is unusual, as it is the only active OEX measurement in which the sensor is located in front of the leading edge spar. The purpose of the sensor was to measure the temperature of the RCC attachment clevis, and to implement this, the RTD is affixed to a metal tab that is installed underneath the head of the lower forward RCC #10 attachment bolt, much like a washer. This places the sensor close to the lower part of the T-seal between RCC panels #9 and #10. The sensor is located at coordinates (X1112.0, Y–239.0, Z289.0). The three leads from the RTD are spliced to a connector plug, whose mating receptacle is installed into the spar fitting. The wires from the receptacle pass through a penetration in the spar where they are in turn spliced into harness V070-776807. The EXC, SIG, and COMMON leads from the sensor are connected to pins 93, 102, and 103, respectively, of connector 65V77W105P113. Integrated schematic VS72-978099 differs from this description in some respects. It shows the EXC, SIG, and RTN leads as coming from pins 1, 2, and 3 of the RTD sensor and going to pins 5, 6, and 4 of 65P305/65J305 located on the spar attachment hardware. From here, the leads go to pins 87, 78, and 75 of 65P103/40J103 with the shield connected to pin 79. The cable then runs to pins 70, 69, and 81 of 40J502/40P502 which takes it into shelf 8. The leads then run to pins 17, 16, and 27 of J11 on PCM1, 40V78A199, with the shield connected to the case. No resolution was found to the discrepancies between the installation drawing and the integrated schematic. Regardless, this sensor was also wired directly to PCM-1, and any failure mode that it may have experienced would not have affected any other sensors in the vehicle.

The MSID # V07T9666A thermocouple temperature sensor has reference designation 65V07TC113 and is installed as sensor part number ME449-0204-0002 (Type R, Pt:Rh/Pt) according to installation drawing V070-192131. The wiring is shown on installation drawing V070-786611 as harness number V070-776803 (different from the other three sensors above). This particular thermocouple measures the left wing lower surface temperature at a point two rows of tile aft of the junction between RCC panels #9 and #10. The coordinates for the sensor are (X1121.7, Y–236.7, Z102.0), and it

is installed in heat tile number 192158-099, as detailed in the James A. Smith document, "OV-102 Modular Auxiliary Data System Measurement Locations," (revised Jan. 1992). This type of thermocouple installation penetrates the heat tile by means of a slot and after the thermocouple bead is threaded through, the tile is glazed over to seal the thermocouple bead into the outer surface layer. The thermocouple wires extend through the tile to a pair of recesses cut into the back of the tile. The SIP tile mounting material has a hole cut into it where the wing penetration occurs, and this is an inch or two laterally offset from where the thermocouple bead is located. The thermocouple wires are spliced to the thermocouple extension wires (type SX) underneath the tile before the tile is bonded to the orbiter skin. After passing through the wing penetration, the thermocouple extension wires are then routed to the thermocouple reference junction (TRJ) box that is mounted on to the surface of the leading edge spar. This TRJ is a 10-channel unit with part number MC476-0133-0050. The signal and power leads from the TRJ unit then run forward along the leading edge spar to interconnect panel 65P. The thermocouple bead is located at the coordinates (X1121.7, Y–236.7, Z102.0). The SIG and SIG RTN leads are connected to pins 19 and 20 of connector 65V77W103P101. Integrated schematic V428-780372 shows the + and – leads from the thermocouple going to TRJ box 65V78Z121-6 (channel 6 of 10). The EXC+ and EXC– leads from the TRJ box then go to pins 91 and 92 on P113/J113 with the shield connected to pin 113. Similarly, the SIG+ and SIG– leads from the TRJ box go to pins 19 and 20 on P101/J101 with the shield connected to pin 21. Two parallel, independent, 2-conductor shielded cables are used for the full length of this run. The excitation cable leads then go to pins 50 and 61 on J546/P546, and the signal cable leads go to pins 51 and 62 on J546/P546, with both shields connected to pin 67. Once on shelf 8, the excitation cable leads go to pins 89 and 101 of J5 (channel ?) of PCM-1, 40V78A199, and the signal cable leads go to pins 119 and 126 on J12 (channel ?). Both shields are connected to the case. Because the power to the TRJ box was obtained from PCM-1 PPS-17,18,89,90 which also supplied several temperature sensors on the lower fuselage surface, a failure in V07T9666A which took down the power supply voltage would also kill the output of these sensors as well.

The V12G9921A strain gauge was the only strain gauge to register any significant anomalous behavior prior to EI + 500 seconds, and its response started to climb away from those of past flights as early as GMT 13:48:39 (EI + 270 sec). From GMT 13:48:39 to 13:50:09 (EI + 270 to 360 sec), the recorded strain climbs anomalously, reaching at peak of +180 μin/in. At GMT 13:51:39 (EI + 450 sec), the strain reverses sign, and then peaks in the opposite direction at GMT 13:52:04 (EI + 475 sec) to a value of –140 μin/in. At GMT 13:52:04 (EI + 475 sec), the strain abruptly reduces by a small amount, and then remains constant and negative up until GMT 13:52:24 (EI + 495 sec), at which point the signal bounces up and down in a completely unphysical manner, continuing on through GMT 13:52:59 (EI + 530 sec), when it flatlines at a bias value slightly above zero. The non-physical behavior beginning at GMT 13:52:24 (EI + 495 sec) is presumed to result from the burn through of the left wing leading edge spar at a point somewhere along the length of the cable to this sensor. The out of family strains that were recorded prior to this are presumed to indicate some significant thermal bowing or buckling of the aluminum honeycomb spar. In particular, reversals in the sign of a strain are rather unusual and indicate either a complete reversal in the direction of loading, which is highly unlikely, or a buckling of the structural element. There was some initial speculation that the erratic behavior over the time span of EI + 495 to 530 seconds was actually a damped mechanical vibration, resulting from some mechanical impact or sudden loading change in the spar. However, the damping rate and the oscillation frequency that would be represented by this response are not consistent with the expected mechanical response from a honeycomb spar which would normally be quite rigid and oscillate at a much higher acoustic frequency. The erratic behavior is also characteristic of the burning or tearing of a cable, and this interpretation aligns better with the observed responses of the other sensors in the vicinity. The strain that is recorded prior to EI + 495 sec is considered valid data, but any response beyond this time is considered invalid. Since the strain gauge is temperature compensated by having both elements of the half bridge attached to the spar, the recorded signal should represent real strain, and not the temperature sensitivity of the gauge. High temperatures acting upon the spar could cause it to bow or deflect, and this deflection would certainly produce strains; however, the strain gauge should have been largely insensitive to the temperature of the spar itself. In several charts NASA labeled this sensor as having gone off scale. In point of fact this is not true. The range of strains that V12G9921A can measure extends from –1500 to +1000 μin/in. The recorded signal came close to these limits during its erratic behavior, but actually never reached them.

The V09T9910A temperature sensor on the RCC attachment clevis recorded a gradual, abnormal rise in temperature, beginning as early as GMT 13:48:59 (EI + 290 sec) and climbing steadily from a nominal 30°F to 65°F at GMT 13:52:22 (EI + 493 sec), after which it fell straight to OSL. This was one of the first sensors in the vehicle to fail during the re-entry flight, and it did so with extreme abruptness. Its data appears valid right up until the abrupt fall to OSL, and the data indicates only a gentle warming of the RCC attachment clevis at that point. This was also the only sensor that was located on the front side of the left wing leading edge spar. Although clearly abnormal, the temperature rise was slow and small in comparison to the temperatures that would be expected if it was exposed to the raw blast from a breach in the RCC panels. This is, however, consistent with the location of the sensor being buried deep beneath layers of inconel and cerachrome insulation that were installed around the spar fitting. The abruptness of the fall in the reading to OSL also suggests that the failure of the sensor could have just as easily been caused by a severe and sharp event, such a mechanical break in part of the leading edge structure which could have either clipped the wires, or otherwise mechanically destroyed the sensor. One possibility is that a piece of T-seal or RCC panel fell away at that time and took the sensor with it. The location of the sensor is actually several inches ahead of the spar surface, and the installation diagram shows its wiring as extending even further forward, offering an easy target to be torn off by any rapid loss of RCC panel or T-seal.

The V09T9895A temperature sensor on the inside of the left wing leading edge spar also recorded a rise in temperature that ended in an abrupt fall to OSL. The anomalous temperature rise began as early as GMT 13:51:14 (EI + 425 sec) and then abruptly fell at GMT 13:52:54 (EI + 525 sec). Unlike V09T9910A, the temperature rise was extreme, going from a nominal 20°F at GMT 13:51:14 (EI + 425 sec), to 40°F at GMT 13:52:14 (EI + 485 sec), and then rising much faster to 120°F at GMT 13:52:44 (EI + 515 sec), and then finally to an OSH at 450°F at GMT 13:52:51 (EI + 522 sec). Although the subsequent fall to OSL at GMT 13:52:55 (EI + 526 sec) was abrupt, the failure signature of this sensor clearly indicates a destruction due to direct thermal causes, which could include any of several processes by which one or more of the three leads of the device became open circuited. The rapid rise of the readings from this sensor, as compared to V09T9910A, are consistent with its location which is directly behind the part of the spar which had the least thermal insulation and obscuring RCC mounting hardware. Burn through of the spar would be expected to occur though this less protected zone first. The readings of this sensor appear to be valid up to the point where they went to an OSH. While all of the sensors with locations or wiring along the leading edge spar failed within the time span of GMT 13:52:16 to 13:52:26 (EI + 487 to 497 sec), this sensor failed at a comparatively later time, GMT 13:52:51 (EI + 522 sec).

The V07T9666A lower wing surface thermocouple showed a reading which had several important aspects. First, the readings starting becoming abnormally high and somewhat erratic as early as GMT 13:50:19 (EI + 370 sec), with several brief high temperature spikes climbing to 2500°F, significantly higher than the nominal 2000°F peak temperatures within a normal flight. Then, at GMT 13:52:25 (EI + 496 sec), the reading began an abrupt chatter between OSH and OSL, and then at GMT 13:52:35 (EI + 506 sec), essentially falling to OSL with some residual erratic noise up until GMT 13:52:52 (EI + 523 sec). This failure signature is indicative of a slower burning or tearing process. Because this thermocouple was located on the wing lower surface directly behind the junction between RCC panels #9 and #10, the high temperatures that it recorded were almost certainly a result of the initial gas jetting through the RCC panel damage area and the subsequent heating of the left wing around that zone. It is important to note that this sensor provided an external temperature measurement, while V09T9910A and V09T9895A both provided internal temperature measurements. Also of note is that this sensor fed immediately into a thermocouple reference junction (TRJ) box that was located on the spar as well. Both the power feed to the TRJ box and the signal conditioned output cables then ran along the spar in the forward direction with the other sensor wiring. Thus, both the sensor signal cable and the power supply feed cable were susceptible to damage from a burn through of the spar.

The timing of the failures of these four sensors and the path of their cable routing lends important information to determining both the timing and location of the breach of the leading edge spar. All of the cables from these sensors, as well as many others, were routed into wiring harnesses that traveled forward along the spar, up to the X1040 cross spar, where they passed through the service opening and then ran along in front of the left wheel well before reaching interconnect panel 65P, where they then entered the fuselage. All of the sensors with wiring in this set of harnesses had failure times within a rather narrow window of EI + 487 to 497 seconds, except for V09T9895A, which lasted up until EI + 522 sec. The diversity of sensor locations and types indicates that their common failure time was caused by their wiring being destroyed as part of the spar burn through, rather than the sensors themselves being destroyed by direct heating at their placement points. Close examination of the close out photographs and the engineering drawings for the wiring installation show that there were five main wiring harnesses running forward along the spar, labeled top-down as A-E in most charts. The upper four, A-D, are spaced within a few inches of each other, while the fifth, E, is routed about 6-8 inches below the rest. While the harness path taken by most of the sensors was fairly clear from the close out photographs, installation drawings, and wire lists, the routing of the wires for sensor V09T9895A was not immediately obvious. Closer inspection of the close out photographs and the geometry of the cable spot ties around the splice area showed that, indeed, this sensor was routed forward as part of the lowermost harness E. The physical separation between harness E and the other four is consistent with the later failure time of V09T9895A by 25-29 seconds, and thereby indicates that the breach of the leading edge spar began within the upper two-thirds of the spar, causing three of the sensors with their cables in this area to fail over EI + 493 to 497 seconds, and then progressed downward, causing the V09T9895A sensor to fail at EI + 522 seconds. This is also quite consistent with the fact that thick layers of inconel and cerachrome insulation protect the spar fitting hardware on the upper third and lower third of the spar. The center third of the spar, which is far less protected on the front, is where the initial breach most likely occurred and also where the upper four wiring harnesses were routed. The relevant close out photographs which show the sensor placement and wire harness routing are A950318L-I06G-jpg, A950318L-J08C-jpg, A950318L-K04C-jpg, A950318L-A03C-jpg within left wing cavity 1, and A950309J-55C.jpg and A950309J-54C.jpg within the left wing glove.

The failure times for these four key sensors behind RCC panel #9 each indicate the timing for which their response was no longer trustworthy by virtue of displaying an impossible physical behavior, rising or falling faster than known thermal time constants would allow. The characteristics of those behaviors were indicative of a wiring fault in their cables at that moment, most likely short circuits, since these occur before open circuits and at lower degrees of applied external stress. The rapid rise in the spar temperature sensor V09T9895A just prior to this sequence of sensor failures clearly indicates that high temperature was the source of the external stress. Comparisons between temperature sensors on the outside of the wing (V07T9666A) versus those on the inside (V09T9910A and V09T9895A) also clearly indicate that the abnormal heating began first on the outside and worked its way inward. As noted previously, while the timing of the electrical anomalies is known and recorded to within one second precision, the initiation of the physical events that caused them is known with far less precision because of the variability in the burn through speed of the sensor cables. Since the aluminum spar would have to burn through before

any of the cable harnesses on the inside would begin their burn through process, the breach of the spar must have occurred some time prior to the first of the sensor failures. The first sensor failure was V09T9910A at EI + 493 seconds, but the sensor and some of its wiring were located on the outside of the spar; therefore, this particular sensor failure cannot be used to conclusively indicate that the spar was breached. The next sensor failures were V12G9921A and V07T9666A at EI + 495 and 496 seconds, respectively. Both of these sensors had all of their wiring within the inside of the wing box and therefore provided a conclusive indication of when the hot gas had actually breached the spar. The shortest recorded burn through times were 2 seconds, and the longest 200 seconds, for any of the sensors in the system. The most conservative assertion is therefore that the breach of the leading edge spar occurred between 2 and 200 seconds prior to the first conclusive sensor wiring burn through failure on the inside of the spar at EI + 495 seconds.

As will be discussed in the next section, there were eleven pressure sensors on the left wing which also had their cable harnesses routed along the leading edge spar. The range of times over which these failed with a cable burn through signature was EI + 487 to 497 seconds and overlaps very closely with the failure times of V09T9910A, V12G9921A, and V07T9666A. The earliest failure among these was V07P8038A out on the wing tip, which NASA reported failing at EI + 487 seconds, but it also had some of its wiring on the outside of the spar and thus cannot be considered a conclusive indicator for a breach of the spar. The next pressure sensor failing with a burn through signature was V07P8023A, which had a clearly defined failure point at EI + 489 seconds. All of its wiring was routed within the inside of the wing box and this provides a conclusive indication of a spar breach that occurred a few seconds prior to those of the V12G9921A and V07T9666A. Thus, the pressure sensor data allows the breach of the leading edge spar to be placed between 2 and 200 seconds prior to the first conclusive sensor wiring burn through failure on the inside of the spar at EI + 489 seconds.

The number of sensors is, however, large enough to make valid use of statistics. The three large cable harnesses that pass above the outboard wall of the left wheel well happen to create a nicely controlled experiment in their own right. These provide a statistically significant test of the average burn through speed of typical sensor cable harnesses under virtually the same conditions as those on the left wing leading edge spar behind RCC panel #9. Bundle #3 contained the cables for 138 sensors of which 134 failed in the time span of EI + 487 to 600 seconds. Bundle #1 contained the cables for 11 out of 11 sensors that failed in the time span of EI + 493 to 560 seconds. And bundle #4 contained the cables for 25 out of 25 sensors which failed during the time span of EI + 516 to 738 seconds. There were actually far more cables in bundles #1 and #4, but they were associated with sensors that were operating in the snap-shot mode, and whose precise failure times could thus not be determined. Overall, it is remarkable that bundles of around 100 or more cables could be burnt through in their entirety within only about two minutes. These larger bundles of 100 or more cables had approximately 8-10 radial layers to them. If one supposes that one layer must burn through before the next begins, the overall burn through process becomes sequential, and the overall burn through time of approximately 100 seconds on the average might actually represent the sequential burn throughs of 10 layers of cables, each roughly 10 seconds in length on the average. Taking this argument as the basis for a more aggressive assertion, the left wing leading edge spar breach could have occurred as late as 10±5 seconds (5 to 15 sec) before the first sensor wiring failure at EI + 489 seconds.

Even within these vagaries, the precise definition of what constitutes a specific breach of the spar remains. The breach could have been defined by a pin hole, a series of pin holes, or a hole greater than some threshold diameter to start admitting gas at a significant flow rate, or several such sufficiently large holes. NASA placed the breach of the leading edge spar as falling within the range of EI + 425 to 487 seconds, with a higher probability toward the EI + 487 second mark, thus taking the wiring failure of pressure sensor V07P8038A at EI + 487 seconds as the indicator and allowing for a burn through time period of 0-62 seconds. Nonetheless, NASA's conclusion and the above analysis are ultimately in fairly close agreement, differing only by a few seconds.

Left Wing Aerodynamic Pressures

From the MADS/OEX recorded data, NASA plotted 97 different aerodynamic pressures for the left wing and 84 for the right. The pressure readings were all MSIDs beginning with V07P, and 91 came from PCM-1, and 90 from PCM-2. Of these, a certain few were of greater importance than the rest because their wiring, like the that of the four key sensors discussed previously, also ran along the inside wall of the left wing leading edge spar. Lying directly behind RCC panel #8 are V07P8010A and V07P8058A on the upper and lower surfaces, respectively, of the left wing. A large number of pressure sensors are also clustered along the length of the Y = –256 plane on both the upper and lower surfaces of the left wing. Proceeding aft from the leading edge of the wing, V07P8022A, V07P8023A, and V07P8024A were on the upper surface, and V07P8071A, V07P8072A, and V07P8073A were on the lower surface. The wiring for all six of these was routed forward along the Y = –256 strut line of the wing and then along the leading edge spar as part of the larger cable harnesses. Out near the tip of the left wing at Y = –448 are V07P8037A, V07P8038A, and V07P8044A, each measuring pressures on the upper surface of the wing. The wiring for each of these three pressure sensors was routed along the full length of the left wing leading edge spar, although the wiring was uncharacteristically routed on the outside of the leading edge spar until it went through a penetration at X = 1164 and then continued along the inside of the leading edge spar along with the other sensor cable harnesses behind RCC panels # 7-10.

Sensor MSIDs V07P8010A and V07P8058A have reference designators 65V07MT310 and 65V07MT358, respectively, and are both sensor part number ME449-0177-2108, manufactured by Statham, with a 0 to +15 psia range. On the upper wing surface along Y = –256, sensor MSIDs V07P8022A, V07P8023A, and V07P8024A have reference designators 65V07MT322, 65V07MT323, and

65V07MT324, respectively, and all three are Kulite miniature pressure sensors with part number ME449-0219-0002 and a 0-16 psia pressure range. Matching to these same Y = –256 locations along the lower wing surface, sensor MSIDs V07P8071A, V07P8072A, and V07P8073A have reference designators 65V07MT371, 65V07MT372, and 65V07MT373, respectively, and are also miniature Kulite pressure sensors with a 0-16 psia range, part number ME449-0219-0002. Finally, out on the left wing tip upper surface, sensor MSIDs V07P8037A, V07P8038A, and V07P8044A have reference designators of 65V07MT337, 65V07MT338, and 65V07MT344, respectively, and these three are also miniature Kulite pressure sensors with a 0-16 psia range, part number ME449-0219-0002. Both of the Statham pressure sensors, V07P8010A and V07P8058A, were installed according to drawing M072-756106, and all nine of the Kulite miniature pressure sensors were installed according to drawing V070-192146. The Statham pressure sensors, because of their larger transducer housing, were typically mounted against a spar and a stainless steel tubing was routed from the transducer to the pressure sensing port fitting on the wing skin. The stainless steel tubing runs were usually routed along the wing strut frames (tube trusses). Sensor wiring was typically run along the spars. The Kulite pressure sensors, because of their smaller bodies, were mounted directly on the wing skin.

Sensor V07P8010A on the upper wing surface was reading essentially zero from EI up to GMT 13:52:26 (EI + 497 sec) at which point it abruptly shot to OSH at 15 psia and then chattered between OSH and OSL until GMT 13:52:34 (EI + 505 sec), after which is remained at a zero reading with occasionally small transient spikes. The failure at EI + 497 sec is both abrupt and clearly defined. The essentially zero pressure reading from the upper wing surface is normal for this phase of the re-entry flight, because most of the pressure is building up on the lower surface of the wing which is facing into the direction of motion due to the pitch of the vehicle. The companion sensor V07P8058A on the lower wing surface was reading a normal rise in pressure starting from a systematic offset value of about 0.2 psia at EI and gradually climbing to about 0.4 psia at GMT 13:52:29 (EI + 500 sec), completely normal with comparison to previous flights. At around GMT 13:52:34 to 13:52:39 (EI + 505 to 510 sec), the reading begins to gradually fall, and hits an absolute zero at GMT 13:53:04 (EI + 535 sec), without any remainder of the original offset. Over EI + 547 to 575 sec, the reading chatters between OSL and OSH, and then remains at zero thereafter. NASA claimed that this sensor failed around EI + 495 sec, but this is only vaguely supported by the plotted data. Because the sensor reading transitioned downward to an absolute level that no longer had the systematic offset, this downward trend, although smooth, is indicative of a soft short wiring failure mode for this sensor. This failure mode is somewhat more subtle than those of other sensors, but still uncharacteristic of the normal operation of an absolute pressure sensor. The disappearance of the systematic offset beyond EI + 535 sec indicates either an open or short circuit in the pressure sensor bridge power, or an open or short circuit in the sensing leads from the two arms of the bridge. A conclusive failure time of GMT 13:52:34 (EI + 505 sec) can be validly claimed from the data, behaving similarly to the soft shorts produced in the Kapton insulated wiring of other sensors. NASA still prefers to claim the failure time as GMT 13:52:24 (EI + 495 sec), 10 seconds earlier. The sensor behavior at EI + 495 sec appears suggestive of a possible failure, but not conclusive. By the slightly later time of EI + 505 sec, the failure signature is clearly evident and conclusive.

NASA claimed that sensors V07P8022A, V07P8023A, and V07P8024A on the upper surface of the left wing along Y = –256 failed at times of EI + 492, 489, and 490 seconds, respectively. The plot for V07P8022A was not among the data provided to the CAIB by NASA, so there was no means by which to verify the behavior of that sensor. Both V07P8023A and V07P8024A indeed showed clearly defined failures at EI + 489 and 490 seconds with the output showing an abrupt onset of erratic signal noise, in many cases approaching OSL and OSH. By EI + 530 sec, both of these outputs had settled down to a zero reading. Both of these sensors also showed a significant offset error over the full re-entry time span for previous flights of about –0.2 psia for V07P8023A and –0.7 psia for V07P8024A. Neither of these offsets appear to have altered the functioning of the sensor, however.

NASA also stated that the matching sensors V07P8071A, V07P8072A, and V07P8073A on the lower surface of the left wing had failure times of EI + 491, 490, and 492 seconds, respectively, and indeed this is shown clearly in the plotted data with each of these showing a very normal slowly rising pressure that had smoothly climbed by about 0.1-0.2 psia over the time period from EI to EI + 490 sec. At the various times of EI + 491, 490, and 492 sec, each sensor reading abruptly shot up with an erratic spiking, occasionally hitting the OSH value of 16 psia, and then quieting down to a zero reading by EI + 530 seconds. Sensor V07P8071A also showed a systematic offset of –0.5 psia over the full time span and for previous flights. Similarly, V07P8072A may have had a systematic offset of +0.4 psia, its value at EI for all previous flights.

For the three sensors in the left wing tip, V07P8037A, V07P8038A, and V07P8044A, NASA claimed failure times of EI + 492, 487, and 495 seconds. This is shown clearly in the plotted data, although the failure time for V07P8038A appears to be closer to EI + 492 than EI + 487 seconds. These sensors show exactly the same failure modes as the preceding six, with an abrupt onset of erratic spiking that occurs at their failure time and which ceases around EI + 530 seconds. Beyond this point, the reading remains at zero with minimal noise transients.

The nine aerodynamic pressure sensors V07P8022A, V07P8023A, V07P8024A, V07P8071A, V07P8072A, V07P8073A, V07P8037A, V07P8038A, and V07P8044A, have nearly simultaneous failures within the range of EI + 489 to 497 seconds and a common wiring route along the middle of the leading edge spar, thereby corroborating the time of the spar burn through. Close-out photographs and engineering blackline drawings confirm the wiring routes from the sensors. There was considerable confusion at first in identifying these wiring runs, but the key to properly identifying their placement is the fact that the larger Statham pressure sensors each have a sizeable stainless steel

tubing that routes the transducer to the sampling port on the wing, while the miniature Kulite pressure sensors were small enough to be mounted on the wing surface directly over their sensing port. The routing of the wiring to sensors V07P8037A, V07P8038A, and V07P8044A out on the left wing tip along the outside of the leading edge spar is very unexpected, but this is confirmed by the wiring penetrations shown in close-out photograph A950318L-G11C.jpg. This wire routing has also been confirmed in the engineering blackline drawings, and the recovered debris from this area of the left wing indeed had wire fragments on the front surface of the spar.

Close-out photograph A950318L-K04C.jpg shows sensors V07P8010A and V07P8058A, which were both the larger Statham type, the stainless steel tubing to their ports, and their wiring as it enters the cable harnesses leading forward along the leading edge spar. The wiring from V07P8010A runs vertically down from the top of the wing and meets the uppermost harness A, and then runs forward along the leading edge spar as part of harness A. Similarly, the wiring from V07P8058A runs vertically upward from the bottom of the wing and also meets the uppermost harness A, and then continues forward along with it. From the wiring routing path, it appears that sensor V07P8010A on the upper wing surface had its wiring damaged at EI + 497 sec, immediately following the first of the key sensors located behind RCC panel #9. Sensor V07P8058A on the lower wing surface was somewhat more protected and failed at a slightly later time. The earliest conclusive failure timing for this sensor is at EI + 505 to 510 seconds, although NASA cites a slightly earlier time of EI + 495 seconds. Because these two sensors were located forward of the four key sensors behind RCC panel #9, the burn through of the leading edge spar must have occurred at least this far forward to support the observed failure timing.

Within the broader picture, all of the aerodynamic pressure sensors were only beginning to record any significant rise in the absolute pressure during this phase of the re-entry flight. Pressure sensors on the upper wing surface experience essentially zero pressure until much further into the re-entry because they are not exposed to the oncoming dynamic pressure of the incident air stream. Only the pressure sensors on the lower surface of the wing experience any observable rise in their readings, typically less than 1.0 psia over this phase of the flight. Boeing engineers in several of their briefings also pointed out that the aerodynamic pressure instrumentation was designed for much lower altitude phases of the vehicle's flight. Because most of these pressure sensors were only beginning to come off of zero, their readings are already near to the OSL points, and thus somewhat more difficult to interpret than a mid-scale reading.

Fuselage Lower Surface Temperatures

Twelve temperature measurements were recorded by the MADS/OEX system along the lower surface of the fuselage. All but one of these were type R thermocouples that were mounted on the outside of the heat tiles, part number ME449-0204-0002. These were calibrated for ranges of either 500-2700°F or 0-2400°F, depending upon the specific location. The remaining sensor (V09T9731A) was a structural skin measurement, taken at the bond line between the heat tiles and the aluminum skin, and used an RTD, part number ME449-0160-0001, that was calibrated for the range of −200 to +450°F. Five of these were placed successively along the centerline of the vehicle (Y = 0.0), one was placed slightly off center 50 inches to the left (Y = −50.0), and the remaining six were placed along the left fuselage edge (Y = −100.0 to −117.0).

Sensor V07T9468A was a surface thermocouple mounted at (X618.9, Y0.0, ZBOT), just below the front of the payload bay area on the vehicle's centerline. This measurement behaved very much like that of prior flights until it momentarily spiked up to nearly OSH of 2650°F at GMT 13:58:31 (EI + 862 sec) and then returned to read within normal limits until it spiked up again at GMT 14:00:09 (EI + 960 sec), just a few seconds before the end of the OEX recorded data. The overall trend of this measurement was for a smoothly increasing temperature from an OSL value of 500°F at EI to approximately 1700°F at EI + 360 seconds, and finally leveling off to a value of approximately 1800°F for the remaining recorded re-entry flight.

Sensor V07T9478A was a surface thermocouple mounted at (X1006.0, Y0.0, Z267.3) below the middle of the payload bay area on the vehicle's centerline. This measurement behaved within normal family limits, also smoothly increasing from an OSL of 500°F at EI up to 1700°F at EI + 360 seconds. It then leveled off to a value of 1800°F until GMT 13:59:44 (EI + 935 sec) after which it started behaving erratically and then started chattering between OSL and OSH at GMT 13:59:59 (EI + 950 sec) and continued this until the last recorded OEX data point.

Sensor V07T9489A was a surface thermocouple mounted at (X1391.5, Y0.0, Z264.0) beneath the front of the main engine compartment and also on the vehicle's centerline. This measurement read an OSL value of 500°F from EI up to GMT 13:46:54 (EI + 165 sec), smoothly climbed to 1230°F at EI + 360 seconds, and then leveled off at 1300°F by EI + 480 seconds, and this was all well within the limits of past flight behavior. At GMT 13:52:22 (EI + 493.33 sec), the recorded data jumped abruptly up by 32 bits, or 250°F, and retained this offset for the remainder of the recorded data. At approximately GMT 13:59:09 (EI + 900 sec), the gently decreasing temperature reversed direction and began climbing upwards and at GMT 13:59:54 (EI + 935 sec) shot up to OSH and then chattered between OSL and OSH until the end of the recorded data.

Sensor V07T9492A was a surface thermocouple mounted at (X1511.1, Y1.3, Z275.6) beneath the rear of the main engine compartment and nearly on the vehicle's centerline. This measurement read an OSL value of 500°F from EI up to GMT 13:47:34 (EI + 205 sec), smoothly climbed to 1150°F at EI + 360 seconds, and then leveled off at 1200°F by EI + 480 seconds, and this was similarly well within the limits of the behavior of prior flights. At GMT 13:52:22 (EI + 493.33 sec), the recorded data from this sensor also abruptly jumped up by nearly exactly the same amount as the previous one, 32 bits, or 250°F, and similarly retained this offset for the

remainder of the recorded data. At GMT 13:59:49 (EI + 940 sec), the temperature shot upwards and continued to behave erratically with drastic chattering up and down (although not hitting OSL or OSH) until the end of the recorded data.

Sensor V07T9502A was a surface thermocouple mounted at (X1561.0, Y0.0, ZBOT) and centered on the lower surface of the body flap. The recorded data smoothly increased from 50°F at EI to 1150°F at EI + 360 seconds, and then leveled off at a maximum of 1250°F. At GMT 13:57:09 (EI + 780 sec), the temperature began to fall slightly, dropping to 1170°F at GMT 13:59:44 (EI + 935 sec), after which it rose sharply and then chattered between OSL and OSH values from EI + 960 seconds through to the end of the recorded data. The dropping temperature reading over EI + 780-935 seconds is out of family behavior, and this cooling trend could potentially be of a similar origin as that which affected the left OMS pod around this same time period.

Sensor V07T9470A was a surface thermocouple that was mounted at (X620.5, Y–50.0, Z278.8) underneath the front of the payload bay and offset 50 inches to the left side of the centerline. This measurement started at an OSL value of 500°F at EI and smoothly rose to 1750°F by EI + 360 seconds. The temperature then more slowly reached a maximum of 1920°F at EI + 780 seconds, mirroring the contour of the aerothermal peak heating curve for the re-entry flight, as did most of these surface temperature sensors on the lower surface of the orbiter. The heating was greater toward the nose as compared to the tail of the vehicle, as would be intuitively expected for its 40° pitch and descent vector, and each of the lower surface temperature sensors placed successively along the centerline showed progressively increasing temperature profiles going from tail to nose. At GMT 13:59:44 (EI + 935 sec), the reading began to rise rapidly and it continued to behave erratically until the end of the recorded data.

Sensor V07T9480A was a surface thermocouple mounted at (X1004.1, Y–99.8, ZBOT) under the middle of the payload bay and offset to the left to roughly match the side of the fuselage. This measurement began with an OSL reading of 500°F at EI, began to rise at GMT 13:46:29 (EI + 140 sec), and reached 1500°F at EI + 360 seconds. At GMT 13:52:22 (EI + 493.33 sec), the recorded data from this sensor also abruptly jumped up by 32 bits, or 250°F, and similarly to V07T9489A and V07T9492A retained this offset for the remainder of the recorded data. At GMT 13:59:09 (EI + 900 sec) the temperature reversed it gentle decrease and began to rise again, then at GMT 13:59:44 (EI + 935 sec), it rose dramatically and began chattering between the OSL and OSH limiting values until the end of the recorded data. As a note, the installation drawings also show a sensor V09T9493A to be installed at nearly the same location as V07T9480A; however, the signal from this sensor was not included in the OEX recorder data, and it is likely that this sensor was broken or simply no longer used.

Three more surface thermocouples were mounted on the fuselage lower surface along the Y–110 left side edge. Sensors V07T9784A, V07T9787A, and V07T9788A were placed toward the rear of the vehicle, midway back underneath the main engine compartment, underneath the aft end of the main engine compartment, and on the lower outboard forward edge of the body flap, respectively. All three of these sensors differed from the rest by having their signals channeled through the MADS PCM-2 unit. The available documentation did not provide any precise coordinates for any of these three. All three of these sensors behaved in essentially the same manner, remaining well within the normal family limits of behavior up until GMT 13:59:44 (EI + 935 sec), when their readings began to rise sharply, fluctuate erratically up and down, and then chatter between OSH and OSL limiting values up until the end of the recorded data. All three started at a value of approximately 75°F at EI, smoothly rose to a knee value at EI + 360 seconds of 1300°F for V07T9784A and V07T9787A and 1150°F for V07T9788A, and then leveled out to a maximum heating temperature of 1450°F for V07T9784A and V07T9787A and 1250°F for V07T9788A. The measurement on the body flap, V07T9788A, showed somewhat more structured variations of temperature over certain periods; however, this was also observed in prior flights and most likely due to the more complex aerothermal dynamics existing around the edges of this unusual control structure.

Sensor V09T9731A as also different from the rest and was a structural RTD temperature sensor that was placed on the bond line between the heat tiles and the aluminum skin of the orbiter at the coordinates (X1443.0, Y–117.0, ZBOT), very close to V07T9784A on the lower fuselage. This reading began at a value of 30°F at EI and very smoothly and gently climbed to 80°F at GMT 14:00:04 (EI + 955 sec), after which it rose sharply to a final value of 180°F as the last recorded value in the OEX data. The behavior over the entire time from EI to EI + 955 seconds was completely normal.
Finally, sensor V07T9508A was a surface thermocouple mounted at (X1558.5, Y–105.0, Z281.3) midway back on the lower left edge of the body flap. This reading began at an OSL value of 500°F at EI and smoothly climbed to a knee value of 1300°F at EI + 360 seconds, and finally leveled out to a maximum temperature of 1400°F. At GMT 13:57:09 (EI + 780 sec), the temperature began an uncharacteristic decrease, falling to 1350°F at GMT 13:59:44 (EI + 935 sec). Beyond this point, the temperature rose abruptly to 2100-2300°F and then chattered between OSL and OSH limiting values until the end of the recorded data. Similar to V07T9502A, this uncharacteristic cooling trend over EI + 780 to 935 seconds could be related to the same origins as the cooling seen on the left OMS pod around the same time.

The fuselage lower surface temperatures thus behaved very much according to their prior flight patterns from EI up until a few seconds before the last recorded MADS/OEX data. In addition, three of these sensors (V07T9480A, V07T9489A, and V07T9492A) each showed an abrupt upward step of very nearly the same magnitude (+32 bits) at precisely the same time of GMT 13:52:22 (EI + 493.33 sec). Boeing and NASA identified that these three sensors, in addition to being of the same type R, using the same type of thermocouple reference junction (TRJ) of part number MC476-0133-0070, being sampled at ten times per second, and using the same second order calibration curve, that they each shared the same +5.0 V precision power supply (PPS) output from the

MADS PCM-1 unit, namely PPS output 89. Besides these three thermocouple sensors, it was also found that sensor V07T9522A on the left side surface of the fuselage jumped down by –5 bits at precisely the same time of EI + 493.33 seconds. Further, sensor V07T9636A, a thermocouple surface temperature sensor on the upper left wing had its reading jump down by –7 bits at the same time of EI + 493.33 seconds. Both sensors V07T9522A and V07T9636A were type K thermocouples, both used a TRJ of type ME476-0133-0001, both were sampled once per second, both used the same first order calibration curve, and notably, both TRJ units were supplied +5.0 V DC power from the same PPS output 89 of PCM-1 unit as the other three measurements. The commonality of these five measurements is electrically traceable to a single terminal junction bar which takes the output from PPS-89 and distributes it to each of the five TRJ units for these thermocouples.

For a Wheatstone bridge-type signal conditioner, as is used for all of the temperature, pressure, and strain sensors on the orbiter, most of the wiring failure modes (open or short circuits between various combinations of the wires) result in a measurement output that is either off scale low (OSL), off scale high (OSH), or zero. There are a few, less probable combinations of faults which can introduce an abrupt and persistent offset in the reading. These would be associated with the power supply leads to the Wheatstone bridge, which, in the case of the thermocouples, is located within the TRJ unit. NASA performed testing and analysis of the ME476-0133-0001 thermocouple reference junction units and found that there were three wiring failures which could produce this offset in the output: an open circuit in the +EXC lead, an open circuit in the –EXC lead, or a short circuit between the +EXC and –EXC leads, each of which has the effect of removing power from the Wheatstone bridge and allowing the bridge to float to whatever common-mode potential exists between the +SIG and –SIG output leads.

While NASA and Boeing identified the electrical commonality of these five thermocouple measurements, they did not identify the cause. They noted that in addition to these five thermocouples, that thermocouple sensor V07T9666A was also powered by this same PPS output from PCM-1, although it did not use the common terminal junction bar. They incorrectly stated that V07T9666A responded nominally all the way through to the terminal period of the re-entry flight, and that the cause for the jump in the other five thermocouple readings was therefore an vaguely defined "terminal block anomaly." In point of fact, thermocouple sensor V07T9666A was one of the four key sensors located behind RCC panel #9, and it failed to OSL at GMT 13:52:24 (EI + 495 sec), only two seconds behind the jump in the other 5 thermocouple sensors. While the burn-through of V07T9666A happens two seconds later than the jumps in the other five thermocouples, this does not discount their connection, since a given burn-through will create several faults within a sensor cable, and it is perfectly conceivable that the power supply fault which caused the jumps occurred a few seconds prior to the signal wire fault which caused V07T9666A to transition to an OSL value. A much better explanation for the abrupt jumps in these five thermocouple readings is offered simply by noting that a burn-through induced short between the power supply wires for the TRJ unit that supplied V07T9666A would pull the overall PCM-1 PPS outputs 17, 18, 89, and 90 to zero, and this effect would propagate to the other five thermocouple reference junction units as well. The jumps seen the these five thermocouples are in all likelihood the propagating electrical effects of the burn through of the left wing leading edge spar behind RCC panel #9.

Fuselage Left Side Surface Temperatures

Seven thermocouple temperature sensors on the left side surface of the fuselage recorded measurements in the MADS/OEX data. These were all instrumented through the MADS PCM-1 unit, and the thermocouples were listed in the Boeing integrated part and component locator (IPCL) as part numbers ME449-0204-0001, -0002, and -0003. The -0003 is probably a typographical error in the locator, since thermocouples only come in the -0001 type K and -0002 type R forms. In general, the thermocouples closer to the nose recorded largely normal behavior up until the last few seconds of the OEX data, while those toward the tail recorded anomalous temperature variations which indicated some unusual aerodynamic flow and heating trends that was most likely the result of damage to the left wing leading edge farther forward.

Starting from the nose of the vehicle and working towards the tail, sensor V07T9880A was the most forward located of all of the thermocouple surface temperature sensors, and it was mounted at (X322.5, Y–56.6, Z340.9), about six feet back from the tip of the nose on the left hand side of the vehicle. The reading from this sensor started at an OSL value of 0°F at EI, smoothly rose to a knee temperature of 960°F at EI + 360 seconds, and then steadily climbed at a much slower rate to 1100°F at GMT 13:59:44 (EI + 935 sec). At this point, it abruptly shot up towards an OSH limit of 1750°F and varied about this level until the end of the recorded data. Prior to this point, the behavior was well within the usual patterns of past flights.

Sensor V07T9522A is a surface thermocouple that is mounted at (X650.0, Y–105.0, Z354.7), about eight feet behind the crew door on the left side of the vehicle. The reading from this sensor began at an OSL value of 0°F at EI, climbed smoothly to 640°F over GMT 13:46:09 to 13:50:09 (EI + 120 to 360 sec), and then more slowly climbed to 940°F at GMT 13:59:44 (EI + 935 sec). At this point, the reading went straight up to an OSH value of 1300°F and remained there until the end of the recorded data. As noted previously, this sensor also exhibited an abrupt jump downward by –5 bits at EI + 493 seconds, and the origin of this was traced to a common power supply feed to its TRJ signal conditioner that was shared with other thermocouples on the lower surface of the fuselage. The cause of these jumps is most likely the wiring burn through of thermocouple sensor V07T9666A which occurred precisely at this time and which also shared this common power supply feed from PCM-1.

Sensor V07T9253A is a surface thermocouple mounted at (X1006.0, Y–105.0, Z355.5), on the left side of the midbody, just below the payload bay door and above the left wing. The reading from this sensor started at an OSL value

of 0°F at EI, and rose smoothly from 0°F to 200°F over GMT 13:47:24 to 13:53:24 (EI + 195 to 555 sec). At this point the behavior deviated sharply from that of prior flights and the temperature soared up to 400°F at GMT 13:54:39 (EI + 630 sec), steadily decreased back down to 240°F at GMT 13:57:49 (EI + 820 sec), and then rose steadily up to 450°F at GMT 13:59:44 (EI + 935 sec). Following this, the reading went up to an OSH limit of 880°F at GMT 13:59:51 (EI + 942 sec) and chattered between this and OSL until the end of the recorded data. Although the heating and cooling rates are large, this thermocouple appears to be measuring accurate data over the time period from EI through EI + 942 seconds where it reached its OSH limit.

Sensor V07T9903A is a surface thermocouple mounted at (X1006.0, Y–105.0, Z399.0), directly above V07T9253A and just below the left payload bay door. The reading from this sensor began at an OSL value of 0°F at EI, rose from 0°F to 480°F over GMT 13:46:09 to 13:53:09 (EI + 120 to 540 sec), and then continued to rise in a somewhat more erratic manner to 520°F at GMT 13:59:27 (EI + 918 sec). From this point, the temperature rapidly climbed to 630°F at GMT 13:59:41 (EI + 932 sec), after which it shot up to an OSH limit of 1300°F and remained there until the end of the recorded data, aside from one subsequent transition to OSL and back.

Sensor V07T9913A is a surface thermocouple mounted at (X1003.8, Y–105.0, Z441.4), directly above V07T9253A and V07T9903A on the payload bay door. The reading from this sensor started at an OSL value of 0°F at EI, rose from 0°F to 730°F over GMT 13:46:39 to 13:53:09 (EI + 150 to 540 sec), and then climbed more slowly and more erratically up to 840°F at GMT 13:59:41 (EI + 932 sec). At this point the reading shot straight up to an OSH value of 1300°F and then subsequently chattered between the OSL and OSH limits until the end of the recorded data. These reading appear accurate up until the failure point at EI + 932 seconds, and show a more erratic than normal heating trend over EI + 540 to 932 seconds, consistent with the timing of the anomalous readings from V07T9253A located just below it.

Sensor V07T9925A is a surface thermocouple mounted at (X1138.4, Y–105.0, Z441.4), also located on the left payload bay door at the same elevation as V07T9913A, but approximately eight feet further back. The reading from this sensor began at an OSL value of 0°F, rose from 0°F to 260°F over GMT 13:47:09 to 13:50:09 (EI + 180 to 360 sec), at which point the heating rate abruptly decreased and the temperature fell below the trend shown by prior flights. This sensor showed an abrupt jump downward by approximately 20°F at EI + 505 seconds, after which the heating rate began to increase again, reaching the normal value of 500°F at GMT 13:53:39 (EI + 570 sec), and continuing up to a peak of 830°F at GMT 13:54:34 (EI + 625 sec). The temperature then fell back to normal trends and values over EI + 780 to 900 seconds, and then it rapidly rose to an OSH limit of 1740°F at GMT 13:59:44 (EI + 935 sec), where it remained until a drop to OSL near the end of the recorded data. Sensor V07T9925A was the first of the left side fuselage temperature readings to show an anomalous behavior, and this occurred at GMT 13:50:09 (EI + 360 sec).

Sensor V07T9270A is a surface thermocouple mounted at (X1486.1, Y–124.8, Z307.1), located at the far tail end of the vehicle, and low on the fuselage to be directly behind the trailing edge of the left wing. The readings began at an OSL value of 0°F at EI, rose from 0°F to a knee temperature of 600°F over GMT 13:47:49 to 13:52:09 (EI + 220 to 480 sec), and then climbed more slowly to 650°F at GMT 13:57:09 (EI + 780 sec). Beyond this point, the temperatures still rose but with significantly more variations than normal and then shot up from 850°F to an OSH value of 1740°F at GMT 13:59:44 (EI + 935 sec), where they remained aside from one brief transition to OSL and back.

While not located on the fuselage left side surface per se, sensor V07T9749A was a surface thermocouple mounted on fuselage upper surface canopy at (X474.2, Y–24.0, Z482.4) and exhibited a similar behavior as the others. The response from this sensor began at an OSL value of 0°F at EI, rose smoothly from 0°F to a plateau at 360°F over GMT 13:46:39 to 13:53:09 (EI + 150 to 540 sec), and then rose smoothly again to 570°F at GMT 13:59:47 (EI + 938 sec), when it abruptly shot up to 990°F and then fell back to 800°F at GMT 14:00:09 (EI + 960 sec).

Collectively, all eight of these surface thermocouple sensors appeared to record valid data up until their failure points at around EI + 935 seconds. The two surface thermocouples with the most severe departures from normal flight behavior were V07T9253A and V07T9925A. Both of these happen to form a straight line that extends forward to the damaged area of the left wing leading edge, and this straight line also extends aft to pass very close to the front of the left OMS pod and the left side tip of the vertical stabilizer, both of which were heavily damaged by hot gas and particulate flow from the damaged left wing. The anomalous variation from normal heating trends over the period of EI + 560 seconds onward is indicative of a significant disruption in the normal air flow patterns across this part of the vehicle, and point to these as being downstream effects of the damage zone on the left wing leading edge.

Left Wing Lower Surface Temperatures

Twelve surface thermocouple measurements were recorded in the MADS/OEX data for the lower left wing. Each was a type R thermocouple that was mounted into the outer surface of the heat tiles, part number ME449-0204-0002, and were calibrated over a range of either 0-2400°F or 0-3000°F. In addition, one surface thermocouple measurement was recorded for the upper surface of the left wing, and this was a type K thermocouple, part number ME449-0204-0001, that was calibrated over a range of 0-900°F. These surface thermocouples were located along lines of constant Y coordinate, primarily Y = –235 and Y = –370, of the left wing.

Sensor V07T9636A was the only surface thermocouple located on the upper surface of the left wing at coordinates (X1352.3, Y–361.3, Z119.4). The reading from this sensor began at an OSL value of 0°F at EI and rose from 0°F to 90°F over GMT 13:47:49 to 13:52:22 (EI + 220 to 493 sec) following the normal behavior of past flights. At GMT 13:52:22 (EI + 493 sec), the reading took an abrupt jump downward by –7

bits or about 15°F. As noted previously, this can be attributed to its thermocouple reference junction sharing a PCM-1 precision power supply output with several other sensors which also showed an abrupt jump at the same instant. The originating cause is most likely the burn through of the wiring to the TRJ unit for thermocouple V07T9666A on the lower surface of the left wing, just behind RCC panel #9. Following this –7 bit jump, the reading then climbed briefly until GMT 13:52:59 (EI + 530 sec), at which point it shot up unphysically to 320°F and then back to 0°F at GMT 13:53:14 (EI + 545 sec). From this point onward, the reading stayed at the OSL level, aside for a few occasional and short lived jumps up from this value. This failure mode is characteristic of a wire burn through and indeed, the wiring for V07T9636A was routed along the X1307 cross spar of the left wing until it reached the access panels and there it joined other cables in forming harness #4 that was routed along the upper outboard surface of the left wheel well along Y = –167.0. From there, the cable went to connector 65P107 on the interconnect panel before passing through into the fuselage.

Sensor V07T9666A was a surface thermocouple on the lower surface of the left wing, located at coordinates (X1121.7, Y–236.7, Z102.0), close to the leading edge of the left wing. This was one of the four key sensors behind RCC panel #9 that provides the strongest evidence for establishing the burn through time of the left wing leading edge spar. The reading from this thermocouple began at 120°F at EI, rose smoothly up to 2000°F at GMT 13:50:09 (EI + 360 sec), and then began to behave anomalously with a higher rate of heating and an erratic spiking up until GMT 13:52:25 (EI + 496 sec), when it started to chatter between OSH and OSL limiting values. Three seconds prior at GMT 13:52:22 (EI + 493 sec) is when the jumps in the readings of V07T9480A, V07T9489A, V07T9492A, V07T9522A, and V07T9636A occurred, and as noted previously, it is wholly possible for the power supply fault which caused these jumps to have preceded the burn-through fault which caused the response of V07T9666A to transition to OSL. Yet, these events could not have been separated by too much time, either, and the three second difference between the two appears well within the range of reasonable time delay for these sequential events. Close inspection of the readings from V07T9666A show that there was a small downward transition in its data at EI + 493, too, which could be the result of the power supply fault. Sensor V07T9666A is also a sensor that NASA has not understood very well. Its position on the leading edge makes it subject to some unusual features of the air flow boundary layers during re-entry. For some flights the overall profile of the response from V07T9666A follows the normal, symmetrical heating curve. For other flights, the response shows portions where the response drops abruptly from 2000°F to 1500°F. The best explanation that NASA has for this phenomenon is that the boundary layer associated with the air flow over the wing surface experiences somewhat randomly timed attachments and releases which cause the heat transfer to the wing to vary greatly and produce the observed effects.

Three other sensors are located on the left wing lower surface and lie close to the Y = –235 plane. Sensor V07T9674A is a surface thermocouple located on the trailing edge of the left wing at coordinates (X1351.1, Y–237.0, Z96.1). The response of this sensor followed normal trends, rising from an OSL limit of 500°F to 1500°F over GMT 13:46:59 to 13:52:29 (EI + 170 to 500 sec). Immediately following this, it took a small dip down to 1450°F over EI + 520 to 550 seconds, and then returned to 1500°F. At GMT 13:53:44 (EI + 575 sec), the sensor exhibited a wire burn through failure mode consistent with a soft short burn-through process of the Kapton insulation. From EI + 595 seconds onward, the reading remained largely at the OSL limit. Sensor V07T9786A is a thermocouple on the left inboard elevon lower forward surface. Its response climbed smoothly from 80°F to 1600°F over EI to GMT 13:52:41 (EI + 512 sec), and the response then shot up briefly to over 3000°F and then plummeted to OSL where it largely remained. Sensor V09T9231A is a thermocouple mounted on the left inboard elevon lower middle surface at the coordinates (X1441.9, Y–234.5, Z101.9). The response of this sensor climbed smoothly from 80°F to 1250°F over EI to GMT 13:52:49 (EI + 520 sec) where it then fell abruptly to OSL. All three of these sensors had their cables routed among the four harnesses that followed Y = –167 forward through the access ports and along the upper outboard wall of the left wheel well.

Two surface temperature thermocouple sensors were located on the inboard edge of the outboard left elevon at approximately Y = –320. Sensor V09T9845A is mounted at mid-gap in the middle of the inboard edge. The response of this sensor climbs smoothly from 50°F to 1800°F over the time from EI to GMT 13:53:04 (EI + 535 sec), when its response drops abruptly, reaching OSL at GMT 13:53:19 (EI + 550 sec). Sensor V09T9849A is mounted on the lower surface edge of the outboard elevon. The response of this sensor climbs smoothly from 100°F to 1900°F over the time from EI to GMT 13:52:51 (EI + 522 sec), after which it falls abruptly to OSL. The wiring from both of these sensors follows nearly the same route, traveling inboard along the cross spar at X1307 and then heading forward along the access ports and upper outboard wall of the left wheel well at Y = –167.

Three other surface thermocouples were located close to the left outboard elevon along the Y = –370 plane. Sensor V07T9711A was mounted on the lower surface of the trailing edge of the left wing at the coordinates (X1363.0, Y–369.0, ZBOT). Sensor V07T9713A was mounted on the lower middle surface of the left outboard elevon at the coordinates (X1402.0, Y–375.3, Z98.2). Sensor V07T9785A was mounted on the lower forward surface of the left outboard elevon. All three of these sensors had essentially the same characteristic behavior, beginning at approximately 100°F at EI and climbing smoothly to a maximum heating value of 1700°F. Close to their normal maximum, each abruptly fell to OSL with a failure signature that is once more typical of a soft-short wiring burn through. The burn through occurred at GMT 13:52:59 (EI + 530 sec) for V07T9711A; at GMT 13:53:09 (EI + 540 sec) for V07T9713A; and at GMT 13:52:59 (EI + 530 sec) for V07T9785A. The wiring for all three of the thermocouples runs inboard along the X1307 cross spar and then forward along Y = –167.

The last three remaining surface thermocouples are located further out on the left outboard elevon. Sensor V09T9893A measures the lower surface temperature of the left outboard

elevon cove, while sensor V09T9894A measures the upper surface temperature at nearly the same location. The lower surface temperature of the elevon cove rose from 50°F at EI up to 1150°F at GMT 13:52:32 (EI + 503 sec), after which it spiked up and then fell to OSL. The upper surface temperature of the elevon cove rose from 70°F at EI up to 300°F at GMT 13:52:32 (EI + 503 sec) also, after which it also spiked up and then fell to OSL. Sensor V09T9860A is another thermocouple that measures the elevon cove insulation surface temperature at the coordinates (X1382.0, Y–422.0, Z289.0). The response of this sensor rose from 50°F at EI up to 780°F at GMT 13:52:32 (EI + 503 sec), after which it, too, spiked up and fell to OSL. The wiring for V09T9893A and V09T9894A is routed identically and first inboard along the X1307 cross spar, and then forward along Y = –167. The wiring for V09T9860A is routed somewhat differently, first traveling inboard along the elevon hinge line, then forward along Y = –254, then inboard along the X1307 cross spar, and then forward along Y = –167.

All thirteen of these left wing surface temperatures experienced an abrupt burn through failure within the rather narrow time frame of EI + 496 to 540 seconds. The one exception to this is V07T9674A, which exhibited an anomalous and inexplicable drop of 50°F at EI + 505 seconds prior to its transition to OSL that began at EI + 575 seconds. Sensor V07T9666A was the earliest to burn through at EI + 496 seconds, since its wiring was routed along the leading edge spar of the left wing. The burn through the aluminum honeycomb spar itself and the time for which hot gases began to enter the wing box falls within the range of EI + 492 to 497 seconds, based upon the four key sensor behind RCC panel #9, for which V07T9666A is one. The other twelve surface temperature sensors all had their wiring routed along the opposite side of the wing box cavity, along the upper outboard wall of the left wheel well. The data shows that these underwent burn through wiring failures as early as EI + 503 seconds, only 6 to 10 seconds after the hot gas breached the wing box cavity. While the observed ordering of the events makes logical sense, the short time delay between the spar breach and the burn through of wires on the opposite wall of the wing box indicates an extremely intense internal heating rate and/or directionality to the intruding flow.

Orbital Maneuvering System (OMS) Pod Temperatures

The MADS/OEX system recorded 8 temperatures on the left OMS pod and 1 on the right OMS pod. All 9 of these were instrumented through PCM-1 of the MADS system. All of these but one were thermocouple temperature sensors with part numbers ME449-0204-0001 or ME449-0204-0003, and the remaining one (V07T9221A) was an RTD temperature sensor of part number ME449-0106-0001. The interesting feature of this set of sensors is that they began to deviate from the normal re-entry pattern at an early time of approximately GMT 13:49:49 (EI + 340 sec), during the execution of the first rightward roll of the vehicle, and just prior to the first set of anomalous communications drop outs. Another interesting feature of these sensors is that most of them recorded a drop in the outside temperature of the left OMS pod during a period of the re-entry flight for which these surface temperatures are normally slowly rising. The sensors will be described in an order going from the rear of the OMS pods forward.

Sensor V07T9219A is a thermocouple mounted into the high temperature reusable surface insulation (HRSI) heat tiles at the most rearward position on the left OMS pod, located toward the bottom of the pod where it meets the fuselage of the orbiter. The recorded temperature from this sensor followed normal re-entry behavior until GMT 13:52:59 (EI + 530 sec), when its previously smooth rising behavior changed directions and started downward. It then followed an approximately constant 800°F until GMT 13:53:44 (EI + 575 sec) at which point it took a more rapid drop in temperature, bouncing up and down between 600-800°F up until its apparent failure at GMT 13:59:48 (EI + 939 sec). The normal pattern for this sensor on re-entry is to continue rising from about 800°F to about 1000°F over the same period. After this, it chattered between an OSH value of 1740°F and an OSL value of 0°F up until the end of the OEX recorded data at GMT 14:00:14 (EI + 965 sec).

Sensor V07T9222A is another thermocouple mounted into the HRSI heat tiles, also toward the bottom of the pod where it meets the fuselage, but a few feet forward of V07T9219A. This sensor recorded a normal heating trend up to 680°F at GMT 13:52:34 (EI + 505 sec), after which it dropped sharply and abnormally to roughly 500°F where it largely remained until its apparent failure at GMT 13:59:48 (EI + 939 sec). The normal trend for this sensor would be for it to continue smoothly climbing up to about 900°F by roughly EI + 850 seconds. After its failure, V07T9222A chattered between its OSH value of 1740°F and its OSL value of 0°F.

Sensor V07T9223A is also a thermocouple that is mounted into the HRSI heat tiles, also toward the bottom of the pod where it meets the fuselage, and a few more feet further forward than the previous two. This sensor similarly recorded a fairly normal rise in temperature up to about 300°F at GMT 13:52:34 (EI + 505 sec), when it abruptly fell by 40°F for 20 seconds, and then started climbing at an abnormally fast rate, recording temperatures much higher than normal. By GMT 13:59:19 (EI + 910 sec), this sensor was reading well above 600°F, whereas normal behavior would have only reached about 400°F by the same time. At this point, the temperature rose extremely rapidly to 1140°F at GMT 13:59:48 (EI + 939 sec), when it failed by starting a chattering behavior between an OSH of 1740°F and OSL of 0°F. The interesting feature, of course, is that two sensors, V07T9222A and V07T9223A, located within only a few feet of each other, could record such drastically different trends, one recording temperatures up to 400°F lower than normal and the other recording temperatures up to 250°F higher than normal.

Sensor V07T9978A is a surface thermocouple that is mounted into the heat tiles at an approximately mid elevation on the pod and approximately six feet back from the front. This is considerably further forward than the previous three sensors. This sensor recorded a normal heating trend up to 520°F at GMT 13:49:49 (EI + 340 sec), when its rate of rise reduced and it began recording cooler than normal temperatures for this time during the re-entry. This temperature then stayed lower than normal by 50-100°F up until GMT 13:52:

29 (EI + 500 sec), after which it rapidly rose to higher than normal temperatures, reaching at first peak at 820°F at GMT 13:53:10 (EI + 541 sec). The temperature then fell rapidly to 670°F at GMT 13:54:09 (EI + 600 sec), and then rose rapidly to 1175°F at GMT 13:56:59 (EI + 770 sec). Normal temperatures at this time would have been only 600-650°F. Over the period from EI + 840-900 seconds, the temperature dipped down by about 200°F, and then soared up to its OSH value of 1300°F at GMT 13:59:30 (EI + 921), just two seconds before the telemetry loss of signal. After this, the recorded temperature chattered between its OSH and OSL limits.

Sensor V07T9976A is also a surface thermocouple that is mounted at approximately mid elevation on the pod and approximately four feet back from the front. This sensor behaved very similarly to V07T9978A, following normal trends up to 550°F at GMT 13:49:49 (EI + 340 sec), when its rate of rise dropped off prematurely and it then followed below the normal temperatures by about 50°F. Over GMT 13:52:54 to 13:53:14 (EI + 525 to 545 sec), the temperature then rapidly rose to 1030°F, and the plummeted to 750°F at GMT 13:54:09 (EI + 600 sec). Following this sharp dip in temperature, which was also recorded by most of the sensors on the forward part of the left OMS pod, the temperature then rapidly climbed up to vary about within the 1100-1300°F range until it dropped by about 300°F over EI + 840-900 seconds, another characteristic that was shared by most of the sensors on the front of the left OMS pods. After this, the temperature very rapidly rose to its OSH value of 1740°F at GMT 13:59:28 (EI + 919), where it failed and began chattering between its OSH and OSL limits.

Sensor V07T9972A is another surface thermocouple that is mounted high on the left OMS pod, approximately two feet back from the front. Its response was also very similar to that of V07T9976A and V07T9978A. It recorded a normal temperature up to 440°F at GMT 13:49:52 (EI + 343 sec), after which its rate of rise fell below normal. It slowly caught back up to a normal temperature of about 640°F at GMT 13:52:49 (EI + 520 sec), and then over GMT 13:53:09 to 13:53:49 (EI + 540 to 580 sec), it rapidly rose to 870°F. It then reached 1000°F at GMT 13:55:44 (EI + 695 sec), and stayed around this value until it dropped by about 150°F over EI + 840-900 seconds. At GMT 13:59:44 (EI + 935 sec), the temperature hit the OSH value of 1300°F and then chattered between the OSH and OSL limits until the end of the recorded MADS/OEX data.

Sensor V07T9220A is a thermocouple that was placed on the outside surface of the low temperature reusable surface insulation (LRSI) heat tiles at approximately mid elevation and approximately two feet back from the front of the pod. This sensor responded normally up to 310°F at GMT 13:49:59 (EI + 350 sec), when its rate of temperature rise fell below normal and its temperature fell about 100°F below the normal values for this time. The temperature began climbing faster at GMT 13:52:39 (EI + 510 sec), reaching a normal value of 500°F at GMT 13:53:14 (EI + 545 sec), and continuing up to around 1000°F at GMT 13:55:39 (EI + 690 sec). At GMT 13:59:37 (EI + 928 sec), it peaked up to 1200°F, and then failed at its OSH value of 1740°F at GMT 13:59:47 (EI + 938 sec), chattering between OSH and OSL limits.

Sensor V07T9221A is an RTD temperature sensor that was placed at the same location as V07T9220A, but on the underside of the LRSI heat tile, on the skin-to-tile bond line of the left OMS pod. This sensor, in contrast to its mate on the outer surface of the LRSI heat tile, recorded a perfectly normal temperature versus time profile over the entire re-entry period, up until it abruptly failed at GMT 13:59:49 (EI + 940 sec). At EI, it read 5°F, and this very slowly and smoothly rose to 12°F at its point of failure, when it then began to chatter between its OSH limit of +450°F and its OSL limit of –200°F. This RTD sensor mounted on the aluminum skin of the bond line shows rather clearly that the abnormal heating that was seen on the other left OMS pod sensors was coming from conditions outside the pod, rather than from within, as could have possibly been the case if, for example, an OMS pod or RCS hydrazine or oxygen cell might have ruptured and/or exploded.

Finally, sensor V07T9224A is a thermocouple that was placed on the outside surface of the LRSI heat tiles at the same location as V07T9220A and V07T9221A, but on the right OMS pod. This was one of the few temperature sensors that was on the right side of the vehicle. While the normal behavior for this sensor involves several gradual variations between 500-700°F over the course of the re-entry flight, the behavior on STS-107 fell largely within the range of these variations. The only substantive departure from normal behavior occurred at GMT 13:59:59 (EI + 950 sec) where the temperature shot up rapidly to 870°F just prior to the end of the MADS/OEX recorded data. This sensor never hit either its OSH limit of 1740°F or its OSL limit of 0°F, and its failure mode was a simple abrupt rise at the end of its data, rather than the characteristic chattering between OSL and OSH that the temperature sensors on the left OMS pod all exhibited.

The collected debris of the *Columbia* included a large section of the front of the left OMS pod which shows quite clearly that it was impacted by an abnormally intense stream of hot gas and particulates. The front of the left OMS pod was also directly downstream from the damaged area of the left wing leading edge, and thus, any material eroded away from that part of the left wing could easily be carried back to impact the front of the OMS pod. The temperatures on the front of the left OMS pod (V07T9220A, V07T9972A, V07T9976A, and V07T9978A) all dropped below normal after EI + 340 seconds, and then rose well above normal after EI + 540 seconds. Each also recorded distinct drops in their elevated temperatures at EI + 600 and over EI + 840-900 seconds. The two most rearward located temperatures (V07T9219A and V07T9222A) both showed normal behavior up to EI + 540 seconds and then significantly lower than normal temperatures. Sensor V07T9223A which was located roughly midway between these two groups, although closer to the rear group, showed only the higher than normal temperatures beyond EI + 540 seconds. If aerodynamic heating is correlated with suspended particulates which could cause surface damage to the front tiles of the left OMS pod, then this damage must have occurred during the post EI + 540 period. Since the temperatures and rate of heating on the front of the left OMS pod were actually lower than normal during EI + 340-540 seconds, it is unlikely that they were receiving any intensified flow or particulate flux from the left wing

damage zone during this time. The drastic difference in the temperature variations between two sensors that were located fairly close together (V07T9222A and V07T92232A) suggests that the air flow over the left OMS pod was either turbulent, unstable, or broken into segments in which the boundary layer was attached in some places, but not in others. Any of these circumstances would be consistent with a drastic disruption in the vehicle's airflow patterns originating from damage to the left wing leading edge.

Chin Panel Temperatures

The chin panel is a rather unusual piece of bodywork that covers the area between the nose cap and the nose wheel door on the underside of the vehicle. It is also constructed of reinforced carbon – carbon (RCC), the same material as the leading edge of the wings, and it also makes use of a T-seal piece for the joint between it and the nose cap. The T-seal and the chin panel itself are attached to the vehicle with a clevis pin assembly, similar to the mounting of the RCC panels for the wings. The location of the temperature sensors is detailed in drawing JSC-ES3-33189, which shows five temperature sensors in cross sectional view C-C. Two are located on the clevis just behind the nose cap, V09T9888A at Y0 (on the vehicle's centerline) and V09T9889A at Y-23 (23 inches to the left of the centerline). One sensor was located on the inside of the aluminum skin behind the chin panel, V09T9890A at Y-8. The two others were located on the inside surface of the RCC chin panel material, V09T9891A at Y-8 and V09T9892A at Y+8. The latter of these, V09T9892A was an unused spare; hence, there were only four measurements recorded for the chin panel area, all on PCM-1 of the MADS/OEX system. The other sensor on the inside surface of the RCC chin panel material, V09T9891A, was know to have been bad as a pre-existing condition to the flight. Its output reads a constant and erroneous 2500°F for all of the recorded re-entry period.

Of the three chin panel temperature sensors that recorded valid data, two of these were perfectly normal in their behavior in comparison to past flight data. Sensor V09T9888A, also described as the "RCC attachment lower clevis temperature," recorded 40°F at EI which then rose slowly and smoothly to 680°F over the period from EI + 260 to 965 seconds, which was the end of the recorded OEX data. Similarly, sensor V09T9890A, also known as the "RCC aluminum structure temperature," toggled between 47.0-49.5°F at EI and then over EI + 700 to 965 seconds rose by 4 bits to a final recorded value of 59.5°F. Neither of these sensors showed any spikes or abnormal transients in their recorded data.

The chin panel temperature sensor with the anomalous behavior was V09T9889A, also known as the "RCC attachment outboard clevis temperature." This sensor recorded a temperature of 20-30°F at EI which began a normal rise starting at EI + 300 seconds. However, at from GMT 13:52:19 to 13:52:34 (EI + 490 to 505 sec) the temperature rose abnormally from 105°F to 180°F, and then somewhat more slowly fell to 155°F at GMT 13:53:04 (EI + 535 sec). From this point onward, the temperature followed a smooth and gradual to climb to 605°F at GMT 14:00:14 (EI + 965 sec) which was the end of the recorded data, although the rate of rise was slightly higher than normal.

While the overall departure of this sensor away from normal behavior is rather minor, the spiking up of the temperature over EI + 490 to 535 seconds is quite distinct. And while there were other significant events occurring within the left wing damage zone within this time frame, this signature is puzzling, because of its very forward location and the lack of any common interconnections or power feeds which could have coupled disruptive signals into this measurement. These events are, however, simultaneous with the OFI telemetry measurements of the fuselage water dump and vacuum vent nozzle temperatures, both of which are also located well forward on the vehicle. The V09T9889A chin panel temperature also has in common with the water dump and vacuum vent nozzle temperatures a location toward the left side of the vehicle and the same relative magnitude of the recorded temperature anomalies. It is reasonable to suspect that the chin panel and the water dump and vacuum vent nozzle temperatures were all responding to the same set of external environmental conditions over the critical time frame of EI + 490 to 535 seconds.

Structural Strain Gauge Measurements

The MADS/OEX strain gauge structural measurements are voluminous, but not as revealing as the temperature and pressure measurements. This is due largely to the more difficult interpretation of structural strain data, often requiring both a strong background in structural mechanics and a detailed model of the structure. Typically, many different strain gauge measurements must be compiled and compared against a computer model to determine the originating forces that would be responsible for such strains, anomalous or normal. Because strain is a vector quantity with six principal components (three axial strains and three shear strains), several different strain gauge measurement combinations must usually be used to resolve the desired strain vector components. Strains also vary strongly with location, much more so than temperatures and pressures, and this is why such a large number of strain gauges are typically used to instrument a given structure. However, the burn through timing and failure modes of the strain gauge wiring further validate the overall sequence of events, and this is generally where the more valuable data lies within this group of measurements.

A total of 422 strain gauge measurements were active when STS-107 lifted off, and these were recorded by the MADS/OEX system on PCM-1, PCM-2, and PCM-3. All of the 184 strain gauge measurements that were recorded on PCM-3 were done in a "snap-shot" mode, in which data is taken for a one minute period, followed by four minutes during which no data is taken. The snap-shot mode is typically used for those sensors whose readings change sufficiently slowly as to not require the faster once or ten times per second rates that the MADS system supports. With a few exceptions, the strain gauge measurements on PCM-1 and PCM-2 were continuous over the recorded time period. Because the snap-shot mode only samples for 20% of the running time, it is considerably less useful for picking out critical timing of events, unless those events just happen to fall within a one minute period that the data is being taken. As such, the PCM-3 data was far less useful than that from PCM-1 and PCM-2.

Within the left wing, 121 strain gauge measurements were made on the wing box structure itself and having MSIDs starting with V12G, with 45 on PCM-2 in continuous mode and 76 on PCM-3 in snap-shot mode. There were 26 strain gauge measurements made on the left elevon hinges in the V13G group, all on PCM-2, with 10 made continuously and 16 made in snap-shot mode. By far the most common pattern for these measurements is a sudden off-scale event occurring in the time period of EI + 500 to 580 seconds, after which the measurement returns to a nearly zero reading. This pattern was evident in 41 of the 45 left wing strain gauges on PCM-2, and in all 10 of the 10 left elevon hinge strain gauges on PCM-2 that were in continuous mode.

A few of the left wing strain gauges deserve particular comment. Sensor V12G9921A was one of the four key sensors on the aluminum honeycomb spar behind RCC panel #9. As discussed previously, this gauge recorded an anomalous reading as early as GMT 13:48:29 (EI + 260 sec) when its recorded strain began to rise above normal behavior, peaking up to a value of +180 μin/in at GMT 13:50:09 (EI + 360 sec), then falling and crossing zero at GMT 13:51:39 (EI + 450 sec), reaching a negative peak of –140 μin/in at GMT 13:52:04 (EI + 475 sec), and then shooting up and down drastically at GMT 13:52:24 (EI + 495 sec). This last event is the failure signature for the wires of this strain gauge and provides a timing mark for the burn through of the spar itself. Following the failure signature, the recorded strain falls to a flat, unresponsive reading which results from the residual offset trim of the strain gauge signal conditioner, in this case about +35 μin/in. Prior to GMT 13:52:24 (EI + 495 sec), the strain readings were well within the range of measurement for the system, and within the range that would be expected for actual strains in the leading edge spar, given that it was being subjected to destructive forces from the broken RCC materials of the left wing leading edge. Thus, the data from this strain gauge appears perfectly valid prior to EI + 495 seconds.

In addition to V12G9921A, sensor V12G9056A is a strain gauge mounted on the top of the spar cap at coordinates (X1365.0, Y–238.0, ZUPR) that Boeing identified as another which showed an anomalous response well before EI + 500 seconds, however this characterization is somewhat debatable. The normal trend for this sensor has been to remain at a constant value of –65 μin/in for the period of EI to EI + 800 seconds, varying up and down by only a bit or two. For STS-107, the reading from this sensor went down by one bit at GMT 13:48:29 (EI + 260 sec), and then down by another bit at GMT 13:49:20 (EI + 311 sec) to a value of about –105 μin/in. At GMT 13:53:29 (EI + 560 sec), the reading shot downward to OSL, and then immediately return back to a flat and unresponsive reading of nearly zero for the remainder of the recorded data. This behavior of falling by two bits over the period of EI + 260 to 311 seconds is different from past flights only in that previously the maximum drop was one bit during the same period. The location of this strain gauge is also far back toward the trailing edge of the left wing, and quite some distance from the damage zone of the leading edge. It is difficult to conceive of any physical means by which a sensor this far back would be responding this early to the left wing damage. This time frame is also earlier than the earliest identified wire burn through, so the additional bit changes during this time cannot be attributed to instrumentation system damage. In any event, the departure from prior flights of the reading from this strain gauge is quite small and can be largely dismissed as a random bit flip that had no conclusive relation to the left wing damage effects. Of the 45 strain gauges on the left wing that were in continuous recording mode, only V12G9921A showed a significant and conclusive departure from normal behavior prior to EI + 500 seconds. The so-called anomalous reading from V12G9056A is very subtle, if present at all, and far from conclusive. Given the large number of structural strain gauges distributed throughout the left wing frame, the fact that only one of these showed any significantly anomalous behavior prior to EI + 500 seconds gives fairly conclusive evidence that the entry of the damage path into the wingbox did in fact occur only at the leading edge spar behind RCC panel #9.

Of the remaining 43 of the 45 left wing strain gauges in continuous recording mode, all but two showed a wiring burn through failure mode within the time span from GMT 13:52:29 to 13:53:49 (EI + 500 to 580 sec). A typical response was like that from V12G9055A, in which the data followed the past flight history perfectly until GMT 13:52:29 (EI + 500 sec) where it started to anomalously decrease, and then at GMT 13:52:54 (EI + 525 sec) it rapidly shot up to OSH and then fell back to a zero, unresponsive level at GMT 13:53:05 (EI + 536 sec) for the remainder of the recorded data. Another typical response was like that from V12G9911A, where the data again followed the prior flight history up until a time of GMT 13:52:44 (EI + 515 sec), after which it chattered back and forth between OSH and OSL until falling permanently to a zero unresponsive state at GMT 13:55:09 (EI + 660 sec). The response from V12G9063A was generally of a similar nature, but appeared to record several sudden events within its wiring burn through failure signature. The response first fell abruptly from past trends at GMT 13:52:34 (EI + 505 sec), going from +150 μin/in to –200 μin/in. It held roughly this value for quite some time, until a series of off-scale spikes that occurred over GMT 13:53:49 to 13:54:39 (EI + 580 to 630 sec), after which it decayed back to the –200 μin/in level until it abruptly dropped to zero at GMT 13:57:59 (EI + 830 sec). The V12G9063A strain gauge is located at coordinates (X1191.0, Y–244.0, ZLW), which is about seven feet directly aft of V12G9921A on the leading edge spar. Its wiring also gets routed along the inside of the leading edge spar, and this can account for a large share of the unusualness of its response.

Two of the 45 left wing strain gauges that were in continuous recording mode also recorded an anomalous event around EI + 500 to 580 seconds, but their readings did not go off-scale, nor behave erratically until the terminal phase at EI + 930 seconds. Both of these strain gauges were located far forward on the left wing X1040 spar. Strain gauge V12G9048A was located at the coordinates (X1040.0, Y–135.0, ZLWR) on the lower spar cap, and strain gauge V12G9049A was located at coordinates (X1040.0, Y–135.0, ZUPR) on the upper spar cap. At GMT 13:52:19 (EI + 490 sec), the reading from V12G9048A began to smoothly rise from +50 μin/in to a peak at +350 μin/in at GMT 13:54:39 (EI + 630 sec), and then smoothly decayed back to a normal value of +150

μin/in at GMT 13:57:49 (EI + 820 sec), with only a minor upward jump of 30 μin/in at GMT 13:55:34 (EI + 685 sec). At GMT 13:59:44 (EI + 935 sec) the response then began spiking up to off-scale values, typical of a wire burn through failure at that point. The reading from V12G9049A followed normal trends until GMT 13:53:39 (EI + 570 sec), when it began to rise smoothly from −40 μin/in to +240 μin/in at GMT 13:55:34 (EI + 685 sec). At this point, the same time as when V12G9048A took a slight jump upward, strain gauge V12G9049A took a larger jump downward to a value of +80 μin/in. From there, the response increased smoothly again to a value of +250 μin/in at GMT 13:59:44 (EI + 935 sec), after which it, too, began spiking up to off-scale values as it began a wire burn through failure signature. The simultaneous jumps in both of these strain gauge readings appears to be the result of a common power supply connection. The responses from both of these two strain gauges on the X1040 spar appears to be the actual strain at that location up until their failures at EI + 935 seconds. Because the X1040 spar crosses in front of the left wheel well, and the exposed wiring for most of the sensors in the left wing runs along the front of this spar, the fact that both of these strain gauges remained operational until EI + 935 seconds indicates that no left wing damage propagated into the wing cavity area in front of the wheel well until at least EI + 935 seconds. This is significant, because it implies that the route that the hot gases must have taken to cause the damage inside the left wheel well must have occurred by way of burning through the outboard wall of the wheel well, rather than snaking around forward and then back through the access panel at the front of the wheel well, as was originally hypothesized. Further, both of these strain gauges record some significant and anomalous strains prior to their failure, indicating strong twisting distortions that were occurring within the wing frame near to the front of the left wheel well.

Within the right wing, 126 strain gauge measurements were made on the wing box structure itself in the V12G group, with 65 on PCM-1 in continuous mode, 21 on PCM-2 in continuous mode, and 40 on PCM-3 in snap-shot mode. There were also 26 strain gauge measurements on the right elevon hinges in the V13G group, all on PCM-1, with 10 made continuously and 16 made in snap-shot mode. One of the right wing upper skin strain gauges, V12G9653A, recorded ascent data, but did not respond for re-entry data, presumably failing somewhere in between the two periods. Thus, there were only 125 recorded measurements for the right wing during the re-entry flight. The most common measurement pattern for the right wing was a completely normal response, matching to the trends and values of past flights, up until the terminal phase that began around EI + 930 seconds. Of the 85 continuous mode right wing strain measurements on PCM-1 and PCM-2, 51 showed this behavior, as did 8 of the 10 continuous mode right elevon strain measurements. The remaining 34 continuous right wing strain measurements and 2 continuous right elevon strain measurements exhibited an anomalous event near EI + 500 seconds, but this did not cause off-scale readings or erratic behavior. One example of this is strain gauge V12G9068A, whose reading at GMT 13:52:29 (EI + 500 sec) reversed its rising trend and fell continuously below its normal trend by about 100 μin/in until its failure at GMT 13:59:44 (EI + 935 sec). Another example is strain gauge V12G9815A, whose reading rose and fell by 3 bits over the time span of GMT 13:52:24 to 13:53:04 (EI + 495 to 535 sec) before returning to normal values and then ultimately failing at GMT 13:59:44 (EI + 935 sec).

A variety of other strain gauges were measured during the re-entry flight, but these were all done completely in snap-shot mode and did not provide much relevant information. There were 15 strain gauge measurements made on the payload bay door hinge lines in the V37G group, and all of these were made on PCM-2 in the snap-shot mode. There were 40 strain gauge measurements made on the midbody fuselage in the V34G group, 28 on PCM-1 and 12 on PCM-2, all in the snap-shot mode. There were 38 strain gauge measurements made on the vertical stabilizer in the V22G group and 12 rudder hinge moment strains in the V23G group, all made in snap-shot mode. Finally, there were 2 aft fuselage strain measurements in the V08G group and 16 aft fuselage OMS deck strains in the V35G group, again, all made in snap-shot mode. Many of these exhibited completely normal behavior over the 1 minute sampled time windows, such as V13G9834A located on the right outboard elevon hinge, while a few showed anomalous behavior during their 1 minute sampled time windows, such as V13G9818A located on the left outboard elevon hinge. However, the lack of any recorded data for this sensor and ones like it over the 4 minute blank time windows makes further investigation of their anomalous behavior difficult at best and rather nonconclusive.

Wide Band FDM Data

The two frequency division multiplex (FDM) units were programmed to interleave a total of 104 different wide bandwidth measurements. Each of the two FMD units can interleave 15 channels on each of their 4 multiplexers for a total of 120 measurements. For STS-107, 16 channels were unused. For FDM-1, multiplexers M1A, M1B, M1C, and M1D were recorded on tracks 6, 8, 10, and 12, respectively, of the OEX recorder during the re-entry flight; for FMD-2, multiplexers M2A, M2B, M2C, and M2D were recorded on tracks 22, 24, 26, and 28, respectively. The ascent and deorbit flight segments were recorded on a different selection of OEX recorder tracks.

The wideband data included two MSIDs which are reserved for FDM timing synchronization, V75W9006D and V75W9016D, filling channel 1 of M1A and M2A, respectively. The main body measurements included 17 vibration sensors with MSIDs beginning with V08D, 4 acoustic measurements with MSIDs beginning with V08Y, and two wideband strain measurements with MSIDs beginning with V08G. The tall vertical stabilizer had 6 wideband strains recorded with MSIDs beginning with V22G, and the rudder had 12 wideband strains with MSIDs beginning with V23G. The midbody fuselage had 9 accelerometer measurements recorded with MSIDs beginning with V34A, and 16 additional wideband strains with MSIDs beginning with V35G. In addition, 12 wideband strains and 24 vibrations were recorded for the main engines with MSIDs beginning with E41G and E41D, respectively. Since the main engines are off, the 36 measurements associated with them do not pro-

vide any useful information for the re-entry flight. Analysis of the FDM data was accomplished rather late in the analysis because the raw OEX recorder data had to be sent to Boeing at Huntington Beach for them to perform the power spectral density (PSD) analyses. The results of that analysis were presented to NASA and the CAIB on May 23.

For the re-entry flight, the primary wideband sensor of interest was V08D9729A, which is an accelerometer that measures the Z-axis motion of the left outboard elevon at the coordinates (X1429.4, Y–435.0, Z). It has a matching counterpart on the right outboard elevon, V08D9737A, located at the coordinates (X1429.4, Y+435.0, Z). The Z-coordinate for both was not specified in the available documentation. Both accelerometers are part number ME449-0163-0002, and measure accelerations of up to 20 G, peak-to-peak. These two accelerometer readings were recorded on the 16 kHz center frequency channel #2 of FDM-1, with V08D9729A on the M1B multiplexer and V08D9737A on the M1C multiplexer. Since both of these accelerometers measure Z-axis motion of the wing tips, they are sensitive to symmetrical or anti-symmetrical "flapping" modes on both wings.

The recorded data for both of these accelerometers showed a normal behavior up through approximately GMT 13:52:19 (EI + 490 sec), which included a normal transient response to the activation of the elevons at GMT 13:47:52 to 13:47:53 (EI + 233 to 234 sec). This transient matched to the known activation of the elevons at this time, and consisted of 6-7 cycles of a damped oscillation with a peak acceleration of slightly less than 1 g in both directions. Two sharp transients then occurred on the left outboard elevon at GMT 13:52:25 (EI + 496 sec) and GMT 13:52:31 (EI + 502 sec), with peaks close to 2.0 g for the first and nearly 2.5 g for the second. The right outboard elevon did not record any significant disturbances during these periods, and its data remained at a fairly normal rms noise level of approximately 0.2 g. The power spectral density (PSD) showed no significant changes before and after these transient events, as all of the expected frequency components that are associated with known vibrational modes of the wings and elevons were present. These included a primary 5.7 Hz mode associated with symmetrical bending of the wings, akin to flapping motion, a 13 Hz mode associated with the first rotational mode of the elevon itself, 19 Hz and 22 Hz modes associated with the second bending mode of the wings, and a 30 Hz mode associated with a torsional mode of the outboard elevon. At GMT 13:53:03 (EI + 534 sec), the left outboard elevon accelerometer recorded a transient which saturated the measurement range at greater than ±10 g. Over EI + 534 to 537 seconds, a displacement grew within the recorded measurement that was unphysical and most likely indicated a failure mode of this type of linear, low-frequency accelerometer. After the displacement caused a saturated output, the 6 Hz wing mode was no longer recognized in the PSD, and this is another indication that the accelerometer or its wiring had been damaged by the event at EI + 534 seconds. Beyond this point, the recorded data shows numerous chattering between OSH and OSL limits of ±10 g, all of the way out to the end of the recorded data. The right outboard elevon accelerometers begins to pick up this activity also from about GMT 13:58:19 (EI + 850 sec) onward.

Among the other wideband re-entry data, there were several other accelerometers which were placed along the longeron of the orbiter, but none of these recorded any significant transient vibrations or displacements. The wideband strain gauges also recorded essentially nominal strain values over the re-entry flight. The PSD of the wideband sensors on STS-107 generally matched well to those of STS-109 in the frequency domain; however, STS-107 exhibited a large number of transient spikes in the time domain that STS-109 did not. Overall, the wideband FDM data did not add any significant new information about the orbiter's damage extent or propagation, but simply reinforced the timing of around EI + 495 seconds onward, during which the damage began to cause wiring burn throughs and other internal structural damage to the left wing that was recorded on many of the different instrumentation systems.

Ascent Data

Ascent data from both the OEX and OFI instrumentation systems is largely unremarkable. Particular interest is in the time frame around 82 seconds Mission Elapsed Time (MET), around which the foam debris strike from the external tank (ET) is best centered. As detailed below, none of the sensors in the PCM OEX suite recorded any significant disturbance which could be linked to a debris strike around this period of time.

The temperature sensors are divided into two systems: the aerothermal sensors on the outer skin of the left wing, left fuselage, and left OMS pod (35 sensors in the V07T set), and the internal structural sensors on the elevon coves, spars, and RCC clevises (14 sensors in the V09T set). Several temperature sensors showed some differences from prior flight histories; however, these deviations are in general not very significant. V07T9222A showed a slight rise at 330 sec MET on the left OMS pod, but this was still well within family. V07T9224A showed widely disparate data on all past flights, but STS-107 was still within this overall band. V07T9468A showed a slightly warmer lower fuselage surface temperature over 120-360 sec MET. V07T9470A showed some transient spiking over 90-120 sec MET, although this was also seen on prior flights. V07T9478A showed a 2-bit higher temperature on the fuselage surface, and this is very faint, if significant at all. V07T9522A showed a slightly warmer fuselage aft penetration area over 120-360 sec MET. Several temperature sensors recorded a slight fall in the fuselage surface temperatures at 380 sec MET, and these included V07T9880A, V07T9903A, V07T9913A, and V07T9925A.

NASA had called attention to temperature sensor V09T9895A, the wing front spar panel 9 temperature, which decreased by 5 bits over 30-180 sec MET, and then slowly rose by 3 bits over 300-900 sec MET. Other prior flights showed a 4 bit drop and then a 1 bit rise over the same periods. Each bit corresponds to approximately 2.5°F. The only substantive difference from prior flights was the 3-bit rise which occurs over a 10 minute span that was well past the event timing for the debris strike; thus, this sensor does not appear to indicate any direct correlation to the ET foam strike.

Aerodynamic pressure readings from both the left and right wings were similar. V07P8026A read 2.5 psi lower than previous flights, and this appeared to be a simple case of the sensor becoming uncalibrated. The overall shape of the response versus time was the same as all previous flights, but simply offset downward by 2.5 psi over the recording period. Similarly, V07P8092A was offset downward by 2.5 psi, and was also erratic prior to launch. Several pressure sensors gave unphysical readings over the recording period, starting at around 1 psia before launch and then flatlining at 0 psi immediately after launch. These were assumed to be dead measurement channels and included V07P8181A, V07P8182A, V07P8188A, V07P8189A, and V07P8190A. V07P8013A only recorded a pressure fall from 15 psia to 2.5 psia over the ascent, indicating a gain and/or offset error in its calibration. V07P8088A recorded readings which bounced up to OSH at 16 psia immediately after launch. V07P8103A only fell from 15 psia to 1.8 psia during ascent, again indicating a loss of calibration. V07P8144A failed and went to OSL at 30 sec MET. V07P8175A started out reading only 1.8 psia, indicating a sensor grossly out of calibration or beginning to fail completely. V07P8191A recorded some spikes at 480 and 670 sec MET. Overall, the aerodynamic pressure sensors showed no deviations from prior flight history aside from the above noted ones for which the behavior was indicative of a loss of calibration in the sensor or a completely dead measurement channel. None of the anomalous events appeared to have any time correlation to the foam debris strike at 82 sec MET.

Aerodynamic pressure sensor V07P8073A deserves special comment, as it was also noted by NASA as having an unusual response near to the 82 sec MET foam debris impact time. This was the only sensor within the OEX suite which had any unusual behavior near to 82 sec MET. This sensor first showed some erratic behavior at 61 sec MET when it recorded an abrupt 2 psi drop for half a second. Up until 84.5 sec MET, its response was fully consistent with prior flight history, when it fell to OSL and largely remained there at 0 psia for the rest of the recorded ascent period. Over 85-88 sec MET, the sensor recorded a parabolic burst, peaking at 2.5 psia at 86.5 sec MET. Shortly thereafter, it recorded an abrupt transition from OSL to OSH which then decayed back to OSL over 93-96 sec MET. This second transient is clearly non-physical and can be attributed to an instrumentation fault or interference pickup. The fast rise and exponential decay are typical for a system impulse response to any sudden charge injection. The first parabolic transient, because of its nearness to the 82 sec MET foam strike, could possibly be interpreted as a piece of foam debris either flying past the pressure sensing port or perhaps becoming temporarily lodged in the port orifice. Neither of these events is likely, because the port is flush with the surface of the heat tile and not prone to trap flying debris, and the duration of the parabolic pulse is too long (3 seconds) to match to any reasonable size piece of foam debris flying past a 3 mm diameter port at 150 mph. Similarly the time of the pulse, starting at 84.5 sec MET, is too far past the debris strike at 82 sec MET to match to the transit time between the wing leading edge and the location of the pressure port in the middle of the left wing. Also notable is the fact this was only one of eight sensors in the $Y_o = -250$ forward band of the left wing, which should have also recorded a similar event. The other 7 sensors in this zone showed completely normal ascent data, and include V07P8071A, V07P8072A, V07P8074A, V07P9186A, V07P9188A, V07P9189A, and V07P9190A. Pressure sensor V07P9186A is located within a few inches of V07P8073A, and it recorded data that was nearly identical to V07P8073A except for those time periods where V07P8073A was behaving erratically. The behavior of pressure sensor V07P8073A can thus be largely attributed to a "normal" failure mode of the sensor, most likely caused by a loss of its vacuum reference chamber. Any leaking in this chamber would cause the sensor to read low, and ultimately go OSL, which is what is observed. Several other pressure sensors in this suite show similar behavior before launch, and it should also be noted that leaking of the vacuum reference chamber on an absolute pressure sensor is the primary failure mode and shelf-life limit for these devices. Of the 181 aerodynamic pressure sensors installed on OV-102, 55 were already known to be bad or producing untrustworthy readings prior to launch.

A small fraction of the strain gauges showed differences with prior flight history, but in most cases this was a systematic offset that merely shifted the response up or down without changing its shape or features. These offset errors were typically small, on the order of 20-30 μin/in. For the 131 strain gauges on the left and right wing structural elements, 13 on the right wing showed some offset errors, including V12G9081A, V12G9442A, V12G9452A, V12G9641A, V12G9642A, V12G9648A, V12G9649A, V12G9651A, V12G9656A, V12G9629A, V12G9635A, V12G9636A, and V12G9637A. By contrast, only 2 strain gauges on the left wing showed any offset errors between STS-107 and prior flights, and these were V12G9058A and V12G9921A. The latter of these, V12G9921A, is one of the key sensors located on the spar panel immediately behind RCC panel #9. Even on the expanded time scale plots covering 50-150 sec MET, there is no evidence of any significant event around the ET foam debris impact at 82 sec MET. There were a total of 52 strain gauges on the right and left elevons, and all of these but one, V13G9749A which showed a slight offset error, responded similar to prior flight history. The middle fuselage area had 40 strain gauges, and of these a few recorded data that contained offset errors: V34G9503A, V34G9934A, V34G9935A, V34G9936A, V34G9937A, V34G9938A, V34G9941A, and V34G9952A. Some of these offsets were more apparent over 80-500 sec MET, but may exist over a wider time span. The 15 strain gauges on the payload bay door hinges (V37GxxxxA) each recorded data that was completely consistent with the behavior of prior flights.

The wideband FDM data, which because of its more complex encoding took longer to extract from the OEX recorder tape, also showed some signatures which are indicative of a debris strike near to 82 sec MET. One of the accelerometers on the left wing elevons, V08D9729A, showed a single cycle sinusoidal pulse at 81.9 sec MET that was approximately ±2 g in amplitude, as compared to a background vibration level which generally stayed well below ±1 g. This is a fairly significant pulse which could easily represent a strike of foam debris upon ascent. The timing and amplitude of this pulse were taken from a preliminary assessment of the wideband

FDM data that was printed out on a strip chart recorder by NASA at JSC.

Boeing of Huntington Beach performed a more thorough analysis of the remainder of the wideband FDM ascent data and in general did not find much that was anomalous. They found that the overall noise levels and power spectral density (PSD) matched very closely to the data from the previous flight, STS-109. They noticed that at approximately 40 sec MET, the vertical stabilizer had some of its higher order modes growing slightly larger than normal, and this was attributed to some wind buffeting that was thought to occur around this time. These modes then decayed shortly thereafter, indicating that the so-called flutter instability was not becoming excited, as can occur when the wing bending modes and the fuselage vertical modes coalesce into a single coupled oscillation. Boeing's analysis also pointed out that the recorded accelerations along the longeron were normal. Detailed analysis of the wideband FDM data over the time frame around 80-85 sec MET was performed. For the left outboard elevon accelerometer, V08D9729A, several wing and elevon oscillation modes were found to be excited during this time, with the strongest being a second order wing bending mode that matched best to the fundamental component of the single cycle sinusoidal pulse at 81.9 sec MET. Boeing's more detailed time scale showed the period of the single sinusoidal pulse to extend over 81.70 to 81.74 sec MET, reaching +3.0 g on the positive peak at 81.71 sec MET, and –2.6 g on the negative peak at 81.72 sec MET.

In addition, another accelerometer on the right wing, V08D9766A, showed a 1.5 cycle sinusoidal pulse response at a slightly earlier time of around 80 sec MET. This accelerometer was located at the coordinates (X1367.0, Y+312.0, Z) towards the middle of the right wing and was sensitive to Z-axis motion. This accelerometer recorded an anomalous pulse beginning at 80.22 sec MET, growing to a first positive peak of +1.5 g at 80.23 sec MET, reaching a negative peak of –1.9 g at 80.24 sec MET, then another positive peak of +2.0 g at 80.26 sec MET, before dying away beyond 80.27 sec MET. The best fit to these peaks was a combination of outboard elevon torsion and the first wing bending mode. There have not been any explanations offered for the cause of this right wing accelerometer response.

Findings and Recommendations

Clearly Defined Features within the Sensor Data Evidence

The vast number of sensors in place in both the OFI and MADS/OEX instrumentation systems of *Columbia* have provided a wealth of information about the circumstances of the accident. Physical sensors that were originally placed to monitor the vehicle as it passed through the harsh environments of ascent and re-entry have provided critical real-time measurements of vehicle temperature, pressure, and strain as the integrity of its left wing deteriorated. In many cases several sensors of the same type recorded different views of the same events, and this redundancy in the measurements provides an even higher degree of confidence in the interpretations. Correlations between different types of physical sensors, for example temperature and strain of the leading edge spar, together paint a more complete picture of the events than that provided by each sensor considered singly. Both the diversity of sensor types, the wide distribution of their placement, and the sheer numbers of them which were installed have provided rich information upon which to base hypotheses of the accident's chain of events and contributing causes, as well as to rule out other possibilities as being inconsistent with this voluminous amount of sensor data.

The fundamental design of the OFI and MADS/OEX instrumentation systems, which places a time stamp on each frame of telemetry or recorded data, inherently provides an extremely accurate, universal, and unambiguous time reference for each measurement, providing a time resolution on the events down to one second accuracy for most and to a tenth second accuracy for some. Since the time stamp is carried along with the measurement data itself, there is practically no uncertainty about when particular events occurred, at least in the electrical instrumentation sense. Any uncertainties in the timing of events are due to the random nature of the physical process which prompted the electrical instrumentation system reaction, for example, the speed at which sensor cables might burn through, or the thermal time constants that would be required for a sensor to reach its steady-state response to a fast changing stimulus.

While most instrumentation systems remain static and simply record unfolding events, the situation with the instrumentation systems on the *Columbia* is fundamentally different, because the instrumentation systems were themselves being injured by the left wing damage and were thus changing along with the rest of the vehicle that they were measuring. The most conservative approach is to simply disqualify any data beyond the time for which its readings imply a physically impossible event, for example, a temperature rising faster than what the thermal time constants of the material would allow. And indeed, after a sensor channel has obviously been damaged, the accuracy of its subsequent readings becomes wholly suspect. However, the manner in which the failures occur and the timing of these failures also provides important information about the events which have precipitated the failure. Considered in this manner, the cables of a given sensor now become a sensor, too. And similarly, drop outs within a barely connected communication link can become a sensitive indicator of obscuring matter or mis-orientation between the receiver and transmitter antennas.

The foremost feature in the accident's sequence of events that is clearly revealed by the sensor readings is the breach of the left wing leading edge spar at a time in the range of 5 to 15 seconds prior to GMT 13:52:18 (EI + 489 sec), when the first sensor whose cable was routed along the leading edge (V07P8023A) failed. The 10±5 second delay represents the best estimate for the burn through time of these sensor cables. Four key sensors were located within the damage zone of the leading edge spar, and included the RCC clevis temperature, V09T9910A, which was located on the outside of the leading edge spar, the spar strain gauge, V12G9921A, the wing lower surface thermocouple, V07T9666A, and the leading edge spar temperature, V09T9895A, which was located on the inside surface of the spar. Each of these four key

sensors recorded anomalous conditions very early into the re-entry flight, and each then failed with a cable burn through signature within a rather narrow span of time immediately following the breach of the leading edge spar. Specifically, the spar strain V12G9921A first recorded anomalous mechanical behavior of the spar at GMT 13:48:39 (EI + 270 sec) and it failed at GMT 13:52:24 (EI + 495 sec). The RCC clevis temperature V09T9910A first recorded anomalous temperatures on the outside of the spar at GMT 13:48:59 (EI + 290 sec) and it failed at GMT 13:52:22 (EI + 493 sec). The lower wing surface temperature V07T9666A first recorded anomalous heating on the bottom of the wing at GMT 13:50: 19 (EI + 370 sec) and it failed at GMT 13:52:23 (EI + 496 sec). The spar surface temperature V09T9895A first recorded an anomalous heating of the spar at GMT 13:51:14 (EI + 425 sec) and it failed at GMT 13:52:51 (EI + 522 sec), slightly later than the rest because of its cable harness lying farther away from the initial entry point of the spar breach. These four key sensor readings compile a very clear picture of abnormally high temperatures on the outside of the wing working their way through the RCC panels and then ultimately through the leading edge spar, accompanied by mechanical distortions and strains in the spar as this happened. These four key sensors, along with eleven other pressure sensors, each had their cable harnesses routed along the center backside of the leading edge spar. All fifteen of these sensors failed with a wiring burn through signature in the time span of GMT 13:52:18 to 13:52:26 (EI + 489 to 497 sec), except for V09T9895A, which failed at GMT 13:52:51 (EI + 522 sec) because of its different cable harness routing. Allowing an estimated 5 to 15 seconds for a cable to burn through on the average, the breach of the leading edge spar can then be placed at 10±5 seconds prior to GMT 13:52:18 (EI + 489 sec), which was the first failure of a sensor whose cable run was entirely behind the leading edge spar (V07P8023A).

An implicit assumption in the above reasoning is that the leading edge spar had to have been breached completely through before the sensor cabling began its burn through process, that is, the two processes were necessarily sequential. This appears well justified, because the melting point for the aluminum honeycomb spar is 1218ºF (659ºC), which is essentially the same the temperature needed to produce a soft short breakdown in the Kapton wiring insulation. In other words, it is unlikely that simple heating of the outside of the leading edge spar would have been sufficient to degrade the wiring insulation on the inside, since by the point at which the insulation would have degraded to failure, the spar itself would have melted.

The direction of the spar breach is also clearly evident, coming into the wing box from the outside, from behind the leading edge RCC panels. The RCC clevis temperature sensor V09T9910A, which was located behind the RCC panels and outside the wing box, was the first to register anomalous and significantly increasing temperatures at EI + 290 seconds, giving a clear picture that the temperature on the outside of the wing box was growing rapidly hotter than anything on the inside. The wing lower surface temperature V07T9666A began recording anomalously high temperatures on the bottom of the wing shortly thereafter at EI + 370 seconds. The inside surface temperature of the spar, V09T9895A, did not begin rising until significantly later, at EI + 425 seconds. The possibility that the left wing damage occurred by something blowing out from the inside of the wing box is not consistent with the timing or the observed temperatures of these sensor readings. Likewise, the timing for destructive events within the left wheel well occurs later than the leading edge spar breach, indicating also that the direction of substantive damage was from RCC leading edge, through the leading edge spar, through the wing box and the cabling it contained, and then finally into the left wheel well.

The locations of the various sensors which exhibited wiring burn through failures and the routing of their cable harnesses also provides fairly conclusive evidence of the location of the leading edge spar breach. In addition to the four key sensors behind RCC panel #9, eleven aerodynamic pressure sensors in the left wing had their sensor cables routed along the leading edge spar. All eleven of these exhibited a wiring burn through failure signature within the time range of GMT 13:52:16 to 13:52:26 (EI + 487 to 497 sec). These pressure sensors included V07P8010A, V07P8058A, V07P8022A, V07P8023A, V07P8024A, V07P8071A, V07P8072A, V07P8073A, V07P8037A, V07P8038A, and V07P8044A. There was also another strain gauge on the leading edge spar behind RCC panel #9, V12G9169A; however, this strain gauge was instrumented through PCM-3 in snap-shot mode and thus its precise time of failure cannot be determined, but it is nonetheless consistent with a burn through failure time in the range of EI + 487 to 497 seconds, too. The time span of EI + 487 to 497 seconds also brackets the burn through failure times of V09T9910A, V07T9666A, and V12G9921A on the leading edge spar behind RCC panel #9. The only sensor whose cable was routed along the leading edge spar whose failure time was different from this was V09T9895A, and is most likely because its cable was routed significantly lower on the spar than the rest.

The most noteworthy feature of the failed aerodynamic pressure sensor readings is that two of these, V07P8010A and V07P8058A, were located quite far forward on the left wing, just a few inches aft of the forward edge of RCC panel #8. The cables to these two pressure sensors did not extend any further aft than this point either, yet both sensors exhibited an unmistakable wire burn through failure signature at EI + 497 seconds for V07P8010A and EI + 495 to 505 seconds for V07P8058A. This implies that the leading edge spar breach must have occurred no farther aft than this point. Also of similar note are two strain gauges that were located on the X1040 cross spar which ran along the front wall of the wheel well. Sensors V12G9048A on the lower spar cap and V12G9049A on the upper spar cap recorded anomalous strain data around the time period of the lead edge spar breach, but neither failed until much later, at EI + 935 seconds, just before the end of the recorded OEX data. The cables to both of these strain gauges must therefore have remained intact until this point, and this implies that the leading edge spar breach must have occurred farther aft than the X1040 cross spar. Otherwise, the hot gas would have surely caused a wire burn through failure in the exposed cables of these two strain gauges. This then brackets the possible location of the leading edge spar breach to a fairly small area extending from the aft end of RCC panel #6 to the front end of RCC panel #8.

Besides the leading edge RCC panels, several other potential points of entry into the wing box could have existed, but these are each clearly refuted by the sensor data. A breach through either the upper or the lower wing surface acreage tiles in one of several areas was originally suggested, but none of these are consistent with the large number of pressure, temperature, and strain sensors on the left wing which did not record any anomalous behavior until nearly the end of the telemetry or recorded data. A breach through the upper or lower wing surfaces would also not explain the clearly evident rise in the V09T9910A RCC clevis temperature which was located outside of the wing box and back behind the RCC panels in what is termed the leading edge chunnel.

Prior to the recovery of the OEX recorder, attention was drawn to what was then the most dramatic events in the OFI telemetry data around the left wheel well, in which the tire pressure and wheel temperatures all exhibited failures within the time span of EI + 858 to 880 seconds. The possibility of a breach into the wing box by way of the wheel well was suggested, in addition to several other hypotheses which suggested that some other destructive event originating from the wheel well might have led to the breach of the wing box. However, the refuting evidence for these is that, within the wheel well, while one of the eight main landing gear hydraulic temperatures did record an anomalous rising temperature as early as EI + 488 seconds, only one actually failed outright, and this was not until EI + 913 seconds, just 10 seconds prior to the loss of the telemetry signal. Of equal importance, the temperature rises in these hydraulic system components were only a few tens of degrees for most, and the largest only rose to 172ºF. Before the OEX recorder data was available, these temperature rises may have been perceived as drastic, but within the larger perspective provided by the OEX sensors which recorded truly significant rises in temperatures near the damage zone of wing leading edge, rises of many hundreds of degrees, these temperature rises inside the wheel well are by comparison rather small, and occurred far too late in the time line to be seriously considered as the entry point for the breach into the wing box. The same sensors also provide rather conclusive evidence that the wheel well door did not open prematurely, that the tires did not explode, and that none of the pyrotechnic actuators fired, at least up until the loss of the telemetry signal. Further, the elevon hydraulic system temperatures, whose sensor cable harnesses were routed along the outboard wall of the wheel well, show wire burn through failures in the time span of EI + 533 to 567 seconds, consistent with and shortly following the timing of the leading edge spar breach. Of the eight main landing gear hydraulic system temperatures measured inside the left wheel well, five of these did not show any anomalous behavior until EI + 610 seconds.

Apart from the three which did show minor temperature rises prior to EI + 610 seconds, this suggests that a breach from the wing box into the wheel well could have occurred in the time frame of approximately EI + 550 to 600 seconds. Regardless of the precise timing of the wheel well breach, the time sequence of the anomalous sensor events shows clearly that the damage zone proceeded from the wing box into the wheel well and not from the opposite direction.

The combination of telemetry and recorded data also establishes the path and timing of several debris shedding events as the leading edge of the left wing began to come apart. Both increased and decreased heating patterns were shown in the temperature readings from sensors distributed across the left OMS pod and the left side of the fuselage, indicating a strongly altered aerodynamic flow pattern across these regions. The most dramatically affected sensors on both the side of the fuselage and the OMS pod lie almost perfectly along a straight line drawn from the supposed damage area of the left wing leading edge backwards along the direction of vehicle motion. This same straight line continues toward the left side of the vertical stabilizer, and this path of debris from the damage area on the leading edge of the wing is corroborated distinctly in the recovered wreckage which included large pieces from the front of the left OMS pod and the top of the vertical stabilizer. Both of these surfaces show an extreme amount of impact debris damage. Moreover, several of the longer communication drop outs that occurred earlier into the re-entry flight happened very close to the times at which the more significant debris shedding events were both observed from the ground and recorded as anomalous surface temperatures on the vehicle. While the debris shedding events cannot conclusively be identified as the actual cause of the anomalous, early communications drop outs, the relatively small and decreasing communications link margins suggest that even a small signal attenuation caused by some debris or vaporized metal could have produced the observed drop outs.

A number of temperature sensors on the lower surface of the fuselage and pressure sensors on the upper and lower surfaces of the right wing also showed anomalous readings during the re-entry flight. In almost all cases, these can be traced to common electrical power supplies within the instrumentation system which are shared between these sensors and ones which were more directly affected on the left wing. Thus, the anomalous readings given by these sensors on the lower fuselage and right wing surfaces do not contradict any of the other conclusions, but rather reinforce the explanations as being consistent with how the overall instrumentation systems of the orbiter should have reacted to the sensor wiring failures created within the left wing.

Remaining, Unexplained Inconsistencies

By far the most puzzling unexplained sensor anomalies are those readings from the sensors which were located forward of the damage area on the left wing leading edge. These are the slight temperature perturbations exhibited by the fuselage supply water dump and vacuum vent nozzles (V62T0439A, V62T0440A, and V62T0551A) and by the chin panel mounting clevis (V09T9889A). Each of these temperature sensors appeared to be working properly, and each recorded small, but still distinctly anomalous readings that began at EI + 499 ± 4 seconds. An explanation for how damage to the left wing leading edge could propagate forward to affect these locations, almost at the nose of the vehicle, has yet to be offered. The aerodynamic engineers have suggested that this was an instrumentation artifact, while the instrumentation engineers have likewise suggested that the cause was an aerodynamic artifact arising from the asym-

metrical vehicle profile that was produced by the left wing damage. The simultaneous occurrence of this unusual temperature rise on the water dump nozzles and vacuum vents, which were both OFI telemetry data, and on the chin panel mounting clevis, which was OEX recorded data, suggests that this was not a simple instrumentation glitch, as both instrumentation systems recorded the event independently. Changes in the overall aerodynamic profile could produce reaction vortices or turbulence further forward, and the thermal perturbations that were recorded in the fuselage nozzles and in the chin panel clevis both occurred around the time of the breach of the left wing leading edge spar.

Although they occurred comparatively late in comparison to the breach of the left wing leading edge spar, events within the left wheel well still raise some unanswered questions. First is the unexplained cause for the slight but distinctly abnormal rise in the temperature of the left hydraulic brake line point D, V58T1703A, located on the aft end of the inboard wheel well wall, at the early time of GMT 13:52:17 (EI + 488 sec). The left hydraulic brake line temperatures at points A and C, V58T1700A and V58T1702A, also recorded anomalous rises slightly thereafter at GMT 13:52:41 (EI + 512 sec). All three of these sensors inside the left wheel well responded anomalously prior to the failures of sensors with their cable harnesses routed on the upper outboard wheel well wall and thus presumably before the breach of the left wheel well wall. It has been hypothesized that the hot gas which began entering the wing box after the breach of the leading edge spar flowed around forward through the X1040 spar access panel and then backward into the wheel well through an approximately 5 inch diameter vent hole further inboard on the X1040 spar. This pathway for the hot gas does indeed exist, but the reason for the gas to take this tortuous path over other directions is not clear, nor is it understood why the heating effects would be registered by only a few sensors on the rear wall of the wheel well and not by others of a similar type and mounting located only inches away. For example, the brake switch return line temperatures V58T0841A and V58T0842A were only a few inches away from V58T1703A which recorded an anomalous rise first, but these other two hydraulic line temperature sensors did not record any anomalous behavior until several minutes later. Another unexplained feature is that every one of the tire pressure and wheel temperature sensors showed a clear wiring burn through failure within a narrow window of EI + 858 to 880 seconds, and this is quite well explained by all of these sensor cables being routed along a similar path on the backside of the left main landing gear strut. The inconsistency is that two of the hydraulic brake line temperatures V58T1700A and V58T1701A also had their cables routed along the same path and these two did not show any wiring burn through failures within any of the telemetry data. It is puzzling why the wiring burn throughs would completely destroy one type of system and leave an adjacent one untouched.

The communication drop outs occurred at times quite close to several major debris shedding events and to the breach of the left wing leading edge spar; however, a definitive link between these two is still largely conjectural. It is known that the link margins were decaying from EI onward, as was normal for the re-entry flight, and they would thus be increasingly sensitive to any events which would cause obscuration, attenuation, or scattering of the radio signal. Whether these events were the shedding of debris or vaporized metal from the damaged area of the left wing or simply some additional radio interference or multipath clutter caused the increasing heating and plasma envelope around the vehicle is unclear. The timing is suggestive of debris shedding events, but it is not conclusive.

A Few Recommendations

The MADS/OEX data has proven extremely valuable to the analysis of the accident and the validation of various scenarios. This, however, has been largely fortuitous. It was only pure happenstance that the *Columbia* (OV-102) was, by far, the most extensively instrumented of all the orbiter fleet and thus had the OEX sensor suite to record such detailed data. It was also fortunate that the orbiter broke up over a desolate area of the US mainland where the debris could be painstakingly and methodically collected. If the break up had occurred several minutes earlier or later, the debris would have been deposited into the Pacific Ocean or the Gulf of Mexico, where virtually none of it could have been collected. It was almost miraculous that the OEX data recorder was found, that it was intact, and that the data on it was in essentially perfect condition. No other avionics box besides the OEX recorder survived the re-entry. If the OEX recorder happened to have landed upside down, the weight of the capstan motors would have crushed the mylar tape spool upon impact. As luck had it, the OEX recorder landed right side up. Furthermore, it was also exceedingly fortunate that the damage occurred on the left wing rather than the right. The left wing contained 15 temperature sensors which recorded anomalous events, while the right wing contained none. The damaged area of the left wing also just happened to be at a place where the leading edge spar was most heavily instrumented with temperature, pressure, and strain sensors. It was also fortuitous that the orbiter flight instrumentation (OFI) telemetry data, that complements the OEX recorded data, was gathered. The communication systems on the orbiter were not originally designed to maintain radio contact during re-entry, but the link margins luckily happened to be sufficient to provide contact for most of the first half of the re-entry flight. Should the unthinkable occur and another space shuttle accident of a similar nature happen, there is only the slimmest of chances that all of these circumstances would occur once more to provide the fairly clear level of information that came from the *Columbia* accident.

Another notable feature is that the sensor suite installed on the *Columbia* was originally designed only for engineering development purposes during the first few flights of the orbiter to insure that it was following design specifications. This instrumentation remained on the vehicle as a historical legacy to the developmental process, but it has since been routinely used to provide vehicle flight data that has been of value to on-going flight analysis and vehicle engineering. Nearly all of the sensors used on the *Columbia* were specified to have only a 10 year shelf life, and in some cases a shorter service life. The *Columbia* was 22 years old in 2003, and thus, the majority of the instrumentation system was dated and was being used twice as long as its originally

designed service life. Many sensors, for example those for aerodynamic pressure, were already failing. Of the 181 active MADS/OEX pressure sensors on the wings, 55 had already failed or were producing questionable readings before the STS-107 mission was launched. The wiring and cabling was also becoming old and in need of repair and updating. In a general sense, the instrumentation systems on the vehicle were never updated from those which were originally installed, and the original systems were being used well beyond their intended length of service. It is a testament to the soundness of the original design that the instrumentation systems have lasted as long as they have and have provided reliable data up through the present.

Based upon the above, some rather obvious recommendations can be suggested to both improve the data gathering capability of the orbiter while in flight, as well as to provide improved vehicle safety by recognition of damaged components prior to their catastrophic failure. These recommendations include:

1. *The existing instrumentation systems which were designed only for developmental purposes should be changed over to instrumentation systems which are designed for assessing vehicle health and prompting preventative maintenance*. This is not to suggest that the existing operational flight instrumentation (OFI) system should be done away with, as it is quite crucial to the flight control of the vehicle. Rather, the large number of sensors in the OEX suite could be reduced to only those needed for critical monitoring of flight behavior, and made more symmetrical between the left and right sides of the vehicle. This OEX-like suite should also be added to each of the remaining orbiters so that vehicle-to-vehicle comparison data can be compiled in addition to flight-to-flight comparison data.
2. *Instrumental measurement and inspection techniques should be used which can detect injured or malfunctioning vehicle components prior to their being called into service, particularly in relation to the thermal protection system (TPS)*. Presently, most of the TPS components are qualified by visual inspection techniques which fail to probe the internal features. X-ray, acoustic, and radio frequency (RF) imaging techniques can provide penetrating examinations of vehicle components which can complement existing visual surface inspection. While this will undoubtedly add time and expense to the orbiter inspection process, it will however provide a more thorough screening and qualification process which should stand a higher probability of catching minute flaws before they become in-service component failures.
3. *The MADS instrumentation system and sensor suite on each of the orbiters should be updated to make use of current sensor and data acquisition technologies*. The temperature, pressure, and strain sensors on the *Columbia*, as well as the remaining orbiters, is a late 1970s vintage which does not take advantage of the revolutionary advances that have occurred in the sensors and instrumentation field since then. Notably absent on the orbiter are micromachined pressure, strain, and inertial sensors which are much more reliable, smaller, lower power, less expensive, and have in general displaced the older style units which were used on the *Columbia* and the rest of the fleet. Signal aggregation and sensor multiplexing can also be greatly improved and would produce improved signal fidelity and savings in wire weight. Wireless sensing systems can also be used to great advantage and could also help alleviate the cabling bird's nest on the orbiters. Similarly, many optical sensing techniques such as infrared thermometry and pyrometry could be used to great advantage to sense the high outer surface temperatures where direct placement of a contact temperature sensor is not possible.
4. *A more robust OEX-like flight data recorder should be developed which can be used analogously to the black boxes on commercial aircraft*. Flight data recorders should be packaged to survive a re-entry breakup and fitted with a homing beacon by which they can be located.
5. *The instrumentation system should be designed to be reconfigurable during flight, allowing certain data to be recorded or telemetered or both, as the needs change*. Reconfigurability in general imparts improved robustness and fault tolerance, and while this has been implemented in the original design of the orbiter to some degree, it can be further improved upon. Specifically, the OEX recorder data is not accessible until the vehicle has landed back on the Earth, yet it also records ascent data which could, in principle, have been examined for abnormalities which might be clues to latent problems.
6. *Instrumentation should be added which can both detect impacts to the vehicle and the extent of damage that was left as a result of such impacts*. One of the original problems with the space shuttle orbiters that has existed from the first flight up through the present, and which has yet to be satisfactorily solved, is that the belly of the vehicle cannot be inspected prior to de-orbit and re-entry. Robotic inspection cameras offer one of the most flexible solutions, but the problems with such robots potentially creating more damage than they discover needs to first be surmounted. Modern accelerometers and acoustic microphones could readily be used to detect sharp impact events and signal the need for closer inspection of the vehicle. Light weight optical fiber sensors could also be put to good use to monitor the conditions along critical sections of the structure.

The *Columbia* accident has been a regrettable tragedy which has set back the progress of manned spaceflight and briefly tarnished many of the truly outstanding aspects of the American space program. However, the aftermath of the accident provides a unique and valuable learning opportunity in view of the detailed information and analysis which has been compiled. While there may be some sentiment by the general public that space flight has become a routine business, akin to commercial air travel, it is important to bear in mind that space travel will always be a venture with significantly and necessarily higher risks for the given rewards. The only fatal error at this juncture would be to fail to learn from the events and circumstances of the *Columbia* accident. Improved instrumentation systems only provide the raw data; properly interpreting this data and making good judgments from it is an exclusively human endeavor.

Volume II
Appendix D.20
Bolt Catcher Debris Analysis

This appendix contains – reproduced at smaller than normal size – the study of radar returns from past Space Shuttle launches to determine whether the Solid Rocket Booster bolt catchers may have failed during the flight of STS-107. The report concluded that there was the possibility that one of the debris items seen on radar during that flight could have been part of a bolt catcher.

This appendix has no recommendations, but the Board did make recommendations related to the bolt catcher issue in Volume I. The conclusions drawn in this report do not necessarily reflect the conclusions of the Board; when there is a conflict, the statements in Volume I of the Columbia Accident Investigation Board Report take precedence.

THIS PAGE INTENTIONALLY LEFT BLANK

Bolt Catcher Debris Analysis

Launching into the Future
CSR Computer Sciences Raytheon

NQA ISO 9001 REGISTERED COMPANY ANSI-RAB QMS ACCREDITED

25 June 2003

Department of the Air Force
45th Space Wing
Patrick Air Force Base, FL 32925

ATTN: 45th Range Management Squadron (45 RMS/RMSS)

SUBJECT: CONTRACT F08650-00-C-0005: **TECHNICAL NOTE – BOLT CATCHER DEBRIS ANALYSIS FOR SHUTTLE STS-107 (CDR A205)**

The attached Technical Note presents an analysis of the STS-107 vehicle debris detected by Eastern Range radar following Solid Rocket Booster separation. The analysis was specifically conducted to determine if any debris detected following Solid Rocket Booster separation was characteristic of an External Tank Bolt Catcher.

If additional information is required, please contact Michael Ignacek at (321) 494-9740.

Original signed by

Susan J. Vaughn
Manager, Systems Performance (CSR 7200)

SJV/ll

Attachment: As stated

cc: 45 SW/TD\Robert Fore
45 MXG/CC\Col. Byron Presley
45 RMS/CC\Lt. Col. Clay Frasier
45 RMS/RMO\Lee Bridges
45 RMS/RMSS\Richard Krizan, John Sienkiewicz
45 RANS/CC\Lt. Col. Cynthia Grey
45 RANS/DOUF\Mike Gawel
NASA\William Haase, Wayne Hale
CSR Project Director\Fran Shill
CSR Instrumentation Systems\Tom White

CSR Range Operations\Charles Oberwetter
CSR Systems Analysis\Michael Maier, Walter Neuhauser, Michael Ignacek, Karen Beauchamp, Charles Cook, Michael VonNiederhausern, George Meixel

FOR OFFICIAL USE ONLY

Launching into the Future
CSR Computer Sciences Raytheon

Technical Note 25 June 2003

BOLT CATCHER DEBRIS ANALYSIS FOR SHUTTLE STS-107

Chuck Cook, Karen Beauchamp, Michael VonNiederhausern

An analysis of debris detected following Solid Rocket Booster separation indicates that one debris item, Item #33, is a good candidate to be an External Tank Bolt Catcher. Peak amplitudes of the debris returns are consistent with those of an External Tank Bolt Catcher. Range Time Intensity data from previous missions indicate that debris items have been detected at or near Solid Rocket Booster separation on 19 past missions. Seven items from five missions exhibit strong similarities to Item #33.

INTRODUCTION

Shuttle STS-107 was launched from Space Launch Complex (SLC) 39A, located at the Kennedy Space Center (KSC), on 16 January 2003. During the ascent phase of this launch, the Orbiter Vehicle, Columbia, was impacted by debris emitted from the External Tank (ET) at approximately T+81 seconds (s). At the request of Mr. William H. Haase, National Aeronautics and Space Administration (NASA) Shuttle Flight Safety Manager, CSR Systems Analysis performed a debris analysis of radar data, optical video, and optical film images collected during the launch.

The analysis was conducted in two parts. The original report, distributed on 14 February 2003 [ref. 1], consisted of analysis of debris detected at T+30 s, T+81 s (near the time of known impact), and from T+150 s to T+230 s. The time frame around Solid Rocket Booster (SRB) separation is typically characterized by abundant plume effects and expulsion of solid fuel debris and was, therefore, not analyzed in the original report. At the request of Mr. Haase, the time period from T+110 s to T+140 s was analyzed for debris, and the results were distributed in a revision to the original report on 4 April 2003 [ref. 2].

This technical note was prepared for the United States Air Force 45th Space Wing by the Systems Analysis Department of Computer Sciences Raytheon (CSR), under contract F08650-00-C-0005, and constitutes a delivery under CDR A205.

For additional information, contact the author at (321) 494-9720 or through e-mail at <karen.beauchamp@patrick.af.mil>.

FOR OFFICIAL USE ONLY

Additionally, 12 samples of selected material from the Orbiter/ET were tested to determine their individual reflectivity coefficients. By using the test material reflectivity values and the maximum Radar Cross Section (RCS) of the detected debris, an approximate size of each of the sample materials relative to each of the detected debris items was determined in the revised report. RCS measurements of an ET Bolt Catcher were not conducted in time to include in the publication of the revised report. At the request of Mr. N. Wayne Hale, Jr., NASA Shuttle Launch Integration Manager, an analysis of debris detected following SRB separation was conducted to determine if any of the debris items were characteristic of an ET Bolt Catcher.

The Eastern Range (ER) radar that supported STS-107 were:

- Radar 1.16 at Cape Canaveral Air Force Station (CCAFS), FL
- Radar 0.14 at Patrick Air Force Base (PAFB), FL
- Radar 19.17 at KSC, FL
- Radar 19.14 at KSC, FL
- Radar 28.14 at Jonathan Dickinson Missile Tracking Annex (JDMTA), FL
- NASA Radar 86.18 at the Wallops Flight Facility, VA
- NASA Radar 86.16R at the Wallops Flight Facility, VA

Only Radar 19.14, Radar 0.14, and Radar 28.14 have the capability to record Full Range Video (FRV) of the track, which may provide an indication of debris presence.

METHODOLOGY

The radar suitable for detection of low RCS particle separations is the C-band FPQ-14 radar (0.14, 19.14, and 28.14). The primary indicator of debris is found in the radar's FRV tape recording. This recording contains returns across the radar's pulse repetition interval (PRI). The FRV tape recording of the radar receiver output is converted at the Data Playback and Digitizing Equipment (DPDE) facility at CCAFS into Range Time Intensity (RTI) charts for documentation of debris separations. The RTI charts are time-tagged with an Inter-Range Instrumentation Group (IRIG) timing format that allows for accurate time correlation.

The time of debris detection, as obtained from the RTI charts, is isolated and then digitized for detailed analysis. Once the data has been digitized, the radar receiver calibration data is used to fit the amplitude data, DPDE counts, to Signal-to-Noise (S/N) values. The radar equation is applied using the specific Radio Frequency Loop Gain (RFLG) value of the radar to get RCS. The data is then plotted in three dimensions (time, relative range, and RCS) to provide a 'picture' of the debris characteristics. It is from these plots that the debris RCS can be estimated. Additionally, the plots reveal the range separation rate relative to the vehicle and the debris flight characteristics (i.e., floating, tumbling, rotating).

Detected debris items from the three-dimensional RTI plots were evaluated as possible candidates for an ET Bolt Catcher. Previous reports [ref. 1 and ref. 2] provided analysis of debris based on the time block when it was first observed. The earlier analyses indicated that the majority of the debris detected from T+150 s to T+230 s was near enough to the noise floor to prevent reasonable estimation of the shape or size. Additionally, it is assumed that if a Bolt Catcher were to detach from the ET and forward bolt assembly, such separation would occur at or near the time of SRB separation. Therefore, the debris detected from T+150 s to T+230 s was eliminated from consideration.

Previous analysis indicated that the debris items detected from T+110 s to T+140 s were largely near the radar noise floor, and a determination of the items' shape and/or size was not possible. Only one debris item, detected by Radar 28.14, had a significant return, and is considered the only possible candidate for an ET Bolt Catcher.

The RCS of an ET Bolt Catcher was determined in tests conducted by the Air Force Research Laboratories (AFRL) at Wright Patterson Air Force Base (WPAFB) [ref. 3]. Data from the candidate debris item was analyzed to determine if it was characteristic of ET Bolt Catcher signal returns as determined by WPAFB. If separation was destructive to a Bolt Catcher, the objects' radar signatures could be greatly different than that of an intact Bolt Catcher. This analysis does not account for a severely damaged Bolt Catcher.

ANALYSIS

Each SRB is attached to the ET with one forward separation bolt enclosed in a forward separation bolt assembly (Fig. 1). At SRB separation, approximately two minutes into flight, the forward separation bolts are broken into halves by explosive charges at each end of the bolts. The SRB half of the bolt is captured in the SRB forward skirt (Fig. 2) and stays with the SRB throughout the remainder of its flight. The ET half of the forward separation bolt is forced into the Bolt Catcher/ET portion of the separation bolt assembly (Fig. 2), which remains attached to the ET and is jettisoned into the Indian Ocean.

Fig. 1 and Fig. 2 have been supplied at the courtesy of Mr. Roger Elliott of United Space Alliance via e-mail on 21 June 2003.

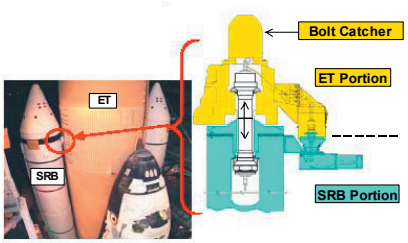


Fig.1. Forward Bolt Assembly and Attachment

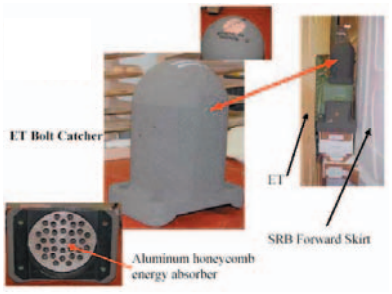


Fig. 2. ET Bolt Catcher

An ET Bolt Catcher is composed of an aluminum casing, covered with a Super Light Ablative (SLA) coating. In the opening at the base of a Bolt Catcher, a honeycombed aluminum disk exists to absorb the explosive energy of the bolt as it separates the SRB from the ET (Fig. 2). Bolt Catcher dimensions are shown in Fig. 3.

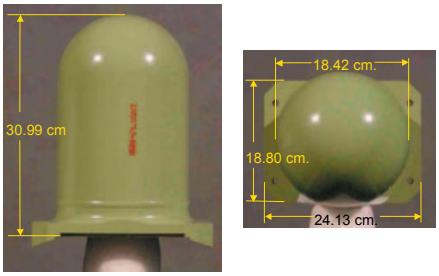


Fig. 3. ET Bolt Catcher Dimensions

A Bolt Catcher's radar return signature characteristics, as well as its mean and maximum RCS, were established in controlled testing at the AFRL, WPAFB. The testing was conducted within the ER radar operating parameters of 5690 MHz frequency and linear vertical polarization. These signatures and measurements were used as an approximation of the signal that may be returned from a Bolt Catcher if captured by the ER tracking radar. Fig. 4 and Fig. 5 present the results of the AFRL C-Band tests. Note that all measurements done at the AFRL were taken from a Bolt Catcher without SLA coating. All comparisons made in this report use these numbers. Although no RCS information is available for a Bolt Catcher with an SLA coating, the maximum RCS magnitudes are not expected to be significantly different from that of an uncovered Bolt Catcher due to the thickness of the coating (1.52 cm) relative to the radar's wavelength (λ), which is 5.27 cm or 0.29λ, and the low radar reflectivity of SLA. A 230-cm^2 plate with SLA coating has an RCS of -32 dBsm vice 3.9 dBsm for a similarly sized metal plate without SLA coating [ref. 4].

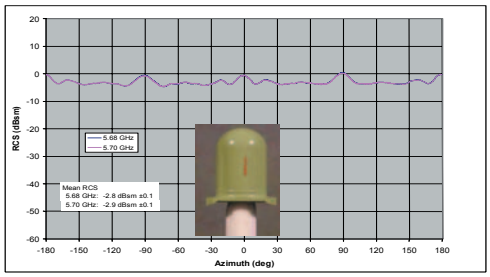


Fig. 4. ET Bolt Catcher, Vertical Mount, Vertical Polarization, C-Band

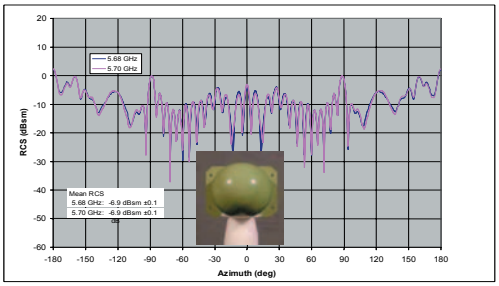


Fig. 5. ET Bolt Catcher, Horizontal Mount, Vertical Polarization, C-Band

The command for SRB separation was issued at T+127 s. Radar 0.14 detected no items around the time of SRB separation, Radar 19.14 detected five items, and Radar 28.14 detected one item. The maximum RCS of the detected items during that time ranged from -15 dBsm to +1 dBsm.

Examination of the RTI charts for Radar 19.14 and Radar 28.14 shows a large cloud of debris particles after SRB separation with some distinct particles discernable from the cloud (Fig. 6 and Fig. 7). The possibility exists that more debris was present than was detected, as the separating SRB and/or its plume may have masked signals from separating objects.

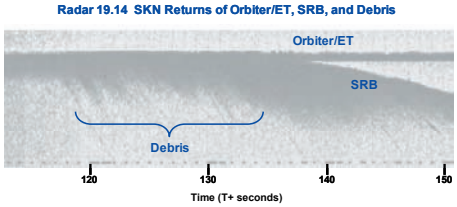


Fig. 6. Radar 19.14 RTI, T+113 s – T+150 s

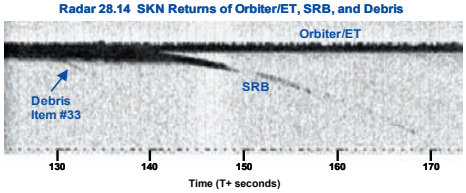


Fig. 7. Radar 28.14 RTI, T+125 s – T+173 s

The digitized data from T+110 s to T+140 s was analyzed in an attempt to determine the basic shape (e.g., flat plate, cone, cylinder, sphere) of the debris. Radar signatures were examined for all objects. For all but a single item, Item #33, the signal returns from the debris could not effectively be distinguished from the radar noise and thus prevented reasonable estimation of the shape. Based on the signal specular analysis, the majority of the debris is assumed to be irregular in shape. As a result, all debris items during this time period were excluded as possible Bolt Catcher candidates, with the exception of debris Item #33. The speculars from Item #33 were well defined, and a detailed analysis of debris Item #33 is provided in the following section.

Debris Item #33

Debris Item #33 (Fig. 8) is first observed at T+128 s, one second after the SRB separation command was issued. The item has a range separation rate of 520 m/s (with a 120 m/s uncertainty), and is visible for two seconds. The signal return of this item is significantly stronger than any of the debris detected by any radar from SRB separation through the remainder of the mission, indicating a larger or a more highly reflective item than any of the other detected debris items. An RTI contour plot depicting debris Item #33 separating from the Orbiter/ET stack is shown in Fig. 8.

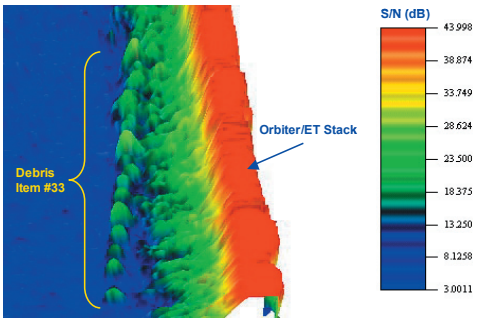


Fig. 8. Item #33 RTI Contour Plot

Item #33 radar signatures are shown in Fig. 9. Analysis of the peaks in this figure suggests a tumble rate of at least 310 degrees per second. At this rate, the 160-PRF of the observing radar limits the speculars to a maximum resolution of 1 point for every 2 degrees. The low resolution of the signature data limits the information that can be extracted from this data. Comparison of the radar spectrals with the Bolt Catcher RCS data gathered at the AFRL (Fig. 4 and Fig. 5) does not eliminate Item #33 as a candidate for a Bolt Catcher, but the low resolution of the signature prevents positive identification. Although the radar signature analysis to determine the shape is inconclusive, the signature peak magnitudes provide information of the maximum RCS of the item, which can be translated into approximate sizes for selected shapes.

Radar 28.14 has a 3-dB beamwidth of 0.38 degrees. As the debris item is moving out of the main radar beam, the debris can be expected to fall out of range for reasonable estimation of true RCS when it exceeds the half-beamwidth point. This is consistent with the signature data; the debris item begins to pass out of the high gain region of the radar beam at T+129.8 s, at which point the item has moved approximately the distance of the radar's half beamwidth. Item #33 spectral data after T+129.8 s was not used in this analysis.

Analysis of the speculars shows that the RCS peak amplitudes of Item #33 returns are consistent with the peak amplitudes for the nose, broadside, and base of an ET Bolt Catcher as determined by measurements at WPAFB (Fig. 4 and Fig. 5). All peak RCS amplitudes for Item #33 are within the uncertainty values established in Revision 1 of the original Technical Report [ref. 2] to be matched to the RCS of the individual facets of a Bolt Catcher; nose, broadside, and base. The AFRL tests indicate that the rounded nose of a Bolt Catcher has a maximum RCS of -3.2±0.1 dBsm. The broadside and the end of a Bolt Catcher have a maximum RCS of -0.3±0.1 and 2.4±0.1 dBsm, respectively. The peak speculars measured at Radar 28.14 ranged from -2 to 2 dBsm with a 3-dBsm uncertainty.

If Item #33 were a metallic cylinder, its theoretical dimensions would be similar to the dimensions of an ET Bolt Catcher. The peak specular amplitudes indicate that the item has a maximum reflective surface of 170±60 cm^2. This reflective area would be produced by a cylinder with a 20±9 cm diameter and a length of 32±9 cm. These tolerances on the Item #33 dimension estimates make it well within the possibility to be the dimensions of an ET Bolt Catcher.

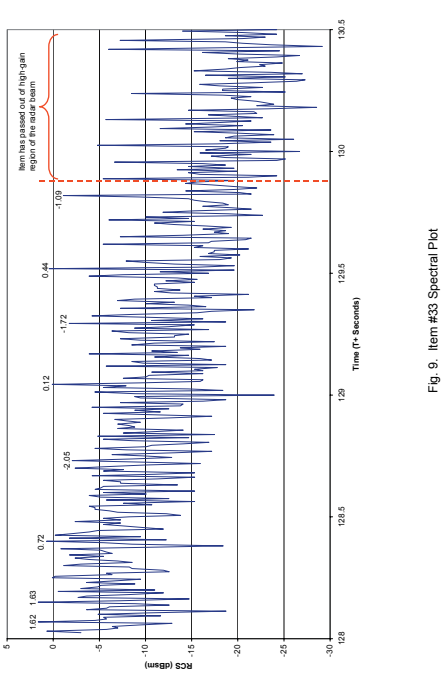


Fig. 9. Item #33 Spectral Plot

Debris Item #33 was evaluated to determine if it could be any other part of the Forward Separation Bolt assembly (Table 1). The ET Bolt Catcher attachment bolts, Bolt Catcher honeycomb particle, and ET separation bolt were eliminated as possible candidates, since none of these items would produce a return of Item #33's magnitude.

Table 1. Forward Separation Bolt Assembly Parts

ITEM	MATERIAL	SIZE (cm)
Bolt Catcher Attachment Bolt	A-286 CRES	0.953 diameter x 6.35 long
Bolt Catcher Honeycomb Particle	AL-5052 Metallic Dust	Typically less than 0.08 diameter x 0.08 long
ET Separation Bolt	4340 Steel	7.62 diameter x 29.21 long

The Item #33 maximum RCS was compared to the maximum RCS that would be returned by a Booster Separation Motor (BSM) aft cover [ref. 4]. The maximum RCS of Item #33 is 1.7±3 dBsm, and the maximum RCS of the BSM aft cover is -9.5±1 dBsm. The much greater RCS of Item #33 eliminates the possibility that it is a BSM aft cover.

Radar 19.14 Debris

The only radar other than Radar 28.14 that detected debris around SRB separation was Radar 19.14. An evaluation of Radar 19.14's debris items was conducted to determine if any of the debris detected could have been any of the forward bolt assembly parts listed in Table 1. The theoretical maximum RCS of a Bolt Catcher attachment bolt is -26 dBsm. At SRB separation, the RCS detection sensitivity for Radar 19.14 was -29 dBsm, so the radar should have been capable of detecting Bolt Catcher attachment bolts if they separated from the Bolt Catcher. Radar 19.14 detected five debris items in close proximity to SRB separation. The maximum RCS of the detected items ranged from -15 dBsm to -13 dBsm. The RCSs of these debris items are too large to be an attachment bolt.

The typical estimated size of a honeycomb particle is too small to be detected by the radar and would have been undetected if present.

The theoretical maximum RCS of the ET separation bolt is -4 dBsm. The maximum RCS of debris items detected by Radar 19.14 (-15 dBsm to -13 dBsm) did not exceed -4 dBsm, so it is possible that one of these items could be an off-aspect return from the bolt. As stated in previous reports [ref. 1 and ref. 2], the signal returns from the debris could not effectively be distinguished from the radar noise and, based on the signal specular analysis, it is assumed that the debris was irregular in shape. As a result, none of these debris items are considered a candidate for the ET separation bolt in the event it separated from the forward separation bolt assembly.

Historical Review

CSR Systems Analysis reviewed 48 previous Shuttle missions for which RTI charts are available, dating back to November 1994. On 19 of these missions, a debris item was detected at a time similar to that of Item #33, specifically, at or near the time of SRB separation. Additionally, on five of these 19 missions, the debris items exhibit a very strong similarity to Item #33 in that they were singular, distinct items, and had similar returns. These five missions were F1642 (STS-110), F1076 (STS-105), F4289 (STS-100), A4651 (STS-95), and A3839 (STS-90). It cannot be determined if these items are identical to Item #33, since all data required to perform a complete analysis may not exist.

CONCLUSIONS

Debris Item #33 was determined to be the only possible candidate for an ET Bolt Catcher. Analysis of speculars from the item shows that the peak amplitudes of the returns are characteristic of the peak amplitudes for the nose, broadside, and bottom of an ET Bolt Catcher as determined by RCS measurements by the AFRL at WPAFB. Additionally, the peak return observed by Radar 28.14 would, theoretically, be indicative of a metal cylinder with similar dimensions of an ET Bolt Catcher.

Full characterization of the signature pattern could not be accomplished due to PRF limitations, and the exact shape of the debris item could not be determined. As a result, this analysis cannot definitely determine if this item is, or is not, an ET Bolt Catcher. However, due to the detection of the item in close proximity to SRB separation, the similar peak amplitudes, and similar theoretical size, this item is considered a reasonable candidate to be an ET Bolt Catcher.

Debris Item #33 was evaluated to determine if it could be any part of the Forward Separation Bolt assembly (Table 1). The ET Bolt Catcher attachment bolts, Bolt Catcher honeycomb particle, and ET separation bolt were eliminated as possible candidates, since none of these items would produce a return of the magnitude observed by Radar 28.14. Additionally, the signal returns from Item #33 were determined to be too large to be a Booster Separation Motor (BSM) aft cover.

RTI data from previous missions indicate that debris items have been detected at or near SRB separation on 19 past missions. Seven items from five missions exhibit strong similarities to Item #33.

ABBREVIATIONS AND ACRONYMS

λ	Wavelength
45 RMS	45th Range Management Squadron
AFRL	Air Force Research Laboratories
AL	Aluminum
BSM	Booster Separation Motor
CCAFS	Cape Canaveral Air Force Station
CRES	Corrosion Resistant Steel
CSR	Computer Science Raytheon
cm	centimeters
dB	decibels
dBsm	Decibels per square meter
DPDE	Data Playback and Digitizing Equipment
ER	Eastern Range
ET	External Tank
FRV	Full Range Video
GHz	Gigahertz
IRIG	Inter-Range Instrumentation Group
JDMTA	Jonathan Dickinson Missile Tracking Annex
KSC	Kennedy Space Center
m/s	Meters per second
MHz	Megahertz
NASA	National Aeronautics and Space Administration
PAFB	Patrick Air Force Base
PRF	Pulse Repetition Frequency
RCS	Radar Cross Section
ref.	Reference
RFLG	Radio Frequency Loop Gain
RTI	Range Time Intensity
s	second
S/N	Signal-to-Noise
SKN	Skin
SLA	Super Light Ablative
SLC	Space Launch Complex
SRB	Solid Rocket Booster
WPAFB	Wright Patterson Air Force Base

REFERENCES

1. CSR Technical Report – Debris Analysis Report for Operation F1120, Shuttle STS-107, 16 January 2003. 14 February 2003.
2. CSR Technical Report – Debris Analysis Report for Operation F1120, Shuttle STS-107, 16 January 2003, Revision 1. 4 April 2003.
3. *RCS Assessment of STS-107 Debris Candidates*, Air Force Research Laboratory, Sensors Directorate, Brian M. Kent, Dan A. Turner, 14 March 2003.
4. Report No. CSR 321-9012, *ETR Radar Support of the STS-27 Tile Damage Investigation*. A.E. Hoffmann-Heyden, 3 February 1989

THIS PAGE INTENTIONALLY LEFT BLANK